WILEY-VCH

Michael Vollmer and Klaus-Peter Möllmann

Infrared Thermal Imaging

Fundamentals, Research and Applications

Second Edition

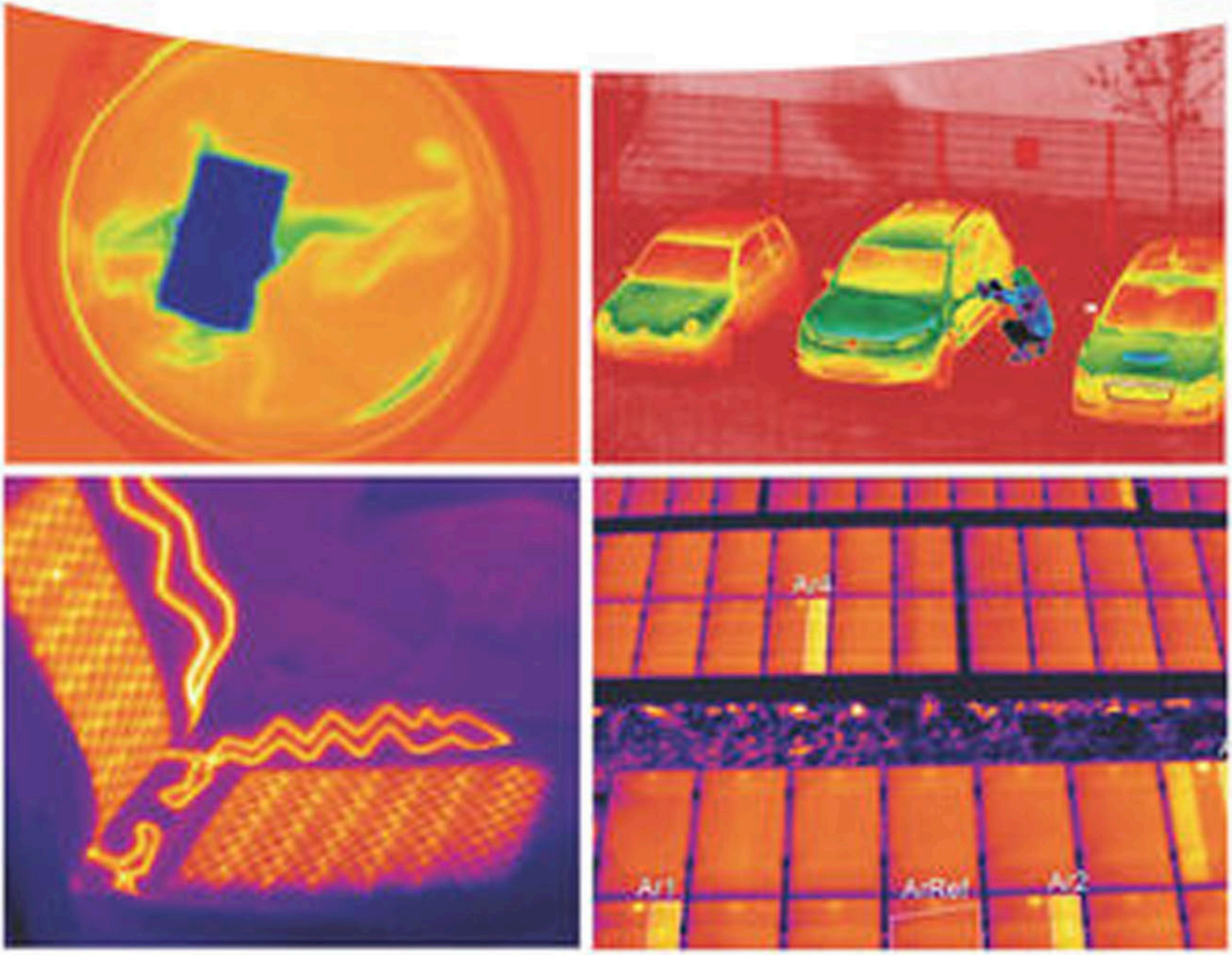

Michael Vollmer and
Klaus-Peter Möllmann

Infrared Thermal Imaging

Michael Vollmer and Klaus-Peter Möllmann

Infrared Thermal Imaging

Fundamentals, Research and Applications

Second Edition

WILEY-VCH
Verlag GmbH & Co. KGaA

Authors

Michael Vollmer
TH Brandenburg
Department of Engineering
Magdeburger Str. 50
14770 Brandenburg
Germany

Klaus-Peter Möllmann
TH Brandenburg
Department of Engineering
Magdeburger Str. 50
14770 Brandenburg
Germany

All books published by Wiley-VCH are carefully produced. Nevertheless, authors, editors, and publisher do not warrant the information contained in these books, including this book, to be free of errors. Readers are advised to keep in mind that statements, data, illustrations, procedural details or other items may inadvertently be inaccurate.

Library of Congress Card No.:
applied for

British Library Cataloguing-in-Publication Data:
A catalogue record for this book is available from the British Library.

Bibliographic information published by the Deutsche Nationalbibliothek
The Deutsche Nationalbibliothek lists this publication in the Deutsche Nationalbibliografie; detailed bibliographic data are available on the Internet at http://dnb.d-nb.de.

© 2018 WILEY-VCH Verlag GmbH & Co. KGaA, Boschstr. 12, 69469 Weinheim, Germany

All rights reserved (including those of translation into other languages). No part of this book may be reproduced in any form – by photoprinting, microfilm, or any other means – nor transmitted or translated into a machine language without written permission from the publishers. Registered names, trademarks, etc. used in this book, even when not specifically marked as such, are not to be considered unprotected by law.

Print ISBN 978-3-527-41351-5
ePDF ISBN 978-3-527-69332-0
ePub ISBN 978-3-527-69329-0
Mobi ISBN 978-3-527-69331-3
oBook ISBN 978-3-527-69330-6

Typesetting le-tex publishing services GmbH, Leipzig, Deutschland

Printed on acid-free paper.

Contents

Preface to Second Edition *XVII*

Preface to First Edition *XIX*

List of Acronyms *XXIII*

1 Fundamentals of Infrared Thermal Imaging *1*
1.1 Introduction *1*
1.2 Infrared Radiation *6*
1.2.1 Electromagnetic Waves and the Electromagnetic Spectrum *6*
1.2.2 Basics of Geometrical Optics for Infrared Radiation *10*
1.2.2.1 Geometric Properties of Reflection and Refraction *10*
1.2.2.2 Specular and Diffuse Reflection *12*
1.2.2.3 Portion of Reflected and Transmitted Radiation: Fresnel Equations *12*
1.3 Radiometry and Thermal Radiation *14*
1.3.1 Basic Radiometry *15*
1.3.1.1 Radiant Power, Excitance, and Irradiance *15*
1.3.1.2 Spectral Densities of Radiometric Quantities *15*
1.3.1.3 Solid Angles *16*
1.3.1.4 Radiant Intensity, Radiance, and Lambertian Emitters *17*
1.3.1.5 Radiation Transfer between Surfaces: Fundamental Law of Radiometry and View Factor *20*
1.3.2 Blackbody Radiation *21*
1.3.2.1 Definition *21*
1.3.2.2 Planck Distribution Function for Blackbody Radiation *22*
1.3.2.3 Different Representations of Planck's Law *24*
1.3.2.4 Stefan–Boltzmann Law *26*
1.3.2.5 Band Emission *26*
1.3.2.6 Order-of-Magnitude Estimate of Detector Sensitivities of IR Cameras *29*
1.4 Emissivity *31*
1.4.1 Definition *31*
1.4.2 Classification of Objects according to Emissivity *32*

1.4.3 Emissivity and Kirchhoff's Law *32*
1.4.4 Parameters Affecting Emissivity Values *34*
1.4.4.1 Material *34*
1.4.4.2 Irregular Surface Structure *34*
1.4.4.3 Viewing Angle *35*
1.4.4.4 Regular Geometry Effects *39*
1.4.4.5 Wavelength *41*
1.4.4.6 Temperature *42*
1.4.4.7 Conclusion *43*
1.4.5 Techniques to Measure/Guess Emissivities for Practical Work *44*
1.4.6 Blackbody Radiators: Emissivity Standards for Calibration Purposes *45*
1.5 Optical Material Properties in IR *49*
1.5.1 Attenuation of IR Radiation while Passing through Matter *50*
1.5.2 Transmission of Radiation through the Atmosphere *51*
1.5.3 Transmission of Radiation through Slablike Solid Materials *54*
1.5.3.1 Nonabsorbing Slabs *54*
1.5.3.2 Absorbing Slabs *55*
1.5.4 Examples of Transmission Spectra of Optical Materials for IR Thermal Imaging *56*
1.5.4.1 Gray Materials in Used IR Spectral Ranges *56*
1.5.4.2 Some Selective Absorbers *61*
1.6 Thin Film Coatings: IR Components with Tailored Optical Properties *62*
1.6.1 Interference of Waves *63*
1.6.2 Interference and Optical Thin Films *64*
1.6.3 Examples of AR Coatings *65*
1.6.4 Other Optical Components *66*
1.7 Some Notes on the History of Infrared Science and Technology *69*
1.7.1 Infrared Science *69*
1.7.1.1 Discovery of Heat Rays and Atmospheric Absorption *69*
1.7.1.2 Blackbodies and Blackbody Radiation *72*
1.7.1.3 Radiation Laws *73*
1.7.2 Development of Infrared Technology *76*
1.7.2.1 Prerequisites for IR Imaging *77*
1.7.2.2 Quantitative Measurements *84*
1.7.2.3 Applications and Imaging Techniques *88*
References *97*

2 Basic Properties of IR Imaging Systems *107*
2.1 Introduction *107*
2.2 Detectors and Detector Systems *107*
2.2.1 Parameters That Characterize Detector Performance *108*
2.2.2 Noise Equivalent Temperature Difference *110*
2.2.3 Thermal Detectors *111*

2.2.3.1 Temperature Change of Detector *111*
2.2.3.2 Temperature-Dependent Resistance of Bolometer *112*
2.2.3.3 NEP and D^* for Microbolometer *113*
2.2.4 Photon Detectors *117*
2.2.4.1 Principle of Operation and Responsivity *117*
2.2.4.2 D^* for Signal-Noise-Limited Detection *119*
2.2.4.3 D^* for Background Noise Limited Detection *120*
2.2.4.4 Necessity to Cool Photon Detectors *123*
2.2.5 Types of Photon Detectors *125*
2.2.5.1 Photoconductors *125*
2.2.5.2 Photodiodes *126*
2.2.5.3 Schottky Barrier Detectors *128*
2.2.5.4 Quantum Well IR Photodetectors *128*
2.2.5.5 Recent Developments in IR Detector Technology *132*
2.3 Basic Measurement Process in IR Imaging *142*
2.3.1 Radiometric Chain *142*
2.3.2 Wavebands for Thermal Imaging *146*
2.3.3 Selecting the Appropriate Waveband for Thermal Imaging *147*
2.3.3.1 Total Detected Amount of Radiation *148*
2.3.3.2 Temperature Contrast–Radiation Changes upon Temperature Changes *151*
2.3.3.3 Influence of Background Reflections *155*
2.3.3.4 Influence of Emissivity and Emissivity Uncertainties *158*
2.3.3.5 Potential use of Bolometers in MW or SW band *168*
2.4 Complete Camera Systems *173*
2.4.1 Camera Design – Image Formation *173*
2.4.1.1 Scanning Systems *174*
2.4.1.2 Staring Systems–Focal-Plane Arrays *176*
2.4.1.3 Nonuniformity Correction *180*
2.4.1.4 Bad Pixel Correction *186*
2.4.2 Photon Detector versus Bolometer Cameras *186*
2.4.3 Detector Temperature Stabilization and Detector Cooling *188*
2.4.4 Optics and Filters *191*
2.4.4.1 Spectral Response *191*
2.4.4.2 Chromatic Aberrations *191*
2.4.4.3 Field of View *192*
2.4.4.4 Extender Rings *195*
2.4.4.5 Narcissus Effect *196*
2.4.4.6 Spectral Filters *199*
2.4.5 Calibration *200*
2.4.6 Camera Operation *204*
2.4.6.1 Switch-On Behavior of Cameras *205*
2.4.6.2 Thermal Shock Behavior *206*
2.4.7 Camera Software – Software Tools *208*
2.5 Camera Performance Characterization *209*

2.5.1 Temperature Accuracy *209*
2.5.2 Temperature Resolution – Noise Equivalent Temperature Difference (NETD) *210*
2.5.3 Spatial Resolution – IFOV and Slit Response Function *213*
2.5.4 Image Quality: MTF, MRTD, and MDTD *216*
2.5.5 Time Resolution – Frame Rate and Integration Time *221*
References *226*

3 Advanced Methods in IR Imaging *229*
3.1 Introduction *229*
3.2 Spectrally Resolved Infrared Thermal Imaging *229*
3.2.1 Using Filters *230*
3.2.1.1 Glass Filters *231*
3.2.1.2 Plastic Filters *233*
3.2.1.3 Influence of Filters on Object Signal and NETD *234*
3.2.2 Two-Color or Ratio Thermography *236*
3.2.2.1 Neglecting Background Reflections *237*
3.2.2.2 Approximations of Planck's Radiation Law *240*
3.2.2.3 T_{obj} Error for True Gray Bodies within Wien Approximation *242*
3.2.2.4 Additional T_{obj} Errors Owing to Nongray Objects *246*
3.2.2.5 Ratio Versus Single-Band-Radiation Thermometry *247*
3.2.2.6 Exemplary Application of Two-Color Thermography *248*
3.2.2.7 Extension of Ratio Method and Applications *254*
3.2.3 Multi- and Hyperspectral Infrared Imaging *256*
3.2.3.1 Principal Idea *256*
3.2.3.2 Basics of FTIR Spectrometry *258*
3.2.3.3 Advantages of FTIR Spectrometers *262*
3.2.3.4 Example of a Hyperspectral Imaging Instrument *263*
3.3 Superframing *265*
3.3.1 Method *266*
3.3.2 Example of High-Speed Imaging and Selected Integration Times *268*
3.3.3 Cameras with Fixed Integration Time *270*
3.4 Polarization in Infrared Thermal Imaging *271*
3.4.1 Polarization and Thermal Reflections *272*
3.4.1.1 Transition from Directed to Diffuse Reflections from Surfaces *272*
3.4.1.2 Reflectivities for Selected Materials in the Thermal Infrared Range *276*
3.4.1.3 Measuring Reflectivity Spectra: Laboratory Experiments *278*
3.4.1.4 Identification and Suppression of Thermal Reflections: Practical Examples *281*
3.4.2 Polarization-Sensitive Thermal Imaging *284*
3.5 Processing of IR Images *285*
3.5.1 Basic Methods of Image Processing *287*
3.5.1.1 Image Fusion *287*
3.5.1.2 Image Building *289*

3.5.1.3 Image Subtraction *290*
3.5.1.4 Consecutive Image Subtraction: Time Derivatives *293*
3.5.1.5 Consecutive Image Subtraction: High-Sensitivity Mode *296*
3.5.1.6 Image Derivative in Spatial Domain *296*
3.5.1.7 Infrared Image Contrast and Digital Detail Enhancement *300*
3.5.2 Advanced Methods of Image Processing *309*
3.5.2.1 Preprocessing *311*
3.5.2.2 Geometrical Transformations *313*
3.5.2.3 Segmentation *314*
3.5.2.4 Feature Extraction and Reduction *316*
3.5.2.5 Pattern Recognition *319*
3.5.2.6 Deblurring of Infrared Images *321*
3.6 Active Thermal Imaging *327*
3.6.1 Transient Heat Transfer – Thermal Wave Description *330*
3.6.2 Pulse Thermography *333*
3.6.3 Lock-in Thermography *337*
3.6.3.1 Nondestructive Testing of Metals and Composite Structures *340*
3.6.3.2 Solar Cell Inspection *343*
3.6.4 Pulsed Phase Thermography *345*
References *346*

4 Some Basic Concepts in Heat Transfer *351*
4.1 Introduction *351*
4.2 The Basic Heat Transfer Modes: Conduction, Convection, and Radiation *352*
4.2.1 Conduction *352*
4.2.2 Convection *355*
4.2.3 Radiation *356*
4.2.4 Convection Including Latent Heats *357*
4.3 Selected Examples of Heat Transfer Problems *359*
4.3.1 Overview *359*
4.3.2 Conduction within Solids: The Biot Number *361*
4.3.3 Steady-State Heat Transfer through One-Dimensional Walls and U-Value *364*
4.3.4 Heat Transfer Through Windows *369*
4.3.5 Steady-State Heat Transfer in Two- and Three-Dimensional Problems: Thermal Bridges *370*
4.3.6 Dew Point Temperatures *372*
4.4 Transient Effects: Heating and Cooling of Objects *373*
4.4.1 Heat Capacity and Thermal Diffusivity *374*
4.4.2 Short Survey of Quantitative Treatments of Time-Dependent Problems *375*
4.4.3 Demonstration of Transient Heat Diffusion *377*
4.4.4 Typical Time Constants for Transient Thermal Phenomena *377*
4.4.4.1 Cooling Cube Experiment *379*

4.4.4.2 Theoretical Modeling of Cooling of Solid Cubes *379*
4.4.4.3 Time Constants for Different Objects *382*
4.5 Some Thoughts on the Validity of Newton's Law *383*
4.5.1 Theoretical Cooling Curves *383*
4.5.2 Relative Contributions of Radiation and Convection *385*
4.5.3 Experiments: Heating and Cooling of Light Bulbs *389*
References *392*

5 Basic Applications for Teaching: Direct Visualization of Physics Phenomena *393*
5.1 Introduction *393*
5.2 Mechanics: Transformation of Mechanical Energy into Heat *394*
5.2.1 Sliding Friction and Weight *394*
5.2.2 Sliding Friction during Braking of Bicycles and Motorcycles *395*
5.2.3 Sliding Friction: the Finger or Hammer Pencil *398*
5.2.4 Inelastic Collisions: Tennis *398*
5.2.5 Inelastic Collisions: The Human Balance *401*
5.2.6 Temperature Rise of Floor and Feet while Walking *402*
5.2.7 Temperature Rise of Tires during Normal Driving of a Vehicle *403*
5.2.8 Generating Heat by Periodic Stretching of Rubber *404*
5.3 Thermal Physics Phenomena *406*
5.3.1 Conventional Hot-Water-Filled Heaters *407*
5.3.2 Thermal Conductivities *407*
5.3.3 Conduction of Heat in Stack of Paper *410*
5.3.4 Convection in Liquids *410*
5.3.5 Convection Effects Due to Gases *414*
5.3.6 Evaporative Cooling *414*
5.3.7 Adiabatic Heating and Cooling *417*
5.3.8 Heating of Cheese Cubes *418*
5.3.9 Cooling of Bottles and Cans *422*
5.4 Electromagnetism *425*
5.4.1 Energy and Power in Simple Electric Circuits *425*
5.4.2 Eddy Currents *427*
5.4.3 Thermoelectric Effects *428*
5.4.4 Experiments with Microwave Ovens *429*
5.4.4.1 Setup *430*
5.4.4.2 Visualization of Horizontal Modes *430*
5.4.4.3 Visualization of Vertical Modes *431*
5.4.4.4 Aluminum Foil in Microwave Ovens *432*
5.5 Optics and Radiation Physics *433*
5.5.1 Transmission of Window Glass, NaCl, and Silicon Wafers *433*
5.5.2 From Specular to Diffuse Reflection *435*
5.5.3 Some Light Sources *437*
5.5.4 Blackbody Cavities *438*
5.5.5 Emissivities and Leslie Cube *440*

5.5.6 From Absorption to Emission of Cavity Radiation *441*
5.5.7 Selective Absorption and Emission of Gases *443*
References *444*

6 Shortwave Infrared Thermal Imaging *447*
6.1 Introduction *447*
6.2 The Why and How of SW Infrared Imaging *447*
6.3 Some Applications of SW Infrared Imaging *450*
6.3.1 Water Optical Material Properties *452*
6.3.2 Cameras Used in the Experiments *452*
6.3.3 Selected Examples of SW Imaging *454*
6.3.3.1 High-Temperature Measurements *454*
6.3.3.2 Vegetation Studies *456*
6.3.3.3 Sky-to-Cloud Contrast Enhancement *458*
6.3.3.4 Sorting Plastics and Detecting Liquid Levels in Plastic Containers *460*
6.3.3.5 Looking Beneath the Surface *461*
6.3.3.6 Undamaged Fresh Fruit/Vegetable Test *466*
6.3.3.7 Material Properties of Liquids *467*
6.3.3.8 Moisture on Walls *470*
6.3.3.9 Other Applications of SW Imaging *470*
6.4 Survey of Commercial Systems *472*
References *472*

7 IR Imaging of Buildings and Infrastructure *477*
7.1 Introduction *477*
7.1.1 Publicity of IR Images of Buildings *478*
7.1.2 Just Colorful Images? *479*
7.1.2.1 Level and Span *480*
7.1.2.2 Choice of Color Palette *480*
7.1.2.3 More on Palette, Level, and Span *480*
7.1.3 General Problems Associated with Interpretation of IR Images *485*
7.1.4 Energy Standard Regulations for Buildings *488*
7.2 Some Standard Examples for Building Thermography *490*
7.2.1 Half-Timbered Houses behind Plaster *490*
7.2.2 Other Examples with Outside Walls *493*
7.2.3 Determining whether a Defect Is Energetically Relevant *494*
7.2.4 The Role of Inside Thermal Insulation *497*
7.2.5 Floor Heating Systems *498*
7.3 Geometrical Thermal Bridges versus Structural Problems *500*
7.3.1 Geometrical Thermal Bridges *500*
7.3.2 Structural Defects *504*
7.4 External Influences *507*
7.4.1 Wind *507*
7.4.2 Effect of Moisture in Thermal Images *509*
7.4.3 Solar Load and Shadows *513*

7.4.3.1 Modeling Transient Effects Due to Solar Load *513*
7.4.3.2 Experimental Time Constants *516*
7.4.3.3 Shadows *518*
7.4.3.4 Solar Load of Structures within Walls *519*
7.4.3.5 Direct Solar Reflections *520*
7.4.4 General View Factor Effects in Building Thermography *525*
7.4.5 Night Sky Radiant Cooling and the View Factor *528*
7.4.5.1 Cars Parked Outside or Below a Carport *529*
7.4.5.2 Walls of Houses Facing a Clear Sky *531*
7.4.5.3 View Factor Effects: Partial Shielding of Walls by Carport *531*
7.4.5.4 View Factor Effects: The Influence of Neighboring Buildings and Roof Overhang *533*
7.5 Windows *534*
7.5.1 General Features *534*
7.5.2 Optically Induced Thermal Effects *539*
7.6 Thermography and Blower-Door Tests *541*
7.6.1 Close-Up Studies *543*
7.6.2 Overview Studies *547*
7.7 Quantitative IR Imaging: Total Heat Transfer through Building Envelope *549*
7.8 New Developments and Conclusions *552*
References *556*

8 Industrial Application: Detection of Gases *561*
8.1 Introduction *561*
8.2 Spectra of Molecular Gases *561*
8.3 Influences of Gases on IR Imaging: Absorption, Scattering, and Emission of Radiation *567*
8.3.1 Introduction *567*
8.3.2 Interaction of Gases with IR Radiation *567*
8.3.3 Influence of Gases on IR Signals from Objects *569*
8.4 Absorption by Cold Gases: Quantitative Aspects *572*
8.4.1 Attenuation of Radiation by a Cold Gas *572*
8.4.2 From Transmission Spectra to Absorption Constants *574*
8.4.3 Transmission Spectra for Arbitrary Gas Conditions and IR Camera Signal Changes *574*
8.4.4 Calibration Curves for Gas Detection *577*
8.4.5 Problem: the Enormous Variety of Measurement Conditions *578*
8.5 Thermal Emission from Hot Gases *580*
8.6 New Developments *582*
8.7 Practical Examples: Gas Detection with Commercial IR Cameras *588*
8.7.1 Organic Compounds *588*
8.7.2 Some Inorganic Compounds *591*
8.7.3 CO_2: Gas of the Century *594*
8.7.3.1 Comparison of Broadband and Narrowband Detection *596*

8.7.3.2 Detecting Volume Concentration of CO_2 in Exhaled Air 597
8.7.3.3 Absorption, Scattering, and Thermal Emission of IR Radiation 597
8.7.3.4 Quantitative Result: Detecting Minute Amounts of CO_2 in Air 599
8.7.3.5 Quantitative Result: Detection of Well-Defined CO_2 Gas Flows from a Tube 599
8.A Appendix: Survey of Transmission Spectra of Various Gases 602
8.A.1 Inorganic Compounds 1 604
8.A.2 Inorganic Compounds 2 605
8.A.3 Simple Hydrocarbons 1 606
8.A.4 Simple Hydrocarbons 2 607
8.A.5 Simple Multiple Bond Compounds and Some Alcohols 608
8.A.6 Some Ketones/Ethers 609
8.A.7 Some Benzene Compounds 610
8.A.8 Some Hydrocarbons With Halogens 611
References 612

9 Microsystems *615*
9.1 Appendix: Survey of Transmission Spectra of Various Gases 615
9.2 Special Requirements for Thermal Imaging 616
9.2.1 Mechanical Stability of Setup 616
9.2.2 Microscope Objectives, Close-up Lenses, Extender Rings 616
9.2.3 High-Speed Recording 618
9.2.4 Temperature Measurement 618
9.3 Microfluidic Systems 619
9.3.1 Microreactors 619
9.3.1.1 Stainless Steel Falling Film Microreactor 619
9.3.1.2 Glass Microreactor 623
9.3.1.3 Silicon Microreactor 625
9.3.2 Micro Heat Exchangers 626
9.4 Microsensors 628
9.4.1 Thermal IR Sensors 628
9.4.1.1 IR Thermopile Sensors 629
9.4.1.2 IR Bolometer Sensors 632
9.4.2 Semiconductor Gas Sensors 635
9.5 Microsystems with Electric to Thermal Energy Conversion 637
9.5.1 Miniaturized IR Emitters 637
9.5.2 Micro Peltier Elements 639
9.5.3 Cryogenic Actuators 640
References 642

10 Selected Topics in Industry *645*
10.1 Introduction 645
10.2 Miscellaneous Industrial Applications 645
10.2.1 Predictive Maintenance and Quality Control 645
10.2.2 Pipes and Valves in a Power Plant 647

10.2.3 Levels of Liquids in Tanks in Petrochemical Industry *648*
10.2.4 Polymer Molding *651*
10.2.5 Rack-Storage Fire Testing *652*
10.3 Low-Voltage Electrical Applications *653*
10.3.1 Early Microelectronic Boards *654*
10.3.2 Macroscopic Electric Boards *655*
10.3.3 Modern Microelectronic Boards *656*
10.4 High-Voltage Electrical Applications *656*
10.4.1 Substation Transformers *657*
10.4.2 Overheated High-Voltage Line *659*
10.4.3 Electric Fan Defects *660*
10.4.4 Oil Levels in High-Voltage Bushings *660*
10.5 Metal Industry and High Temperatures *662*
10.5.1 Direct Imaging of Hot Metal Molds *662*
10.5.2 Manufacturing Hot Solid Metal Strips: Thermal Reflections *663*
10.5.3 Determination of Metal Temperatures if Emissivity Is Known *665*
10.5.4 Determining Metal Temperatures for Unknown Emissivity: Gold Cup Method *666*
10.5.5 Determining Metal Temperatures for Unknown Emissivity: Wedge and Black Emitter Method *667*
10.5.6 Other Applications of IR Imaging in Metal Industry or at High Temperatures *669*
10.6 Automobile Industry *670*
10.6.1 Quality Control of Heating Systems *671*
10.6.2 Active and Passive IR Night Vision Systems *672*
10.6.3 IR Imaging of Race Cars *675*
10.6.4 Motorcycles *676*
10.7 Airplane and Spacecraft Industry *676*
10.7.1 Imaging of Aircraft *676*
10.7.2 Imaging of Spacecraft *678*
10.8 Plastic Foils *683*
10.8.1 Spectra: Selective Emitters *683*
10.8.2 Images: Looking through Plastics *685*
10.9 Surveillance and Security: Range of IR Cameras *687*
10.9.1 Applications in Surveillance *687*
10.9.2 Range of IR Cameras *688*
10.10 Line Scanning Thermometry of Moving Objects *694*
10.11 Remote Sensing Using IR Imaging *695*
10.11.1 Survey of Methods *695*
10.11.2 Some IR Imaging Applications Using Drones *699*
References *702*

11 Selected Applications in Other Fields *709*
11.1 Medical Applications *709*
11.1.1 Introduction *709*

11.1.2 Diagnosis and Monitoring of Pain *712*
11.1.3 Acupuncture *716*
11.1.4 Breast Thermography and Detection of Breast Cancer *718*
11.1.5 Other Medical Applications *719*
11.1.5.1 Raynaud's Phenomenon *719*
11.1.5.2 Pressure Ulcers *720*
11.2 Animals and Veterinary Applications *721*
11.2.1 Pets *722*
11.2.2 Zoo Animals *723*
11.2.3 Equine Thermography *725*
11.2.4 Wildlife *726*
11.3 Sports *729*
11.3.1 High-Speed Recording of Tennis Serve *729*
11.3.2 Squash and Volleyball *732*
11.3.3 Other Applications in Sports *734*
11.4 Arts: Music, Contemporary Dancing, and Paintings *735*
11.4.1 Musical Instruments *735*
11.4.2 Contemporary Dance *737*
11.4.3 Paintings *740*
11.5 Nature *742*
11.5.1 Sky and Clouds *742*
11.5.2 Wildfires *746*
11.5.3 Sun and Moon *749*
11.5.4 Infrared Mirages *752*
11.5.5 Geothermal Phenomena *754*
11.5.5.1 Geysers and Hot Springs *754*
11.5.5.2 IR Thermal Imaging in Volcanology *756*
References *760*

Index *765*

Preface to Second Edition

In Infrared Thermal Imaging, seven years is a long time. On the one hand, the development cycles are short which means that many new devices have meanwhile become commercially available and others are in the pipeline. On the other hand, many new application fields have been opened up and partially breathtaking new IR imagery has been published.

Therefore a second edition of this up-to date textbook was nearly overdue. Again it is designed as a desk reference for practitioners as well as a textbook for beginners. We have taken this opportunity not only to add a completely new chapter and many new subsections of preexisting chapters but also to very carefully revise the whole text including necessary corrections of usually unavoidable small misprint errors. Overall this second edition has been largely extended including more than 100 new IR images and graphs.

In the first three more theoretical and technology based fundamental chapters, we added a detailed discussion of the history of IR science and technology (Section 1.7), elaborated on recent detector developments and the problem of the proper waveband selection (Sections 2.2.5.5 and 2.3.3), and discussed potentials of polarization sensitive IR imaging and the theoretical deblurring algorithms for images (Sections 3.4.2 and 3.5.2.6).

Chapter 4 on physics of heat transfer and some respective applications was only very slightly modified. In Chapter 5 on the use of IR imaging for teaching and education purposes we added quite a few new examples including for example, imagery from a formula one racing car, the thermal properties of stretching rubber bands , or visualization of heat transfer through paper and more. We then also added a completely new chapter on Short Wave IR imaging which has become more important within the last decade (new Chapter 6). All subsequent old Chapters 6 to 10 were accordingly shifted in the second edition. In the building thermography chapter we added an extended section on proper choice of palette, level, and span, optically induced thermal effects and other new developments (Sections 7.1.2.3, 7.5.2 and 7.8). Quite a few new developments in the field of optical gas imaging have been achieved within the last few years which we accounted for by a new subsection (Section 8.6). The chapter on microsystem was just revised, but not extended. In contrast the two final chapters on other application fields have been thoroughly revised, restructured and extended. Besides new examples on for instance storage rack fires and investigation of furnace tubes, and newly reported space shuttle investigations we also focus on remote sensing with IR cameras, in particular with drones (new Section 10.11). Finally we also included a number of new applications of IR imaging in nature such as imaging of clouds, sun, moon, mirages and some new geothermal phenomena (Sections 11.5.1, 11.5.3 to 11.5.5).

Books on evolving fields in science and technology can never reach perfection, they can always only present snapshots of the state of the art. Still we hope that the content provides a comprehensive coverage of the field and that all readers will enjoy this second edition.

Preparing this edition meant a lot of work and we need to thank again many colleagues who send us comments to the first edition, who contributed by providing new fantastic IR images and who had helpful discussions at conferences with us. We did of course get very professional support by the publisher and we want to thank in particular Mrs. Gudrun Wüst for her ongoing support and always fast response to queries and help in problem solving of any technical issues. In addition we appreciated the professional help of Mrs. Petra Moews and Mrs. Annegret Krap from le-tex publishing services during production as well as corrections due to an anonymous professional language check. Last not least, we need of course again thank our families for their permanent support, in particular in the final stages within the editing stage and proofreading.

We also thought about adding new author photos, but refrained from doing so. The old IR images are still perfect since they do not change as rapidly with time as do, for example, visible photos concerning the color of our hair.

Brandenburg, June 2017 *Michael Vollmer* and *Klaus-Peter Möllmann*

Preface to First Edition

The really large steps in the history of thermal imaging took place in intervals of hundred years. First, infrared radiation was discovered in 1800 by Sir William Herschel while studying radiation from the sun. Second, Max Planck was able to quantitatively describe the laws of thermal radiation in 1900. It took more than 50 years thereafter before the first infrared-detecting cameras were developed; initially, these were mostly quite bulky apparatus for military purposes. From about the 1970s, smaller portable systems started to become available; these consisted of liquid nitrogen cooled single photon detector scanning systems. These systems also enabled the use of infrared imaging for commercial and industrial applications. The enormous progress due to microsystem technologies toward the end of the twentieth century – the first uncooled micro bolometer cameras appeared in the 1990s – resulted in reliable quantitatively measuring infrared camera systems. This means, that the third large step was taken by about the year 2000. Infrared thermal imaging has now become affordable to a wider public of specialized physicists, technicians and engineers for an ever growing range of applications. Nowadays, mass production of infrared detector arrays leads to comparatively low price cameras which – according to some advertisements – may even become high-end consumer products for everyone.

This rapid technological development leads to the paradoxical situation that there are probably more cameras sold worldwide than there are people who understand the physics behind and who know how to interpret the nice and colorful images of the false color displays: IR cameras easily produce images, but unfortunately, it is sometimes very difficult even for the specialist to quantitatively describe several of the most simple experiments and/or observations.

The present book wants to mitigate this problem by providing an extensive background knowledge on many different aspects of infrared thermal imaging for many different users of IR cameras. We aim at least for three different groups of potential users.

First, this book addresses all technicians and engineers who use IR cameras for their daily work. On the one hand, it will provide extensive and detailed background information not only on detectors and optics but also on practical use of camera systems. On the other hand, a huge variety of different application fields is presented with many typical examples with hints of how to notice and deal with respective measurement problems.

Second, all physics and science teachers at school or university level can benefit since infrared thermal imaging is an excellent tool for visualization of all phenomena in physics and chemistry related to energy transfer. These readers can particularly benefit from the huge variety of different examples presented from many fields, a lot of them given with qualitative and/or quantitative explanations of the underlying physics.

Third, this text also provides a detailed introduction to the whole field of infrared thermal imaging from basics via applications to up to date research. Thus it can serve as a textbook for newcomers or as a reference handbook for specialists who want to dig deeper. The large number of references to original work can easily help to study certain aspects in more depth and thus get ideas for future research projects.

Obviously, this threefold approach concerning the addressed readers does have some consequences for the structure of the book. We tried to write the ten chapters such that each may be read separately from the others. In order to improve the respective readability, there will be some repetitions and also cross references in each chapter (that more information can be found in other chapters or sections).

For example, teachers or practitioners may initially well skip the introductory more theoretical chapters about detectors or detectors systems and jump right away into the section of their desired applications. Obviously, this sometimes means that not every detail of explanation referring to theory will be understood, but the basic ideas should become clear – and maybe later on, those readers will also get interested in checking topics in the basic introductory sections.

The organization of this book is as follows: the first three chapters will provide extensive background information on radiation physics, single detectors as well as detector arrays, camera systems with optics, and IR image analysis. This is followed by a partly theoretical chapter on the three different heat transfer modes, which will help enable a better understanding of the temperature distribution that can be detected at the surfaces of various objects as for example, buildings. Chapter 5 then gives a collection of many different experiments concerning phenomena in physics. This chapter was particularly written with teaching applications in mind. The subsequent three chapters discuss three selected application as well as research topics in more detail: building thermography as a very prominent everyday application, the detection of gases as a rather new emerging industrial application with very good future prospects and the analysis of microsystems for research purposes. Finally, the last two chapters give a large number of other examples and discussions of important applications ranging for example from the car industry, sports, electrical, and medical applications via surveillance issues to volcanology.

Our own background is twofold. One of us had originally worked in IR detector design before switching to microsystem technologies whereas the other worked on optics and spectroscopy. Soon after joining our present affiliation, a fruitful collaboration in a common new field, IR imaging, developed, starting with the purchase of our first MW camera in 1996. Meanwhile, our infrared group has access to three different IR camera systems from the extended MW to the LW range including a high speed research camera and a lot of additional equipment such as microscope lenses and so on. Besides applied research, our group focuses also on teaching the basics of IR imaging to students of Microsystem and Optical Technologies at our university.

Obviously, such a book cannot be written without the help of many people, be it by discussions, by providing images, or just by supporting and encouraging us in phases of extreme work load towards the end of this endeavor. We are therefore happy to thank in particular our colleagues Frank Pinno, Detlef Karstädt, and Simone Wolf for help with various tasks that had often to be done at very short notice.

Furthermore, we want to especially thank Bernd Schönbach, Kamayni Agarwal, Gary Orlove, and Robert Madding for fruitful discussions on selected topics and also for permission to use quite a large number of IR images.

We are also grateful to S. Calvari, J. Giesicke, M. Goff, P. Hopkins, A. Mostovoj, M. Ono, M. Ralph, A. Richards, H. Schweiger, D. Sims, S. Simser, C. Tanner, and G. Walford for providing IR images and to A. Krabbe & D. Angerhausen, as well as DLR for providing other graphs. Also the following businesses have given permission to reproduce images, which we gratefully acknowledge: Alberta Sustainable Resource development, BMW, Daimler, FLIR systems, IPCC, IRIS, ITC, MoviTHERM, NAISS, NASA, Nature, NRC of Canada, PVflex, Raytek, Telops, Ulis, as well as United Infrared Inc.

Finally we need to especially thank our families for their tolerance and patience, in particular during the final months. Last not least we also need to express special thanks for the effective working together with Mrs. Ulrike Werner from Wiley/VCH.

Brandenburg, June 2010 *Michael Vollmer* and *Klaus-Peter Möllmann*

List of Acronyms

AGC	Automatic Gain Control
APE	Advanced Plateau Equalization
BLIP	Background Limited Infrared Photodetection
BP	Band Pass (filter)
CCS	Carbon Capture and Storage
CM	Condition Monitoring
DDE	Digital Detail Enhancement
DoLP	Degree of Linear Polarization
DSLR	Digital Single-Lens Reflex (camera)
EM	ElectroMagnetic (waves, spectrum, …)
FLIR	Forward Looking InfraRed (camera)
FOV	Field Of View
FPA	Focal Plane Array
FTIR	Fourier Transform InfraRed (spectroscopy)
FWHM	Full Width at Half Maximum
GPS	Global Positioning System
HITRAN	HIgh resolution atmospheric TRANsmission
HOT	High Operating Temperature
HSM	High Sensitivity Mode (FLIR cameras)
IFOV	Instantaneous Field Of View
IR	InfraRed spectral range
ITC	Infrared Training Center
LDAR	Leak Detection And Repair
LOWTRAN	LOW resolution atmospheric TRANsmission
LW	Long Wave (IR)
MEMS	Micro Electro Mechanical Systems
MCT	Mercury Cadmium Telluride
MDTD	Minimum Detectable Temperature Difference
MODIS	MODerate-resolution Imaging Spectroradiometer
MODTRAN	MODerate resolution atmospheric TRANsmission
MQW	Multiple Quantum Wells
MRTD	Minimum Resolvable Temperature Difference

MST	Micro System Technologies
MSX	MultiSpectral dynamic imaging (FLIR patented image software tool)
MTF	Modulation Transfer Function
MW	Mid Wave (IR)
NBP	Narrow Band Pass (Filter)
NDT	Non Destructive Testing
NEP	Noise Equivalent Power
NESR	Noise Equivalent Spectral Radiance
NETD	Noise Equivalent Temperature Difference
NIR	Near InfraRed (Spectral Range)
NUC	Non Uniformity Correction
OGI	Optical Gas Imaging
PdM	Predictive Maintenance
PE	Plateau Equalization (FLIR software)
PET	PolyEthylene Terephthalate
PSF	Point Spread Function
PVC	PolyVinyl Chloride
QWIP	Quantum Well Infrared Photodetetor
R&D	Research and Development
ROI	Region Of Interest
ROIC	Read Out Integrated Circuit
SNR	Signal to Noise Ratio
SRF	Slit Response Function
STS	Space Transportation System (numbers for space shuttle missions)
SW	Short Wave (IR)
T2SLS	Type II Strained Layer Superlattice
TSR	Total Solar Reflection
UAV	Unmanned Aerial Vehicle
UV	UltraViolet spectral range
VGA	Video Graphics Array (standard for images with 640 · 480 pixels)
VIS	VISible spectral range
VOC	Volatile Organic Compounds
1D	one-dimensional
2D	two-dimensional
3D	three-dimensional

Chapter 1
Fundamentals of Infrared Thermal Imaging

1.1
Introduction

Infrared (IR) thermal imaging, also often called *thermography* for short, is a very rapidly evolving field in science as well as industry owing to the enormous progress made in the last three decades in microsystem technologies of IR detector design, electronics, and computer science. Thermography nowadays is applied in research and development as well as in a variety of different fields in industry, such as nondestructive testing, condition monitoring, and predictive maintenance, reducing energy costs of processes and buildings, detection of gaseous species, and many more areas. In addition, competition in the profitable industry segment of camera manufacturers has recently led to the introduction of low-cost models at a price level of just several thousand dollars or euros, and smartphone accessories even below five hundred dollars, which has opened up new application fields for the cameras. Besides education (obviously schools' problems with financing expensive equipment for science classes are well known), IR cameras will probably soon be advertised in hardware stores as "must-have" do-it-yourself products for analyzing building insulation, heating pipes, or electrical components in homes. This development has both advantages and drawbacks.

The advantages may be illustrated by an anecdote based on personal experiences concerning physics teaching in school. Physics was, and still is, considered to be a very difficult subject in school. One of the reasons may be that simple phenomena of physics, for example, friction or the principle of energy conservation in mechanics, are often taught in such an abstract way that rather than being attracted to the subject, students are scared away. One of us clearly remembers a frustrating physics lesson at school dealing first with free-falling objects and then with the action of walking on a floor. First, the teacher argued that a falling stone would transfer energy to the floor such that the total energy was conserved. He only used mathematical equations but stopped his argument at the conversion of initial potential energy of the stone to kinetic energy just prior to impact with the floor. The rest was a hand-waving argument that, of course, the energy would be transformed into heat. The last argument was not logically developed; it was just one of the typical teacher arguments to be believed (or not). Of course, at

Infrared Thermal Imaging, Second Edition. M. Vollmer and K.-P. Möllmann.
© 2018 WILEY-VCH Verlag GmbH & Co. KGaA. Published 2018 by WILEY-VCH Verlag GmbH & Co. KGaA.

those times, it was very difficult in schools to actually measure the conversion of kinetic energy into heat. Maybe the students would have been more satisfied if the teacher had at least attempted to visualize the process in more detail. The second example – explaining the simple action of walking – was similarly frustrating. The teacher argued that movement was possible owing to the frictional forces between shoe and floor. He then wrote down some equations describing the underlying physics, and that was all. Again, there were missing arguments: if someone walking has to do work against frictional forces, there must be some conversion of kinetic energy into heat, and shoes as well as the floor must heat up. Again, of course, at those times, it was very difficult in school to actually measure the resulting tiny temperature rises of shoes and floors. Nevertheless not discussing them at all was a good example of bad teaching. And again, maybe some kind of visualization would have helped. But visualizations were not a strength of this old teacher, who rather preferred to have Newton's laws recited in Latin.

Visualization refers to any technique for creating images, diagrams, or animations to communicate an abstract or a concrete argument. It can help bring structure to a complex context, it can make verbal statements clear, or it can give clear and appropriate visual representations of situations or processes. The underlying idea is to provide visual concepts that help to better understand and better recollect a context. Today, in the computer age, visualization is finding ever-expanding applications in science, engineering, medicine, and other fields. In the natural sciences, visualization techniques are often used to represent data from simulations or experiments in plots or images in order to make analysis of the data as easy as possible. Powerful software techniques often enable the user to modify the visualization in real time, thereby allowing easy perception of patterns and relations in the abstract data in question.

Thermography is an excellent example of a visualization technique that can be used in many different fields of physics and science. Moreover, it has opened up a totally new realm of physics in terms of visualization. Nowadays, it is possible to visualize easily the (to the human eye) invisible effects of temperature rise of the floor upon impact of a falling object or upon interaction with the shoe of a walking person. This will allow totally new ways of teaching physics and the natural sciences starting in school and ending in the training of professionals in all kinds of industries. Visualization of "invisible" processes of physics or chemistry with thermography can be a major factor creating fascination for and interest in these subjects, not only in students at school and university but also for the layperson. Nearly every example described later in this book can be studied in this context.

The drawbacks of promoting IR cameras as mass products for a wide range of consumers are less obvious. Anyone owning an IR camera will be able to produce nice and colorful images, but most will never be able to fully exploit the potentials of such a camera – and most will never be able to correctly use it.

Typically, the first images recorded with any camera will be the faces of people nearby. Figure 1.1 gives an example of IR images of the two authors. Anyone confronted with such images for the first time would normally find them fascinating since they provide a totally new way of looking at people. The faces can still be

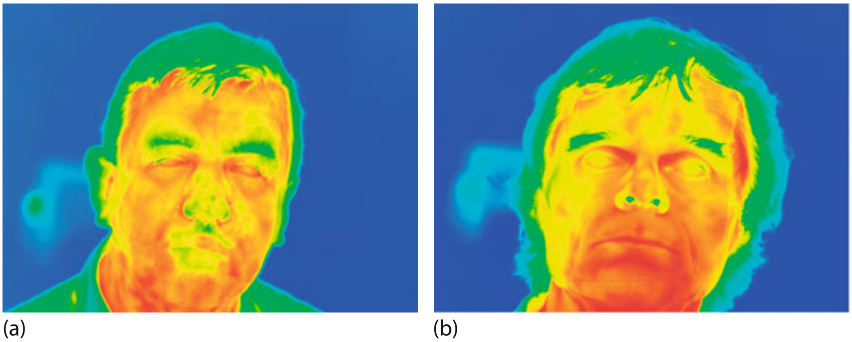
(a) (b)

Figure 1.1 IR thermal images of (a) K-P. Möllmann and (b) M. Vollmer.

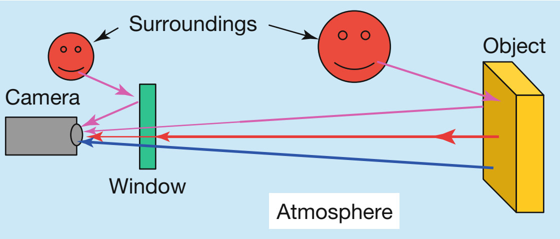

Figure 1.2 Various signal contributions entering an IR camera due to external influences.

recognized, but some parts look strange, for example, the eyes. Also, the nostrils (Figure 1.1b) seem to be distinctive and the hair to be surrounded by an "aura."

For artists who want to create new effects, such images are fine, but thermography – if it is to be used for the analysis of real problems like building insulation, for example – is much more than this. Modern IR cameras may give qualitative images, colorful images that look nice but mean nothing, or they can be used as quantitative measuring instruments. The latter use is the original reason for developing these systems. Thermography is a measurement technique that, in most cases, is able to quantitatively measure surface temperatures of objects. To use this technique correctly, professionals must know exactly what the camera does and what the user must do to extract useful information from images. This knowledge can only be obtained through professional training. Therefore, the drawback in IR cameras is that they require professional training before they can be used properly. A multitude of factors can influence IR images and, hence, any interpretation of such images (Figure 1.2 and Chapters 2 and 7).

First, radiation from an object (red) is attenuated via absorption or scattering while traveling through the atmosphere (Section 1.5.2), IR windows, or the camera optics (Section 1.5.4). Second, the atmosphere itself can emit radiation owing to its temperature (blue) (this also holds for windows or the camera optics and housing itself), and third, warm or hot objects in the surroundings (even the thermographer is a source) may lead to reflections of additional IR radiation from the

Table 1.1 Several parameters and factors affecting images recorded with modern IR cameras systems.

Parameters affecting IR images generated from raw detector data within camera that can usually be adjusted using camera software; quantitative results can strongly depend on some of these parameters! They can often be changed while analyzing images (after recording) if proper software is used (this may not be possible for the cheapest models!)	• Emissivity of object • Distance of camera to object (usually in meters, feet in the USA) • Size of object • Relative humidity • Ambient temperature (usually in degrees Celsius or Kelvin, degrees Fahrenheit in the USA) • Atmospheric temperature • External optics temperature • External optics transmission
Parameters affecting how data are plotted as an image; if chosen unfavorably, important details may be disguised	• Temperature span ΔT • Temperature range and level • Color palette
Some parameters that can significantly affect quantitative analysis and interpretation of IR images	• Wavelength dependence of emissivity (wavelength range of camera) • Angular dependence of emissivity (angle of observation) • Temperature dependence of emissivity • Optical properties of matter between camera and object • Use of filters (e.g., high temperature, narrowband) • Thermal reflections • Wind speed • Solar load • Shadow effects of nearby objects • Moisture • Thermal properties of objects (e.g., time constants)

object or windows, and so on (pink arrows). The contributions from the object or windows may, furthermore, depend on the material, the surface structure, and so on, which are described by the parameter emissivity. These and other parameters are listed in Table 1.1; they are all discussed in subsequent sections.

Even if all of these parameters are dealt with, some remaining open questions will need to be answered. Consider, for example, someone who uses IR imaging in predictive maintenance doing electrical component inspections. Suppose the recording of an IR image shows a component with an elevated temperature. The fundamental problem is the assessment criterion for the analysis of IR images. How hot can a component become and still be okay? What is the criterion for an immediate replacement, or how long can one wait before replacement? These questions involve a lot of money if the component is involved in the power supply of an industrial complex, the failure of which can lead to a shutdown of a facility for a certain period of time.

Obviously, buying a camera and recording IR images may shift the problem from not knowing anything at all to the problem of understanding the IR technology being used and all aspects of IR image interpretation. This book deals with the second problem. In this respect, it is addressed to at least three different groups of people. First, it will benefit interested newcomers to the field by giving an introduction to the general topic of IR thermal imaging, by discussing the underlying fundamental physics, and by presenting numerous examples of the technique in research as well as in industry. Second, it will benefit educators at all levels who want to include IR imaging in their curriculum in order to facilitate the understanding of physics and science topics as well as IR imaging in general. Third, it is addressed to all practitioners who own an IR camera and want to use it as a quantitative or qualitative tool for business. The text complements any kind of modern IR camera training/certification course as is offered by nearly every manufacturer of such camera systems.

The authors sincerely hope that this text will help reduce the number of colorful, but often quite wrongly interpreted, IR images of buildings and other objects in daily newspapers. In one typical example, a (probably south) wall of a house that had been illuminated by the sun for several hours before the IR image was taken was – of course – showing up as being warmer than the windows and other walls of the house. The interpretation that the wall was obviously very badly insulated was, however, pure nonsense (Chapter 7). In addition, we hope that in the future trained specialists will no longer call up their manufacturer and ask, for example, why they are not able to see any fish in their aquarium or in a pond with a long-wave (LW) camera. When that happens, there will be no more complaints about system malfunctions because the IR camera measures skin temperatures well above 45 °C. Or, to give a last example, people will no longer ask whether they are also able to measure the temperature of hot noble gases or oxygen using IR imaging.

We next come to the reason for bringing out the second edition of our book on IR thermal imaging. Of course, various handbooks have been published [1–6] that contain articles on several related topics, a number of books are available on certain aspects like the principles of radiation thermometry [7–9], detectors and detector systems, and their testing [10–16], IR material properties [17, 18], the fundamentals of heat transfer [19, 20], and an overview of the electromagnetic (EM) spectrum in the IR and adjacent regions [21], and, finally, some concise books on practical applications have also been released [22–24]. However, not only the detector technologies but also the range of applications have increased enormously over the past decade and since the first edition of this textbook. Therefore, an up-to-date review of the 2017 state of the art in technology and applications seems overdue.

This text uses the international system of units. The only deviation from this rule concerns temperature, probably the most important quantity for thermography. Temperatures in science should be given in Kelvin; IR camera manufac-

Table 1.2 Relation between three commonly used temperature scales in thermography.

T (K)	*T* (°C)	*T* (°F)
0 (absolute zero)	−273.15	−459.67
273.15	0	32
373.15	100	212
1273.15	1000	1832

ΔT (K) = ΔT(°C); ΔT (°C) = (5/9) · ΔT (°F);
T (K) = T (°C) + 273.15; T (°C) = (5/9) · (T (°F) − 32);
T (°F) = (9/5) · T (°C) + 32.

turers, however, mostly use the more common Celsius scale for their images. For North American customers, there is the option of presenting temperatures on the Fahrenheit scale. Table 1.2 gives a short survey of how these temperature readings can be converted from one unit to another.

1.2
Infrared Radiation

1.2.1
Electromagnetic Waves and the Electromagnetic Spectrum

In physics, visible light (VIS), ultraviolet (UV) radiation, IR radiation, and so on can be described as waves – to be more specific, as EM waves (for some properties of IR radiation, e.g., in detectors, a different point of view with radiation acting like a particle is adopted, but for most applications, the wave description is more useful).

Waves are periodic disturbances (think, e.g., of vertical displacements of a water surface after a stone has been thrown into a puddle or lake) that keep their shape while progressing in space as a function of time. The spatial periodicity is called *wavelength*, λ (given, for example, in meters, micrometers, nanometers), the transient periodicity is called the *period of oscillation*, T (in seconds), and its reciprocal is the *frequency*, $\nu = 1/T$ (in s^{-1} or Hertz). Both are connected via the speed of propagation c of the wave by Eq. (1.1):

$$c = \nu \cdot \lambda \tag{1.1}$$

The speed of propagation of waves depends on the specific type of wave. Sound waves, which exist only if matter is present, have typical speeds of about 340 m s^{-1} in air (think of the familiar thunder and lightning rule: if you hear the thunder 3 s after seeing the lightning, it has struck at a distance of about 1 km). In liquids, this speed is typically at least three times higher, and in solids, the speed of sound can reach about 5 km s^{-1}. In contrast, EM waves propagate at the much higher speed

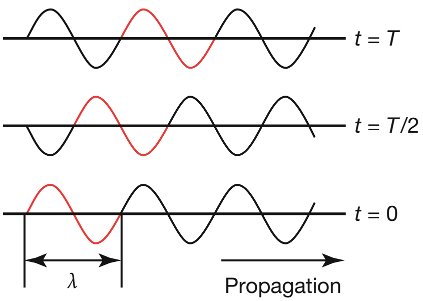

Figure 1.3 Three snapshots of a sinusoidal wave traveling from left to right. Part of the wave (one wavelength) is marked (red line) to demonstrate how the wave propagates as a function of time. The snapshots start at $t = 0$ then show the wave after half a period and a full period. In one period T, the wave has traveled one wavelength λ.

of light, which is $c = 299\,792\,458\ \mathrm{m\,s^{-1}} \approx 300\,000\ \mathrm{km\,s^{-1}}$ in a vacuum and $v = c/n$ in matter, with n being the index of refraction, which is a number of the order of unity.

In nature, the geometric form of a disturbance is very often sinusoidal, that is, it can be described by the mathematical sine function. Figure 1.3 schematically depicts snapshots of a sinusoidal wave traveling from left to right in space. The bottom snapshot refers to a starting time of $t = 0$. One wavelength λ is marked by a red bold line. After half a period of oscillation (when $t = T/2$), the wave has moved by $\lambda/2$, and when $t = T$, it has moved by one wavelength in the propagation direction.

Disturbances, which resemble waves, can be of a great variety. For example, sound waves in gases are due to pressure variations and water waves are vertical displacements of the surface. According to the type of disturbance, two wave types are usually defined: in longitudinal waves (e.g., sound waves in gases), the disturbance is parallel to the propagation direction, whereas in transverse waves (e.g., surface-water waves), it is perpendicular to it. With springs (Figure 1.4), both types of waves are possible (e.g., sound waves in solids). In transverse waves, the disturbances can oscillate in many different directions. This is described by the property called *polarization*. The *plane of polarization* is the plane defined by the disturbance and the propagation direction.

Light and IR radiation are EM waves. In EM waves, the disturbances are electric and magnetic fields. They are perpendicular to each other and also perpendicular to the propagation direction, that is, EM waves are transverse waves (Figure 1.5). The maximum disturbance (or elongation) is called the *amplitude*.

The polarization is defined by the electric field and the propagation direction, that is, the wave is polarized in the x–z plane in Figure 1.5. Sunlight and light from many other sources like fire, candles, or light bulbs is unpolarized, that is, the plane of polarization of these light waves can have all possible orientations. Such unpolarized radiation may, however, become polarized by reflections from surfaces or on passing a so-called polarizer.

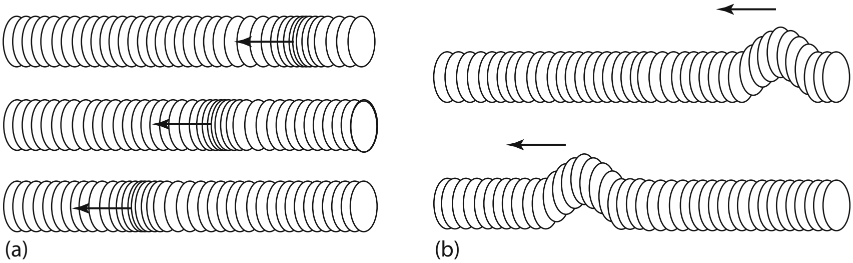

Figure 1.4 Illustration of longitudinal (a) and transverse waves (b). The latter have the additional property of polarization.

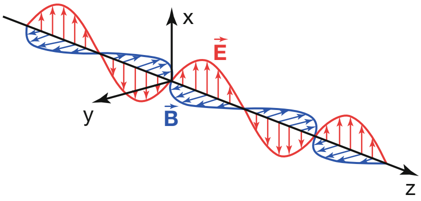

Figure 1.5 IR radiation involves a special kind of EM waves. In EM waves, the electric field and the magnetic induction field are perpendicular to each other and to the direction of propagation (here the *z*-direction).

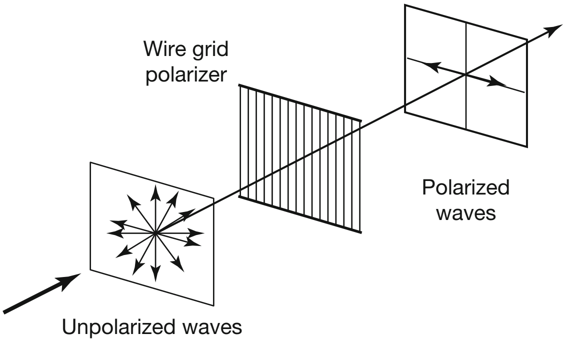

Figure 1.6 Microscopic wire grids can act as polarizers for IR radiation. The transmitted electric field oscillates perpendicular to the direction of the wires.

For VIS and IR radiation the simplest polarizer consists of a microscopically small conducting grid (similarly, a metal wire grid can polarize microwave radiation). If unpolarized radiation is incident on such a grid, only those waves whose electric field is oscillating perpendicular to the grid wires are transmitted (Figure 1.6). Such polarizing filters can help suppress reflections when taking photos with a camera (for more details, see [25, 26] and Section 3.4).

Figure 1.7 gives an overview of EM waves, ordered according to their wavelength or frequency. This spectrum consists of a great variety of different waves. All of them can be observed in nature, and many have technical applications.

Starting from the top of the figure, for example, γ-rays have the highest frequencies, that is, the shortest wavelengths. X-rays are well known from their medical applications, and UV radiation is important in the context of the ozone hole

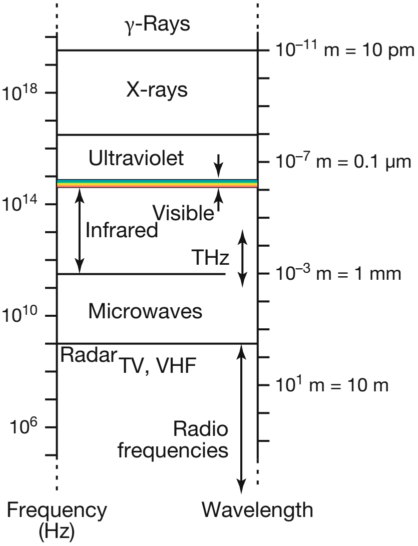

Figure 1.7 Overview of most common types of EM waves. The visible spectral range (VIS) covers only a tiny part with wavelengths from 0.38 to 0.78 µm, followed at longer wavelengths by the infrared (IR) from 0.78 µm to 1 mm.

since less ozone in the upper atmosphere means more UV radiation from the sun reaches the surface of the earth, which can cause skin cancer. The visible light, defined by the sensitive range of the light receptors in our eyes, only covers a very small range within this spectrum, with wavelengths from 380 to 780 nm. The adjacent spectral region with wavelengths from 780 up to 1 mm is usually called *infrared*, which is the topic of this book. This range is followed by microwaves, RADAR, and all EM waves that are used for radio, TV, and so on. Recently, new sensing developments in the frequency range from 0.1 to 10 THz have led to the newly defined range of terahertz radiation, which overlaps part of the IR and microwave ranges.

For IR imaging, only a small range of the IR spectrum is used. It is shown in an expanded view in Figure 1.8. Typically, three spectral ranges are defined for thermography: the long-wave (LW) region from around 8 to 14 µm, the mid-wave (MW) region from around 3 to 5 µm, and the short-wave (SW) region from 0.9 to 1.7 µm. Commercial cameras are available for these three ranges (note that the limiting wavelengths for these ranges, also called *bands*, can vary depending on the actual detector sensitivities (Figure 2.71) and additional optical filter elements; for most simple estimates we use the aforementioned values). The restriction to these wavelengths follows firstly from considerations of the amount of thermal radiation to be expected (Section 1.3.2), secondly from the physics of detectors (Chapter 2), and thirdly from the transmission properties of the atmosphere (Section 1.5.2).

The origin of naturally occurring EM radiation is manifold. The most important process for thermography is the so-called thermal radiation, which will be discussed in detail in the next section. In brief, the term *thermal radiation* implies that every body or object at a temperature $T > 0\,\mathrm{K}$ (−273.15 °C) emits EM radiation. The amount of radiation and its distribution as a function of wavelength

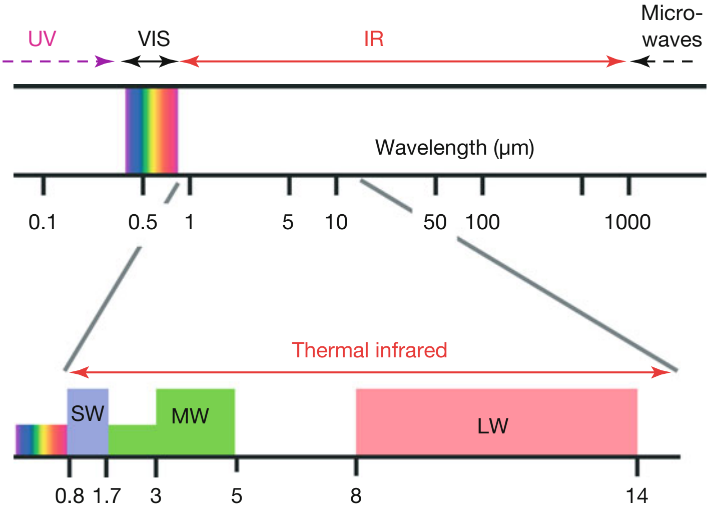

Figure 1.8 Infrared (IR) and adjacent spectral regions and expanded view of so-called thermal IR. This is the region where IR imaging systems for short-wave (SW), mid-wave (MW), and long-wave (LW) cameras exist. Special systems have extended ranges.

depend on temperature and material properties. For temperatures in the range of natural and technological processes, this radiation is in the thermal IR spectral region.

1.2.2
Basics of Geometrical Optics for Infrared Radiation

1.2.2.1 Geometric Properties of Reflection and Refraction

From the observation of shadows or the use of laser pointers, it is an everyday experience that visible light propagates more or less in straight lines. This behavior is most easily described in terms of geometrical optics. This description is valid if the wavelength of the light is much smaller than the size of the objects/structures on which the light is incident. IR radiation has a behavior very similar to that of visible light; hence, it can also often be described using geometrical optics:

- In homogeneous materials, IR radiation propagates in straight lines. It can be described as rays whose propagation follows from geometrical laws. Usually the rays are indicated by arrows.
- At the boundary between two materials, part of the incident radiation is reflected, and part of it is transmitted as refracted IR radiation (Figure 1.9).
- The optical properties of homogeneous materials, for example, those of a lens of an IR camera, are described by the index of refraction n. This index n is a real number larger than unity for nonabsorbing materials and a complex mathematical quantity for absorbing materials. The properties of materials for the thermal IR spectral range are described in detail in Section 1.5.

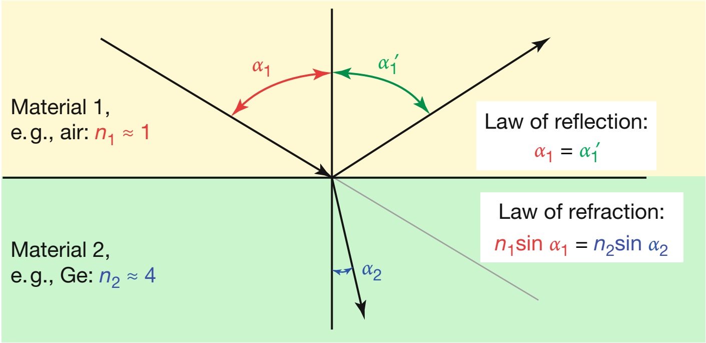

Figure 1.9 Laws of reflection and refraction in geometrical optics. The examples given in the figure refer to IR radiation, which is incident from the air on a germanium surface.

- The orientation between the incident radiation and surface normal of the boundary between two materials is called the *angle of incidence*, α_1. The corresponding angle between the reflected ray and the surface normal is the angle of reflection, α_1'. The law of reflection – which is the basis for mirror optics – states that

$$\alpha_1' = \alpha_1 \tag{1.2}$$

- The orientation between the transmitted refracted radiation and surface normal of the boundary between two materials is called the *angle of refraction*, α_2. If the index of refraction of the two materials are given by n_1 and n_2, the law of refraction (also called *Snell's law*) – which is the basis for lens optics – states that

$$n_1 \sin \alpha_1 = n_2 \sin \alpha_2 \tag{1.3}$$

The propagation of radiation in matter can be described using these two laws. Nowadays, this is mostly done using ray-tracing programs, which make it possible to follow the path of radiation through many different materials and a large number of boundaries, as are usual, for example, in complex lens systems used in optical instruments such as IR cameras.

Refraction is also the basis for studying spectra and defining the IR spectral region. In the seventeenth century, Isaac Newton demonstrated that the index of refraction of materials depends on the wavelength of visible light. The same holds for IR radiation. Typical optical materials show a normal dispersion, that is, the index of refraction decreases with increasing wavelength. If radiation is incident on a prism, the angles of refracted light within the prism are determined from the law of refraction. If the index of refraction decreases with increasing wavelength, the radiation with longer wavelength is refracted less than the short wavelength radiation. The same holds for the second boundary of the prism. As a result, the incident EM radiation is spread out into a spectrum behind the prism. If thermal IR radiation is incident and the prism is made of an IR transparent

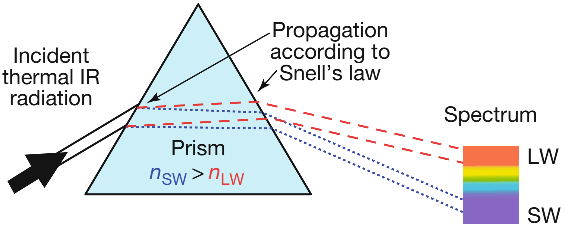

Figure 1.10 Generating a spectrum from a collimated narrow beam of EM radiation using a nonabsorbing prism.

material, the LW radiation will end up on top and the SW radiation on the bottom of the spectrum in Figure 1.10.

1.2.2.2 Specular and Diffuse Reflection

Finally, IR imaging is often used to study objects with rough surfaces. In such cases, reflection need not be directed but can also have a diffuse component. Figure 1.11 illustrates the transition from directed reflection, also called *specular reflection*, to diffuse reflection.

1.2.2.3 Portion of Reflected and Transmitted Radiation: Fresnel Equations

Equations 1.2 and 1.3 give the directions of reflected and transmitted radiation. The portions of reflected and transmitted light, which depend on angle of incidence, can also be computed from the so-called Fresnel equations of wave optics [25, 27]. For the purpose of this book, graphical results will be sufficient. Fig-

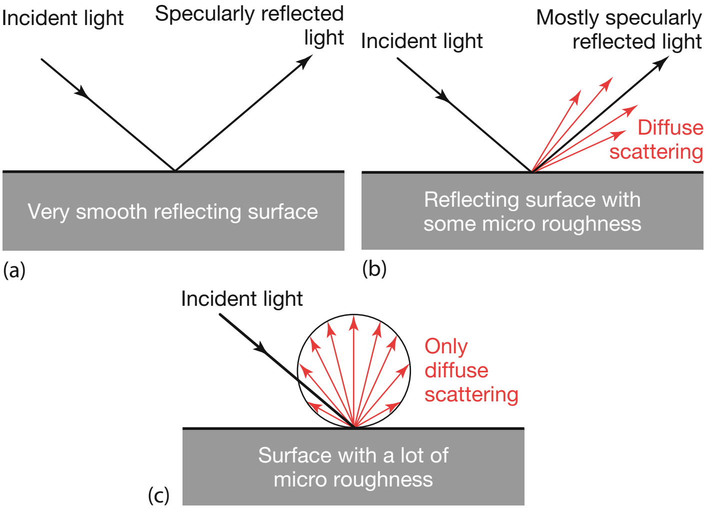

Figure 1.11 During the transition from smooth to rough surfaces, optical reflections change from specular mirrorlike (a) to diffuse reflection (c). The most common case is a combination of both types of reflection (b).

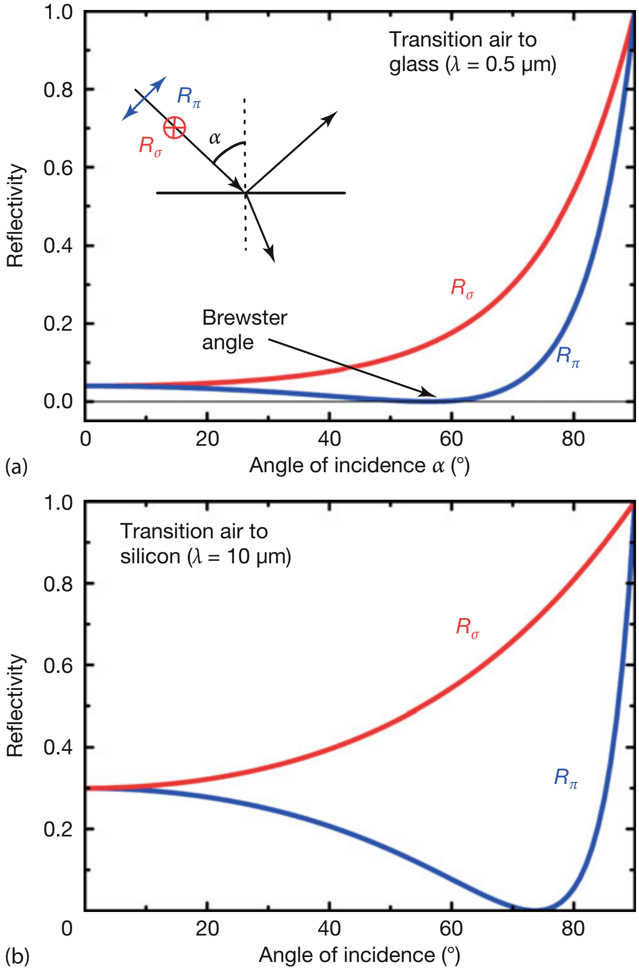

Figure 1.12 The portion of reflected visible light from an air–glass boundary (a) or of IR radiation from an air–silicon boundary (b) depends on the polarization of the radiation.

ure 1.12 shows representative results for the reflection of visible light ($\lambda = 0.5$ μm) for a boundary between air and glass and for IR radiation ($\lambda = 10$ μm) for a boundary between air and silicon.

Reflected light consists of two contributions: the first is light that is polarized parallel (R_π) and the second is light that is polarized perpendicular (R_σ) to the plane of incidence. The latter is defined as the plane made up by the surface normal of the boundary and the propagation direction of the EM radiation. In Figure 1.9 and the inset in Figure 1.12, the drawing plane is the plane of incidence. For the perpendicular component, the portion of reflected radiation, called *reflectivity*, slowly increases from 0.04 for the VIS case (and about 0.3 for IR) at normal incidence ($\alpha = 0°$) up to the maximum value of 1.0 at grazing incidence ($\alpha = 90°$).

In contrast, the parallel component first decreases from the same starting value at $\alpha = 0°$, reaches a specific angle, called the *Brewster angle*, with zero reflectivity, and then steeply rises to the maximum value of 1.0 at grazing incidence.

In general, the Brewster angle α_{Br} for a transition from a transparent, that is, nonabsorbing material A (e.g., air) to a transparent material B (e.g., glass) is defined by the condition

$$\tan(\alpha_{\mathrm{Br}}) = \frac{\sin(\alpha_{\mathrm{Br}})}{\cos(\alpha_{\mathrm{Br}})} = \frac{n_{\mathrm{B}}}{n_{\mathrm{A}}} \tag{1.4}$$

which, for the preceding examples, gives $\alpha_{\mathrm{Br}} = 56.3°$ for air–glass (VIS) and $\alpha_{\mathrm{Br}} = 75°$ for air–silicon (IR). For absorbing materials, the general form of the curves stays the same; however, the minimum may not reach zero and the Brewster angles may shift.

Thermal reflections are important in many applications of thermography. For quick numerical estimates, we mention Eq. (1.5), which gives the reflectivity R (portion of reflected radiation) in terms of the refractive indices for the case of normal incidence ($\alpha = 0°$). The material A from which radiation is incident is considered to be transparent (e.g., air), whereas the material B from which radiation is reflected can be transparent or opaque to the radiation. In the latter case, the index of refraction, which can be found as a function of wavelength in tables of several handbooks [18], is mathematically a complex number $n_{\mathrm{B}} = n_1 + \mathrm{i}n_2$ and

$$R(\alpha = 0°, n_{\mathrm{A}}, n_{\mathrm{B}} = n_1 + \mathrm{i}n_2) = \frac{(n_1 - n_{\mathrm{A}})^2 + n_2^2}{(n_1 + n_{\mathrm{A}})^2 + n_2^2} \tag{1.5}$$

In the preceding examples, $n_{\mathrm{A}} = 1.0$, $n_1 = 1.5$, and $n_2 = 0$, which gives $R = 0.04$ for air–glass at $\lambda = 0.5\,\mu\mathrm{m}$ and $n_{\mathrm{A}} = 1.0$, $n_1 = 3.42$, and $n_2 = 6.8 \cdot 10^{-5}$, which gives $R = 0.30$ for air–silicon at $\lambda = 10\,\mu\mathrm{m}$. Some applications of these results are discussed in the section on suppression of thermal reflections (Section 3.4).

1.3
Radiometry and Thermal Radiation

In any practical measurement with an IR camera, an object emits radiation in the direction of the camera, where it is focused on the detector and measured quantitatively. Since thermography is mostly done with solid objects, which are, furthermore, opaque to IR radiation, the emission refers to the surfaces of the objects only (the most important exception – gases – will be treated separately in Chapter 8). Let us consider a small surface area element $\mathrm{d}A$ that emits thermal radiation in the specific direction of the detector, which occupies a certain solid angle. To characterize the emission, propagation, and irradiance of any kind of radiation – that is, also the thermal radiation discussed here – with respect to the detector, a set of several radiometric quantities has been defined, which will be introduced in Section 1.3.1. As will become evident, a certain class of emitters – so-called black-

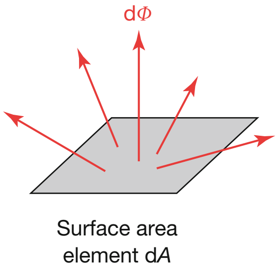

Figure 1.13 The total energy flux, dΦ, emitted by a surface area element, dA, is emitted in a hemisphere above dA.

bodies – has unique properties concerning the total amount of emitted radiation as well as their geometrical distribution. This will be discussed in Section 1.3.2.

1.3.1
Basic Radiometry

1.3.1.1 Radiant Power, Excitance, and Irradiance

Consider an element dA of the radiating surface of an object. The total energy flux dΦ from this surface element dA into the hemisphere is called *power*, *radiant power*, or *energy flux* with the SI unit W (watt) (Figure 1.13). This quantity can only be measured directly if the detector collects radiation from the hemisphere completely. This is usually not the case.

If this radiant power is related to the emitting surface area, we find the excitance, M, in W m^{-2}, using

$$M = \frac{\mathrm{d}\Phi}{\mathrm{d}A} \tag{1.6}$$

Obviously excitance (sometimes also called *emittance* or *emissive power* [16, 20]) characterizes the total radiant power within the hemisphere divided by the surface area. It contains the contributions of all emitted wavelengths (for the sake of simplicity, we write total derivatives; note, however, that these are partial derivatives, since the radiant power depends also on angles and wavelength).

If, in contrast, we consider the total incident power from a hemisphere on a given surface dA, the same definition leads to the irradiance $E = \mathrm{d}\Phi/\mathrm{d}A$. Obviously, excitance and irradiance refer to the same units of measurement, namely, watts per meter squared (W m^{-2}), but the corresponding energy flux is either emitted or received by a particular surface area dA.

1.3.1.2 Spectral Densities of Radiometric Quantities

So far, radiant power, excitance, and irradiance for an area dA refer to the total power emitted to or received from a hemisphere. In practice, all radiometric quantities do, however, also depend on wavelength. Therefore, one can easily define the spectral densities of the various radiometric quantities. As an example, Figure 1.14 illustrates the relation between radiant power Φ and its spectral den-

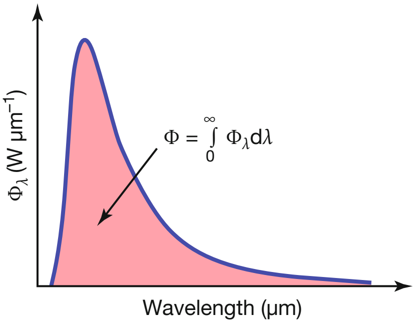

Figure 1.14 Relation between radiant power Φ and its spectral density: The total radiant power Φ (red area) is found by summing up the contribution of Φ_λ (blue curve) over the whole wavelength range.

Table 1.3 Overview of important radiometric quantities.

Name	Symbol	Unit	Definition
Energy flux or radiant power	Φ	W	Emission of energy per time in hemisphere
Excitance	M	W m^{-2}	$M = \frac{\mathrm{d}\Phi}{\mathrm{d}A}$ dA: emitting surface, into hemisphere
Irradiance	E	W m^{-2}	$E = \frac{\mathrm{d}\Phi}{\mathrm{d}A}$ dA: receiving surface, from hemisphere
Radiant intensity	I	W (sr)$^{-1}$	$I = \frac{\mathrm{d}\Phi}{\mathrm{d}\Omega}$
Radiance	L	W (m^2 sr)$^{-1}$	$L = \frac{\mathrm{d}^2\Phi}{\cos\delta\,\mathrm{d}\Omega\,\mathrm{d}A}$
Spectral density X_λ of any chosen radiometric quantity X	X_λ	(unit of X) (µm)$^{-1}$ or (unit of X) (nm)$^{-1}$ or (unit of X) m^{-1}	$X_\lambda = \frac{\mathrm{d}X}{\mathrm{d}\lambda}$

sity Φ_λ.

$$\Phi_\lambda = \frac{\mathrm{d}\Phi}{\mathrm{d}\lambda} \tag{1.7}$$

Similar relations hold for all other radiometric quantities (Table 1.3). The excitance, that is, emissive power, would then be called, for example, *spectral excitance* or *spectral emissive power*.

1.3.1.3 **Solid Angles**

Most often, surfaces of objects do emit radiation, but not uniformly in the hemisphere. To account for this directionality of emitted radiation, we must introduce angles in three-dimensional coordinate systems and the concept of the solid angle. Figure 1.15a depicts the geometry: the emitting area is located in the x–y plane,

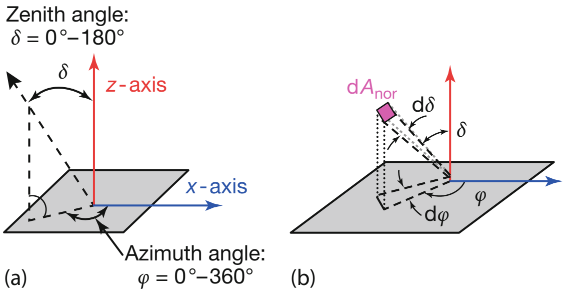

Figure 1.15 (a) Definition of angles in space and visualization of solid angle, which, (b) at a given distance from the surface, is related to the area $\mathrm{d}A_{\mathrm{nor}}$, which is normal to the chosen direction.

that is, the z-axis is perpendicular to the area. Then, any direction in space (broken arrow) can be defined by two angles, the azimuth angle φ, which is measured from the x-axis to the projection line of the chosen direction onto the x–y plane, and the zenith angle δ.

Usually, the direction itself is not important; rather, radiation is emitted toward a detector of a given surface area. For simplicity we assume an area $\mathrm{d}A_{\mathrm{nor}}$ that is oriented perpendicular to the chosen direction at a distance R from a chosen point on the emitting surface. The area can be characterized by the small increments of angles $\mathrm{d}\varphi$ and $\mathrm{d}\delta$, as shown in Figure 1.15b. This leads to the definition of the solid angle element $\mathrm{d}\Omega$ (for details, see textbooks on mathematics):

$$\mathrm{d}\Omega(\delta,\varphi) = \sin\delta\cdot\mathrm{d}\delta\cdot\mathrm{d}\varphi = \frac{\mathrm{d}A_{\mathrm{nor}}}{R^2} \tag{1.8}$$

The unit of solid angle is the steradian (sr), similar to the radian (rad) for the planar angle. The full solid angle is 4π. Using δ, φ, and $\mathrm{d}\Omega(\delta,\varphi)$, any emission of radiation in any given direction can be characterized using the quantities radiant intensity and radiance.

1.3.1.4 Radiant Intensity, Radiance, and Lambertian Emitters

The radiant intensity I is the radiant power that is emitted from a point source of a radiating object into a solid angle element $\mathrm{d}\Omega$ in a given direction, characterized by (δ,φ). Mathematically it is given by $I = \mathrm{d}\Phi/\mathrm{d}\Omega$, with unit watt/steradian ($\mathrm{W\,sr^{-1}}$).

Radiant intensity (which, by the way, is the only quantity in optics where intensity is properly defined [28]) is related to the most often used quantity in radiometry, the radiance L. Radiance is used to characterize extended sources. It is defined as the amount of radiant power per unit of projected source area and per unit solid angle:

$$L = \frac{\mathrm{d}^2\Phi}{\cos\delta\,\mathrm{d}\Omega\,\mathrm{dA}}, \quad \text{i.e.,} \quad \mathrm{d}^2\Phi = L\cos\delta\,\mathrm{d}\Omega\,\mathrm{dA} \tag{1.9a}$$

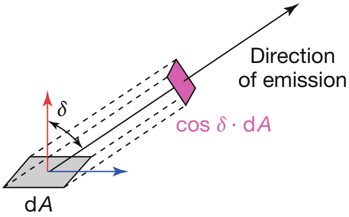

Figure 1.16 For a given direction, only the projection dA · cos δ can be seen from the emitting area dA.

The significance of this slightly more complicated definition of radiance may become obvious if Eq. (1.9a) is written in such a way as to calculate the total radiant power from the radiance:

$$\Phi = \iint L \cos\delta \,\mathrm{d}\Omega \,\mathrm{dA} \tag{1.9b}$$

The total radiant power results from summing up radiance contributions over the area and solid angle of the hemisphere. If only integration over a solid angle is done, one ends up with the excitance:

$$M = \frac{\mathrm{d}\Phi}{\mathrm{d}A} = \int_{\text{hemisphere}} L \cos\delta \,\mathrm{d}\Omega \tag{1.10a}$$

whereas only integration over a surface area results in radiant intensity:

$$I = \frac{\mathrm{d}\Phi}{\mathrm{d}\Omega} = \int_{\text{source area}} L \cos\delta \,\mathrm{d}A \tag{1.10b}$$

The geometrical factor cos δ can be easily understood from Figure 1.16. Any emitting surface area dA is observed to be largest for a direction that is perpendicular to the surface. For any other direction, only the projection of dA perpendicular to it can contribute to the emitted radiation.

Hence, radiance is a measure of the radiant power of an emitter with surface area dA that passes through a surface that is normal to the emission direction. Since this surface defines a solid angle in this direction, radiance is a true measure of the amount of radiation that is emitted in a certain direction and per unit solid angle.

A summary of important radiometric quantities is listed in Table 1.3. SI units are used; however, for the spectral densities the wavelength interval is often given in micrometers or nanometers. This helps to avoid misinterpretations. Consider, for example, the spectral density of the excitance, which is the total radiant power per area and wavelength interval. Its unit can be expressed as $\mathrm{W\,(m^2\,\mu m)^{-1}}$ or also as $\mathrm{W\,m^{-3}}$. The first choice is much better since it avoids any misunderstanding. For example, a quantity with unit $\mathrm{W\,m^{-3}}$ could be wrongly interpreted as the power density per volume.

The difference between radiant intensity and radiance will become most obvious for so-called Lambertian radiators (after J.H. Lambert, an eighteenth-century

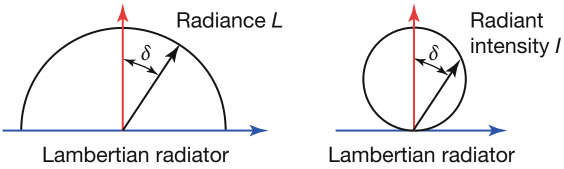

Figure 1.17 Lambertian radiators have constant radiance, but the radiant intensity depends on the direction of emission.

scientist who made significant contributions to the field of photometry). A Lambertian radiator is one that emits or reflects a radiance that is independent of angle, that is, it emits uniformly into the hemisphere. Lambertian radiators are theoretical constructs that can be approximated in the real world by blackbody sources (Section 1.4.6) or perfect diffusely scattering surfaces. In this case, L = constant and $I = L \cdot A \cdot \cos\delta = I_0 \cdot \cos\delta$. This angular dependence of radiant intensity and radiance is schematically depicted in Figure 1.17.

Why is constant radiance important? As stated earlier, radiance describes the amount of radiation emitted by an emitting area in a given direction and per unit solid angle; therefore, a Lambertian source appears to emit equal amounts of radiation in every direction. A typical example of such behavior is known from visual optics. Diffusely scattering surfaces like, for example, a tapestry, reflect the same amount of radiation in every direction. This means that, visually, the illuminated surface has the same brightness irrespective of the direction of observation. Similarly, IR cameras detect radiance from objects since the area of the camera lenses defines the solid angle, which is used for detection in the direction of the camera. If an object emits like a Lambertian source, the detected IR radiation will therefore be independent of the direction of observation. More practically speaking, the detected radiation relates to the temperature of an object. Therefore, a Lambertian source observed with an IR camera will appear to have the same temperature irrespective of the observation direction – which is, of course, a prerequisite for useful and accurate temperature measurements. Conclusion: objects studied with IR cameras should ideally behave like Lambertian sources; otherwise, complicated angle-dependent corrections would be needed.

For Lambertian surfaces, the relation between the excitance M and radiance L of a surface is given simply by $M = \pi L$. This also holds for the corresponding spectral densities, that is, in general, the excitance of Lambertian radiators equals π times their radiance. A summary of properties of Lambertian radiators is given in Table 1.4.

Table 1.4 Some relations holding for Lambertian radiators or reflectors.

Radiance	L = constant	Isotropic
Radiant intensity	$I = I_0 \cos\delta$	δ angle of direction to surface normal
Relation of excitance to radiance	$M = \pi \cdot L$; $M(\lambda) = \pi \cdot L(\lambda)$	

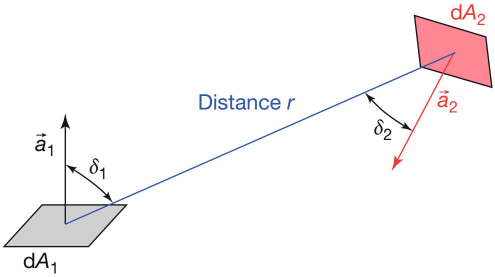

Figure 1.18 Geometry for radiation transfer between two surfaces dA_1 and dA_2.

1.3.1.5 Radiation Transfer between Surfaces: Fundamental Law of Radiometry and View Factor

The concept of radiance helps to formulate radiation exchange between two surfaces. This will become important later when we discuss practical examples such as building thermography, where neighboring buildings or objects have a significant influence on the measured surface temperature of a wall or a roof (Section 7.4). The basic relations are introduced here.

Consider two surface area elements, dA_1 and dA_2, that are arbitrarily positioned and oriented in space (Figure 1.18).

According to Eq. (1.9a), the radiant power $\mathrm{d}^2\Phi$ that is emitted by area dA_1 and intercepted by dA_2 can be written

$$\mathrm{d}^2\Phi = L_1 \cos\delta_1 \,\mathrm{d}A_1\,\mathrm{d}\Omega_2 \tag{1.11}$$

where L_1 is the radiance from dA_1, and dΩ_2 is the solid angle under which dA_2 is seen from dA_1. The latter is given by $(\cos\delta_2)\,\mathrm{d}A_2/r^2$, which leads to the *fundamental law of radiometry*:

$$\mathrm{d}^2\Phi = \frac{L_1 \cos\delta_1 \cos\delta_2}{r^2}\,\mathrm{d}A_1\,\mathrm{d}A_2 \tag{1.12}$$

The radiant power that is emitted by dA_1 and received by dA_2 depends on the distance and relative orientation of the two areas with respect to the connecting line. Equation 1.12 makes it possible to calculate the portion of the total radiant power of a finite area A_1 of an emitting object that is incident on a finite area A_2 of a receiving object (Figure 1.19).

From Eq. (1.12), the total radiant power Φ_{12} from area A_1 that is incident on area A_2 is given by

$$\Phi_{12} = L_1 \iint\limits_{A_1,A_2} \frac{\cos\delta_1 \cos\delta_2}{r^2}\,\mathrm{d}A_1\,\mathrm{d}A_2 \tag{1.13}$$

Since the total radiant power Φ_1 that is emitted by A_1 into the hemisphere can be computed to be $\Phi_1 = \pi L_1 A_1$, one needs to find the portion of Φ_1 that is inter-

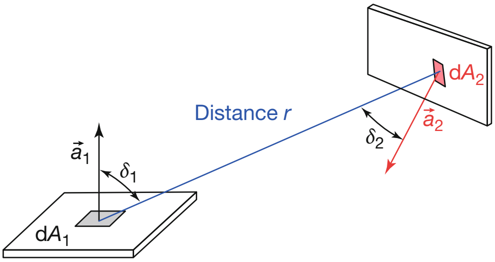

Figure 1.19 Geometry for definition of view factor. For simplicity, areas A_1 and A_2 are plotted as planar, but any kind of arbitrarily curved surface would also work.

sected by A_2, the so-called view factor:

$$F_{12} = \frac{\Phi_{12}}{\Phi_1} = \frac{1}{\pi A_1} \iint\limits_{A_1,A_2} \frac{\cos\delta_1 \cos\delta_2}{r^2}\, \mathrm{d}A_1\, \mathrm{d}A_2 \tag{1.14a}$$

Similarly, one may define the view factor F_{21} that describes the portion of Φ_2 that is intersected by A_1. From these definitions it follows that

$$A_1 F_{12} = A_2 F_{21} \tag{1.14b}$$

For any practical situation, one usually deals with at least two objects (the object under study and the IR camera itself) at different temperatures; hence, view factors will be used to help analyze the total net energy flux from an object to an IR camera. We return to the topic of view factors when discussing radiation exchange between objects (Section 7.4.4).

1.3.2
Blackbody Radiation

1.3.2.1 Definition

On the basis of fundamental physics, every object at any given absolute temperature above 0 K emits radiation. The maximum radiant power that can be emitted by any object depends only on the temperature of the object. Therefore, this emitted radiation is called *thermal radiation*. For real bodies, an additional material property, the emissivity, comes into play (Section 1.4).

In this section, we only deal with perfect emitters (see also Section 1.4.5) of thermal radiation, that is, those that emit the maximum radiant power. These are called *blackbodies*. Blackbodies resemble ideal surfaces having the following properties [20]:

1. A blackbody absorbs all incident radiation, regardless of wavelength and direction.
2. For a given temperature and wavelength, no surface can emit more energy than a blackbody.

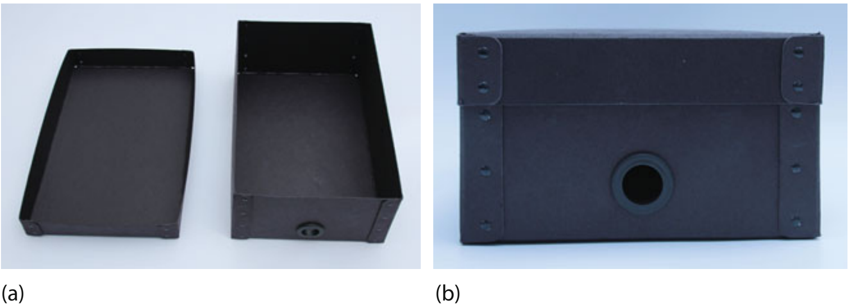
(a) (b)

Figure 1.20 A shoebox-like container, made of black cardboard with a small hole and a lid (a) resembles a cavity. Similar cavities are used as blackbody sources. The hole looks very black in the VIS, nicely illustrating the name *black*body (b).

3. Radiation emitted by a blackbody depends on wavelength; however, its radiance does not depend on direction, that is, it behaves like a Lambertian radiator.

As perfect absorbers and emitters, blackbodies serve as standards in radiometry.

Experimentally, the most simple commercial blackbodies are cavities whose walls are kept at constant temperature. The notion of black (as defined by property 1) can easily be understood from an optical analog in the visible spectral range. If one observes a distant building with an open window, the inner part of the window looks black indeed. A small box, preferably with inner black surfaces, with a small hole serves the same purpose (Figure 1.20).

1.3.2.2 Planck Distribution Function for Blackbody Radiation

Very precise spectral measurements of thermal radiation of cavities, that is, experimental blackbodies, existed by the end of the nineteenth century. However, it was not before 1900, when Max Planck introduced his famous concept of the Planck constant h, that measured spectra could be satisfactorily explained. Planck's theory was based on thermodynamics, but with the quantum nature of the emission and absorption of radiation, he introduced a totally new concept not only in the theory of blackbody radiation but in the whole world of physics. In modern language, the spectral excitance, that is, total radiant power into the hemisphere, of a blackbody of given temperature T in wavelength interval $(\lambda, \lambda + \mathrm{d}\lambda)$ can be written as

$$M_\lambda(T)\,\mathrm{d}\lambda = \frac{2\pi hc^2}{\lambda^5}\frac{1}{e^{hc/(\lambda kT)} - 1}\,\mathrm{d}\lambda \tag{1.15}$$

The corresponding radiance is $L_\lambda(T) = M_\lambda(T)/\pi$. Here, $h = 6.626 \cdot 10^{-34}\,\mathrm{J\,s}$ is Planck's constant, $c = 2.998 \cdot 10^8\,\mathrm{m\,s^{-1}}$ is the speed of light in a vacuum, λ is the wavelength of the radiation, and T is the absolute temperature of the blackbody given in Kelvin. The currently accepted values for the fundamental physical constants such as c, h, and others can be found on the NIST web site [29].

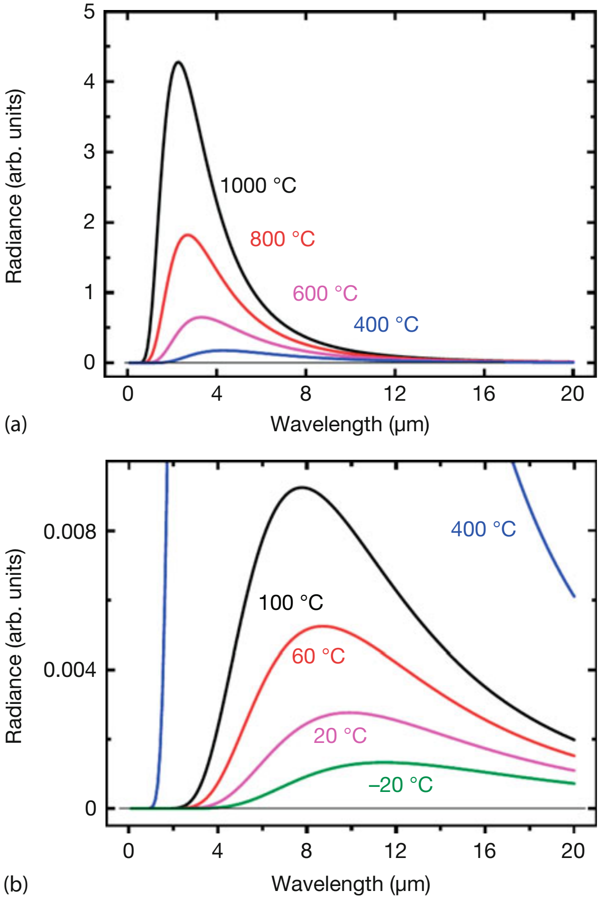

Figure 1.21 Radiance of blackbodies of temperatures between –20 and 1000 °C. Radiance is given in the same arbitrary units for (a) and (b).

Figure 1.21 depicts a series of blackbody spectra for various temperatures. The spectra refer to either radiance or excitance (the scale has arbitrary units; for absolute values see Figure 1.22). They have several characteristic features:

1. In contrast to emission from spectral lamps, these spectra are continuous.
2. For any fixed wavelength, radiance increases with temperature (i.e., spectra of a different temperature never cross each other).
3. The spectral region of emission depends on temperature. Low temperatures lead to longer wavelengths, high temperatures to shorter wavelength emission.

The wavelength of peak transmission in this representation is found by locating the maximum via the condition $\mathrm{d}M_\lambda(T)/\,\mathrm{d}\lambda = 0$. This leads to Wien's displacement law:

$$\lambda_{\max} \cdot T = 2897.8\,\mu\mathrm{m\,K} \tag{1.16}$$

For blackbodies at 300, 1000, and 6000 K, maximum emission occurs around 10, 3, and 0.5 μm, respectively. The first case resembles environmental radiation, the second, for example, a hot plate from an electric stove, and the third, the apparent average temperature of the outer layers of the Sun. From daily experience, hot plates start to glow red because the short-wavelength part of the thermal emission enters the red part of the visible spectrum. Radiation from the Sun appears white to us since it peaks in the middle of the visible spectrum.

1.3.2.3 **Different Representations of Planck's Law**

Besides the usual textbook representation of Planck's law in terms of radiance or excitance as a function of wavelength (Eq. (1.15)), other equations can be found illustrating the same phenomenon. Many spectrometers that are used to measure the spectra of blackbody radiation measure, for example, signals as a function of frequency $\nu = c/\lambda$ (in Hz) or wavenumber $\tilde{\nu} = 1/\lambda$ (in cm^{-1}). The corresponding representation of spectra reveals important differences compared to the wavelength representation. For example, Eq. (1.17) gives the frequency distribution of blackbody radiation:

$$M_\nu(T)\,\mathrm{d}\nu = \frac{2\pi h\nu^3}{c^2}\frac{1}{\mathrm{e}^{h\nu/(kT)} - 1}\,\mathrm{d}\nu \tag{1.17}$$

Figure 1.22 compares a set of blackbody spectra in terms of excitance (i.e., spectral emissive power) as a function of wavelength $M_\lambda\,\mathrm{d}\lambda$ and as a function of frequency $M_\nu\,\mathrm{d}\nu$ in double log plots. Similar to Wien's displacement law for wavelength (Eq. (1.16)), a displacement law also exists for the frequency representation:

$$\frac{\nu_{\max}}{T} = 5.8785 \cdot 10^{10}\,\mathrm{Hz/K} \tag{1.18}$$

A note of caution: obviously the two representations have their peaks at different parts of the spectrum at the same temperature since the distribution functions include $\mathrm{d}\lambda$ and $\mathrm{d}\nu$, which are related via a nonlinear equation [30]. For example, $M_\lambda\,\mathrm{d}\lambda$ for $T = 5800\,\mathrm{K}$ peaks in the VIS range at 500 nm, whereas $M_\nu\,\mathrm{d}\nu$ peaks at $3.41 \cdot 10^{14}$ Hz, which, according to $c = \nu\lambda$, corresponds to a wavelength of 880 nm. This behavior is a consequence of using distribution functions. One needs to be very careful when arguing about the maxima of Planck blackbody spectra. The position of a maximum actually depends on the chosen representation. For IR cameras, this has no effect, of course, since we are always interested in the total radiant power within a certain spectral interval; and, of course, in the total radiant power within a certain spectral range, for example, the VIS for $T = 5800\,\mathrm{K}$ (or the range 8–14 μm for 300 K radiation or any other range) is the same in both representations.

Blackbody radiation is one of the few topics that have inspired several Nobel Prizes in physics. First, Wilhelm Wien received the prize in 1911 for his work

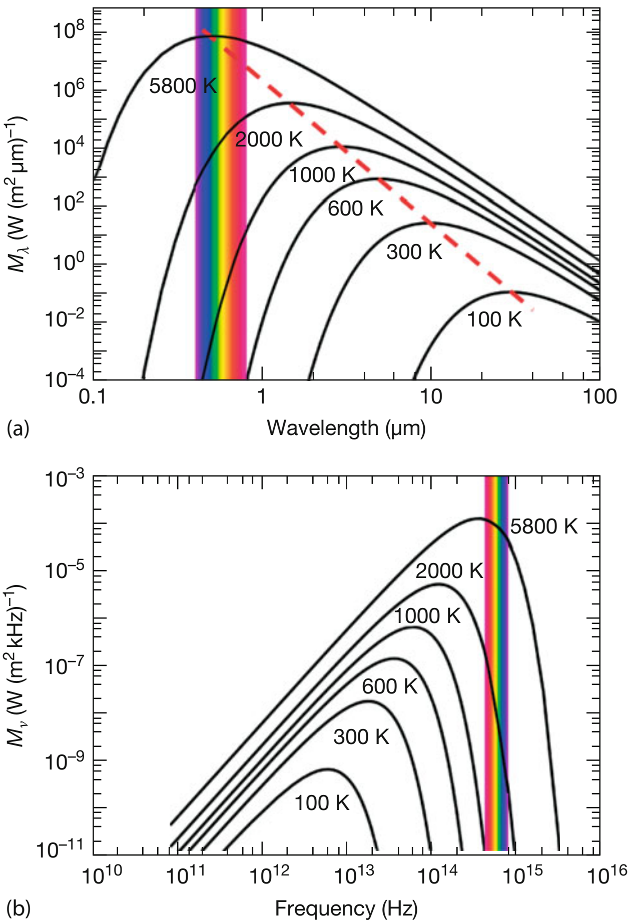

Figure 1.22 (a,b) Comparison of two representations of Planck's law for blackbody radiation. The maxima of the curves lie at different spectral positions, depending on the choice of the variable. The dotted line in the wavelength representation (a) gives the position of the maxima according to Wien's displacement law.

on thermal radiation, although it was Max Planck who finally solved the theoretical puzzle of correctly describing blackbody radiation. Nevertheless, Planck received the prize in 1918 for his general concept of the quantum nature of radiation, which had consequences reaching far beyond thermal radiation in the entire field of physics. The third prize in this field was awarded in 2006 to George Smoot and John Mather. They succeeded in recording the most famous blackbody radiation spectrum in astrophysics. This spectrum of cosmic background radiation is thought to resemble a kind of echo of the Big Bang of our Universe. It was recorded in the early 1990s by the NASA satellite COBE. Figure 1.23 depicts the results of this spectrum, which can be fitted with very high accuracy to a Planck function of temperature 2.728(±0.002) K.

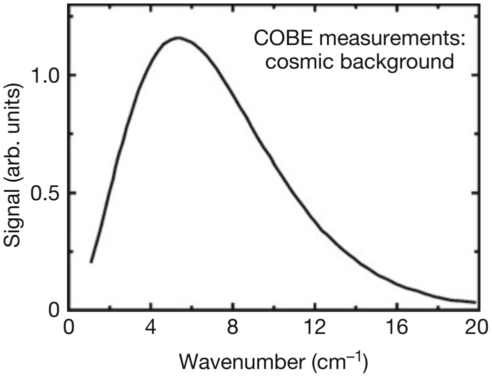

Figure 1.23 Cosmic ray background spectrum measured with COBE satellite. The theoretical fit refers to $T = 2.728\,\mathrm{K}$ (Courtesy NASA).

Usually, only part of the spectrum of blackbody radiation is utilized in IR imaging. In the following two subsections, we deal with the total amount of radiation within certain spectral limits. The Stefan–Boltzmann law deals with the whole spectrum, extending from zero to infinity, whereas band emission is slightly more complicated.

1.3.2.4 **Stefan–Boltzmann Law**

The excitance of a blackbody source is calculated from

$$M(T) = \int_0^\infty M_\lambda(T)\,\mathrm{d}\lambda = \int_0^\infty M_\nu(T)\,\mathrm{d}\nu = \sigma T^4 \tag{1.19}$$

Here, $\sigma = 5.67 \cdot 10^{-8}\,\mathrm{W\,m^{-2}\,K^{-4}}$ denotes the Stefan–Boltzmann constant.

The area under the spectral excitance (spectral emissive power) curve (Figure 1.24) gives the excitance (emissive power), which depends exclusively on the temperature of the blackbody. Hence, the total radiance associated with blackbody radiation is M/π. In astrophysics, the Stefan–Boltzmann law is used to calculate the total energy production of stars, for example, of the sun, from its known surface area and surface temperature.

1.3.2.5 **Band Emission**

In IR imaging, one never detects radiation of the whole spectrum, but rather the radiation in a predefined spectral range, which is determined by the detector and material properties of the optics and the atmosphere. Unfortunately, the integral of Eq. (1.19) does not have analytical solutions for arbitrary values of lower and upper limits. To simplify the results, one defines a blackbody radiation function $F_{(0\to\lambda)}$ as the fraction of blackbody radiation in the interval from 0 to λ, compared

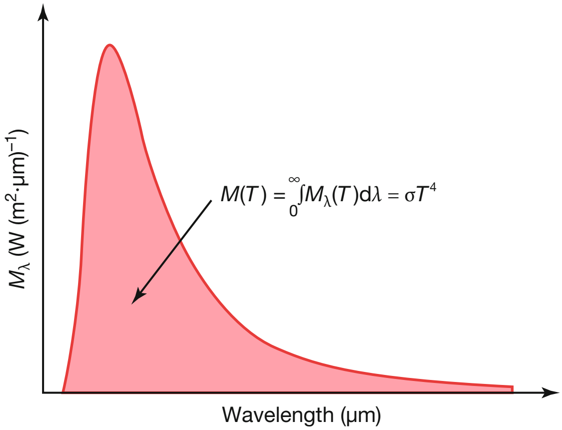

Figure 1.24 Visualization of Stefan–Boltzmann law.

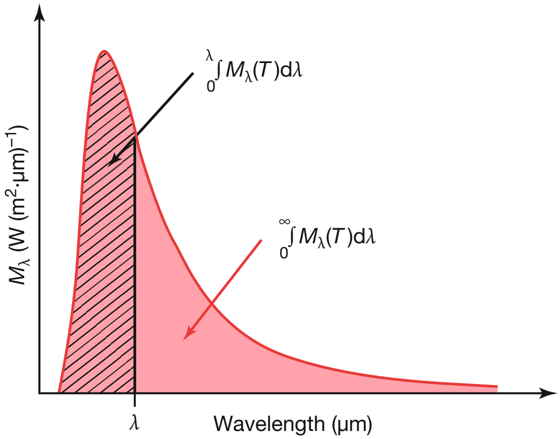

Figure 1.25 Definition of blackbody function: fraction of emitted excitance in spectral band (see text for details).

to the total emission from 0 to ∞ (Figure 1.25):

$$F_{(0\to\lambda)} = \frac{\int_0^\lambda M_\lambda \, \mathrm{d}\lambda}{\int_0^\infty M_\lambda \, \mathrm{d}\lambda} \tag{1.20}$$

We note that, unfortunately, view factors F_{ij} and this blackbody radiation function $F_{(0\to\lambda)}$ are denoted by the same letter F, the only difference being the subscripts. The context of the two quantities is, however, quite different and can be easily guessed from the subscripts. We therefore adopt this general similar notation for both.

The mathematical analysis shows that the integrand only depends on the parameter $\lambda \cdot T$; therefore, integrals can be evaluated numerically for this parameter,

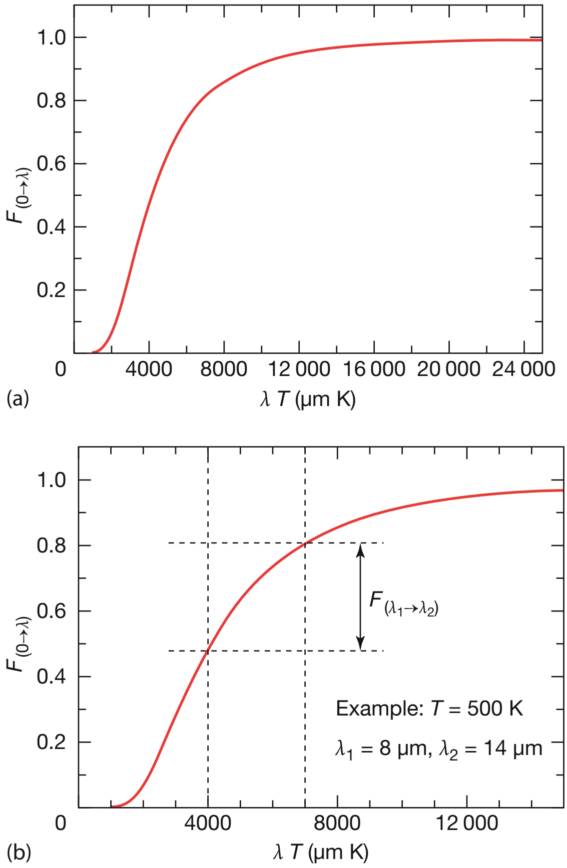

Figure 1.26 Fraction $F_{(0\to\lambda)}$ of excitance of blackbody radiation in wavelength interval 0–λ as function of λT (a) and how it can be used to estimate the fraction $F_{(\lambda_1\to\lambda_2)}$ in a wavelength interval λ_1–λ_2 (b).

and hence, $F_{(0\to\lambda)}$ is tabulated as a function of λT (e.g., [20]). Figure 1.26a depicts the corresponding results.

Obviously, the function $F_{(0\to\lambda)}$ can be easily used to calculate the fraction of blackbody radiation in an arbitrary wavelength interval (λ_1, λ_2):

$$\mathrm{F}_{(\lambda_1\to\lambda_2)} = F_{(0\to\lambda_2)} - F_{(0\to\lambda_1)} \tag{1.21}$$

Figure 1.26b illustrates an example of how quick graphical estimates of $\mathrm{F}_{(\lambda_1\to\lambda_2)}$ are possible for $T = 500$ K and a wavelength range between 8 and 14 μm. In general, a given temperature and wavelength range $\lambda_1 \to \lambda_2$ defines $\lambda \cdot T$ values (vertical broken lines). They intercept the $F(0, \lambda)$ curve at two specific values. Their difference (the distance between the horizontal broken lines) gives $F_{(\lambda_1\to\lambda_2)}$.

We present three examples for object temperatures of 300, 500, and 2800 K (Table 1.5). The fraction of blackbody radiation within the hemisphere of an object of

Table 1.5 Examples of band emission.

Range T	VIS $F_{0.38-0.78\,\mu m}$	SW $F_{0.9-1.7\,\mu m}$	MW $F_{3-5\,\mu m}$	LW $F_{8-14\,\mu m}$
300 K	$\approx 10^{-22}$	$\approx 3 \cdot 10^{-9}$	$\approx 1.3 \cdot 10^{-2}$	$\approx 37.6 \cdot 10^{-2}$
500 K	$\approx 10^{-12}$	$\approx 4 \cdot 10^{-5}$	$\approx 14.9 \cdot 10^{-2}$	$\approx 32.7 \cdot 10^{-2}$
2800 K	$\approx 9.9 \cdot 10^{-2}$	$\approx 43.6 \cdot 10^{-2}$	$\approx 9.2 \cdot 10^{-2}$	$\approx 0.84 \cdot 10^{-2}$

500 K in the LW wavelength interval is approximately 32.7%, but only 14.9% in the MW range. A very hot object, for example, a filament of a light bulb at a temperature of 2800 K, leads to a fraction of approximately 10.0% in the VIS wavelength interval, more than 43% in the SW infrared, and, similarly, approximately 9.2% in the MW range and less than 1% in the LW.

More examples of band emission and detection and further relevant radiometric quantities for complete IR camera systems will be discussed in Section 2.3.2.

1.3.2.6 **Order-of-Magnitude Estimate of Detector Sensitivities of IR Cameras**

Usually, blackbody radiators are used to calibrate IR cameras (Chapter 2). Using the concepts of radiometry and the laws of blackbody radiation, we can estimate the typical order of magnitude for the sensitivity of thermal radiation detectors, that is, how many watts of input power on a detector element are needed to detect, for example, a 1 K temperature difference between two objects. Consider, for example, a blackbody radiator of temperature T_{BB} at a distance of $R = 1$ m in front of a LW IR camera at ambient temperature T_{cam}. The blackbody radiator has a circular shape and diameter $2r_{BB} = 5$ cm, and the front lens of the IR camera should also have a diameter of $2r_{cam} = 5$ cm. The camera detects radiation in the spectral range from 8 to 14 μm.

The total radiant power that is incident on the camera from the object is given by Eq. (1.11):

$$d^2\Phi = L_1 \cos\delta_1 \, dA_1 \, d\Omega_2$$

Here, $\cos\delta_1 \approx 1$, the integral over the blackbody area gives $A_1 = \pi r_{BB}^2$, $L_1 = M_{BB}/\pi$, and $d\Omega_2 = \pi r_{cam}^2/R^2$. Therefore the spectrally integrated radiant power incident on the camera is given by

$$\Phi_{BB\to cam} = M_{BB}(T_{BB}) \frac{r_{BB}^2 \cdot r_{cam}^2 \cdot \pi}{R^2} \tag{1.22}$$

Of course, there is also a similar radiant power emitted from the detector toward the blackbody source; however, the corresponding contributions to Φ due to the detector temperature cancel since we are dealing only with changes in radiant power with object temperature. Therefore, this argument should also hold for all detector types (cooled as well as room-temperature ones).

In the following numerical example, we consider a LW camera system (a similar calculation can also be done for a MW or SW system). The emitted energy flux from a blackbody of temperature T_{BB} in the detector wavelength range is given by

$$\Phi_{\mathrm{BB}\to\mathrm{cam}} = \frac{r_{\mathrm{BB}}^2 \cdot r_{\mathrm{cam}}^2 \cdot \pi}{R^2} \int_{8\,\mu\mathrm{m}}^{14\,\mu\mathrm{m}} M_{\mathrm{BB}}(T_{\mathrm{BB}})\,\mathrm{d}\lambda \tag{1.23}$$

The integral is given by $\mathrm{F}_{(\lambda_1\to\lambda_2)}\sigma T^4$. Any further calculation requires numerical temperature values. For simplicity, let us assume $T_{\mathrm{BB1}} = 303\,\mathrm{K}$, $T_{\mathrm{BB2}} = 302\,\mathrm{K}$, since most detector sensitivities are rated at $T = 30\,°\mathrm{C}$. The integral values can be easily derived from $F_{(\lambda_1\to\lambda_2)}$. For 303 and 302 K, they are very similar (0.378 and 0.377); therefore a single value of 0.38 is assumed.

In this case, the difference in incident radiative power for a variation from 303 to 302 K of the blackbody temperature is given by

$$\Delta\Phi \approx \frac{r_{\mathrm{BB}}^2 \cdot r_{\mathrm{cam}}^2 \cdot \pi}{R^2} \cdot F_{\lambda_1\to\lambda_2} \cdot \sigma\left(T_{\mathrm{BB1}}^4 - T_{\mathrm{BB2}}^4\right) \tag{1.24}$$

Inserting the preceding values, we find $\Delta\Phi/\Delta T = 2.9 \cdot 10^{-6}\,\mathrm{W\,K^{-1}}$ (the total radiative power Φ_{BB} (8–14 μm) due to a blackbody of 303 K is about $2.2 \cdot 10^{-4}\,\mathrm{W}$).

A typical standard lens of an IR camera has an acceptance angle of 24°. At a distance of 1 m, the blackbody source will only occupy an angular diameter of 2.86°. If 24° corresponds to the 320 pixel width of the detector, the blackbody source will be imaged on an angular diameter of about 38 pixels, corresponding to a circular area with about 1140 pixels. This means that each pixel will receive on average a difference in radiant power of $2.54\,\mathrm{nW\,K^{-1}}$.

These numbers are probably still a factor of at least 3 too large since, first, part of the radiation may be attenuated within the atmosphere on its way from the source to the camera (Section 1.5.2), second, the camera optics has a transmission smaller than 100%, and third, the active detector area is only about 50% of the complete pixel area. As a final result, one may expect values on the order of $1\,\mathrm{nW\,K^{-1}}$ for the difference in radiative power received by each detector pixel for a 1 K difference. For a camera with the same 24° optics, but a 640 pixel width of the detector, values would be smaller by a factor of 4. We return to this estimate when discussing detectors and relate it to the noise-equivalent temperatures (Section 2.2.2).

One may gain confidence in this kind of estimate by similarly deriving the solar constant, that is, the total radiant flux onto an area of $1\,\mathrm{m}^2$ outside of the (attenuating) atmosphere of the earth. Starting again with Eq. (1.11) and using $A_1 = \pi r_{\mathrm{sun}}^2$, $L_1 = M_1/\pi$, and $\mathrm{d}\Omega_2 = 1\,\mathrm{m}^2/R_{\mathrm{sun-earth}}^2$, we find

$$\Phi_{\mathrm{solar\ constant}} = M_{\mathrm{BB}}(T_{\mathrm{sun}})\frac{r_{\mathrm{sun}}^2 \cdot 1}{R_{\mathrm{sun-earth}}^2} \tag{1.25}$$

$r_{\mathrm{sun}} = 6.96 \cdot 10^5\,\mathrm{km}$, $R_{\mathrm{sun-earth}} = 149.6 \cdot 10^6\,\mathrm{km}$, and $T = 5800\,\mathrm{K}$ gives $\approx 1390\,\mathrm{W\,m^{-2}}$, which, considering that the sun is not a true blackbody emitter, is a very good approximation for the solar constant.

1.4
Emissivity

1.4.1
Definition

Blackbodies are idealizations, and no real object can emit the maximum thermal radiation at a given temperature. The real emission of thermal radiation from any object can, however, be easily computed by multiplying the blackbody radiation by a quantity that describes the influence of the object under study, the emissivity ε. In other words: *the emissivity of an object is* the ratio of the amount of radiation actually emitted from the surface to that emitted by a blackbody at the same temperature.

Differing definitions of emissivity are possible (Eq. 1.26), depending on which quantity is used to describe the radiation. In radiometry, four definitions are used based on radiance L and excitance M. The relevant radiometric quantities are (i) spectral directional emissivity, (ii) spectral hemispherical emissivity, (iii) total directional emissivity, and (iv) total hemispherical emissivity.

They are defined as follows:
Spectral directional emissivity (L, spectral radiance)

$$\varepsilon(\lambda, \delta, \varphi, T) = \frac{L(\lambda, \delta, \varphi, T)}{L_{\mathrm{BB}}(\lambda, T)} \tag{1.26a}$$

Spectral hemispherical emissivity, directionally averaged (M, spectral excitance):

$$\varepsilon(\lambda, T) = \frac{M(\lambda, T)}{M_{\mathrm{BB}}(\lambda, T)} \quad \text{with} \quad M = \int\limits_{\text{hemisphere}} L \cos\delta \, \mathrm{d}\Omega \tag{1.26b}$$

Total directional emissivity (wavelength averaged):

$$\varepsilon(\delta, \varphi, T) = \frac{L(\delta, \varphi, T)}{L_{\mathrm{BB}}(T)} \tag{1.26c}$$

Total hemispherical emissivity (wavelength and direction averaged):

$$\varepsilon(T) = \frac{M(T)}{M_{\mathrm{BB}}(T)} = \frac{M(T)}{\sigma T^4} \tag{1.26d}$$

Unfortunately, none of these definitions refers to the required conditions for practical IR imaging, where one first usually deals with objects that are observed near normal incidence or at small angles. Hence, a directional quantity, averaged over the desired angular range, is needed. Second, IR cameras operate at predefined wavelength ranges. Obviously, the required emissivity needs to be averaged over the desired wavelength range. Symbolically, we need an emissivity ε ($\Delta\lambda$,

$\Delta\Omega$, T). In practice, mostly the directional, near-normal emissivity is used, which is furthermore assumed to be independent of wavelength and temperature. We will return to the consequences of this for practical work at the end of this chapter.

1.4.2
Classification of Objects according to Emissivity

From the definition of emissivity it is clear that $0 \leq \varepsilon \leq 1$. Figure 1.27 illustrates spectral hemispherical emissivities and corresponding spectra of emissions of thermal radiation at given temperatures first for a blackbody, second for a so-called gray body with constant ε value, that is, ε is independent of wavelength, and third for a so-called selective emitter where ε varies as a function of wavelength.

For most practical applications in thermography, ε is independant of wavelength resembling a gray body. Whenever substances are studied that have absorption and emission bands in the thermal IR spectral range, for example, gases or plastic foils, one must deal with selective emitters, which may complicate the quantitative analysis.

1.4.3
Emissivity and Kirchhoff's Law

The emissivity can be guessed from *Kirchhoff's law* (e.g., [20, 31]), which states that the amount of radiation absorbed by any object is equal to the amount of radiation that is emitted by this object. This is usually written in the form

$$\varepsilon = \alpha \tag{1.27}$$

where ε and the so-called absorptivity α denote the fraction of radiation that is either emitted or absorbed. Energy conservation requires that any radiation (Φ_0) incident on any object must be reflected (Φ_R) (whether it is directed according to the law of reflection or diffusely scattered from rough surfaces), transmitted (Φ_T) through the object, or absorbed (Φ_A) within the object:

$$\Phi_0 = \Phi_\mathrm{R} + \Phi_\mathrm{T} + \Phi_\mathrm{A} \tag{1.28a}$$

Considering the fraction of the incident radiation (e.g., in excitance or radiance), this law reads

$$1 = R + T + \alpha \tag{1.28b}$$

where R and T denote the fraction of radiation that is either reflected or transmitted. Combining Eqs. (1.27) and (1.28b) allows for estimates of the emissivity ε. The simplest examples are opaque solids with $T = 0$. In this case,

$$\varepsilon = 1 - R \tag{1.29}$$

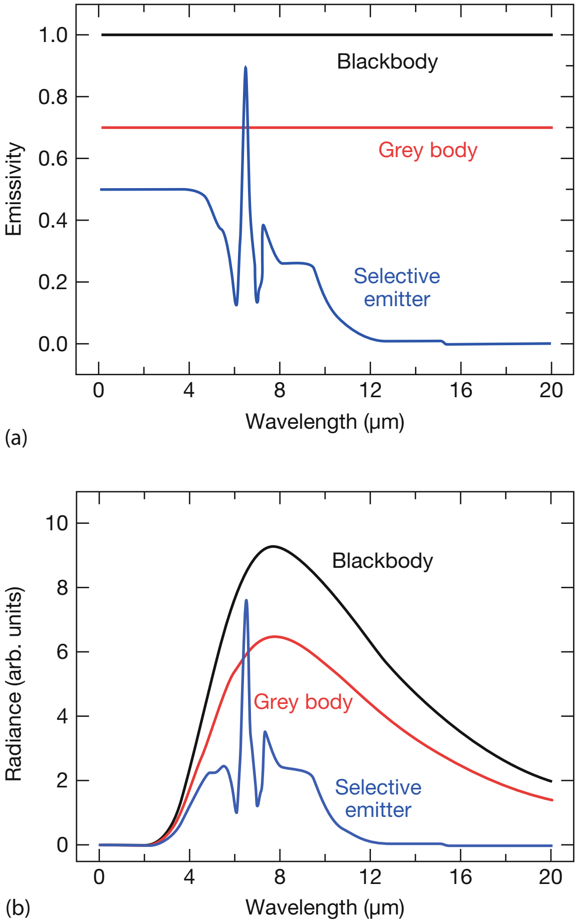

Figure 1.27 Spectral hemispherical emissivities (a) and corresponding thermal radiation (b) spectra for blackbodies, gray bodies, and arbitrary selective emitters.

that is, the emissivity follows directly from known values for the total reflectivity. It is important to note that R includes not only directed reflectivity (Figure 1.9), as is usual for polished surfaces, but also diffuse reflectivity (Figure 1.11), which additionally occurs for rough surfaces. Equation 1.29 makes it possible to guess ε values. For example, glass, which is more or less opaque in the IR with reflectivities in the IR range of a small percentage, will have emissivities of $\varepsilon > 0.95$. In contrast, metals with high reflectivities above 90% will have emissivities below 0.1. Some very well-polished metal surfaces can have the lowest possible emissivities of order 0.01, which practically render IR imaging impossible.

Table 1.6 Parameters that affect emissivity ε.

Intrinsic object properties	Variations due to other parameters
Material (e.g., metal, insulator)	Regular geometry (e.g., grooves, cavities)
Surface structure (rough/polished)	Wavelength (e.g., LW/MW/SW)
Observation direction (viewing angle)	Temperature (e.g., phase changes)

1.4.4
Parameters Affecting Emissivity Values

As a material property, the emissivity depends on the following parameters (Table 1.6).

1.4.4.1 Material

The major parameter is the kind of material. Depending on the measurement techniques used, averages are taken over certain angular and spectral ranges as is useful in thermography. In a simplified classification, one can separately discuss nonmetals and metals, because – fortunately – most nonmetallic materials that are needed for practical thermography applications like skin, paper, paints, stones, glass, and so on are gray emitters and have fairly high emissivity values of above 0.8. In contrast, metals and, in particular, polished metals pose problems owing to their often very low emissivities with values below 0.2.

1.4.4.2 Irregular Surface Structure

For any given material, the emissivity may vary considerably as a result of the surface structure. This leads to the unfavorable situation where, for the same material, many different values for emissivity are reported. This effect is most pronounced for metals. Whereas some polished metals can reach values of ε as low as 0.02, the emissivity can be much larger and even reach values above 0.8 if the surfaces are roughened. The highest values for originally metallic parts are found where the surfaces are modified via oxidation/corrosion over the course of time. Imagine, for example, a metallic bolt of an electrical connection that is operated for many years while being exposed to the elements, oxygen from the air, water from rain, and so on. A value as high as 0.78 has been reported for strongly oxidized Cu and 0.90 for some steel compounds owing to such chemical modifications of the surface. This factor is most important for any inspection of, for example, bolts, nuts, electrical clamps, and similar parts in electrical components since a thermographer must have criteria for determining whether a components fails or passes. Therefore, a quantitative analysis is necessary, that is, one must know the exact temperature difference of these components compared to their surroundings of known emissivity, and the measured temperature will very strongly depend on the actual value of emissivity.

To illustrate the effect of material as well as surface structure on emissivity, we used a so-called Leslie cube. This is a hollow copper metal cube (with a side length of around 10 cm) whose side faces are treated in different ways. One side is covered with a white paint, one with black paint, one is not covered but just resembles polished copper, and the fourth side consists of roughened copper.

The cube is placed on some Styrofoam as thermal insulation and then filled with hot water. Owing to the good thermal conductivity of the metal, all the side faces of the cube will quickly have the same temperature. The emission of thermal radiation by each side face can easily be analyzed with an IR camera. Figure 1.28 depicts some results (for details of how temperatures are calculated within the used LW camera, see Section 2.3).

For the two painted side faces, the chosen ε value of 0.96 produced more or less the correct temperature (as can be verified by a contact probe). The rough copper surface had much less emission of thermal radiation and the polished copper surface even less. Using the camera software, one can adjust the emissivity values such that the copper surfaces also give the correct value of the wall temperatures. For our example we find emissivities of the polished copper surface to be around 0.03 and of the roughened copper surface to be about 0.11.

Figure 1.28 illustrates one way of finding correct values for emissivities: measure object temperatures with a contact probe, then adjust the emissivity in the camera until the camera shows the correct temperature reading (assuming, of course, that all other camera parameters are chosen correctly; see Section 2.3).

1.4.4.3 **Viewing Angle**

We have defined *emissivity* as the ratio of the amount of radiation actually emitted from a surface to that emitted by a blackbody at the same temperature. In particular, the spectral directional emissivity (Eq. 1.26a) is the ratio of the radiance of the radiation, emitted at given wavelength λ and in a direction defined by the two angles δ and φ (Figure 1.15), to the radiance emitted by a blackbody at the same temperature and wavelength.

Blackbodies behave like perfect isotropic emitters, that is, the radiance of any emitted radiation is independent of the direction in which it is emitted (compare the discussion of Lambertian radiators, Figure 1.17). Unfortunately, any real surface shows a different behavior, that is, its radiance shows variations depending on the direction of emission. This is schematically illustrated in Figure 1.29. In addition to the fact that any real surface emits less radiation than a blackbody at the same temperature (left side: red solid line), the radiance from a real gray object usually also depends on the angle of emission. In Figure 1.29, this manifests itself as a deviation between the real radiance (right side: solid blue line) and the Lambertian behavior of a gray object (right side: red broken line). Azimuthal symmetry is assumed in Figure 1.29, hence only the angle δ is shown.

This behavior can strongly affect any contactless temperature measurement using IR cameras, since an object that is observed from a direction normal to its surface ($\delta = 0°$) will emit more radiation than when observed at oblique angles. This means that the emissivity depends on the angle of observation with respect

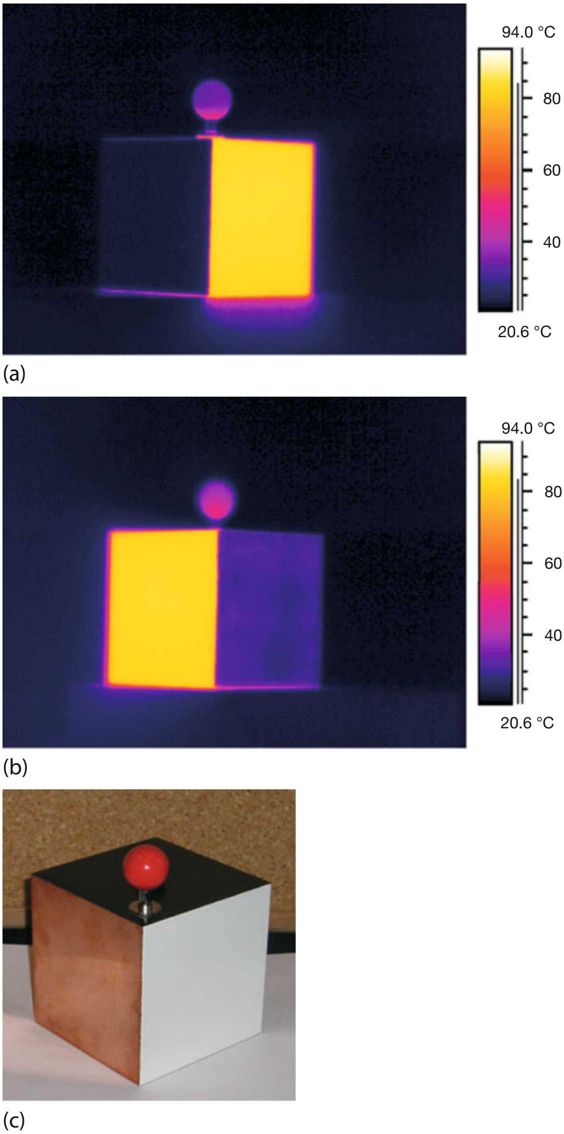

Figure 1.28 (a,b) Leslie cube, filled with hot water and viewed at an angle of 45° with respect to the side faces. The emissivity of the whole image was set to $\varepsilon = 0.96$, resulting in the following temperature readings (left to right). (a) Polished copper ($T = 22.6$ °C), white paint ($T = 84.3$ °C). (b) Black paint ($T = 83.4$ °C), roughened copper ($T = 29.3$ °C). The knob on top is a stirrer for reaching thermal equilibrium faster. (c) Visible image of such a cube.

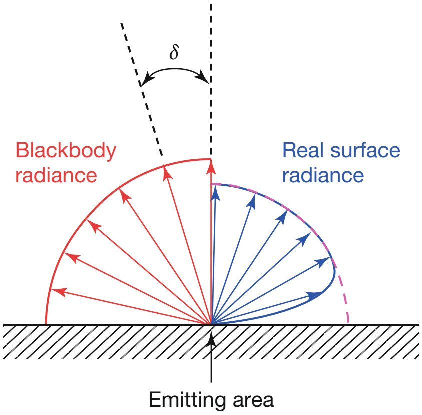

Figure 1.29 Schematic illustration of angle-independent radiance for blackbodies (left/red) and directionally dependent radiance of real surfaces (right side/blue).

to the surface normal. Fortunately, many measurements have been performed and a wide variety of materials has been studied in relation to their directional emissivities. A typical setup for such an experiment is shown in Figure 1.30a.

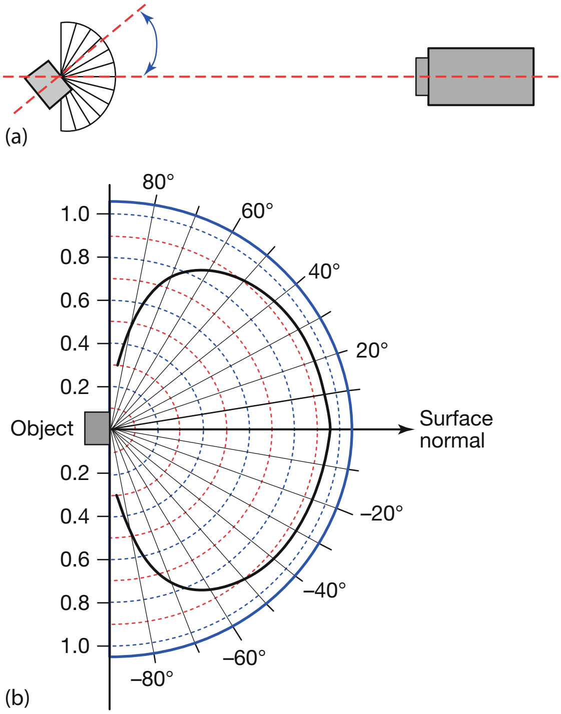

Figure 1.30 A Leslie cube with a painted side face (high emissivity) was used as object to measure the directional emissivity (averaged in the LW range) as a function of the viewing angle from 0 to 85° with respect to the surface normal. The cube was rotated with respect to the camera (a) and temperatures recorded. (b) The emissivity as a function of the viewing angle was then found by varying the emissivity in the camera software until the temperature readings of the rotated side face gave correct values.

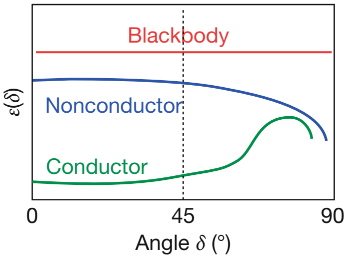

Figure 1.31 Overview of typical directional dependence of emissivities of nonconductors and conductor with respect to blackbodies.

An angular scale from 0 to 180° is attached to a table with 90° pointing to the IR camera. The (warm or hot) object to be studied is placed on top of the scale with its surface normal facing 90°, that is, the IR camera. Then measurements of the emitted radiation are recorded as a function of the angle while rotating the object. In Figure 1.30b, we show an example for the white paint side of a Leslie cube that was filled with hot water. The actual surface temperature can be measured by contact thermometry, which gives the correct value of the normal-direction emissivity. The angle-dependent values are found by changing the emissivity value in the camera software until the real temperature is shown (for details of signal processing in the camera, see Chapter 2). Another experiment on $\varepsilon(\delta)$ is discussed in Section 5.5.5.

Figure 1.30b nicely demonstrates an effect that fortunately holds for nearly all practically important surfaces: the emissivity is nearly constant from the normal direction 0° to at least 40° or 45°. The behavior at larger angles differs for metallic and nonmetallic materials (Figure 1.31). For nonconductors, one observes a characteristic drop of ε for larger angles, whereas metallic surfaces usually show first an increase toward larger angles before decreasing again at grazing incidence [7, 20, 32].

Neglecting diffuse reflections for the moment, this behavior can already be understood from the characteristic properties of directed reflection for different polarizations of radiation. Figure 1.32 schematically depicts plots for the portion R of directly reflected radiation in the IR spectral region for nonmetals and metals with polished surfaces (similar to Figure 1.12) as a function of the angle of incidence.

The directed reflectivity depends on the polarization of the radiation. Unpolarized radiation is characterized by the broken line, which represents the average of both polarizations. Obviously, the reflectivity for nonconductors exhibits a monotonous increase with angle of incidence, whereas metals show first an decrease before increasing again at larger angles. This characteristic feature (which can be explained theoretically by the Fresnel equations) explains the observed angular plots of emissivity, since $\varepsilon = 1 - R$ for opaque materials according to Eq. (1.29). However, we also note that most metallic objects have rough surfaces, which induce additional contributions to the emissivity and which can also induce changes in the observed angular distributions.

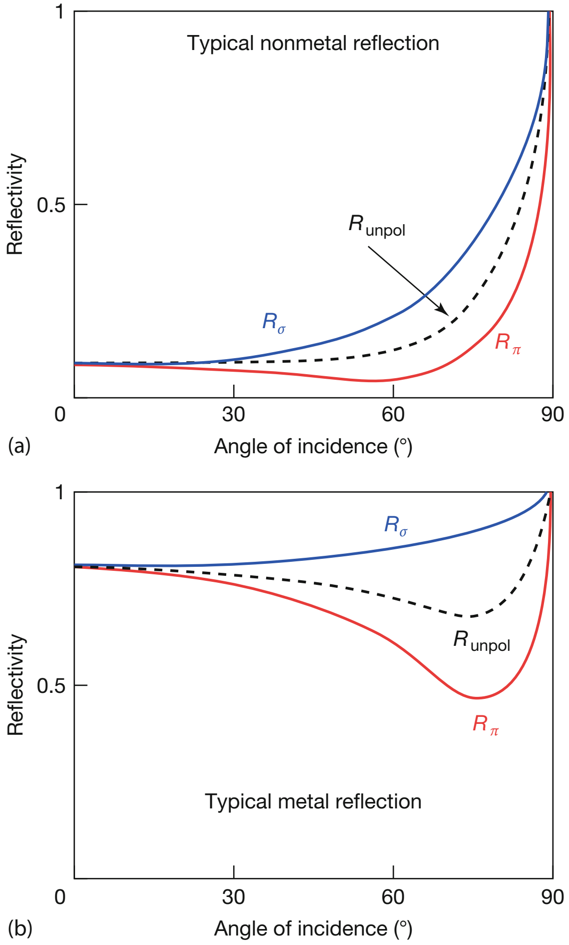

Figure 1.32 Schematic plot of reflectivities of polarized and unpolarized IR radiation of metals (a) and nonmetals (b) as a function of the angle of incidence.

1.4.4.4 **Regular Geometry Effects**

The geometry of a surface is related to the surface structure; however, in contrast to irregular surface roughness (Section 1.4.4.2), here we refer to well-defined geometric structures like grooves, which are used to systematically change emissivity. Cavities are discussed in detail separately in the context of blackbody calibration sources (Section 1.4.6).

Consider a polished metal surface (of, for example, $\varepsilon_{\text{normal}} = 0.04$) with a well-defined surface structure in the form of grooves of a given slope angle (Figure 1.33, here with an apex angle of 60°).

The grooves enhance the emissivity in the vertical direction, that is, perpendicular to the macroscopic surface, as can be understood from the following argument.

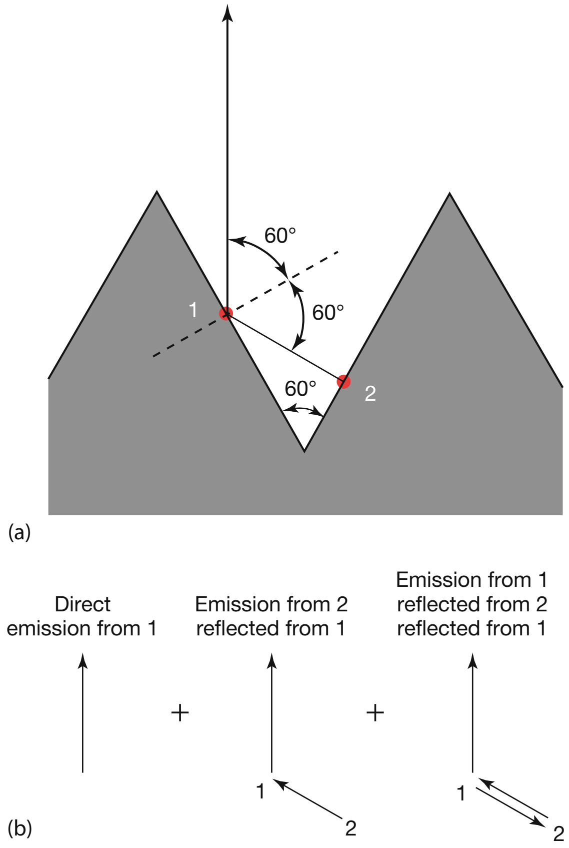
60°
1
60°
60°
2
(a)
Direct emission from 1
+
Emission from 2 reflected from 1
+
Emission from 1 reflected from 2 reflected from 1
1
2
1
2
(b)

Figure 1.33 V-groove model of a polished metal surface with low emissivity (a). The macroscopic surface is horizontal. There are three contributions to radiance and, hence, emissivity for the groove surface in the vertical direction (b).

Radiation that is emitted from spot 1 in a direction normal to the macroscopic groove surface is composed of three radiance contributions:

1. Direct radiation emitted from spot 1: this contribution is characterized by $\varepsilon(60^\circ)$ with regard to the real groove surface;
2. Radiation emitted from spot 2, which is then reflected from spot 1 in the normal direction: this contribution is characterized by $\varepsilon(0^\circ) \cdot R(60^\circ) = \varepsilon(0^\circ) \cdot [1 - \varepsilon(60^\circ)]$ with regard to the groove surface;
3. Radiation emitted from spot 1 in direction of spot 2, reflected back from spot 2 to spot 1, and then reflected in the normal direction: this contribution is characterized by $\varepsilon(60^\circ) \cdot R(0^\circ) \cdot R(60^\circ) = \varepsilon(60^\circ) \cdot [1 - \varepsilon(0^\circ)] \cdot [1 - \varepsilon(60^\circ)]$ with regard to the groove surface.

Adding up these radiance contributions and dividing by the blackbody radiance, one can easily see that the normal emissivity of the grooved surface has increased.

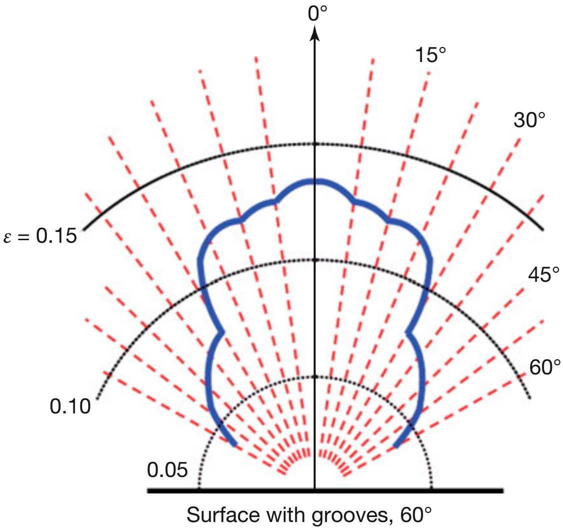

Figure 1.34 Polar diagram for expected dependence of emissivity as a function of observation angle for 60° V-groove model of a polished metal surface with flat surface emissivity of 0.04 (after [33]).

For a numerical estimate, we assume a polished surface emissivity of $\varepsilon(0°) = 0.04$ and $\varepsilon(60°) = 0.05$. In this case, the total normal emissivity of the grooved surface $\varepsilon_{\text{total,normal}} = 0.04 + 0.04 \cdot (1 - 0.05) + 0.05 \cdot (1 - 0.04) \cdot (1 - 0.05) = 0.124$, that is, the emissivity has increased by a factor of nearly 3 owing to this surface structure. The basic idea behind this enhancement explains why any rough surface has a higher emissivity than polished flat surfaces.

Regular surface structures often lead to nonuniform angular distributions of emissivity. Repeating the preceding calculation for different emission angles [33] with respect to the macroscopic groove surface (Figure 1.34) reveals strong variations of emissivity as a function of observation angles.

1.4.4.5 Wavelength

As is well known in optics, material properties usually depend on wavelength. Consider, for example, the reflectivity of the noble metals gold (Au), silver (Ag), and copper (Cu). Au and Cu have electronic interband transitions in the VIS range, which give rise to the wavelength-dependent reflectivities, finally resulting in the characteristic golden-yellow as well as red-brown color of these metals. Reflectivity is strongly related to the emissivity of materials, so any wavelength dependence on reflectivity will also show up in emissivity. Detailed theoretical arguments are beyond the scope of this book, so we refer the interested reader to the corresponding literature [20, 31, 34, 35] and give schematic diagrams of how the emissivities of certain materials change in general (Figure 1.35).

As can be seen from Figure 1.35, the emissivity of metals usually decreases with wavelength (an effect opposite to that of reflectance), whereas oxides and other

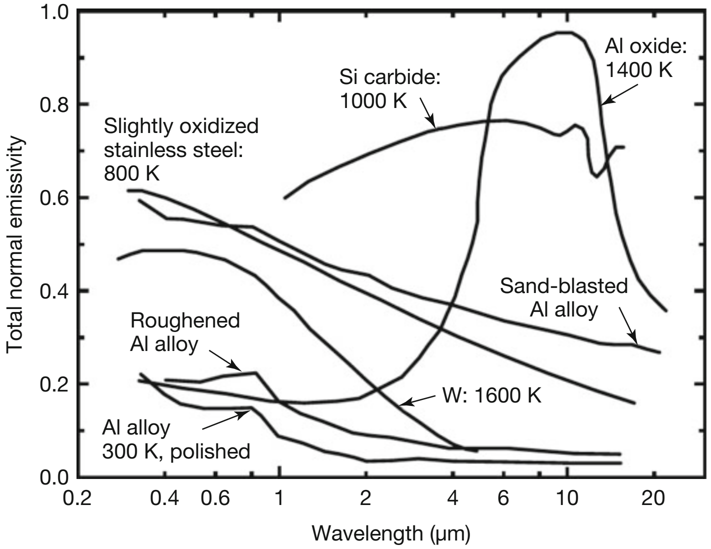

Figure 1.35 Examples of wavelength dependence of normal emissivity for different materials (after [20, 31]).

nonmetals can show increases as well. The examples of aluminum alloys clearly emphasize the effect that increasing surface roughness from polished surfaces to those roughened by grid paper or finally being sand blasted leads to drastic increases of emissivity. Whenever dealing with substances that have wavelength-dependent emissivity, one must first determine whether emissivities are constant in the IR camera spectral range being used. If not, it is advisable to use narrowband filters or another wavelength band for thermography where emissivities are nearly constant. If this is not possible, one must be aware that any quantitative analysis will be much more complicated since signal evaluation must then use the known variation of emissivity.

We finally mention that in addition to these slowly varying emissivities as a function of wavelength, there are several examples of selective absorbers and emitters such as plastic foils or many gaseous species. These have special applications in IR imaging and are treated in detail in other chapters (Chapter 8, Section 10.8).

1.4.4.6 **Temperature**

Material properties usually change with temperature, and it is no surprise that this also holds for emissivity. Figure 1.36 gives some examples. Some materials show fairly strong variations, so it may be necessary for practical purposes to know whether the temperature of a process under IR observation will remain within a certain temperature interval such that the emissivity for this study can be considered constant. In addition, if the literature values for emissivity are used, one must know the corresponding temperatures. Particular care should be taken when

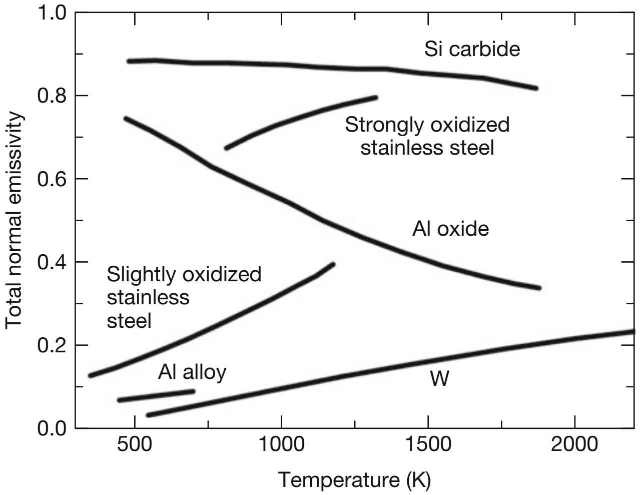

Figure 1.36 Examples of temperature dependence of emissivity for different materials (after [20, 31]).

studying materials that undergo phase changes, for example, when observing the melting of metals.

1.4.4.7 **Conclusion**

The material property of emissivity, which is essential in IR imaging, depends on many parameters. Accurate temperature measurement with thermography requires precise knowledge of this quantity. Several sets of tables of emissivities for various materials are available in books [1, 10, 23, 31] and from the manufacturers of related camera systems. Unfortunately, these cannot be used without a word of caution. Measurements always refer to specific experimental conditions, for example, temperature range, wavelength range (LW, MW, SW), or angles (directional or hemispherical measurement). These three factors are usually not critical since, for most (not all) practical cases in thermography, wavelength and temperature dependencies are not relevant. Furthermore, most practical emitters show directional dependencies only for observation angles larger than 45° with respect to the surface normal. This means that we mostly deal with gray objects of nearly Lambertian behavior whose emissivity can be guessed within a certain range of accuracy.

Unfortunately, however, metallic objects pose severe problems. Polished metals have very small values of emissivity. Small variations in ε can cause large errors in temperature; therefore, the smaller the emissivity, the more precisely must its value be determined (see also discussion in Section 2.3.3). This poses serious challenges since polished metals have ε values that are quite different compared to roughened or oxidized ones. In electrical inspections, one may often deal with highly oxidized or corroded metallic parts. In such cases, guessing the emissivity from tables may lead to results that are quite erroneous [36, 37]. In addition, the metal industry (e.g., aluminum or steel production) may also need to consider variations of emissivity with temperature.

1.4.5
Techniques to Measure/Guess Emissivities for Practical Work

Owing to the problems in guessing accurate values for emissivity, it is common practice to measure ε directly. This can be done in various ways; some of those often used are listed in Table 1.7. In all cases, by "emissivities" we mean directional near normal emissivities, which are integrated over the selected wavelength range of the IR camera.

The easiest method is to attach tape or paint of known emissivity to the object under study. In the analysis, the surface temperatures of the tape or paint follow from their known ε. Assuming good thermal contact and waiting until thermal equilibrium is established, adjacent surface temperatures of the object are assumed to be the same; hence, the object emissivity is found by varying ε in the camera software until the object temperature is equal to known tape surface temperature. The accuracy of this method depends on the accuracy of the known emissivity. Owing to the lab measurements, they are related to the temperature accuracy of the contact probe (thermocouple).

One may also directly measure several spot surface temperatures with thermocouples and use them to calibrate the IR images. In this case, one must make sure that good thermal contact is achieved, thermal equilibrium is established, and – which is crucial for small objects – that the thermocouple itself does not change the object temperature via heat conduction. A useful condition is that the heat capacity of the thermocouple must be much smaller than that of the object. This method need not, but may, be more time consuming if objects made of many

Table 1.7 Some practical methods of adjusting normal emissivities in thermography.

Method	Tape	Paint, correction fluid, and so on	Contact thermometer	Hole drilling
Equipment needed	Tape	Paint	Thermocouple	Electric drill
Idea behind method	Known emissivity from lab experiments, calibrated with contact probe (usually thermocouple)		Spot measurements with contact probe	Known increased emissivity due to cavity effect
Advantage/ disadvantage	Nondestructive, removable, problem of good thermal contact for very rough surfaces	Nondestructive, problem in removing paint, works also for rough surfaces	Nondestructive, may be time consuming	Destructive, independent of object surface structure

different materials are investigated. Also, one must make sure that no thermal reflections are present in IR images (Section 3.4) since these would introduce errors into the analysis.

Sometimes, in building thermography, one may have the chance to drill a hole in the wall, thereby creating a cavity with very high emissivity values that can then be used in images for a correct temperature reading. In a manner similar to the tape method, emissivity can then be estimated for adjacent regions.

1.4.6
Blackbody Radiators: Emissivity Standards for Calibration Purposes

In IR imaging, all commercial camera manufacturers must calibrate their cameras such that the user will be able to obtain temperature readings in IR images whenever the proper emissivity is chosen. In addition, some research cameras must be calibrated by the users themselves.

Calibration is usually done by observing the best available experimental approximations to blackbody radiation, so-called blackbody calibration standards. The national institutes that are responsible for standards (e.g., in the USA, NIST, in Germany, PTB) have developed standards (e.g., $\varepsilon > 0.9996$ in the form of heat pipe cavity-type blackbodies [38]). Commercial blackbody radiators, in particular, large area instruments, are used as secondary standards by IR camera manufacturers and other users in laboratory experiments (Figure 1.37). They can be tracked back to the primary cavity-type standards but usually have smaller emissivities of around $\varepsilon = 0.98$. They are made of high-emissivity materials with additional surface structures (e.g., pyramids) whose surfaces are temperature stabilized.

The principle for achieving high emissivities for primary standards is based on Kirchhoff's law (Eq. (1.27)). One needs to construct an object that has high absorptivity. As mentioned earlier, when introducing blackbody radiation, an open window of a distant building usually looks very black. The reason for this is illustrated in Figure 1.38.

Radiation is directed into the hole of an otherwise opaque cavity whose walls are stabilized at a given temperature. There is a certain absorption per interaction with the wall, and the radiation will be gradually attenuated. Usually, the inner surface is not polished, that is, it is not a reflecting surface according to the law of reflection (Eq. (1.2)) but rather it is diffusely scattering (Figure 1.11). If the hole is small compared to the total surface area of the cavity, the radiation will undergo many absorption losses before there is a chance of its leaving the cavity again through the entrance hole. For example, if $\alpha = 0.5$ (absorptivity of 50% per interaction), the radiation will be attenuated after 10 reflections already to $(0.5)^{10}$, which is less than 10^{-3}. This means that the overall absorptivity is larger than 99.9%, and therefore the corresponding emissivity has the same value.

The same thing happens, of course, to any radiation that is thermally emitted within the cavity. It interacts with the inner walls many times before leaving the cavity through the only hole. This is why such cavities are considered to be perfect emitters of thermal radiation. As a matter of fact, attempts to explain the results of

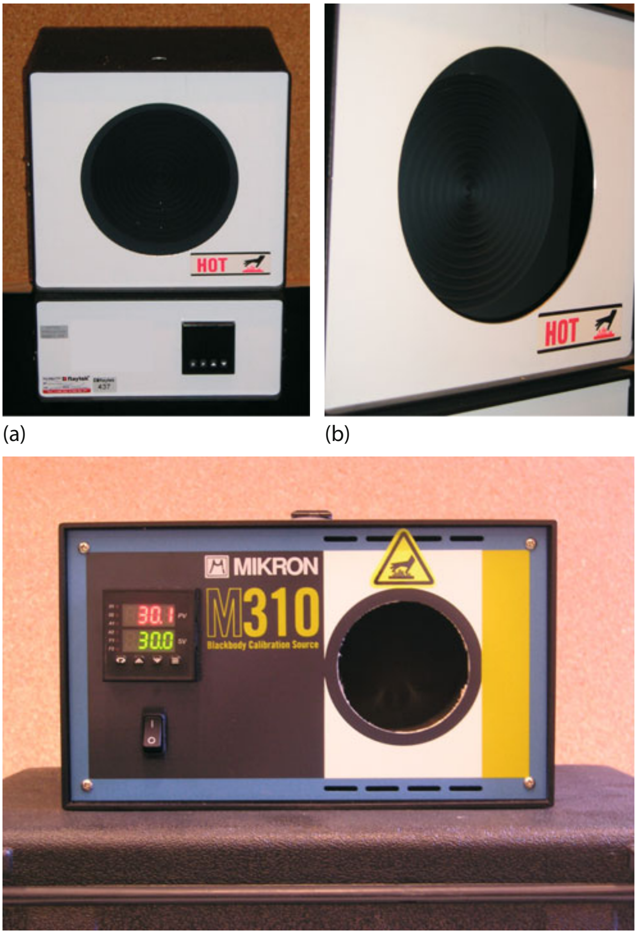

(a) (b)

(c)

Figure 1.37 Photograph of two commercial secondary standard blackbody source with $\varepsilon = 0.98$. (a,b) With circular symmetry structures, which are visible at grazing incidence. (c) Without structures.

very accurate cavity measurements of thermal radiation led Planck to his famous radiation law.

Many different geometries and sizes of cavities and holes have been studied (Figure 1.39) for a variety of different materials over the years [1, 31]. The simple geometries of sphere and cylinder are usually replaced by either conical shapes or at least cylinders with conical end faces. For high-emissivity sources, the inner surfaces are rough and of materials with high emissivity (see also Section 5.5.4).

It is now easy to generate very high emissivities, but it has also been shown that, using low ε wall materials, it is possible to design cavities with intermediate emissivity values in the range 0.3–0.7 [39]. As an example, Figure 1.40a shows the

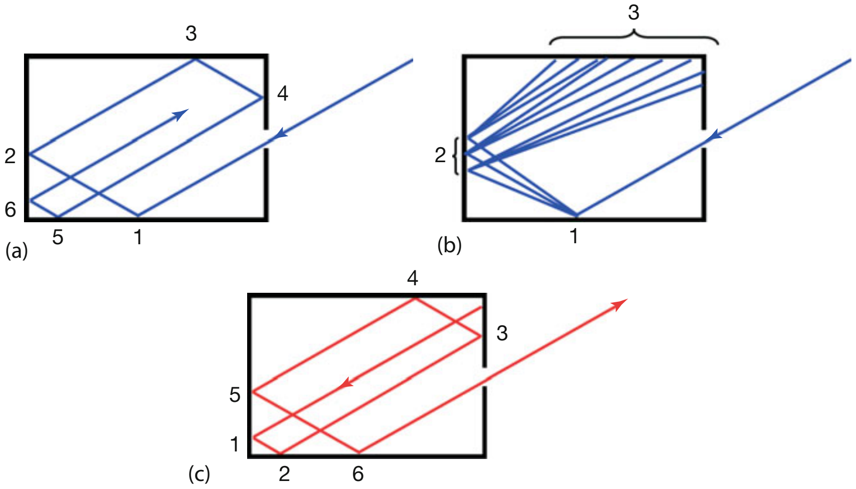

Figure 1.38 A cavity with a hole can trap incident radiation (blue) even if the absorption per interaction with the surface is small since radiation undergoes many reflections before there is a chance of being emitted again (a). If the inner surfaces are diffusely reflecting (b), the effect is even stronger. Similarly, any thermal radiation emitted from some spot on the wall (c, red) will be in thermal equilibrium before leaving the opening.

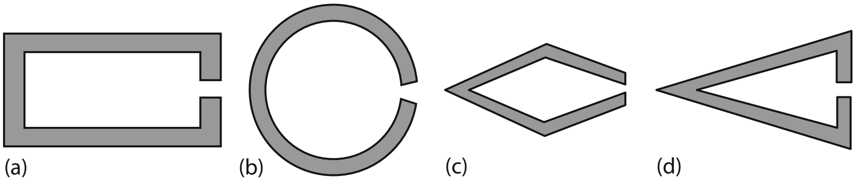

Figure 1.39 Various geometries for cavity blackbody radiators.

geometry of a polished metal cavity. Figure 1.40b depicts the resulting theoretical emissivity as a function of material emissivity, and Figure 1.40c demonstrates the effect of cavity geometry on the resulting emissivity. The latter result is easy to understand: the larger the inner surface area, the lower the chance of radiation hitting the small-opening hole, hence the larger the emissivity.

Polished wall materials within well-defined geometries do, however, have the side effect of angular dependence of emissivity. As illustrated in Figure 1.34, there are specific angles at which more (or less) radiation is emitted with regard to other angles. These so-called geometrical resonances are illustrated in Figure 1.41, which depicts IR measurement results from the heated cavity shown in Figure 1.40 for $L = 5\,\text{mm}$.

In conclusion, for cavity blackbody sources, whenever the inner surfaces are made of polished metals, it may be possible to obtain low and medium emissivities in the range 0.2–0.6; however, the directional character of emissivity usually still shows up, that is, the cavities do not yet resemble Lambertian sources. The

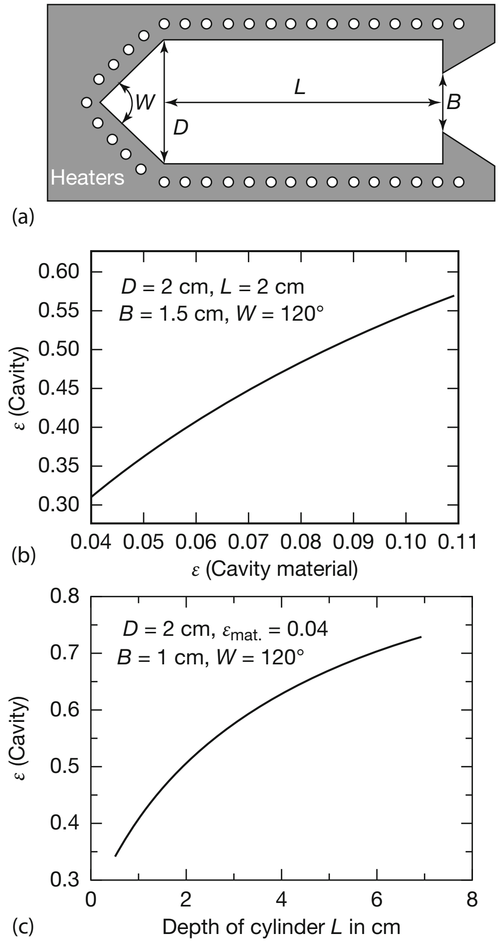

Figure 1.40 (a–c) Design of a blackbody radiator cavity and theoretical expectations for cavity emissivities as function of wall material and geometry.

best high-emissivity Lambertian blackbody sources are made of cavities with wall materials of high emissivity in the first place, perhaps additionally roughened.

Finally, a rather recent new development of a large area, high-emissivity blackbody was developed for in-flight blackbody calibration of an interferometer on research airplanes. It consists of 49 aluminum pyramids having a Nextel coating with $\varepsilon > 0.967$ from 5 to 12 μm and covering an area of $126 \cdot 126\,\text{mm}^2$. Three different pyramid base types – all with steep angles of around 80° – were arranged to form light traps. In this way, a large area blackbody with an emissivity exceeding 0.9996 could be designed (Figure 1.42) [40].

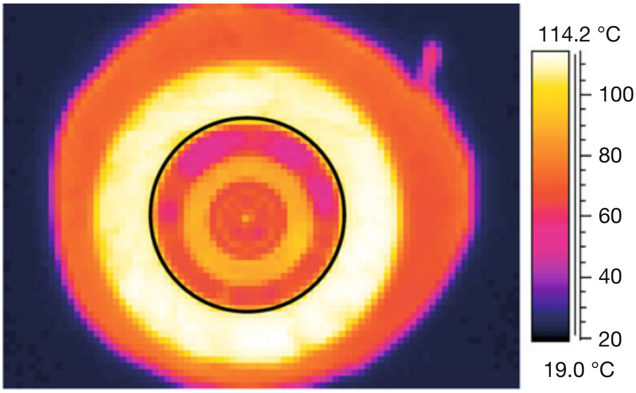

Figure 1.41 Geometrical resonances in emissivity of metallic cavities. The black circle indicates the size of the aperture.

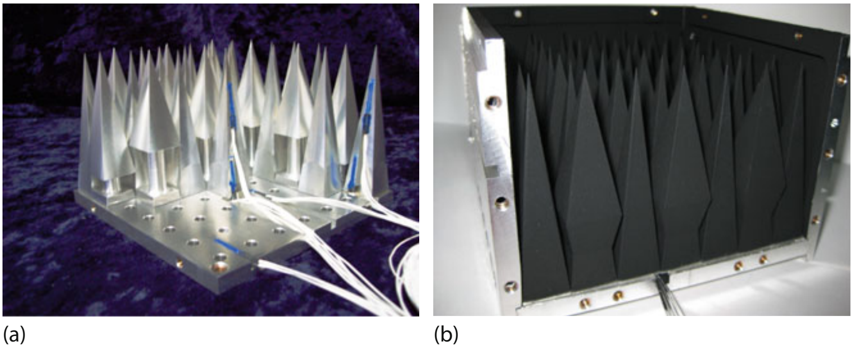
(a)
(b)

Figure 1.42 Pyramid-based blackbody calibration source for airborne instruments (after [40]. Image courtesy F. Olschewski).

1.5
Optical Material Properties in IR

In any practical contactless temperature measurement with either pyrometry or IR imaging, the radiation from an object under study must reach the detector. However, this requires the IR radiation to pass through the space between object surface and detector within the camera housing (Figure 1.43). The radiation is usually attenuated on this path since it must pass through various kinds of matter, usually at least the gaseous atmosphere and the solid focusing optics materials. Additional solid materials, for example protection windows, can lead to additional attenuation and thermal reflections and – if at elevated temperatures – to additional emission of thermal radiation, which may contribute to the object signal. Certain special applications may include additional matter between object and detector, such as other gases, liquids, or additional solid filters.

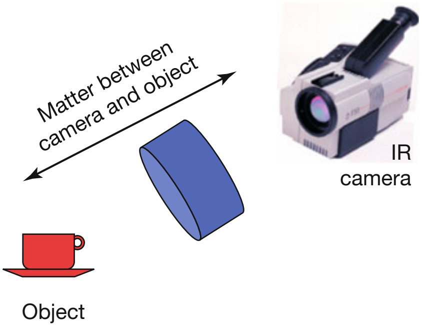

Figure 1.43 Typical setup for thermography. The object is observed through matter, which can be a gas, a liquid, or a solid material, so it can become attenuated. The same holds for the camera optics in front of the detector.

Here, we summarize optical material properties due to the atmosphere and common solid window or lens materials in the thermal IR spectral range. Additional materials, for example special gases or plastics, are dealt with separately in Chapter 8 and Section 10.8. More information can be found in the literature [1, 4, 12, 13, 17, 31, 41–43].

1.5.1
Attenuation of IR Radiation while Passing through Matter

The most common case is the study of objects already present in the atmosphere, that is, objects and the camera already immersed in a gas. IR radiation is emitted from the object surface into the atmosphere. Once the scattering, absorption, or emission processes within the gas are known, one may calculate the modification of the object IR radiation.

Similarly, for any kind of solid material, incident radiation will be modified as it is regularly reflected, diffusely scattered, absorbed, or emitted (Figure 1.44).

In most cases, emission can be neglected. A general treatment of attenuation of IR radiation must therefore be able to compute absorption/scattering within matter as well as reflection losses at material boundaries.

Attenuation of radiation along its original direction within matter is described by the Bouguer–Lambert–Beer law (Eq. (1.30)), which yields the transmitted portion T of the radiance as a function of traveled distance d within matter:

$$T(\lambda, d) = \frac{I(\lambda, d)}{I(\lambda, 0)} = \mathrm{e}^{-\gamma(\lambda)\cdot d} \tag{1.30}$$

Here, $\gamma(\lambda) = \alpha(\lambda) + \sigma(\lambda)$ denotes the total attenuation coefficient, which is due to the absorption (α) of radiation as well as scattering (σ), that is, a change in the direction of radiation. Both absorption and scattering can be calculated from first principles. In gases, both are due to electronic, vibrational, or rotational excitations, and γ can be expressed as

$$\gamma_{\text{gases}}(\lambda) = n \cdot (\sigma_{\text{abs}}(\lambda) + \sigma_{\text{sca}}(\lambda)) \tag{1.31}$$

where n is the volume concentration of the gas (in number of particles/volume), and σ_{abs} and σ_{sca} are the so-called absorption and scattering cross sections. Re-

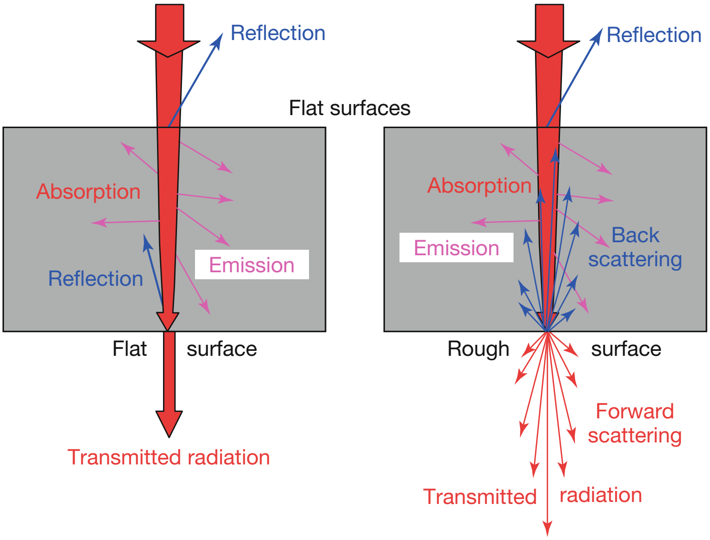

Figure 1.44 IR radiation that is incident on matter with flat surfaces can be reflected, absorbed, or emitted. For rough surfaces, diffuse scattering may take place.

sults for atmospheric gases – in the thermal IR range these refer more or less exclusively to ro-vibrational excitations – are known from many laboratory experiments (Chapter 8).

For solid matter, attenuation is due to excitations within electronic bands and lattice vibration processes. The attenuation coefficient in nondiffusely scattering solids (e.g., glasses or crystalline materials with polished surfaces) can be related to a macroscopic well-known quantity, the imaginary part of the index of refraction $n = n_1 + \mathrm{i}n_2$ (Eq. (1.32)):

$$\gamma_{\text{solids}}(\lambda) = \alpha_{\text{solids}}(\lambda) = \frac{4\pi \cdot n_2}{\lambda} \tag{1.32}$$

The index of refraction has been measured for many solids and is tabulated in a series of handbooks [18].

1.5.2
Transmission of Radiation through the Atmosphere

The dry atmosphere is composed of several natural gases (Table 1.8). In addition, there is a varying amount of water vapor of several percent volume concentration. Atomic gases (e.g., Ar) and diatomic gases of the same atomic species (N_2 and O_2) cannot absorb IR radiation in the thermal IR range. However, molecules, made up of two or more different atomic species, for example, NO, CO, CO_2, CH_4, and, of course, H_2O, are, in principle, able to absorb IR radiation. Figure 1.45 depicts two overview transmission spectra of horizontal atmospheric paths of lengths 10 and 1000 m, demonstrating that mostly CO_2 and H_2O dominate attenuation in

Table 1.8 Composition of dry air (for CO_2, August 2016: http://www.esrl.noaa.gov/gmd/ccgg/trends/).

Gas	Symbol	Volume (%)	Concentration (ppm)
Nitrogen	N_2	78.08	–
Oxygen	O_2	20.95	–
Argon	Ar	0.93	–
Carbon dioxide	CO_2	0.040 2	402
Neon	Ne	0.001 8	18
Helium	He	0.000 5	5
Methane	CH_4	0.000 19	1.9

otherwise pure air. Aerosols and clouds can induce additional attenuation (see also Section 11.5.1).

Several characteristic absorption features are present, in particular, some bands around 2.7 μm (H_2O and CO_2), around 4.2 μm (CO_2), between 5.5 and 7 μm (H_2O), and above 14 μm (H_2O, CO_2). These absorption bands are important for defining the spectral bands of IR cameras (Figure 1.8).

In addition to Table 1.8, there are gases with lower concentrations like krypton (Kr), hydrogen (H_2), nitrous oxides (N_2O, NO), xenon (Xe), ozone (O_3), and so on. The composition depends on the height above sea level. Some gas concentrations vary with time, e.g. the current increase in CO_2 is about 2 ppm/year, and for methane it is about 7 ppb/year.

Several computer models compute very precise transmission spectra of IR radiation within the atmosphere, the best-known being the Low Resolution Transmittance (LOWTRAN), Moderate Resolution Transmittance (MODTRAN), or High Resolution Transmittance (HITRAN) codes. These radiative transfer models for the atmosphere incorporate absorption and scattering constants for all relevant gaseous species in the atmosphere, and they also include vertical distributions of the constituents in order to provide an adequate modeling for the gas attenuation. LOWTRAN is a low-resolution propagation model and computer code for predicting atmospheric transmittance and background radiance. MODTRAN is similar to LOWTRAN, but with better spectral resolution. Similarly, HITRAN works with even higher resolution. The 2004 HITRAN model included 1 734 469 spectral lines for as many as 37 different molecules. For IR imaging, however, we mostly deal with two species and a few spectral bands, as shown in Figure 1.45.

Two aspects are particularly important for practical IR thermography. First, attenuation depends on the concentration of the absorbing gas species (Eq.(1.31)). For most gases of the atmosphere, concentrations are constant or slowly varying with time; water vapor, however, can have strong fluctuations; therefore, the relative humidity is an important quantity that needs to be measured for accurate compensation of water vapor attenuation between object and camera. Second, attenuation depends on the distance from an object to the camera (Eq.(1.30)), so

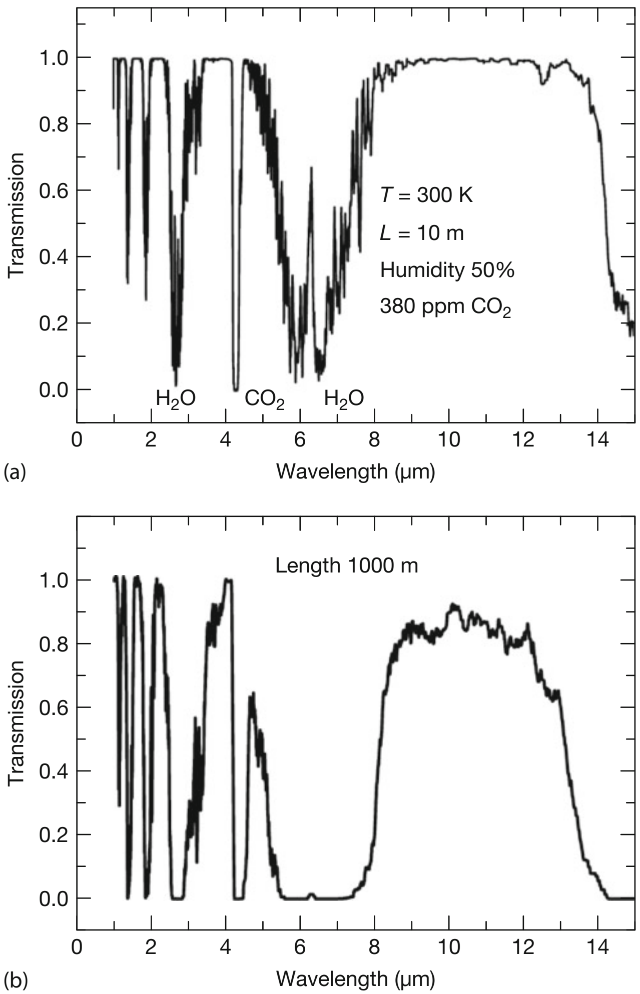

Figure 1.45 Atmospheric transmission $T(\lambda)$ for (a) 10 m and (b) 1000 m horizontal atmospheric paths. The spectra are nearly identical for the meanwhile slightly changed CO_2 concentration (400 rather than 380 ppm).

this quantity also needs to be known. Both humidity and distance are input parameters within the camera software packages.

Finally, for long atmospheric paths (e.g., hundreds of meters to kilometers) that are not usually encountered in thermography, additional effects due to aerosol scattering may become important, and the corresponding modeling must then include aerosol size and height distributions. If particles are small, as is the case, for example, in typical haze with water droplets of, say, 500 nm, visible light is scattered very effectively, whereas longer IR radiation is much less affected (Chapter 6, Section 10.9.2).

1.5.3
Transmission of Radiation through Slablike Solid Materials

1.5.3.1 Nonabsorbing Slabs

The attenuation of IR radiation in solid materials happens, for example, for lenses in IR cameras, but quite often objects are also observed through some windows. Mostly, flat (polished) surfaces are used such that scattering from surface roughness is neglected. The attenuation is then due to reflection at the boundaries as well as to absorption within the material. For the sake of simplicity we now discuss planar geometry, that is, slabs of material of a given thickness and well-defined index of refraction and IR radiation at normal incidence. For camera lenses with curved surfaces, one should redo the argument for finite angles of incidence. In this case, reflection coefficients will change according to the Fresnel equations, giving rise to polarization-dependent effects (Figures 1.12 and 1.32). However, if the distance from the object to the lens is large compared to the diameter of the lens, then the angles are small, and the general argument will still be valid.

Consider first a slab (coplanar plate) of a nonabsorbing material surrounded by a nonabsorbing material, usually the atmosphere (Figure 1.46). IR radiation of radiance L_0 is incident at normal incidence (in Figure 1.46, the propagation is drawn at oblique angles in order to visualize the various contributions separately).

In the simplest description (Figure 1.46a), there will be reflection losses L_R (characterized by the reflectivity $R = L_R/L_0$) of the radiation at the first interface. If the losses are small, the wave encounters similar losses at the second interface, that is, the total losses amount to about $2RL_0$ and the total transmission $T_{\text{total}} = L_{\text{trans}}/L_0$ can be written as $T_{\text{total}} \approx 1 - 2R$, with R from Eq. (1.5). A typical example for visible light and a glass plate in air would be $n_{\text{air}} = 1.0$, $n_{\text{glass}} = 1.5 + \text{i}0.0$, $R = 0.04$, and $T_{\text{total}} \approx 0.92$. This means that a typical glass plate transmits about 92% of incident visible light, which is why we can see quite clearly through windows. Before turning to IR windows, let us briefly generalize this result.

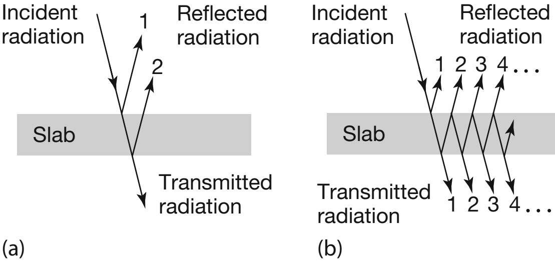

Figure 1.46 Scheme for calculating transmission of a slab in air. (a) Simplest approximation for small losses. (b) Complete analysis including all reflection contributions. The propagating radiation is drawn as oblique lines for clarity. In the calculation, however, they are assumed to be at normal incidence.

If the reflection losses upon hitting the first interface become larger (which will be the case for most IR transparent materials in the IR region), the derivation for the transmission must take into account all contributions of multiple reflections. Figure 1.46b depicts the idea behind the calculation. Part of the incident radiation is reflected at the first encounter with the slab. Using the symbols $R = L_\mathrm{R}/L_0$ and $T = L_\mathrm{T}/L_0 = (1 - R)$ for reflectivity and transmission at a single interface, this first reflection contribution (1) is given by $L_0 \cdot R$. The transmitted part $L_0 \cdot T$ enters the medium, which is initially assumed to be nonabsorbing. After the second transmission, and exiting the material, the radiance has decreased to $L_0 \cdot T^2$ (transmitted beam number 1). Following the beam, which is internally reflected within the slab, and subsequently studying more reflections and transmissions upon interactions with the slab surfaces, we end up with a number of rays (1, 2, 3, 4, …) contributing to the total reflected radiance and to the total transmitted radiance. For nonabsorbing materials, $T = 1 - R$; hence, the sum of all reflected contributions can be written as a geometrical sum

$$T_\mathrm{slab} = (1-R)^2 \cdot (1 + R^2 + R^4 + R^6 + \ldots) = \frac{(1-R)^2}{1-R^2} \tag{1.33}$$

Using Eq. (1.5) again for the air–glass example ($n_\mathrm{A} = 1.0, n_\mathrm{B} = 1.5 + \mathrm{i}0.0$), the transmission can easily be evaluated to give

$$T_\mathrm{slab} = \frac{2n_\mathrm{B}}{n_\mathrm{B}^2 + 1} \tag{1.34}$$

For $n_\mathrm{B} = 1.5$ this gives $T_\mathrm{slab} = 0.923$, which is only slightly higher than the previously estimated 0.92 value.

In contrast, a material like germanium at a wavelength of 9 μm has $n_\mathrm{B} \approx 4.0 + \mathrm{i}0.0$. The simple derivation of a Ge slab in air would give $T_\mathrm{total} = 1 - 2 \cdot 0.36 = 0.28$, whereas the correct treatment according to Eq. (1.34) gives $T = 0.47$.

1.5.3.2 **Absorbing Slabs**

The propagation of radiation within an absorbing slab has the same type of contributions as in Figure 1.46b, the only difference being that during each successive passage through thickness d of the slab, there will be an additional attenuation described by Eq. (1.30).

Repeating the preceding calculation of the transparent-slab transmission and inserting R from Eq. (1.5) we finally find the transmission of an absorbing slab ($n_\mathrm{B}(\lambda) = n_1(\lambda) + \mathrm{i}n_2(\lambda)$) in air ($n_{1\mathrm{A}} = 1$):

$$T_\mathrm{slab}(\lambda, d) = \frac{16 n_1^2 \cdot \mathrm{e}^{-(4\pi n_2 d)/\lambda}}{\left[(n_1+1)^2 + n_2^2\right]^2 - \left[(n_1-1)^2 + n_2^2\right]^2 \cdot \mathrm{e}^{-(8\pi n_2 d)/\lambda}} \tag{1.35}$$

Equation 1.35 makes it easy to compute slab transmission spectra, provided the thickness d of the slab as well as the optical constants $n_1(\lambda)$ and $n_2(\lambda)$ of the slab material are known.

1.5.4
Examples of Transmission Spectra of Optical Materials for IR Thermal Imaging

1.5.4.1 Gray Materials in Used IR Spectral Ranges

A number of common materials are available in the thermal IR spectral range [4, 9, 17]. These include crystals like BaF_2, NaCl, CdTe, GaAs, Ge, LiF, MgF_2, KBr, Si, ZnSe, and ZnS, and inorganic as well as organic glasses like fused silica IR grade or AMTIR-1. The materials can be characterized according to the corresponding wavelength range in which they are used. A number of examples are presented in what follows.

Figure 1.47a depicts the transmission, reflection, and absorption spectra for a 7.5 mm slab of NaCl. Obviously, NaCl has an excellent IR transmission of greater

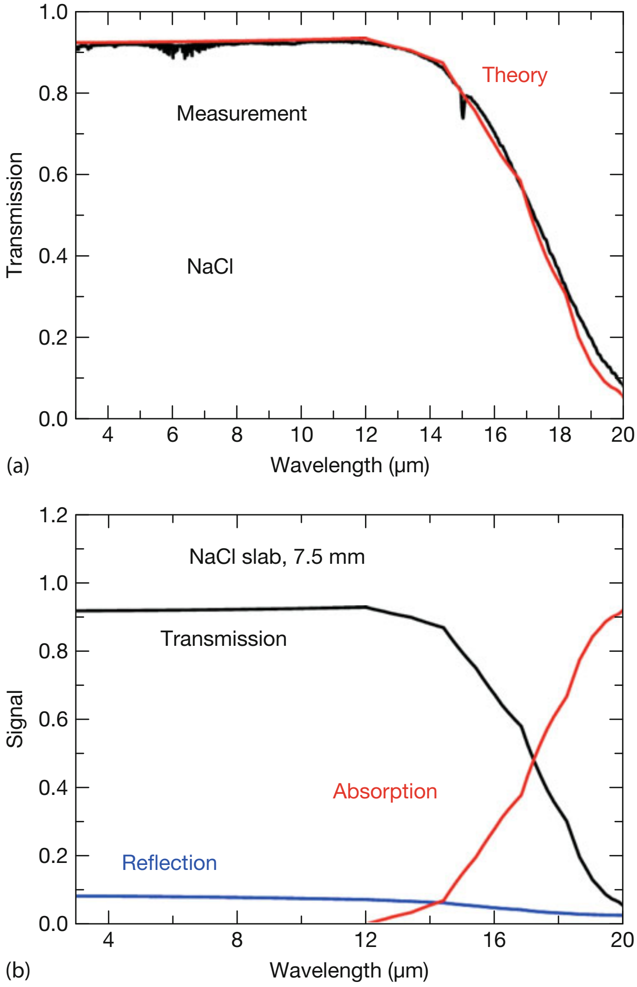

Figure 1.47 Experimental (black) and theoretical (red) transmission spectra of a 7.5 mm thick slab of NaCl (a) as well as the reflection and absorption contributions (b).

than 0.90 up to about 12 μm, and it still has a transmission of about 0.87 at 14 μm. The transmission depends on the slab thickness wherever absorption plays a role, here for $\lambda > 12$ μm. However, NaCl – as well as other alkali halides – has the disadvantage of being hygroscopic, that is, it must be protected from water moisture and humidity. Therefore, alkali halides are not used to manufacture lenses for IR camera systems. They are, however, sometimes used as special windows.

As is the case with all literature data, a word of caution is necessary for the theoretical spectra. Accurate measurements of optical constants of materials are difficult, and those collected over the years were subsequently refined after better sample preparation techniques became available. All of the following theoretical plots are based on the collection of data of optical constants from the literature [18]. Often, several slightly different sets of data are available. This is due to the fact that such measurements are usually made under ideal conditions, for example, clean samples, very good crystal or sample film quality, very few surface defects, scratches, and so on, with little sideways scattering. Hence, when comparing these data to real-world windows or lenses of the same materials, several percent deviations are common; in the case of severe surface damage with considerable side scattering, even larger deviations are possible. Hence, theoretical spectra should be regarded as order-of-magnitude expectations, and experimental spectra should be recorded for comparison whenever quantitative analysis is needed. In Figure 1.47b, the comparison of experimental spectra, recorded with Fourier transform infrared (FTIR) spectroscopy, and theoretical spectra based on tabulated optical constants shows very good agreement.

All data presented here refer to normal incidence. Spectra for obliquely incident radiation must take into account polarization-dependent effects described by the Fresnel equations (Figure 1.32). Lenses, windows, and filters for IR cameras are

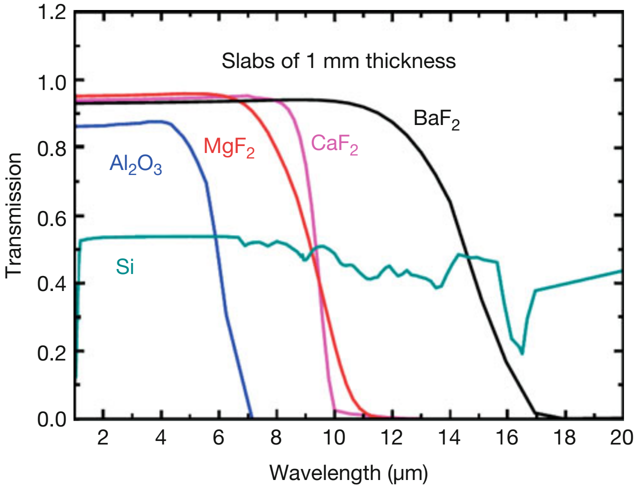

Figure 1.48 Overview of typical theoretical transmission spectra for 1 mm thick slabs of various materials that are used in the MW IR spectral region.

often manufactured from materials like BaF_2, CaF_2, MgF_2, Al_2O_3 (sapphire), and Si for a wavelength range up to 5 μm and Ge, ZnS, and ZnSe for the LW region. Some of these ideally suited materials for IR imaging are manufactured by special hot-pressing techniques and have special names like Irtran (acronym for IR transmitting).

Figures 1.48 and 1.49 show some examples of transmission spectra of materials that are used in the MW range.

Similar to the NaCl results (Figure 1.47), absorption features become important for longer wavelengths. In this case, the transmission spectra depend on the material thickness, as shown for BaF_2 and MgF_2 in Figure 1.49. Therefore, it is important to know the exact thickness of windows made of such materials if the

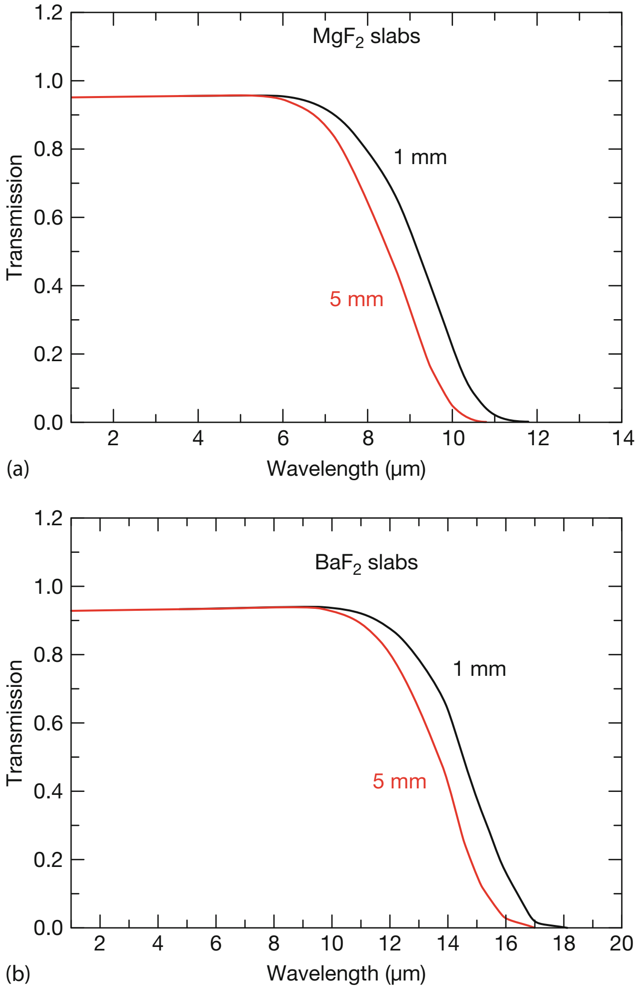

Figure 1.49 Transmission spectra depend on the thickness of the slabs owing to the onset of absorption.

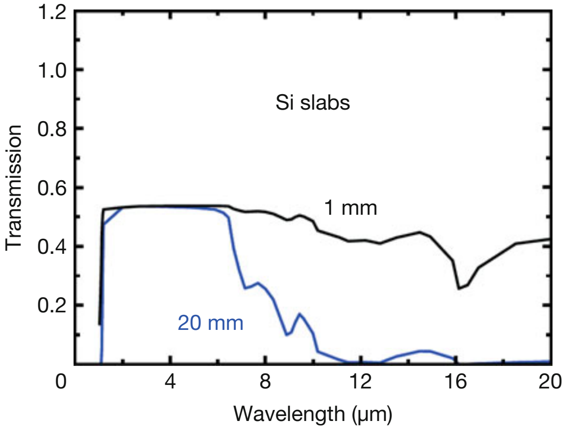

Figure 1.50 Transmission spectra of silicon slabs for different thicknesses. Absorption features are prominent for wavelengths above 5 μm.

IR camera used is sensitive in the corresponding spectral range of absorption features. Obviously, BaF_2 may also be used for LW cameras; however, one must take care to keep the thickness of window materials small.

Figure 1.51 provides an overview of spectra for materials that can be used in the LW range.

Figure 1.48 proves that the transmission for silicon is rather flat in the MW range; however, absorption features dominate the spectra in the LW range. This is illustrated in Figure 1.50, which presents a closer look of a silicon plate for different thicknesses. In the last few decades, the purity of silicon crystals has improved considerably. This means that high-quality oxygen-free silicon crystals may have appreciably less absorption than the sample shown here, which is based on a compilation of measured optical data from 1985 [18].

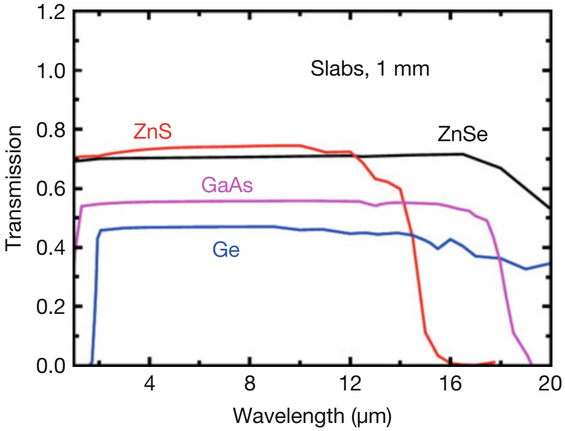

Figure 1.51 Overview of typical theoretical transmission spectra for 1 mm thick slabs of various materials that are used in the LW IR spectral region.

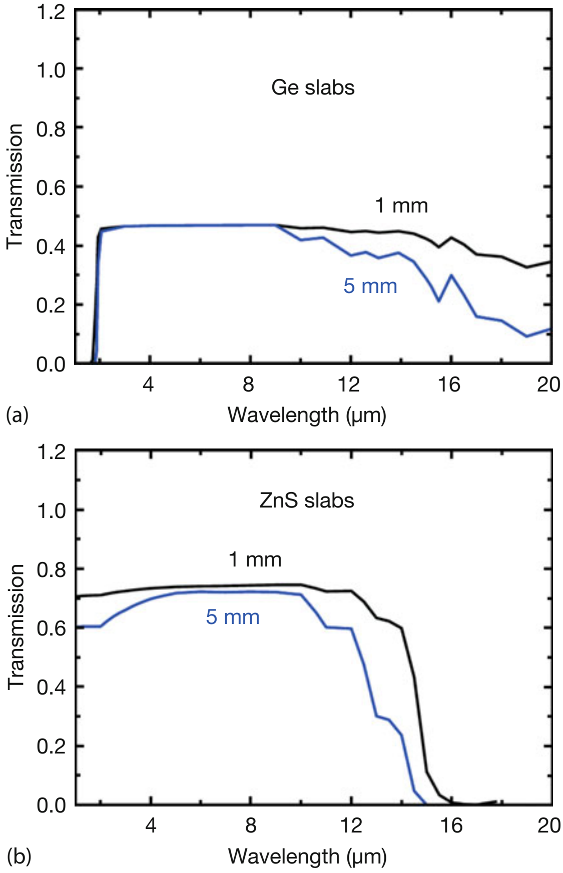

Figure 1.52 Transmission spectra of Ge (a) and ZnS (b) depend on slab thickness owing to onset of absorption.

It is should be mentioned that some of these materials have special trade names if manufactured in a certain way. For example, hot-pressed polycrystalline ZnS with about 95% cubic and 5% hexagonal crystals was called Irtran-2 by the manufacturer Eastman Kodak. Similar other trade names exist, like Irtran 4 for ZnSe, and so on. Since optical properties depend on crystalline structure, mixtures of different crystal forms can lead to differences in optical transmission spectra. ZnSe can be used throughout the LW range; for ZnS or Ge, however, thick samples show significant absorption features even below wavelengths of 15 μm (Figure 1.52). This effect is less pronounced for GaAs; however, GaAs is very expensive compared to the other materials, which affects its commercial use for lenses.

For comparison, Figure 1.53 depicts the respective spectra for regular laboratory glass BK7 (Schott) or fused silica, that is, amorphous silicon dioxide. Obviously, common glass cannot be used in either MW or LW IR cameras. Synthetic fused silica can, in principle, be used for MW systems, acting as bandpass filters.

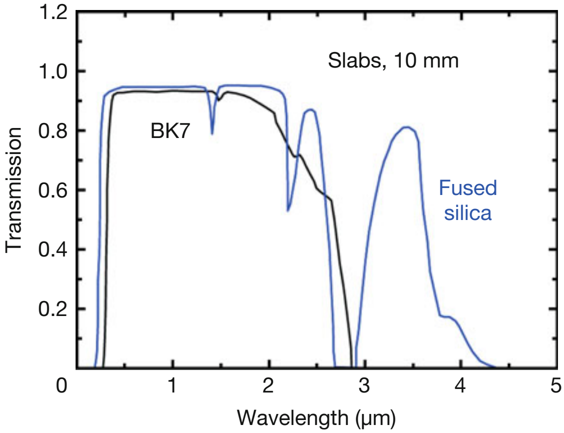

Figure 1.53 Transmission spectra of common laboratory glass BK7 and fused silica. There are usually batch-to-batch variations in the range around the water absorption band at 2.7 μm owing to fluctuations in the OH chemical bond contents in these materials.

1.5.4.2 Some Selective Absorbers

A common misconception among beginners in IR imaging is the expectation that they will be able to observe warm or hot objects immersed in water. This is more or less impossible, as can be seen from Figure 1.54, which depicts theoretical transmission spectra of thin slabs of water. For direct comparison with Figures 1.47–1.53, the slabs are assumed to be surrounded by air. Obviously, only the very thinnest layers of water still allow the transmission of radiation in the thermal IR spectral range.

Water that is 1 mm thick is sufficient to completely suppress any IR transmission in the MW and LW spectral range. In principle, SW IR imaging ($\lambda < 1.7$ μm) seems possible; however, the thermal radiation of objects at temperatures less than 600 K is very low in this spectral range (Figures 1.21 and 1.22).

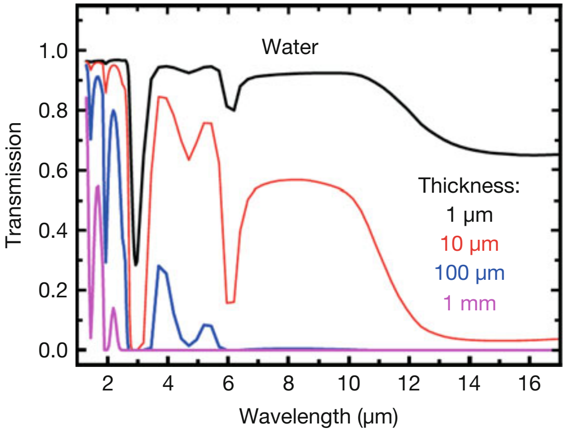

Figure 1.54 Transmission spectra of slabs of water of varying thickness.

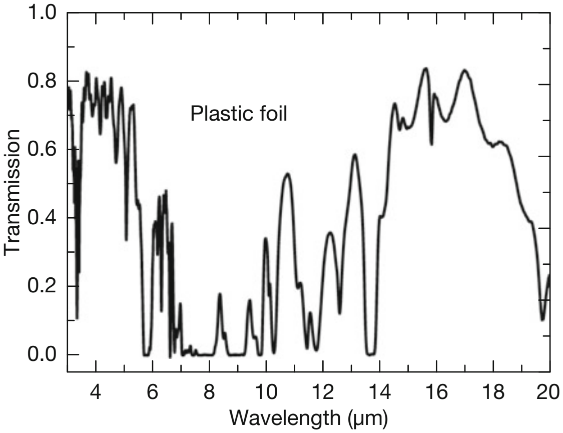

Figure 1.55 Experimental IR transmission spectrum of a plastic foil.

In principle, other liquids like oils or organic compounds can have finite IR transmission; they are, however, only used for special applications and are not treated here.

A final example of another frequently encountered material in IR imaging is shown in Figure 1.55, which depicts the IR transmission of a plastic foil. Plastics are complex organic compound materials that, depending on their type, show a huge variety in chemical composition. Therefore, they can also have large variations in their IR spectra. Obviously, the chosen example may be used for MW cameras. It has several absorption features in the LW range but could perhaps be used as band filter material for special investigations.

1.6
Thin Film Coatings: IR Components with Tailored Optical Properties

Many IR transparent optical materials have transmission values much lower than 100%, some of them being in the range of 70% and others like Ge or Si even in the range of only 50% (Figures 1.48–1.52). These transmission losses are mostly due to the reflection losses from air to the material, with a high index of refraction. Obviously, any optical system using such materials would suffer from substantial losses of IR radiation reaching the detector. To reduce these losses, the lenses and optical components of IR cameras are usually treated with antireflection (AR) coatings. In addition, the coating technique can also be used to tailor desired optical properties like, for example, band filters for IR radiation. The technique to modify optical properties by deposition with thin film coatings is well known from the visible spectral range [25, 27, 44–46] and also has been successfully applied to the IR spectral range [2, 4, 17].

1.6.1
Interference of Waves

The principle behind AR coatings is based on the wave nature of radiation, in particular the phenomenon of interference. Figure 1.56 illustrates interference schematically. IR radiation is an EM wave, which may be described by the oscillation of the electric field vector (Section 1.2.1). Whenever two individual waves (e.g., light waves, sound waves, water waves) meet each other at the same time and location, their elongations (here the electric field) superimpose, that is, they add up to give a new total wave elongation and a new maximum elongation, or wave amplitude. In Figure 1.56a, the two waves superimpose in such a way that the first wave is just shifted by half a wavelength, that is, it is out of phase with the second wave. In this case, the adding up of the two elongations results in complete cancellation of the electric field, and the new total elongation is zero. This is called *destructive interference*. In Figure 1.56b, the two waves superimpose in such a way that the first wave has no shift, meaning it oscillates in phase with the second wave. In this case, the adding up of the two elongations results in a larger elongation of the electric field, that is, the new total amplitude is twice as large as the one from each individual wave. This is called *constructive interference*. The overall energy transported by a wave is then proportional to the square of the amplitude of the wave, that is, in the first case, there is no net energy flux, whereas in the second case, there is twice as much energy flux with regard to the two individual

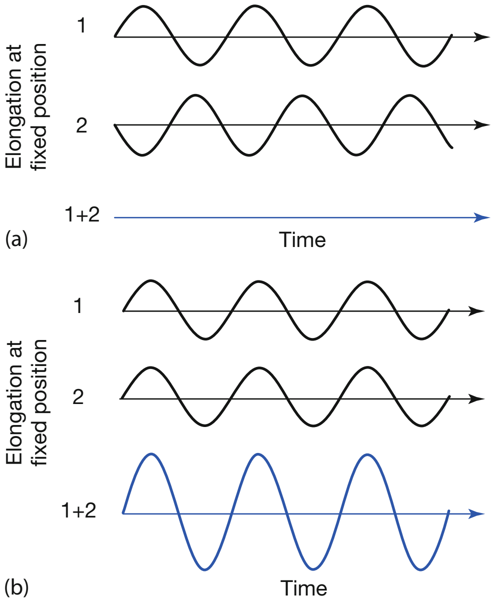

Figure 1.56 Destructive (a) and constructive (b) interference of waves as observed at a fixed location.

waves. Whenever interference happens, the energy flux of waves is redistributed such that in certain directions, destructive interference reduces the flux, whereas in other directions, there is constructive interference with larger flux. Of course, energy conservation is satisfied overall.

1.6.2
Interference and Optical Thin Films

Interference can be utilized to tailor the optical properties of materials by depositing thin films on top of the desired optical material. The idea behind this is schematically illustrated in Figure 1.57. Suppose IR radiation is incident on an optical component made up of a certain material, for example, Ge, Si, or ZnSe. This component material is called the *substrate*. For the sake of simplicity, we assume the substrate to be thick, that is, we only treat the first reflection from the top surface (Figure 1.57a). We can easily calculate the reflectivity for normal incidence from Eq. (1.5).

If a thin transparent film is deposited onto the substrate (Figure 1.57b), there are at least two dominant reflections, one from the top surface of the film and the other from the interface between film and substrate (for the sake of simplicity of argument, we neglect additional reflections). For normal incidence, the two contributions overlap spatially, and at the top surface of the film, the two reflected waves can interfere with each other. With regard to the top reflection (1), the radiation (2) reflected from the interface has traveled an additional distance of twice the film thickness before interfering with the first wave. In this way, a phase shift is induced. For proper film thickness and index of refraction, the phase shift can be chosen such that the two waves interfere destructively. In this case, the thickness of the film needs to be $\lambda/4$, with λ being the wavelength of the EM radiation within the film material. If in addition the amplitudes of the two reflected waves can be made equal, destructive interference can lead to a total suppression of reflected radiation. Alternatively, it is possible to enhance the reflected portion of the radiation using constructive interference. Five parameters determine the optical properties of reflected or transmitted radiation: first, the index of refraction of

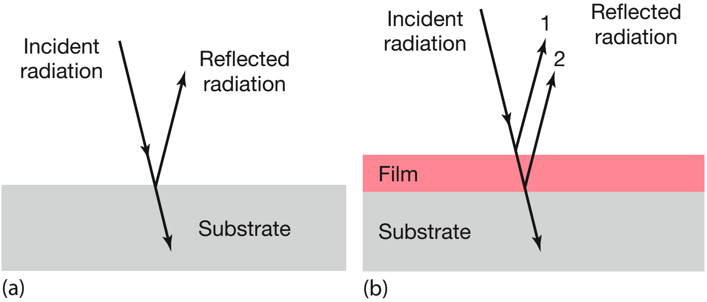

Figure 1.57 (a,b) Idea behind optical coatings (see text for details).

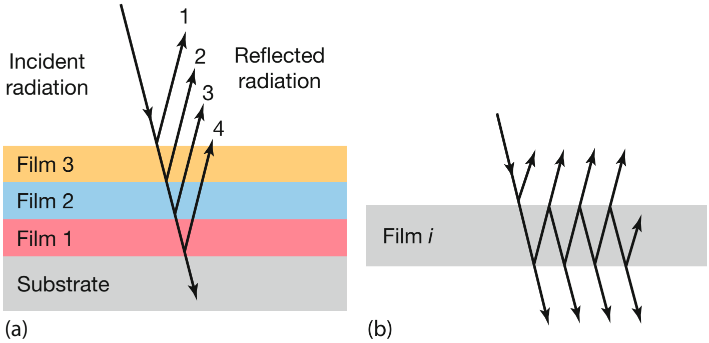

Figure 1.58 Schematic of a multilayer thin film optical coating. In a simplified overview (a), there is a reflection component from each interface; in reality, there are multireflection contributions from each film (b) that need to be summed up.

the substrate material; second, the index of refraction of the film material; third, the thickness of the film material; fourth, the angle of incidence; and finally, the wavelength of the IR radiation.

Optical interference coatings have been studied for many decades in the visible spectral range, the most common and well-known example being AR coatings for eyeglasses. Research has shown that single layers work only for one specific wavelength but are less effective for neighboring wavelengths. If special properties like AR coatings, mirrors, or bandpass filters are needed for broader wavelength ranges, multilayer coatings are used (Figure 1.58). They can range from a few (like three) to several hundreds of layers. Matrix formulations have been developed to analytically treat such multilayer films [44–46]; however, it is obvious that such solutions become very complex, and nowadays computer codes are used to compute the optical properties. We show a few selected results in what follows. However, a word of caution is needed when theoretically discussing thin film properties. Besides the aforementioned theoretical parameters that influence optical properties, one also needs to consider the availability of transparent film materials as well as their growth properties on the given substrate materials. If the lattice constants of the selected film material deviate too much from those of the substrate, it may be that the coating cannot be manufactured.

1.6.3
Examples of AR Coatings

The effectiveness of thin film optical coatings is first illustrated by an example with visible light. Figure 1.59 depicts the reflectivity for normal glass as well as for the same glass substrate coated with either a single layer of MgF_2 (thickness ≈ 90 nm, corresponding to $\lambda/4$ for the chosen reference wavelength of 500 nm) or a triple layer using MgF_2, ZrO_2, and Al_2O_3. The typical glass reflectivity of a single interface is reduced from around 4% to a minimum of about 1.5% for a single-layer coating and to less than 0.1% for an appropriate three-layer coating. The

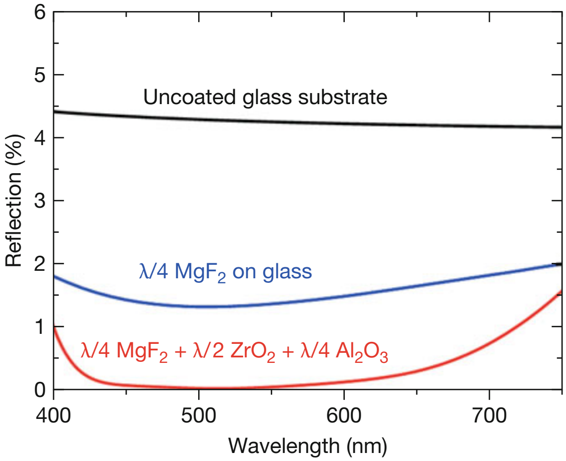

Figure 1.59 Optical antireflection (AR) coatings for glass in the visible spectral range, optimized for a reference wavelength of 500 nm. Multilayer coatings can lead to a broadband reduction of reflectivity (computed with the commercial program Essential McLeod [46]).

multilayer coating has the additional advantage of a very broadband reduction of reflectivity within the visible spectral range. Nowadays such AR coatings are of standard use in eyeglasses and glass lenses (of course, both glass surfaces must be treated).

Similarly, AR coatings can be applied to materials used for IR optical components like IR cameras. For example, silicon has a reflectivity well above 40% and a corresponding low transmission in the MW range. Again, a simple two-layer coating made of MgF_2 and ZrO_2 could easily reduce the reflectivity to below 10% (Figure 1.60), that is, enhance transmission to over 90% (the sum of both is slightly less than 100% because of absorption). Similar AR coatings can be applied to other materials in the LW range. In practice, all component surfaces are treated with AR coatings, not just the front surface.

In conclusion, AR coatings of IR optical components can be easily produced. The exact multilayer composition of manufacturers is usually not known, but the principle behind the method is obvious. Figure 1.61 depicts transmission spectra of a simple single-layer AR coating made of 530 nm ZnS on a silicon wafer. The model result (blue solid line) corresponds quite well with the corresponding real system, which was produced by evaporation techniques in a vacuum chamber and subsequently analyzed using FTIR spectroscopy.

1.6.4
Other Optical Components

Finally, some applications in IR imaging require special optical coatings. There are several common examples. First, one might want to use high-pass or low-pass filters, that is, either long or only short wavelengths are transmitted

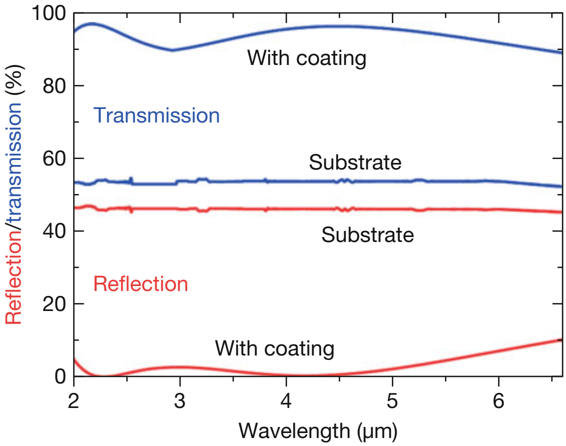

Figure 1.60 Example of antireflection (AR) coatings for silicon in MW IR spectral range (computed using commercial program Essential McLeod [46]).

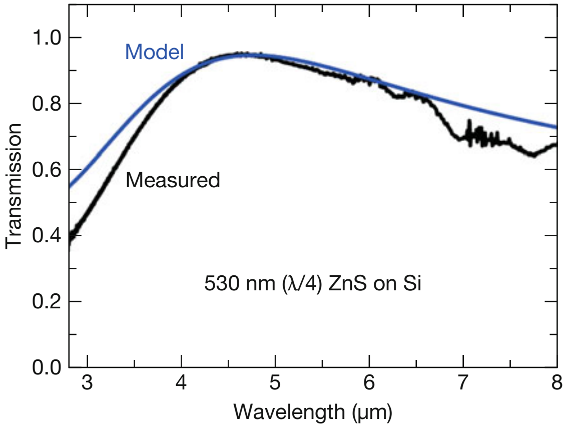

Figure 1.61 Example of a modeled (blue curve) and experimental single-layer antireflection coating of ZnS on top of a silicon wafer.

with respect to a defined reference wavelength. This may be useful if background radiation of well-defined wavelengths need to be suppressed. Second, so-called neutral density filters may be useful if the total radiance incident on a camera is attenuated in a well-defined way. These filters can have a transmission (which can be chosen more or less arbitrarily over a wide range) that is independent of wavelength. Third, several applications require bandpass filters. Such filters are similar to interference filters known from the visible spectral range. Figure 1.62 depicts a typical commercial filter whose transmission corresponds to the CO_2 absorption lines at $\lambda \approx 4.23$ μm. It is characterized by maximum transmission, a bandwidth at half maximum, and sometimes the slope of the curve. Commercially,

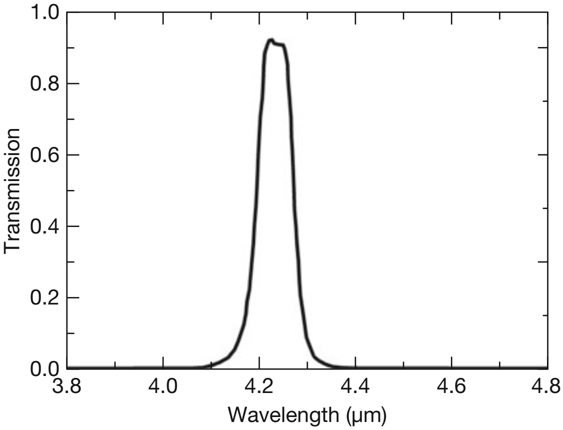

Figure 1.62 Typical example for transmission spectrum of commercially available narrowband IR filter at 4.23 μm.

a wide variety of broadband or narrowband filters are available for nearly every wavelength in the thermal IR range (e.g., [47]).

In conclusion, using thin optical film coatings, it is possible, within certain limits, to tailor desired optical properties of IR optical components. The only important issue to keep in mind is that the materials for the thin films must not absorb in the respective spectral range. Otherwise, they would behave in a manner similar to absorbing windows, that is, absorb part of the radiation, thereby heat up and emit IR radiation, which would introduce an error in the measurement of object temperatures.

Interference filters in the IR are usually a combination of a cut-on and a cutoff filter (Figure 1.63). The use of filters is discussed in Section 3.2.1 and Chapter 8. Many filter materials transmit short IR waves and start to absorb wavelengths larger than a certain wavelength. Ideally, a filter substrate material should absorb only at wavelengths larger than the filter cutoff wavelength. However, in this case, it is important to choose the direction of IR object radiation through the filter. It should pass first through the cutoff filter such that longer wavelengths are reflected, that is, cannot be absorbed in the filter. If radiation passed through the filter in the wrong direction, the filter itself would absorb longer wavelengths and thereby heat up, leading to an additional source of thermal radiation, which would affect the signal-to-noise ratio (Chapter 2). Unfortunately, however, whenever a filter substrate material is absorbing in the used spectral range, it is itself also a source of IR radiation (Eq.(1.27)). Therefore, any warm filter (irrespective of being potentially heated up by absorbing object radiation) will also emit additional broadband background radiation toward the detector. Therefore, the selection of available filters does depend on the application. IR radiation emitted from a filter, in particular if uncooled, may still be tolerated in IR spectroscopy. In contrast, the additional filter radiation – if used as warm filters (Section 8.3) – would dramati-

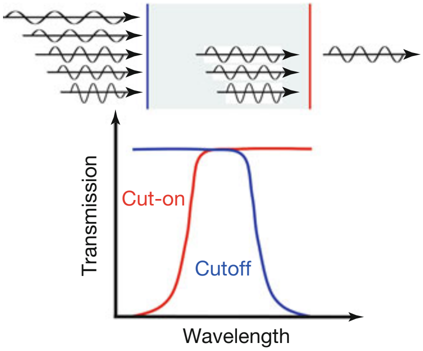

Figure 1.63 An interference filter that has interference coatings on both sides, one acting as a cutoff filter (blue, reflecting long wavelengths), the other acting as cut-on filter (red, reflecting short wavelengths). Together they result in a bandpass filter. Only incident IR radiation with suitable wavelength is transmitted; the rest is reflected, and ideally none is absorbed within the filter.

cally reduce the signal-to-noise ratio in IR imaging. As a remedy, absorbing filters are cooled or filters from nonabsorbing materials must be used. Both absorbing and nonabsorbing filter materials for IR are available [47].

1.7
Some Notes on the History of Infrared Science and Technology

Nowadays, science and technological developments often go hand on hand, stimulating each other. Concerning the beginning of IR thermal imaging, science and technology developed more or less independently. Therefore, we will begin discussing the science alone up to about 1900 before dealing with developments in IR technology.

1.7.1
Infrared Science

Table 1.9 gives a brief overview of early IR science. It may be subdivided into three parts: the discovery of IR radiation, the introduction of the concepts of blackbodies and their radiation, and the development of the laws of radiation. Some concepts and laws were discussed earlier in the introductory sections to provide a scientific basis of the discussed topics; here, however, we focus on the historical perspective.

1.7.1.1 **Discovery of Heat Rays and Atmospheric Absorption**

The modern history of IR science started around 1737, when Émilie du Châtelet first predicted IR radiation. Châtelet was a French mathematician and physicist who, for example, also translated Newton’s *Principia*. In 1737, she entered a contest sponsored by the French Academy of Sciences on the nature of light, heat, and fire. Although she did not win the contest, her work was later published. In this paper, “Dissertation sur la nature et la propagation du feu,” she suggested that different colors of light carried different heating power, that is, she anticipated the existence of what is now known as IR radiation [48, 49].

Table 1.9 Timeline of important early IR science discoveries.

Year	Person	Important event in IR science	
1737	E. du Châtelet	Prediction of IR radiation	
1786	B. Thompson	Transport of heat through vacuum	
1800	W. Herschel	Discovery of IR radiation	
1804	J. Leslie	Emissivities of different surfaces, Leslie cube	
1830s	M. Melloni	Absorption spectrum of liquids and solids	
1840	J. Herschel	Atmospheric windows	
1859	G.R. Kirchhoff	Blackbody theorem: absorption ↔ emission	
1879	J. Stefan	Stefan–Boltzmann law	Empirical
1884	L. Boltzmann		Derived from thermodynamics
1893/1896	W. Wien	Wien radiation and displacement laws	
1898	O. Lummer/ F. Kurlbaum/ E. Pringsheim	Very precise measurements of cavity (blackbody) radiation at PTR in Berlin	
1900/1905	Lord Rayleigh/ J. Jeans	Radiation law	
1900	M. Planck	General blackbody radiation law: birth of quantum theory	

However, more than 60 years would pass before IR radiation was experimentally discovered by Sir William Herschel. In 1800, Herschel studied the heating power of solar radiation [50, 51]. Radiation from the sun was passed through a prism before different parts of the spectrum would hit sensitive thermometers (Figure 1.64). Herschel found that the resulting temperature rise depended strongly on the location of the thermometer in his spectrum, the visible part of which extended around 10 cm. Herschel found that violet light raised the temperature by 2 °F (for conversions from Fahrenheit into Celsius or Kelvin, see Table 1.2), green by around 3.5 °F, and red light by as much as 7 °F above ambient temperature. Surprisingly, however, the maximum heating effect occurred way beyond the red edge of his visible spectrum, where he measured 9 °F. No effect was observed beyond the violet edge. Herschel observed that these so-called heat rays obeyed the same laws of reflection and refraction as light.

Herschel's work was immediately subjected to severe criticism by Leslie, who challenged the accuracy of the experiments and completely denied the existence of invisible heat rays [52–54]. At that time, the majority of scientists still thought heat could only be transferred by matter. However, it was already proposed in Query 18 by Newton in his *Opticks* [55] that the transfer of heat through a vacuum was possible.

"If in two large tall cylindrical Vessels of Glass inverted, two little Thermometers be suspended so as not to touch the Vessels, and the Air be drawn out of one of these Vessels, and these Vessels thus prepared be carried out of a cold place into a warm one; the Thermometer in vacuo will grow warm as much, and almost as soon as the Thermometer which is not in vacuo." Newton concludes that heat, like

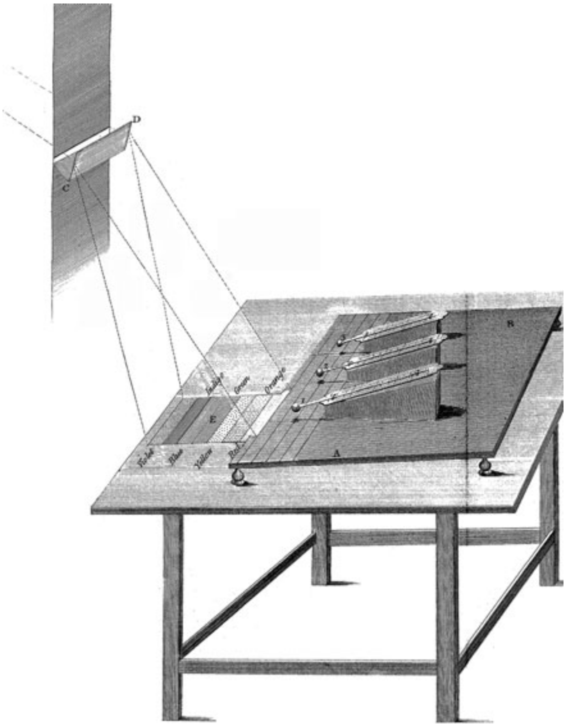

Figure 1.64 Experimental setup used by William Herschel that was used to discover IR radiation (after [51]).

light, is transferred by what others called the ether, a much more subtle medium than air, which remained in the vacuum even after the air was drawn out.

In 1786, Benjamin Thompson, also known as Count Rumford, reported more experiments along these lines. He described some experiments using the vacuum of Torricelli tubes to measure heat transfer through a vacuum [56].

Assuming, therefore, that heat could indeed be transported even in the absence of regular matter (nowadays we no longer need the hypothesis of the ether), it is obvious that Herschel – had he surrounded his thermometers by a vacuum – would have observed more or less the same effect.

Although Leslie, with his denial of invisible heat rays, was not successful in the long run, his rather ingenious attempts to verify his own ideas led to an instrument that is widely known today as the Leslie cube [57] (see Figure 1.28 for modern version of this cube). This instrument makes it possible to directly prove that different surfaces have characteristic abilities to emit heat and that dark or rough surfaces emit heat better than polished ones. He had even already formulated the law that the sum of reflection and absorption (i.e., emission) is the same for all opaque objects.

The first investigation into atmospheric gas absorption in the IR spectral range had to wait a few more decades. In 1840, Sir John Herschel, son of William, while

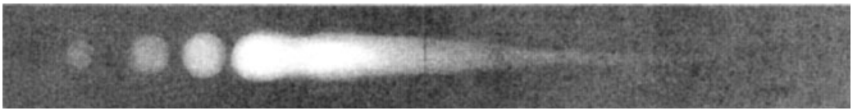

Figure 1.65 Example spectrum (horizontal coordinate related to wavelength) from wet-paper method to demonstrate absorption spectra (after [58]).

focusing his work on the then newly discovered method of photography, discussed the distribution of so-called calorific rays (as they were called at the time) in the solar spectrum by visualizing not only their spectrum but also their absorption features using a wet-paper method (Figure 1.65) [58]. The wet paper dries more efficiently at locations where it is hit by IR radiation. He concluded that the absorption features may be due to the earth's atmosphere, and, if future work supports this idea, "we should see reason to believe that a large portion of solar heat never reaches the earth's surface …" In modern language, the results indicated that IR radiation is strongly attenuated by the atmosphere in certain spectral regions, a discovery that later led to the definition of the atmospheric windows that define the thermal IR wavebands (SW, MW, and LW) used for IR astronomy as well as IR thermal imaging. Much like Herschel, his contemporary M. Melloni also studied absorption spectra, but mostly for liquids and solids (see following discussion).

1.7.1.2 Blackbodies and Blackbody Radiation

The next milestone in understanding thermal radiation was reached in 1859, when German physicist Gustav Kirchhoff, while at the University of Heidelberg in Germany, formulated his famous radiation law. Kirchhoff was collaborating with Bunsen on methods of spectral analysis. In an attempt to understand absorption and emission from a general point of view, he also studied the absorption and emission of thermal radiation emitted from cavities and invented the term *blackbody*. Based on thermodynamics, he formulated what is now known as Kirchhoff's radiation law, which states that the amount of absorption of a blackbody at any given temperature is the same as the amount of emission of the same body provided it is in thermal equilibrium [59–61]. Furthermore, the amount of emitted radiation only depends on wavelength and temperature. The correct corresponding radiation laws were not discovered before the turn of the next century. The main difficulties were, first, to accurately produce and, second, to accurately measure the spectrum of blackbody radiation for a wide temperature range. These problems were solved in the group of Lummer in Berlin first by constructing very precisely temperature-stabilized cavity blackbodies and second by developing very accurate bolometer detectors [62].

Figure 1.66 depicts two of the most famous and precise blackbody spectra of the nineteenth century, which – after Rubens added some at even longer wavelengths [63, 64] – later led Max Planck to his famous radiation law (see subsequent discussion). The spectra were recorded at the Physikalisch Technische Reichsanstalt in the late 1890s by Lummer and coworkers. Besides the observ-

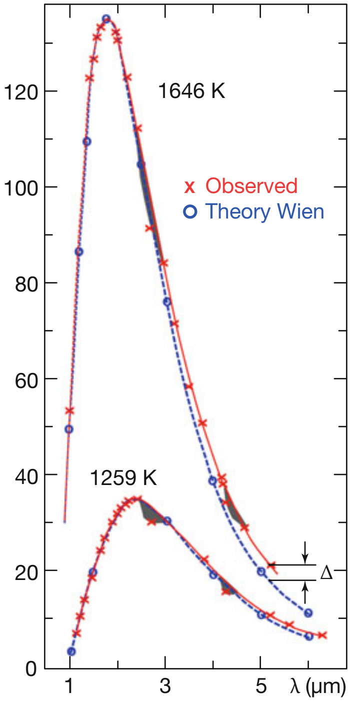

Figure 1.66 Two examples of observed (x) blackbody spectra and those calculated from Wien's radiation law (o) (detail from [62]). Although deviations between theory and experiment seem small (indicated by Δ), they are reproducible and call for improvements in the theory. Gray areas around 2.7 to 3 μm and 4.2 to 4.3 μm refer to H_2O and CO_2 absorption bands.

able residual absorption features of H_2O (between 2.7 and 3 μm) and CO_2 (4.2 to 4.3 μm) from the ambient air, students might think that there was very good agreement between theory and experiment. However, the measurements were so accurate that the experimenters claimed that there was a systematic disagreement between theory and experiment for long wavelengths at high temperature and that the theory of Wien, one of the leading theoreticians of the time, was wrong. Think about how self-confident you must be regarding your own experiments in order to make such a statement!

1.7.1.3 Radiation Laws

Rather than presenting an exhaustive historical discussion on the laws of radiation (which is beyond the scope of this section), we will summarize the most important laws describing thermal radiation for blackbodies in the 40 years between Kirchhoff (1860) and about 1905.

An often used and quite accurate radiation law based on thermodynamics was the one formulated by Wien in the 1890s [65]. As can be seen from Figure 1.66, it described blackbody radiation spectra very well, with only very small deviations for long wavelengths and high temperatures. In modern language, his radiation law in terms of spectral excitance is written

$$M_\lambda^{\text{Wien}}(T)\,\mathrm{d}\lambda = \frac{A}{\lambda^5}\mathrm{e}^{-B/(\lambda T)}\,\mathrm{d}\lambda \tag{1.36}$$

Wien used unspecified constants in the exponent and the nominator in front of the exponential function. This Wien law describes nicely the existence of a maximum and yielded reasonable fits to experimental data at the time. Only later, when Lummer, Pringsheim, and Rubens published more accurate measurements (Figure 1.66), did it become evident that Wien's law was only an approximation that worked very well for short wavelengths, that is, high frequencies, but a better description had to be found for the long-wavelength regime.

Surprisingly, it is also possible to use classical physics to derive a good approximation of blackbody radiation spectra for long wavelengths [66, 67]. This was done by Rayleigh (1900) and Jeans (1905). Their approximation, known today as the Rayleigh–Jeans law (see Eq. (1.37) as a function of wavelength or frequency) faces, however, the issue of the so-called UV catastrophe: according to the law, radiation should increase to infinity for high frequencies (short wavelengths), which is, of course, not the case:

$$M_\lambda^{\text{Rayleigh–Jeans}}(T)\,\mathrm{d}\lambda = \frac{C \cdot T}{\lambda^4}\,\mathrm{d}\lambda \quad \text{or} \quad M_\nu^{\text{Rayleigh-Jeans}}(T)\,\mathrm{d}\nu \propto T\nu^2\,\mathrm{d}\nu \tag{1.37}$$

Both laws, Wien's (Eq. (1.36)) and the Rayleigh–Jeans law (Eq. (1.37)), are nowadays simple approximate derivations from Planck's law (Eq. (1.15) or (1.17); see also Section 3.2.2.2 and Figure 3.10). Initially Planck believed in Wien's law, which can be derived from general thermodynamic arguments of minute entropy changes for a system in thermodynamic equilibrium. However, in 1900, when confronted with the experimental spectra by Lummer, Pringsheim, and especially by Rubens at even longer wavelengths, Planck changed his mind. It is reported [68–70] that Rubens told Planck on 7 October 1900, about his very-long-wavelength measurements and the problem with the theory. His measurements unequivocally demonstrated that Wien's law could not explain the data. Just one day later, Planck wrote a postcard to Rubens and explained that he had guessed the correction needed. What he had done and what he spoke about some days later on 19 October, directly after Rubens and Pringsheim presented their measurements, was extremely simple: he just changed Wien's law ever so slightly by writing the exponential function as a fraction and adding a 1 in the denominator. As a matter of fact, this change was also supported by some general thermodynamic arguments, though Planck himself noted that he arbitrarily constructed expressions for the entropy that gave similar but improved versions of Wien's radiation law [71]. Therefore, science historians later referred to a very lucky guess. Though Planck's change may appear simple, it has enormous consequences. Only after six grueling weeks of intensive work was Planck able to theoretically derive the new radiation law. In the derivation he had to introduce a new constant and in particular the fact that radiation is not a continuous quantity but only happens in steps of h. This marks the birth of quantum theory.

Spectra of blackbody radiation according to Planck's law were discussed in detail in Sections 1.3.2.2 and 1.3.2.3. Here we briefly add that using Planck's law it is now easy to derive two other very famous radiation laws. Historically they were derived differently and still in the nineteenth century. The first, called Wien's displacement law (Eq. (1.38), see also Eq. (1.16), [72]), relates the wavelength of maximum spectral emission of radiation with the blackbody object temperature. In brief, it explains that the product of maximum wavelength and temperature is constant (more details can be found in Section 1.3.2.2, Eq. (1.16)):

$$\lambda \cdot T = const \tag{1.38}$$

The second law, the Stefan–Boltzmann law, is again named after two scientists who dealt with blackbody radiation at different times. In 1879, the Slovenian-Austrian physicist Josef Stefan [73, 74], based on experimental data for cooling of mercury thermometers of different initial temperatures (experiments from Dulong and Petit), stated that the total amount of radiation emitted from an object is proportional to the fourth power of its absolute temperature. In modern parlance (see also Eq. (1.19)), we write

$$P_{\text{total}}(T) = \varepsilon A \sigma T^4 \quad \text{in W with} \quad \sigma = 5.67 \cdot 10^{-8}\ \text{W}/(\text{m}^2\ \text{K}^4) \tag{1.39}$$

where ε is emissivity and A the emitting area. (It was subsequently questioned whether Stefan really deserved to be mentioned in the context of this law [75], but here we stick with the general story.) About 5 years later, Ludwig Boltzmann theoretically derived this relation [76]. Similar to the Wien displacement law, the Stefan–Boltzmann law can be directly derived from Planck's law by integrating it over the whole spectral range (Section 1.3.2.4).

The great popularity of the Stefan–Boltzmann law stems from the fact that it allows for easy and quick estimates of surface temperatures and, on the basis of those estimates, estimates of the energy production of stars as derived from their spectra. Stefan in his 1879 paper already compared the estimates available at that time of the surface temperature of the sun and, assuming it to be a blackbody, estimated it be around 5586 °C. Since the sun is not a blackbody emitter, modern estimates derived from its spectrum typically range between 5700 and 6000 K, that is, quite close to Stefan's estimate. Let us briefly demonstrate the usefulness of the Stefan–Boltzmann law, knowing the value of the constant, by considering the total energy flux of the sun. Assuming a temperature of 5800 K, $\varepsilon = 1$, and a sun radius of 696 000 km, we immediately find the total energy flux from the sun to be

$$P_{\text{total}}(T) = 5.67 \cdot 10^{-8} \cdot 5800^4 \cdot 4\pi \cdot (696 \cdot 10^6)^2\ \text{W} \approx 4 \cdot 10^{26}\ \text{W} \tag{1.40}$$

Obviously, only fusion processes within the interior of the sun can permanently produce this huge energy flux, and its value must be consistent with stellar fusion models.

Coming back to earth, this energy flux from the solar surface must also equal the energy flux passing through a sphere with a radius corresponding to the sun–earth distance, that is, a sphere with a radius of around 150 million km:

$$P_{\text{total}}(\text{sun}) = S 4\pi R^2_{\text{sun–earth}} \tag{1.41}$$

This immediately gives a solar constant of around $S \approx 1370\,\mathrm{W/m^2}$ outside of the earth's atmosphere.

1.7.2
Development of Infrared Technology

After the establishment of IR science by 1900, a huge field of applications lay ahead. For the purposes of this book, we will discuss only the following fields:

- Quantitative IR spectroscopy either analytically in laboratories or in astronomy
- Quantitative spot measurements of temperature with either band-pass or broadband pyrometers
- First qualitative and then quantitative thermal imaging

All of these applications are strongly correlated with, first, the development of detector technologies (see details of detector principles in Chapter 2) and, second, further scientific developments in precise definitions in radiometry and technological developments of IR optics (e.g., optical materials, windows, lenses, prisms, filters), as well as calibration sources (blackbodies). With regard to IR imaging, there are obviously two ways to review the further development of IR technology. First, we could just give a chronological discussion, which would have the disadvantage that contributions to the various fields would be strongly mixed, or, second, we could divide this huge field into various subfields, which would help in following the developments in the various fields. We will proceed with the second option and divide the subsequent discussion into three parts:

A. Prerequisites for IR imaging
   1) Detectors and underlying physics
   2) Materials
   3) Blackbodies and radiation sources
   4) Radiometry
B. Development of quantitative measurement techniques
   1) Spectroscopy and IR astronomy
   2) Beginning of contactless T measurement
   3) Vanishing filament band-pass pyrometers
   4) Broadband pyrometers
C. Applications and imaging techniques
   1) Industrial/military applications
   2) Qualitative imaging
   3) Quantitative imaging

We would like to add two general remarks. First, we will make mention of quite a few – mostly freely available – early references that in the nineteenth and early twentieth centuries were often published in German, the then dominant scientific language. One of the most important journals at the time were the *Annalen der Physik*. Unfortunately, the volume count started several times anew with new series, which means that the same volume number refers to different series and different years. To overcome this sometimes puzzling situation (e.g., when the series number is not mentioned), it was decided to only use a new counting system when the old journals started to be digitized. The relation between the various counting schemes is described in [77]. There, links to web sites are given for free downloads.

We also mention that, in Germany, the IR spectral range was initially called *ultrarot* (or ultrared, "rot" being German for "red"). Similarly, there are a number of other synonyms in the older English literature, such as *caloric rays* or *radiant heat*. This lasted to about World War II, after which the general term *infrared* took over in scientific publications. Another German term lasted for a while, the so-called *Reststrahlen* (Table 1.10). However, this term is no longer important in research or technological applications.

1.7.2.1 **Prerequisites for IR Imaging**

Table 1.10 presents a timeline for many important discoveries and developments in connection with IR detectors, materials, and other prerequisites for quantitative thermal imaging. We will just mention some milestones here and refer to the extensive literature with reviews of this huge field concerning detectors (e.g., [78–82]), materials [17, 83], and radiometry and instrumentation [1, 84, 85], as well as other early developments including military ones (e.g., [86]).

The discovery of IR radiation by Herschel was accomplished by measuring temperature rises within rather large and bulky thermometers due to the absorption of radiation. Even before these first quantitative measurements, human senses were used to detect radiant heat, that is, IR radiation. There are reports from the sixteenth century [87] that a hand or face in front of a curved mirror that collects radiation, for example from a candle or ice, senses the radiation, that is, acts as a detector. Around 1600, this kind of experiment was supposedly conducted repeatedly using thermometers as detectors [87]. An account of this and related experiments [88] not only demonstrated that a pane of glass in between a source and the skin strongly attenuated the heat perception from a fire (Figure 1.67a) [89, 90], but in particular it described an ice experiment, often named after Pictet. This experiment, performed in the late eighteenth century, seems counterintuitive for many physicists.

Figure 1.67b depicts a setup with the main difference from earlier demonstrations that thermometers were used instead of skin to quantitatively measure the effect. Cold or hot objects are located close to the focal region of a mirror such that emitted radiation is made more or less parallel. It is focused by a second mirror, and a thermometer is placed close to its focal region. The obvious experiment is to have a hot object and detect a temperature rise. Saussure and Pictet used a red glowing metal bullet (about 5 cm in diameter), which they allowed to cool down, such that no visible emission was detectable by the eye. Still, however, there was a strong thermometer signal. Inserting a glass pane reduced the signal. They reproduced these results also with a pot of water that had just boiled. However, when the hot object was replaced by a container of ice or an iced liquid, the temperature dropped several degrees below ambient temperature. At the time, this initially un-

Table 1.10 Prerequisites for IR imaging: detectors, materials, blackbodies, radiometry.

Subfield	Year	Person/reference	Important event of infrared technology
A2	1682	Mariotte [89]	Glass in front of fire decreases sensed radiation. Lambert: glass pane in front of face, even if lens-focused fireplace radiation is directed toward face: no feeling of heat
A2	1779	Lambert [90]	
A3	ca. 1790	Pictet [88]	So-called cold rays emitted from cold objects
A3	1800	Herschel [51]	Discovery of IR radiation in sun spectrum
A1	1821	Seebeck [92]	Thermoelectric effect, ΔT generates voltage
A1	1830	Nobili [93]	Applied thermal element to detect IR radiation
A1	1830/1833	Nobili/Melloni [94]	From thermocouple to thermopile: 10 Sb-Bi pairs in series
A2	1830s	Melloni [97–101]	Transmission IR transparent materials
A1	1834	Peltier [102]	Peltier effect: current generates ΔT, application: cooling system of IR cameras
A1	1839	Becquerel [105, 106]	Photovoltaic effect discovery
A1	1857	Svanberg [110]	Wheatstone Bridge coupled with galvanometer, ΔR due to ΔT, i.e., sensitive thermometer. If hand approaches apparatus: signal due to radiant heat
A1	1873	W. Smith [107]	Photoconductive effect in selenium
A1	1876	W.G. Adams, A.E. Day [108]	Photovoltaic effect selenium (photoelectric currents) “the question … as to whether it would be possible to start a current in the selenium merely by the action of the light”
A1	1880	S.P. Langley [104]a	Platinum foil bolometer. Wheatstone Bridge measurement, sensitivity greater than contemporary thermopiles with similar accuracy. Bolometer: radiation balance
A3	1897	Rubens [63, 64]; see also [112]	Reststrahlen: method to generate large amount of long-wavelength IR radiation
A1	1901	Langley [104]b	Improved bolometer, IR sun spectrum up to 5.3 μm using a 60° rock salt prism
A4	1903	W.W. Coblenz [84, 85]	IR radiometry
A1	1917	T.W. Case [124]	First IR photoconductor Tl_2S up to 1.2 μm and its use for IR telegraphy
A1	1930	[125]	Schäfer/Matossi book: sensitive thermopiles important, in contrast: bolometer seldom used
A1	1938	Ta [109, 126]	Use of pyroelectric crystals for IR radiation, review: [127]
A2	1940s	[117]	KRS5 synthesis of crystals, characterization for IR applications
A1,2	1952	Welker [128]	First synthetic InSb crystal

Table 1.10 Continued.

Subfield	Year	Person/reference	Important event of infrared technology
A4	1950–1960s	Nicodemus, Zissis, Jones [114–116]	Nomenclature, radiometry
A1	1959	W.D. Lawson *et al.* [129]	First studies on HgCdTe, also acronym MCT for mercury cadmium telluride
A2	1950s	[83, 118, 119]	Coatings, filters for IR components
A1	1960s	[78, 160, 204]	Extrinsic detectors Ge:Hg
A1	1970	W.S. Boyle, G.E. Smith [120–122]	Charge-coupled devices (CCDs), Nobel Prize 2009: start signal for multielement detectors in IR
A1	1970s	[123]	Replacement of LN2 cooling by other methods like Stirling coolers
A1	1980s	[130]	Hybrid focal-plane arrays (FPAs): interconnecting detector array to multiplexing (silicon-based) readout, allows independent optimization of detector array and readout Second-generation systems: hybrid HgCdTe(InSb)/Si (readout) FPAs
A1	1982	T.S. Elliott (e.g., [131–133])	Signal Processing In The Element (SPRITE) sensor used with MCT photoconductors
A1	1985	[134–138]	From idea (1973) to 1040 × 1040 Schottky diode FPAs from PtSi
A1	1990s	[139–143]	Quantum well IR photoconductor (QWIP), Stirling coolers, thermoelectric coolers
A1	After 1990s	[144–148]	Cameras with uncooled microbolometer FPAs Peltier T stabilization

expected result led famous physicists such as Lord Rumford to conclude [88] that there is also “emission of frigorific rays from … bodies when they are cold.”

The main problem of researchers in thermal physics at the time was the lack of availability of very precise thermometers. Therefore, many physicists„ such as Leslie [57] or Benjamin Thompson, later called Count Rumford [91], built their own apparatus.

A breakthrough, which subsequently spurred the development of much smaller temperature sensors, was made in 1821 by Seebeck, who discovered the thermoelectric effect for a Sb–Cu sample [92]. The principle of this fundamental physical effect is depicted in Figure 1.68a. A temperature difference results in a voltage that is proportional to ΔT:

$$U = C(T_2 - T_1) \tag{1.42}$$

It was soon understood that this effect could be used in measuring absorbed radiation and building sensitive thermometers. Already in 1830, Nobili for the first time used a thermal element of this kind to detect IR radiation [93]. Together

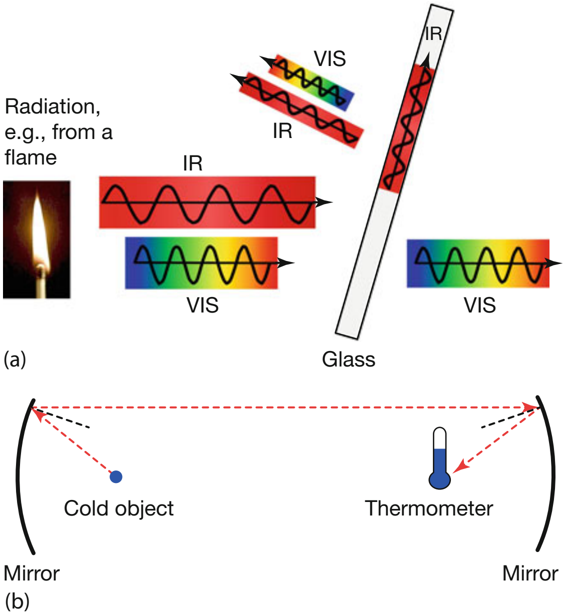

Figure 1.67 (a) Illustration of experiments described by Mariotte and Lambert. In modern terms, most of the IR radiation will be absorbed and some parts will be reflected. (b) Schematic setup to demonstrate so-called cold rays after Pictet.

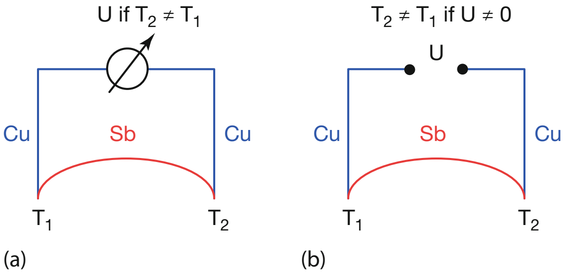

Figure 1.68 Principal setup for thermoelectric effect (a) and Peltier effect (b). If two contacts from two different metals are held at different temperatures, a voltage $U = const. (T_2 - T_1)$ results that is characteristic of the two materials. Conversely, if a voltage is applied, then a temperature difference results that can be used, for example, for cooling.

with Melloni [94] he greatly improved sensitivity by adding many of these thermocouple elements together to form a so-called thermopile detector. For example, in 1833 Nobili and Melloni used 10 Sb–Bi pairs in a series circuit. The resulting thermopile was 40 times more sensitive than the best available conventional thermometer, and they could detect the thermal signatures of humans from a distance of up to about 10 m (30 feet) (see also [95, 96]). To obtain the most sensitive instruments, a thermopile was combined with a sensitive galvanometer, and the resulting device was called a *thermo-multiplicator*. Melloni was very productive

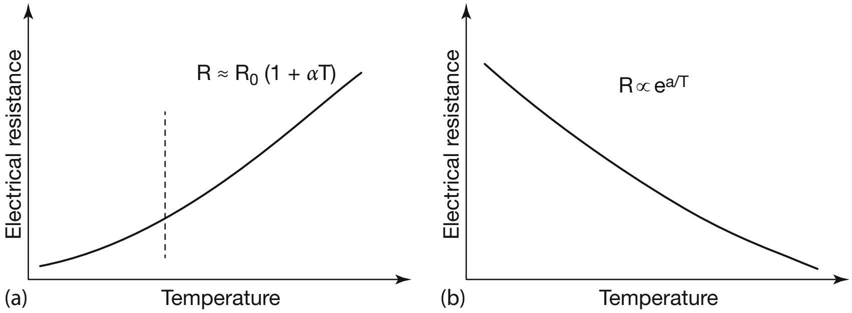

Figure 1.69 Schematic temperature dependence of electrical resistance of metals or alloys (a) and semiconductors (b). Conductors show a nearly linear increase in resistance with temperature, whereas semiconductors show a decrease. Both materials can be used for temperature measurements.

and investigated many thermal effects in the IR range, such as the transmission of solids and liquids for IR radiation [97–101].

The inverse of the photoelectric effect, the so-called Peltier effect (Figure 1.68b), was discovered as early as 1834 [102]. It was also used in IR cameras, for example, as a temperature stabilization unit in uncooled bolometer cameras.

In the following decades, many researchers used thermopiles by building their own devices. A typical commercial device is the thermopile named after Moll made from 16 thermocouples of constantin-manganin. The response time is several seconds, and sensitivity is around 0.16 mV/mW for wavelengths from 150 nm to 15 μm (e.g., [103]).

Another typical thermal detector, the bolometer, followed soon after [104]a. In strongly modified versions this detector type is currently used in many LW IR cameras. It is based on the temperature dependence of the electrical resistance of the materials used. Absorbed radiation leads to a temperature increase, which in turn leads to a change in electrical resistance (Figure 1.69) that is measured.

The next development came with the discovery of photoelectric detectors. Shortly after Becquerel [105, 106] discovered the photovoltaic effect in 1839, photoconductivity [107] and photovoltaic effects [108] were discovered in selenium. In 1938, the first pyroelectric detectors for IR radiation were investigated [109]. The principle of photoelectric radiation detection is schematically shown in Figure 1.70.

It was only a matter of time before other promising materials were investigated, for example, Tl_2S, InSb, HgCdTe, and many others.

Parallel to the development of IR radiation detectors, researchers studied three more fields. The first one dealt with sources of IR radiation. Around the turn of the nineteenth to the twentieth century blackbody sources that emitted broadband IR spectra (Figure 1.66) were widely available. The most precise ones were constructed at the Physikalisch Technische Reichstanstalt in Berlin ([111], Figure 1.71).

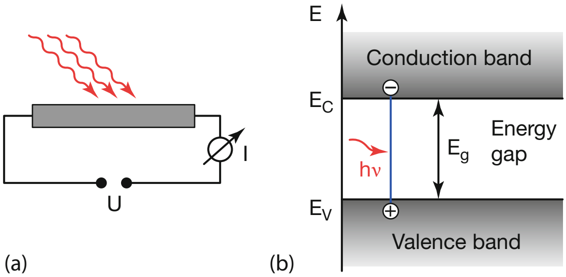

Figure 1.70 (a) Incident radiation on a photoelectric element leads to a change in electrical signals, for example, the current. (b) Simple band structure model: the incident radiation leads to charge carriers within the conduction and valence bands of the material (for more details, see Chapter 2).

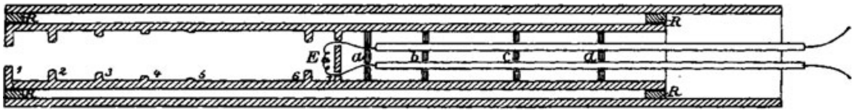

Figure 1.71 Cavity blackbody radiation source (after [111]). Only the inner part near the thermocouple *E* was at the desired stable temperature such that blackbody radiation was emitted through the cavity with diaphragms 1 to 6. The inner cylinder of 0.01 mm thin platinum had a length of 40 cm and diameter of 4 cm.

Intense IR sources for selected wavebands were more difficult to obtain. An ingenious nonspectroscopic and quite easy way to obtain more or less pure IR radiation is the *Reststrahlen* method developed by Rubens [63, 64, 112]. Rubens had discovered that alkali halide crystals showed strong wavelength-dependent absorption bands even for thicknesses of only a few micrometers (excitation of optical phonons plus higher-order additional acoustic phonons that broaden the feature). If broadband IR radiation, for example from an incandescent source such as a blackbody, is incident on alkali halide crystals, these selected bands are reflected better than adjacent wavelengths (Figure 1.72a). Repeating the reflections a few times (Figure 1.72b) leads to rather pure IR radiation wavebands, the so-called *Reststrahlen* (which translates as residual rays that are still there after the multiple reflections), which can be used for further experiments. For example, LiF crystals favor wavebands around 20–30 μm, whereas NaCl results in bands around 50–60 μm.

The second parallel field, developed mostly after around 1950, had to do with how to correctly and quantitatively describe the various quantities associated with IR thermal radiation. As discussed in detail in Section 1.3.1, there are a number of quantities, and some of them, like radiance, are more important for IR imaging than others. Although nomenclature and radiometry may be a dry topic, its development (e.g., [114–116]) was particularly important for any later quantitative application.

The third field, which partially developed independently of the others, concerns optical materials for the IR spectral range. Of course, a huge number of materi-

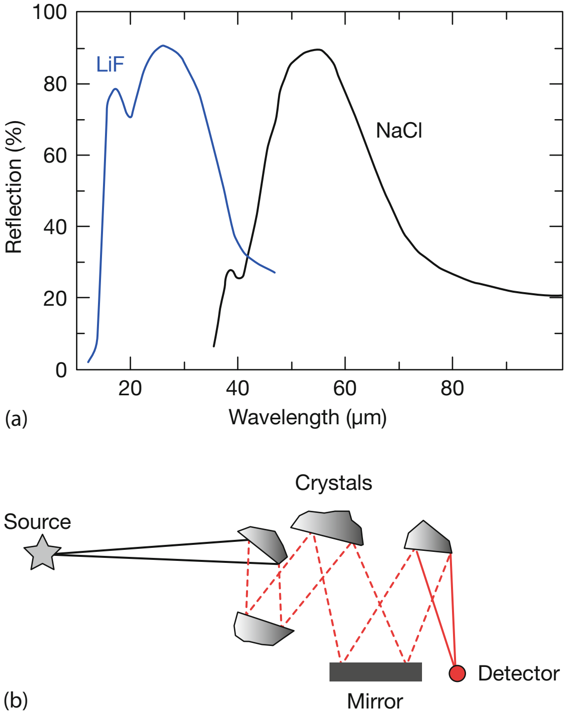

Figure 1.72 (a) Reflectivity from two alkali halide crystals: selected bands are reflected better than other wavelengths (after [113]). (b) Setup to generate *Reststrahlen* using multiple reflections from alkali halide crystals (after [64]).

als have virtually no absorption in the IR range. Some of them were given special names, such as IRTRAN (for IR transmission), for example, Irtran-1 to Irtran-5 are MgF_2, ZnS, CdF_2, ZnSe, and MgO, respectively. In addition, other IR transparent materials are known in industry with acronyms that seem totally unrelated to their chemical composition, such as KRS-5 or KRS-6 for thallium-bromide-iodide or thallium-chloride-bromide. Early research along these lines dates back to the first half of the twentieth century (e.g., [117]). Unfortunately, most IR transparent materials have high refractive index values, which means that they have large reflection losses at the air–material interface. This problem was tackled by optical interference coatings for IR components (e.g., [17, 83, 118, 119]).

A new revolutionary change in detector technology with enormous influence on IR imaging dates back to 1970 when – at first only for the visible spectral range – CCD sensors were introduced by Boyle and Smith [120, 121]. This invention was considered so important that both researchers received the 2009 Nobel Prize in Physics for their work [122]. CCDs are devices that can be used as detectors to record images in electronic digital form. This led to the development of consumer product digital cameras. The CCD surface structure resembles a matrix of a large number of radiation-sensitive cells, called pixels, arranged horizontally in rows and vertically in columns. Each pixel comprises a metal oxide semiconductor (MOS) capacitor. When a photon impinges upon a pixel, it is converted via the photoelectric effect into one or several electrons that are stored in the capacitor. The number of electrons in a pixel is proportional to the irradiation.

Therefore, the charge distribution in the pixels is a representation of an image.

By reading out the contents of the different pixels using successive charge shifting row by row and within each row column by column (this is done by a readout circuit, ROC), one can reconstruct the image in digital form. A huge advantage of CCD sensors is that they are manufactured on silicon wafers by large-scale integration processes including photolithographic steps, which are well known from microelectronics.

The development of IR detector systems changed rapidly with the introduction of IR multielement sensors, similar to visible CCD chips. In brief, detector elements have been developed as sensor arrays using MCT, PtSi, pyroelectric detectors, microbolometers, and quantum well IR photodetectors (QWIPs). Depending on the required operation temperature, the photoelectric systems were originally cooled by liquid nitrogen. This was later simplified by compact closed cycle cooling systems using the Stirling process or multistage thermoelectric Peltier coolers [123]. Better signal processing became available with the development of SPRITE sensors, which had signal processing already on their sensor elements. The latest and most advanced detectors available now are multiwaveband sensors, which can detect MW as well as LW bands separately.

1.7.2.2 **Quantitative Measurements**

The development of quantitative IR measurements started in two different fields, pyrometry (i.e., quantitative temperature spot measurements) and spectroscopy (quantitative λ-measurements).

Obviously, generations of potters, metal workers, blacksmiths, and glass blowers had the personal experience to estimate the amount of heat during their process from the color of the kiln, metal melt, or glass. The ideas for measurements of temperature started as early as 1836, when Pouillet suggested estimating temperatures from the color of incandescent bodies [149] (Table 1.11).

Keeping in mind that more than 50 years earlier Wedgewood had noted that it is quite difficult to judge the temperature from the color and brightness of heated objects, and that the brightness of a fire increases through numerous gradations, which can neither be expressed in words nor discriminated by the eye [150], we may be surprised by Pouillet's table. His description of colors was indeed very subjective; however, he was the first to come up with a rule for color change with temperature, although today we are surprised that the perception of white color should start already at temperatures of 1300 °C.

In 1862 Becquerel [151] referred to Pouillet when he suggested that one may indeed use the color to measure temperatures of incandescent bodies. However, since the eye was used as sensor, only very rough estimates could be achieved. This changed by the end of the century when the first laboratory radiative thermome-

Table 1.11 Perceived color of a hot body as a function of its temperature (after [149]).

Dull red	525 °C
Dark red	700 °C
Start of cherry red	800 °C
Cherry red	900 °C
Clear cherry red	1000 °C
Dark orange	1100 °C
Clear orange	1200 °C
White	1300 °C
Shining white	1400 °C
Dazzling white	1500 to 1600 °C

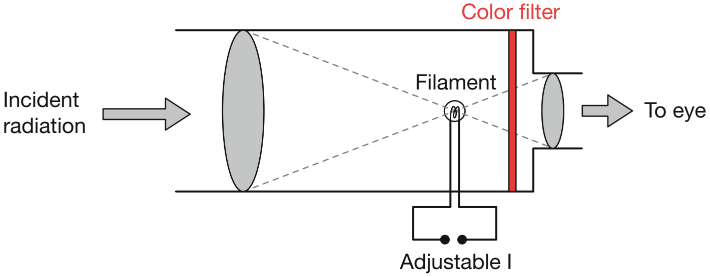

Figure 1.73 Scheme of vanishing filament pyrometer. Radiation from an unknown source is matched to one from a filament whose electrical input power is adjustable.

ters were developed (Table 1.12). The most commonly used type is the vanishing filament pyrometer (Figure 1.73) [152, 153]. In brief, its working principle is similar to that of a telescope that has an electrically heated tungsten filament in the focal plane of the objective lens. Therefore, the image of the lamp filament and its radiation are superimposed on the target radiation. The brightness of the filament is then adjusted until it matches that of the target. This means that within the image the filament disappears against the target. The red filter avoids any misinterpretation thanks to the color differences. Furthermore, it enhances the instrument's sensitivity. The device is calibrated by viewing blackbodies of known temperatures. Errors estimated around 1900 were around 100 °C. Meanwhile, the accuracy of typical commercial devices – if properly operated – is around 1 °C at 775 °C to 5 °C for temperatures at 1225 °C [153]. The most precise modern photoelectric laboratory pyrometers achieve uncertainties better than 0.1 K at 1063 °C and about 2 K at 3525 °C [154] by using much narrower red pass-band filters and photomultiplier tubes as detectors. Additional gray filters may be used to deal with different brightness levels.

Nowadays the vanishing filament pyrometer is rarely used in industry, mostly because it does not allow automated operation, and this is due to the availability of easier-to-operate modern pyrometers [31] that have direct readouts and do not

Table 1.12 Timeline of some important developments in quantitative IR measurements with pyrometers.

Subfield	Year	Person/Ref.	Event
B2	1836	Pouillet [149]	Incandescent color relates to temperature
	Around 1860	Bunsen–Kirchhoff [125]	Start of spectral analysis of atoms; however, initially there was a lack of suitable means to decompose spectrum in IR
B2	1862	Becquerel [151]	Proposed to use red glow of hot bodies to measure T
B2	1892	Le Chatelier [156]	First laboratory radiative thermometer, compared luminance of a target with central part of oil lamp flame, red filter
B3	1899	Morse [157]	US patent, disappearing filament pyrometer; for more details see, for example, [153] for comparison of various temperature measurement methods: accuracies, for example, 61 °C at 775 °C and 65 °C at 1225 °C
B3	1901	Holborn–Kurlbaum [158]	Similar pyrometer, unaware of Morse patent
B4	1901	Fery	Patent on total radiation pyrometer with thermoelectric sensor [31]
	After 1890	Many researchers	First investigations of IR spectra with grating spectrometers of atoms (e.g., [159, 160]); molecular spectra, initially unresolved broadbands [161], later resolved fine structure (e.g., [162]) (e.g., reviews [125, 163])
B3	1923	Fairchild [164, 165]	Changes of pyrometer design into approximately the present form
	1966	Lee [154]	Example of very precise modern photoelectric pyrometers, for example, uncertainties better than 0.1 K at 1063 °C and about 2 K at 3525 °C achieved owing to much narrower pass band in red and VIS photomultiplier tube

rely on the human eye as detector. Three types are common, all of which rely on the same principle as all modern IR cameras do, the main difference being that only one detector element is used. They all detect absorbed IR radiation giving rise to some signal (see corresponding sections in Chapter 2). First, narrowband pyrometers detect IR radiation within a narrow spectral band, much like IR cameras detect in the SW, MW, or LW band.

Second, to avoid the need to know correct emissivity values, ratio or two-color pyrometers were developed, which assume that emissivity does not change when two different wavelengths are used. Third, multiple-wavelength pyrometers were introduced (e.g., [155]) with the aim of becoming totally independent of emissivity (Section 3.2.2).

Parallel to the development of quantitative pyrometry, the first applications of IR spectrometry started as early as the nineteenth century. The birth of spectroscopy probably dates back to Fraunhofer, who in 1814 discovered dark lines within the continuous solar spectrum. In 1859, Bunsen and Kirchhoff interpreted the Fraunhofer lines as absorption lines due to gases in the solar atmosphere, and they developed the method of spectral analysis. Initially, it was mostly applied to atoms in the visible spectral range, and results were used to analyze spectra of stars to learn about their elemental composition. However, it was just a matter of time before the IR spectral range was used as well thanks to the increasing knowledge about it and technologies for generating and detecting the corresponding radiation.

For example, an extensive set of IR spectra of gases, liquids, solids, and minerals is due to Coblentz between 1900 and 1910 (e.g., [166–169]) and others, for example, near-IR (NIR) line spectra of atoms of hydrogen, helium, alkalis, and others were recorded shortly after 1900 by Paschen [159].

After the Bohr model of the atom was developed in 1913, other line spectra, for example, the Brackett and Pfund series of hydrogen in the IR region were predicted and experimentally investigated (e.g., [160, 170]). In parallel, the first investigations of molecular IR spectra started around the turn of the nineteenth to the twentieth century. The development was initially slow, as may be seen in Figure 1.74, which displays the rotational-vibrational spectra of HCl over a period of more than 30 years from 1893 until 1929.

At this time, Angstrom had just succeeded in detecting the location of absorption bands; however, these were very broad and showed no fine structure at all due to the then available low resolution of around 400 nm. In subsequent years the resolution of the spectrometers in the IR range was undergoing continual improvement. In Figure 1.74 this is illustrated by the single broad-band feature

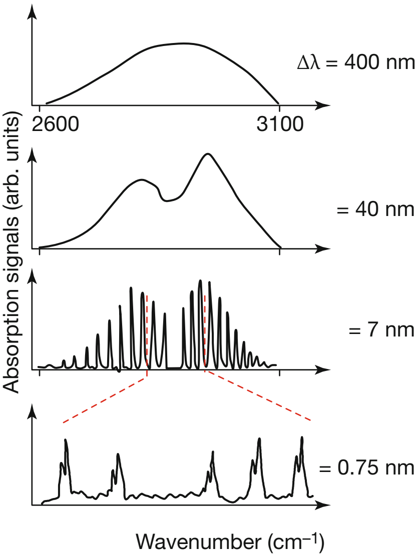

Figure 1.74 Improvements in optical resolution in spectrometers allowed a much better recording of spectra. Here a schematic overview is given for HCl ro-vibrational molecular spectra around 3.4 μm wavelength, which were recorded between around 1890 (top) and 1939 (bottom) (data after [163, 171]).

showing two peaks, then a large number of a few dozen individual peaks, separated by a characteristic missing line in the middle of the spectrum. This spectrum, with 7 nm resolution, represents a typical spectroscopic fingerprint spectrum of a given molecule, here the HCl molecule. Owing to the distinct spectral features that resemble coupled rotational-vibrational excitations in the spectral range, which sensitively depend on the molecule under study, the corresponding spectral region between $\lambda = 2$ to about 25 μm is the fingerprint region for molecules, which is optimally suited for quantitative analysis.

However, it did not end there. With the finest optical resolution available, one could determine that a single one of these individual peaks could still be split into two individual lines. The interpretation in this case is that the nuclear mass of HCl, which has an influence on the rotational motion of the molecule, depends on the isotopes. Two Cl isotopes exist, ^{35}Cl and ^{37}Cl, and the molecular spectra even allow one to investigate isotope effects and the composition of molecules. Besides these coupled rotational-vibrational excitations of molecules in the thermal IR range, purely rotational excitations at larger wavelengths of around 40 to 100 μm were also analyzed (e.g., HCl [172]).

In parallel to these experiments, the further development of quantum mechanical methods in the first decades of the twentieth century led to a very good theoretical understanding of electronic, vibrational, and rotational molecular excitations [173]. However, real experimental progress was made only after fully automated spectroscopic instruments became available after around 1940. Initially they were based on prisms and gratings, but following the invention of the fast Fourier transform (FFT), Fourier transform infrared (FTIR) spectroscopy began to dominate spectroscopic investigations in the thermal IR region starting in the 1980s [174, 175].

Astronomy also started to use the IR spectral range once the first detectors became available (e.g., review [176, 177]). Early applications included measuring the moon or planets and the thermal radiation of stars. In addition, NIR spectroscopy was used to identify corresponding lines from elements within star spectra [178]. The first interstellar and extragalactic molecules, CO, ammonia, and other polyatomic molecules, were detected in the microwave region; however, the IR range was being used, too. A prominent current example is the detection of methane on Mars using ground-based telescopes [179].

1.7.2.3 Applications and Imaging Techniques

There is a huge amount of IR applications, and it is impossible to list them all. Here a short survey of some of the most important milestones is given (Table 1.13). Coming closer to the present time, most advances are being made in modern IR cameras, which is a rapidly growing field in terms of both applications and new developments in detector and imaging technologies. Therefore, the timeline in this section stops at around the year 2000. Later developments are discussed in Chapter 2 on detectors.

The earliest visualizations of thermal signatures are probably medical applications [180] dating back to the Egyptians, who moved hands across the bodies of ill people to detect temperature changes with their fingers. Later, the Greek Hippocrates (around 400 BC) asserted that body heat was a useful diagnostic indicator of acute diseases [181]. Consequently, it is stated [182, 183] that the Greeks immersed bodies in wet mud and examined the drying process. Areas that dried more quickly were warmer regions, which helped to identify diseased regions of a body.

It took more than 2000 years before new techniques for visualizing temperature distributions on objects were developed [80]. The principle is simple: one needs a specially prepared surface such that incident absorbed radiation causes some observable change in the surface. Herschel in 1840 was the first to come up with the idea of recording/visualizing the invisible IR spectrum of the sun [58]. This may be regarded first as the birth of IR astronomy and, second, as the year of the first IR image of an object, here the spectrum of the sun (Figure 1.65), with absorption bands due to the atmosphere. Herschel moistened a strip of black paper with alcohol. Incident IR radiation led to evaporating alcohol whose pattern was immediately observable to the naked eye. Working on photography, Herschel also tried to produce permanent results by fixing images using a dye that remained on the surface after the evaporation of the alcohol. The dye concentration depended on the velocity of evaporation [58].

Owing to the low sensitivity of the method, it only works well for intense radiation sources, in this case, the sun. Some 25 years later, Tyndall wanted to convert IR images into visible ones [184]. He noted that “We must discover a substance which shall filter the composite radiation of a luminous source by stopping the visible rays and allowing the invisible ones free transmission.” Tyndall used carbon arc lamps as intense IR radiation sources, with the VIS filtered out by saturated solution of iodine in carbon disulfide. Tyndall used various detectors, for example, very thin platinum foils (thin to reduce thermal conduction) in a vacuum. The side facing the source was coated with aluminum black and absorbed IR radiation. This led to a permanent image of the carbon arc on the detector owing to the chemical reduction of platinum (Figure 1.75). Tyndall also noted that

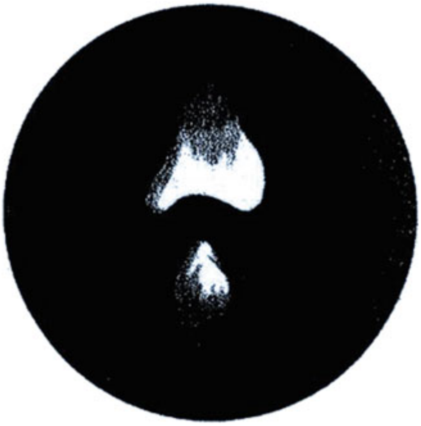

Figure 1.75 Permanent thermal image of arc of carbon arc lamp from 1866 (after [184]).

Table 1.13 Timeline of important developments: IR applications and imaging techniques up to around 2000.

Subfield	Year	Person/company/ reference	Important event in IR imaging technology
C2		Egypt, Greece	[181]: Temperature measurement for illness, detect heat with hands above body [180], also Greeks: drying mud [182, 183]
B1,C2	1840	Herschel [58]	First image spectrum
C2	1866	Tyndall [184, 185]	Thermal images by (1) chemical reduction and (2) color changes
	1880	Abney [186]	Photographic plates, sun spectrum
C2	1929–1938	Czerny, Willenberg, Mollet, Röder [187–190]	Ultrared photography: naphthalene on celluloid membranes, IR absorbed, heating ⇒ sublimation of naphthalene at those locations
C1	1930s/ 1940s	Gudden, Kutzscher	Military research on PbS IR detectors [78]
	1933	Mees *et al.* [195, 196]	Sensitive IR films
C1	1933	Ford Motor Company	First patents for IR drying ($\lambda \approx 1{-}1.6\,\mu$m) in automotive industry
C2	1934	G. Holst *et al.* [197]	First IR image converter (photocathode), more advanced developments in following decades [198]
B2, C1	1940s	Military applications in WWII	First IR display unit, image converter tube, sensitive up to 1.2 μm, used as sniper scopes
C2	1940s	G. Eastman Kodak	Commercial IR sensitive films
	1946 1954 1960	Some military camera developments	First military IR line scanner, line-by-line image, 1 h/image; mounted on aircraft, looking down, scan perpendicular to motion 1954: additional scanner reduced time to 45 min; by 1960: time 5 min/image (after Holst [23])
C2	1953	Gobrecht, Weiss [191]	IR images of hands, face, and so on, evaporography
C2	1950s	P. Kruse/Honeywell, Texas Instruments	IR images [148, 202]
C2	1954	First IR camera	Thermopile (20 min/image); bolometer (4 min/image)
C1	1955	Military	IR seeker heads; detectors PbS, PbTe, later InSb [78]
	1960	Texas Instruments	Camera looking forward/system with two moving mirrors Name: Forward Looking InfraRed system (FLIR)

Table 1.13 Continued.

Subfield	Year	Person/company/ reference	Important event in IR imaging technology
C2	1960s		Ge:Hg, first astronomical applications [78, 205]
C3	1964/ 1965/ 1966	Aga/Agema	Mass-produced cameras for civilian use: AGA 660/Sweden (single-element sensor, optomechanical scanner); 1966: 20 images/s; first camera of modern type, as known today [23, 78]
C2/A1	1970	W.S. Boyle, G.E. Smith [120–122]	CCDs, Nobel Prize 2009
C3	1975		Start of high spatial resolution systems, multielement detectors in mini coolers (first-generation systems, common module in USA) [78, 206]
C3	1980		Second-generation systems: hybrid HgCdTe(InSb)/Si (readout) FPAs
B1	1983	[207]	IRAS satellite for IR astronomy
C3	1985		Schottky diode FPAs (PtSi) commercial systems
C3	1986	Agema	Agema 870 camera with SPRITE sensor
B1	1990s	NASA	NIR instruments on board Hubble Space Telescope, for example, WFC3 [201]
C3	1990		Quantum well IR photoconductor (QWIP), hybrid second-generation systems, Stirling coolers
C3	1995		Cameras with uncooled FPAs, microbolometer, and pyroelectric
C3	> 2000		Start of third-generation system development

mercury iodide changed color from red at room temperature to yellow at 150 °C, that is, the recorded color changes refer to temperature differences. Tyndall finally realized that experiments could be dangerous. His filter solution of iodine in carbon-disulfide was extremely inflammable, and the equipment in his lab caught fire several times.

The next people to try recording thermal images were Czerny and coworkers [187–190]. Whereas Herschel and Tyndall had high temperature sources (sun or arc lamp) and therefore operated at short IR wavelengths, Czerny wanted to detect IR radiation of room temperature.

Obviously regular photography was not possible at long wavelengths because of dark reactions at room temperature.

For his new method, called *ultrared photography*, he used naphthalene or camphor on one side of a celluloid membrane. The other side facing the source

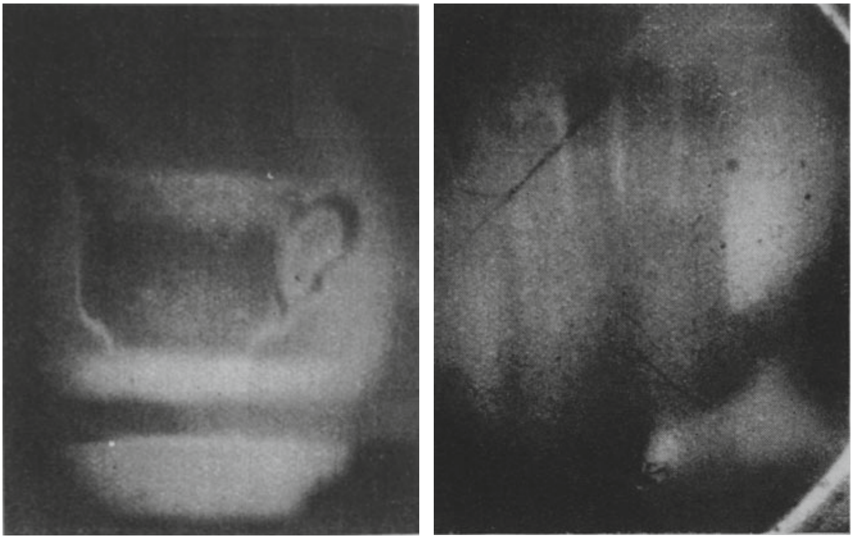

Figure 1.76 Thermographic images of a coffee mug and hand from 1953 (after [191]).

was covered with soot (later other absorbers). Absorbed IR radiation heated the membrane, leading to sublimation of the naphthalene at the respective locations. As a consequence, the irradiated parts of the coated membrane became thinner. Initially, Czerny recorded absorption spectra (with integration times of about 20 min!). A later modification entailed the use of absorbed layers of paraffin oil that evaporated when the membrane was heated. The thickness change resulted in an observed change in interference colors. Image quality depended on the thickness of the absorber layer. For thin layers, sharp images were produced; however, the method was then not very sensitive because of the reduced absorption. But if the absorber layers were thick, strong absorption also led to heat diffusion in the layer, giving slightly fuzzy images. The technique was used to analyze many spectra of fluids or gaseous samples. Also, beakers filled with near boiling water were recorded with exposure times of around 30 s. Drastic improvements in this method were later reported by Gobrecht and Weiss. They were (to our knowledge) the first to publish images of hot coffee mugs, a hand, and even the profile of a face (Figure 1.76, after [191]).

In parallel to these imaging methods based on thermal effects on absorption, research in photography was partly also focusing on the development of films sensitive to NIR radiation. Initially, the creation of IR-sensitive photographic layers and plates was an art in science [186, 192]. The first photographic images of scattered NIR radiation in nature [193] looked very strange compared to visible photos, and there is a lot of interesting physics behind the phenomena [194]. Eastman Kodak was developing the first commercial films based on fundamental research by Mees and coworkers after World War I [195, 196]. IR-sensitive films were soon being sold by at least five companies. Most films were only usable in the very NIR with

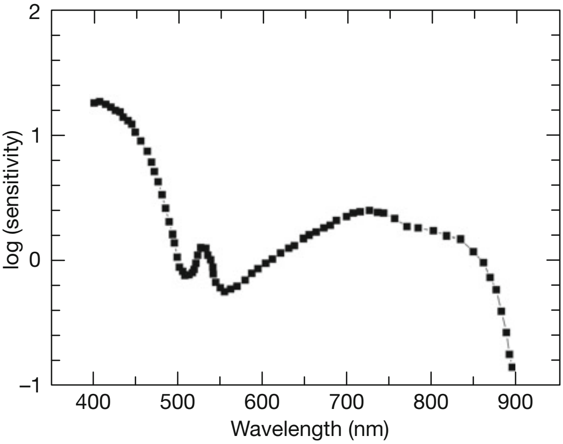

Figure 1.77 Example of sensitivity of Kodak Ektachrome Professional IR-sensitive film (after Kodak).

an upper wavelength of around 900 nm (Figure 1.77). Owing to the shift from film to digital cameras, demand for IR films decreased, and most if not all companies have meanwhile stopped producing IR films altogether.

A typical military development with later commercial use was the invention of image intensification systems, starting during World War II, based on image conversion systems that had been demonstrated as early as 1934 [197]. Image conversion means that red or IR radiation is used to create photoelectrons, which are accelerated and converted back to photons upon hitting a fluorescent layer, which emits shorter-wavelength radiation (Figure 1.78).

In principle, image intensification systems were the basis for early night vision systems [198]. Incident radiation (typically residual light or NIR radiation) is focused with an objective lens on a photocathode. There photoelectrons are created via the photoelectric effect (first conversion). The energy of these electrons is increased by accelerating them using a high electric voltage and they are then directed onto a phosphor screen where they generate photons (second back conversion), which can be viewed through an eyepiece. Early versions used photocathodes of rather low quantum efficiency (compared to today's technology). Owing to their relatively low price (compared to IR cameras), such systems are still used and sold as standard night vision goggles. The reduction in size, weight, and price of modern IR cameras may, however, soon lead to an end of these products. The principle of image intensifiers is also used in many other fields, for example, medical and industrial endoscopes.

An early example of a nonmilitary application of IR radiation is the drying of paints in the automotive industry, dating back to 1993 and operating with IR wavelengths in a range from 1 to 1.6 μm [199].

Another important nonmilitary application of IR radiation is IR astronomy. Following detector development advances, modern IR astronomy started around the

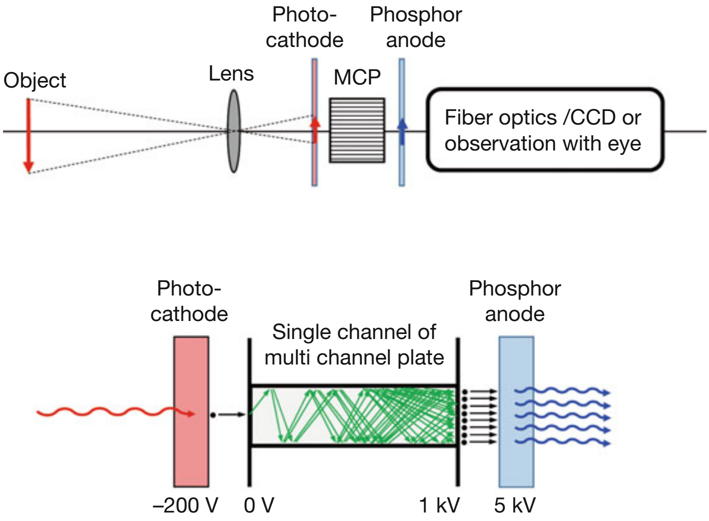

Figure 1.78 Principal setup of an image intensifier (or residual light amplifier). Top: scheme, bottom: enlarged view of main components. A small amount of object scene long-wavelength radiation is directed onto a photocathode. The ejected photoelectrons are accelerated, and their number increases, for example, with a microchannel plate (MCP). The electrons then hit a phosphor, which emits a large amount of shorter-wavelength radiation, which can either be observed by the naked eye or detected with suitable image sensors.

1960s (for a good overview of the topic, see [176]). The best systems nowadays all avoid attenuation due to the earth's atmosphere. The first pure IR satellite (IRAS) was launched in 1983, and more modern systems, such as the Hubble Space Telescope, owed their development to IRAS's success. At present, alternatives to satellites are high flying observatories such as SOFIA, a 2.5 m telescope located on board a 747 airplane [200]. The future of IR astronomy will probably start with the launch of Hubble's successor – currently planned for late 2018 – the James Webb telescope [210], which will have a 6.6 m aperture and detect radiation with wavelengths between 0.7 and 28 μm.

An example of satellite-based IR astronomy is shown in Figure 1.79. It depicts the Carina Nebula at a distance of about 7500 light years, recorded in July 2009 with the Wide Field Camera (WFC3) instrument of the Hubble Space Telescope [201]. The Hubble Space Telescope, put into orbit in April 1990 and fully operational after a service mission in late 1993, has enlarged our knowledge about the universe enormously, partly also because of its amazing capability to detect NIR radiation. Many nebulas are called as such because they have a characteristic appearance in VIS images, as shown in Figure 1.79. It is dominated by scattered light from enormous amounts of dense gas and dust. Therefore stars nestled within the dust cannot be detected in the VIS. However, they can easily be detected in the bottom image, recorded at NIR wavelengths that are scattered much less than VIS light and thus penetrate the gas and dust region (see also

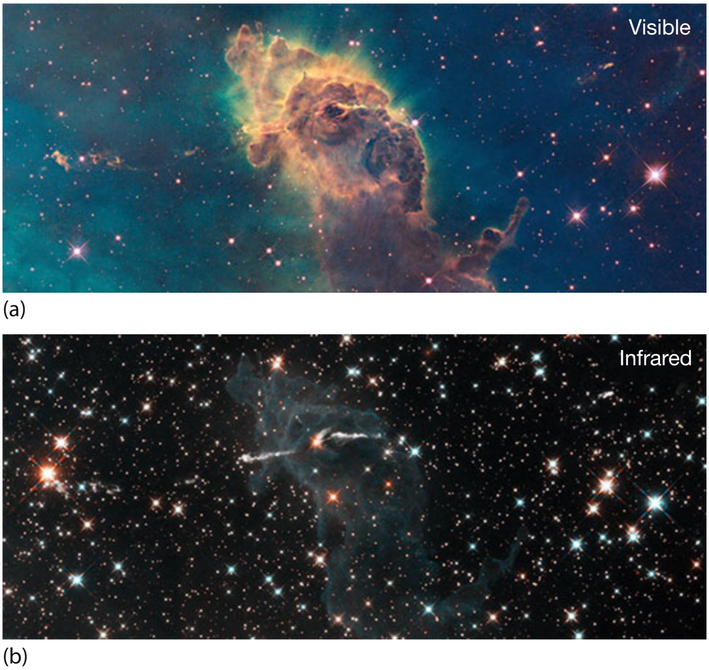

Figure 1.79 Comparison of VIS (a) and NIR (b) images of Carina Nebula. The VIS image is a composite and was recorded with a 16 megapixel CCD sensor using narrowband filters with center wavelengths of 502, 656, and 673 nm (false colors assigned are blue, green, and red, respectively). The NIR image was recorded with a 1 megapixel HgCdTe CMOS sensor with center wavelengths of 1.26 and 1.64 μm (false colors are cyan and orange, respectively). Images courtesy NASA, ESA, and the Hubble SM4 ERO team.

Section 6.3.3.3 on NIR imaging examples and Section 10.9 on the range of IR cameras).

Modern IR imaging with electronic detectors started in the late 1940s. The first systems were for the military and consisted of line scanners with a single detector. They were mounted on airplanes looking down while scanning perpendicular to the plane's motion. The forward motion of the plane led to two-dimensional images created from many line scans placed side by side. Recording times were later reduced by the addition of a scanner. A revolutionary design emerged in 1960 when Texas Instruments designed the first system capable of looking at other angles (i.e., not downward) and in particular looking in the forward direction. These systems were therefore called *forward looking IR* and later gave the acronym to the company FLIR Systems, probably the largest worldwide in this field. Many names are associated with the early research in IR detector and camera technology, but here only one of them will be singled out as an example. Paul Kruse (1927–2012) [148, 202], working at Honeywell, started working on IR imaging in the 1950s and pursued this topic until well after his retirement. He made many contributions to the field, in particular on HgCdTe detectors and uncooled microbolometer two-dimensional arrays.

Around 1960, IR detector technology was increasingly being applied to study not only intrinsic materials such as PbS or InSb but also extrinsic, that is, impurity-activated ones that offer the possibility to shift energies by the concentration and kind of doping material [203]. Mercury-doped germanium [204] soon became a new material of choice for IR applications (e.g., [205]) in the 8–14 μm range.

FLIR imagers – produced mostly, of course, for the military – were highly customized, each having unique requirements. For example, between 1964 and 1972, Texas Instruments produced 385 FLIR systems, but with 55 different configurations [206]. Obviously, because of the small numbers per configuration, these were expensive systems. In the 1970s, the need to reduce costs finally led to the development of common modules (CMs), dramatically reducing the number of configurations. The currently accepted idea behind CM systems is that certain functions of an IR sensor are not sensitive to a specific application and can therefore be made universal. This decision marked the start of rapid development in IR imaging.

The first mass-produced civilian-use camera had already been introduced earlier in 1966 with the AGA 660 by Aga (later Agema) in Sweden. Such early cameras were quite heavy and could easily weigh 20 kg, including the control unit. Aga 660 cameras had a single element sensor and an optomechanical scanner unit and pro-

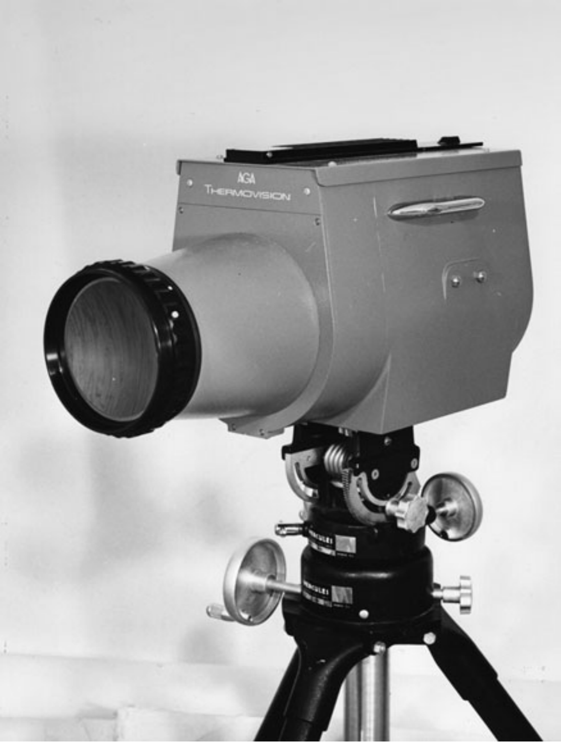

Figure 1.80 AGA Thermovision 665 camera This camera type was sold starting around 1965. Image courtesy FLIR systems, Inc. (2016).

duced about 20 images/s. Figures 1.80 and 1.81 depict two other early commercial models, a Thermovision 665 and a later example of a 1980s medical 30 Hz IR camera (Inframetrics 535) with a single HgCdTe sensor cooled by liquid nitrogen. It was advertised as requiring little space and having video output, and it allowed for recording screen images with a Polaroid camera.

Subsequent changes in IR camera technology included so-called second-generation systems where sensor and ROC were produced as hybrid focal-plane arrays. These required less power consumption and allowed for a more compact design at affordable prices and, hence, led to a real breakthrough for nonmilitary, that is, civilian, applications.

The next milestone was 1995, when the first IR cameras with uncooled microbolometer arrays were produced. The turn of the century marked the start of the development of so-called third-generation systems, which, besides bringing improvements in frame rates, number of pixels, and thermal resolution, saw the emergence of other functions, for example, multiwaveband detection.

The current world leader in IR camera sales, commercial, scientific, and military, is probably FLIR Systems. Founded in 1978, it bought out many successful competitors, such as Agema (formerly Aga Infrared) in 1997, Inframetrics in 1999, Indigo Systems in 2003, and Cedip in 2008.

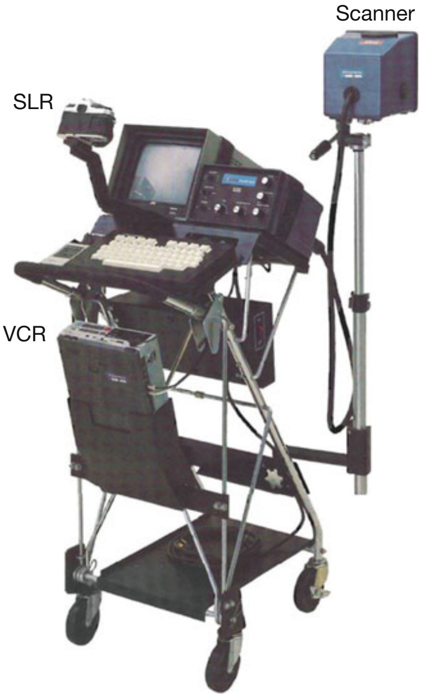

Figure 1.81 Liquid-nitrogen-cooled Inframetrics 535 IR camera from 1980s producing images of 130 × 200 pixels. The camera was cooled with liquid nitrogen (funnel on top). Hard copy recording was performed on 35 mm film (photo of computer screen) and half-inch VCR (VHS). The needed floor area of 17.5 × 22.5 in^2 was advertised as space saving (see Inframetrics PDF brochure from FLIR web site [209]).

References

1 Wolfe, W.L. and Zissis, G.J. (eds) (1993) *The Infrared Handbook*, revised 4th printing, The Infrared Information Analysis Center, Environmental Research Institute of Michigan.

2 Bass, M. (ed.) (1995) *Handbook of Optics*, Sponsored by the Optical Society of America, vol. 1, McGraw Hill, Inc.

3 Dakin, J.R. and Brown, R.G.W. (eds) (2006) *Handbook of Optoelectronics*, vol. 1, Taylor and Francis, New York.

4 Laurin, T.F. (2005) *The Photonics Handbook, Book 3: The Photonics Directory*, 51st edn, Laurin Publishing Company, Pittsfield.

5 Gross, H. (ed.) (2005) *Handbook of Optical Systems*, vol. 1, Wiley-VCH Verlag GmbH, Weinheim.

6 Gross, H. (ed.) (2008) *Handbook of Optical Systems*, vol. 4, Wiley-VCH Verlag GmbH, Weinheim.

7 Bentley, R.E. (ed.) (1998) *Handbook of Temperature Measurement, Temperature and Humidity Measurement*, vol. 1, Springer, Singapore.

8 Michalski, L., Eckersdorf, K., Kucharski, J., and McGhee, J. (2001) *Temperature Measurement*, 2nd edn, John Wiley & Sons, Ltd, Chichester.

9 Hermann, K. and Walther, L. (eds) (1990) *Wissensspeicher Infrarottechnik*, Fachbuchverlag, Leipzig (in German).

10 Dereniak, E.L. and Boreman, G.D. (1996) *Infrared Detectors and Systems*, John Wiley & Sons, Inc., New York.

11 Holst, G.C. (1993) *Testing and Evaluation of Infrared Imaging Systems*, JCD Publishing Company, Maitland.

12 Jha, A.R. (2000) *Infrared Technology: Applications to Electro-Optics, Photonic Devices, and Sensors*, John Wiley & Sons, Inc., New York.

13 Schlessinger, M. (1995) *Infrared Technology Fundamentals*, 2nd edn, Marcel Dekker, New York.

14 Schneider, H. and Liu, H.C. (2007) *Quantum Well Infrared Photodetectors*, Springer Series Optical Science, vol. 126, Springer, Heidelberg.

15 Schuster, N. and Kolobrodov, V.G. (2000) *Infrarotthermographie*, Wiley-VCH Verlag GmbH, Berlin.

16 Wolfe, W.L. (1996) Introduction to infrared system design, in *Tutorial Texts in Optical Engineering*, vol. TT24, SPIE Press, Bellingham and Washington, DC.

17 Savage, J.A. (1985) *Infrared Optical Materials and Their Antireflection Coatings*, Adam Hilger, Bristol.

18 Palik, E.P. (ed.) (1985) *Handbook of Optical Constants of Solids*, vol. 1, Academic Press, Boston; vol. 2 (1991); vol. 3 (1998).

19 Baehr, H.D. and Karl, S. (2006) *Heat and Mass Transfer*, 2nd revised edn, Springer, Berlin, New York.

20 Incropera, F.P. and DeWitt, D.P. (1996) *Fundamentals of Heat and Mass Transfer*, 4th edn, John Wiley & Sons, Inc., New York.

21 Richards, A. (2001) *Alien Vision, Exploring the Electromagnetic Spectrum with Imaging Technology*, SPIE Press, Bellingham and Washington, DC.

22 Kaplan, H. (1999) Practical applications of infrared thermal sensing and imaging equipment, in *Tutorial Texts in Optical Engineering*, vol. TT34, 2nd edn, SPIE Press, Bellingham.

23 Holst, G.C. (2000) *Common Sense Approach to Thermal Imaging*, SPIE Optical Engineering Press, Washington, DC.

24 Moore, P.O. (ed.) (2001) Infrared and thermal testing, in *Nondestructive Testing Handbook*, vol. 3, 3rd edn, American Society for Nondestructive Testing, Inc., Columbus.

25 Hecht, E. (1998) *Optics*, 3rd edn, Addison-Wesley, Reading.

26 Falk, D.S., Brill, D.R., and Stork, D.G. (1986) *Seeing the Light: Optics in Nature, Photography, Color Vision, and Holography*, Harper & Row, New York.

27 Pedrotti, F. and Pedrotti, L. (1993) *Introduction to Optics*, 2nd edn, Prentice Hall, Upper Saddle River.

28 Palmer, J.M. (1993) Getting intense on intensity. *Metrologia*, **30**, 371–372.

29 Codata values of fundamental constants 2014, www.nist.gov/pml/div684/

fcdc/upload/wall2014.pdf (accessed May 2017).

30 Soffer, B.H. and Lynch, D.K. (1999) Some paradoxes, errors, and resolutions concerning the spectral optimization of human vision. *Am. J. Phys.*, **67**, 946–953.

31 De Witt, D.P. and Nutter, G.D. (eds) (1988) *Theory and Practice of Radiation Thermometry*, John Wiley & Sons, Inc., New York.

32 Fronapfel, E.L. and Stolz, B.-J. (2006) Emissivity measurements of common construction materials. Inframation 2006, Proceedings vol. 7, pp. 13–21.

33 Kanayama, K. (1972) Apparent directional emittance of V-groove and circular-groove rough surfaces. *Heat Transf. Jpn. Res.*, **1** (1), 11–22.

34 Wen, C.-D. and Mudawar, I. (2004) Emissivity characteristics of roughened aluminum alloy surfaces and assessment of multispectral radiation thermometry (MRT) emissivity models. *Int. J. Heat Mass Transf.*, **47**, 3591–3605.

35 Rose, S.R., Watson, I.M., Ramsey, M.S., and Hughes, C.G. (2014) Thermal deconvolution: Accurate retrieval of multispectral infrared emissivity from thermally-mixed volcanic surfaces. *Remote Sens. Environ.*, **140**, 690–703

36 deMonte, J. (2008) Guess the real world emittance. Inframation 2008, Proceedings vol. 9, pp. 111–124.

37 Cronholm, M. (2003) Geometry effects: Hedging your bet on emissivity. Inframation 2003, Proceedings vol. 4, pp. 55–68.

38 Hartmann, J. and Fischer, J. (1999) Radiator standards for accurate IR calibrations in remote sensing based on heatpipe blackbodies. Proc. EUROPTO Conf. Environ. Sens. Appl., SPIE, vol. 3821, pp. 395–403.

39 Henke, S., Karstädt, D., Möllmann, K.P., Pinno, F., and Vollmer, M. (2004) Challenges in infrared imaging: Low emissivities of hot gases, metals, and metallic cavities. Inframation 2004, Proceedings vol. 5, pp. 355–363.

40 F. Olschewski *et al.* (2013) The in-flight blackbody calibration system for the GLORIA interferometer on board an airborne research platform. *Atmos. Meas. Tech.*, **6**, 3067–3082.

41 Madding, R.P. (2004) IR window transmittance temperature dependence. Inframation 2004, Proceedings vol. 5, pp. 161–169.

42 Richards, A. and Johnson, G. (2005) Radiometric calibration of infrared cameras accounting for atmospheric path effects, in *Thermosense XXVII*, Proceedings of SPIE, vol. 5782 (eds G.R. Peacock, D.D. Burleigh, and J.J. Miles), SPIE Press, Bellingham, pp. 19–28.

43 Vollmer, M., Möllmann, K.-P., and Pinno, F. (2007) Looking through matter: quantitative IR imaging when observing through IR windows. Inframation 2007, Proceedings vol. 8, pp. 109–127.

44 Kaiser, N. and Pulker, H.K. (eds) (2003) *Optical Interference Coatings*, Springer, Berlin, Heidelberg.

45 Bach, H. and Krause, D. (eds) (1997) *Thin Films on Glass*, Springer, Berlin, Heidelberg.

46 MacLeod, H.A. (2010) Thin Film Optical Filters, 4th ed., CRC Press. www.thinfilmcenter.com (accessed May 2017).

47 www.spectrogon.com; https://www.jenoptik.com/-/media/websitedocuments/optical-systems/optik/filter_ir_spektralbereich_en.pdf (accessed May 2017).

48 *This month in Physics History: Birth of Émilie du Châtelet*, APS news 17/11, p. 2 (2008), http://www.aps.org/publications/apsnews/200812/physicshistory.cfm (accessed May 2017).

49 du Châtelet, É. (1744) Dissertation sur la nature et la propagation du feu, Paris, Chez Prault, fils, 1744, avail. via Bibliothèque nationale de France, see http://gallica.bnf.fr/ark:/12148/bpt6k756786/f6.image (accessed May 2017).

50 Hearnshaw, J.B. (1986) *The Analysis of Starlight*, Cambridge UP.

51 Herschel, W. (1800) Experiments on the refrangibility of the invisible rays of the sun. *Philos. Trans. R. Soc. Lond.*, **90**, 284–292, doi:10.1098/rstl.1800.0015

52 Cornell, E.S. (1938) The radiant heat spectrum from Herschel to Melloni. – I.

The work of Herschel and his contemporaries. *Ann. Sci.* **3** (1), 119–137 and Cornell, E.S. (1938) II. The work of Melloni and his contemporaries. *Ann. Sci.* **3** (4), 402–416.

53 Olson, R.G. (1969) A note on Leslie's cube in the study of radiant heat. *Ann. Sci.*, **25** (3), 203–208.

54 Olson, R.G. (1970) Count Rumford, Sir John Leslie, and the study of the nature and propagation of heat at the beginning of the nineteenth century. *Ann. Sci.*, **26** (4), 273–304.

55 Newton, I. (1730) *Opticks or, a Treatise of the Reflections, Refractions, Inflections, and Colours of Light,* corrected 4th edn, The Project Gutenberg, EBook #33504

56 Thompson, B. (1786) New experiments upon heat. *Philos. Trans. R. Soc. Lond.*, **76**, 273–304.

57 Leslie, J. (1804) *An Experimental Inquiry Into the Nature and Propagation of Heat*, J. Mawman, London, Edinburgh, reprint Cambridge Univ. Press (2014).

58 Herschel, J.F.W. (1840) On the chemical action of the rays of the solar spectrum on preparations of silver and other substances, both metallic and non-metallic, and on some photographic processes. *Philos. Trans. R. Soc. Lond.* **130,** 1–59, http://www.jstor.org/stable/108209?seq=1#page_scan_tab_contents (accessed May 2017).

59 Kirchhoff, G. (1860) Über das Verhältnis zwischen dem Emissionsvermögen und dem Absorptionsvermögen der Körper für Wärme und Licht. *Pogg. Ann. Phys.* Bd. 19, new count: **185** (2), 275–301.

60 Agassi, J. (1967) The Kirchhoff–Planck radiation law. *Science*, **156**, 30–37.

61 Schirrmacher, A. (2003) Experimenting theory: The proofs of Kirchhoff's radiation law before and after Planck. *Hist. Stud. Phys. Biol. Sci.*, **33** (2), 299–335, University of California Press.

62 Lummer, O. and Pringsheim, E. (1901) Kritisches zur schwarzen Strahlung. *Ann. Phys.*, 4. Folge **6**, new count: **311** (9), 192–210.

63 Rubens, H. and Nichols, E.F. (1897) Versuche mit Wärmestrahlen von grosser Wellenlänge. *Wied. Ann. Phys.*, **60**, new count: *Ann. Phys.*, **296** (3), 418–462.

64 Rubens, H. and Kurlbaum, F. (1901) Anwendung der Methode der Reststrahlen zur Prüfung des Strahlungsgesetzes. *Ann. Phys.*, 4. Folge, Bd. **4**, new count: **309** (4), 649–666.

65 Wien, W. (1896) Über die Energieverteilung im Emissionsspektrum eines schwarzen Körpers. *Ann. Phys.*, **58**, new count: vol **294** (8), 662–669,
in English: (1897) On the division of energy in the emission-spectrum of a black body. *Philos. Mag.*, **43** (262), 214–220.

66 Lord Rayleigh (1900) Remarks upon the law of complete radiation. *Philos. Mag. Ser. 5*, **49** (301), 539–540.

67 Jeans, J.H. (1905) On the partition of energy between matter and ether. *Philos. Mag. Ser. 6*, **10** (55), 91–98.

68 Hollandt, J. (2012) 125 Jahre Forschung an und mit dem schwarzen Körper. *PTB Mitteilungen*, **122** (3), 87–91.

69 Hoffmann, D. (2000) Schwarze Körper im Labor – Experimentelle Vorleistungen für Plancks Quantenhypothese. *Phys. Bl.*, **56** (12), 43–47.

70 Hettner, G. (1922) Die Bedeutung von Rubens Arbeiten für die Planck'sche Strahlungsformel. *Naturwissenschaften*, **10**, 1033–1038.

71 Planck, M. (1900) Zur Theorie des Gesetzes der Energieverteilung im Normalspektrum. *Verh. Dtsch. Phys. Ges.*, **2**, 202 refers to oral presentation of 19 October, see also (1900) Über eine Verbesserung der Wien'schen Spektralgleichung. *Verh. Dtsch. Phys. Ges.*, **2**, 237 refers to oral presentation of 14 December.

72 Wien, W. (1894) Temperatur und Entropie der Strahlung. *Ann. Phys.*, **52**, new count: vol. **288** (5), 132–165.

73 Stefan, J. (1879) Über die Beziehung zwischen der Wärmestrahlung und der Temperatur. *Sitzungsber. Math.-Naturwiss. Classe Kais. Akad. Wiss. Wien*, **79**, 391–428.

74 Wisniak, J. (2006) Josef Stefan. Radiation, conductivity, diffusion, and other phenomena. *Rev. CENIC Cienc. Quím.*, **37** (3), 188–195.

75 Douglas, R.C. (1979) The centenary of the fourth-power law. *Phys. Educ.*, **14**, 234–238.

76 Boltzmann, L. (1884) Ableitung des Stefan'schen Gesetzes betreffend die Abhängigkeit der Wärmestrahlung von der Temperatur aus der electromagnetischen Lichttheorie. *Wiedem. Ann.*, **22**, 291–294, new count: (1884) *Ann. Phys.* **258** (6), 291–294, http://onlinelibrary.wiley.com/doi/10.1002/andp.18842580616/abstract (accessed May 2017).

77 Volume numbers Annalen der Physik: https://de.wikisource.org/wiki/Annalen_der_Physik (accessed May 2017).

78 Rogalski, A. (2012) History of infrared detectors. *Opto-Electron. Rev.*, **20** (3), 279–308.

79 Putley, E.H. (1982) History of infrared detection – Part I. The first detectors of thermal radiation. *Infrared Phys.*, **22**, 125–131.

80 Putley, E.H. (1982) History of infrared detection – Part II. The first thermographs. *Infrared Phys.*, **22**, 189–191.

81 Lovell, D.J. (1969) The development of lead salt detectors. *Am. J. Phys.*, **37**, 467–478.

82 Kutzscher, E.W. (1974) Review on detectors of infrared radiation. *Electro-Opt. Syst. Des.*, **5**, 30–34.

83 Wolfe, W.L. and Ballard, S.S. (1959) Optical materials, films, and filters for infrared instrumentation. *Proc. IRE*, **47** (9), 1540–1546.

84 Coblentz, W.W. (1908) Instruments and Methods used in radiometry. *Bull. Bureau Stand.*, **4** (3), 391–460, Washington, https://archive.org/details/NBSBulletin (accessed May 2017).

85 Coblentz, W.W. (1913) Instruments and Methods used in radiometry II. *Bull. Bureau Stand.*, **9**, 7–63, Scientific Paper 188, https://archive.org/details/NBSBulletin (accessed May 2017).

86 Arnquist, W.N. (1959) Survey of early infrared developments, Proc. IRE 47/9, 1420–1430.

87 Della Porta, G.B. (1589) *Magiae Naturalis*, Naples.
English translation, London (1658) See short description on page 361, book download from the library of congress researchers rare book and special collections room: http://www.loc.gov/rr/rarebook/digitalcoll/digitalcoll-magic.html (accessed May 2017).

88 Evans, J. and Popp, B. (1985) Pictet's experiment: The apparent radiation and reflection of cold. *Am. J. Phys.*, **53** (8), 737–753.

89 Mariotte, M. (1733) 1682 – a short note on an experiment with changed perception, if glass is put in front of fireplace, Histoire de l'Académie Royale des Sciences depuis son établissement en 1666 jusqu' à 1686 vol. 1, Paris, p. 344.

90 Lambert, J.H. (1779) *Pyrometrie oder vom Maaße des Feuers und der Wärme*, Haude und Spener, Berlin, pp. 210–211, Sect. 78, https://books.google.de/books?id=G5I_AAAAcAAJ&printsec=frontcover&hl=de#v=onepage&q&f=false (accessed May 2017).

91 Count of Rumford (1804) An enquiry concerning the nature of heat. *Philos. Trans. R. Soc. Lond.* 94, 77–182.

92 Seebeck, T.J. (1822) Magnetische Polarisation der Metalle und Erze durch Temperatur-Differenz. *Abh. Dtsch. Akad. Wiss. Berlin*, 265–373; also available as: (1895) *Ostwald's Klass. Exakten Wiss.*, **70**, 3–120.

93 Nobili, L. (1830) Beschreibung eines Thermo-Multiplicators oder elektrischen Thermoskops. *Pogg. Ann. Phys.*, **20**, new count: vol. **96**, 245–252.

94 Nobili, L. and Melloni, M. (1833) Untersuchungen über mehrere Wärme-Erscheinungen mittelst des Thermomultiplicators. *Pogg. Ann. Phys.*, **27**, new count: vol. **103**, 439–455.

95 Barr, E.S. (1962) The infrared pioneers – 2. Macedonio Melloni. *Infrared Phys.*, **2**, 67–73, see also: Sir William Herschel. (1961) *Infrared Phys.* **1**, 1–4 and (1963) Samuel Pierpont Langley. *Infrared Phys.*, **3**, 195–206.

96 Hentschel, K. (2005) Macedonio Melloni über strahlende Wärme. *NTM Int. J. Hist. Ethics Nat. Sci. Technol. Med.*, **13** (4), 216–237.

97 Melloni, M. (1833) Ueber den Durchgang der Wärmestrahlen durch verschiedene Körper. *Ann. Phys.*, **28** (2), new count: vol. **104** (6), 371–378.

98 Melloni, M. (1835) Ueber den freien Durchgang der strahlenden Wärme durch verschiedene starre und flüssige Körper. *Ann. Phys.*, **111** (6), 112–139, 277–308.

99 Melloni, M. (1835) Neue Untersuchungen über den unmittelbaren Durchgang der strahlenden Wärme durch verschiedene starre und flüssige Körper. *Ann. Phys.* **111** (7), 385–413 and **111** (8), 529–558.

100 Melloni, M. (1835) Nachtrag zu den Abhandlungen des Herrn Melloni. *Ann. Phys.*, **35** (2), new count: vol. **111** (8), 559–578.

101 Melloni, M. (1835) On the immediate transmission of calorific rays through diathermal bodies. *Philos. Mag.*, **7** (3), 475–478.

102 Peltier, J.C.A. (1834) Nouvelles Expériences sur la Caloricité des courans électriques. *Ann. Chim. Phys.* **56**, 371–386, http://gallica.bnf.fr/ark:/12148/cb343780820/date.r=Annales+de+chimie+et+de+physique.langEN (accessed May 2017).

103 http://www.leybold-shop.com/physics/physics-equipment/heat/heat-transfer/heat-radiation/moll-s-thermopile-55736.html (accessed May 2017).

104 (a) Langley, S.P. The bolometer and radiant energy. *Proc. Am. Acad. Arts Sci.*, **16**, 342–358 (May 1880–June 1881), see also (b) (1901) The new spectrum. *Philos. Mag. Ser. 6*, **2** (7), 119–130.

105 Becquerel, E. (1839) Recherches sur les effets de la radiation chimique de la lumière solaire, au moyen des courants électriques, *C. R. Acad. Sci.*, **9**, 145–149, see http://gallica.bnf.fr/ark:/12148/bpt6k2968p.image.langDE.r=comptes%20rendus%201839 (accessed May 2017).

106 Becquerel, E. (1841) Ueber die elektrischen Wirkungen unter Einfluß der Sonnenstrahlen. *Ann. Phys.*, **54**, new count **130**, 35–42.

107 Smith, W. (1873) Effect of light on selenium during the passage of an electric current. *Nature*, **7**, 303.

108 Adams, W.G. and Day, R.E. (1877) The action of light on selenium. *Philos. Trans. R. Soc. Lond.*, **167**, 313–349.

109 Ta, Y. (1938) Effects des radiations sur les cristaux pyroelectriques, *Compt. Rend.*, **207**, 1042–1044, see http://gallica.bnf.fr/ark:/12148/cb343481087/date.langDE (accessed May 2017).

110 Svanberg, A.F. (1851) Ueber Messung des Leitungswiderstandes für elektrische Ströme und über ein galvanisches Differentialthermometer. *Ann. Phys Chem.*, **24** (3), 411–418 (gesamte Reihe Bd. 160).

111 Lummer, O. and Kurlbaum, F. (1901) Der elektrisch geglühte "schwarze" Körper. *Ann. Phys.*, new count **310** (8), 829–836.

112 Czerny, M. (1923) Über eine neue Form der Rubensschen Reststrahlenmethode. *Z. Phys.*, **16** (1), 321–331.

113 Pohl, R.W. (1954) *Optik und Atomphysik*, 9th edn, Springer.

114 Nicodemus, F.E. and Zissis, G.F. (1962) Methods of radiometric calibration, Report 4613-20-R, Infrared Laboratory, University of Michigan, see http://deepblue.lib.umich.edu/bitstream/handle/2027.42/6821/bac9793.0001.001.pdf?sequence=5 (accessed May 2017).

115 Nicodemus, F. (1963) Radiance. *Am. J. Phys.*, **31**, 368–377.

116 Spiro, I.J., Clark Jones, R., and Wark, D.Q. (1965) Atmospheric transmission: Concepts, symbols, units and nomenclature. *Infrared Phys.*, **5**, 11–36.

117 Tilton, L.W., Plyler, E.K., and Stephens, R.E. (1949) Refractive indices of thallium bromide-iodide crystals for visible and infrared radiant energy. *J. Res. Nat. Bureau Stand.*, **43**, RP2008, http://nvlpubs.nist.gov/nistpubs/jres/43/jresv43n1p81_A1b.pdf (accessed May 2017).

118 Hass, G., Schroeder, H.H., and Turner, A.F. (1956) Mirror coatings for low visible and high infrared reflectance. *J. Opt. Soc. Am.*, **46**, 31–35.

119 Cox, J.T. and Hass, G. (1958) Antireflection coatings for germanium and silicon in the infrared. *J. Opt. Soc. Am.*, **48**, 677–680.

120 Boyle, W.S. and Smith, G.E. (1970) *Bell Syst. Tech. J.*, **49**, 587–593.

121 Amelio, G.F., Tompsett, M.F., and Smith, G.E. (1970) *Bell Syst. Tech. J.*, **49**, 593–600

122 Scientific Background on the Nobel Prize in Physics 2009: Two revolutionary optical technologies, Royal Swedish Academy of Sciences, (2009), http://www.nobelprize.org/nobel_prizes/physics/laureates/2009/ (accessed May 2017).

123 Rogalski, A. (2012) Progress in focal plane array technologies. *Progr. Quant. Electron.*, **36**, 342–473.

124 Case, T.W. (1917) Notes on the change of resistance of certain substrates in light. *Phys. Rev.*, **9**, 305–310.

125 Schäfer, C. and Matossi, F. (1930) *Das Ultrarote Spektrum*, Springer, Berlin.

126 Putley, E.H. (1971) Infrared applications of the pyroelectric effect. *Opt. Laser Technol.*, **3** (3), 150–156.

127 Lal, R.B. and Batra, A.K. (1993) Growth and properties of triglycine sulfate (TGS) crystals: Review. *Ferroelectrics*, **142** (1), 51–82.

128 Welker, H. (1952) Über neue halbleitende Verbindungen. *Z. Naturforsch.*, **7a**, 744–749 and (1954) Semiconducting intermetallic compounds. *Physica*, **XX**, 893–909.

129 Lawson, W.D., Nielsen, S., Putley, E.H., and Young, A.S. (1959) Preparation and properties of HgTe and mixed crystals of HgTe-CdTe. *J. Phys. Chem. Solids*, **9**, 325–329.

130 Kozlowski, L.J. and Kosonocky, W.F. (1995) Infrared detector arrays, in *Handbook of Optics*, Chapt. 23, McGraw Hill.

131 Elliott, C.T. (1981) New detector for thermal imaging systems. *Electron. Lett.*, **17** (8), 312–313.

132 Elliott, C.T., Day, D., and Wilson, D.J. (1982) An integrating detector for serial scan thermal imaging. *Infrared Phys.*, **22**, 31–42.

133 Elliott, C.T. (1985) Cadmium mercury telluride infrared detectors. *J. Cryst. Growth*, **72**, 453–461.

134 Shepherd, F.R. and Yang, A.C. (1973) Silicon Schottky retinas for infrared imaging. IEEE Int. Electron. Dev. Meet. (IEDM73) Tech. Dig., 310–313.

135 Kimata, M., Denda, M., Fukumoto, T., Tsubouchi, N., Uematsu, S., Shibata, H., Higuchi, T., Saheki, T., Tsunoda, R.E., and Kanno, T. (1982) Platinum silicide Schottky-barrier IR-CCD image sensors. *Jap. J. Appl. Phys.*, **21** (1), 231–235.

136 Kosonocky, W.F., Shallcross, F.V., Villani, T.S., and Groppe, J.V. (1985) 160 · 244 element PtSi Schottky-barrier IR-CCD image sensor. *IEEE Trans. Electron. Dev.*, **ED-32** (8), 1564–1573.

137 Kimata, M., Denda, M., Yutani, N., Iwade, S., and Tsubouchi, N. (1987) A 512 × 512-element PtSi Schottky-barrier infrared image sensor. *IEEE J. Solid State Circuits Soc.*, **22** (6), 1124–1129.

138 Yutani, N., Yagi, H., Kimata, M., Nakanishi, J., Nagayoshi, S., and Tubouchi, N. (1991) 1040 × 1040 element PtSi Schottky-barrier IR image sensor. IEEE Int. Electron. Dev. Meet. (IEDM 91) Tech. Dig., 175–178.

139 Levine, B.F. (1993) Quantum-well infrared photodetectors. *J. Appl. Phys.*, **74**, R1–R81.

140 Rogalski, A. (2003) Quantum well photoconductors in infrared detector technology. *J. Appl. Phys.*, **93**, 4355.

141 Veprik, A.M., Babitsky, V.I., Pundak, N., and Riabzev, S.V. (2000) Vibration control of linear split Stirling cryogenic cooler for airborne infrared application. *Shock Vib.*, **7**, 363–379.

142 Korf, H., Rühlich, I., Mai, M., and Thummes, G. (2005) Pulse tube cryocooler for IR applications. Proc. SPIE, vol. 5783, Infrared Technology and Applications XXXI, 164.

143 Mongellaz, F., Fillot, A., Griot, R., and De Lallee, J. (1994) Thermoelectric cooler for infrared detectors. Proc. SPIE, vol. 2227, Cryogenic Optical Systems and Instruments VI, 156.

144 Wood, R.A., Han, C.J. and Kruse, P.W. (1992) Integrated uncooled infrared detector imaging arrays. Solid-State Sens. Actuator Workshop, 1992. 5th Tech. Dig., IEEE, 132–135.

145 Niklaus, F., Vieider, C., and Jakobsen, H. (2007) MEMS-based uncooled infrared bolometer arrays – A review, in *MEMS/MOEMS Technologies and Applications III*, (eds J.-C. Chiao,

X. Chen, Z. Zhou, and X. Li), Proc. SPIE, vol. 6836, 68360D.

146 Roxhed, N. *et al.* (2010) Optical Sensing and Detection, in *Low-Cost Uncooled Microbolometers for Thermal Imaging* (eds F. Berghmans, A.G. Mignani, and C.A. van Hoof), Proc. SPIE, vol. 7726, 772611.

147 Budzier, H. and Gerlach, G. (2011) *Thermal Infrared Sensors*, John Wiley & Sons.

148 Kruse, P.W. (2001) Uncooled thermal imaging – arrays, systems, and applications, in *Tutorial Texts in Opt. Eng.*, vol. TT51, SPIE, Bellingham.

149 Pouillet, C.S.M. Recherches sur le hautes temperatures et sur plusieurs phénomènes qui en dependent. *C. R. Acad. Sci.*, **3**, 782–790 (1836), see also http://gallica.bnf.fr/ark:/12148/cb343481087/date.r=Comptes+rendus+de+l%27Acad%C3%A9mie+des+sciences+1838.langDE (accessed May 2017).

150 Wedgewood, J. (1782) An attempt to make a thermometer for measuring the higher degrees of heat from a red heat up to the strongest that vessels made of clay can support. *Philos. Trans. R. Soc. London*, **72**, 305–326.

151 Becquerel, A.E. (1862) Recherches sur la détermination des hautes températures au moyen de l'intensité de la lumiere émise par les corps incandescents. *C. R. Acad. Sci.* **55**, 826–829, Mallet-Bachelier, Paris.

152 Waidner, C.W. and Burgess, G.K. (1904/1905) Optical pyrometry. *Bull. Bureau Stand.*, **1** (2), 189–254, http://nvlpubs.nist.gov/nistpubs/bulletin/01/nbsbulletinv1n2p189_A2b.pdf (accessed May 2017).

153 Childs, P.R.N., Greenwood, J.R., and Long, C.A. (2000) Review of temperature measurement. *Rev. Sci. Instrum.*, **71** (8), 2959–2978.

154 Lee, R.D. (1966) The NBS photoelectric pyrometer and its use in realizing the international practical temperature scale above 1063 °C. *Metrologia*, **2** (4), 150–162.

155 Ng, D. and Fralick, G. (2001) Use of a multiwavelength pyrometer in several elevated temperature aerospace applications. *Rev. Sci. Instrum.*, **72**, 1522–1530.

156 le Chatelier, H. (1892) Sur la mesure optique des temperatures élevés. *C. R. Acad. Sci.*, **114**, 214–216, http://gallica.bnf.fr/ark:/12148/bpt6k918488/f164.image.r=h%20de%20chatelier%201892.langDE, (accessed May 2017),
also H. le Chatelier, O. Boudouard, *Mesure des Températures élevées*, Carré et Naud, Paris.

157 Morse, E.F. (1899) US Patent 696916, Apparatus for gaging temperatures of heated substances (filed 9 November 1899; patent issued 1 April 1902).

158 Holborn, L. and Kurlbaum, F. (1903) Über ein optisches Pyrometer. *Ann. Phys.*, 4. Folge, Bd. **10**, 225–241, new count: vol. **315** (2).

159 Paschen, F. (1908) Zur Kenntnis ultraroter Linienspektra. I. (Normalwellenlängen bis 27 000 Å.-E.). *Ann. Phys.*, **332** (13), 537–570.

160 Brackett, F.S. (1922) Visible and infrared radiation of hydrogen. *Astrophys. J.*, **56**, 154–161.

161 Ångström, K. (1900) Ueber die Bedeutung des Wasserdampfes und der Kohlensäure bei der Absorption der Erdatmosphäre. *Ann. Phys.*, **308** (12), 720–732.

162 Meyer, C.F. and Levin, A.A. (1929) On the absorption spectrum of hydrogen chloride. *Phys. Rev.*, **34**, 44–52.

163 Randall, H.M. (1938) The spectroscopy of the far infra-red. *Rev. Mod. Phys.*, **10**, 72–85.

164 Fairchild, C.O. and Hoover, W.H. (1923) Disappearance of the filament and diffraction effects in improved form of an optical pyrometer. *J. Opt. Soc. Am.*, **7**, 543–579.

165 Foote, P.D., Fairchild, C.O., and Harrison, T.R. (1948) *Pyrometric Practice*, Department of Commerce – Technologic papers of the bureau of standards No. 170, Bureau of Standards, 16 February 1921, US Government printing office Washington.

166 Coblentz, W.W. (1905) Infra-red absorption spectra, I. Gases. *Phys. Rev. (Ser. I)*, **20** (5), 273–291.

167 Coblentz, W.W. (1905) Infra-red absorption spectra, II. Liquids and solids. *Phys. Rev. (Ser. I)*, **20** (6), 337–363.

168 Coblentz, W.W. (1906) Infra-red absorption and reflection spectra (minerals). *Phys. Rev. (Ser. I)*, **23** (2), 125–153.

169 Coblentz, W.W. (1907) Infra-red emission spectrum of burning carbon disulphide. *Phys. Rev. (Ser. I)*, **24** (1), 72–76.

170 Pfund, A.H. (1924) The emission of nitrogen and hydrogen in infrared. *J. Opt. Soc. Am.*, **9** (3), 193–196.

171 Ogilvie, J.F. (1989) Infrared spectroscopy of diatomic molecules – the first century, *Chin. J. Phys.*, **27** (4), 281–296.

172 Czerny, M. (1925) Messungen im Rotationsspektrum des HCl im langwelligen Ultrarot. *Z. Phys.*, **34** (1), 227–244.

173 Herzberg, G. (1939) *Molecular Spectra and Molecular Structure, 1. Diatomic Molecules*, Prentice Hall.

174 Bell, R.J. (1972) *Introductory Fourier Transform Spectroscopy*, Academic, New York.

175 Möllmann, K.-P. and Vollmer, M. (2013) Fourier transform infrared spectroscopy in physics laboratory courses. *Eur. J. Phys.*, **34**, S123–S137.

176 Rieke, G.H. (2009) History of infrared telescopes and astronomy. *Exp. Astron.*, **25**, 125–141.

177 Clements, D.L. (2015) *Infrared Astronomy – Seeing the Heat*, CRC Press.

178 Merrill, P.W. (1934) Photography of the near infra-red region of stellar spectra. *Astrophys. J.*, **79**, 183–202.

179 Mumma, M.J. *et al.* (2009) Strong release of methane on Mars in northern summer 2003. *Science*, **323** (5917), 1041–1045.

180 Berz, R. and Sauer, H. (2007) The medical use of infrared thermography – History and recent applications, paper 04, 12 pages, online-Proceedings Thermographie Kolloquium 2007, DGZfP, Stuttgart/Germany, see http://www.ndt.net/search/docs.php3?MainSource=61 (accessed May 2017).

181 Wunderlich, C.A. (1871) *On the Temperature in Diseases, a Manual of Medical Thermometry*, translation of 2nd German edn, New Sydenham Soc., London.

182 Ring, E.F.J. (2004) The historical development of thermal imaging in medicine. *Rheumatology*, **43**, 800–802.

183 Niumsawatt, V., Rozen, W.M., and Whitaker, I.S. (2015) Digital thermographic photography for preoperative perforator mapping, in *Imaging for Plastic Surgery*, Chapt. 10, (eds L. Saba *et al.*), CRC Press, Taylor and Francis.

184 Tyndall, J. (1866) On calorescence. *Philos. Trans. R. Soc. Lond.*, **156**, 1–24.

185 Tyndall, J. (1868) *Heat – A Mode of Motion*, 3rd edn, Longmans, Greens and Co, London.

186 Abney, W.W. (1880) The Bakerian lecture: On the photographic method of mapping the least refrangible end of the solar spectrum. *Philos. Trans. R. Soc. Lond.*, **171**, 653–667.

187 Czerny, M. (1929) Über Photographie im Ultraroten. *Z. Phys.*, **53** (1/2), 1–12.

188 Willenberg, H. (1932) Ultrarotphotographie. *Z. Phys.*, **74** (9–10), 663–680.

189 Czerny, M. and Mollet, P. (1938) Neue Versuche zur Photographie im Ultraroten. *Z. Phys.*, **108** (1–2), 85–100.

190 Czerny, M. and Röder, H. (1938) Fortschritte auf dem Gebiete der Ultrarottechnik. *Ergeb. Exakt. Naturwiss.*, **17**, 70–107.

191 Gobrecht, H. and Weiss, W. (1953) Zur photograpischen Aufnahme im Ultrarot nach der Methode von Czerny. *Z. Angew. Phys.*, **5** (6), 207.

192 Hentschel, K. (2002) *Mapping the Spectrum – Techniques of Visual Representation in Research and Teaching*, Oxford UP.

193 Wood, R.W. (1910) A new departure in photography. *Century Mag.*, Volume 79, 565–572.

194 Mangold, K., Shaw, J.A., and Vollmer, M. (2013) The physics of near-infrared photography. *Eur. J. Phys.*, **34** (6), 51–71.

195 Brooker, L.G.S., Hamer, F.M., and Mees, C.E.K. (1933) Recent advances in sensitizers for the photography of the infrared. *J. Opt. Soc. Am.*, **23** (6), 216–222.

196 Kenneth Mees, C.E. (1961) *From Dry Plates to Ektachrome Film: A Story of Photographic Research*, Ziff-Davis Pub. Co.

197 Holst, G., de Boer, J.H., Teves, M.C., and Veenemans, C.F. (1934) An apparatus for the transformation of light of long wavelength into light of short wavelength. *Physica*, **1**, 297–305.

198 Montoro, H.P. (2005) Image intensification: The technology of night vision, in *The Photonics Handbook 2005, Book 3 of The Photonics Directory*, 51st Int. edn, Laurin Publishing, Pittsfield, p. H114–H117, see www.photonics.com (accessed May 2017).

199 Groven, F.J. (1933) Ford Motor Company, patents US 1998615 A and US 2057776 A, Paint baking process, registered 21. July 1933 and 29. October 1934.

200 https://www.sofia.usra.edu (accessed May 2017).

201 https://www.nasa.gov/mission_pages/hubble/main/index.html (accessed May 2017).

202 Reine, M.B., Norton, P.R., and Stelzer, E.L. (2013) Paul E. Kruse (1927–2012, in memoriam), in *Infrared Technology and Applications XXXIX*, (eds B.F. Andresen, G.F. Fulop, C.M. Hanson, and P.R. Norton), Proc. SPIE, vol. 8704, 87041F.

203 Bratt, P., Engeler, W., Levinstein, H., Mac Rae, A., and Pehek, J. (1961) A status report on infrared detectors, *Infrared Phys.*, **1**, 27–38.

204 Borrello, S.R. and Levinstein, H. (1962) Preparation and properties of mercury-doped germanium. *J. Appl. Phys.*, **33**, 2947–2950.

205 Westphal, J.A., Murray, B.C., and Martz, D.E. (1963) An 8–14 micron infrared astronomical photometer, *Appl. Opt.*, **2**, 749–753.

206 http://www.ti.com/corp/docs/company/history/timeline/defense/1970/docs/72-common-module.htm (accessed May 2017)

207 Neugebauer, G. *et al.* (1984) The infrared astronomical satellite (IRAS) mission. *Astrophys. J.*, **278,** L1–L6.

208 Tekniska museet in Stockholm, http://www.tekniskamuseet.se/objekt.html?Id=http://kulturarvsdata.se/tekm/object/TM40091 (accessed May 2017).

209 http://www.flir.com/uploadedFiles/CVS/Markets/Legacy/Documents/Model%20535%20Inframetrics.pdf (accessed May 2017).

210 http://www.jwst.nasa.gov/ (accessed May 2017).

Chapter 2

Basic Properties of IR Imaging Systems

2.1

Introduction

This chapter presents a brief overview of the radiation detector principles used in thermal imaging systems. It provides background knowledge on operation principles, limiting factors for detector performance, and imaging systems. For a practitioner, a detailed knowledge on detectors is not necessary to be able to use an infrared (IR) imaging system. However, the interpretation of IR images requires some background knowledge on the limiting factors for camera parameters, such as temperature accuracy, temperature resolution (noise equivalent temperature difference, or NETD), spatial resolution (modulation transfer function, or MTF), and so on.

2.2

Detectors and Detector Systems

An IR detector or detector system acts as a transducer that converts radiation into electrical signals. It forms the core of an IR imaging system. The quality of this transduction largely determines the performance of the imaging system.

IR detectors can be divided into two groups: photon detectors and thermal detectors. In photon (or quantum) detectors, a single-step transduction leads to changes in the concentration or mobility of the free charge carriers in the detector element upon absorption of photons from IR radiation [1]. If the incident radiation generates nonequilibrium charge carriers, the electrical resistance of the detector element is changed (e.g., photoconductors [2, 3]) or an additional photocurrent is generated (e.g., photodiodes [2, 3]).

Thermal detectors can be treated as two-step transducers. First, the incident radiation is absorbed to change the temperature of a material. Second, the electrical output of the thermal sensor is produced by a corresponding change in some physical property of the material (e.g., temperature-dependent electrical resistance in a bolometer).

Infrared Thermal Imaging, Second Edition. M. Vollmer and K.-P. Möllmann.
© 2018 WILEY-VCH Verlag GmbH & Co. KGaA. Published 2018 by WILEY-VCH Verlag GmbH & Co. KGaA.

2.2.1
Parameters That Characterize Detector Performance

In general, radiation detectors are characterized by a large number of parameters [4]. With respect to the performance of an imaging system, the detector parameters listed in Table 2.1 are of particular importance.

The important figure for radiation detectors is the value of D_λ^*. Using the D_λ^* value, the performance of all different radiation detectors can be compared (see Figure 2.1 for spectral specific detectivity curves of commercially available IR detectors). The D_λ^* value is determined experimentally from spectral responsivity and frequency-dependent noise measurements.

Knowledge of the D_λ^* value makes it possible to estimate the noise-equivalent power (NEP) for a given detector geometry and bandwidth of signal detection. For example, if we assume an indium antimonide (InSb) photodiode at 5 μm wavelength with a specific detectivity of about $10^{11}\,\mathrm{cm\,Hz^{1/2}\,W^{-1}}$, a detector area of $25 \times 25\,\mu\mathrm{m}^2$, and a bandwidth of 10 kHz for signal detection, we find a value of NEP_λ of 2.5 pW.

As shown in Section 1.3.2, the incident radiant power on a detector element depending on the object temperature can be estimated for any given optics of an IR camera. A change in the blackbody temperature ΔT_{BB} causes a difference in

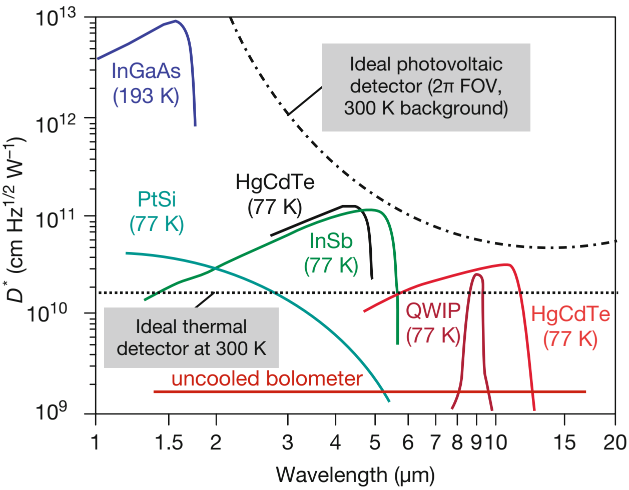

Figure 2.1 Specific spectral detectivity D_λ^* of various photon and thermal detectors for IR radiation in comparison to theoretical limits of D^* for ideal photon and thermal detectors, respectively (after [6]) (operating detector temperature as indicated, all detectors with a hemispherical field of view (FOV) to 300 K background, a chopping frequency of 1 kHz for photon detectors, and 10 Hz for thermal detectors are assumed).

Table 2.1 Several detector parameters with a significant influence on IR imaging system performance.

Name, symbol, preferred units	Definition, description	Functional relationship
A_D (cm^2) responsive area of a single pixel	Usually equals geometric area of a single pixel. Typically $50 \times 50\ \mu\mathrm{m}^2$ or $25 \times 25\ \mu\mathrm{m}^2$ for thermal detectors and $50 \times 50\ \mu\mathrm{m}^2$ down to $15 \times 15\ \mu\mathrm{m}^2$ for photon detectors in IR focal plane arrays.	–
τ (s) Time constant	Characterizes detector response time (see also Figure 2.2).	Equals decay time or rise time necessary for detector signal to reach 1/e value or (1 − 1/e) value, respectively, for incident radiation in terms of rectangular wave pulse.
R_λ^U (V W^{-1}) or R_λ^I (A W^{-1}) Spectral responsivity	Ratio of detector signal voltage or current to incident monochromatic radiant flux on detector area at wavelength λ.	$R_\lambda^U = \dfrac{U_\mathrm{signal}}{\Phi_\mathrm{radiation}}$ or $R_\lambda^I = \dfrac{I_\mathrm{signal}}{\Phi_\mathrm{radiation}}$
$\dfrac{U_N}{\sqrt{\Delta f}}$ (V Hz$^{-1/2}$) or $\dfrac{I_N}{\sqrt{\Delta f}}$ (A Hz$^{-1/2}$) rms–noise voltage or current density	Detector output noise voltage U_N or current I_N with respect to square root of applied bandwidth $\sqrt{\Delta f}$ of signal measurement.	Depends on noise mechanism. Example: $\dfrac{U_N}{\sqrt{\Delta f}} = \sqrt{4kT_\mathrm{D}R_\mathrm{D}}$ for dominating Johnson–Nyquist noise (R_D-detector resistance)
NEP$_\lambda$ (W) Spectral noise equivalent power	Necessary incident monochromatic radiant power on detector area to produce a signal-to-noise ratio (SNR) of unity; this value mostly depends on detector area and bandwidth of signal detection [3, 5].	$\mathrm{NEP}_\lambda = \dfrac{U_N}{R_\lambda^U}$ or $\mathrm{NEP}_\lambda = \dfrac{I_N}{R_\lambda^I}$
Specific spectral detectivity D_λ^* (cm Hz$^{1/2}$ W^{-1})	Reciprocal of spectral noise equivalent power normalized to eliminate dependence of detector area and bandwidth of signal detection.	$D_\lambda^* = \dfrac{\sqrt{A_\mathrm{D}\Delta f}}{\mathrm{NEP}_\lambda}$
T_D (K) Operating temperature	Equals temperature of detector.	–

the radiant power $\Delta\Phi_{\mathrm{BB}}$ received by the detector according to

$$\Delta\Phi_{\mathrm{BB}} = \frac{\partial\Phi_{\mathrm{BB}}}{\partial T_{\mathrm{BB}}}\Delta T_{\mathrm{BB}} \tag{2.1}$$

The object temperature difference ΔT_{BB} can be calculated from the measured radiant power difference $\Delta\Phi_{\mathrm{BB}}$:

$$\Delta T_{\mathrm{BB}} = \left(\frac{\partial\Phi_{\mathrm{BB}}}{\partial T_{\mathrm{BB}}}\right)^{-1}\Delta\Phi_{\mathrm{BB}} \tag{2.2}$$

If the radiant power difference $\Delta\Phi_{\mathrm{BB}}$ equals the NEP, the limit for possible signal detection (with SNR equal to unity) is achieved.

2.2.2
Noise Equivalent Temperature Difference

The lower limit of the detectable radiant power difference is the NEP. Inserting the NEP in Eq. (2.2) results in the minimum temperature difference of the blackbody $\Delta T_{\mathrm{BB}}^{\mathrm{min}}$ that can be measured.

This minimum temperature difference giving a radiant power difference equal to the NEP is defined as the NETD:

$$\Delta T_{\mathrm{BB}}^{\mathrm{min}} = \mathrm{NETD} = \left(\frac{\partial\Phi_{\mathrm{BB}}}{\partial T_{\mathrm{BB}}}\right)^{-1}\mathrm{NEP} \tag{2.3a}$$

$$\mathrm{NETD} = \left(\frac{\partial\Phi_{\mathrm{BB}}}{\partial T_{\mathrm{BB}}}\right)^{-1}\frac{\sqrt{A_{\mathrm{D}}\Delta f}}{D_{\lambda}^{*}} \tag{2.3b}$$

For a given D_{λ}^{*} the NETD of the detector depends on the square root of the detector area and the bandwidth of signal detection. For example, a detector is assumed to have a very low time constant, allowing signal detection at 10 kHz and a frequency-independent D_{λ}^{*}. If the bandwidth is increased from 100 Hz to 10 kHz, then the necessary D_{λ}^{*} value of the detector to achieve the same NETD (i.e., temperature resolution of an IR camera) must be increased by a factor of 10. If the detector area is decreased by a factor of 4 (e.g., detector size from $50 \times 50\ \mu\mathrm{m}^2$ to $25 \times 25\ \mu\mathrm{m}^2$), then the D_{λ}^{*} value must be doubled to achieve the same NETD. Furthermore, the NETD is influenced by the camera optics, and all attenuation factors for the incident radiation (e.g., limited transmittance of the atmosphere and the optics, filling factor) will increase the NETD.

If D^{*} is wavelength dependent (Figure 2.1) and the detector receives the blackbody radiation within the wavelength region $\lambda_1 \le \lambda \le \lambda_2$ according to Eqs. (1.23), (2.3a) and (2.3b), we find

$$\mathrm{NETD} = \frac{1}{\mathrm{FOV}\int_{\lambda_1}^{\lambda_2}\tau_{\mathrm{optics}}(\lambda)D_{\lambda}^{*}(\lambda)\frac{\partial M_{\lambda,\mathrm{BB}}(\lambda,T_{\mathrm{BB}})}{\partial T_{\mathrm{BB}}}\,\mathrm{d}\lambda}\sqrt{\frac{\Delta f}{A_{\mathrm{D}}}} \tag{2.4}$$

with the field of view (FOV) related to the hemisphere FOV and the spectrum-dependent attenuation factor of camera optics $\tau_{\text{optics}}(\lambda)$.

According to the order-of-magnitude estimate of detector sensitivities of IR cameras (Section 1.3.2.6), all attenuation factors for the incident radiation on the NETD have been neglected.

A simple estimate of the necessary D^* for a detector to achieve a given NETD value uses the results of Section 1.3.2.6. For a long-wavelength camera system (8–14 μm) with a standard 24° objective and an object temperature change from 302 to 303 K, the difference of incident radiant power received by each single detector pixel amounts to 2.54 nW.

We treat this difference in radiant power as the NEP for a detector size of $50 \times 50\,\mu\text{m}^2$ and a signal detection with an effective noise bandwidth of 100 Hz. In this case the necessary average D^* value (average spectral value of $D^*(\lambda)$ within the 8–14 μm wavelength region) can be calculated according to the functional relationship for the D^* value in Table 2.1. The necessary D^* value from this estimate amounts to $2 \cdot 10^7\,\text{cm}\,\text{Hz}^{1/2}\,\text{W}^{-1}$. If the object temperature difference is decreased to NETD = 0.1 K, the necessary D^* of the detector increases to $2 \cdot 10^8\,\text{cm}\,\text{Hz}^{1/2}\,\text{W}^{-1}$. For a more realistic situation, only a decreased value of radiant power will generate the detector signal because of the attenuation factors. In this case, the minimum D^* must exceed $5–8 \cdot 10^8\,\text{cm}\,\text{Hz}^{1/2}\,\text{W}^{-1}$.

2.2.3
Thermal Detectors

2.2.3.1 Temperature Change of Detector

Thermal detectors convert absorbed electromagnetic radiation into thermal energy, causing a rise in the detector temperature. The efficiency of this energy conversion is determined by the absorptance α, (also called absorptivity, Eq. (1.27)) that is, the portion of absorbed radiation $\Phi_{\text{absorbed}}/\Phi_{\text{incident}}$.

Therefore, the spectral dependence of the responsivity is determined by the spectral distribution of the absorptance $\alpha(\lambda)$. The energy conversion can be expressed by the following differential equation resembling energy conservation:

$$\alpha \Phi_0 = C_{\text{th}} \frac{\mathrm{d}\Delta T}{\mathrm{d}t} + G_{\text{th}} \Delta T \tag{2.5}$$

with C_{th} the heat capacitance and G_{th} the heat conductance of the detector. The heat conductance G_{th} contains all heat exchange mechanisms of the detector as conduction, convection, and radiation. The radiation power $\Phi_0 = \Phi(T_{\text{object}}) - \Phi(T_{\text{detector}})$ in Eq. (2.5) represents the net radiation power transferred to the detector, which is given by the difference between the radiation power received from the object $\Phi(T_{\text{object}})$ and the radiation power emitted by the detector $\Phi(T_{\text{detector}})$ itself. The absorbed radiant power $\alpha\Phi_0$ leads to an increase in the detector temperature ΔT.

For a square-wave pulse of radiation, the change in detector temperature ΔT exhibits an exponential rise and decay with a time constant τ (Figure 2.2).

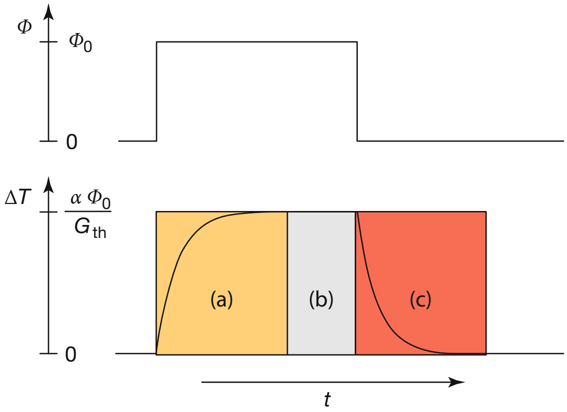

Figure 2.2 Time-dependent temperature change for a square-wave pulse of radiation (after [6]).

Equation 2.5 can be readily solved. One finds for the temperature response $\Delta T(t)$ of the sensor during the rise period

$$\Delta T = \frac{\alpha \Phi_0}{G_{th}} \left(1 - e^{-\frac{t}{\tau}}\right) \tag{2.6}$$

with time constant

$$\tau = \frac{C_{th}}{G_{th}} \tag{2.7}$$

for the steady-state conditions ($t \to \infty$)

$$\Delta T = \frac{\alpha \Phi_0}{G_{th}} \tag{2.8}$$

and for the decay period

$$\Delta T = \frac{\alpha \Phi_0}{G_{th}} e^{-\frac{t}{\tau}} \tag{2.9}$$

The time constant τ for a thermal detector is a measure of the detector's speed of response. It is determined by the ratio of the heat capacitance to the heat conductance of the sensor. If the temperature difference ΔT due to absorbed radiation is linearly transformed into an electrical signal, then the responsivity of the detector is determined by the ratio of the absorptance α to the heat conductance G_{th} of the detector. Obviously, a fast and sensitive thermal detector requires low heat conductance for an optimum temperature increase and, as a consequence, also low heat capacitance (or mass) to exhibit a small time constant. For measurements, see Section 9.4.1.2.

2.2.3.2 Temperature-Dependent Resistance of Bolometer

For the complete detector operation, transduction of the temperature rise to an electrical output signal is necessary. This can be done using any temperature-dependent physical property, such as the temperature dependence of the electrical resistance (bolometer), the creation of a voltage by a temperature difference (thermoelectricity or Seebeck effect in thermocouples and thermopiles), the temperature dependence of electrical polarization (pyroelectric detectors), and others. At present, the bolometer principle is the dominating detector used for IR cameras. Therefore, only the bolometer is discussed here in detail.

The bolometric effect is a change in the electrical resistance of a material due to the temperature increase caused by the absorbed radiation in the detector element. The temperature dependence of the electrical resistance $R(T)$ is given by the temperature coefficient β, defined by

$$\beta = \frac{1}{R}\frac{\partial R}{\partial T} \tag{2.10}$$

If the bolometer temperature is increased by ΔT, we find for the resistance change

$$\Delta R = \frac{\partial R}{\partial T}\Delta T = \overline{\beta R}\Delta T \tag{2.11}$$

where $\overline{\beta R}$ is the average value in the temperature interval ΔT.

This resistance change for steady-state conditions can be expressed with the absorbed radiant power $\alpha \Phi_0$ using Eq. (2.8):

$$\Delta R = \frac{\beta R \alpha \Phi_0}{G_{\text{th}}} \tag{2.12}$$

2.2.3.3 NEP and D^* for Microbolometer

If a steady-state bias current I is applied to the bolometer, the signal voltage $U_{\text{signal}} = I\Delta R$ can be measured. According to the definition of R_λ^U, the bolometer responsivity equation is given by

$$R_\lambda^U = \frac{\beta I R \alpha(\lambda)}{G_{\text{th}}} \tag{2.13}$$

The responsivity is strongly influenced by the temperature coefficient β of the material used. Therefore, today semiconductors with $\beta = -2$ to $-3\%\,\text{K}^{-1}$, such as vanadium oxide VO_x or amorphous silicon α-Si, are used as bolometer materials instead of metals with β values on the order of $0.1\,\%\,\text{K}^{-1}$. The responsivity increases with the current applied to the bolometer. However, with increasing current an additional self-heating of the bolometer occurs associated with a bolometer resistance decrease owing to the negative temperature coefficient of the bolometer material. This behavior defines an optimum operating point of the detector.

For a discussion of the specific detectivity D^*, it is necessary to fix the dominant noise mechanisms in bolometer detectors. If no $1/f$-noise occurs, we can assume two dominating noise mechanisms: Johnson noise and noise resulting from temperature fluctuations [4, 5]. Neglecting an additional amplifier noise, these two dominating noise mechanisms of the NEP lead to

$$\text{NEP} = \sqrt{4kT_{\text{D}}^2 G_{\text{th}}\left(1 + \frac{I^2 R}{T_{\text{D}} G_{\text{th}}}\right)\Delta f + \frac{4kT_{\text{D}} G_{\text{th}}^2 \Delta f}{\beta^2 I^2 R}} \tag{2.14}$$

where the current heating of the bolometer is included. For Eq. (2.14), we have used the fact that the temperature differential due to current heating is small compared to the detector temperature before applying a current flow. The first term in Eq. (2.14) resulting from the temperature fluctuation noise indicates an increasing NEP with current heating. The second term resulting from the Johnson noise describes a decreasing NEP with increasing current associated with the increasing signal response of the detector Eq. (2.13). These opposite tendencies result in an optimum current flow with a minimum NEP. The minimum NEP is found by differentiating the NEP with respect to the current. The minimum NEP is found for optimum bolometer current $I(\mathrm{NEP}_{\min})$,

$$I(\mathrm{NEP}_{\min}) = \sqrt{\frac{G_{\mathrm{th}}}{|\beta| R}} \tag{2.15}$$

which defines the minimum NEP as

$$\mathrm{NEP}_{\min} = \sqrt{4kT_{\mathrm{D}}^2 G_{\mathrm{th}} \left(1 + \frac{2}{|\beta| T_{\mathrm{D}}}\right) \Delta f} \tag{2.16}$$

This expression shows that the temperature coefficient β, the heat conductance G_{th}, and the detector temperature T_{D} represent optimization parameters for the NEP of a bolometer detector. In IR cameras with bolometer arrays, the focal-plane array (FPA) is operated near room temperature ($T_{\mathrm{D}} \approx 300\,\mathrm{K}$). The β value for the materials used is about -2 to $-3\%\,\mathrm{K}^{-1}$, as mentioned earlier; hence, the factor $2/(|\beta| T_{\mathrm{D}})$ varies between 0.22 and 0.33. The most interesting parameter in bolometer detector technology is the thermal conductance, G_{th}, which directly affects the NEP Eq. (2.16). For a bolometer detector, the heat transfer can be described by the three fundamental heat transfer processes conduction, convection, and radiation. Bolometer arrays in IR cameras operate under vacuum conditions. Therefore, convection and conduction due to a surrounding gas atmosphere can be excluded. The only remaining heat transfer processes are radiant heat exchange and heat conduction via the solid-state material of the bolometer (support legs; Figure 2.3). The total thermal conductance G_{th} can be calculated from the conductances caused by radiation and conduction:

$$G_{\mathrm{th}} = G_{\mathrm{th}}^{\mathrm{radiation}} + G_{\mathrm{th}}^{\mathrm{conduction}} \tag{2.17}$$

The thermal conductance caused by the radiant loss of a detector with area A_{D} at temperature T_{D} assuming unit emissivity and hemispherical FOV can be calculated by differentiating the Stefan–Boltzmann equation with respect to the temperatures:

$$G_{\mathrm{th}}^{\mathrm{radiation}} = \frac{\mathrm{d}(A_{\mathrm{D}} \sigma T_{\mathrm{D}}^4)}{\mathrm{d}T} = 4 A_{\mathrm{D}} \sigma T_{\mathrm{D}}^3 \tag{2.18}$$

The conduction contribution $G_{\mathrm{th}}^{\mathrm{conduction}}$ can be estimated using a simplified model of one-dimensional heat transport Eq. (2.19):

$$G_{\mathrm{th}}^{\mathrm{conduction}} = \lambda \frac{A_{\mathrm{cross}}}{l} \tag{2.19}$$

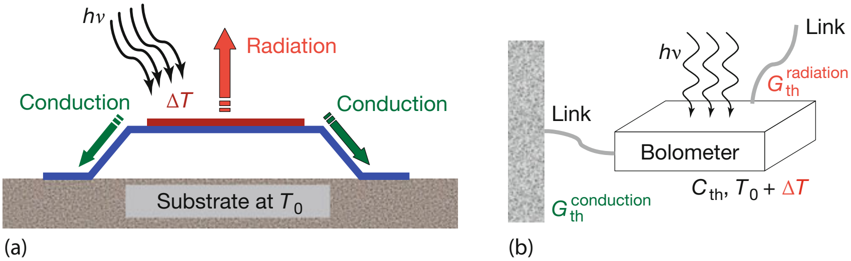

Figure 2.3 (a) Heat transfer from a bolometer membrane by radiative losses from membrane and conductive losses via support legs of membrane. (b) Equivalent circuit for energy transfer.

where λ is the thermal conductivity of the material suspending the bolometer membrane, A_{cross} the cross-sectional area, and l the length of the support legs of the bolometer.

To get low NEP values, and hence low NETD values, the total heat conductance must be as small as possible. The minimum value of G_{th} results if conduction can be neglected and the radiation dominates the heat transfer. In this case, and if only thermal fluctuation noise occurs in the thermal detector (Johnson noise is neglected), we will get the minimum NETD possible or, in other words, the theoretical limit of the specific detectivity D^* (Eqs. (2.20) and (2.21), respectively):

$$\text{NEP}_{\text{ideal}} = 4\sqrt{A_{\text{D}}\sigma k T_{\text{D}}^5 \Delta f} \tag{2.20}$$

$$D_{\text{ideal}}^* = \frac{1}{4\sqrt{\sigma k T_{\text{D}}^5}} \tag{2.21}$$

As a numerical example for detector temperature $T_{\text{D}} = 300\,\text{K}$, the specific detectivity becomes $1.8 \cdot 10^{10}\,\text{cm}\,\text{Hz}^{1/2}\,\text{W}^{-1}$. If this value is compared to the 2π FOV and 300 K background-limited IR photodetection (BLIP) limit for quantum detectors (Figure 2.1), one can conclude that thermal detectors are only competitive in the LW region (8–14 μm).

For a $35 \times 35\,\mu\text{m}^2$ bolometer, this corresponds to a thermal conductance value of $7.5 \cdot 10^{-9}\,\text{W}\,\text{K}^{-1}$.

For a real bolometer, the thermal conductance is also influenced by the heat conduction via the suspension legs of the membrane connecting the bolometer with the substrate, which acts as a heat sink.

To achieve only small additional contributions to the thermal conductance, a small cross-sectional area and a comparatively large length of the insulation legs are required. The limits for the length of the legs are given by the area of a single pixel (Figure 2.4a). The insulation legs are responsible for a decrease of the filling factor below 100%. Improvements in micromechanical technologies have increased the filling factor to about 80%.

For a simple estimate of the heat conductance of the legs, neglecting the temperature coefficient of resistivity (TCR) of the material, we assume a heat conductivity of the material Si_3N_4 used of about $2\,\text{W}\,\text{m}^{-1}\,\text{K}^{-1}$, a leg length of 50 μm,

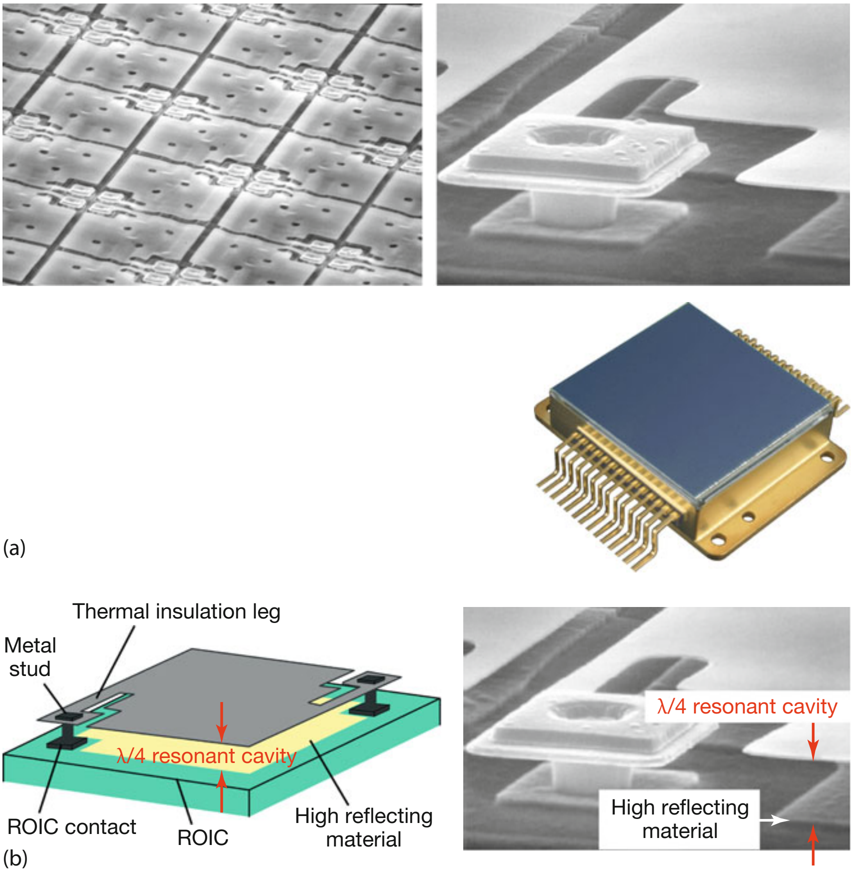

Figure 2.4 (a) Uncooled bolometer FPAs. Left: bolometer array; top right: contact of bolometer detector; bottom right: complete bolometer 640 × 480 pixels FPA chip. Image courtesy: ULIS, France. (b) Bolometer pixel with $\lambda/4$ resonant cavity. Image courtesy: ULIS, France.

with a cross-sectional area of $2 \times 0.5\,\mu\text{m}^2$ [7]. For these parameters, the thermal conductance caused by the thermal conduction via the two bolometer legs is $8 \cdot 10^{-8}\,\text{W}\,\text{K}^{-1}$. The vacuum-operated bolometer will therefore have a total heat conductance of $8.8 \cdot 10^{-8}\,\text{W}\,\text{K}^{-1}$. According to Eq. (2.9), the time constant equals the ratio of the heat capacitance to the heat conductance. For a bolometer with a heat conductance of $8.8 \cdot 10^{-8}\,\text{W}\,\text{K}^{-1}$ and a time constant of 10 ms, a heat capacitance of $8.8 \cdot 10^{-10}\,\text{J}\,\text{K}^{-1}$ must be achieved. Assuming a specific heat capacity of $500\,\text{J}\,\text{kg}^{-1}\,\text{K}^{-1}$ of the main bolometer material Si_3N_4, this results in a mass of the bolometer pixel of about 0.6 ng. For a Si_3N_4 density of $3.2\,\text{g}\,\text{cm}^{-3}$ and a bolometer area of $35 \times 35\,\mu\text{m}^2$, this corresponds to a detector membrane thickness of about $0.2\,\mu\text{m}$. Such a detector membrane would be too thin for efficient absorption of IR radiation. For enhanced long-wavelength IR absorption, a quarter-wavelength resonant cavity is used (Figure 2.4b). The metal studs connecting the bolometer of a FPA to a complementary metal oxide semiconductor (CMOS) readout integrated circuit (ROIC) also adjust the cavity width. The ROIC is an integrated circuit multiplexer that couples to a FPA sensor that reads the individual electrical FPA outputs. The ROIC transforms the small detector signal to a relatively large measurable output voltage.

For an application of these detectors in thermal imaging systems, it must be considered that bolometers are not perfect in DC operation. The previously discussed 2.54 nW change of incident radiation power for a long-wavelength camera system (8–14 μm) with a standard 24° objective and an object-temperature change from 303 to 302 K will cause a radiation-induced bolometer temperature change (total conductance of $8.8 \cdot 10^{-8}\,\mathrm{W\,K^{-1}}$ assumed) of only about 29 mK. However, the correct object-temperature change e of 1 K can only be measured by the bolometer if the intrinsic bolometer temperature is stable compared to the temperature change caused by the radiation power change. This means that if the detector temperature is changed by 29 mK owing to other mechanisms, for example, a change in temperature of the whole detector assembly, this also leads to an apparent 1 K object temperature change. Therefore, in most bolometer research and development (R&D) cameras, the array in a thermal imaging system is mounted on a Peltier element and its temperature is thermoelectrically stabilized. Additionally, a flag with known temperature is placed with a period of some minutes into the optical path of the camera for a recalibration of the detector array.

Nowadays bolometer arrays are also operated without temperature stabilization [8]. This lowers the energy consumption of the cameras and allows a more compact camera design but increases the demands on the calibration process and the exact temperature determination of the detector array. Additional attempts are being made to develop a camera calibration process that makes the shutter dispensable [9, 10].

2.2.4
Photon Detectors

2.2.4.1 Principle of Operation and Responsivity

Photon detectors convert absorbed electromagnetic radiation directly into a change in the electronic energy distribution in a semiconductor by the change in the free charge carrier concentration. This process is called the *internal photoelectrical effect*. Solids as semiconductors exhibit a typical electronic band structure with energy bands or energy states (“allowed” electron energies) and energy gaps (“forbidden” electron energies) (Figure 2.5a,b). For radiation detection, the quantum energy of the photons, $E = h\nu$, must exceed an energy threshold, ΔE, which is the excitation energy of an electronic transition between the valence (uppermost band almost fully occupied by electrons) and the conduction band (lowermost band, almost completely unoccupied) or between an energy state within the energy gap (caused by an impurity energy level) and an energy band. Figure 2.5c depicts different excitation processes. For the intrinsic photoeffect, there occurs an interband excitation of an electron–hole pair at photon energies exceeding the

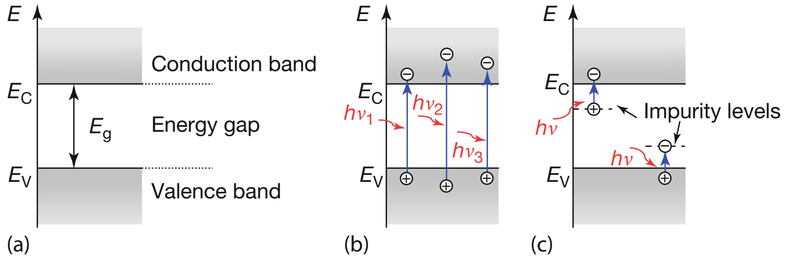

Figure 2.5 (a) Simplified energy-band structure of solids. E_V and E_C denote the upper edge of the valence band and lower edge of the conduction band, respectively. (b) Intrinsic photoeffect: photons of varying energy $h\nu$ (length of arrows) may excite electrons into the conduction band while leaving holes in the valence band. (c) Extrinsic photoeffect: impurities form localized electronic states within the energy gap. Photons need much lower energy for transitions between impurity levels and electronic bands.

energy gap of the semiconductor. The extrinsic photoeffect describes the excitation of an electron or hole from an impurity level to the conduction or the valence band of the semiconductor, respectively. For this excitation, the photon energy must exceed the ionization energy of the impurity that is the energy difference between the impurity energy level and the corresponding band edge.

Because of the energy threshold ΔE for photon detectors, the spectral sensitivity region is limited by a cutoff wavelength λ_{cutoff}:

$$\Delta E = h\nu_{\text{cutoff}} = \frac{hc}{\lambda_{\text{cutoff}}} \tag{2.22a}$$

$$\lambda_{\text{cutoff}} = \frac{hc}{\Delta E} \tag{2.22b}$$

The photon detector is only sensitive for $\nu \geq \nu_{\text{cutoff}}$, that is, $\lambda \leq \lambda_{\text{cutoff}}$. The responsivity and the specific detectivity are strongly wavelength dependent. This behavior is caused by the fact that the detector acts as a photon counter and the detector signal corresponds to the number of incident photons $Z_{\text{radiation}}$ per unit of time, also known as the *quantum flux*. The responsivity is defined by the ratio of the detector signal to the incident radiative power $\Phi_{\text{radiation}}$ (Table 2.1). If we assume a monochromatic radiation at a wavelength λ, the quantum flux Z can be calculated from the incident radiative power $\Phi_{\text{radiation}}$, and vice versa:

$$Z_{\text{radiation}} = \frac{\Phi_{\text{radiation}}}{h\nu} = \lambda\frac{\Phi_{\text{radiation}}}{hc} \quad \text{or} \quad \Phi_{\text{radiation}} = \frac{1}{\lambda}hcZ_{\text{radiation}} \tag{2.23}$$

The responsivity is defined by the ratio of the detector signal to the incident radiant power $\Phi_{\text{radiation}}$ (Table 2.1). We may write the signal current from the detector as

$$I_{\text{signal}} = e\eta Z_{\text{radiation}} = \frac{e\eta\lambda\Phi_{\text{radiation}}}{hc} \tag{2.24}$$

where η is the quantum efficiency, which means the number of free charge carriers per incident photon.

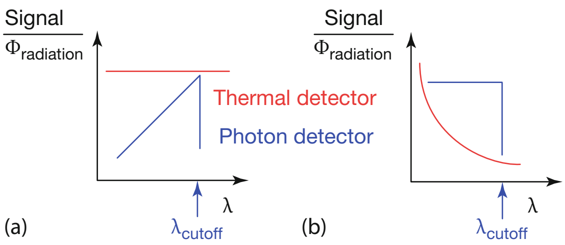

Figure 2.6 Wavelength dependence of photon detector and thermal detector signals for constant incident radiant power (a) and quantum flux (b), respectively.

Therefore,

$$R_\lambda^I = \frac{I_{\text{signal}}}{\Phi_{\text{radiation}}} = \frac{e\eta\lambda}{hc}\,, \quad \frac{I_{\text{signal}}}{Z_{\text{radiation}}} = e\eta \tag{2.25}$$

The responsivity and the specific detectivity exhibit a spectral dependence proportional to the wavelength λ (Figure 2.6). The highest possible responsivity of a photon detector for a quantum efficiency equal to unity ($\eta = 1$) depends only on the wavelength.

This results in a theoretical triangular shape of the spectrally dependent responsivity and detectivity curves for photon detectors. The deviation of the real spectral dependence (Figure 2.1) compared to the triangular-shaped curve results from the dependence of the quantum efficiency η near the cutoff wavelength. For our simplified model, we have used a step function for the quantum efficiency η, with $\eta = 0$ for $\lambda > \lambda_{\text{cutoff}}$ and $\eta = 1$ for $\lambda \leq \lambda_{\text{cutoff}}$. Deviations from the step function model $\eta(\lambda)$ are due to different parameters, such as the spectral dependence of absorption coefficient, nonequilibrium carrier lifetime, carrier diffusion length, detector geometries, and so on.

The quantum detector noise is dominated by different noise sources. Two groups of noise can be distinguished: dark current noise (e.g., Johnson–Nyquist noise, current noise, generation and recombination noise [1, 5]) and radiation-induced noise. For an ideal detector, noise is due only to radiation-induced noise contributions. The signal detection can then be limited by the signal noise or by the background radiation.

2.2.4.2 *D** for Signal-Noise-Limited Detection

We assume that the detector receives only signal radiation causing a signal current I_{signal} without any additional radiation from the background. The shot noise current caused by the signal current (Eq. (2.24)) is [5, 11]

$$I_N = \sqrt{2eI_{\text{signal}}\Delta f} = \sqrt{\frac{2e^2\eta\lambda\Phi_{\text{signal}}\Delta f}{hc}} \tag{2.26}$$

and the $\mathrm{NEP}_{\mathrm{SL}}$ for a signal-noise-limited detector becomes

$$\mathrm{NEP}_{\mathrm{SL}}(\lambda) = \frac{2hc\Delta f}{\eta\lambda} = \frac{2E_{\mathrm{photon}}}{\eta}\Delta f \tag{2.27}$$

The $\mathrm{NEP}_{\mathrm{SL}}$ depends only on the photon energy. For a wavelength $\lambda = 10\,\mu\mathrm{m}$, a quantum efficiency $\eta = 1$, and a bandwidth of $\Delta f = 1\,\mathrm{Hz}$, we estimate an extremely low NEP of about $4 \cdot 10^{-20}$ W. In this case, a photon flux of only two photons per second will produce a SNR equal to unity.

The specific spectral detectivity $D^*(\lambda)$ becomes dependent on the detector area:

$$D^*(\lambda) = \frac{\eta\lambda}{2hc}\sqrt{\frac{A_{\mathrm{D}}}{\Delta f}} \tag{2.28}$$

and for a detector area of $25 \times 25\,\mu\mathrm{m}^2$, we obtain $D^*(\lambda = 10\,\mu\mathrm{m}, \eta = 1, \Delta f = 1\,\mathrm{Hz}) = 6.3 \cdot 10^{16}\,\mathrm{cm\,Hz^{1/2}\,W^{-1}}$. This value must be considered an ideal theoretical result. It does not reflect the situation of a photon detector in an IR camera, which also receives background radiation.

2.2.4.3 D^* for Background Noise Limited Detection

Now we consider a more realistic situation of a photon detector in our camera. The detector will be exposed to signal as well as background radiation.

We can use Eq. (2.24) again for the calculation of the signal current. The noise current is modified by additional background radiation generating an additional noisy detector current. Modifying Eq. (2.26) we find

$$I_N = \sqrt{2\mathrm{e}I_{\mathrm{signal}}\Delta f} = \sqrt{\frac{2\mathrm{e}^2\eta\lambda(\Phi_{\mathrm{signal}} + \Phi_{\mathrm{background}})\Delta f}{hc}} \tag{2.29}$$

Earlier we discussed the extreme case where background radiation was negligible. The other extreme would be if the photocurrent due to background radiation were the dominant noise contribution.

Assuming that the signal radiation power can be neglected compared to the background radiation power and using the expressions for the signal current from Eq. (2.24) and the noise current from Eq. (2.29), we can write the specific spectral detectivity D^*_{BLIP} for a detector characterized by BLIP as

$$D^*_{\mathrm{BLIP}}(\lambda) = \sqrt{\frac{\eta\lambda}{2hc\left(\frac{\Phi_{\mathrm{background}}}{A_{\mathrm{D}}}\right)}} = \sqrt{\frac{\eta\lambda}{2hcE_{\mathrm{background}}}} \tag{2.30}$$

with the irradiance $E_{\mathrm{background}}$ from the detector background. Note that Eq. (2.30) is valid for monochromatic background radiation with wavelength λ. It can be rewritten in terms of photon flux $Z_{\mathrm{background}}$, which for a hemisphere is given by the absorbed background photon flux:

$$Z_{\mathrm{background}} = A_{\mathrm{D}} \int_0^{\lambda_{\mathrm{cutoff}}} M_\lambda(\lambda, T_{\mathrm{background}})\frac{\eta\lambda}{hc}\,\mathrm{d}\lambda \tag{2.31}$$

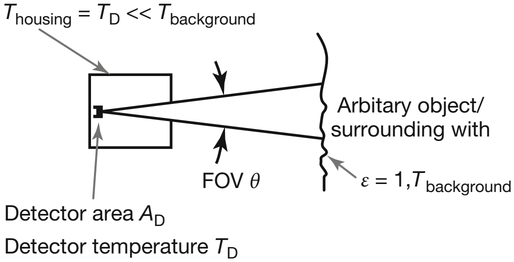
$T_{\text{housing}} = T_D << T_{\text{background}}$
Arbitary object/
surrounding with
FOV θ
$\varepsilon = 1, T_{\text{background}}$
Detector area A_D
Detector temperature T_D

Figure 2.7 Detector-aperture-defined FOV of a cooled detector for thermal background radiation.

Now the value of $D^*_{\text{BLIP}}(\lambda)$ can be derived for a detector in the presence of thermal background radiation (background temperature $T_{\text{background}}$) within a FOV characterized by the full cone angle θ of the received background radiation (Figure 2.7). For hemispherical background, Eq. (2.31) gives the number of background photons. For a limited FOV of a θ linear angle as seen from the detector, the result of Eq. (2.31) must be multiplied by $\sin^2(\theta/2)$.

For the calculation of $D^*_{\text{BLIP}}(\lambda)$, we assume a black background $\varepsilon_{\text{background}} = 1$ with uniform temperature $T_{\text{background}}$, the triangular-shaped spectral responsivity distribution of the photon detector with quantum efficiency $\eta = 1$ for $\lambda \leq \lambda_{\text{cutoff}}$, and 0 for $\lambda > \lambda_{\text{cutoff}}$ according to Eq. (2.25):

$$D^*_{\text{BLIP}}(\lambda) = \frac{\lambda}{hc} \sin^{-1}\left(\frac{\theta}{2}\right) \left\{ \int_0^{\lambda_{\text{cutoff}}} \frac{2\pi c}{\lambda^4 (e^{hc/(\lambda k T_{\text{background}})} - 1)} \, d\lambda \right\}^{-1/2} \tag{2.32a}$$

which can be approximated by

$$D^*_{\text{BLIP}}(\lambda) = \left\{ \sin\left(\frac{\theta}{2}\right) \left[\frac{4\pi (k T_{\text{background}})^5}{c^2 h^3} \right]^{1/2} \cdot x_c \left(x_c^2 + 2x_c + 2\right)^{1/2} e^{-\frac{x_c}{2}} \right\}^{-1} \tag{2.32b}$$

with dimensionless parameter x_c for $x_c \gg 1$:

$$x_c = \frac{hc}{\lambda k T_{\text{background}}} \tag{2.33}$$

Figure 2.8 depicts $D^*_{\text{BLIP}}(\lambda)$ according to Eq. (2.32b) calculated for a background temperature of 300 K and different aperture sizes. We assume that the housing that contains the detector and forms the aperture for the background radiation exhibits a temperature much lower than the background, for example, the temperature of liquid nitrogen $T_{\text{chamber}} = 77$ K. Therefore, the influence of the radiation from inside the detector housing on the D^* value can be neglected.

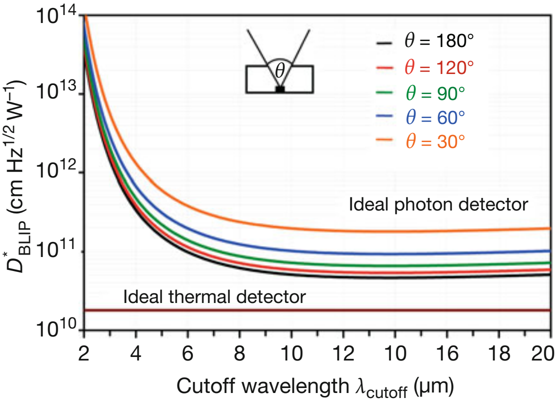

Figure 2.8 D^*_{BLIP} for an ideal photon detector depending on cutoff wavelength and field of view θ for background radiation with $T_{\mathrm{background}} = 300$ K (ideal thermal detector for comparison).

According to the results shown in Figure 2.8, the specific detectivity of a BLIP photon detector can be increased by decreasing the FOV for thermal background radiation. The minimum aperture size in a thermal imaging system is given by the FOV of the camera optics. In addition to this limit, one must consider that we have disregarded all other detector noise processes (as dark current noise of the detector) for calculating D^*_{BLIP}. If the noise caused by background radiation is decreased by reducing the aperture size, the other noise processes become more important or even dominant. In this case, the aperture D^* dependence saturates and the D^* value is no longer background radiation limited.

From this discussion we can draw another conclusion. If we want to limit the spectral range of a camera using spectral filters, these filters should be cold. The background radiation emitted by a cold filter at a low temperature, such as 77 K, can be disregarded. The detector receives only the background radiation within the spectral range given by the filter transmittance. This results in a decrease in background radiation striking the detector and can cause a further increase in the specific detectivity D^*.

If we assume the detector D^*_{BLIP} to be at 2π FOV, the possible temperature resolution of thermal imaging systems in the LW and MW regions can be compared. As will be shown subsequently in Section 2.3.3.2, the radiation temperature contrast (change of excitance with object temperature change) can be calculated from the derivative of the spectral excitance $M_\lambda(\lambda, T)$ with respect to the object temperature T. This result can be related to the NEP by multiplying the derivative of $M_\lambda(\lambda, T)$ by $D^*(\lambda)$. Finally, we must integrate this expression with respect to the wavelength region of the camera.

In this case (see also Eq. (2.3)),

$$\int_{\lambda_1}^{\lambda_2} D^*(\lambda)\frac{\mathrm{d}M}{\mathrm{d}T}\Delta T\,\mathrm{d}\lambda \propto \int_{\lambda_1}^{\lambda_2} \frac{\mathrm{d}M}{\mathrm{d}T}\frac{\Delta T}{\mathrm{NEP}}\,\mathrm{d}\lambda \propto \frac{\text{signal change induced by } \Delta T}{\text{noise}} \tag{2.34}$$

The result gives a measure of the possible temperature resolution of the detector.

Figure 2.9 depicts the results of such a calculation for MW and LW systems. All influences of camera optics have been neglected, that is, only the detector properties will affect the result. For the calculation, a triangular-shaped wavelength dependence of the responsivity has been assumed for the photon detector and a constant responsivity for the bolometer detector. The marked areas in Figures 2.9b, c represent the results of the integration and are a measure of the SNR for an infinitesimal temperature change of a 303 K object. The possible temperature resolutions are related to the reciprocal surfaces of the colored areas in the LW and MW regions depicted in Figure 2.9.

The ratio between the minimum resolvable temperatures in the LW and SW regions for both types of detectors can be calculated using the ratio of the colored areas. For the photon detector operated at the BLIP limit (FOV 2π with 300 K background), the LW : MW ratio is 1 : 2.9 for 300 K object temperature. Photon detectors with BLIP performance allow a comparable temperature resolution of an IR camera in the LW and MW spectral regions. At higher object temperatures the MW detector surpasses the temperature resolution of the LW detector (Section 2.3.3).

For a thermal detector with ideal performance, the LW : MW ratio is 1 : 11.2 for a 300 K object temperature. Compared to the LW region, the temperature resolution of a thermal imaging system equipped with thermal detectors will drop by almost one order of magnitude if it is used in the MW region. Therefore, thermal detectors are suitable only for MW imaging systems for higher object temperatures.

Finally, we can compare the detector capabilities of the BLIP photon (FOV 2π with 300 K background) and the ideal thermal detectors for thermal imaging in the LW region. The LW (thermal detector) : LW (photon detector) ratio between the minimum resolvable temperatures is 1 : 0.51 for a 300 K object temperature. This demonstrates the capability of thermal sensors for thermal imaging in the LW region, although we must consider that the performance of a photon detector can be further improved by decreasing the FOV for background radiation and the fact that the performance of available thermal detectors does not achieve the theoretical D^* limit.

2.2.4.4 **Necessity to Cool Photon Detectors**

IR photon detectors operating at BLIP conditions require cooling to low temperatures, as can be seen by the following argument. The cutoff wavelength of the detector corresponds to the gap energy (Figure 2.5 and Eqs. (2.22a) and

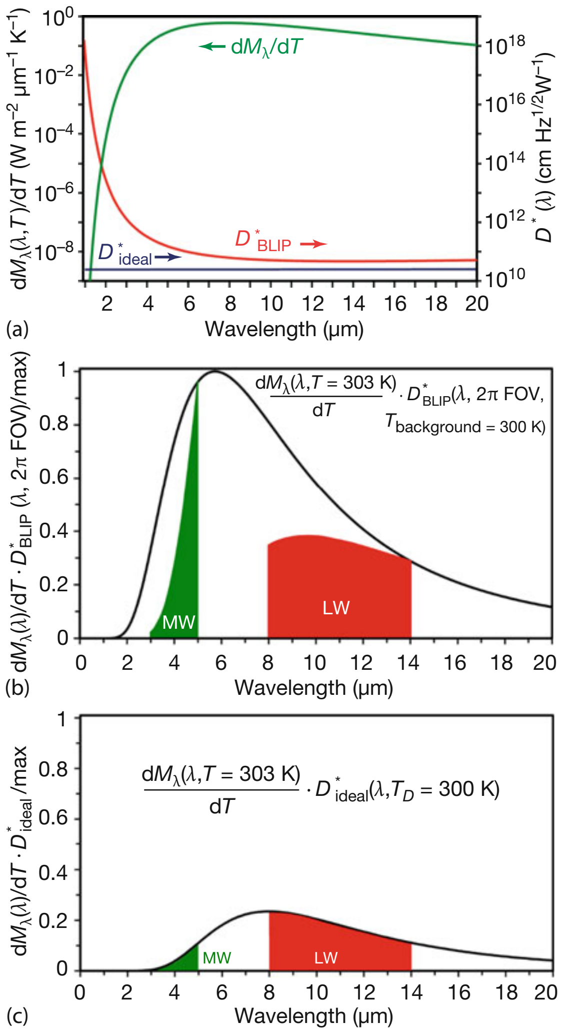

Figure 2.9 (a) Comparison of spectral dependent D^* for BLIP photon detector (FOV 2π with 300 K background) and ideal thermal detector with 300 K detector temperature with dM_λ/dT spectral dependence for an object temperature of $T_{\text{object}} = 300$ K. (b) Comparison of temperature resolutions of BLIP photon detectors in LW (8–14 µm) and MW (3–5 µm, InSb detector at 77 K assumed) regions. (The curve is normalized with the maximum value of its spectral dependence.) (c) Comparison of temperature resolutions of ideal thermal detector in LW and MW regions. (The curve is normalized with the maximum of the spectrally dependent photon detector curve from (b).)

(2.22b)). For a photon detector with a 10 µm cutoff wavelength, the energy gap is 124 meV. In general, the energy of photons is related to their wavelength via E(eV) = 1.24/λ (µm). The optimum situation for detector operation is achieved if only incoming photons with $\lambda < \lambda_{\text{cutoff}}$ generate free charge carriers. Based on the discussion of noise in photon detectors, one would expect that any additional thermal excitation process of charge carriers over the energy gap would increase the noise. At a temperature of $T = 300\,\mathrm{K}$, the thermal energy kT equals 25.9 meV. Using the energy gap of the 10 μm detector and this thermal energy, we can estimate the probability W of thermal carrier excitation using the Boltzmann equation (simplified model used):

$$W = const.\ \exp\left(-\frac{\Delta E}{kT}\right) \tag{2.35}$$

where const. accounts for transition probabilities, density of states, and so on. For $\lambda = 10\,\mu\mathrm{m}$ and $T = 300\,\mathrm{K}$, we obtain for the exponential part $8.3 \cdot 10^{-3}$. Because of this rather large factor for the excitation probability and the high density of states in the semiconductor material, the equilibrium concentration of thermally excited free carriers is much larger than the nonequilibrium carrier concentration caused by the radiation absorption. This causes a large noise and a reduced sensitivity of the photon detector.

However, if the temperature of the 10 μm detector is reduced to the temperature of liquid nitrogen $T = 77\,\mathrm{K}$ ($kT = 6.63\,\mathrm{meV}$), the Boltzmann factor for the probability of thermal carrier excitation is reduced by six orders of magnitude to a value of $7.6 \cdot 10^{-9}$. Cooling down to low temperatures very efficiently decreases the free charge carrier concentration and therefore the noise in the photon detector. The demand for cooling the photon detector to low temperatures increases with increasing cutoff wavelength owing to the decreasing energy for carrier excitation. Almost all 8–14 μm photon detectors (for LW cameras) operate at about 77 K. Detectors for the 3–5 μm MW region are thermoelectrically cooled to about 200 K or also to 77 K. The detectors for the 0.9–1.7 μm SW region are thermoelectrically cooled or are operated at room temperature.

2.2.5
Types of Photon Detectors

Photon detectors can be subdivided into different types depending on the operation principles. The most important photon detectors are classical semiconductor detectors, including photoconductors and photodiodes, and novel semiconductor detectors, including photoemissive Schottky barrier, bandgap-engineered quantum well IR photodetectors (QWIPs), and InAs/GaSb–type II strained layer superlattices (T2SLSs).

2.2.5.1 Photoconductors

A photoconductor is a detector device composed of a single uniform semiconductor material. Photoconductors monitor incident radiation via changes in the semiconductor bulk resistivity. It is due to a creation of free charge carriers induced by absorbed photons. Any change in photoconduction is detected by measuring the current–voltage characteristic.

The responsivity of a photoconductor can be derived from Eq. (2.25), but with the addition of a gain factor g. This gain factor represents the ratio of the carrier lifetime τ to the transit time for the carrier in the photoconductor. The latter is given by the ratio of the detector length to the carrier drift velocity [2]. If the carrier lifetime is greater than the transit time, the photocurrent is amplified ($g > 1$). This gain can be understood from the following argument: if charge carriers live longer than their transit time, they will leave the detector at one electrical contact. For charge conservation reasons, they will be replaced by new (secondary) carriers at the opposite contact. The process will repeat again and again until the time reaches the carrier lifetime. As a result, many charge carriers are due to a single excitation mechanism, that is, the process can be regarded as a photocurrent gain. All D^* values calculated in Section 2.2.4 must be divided by a factor of $\sqrt{2}$ for photoconductors owing to additional recombination noise [3, 5].

The sensitivity of a photoconductor increases with the applied voltage or current. However, this goes along with the increased heat dissipation at the detector. As a consequence, large photoconductor arrays are difficult to cool. Moreover, the increase in operating current often leads to an increased $1/f$-noise behavior [5], which decreases the D^* value. The photocurrent gain can also be increased by an increased carrier lifetime. Very sensitive photoconductors often exhibit much larger time constants than photodiodes. Regarding IR camera systems, long time constants are, however, not desirable. Detectors with larger time constants can only be operated at lower frame rates. As a result of these properties, photoconductors are not the photon detectors of choice for thermal imaging.

2.2.5.2 **Photodiodes**

Photodiodes consist of a p–n junction in a semiconductor. It is a photon-sensitive diode, producing a current or voltage output in response to incident optical radiation flux. The cutoff wavelength is determined by the energy gap of the semiconductor used.

For FPAs used in LW thermal imaging systems, mercury–cadmium–telluride (MCT) ($Hg_{1-x}Cd_xTe$) is the favorite semiconductor material. This II–VI compound is an alloy composition of the wide energy gap semiconductor CdTe (energy gap 1.6 eV) and the semimetallic compound HgTe (energy gap –0.3 eV). The energy gap of $Hg_{1-x}Cd_xTe$ is controlled by the relative portions of the two binary semiconductors. The dependence of the energy gap on composition can be approximated by a linear dependence. For a composition of $x = 0.196$ at $T = 77$ K, a cutoff wavelength of 14 μm is observed [3].

Because of the strong dependence of the energy gap on composition caused by the strong variation of 1.9 eV from CdTe to HgTe and the low energy gap of 0.089 eV for a cutoff wavelength of 14 μm, a composition uncertainty of only 2% ($x = 0.196 \pm 0.004$) will cause a variation of the cutoff wavelength by $\Delta\lambda_{\text{cutoff}} = \pm 0.51$ μm, that is, $\lambda_{\text{cutoff}} = (14 \pm 0.51)$ μm. Therefore, MCT detectors pose problems in detector arrays. Small composition changes lead to changes in cutoff wavelengths and, therefore, also changes in NEP and D^* at fixed wavelength.

Therefore, the very complex technology and the demand for composition homogeneity of this material result in very high prices for two-dimensional detector arrays with a large number of detectors. Modern fabrication methods such as molecular beam epitaxy (MBE) and metalorganic chemical vapor deposition (MOCVD) increase the manufacturability of this material and will hopefully lead to lower prices in the future.

MCT is also used for FPAs in the MW spectral region (3–5 μm). However, in this spectral region, it competes directly with InSb. InSb is the most highly developed and widely used semiconductor material in the 1–5 μm spectral region and one of the most sensitive detector materials available in the MW spectral region. Compared to $Hg_{1-x}Cd_xTe$, the technology of InSb is less complicated [12] and enables large detector arrays of reasonable uniformity with more than 1 megapixel. The energy gap of this material is only temperature dependent and amounts to 0.23 eV at $T = 77$ K, causing a cutoff wavelength of about 5.4 μm. The excellent detector performance results in an operation that, similar to MCT, has a D^* value close to the BLIP limit (Figure 2.1). Many modern MW IR cameras use InSb detectors.

In recent years, progress for the SW spectral region (0.9–1.7 μm) was due to intensive technology development of the III–V compound semiconductors based on the binary semiconductor compounds GaAs and InAs. Today, it is possible to obtain high-sensitive and high-speed $In_{1-x}Ga_xAs$ photodiodes and photodiode arrays for the near-IR spectral region. $In_{1-x}Ga_xAs$ is an alloy consisting of GaAs (energy gap 1.43 eV corresponding to a cutoff wavelength of 0.87 μm) and InAs (energy gap 0.36 eV corresponding to a cutoff wavelength of 3.4 μm). The energy gap of the alloy can be tailored to the wavelength of interest by controlling the mixing of the two binary compounds.

The basic operational principle used in photodiode arrays of imaging systems is the external current flow to a readout circuit (short circuit current or reverse bias operation) caused by the incident IR radiation. The incident photon with a quantum energy larger than the gap energy of the semiconductor is absorbed, exciting an electron–hole pair. During their lifetime (average time from generation to recombination), the charge carriers move within the diode owing to diffusion processes. The average distance is the diffusion length. If the electron–hole pair is generated inside the depletion layer or at a maximum distance of one diffusion length from the depletion layer, the electron–hole pair will be separated by the electric field of the p–n junction. The electron moves into the p-type region and the hole moves into the n-type region, causing a current to flow. This photogenerated current is given by Eq. (2.24) and resembles a reverse current in the photodiode. Mostly photodiodes are operated with reverse bias. The reverse bias widens the depletion layer that causes a decrease in the junction capacitance and allows a faster detector response due to the decreased time constant $\tau = RC$ of the photodiode. Typical photodiode time constants range from nanoseconds to microseconds, which allow frame rates of some 100 kHz. Additional limitations on the readout process are discussed in Section 2.4.

Using the reversed bias operation mode, the photodiode can also decrease the dark current noise [5]. The maximum increase in the specific detectivity D^*

amounts to a factor of $\sqrt{2}$ if Johnson–Nyquist noise is the dominant noise process in the photodiode.

2.2.5.3 Schottky Barrier Detectors

A variety of metal films on semiconductors can form Schottky barriers [2]. For IR applications, Schottky barriers on silicon are used [3]. The use of a silicon-based technology for IR detectors is advantageous for the construction of FPAs since monolithic integration of the IR sensor arrays with the readout circuit becomes possible. The complete technological process is similar to the well-developed standard silicon very-large-scale integration/ultra-large-scale integration (VLSI/ULSI process) for silicon-integrated circuits. This results in lower defect rates, excellent homogeneity of the detectors in FPAs (response nonuniformity of less than 1% in large arrays), and cheaper manufacturing.

The most important metal used is platinum (Pt). Figure 2.10 depicts the typical structure of a Schottky barrier photodiode formed by Si/PtSi. These detectors act via the process of internal photoemission over the Schottky barrier height Ψ (Ψ = 0.22 eV for Pt/PtSi). The Si/PtSi Schottky barrier detector is cooled to $T = 77$ K. IR photons of energy $h\nu$ with $E_g^{Si} > h\nu \geq \Psi$ can pass the silicon ($E_g^{Si} = 1.1$ eV) but are absorbed in the silicide, thereby generating an electron–hole pair.

Photoexcited holes can diffuse to the Si/PtSi interface. The electrons accumulate on the silicide electrode and can be transferred to a readout circuit. The low quantum efficiency of Schottky barrier detectors (typically 0.1–1%) is due to the fact that the absorption of the IR photons is weak (thin silicide layer) and only a small number of photoexcited holes can cross the barrier. Therefore, an additional $\lambda/4$ cavity with a dielectric layer and an aluminum reflector is used to enhance the photoemission process.

2.2.5.4 Quantum Well IR Photodetectors

The development of modern methods of crystal growth such as MBE and MOCVD allows for the fabrication of semiconductor heterostructures. Different lattice-matched semiconductor materials can be deposited in a perfect crystalline structure with atomic thickness resolution. The combination of different semiconduc-

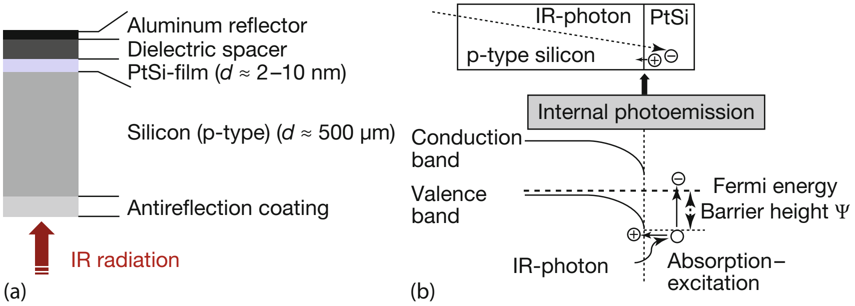

Figure 2.10 (a) Typical structure of a Schottky barrier IR sensor and (b) the operation principle (for detailed description, see [3]).

tor materials with different bandgaps in heterostructures causes a spatial variation of the conduction and valence band edge. Tailoring of the band edge distribution becomes possible by variation of semiconductor materials and the layer thickness. This method is called *bandgap engineering*. For the simplest case, an alternating sequence of abruptly changing materials such as GaAs and $Al_{1-x}Ga_xAs$ results in a cascaded band edge distribution (Figure 2.11). For small layer thickness in the nanometer range, drastic changes in the electronic and optical properties are observed due to quantum effects.

The band edge distribution forms alternating quantum wells and barriers for the electrons and holes. For an adequate layer composition and thickness in the nanometer range, quantized energy levels occur within the quantum wells (for a more detailed discussion of charge carrier behavior and thewavefunctions of charge carriers within a box-shaped potential, see [14]). These energy levels are called *subbands*. An incident photon can excite an electron from the ground to the

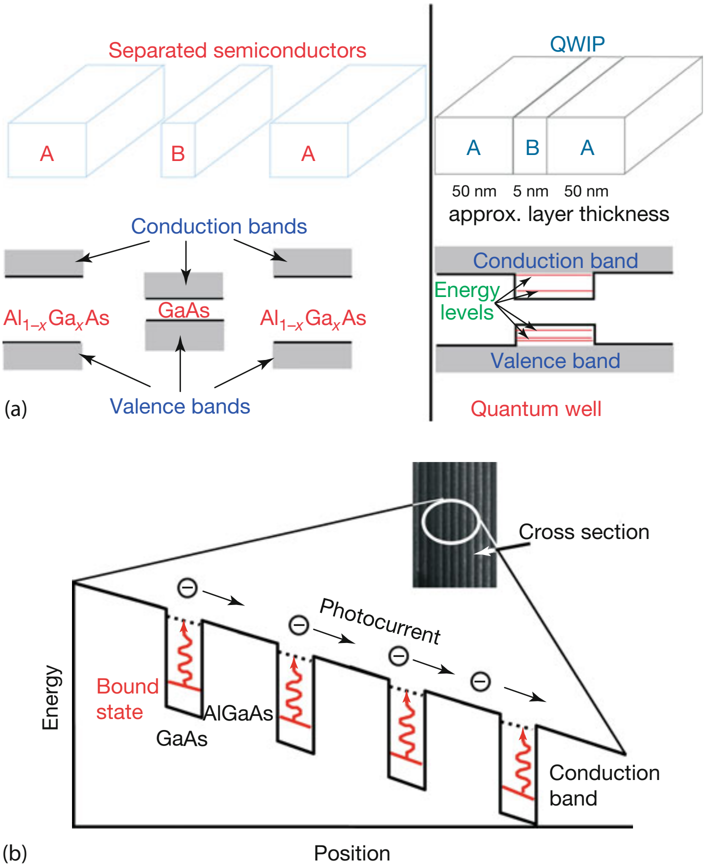

Figure 2.11 Structure and energy-band diagram (a) as well as excitation of electrons (b) in biased GaAs/AlGaAs QWIP, after [13].

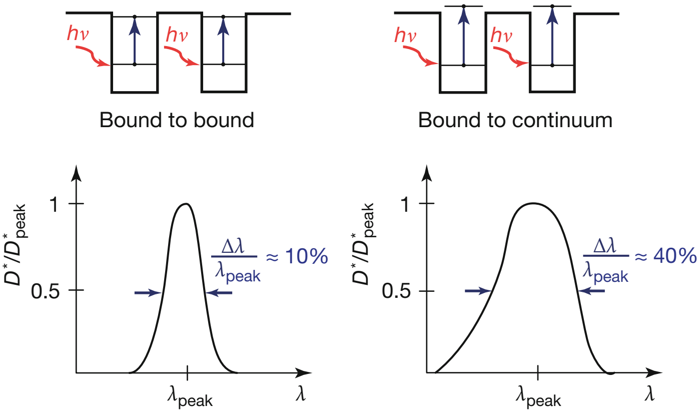

Figure 2.12 Typical spectral responsivities of bound excited state and continuum QWIPs.

first excited state subband if the photon energy equals the energy gap of these two subbands (Figure 2.11). This energy gap is much smaller than the energy gaps of the two semiconductors used and corresponds to quantum energies of photons within the IR spectral region. The narrow quantum well causes very low quantum absorption efficiency. To increase this efficiency, a multiple-quantum-well (MQW) structure with 50 or more quantum wells is used. The QWIP responsivity spectra are much narrower and sharper than the spectra of intrinsic detectors owing to their resonance intersubband absorption. The spectral dependence of the responsivity of QWIPs can be tailored from narrow ($\Delta\lambda/\lambda \sim 10\%$) for bound excited states to wide ($\Delta\lambda/\lambda \sim 40\%$) for excited states in the continuum band just above the energy barrier [13, 15] (Figure 2.12).

The spectral bandwidth of QWIPs can be further increased by replacing a single quantum well staple with a superlattice structure consisting of staples of several quantum well types separated by very thin barriers [16].

In QWIPs, the photocurrent gain depends on the operating bias voltage and varies from about 10 to about 50%. This behavior is connected to the probability of electron capture into the quantum wells while traveling to the contact of the detector. Typical time constants of QWIPs are in the millisecond range, that is, higher than the time constants of photodiodes. This limits the maximum frame rate of a QWIP FPA camera.

For the operation of QWIPs, low detector temperatures are required, typically $T = 77$ K. With decreasing temperatures, the number of thermally excited charge carriers decreases strongly according to the Boltzmann distribution function. This results in an increasing responsivity. Furthermore, the noise current in a QWIP, which limits the NEP or its D^* value, also strongly decreases with detector temperature. The dominant noise in QWIP devices is due to the shot noise resulting from the dark current in the detector. The dark current originates from three main processes: quantum-well-to-quantum-well tunneling, thermally assisted tunneling, and classical thermionic emission. The last mechanism de-

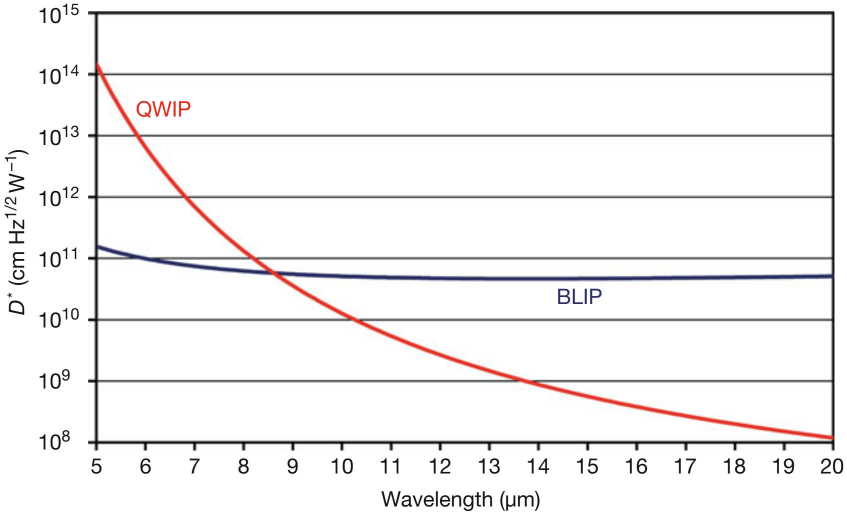

Figure 2.13 Predicted spectrum-dependent maximum D^*_{QWIP} at peak wavelength for QWIP detectors operated at 77 K [17] compared to D^*_{BLIP} for photon detectors at 2π FOV and 300 K background temperature.

creases the responsivity and establishes the major source of the dark current at higher operation temperatures. The maximum D^* values for a given peak response wavelength (λ_{peak}) and detector temperature for GaAs/AlGaAs QWIPs were empirically fitted to measurement results [17]:

$$D^*_{\text{QWIP}} = 1.1 \cdot 10^6 \exp\left(\frac{hc}{2\lambda_{\text{peak}} kT}\right) \text{ cm Hz}^{1/2}\text{ W}^{-1} \tag{2.36}$$

This equation was used to predict the limit of D^* of a QWIP as a function of peak wavelength and for $T = 77$ K (Figure 2.13).

A variety of III–V semiconductor combinations are used for QWIPs, such as GaAs/AlGaAs, InGaAs/InP, InGaAs/InAlAs, and AlGaInAs/InP, covering the spectral range from 3 to 20 μm. QWIPs are the only genuine narrowband IR detectors and are therefore ideally suited for narrowband applications (Chapter 8). In addition, they can be used as bi- or multispectral sensors. Such multispectral sensors can be assembled in a stack arrangement of QWIPs (independently contacted) with different peak wavelengths [18]. A modern approach to bispectral detectors are QWIPs operating in two different spectral regions with switchable sensitivity from the LW to the MW by increasing the bias voltage.

QWIPs have made their way from the laboratory to commercial high-performance thermal imaging systems with megapixel FPAs [19]. QWIPs offer high thermal resolution (some mK), spatial resolution, excellent homogeneity, low fixed pattern noise, low $1/f$ noise, high pixel functionality, and high yield at moderate cost.

2.2.5.5 Recent Developments in IR Detector Technology

Many new IR detectors have been designed in recent years. This section will provide a brief overview of selected new developments in photon detectors [20]. In short, the main hot topic nowadays is superlattice detectors. These can be combined with barrier layers to reduce dark currents, and they can be specifically tuned to wavebands and allow for multiple-waveband detection.

One of the main objectives for improvements in IR photon detectors is the reduction of dark currents as the limiting noise source. In other words, decreasing dark currents in detector technology is the key factor to improving detector performance.

MCT will continue to be the semiconductor material of choice for the highest-quality IR FPA devices [20]. The intense research and technological work being conducted on MCT concentrate on improving epitaxial layer growth and substrate materials for the epitaxy, extrinsic doping, reduction in dark currents using a heterostructure or barrier devices, and reduction in pixel size.

One of the driving forces in detector development resulting in new detector architectures is an external one: many applications nowadays require a fast response and–even more importantly–increased detector operating temperature because of the need for reduced power consumption for detector cooling. Therefore, high operation temperature (HOT) detectors made from MCT in the MW band represent a current research interest [21, 22].

Conventional MCT p–n junction photodiodes are operated at very low temperatures, typically at 77 K. At these temperatures the diffusion current dominates within the p–n junction. It arises from the thermal excitation of charge carriers over the semiconductor bandgap. In MCT as well as in other compound semiconductors, imperfections in the crystal lattice, for example vacancies or interstitial atoms, lead to energy levels within the bandgap of the semiconductor, called Shockley–Read–Hall (SRH) traps (Figure 2.14a). These traps act as additional sources of generation and recombination processes in the semiconductor and thus make additional dark current contributions, in particular since their associated excitation energies are below the actual bandgap energy. Therefore, SRH trap generation–recombination (G–R) currents become dominant at higher detector temperatures, leading to a strong increase in the total dark current in the diode (Figure 2.14b).

If it is possible to suppress these G–R currents, the detector performance will improve at any given operating temperature. Alternatively, the detector may be operated at a higher temperature without any loss of detector performance compared to a conventional detector at a lower operating temperature.

With the improvements in MCT detector technology, the first complete camera systems were demonstrated at an operating temperature of 150 K with a cutoff wavelength of 5 μm, a pixel pitch of 15 μm, and a temperature resolution better than 20 mK. The elevated operating temperature enabled a decrease in power consumption to less than 2 W [23]. Such systems meet the application requirements for small size, weight, and power (SWaP) configurations.

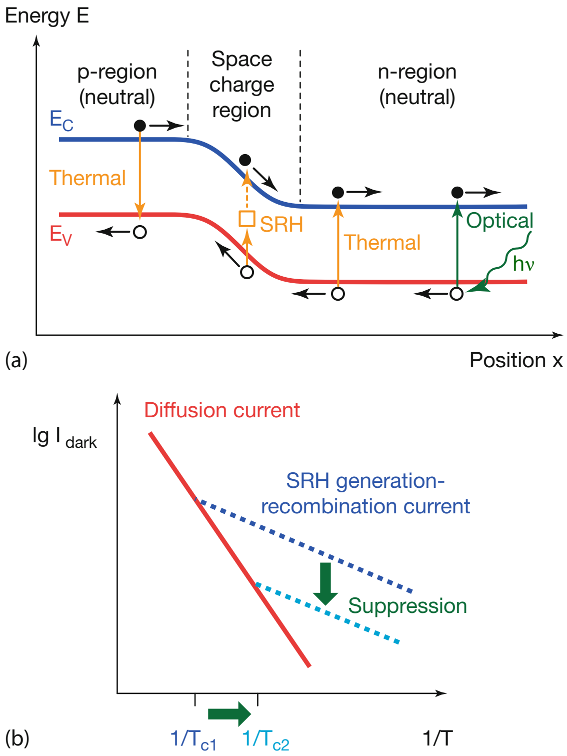

Figure 2.14 (a) Conventional p–n junction photodiode with dark and photocurrent mechanisms. (b) Temperature-dependent dark current in a photodiode, and the effect of generation–recombination current suppression.

A promising idea for suppressing the trap-induced G–R currents (or other leakage currents) was first discussed by A.M. White in 1983 [24]. He proposed to change the conventional detector architecture by introducing a blocking barrier for these kinds of charge carrier transport (Figure 2.15a). In his concept White assumed a heterostructure consisting of a thin wide-bandgap layer sandwiched between two narrow-bandgap regions. One of the narrow-bandgap regions acts as the absorption layer, the other as the contact layer. The typical problem with two adjacent layers is that they simultaneously shift the energies of both the valence and the conduction bands.

White's layer model (Figure 2.15b) assumes that only one of the bands shifts (in the figure, the conduction band). In such a structure, the thin wide-bandgap layer forms a blocking layer for the majority carriers of the narrow-bandgap regions (here the electrons in the n-type semiconductor) but allow the minority carrier to flow (here the holes) [25]. Therefore, G–R currents are effectively suppressed. In contrast, IR radiation in this example is absorbed in the n-type region to the left of the barrier. Therefore, both photoelectrons and holes can move freely and generate the detected photocurrent.

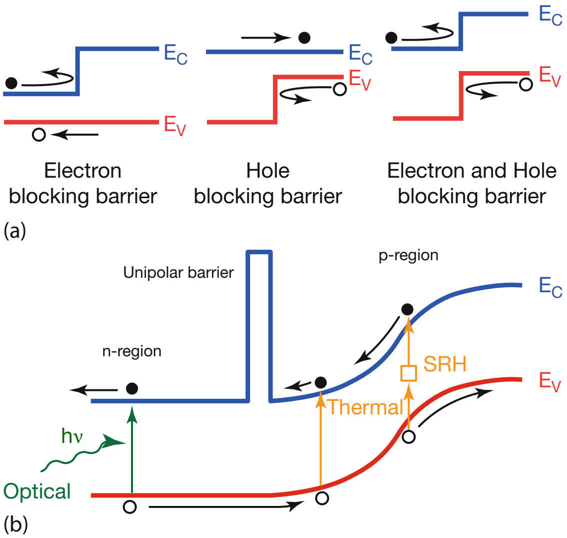

Figure 2.15 (a) Heterojunction as a charge-carrier-blocking barrier. (b) Suppression of SRH G–R current by introducing wide bandgap layer.

Theoretically this new concept for IR detector architecture is in principle not limited to specific semiconductor materials; however, in practice the associated solid-state physics imposes restrictions. Unfortunately, the standard IR detector materials, such as MCT and InSb, do not allow one to easily use such heterostructures with zero band-offset barriers. There have been successful attempts at implementing such heterostructure architecture in MCT [26]. However, the existence of band offsets for minority carriers limits the performance of these detectors [25].

However, such structures can be implemented with a new system type, so-called superlattice detectors. In general, superlattices are periodic heterostructures of the type ABABAB… made of two semiconductor materials, A and B. Let us first discuss superlattice IR detectors before returning to additional barriers for noise reduction.

Superlattices of InAs/GaSb for IR detection were first suggested in 1977 [27]. The nanolayers of the two different semiconductors are alternately deposited on each other, forming a periodic structure in growth direction (Figure 2.16a). Such artificial periodic (super-)lattices have completely new semiconductor properties similar to quantum wells (Section 2.2.5.4). Their band structure is caused by the overlapping electron wavefunctions between the nanometer-wide adjacent thin layers.

The first high-performance IR detectors and FPAs based on superlattices were reported in the late twentieth century [28] using strained layers of III–V compound semiconductors InAs and InGaSb on GaSb substrates [29]. The LW detec-

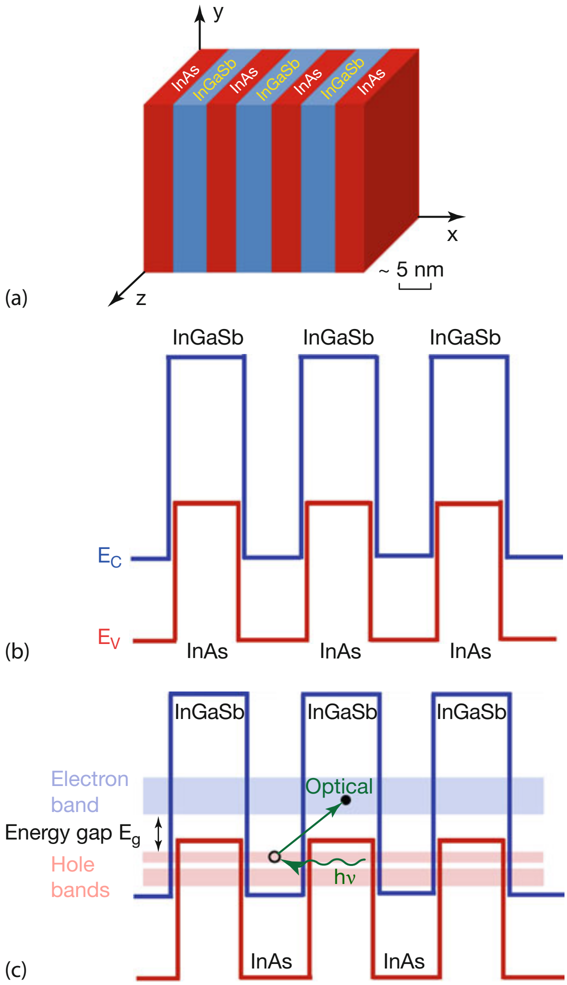

Figure 2.16 (a) Alternating layer structure forming an InAs/(InGa)Sb superlattice. (b) Alternating band structure in a type II InAs/(InGa)Sb superlattice. (c) Formation of minibands and bandgap in an InAs/GaSb superlattice.

tor had a photoresponse up to a wavelength of 10.6 μm at an operation temperature of 78 K. This initiated significant advances in IR detector technology [28].

In the last few years most of the research and technological development has been done in connection with InAs/(In,Ga)Sb systems. Superlattices made from these two materials are called type II strained layer superlattices. The strain is due to the small lattice mismatch of less than 1% of InAs on GaSb. If both the valence and the conduction band edge of the second material are above the band edges of the first material, the system is called a type II band-aligned superlattice (Figure 2.16b).

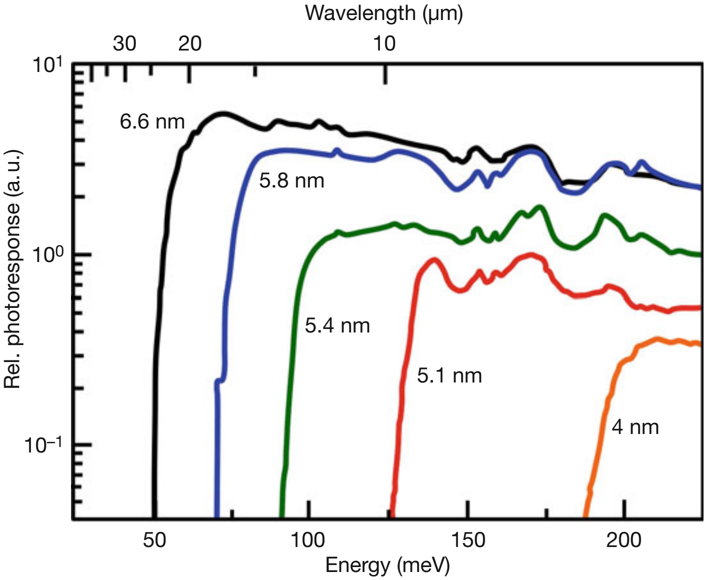

Figure 2.17 Photoresponse spectrum of a series of GaSb/InAs superlattices grown under identical conditions with fixed GaSb layer thickness of 4 nm (13 monolayers) at a temperature of 80 K. The layer thickness of InAs changed from 4 nm (13 monolayers) up to 6.6 nm (22 monolayers) (after [30]).

As a result of the quantum effects in the nanolayer superlattice structure, minibands for electrons and holes are formed in the superlattice (Figure 2.16c). The bandgap between the minibands is used for the detection of IR radiation. It can be tailored by varying the thickness of the constituent superlattice layers, that is, number of monolayers. This offers the possibility of tuning the sensitivity of such superlattice structures within a broad spectral range. For InAs/GaSb superlattices the tunable bandgap range makes it possible to use these structures for IR detection in a range from 3 to 30 μm, as illustrated by the photoresponse signals in Figure 2.17 [30].

IR detectors made from InAs/(In,Ga)Sb type II strained layer superlattices combine the advantages of InSb of, first, increased uniformity and, second, significantly lower cost per pixel compared to MCT. Therefore, they are the material of choice for large-scale FPAs. They exhibit smaller dark currents than InSb photodiodes, resulting in less noise, that is, lower NETD values.

The construction of superlattice detectors allows for an independent tuning of the valence and conduction band edge positions. This makes it possible to introduce the previously discussed barrier layers for noise reduction. Klipstein [31, 32] proposed the so-called bariode (short for "barrier diode") with a unipolar charge-carrier-blocking barrier. A broad family of eight different band profile configurations in such barrier detectors has been considered [25, 33]. Such III–V superlattices constitute a very flexible system, and a combination with barrier heterojunctions is straightforward and fundamental for the future development of IR detectors.

Bandgap engineering within modern technological processes allow complex layer systems with homo- and heterojunction structures, additional unipolar carrier structures with an accuracy in the range of monolayer thickness. This will lead to the development of a large variety of new IR detector structures.

The great potential of III–V strained layer superlattice IR detectors, especially of an InAs/(In,Ga)Sb material system, which will most probably form the basis for the next generation of IR imagers, can be summarized as follows [28, 31, 32, 34]:

- III–V superlattice technology is well known and established using molecular beams.
- The growth of lattices on inexpensive GaAs substrates (instead of GaSb) has been successfully demonstrated.
- The performance of type II strained layer superlattice (T2SLS) detectors has reached a comparable level with state-of-the-art MCT detectors.
- T2SLS detectors will cover a much wider range of the IR spectrum from the SW to way beyond the presently used LW (this may be particularly interesting for IR astronomy).
- Barrier structures can be introduced in T2SLS detectors to lower the dark current and to improve the detector's detectivity.
- T2SLS detectors with barriers allow high operating temperatures up to 150 K for MW arrays with lower cooling power requirements.
- T2SLSs allow megapixel FPAs.
- Last but not least multispectral IR photodetectors and imagers can be made from T2SLS (see subsequent discussion).

A few examples of complete camera systems will confirm these statements.

a) High-Operating-Temperature Cameras

High-operating-temperature T2SLS arrays in MW cameras have been successfully demonstrated (Figure 2.18) [33, 35, 36]. These detector arrays can be operated in the BLIP regime up to 180 K, and the camera offers a NETD of 20 mK limited only by shot and readout noise. Qualitative images may even be recorded for temperatures up to 225 K!

This excellent detector performance became possible by the introduction of a heterostructure barrier into the detector architecture (Figure 2.19a) [33, 35].

The absorption layer can be made of (In,As)Sb or InAs/GaSb type II SLS. The barrier layer made of (Al,As)Sb suppresses the G–R currents in the detector (Figure 2.19b). The decreasing dark current causes lower noise and results in an increased detector detectivity. Moreover, the barrier detector offers the same performance as conventional detectors without the barrier structure, such as InSb photodiodes, however at higher operating temperatures.

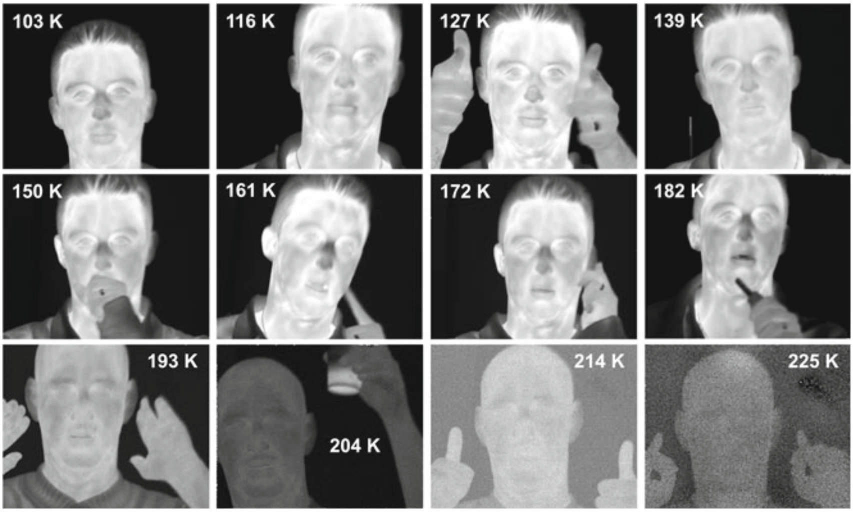

Figure 2.18 MW images of a person at FPA temperatures between 103 and 225 K for an n-type bariode InAs/(In,Ga)Sb superlattice FPA. © Courtesy of SemiConductor Devices (SCD), Haifa, Israel.

b) Dual-Band MW Camera

Compared to state-of-the-art conventional "monospectral" broadband IR cameras, which measure the spectrally integrated object radiation within a given IR band (SW, MW, or LW), a multispectral camera will also give information about the spectral signature of the emitted radiation. This can be a decisive advantage for the characterization of nongray emitters like, for example, gases or plastics.

Owing to the development of InAs/GaSb superlattice detector technology in recent years, dual-color detector arrays for the MW became available [37–39]. These detectors are characterized by a backside-illuminated sandwich structure of two pin-photodiodes (Figure 2.20) [38].

The different structures of the superlattices used in the two sandwich diodes allow the simultaneous detection of IR radiation in two spectral channels. The bottom diode (blue channel) detects the shorter MW and the top diode (red channel) detects the longer MW IR radiation. Today FPAs with 288 × 384 pixels are available and arrays with 640 × 512 pixels are under development. The detectors are sensitive in the 3–4 μm wavelength range for the blue channel and in the 4–5 μm range for the red channel. For short integration times of 0.2 ms the blue channel offers about 25 mK and the red channel about 15 mK NETD, respectively [38]. These dual-color detectors are ideally suited, for example, for the remote detection of carbon dioxide as a result of the strong CO_2 absorption around 4.3 μm, which only affects the radiation signal of the red channel (4–5 μm). Figure 2.21 depicts the IR images of a man holding a burning candle in the blue and red channels, respectively. The subtraction image clearly demonstrates the hot carbon dioxide emission around the central flame (details on gases can be found in Chapter 8).

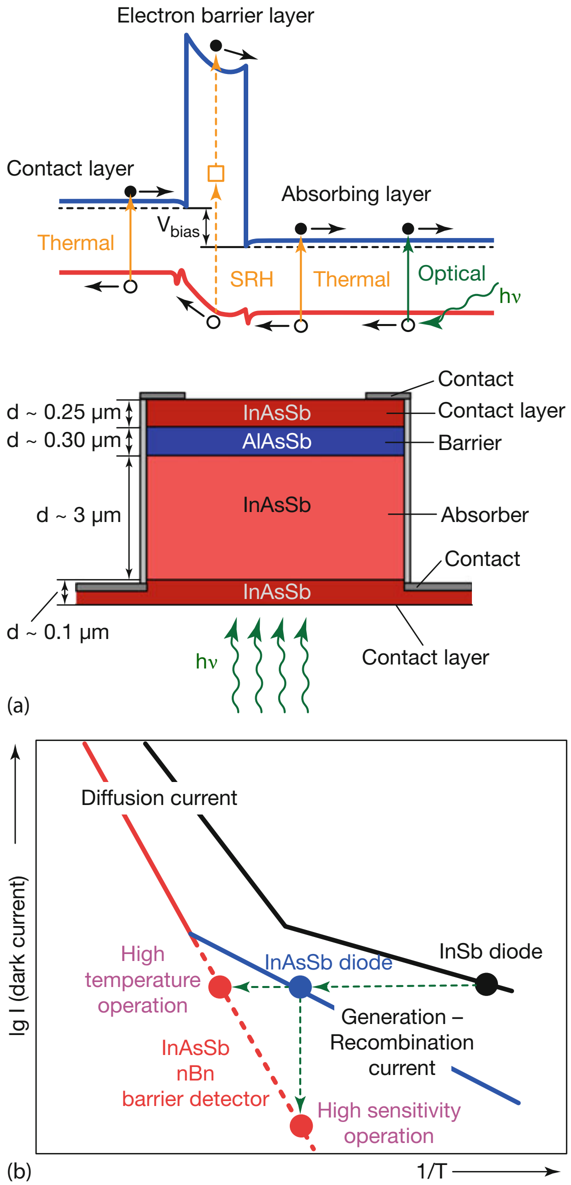

Figure 2.19 (a) Bandgap diagram of nBn barrier detector (n-type bariode InAs/(In,As)Sb superlattice detector) and typical device structure with absorber thickness of a few micrometers. (b) Dark current reduction by barrier structure compared to InSb standard photodiodes.

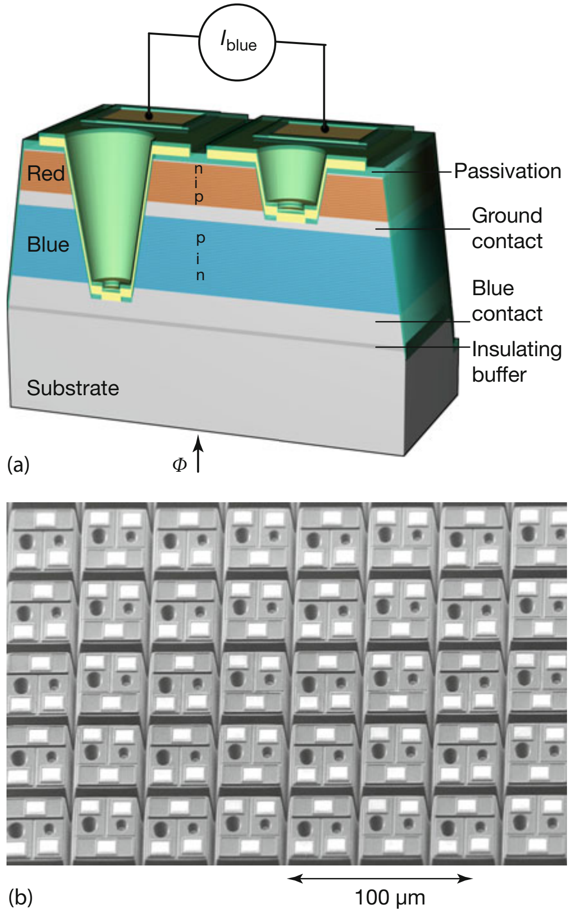

Figure 2.20 (a) Schematic cross section (side view) of a backside-illuminated dual-color photodiode. Short wavelengths are absorbed in the lower photodiode, longer wavelengths in the upper diode. (b) Scanning electron microscope image (front view) showing pixels of a completely processed 288 × 384 InAs/GaSb SL dual-color FPA. © Courtesy of Fraunhofer-Institut für Angewandte Festkörperphysik IAF, Freiburg 2007.

c) Dual-Band LW Camera

Dual-band IR detection in the LW was demonstrated for the first time on type II superlattices. The quantum efficiencies in the two spectral channels (blue channel with a cutoff wavelength of 9.5 µm and red channel with 12.5 µm cutoff) can be controlled by the applied detector voltage (Figure 2.22) [40]. At an operating temperature of 81 K, a detector with 640 × 512 pixels (and 30 µm pixel pitch) has minimum NEDTs of about 20 mK (30 °C object temperature) in both spectral channels at integration times below 1 ms. Therefore, these superlattice dual-band FPAs are competitive with state of-the-art single-band conventional LW imagers using low integration times.

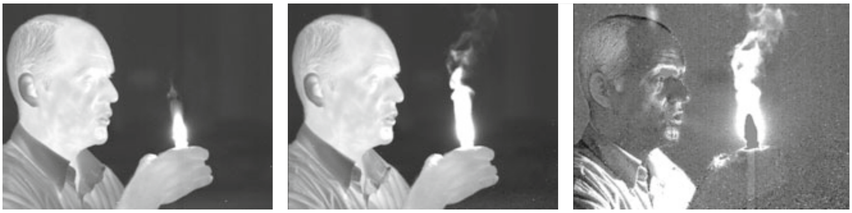
(a) (b) (c)

Figure 2.21 IR images of a man holding a burning candle taken with a 288 × 384 dual-color InAs/GaSb SL camera. (a) Blue channel (3–4 μm). (b) Red channel (4–5 μm). (c) Subtraction image after [38]. © Courtesy of Fraunhofer-Institut für Angewandte Festkörperphysik IAF, Freiburg 2007.

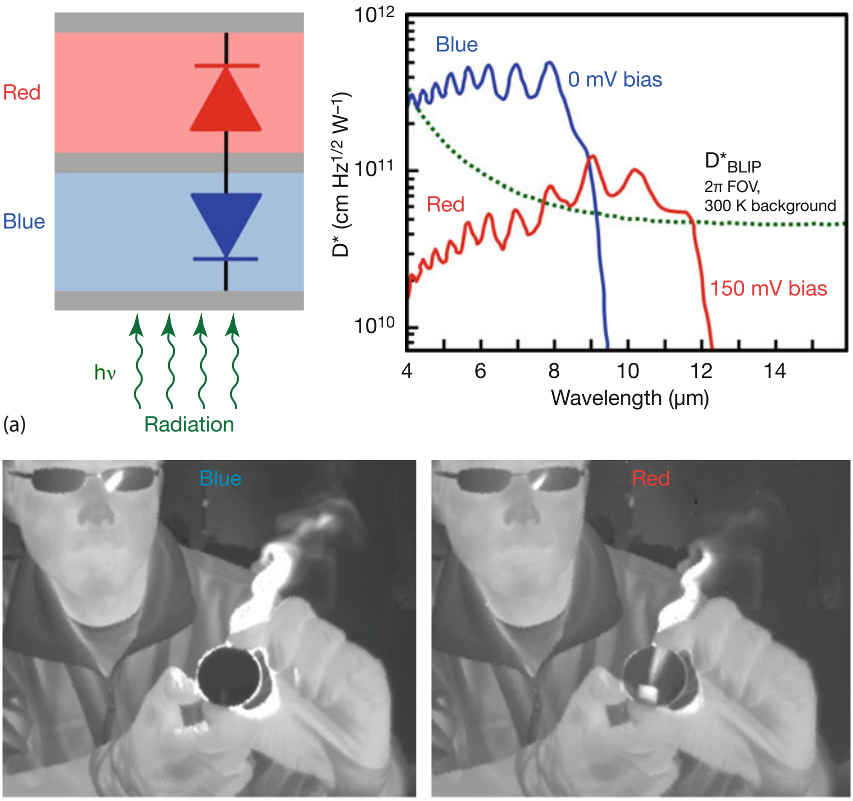

(b) (c)

Figure 2.22 (a) Principal structure of dual-channel detector and spectrum-dependent D^* for different detector biases at 77 K operating temperature (after [40]). (b) IR image in blue channel ($\lambda < 9.5$ μm). (c) IR image in red channel ($\lambda < 12.5$ μm). An 11.3 μm narrow-band filter was held in front of a flame. Image courtesy M. Razhegi, Center for Quantum Devices, Northwestern University, Evanston, IL, USA.

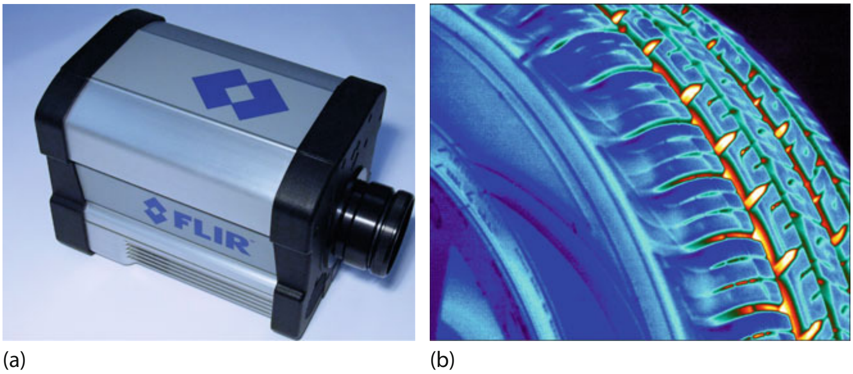
(a) (b)

Figure 2.23 (a) FLIR SC6750SLS LW camera at 640 × 512 pixels. (b) Example image of a tire at a speed of 85 mph (137 km/h) with 50 μs camera integration time. Image courtesy for the IR image: FLIR Systems Inc.

d) Commercial System

The first cameras with strained layer superlattice detector arrays are now commercially available. Figure 2.23 depicts the FLIR SC6750SLS sensitive in the 7.5–9.5 μm LW wavelength range at 640 × 512 pixels with a detector pitch of 15 μm (for details see [41]). The SLS detector is operated at 77 K by a closed cycle Stirling cooler. The temperature resolution of the camera is characterized by a NETD below 30 mK for 30 °C object temperature. The very fast SLS detectors allow user-selectable integration times down to 500 ns.

2.3
Basic Measurement Process in IR Imaging

2.3.1
Radiometric Chain

The basic measurement process in radiation thermometry is described using the concept of the radiometric chain, including all phenomena influencing the detection of the radiation emitted by an object at a certain temperature (Figure 2.24).

The radiometric chain starts with the emission of thermal radiation by the object at a temperature T_{object}. To describe the basic measurement process, we always use radiant power contributions Φ_i (i indicates the contribution mechanism) to the detector signal. These values are related to other radiometric quantities (Table 1.3), and they shall include such camera properties as the detector FOV, the spectral response of the detector, the transmittance of the camera optics, and so on.

To simplify matters, we limit the following discussion to opaque gray body objects (Section 1.4.2). The radiant power of the object $\Phi_{\text{object}}(T_{\text{object}})$ compared

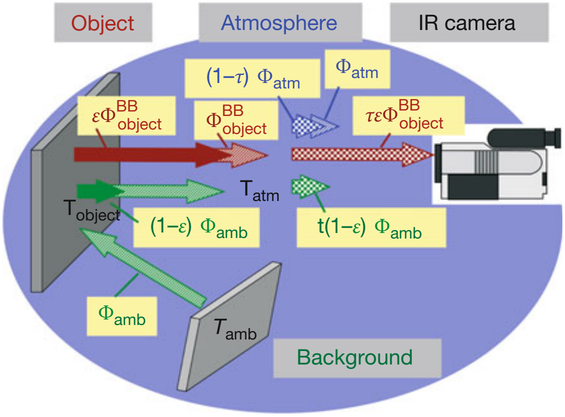

Figure 2.24 Radiometric chain – basic measurement process for opaque objects.

to the radiant power of a blackbody $\Phi_{\text{object}}^{\text{BB}}(T_{\text{object}})$ is given by $\Phi_{\text{object}}(T_{\text{object}}) = \varepsilon\Phi_{\text{object}}^{\text{BB}}(T_{\text{object}})$. The reflectivity of the opaque gray object is given by $R = 1 - \varepsilon$, according to Eq. (1.29). The object receives thermal radiation from its surrounding at ambient temperature T_{amb} and will reflect the radiant power $R\Phi_{\text{amb}}(T_{\text{amb}}) = (1 - \varepsilon)\Phi_{\text{amb}}(T_{\text{amb}})$. The ambient temperature is often indicated as apparent reflected temperature. The radiant power emitted and reflected by the object toward the camera must pass through the atmosphere. Because of the absorption and scattering processes in the atmosphere, the radiant power is attenuated. This can be described by multiplying the radiant power contribution from the object and the surroundings by the atmospheric transmittance τ_{atm}. If one assumes that the atmospheric transmittance is dominated by only absorption losses (scattering mechanism neglected), the atmosphere at a temperature T_{atm} will also emit a radiant power $(1 - \tau_{\text{atm}})\ \Phi_{\text{atm}}\ (T_{\text{atm}})$.

Therefore, the camera detects a radiant power mixture with contributions from the object, the surroundings, and the atmosphere. The total radiation power incident on the detector Φ_{det} can be written as

$$\Phi_{\text{det}} = \tau_{\text{atm}}\varepsilon\Phi_{\text{object}}^{\text{BB}}(T_{\text{object}}) + \tau_{\text{atm}}(1-\varepsilon)\Phi_{\text{amb}}(T_{\text{amb}}) + (1-\tau_{\text{atm}})\Phi_{\text{atm}}(T_{\text{atm}}) \tag{2.37a}$$

Strictly speaking, Eq. (2.37a) represents the spectral radiant power. To calculate the detector signal, this equation must be integrated over the wavelength to account for the spectral dependence of detector responsivity and atmospheric transmission.

For blackbody radiation ($\varepsilon = 1$) and short measurement distances ($\tau_{\text{atm}} = 1$), the radiant power Φ_{det} equals the object radiant power. This behavior is used for the camera calibration process (Section 2.4.5).

An IR camera measures radiance. Therefore, from energy conservation, the signal “brightness” will be independent of the measurement range if $\tau_{\text{atm}} = 1$.

The radiant power emitted by the object can be calculated from

$$\Phi_{\text{object}}^{\text{BB}}(T_{\text{object}}) = \frac{\Phi_{\text{det}}}{\tau_{\text{atm}}\varepsilon} - \frac{(1-\varepsilon)}{\varepsilon}\Phi_{\text{amb}}(T_{\text{amb}}) - \frac{(1-\tau_{\text{atm}})}{\tau_{\text{atm}}\varepsilon}\Phi_{\text{atm}}(T_{\text{atm}}) \tag{2.37b}$$

The value of Φ_{det} is determined from the measured sensor signal. According to Eq. (2.37b), the following parameters are necessary for the correct evaluation of $\Phi_{\text{object}}^{\text{BB}}(T_{\text{object}})$:

- object emissivity ε,
- ambient temperature T_{amb},
- atmospheric temperature T_{atm}, and
- atmospheric transmittance τ_{atm}.

The values for object emissivity, the ambient temperature, and the atmospheric temperature can be entered directly into the camera software. The atmospheric transmittance is calculated by the camera software using the LOWTRAN model (Section 1.3.2). For the calculation of the atmospheric transmittance, the atmospheric temperature, the relative humidity, and the measurement distance are the necessary input parameters.

The object temperature is determined on the basis of the object radiation power $\Phi_{\text{object}}(T_{\text{object}})$ (Eq. (2.37b)) using the calibration curve of the camera (Section 2.4.5).

It is quite obvious that the described radiometric chain is very sensitive to any external influences on the radiation power detected by the camera. Any variation in the object emissivity within the measured area or a background with a spatial temperature variation requires a correction of the measured radiation power for all camera pixels. The necessary accuracy of the correction increases with decreasing object emissivity, that is, increasing reflectance contributions. Figure 2.25 illustrates the portion of object radiation (first term in Eq. (2.37a)) with regard to the total detected radiation as a function of emissivity for MW and LW cameras with constant spectral sensitivities in the 3–5 or 8–14 μm wavelength ranges, respectively.

On the one hand, object radiation contributions are lower for the LW than for the MW range; on the other hand, they are decreasing for decreasing object temperature. The background is not only a source for reflected radiation from the object, but it also serves as a reference. The object is seen in front of a background of given temperature, and whether the object can be distinguished from the background depends on the thermal contrast between object and background.

Figure 2.26 depicts the difference between object radiation and background radiation normalized to the object radiation. Obviously, if the object and background have identical temperatures, thermal imaging cannot identify any object, irrespective of emissivity. Differentiation starts if $|T_{\text{object}} - T_{\text{amb}}| > \text{NETD}$.

Additional optics, filters, windows, and so on can have a strong influence on the detected radiant power and its object-temperature dependence. For a correct

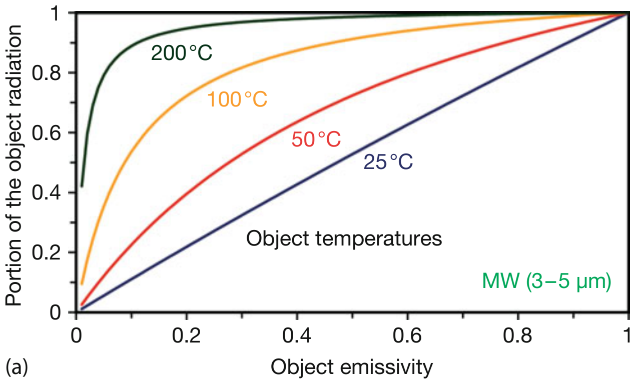

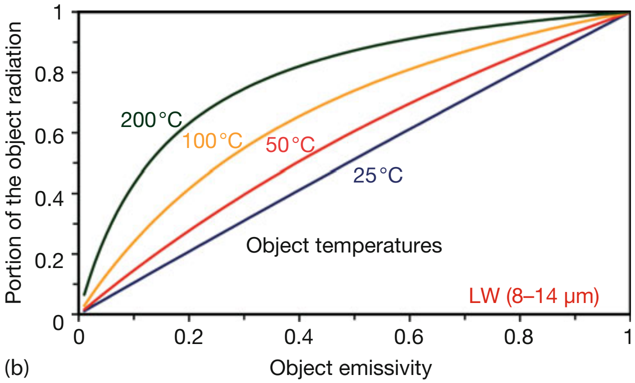

Figure 2.25 Portion of object radiation with regard to total radiation received by camera for different object emissivities at different object temperatures and at an ambient temperature of 22 °C.

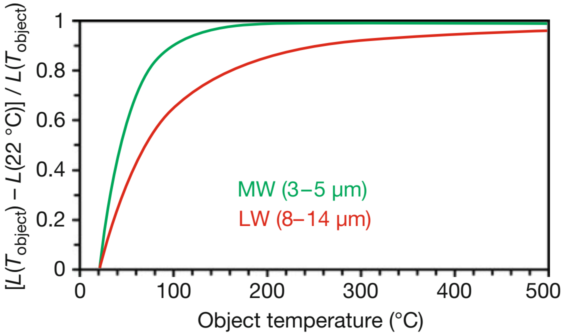

Figure 2.26 Difference in object radiance and background radiance normalized to object radiance at background temperature of 22 °C and different object temperatures.

temperature measurement or signal correction, the complete radiometric chain with all additional elements must be analyzed carefully. This consideration results in a more complex relationship, as shown in Eq. (2.37b), with all computable influences of the additional elements in the radiometric chain.

2.3.2
Wavebands for Thermal Imaging

Adapted to the atmospheric transmission windows for IR radiation, commercial IR cameras are available mostly for the following three spectral ranges (Figure 1.8): SW (0.9–1.7 μm), MW (3–5 μm), and LW (8–14 μm). Figure 2.27 depicts these ranges as blue (SW), green (MW), and red (LW), shaded areas together with the normalized spectral responsivity curves of the detectors of a number of IR cameras.

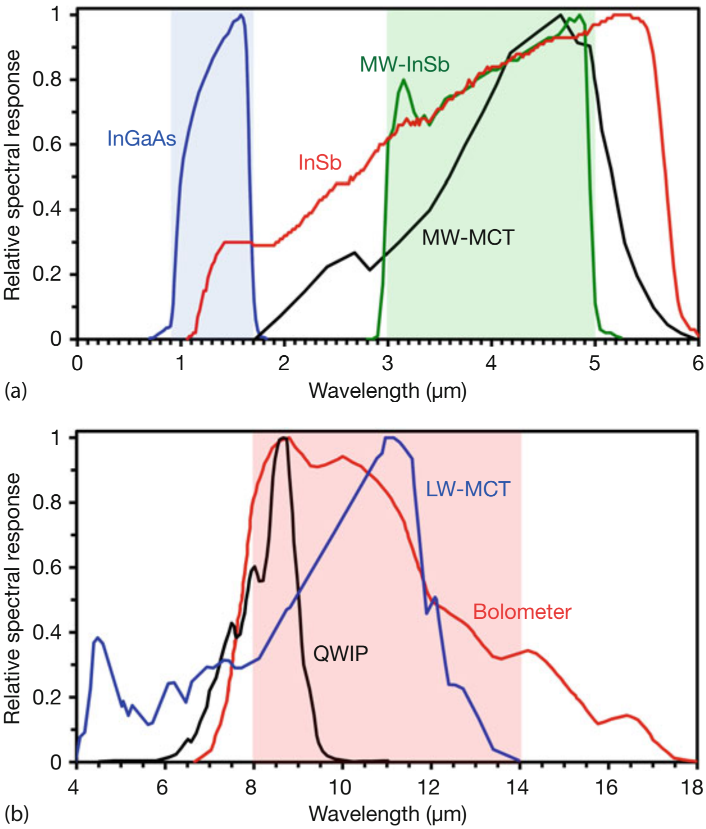

Figure 2.27 Typical relative spectral responsivity curves Res_λ of various thermal imaging systems at shorter (a) and longer (b) IR wavelengths.

For any given spectral response Res(λ) the temperature-dependent object signal (camera output signal, Section 2.4.5) can be easily calculated when assuming blackbody objects of temperature T_{object} characterized by their spectral excitance $M(\lambda)$:

$$S_{\text{camera}}(T_{\text{object}}) = \textit{const.} \int \text{Res}_\lambda M_\lambda(T_{\text{object}})\,\mathrm{d}\lambda \tag{2.38}$$

For quick estimates it is sometimes useful to simplify this calculation. First, one may use the top-hat approximation, that is, assuming a constant spectral response within the camera waveband and zero response outside this waveband. This gives

$$S_{\text{camera}}(T_{\text{object}}) = \textit{const.} \int_{\lambda_1}^{\lambda_2} M_\lambda(T_{\text{object}})\,\mathrm{d}\lambda \tag{2.39a}$$

with

$$[\lambda_1, \lambda_2] = \begin{cases} [0.9\ \mu\text{m}, 1.7\ \mu\text{m}] & \text{for SW} \\ [3\ \mu\text{m}, 5\ \mu\text{m}] & \text{for MW} \\ [8\ \mu\text{m}, 14\ \mu\text{m}] & \text{for LW} \end{cases} \tag{2.39b}$$

Obviously, in this case, one just needs to compute the corresponding band emission (Section 1.3.2.5).

As a second (slightly less accurate) approximation, the spectral excitance M_λ for a given object temperature may be approximated by its value at the center wavelength of the waveband multiplied by the width of the waveband:

$$S_{\text{object}}(T_{\text{object}}) = \textit{const.}\quad M_{\lambda(\text{center})}(T_{\text{object}}) \cdot (\lambda_2 - \lambda_1) \tag{2.40}$$

When using this approximation we employ the following center wavelengths:

$$\lambda(\text{center}) = \begin{cases} 1.3\ \mu\text{m} & \text{for SW} \\ 4\ \mu\text{m} & \text{for MW} \\ 11\ \mu\text{m} & \text{for LW} \end{cases} \tag{2.41}$$

Figure 2.28 compares the two approximations of Eqs. (2.39) and (2.40) with the full calculation according to Eq. (2.38) for an InGaAs SW camera, an InSb MW camera, and a bolometer LW camera. Obviously, the temperature dependence of the true camera object signal, which takes into account the spectral camera response, can be approximated with reasonable accuracy using the corresponding waveband or center wavelength of the waveband.

2.3.3
Selecting the Appropriate Waveband for Thermal Imaging

Anyone planning to use IR cameras must first decide upon the type of camera for the problem to be investigated. The focus here will be only on measuring object temperatures using black or gray body objects (selective absorbers/emitters,

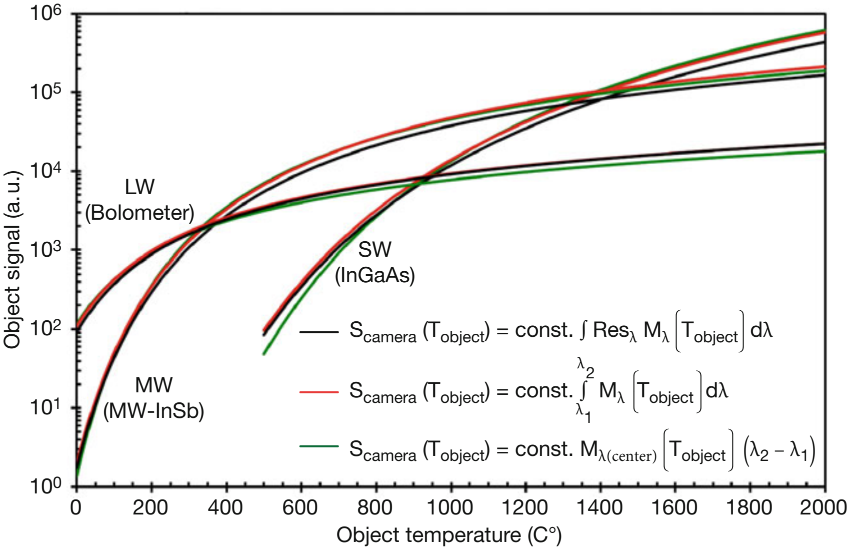

Figure 2.28 Temperature-dependent object signal Eq. (2.38) (black) may be described reasonably well with approximations according to Eqs. (2.39) (red) and (2.40) (green).

discussed in Section 3.2 and Chapter 8). For any given problem, the two most important experimental parameters that have an influence on camera choice are usually predefined: first the expected object temperature, and second the object material and orientation, described by the emissivity. These two parameters define the amount of object radiation that is directed toward the lens of an IR camera. In addition, the medium between object and camera, usually the atmosphere, will alter the radiation spectrum owing to the selected absorption (Figure 1.45).

Assuming that, in principle, IR cameras of all three commercially available wavebands (SW, MW, and LW) are suitable for thermal imaging, the obvious first question is which camera waveband is best suited for a given problem (the second, perhaps more important, question would be whether the most suitable camera is also affordable). The important criteria will be temperature accuracy and resolution and how object signals are disturbed by background reflections or emissivity uncertainties.

2.3.3.1 Total Detected Amount of Radiation

Figure 2.29 depicts a series of blackbody spectra (spectral excitance of a blackbody of given temperature T in wavelength interval $(\lambda, \lambda + d\lambda)$, as described in Eq. (1.15); see also Figure 1.22). For blackbodies at 300, 1000, and 2000 K, maximum emission occurs around 9.7, 2.9, and 1.4 μm, respectively. The first case resembles environmental radiation as used, for example, in building thermography, the second could be a hot plate from an electric stove, and the third liquid hot metals in the metal industry. Obviously, the 300 K objects emit nearly no radiation in the SW band, that is, quantitative SW cameras are only used for high-

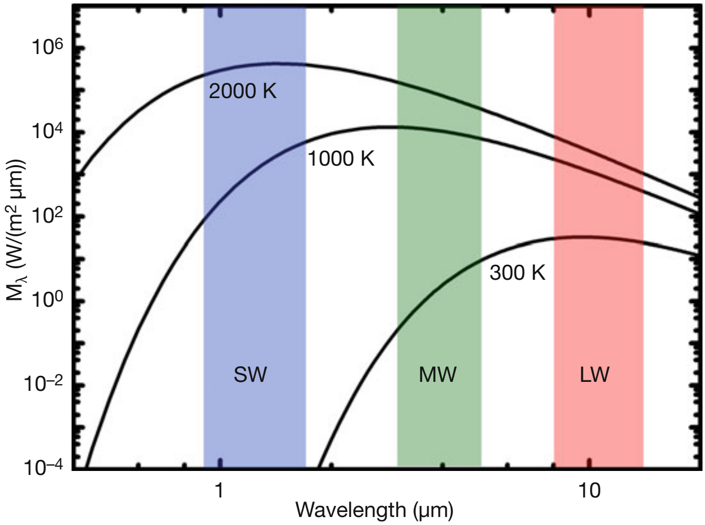

Figure 2.29 Blackbody spectra for three different temperatures. The colored regions indicate the typical wavebands, SW, MW, and LW, of thermography. Note logarithmic scales.

temperature applications. However, the amount of radiation in the MW band is of the same order of magnitude as that in the LW region. The situation changes for increasing temperature because shorter wavelengths receive more radiation. The hottest objects (2000 K) definitely favor SW band detection.

The portions of blackbody radiation (i.e., $F_{(\lambda_1 \to \lambda_2)}$) at a given temperature that fall into the three predefined spectral bands SW (0.9–1.7 µm), MW (3–5 µm), and LW (8–14 µm) are shown in more detail in Figure 2.30a. Similarly, Figure 2.30b depicts the total amount of radiation in the wavebands, that is, $F_{(\lambda_1 \to \lambda_2)}\sigma T^4$, as a function of object temperature. The dotted lines indicate transition regions. For temperatures below around 350 °C, most of the blackbody radiation is emitted in the LW band. Between 350 °C and around 1420 °C, most of the radiation is emitted in the MW band, and above 1420 °C the SW band wins. In addition, at temperatures of around 920 °C, the SW band contribution overtakes that from the LW band.

From these general radiation considerations alone one could guess that cameras detecting in the LW band would be superior to all other cameras up to 350 °C. This is, however, not the case–for several reasons.

First, the properties of actual detectors must be considered. The graphs of Figure 2.30 would shift a bit if the detected radiation, that is, the blackbody radiation, were weighted by the detector sensitivity. Still, the situation would look similar to Figure 2.30. However, in addition, and much more importantly, the detector performance of photon detectors operating in the MW and SW regions are much better than those of bolometers operating in the LW band. The detectivities of photon detectors are usually one to two orders of magnitude better than those of thermal detectors (Figure 2.1). Therefore, a photon detector camera, operating

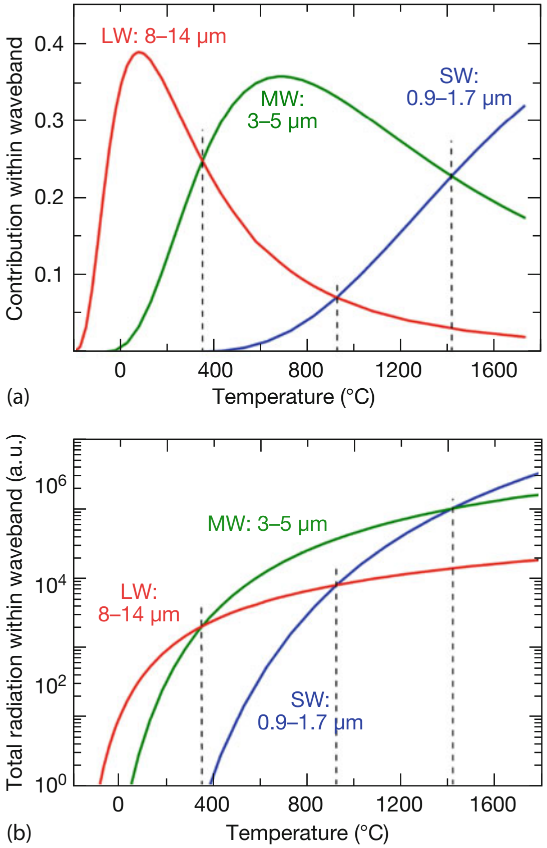

Figure 2.30 (a) Portions of blackbody radiation at given temperature that fall in various waveband regions. (b) Total amount of blackbody radiation within these bands (note logarithmic scale). Broken lines at temperatures at which two wavebands receive the same amount of radiation.

in the MW band, detects signals comparable to those of bolometer cameras in the LW band at room temperature, that is, detector properties enhance camera performance at shorter wavelengths. Since photon detectors usually can achieve lower NETD values, they are in addition usually superior to bolometer detectors.

As a first conclusion, photon detectors of MW cameras lead to superior camera performance even in room temperature conditions. Therefore, if the highest temperature resolution is required, MW cameras should be used. For most regular analyses (e.g., in building or maintenance studies under well-defined conditions), the temperature resolution of bolometer cameras is sufficient, and these – less expensive – systems may be used for such thermal investigations. In contrast, SW camera systems do suffer from missing thermal object radiation and are not suitable in the room temperature range.

There are, however, a number of important additional arguments in favor of shorter wavelength cameras; they will be discussed in what follows. These include temperature contrast, influence of background reflections, and emissivity issues. Therefore, MW cameras are almost always better suited for a given problem than LW cameras. In addition, above around 1000 K, SW cameras become competitive. The same arguments, that is, preferring detectors with shorter wavelengths, also apply to pyrometers.

2.3.3.2 **Temperature Contrast–Radiation Changes upon Temperature Changes**

Whenever minute temperature differences within a scene or transient temperature differences are to be detected, it is important to know how the object radiation changes with temperature. In this respect one can define the temperature contrast as object signals change with changes in temperature. Various possibilities exist. First, a rather practical description of temperature contrast just uses the relative signal change with temperature, that is (e.g., [42]),

$$\text{Temperature contrast} = \frac{1}{\delta T} = \frac{1}{M}\frac{\mathrm{d}M}{\mathrm{d}T} \tag{2.42}$$

Results are then typically given as a signal change in %/K. For single-wavelength radiation thermometers, one may readily calculate $1/\delta T$ from the blackbody functions (Eq. (1.17)). This gives

$$\frac{1}{\delta T}(\lambda, T) = \frac{1}{M_\lambda} \cdot \frac{\mathrm{d}M_\lambda}{\mathrm{d}T} = \frac{hc}{\lambda k T^2} \frac{\mathrm{e}^{(hc)/(\lambda k T)}}{\mathrm{e}^{(hc)/(\lambda k T)} - 1} \tag{2.43}$$

Results for monochromatic wavelengths of 1.3 μm (SW), 4.0 μm (MW), and 11 μm (LW) are shown in Figure 2.31a as a function of object temperature. Alternatively and better suited for IR imaging, one can numerically integrate the blackbody radiation spectra within the wavebands as a function of temperature and evaluate T_{contrast}. Figure 2.31a also depicts the results for the SW, MW, and LW bands. These results are very similar to those in the simplified monochromatic plots.

Figure 2.31b depicts the results for fixed temperatures as a function of wavelength. At any given temperature, the contrast is higher for shorter wavelengths; for example, a temperature change from 1000 to 1001 K would lead to a band excitance increase of only around 0.2% for the LW band, about 0.4% for the MW band, and already about 1% for the SW band. Obviously, the shorter the wavelength, the higher the temperature contrast. This means that whenever a short waveband has enough signal (Figure 2.30), its temperature contrast suggests, again, that the shorter, the better.

Second, a rather universal approach to discussing temperature contrast is in terms of the relative signal change with regard to relative temperature change [43]. This means that we study how a fractional change in the temperature $\mathrm{d}T/T$ of an object leads to a fractional change in incident radiance $\mathrm{d}L/L$ or excitance $\mathrm{d}M/M$ of a blackbody at temperature T.

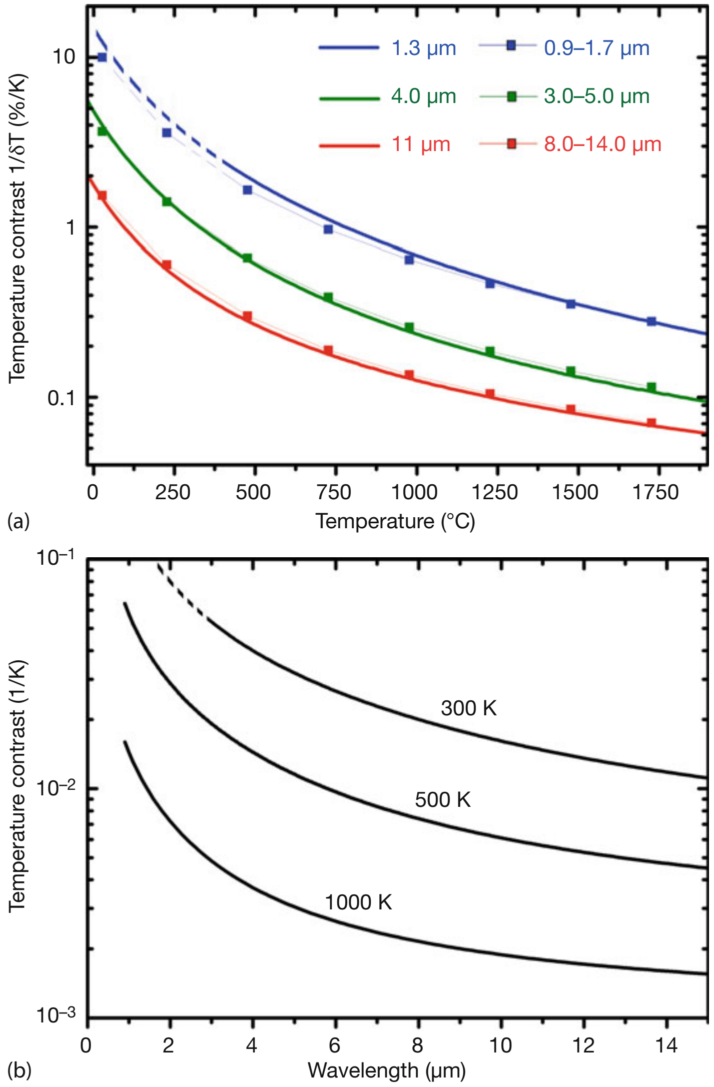

Figure 2.31 (a) Temperature contrast as a function of object temperature for three bands in percent signal change per Kelvin. Thick solid lines: monochromatic results for indicated wavelengths; squares connected by thin lines: corresponding band-integrated results. (b) Temperature contrast as a function of wavelength for three temperatures (note logarithmic scales).

Differentiating Eq. (1.15) with respect to T or simply rearranging the quantities in Eq. (2.43), one finds

$$\frac{\mathrm{d}M_\lambda(T)}{M_\lambda(T)} \Bigg/ \frac{\mathrm{d}T}{T} = \frac{c_2}{\lambda T}\,\frac{\mathrm{e}^{c_2/(\lambda T)}}{\mathrm{e}^{c_2/(\lambda T)} - 1} \tag{2.44}$$

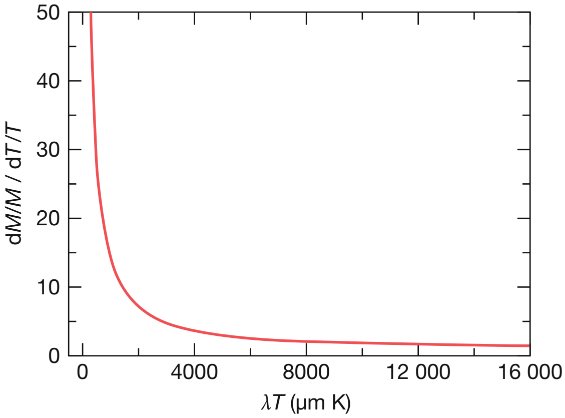

Figure 2.32 Fractional change in excitance of a blackbody owing to a fractional change in temperature according to Eq. (2.44).

where $c_2 = hc/k = 14\,387.7$ μm K. Figure 2.32 depicts a plot of this quantity as a function of $\lambda \cdot T$.

For most practical applications, Eq. (2.44) can be simplified. If $\lambda \cdot T < 2898$ μm K (Eq. (1.16)), the exponential is much larger than unity, and the second fraction is close to unity. In this case,

$$\frac{\mathrm{d}M_\lambda(T)}{M_\lambda(T)} \bigg/ \frac{\mathrm{d}T}{T} \approx \frac{c_2}{\lambda T} \tag{2.45}$$

with a maximum deviation of 0.7%. For larger $\lambda \cdot T$ values, for example, if $\lambda \cdot T$ reaches 4000 μm K, the deviations of Eq. (2.45) from the exact solution of Eq. (2.44) still come in under 2.8%.

Equations 2.44 and 2.45 allow one to estimate detector signal changes upon a change in object temperature as a function of wavelength. As an example, we discuss how a fractional change of 1% in temperature from $T = 400$ K to $T = 404$ K results in different fractional changes in excitance in the MW and LW spectral regions. Again, for simplicity, the MW is characterized by $\lambda_1 = 4$ μm and the LW by $\lambda_2 = 11$ μm. Using Eq. (2.44) with $\lambda_1 \cdot T = 1600$ μm K and $\lambda_2 \cdot T = 4400$ μm K, one finds

$$\frac{\mathrm{d}M_{4\,\mu\mathrm{m}}(T)}{M_{4\,\mu\mathrm{m}}(T)} \bigg/ \frac{\mathrm{d}T}{T} \approx 2.65 \cdot \frac{\mathrm{d}M_{11\,\mu\mathrm{m}}(T)}{M_{11\,\mu\mathrm{m}}(T)} \bigg/ \frac{\mathrm{d}T}{T} \tag{2.46}$$

This means that a 1% object-temperature change from 400 to 404 K leads to a 2.65 larger fractional change in MW radiation than for LW radiation. As a consequence, MW (or generally shorter waveband) cameras will have advantages compared to LW cameras owing to the more pronounced dependence of signal on object temperatures.

Mathematically, changes in signal with temperature manifest themselves in the different slopes of tangents to the total radiation curves of Figure 2.30b. For any

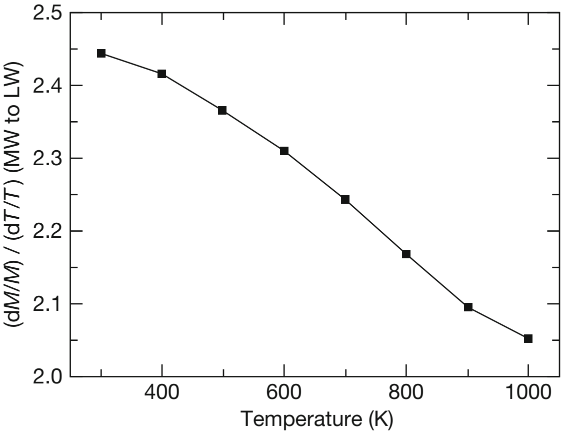

Figure 2.33 Ratio of fractional signal changes to temperature for MW to LW ranges with center wavelength approximation.

given temperature, the slope of tangents to the 3–5 μm curve is much steeper than for the 8–14 μm curve. A detailed analysis of fractional signal changes of the MW versus the LW band (using approximations of the center wavelengths) as a function of object temperature is shown in Figure 2.33.

The exact calculation using waveband ranges of 3–5 μm versus 8–14 μm and a top-hat approximation reveals a slight change from the preceding simple expectation based on Eq. (2.44). For 400 K the result is 2.45 rather than 2.65. In addition, one observes a decrease with temperature. In any case, the overall statement holds that the shorter the wavelength, the more signal change results from any given temperature change.

We present a final related example of how temperature contrast affects measurement results. A typical practical question is how precise the temperature of a (blackbody) source must be stabilized to $T \pm \Delta T$ such that the variation in radiation reaching a detector is less than a predefined value. Let us consider three temperatures of 300, 500, and 1000 K, assume monochromatic detection for the SW (1.3 μm), MW (4.0 μm), and LW (11.0 μm) bands, and allow for a maximum signal variation of 1%. The results are given in Table 2.2.

Table 2.2 Temperature variation of an object that results in a 1% signal change for monochromatic detection at 1.3 μm (SW), 4 μm (MW), and 11 μm (LW).

	$T_{\text{object}} = 300\,\text{K}$	$T_{\text{object}} = 500\,\text{K}$	$T_{\text{object}} = 1000\,\text{K}$
ΔT (SW)	0.08 K	0.22 K	0.9 K
ΔT (MW)	0.25 K	0.69 K	2.7 K
ΔT (LW)	0.68 K	3.54 K	5.6 K

Obviously the same signal change of 1% is due to much smaller temperature variations at shorter wavelengths. In other words, the shorter the wavelength of an IR camera, the more sensitive is the radiation detection.

2.3.3.3 **Influence of Background Reflections**

All real camera signals contain contributions from reflected background radiation (Figure 2.24, Eq. (2.37b)), which can dramatically affect the measured object temperatures. In this section, quantitative estimates will be given on how background reflection influence varies with wavelength, that is, with the waveband of the camera. Again, it will be demonstrated that in this respect shorter-wavelength systems are superior to longer-wavelength systems.

The discussion will be based on the object and background radiation that a camera may receive. We assume an opaque object of emissivity ε, that is, its reflectivity is given by $(1-\varepsilon)$ (Eq. (1.29)). Therefore, the object radiation is determined by its radiance, $L_{\text{obj}}(T_{\text{obj}}) = \varepsilon \cdot L_{\text{BB}}(T_{\text{obj}})$, and the reflected background radiation by $L_{\text{amb}}(T_{\text{amb}}) = (1-\varepsilon) \cdot L_{\text{amb}}(T_{\text{amb}})$. Figures 2.34 and 2.35 depict two examples for these quantities. In Figure 2.34, the object temperature was 200 °C and the background was at 25 °C. Figure 2.35 depicts the situation for higher temperatures as encountered in the aluminum and steel industries.

Figures 2.34 and 2.35 show that the portion of reflected background radiation with respect to the object radiation depends strongly on emissivity. This ratio is plotted for MW and LW detection in Figure 2.36 for the high-temperature regime. Obviously, this ratio is always lower for the MW region compared to the LW region, that is, the MW band is less affected by background reflection than the LW band. In other words, whenever background reflections cannot be properly corrected or if there are unnoticed reflection contributions, the MW regime is always less sensitive to these disturbances.

As an example for the chosen temperatures, the region below the dotted line means that the background reflection signal accounts for at most 10% of the object signal. With this restriction, LW cameras would require emissivities of around 0.8, whereas MW cameras could operate at values as low as 0.6.

As a practical example, we illustrate the relative contributions of background reflections using a homogeneously heated hot stainless steel plate of 200 °C and observe the reflections of a human hand using LW and MW cameras. This situation corresponds approximately to the radiance signals of Figure 2.34. The emissivity of stainless steel is not easy to guess–too many factors play a role. However, we can safely assume that ε is smaller than 0.3, probably even below 0.2 (see following discussion). Whatever value we actually choose is not important since for all emissivities the MW camera should be less sensitive to the thermal reflections of the hand. This is nicely demonstrated in Figure 2.37. Both cameras used the same level and span as well as palette settings for better comparison. As expected, the hand reflection is easily seen with the LW camera, whereas it is much more difficult to detect in still IR images of the MW camera. Assuming, for example, $\varepsilon = 0.2$, the reflection as incident onto the MW camera would be around 6.3% of the object signal, whereas this ratio would increase by more than a factor of ten

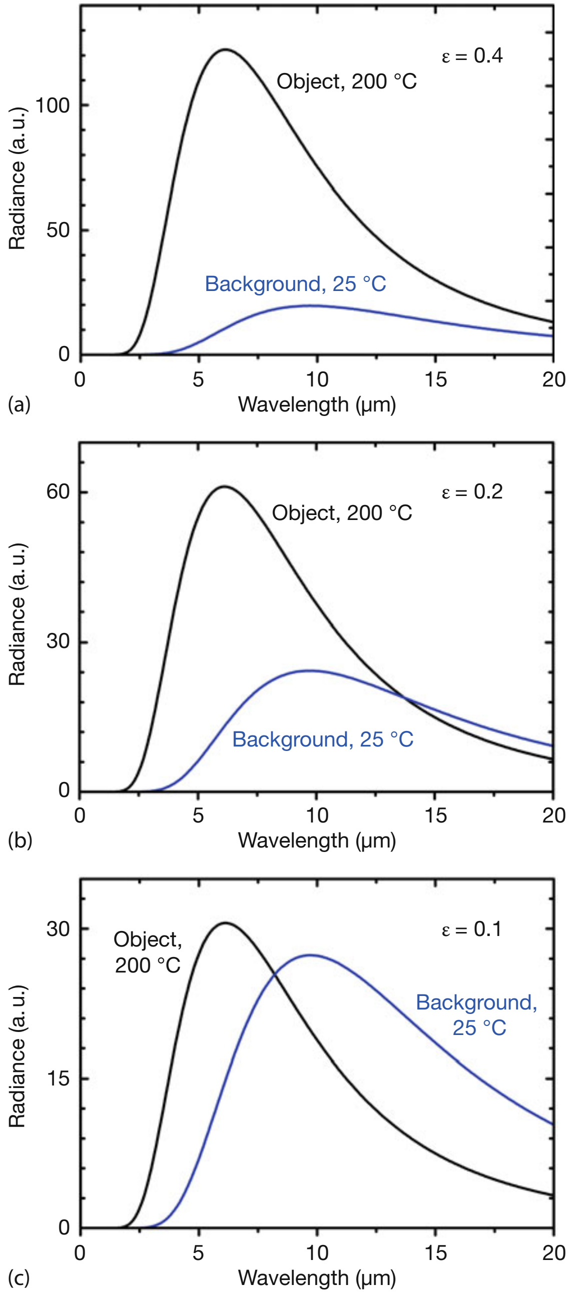

Figure 2.34 Object radiance (T_{obj} = 200 °C) and reflected background radiance (T_{amb} = 25 °C) for different emissivities of opaque objects.

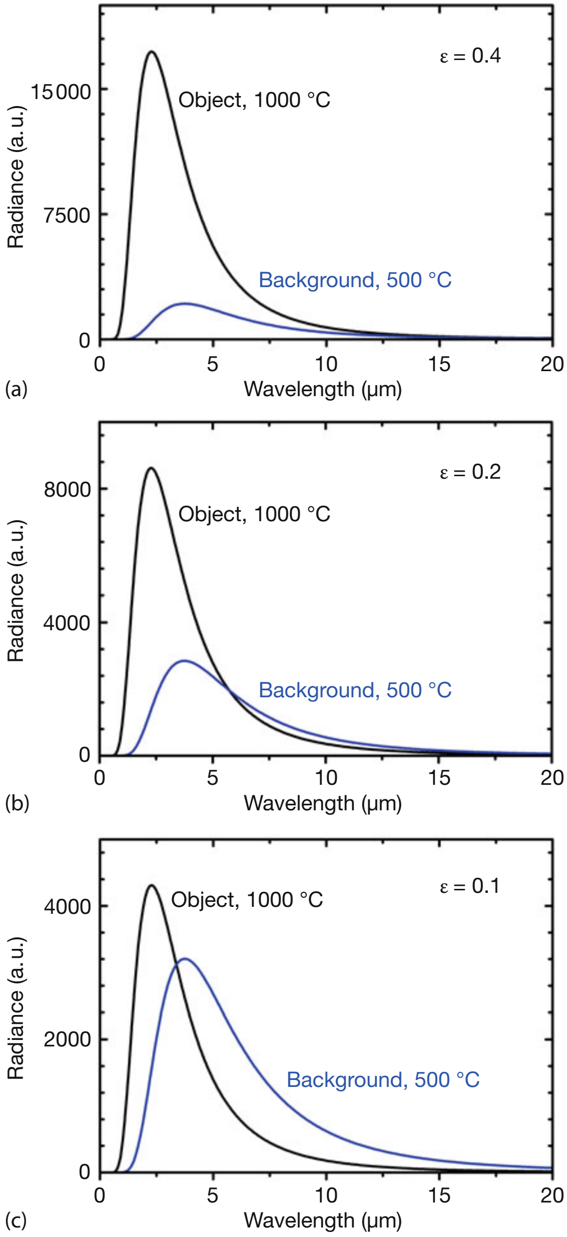

Figure 2.35 Object radiance ($T_{obj} = 1000\,°C$) and reflected background radiance ($T_{amb} = 500\,°C$) for different emissivities of opaque objects.

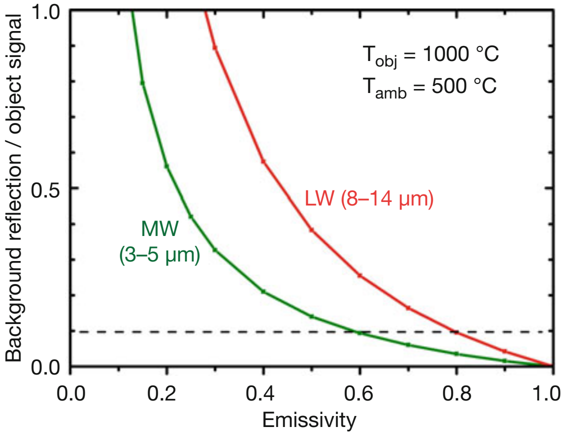

Figure 2.36 Ratio of reflected background radiance versus object radiance as a function of object emissivity for $T_{\text{obj}} = 1000\,°\text{C}$ and $T_{\text{amb}} = 500\,°\text{C}$.

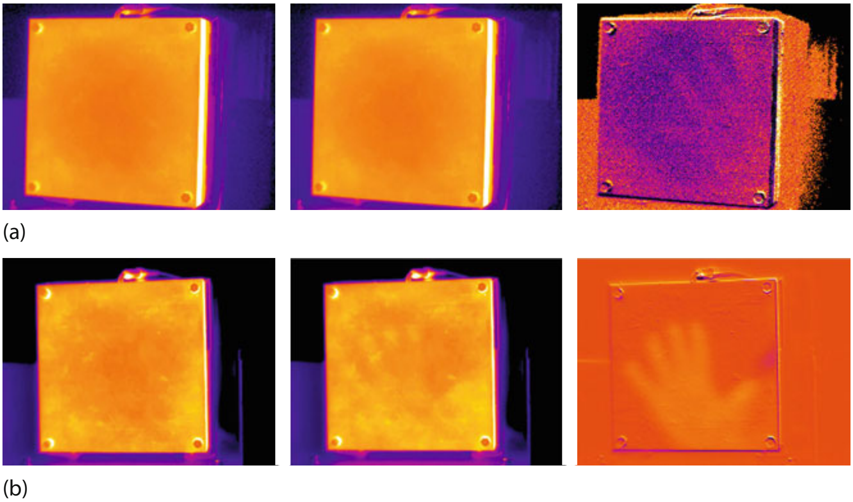

Figure 2.37 Homogeneously heated stainless steel plate ($T_{\text{obj}} = 200\,°\text{C}$) attached to temperature-stabilized blackbody source. (a) MW and (b) LW images. Left to right: without hand, with hand, and image subtraction.

to about 68.4% for the LW camera. Although the MW hand signal is quite small, it may still be detected using techniques of image subtraction (Section 3.5.1.3).

2.3.3.4 **Influence of Emissivity and Emissivity Uncertainties**

Besides the role of emissivity in background reflections, low emissivity values as well as emissivity uncertainties additionally favor short wavebands for quantitative measurements.

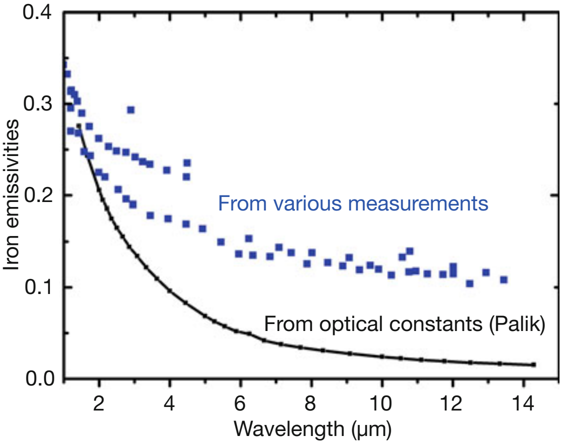

Figure 2.38 Emissivity of iron as function of wavelength. Solid black line: ideal directed normal emissivity from Eq. (2.47) using optical constants from [44]. Blue squares: from various measurements (after [45]).

a) Imaging of Objects with Low Emissivity

Typical objects with low emissivity values are metals. Figure 2.38 depicts the expected normally directed spectral emissivity of a typical metal, iron, based on optical constants from the literature [44] (solid black line with dots) as well as various experimental data (blue squares). The theoretical data, based on carefully selected literature data of optical constants (i.e., real and imaginary parts of index of refraction $n(\lambda) = n_1(\lambda) + in_2(\lambda)$) resemble the most ideal case of polished smooth metal surfaces. n_1 and n_2 allow one to calculate the reflectivity R for normal incidence (adjacent medium air, $n_{\text{air}} = 1$, see Eq. (1.5)) according to

$$R_{\text{normal}} = \frac{(n_1(\lambda) - 1)^2 + n_2(\lambda)^2}{(n_1(\lambda) + 1)^2 + n_2(\lambda)^2} \tag{2.47}$$

and the directed normal emissivity is computed from that (Eq. (1.29)) for opaque objects according to $\varepsilon = 1 - R_{\text{normal}}$.

One sees nicely the general trend for all such metals: emissivity increases toward the short wavelengths, reaching values of up to 0.3 in the SW range, and is very low for the LW range, here below 0.035.

In contrast, the measured data are widely scattered. In the SW region, they still coincide with the ideal values, but for the MW and LW regions, they are much larger, with values above 0.1. Figure 2.38 is a typical example, showing the general problem with all metals. If they are very pure and have smooth surfaces, they behave ideally. However, impurities of any kind, oxidation, and corrosion of the surfaces and residual or additionally introduced surface roughness immediately alter the emissivity. This is why one can never trust literature data on metal emissivities. Theoretical literature data on a certain metal and a real sample of the same metal may differ appreciably on a microscopic scale, although this may not be obvious macroscopically.

One general feature is, however, also present for any realistic metal sample, as can be seen for the measured data here as well as from survey data of Figure 1.35: metal or metal alloy emissivities always increase toward shorter wavelengths.

This trend favors shorter waveband detection for two reasons. First, as discussed previously, at any given low emissivity, shorter waveband detection suffers less from reflected background radiance than LW band detection (Figure 2.36). Second, for any given metal object, detection in the MW band is always associated with higher emissivities compared to the LW region, which additionally improves the performance regarding reflections.

This general statement is visualized in Figure 2.39a. Some objects (a hand and a face) are close to a slightly corroded brass plate in such an alignment that a camera is able to observe direct reflections, if there are any. The scene is observed with four different cameras, operating in the visible spectral range (0.4–0.8 μm) as well as the SW (0.9–1.7 μm), the MW (3–5 μm), and the LW (8–14 μm) thermal IR range. Whereas mirror images due to direct reflections can hardly be seen in the VIS and SW ranges, mirror image quality gets progressively better, that is, background reflections get progressively worse toward the LW range. The direct reflectivity of the brass sample was analyzed and is depicted in Figure 2.39b (in addition, diffuse reflections will also contribute). As expected, reflectivity is larger, that is, emissivity is lower for longer wavelengths, which, like Figure 2.37, explains the respective better visibility of thermal reflections at these wavelengths.

b) Influence of Emissivity Uncertainties in General

For any quantitative measurement the resulting temperature reading depends on the emissivity. The precision of a measurement therefore sensitively depends on the accurate knowledge of the value of emissivity. Here, we want to discuss the influence of emissivity uncertainties on the accuracy of temperature measurements and in the next subsection how these results depend on the choice of a specific waveband. Arguments here are based on the radiometry of black and gray bodies using the top-hat approximation.

First, let us consider a gray body radiance function $\varepsilon_1 \cdot L(\lambda, T_1)$ at a given object temperature T_1, which is shown as solid black line in Figure 2.40. The camera will detect a signal proportional to the in-band radiance. For a LW camera this would be the area below the black graph between the two boundaries at 8 and 14 μm (vertical thin black lines). This signal would then be used to calculate the object temperature according to the calibration curve (Section 2.4.5). However, if the camera user does not know the exact emissivity, it may well be that he is using the wrong emissivity value for the internal corrections. Consider, for example, an emissivity ε_2 that is smaller than the actual object emissivity. The corresponding gray object radiance $\varepsilon_2 \cdot L(\lambda, T_1)$ (blue graph in Figure 2.40) and the in-band radiance as well would be lower, indicated by the blue arrow. Referring to the detected in-band radiance (the area below $\varepsilon_1 \cdot L(\lambda, T_1)$), the user would find a much higher temperature $T_2 > T_1$ (indicated by red arrow) such that the in-band radiance of $\varepsilon_2 \cdot L(\lambda, T_2)$ in the LW band would be the same (the area below the red graph between 8 and 14 μm is the same as below the black graph).

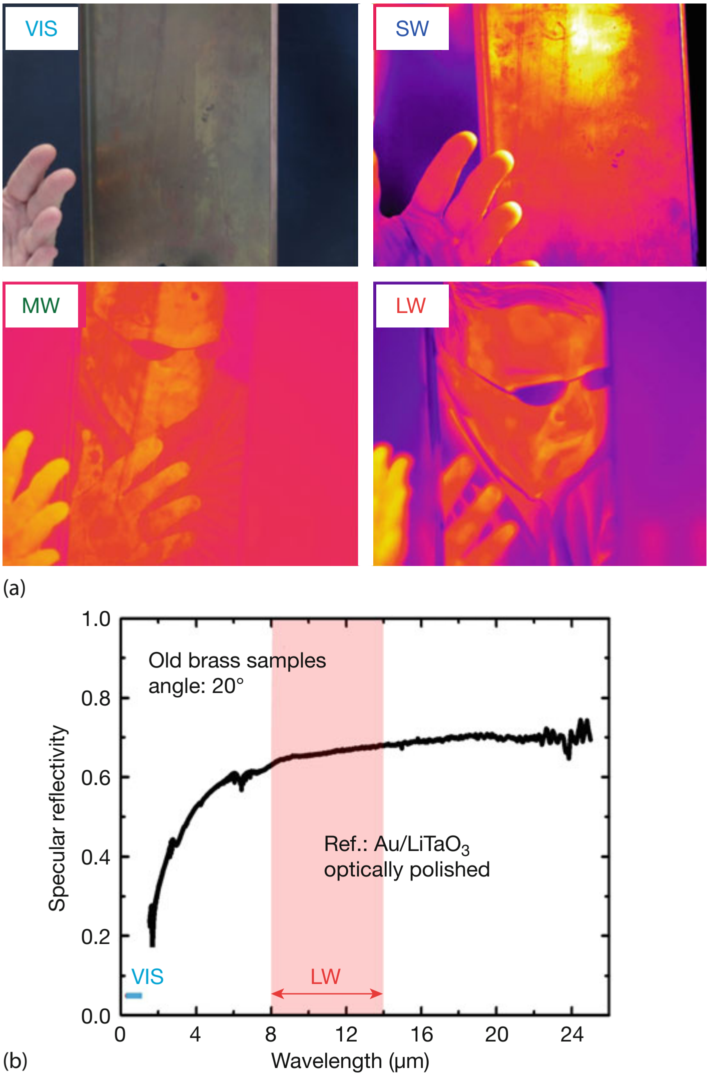

Figure 2.39 Waveband-dependent influence of reflections from corroded brass plate (a) and measured directed reflectivity of plate (b).

We summarize the main result: assuming an emissivity below the actual one results in an object temperature higher than the actual one – and vice versa. As a consequence, any uncertainty in the emissivity will lead to an uncertainty in the measured object temperatures. To estimate associated temperature errors, one would need to include all camera parameters, detector sensitivities, properties of optics, and so forth. In this general discussion, we only use radiometry to indicate the effects with the proper order of magnitude. Specific numbers for any given camera may differ slightly.

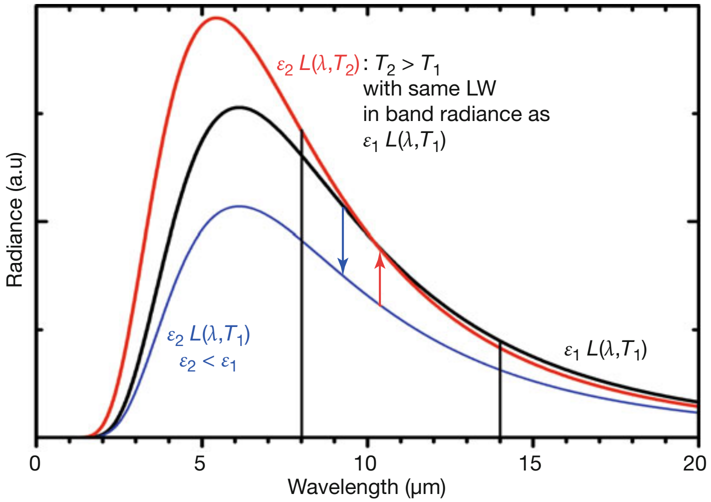

Figure 2.40 Scheme to explain influence of emissivity uncertainties on resulting temperature errors. For details see text.

Let us start with gray body radiation spectra of known emissivities as a function of temperature. From there we compute the relevant in-band radiances as a function of temperature that serve the same purpose here as camera calibration curves for any real camera. Figure 2.41 shows examples of in-band radiance of LW IR due to three different emissivities, here 0.8 as well as 10% lower and higher values 0.72 and 0.88. We now assume that $\varepsilon = 0.8$ is the correct emissivity, and we want to guess the temperature offset resulting when using the emissivity variation of ±10%. Obviously we just need to find the temperature values for the same in-band radiance, which is depicted as a horizontal line in the plot. As a numerical example we assume that at $\varepsilon = 0.8$ the correct temperature would be 1500 °C. The horizontal in-band radiance line intersects the in-band-radiance graphs for the other emissivity values, as is shown enlarged in Figure 2.41b. For an emissivity of 0.72, the resulting temperature error would be as large as +134 K, and for $\varepsilon = 0.88$ it would be −110 K.

c) Influence of Emissivity Uncertainties: Comparison of Different Wavebands

Knowing that all emissivity uncertainties result in temperature errors, we now investigate whether certain wavebands are superior by giving smaller errors.

Figure 2.40 demonstrated that the gray body radiance for lower emissivity $\varepsilon_2 < \varepsilon_1$ required a higher apparent temperature T_2 such that $\varepsilon_2 L(\lambda, T_2)$ had the same in-band radiance in the LW band as one with a correct emissivity, that is, $\varepsilon_1 L(\lambda, T_1)$ at lower temperature T_1. However, in order for MW in-band radiances to be equal, one would have required a lower temperature rise. This is illustrated in Figure 2.42 for a specific example with object temperature $T_1 = 200\,°\mathrm{C}$ and object emissivity $\varepsilon_1 = 1.0$ (black solid line is the black body radiance). The red and green solid lines represent gray body radiances for emissivities of 0.7 such that

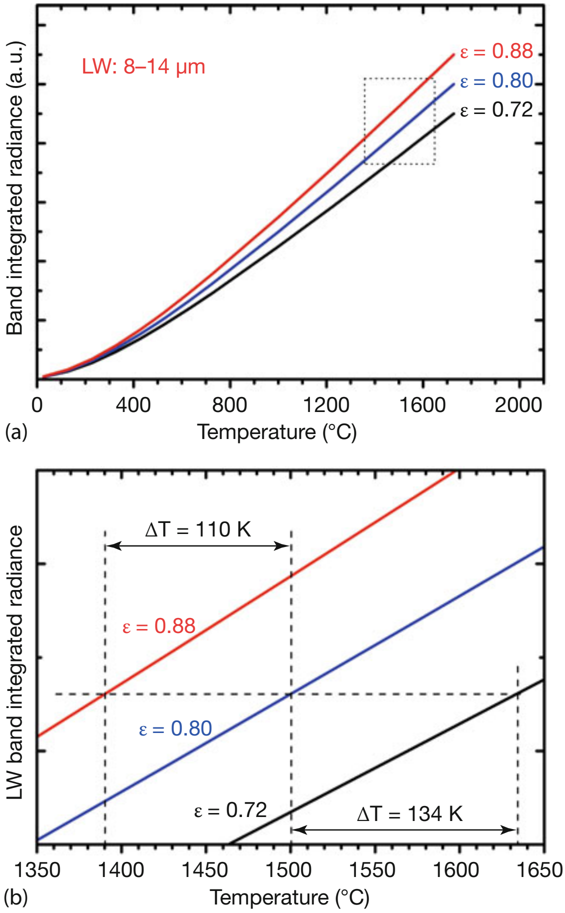

Figure 2.41 Integrated band emission in interval of 8–14 μm plotted as function of *T* for three different emissivities. (a) The content of the broken rectangle is shown enlarged in (b). A 10% ε variation leads to temperature errors well above 100 K.

either the LW in-band radiance (red line) or the MW in-band radiance (green) matches the one from the blackbody.

Obviously, the wrongly guessed emissivity of 0.7 leads only to a temperature error of 24 K for the MW, but to 60 K for the LW band. The result from this specific example holds in general: the MW temperature error is always smaller than that for LW bands.

The calculations presented previously for predefined wavebands are simple but tedious. Trends can be seen easier by using the approximation of monochromatic radiances at the center of the respective bands.

We start with the blackbody excitance $M(\lambda, T_1)$ for an object with temperature T_1 (Eq. (1.15)), which leads to the gray body radiance $L(\lambda, T) = M(\lambda, T)/\pi$

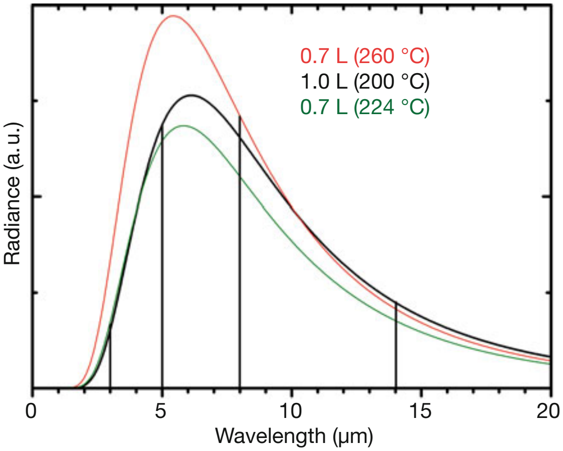

Figure 2.42 Comparison of a black body spectrum at 200 °C (black line) with two spectra for emissivity of 0.7, which have the same in-band radiance for the MW (3–5 μm, green line) and the LW (8–14 μm, red line) bands. The MW-related spectrum corresponds to a 24 K and the LW related spectrum to a 60 K increase in object temperature.

(Table 1.4).

$$L_\lambda(\varepsilon, T_1) = \varepsilon \frac{2hc^2}{\lambda^5} \frac{1}{e^{(hc)/(\lambda k T_1)} - 1} \tag{2.48}$$

Now we allow for an emissivity variation by a factor of α, that is, $\varepsilon' = \alpha \cdot \varepsilon$. For example, a 10% decrease would correspond to $\alpha = 0.9$ and a 10% increase to $\alpha = 1.1$. The problem now consists in finding the temperature T_2 of the gray object with emissivity $\alpha \cdot \varepsilon$ which has the same monochromatic radiance at any given wavelength, that is, $L(\lambda, \varepsilon, T_1) = L(\lambda, \alpha\varepsilon, T_2)$, giving

$$\frac{1}{e^{(hc)/(\lambda k T_1)} - 1} = \alpha \frac{1}{e^{(hc)/(\lambda k T_2)} - 1} \tag{2.49}$$

Solving for T_2 we find

$$T_2 = \frac{(hc)/(\lambda k)}{\ln\left[1 + \alpha\left(e^{(hc)/(\lambda k T_1)} - 1\right)\right]} \tag{2.50}$$

Figure 2.43 shows resulting temperature errors $(T_2 - T_1)$ for an emissivity uncertainty of 10% for the three monochromatic wavelengths at the center of the SW, MW, and LW bands.

The accuracy of the approximation can be judged when analyzing the data for the parameters of Figure 2.42 with 200 °C and 30% ε-decrease. We find a temperature of 264 K instead of 260 K for the LW band and 223 K instead of 224 K for the MW band.

Similarly, comparison with the LW in-band radiance results of Figure 2.43 at 1500 °C with 10% ε-variation gives monochromatic values of 1639 and 1386 °C

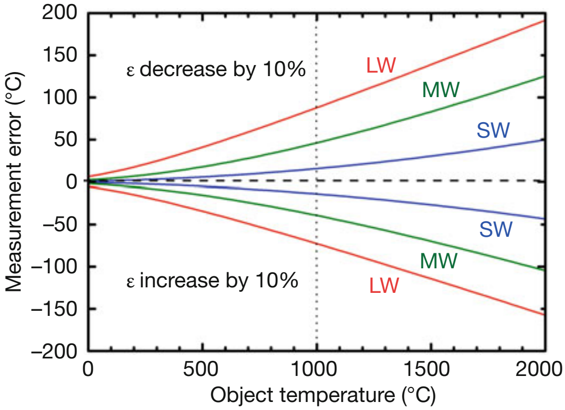

Figure 2.43 Influence of emissivity variations on temperature errors for monochromatic thermal IR radiation (SW: $\lambda = 1.3\ \mu m$; MW: $\lambda = 4\ \mu m$; LW: $\lambda = 11\ \mu m$).

instead of the in-band values 1634 and 1390 °C respectively. Both comparisons are in very good agreement. Therefore, the data of Figure 2.43 can be considered reasonably accurate temperature error results upon emissivity uncertainties.

The general trend is obvious: the shorter the wavelength, the lower the temperature error for the same emissivity uncertainty. This is again a strong argument for MW rather than LW cameras.

There is an additional argument that favors shorter wavelength detection. Very often one does not deal with relative emissivity uncertainties but, rather, absolute ones. As an example, we discuss temperature errors for an absolute variation of $\Delta\varepsilon = 0.04$ as a function of the emissivity of an object (Figure 2.44).

Again, Eq. (2.50) is used within the monochromatic approximation. The only difference is that the factor α now changes with the absolute value of ε. For $\Delta\varepsilon = 0.04$ and $\varepsilon = 0.8$, we find, for example, $\alpha = 0.95$ (giving $\varepsilon = 0.76$) and 1.05 (giving 0.84). Similarly $\Delta\varepsilon = 0.04$ and $\varepsilon = 0.5$ gives $\alpha = 0.92$ and 1.08, and for $\varepsilon = 0.1$ we find $\alpha = 0.6$ and 1.4. Figures 2.44 and 2.45 depict some results for MW (4.0 μm) and LW (11.0 μm) radiation and chosen temperatures of 500, 1000, and 1500 °C. In all cases, the temperature errors are smaller for shorter wavelengths. In addition, errors get very large for small emissivities. If polished metals with ε on the order of 0.1 are to be investigated, an uncertainty of 0.04, that is, ε within the interval (0.06 to 0.14), already leads to very large temperature uncertainties: for MW radiation T lies in the interval (≈ 870 to 1255 °C). Using LW cameras further expands the temperature interval to (≈ 770 to 1520 °C). If the uncertainty were half of these values, that is, $\Delta\varepsilon = 0.02$, the temperature intervals would still be quite large: ≈ 925 to 1100 °C for MW and ≈ 865 to 1200 °C for LW.

A final practical example will illustrate the different influence of emissivity variations on the temperature measurement results in the MW and LW bands, respectively. A stainless steel plate was homogeneously heated to 210 °C (Figure 2.46). Using the known temperature of 210 °C from a contact temperature measure-

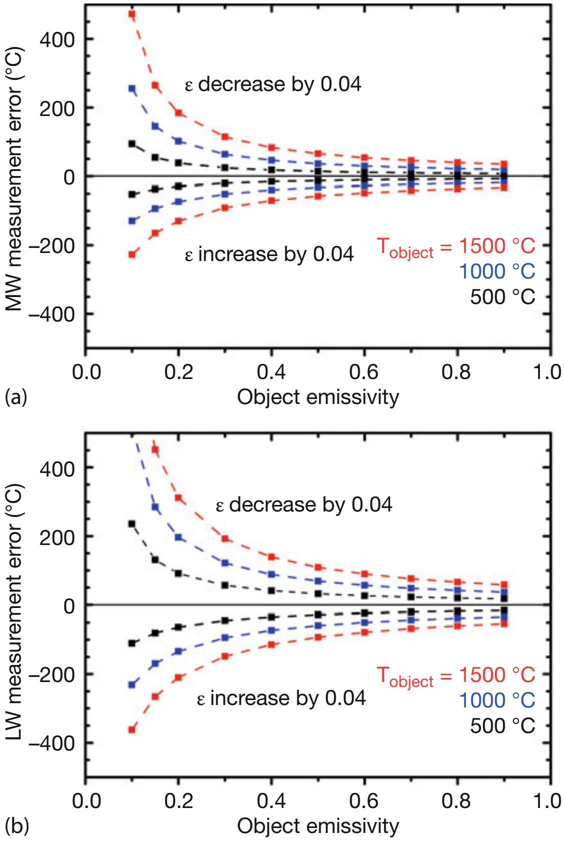

Figure 2.44 Influence of absolute emissivity uncertainty on temperature errors as a function of emissivity for the (a) MW band and (b) LW band and object temperatures varying from 500 to 1500 °C.

ment, the average emissivity in the marked circular area was determined for both spectral ranges. The average emissivity within the area slightly decreased from 0.2 in the MW band to about 0.16 in the LW band.

A variation of the object emissivity within the marked area owing to surface property variations causes respective variations of the measured pixel temperatures. As expected, emissivity variations cause a larger spread of the measured temperatures for the LW camera ($\Delta T_{\text{LW}} = T_{\text{max}} - T_{\text{min}} = 29\,°\text{C}$) compared to only 13 °C for the MW camera. The measured increase in the temperature measurement error by a factor of about 2 corresponds nicely to the results of the calculations depicted in Figure 2.43.

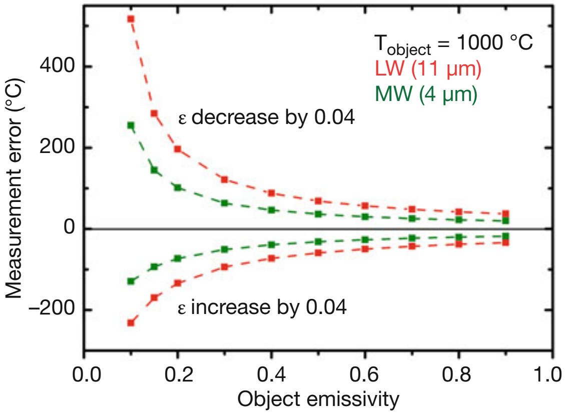

Figure 2.45 Comparison of absolute temperature errors between MW and LW bands owing to an emissivity uncertainty of 0.04. The object temperature was 1000 °C.

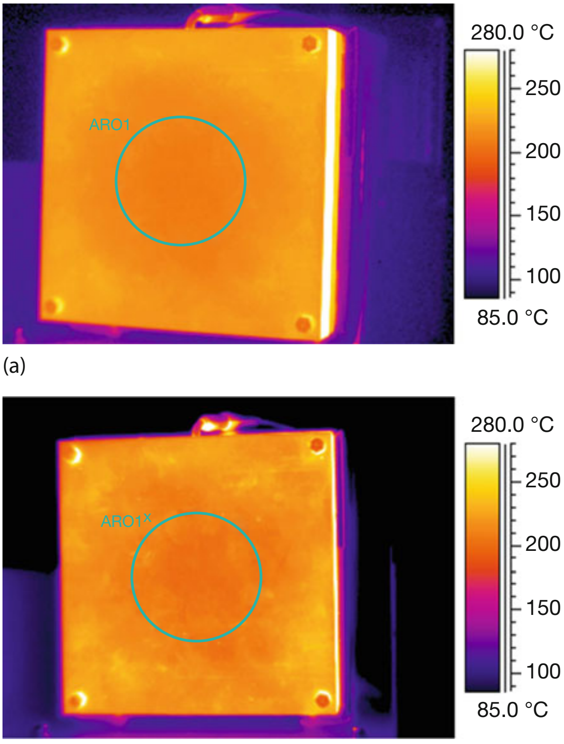

(a)

(b)

Figure 2.46 Homogeneously heated stainless steel plate (T_{obj} = 210 °C) attached to a temperature-stabilized blackbody source. (a) MW with $\varepsilon = 0.2$ and (b) LW with $\varepsilon = 0.16$.

2.3.3.5 Potential use of Bolometers in MW or SW band

So far, the question of which waveband is most suitable with respect to sensitivity and small temperature measurement errors for a given problem has been based solely on radiometric arguments. The answer up to this point can be summarized as follows: the shorter the wavelengths, the better – provided enough radiation is available in the shorter wavebands.

Unfortunately for the practitioner, cameras in the shorter waveband ranges are usually photodetector cameras whose detectors need to be cooled. As a consequence, these cameras are much more expensive than the cheaper bolometer cameras, which nowadays dominate the inexpensive LW camera segment.

However, we want to suggest that for certain high-temperature applications, less expensive bolometer cameras may well find an application niche also for the MW band. Here we briefly summarize the underlying physics reasons–again based solely on radiometry, that is, the in-band radiance estimated with the top-hat approximation–why bolometers may indeed be useful at shorter wavelengths, too.

Same In-Band Radiances for Different Temperatures

Figure 2.47 depicts a small segment of the total in-band radiance of the LW, MW, and SW bands as a function of temperature (see also Figure 2.30). We start with an object at a temperature of 30 °C, which gives an in-band radiance indicated by the red arrow. If we require that the same signal, that is, the same in-band radiance, be detected within the MW and SW wavebands, we find that this would happen at temperatures of 160 and 540 °C, respectively. Assuming that we use the same detector with the same sensitivity and the same noise level, we can describe the result of Figure 2.47 in other words: an object of 30 °C detected in the LW band gives the same SNR as an object of 160 °C detected in the MW as well as an object of 540 °C detected in the SW band.

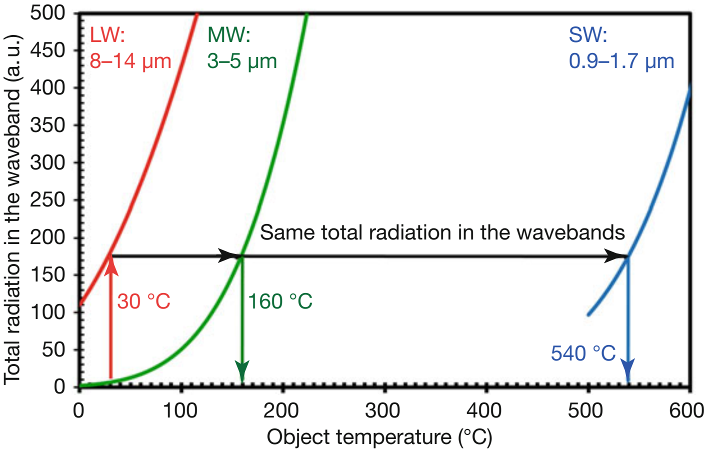

Figure 2.47 Object-temperature-dependent total in-band radiance in LW, MW, and SW bands (see text for details).

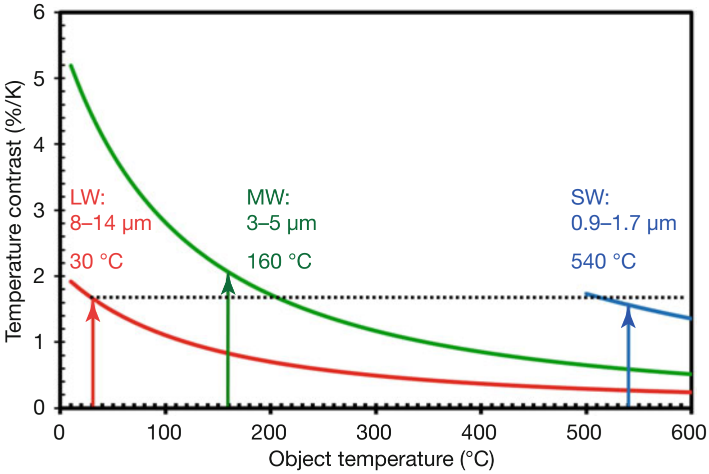

Figure 2.48 Temperature contrast according to Eq. (2.44) for LW, SW, and MW bands as function of object temperature.

According to Eq. (2.3a) the NETD of a measurement is inversely proportional to the in-band radiance change with temperature. Therefore, the NETD is governed by the temperature contrast discussed in Section 2.3.3.2.

Figure 2.48 depicts the temperature contrast of the in-band radiance in the LW, MW, and SW bands as a function of object temperature. Compared to the NETD for the LW measurement at 30 °C object temperature, the MW measurement at a 160 °C object temperature has a slightly greater temperature contrast, that is, a slightly lower NETD (about 0.9 of the NETD of the LW camera). Similarly, a SW measurement at an object temperature of 540 °C will have a slightly higher NETD (about 1.02) compared to the LW measurement at a 30 °C object temperature.

Overall one can conclude that NETD values are comparable. The conclusion drawn so far is that, given detectors of comparable sensitivity in different wavebands, the achievable temperature errors would also be comparable provided measurements are made at correspondingly higher temperatures.

Modifications of Bolometer Detectors for Use in MW Cameras

Bolometer detectors so far are mostly used and therefore also optimized for the LW band. Owing to the thin bolometer membranes, IR absorption is low. Therefore (Figure 2.4), a quarter-wavelength cavity is used to increase IR absorption. For example, a 2.5 μm cavity is used for optimized absorption at a 10 μm wavelength. Figure 2.49 compares some measured and theoretical bolometer response spectra.

Obviously, a bolometer has broadband sensitivity from around 2 μm well beyond 16 μm. Typically the MW detection is suppressed in LW bolometer cameras by adding a cut-on spectral filter (at a wavelength of about 7.5 μm) to the detector window. Without such a filter, the MW response for such bolometer structures is

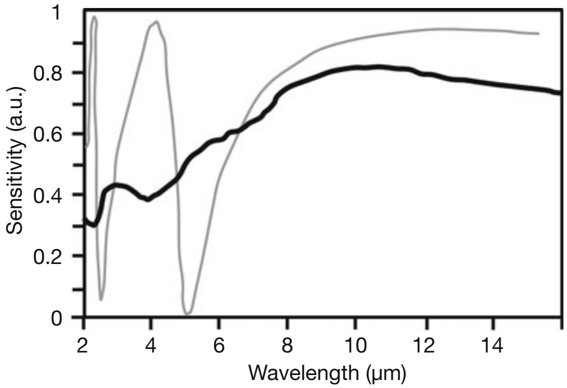

Figure 2.49 Typical theoretical (thin gray line) and measured (thick black line) spectral sensitivity of a LW bolometer with 2.5 μm cavity (after [46]).

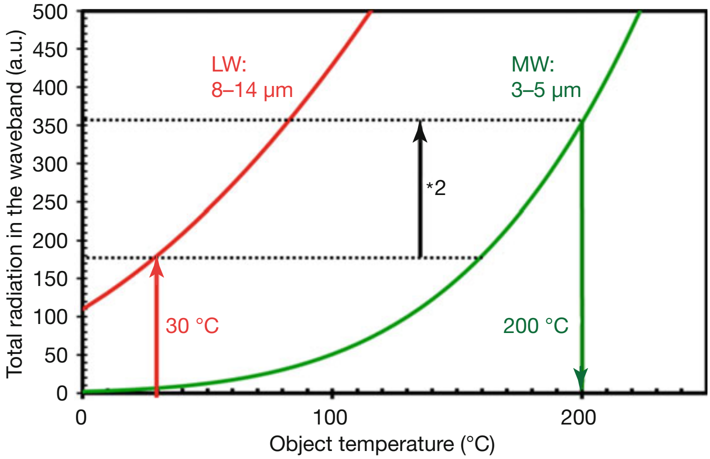

Figure 2.50 Object-temperature-dependent total in-band radiance in LW and MW bands. An object of 200 °C detected in MW has about the same detector signal as a 30 °C object detected in the LW band.

about 50% of the LW response. Therefore, MW bolometer detectors could just be implemented–without any change in detector technology–by replacing the cut-on filter with a MW bandpass filter.

The reduction of sensitivity by a factor of two, however, means that we need twice the in-band radiance in the MW band as in the LW. Therefore, the preceding estimates need to be changed slightly (Figure 2.50). To achieve the same signal owing to the doubled in-band radiance we now have the same signal in the MW band for $T_{\text{object}} = 200\,°\text{C}$. The temperature contrast will again lead to a very similar NETD.

Obviously, this example shows that it is quite possible to use bolometer cameras within the shorter MW waveband for higher object temperatures typical for many industrial temperature measurement applications without any change in bolometer technology.

Fast Bolometers with Smaller Time Constants

Bolometers also make it possible to reduce time constants, thereby allowing for faster temperature measurements. Although such modified bolometers would still be much slower than photon detectors, they may find an industrial application niche, too.

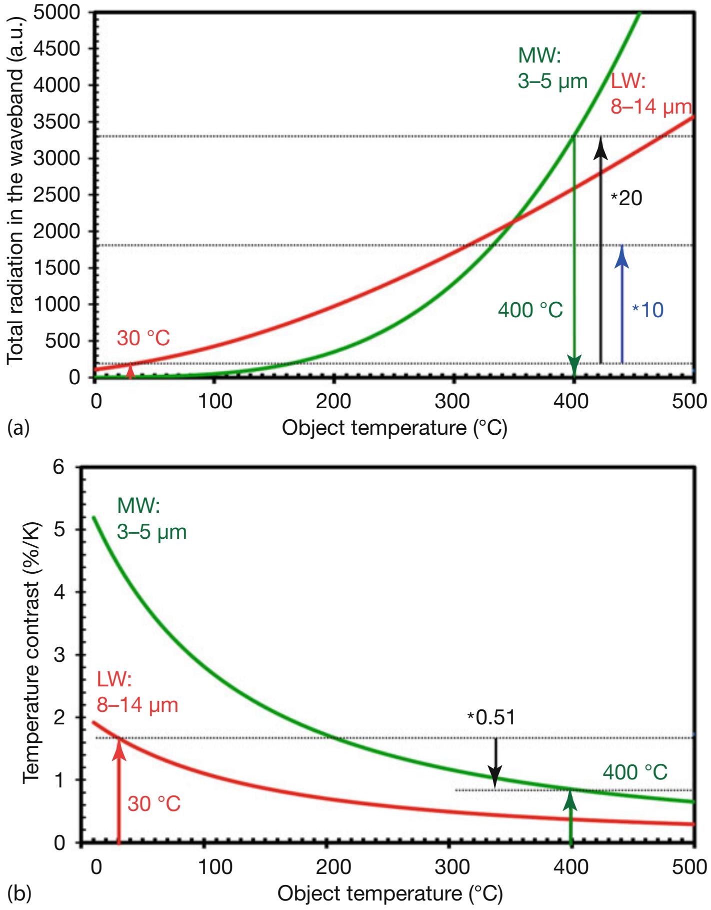

Figure 2.51 Object-temperature-dependent total in-band radiance in LW and MW bands. (a) An object of 400 °C detected in MW with 1 ms time constant bolometer has about the same detector signal as a 30 °C object detected in LW band. (b) Temperature contrast according to Eq. (2.44) for LW and MW bands as a function of object temperature.

Vacuum-operated bolometer arrays in LW cameras are quite slow and are characterized by time constants of about 10 ms (Section 2.2.3). A change in the time constant can be brought about by an increase in the detector heat conductance (Eq. (2.7)), for example by a gas filling. This will decrease the time constant; however, it will also decrease the bolometer responsivity by the same factor. A 10 times higher conductance will result in a 10 times lower time constant (1 ms). However, the incident object radiance must also be increased by a factor of 10 to get the same detector signal as for a vacuum-operated bolometer (Eq. (2.6)).

Let us estimate how such a fast 1 ms time constant bolometer may be used in the MW band. Its in-band radiance must be a factor of 10 larger due to the reduced time constant and – as previously – another factor of 2 larger due to reduced sensitivity in the MW band. Figure 2.51 illustrates that, compared to a LW band detected object of 30 °C, we have a similar signal for a MW band detected object of 400 °C.

However, the temperature contrast at this temperature is smaller by a factor of two (Figure 2.51b), that is, the NETD will be larger by the same factor. But this somewhat reduced thermal response should still be good enough for most industrial high-temperature applications. One just does not need to have a NETD well below 1 K when dealing with temperatures above 400 or 500 °C.

Research on the use of bolometers for other wavebands has already started. For example, it was recently demonstrated that bolometer detector sensitivity can be fine-tuned to the desired MW band [35].

Figure 2.52 depicts the comparison between the spectral absorption of a standard LW bolometer structure (broken line) to a bolometer structure optimized for both LW and MW band use.

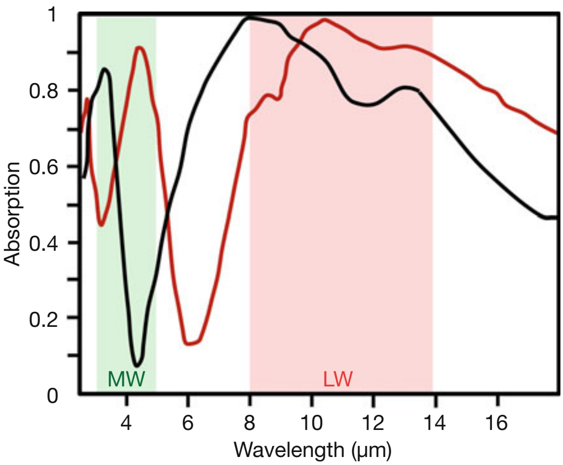

Figure 2.52 Comparison of absorption spectra of LW standard bolometer detector (black) and bolometer detector with increased MW absorption (red) after [35].

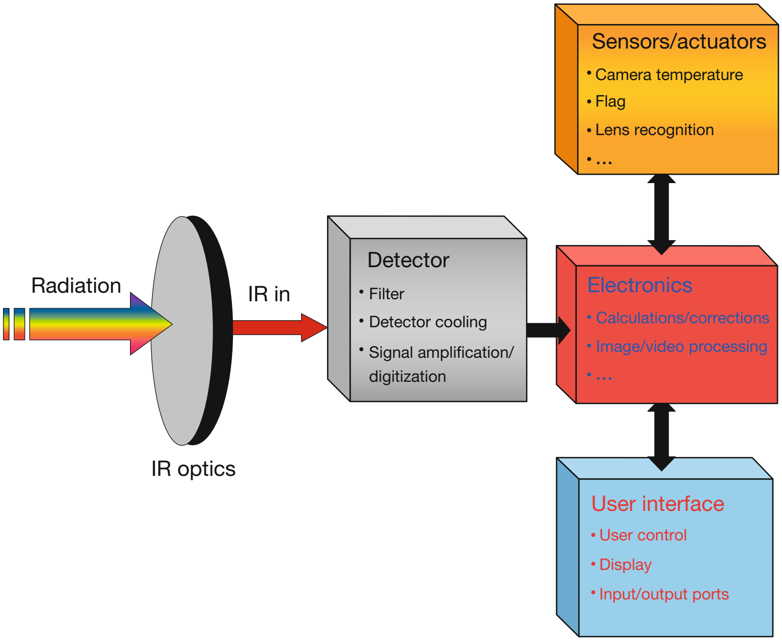

Figure 2.53 Block diagram with main IR camera components.

2.4
Complete Camera Systems

The main purpose of an IR camera is to convert IR radiation into a false color (including gray scale) visual image. This visual image should represent the two-dimensional distribution of the IR radiation emitted by an object or a scene. For a temperature-measuring system, the visual image displays the object temperatures. Therefore, the main components of an IR camera are the optics, the detector, the cooling or temperature stabilization of the detector, the electronics for signal and image processing, and the user interface with output ports, control ports, and the image display (Figure 2.53).

Complete understanding of the camera's operation requires a more detailed discussion of these main camera components and their interaction in the measurement process. The different IR camera systems (partly with additional accessories) used for most of the experiments described in this book are listed in Table 2.3. They range from the SW via the MW to the LW.

2.4.1
Camera Design – Image Formation

Two basic camera concepts for thermal imaging are scanning and staring systems (Figure 2.54). In scanning systems, the image is generated as a function of time row

Table 2.3 IR cameras used by authors.

SW	FLIR SC2600 InGaAs 0.9–1.7 μm 640 × 512 pixels		
MW	FLIR SC6000 InSb 1.5–5.5 μm 640 × 512 pixels	Agema THV 550 PtSi 3–5.5 μm 320 × 240 pixels	
LW	FLIR T650sc Bolometer 7.5–14 μm 640 × 480 pixels	FLIR A35sc Bolometer 7.5–14 μm 320 × 240 pixels	FLIR SC2000 Bolometer 7.5–14 μm 320 × 240 pixels

by row, like TV screens (Figure 2.54a); in staring systems, the image is projected simultaneously onto all pixels of the detector array (Figure 2.54b).

2.4.1.1 Scanning Systems

The heart of a scanning system consists mostly of a two-dimensional optical scanner with a single-element IR detector. Some systems also use a linear detector array or more complex detectors [47, 48]. In all cases, the image is built up sequentially. The detector's instantaneous field of view (IFOV) is moved across the FOV of the camera (Figure 2.54). A rotating mirror for horizontal scan allows for radi-

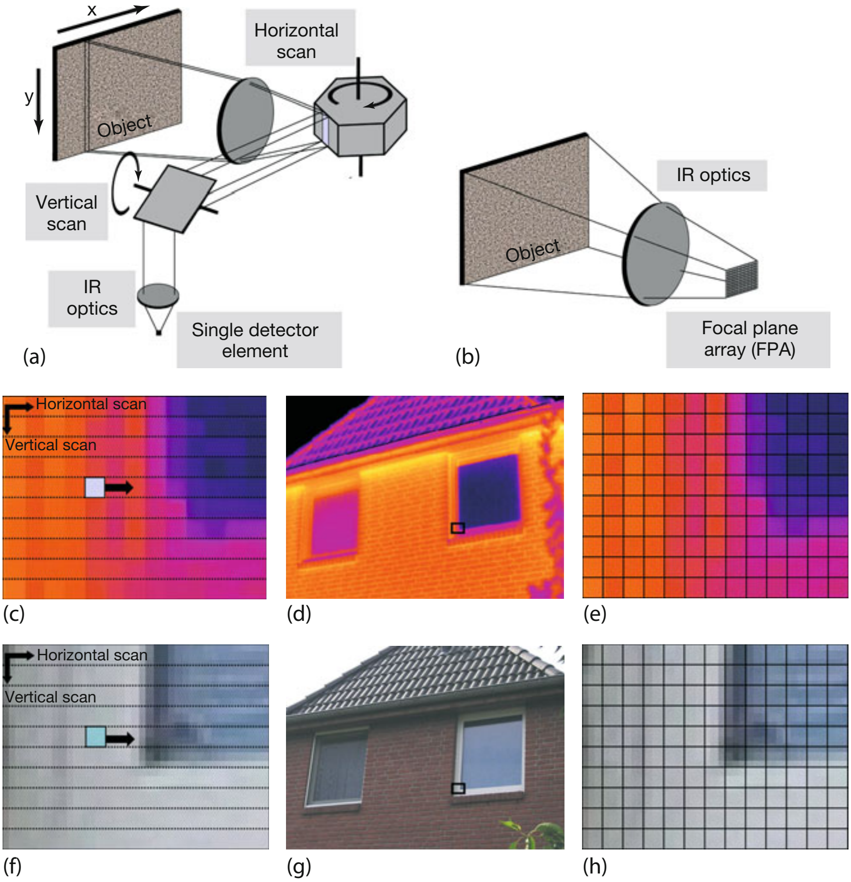

Figure 2.54 Basic principles of image formation for scanning (a) and FPA cameras (b). VIS image of a house (g) recorded with 2987 × 2177 pixels. The small black rectangle is shown enlarged at the sides (f,h). The left-hand-side image illustrates line-after-line scanning, whereas the right-hand-side image refers to the pixel grid of a FPA. (c–e) IR image of a LW camera (320 × 240 pixels) and scan (c) as well as FPA mode (e) of image formation.

ation measurement along a horizontal line of the scene. Mostly a polygon-shaped mirror is used to reach a very high scanning efficiency [47]. A second mirror is used to switch the vertical position of the scanned line. For short image formation times at satisfactory pixel numbers, fast photon detectors and short signal integration times are needed. The following simplified estimate will show the limitations of a scanning imaging system. A scanning camera, such as AGEMA ThermoVision 900 [41] with a single detector element at an image size of 272 × 136 pixels (136 lines and 272 pixels in one line) offers a full frame rate of 15 Hz. In a simplified version, the sequential readout process results in a time frame for one pixel of 1.8 μs. In line scan mode at 272 pixels per line, a line frequency of 2500 Hz (or lines per second) is achieved corresponding to a time frame per pixel of 1.5 μs.

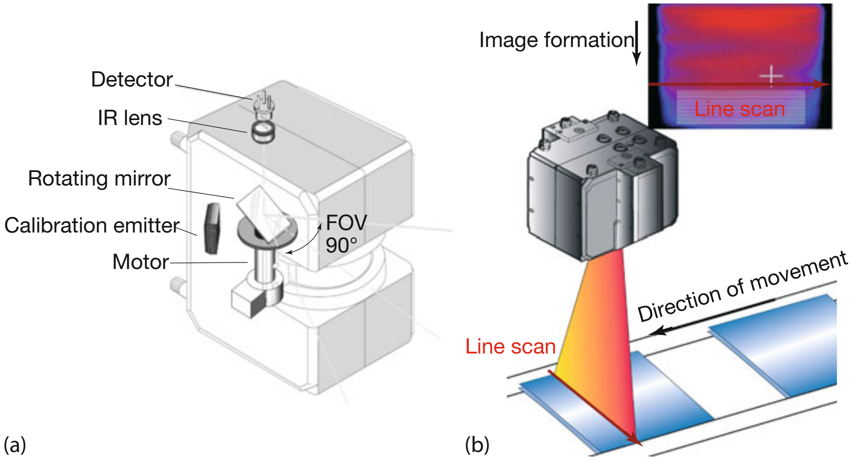

Figure 2.55 (a) Operational principle of a line scanner MP 150 [50] and (b) image formation at a band process. Image courtesy Fluke Process Instruments GmbH, Germany.

Assuming that the scanning system can also deal with larger pixel numbers, one can estimate that the line frequency and the frame rate would decrease for 320 × 240 pixels to about 2100 lines per second or a 7.2 Hz full-frame rate and for 640 × 480 pixels to 1050 lines per second or a 1.8 Hz full-frame rate.

In principle, faster frame rates seem possible by reducing the time frame for one pixel. However, it would not make sense to reduce this time interval since the object signal would decrease and, hence, the SNR would decrease.

Because of the continual improvements in focal-plane detector technology and the limited number of pixels and limited frame rates, the scanning systems for thermal imaging became less important. Nevertheless, scanning systems offer some advantages over staring systems, for example, the radiometric accuracy caused by the fact that radiation from all image pixels is detected by only one detector element.

Today, IR line scanners are used for the thermal imaging of moving objects or scenes such as band processes (Figure 2.55). For the imaging, only the line scan mode is necessary. The second dimension of the thermal image is built up by the object or scene movement. Line scanners allow very high scan rates, up to 2500–3000 lines per second (for lower pixel numbers), variable pixel numbers in a measured line up to about 5000 (for lower scan rates), and a large FOV up to 140° [49–51]. Such line scanners often use one or two (at different temperatures) internal IR emitters with known emissivities and temperature for recalibration during each mirror revolution. For this purpose, the emitters are positioned outside the object FOV and the recalibration process is made between line scans (Figure 2.55).

2.4.1.2 Staring Systems–Focal-Plane Arrays

In FPAs, the detectors are arranged in a matrix of columns and rows. Compared to scanning systems, FPAs allow higher frame rates at higher pixel numbers. The main advantage of a staring system, in addition to the absence of moving mechan-

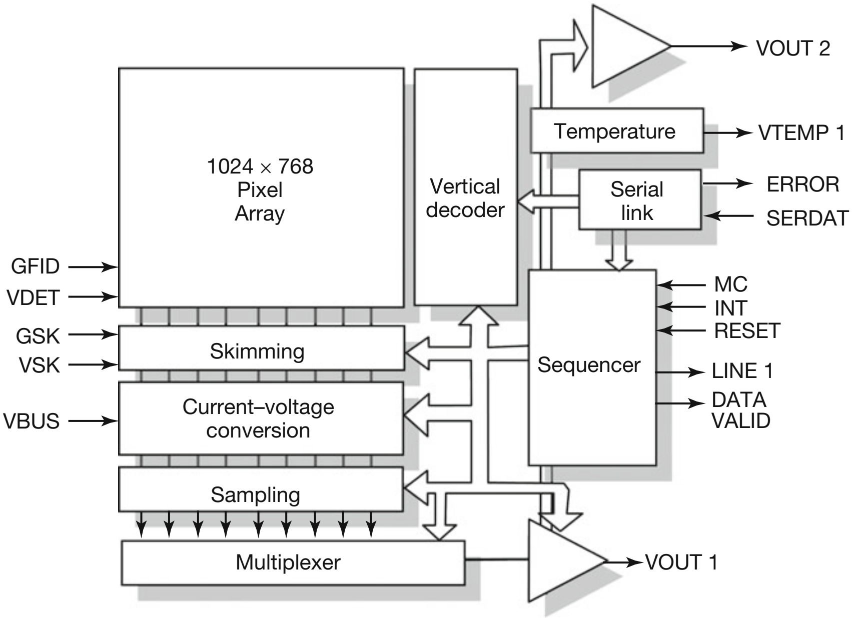

Figure 2.56 ROIC for a 1024 × 768 pixels bolometer array. Image courtesy: ULIS, France.

ical parts and the possibility of using thermal IR detectors, is that the detector array covers the whole FOV simultaneously for the entire frame time [3]. This causes a reduced bandwidth for each detector, resulting in a SNR improvement. Theoretically the SNR is increased by the square root of the image pixel format. Practically this gain cannot be obtained because the FPA consists of individual detector elements, causing a spatial or fixed pattern noise due to their nonuniform properties [52].

An FPA for IR imaging itself consists of two parts: an IR sensor made from an IR radiation-sensitive material and a ROIC made from silicon. Nowadays, ROICs have two functions (Figure 2.56). First, they produce the simple signal readout and, second, they contribute to signal processing with signal amplification and integration or with multiplexing and analog-to-digital conversion.

One of the most important problems in technology results from the fact that, in contrast to FPAs for the visible spectral range, two different material classes must be electrically integrated. This can be done by either monolithic or hybrid integration technology. For a hybrid system, both parts are made separately. Later they will be mechanically and electrically joined by special mounting processes such as flip-chip bonding [53]. For monolithic arrays, first the ROIC is made from silicon. After this process, the IR sensors are built up on top of the ROIC by IR material thin film deposition, lithography, and etching. This is a very complex process because all technological processes and materials used for the fabrication of the IR sensor matrix must be compatible with the CMOS process used for the fabrication of the ROIC and must not change the ROIC properties. Because of lower fabrication costs, higher performance, durability, and reliability, there is a trend toward monolithic integration as, for example, for microbolometer FPAs [54]. Improvements in FPA technology have led to the following trends:

- The number of pixels in arrays is increasing. FPA cameras with up to 1024 × 1024 pixels are commercially available [41]. Figure 2.57 illustrates the different array sizes for a VIS 1 megapixel image. Figure 2.58 depicts IR images of the same object scene for different pixel numbers.
- The pixel size is decreasing. Today, FPAs with $17 \times 17\,\mu m^2$ microbolometer [55] pixels or $15 \times 15\,\mu m^2$ photon detector pixels are available. The decreasing array size reduces the cost of the optics by reducing the size at a given F-number. At a given F-number, the cost for lens material will depend approximately on the square of the lens diameter.
- The NETD is decreasing. This requires a strong improvement in detector performance (D^*) to overcompensate for the effect that a simple decrease in de-

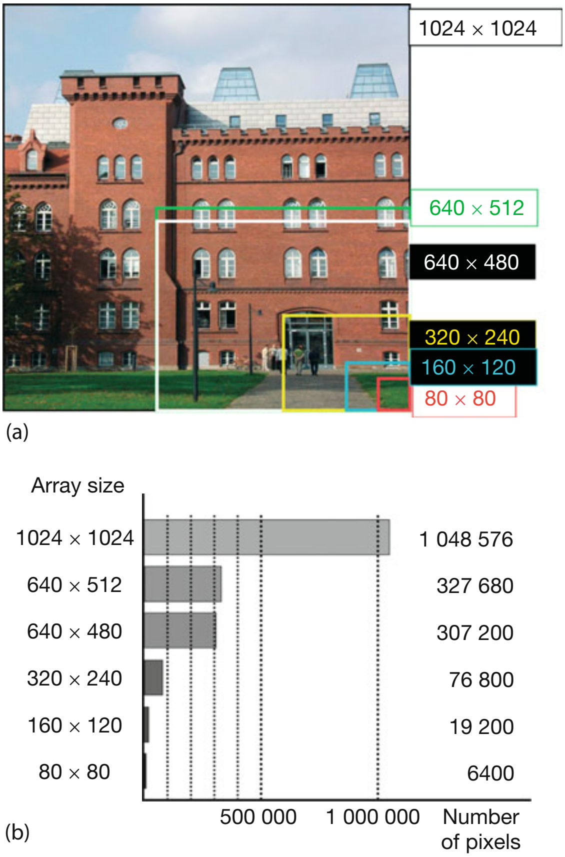

Figure 2.57 Illustration of displayed image sections for different array sizes with the same optics (a) and with detectors at the same distance. Comparison of total pixel numbers for different array sizes (b).

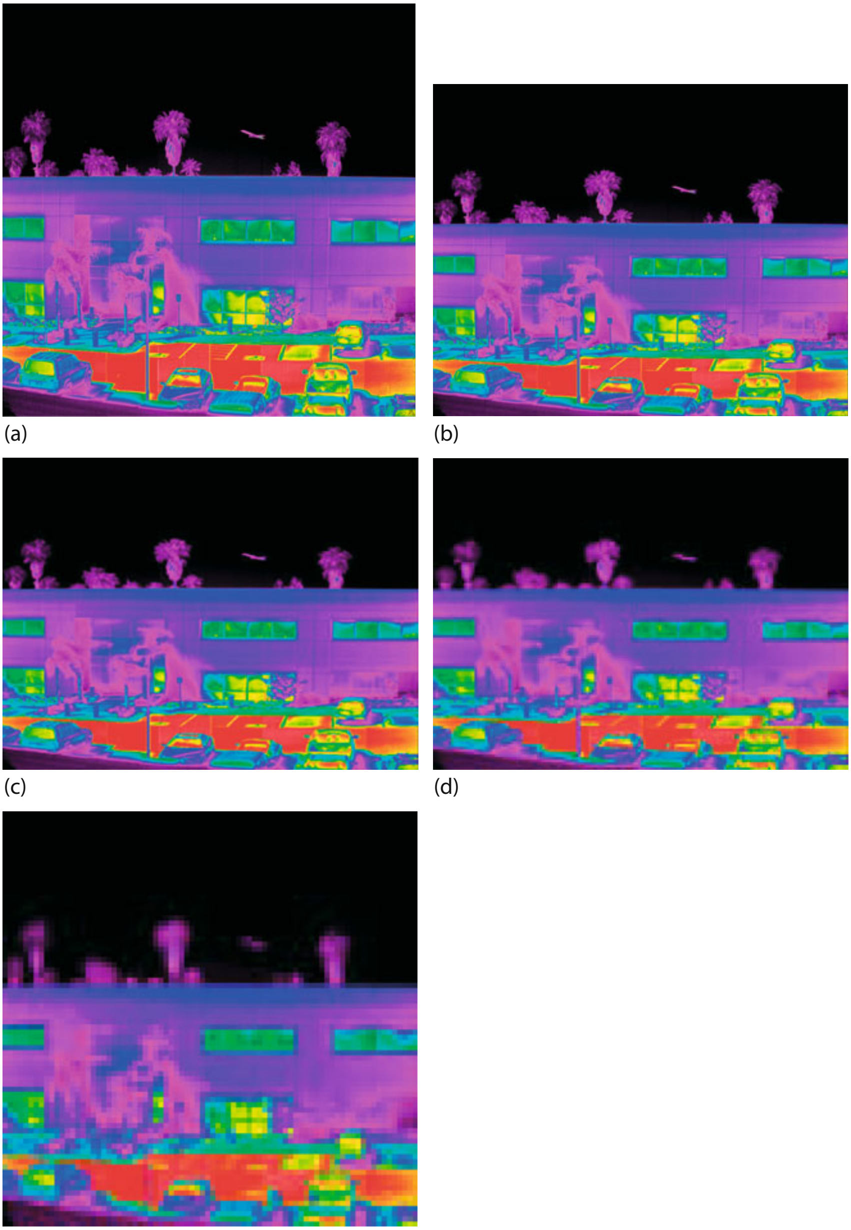

(a) (b) (c) (d) (e)

Figure 2.58 IR images with different pixel numbers generated from the same megapixel image. (a) 1024 × 1024 pixels; (b) 640 × 512 pixels; (c) 320 × 240 pixels; (d) 160 × 120 pixels; and (e) 80 × 80 pixels. Image courtesy: FLIR Systems Inc.

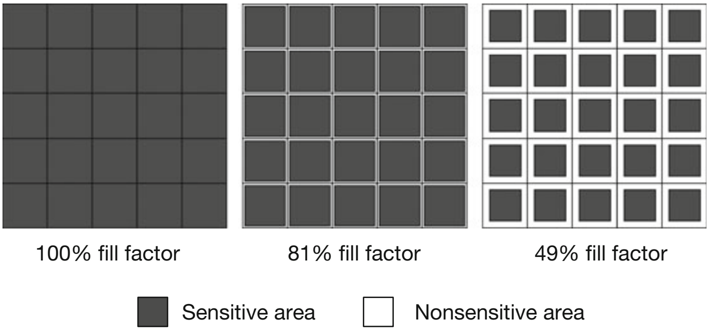

Figure 2.59 Fill factor of a FPA.

tector size will result in an increase in the NETD. Today IR cameras achieve NETDs of about 45 mK for microbolometer detectors and about 10 mK for photon detectors at a 30 °C object temperature.

- The trend toward decreasing pixel size is accompanied by an increasing fill factor. The *fill factor* is defined as the ratio between the IR-sensitive cell area and the whole cell area of a FPA (Figure 2.59). It is not possible to arrange the detectors to be fully contiguous in a FPA. Single-detector elements must be electrically and thermally (for microbolometer arrays) separated from each other and be connected to the ROIC. Therefore, the IR-sensitive area remains smaller than the cell area. This finite fill factor influences the camera performance such as, for example, the spatial resolution and MTF (Section 2.5.3). Today, microbolometer FPAs achieve a fill factor larger than 80% and photon detector FPAs achieve ones larger than 90%. Figure 2.59 illustrates the increase of the fill factor. If a typical quadratic cell is assumed, a fill factor of 49% requires that the side length of the sensitive cell must account for 70% of the whole cell side length. If the fill factor is increased to 81%, this side-length ratio must be increased to 90%.
- The time constant for microbolometers has decreased to about 4 ms [55]. This makes it possible to increase the time resolution of the camera and to use higher frame rates. As discussed in Section 2.2.3, the thermal properties of the bolometer structure influence the time constant. In a complex manner, they affect all detector performance parameters. Therefore, the decrease in the bolometer time constant, while simultaneously decreasing the detector area and NETD, results in a very complex problem. Overall, these trends result in an increase in image spatial and thermal resolution, image information content, and time resolution of the imaging process.

2.4.1.3 **Nonuniformity Correction**

Before IR detectors can be used for quantitatively measuring temperatures, two important image-processing procedures must be performed. First, the differing gains and possible signal offsets of different individual detectors must be accounted for. Second, an absolute temperature calibration (Section 2.4.5) is re-

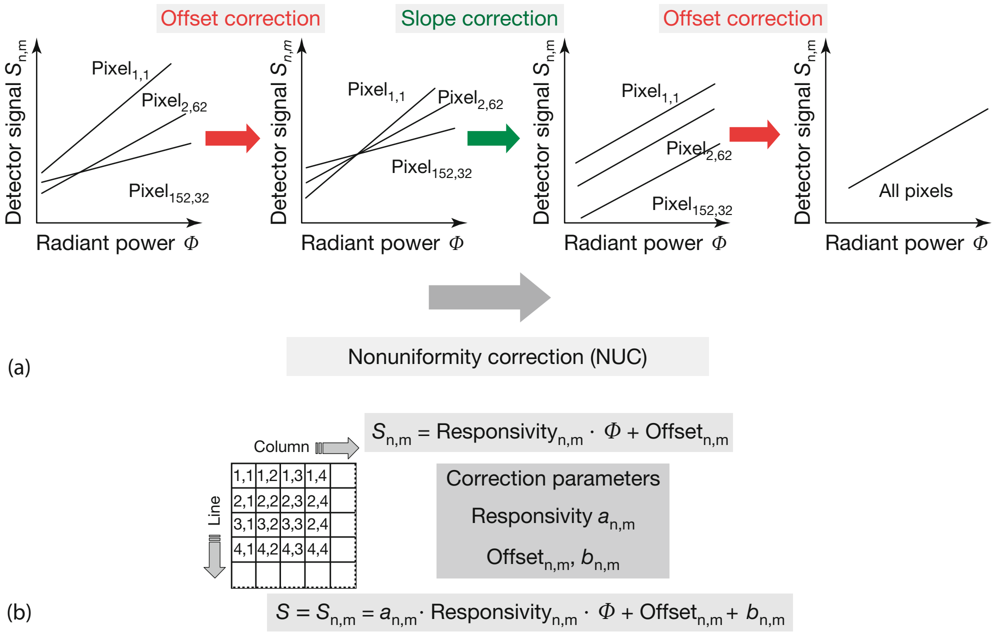

Figure 2.60 (a) Detector nonuniformity in a FPA and the nonuniformity correction to normalize the different FPA detector responsivities and offsets shown for three selected pixels. (b) Mathematical model of NUC corrections.

quired for quantitative analysis. Both procedures are interrelated, although in principle they can be distinguished from each other.

As mentioned earlier, FPAs are composed of many individual detector elements having different signal responsivities (gain or slope) and signal offsets. The same applies to scanning systems with detector lines. Figure 2.60a depicts this situation for some detector elements.

The spread in gain and offset results in a spread of detector signals of different pixels for the same incident radiant power. If this nonuniformity of the individual detectors becomes too large, the image becomes unrecognizable. Therefore, for all imaging systems consisting of more than one detector, the nonuniformity must be corrected [56] (Figure 2.60). This is called *nonuniformity correction* (NUC).

For most commercial cameras, the NUC procedure is performed during the factory camera calibration process, and the correction parameters are stored in the camera firmware. Only some R&D cameras allow users to perform the calibration procedure and NUCs.

The correction procedure (Figure 2.60a) starts mostly with a signal offset correction to bring the response of each detector for a given object temperature range within the dynamic range of the electronics. In the second step, the signal slope (detector signal dependence on the object temperature) is corrected. After this second step, all detectors should have the same signal slope and their response

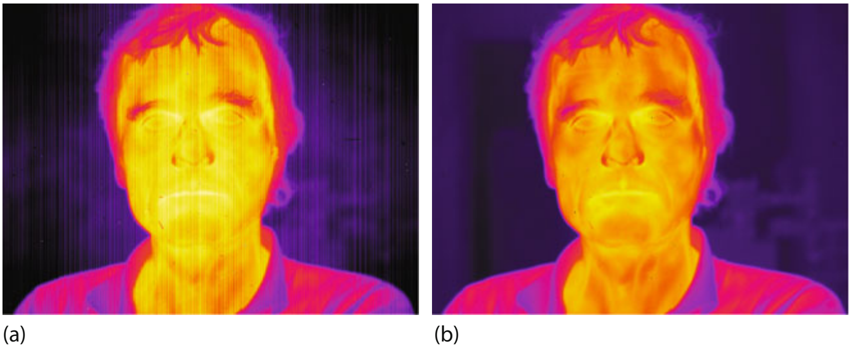
(a) (b)

Figure 2.61 IR images of the same scene before (a) and after (b) NUC.

should be within the dynamic range of the electronics. Finally, an additional offset correction is necessary to get identical response curves for the different detector elements.

In practice, the NUC is performed by placing a rough (nonreflecting) gray body ($\varepsilon > 0.9$) of homogeneous temperature directly in front of the detector or camera lens. As a consequence, each pixel should yield the same signal. The deviations are corrected electronically. If this procedure is done for a single temperature (one-point NUC), the correction works only close to the used temperature. Usually two different temperatures are used (two-point NUC), which gives a reasonable correction between and in the vicinity of the chosen temperatures. As a result, a detector array will yield a very uniform signal. Figure 2.61 depicts two IR images of the same scene, the only difference being that before the second was recorded, a NUC was performed. The improvement in image quality via noise reduction is obvious.

However, perfect detector uniformity in between the calibration points cannot be achieved because of the possible slightly different nonlinear responsivity curves. This situation for a correction at two calibration points is illustrated in Figure 2.62. The remaining detector nonuniformity causes the so-called fixed pattern noise.

The NUC procedure forces the detector pixels to a uniform signal due to the uniform input of a homogeneous object. In principle, it is, however, also possible to perform NUCs based on arbitrary objects. Figure 2.63a depicts the IR image of a person; it was recorded immediately after using a homogeneous background for a NUC. Figure 2.63b depicts the IR image of the person recorded immediately after using the same scene for a NUC. The large radiance differences between background and object (person) were corrected to vanish via the NUC; therefore, the person is (nearly) invisible. In Figure 2.63c, the person has left and the camera only observes a homogeneously tempered background. Still, the camera now detects a feature where the person was standing, although the radiance of the wall is the same everywhere. Figure 2.63 thus illustrates that electronic correction of

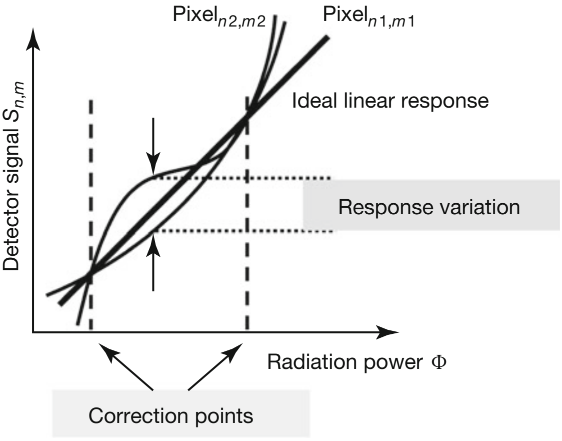

Figure 2.62 Two-point NUC as detectors deviate from linearity in their responsivity. The remaining response variation between the correction points due to the deviation from linearity is responsible for the fixed pattern noise. Deviations from linearity are strongly exaggerated to illustrate the effect.

detector gain and offset can change apparent radiance distributions appreciably. Therefore, NUCs must be performed with great care.

In principle, a NUC only requires that objects of homogeneous temperature be placed in front of the camera. The exact value of the temperature need not be known to obtain an IR image with low noise level. If, however, a quantitative analysis is needed, a temperature calibration must be performed. This is done by detecting objects of known fixed temperatures–usually stabilized blackbody scenes–with the camera for a number of different object temperatures. These temperature-versus-signal-calibration curves are also stored in the firmware.

The quality of the NUC and the corresponding correctness of measured object temperatures rely on the stability of the detector operation. Thermal drifts will change the detector response curve of the pixels and a new NUC must be performed. This means that to ensure a proper correction, FPA cameras must be recalibrated periodically. For a correction during camera operation, mostly a tempered flag or autoshutter is used for a single point offset NUC. If this autoshutter operation is switched off, the periodic camera recalibration NUC will be disrupted. The missing internal correction will lead to a drift in the indicated temperature. Figure 2.64 depicts the situation for a LW thermal detector (bolometer) camera and a MW photon detector (PtSi) camera. For a period of about 2 h, the temperature of a 70 °C blackbody emitter (temperature-stabilized calibration source) was simultaneously measured with both cameras. The average temperature within the marked area was analyzed. At $t = 0$, the autoshutter operation of the cameras was switched off. The bolometer-equipped LW camera shows a much stronger drift behavior of the indicated temperature (about 3 K) than the photon-detector-equipped MW camera (less than 0.5 K).

The physical reason for the drift follows from the discussion in Section 2.2.3. The bolometer detector signal is generated by the net radiation power transferred to the detector, which is given by the difference between the radiation power received from the object and the radiation power emitted by the detector itself. In addition, the thermal detector exchanges radiation with, for example, the camera housing and the optics. Therefore, a small change in the temperature balance inside the camera will also change the transferred net radiation power and cause measurement errors.

In contrast, in photon detectors the signal is generated from the incident radiation alone. A temperature change in the camera will also cause a change in the detector signal, but the deviations are much smaller than for the bolometer. Moreover, bolometer responsivity strongly depends on the detector temperature owing to the high temperature coefficient (Section 2.2.3). Small temperature changes in the bolometer will cause strong signal changes, that is, wrong temperature measurements if automatic periodic recalibration is turned off. Based on a quantitative estimate (Section 2.2.3), the error of the indicated temperature at the end of a long-term measurement of about 3 K after 2 h corresponds to a temperature change of about 100 mK in the bolometer. This example demonstrates the importance of a proper autoshutter operation for correct temperature calibration, especially in bolometer FPA cameras.

Finally, it should be stressed that the detector signal is linear only in a certain output range, for example, from 20 to 80% of the detector saturation signal. The

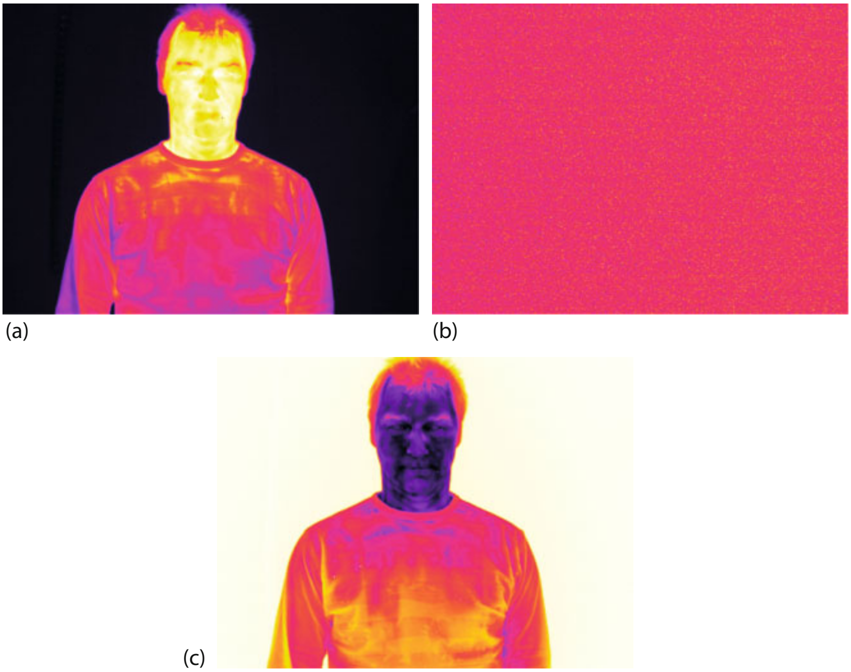

Figure 2.63 IR images of a person (a) after NUC using a homogeneous background, (b) after NUC using the scene shown in (a) image, (c) observing homogeneous background after the person has left with the NUC of the (b) image.

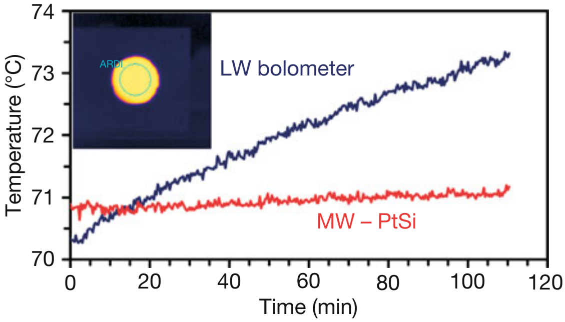

Figure 2.64 Results of a long-term temperature measurement at a stabilized 70 °C blackbody emitter with switched-off operation of camera autoshutter.

NUC works well only within these limits. For very low signals as well as close to saturation, an increased fixed pattern noise level will show up, that is, the NUC will no longer work. Figure 2.65 presents an example of an object (light bulb)

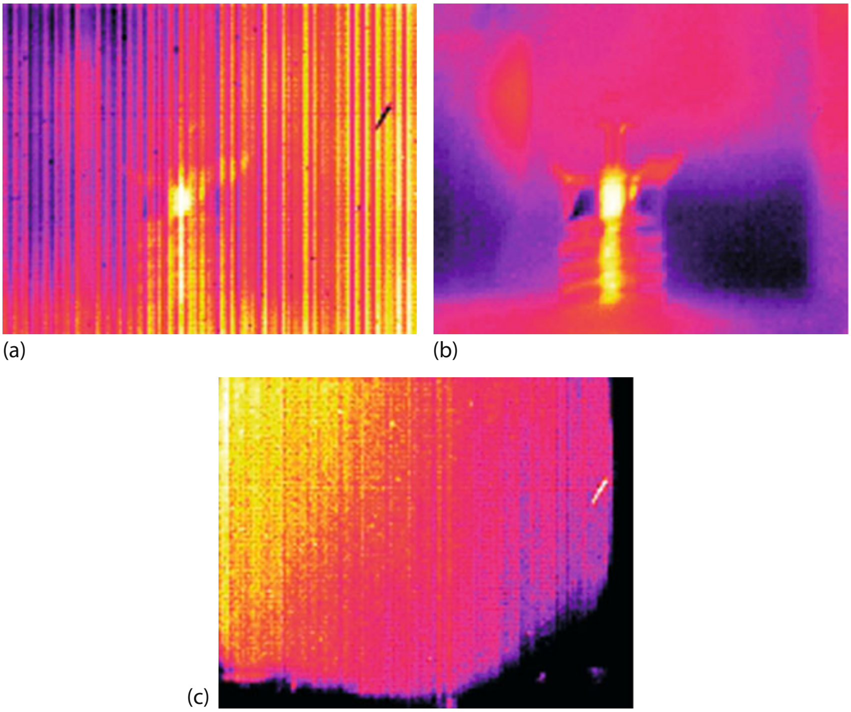

Figure 2.65 Illustration of NUC limitations due to detector signal saturation at high radiance levels. (a) Image of a cold light bulb without NUC, (b) image of the light bulb at room temperature after NUC with homogeneous room temperature background, and (c) image immediately after bulb explosion due to high-voltage pulse application (extremely high temperatures cause detector signals close to saturation level).

recorded before a NUC (a), after the NUC (b), and after the NUC but with saturated signals (c).

2.4.1.4 Bad Pixel Correction

An ideal detector array consists of 100% perfect detectors, which–after performing a NUC–will all give the same output signal when receiving the same radiant power. Unfortunately, however, while manufacturing large detector arrays, yields are less than 100%. This means that there are so-called bad pixels consisting either of really nonfunctionary detectors or of detectors whose gain and offset are too far off the average that they cannot be corrected for by a NUC. Very good manufacturers state that their detector arrays are only allowed less than 0.01% of bad pixels. For example, a 640 × 512 pixel camera would only be allowed to have at maximum 32 bad pixels in the whole array of 327 680 pixels. Probably all commercial cameras have bad pixels. They are usually corrected electronically by replacing the signal of the bad pixel by the weighted average of its neighbor pixels. Problems arise only if bad pixels form clusters. In this case, the corresponding array location is not suitable for accurate temperature measurements of very small objects.

2.4.2
Photon Detector versus Bolometer Cameras

Today, the majority of IR cameras are equipped with microbolometer FPAs. These thermal imagers meet the demands of most practical applications and are much less expensive than photon detector FPA cameras. Microbolometers are characterized by relatively low sensitivities/detectivities, broad/flat spectral response curves, and slow response times on the order of 10 ms. Microbolometer FPAs are mostly temperature stabilized by a Peltier element. Because of their operation as thermal detectors, bolometers do not offer the possibility of fixing the integration time (Figure 2.66). Rather, the integration time is given by the thermal time constant of the bolometer detectors. The frame rate of these cameras cannot be changed by the user. The image formation of microbolometer FPA cameras is characterized by a sequential readout of the detector lines within the full frame time, also called a *rolling readout*.

For more demanding applications requiring higher sensitivities or time resolutions such as in R&D, photon detector FPA cameras are used. For the MW and LW spectral regions, the FPA is cooled to liquid nitrogen temperature, $T = 77$ K. For the SW region, the detectors are cooled by multistage Peltier elements. Photon detector FPAs exhibit a much larger responsivity/detectivity and a spectral response varying with wavelengths (Figure 2.1). Photodiode arrays offer time constants down to about 1 μs. Therefore, photon detector cameras offer smaller NETD values and higher frame rates than microbolometer cameras.

The direct conversion of the photon flux into an electrical signal (photocurrent) and the small time constants allow a snapshot operation of photon detector FPA cameras. The photocurrent of each pixel charges a capacitor during a user-

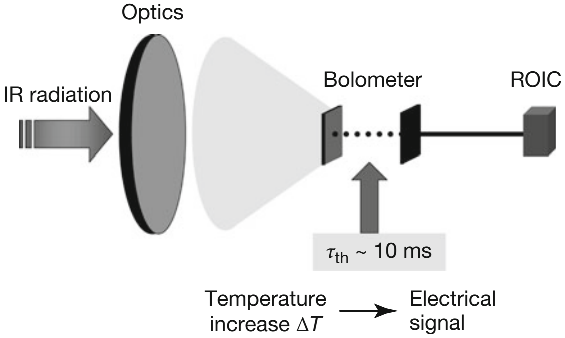

Figure 2.66 Signal generation process and signal readout in a bolometer camera (dotted line illustrates the time delay of bolometer temperature increase with τ_{th}).

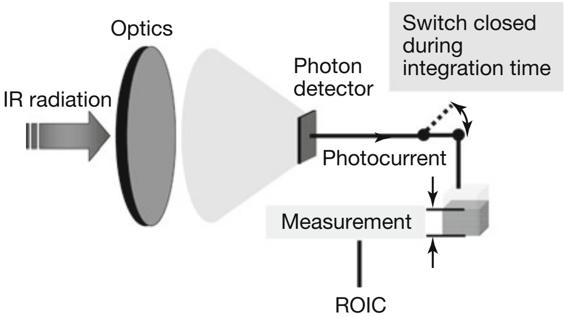

Figure 2.67 Signal generation process and signal readout in a photon detector camera.

selected integration time (several microseconds to full frame time) (Figure 2.67). The readout by the ROIC is mostly possible in integrate-while-read or integrate-then-read mode. Because of the fast direct signal generation by the photon detectors and the readout process, the camera measurement can be triggered.

The maximum achievable frame rate is limited by the speed of data transfer and storage. If we assume a detector with a time constant much below 1 μs and a full frame integration time of 1 μs, a frame rate of 1 MHz is theoretically possible. For the readout, mostly a dynamic range of 14 bits is used. This would result in a data rate of 14 Mbit/s per pixel. If the array size increases to a common size of 320 × 240 pixels (76 800 pixels), such a high frame rate would require a data rate of about 1 Tbit/s. Today, the practical limit of the maximum data rate given by readout electronics is significantly below this value. For example, the FLIR SC8000 MW camera, equipped with an InSb FPA of 1024 × 1024 pixels, allows a maximum full frame rate of 132 frames/s using a 16-channel readout [41]. This results in a practical overall data rate of about 2 Gbit/s. For higher frame rates, the windowed readout mode is used. This mode mostly allows a user-selected random size and location FPA windowing. The decreased pixel number allows for a faster frame rate. For example, the SC8000 at 160 × 120 pixels achieves 909 frames/s. To

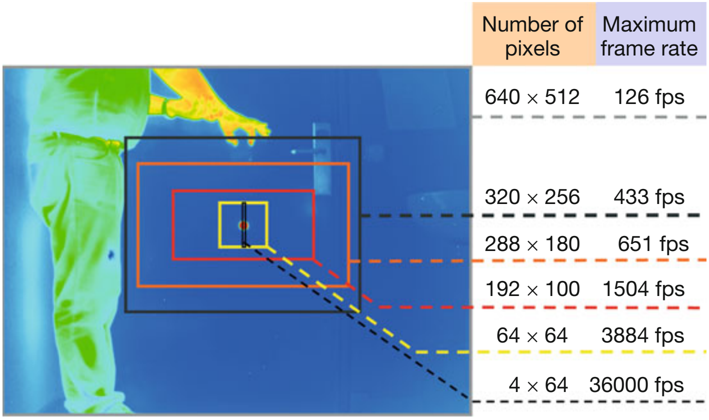

Figure 2.68 FPA window sizes of FLIR SC6000 and maximum frame rates (random and user-defined windowing possible). fps: frames/s.

capture high-speed events, the FLIR SC4000 and the SC6000 high-speed cameras offer maximum frame rates of 48 kHz (2 × 64 pixels) and 36 kHz (4 × 64 pixels), respectively [41]. Figure 2.68 depicts the FPA window size of a FLIR SC6000 camera relative to the maximum frame rates.

With respect to the characteristics given for photon detector FPAs, IR cameras with a PtSi FPA form an exception. This is due to the low quantum efficiency. As discussed in Section 2.2.5, the sensitivity of PtSi detectors is limited and large integration times are necessary to achieve sensitive detection. Therefore, cameras equipped with PtSi detectors commonly use a full frame time constant of 20 ms for signal integration.

2.4.3
Detector Temperature Stabilization and Detector Cooling

For optimum operation of IR detectors in thermal imaging systems, the detector temperature (thermal detectors) or detector cooling (photon detectors) must be stabilized.

For bolometer FPA and SW InGaAs FPA cameras, thermoelectric heaters/coolers are used. Thermoelectric cooling/heating uses the Peltier effect [57] to create a heat flux between the junctions of two different materials (Figure 2.69). A DC current is forced through the thermoelectric materials. During operation, heat is removed from one type of junction and creates the cold side of the element. At the other type of junction heat is generated, forming the hot side of the element. If the current direction is changed, the heat flux direction will also be changed. This causes a cooling of the former hot side and a heating of the former cool side of the Peltier element. The cooling efficiency depends on the materials used. The best performance is achieved using semiconductor materials. The Peltier coolers are arranged in one- to more than three-stage arrangements (Fig-

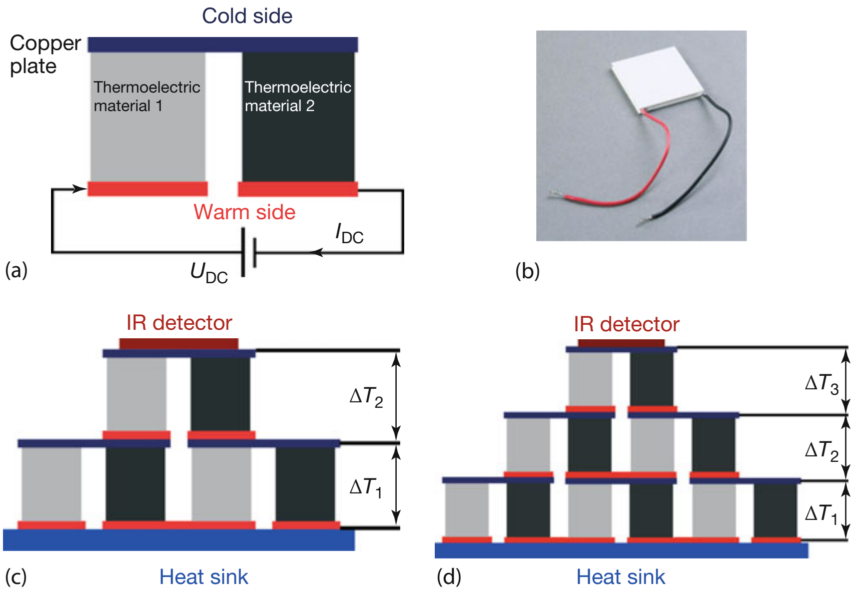

Figure 2.69 Operational principle of Peltier coolers (a), example of a Peltier cooler (b), two- and three-stage Peltier coolers (c and d).

ure 2.69). Peltier elements are used for both cooling InGaAs detector arrays in SW cameras and stabilizing the temperature of microbolometer arrays in LW cameras. Detectors in bolometer cameras are usually operated at temperatures of around 30 °C, which is mostly above ambient temperature. In principle, the temperature stabilization could also work by cooling the detector if ambient temperature exceeded the chosen detector temperature. Bolometer temperatures should be different from ambient temperatures so as to avoid a temperature change of the bolometer detector sensitivity with changing ambient temperature (camera temperature) (Section 2.2.3). A one-stage cooler offers maximum temperature differences of about 50–75 K between the hot and cold sides, which is sufficient for FPA temperature stabilization.

In contrast, photon detectors require increased cooling with increasing wavelength (Section 2.2.4.4). MW and LW photon detectors mostly operate at about 77 K.

Multistage Peltier coolers are used to increase the temperature difference. Unfortunately, the cooling efficiency decreases with decreasing temperature, which means that temperature differences decrease from stage to stage [57]. Therefore, the number of cooling stages is mostly limited to three. With a three-stage cooler, a maximum temperature difference of about $\Delta T = 120–140$ K can be reached, that is, $T = 150–170$ K. Therefore, the application of thermoelectric cooling for FPAs is restricted to the near-IR or SW spectral region.

In the early stage of IR camera technology for detector cooling in MW and LW cameras, liquid nitrogen at 77 K (−196 °C) was used. Later, an electrical solution to

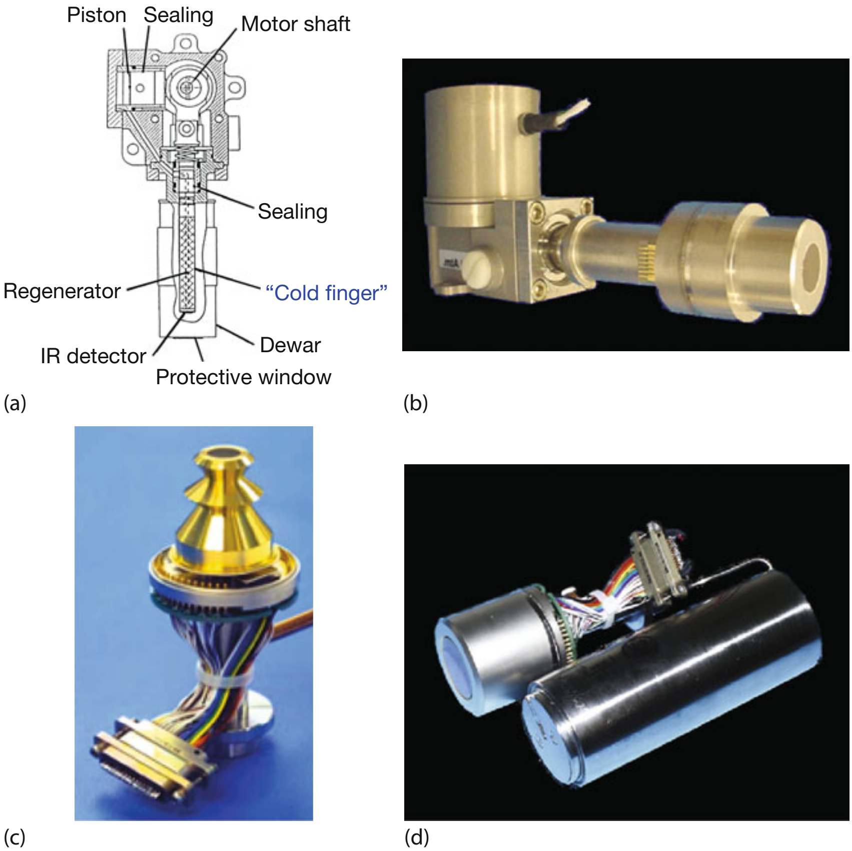

Figure 2.70 (a) Stirling cooler working with helium gas for IR detector cooling and (b–d) examples of cooled FPA assemblies. Image courtesy: Infrared Training Center, FLIR.

cryogenic cooling using the Stirling process [58] was developed (Figure 2.70). The Stirling process removes heat from a cold finger with the FPA by a thermodynamic cycle. This heat is dissipated at the warm side. The efficiency of the Stirling process is relatively low but meets the requirements of the necessary IR detector cooling owing to the low heat capacity and small heat losses. Stirling coolers allow detector temperatures of 77 K and below. The small cooler size and weight, electrical (e.g., electrical power consumption), and mechanical (e.g., mechanical vibrations) properties, reliability, and lifetime (more than 8000 h of operation guaranteed) of Stirling coolers led to their widespread use in thermal imaging systems.

2.4.4
Optics and Filters

2.4.4.1 Spectral Response

Most IR cameras are characterized by a broad spectral response. Figure 2.71 depicts the spectral response curves of a number of IR cameras, normalized to their maximum value.

2.4.4.2 Chromatic Aberrations

Broadband detection is mostly accompanied by considerable chromatic aberrations of the lenses, which cannot be corrected completely. These and other aberrations affect the object–image transformation by the optics and limit the important image quality parameters, for example, spatial resolution or MTF (Sections 2.5.3 and 2.5.4). Figure 2.72 depicts the aberration-induced blurring of an object field during the transformation into an image.

Ideal optical imaging means that the detector element receives radiation only from a well-shaped object field as depicted in Figure 2.72a. Aberrations will cause a spreading of the object radiance distribution, that is, a blurring effect: the radiation of the object field is also detected by the neighboring detector elements (Figure 2.72b). On the one hand, if this detector signal was the result of optical image generation owing to an ideal aberration-free lens, the blurring would be inter-

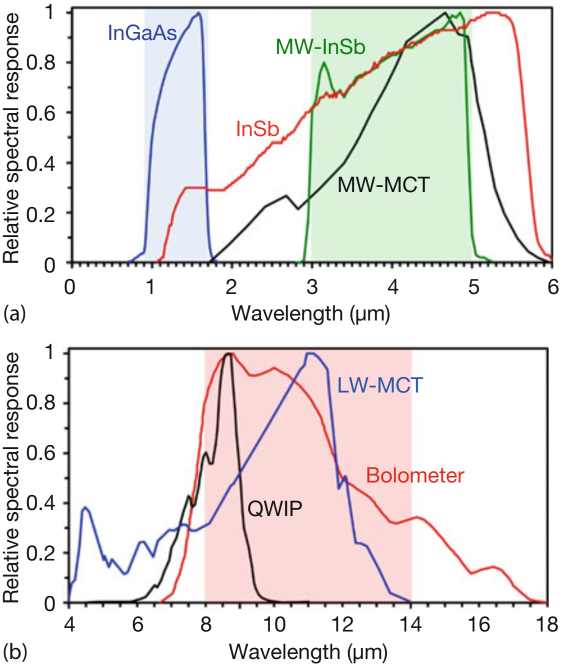

Figure 2.71 Typical spectral response curves of various thermal imaging systems.

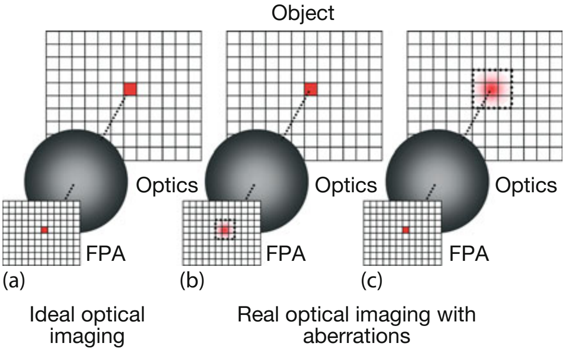

Figure 2.72 Comparison of ideal and real optical imaging. Ideal system (a) and realistic situation due to optics aberrations (b,c).

preted as being due to a large object size, that is, aberrations diminish the spatial resolution. On the other hand, the object radiance on the detector pixel decreases owing to the blurring. This can also cause an incorrect temperature reading since the chosen pixel receives less radiation from the corresponding object area plus additional radiance contributions (of differing amount) from neighboring pixels (Figure 2.72c).

2.4.4.3 Field of View

The object field is transformed to an image within the FOV of the camera. The FOV is the angular extent of the observable object field (Figure 2.73). Sometimes the FOV is also given as the area seen by the camera.

The FOV can be easily constructed from geometrical optics. Rays passing through the center of a (thin) lens are not refracted. Therefore, rays that finally hit the four edges of the detector array limit the FOV.

The FOV depends on the camera lens and the FPA dimensions. For a camera lens with a focal length f and a FPA with linear dimension b, the FOV can be calculated as follows:

$$\mathrm{FOV} = 2\arctan\left(\frac{b}{2f}\right) \tag{2.51}$$

The object area with length x captured by the camera at a given object distance D can be calculated from

$$x = 2D\tan\left(\frac{\mathrm{FOV}}{2}\right) \tag{2.52}$$

The rectangular shape of the FPA causes different horizontal fields of view (HFOV) and vertical fields of view (VFOV).

Different camera optics allow a change of the camera FOV. Figure 2.74 shows some camera lenses for the MW FLIR SC6000 and the LW SC2000 cameras with different focal lengths.

The corresponding fields of view are given in Table 2.4.

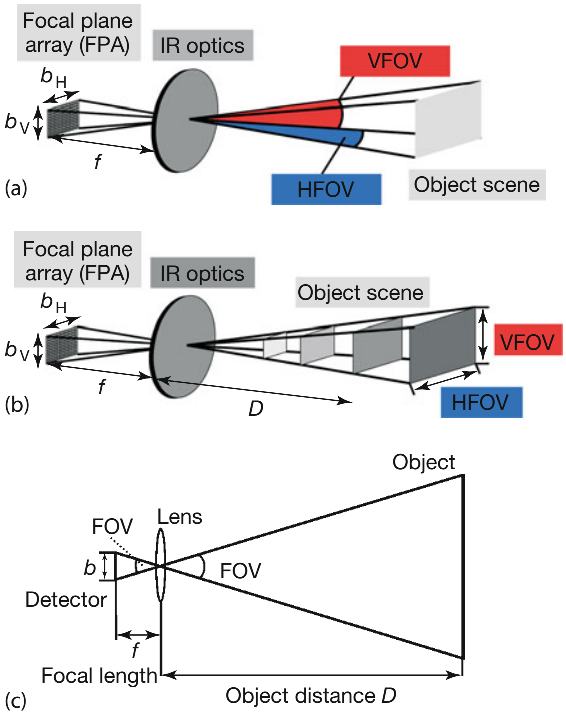

Figure 2.73 (a) Calculation of camera's angular field of view and (b) area seen by camera. (c) Two-dimensional cross section.

Table 2.4 Camera fields of view for different lenses.

Camera lens	**FLIR SC6000 (640 × 512 pixels) HFOV°/VFOV°**	**FLIR SC2000 (320 × 240 pixels) HFOV°/VFOV°**	**FLIR T 650sc (640 × 480 pixels) HFOV°/VFOV°**
7°	–	–	7°/5.3°
12°	–	12°/9°	–
15°	–	–	15°/11.3°
Standard 24°	–	24°/18°	–
25°	–	–	25°/18.8°
45°	–	45°/33.8°	45°/33.8°
Close-up 34/80	–	24°/18°	–
Close-up 64/150	–	24°/18°	–
25 mm (focal length)	35.5°/28.7°	–	–
50 mm (focal length)	18.2°/14.6°	–	–

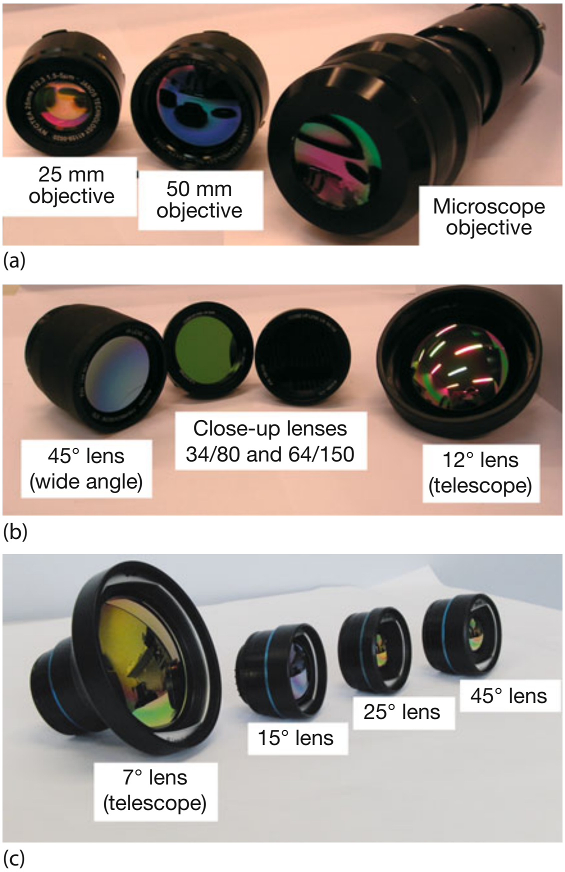

Figure 2.74 (a) Different lenses for MW SC6000 camera, (b) LW camera SC2000, and (c) T650 SC LW camera.

The label x/y for the close-up lenses is related to the FOV; however, the numbers also directly give the minimum object distance (y) and the corresponding horizontal object size (x) at this distance. If the horizontal number of pixels is known, one can immediately estimate the best possible spatial resolution. For example, $x = 34$ mm with 320 pixels means that each pixel reflects an object size of $34\,\text{mm}/320 \approx 0.1$ mm.

Figure 2.75 depicts the IR images of an object scene for the different LW camera lenses. The smaller the FOV of the camera, the better the spatial resolution of the IR image. The knowledge of the camera FOV is necessary to estimate the smallest object that can be detected and to ensure a correct temperature measurement. From the FOV, the IFOV can be determined by dividing the FOV by the number of FPA pixels in a line (horizontal or HIFOV) or in a column (vertical or VIFOV) (Section 2.5.3).

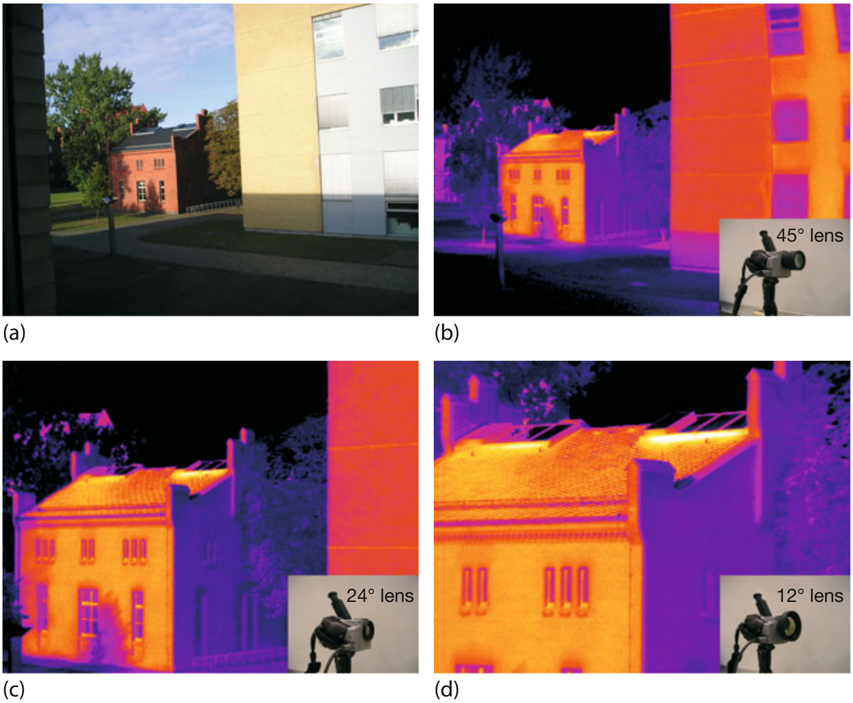

Figure 2.75 Images of an object scene (a), FLIR SC2000 LW images with different lenses: 45° wide angle (b), standard 24° camera lens (c), and 12° telescope lens (d). The angle refers to the horizontal direction.

2.4.4.4 Extender Rings

Some IR cameras allow for the use of extender rings between the camera and the camera objective. Extender rings are known from macrophotography and offer an inexpensive and easy way to increase the magnification. The purpose of extender rings is to move the objective lens farther from the FPA to magnify an image (Figure 2.76). Extender rings decrease the distance between camera and object.

A simplified estimate is possible using the thin lens formula. It relates object distance x_o, image distance x_i, and lens focal length via

$$\frac{1}{f} = \frac{1}{x_o} + \frac{1}{x_i} \tag{2.53}$$

When observing objects in distances measured in meters and using lenses with focal lengths in the centimeter range, $x_o \gg f$ and $x_i = f + z$ with $z \ll f$. Therefore,

$$\frac{1}{f} = \frac{1}{x_o} + \frac{1}{f + z} \tag{2.54}$$

which gives

$$x_o = \frac{f(f + z)}{z} \tag{2.55}$$

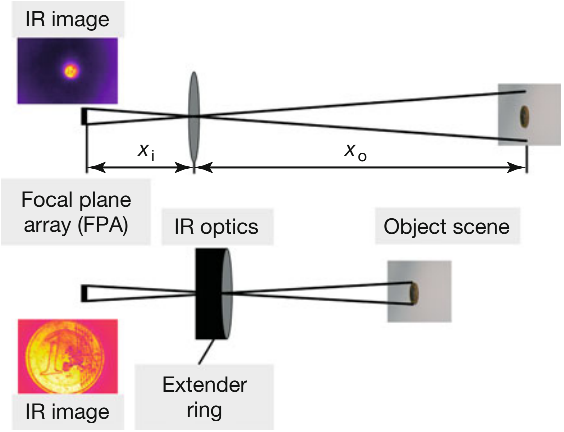

Figure 2.76 Increasing object magnification using extender rings by increasing distance from lens to detector and decreasing distance from camera to object.

The ratio of image size C_i to object size C_o is given by

$$\frac{C_i}{C_o} = \frac{x_i}{x_o} = \frac{(f+z)z}{f(f+z)} = \frac{z}{f} \tag{2.56}$$

Assume, for example, a 50 mm lens that, without an extender ring, has $z = 5$ mm, corresponding to an object distance of $x_o = 0.55$ m and $C_i/C_o = 1/10$. Introducing an extender ring of $0.25'' \approx 6$ mm gives $z^* = 11$ mm, $x_o^* = (50 \cdot 61)/11 \approx 0.277$ m, and $C_i^*/C_o^* = 11/50 \approx 1/4.54$. Obviously, the image size has increased to

$$C_i^* = C_i \frac{z^*}{z} \approx 2.2 \cdot C_i \tag{2.57}$$

Figure 2.77 depicts thermal images of a €1 coin for different extender rings, recorded at minimum possible object distances, as well as the result using the microscope objective.

The use of extender rings has some drawbacks, such as decreasing the FOV with a corresponding loss of radiation with increasing extender ring thickness. This will cause significant uncertainties in the object temperature determination. The strongest degradation of the image quality is observed at the image corners. A much better image quality is observed if close-up lenses or a microscope objective is used (Figure 2.77j).

2.4.4.5 Narcissus Effect

In IR imaging, an optical reflection effect occurs that is unknown from imaging in the visible spectral range. The so-called Narcissus effect occurs when there is a reflection from the camera lens, a window, or an object such that the camera detects the reflection of itself. The Narcissus effect becomes pronounced if the reflecting object is in the focus of the camera. This effect results in a dark (cold) or bright (warm) spot in the IR image depending on the detector temperature. Figure 2.78 illustrates the Narcissus effect for a cooled InSb MW camera and a

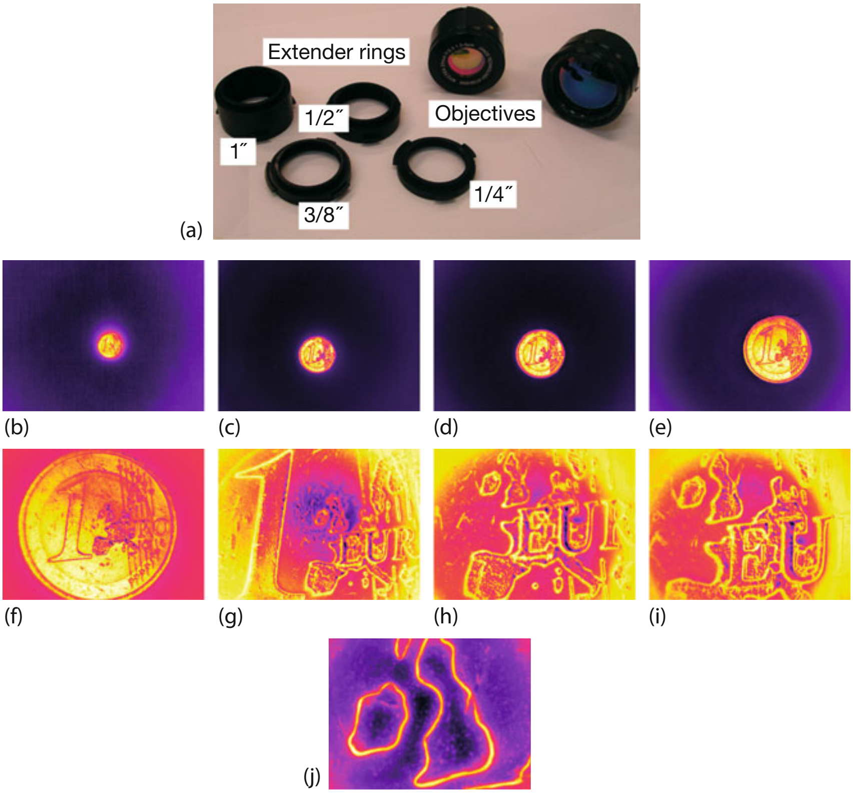

Figure 2.77 Image magnification using a 50 mm lens and extender rings (b–i) and a microscope optics (j). Extender ring sizes: (c) 0.25″, (d) 0.375″, (e) 0.5″, (f) 1″, (g) 2.125″, (h) 3.125″, (i) 4.125″ (″ = inches).

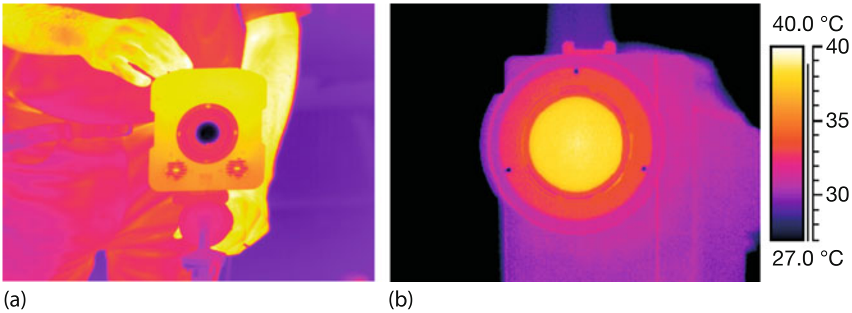

Figure 2.78 Narcissus effect looking at a polished room temperature metal plate for a MW camera (77 K cooled InSb FPA), (a) and with a LW camera (temperature-stabilized microbolometer FPA) (b).

bolometer LW camera viewing a polished steel plate at room temperature (about 22 °C). The LW camera is measuring a maximum temperature of 39 °C for an object emissivity of 1 (perfect 100% mirror) on the lens area. The MW camera is measuring a temperature below −60 °C. One way to avoid this effect is to change the viewing angle to a value such that there is no incident reflected radiation from the camera detector area on the camera objective.

The Narcissus effect is particularly important when using filters, for example, for narrowband detection or other plane-parallel partially transparent plates between camera and object.

Some R&D cameras, such as the FLIR SC6000, allow users to perform NUCs. A one-point NUC can be performed by placing a homogeneous tempered blackbody in front of the camera objective. Figure 2.79 illustrates that such a one-point NUC can be used to eliminate the Narcissus effect if a reflecting object, for example a silicon wafer optically polished on both sides, is placed in front of the camera. Silicon is transparent in the MW spectral region but reflects about 50%

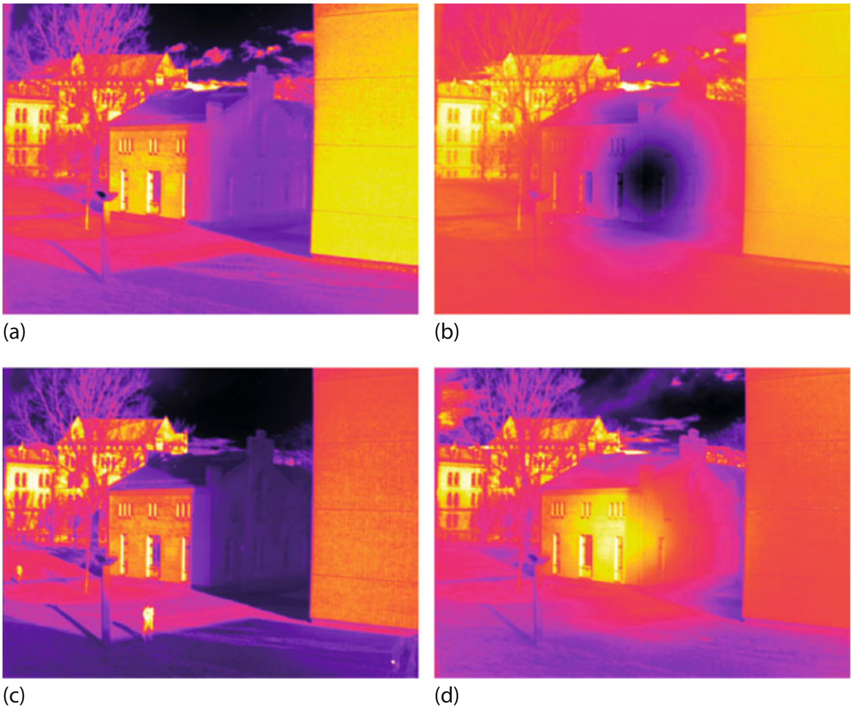

Figure 2.79 Elimination of Narcissus effect caused by a dual-side polished silicon wafer positioned in front of the camera objective performing a NUC of a FLIR SC6000 camera. (a) Object image without silicon wafer after NUC. (b) Object image with silicon wafer in front of camera objective showing Narcissus in center of image. (c) Object image with silicon wafer in front of camera objective after performing an additional NUC (silicon wafer during NUC in front of camera objective). (d) Object image after removing silicon wafer showing inverse Narcissus effect in center of image.

(Figure 1.50). Figure 2.79a depicts an object scene after a NUC with a homogeneous background. If the silicon wafer is placed in front of the camera, the Narcissus effect is clearly seen (Figure 2.79b). Now an additional NUC is performed using a homogeneous background but with the wafer in front of the camera. After this procedure, the Narcissus effect is eliminated (Figure 2.79c). Removing the silicon wafer will now lead to an inverse Narcissus effect, as shown in Figure 2.79d.

2.4.4.6 **Spectral Filters**

The additional use of spectral filters can expand the applications of thermal imaging. As discussed in Chapter 1, the object optical IR properties, for example emissivity, are important for thermal imaging. Not only materials such as glass or plastics but also combustion flames can be characterized as selective emitters and are characterized by a wavelength-dependent emissivity. An analysis of such selective emitters becomes possible at wavelengths with strong absorption in these materials. The camera can be spectrally adapted to these wavelengths by inserting appropriate filters. The spectral filters are described as short-pass (SP), long-pass (LP), bandpass (BP), and narrow bandpass (NBP) filters (Figure 2.80).

In addition to these spectral filters, neutral density (ND) filters are used to attenuate IR radiation without a spectral filtering (wavelength-independent transmittance below 100%), for example, to prevent detector saturation at higher signal levels. It is important that only interference or dichroic filters be used. The spectral filtering is based on the reflectance and transmittance by the interference effect; it is not due to absorption by the filter. Filter absorption would cause a temperature increase in the filter. According to Kirchhoff's law, any absorbing filter would also emit very efficiently (Chapter 1). The detection of this additional radiation by the camera would lead to measurement errors. Sometimes the optical layers on both sides of the filter are the reason behind the spectrally dependent transmittance of the filter (Figure 2.81). The optical layers on one side of the filter substrate will only partially block the incident radiation (SP filter with cutoff wavelength λ_{cutoff} on one side of the substrate and LP filter with cut-on wavelength $\lambda_{\text{cuton}} < \lambda_{\text{cutoff}}$ on the other side of the substrate). The spectral transmittance of the BP filter is formed by the cut-on and cutoff behavior of the combined SP and LP filters. If the filter substrate material is not transparent in the entire IR spectral region, for example, sapphire (used for MW filters), the object radiation must be

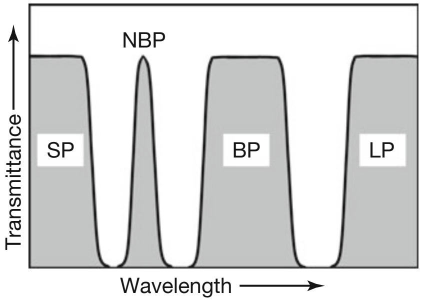

Figure 2.80 Spectral transmittance of different types of optical filters.

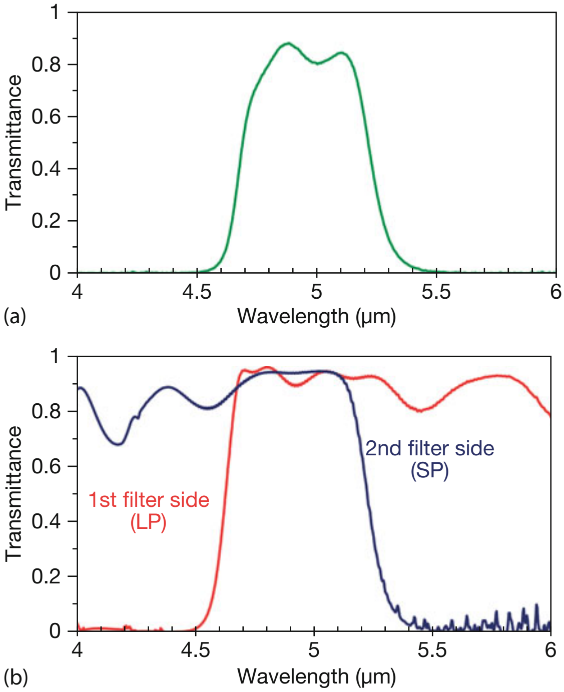

Figure 2.81 NBP filter for glass temperature measurement of (a) spectral filter transmittance and (b) separate spectral transmittance of interference filter layers acting as LP and SP filters on both sides of sapphire substrate.

incident on the filter side with the SP filter that blocks the longer wavelengths of substrate absorption (e.g., owing to the strong absorption behavior of sapphire at wavelengths above 5 µm, the LW region must be blocked) (see also Figure 1.63).

Table 2.5 gives a compilation of some standard filters used in thermal imaging.

For demanding applications with spectral adaptation, cold filters are used in front of the photon detector housing. Cold filters reduce the detector signal generated from the 300 K background radiation (e.g., inside camera parts) and cause an increased signal contrast.

2.4.5
Calibration

An IR camera as a radiometer allows one to measure some radiometric quantities, such as radiance or radiant power. The purpose of calibration is to determine the accurate quantitative relations between camera output and incident radiation. For the calibration procedure, blackbodies (emissivity close to unity) at different temperatures are used since their radiometric quantities, such as excitance M or radiance L, and their spectral quantities are well defined (Section 1.3). Therefore, the calibration process gives a relation between camera signal and blackbody temper-

Table 2.5 Some standard IR filters for thermography.

Wavelength (μm)	Type	Application
2.3	NBP	Measurement through glass
3.42	NBP	Measurement of plastics temperature (polyethylene)
3.6–4	BP	Reduction of atmospheric influences at longer measurement distances
3.6	LP	Reduction of influence of sun reflections
3.7–4	BP	Measurement through flames
3.9	BP	Measurement of high object temperatures (reduces incident radiation on detector)
4.25	NBP	Measurement of flame temperatures
5.0	NBP	Measurement of glass temperature
7.5	LP	Measurement only in LW spectral region
8.3	NBP	Measurement of Teflon temperatures

SP, short pass; NBP, narrow bandpass; BP, bandpass; LP, long pass.

ature. During camera calibration, the signal of each pixel depending on the blackbody temperature is determined. Therefore, the calibration process also forms a NUC of the detector array. Following camera calibration, all pixels will give the correct temperature information of the object. This is a NUC on the quantitative temperature scale, whereas the NUC discussed in Section 2.4.1.3 qualitatively adjusted all detector pixel responses as depending on incident radiance.

During calibration, the camera aperture is completely covered by the blackbody. The distance between the camera and the black body is small so that an atmospheric transmittance of unity can be assumed. This also means that atmospheric emittance is zero, that is, the incident radiance L and, hence, the camera output signal $S_{\text{out}}(T_{\text{BB}})$ for a given IR camera with range $[\lambda_1, \lambda_2]$ depend only on the temperature of the blackbody (Eq. (2.58)):

$$S_{\text{out}}(T_{\text{BB}}) = \textit{const.} \int_{\lambda_1}^{\lambda_2} \text{Res}_\lambda L_\lambda(T_{\text{BB}})\, \text{d}\lambda \tag{2.58}$$

The output signal depends on the spectral camera response, Res_λ, determined by the spectral detector responsivity, the spectral dependence of the optics transmittance, and the camera characteristic constant value, including the properties of the camera optics, such as the F-number of the camera lens. Changing the camera lens may change the F-number and the spectral transmittance of the optics. Therefore, the calibration must be performed for each lens separately. If filters are used, the spectral camera response is changed and a recalibration of the camera with the filter is necessary. The calibration parameters for different configurations

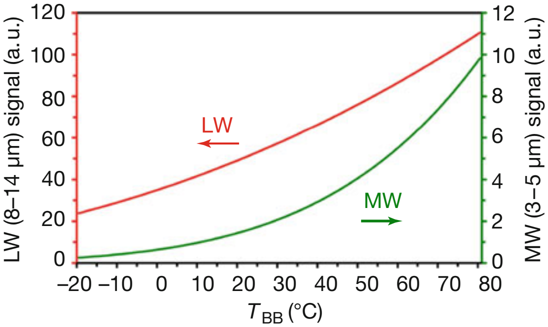

Figure 2.82 Blackbody-temperature-dependent camera output signal generated by incident blackbody object radiation for PtSi MW (3–5 μm) and LW (8–14 μm) cameras with constant spectral response.

(e.g., different additional lenses of the camera) are generally stored in the camera firmware. The use of additional lenses can be detected by the camera itself if the camera can detect a lens code. This can be done, for example, by a magnetic coding of the lens and a Hall-sensor reading at the camera. If the camera detects an additional lens, the corresponding calibration curve will be uploaded to the firmware.

The relative output signal dependence on blackbody temperature $S_{\mathrm{out}}(T_{\mathrm{BB}})$ calculated for MW (3–5 μm) and LW (8–14 μm) cameras is shown in Figure 2.82. For the calculation, the spectral camera response Res_λ was assumed to be constant (boxcar assumption) within the given wavelength limits and zero outside.

The calibration curve is then approximated by a mathematical fit function $S_{\mathrm{out}}(T_{\mathrm{BB}})$. A polynomial or a typical exponential fit function can be used:

$$S_{\mathrm{out}}(T_{\mathrm{BB}}) = \frac{R}{\exp\left(B/T_{\mathrm{BB}}\right) - F} \tag{2.59}$$

Using a least-squares-fit procedure, this function is adjusted to the calibration curve, calculating the values R (response factor), B (spectral factor), and F (form factor) for the best fit. Most IR cameras offer overall temperature measurement ranges from below 0 °C up to 1000–2000 °C. With respect to the object-temperature dependence of the radiance, the whole temperature range must be divided into smaller temperature intervals to ensure optimum temperature sensitivity and to avoid a saturation of the detector signal. Therefore, the overall temperature range of the camera is divided into different measurement subranges and the dynamic range of a specific measurement is limited to the used measurement subrange. If a scene with a larger temperature dynamic range is observed, a decision must be made as to the best measurement subrange for the analysis or some images with different measurement subranges must be taken. R&D cameras offer the possibility of capturing large dynamic range scenes using superframing (Section 3.3). The measurement subrange is changed by changing the signal amplification or by using additional optical filters (ND or spectral filters)

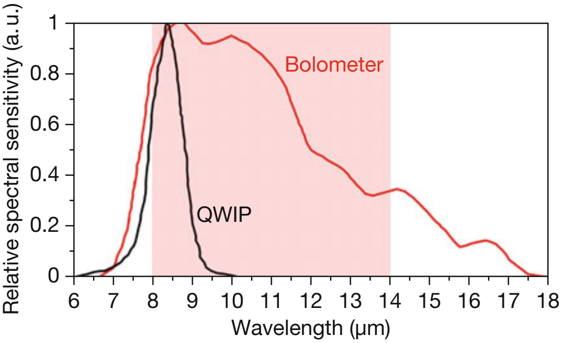

Figure 2.83 Typical spectral sensitivities for LW bolometer and LW QWIP camera.

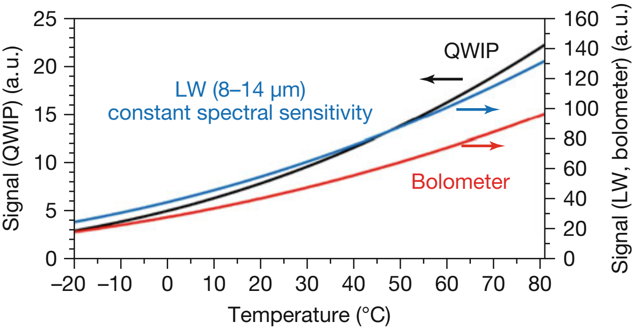

Figure 2.84 Blackbody-temperature-dependent camera output signal for LW bolometer camera and QWIP camera generated by incident blackbody object radiation (for spectral sensitivities according to Figure 2.83).

to attenuate the incident radiation on the detector to ensure detector operation within its linearity range.

The real camera sensitivities (Figure 2.83) differ from boxcar-shaped spectral responses, which was assumed for Figure 2.82.

The spectral sensitivity of the camera has an effect on the characteristics of the calibration curve (Figure 2.84). Compared to the actual bolometer curve, the boxcar spectral sensitivity curve has a slightly larger slope, that is, it should have a slightly better temperature sensitivity. The real bolometer and also QWIP camera calibration curves can be fitted using Eq. (2.59). Because of the limited bandwidth of the QWIP spectral sensitivity, this camera will exhibit a much smaller signal for the same object temperature as a bolometer camera. However, the slope of the signal to object temperature dependence is larger for the QWIP camera. In connection with the large D^* values of the QWIP sensors, this behavior will cause a better temperature resolution.

Besides spectral dependencies, the camera output signal is affected by the incident object radiation as well as by the additional radiation from camera parts such as the optics, the detector window, and the inner parts of the camera. The output signal of the camera, therefore, represents the sum of these two radiation fractions. The additional radiation depends on the camera temperature and causes a signal offset. The effect of this additional radiation can be corrected by a camera-temperature-dependent calibration. The quality of this correction determines the temperature measurement accuracy.

During the measurement process, the camera temperature is measured by temperature sensors inside the camera, and the camera output signal is corrected using the data from the camera-temperature-dependent calibration. The additional use of a tempered flag inside the camera offers the possibility of a one-point camera recalibration. This corrects the output signal by an offset and can be used to perform a NUC of the detector array (Section 2.4.1.3). These corrections will work only if the camera state is characterized by a thermal equilibrium. A rapid change in the ambient temperature will cause thermal shock behavior, which will lead to incorrect temperature measurements. This thermal shock behavior results from the thermal nonequilibrium inside the camera connected with temperature gradients. Because of the thermal mass of the camera, it can take a long time to achieve the equilibrium state (Section 2.4.6).

Today, thermal imaging systems offer a dynamic range of 12 to 16 bits. This is the equivalent of 4096 to 65 536 signal levels and offers the option of expanding the measurement range. If, for example, a camera is operated within a measurement range of −20 to 80 °C, it is also possible to measure temperatures slightly below or above the measurement range limits. As an example, Figure 2.85 depicts the detector digitization for a 12 bit system. The temperature information of the whole measurement range is captured and available for image analysis. For the representation and the analysis, it is possible to fix a level and a span (Figure 2.85). These two parameters only affect the image representation and correspond to the brightness and contrast of the image, respectively. The temperatures within the span range can be depicted in levels of gray or false colors (palette). Mostly 8 bit scales with 256 colors are used with predefined color palettes.

2.4.6
Camera Operation

Accurate temperature measurement using thermal imaging requires correct camera operation. If, for example, the camera is not yet in thermal equilibrium, it will not perform well in field measurements, although it would have passed all camera specifications during tests in the laboratory. In the latter, the cameras are started several hours before the tests so that they are in thermal equilibrium. As a consequence, all manually or automatically performed camera correctives refer only to thermal equilibrium conditions. To enable accurate calibrations, most IR cameras have internal temperature sensors to monitor temperatures of camera parts. During the calibration process, the cameras are placed in an environmental chamber. The data collected from measurements at different camera ambient and object (blackbody) temperatures are stored in the firmware. These data are used to correct the camera temperature output. This correction, referred to as *ambient drift*

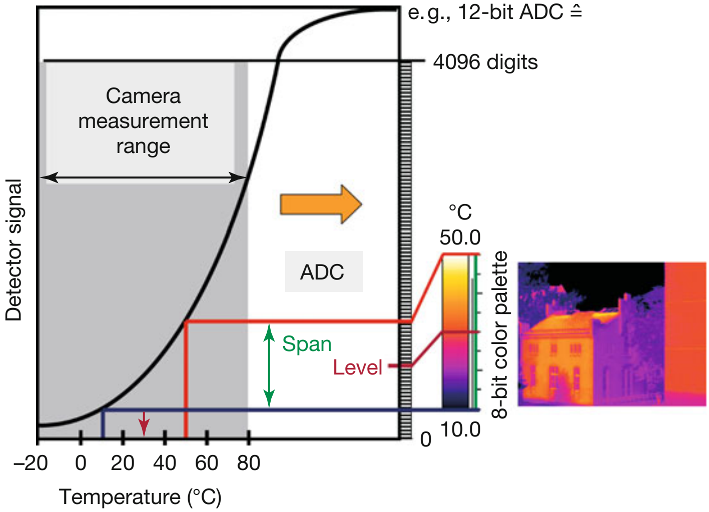

Figure 2.85 Digitization of the detector signal for a 12-bit system, level, and span.

correction, is hence accurate for a thermal steady-state camera behavior similar to that during the calibration process.

To demonstrate the associated uncertainties in temperature measurements, two typical situations of camera operation with possibly transient thermal camera conditions are discussed. First, incorrect temperature readings may occur right after the camera is switched on. Second, measurements following rapid changes in the camera's ambient temperature can also result in measurement errors.

2.4.6.1 Switch-On Behavior of Cameras

The apparent object temperature drifts due to the camera temperature drift following switch-on were measured using a cooled MW PtSi camera and a LW microbolometer camera. Figure 2.86 depicts measured blackbody temperatures after the cameras were switched on, using stabilized blackbodies at 30 and 70 °C (long-term temperature stabilization for more than 2 h prior to the start of measurement with $\Delta T_{BB} \leq 0.1\,°C$). The measurements started immediately after the cameras were ready for image acquisition. This switch-on process takes about 5 min for the LW microblometer camera and 10 min for the cooled MW PtSi camera.

Both cameras show characteristic signal changes within the first 90–120 min after switch-on. The LW microbolometer camera exhibits a more distinctive change in the temperature measured. Immediately after switch-on, the LW camera measures 2–3 K higher temperatures depending on the object temperature. For the MW camera, smaller deviations between 0.5 and 1 K were measured. For both cameras, the autoshutter operation (periodic measurement of tempered flag for one-point recalibration) was activated. The observed steps of time-dependent temperature measurement result from the autoshutter operation. The auto-adjust

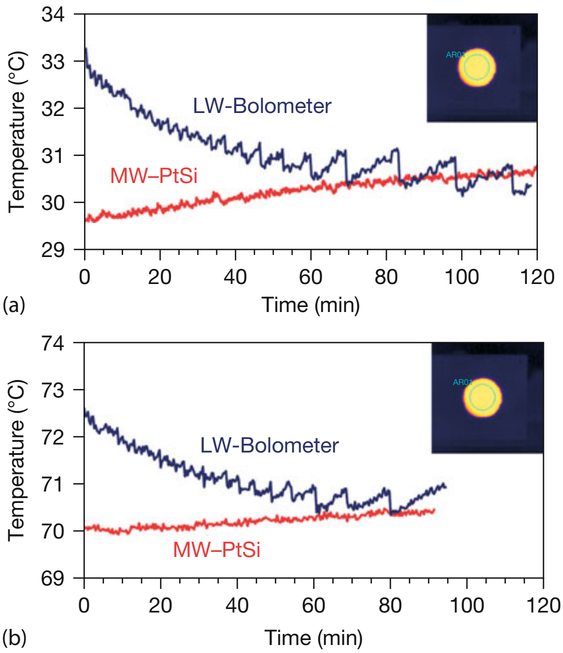

Figure 2.86 Results of long-term temperature measurement at blackbody emitter stabilized at 30 °C (a) and 70 °C (b) with MW and LW IR cameras after camera switch-on.

procedure strongly influences the temperature measurement of the LW camera. The bolometer detector signal is generated by the net radiation incident on the detector (Section 2.2.3). Furthermore, the bolometer sensitivity strongly depends on its temperature. Therefore, thermal nonequilibrium conditions as well as bolometer temperature drift will affect the temperature measurement more strongly.

The time to reach thermal equilibrium within the cameras takes more than 90 min, but the temperature readings of both cameras achieve the given camera specification of a temperature accuracy of ±2 K after about 10 min.

2.4.6.2 **Thermal Shock Behavior**

The second situation to be discussed is known as the *thermal shock behavior* of cameras. During field measurements the ambient temperature often changes rapidly, for example, while taking the camera from outside into a heated building during winter or vice versa. This can cause a thermal shock to the IR camera and result in an incorrect temperature reading since the camera is not in thermal equilibrium, although it may have been switched on hours earlier. As discussed in Section 2.4.5, the accuracy of the radiometric temperature measurement depends on the accuracy of the object signal calculation. The measured detector signal must be corrected for the additional radiation from, for example, the camera optics or other parts within the camera housing. If the ambient temperature changes rapidly, the camera will exhibit transient temperature changes with temperature

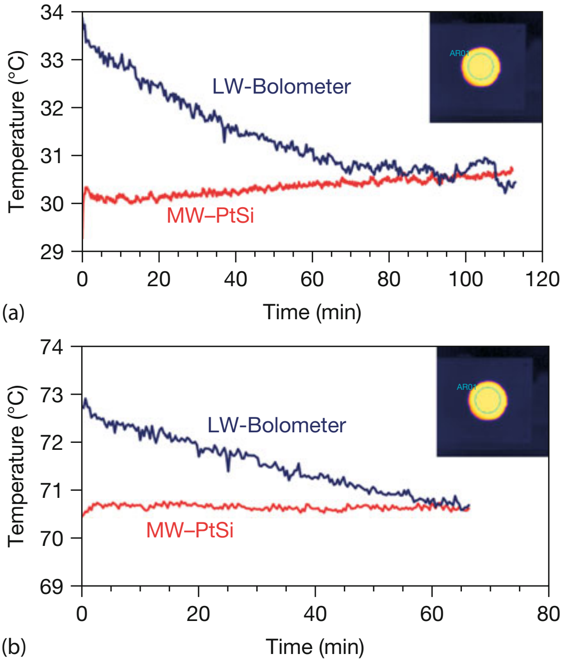

Figure 2.87 Results of long-term temperature measurement at blackbody emitter stabilized at 30 °C (a) and 70 °C (b) with MW and LW IR cameras following rapid change in camera ambient temperature from 13 to 23 °C and camera switch-on.

gradients inside the camera. This limits the accuracy of the detector signal correction algorithms and causes measurement errors. Because of the large camera thermal mass, one must expect large thermal time constants of minutes to hours.

To analyze this thermal shock behavior, the same two cameras of Figure 2.86 were tempered to 13 °C in an environmental chamber for 2 h in order to obtain steady-state temperature camera conditions. The ambient temperature was 23 °C and the relative humidity 50% (dew-point temperature below 13 °C). After 2 h, the cameras were taken out and switched on. Measurements started ($t = 0$) immediately after the cameras were ready for temperature recordings (Figure 2.87). Similar to Figure 2.86, temperature-stabilized blackbodies were studied at 30 and 70 °C.

In this experiment, both the switch-on and the thermal shock behavior are observed simultaneously. Results similar to those for pure switch-on measurements are observed. The LW bolometer camera is more sensitive to the thermal shock because of the 10 K increase in the ambient temperature with a temperature inaccuracy of 3–4 K at the beginning of the measurements. The MW camera is within the accuracy specification immediately after the start of the measurements. For the LW bolometer camera, it takes 20–30 min to reach the ±2 K accuracy specification of the camera.

From Figures 2.86 and 2.87 it can be concluded that steady-state camera temperature conditions are necessary for accurate temperature measurements. Because of the more sensitive signal correction process in bolometer cameras, their measurement accuracy is more sensitive to transient temperature changes due to either switch-on or thermal shock.

2.4.7
Camera Software – Software Tools

IR cameras without analysis software would just provide qualitative false color images of objects. However, whenever quantitative results are needed like temperatures, line plots, or reports, software tools are indispensable.

All manufacturers of thermal imaging systems provide a variety of software tools ranging from general-purpose software packages, including, for example, thermal image analysis and generation of IR inspection reports, to sophisticated software packages that, for example, offer camera control functions, real-time image storage at selectable integration times, and frame rates or radiometric calculations.

The general-purpose software mostly contains the following key features:

- Level and span adjustment;
- Selectable color palette and isotherms;
- Definition of spot analysis, lines, and areas with temperature measurements for maximum, minimum, and average temperatures;
- Adjustment of object parameters (emissivity) and measurement parameters (e.g., humidity, object distance, ambient temperature);
- Creation of professional customized reports with flexible design and layout (e.g., export to other software such as Microsoft Office, including visible images).

For a very detailed analysis of static or transient thermal processes sophisticated software specially designed for R&D is available. Beyond the features of the general-purpose software, such software usually includes more complex data storage, analysis, and camera operation tools:

- Remote control of camera from PC (most or all camera parameters can be controlled by the PC);
- High-speed IR data acquisition, analysis, and storage;
- Digital zoom of IR images, use of subframes;
- Raw data acquisition and analysis, radiometric calculations;
- Automatic temperature vs. time and three-dimensional temperature profile plotting, additional graphic, and image processing tools;
- Different data format export, automatic conversion to, for example, JPEG, BMP, AVI, or MATLAB format;
- Data export to other common software applications such as Microsoft Office;
- Thermal image subtraction;

- Definition of different regions of interest with different shapes, separate emissivity, and so on;
- Customized camera calibration and NUCs.

2.5
Camera Performance Characterization

The system performance evaluation of thermal imagers is well standardized and a lot of research has been done on the characterization and testing of imaging systems [47, 48, 59–61]. In general, however, it is difficult for most practitioners to relate the relevance of the system performance parameters to their applications and the measurement results.

The performance of a thermal imaging system is described by a number of parameters, such as thermal response, detector and electronic noise, geometric resolution, accuracy, spectral range, frame rate, integration time, and so on. These parameters can be divided into two groups: objective and subjective parameters (Table 2.6).

The temperature resolution given by NETD and the spatial resolution given by IFOV are important objective performance parameters. They both significantly affect image quality. An evaluation of the quality and performance limits of thermal imagers more oriented toward practical applications requires a combination of these parameters. Additionally, the subjective factor (the ability to detect, recognize, and identify temperature differences while using the camera system) due to the human observer must be taken into consideration. The MRTD and the MDTD combine the objective and subjective parameters and are directly related to applications.

For any practical thermal imaging, the following question must eventually be answered: Is the camera suited to my application on the basis of its performance parameters? Accurate knowledge of the most important performance limits of the thermal imaging system used and their relevance to the application is crucial for correct temperature measurements and interpretation of the results. Therefore, camera performance parameters and their influence on practical measurement results are discussed in more detail in what follows.

2.5.1
Temperature Accuracy

The specification of accuracy (or, more precisely, inaccuracy) gives the absolute value of the temperature measurement error for blackbody temperature measurements. For most IR cameras, the absolute temperature accuracy is specified to be ±2 °C or ±2% of the measured temperature. The larger value is valid. The temperature measurement errors arise as a consequence of errors in radiometry connected with the calibration procedure, the long- and short-term variability of the camera sensitivity, the limited accuracy of object radiation calculation from the

Table 2.6 Camera performance parameters.

	Name	**Definition, description**	**Unit**	**Significance**
Objective parameters	Temperature accuracy	Absolute error of blackbody temperature measurement	K, °C, °F	Absolute measurement accuracy
	NETD	Minimum temperature difference for SNR = 1	K, °C, °F	Temperature resolution
	FOV	Angular extent of camera observable object field	Degree, °	Detected object field
	IFOV	Angular extent of object field from which radiation is incident on a detector pixel	mrad	Spatial resolution
	Frame rate	Frequency at which unique consecutive images are produced	1/s, Hz	Time resolution
	Integration time	Period of signal integration	s	Time resolution, sensitivity
	SRF (slit response function)	Ratio of signal response for a slit size emitting object depending on slit width and infinite object width	–	Spatial resolution
	MTF	Fourier transform of the camera response when viewing an ideal point source	–	Spatial resolution
Subjective parameters	MRTD (minimum resolvable temperature difference)	Minimum temperature difference at which a 4 bar target can be resolved by a human observer dependent on spatial frequency of bar target	K, °C, °F	Recognition of temperature difference (dependent on spatial frequency)
	MDTD (minimum detectable temperature difference)	Minimum temperature difference at which a circular or square object can be detected by a human observer dependent on the object size	K, °C, °F	Detection of small objects with low temperature difference (dependent on object size)

measured radiant power (Section 2.3), and so on. For the short-term reproducibility of a temperature measurement, a value of ±1% or ±1 °C is typical.

2.5.2
Temperature Resolution – Noise Equivalent Temperature Difference (NETD)

The temperature resolution of a radiometric system is given by the NETD (see also Section 2.2.2), which quantifies the thermal sensitivity of the thermal imager. This parameter gives the minimum temperature difference between a blackbody object

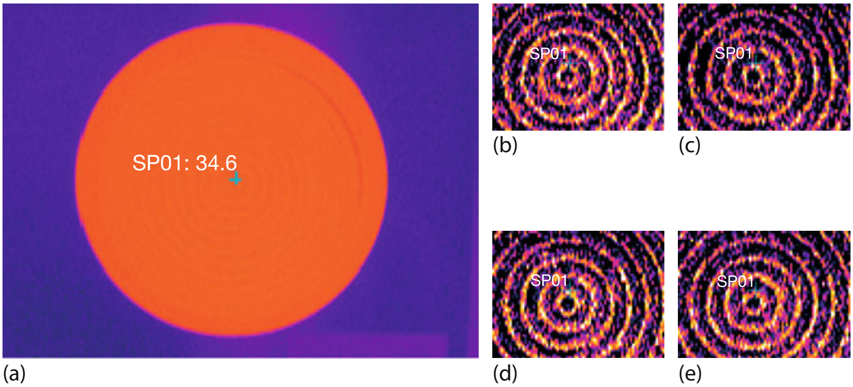

Figure 2.88 NETD measurement: experimental setup, blackbody image (a), and thermal fluctuations (b–e).

and a blackbody background at which the SNR of the imager is equal to unity. The NETD is determined by the system noise and the signal transfer function [4, 43].

Experimentally the temperature-dependent NETD can be determined from the fluctuations of the measured temperature, analyzing the radiation from a heated and temperature-stabilized blackbody.

Figure 2.88a depicts a thermal image while the camera is directed at the blackbody source. A temperature-stabilized source was used with typical circular structures because of the geometry. For each blackbody temperature, a spot temperature measurement was recorded using a thousand images (with 50 images/s, this takes approximately 20 s). Figure 2.88b–d gives a magnified view of the marked area at different times, demonstrating temperature fluctuations. The experiments were performed with a 3–5 μm PtSi MW camera (AGEMA THV550).

Figure 2.89a is a graph of the measured temperatures of a specific pixel as a function of time. It nicely illustrates the thermal noise of the imaging system since the thermal changes of the source happen on a much larger timescale.

The frequency distribution of measured spot temperatures can be approximated by a standardized normal distribution, as expected for random noise processes (Figure 2.89b).

Using the measured temperature data, the root-mean-square (rms) value of these temperature fluctuations, which defines the NETD, can be calculated. For the example shown in Figure 2.89, the NETD equals 0.065 K.

The experimental NETD represents the half-width of the standardized normal distribution. This means that 68.3% of the measured temperatures are within the range $T = (34.50 \pm 0.065)$ °C.

From this measurement we can conclude that the deviation from the correct temperature value in a single measurement can be much higher than the NETD because the NETD represents the root-mean-squared deviation. It can be seen that 95.4% of the temperatures measured are within the range $T = (34.50 \pm$

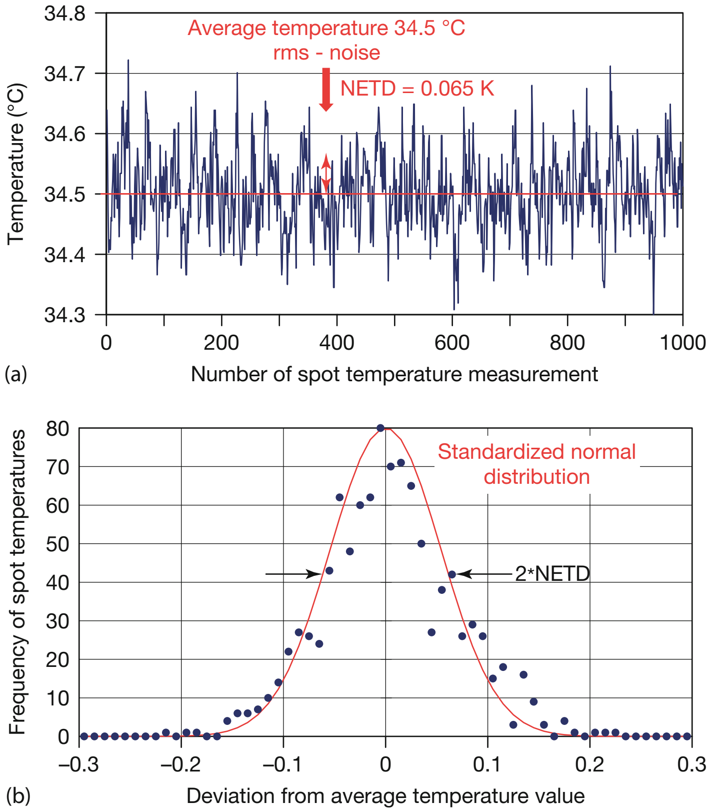

Figure 2.89 Results of a NETD measurement. (a) Time dependence of spot temperatures (marked in Figure 2.88) measured over 20 s with a frame rate of 50 Hz. (b) Frequency distribution of measured spot temperatures centered around average object temperature.

0.13) °C. This corresponds to the 2σ value and 99.7% within $T = (34.50 \pm 0.195)$ °C (3σ value).

Theoretically the NETD is defined as the ratio of the signal noise to the signal transfer function (differential ratio of signal changes $\mathrm{d}S$ to temperature changes $\mathrm{d}T$: $\mathrm{d}S/\mathrm{d}T$). The noise is given by the system (e.g., detector noise, amplifier noise) and independent of the object temperature measured. Because of the change in the signal transfer function with the object temperature T_{obj} the NETD decreases with increasing T_{obj} (Figure 2.90). This is caused by the temperature-dependent thermal derivative owing to the spectral response of the imager. The measured object signal strongly increases with increasing temperature (stronger than a linear dependence). For the complete wavelength range ($\lambda = 0 \rightarrow \infty$), the temperature-dependent signal $S(T) \sim T^4$ (Section 1.3.2.4), that is, the NETD $\sim T^{-3}$. For limited spectral ranges, however, $S(T) = \int_{\lambda_1}^{\lambda_2} S_\lambda(T)\,\mathrm{d}\lambda$ varies, as shown in Figure 2.82. For the MW range, the signal change is governed by an exponential, leading to a strong decrease in the NETD with increasing ob-

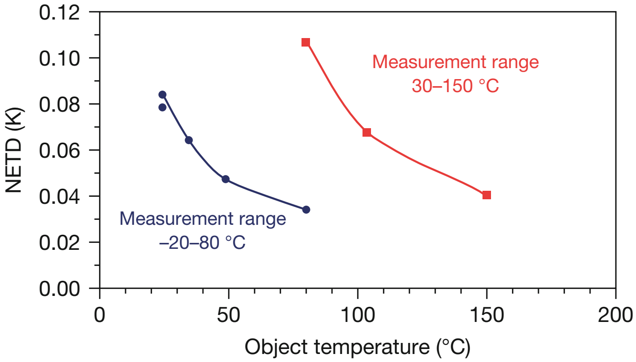

Figure 2.90 Temperature dependence of NETD (root-mean-squared value of temperature fluctuations measured) as function of object temperature and measurement range.

ject temperature. Therefore, within a measurement range selected at the thermal camera (e.g., −20 to 80 °C), the NETD decreases with increasing temperature (Figure 2.90).

If the measurement range is changed to a higher temperature range as shown in Figure 2.90, the NETD is strongly increased owing to the decreased sensitivity of the camera (signal decrease owing to the insertion of a filter but unchanged noise resulting in a smaller SNR or higher NETD). The lowest NETD values are always obtained at the upper temperature limits of the measurement ranges. Because of the temperature dependence of NETD, it only makes sense to give values at well-defined temperatures.

In Figure 2.91, some temperature measurement results using different measurement ranges of the camera are shown. For the measurements, an 80 °C blackbody was used as the target and all other measurement conditions are the same. Obviously the temperature measurement within the −20 to 80 °C range exhibits the lowest noise (or NETD). The measurement within the highest temperature range is already outside of the useful part of the calibration curve.

In addition, Figure 2.91 also illustrates the changes in absolute temperature values. The two lower ranges are well within the stated accuracy range, in contrast to the 100–250 °C range result. This illustrates the fact that although cameras may still be used outside the specified ranges, the results must be interpreted with care.

2.5.3
Spatial Resolution – IFOV and Slit Response Function

The IFOV gives the angle over which one detector element of the FPA senses the object radiation [48] (Figure 2.92). Using the small angle approximation, the minimum object size whose image fits on a single detector element for a given distance can be calculated from object size = IFOV · distance (Table 2.7).

For example, a focal length of $f = 50$ mm and a single pixel size of 50 μm give a IFOV of 1 milliradian (mrad).

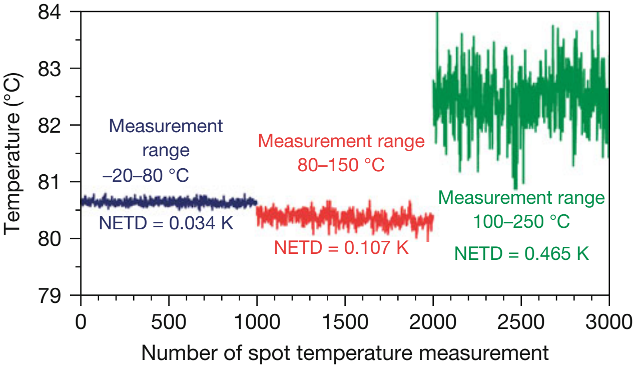

Figure 2.91 Temperature measurement at 80 °C blackbody using different measurement ranges of thermal camera; NETD was calculated from the root-mean square of the observed temperature fluctuations.

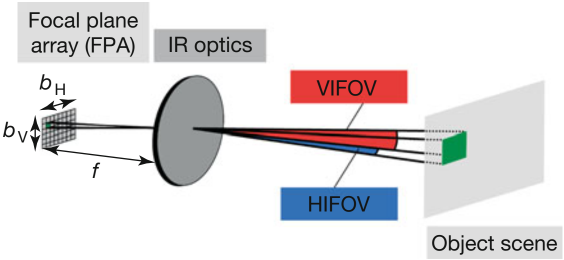

Figure 2.92 Angular IFOV for a detector pixel. (HIFOV: horizontal IFOV, VIFOV: vertical IFOV).

Table 2.7 Minimum object size corresponding to IFOV = 1 mrad at different object distances.

Distance (m)	Minimum object size (mm)
1	1
2	2
10	10
50	50

At a distance $D = 5.5$ m, this IFOV refers to a minimum object size of 5.5 mm.

It is important to keep in mind that the IFOV is only a geometric value calculated from the detector size and the focal length of the optics (Figure 2.93a). The IFOV can also be determined by dividing the FOV by the number of pixels, for example, the IFOV amounts to 1 mrad for 20° FOV and 320 pixels. The system resolution is additionally influenced by the diffraction of the optics. This is described by the SRF, which is defined as a normalized dependence of the system response to a slit-size object with a variable slit width. Experimental analysis of

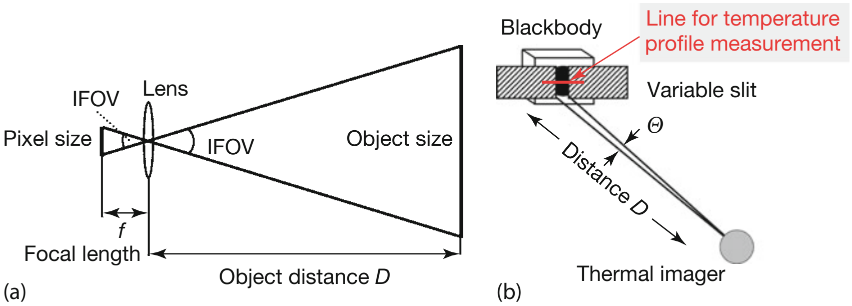

Figure 2.93 Spatial resolution: (a) two-dimensional definition of IFOV; (b) experimental determination of SRF.

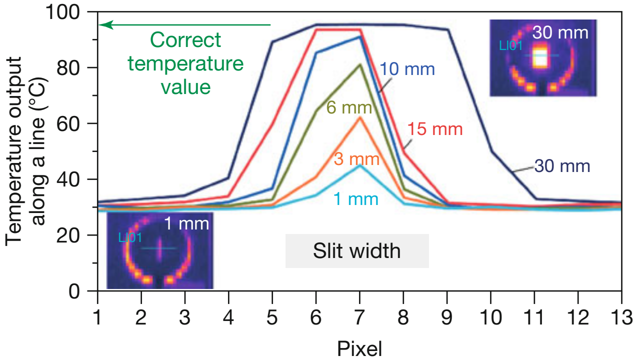

Figure 2.94 Measured temperature of object viewed through a slit with variable width along a line for a measurement distance of 5.5 m between the thermal camera with 20° lens (FOV) and the blackbody with variable slit.

the SRF has been carried out. The test configuration is shown in Figure 2.93b. The angle Θ is the observable slit angle at the given slit width seen from the detector.

The blackbody was heated to a temperature of 95 °C at a distance of 5.5 m from the thermal camera. The object size was changed by a variable slit from 30 to 1 mm. The temperature was measured along a line perpendicular to the slit width (Figure 2.94). With decreasing object size, that is, slit width, the peak output became smaller.

The SRF represents a function of the measured object signal difference at a defined slit width normalized to that measured with a very wide slit (correct object signal difference of the slit size target). The SRF can be calculated from the peak output for each slit width (Figure 2.95). This function provides both the imaging and the measurement resolution.

The *imaging resolution* is usually defined as the angular width of the object seen from the camera that gives a 50% response in the SRF. However, the absolute minimum size of the object for an accurate temperature measurement is two or three times the IFOV (in our case at a slit width of 12 or 18 mm at a measuring distance

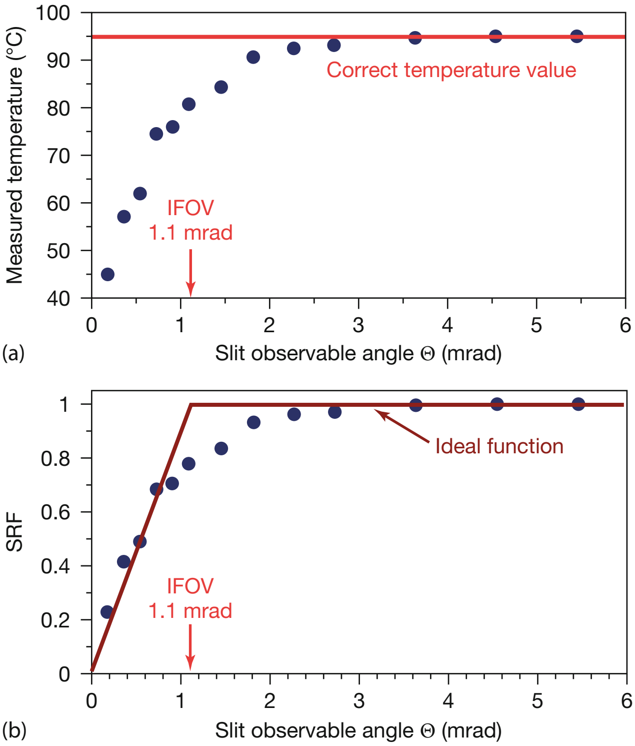

Figure 2.95 Measured peak output temperatures at different slit widths (a) and slit response function SRF (b) as a function of the angular width of the object as seen from the camera (slit widths of 1, 2, 3, 4, 5, 6, 8, 10, 12.5, 15, 20, 25, and 30 mm, respectively).

of 5.5 m using the THV 550) to reach 95% or 99% of the SRF, respectively. The deviation from the ideal SRF is caused by the aberrations of the camera optics, as discussed in Section 2.4.4.

From these results the minimum necessary object size for accurate temperature measurements can easily be calculated using the formula given earlier for the actual measurement distance, multiplying the object size by a factor of 2 or 3.

2.5.4
Image Quality: MTF, MRTD, and MDTD

The MRTD measures the compound ability of a thermal imaging system and an observer to recognize periodic bar targets within an image shown on a display. It is the minimum temperature difference between the test patterns and the blackbody background at which the observer can detect the pattern. This capability is governed by the thermal sensitivity (NETD) and the spatial resolution (IFOV) of the imaging system but strongly depends on other influencing variables such as the palette used, the ability of the observer to distinguish between different col-

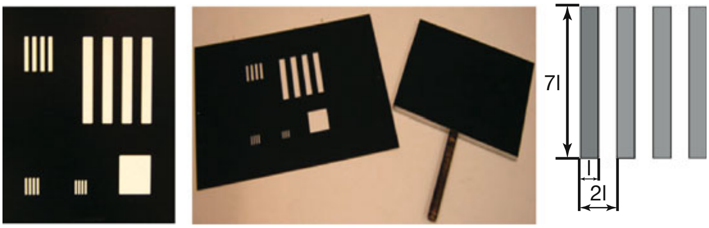

Figure 2.96 Test patterns (four-bar target and a black plate as background).

ors, and so on. ASTM standard MRTD and MDTD test methods are described in [62, 63].

The MRTD is measured by determining the minimum temperature difference between the bars of a standard four-bar target (Figure 2.96) and the background required to resolve the thermal image of the bars by the observer. Different bar dimensions are used to do the analysis with different spatial resolutions. The regular four-bar target is characterized by a spatial frequency (cycles per length or cycles per milliradian).

The contrast in the thermal image measured for different spatial frequencies of the bar targets decreases with increasing frequencies or narrower line pairs owing to the limited resolution of the camera (SRF as a result of given IFOV and limited optics quality) (Figure 2.97). The black plate was heated in an environmental chamber to 60 °C and was then placed as the hot background behind the four-bar target structures. The function contrast measured at the four-bar target structures versus spatial frequency is called the *modulation transfer function* (MTF). For standard determination of MTF, measured object signals (raw signals) are used. Researcher software (e.g., FLIR ExaminIR or ResearchIR) was used to access the raw signals.

The MTF shown in Figure 2.97 was calculated from the ratio of the measured object signal differences (detected raw signals) to the true object signal difference of the four-bar target and the background. For the MRTD measurements, the same equipment was used. The thermal images (50 frames/s) were stored during the cooling of the hot background plate down to room temperature. For the determination of target and background temperatures, the average temperature from the areas marked in Figure 2.98 was used. By analyzing the temperature difference between these two temperatures during the cooling of the background from 60 °C to room temperature, a functional fit for the time-dependent temperature difference can be found. With this fit, we can assign a temperature difference to every image during the cooling period. Such a procedure is necessary to determine the correct values for the very low temperature differences where the measured temperature differences are strongly influenced by temperature fluctuations because of the system noise (Figure 2.98).

Figure 2.99 depicts a series of images observed during the cooling period using the auto-adjust scale and the iron palette. Images at different temperature differences between bar target and background are shown. With decreasing tem-

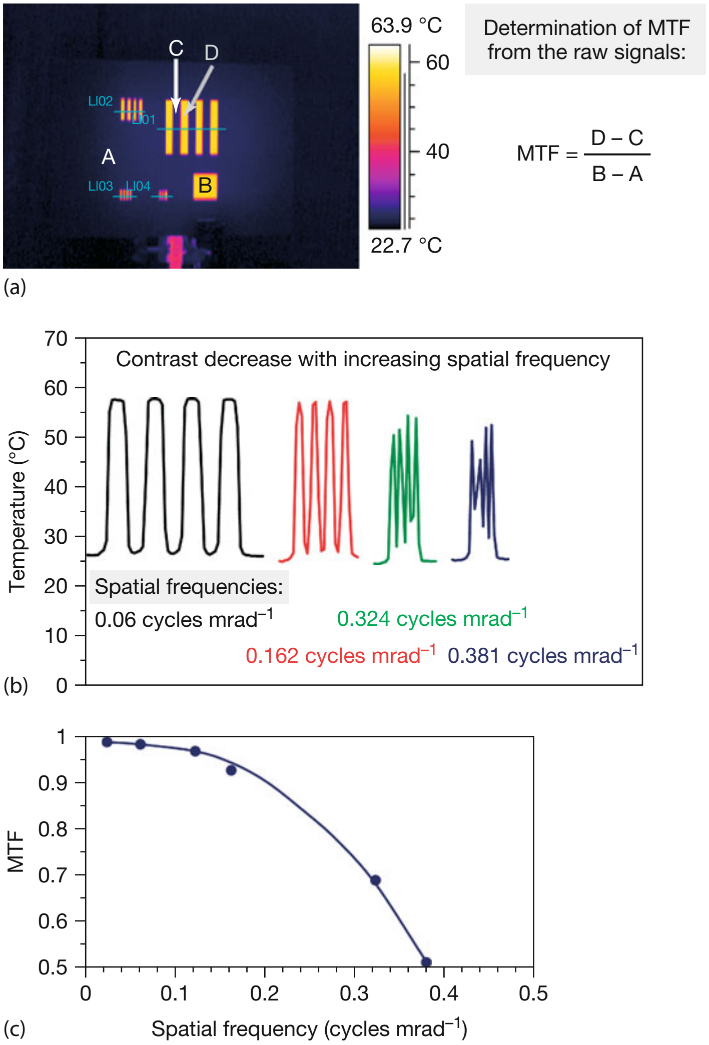

Figure 2.97 Temperature contrast measured at different spatial frequencies. (a) Thermal image of test patterns during measurement (1.2 m measurement distance). (b) Temperature line profiles for different test patterns. (c) Spatial frequency-dependent MTF.

perature differences, lower contrast details cannot be seen. First, the bar target corresponding to the largest spatial frequency can no longer be observed.

Figure 2.100 shows the images that correspond to the individual subjective MRTD of one of the authors for the targets with different spatial frequencies. Using these results, one can get the MRTD dependent on the spatial frequency (number of line pairs per milliradian or cycles per milliradian) for a 24 °C temperature level. We note that the selection is much easier when analyzing the time sequences compared to presenting still images since human perception is very sensitive to changes as a function of time.

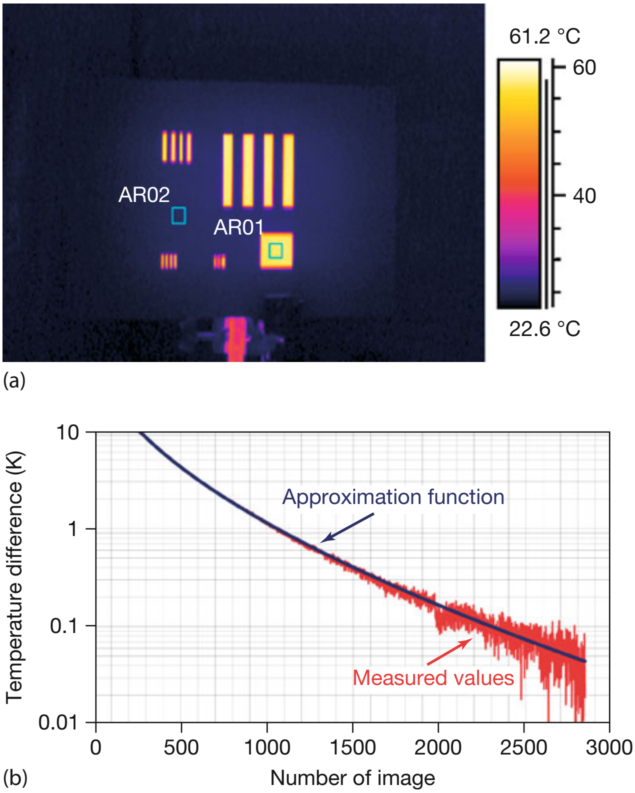

Figure 2.98 MRTD measurement determination of temperature difference between bar target and background.

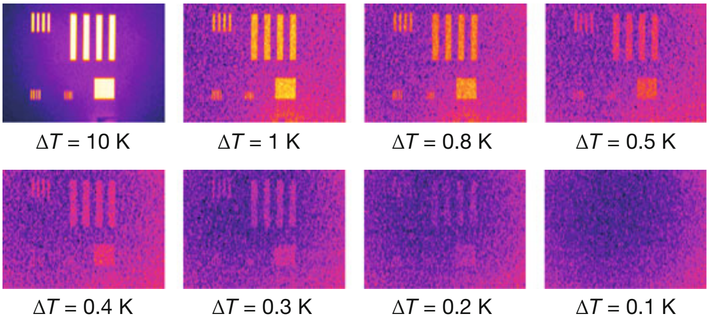

$\Delta T = 10$ K

$\Delta T = 1$ K

$\Delta T = 0.8$ K

$\Delta T = 0.5$ K

$\Delta T = 0.4$ K

$\Delta T = 0.3$ K

$\Delta T = 0.2$ K

$\Delta T = 0.1$ K

Figure 2.99 Images at different temperature differences between bar target and background for a PtSi MW camera.

Because the MRTD is determined not only by the objective parameters (NETD, IFOV) but also by a lot of subjective parameters (observers ability to distinguish between different colors, display quality, etc.), it is important to look for opti-

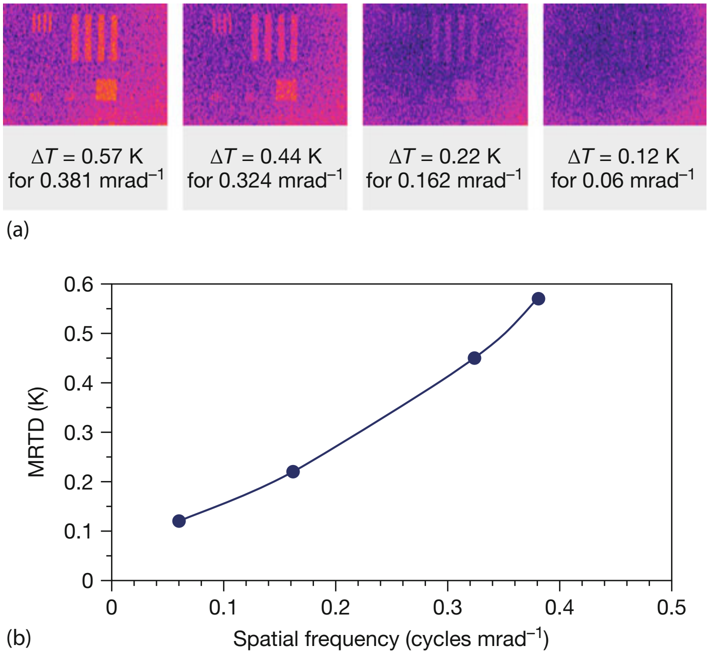

Figure 2.100 (a) Images at temperature differences equal to determined MRTD for different spatial frequencies and (b) determined spatial-frequency dependence of MRTD.

mum camera parameters to get low MRTD values. Figure 2.101 shows the same image using different palettes. The different contrast behavior within the images is clearly demonstrated.

The MRTD result is strongly influenced by the used level and span. Small temperature differences can be detected only if the span and level are set to a maximum color contrast (Figure 2.102).

The MDTD measures the combined ability of a thermal imaging system and an observer to detect a small object. It is the minimum temperature difference between a circular or square object and the background necessary to detect the object. It is measured as MRTD versus the inverse spatial size or the angular size of the object. Figure 2.103 depicts a series of images of a square object with an angular size of 23 mrad during the cooling period.

The individual subjective MDTD for this square object with an inverse angular size of 0.043 mrad^{-1} was determined by one of the authors to be 0.05 K.

The MRTD and MDTD are also very important when estimating the range for the IR camera detection of objects (Section 10.11).

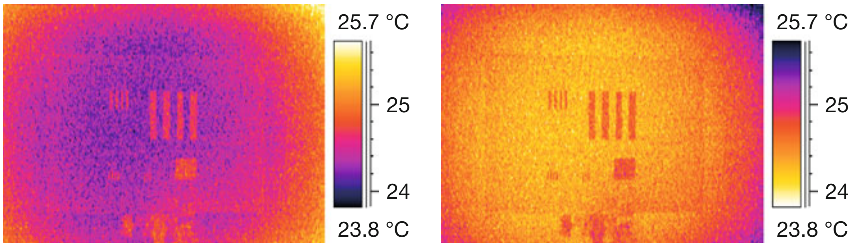

Iron

Iron-inverted scale

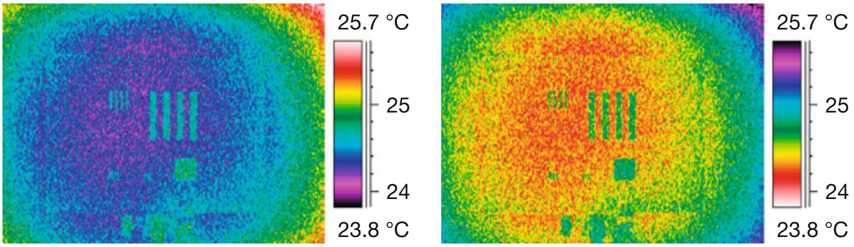

Rain

Rain-inverted scale

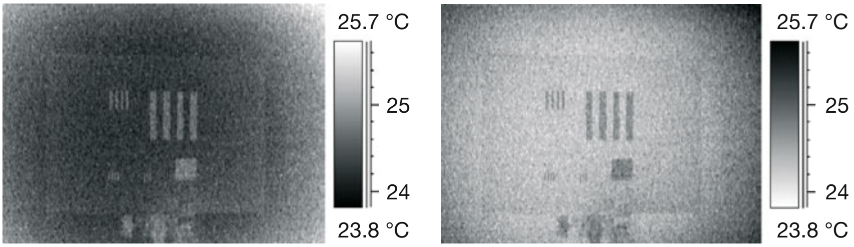

Grey

Grey-inverted scale

Figure 2.101 Image at a temperature difference of 0.5 K using different palettes and auto-adjust scale.

2.5.5
Time Resolution – Frame Rate and Integration Time

The accurate analysis of transient thermal processes requires a sufficient time resolution of thermal imaging compared to the characteristic thermal time constant of the process to be investigated. Most practitioners use bolometer cameras. As described in Section 2.4.2, bolometer cameras usually do not offer the possibility of a selectable integration or exposure time in contrast to photon detector because their time constants are more than a factor of 1000 larger.

In data sheets of imaging systems equipped with bolometer FPAs, the time resolution is usually just characterized by the frame rate as the relevant camera parameter. This value is generally assumed to be connected with the time resolution for the imaging analysis. A simple experiment demonstrates that the frame rate alone will not give the time resolution of a camera. For this experiment, a free-falling

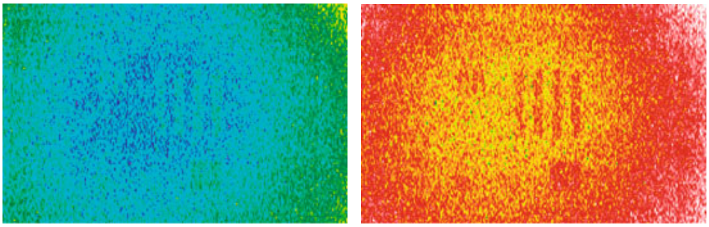

Span 2.5 K, level 24.9 °C

Span 2.5 K, level 24 °C

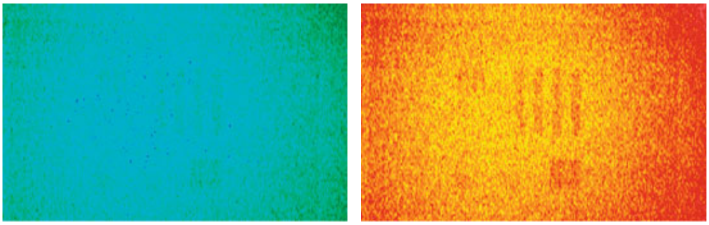

Span 5 K, level 25 °C

Span 5 K, level 23.4 °C

Figure 2.102 Image at a temperature difference of 0.2 K with different level and span adjustment for rain palette.

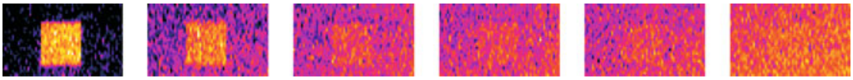

$\Delta T = 1$ K

$\Delta T = 0.5$ K

$\Delta T = 0.2$ K

$\Delta T = 0.1$ K

$\Delta T = 0.08$ K

$\Delta T = 0.05$ K

Figure 2.103 Images at different temperature differences between a square object of 23 mrad angular size and the background.

rubber ball 3 cm in diameter was used. The rubber ball was heated to about 70 °C. Starting at a height of 1 m above the ground, the free-falling ball was analyzed by thermal imaging with IR cameras for an object distance of about 4 m. Figure 2.104 depicts the results of the measurement using a FLIR SC2000 bolometer camera and an InSb camera FLIR SC6000 (photon detector camera with selectable integration time) both operating at a frame rate of 50 Hz.

With increasing velocity of the ball during the free-fall motion, the FLIR SC2000 image of the ball becomes blurred due to the increasing speed of the ball.

The time dependence of the measured ball temperature during the movement of the ball can be analyzed. The ball, with a temperature of about 70 °C, always exhibits the maximum temperature in the IR image. Figure 2.105 depicts the measured ball temperature during the movement of the ball. The measured temperature decreases with increasing ball velocity until the ball hits the ground. After bouncing off the ground, the velocity of the ball decreases and the determined temperature increases to about the actual ball temperature measured at the top, where the ball is at rest. This process of measured temperature change recurs during the periodic down and up movement of the bouncing ball. The correct ball temperature can only be determined when the ball is at rest. From these results it

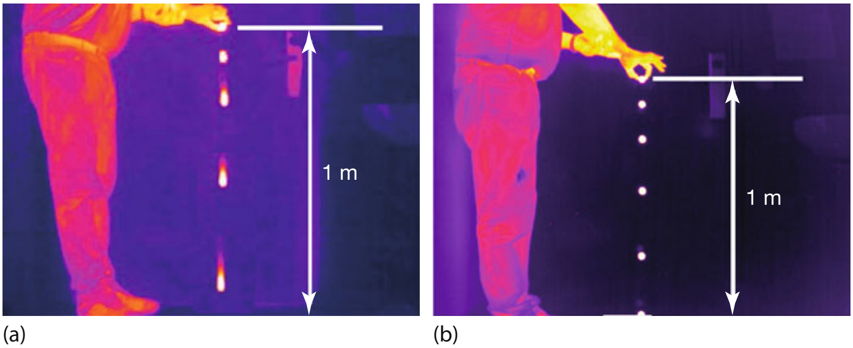

Figure 2.104 Thermograms at 50 Hz frame rates of a free-falling ball (heated to a temperature of 70 °C, starting at a height of 1 m) measured with a LW bolometer camera FLIR SC2000 (a) and a MW InSb camera FLIR SC6000 with 1 ms integration time (b).

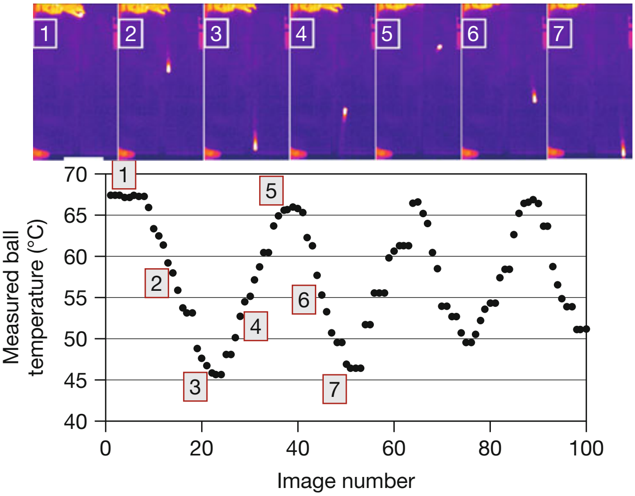

Figure 2.105 Measured temperature of free-falling ball with LW bolometer camera.

can be concluded that the analysis of transient thermal processes or temperatures from moving objects for bolometer cameras requires a detailed investigation of the camera limits given by the thermal detector time constant. For photon detector cameras, the selectable integration time must be adjusted to the process to be analyzed.

The large camera response time causes another result. The blurring of the image of the ball also shows that the IR image will not reflect the real spatial temperature distribution. This can be discussed in more detail using the temperature distribution in the thermal image connected with the movement of the ball. Figure 2.106 illustrates the results of a temperature profile measurement along the falling line of the ball, which for this image had already fallen about 92 cm. It is obvious that

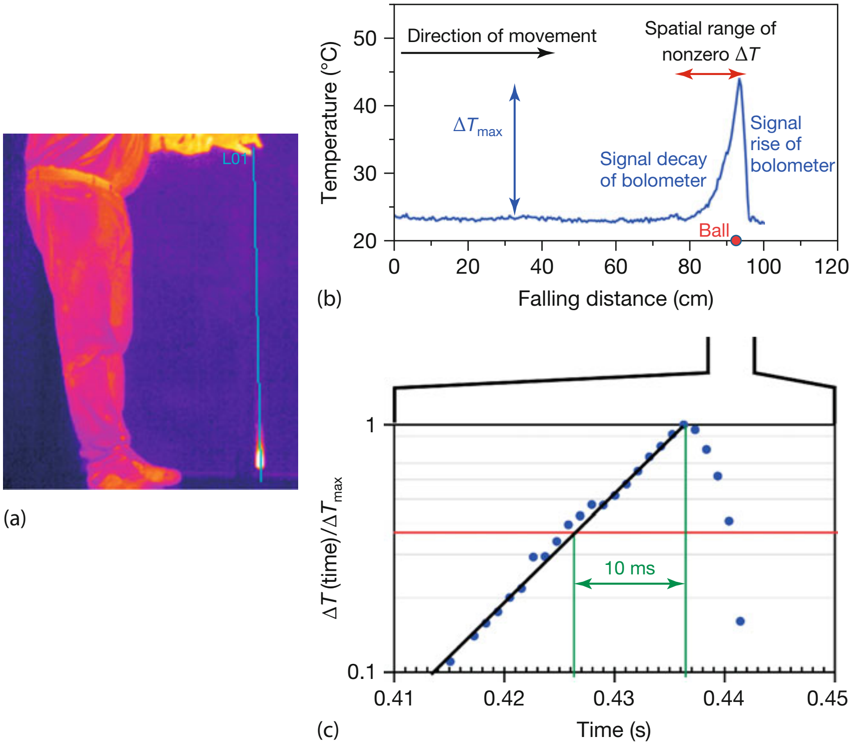

Figure 2.106 Temperature measurement at a free-falling ball (heated up to 70 °C) with LW FLIR SC2000 bolometer camera. Thermal image of falling ball at 93 cm falling height (a). Profile of temperature distribution along line in image (b). Ball size has correct scaling. Time dependence of temperature measured along falling line with timescale calculated from falling distance s using $s = (1/2)gt^2$ (c).

nonzero temperature differences in a 16 cm range of the measured line profile are observed, although the falling ball had a diameter of only 3 cm.

This behavior is caused by the time constant of the bolometer detectors in the FLIR SC2000 camera. Thermal detectors such as bolometers exhibit a time constant within the millisecond range (Section 2.2.3). The measured temperature line profile corresponds to the temperature rise and decay process of the bolometer sensors of the camera. It is not caused by the rolling readout process of the bolometer FPA. If the camera is rotated by 90°, the signal will be essentially the same.

From the falling distance s the speed of the ball v can be calculated using $v = gt$ with gravitational acceleration $g = 9.81\ \mathrm{m\,s^{-2}}$. Therefore, the falling distance shown in Figure 2.106b can be transformed into a timescale using $s = (1/2)gt^2$ (Figure 2.106c).

At the lower end of the ball at the largest falling distance in the IR image, that is, for the largest falling time, the corresponding bolometer detector signal starts to rise owing to IR radiation from the ball. Behind the actual position of the ball

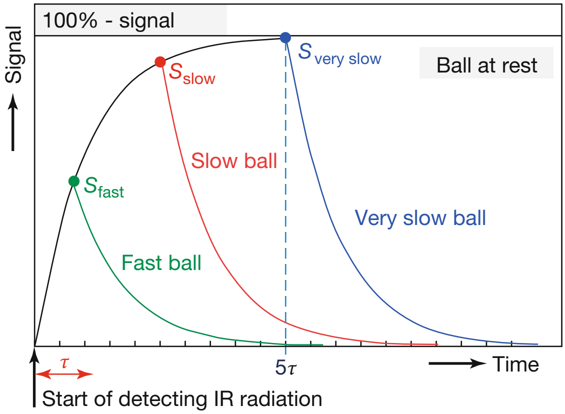

Figure 2.107 Signal rise and decay at bolometer for different speeds v of ball (ball diameter d) compared to bolometer time constant τ-fast ball $d/v < \tau$-slow ball $\tau < d/v < 5\tau$-very slow ball $d/v = 5\tau$.

in the image, that is, at those detectors that no longer receive IR radiation from the ball, there is a drop in the signal characterized by the detector time constant. Therefore, the observed signal decay at the small time side of the signal directly reflects this time constant. Figure 2.106c depicts this detector signal rise and decay. For easier analysis, the signal was normalized to the maximum temperature difference ΔT_{max}. One can estimate an exponential time dependence with a time constant τ of about 10 ms. The time resolution of the camera is limited by this time constant τ.

To get a correct temperature reading with an uncertainty of about 1 °C, one needs at least a 99% signal measurement (Section 2.2.3.1). This corresponds to a measurement time of $5\tau = 50$ ms. At a frame rate of 50 Hz, an image is recorded every 20 ms, but the detector responds more slowly to temperature changes. Therefore, not only is the image of the falling ball blurred but also the measured temperature of the falling ball will be incorrect (Figures 2.105 and 2.106). At a falling distance of 93 cm, the ball has a speed of $4.27\ \text{m}\,\text{s}^{-1}$. Therefore, a pixel receives thermal radiation from the ball for only about 6 ms (1.3 mrad IFOV, 4 m measurement distance, and a ball diameter of 3 cm), which is usually less than the time constant of the bolometer. As a consequence, the maximum signal is much lower than the 100% correct signal (Figure 2.107). Furthermore, the single bolometer signal itself from a 6 ms time window cannot be accurately analyzed since it also depends on the quality of the optics. Because of the extended λ range, aberrations of the lenses may introduce additional uncertainties. Therefore, the signal rise of the bolometer close to the end of the ball should not be analyzed quantitatively. In contrast, the signal decay is only governed by the time constant of the detector.

It is possible to derive a condition for correct temperature measurement that depends on the object speed and size. It represents the combination of time and spatial resolution of the camera. If we require a measurement time of 5τ to get a 99% measurement signal, an object length l_{object}, and the length l_{IFOV} determined by the camera IFOV in the object plane, the object speed is limited to

$$v_{\text{object}} \leq \frac{l_{\text{object}} - l_{\text{IFOV}}}{5\tau} \tag{2.60}$$

At higher object speeds the image can show a significant blurring effect and a corresponding temperature measurement error. Only for well-defined conditions does image processing allow one to reduce the blurring in the images and calculate the correct object temperatures (Section 3.5.2.6).

For InSb photon detectors of the FLIR SC6000, the detector time constants are much lower (nanoseconds to microseconds), and so these detectors respond much faster. For the FLIR SC6000 variable, integration time settings from 9 μs to full frame time are possible. For the experiment with the falling ball (Figure 2.106) an integration time of 1 ms was used. No blurring of the image of the ball is observed, and the temperature of the ball can be correctly determined over the whole falling distance.

References

1 Hudson, R.D. and Hudson, J.W. (eds) (1975) *Infrared Detectors*, John Wiley & Sons, Inc., Dowden, Hutchinson, and Ross.

2 Lutz, G. (1999) *Semiconductor Radiation Detectors*, Springer, Berlin, Heidelberg, New York.

3 Dereniak, E.L. and Boreman, G.D. (1996) *Infrared Detectors and Systems*, John Wiley & Sons, Inc.

4 Wolfe, W.L. and Zissis G.J. (Eds) (1993) *The Infrared Handbook*, Infrared Information Analysis Center, Environmental Research Institute of Michigan.

5 Kingston, R.H. (1978) *Detection of optical and infrared radiation*, Springer Series in Optical Sciences, Springer, Berlin, Heidelberg, New York.

6 Rogalski, A. (2012) Review: Progress in focal plane array technologies. *Progr. Quant. Electron.*, **36**, 342–473.

7 Li, B., Huang, S., and Zhang, X. (2004) Transient mechanical and electrical properties of uncooled resistive microbolometer focal plane arrays, Infrared detector materials and devices. Proc. SPIE, vol. 5564, 123–132.

8 Budzier, H. and Gerlach, G. (2011) *Thermal Infrared Sensors*, John Wiley & Sons, Chichester.

9 Budzier, H. and Gerlach, G. (2015) Calibration of uncooled thermal infrared cameras. *J. Sens. Sens. Syst.*, **4**, 187–197, doi:10.5194/jsss-4-187-2015.

10 Tempelhahn, A., Budzier, H., Krause, V., and Gerlach, G. (2016) Shutter-less calibration of uncooled infrared cameras. *J. Sens. Sens. Syst.*, **5**, 9–16, doi:10.5194/jsss-5-9-2016.

11 Bonani, F. and Ghigne, G. (2001) *Noise in Semiconductor Devices*, Springer, Berlin, Heidelberg, New York.

12 Capper, P. and Elliot, C.T. (Eds) (2001) *Infrared Detectors and Emitters: Material and Devices*, Kluwer Academic Publishers.

13 Gunapala, S., Bandara, S., Bock, J., Ressler, M., Liu, J., Mumolo, J., Rafol, S., Werner, M., and Cardimona, D. (2002) GaAs/AlGaAs based multi-quantum well infrared detector arrays for low-background applications. Proc. SPIE, vol. 4823, 80–87.

14 Hudson, R.D. (1969) *Infrared Systems Engineering*, John Wiley & Sons, Inc.

15 Ryzhii, V. (2003) *Intersubband Infrared Photodetectors*, Selected Topics in Electronics and Systems, vol. 27, World Scientific Publishing Co. Pvt. Ltd.

16 Bandara, S.V., Gunapala, S., Rafol, S., Ting, D., Liu, J., Mugolo, J., Trinh, T., Liu, A.W.K., and Fastenau, J.M. (2001) Quantum well infrared photodetectors for low background applications. *Infrared Phys. Technol.*, **42** (3–5), 237–242.

17 Rogalski, A. (1994) GaAs/AlGaAs quantum well infrared photoconductors versus HgCdTe photodiodes for long-wavelength infrared applications. Proc. SPIE, vol. 2225, 118–129.

18 Soibel, A., Bandara, S., Ting, D., Liu, J., Mumolo, J., Rafol, S., Johnson, W., Wilson, D., and Gunapala, S. (2009) A super-pixel QWIP focal plane array for imaging multiple waveband sensor. *Infrared Phys. Technol.*, **52** (6), 403–407.

19 Simolon, B., Aziz, N., Cogan, S., Kurth, E., Lam, S., Petronio, S., Woolaway, J., Bandara, S., Gunapala, S., and Mumolo, J. (2009) High performance two-color one megapixel cmos roic for qwip detectors. *Infrared Phys. Technol.*, **52** (6), 391–394.

20 Rogalski, A. (2012) Progress in focal plane array technologies. *Progr. Quant. Electron.*, **36**, 342–473

21 Martyniuk, P. and Rogalski, A. (2013) HOT infrared detectors. *Opto-Electron. Rev.*, **21**, 239–257.

22 Martyniuk, P., Gawron, W., Pusz,W., Stanaszek, D., and Rogalski, A. (2014) Modeling of HOT (111) HgCdTe MWIR detector for fast response operation, *Opt. Quant. Electron.*, **46**, 1303–1312.

23 www.sofradir.com/sofradir-boosts-performance-of-high-operating-temperature-hot-infrared-detector/ (accessed May 2017).

24 White, A.M. (1983) Infrared detectors, US Patent 4679063.

25 Martyniuk, P., Kopytko, M., and Rogalski, A. (2014) Barrier infrared detectors. *Opto-Electron. Rev.*, **22** (2), 127–146.

26 Martyniuk, P., Gawron, W., Madejczyk, P., Rogalski, A., and Piotrowski, J. (2013) Modelling of HgCdTe LWIR detector for high operation temperature conditions. *Metrol. Meas. Syst.*, **XX** (2), 159–170.

27 Sai-Halasz, G.A., Tsu, R., and Esaki, L. (1977) A new semiconductor superlattice. *Appl. Phys. Lett.*, **30** (12), 651–653.

28 Plis, E.E. (2014) *InAs/GaSb Type-II Superlattice Detectors*, Advances in Electronics, vol. 2014, Hindawi Publishing Corporation

29 Johnson, J.L., Samoska, L.A., Gossard, A.C., Merz, J.L., Jack, M.D., Chapman, G.H., Baumgratz, B.A., Kosai, K., and Johnson, S.M. (1996) Electrical and optical properties of infrared photodiodes using the InAs/$Ga_{1-x}In_xSb$ superlattice in heterojunctions with GaSb. *J. Appl. Phys.*, **80**, 1116–1127.

30 Wei, Y. and Razeghi, M. (2004) Modeling of type-II InAs/GaSb superlattices using an empirical tight-binding method and interface engineering. *Phys. Rev. B*, **69**, 085316.

31 Klipstein, P.C. (2003) Depletionless photodiode with suppressed dark current, US Patent 7795640, 2 July 2003

32 Klipstein, P.C. (2006) Unipolar semiconductor photodetector with suppressed dark current, US Patent 8004012, 6 April 2006.

33 Klipstein, P., Klin, O., Grossman, S., Snapi, N., Lukomsky, I., Brumer, M., Yassen, M., Aronov, D., Berkowicz, E., Glozman, A., Fishman, T., Magen, O., Shtrichman, I., and Weiss, E. (2011) MWIR InAsSb XBnn detector (bariode) arrays operating at 150 K. Proc. SPIE, vol. 8012 (80122R), doi:10.1117/12.883238.

34 Razeghi, M., Haddadi, A., Hoang, A.M., Huang, E.K., Chen, G., Bogdanov, S., Darvish, S.R., Callewaert, F., and McClintock, R. (2013) Advances in antimonide-based Type-II superlattices for infrared detection and imaging at center for quantum devices. *Infrared Phys. Technol.*, **59**, 41–52.

35 Klipstein, P., Mizrahi, U., Fraenkel, R., and Shtrichman, I. (2013) Status of cooled and uncooled infrared detectors at SCD, Israel. *Def. Sci. J.*, **63** (6), 555–570.

36 Razeghi, M., Pour, S.A., Huang, E., Chen, G., Haddadi, A., and Nguyen, B.-

M. (2011) High operating temperature MWIR photon detectors based on Type II InAs/GaSb superlattice. Proc. SPIE, vol. 8012 (80122Q), doi:10.1117/12.888060.

37 Rehm, R., Schmitz, J., Fleißner, J., Walther, M., Ziegler, J., Cabanski, W., and Breiter, R. (2006) InAs/GaSb type-II superlattices for single- and dual-color focal plane arrays for the mid-infrared spectral range. *Phys. Stat. Solidi (c)*, **3** (3), 435–438.

38 Rehm, R., Walther, M., Schmitz, J., Rutz, F., Fleissner, J., Scheibner, R., and Ziegler, J. (2009) Status of mid-infrared superlattice technology in Germany. Proc. SPIE, vol. 7222, 72220T-1.

39 Rehm, R., Masur, M., Schmitz, J., Daumer, V., Niemasz, J., Vandervelde, T., DeMeo, D., Luppold, W., Wauro, M., Wörl, A., Rutz, F., Scheibner, R., Ziegler, J., and Walther, M. (2013) InAs/GaSb superlattice infrared detectors. *Infrared Phys. Technol.*, **59**, 6–11.

40 Huang, E.K.-W. and Razeghi, M. (2012) World's first demonstration of type-II superlattice dual band 640x512 LWIR focal plane array. Proc. SPIE, vol. 8268, 82680Z-1.

41 http://www.flir.com (accessed May 2017).

42 Schuster, N. and Kolobrodov, V.G. (2000) *Infrarotthermographie*, John Wiley & Sons.

43 DeWitt, D.P. and Nutter, G.D. (1989) *Theory and Practice of Radiation Thermometry*, John Wiley & Sons, Inc.

44 Palik, E.D. (ed.) (1991) *Handbook of Optical Constants of Solids II*, Academic Press, San Diego.

45 Touloukian, Y.S. and DeWitt, D.P. (1970) Thermal radiative properties, in *Thermophysical Properties of Matter*, vol. 7, IFI/Plenum, New York.

46 Tissot, J.L., Trouilleau, C., Fieque, B., Crastes, A., and Legras, O. (2006) Uncooled microbolometer detector: recent developments at ULIS. *Opto-Electron. Rev.*, **14** (1), 25–32.

47 Holst, G.C. (1993) *Testing and Evaluation of Infrared Imaging Systems*, JCD Publishing Company.

48 Holst, G.C. (2000) *Common Sense Approach to Thermal Imaging*, SPIE Press, Bellingham.

49 http://www.laser2000.de (accessed May 2017).

50 http://www.raytek.com (accessed May 2017).

51 http://www.ircon.com (accessed May 2017).

52 Milton, A.F., Barone, F.R., and Kruer, M.R. (1985) Influence of nonuniformity on infrared focal plane array performance. *Opt. Eng.*, **24** (5), 885–862.

53 Lau, J.H. (ed.) (1995) *Flip Chip Technologies*, McGraw-Hill Inc.

54 Kruse, P.W. (2002) *Uncooled Thermal Imaging–Arrays, Systems and Applications*, SPIE Press, Bellingham, Washington.

55 http://www.ulis-ir.com (accessed May 2017).

56 (2009) *The Ultimate Infrared Handbook for R&D Professionals*, FLIR Systems Inc.

57 Rowe, D.M. (ed.) (1995) *CRC Handbook of Thermoelectrics*, CRC Press.

58 Organ, A.J. (2005) *Stirling and Pulse-tube Cryo-coolers*, Professional Engineering Publishing, Antony Rowe Ltd.

59 Chrzanowski, K. (2002) Evaluation of commercial thermal cameras in quality systems. *Opt. Eng.*, **41** (10), 2556–2567.

60 Sousk, S., O'Shea, P., and Van Hodgkin (2004) Measurement of uncooled thermal imager noise. Infrared imaging systems: Design, analysis, modeling and testing XV. SPIE, vol. 5407, 1–7.

61 Levesque, P., Brémond, P., Lasserre, J.-L., Paupert, A., and Balageas, D.L. (2005) Performance of FPA IR cameras and their improvement by time, space and data processing. *QUIRT-Quant. Infrared Thermogr. J.*, **2** (1), 97–111.

62 ASTM E 1213-2002 (2002) Standard test method for minimum resolvable temperature difference for thermal imaging systems.

63 ASTM E 1311-2002 (2002) Standard test method for minimum detectable temperature difference for thermal imaging systems.

Chapter 3
Advanced Methods in IR Imaging

3.1
Introduction

This chapter gives a brief overview of some advanced methods used in IR thermal imaging. Compared to the basic methods of recording and manipulation of infrared (IR) images, for example, by the adjustment of measurement parameters (Chapter 2), these methods contain additional features for data collection and data processing. Examples are the use of additional components such as narrowband spectral filters, the application of heat sources for thermal stimulation of the investigated object, the use of polarization of the IR radiation, or various image-processing tools.

3.2
Spectrally Resolved Infrared Thermal Imaging

IR thermal imaging is a spectral measurement within limited bands (SW, MW, LW) of the electromagnetic spectrum (Chapter 1). The image results from the integration of all spectral signal contributions within the band used, that is, 0.9–1.7 μm (SW), 3–5 μm (MW), or 8–14 μm (LW).

The use of wide spectral bands increases the object radiance detected by a camera and enables the measurement of objects with low temperatures at room temperature or lower with good signal-to-noise ratio (SNR) (Chapter 2).

Reducing the spectral bandwidth is particularly useful when dealing with nongray, that is, spectrally selective emitters with $\varepsilon = \varepsilon(\lambda)$ (Figure 1.27). For such objects, broadband detection must first deal with the problem of a reasonable assumption for the average value of ε within the chosen IR band. Second, for some selective emitters such as gases, only a tiny part of the spectrum is used and broadband detection automatically leads to a poor signal-to-background ratio (Section 8.3, Figure 8.7).

In contrast, spectrally resolved IR thermal imaging will have the advantage of, first, a better-defined emissivity owing to the reduced bandwidth, which will make it possible to also quantitatively characterize spectrally selective emitters such as

Infrared Thermal Imaging, Second Edition. M. Vollmer and K.-P. Möllmann.
© 2018 WILEY-VCH Verlag GmbH & Co. KGaA. Published 2018 by WILEY-VCH Verlag GmbH & Co. KGaA.

plastics (Section 10.2). Second, for gases, it can drastically increase the signal-to-background ratio by only detecting signal changes in the relevant part of the spectrum (Chapter 8). Narrow spectral-band and dual-band measurements using pyrometry have already been successfully applied for a long time. They allow, for example, radiation thermometry in steel and glass production or plastics processing [1], that is, in cases where product temperature is the most critical operating parameter during manufacturing.

The most advanced spectrally resolved thermal imaging techniques combine the spatially resolved measurements of an IR camera with IR spectroscopy, ultimately allowing measurements for each individual pixel.

3.2.1
Using Filters

The use of spectral bandpass (BP) or narrow bandpass (NBP) filters (Section 2.4.4) is the easiest way to perform spectrally resolved IR thermal imaging. A large variety of these NBP and BP filters covering the complete spectral region from the SW to the LW IR are available [2]. Usually, research and development (R&D) cameras offer the possibility to mount an additional spectral filter between the camera lens and the detector (Figure 3.1). These filters mostly exhibit the same temperature as the optics, hence they are called *warm filters*. They should be made from nonabsorbing materials to prevent self-heating and radiation emission toward the detector. They block radiation transmission outside the spectral BP by reflection using interference from a thin layer of IR-transparent films (alternating layers) made from different materials with different refractive indices (Section 1.6).

For some applications such as GasFind cameras (Chapter 8) cold filters with temperatures close or equal to the detector temperature are used to increase the sensitivity by avoiding self-radiation of the filter and by blocking the radiation from warm parts of the camera. These cold filters form an integral part of the cold detector engine of the camera, as depicted in Figure 3.1b for a GasFind camera.

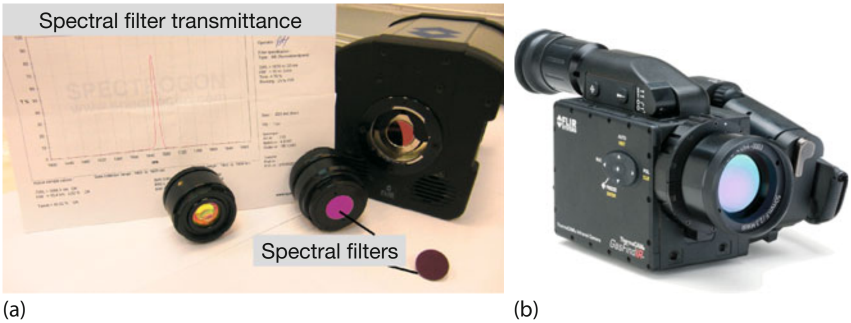

(a) (b)

Figure 3.1 MW cameras for operation with spectral filters. (a) FLIR SC6000 camera. The warm filters can be mounted between the camera lens and the window of the detector housing. (b) FLIR GasFindIR GF300 camera with cold filter. (Image for (b) courtesy FLIR Infrared Training Center.)

Some research cameras that can house more than four cold filters are available with wheels. Cold filters may be made from partially absorbing materials in the used camera range.

3.2.1.1 Glass Filters

Narrow spectral band thermal imaging using filters can be applied to analyze the temperature and temperature distribution of selective emitters, for example, glass. Thermal images obtained using glass filters are depicted in Figure 3.2 using a MW camera (3–5 μm).

Glasses are characterized by transparency from the visible to the near-IR region. At about 2 μm wavelength many glasses become semitransparent because of absorption and opaque between 3 μm and at most about 5 μm (Figure 3.2, for details see [3]). Transmission as a function of wavelength varies with glass composition and depends on glass thickness (Section 1.5.4 and Figure 1.53). Therefore, measurement of the temperatures of the glass itself (rather than of objects behind it) by radiation thermometry requires the application of a spectral filter with nar-

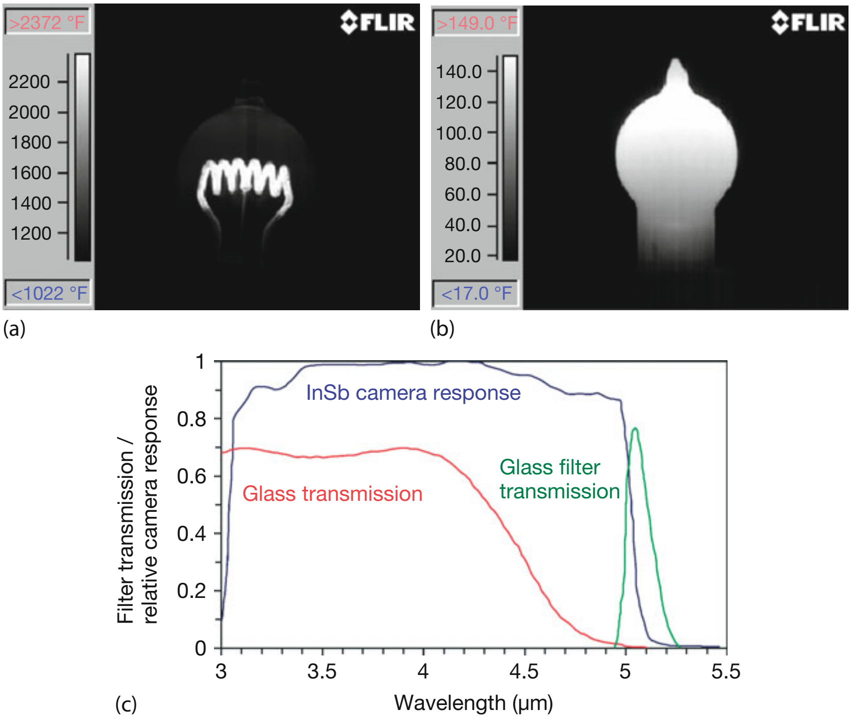

Figure 3.2 Application of a glass spectral filter to eliminate transparency for correct temperature measurement of glass itself. (a) Thermal image in MW region of a light bulb in operation without additional spectral filtering, (b) thermal image in the MW region of the light bulb with an additional spectral glass filter, and (c) comparison of InSb MW camera spectral sensitivity distribution and transmission spectra of glass (exemplary) and the used glass spectral filter. (Image courtesy FLIR Infrared Training Center.)

rowband transmission above 5 μm. However, the spectral response of detectors like InSb used in the MW, strongly decreases for $\lambda > 5$ μm. Furthermore, absorption due to water vapor strongly affects atmospheric transmission above 5 μm, where glass is opaque. Obviously, a compromise must be found. The spectral filters commonly used are transparent in the 5–5.2 μm region.

Figure 3.2a depicts an example of a light bulb that was analyzed during operation. In broadband mode (or using a filter at $\lambda < 4$ μm), the glass transmits a large part of the radiation. Therefore, the camera looks through it and the hot filament is clearly seen. The measured temperatures do not accurately resemble the filament temperature unless the proper attenuation owing to glass transmission is taken into account.

With a narrowband glass filter, the camera only detects radiation from the bulb because the glass is opaque in this spectral region. The temperature scale in Figure 3.2b refers to camera calibration without the filter. Therefore, correct temperature readings require a recalibration of the camera with the filter (Section 2.4.4).

The question might arise as to why one would not measure glass temperatures with LW cameras. Glasses are characterized by large absorption coefficients in the LW spectral band. The absorption coefficient at $\lambda = 8$ μm is about $5.1 \cdot 10^3$ cm^{-1} [4], that is, that glass becomes opaque for very small thicknesses in the micrometer range. This is associated with a significant reflectivity R in neighboring spectral regions of up to about 30% at 9.5 μm (Figure 3.3). Glass obviously represents a selective emitter in the LW spectral range, and an accurate 8–14 μm broadband measurement is not possible unless the correct average emissivity value $\varepsilon = 1 - R$ is known. In Figure 3.3 the average value would be around 0.87 (i.e., reflectivity around 0.13) for a boxcar model of detector sensitivity.

However, rather than using a broadband detecting LW camera, one can also use a NBP filter. Minimum reflectivity occurs at the short-wave edge of the LW spectral range at 7.9 μm. At this wavelength glass, with an emissivity larger than 0.99, is almost a perfect blackbody. Furthermore, at 7.9 μm the atmospheric transmission is only weakly influenced by water vapor (Figure 1.54). This may explain why one

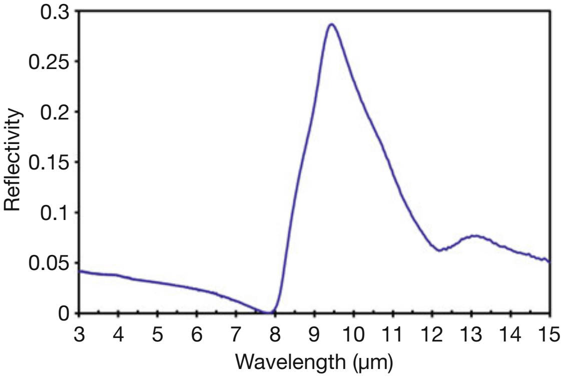

Figure 3.3 Spectrally dependent reflectivity of glass.

IR camera manufacturer (Optris GmbH, Berlin, Germany) offers a thermal imager for industrial glass temperature measurements at 7.9 μm based on a bolometer array detector with a narrow spectral band filter. LW bolometer arrays are sensitive to IR radiation at 7.9 μm (Figure 2.83). The Optris PI 450 G7 IR camera (for details see [5]) has 382 × 288 pixels, a measurement range of 200–1500 °C, a noise equivalent temperature difference (NETD) of 0.13 K at 650 °C object temperature and can be operated in line scan function mode for industrial band processes.

Note that throughout this book we use conventional values of 3–5 μm for MW and 8–14 μm for the LW IR range. Real detector sensitivities extend slightly beyond these ranges such that a LW camera detector may well detect radiation at 7.9 μm (Figure 2.83).

3.2.1.2 Plastic Filters

Plastic films are typical examples of selective emitters. Being organic molecules, most polymers have carbon-hydrogen (C–H) bonds and exhibit the fundamental C–H absorption band around 3.4 μm (see Figure 3.4 and the discussion of Gas-

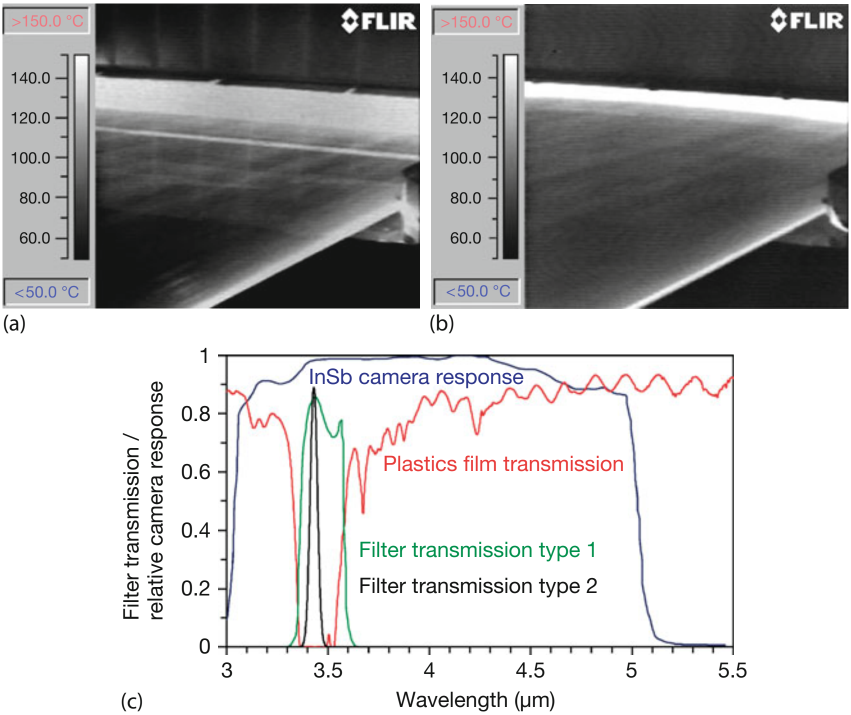

Figure 3.4 Application of a plastic spectral filter for correct temperature measurements with MW cameras. (a) Thermal image of a plastic film with broadband detection, (b) thermal image of a plastic film with an additional spectral plastics filter, and (c) comparison of InSb MW camera spectral sensitivity distribution and transmission spectra of polyethylene plastic film and spectral filters made of two different plastics. (Image courtesy FLIR Infrared Training Center.)

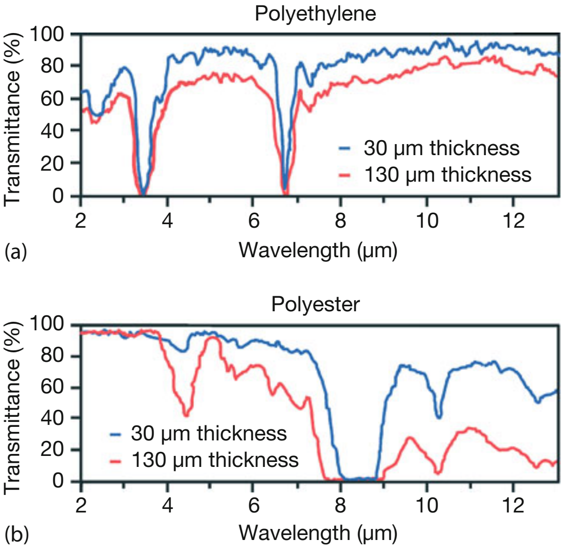

Figure 3.5 Spectral transmittance of polyethylene (a) and polyester (b) films with different thicknesses, showing strong absorption bands at around 6.7 μm (a) and 8.3 μm (b). (Image courtesy Fluke Process Instruments GmbH Berlin, Germany; www.flukeprocessinstruments.de.)

Find cameras in Chapter 8). At this wavelength plastic films become opaque and reach high emissivity values depending on the film thickness. However, the plastic film absorption only covers a small part of the spectral response region of the camera. Therefore, without spectral filtering, the camera will mostly look through the plastic film, and its temperature cannot be measured (see also Section 10.8). Since absorption bandwidth varies with film thickness, measurements depend on the spectral filter width. If it is too large, as shown for filter type 1 in Figure 3.4, the camera signal will strongly change with changing film thickness.

For a NBP filter, measurements are more accurate unless the plastic film is too thin, that is, not completely opaque at the respective wavelength. For some plastics, such as polyester and other ester-related polymers, there is also a strong carbon–oxygen (C–O) stretching band around 8.3 μm in the LW region that can be used for radiation thermometry [1] with thermal detectors in pyrometers or cameras (Figure 3.5).

Another very popular thermal imaging application with spectral filters is the detection of gases. This will be discussed at length in Chapter 8.

3.2.1.3 Influence of Filters on Object Signal and NETD

The use of spectral filters will decrease the SNR and, consequently, increase the NETD. Therefore, the application of NBP filters requires sufficiently high object temperatures. This situation is exemplarily analyzed for the NBP plastic filters such as the type 2 kind in Figure 3.4, with a maximum transmittance of 89% at $\lambda = 3.43$ μm. Figure 3.6 depicts the ratio of the signal for a MW camera and NBP

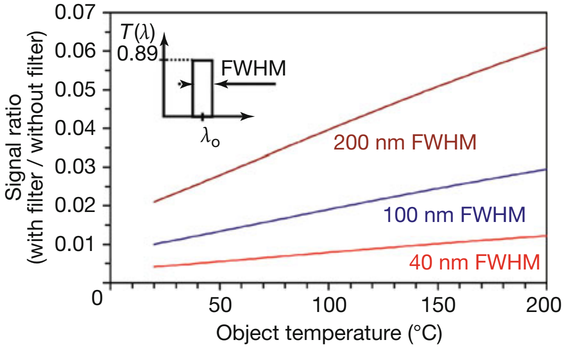

Figure 3.6 Signal ratio for MW camera operated with and without narrow BP spectral filter at 3.43 μm with different FWHM (see inset).

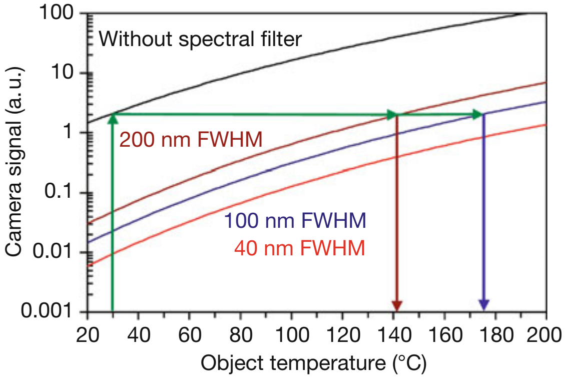

Figure 3.7 Object-temperature-dependent signal for MW camera with different 3.43 μm spectral filters.

filter with respect to the signal without filter as a function of object temperature for different bandwidths (full width at half-maximum, FWHM) of the filter. Similarly, Figure 3.7 depicts the camera signals themselves for the different filter configurations.

As expected, the signals increase with the FWHM of the filters. For simplicity, theoretical signals were computed for top-hat filter transmission curves and a constant detector sensitivity was assumed for the 3–5 μm spectral range.

For a 100 nm FWHM with a maximum transmittance of 89%, the signal drops by a factor of about 100 at a 20 °C object temperature and 50 at 120 °C. Consequently, the NETD is increased by this factor, that is, if the NETD without filter is 25 mK, it increases to ≈ 2.5 K at 20 °C and ≈ 1.25 K for 120 °C.

Figure 3.7 can be used to determine either the minimum object temperature necessary for the same camera signal or the NETD compared to the camera operation without the spectral filter. The camera signal at a 30 °C object temperature is equivalent to that with a 200 nm FWHM filter at 141 °C and for the 100 nm filter at 175 °C. If a 40 nm FWHM filter is used, the necessary object temperature is above 220 °C.

3.2.2
Two-Color or Ratio Thermography

A thermal image results from both the radiance emitted from an object and the radiance reflected from the object because of the surroundings. For large ε values, reflection contributions of opaque objects are small. However, objects like metals with very low emissivities pose problems since emitted radiance is low and reflected radiance is high. Therefore, many approaches have been proposed to develop a so-called emissivity-free radiation thermometry [1]. One of the ideas is to measure the radiance within two or more narrow spectral bands and determine the object temperature from the signal ratio [6–8] while at the same time eliminating the influence of the emissivity under certain conditions.

In what follows, we initially assume measurements at two monochromatic wavelengths. If spectral bands are used, the monochromatic radiance values must be replaced by the integral of the corresponding spectral radiance densities (see Eq. (3.13) and others in what follows).

Neglecting a possible signal reduction owing to atmospheric transmission along the path (short measurement path $\tau_{\text{atm}} = 1$) for the radiance L_{inc} incident on the detector at wavelength λ, object temperature T_{obj}, object emissivity ε_{obj}, and background temperature T_{bgr}, we assume (cf. Eq. (2.37a))

$$L_{\text{inc}}(\lambda) = \varepsilon_{\text{obj}}(\lambda, T_{\text{obj}}) L_{\text{BB}}(\lambda, T_{\text{obj}}) + (1 - \varepsilon_{\text{obj}}(\lambda, T_{\text{obj}})) L_{\text{BB}}(\lambda, T_{\text{bgr}}) \tag{3.1}$$

If the radiance is measured at two different wavelengths ($\lambda_2 > \lambda_1$), the ratio can be determined as follows:

$$\frac{L_{\text{inc}}(\lambda_2)}{L_{\text{inc}}(\lambda_1)} = \frac{\varepsilon_{\text{obj}}(\lambda_2, T_{\text{obj}}) L_{\text{BB}}(\lambda_2, T_{\text{obj}}) + (1 - \varepsilon_{\text{obj}}(\lambda_2, T_{\text{obj}})) L_{\text{BB}}(\lambda_2, T_{\text{bgr}})}{\varepsilon_{\text{obj}}(\lambda_1, T_{\text{obj}}) L_{\text{BB}}(\lambda_1, T_{\text{obj}}) + (1 - \varepsilon_{\text{obj}}(\lambda_1, T_{\text{obj}})) L_{\text{BB}}(\lambda_1, T_{\text{bgr}})} \tag{3.2}$$

The emissivity can affect the ratio of Eq. (3.2) via two different effects. First, the absolute value of ε is significant for the relative importance of the reflected background radiance. Second, the wavelength-dependent variation of ε may lead to considerable differences between the radiance contribution at λ_1 and λ_2. We deal with both topics separately in this chapter.

The ratio given by Eq. (3.2) generally exhibits a complex relation between the signals at the two wavelengths and will not allow a simple object-temperature determination. For certain conditions, however, the analysis can be simplified. The simplest result is obtained if, first, the reflected background contributions can be neglected with respect to the object radiation, and second, the objects are true gray bodies, that is, $\varepsilon_{\text{obj}}(\lambda_1, T_{\text{obj}}) = \varepsilon_{\text{obj}}(\lambda_2, T_{\text{obj}})$. In this case, the ratio

$$\frac{L_{\text{inc}}(\lambda_2)}{L_{\text{inc}}(\lambda_1)} = \frac{L_{\text{BB}}(\lambda_2, T_{\text{obj}})}{L_{\text{BB}}(\lambda_1, T_{\text{obj}})} = \frac{\lambda_1^5}{\lambda_2^5} \frac{\mathrm{e}^{\frac{hc}{\lambda_1 k T_{\text{obj}}}} - 1}{\mathrm{e}^{\frac{hc}{\lambda_2 k T_{\text{obj}}}} - 1} \tag{3.3}$$

is independent of the emissivity and depends only on the chosen wavelengths and the object temperature.

For a given object temperature the accuracy of the temperature determination according to Eq. (3.3) will depend on $\partial L/\partial\lambda$, that is, on how the object signal changes with wavelength. If $\partial L/\partial\lambda$ is large, the signal ratio will change considerably. In addition, however, the ratio does also depend on the object temperature itself. Therefore, to find the condition for the largest signal ratio change, that is, the largest sensitivity of the ratio method, we must find the largest change in $\partial L/\partial\lambda$ with object temperature, that is, we look for the maximum of $\partial/\partial T(\partial L/\partial\lambda)$. This quantity represents the second derivative of the object radiance $(\partial^2 L_{\text{BB}}(\lambda, T))/(\partial\lambda\partial T)$ depicted in Figure 3.8 for six different object temperatures in a range from 25 to 1000 °C as a function of λT_{obj}. $(\partial^2 L_{\text{BB}}(\lambda, T))/(\partial\lambda\partial T)$ has its maximum value at $\lambda T_{\text{obj}} \approx 1500$ μm K (broken green line), that is, one can expect the most sensitive measurements with the ratio method around this λT value. This may be compared to the largest radiance values of the Planck curves defined by Wien's displacement law. In the wavelength representation, they occur at $\lambda T_{\text{obj}} \approx 2900$ μm K (broken red line). At room temperature (300 K), radiance maxima are around $\lambda = 10$ μm, whereas the most sensitive ratio occurs for about $\lambda = 5$ μm, that is, short-wavelength measurements are advantageous.

In what follows, we will discuss the three major sources of error for the determination of object temperatures from Eq. (3.3) and estimate its range of validity. First, there can be errors as a result of the influence of reflected background radiation. Even if reflected radiation can be neglected, Eq. (3.3) is usually simplified for the analysis of T_{obj} by replacing Planck's law with the so-called Wien approximation. This leads, second, to wavelength-dependent errors even for true gray bodies. Third, any unknown additional variation of emissivity between the two chosen wavelengths λ_1 and λ_2 can lead to very large measurement errors for the resulting object temperatures. We will give critical emissivity and object temperature values above which the approximation of Eq. (3.3) holds.

3.2.2.1 **Neglecting Background Reflections**

The transition from Eq. (3.2) to Eq. (3.3) is nontrivial. For small ε_{obj} values, it follows from Eq. (3.2) that if the reflected radiation cannot be neglected even for objects with true gray-body behavior $\varepsilon_{\text{obj}}(\lambda_1, T_{\text{obj}}) = \varepsilon_{\text{obj}}(\lambda_2, T_{\text{obj}})$, the measured ratio is not independent of the emissivity. Figure 3.9 depicts the wavelength-dependent ratio of emitted object radiance and reflected background radiance for a background temperature of 27 °C at different object temperatures and emissivities. The ratio is strongly decreasing with increasing wavelength. Low object emissivities require a measurement at short wavelengths to obtain an insignificant error if the reflected background radiance is to be neglected. A useful measure is

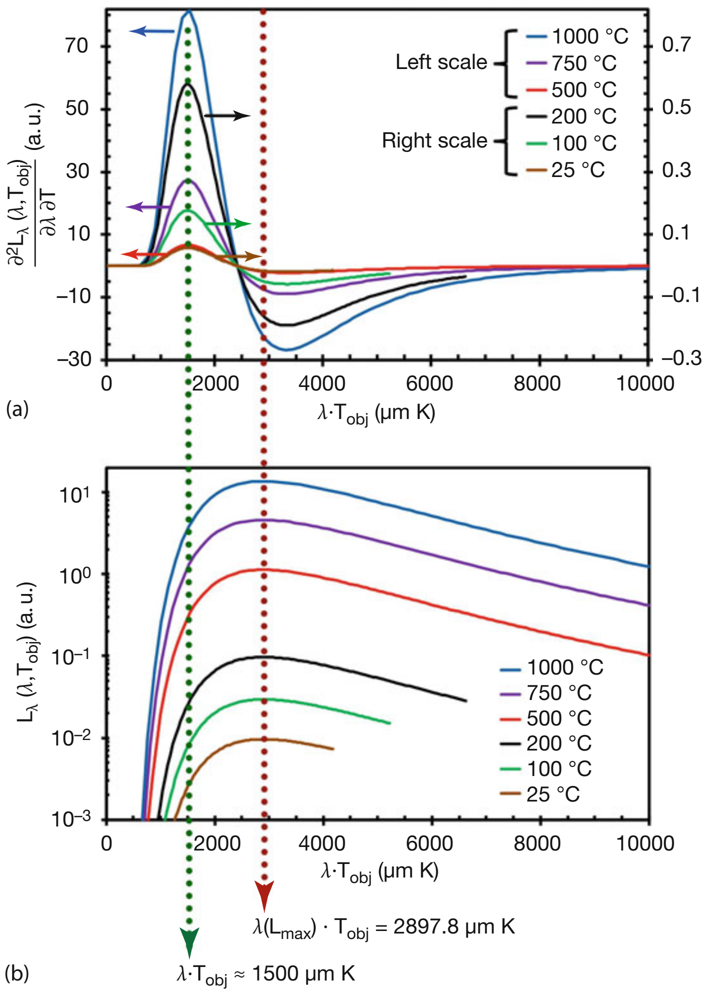

Figure 3.8 Second derivative of object blackbody radiance (a) and corresponding object radiance (b) as a function of $\lambda \cdot T_{\mathrm{obj}}$ for different object temperatures. The broken lines indicate the positions of maximum signals.

that $L_{\mathrm{obj}}/L_{\mathrm{bgr}} > 100$. In this case, typical errors by reducing Eq. (3.2) to Eq. (3.4)

$$\frac{L_{\mathrm{inc}}(\lambda_2)}{L_{\mathrm{inc}}(\lambda_1)} = \frac{\varepsilon_{\mathrm{obj}}(\lambda_2, T_{\mathrm{obj}})L_{\mathrm{BB}}(\lambda_2, T_{\mathrm{obj}})}{\varepsilon_{\mathrm{obj}}(\lambda_1, T_{\mathrm{obj}})L_{\mathrm{BB}}(\lambda_1, T_{\mathrm{obj}})} \tag{3.4}$$

will be on the order of a few percent only. The dotted lines in Figure 3.9 refer to this criterion.

Consider, for example, an object emissivity of 0.02. At a 200 °C object temperature, the measurement wavelengths need to be below 2 μm, whereas higher temperatures of 500 or 1000 °C weaken the constraint to wavelengths below 3.5 and

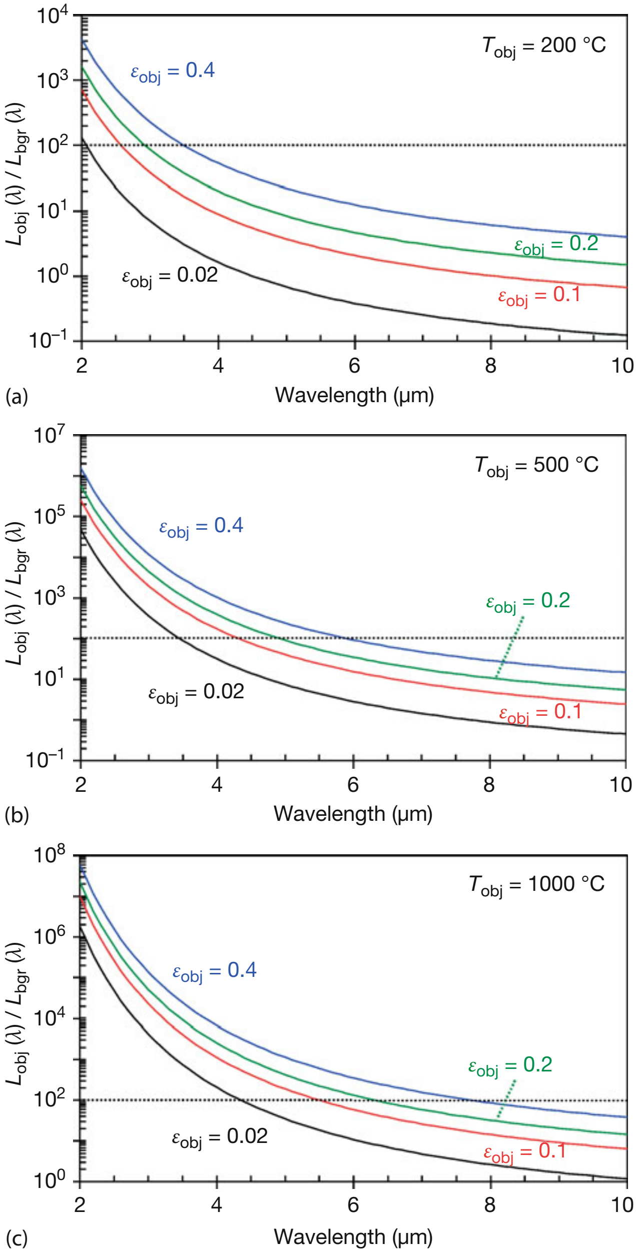

Figure 3.9 Ratio of emitted object radiance to reflected background radiance as a function of wavelength for different object emissivities at different object temperatures and a 27 °C background (300 K).

4.5 μm, respectively. If an object with $\varepsilon = 0.02$ would be measured at $\lambda = 4.5$ μm for $T_{\mathrm{obj}} = 200\,°\mathrm{C}$, the object radiance and reflected background radiance would be equal, resulting in large errors if the reflection contribution is neglected.

It is very important to note that even at very high object temperatures of about 1000 °C, the use of long wavelengths above 8 μm would only make it possible to quantitatively measure with percentage accuracy for emissivities of $\varepsilon_{\mathrm{obj}} > 0.4$. The longer the operating wavelength, the higher the emissivity needed for correct measurements. This explains why two-color measurements always use short wavelengths.

Once it is obvious that Eq. (3.4) can be used for measurements, one benefits from the following advantage for actual measurements: if the transmission between object and detector changes, for example, owing to transient contamination of the atmosphere or possible windows by dust, smoke, and so on, the ratio of Eq. (3.4) changes only if attenuation differs for the two chosen wavelengths. If they are close to each other and object signal changes are the same for both wavelengths, the ratio signal is not affected at all.

3.2.2.2 **Approximations of Planck's Radiation Law**

In what follows, we will neglect any reflection contributions, that is, start with Eq. (3.4). We first discuss the ratio of detected radiance as a result of object excitance at different wavelengths using the Planck distribution function (Eq. (3.5)):

$$\frac{\varepsilon_{\mathrm{obj}}(\lambda_2, T_{\mathrm{obj}}) L_{\mathrm{BB}}(\lambda_2, T_{\mathrm{obj}})}{\varepsilon_{\mathrm{obj}}(\lambda_1, T_{\mathrm{obj}}) L_{\mathrm{BB}}(\lambda_1, T_{\mathrm{obj}})} = \frac{\varepsilon_{\mathrm{obj}}(\lambda_2, T_{\mathrm{obj}})}{\varepsilon_{\mathrm{obj}}(\lambda_1, T_{\mathrm{obj}})} \frac{\lambda_1^5}{\lambda_2^5} \frac{\mathrm{e}^{(hc)/(\lambda_1 k T_{\mathrm{obj}})} - 1}{\mathrm{e}^{(hc)/(\lambda_2 k T_{\mathrm{obj}})} - 1} \tag{3.5}$$

The ratio of the Planck functions can be simplified for both the long- and short-wavelength regions. For the long-wavelength spectral region, the exponential can be linearized, $\mathrm{e}^x \approx 1 + x$ if $x = hc/(\lambda k T) \ll 1$, that is, $\lambda T \gg 14\,400$ μm K. This spectral region of the Planck distribution function can then be replaced by the Rayleigh–Jeans radiation law (Figure 3.10):

$$L_{\mathrm{BB}}^{\mathrm{Rayleigh-Jeans}}(\lambda, T_{\mathrm{obj}}) = 2c \frac{k T_{\mathrm{obj}}}{\lambda^4} \tag{3.6}$$

If the Planck law in Eq. (3.5) were replaced by this Rayleigh–Jeans approximation, a ratio measurement to determine the object temperature in this spectral region would fail since the temperature in numerator and denominator would cancel each other in Eq. (3.5). In addition, the restriction $\lambda T \gg 14\,400$ μm K requires very high temperatures. Even for $\lambda = 10$ μm, the restriction is $T \gg 1440$ K. Conversely, a measurement at $T = 1000$ K would require $\lambda \gg 14.4$ μm, that is, beyond the accessible range of IR cameras.

The other extreme exists for short wavelengths. If $x > 5$, we find that $1/(\mathrm{e}^x - 1) \approx \mathrm{e}^{-x}$ (accuracy better than 1%). This condition is fulfilled for $\lambda T < 2897.8$ μm K $\approx (1/5) \cdot 14\,400$ μm K, where $\lambda T = 2897.8$ μm K resembles the maximum of the

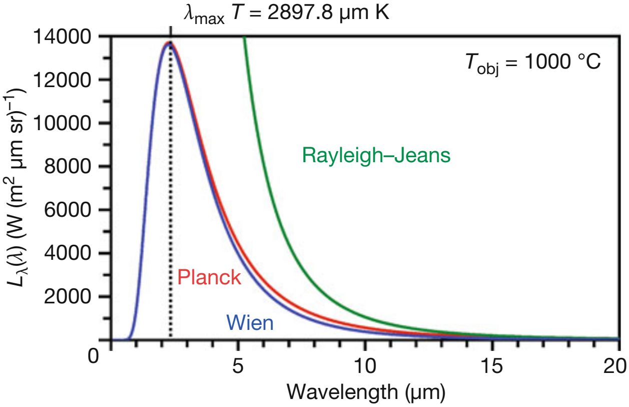

Figure 3.10 Comparison of Planck distribution function, Wien approximation, and Rayleigh–Jeans approximation.

Planck radiance function (Eq. (1.16)). In this case, we find

$$L_{BB}^{Wien}(\lambda, T_{obj}) = \frac{2hc^2}{\lambda^5} e^{-\frac{hc}{\lambda kT}} \tag{3.7}$$

which holds rather well for all short wavelengths below the maximum, as can be seen in Figure 3.10.

In this case, the temperature dependence of the spectral radiance is exponential. An object-temperature change will have a much stronger effect on the radiance than any emissivity changes. Therefore, the ratio method is applied in this spectral region.

Using this Wien approximation, one can easily determine the object temperature needed to ensure that background radiation may be neglected. For $\lambda T <$ 2897.8 μm K the ratio of emitted object radiance and reflected background radiance at a given wavelength λ can be written in the Wien approximation as

$$\frac{L_{obj}(\lambda, T_{obj})}{L_{bgr}(\lambda, T_{bgr})} = \frac{\varepsilon_{obj}}{(1-\varepsilon_{obj})} e^{-\frac{hc}{\lambda k}\left(\frac{1}{T_{obj}} - \frac{1}{T_{bgr}}\right)} \tag{3.8}$$

Provided the Wien approximation holds, Eq. (3.8) can be rewritten to estimate the minimum object temperature that is needed to obtain a predefined ratio of object to reflected background radiation:

$$T_{obj}^{min} = \left\{ \frac{1}{T_{bgr}} - \frac{\lambda k}{hc} \ln \left[\frac{L_{obj}(\lambda, T_{obj})}{L_{bgr}(\lambda, T_{bgr})} \left(\frac{1-\varepsilon_{obj}}{\varepsilon_{obj}} \right) \right] \right\}^{-1} \tag{3.9}$$

For example, $T_{bgr} = 300\,K$, $\varepsilon = 0.02$, $\lambda = 2$ μm, and a ratio of 100 yields $T_{obj}^{min} \approx$ 192 °C, which correlates well with Figure 3.9.

A word of caution regarding the use of Eq. (3.9): if values are chosen for which the Wien approximation does not work, for example, ratio = 100, $\varepsilon = 0.2$, $T_{bgr} =$ 300 K, $\lambda = 10$ μm, unreasonably high temperatures result.

3.2.2.3 T_{obj} Error for True Gray Bodies within Wien Approximation

Using Eq. (3.7), Eq. (3.4) can be written as

$$\frac{L_{\text{inc}}(\lambda_2)}{L_{\text{inc}}(\lambda_1)} = \frac{\varepsilon_{\text{obj}}(\lambda_2, T_{\text{obj}})}{\varepsilon_{\text{obj}}(\lambda_1, T_{\text{obj}})} \frac{\lambda_1^5}{\lambda_2^5} e^{-\frac{hc}{kT_{\text{obj}}}\left(\frac{1}{\lambda_2}-\frac{1}{\lambda_1}\right)} \tag{3.10}$$

The object temperature can be calculated using the measured signal ratio by taking the natural logarithm of both sides of Eq. (3.10) and solving for T:

$$\frac{1}{T_{\text{obj}}} = \frac{k}{hc} \frac{\lambda_1\lambda_2}{(\lambda_2-\lambda_1)} \left[\ln\left(\frac{L_{\text{inc}}(\lambda_2)}{L_{\text{inc}}(\lambda_1)}\right) + 5\ln\left(\frac{\lambda_2}{\lambda_1}\right) + \ln\left(\frac{\varepsilon_{\text{obj}}(\lambda_1, T_{\text{obj}})}{\varepsilon_{\text{obj}}(\lambda_2, T_{\text{obj}})}\right)\right] \tag{3.11}$$

The last term represents the temperature error due to unequal emissivities at λ_1 and λ_2. Therefore, we can write the object temperature in terms of an apparent temperature $T_{\text{app,mono}}$:

$$\frac{1}{T_{\text{obj}}} = \frac{1}{T_{\text{app,mono}}} + \frac{k}{hc} \frac{\lambda_1\lambda_2}{(\lambda_2-\lambda_1)} \ln\left(\frac{\varepsilon_{\text{obj}}(\lambda_1, T_{\text{obj}})}{\varepsilon_{\text{obj}}(\lambda_2, T_{\text{obj}})}\right) \tag{3.12a}$$

with

$$\frac{1}{T_{\text{app,mono}}} = \frac{k}{hc} \frac{\lambda_1\lambda_2}{(\lambda_2-\lambda_1)} \left[\ln\left(\frac{L_{\text{inc}}(\lambda_2)}{L_{\text{inc}}(\lambda_1)}\right) + 5\ln\left(\frac{\lambda_2}{\lambda_1}\right)\right] \tag{3.12b}$$

The apparent temperature for monochromatic wavelengths λ_1 and λ_2 results from Eq. (3.11) for true gray bodies, that is, $\varepsilon_{\text{obj}}(\lambda_1, T_{\text{obj}}) = \varepsilon_{\text{obj}}(\lambda_2, T_{\text{obj}})$. This assumption is usually made, that is, the interpretation of measurements assumes $\varepsilon_{\text{obj}}(\lambda_1, T_{\text{obj}}) = \varepsilon_{\text{obj}}(\lambda_2, T_{\text{obj}})$, and hence the ratio signal is analyzed for blackbody temperatures, giving $T_{\text{app,mono}}$. If, however, ε-differences occur ($\varepsilon_{\text{obj}}(\lambda_1, T_{\text{obj}}) \neq \varepsilon_{\text{obj}}(\lambda_2, T_{\text{obj}})$), the real object temperature, which can be deduced from the ratio, differs from the apparent temperature (see subsequent discussion).

Equations 3.12a and 3.12b contain two conflicting requirements for the selection of λ_1 and λ_2. T_{obj} is only close to $T_{\text{app,mono}}$ if $(\lambda_1\lambda_2)/(\lambda_2-\lambda_1)\ln(\varepsilon(\lambda_1)/\varepsilon(\lambda_2))$ is very small. Obviously, a large $\Delta\lambda = \lambda_2 - \lambda_1$ is favorable for this condition; however, for large values of $\Delta\lambda$ the gray-body assumption will become less valid. The influence of these conflicting requirements on measurement errors must be analyzed in detail to determine the optimum measurement conditions [9].

The difference $\Delta T = T_{\text{obj}} - T_{\text{app,mono}}$ between real object and apparent object temperatures, evaluated for two monochromatic wavelengths (Eqs. (3.12a) and (3.12b)) resembles the easiest analyzable case. Unfortunately, there are, however, additional temperature errors that occur owing to

- Finite transmission of used filters, in particular, if they differ for the two wavelengths;
- Finite spectral widths FWHM of the filters;
- Different spectral widths of the two filters.

For simplicity, let us assume two top-hat filters with $\tau(\lambda_1) = \tau(\lambda_2) = 1$ and the same finite FWHM. This finite width will induce additional errors.

For a finite spectral filter width the detector signals are determined by the integrals

$$L_{\text{inc}}^{\text{Planck}}(\lambda_1, \Delta\lambda) = \frac{1}{\Delta\lambda} \int_{\lambda_1-\frac{\Delta\lambda}{2}}^{\lambda_1+\frac{\Delta\lambda}{2}} L_{\text{BB}}^{\text{Planck}}(\lambda, T_{\text{obj}})\, \mathrm{d}\lambda \tag{3.13a}$$

$$L_{\text{inc}}^{\text{Planck}}(\lambda_2, \Delta\lambda) = \frac{1}{\Delta\lambda} \int_{\lambda_2-\frac{\Delta\lambda}{2}}^{\lambda_2+\frac{\Delta\lambda}{2}} L_{\text{BB}}^{\text{Planck}}(\lambda, T_{\text{obj}})\, \mathrm{d}\lambda \tag{3.13b}$$

The object temperature is calculated from the ratio of Eq. (3.13a) and (3.13b) using Eq. (3.11).

For finite FWHM $\Delta\lambda$ the signal ratio differs from the signal ratio for monochromatic measurement by a factor $A_{\Delta\lambda}$:

$$\frac{L_{\text{inc}}^{\text{Planck}}(\lambda_2, \Delta\lambda)}{L_{\text{inc}}^{\text{Planck}}(\lambda_1, \Delta\lambda)} = A_{\Delta\lambda} \frac{L_{\text{inc}}^{\text{Planck}}(\lambda_2, \Delta\lambda = 0)}{L_{\text{inc}}^{\text{Planck}}(\lambda_1, \Delta\lambda = 0)} \approx A_{\Delta\lambda} \frac{L_{\text{BB}}^{\text{Wien}}(\lambda_2, T_{\text{obj}})}{L_{\text{BB}}^{\text{Wien}}(\lambda_1, T_{\text{obj}})} \tag{3.14}$$

Figure 3.11 depicts an enlarged schematic drawing of the Planck function, strongly exaggerating the deviations. Monochromatic radiances at λ_1 and λ_2 are indicated by solid lines. For spectral BPs with the same center wavelengths and width $\Delta\lambda$, the average radiance in the corresponding spectral bands (broken lines) is larger than that in the monochromatic case. If one interprets this as

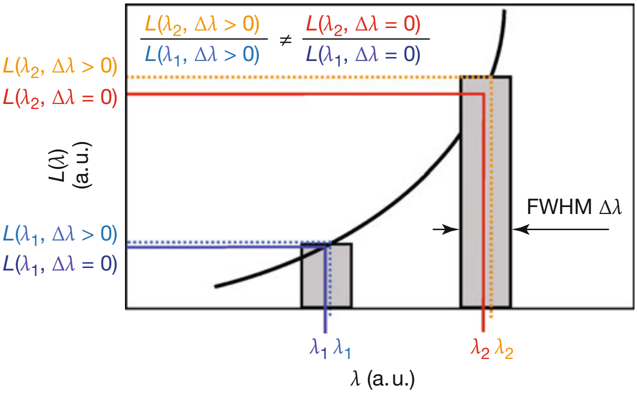
$\frac{L(\lambda_2, \Delta\lambda > 0)}{L(\lambda_1, \Delta\lambda > 0)} \neq \frac{L(\lambda_2, \Delta\lambda = 0)}{L(\lambda_1, \Delta\lambda = 0)}$
$L(\lambda_2, \Delta\lambda > 0)$
$L(\lambda_2, \Delta\lambda = 0)$
$L(\lambda)$ (a.u.)
$L(\lambda_1, \Delta\lambda > 0)$
$L(\lambda_1, \Delta\lambda = 0)$
FWHM $\Delta\lambda$
λ_1 λ_1
λ_2 λ_2
λ (a.u.)

Figure 3.11 Schematic drawing of Planck function illustrating different radiance ratios for monochromatic measurements and measurements with finite filter FWHM, $\Delta\lambda$. The finite filter width leads to apparent shifts of the center wavelengths, which are different for λ_1 and λ_2, giving rise to errors.

being due to monochromatic radiation, one observes a center wavelength shift. The resulting radiance and center wavelength differences give rise to errors of T_{obj} determination, described by $A_{\Delta\lambda}$. The correction factor $A_{\Delta\lambda}$ depends on the chosen wavelengths as well as on the respective spectral widths of the filters and obviously leads to a modification of Eq. (3.12a) and (3.12b) for broadband detection according to

$$\frac{1}{T_{\text{obj}}} = \frac{1}{T_{\text{app},\Delta\lambda}} + \frac{k}{hc}\frac{\lambda_1\lambda_2}{(\lambda_2-\lambda_1)}\ln\left(\frac{\varepsilon_{\text{obj}}(\lambda_1, T_{\text{obj}})}{\varepsilon_{\text{obj}}(\lambda_2, T_{\text{obj}})}\right) \tag{3.15a}$$

with

$$\frac{1}{T_{\text{app},\Delta\lambda}} = \frac{1}{T_{\text{app,mono}}} + \frac{k}{hc}\frac{\lambda_1\lambda_2}{(\lambda_2-\lambda_1)}\ln A_{\Delta\lambda} \tag{3.15b}$$

The deviation from $T_{\text{app,mono}}$ and $T_{\text{app},\Delta\lambda}$ depends on the difference in the ratio of the radiances in the Wien approximation and that using Planck's law.

Using the correction factor $A_{\Delta\lambda}$, the relative difference between the incident radiance ratio and the Wien approximation ratio is given by

$$\frac{\dfrac{L_{\text{inc}}^{\text{Planck}}(\lambda_2)}{L_{\text{inc}}^{\text{Planck}}(\lambda_1)} - \dfrac{L_{\text{BB}}^{\text{Wien}}(\lambda_2)}{L_{\text{BB}}^{\text{Wien}}(\lambda_1)}}{\dfrac{L_{\text{inc}}^{\text{Planck}}(\lambda_2)}{L_{\text{inc}}^{\text{Planck}}(\lambda_1)}} = \frac{A_{\Delta\lambda}-1}{A_{\Delta\lambda}} \tag{3.16}$$

Figure 3.12a depicts this quantity, that is, the relative change in the radiance ratio due to the Wien approximation for two chosen center wavelengths of 1.8 and 2.0 μm of the filter transmission curves. For monochromatic wavelengths (FWHM = 0), deviations occur for high temperatures (due to the limited applicability of the Wien approximation), whereas an increasing filter width leads to errors in the percentage range for low temperatures.

These deviations have consequences for the deduced object temperatures according to Eq. (3.15a) and (3.15b). Figure 3.12b depicts the difference in object and apparent temperatures. The largest temperature errors occur first for large filter widths at low object temperatures but also for very high object temperatures. Obviously, it is possible to perform measurements that are quite accurate (error < 2%) for gray bodies over an extended temperature range from 200 to about 800 °C and filter width below 0.1 μm.

The discussion on errors so far has only referred to idealized conditions such as top-hat filters with $\tau_{\max} = 1$. In experimental studies, real filter transmission curves need to be used. Quite often, the filter curves differ in $\tau_{\max}$ as well as FWHM for the two wavelengths, which may introduce additional errors. Real filter transmission curves $[\tau_1(\lambda), \tau_2(\lambda)]$ will modify Eq. (3.13a) and (3.13b) to

$$L_{\text{inc}}(\lambda_1, \Delta\lambda, \tau) = \frac{1}{\Delta\lambda}\int_{\lambda_1-\frac{\Delta\lambda}{2}}^{\lambda_1+\frac{\Delta\lambda}{2}} \tau_1(\lambda) L_{\text{BB}}^{\text{Planck}}(\lambda, T_{\text{obj}})\,\mathrm{d}\lambda \tag{3.17a}$$

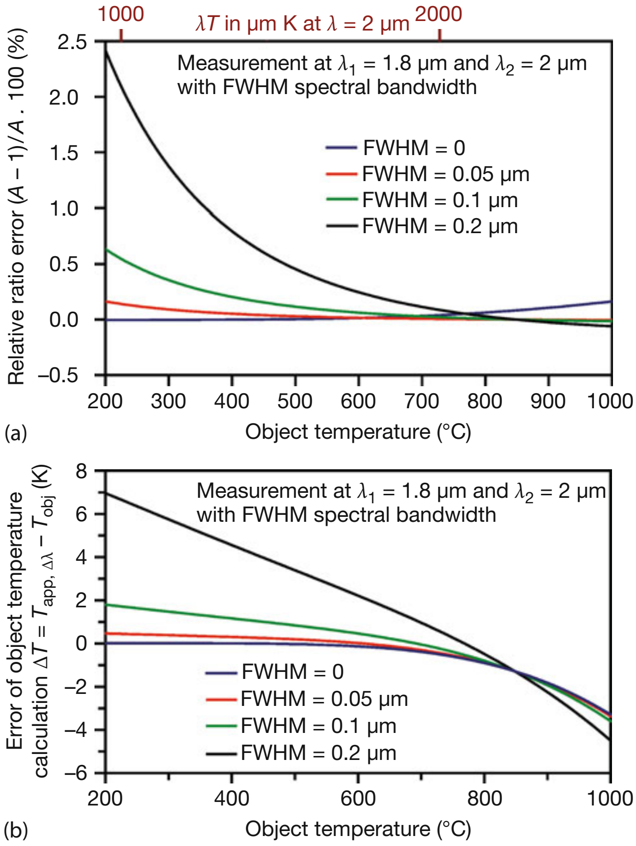

Figure 3.12 Object-temperature-dependent relative error of 1.8 and 2 µm signal ratio $(A_{\Delta\lambda} - 1)/A_{\Delta\lambda} \cdot 100\%$ (according to Eq. (3.16)) applying the Wien approximation compared to Planck's function for different spectral bandwidths of measurement spectral bands (a). The top scale refers to $\lambda = 2$ µm. The resulting error of the calculated object temperature using the signals at 1.8 and 2 µm and applying the Wien approximation (b).

$$L_{\text{inc}}(\lambda_2, \Delta\lambda, \tau) = \frac{1}{\Delta\lambda} \int_{\lambda_2 - \frac{\Delta\lambda}{2}}^{\lambda_2 + \frac{\Delta\lambda}{2}} \tau_2(\lambda) L_{\text{BB}}^{\text{Planck}}(\lambda, T_{\text{obj}})\, \mathrm{d}\lambda \tag{3.17b}$$

The different filter transmission behavior will therefore additionally influence the incident object radiances. The correction factor $A_{\Delta\lambda}$ from Eq. (3.14) will be modified to $A_{\Delta\lambda,\tau(\lambda)}$,

$$\frac{L_{\text{inc}}(\lambda_2, \Delta\lambda, \tau)}{L_{\text{inc}}(\lambda_1, \Delta\lambda, \tau)} = A_{\Delta\lambda,\tau(\lambda)} \frac{L_{\text{BB}}^{\text{Planck}}(\lambda_2, T_{\text{obj}})}{L_{\text{BB}}^{\text{Planck}}(\lambda_1, T_{\text{obj}})} \tag{3.18}$$

and must be determined from a blackbody calibration procedure.

3.2.2.4 Additional T_{obj} Errors Owing to Nongray Objects

So far, we have been considering only true gray objects and resulting errors due to the Wien approximation, which is usually used to evaluate object temperatures. However, this most important gray object assumption of ratio thermography, that is, $\varepsilon(\lambda_1, T_{\text{obj}}) = \varepsilon(\lambda_2, T_{\text{obj}})$ is often only fulfilled approximately. The consequences are obvious: if the object exhibits a nongray behavior, the error of the temperature calculation will increase. The second term in Eq. (3.15a) represents the additional error due to the emissivity change. If we assume an emissivity difference of 1% or 5% for a wavelength change from 2 to 1.8 μm, the ratios of the measured signal will change by a factor of 1.01 or 1.05, respectively. Figure 3.13 depicts the resulting temperature measurement error depending on object temperature and filter FWHM.

This error was calculated in a manner similar to that in Figure 3.12, that is, it includes also the error due to the Wien approximation, the only difference being that the last term in Eq. (3.11) is zero in Figure 3.12 and nonzero in Figure 3.13.

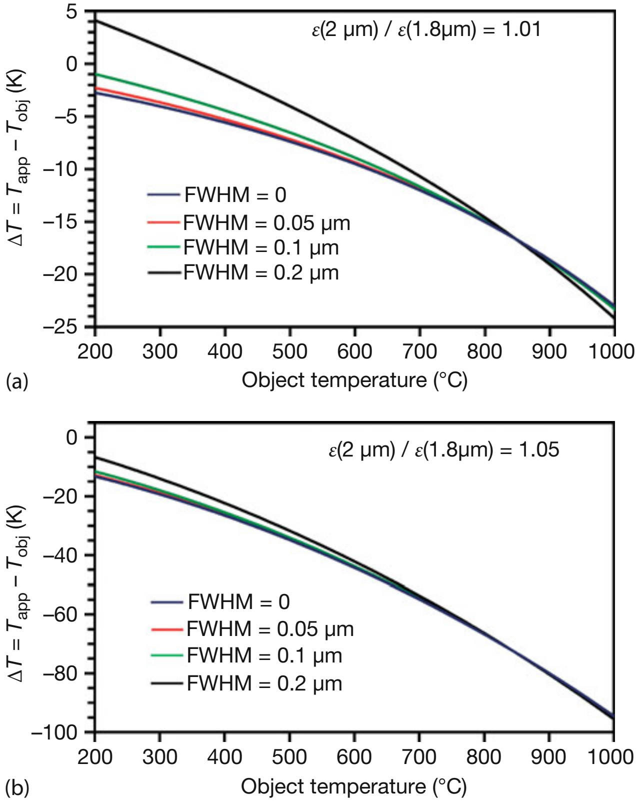

Figure 3.13 Error of calculated object temperature using signals at 1.8 and 2 μm, as in Figure 3.12, with additional emissivity ratio $\varepsilon(2\ \mu\text{m})/\varepsilon(1.8\ \mu\text{m}) = 1.01$ (a) and 1.05 (b) and different FWHM spectral bandwidths.

The apparent object temperature is strongly affected by emissivity change. The temperature error increases with object temperature owing to the decreasing slope of the Planck function for increasing object temperatures, that is, for increasing values of $\lambda T_{\text{object}}$.

Figure 3.13 illustrates that the single most important error source in dual-wavelength pyrometry or thermography is the possibility of nongray bodies. Deviations of 5% can easily lead to temperature errors on the order of 10%. Therefore, any pyrometry or thermography object-temperature measurement using the ratio method with two wavelengths must fulfill the following requirements:

- Reflected background radiance should be at least smaller than 1% of the respective object radiance.
- If the Wien approximation is used, the wavelengths should be in the SW spectral region, preferably below 2 μm.
- Both filters should be narrow and have similar transmissions and widths.
- Wavelengths should be close to each other to reduce the probability of ε changes in gray-looking bodies.
- Never use the method for selective emitters such as plastics unless IR spectra are well known and filters selected accordingly. Whenever IR spectra are measured, they should refer to the same temperature region in order to avoid $\varepsilon(T)$ dependencies.

3.2.2.5 Ratio Versus Single-Band-Radiation Thermometry

Ratio thermometry was motivated by a desire to eliminate unknown emissivities and still measure object temperatures. The difficulties and restrictions of ratio thermometry, however, suggest the need to define the criteria when ratio thermometry should be used, that is, when it is advantageous compared to conventional thermometry.

We assume high object temperatures and short wavelength measurement such that the Wien approximation can be used and background reflections neglected. The temperature measurement error for the ratio method was discussed earlier. Equation 3.7 can be used to estimate the measurement error for a single-band measurement, that is, conventional thermal imaging. We assume a known emissivity except for an uncertainty factor f_ε. The object emissivity can be written as $\varepsilon_{\text{obj}}(\lambda, T_{\text{obj}}) = f_\varepsilon \cdot \varepsilon_{\text{o}}(\lambda, T_{\text{obj}})$. Using the Wien approximation (Eq. (3.7)), we can calculate the object temperature,

$$\frac{1}{T_{\text{obj}}} = \frac{1}{T_{\text{app,single}}} + \frac{k}{hc}\lambda \ln f_\varepsilon \tag{3.19}$$

with

$$\frac{1}{T_{\text{app,single}}} = \frac{\lambda k}{hc} \ln\left(\frac{\varepsilon_{\text{o}}(\lambda, T_{\text{obj}})2hc^2}{\lambda^5 L_{\text{inc}}(\lambda)}\right) \tag{3.20a}$$

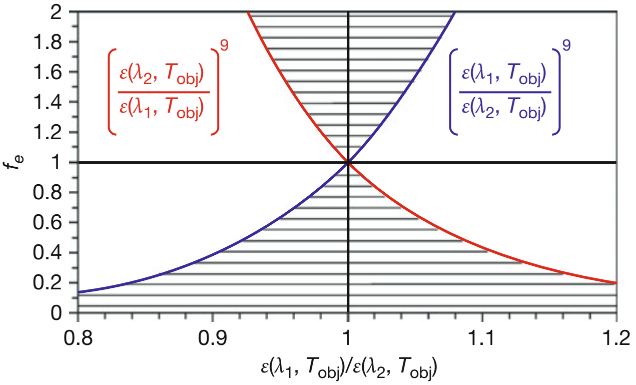

Figure 3.14 Limits of emissivity uncertainty factor f_ε for one-color temperature measurement at $\lambda = 2$ μm depending on object emissivity ratio for a ratio temperature measurement at $\lambda_1 = 1.8$ μm and $\lambda_2 = 2$ μm. The two-color temperature measurement exhibits a higher accuracy within the shaded area. Outside that area, the one-color measurement makes more sense.

The ratio measurement will have equal or better performance if

$$\lambda |\ln f_\varepsilon| \geq \frac{\lambda_1 \lambda_2}{(\lambda_2 - \lambda_1)} \left| \ln \left(\frac{\varepsilon_{obj}(\lambda_1, T_{obj})}{\varepsilon_{obj}(\lambda_2, T_{obj})} \right) \right| \tag{3.20b}$$

For our specific example of ratio measurement at $\lambda_1 = 1.8$ μm, $\lambda_2 = 2$ μm, and a single-band measurement at $\lambda = \lambda_2 = 2$ μm, we get

$$|\ln f_\varepsilon| \geq 9 \left| \ln \left(\frac{\varepsilon_{obj}(\lambda_1, T_{obj})}{\varepsilon_{obj}(\lambda_2, T_{obj})} \right) \right| \tag{3.21}$$

If this relation is fulfilled, the ratio measurement will be equal to or more accurate than the single-band measurement. Figure 3.14 depicts the limits for f_ε (single-band temperature measurement at $\lambda = 2$ μm) depending on the ratio of the object emissivities for the two-color measurement at $\lambda_1 = 1.8$ μm and $\lambda_2 = 2$ μm.

3.2.2.6 Exemplary Application of Two-Color Thermography

A number of narrowband spectral filters from Spectrogon [2] have been used for experimental tests of ratio thermography (Figure 3.15). The filters have been selected to fit the spectral camera sensitivity of our SC6000 camera with an extended MW spectral range from 1.5 to 5.5 μm.

The use of filters below a 2 μm wavelength requires large object temperatures above 500 °C due to the small object signal, combined with low camera sensitivity and narrow spectral filter transmission. Measurements at $\lambda = 1.95$ μm and $\lambda = 4.35$ μm are influenced by water vapor and carbon dioxide absorption in the atmosphere, respectively. For the experiments only object temperatures at a maximum of 350 °C were analyzed since this was the maximum temperature of the

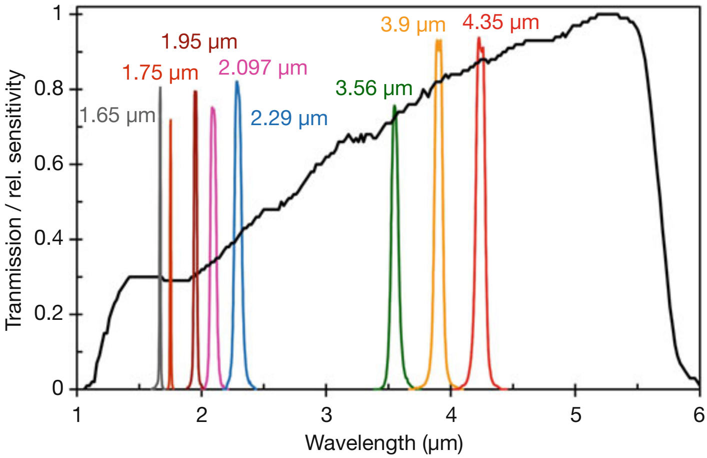

Figure 3.15 Transmission of different NBP spectral filters and relative spectral sensitivity of the used FLIR SC6000 camera (InSb detector).

blackbody used for camera calibration. The tests discussed in what follows were performed with NBP filters at $\lambda = 2.29$, 3.56, and 3.9 μm.

Expected Signal Ratios

To find the theoretically expected signal ratio as a function of temperature for our setup, we first calculate the detected object radiance $L_{\text{filt}}(T_{\text{obj}})$ assuming a gray-body object, and using, first, the known spectral filter transmission $\tau_{\text{filt}}(\lambda)$ (of nonabsorbing filter materials) and, second, the known spectral camera sensitivity Sens (λ). Otherwise ideal optics is assumed (no further losses):

$$L_{\text{filt}}(T_{\text{obj}}) = \int_0^\infty \tau_{\text{filt}}(\lambda)\,\text{Sens}\,(\lambda) L_\lambda(\lambda, T_{\text{obj}})\,\text{d}\lambda \tag{3.22}$$

Results are presented in Figure 3.16a. For an object temperature range of 25 to 500 °C the Planck distribution function is perfectly fitted by the Wien approximation. Therefore, the radiance depends exponentially on the inverse absolute object temperature (Figure 3.16a):

$$L_{\text{filt}}(T_{\text{obj}}) \sim \text{e}^{-\frac{hc}{\lambda_{\text{filt}} k T_{\text{obj}}}} \sim \text{e}^{-\frac{const.(\lambda_{\text{filt}})}{T_{\text{obj}}}} \tag{3.23}$$

The slope of the signal vs. inverse object temperature increases with decreasing filter wavelength.

The signal ratio for different filter combinations can be easily calculated from the object radiances $L_{\text{filt}}(T_{\text{obj}})$. Results are shown in Figure 3.16b. The slope signal ratio versus inverse temperature increases with decreasing filter wavelength and increasing spectral separation $\Delta\lambda = \lambda_2 - \lambda_1$ of the filters. For the assumed

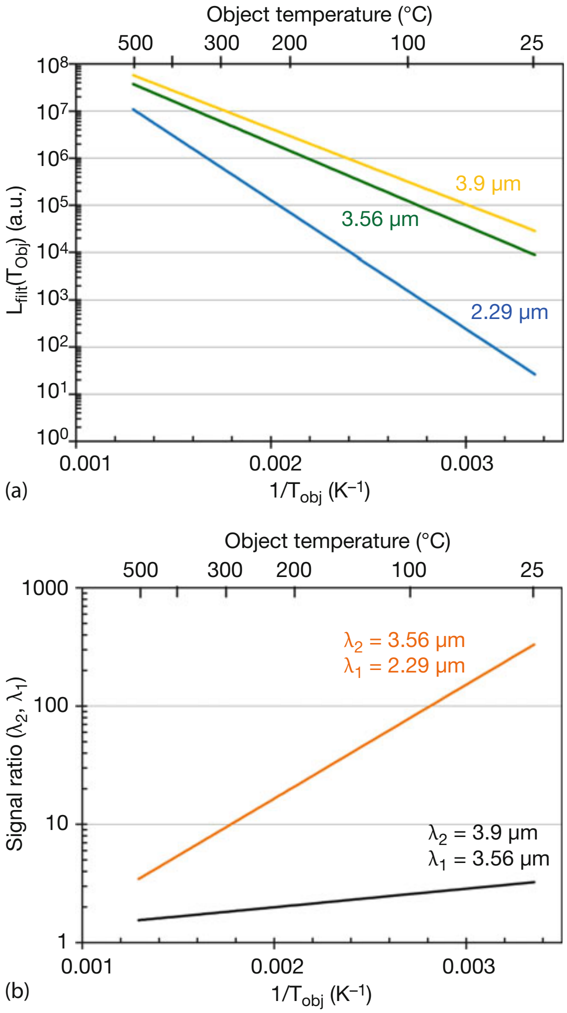

Figure 3.16 (a) Object-temperature-dependent camera signal for different spectral filters and (b) object-temperature-dependent signal ratio for different filter combinations.

ideal conditions the theoretical plots in Figure 3.16b contain all information that is needed to extract the temperature. First, IR images are recorded for the different filters, second the signal ratios are computed for each pixel, which, third, according to the data of Figure 3.16 or respective figures, give the object temperatures. Obviously, this method works correctly only if $\tau_{\text{filt}}(\lambda)$ and Sens (λ) are accurately known.

Experimental Calibration Using NBP Filters

The experimental analysis requires a calibration of camera signal versus object temperature (Section 2.4.5) for both used filters. Because of the largest slope of the object signal ratio (Figure 3.16) the filter combination 3.56 μm/2.29 μm was used. The calibration was performed using a MIKRON M310 [10] blackbody emitter in a temperature range of 25–350 °C. Figure 3.17a,c depicts the determined temperature dependence of the camera raw signal (dots) and the theoretically expected signals (solid lines). Unfortunately, there is a large offset between the two sets of data. This is caused by the emission of IR radiation by the warm spectral filters placed between the camera objective and the camera sensor. This at first glance unexpected behavior is due to the fact that most commercially available filters (as well as ours used here) are usually optimized for spectroscopy. They are made from sapphire substrates that start to absorb IR radiation for wavelengths around and larger than 5 μm (Figure 1.48, Al_2O_3). The used SC6000MW camera does, however, detect radiation up to about 6 μm (Figure 3.15). Therefore, it detects the emitted thermal radiation from the spectral filter, causing the signal offset. This offset can be suppressed by cooling the filter, as is common in GasFind cameras (Chapter 8). Future work on ratio thermal imaging should also deal with filters made from truly nonabsorbing substrate materials.

To still use the calibration data of Figure 3.17, we corrected the camera signals by their offset values. Following offset correction, the expected temperature-dependent radiance was compared to the camera signals. Figure 3.17b,d depicts the signal in a semilogarithmic plot as a function of the inverse absolute object temperature. Now, the observed camera signal (dots) agrees quite well with the expected radiance (solid lines). Note that the calibration results depend on the absolute camera detector sensitivity and the camera integration time.

Using the calibration results (Figure 3.17b,d) the signal ratios of several filter combinations were calculated.

Figure 3.18 depicts the object-temperature signal ratio for the filter combination 3.56 and 2.29 μm. This signal ratio represents the calibration curve for the object-temperature measurements using the two-color method. For the experiments, Figure 3.18 (or a corresponding one plotted versus $1/T$) therefore replaces the theoretical signal ratio of Figure 3.16.

Experimental Results of Ratio Thermal Imaging

An electrically heated, partially oxidized, and scratched aluminum plate ($T_{\text{obj}} \approx$ 250 °C) was used as object to test the ratio thermal imaging method. The emissivity of a crosslike part of the plate was increased by blackening it with soot. Figure 3.19 depicts a visible image (a) and a typical constant emissivity MW (3–5 μm) thermal image of the plate. The soot part of the plate exhibits good temperature homogeneity, as demonstrated by a temperature measurement along the line across the plate (Figure 3.19c,d). At other locations on the plate strong emissivity variations are clearly seen. The table in Figure 3.19e gives the measured spot temperatures for a constant emissivity of 0.96 as well as the emissivity values at all different spots calculated using the emissivity calculator of the FLIR ThermaCamResearcher software, assuming a plate temperature of 250 °C, an ambient temperature of 25 °C, and the known emissivity $\varepsilon = 0.96$ of soot. Obviously, the

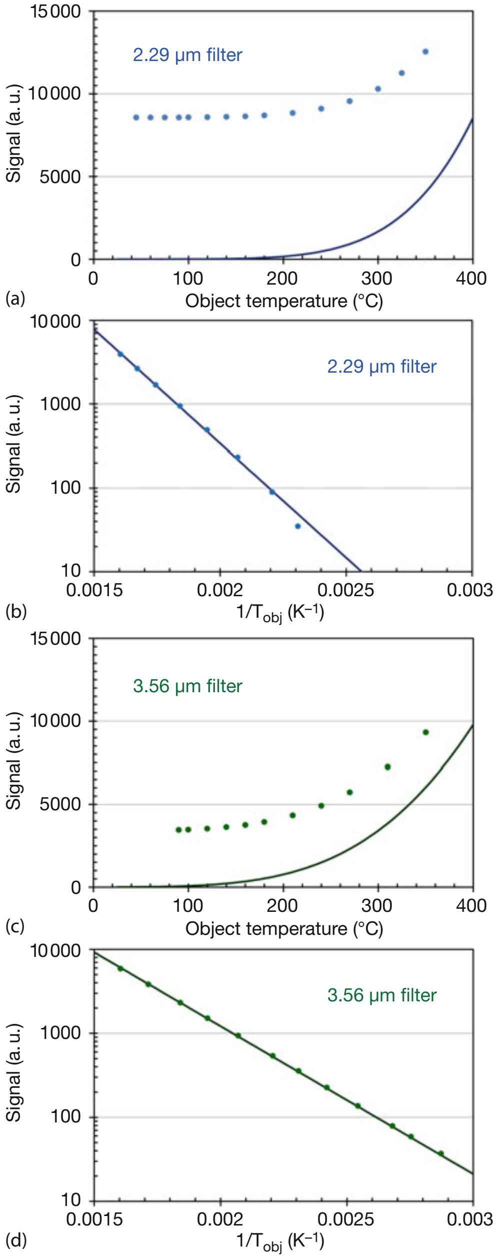

Figure 3.17 Camera calibration as a function of object temperature for different spectral filters using a blackbody emitter. (a,c) Measured raw data camera signals (dots) and data calculated according to Eq. (3.22) (solid lines). Measurements at 2.29 μm with 1 ms camera integration time (a) and at 3.56 μm with 0.2 ms integration time (c). (b,d) Comparison of offset-corrected signal values (dots) with calculated values using Eq. (3.22) (solid lines).

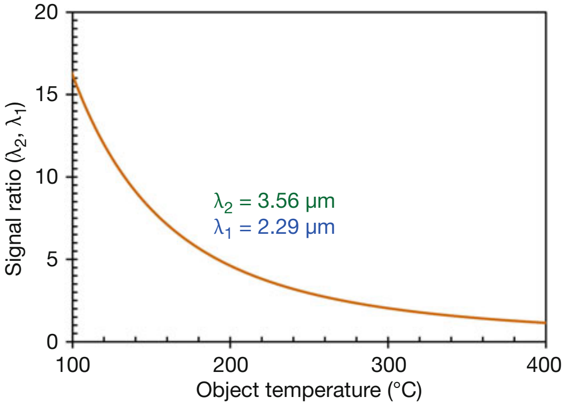

Figure 3.18 Object-temperature-dependent signal ratio for a given filter combination (λ_2, λ_1) calculated from calibration results.

emissivity varies between 0.229 up to 0.96 across the plate, which is therefore a good test object for the ratio method.

For the ratio test measurement the plate temperature was increased to 320 °C. We only used a well-defined subregion of the thermal images (center of the heated plate) for quantitative evaluation of the ratio measurement.

Figure 3.20 depicts the thermal images of the plate subregions at 320 °C for the 3.56 and 2.29 μm filters. As expected, both images indicate temperature differences in this constant emissivity representation. The ratio of the (offset-corrected) signals of these two images, however, leads to a more or less constant value that, according to Figure 3.18, gives an emissivity-independent temperature plot. Figure 3.21 depicts the result. The calculation of the average temperature and its standard deviation across the whole image range gives $T_{\text{obj}} = (317.7 \pm 10.8)\,°\text{C}$ for the 3.56 μm/2.29 μm filter combination for the heated plate at a temperature of 320 °C. Compared to the temperature fluctuations of ±39.2 °C for the broadband MW detection of Figure 3.19, the improved accuracy of the ratio measurement is obvious.

A more detailed analysis of the temperature-dependent ratio signal demonstrates that very accurate measurements are needed to reduce the still detectable deviations. From the signal ratios of the measurement depicted in Figure 3.18 one can calculate the allowed relative ratio error that causes a 1 K error in the resulting temperature. For the plate with 320 °C and our filters of 3.56 and 2.29 μm we find a corresponding allowed ratio error of only 0.011, that is, on the order of 1%.

Although the result is not perfect (mostly owing to the use of warm filters and the therefore necessary offset corrections), it shows that the ratio procedure using a two-wavelength measurement can help to eliminate the influence of the object emissivity on the temperature measurement. The most important error sources for the ratio measurement are image misalignments occurring during the filter

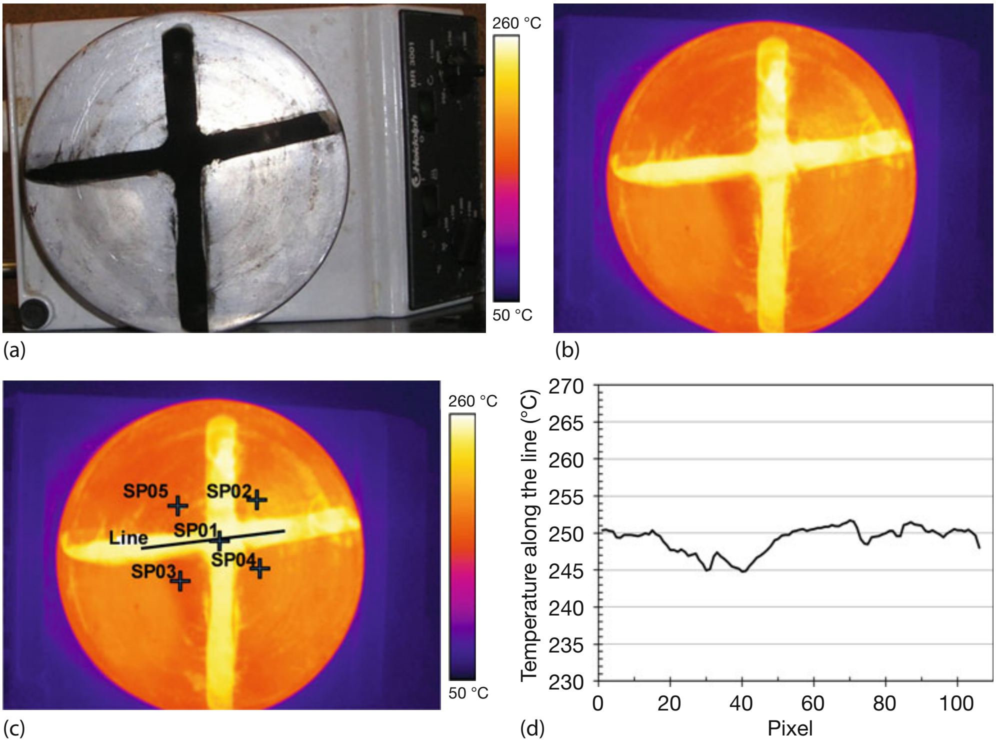

Spot	Spot temperature at ε = 0.96	Spot emissivity T_{obj} = 250 °C T_{bgr} = 25 °C
SP01	250.2	0.960
SP02	206.7	0.507
SP03	161.5	0.229
SP04	185.0	0.353
SP05	171.6	0.277

(e)

Figure 3.19 Heated aluminum test object partially blackened with soot at 250 °C. (a) Visible image. (b) IR image (MW camera THV 550) for an emissivity of 0.96. (c) Analysis labels for temperature line/spot measurements and spot emissivity calculations. (d) Temperature line profile for line shown in (c). (e) Result table with calculated spot emissivities.

change and – if applicable – IR radiation emission by the spectral filters, which generate an object-temperature-independent offset of the camera signal.

3.2.2.7 Extension of Ratio Method and Applications

A natural extension of the dual-wavelength ratio method seems to be multi-wavelength radiation thermometry, which can in principle deal with wavelength-dependent emissivities. The temperature is determined from the ratios of three or more signals, taken at the same temperature but at different wavelengths. In

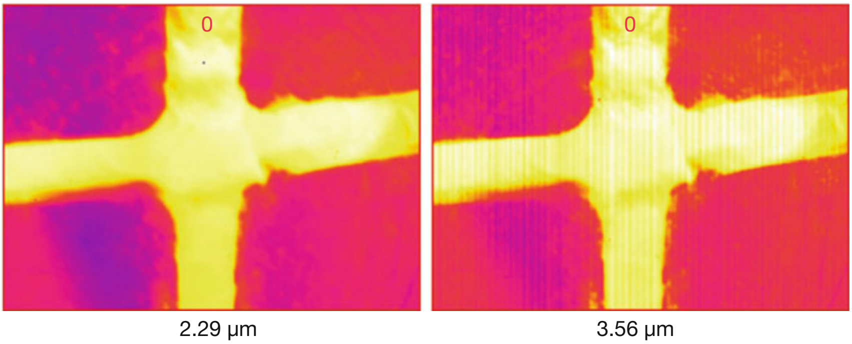

Figure 3.20 Thermal images of a heated plate subregion with 238 × 175 pixels as detected with different spectral filters.

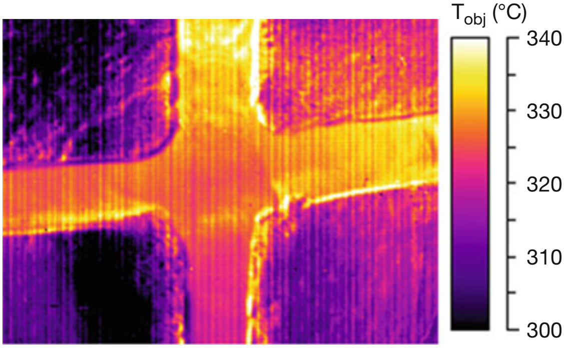

Figure 3.21 Temperature distribution determined from ratio measurement for a plate temperature of 320 °C, ambient temperature of 25 °C, and filter combination of 3.56 and 2.29 μm. The linelike features are artifacts owing to the fact that only a one-point NUC was performed.

this case, it is usually assumed that the problem of the wavelength dependence of emissivity can be solved by describing the logarithm of the emissivity as a series expansion in wavelength [11]. However, the sensitivity of the multiwavelength radiation measurement to errors increases rapidly with the number of parameters in the emissivity model, that is, the number of wavelengths. Thus, in practice, the use of such thermometers cannot be regarded as a general solution to the emissivity problem, and very significant temperature errors can result even for materials that differ only slightly from gray-body conditions [12]. A critical analysis of the potential of multiwavelength radiation thermometry to derive true temperatures is given in [13]. To improve the accuracy of two-color and multicolor temperature measurements, new methods using laser absorption [1] or relative laser reflectometry [14] have been developed.

Despite the difficulties with temperature accuracy, ratio radiation thermometry is being successfully applied in industrial processes for temperature measurement, for example, in steel production [15, 16] or in-process measurements of semiconductor manufacturing [17]. Also, dual-wavelength IR imaging is applied in automated online control [18].

Sometimes dual-band analysis combining measurements in the MW and LW regions are recommended [19]. LW operation can optimize detection at lower object temperatures or in the presence of dust, fog, or smog. The MW can enhance performance at higher object temperatures and higher humidity.

However, correct temperature measurements can be successful only if the emissivity is independent of wavelength, that is, has the same value in both bands. Obviously, the large differences in wavelengths between LW and MW can more easily lead to changes in emissivity than using filters within one spectral band. Therefore, with respect to the real material properties, such dual-band measurements will be successful only for a few applications [20]. This technique is mostly used for qualitative analysis using differences in the radiative properties of the materials within the different spectral regions. The comparison and combination of thermal images taken in two different spectral bands can, for example, improve defect analysis (such as the detection of corrosion damage and delamination problems [21] or building material and conservation performance [22]).

3.2.3
Multi- and Hyperspectral Infrared Imaging

3.2.3.1 Principal Idea

Multispectral images capture image data at a variety of specific wavelength bands across the electromagnetic spectrum. A distinction is made between multispectral and hyperspectral imaging depending on the number of bands used (up to 100 for multispectral and many more than 100 – usually a continuous spectrum – for hyperspectral imaging) (Figure 3.22).

Multispectral imaging uses discrete spectral bands that are mostly separated, for example, by the use of spectral filters or detectors with different spectral sensitivity distributions.

In contrast, hyperspectral imaging uses dispersive or interferometer instruments, which, in principle, allow for the detection of continuous spectra. Available technologies of IR spectrometry provide systems with excellent spectral properties. They essentially make it possible to sample the full continuum of a predefined wavelength region with excellent spectral resolution. The data are stored in so-called three-dimensional 3D data cubes, as depicted in Figure 3.22. One cube refers to a given time and consists of a series of separate IR images as a function of wavelength. Two dimensions are given by the spatial resolution of the IR camera (2D focal-plane array (FPA) sensor), and the third dimension is given by a wavelength or wavenumber scale generated by the spectrometer. In spectrometry, wavenumbers are often used instead of wavelength. The wavenumber is the reciprocal wavelength (in cm^{-1}) and is therefore proportional to photon energy.

Each separate image represents the spatial radiance distribution within a narrow spectral band whose width is determined by the spectral resolution of the in-

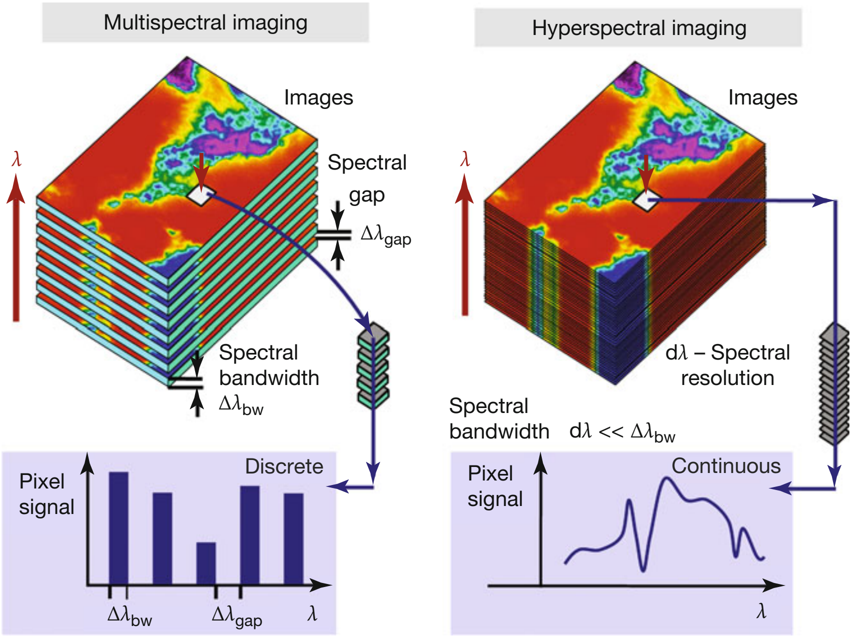

Figure 3.22 Schematic comparison of multispectral and hyperspectral imaging.

strument. Therefore, each single pixel contains an IR spectrum, that is, it contains the same information as a point measurement with a nonimaging IR spectrometer. Such systems are becoming popular in gas imaging (Section 8.6).

In practice, two types of different spectrometer arrangements are used: slit-based and interferometer-based systems. Both systems use FPA detectors, but in different ways. In slit-based systems, single lines of the array are used (such detector linear arrays are used in line scanners), that is, one direction, for example, the horizontal, provides spectral information along a line of an object. Adjacent lines of the array receive signals of the same object line, but from a different spectral region. This is accomplished by using prismatic dispersion elements or a grating [23, 24]. The principal setup with a prism is shown in Figure 3.23.

The FPA detector therefore records spatial information along a line and spectral information in the pixel rows perpendicular to this line. Two-dimensional spatial images are recorded similarly by line scanners (Section 2.4), that is, spatial information such as the second coordinate is recorded sequentially either due to a relative increment between imager and object or, if there is no possibility for moving the object or the imager, using an additional scan mirror to shift the image across the slit [23]. The number of spectral bands will be given by the number of pixels in one FPA row [23].

The second type of hyperspectral imagers uses the concept of interferometer-based spectrometers, which is a well-known and extremely successful technique in IR spectrometry. The combination of IR imaging with the so-called Fourier

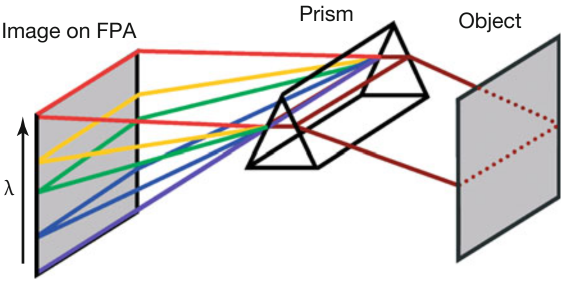

Figure 3.23 Principal setup of a slit-based system with a prism.

(a)

(b)

Figure 3.24 (a) Hyperspectral imager "FIRST Hyper-Cam" and (b) scheme of setup for an environmental application. (Image courtesy Telops Inc., Quebec, Canada; www.telops.com.)

transform IR (FTIR) spectrometry gives the most powerful quantitative measurement devices available in IR imaging with regard to spectral resolution [25, 26]. The IR hyperspectral imager depicted in Figure 3.24 uses a Michelson-type interferometer to spectrally modulate object signals on a detector array with a 320 × 256 pixel format. The use of InSb and MCT FPAs allows for operation within the extended MW (1.5–5 μm) and part of LW (8–11 μm). The spectral resolution is defined by the spectrometer and can be varied within a range of 0.25 to 150 cm^{-1}. The radiometric accuracy of the imager allows a temperature accuracy of better than 1 K after a calibration procedure.

3.2.3.2 Basics of FTIR Spectrometry

In what follows, a brief, simplified description of the FTIR principle [27] is given in order to get an understanding of hyperspectral IR imaging. Most FTIRs are based on a Michelson interferometer as shown in Figure 3.25.

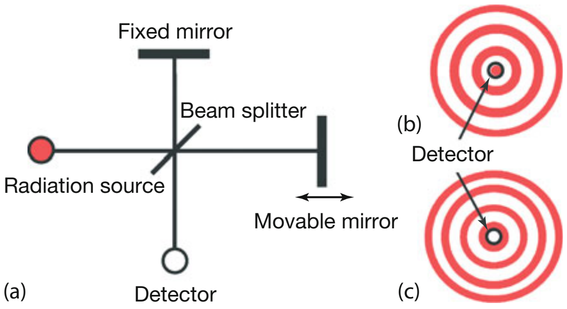

Figure 3.25 Michelson interferometer with movable mirror to change optical path difference of two beams generated by beam splitter (a). Radiance distribution within plane of axially arranged detector for constructive (b) and destructive (c) interference for monochromatic radiation.

The interferometer consists of a radiation source, a beam splitter, a fixed and a movable mirror, and a detector. The movable mirror can be moved forward and backward very precisely. The incident radiation is split into two beams at the beam splitter. One beam is transmitted to the movable mirror and the other is reflected to the fixed mirror of the interferometer. After being reflected from the mirrors, these two beams hit the beam splitter for a second time. Again, one will be partially transmitted and the other reflected. As a result, two recombined beams are formed, one traveling toward the detector and the other to the radiation source. In what follows, we only focus on the beam hitting the detector. This beam is due to a superposition of the two light beams that have traveled along different optical paths. The path difference, which depends on the geometric path difference induced by the movable mirror, leads to a phase difference of the two recombining waves of IR radiation. For the two waves in phase, constructive interference results, whereas a phase shift by π (geometrically a shift by $\lambda/2$) leads to destructive interference. This means that the detector will either receive a maximum signal (constructive interference) or a minimum signal (destructive interference).

To simplify the problem, we assume monochromatic radiation initially. The superposition of the two beams will produce an interference pattern as shown at the top of Figure 3.26.

Suppose the detector receives a maximum signal. If the movable mirror is moved a distance $\lambda/4$, the reflected radiation has passed an additional distance $2 \cdot \lambda/4 = \lambda/2$, which means that it interferes destructively with the other light beam from the fixed mirror, giving rise to a minimum signal. For a mirror distance of $\lambda/2$, the total shift is λ, that is, there will be a maximum signal again. Continuous movement leads, therefore, to a wavelike signal that can be described by a sine function.

This is registered depending on the movable mirror position and is called an *interferogram*, representing the raw FTIR data. If the radiation source additionally emits a second wavelength with a minor wavelength difference, we get an interferogram that is the superposition of the two single interferograms (Figure 3.26 middle). One could proceed to add more wavelengths with successively more complex

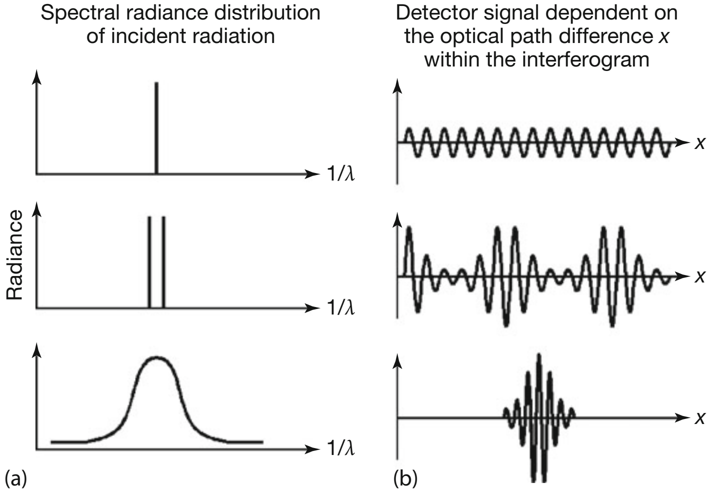
Spectral radiance distribution of incident radiation
Detector signal dependent on the optical path difference x within the interferogram
Radiance
1/λ
1/λ
1/λ
x
x
x
(a)
(b)

Figure 3.26 Basic principle of FTIR. The interferogram (b) generated from the detector signal during mirror movement depends on the spectral radiance distribution (a) of the incident radiation. For the interferograms the average detector signals (DC part) have been subtracted.

interferograms. Figure 3.26 bottom shows the result if the radiation source emits a broad continuous spectrum, for example, that of the thermal IR radiation of an object. The resulting interferogram will now be the superposition of the interference contributions of all wavelengths and will look significantly more complex than a single-wavelength interferogram. It contains the information about the source radiance at all wavelengths, the sinusoid frequency of each wavelength in the interferogram being inversely proportional to its wavelength.

The interferogram of a broadband radiation source is characterized by a big spike (centerburst) at zero optical path difference (OPD; Figure 3.26). At this point all waves are in phase. This causes a maximum signal contribution, resulting in a maximum detector signal. If the optical path difference is increased, the detected radiance will decrease and become an oscillating one.

The FTIR raw-data file consists of a large number of data pairs representing the detector signal as a function of different optical path differences during mirror movement.

If FTIR spectrometry is applied to an imaging system, we need to multiply the number of data pairs by the number of detector pixels of the focal plane array. All wavelengths contributing to the interferograms are analyzed to extract the spectral information. Fourier transformation is applied in detail to the interferogram to get the spectral radiance of all wavelengths forming the observed interferogram. The extremely large number of data points requires a fast algorithm (Cooley–Tukey algorithm, discovered in 1965) and high computational power [28]. Today, specially designed Fourier microprocessors are used most often to achieve a very high transformation speed. The Fourier transformation converts the interferogram into a spectrum (Figure 3.27). In spectral imaging, these spectra form the third dimension of the data cube.

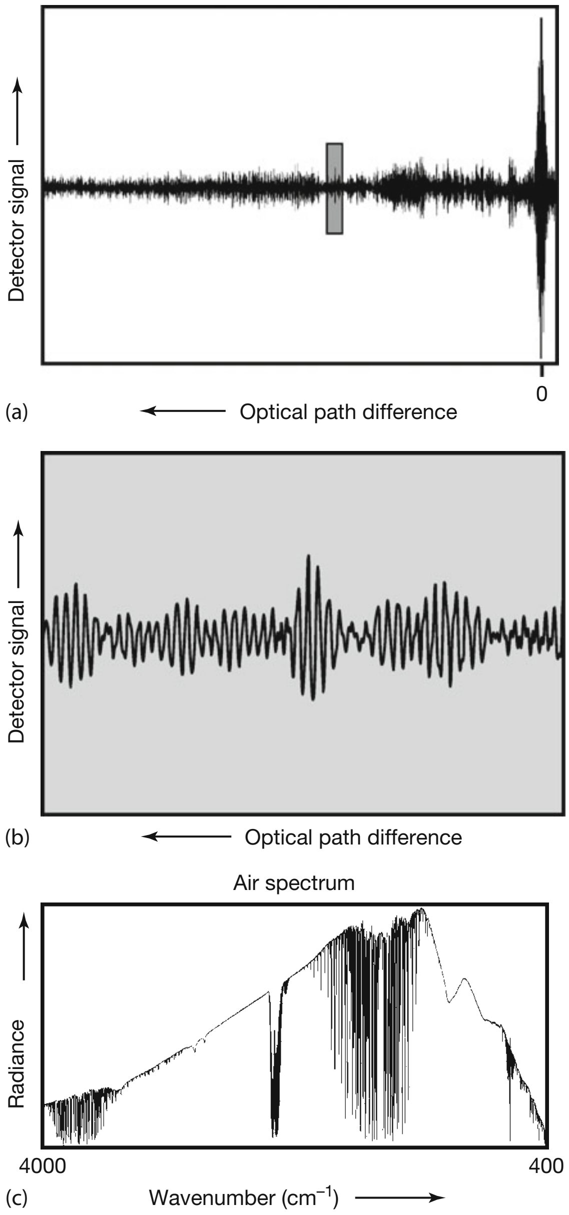

Figure 3.27 A Fourier transformation is used to convert interferogram (a) into wavenumber-dependent spectrum (c). For the example, a spectrum of air was chosen. The feature in the middle of the spectrum corresponds to CO_2, and the absorption close to the maximum of the radiance curve reflects water vapor. Obviously, it is impossible to guess, just from looking at the interferogram, which absorption feature will be present. Besides the complete interferogram (a), an expanded view to the left-hand side of the centerburst is shown (b) to better resolve the rapid oscillations in the interferogram.

3.2.3.3 Advantages of FTIR Spectrometers

The importance of interferometers for spectrometry is based on two fundamental advantages compared to dispersive instruments known as *Fellgett* and *Jacquinot* advantages [29]. These advantages, in addition to a few others, also enable the adaptation of an IR spectrometer to an IR camera.

The Fellgett advantage is also called the *multiplex advantage*. In a conventional dispersive spectrometer, the wavelengths are observed sequentially while the grating is being scanned. In a FTIR spectrometer, the detector signal at any given time already contains the contribution of all wavelengths. This causes a strongly increased SNR. As a consequence, FTIR can provide a spectrum much faster than dispersive spectrometers can with the same SNR.

For spectral imaging, this is a crucial point, in particular if scenes are studied with rapid radiance changes as a function of observation time. The longer the time needed to record a spectrum for a given object point, the larger can be the effect of transient changes. Unfortunately, any time dependence of the radiance received from the source during the recording time of the interferogram (i.e., while the movable mirror is still moving) will lead to mathematical artifacts in the subsequent Fourier transformation. This can cause complete misinterpretation of the spectrum (Figure 3.28).

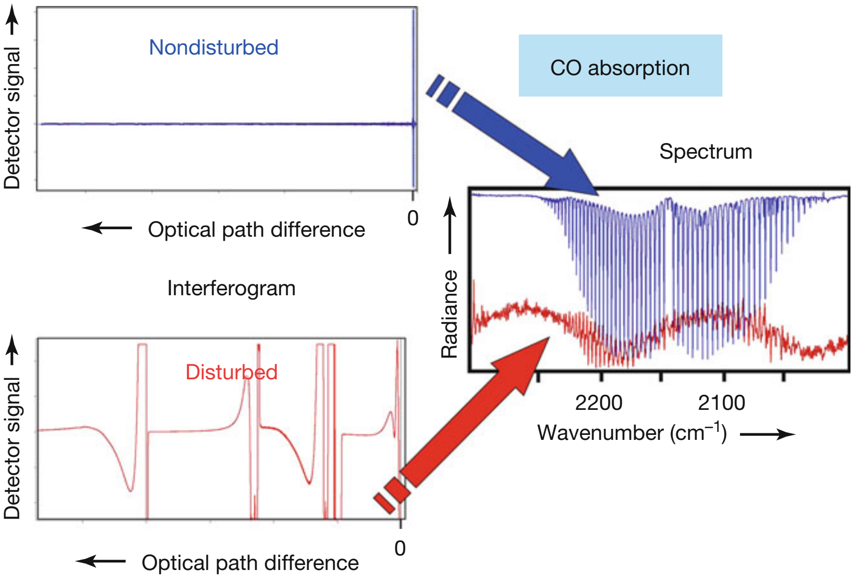

Figure 3.28 Influence of radiance variations during mirror scan and interferogram data acquisition on resulting spectrum of a CO gas sample after Fourier transformation. Disturbance was artificially introduced by briefly blocking the signal three times during data recording. The spectrum calculated from the disturbed interferogram does not allow for detecting the characteristic CO spectral absorption lines.

Therefore, fast mirror movement in the interferometer and high frame rates in the spectral imagers are necessary to prevent these problems. This requires low integration times or, in other words, very fast photon detectors. Lowering the integration times will, however, decrease the detector signal, which means that the SNR of radiation detection during acquisition of the interferogram becomes important.

To quantitatively characterize the SNR in thermal imagers with spectrometers, beyond the NEP and NETD quantities, the noise-equivalent spectral radiance (NESR) is introduced [30]. The spectrally dependent NESR determines the minimum incident spectral radiance necessary to reach a SNR equal to unity at a given spectral resolution and wavelength. The NESR is given in terms of nW $(\mathrm{cm}^2\,\mathrm{sr}\,\mathrm{cm}^{-1})^{-1}$, depending on the wavelength and the spectral resolution for a single scan (single interferogram measurement).

The Jacquinot or *throughput advantage* of FTIR spectrometers over dispersive spectrometers stems from the fact that no slits are used to define the spectral resolution. This causes a much higher detector signal and therefore a higher SNR at each point of the interferogram. However, in reality, there are also some slitlike limits in interferometers. The spectral resolution is affected by the level of collimation of the beams in the two paths of the interferometer. This defines a useful input aperture of the spectrometer especially if a high level of spectral resolution is reached.

One additional advantage of FTIR spectrometry is the so-called Connes advantage. Usually, a frequency-stabilized laser operating in the visible spectral range, for example, a He–Ne laser, is used as an internal wavelength standard. The corresponding FTIR instruments are self-calibrated spectrometers because the moving mirror position is measured very accurately from the laser interferogram. The laser wavelength or frequency stability determines the wavelength accuracy of the FTIR.

Another advantage of FTIR spectrometers is the achievable spectral resolution. As a first approximation, the spectral resolution of a FTIR spectrometer is given by the reciprocal of the maximum achievable optical path difference in a Michelson interferometer. For example, a spectral resolution of $2\,\mathrm{cm}^{-1}$ requires an optical path difference of at least 0.5 cm, whereas the typical best resolution of $0.25\,\mathrm{cm}^{-1}$ requires path differences of at least 4 cm (which, of course, results in a longer time for recording the spectrum). Figure 3.29 depicts an example of analyzing a CO sample with poor ($2\,\mathrm{cm}^{-1}$) and good ($0.25\,\mathrm{cm}^{-1}$) spectral resolution. The center of the absorption band at a wavenumber of about $2150\,\mathrm{cm}^{-1}$ corresponds to a wavelength $\lambda = 1/(2150\,\mathrm{cm}^{-1}) = 4.65\,\mu\mathrm{m}$.

3.2.3.4 **Example of a Hyperspectral Imaging Instrument**

Imaging spectrometers have recently become commercially available for general scientific use. Both the spatial and spectral information of an object scene can be captured simultaneously by IR hyperspectral imagers. Today this technology is applied to military, airborne (combustion processes), research, and environmental (chemical agent detection and investigation) applications [30–32]. As a

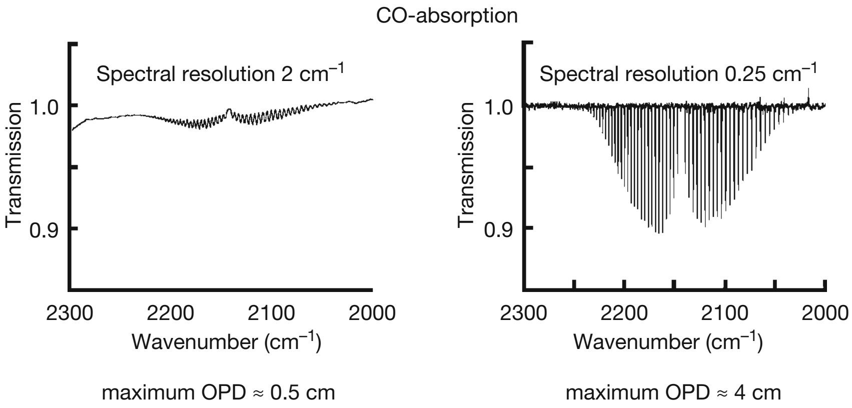

Figure 3.29 Influence of maximum optical path difference in interferometer on spectral resolution of FTIR spectrometry using example of ro-vibrational MW absorption spectrum of CO molecule.

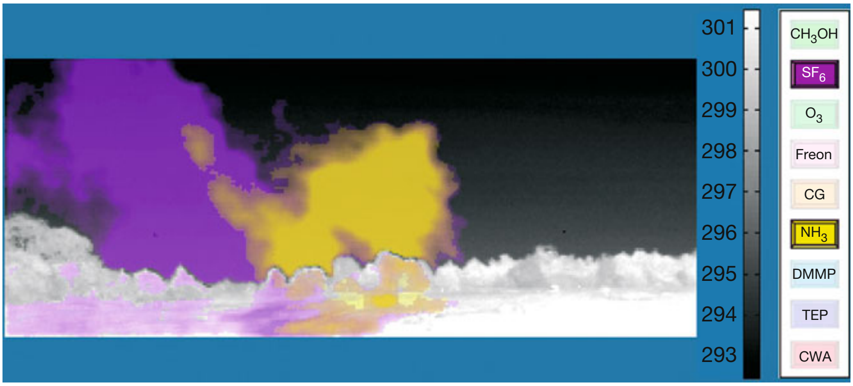

Figure 3.30 Detection and identification of constituents in a gas mixture using hyperspectral imaging. Different spectral channels for the absorption features of NH_3 (yellow) and SF_6 (violet) easily allow one to distinguish several gas species simultaneously. In addition, the temperature of the nongaseous opaque object is indicated by the grayscale. (Image courtesy Telops Inc., Quebec, Canada; www.telops.com.)

unique investigation tool for the identification of chemical substances or constituents of gas mixtures and solids, IR hyperspectral imaging will most probably find many additional application fields. Figure 3.30 depicts the detection and identification of a cloud consisting of a SF_6/NH_3 gas mixture with a LW (8–11 μm) hyperspectral camera. The temperature distribution of the object scene is shown in grayscale. The SF_6 and NH_3 identified from their spectral absorption signature (see Chapter 8 and spectra in Appendix 8.A) are depicted in different colors. The data were captured at an image size of 320 × 128 pixels and a spectral resolution of 4 cm^{-1} [31]. A complete data cube was measured within 5 s. This even makes it possible to detect cloud displacement in nearly real time (frame rate: 0.2 Hz).

3.3
Superframing

High-dynamic-range scenes with large temperature differences often cause serious problems in thermal imaging. Throughout any thermal image a high temperature contrast should be present. This allows to show small temperature differences. In general this is possible, but only within a defined and user-selectable temperature range. However, if we have an object scene with object temperatures ranging, for example, from 10 to 140 °C and we use a thermal camera with the two measurement ranges −20 to 80 °C and 30 to 150 °C, it is not possible to get an image with high contrast for all object temperatures within either of the chosen ranges. If the lower temperature range is used, all objects at higher temperatures are presented as saturated. If the higher temperature range is used, objects with temperatures below the lower temperature limit of this range will be presented as being very noisy. Obviously, it would be desirable to combine the complete information contained in these two images in a single image in such a way that the pixels representing lower-temperature regions are measured in the lower range and those of higher temperatures in the upper range.

The easiest way to define the temperature measurement ranges is by selecting the signal integration time. This method is used for photon detector cameras. The time constants for IR detectors strongly differ between photon detectors and thermal detectors (Section 2.4.2). Typical time constants of photon detectors are in the microsecond range and sometimes also below 1 μs. Therefore, signal integration with a user-selectable integration time from microseconds to milliseconds can be applied to photon detector cameras.

Figure 3.31 shows two typical signal responses for a low- and a high-sensitivity detector (for a well-defined spectral band) versus object temperature for a defined integration time. The signal is usually represented by a 12–14 bit number,

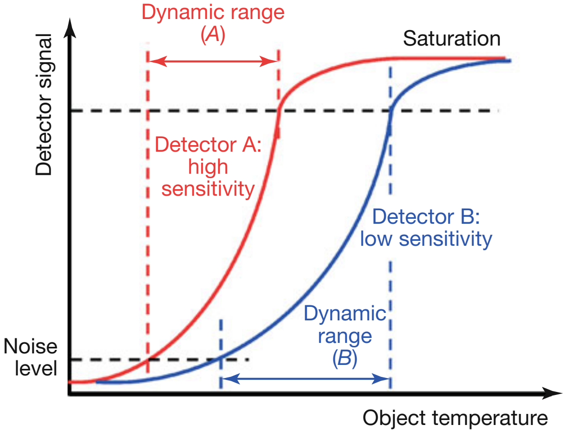

Figure 3.31 Schematic plot of object-temperature-dependent detector signal for low- and high-sensitivity detectors, respectively.

that is, a count rate. This signal is almost linearly proportional to the in-band radiance, that is, the radiance detected within the detector spectral band. On the other hand, the in-band radiance depends nonlinearly on object temperature (integration of the Planck function across a chosen wavelength band of detector). Therefore, the detector signal depends nonlinearly on object temperature, as shown in the schematic plot of Figure 3.31. For very low temperatures, the signal is below the noise level. For ranges between about 10%–20% and 80%–90% of the maximum signal, there is a well-defined relation between object temperature and detector signal. This region may be used for quantitative analysis and defines the dynamic range of the detector for the given integration time. For higher temperatures, the detectors will be saturated.

Both detectors in Figure 3.31 were chosen to start with their response at about the same object-temperature level. Obviously, the lower-sensitivity detector has a larger dynamic range, that is, a larger object-temperature range can be simultaneously recorded. Photon detectors usually have smaller dynamic ranges. This fact is well known to users of MW and LW systems: the temperature ranges of bolometer cameras are usually larger than that of photon detector cameras (Section 2.4.2). To deal with the obvious disadvantage of smaller temperature ranges for photon detector cameras, a method to extend the dynamic range, called *superframing*, has been introduced [33].

3.3.1
Method

Superframing uses the fact that photon detector response curves depend on integration times. First, they are shifted to a higher temperature, and, second, the slopes of the response curves decrease for smaller integration times. Figure 3.32 schematically depicts three response curves of the same detector for three different integration times.

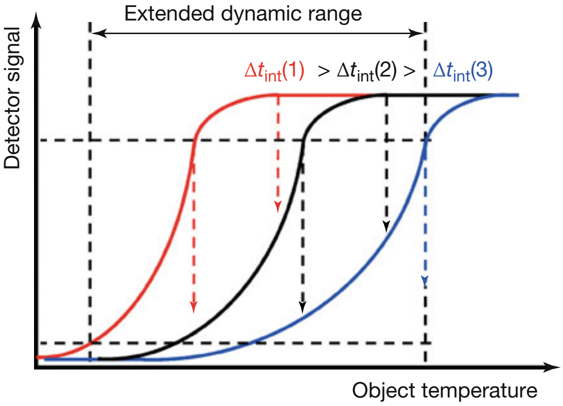

Figure 3.32 Response curves of a detector for different integration times.

The response for the longest integration time (red curve) is steepest and only has a small dynamic range. However, the signals close to the saturation limit can be easily recorded well within the dynamic range of the detector response with a slightly smaller integration time (black curve). This response curve has a dynamic range that partially overlaps with that of the longest integration time. For sufficiently large object temperatures, the detector will again be saturated for the chosen integration time, but it is also possible to record the object scene with an even smaller integration time (blue curve). Each integration time will have its own dynamic range, and within this range, a quantitative determination of the object temperature is possible once the detector is calibrated for the corresponding integration time. Overall, the recording of the same object scene with a certain number of differing integration times (e.g., up to four) will increase the overall dynamic range. It is then possible to combine the temperature information from all integration time measurements to receive a single result with a much higher dynamic range.

Such a procedure is useful whenever an object scene contains sources with very large temperature differences whose span is beyond the temperature region within the dynamic range for the chosen integration time. Besides using IR images of the same object scene for different integration times (typical use for photon detector cameras), it is also possible to use superframing for any camera by combining IR images of the same scene recorded for different temperature ranges, for example, by inserting a filter.

However, if the integration time is changed using, for example, four preset times, the superframed images can only be recorded at one-fourth of the possible image frame rate for a single integration time. As an example, a camera operating at a maximum frame rate of 120 Hz and using four subframes would achieve a maximum superframe rate of 30 Hz because of the four subcycles recorded for each full frame of the object scene. Figure 3.33 illustrates how a superframe image is practically formed from a series of IR images.

The four subframes show images of the same scene, here the wheel of a car with hot brake disc behind. Subframe 1 is almost entirely saturated, with the exception of background around the wheel and a few parts between the brake disc and outer wheel. The subsequent subframes (recorded with either shorter integration time or additional filters) allow one to observe more and more details of the hot parts of the scene, and, finally, subframe 4 only detects the hottest parts of the scene without saturation. The superframe image, shown below, is a superposition of the subframes generated after the recording using the following algorithm. The procedure starts with the subframe representing the lowest measurement range. If a pixel in the first subframe is saturated, the corresponding pixel of the next subframe is analyzed. If its pixel signal is within the dynamic range of the detector, then its signal representing radiance or via the calibration curve the temperature is used to build up the superframe. If the pixel is saturated in the second subframe as well, the algorithm analyzes the third subframe, and so on. This procedure is repeated for all cycles. The algorithm results in one superframe for the chosen pixel per cycle. The procedure is performed for all pixels, and the

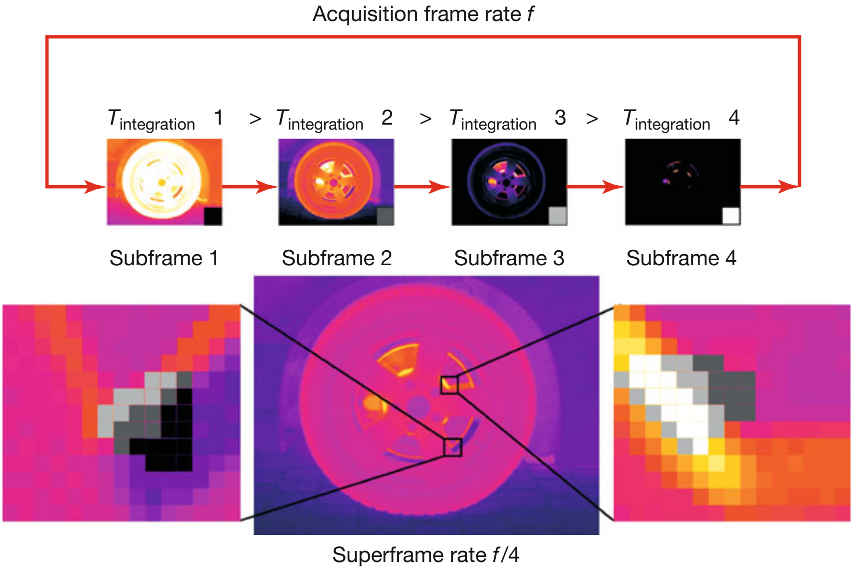

Figure 3.33 Scheme for the generation of a superframe image from four subframes (see text for details). The method is also known as *dynamic range extension* (DRX).

resulting superframe image will have high contrast and wide temperature range offering an increased dynamic range that corresponds to a signal depth of 18–22 bit compared to the typical 14 bit of single images. In Figure 3.33, two enlarged image sections of $15 \times 13 = 195$ pixels are shown directly illustrating how various subframes contribute to the resulting superframe image. In each small image, a smaller subset of about 30–35 pixels was selected and replaced by black (subframe 1), dark gray (subframe 2), light gray (subframe 3), or white (subframe 4) colored areas. Consider, for example, the image section to the right. No part in it is saturated: the yellow colors resembling high temperatures were taken from subframe 4, indicated by the white pixels, the medium temperatures, represented by orange, stem from subframe 3, and the lower temperatures indicated by pink were taken from subframe 2. Similarly, the left-hand-image section uses only pixels from subframes 1–3. Superframing operates well if the object scene does not change during the recording of the subframes, that is, during one recording cycle. Obviously, only high-frame-rate IR cameras can be used for the superframing of temporarily dynamic scenes with a large brightness dynamic range.

3.3.2
Example of High-Speed Imaging and Selected Integration Times

Figure 3.34 depicts FLIR SC6000 thermal images of a propeller-driven aircraft, the Beachcraft King Air, for two different integration times.

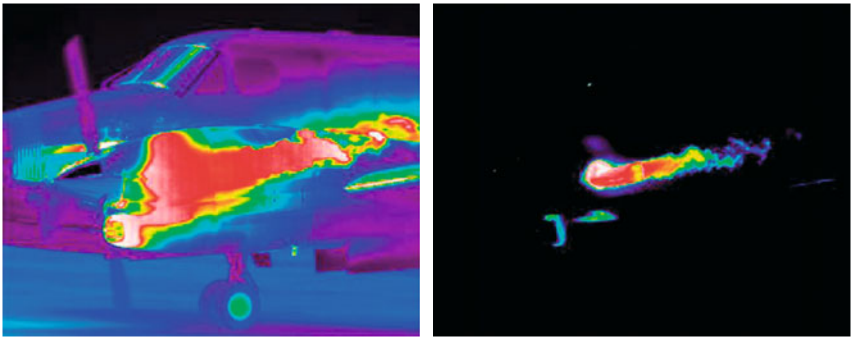

(a) (b)

Figure 3.34 Thermal images of a Beachcraft King Air grabbed using the FLIR MW SC6000 camera at 2 ms (a) and 30 μs (b) integration time. (Image courtesy FLIR Infrared Training Center.)

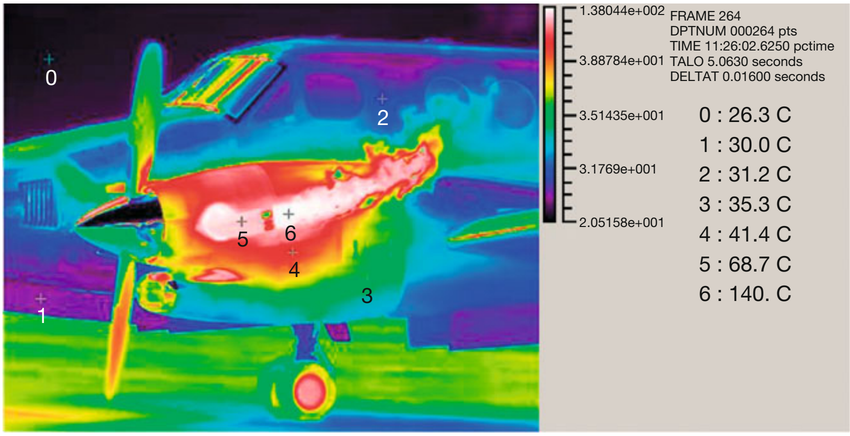

Figure 3.35 Superframe of four subframe images with 2 ms, 500 μs, 125 μs, and 30 μs integration times. (Image courtesy FLIR Infrared Training Center.)

The image in Figure 3.34a was captured with a long integration time of 2 ms in a temperature range of about 20–80 °C. Signal saturation occurs for the hot parts of the aircraft, especially the exhaust fumes. If the integration time is reduced to 30 μs, the range of the temperature measurement is changed to 80–300 °C. The image in Figure 3.34b only depicts the temperatures of the hot parts of the aircraft and some of the hot exhaust gases.

Figure 3.35 depicts the result of the superframing procedure using four subframes, the two shown in Figure 3.34 as well as those with integration times of 500 and 125 μs. This superframe presents an increased dynamic range of 20–300 °C without any loss of temperature resolution compared to each individual subframe.

3.3.3
Cameras with Fixed Integration Time

For thermal detectors the sensitivity and the time constant of the detector cannot be chosen independently (Section 2.2.3). Therefore, bolometer cameras do not offer a user-selectable integration time. Rather, the time is fixed and given by the thermal time constant of the microbolometer detector, which is in the range of several milliseconds, for example, 10 ms (Figure 2.106). In principle a signal integration similar to the procedure used for photon detectors can still be carried out by increasing the integration time above this detector time constant. This would, however, result in very slow signal detection (bad time resolution) and decreased frame rates. Therefore, external signal integration with an increased integration time is normally not used for bolometer cameras.

Nevertheless, the superframing algorithm can also be applied to standard IR cameras equipped with bolometer FPAs in a modified manner with the help of

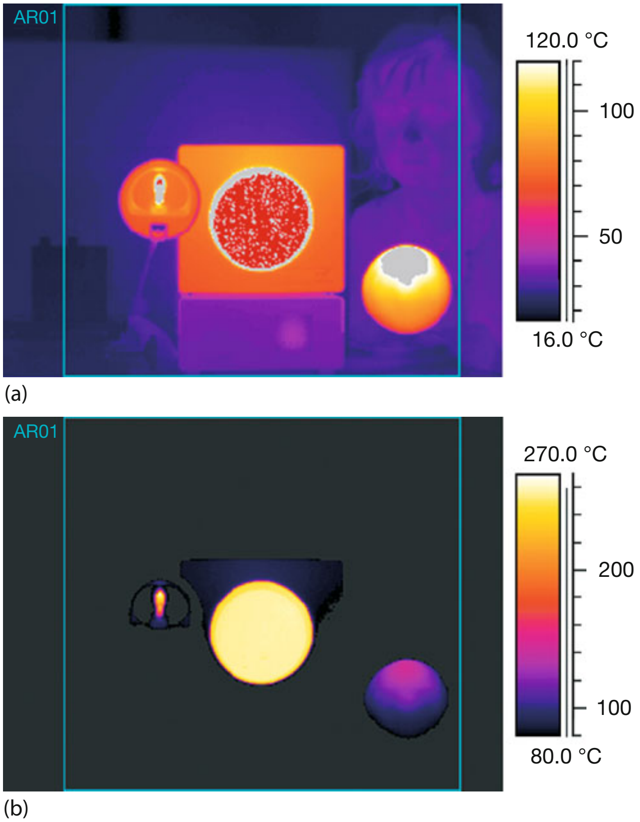

Figure 3.36 Thermal images of a high-dynamic-range scene. (a) Image captured using measurement range 40–120 °C. Temperatures above the upper limit of the measurement range (saturated pixels) are shown in white, gray, or red. (b) Image captured in measurement range 80–500 °C.

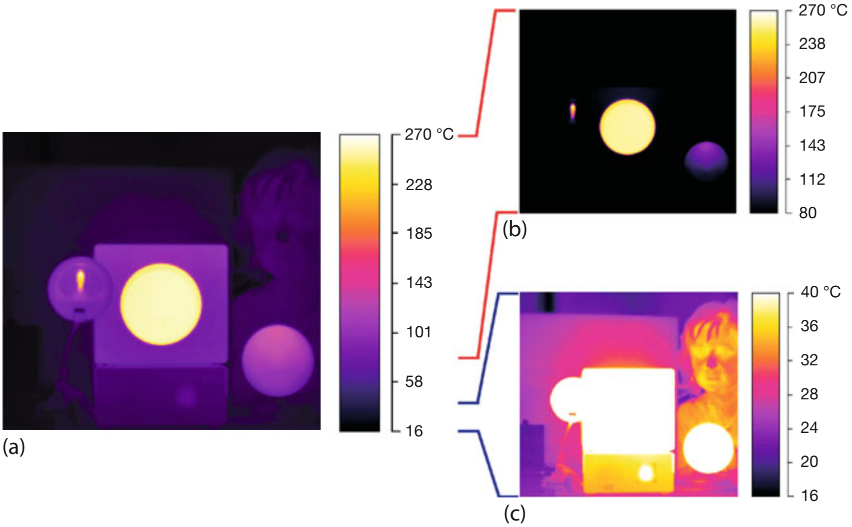

Figure 3.37 (a) Superframe generated by image postprocessing from marked regions of subframes depicted in Figure 3.36. (b,c) Superframe depicted with two different level and span parameters to demonstrate increased signal dynamic range.

the filters that are used to switch between the temperature ranges. For quantitative measurements, the object scene must, however, be characterized by steady-state conditions during the subframe recording. Figure 3.36 depicts a stationary object scene with temperatures in the range of 16–270 °C. The measurement ranges of the FLIR SC2000 LW bolometer camera used to grab these images are 40–120 °C (Figure 3.36a) and 80–500 °C (Figure 3.36b). The hot parts of the image (a halogen lamp with a maximum temperature of 270 °C, a blackbody emitter at 260 °C, and a lamp with a maximum temperature of 150 °C) are above the measurement range in Figure 3.36a and the cold objects are below the measurement range in Figure 3.36b.

A superframe is generated by using the described process. In Figure 3.36a, all temperatures above 120 °C have been replaced by the temperatures of the other image. Figure 3.37 depicts the superframe condensed from the possible extended dynamic range of 40–500 °C to a temperature range of 16–270 °C, which is adapted to the object scene. This image has the same temperature resolution as in the subranges.

3.4
Polarization in Infrared Thermal Imaging

Thermal radiation, being electromagnetic radiation, is described as a transverse wave. As such, it can have the property of being polarized either when unpolarized thermal radiation is reflected from surfaces or just when being emitted from

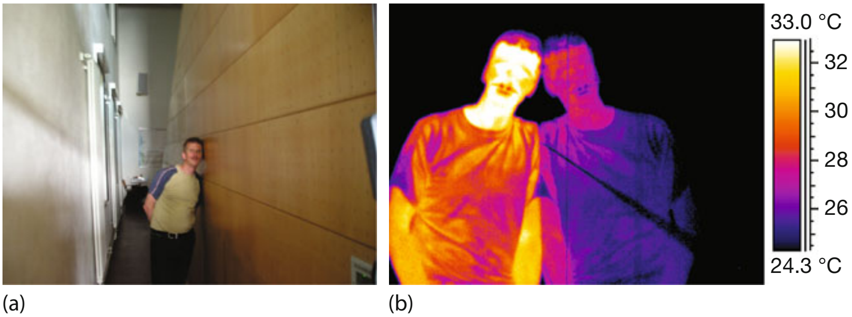

Figure 3.38 Example of thermal reflections from a man standing close to a wall made of varnished wood. (a) Visual image and (b) close-up view with LW IR camera.

various surfaces. In this section we first discuss polarization upon reflection and then potential image improvement procedures of thermal images by utilizing polarization upon emission from objects.

3.4.1
Polarization and Thermal Reflections

Thermal IR images often suffer from thermal reflections, which are a common source of problems when it comes to quantitatively interpreting images. Here, we want to present some exemplary experimental results that demonstrate the physics behind this feature and explain how to reduce them experimentally utilizing the property of polarization of thermal radiation upon reflection.

Not only atomically smooth surfaces such as glass, polished and varnished wood, metals, or wet surfaces but also brick and concrete may easily give rise to reflections of IR radiation from often unexpected sources. Most often people, including thermographers, are the origin of thermal reflections (Figure 3.38).

If unnoticed, such thermal reflections may give rise to misinterpretations of the object temperature. We will now analyze the differences between object IR radiation and thermal reflections and discuss ways to suppress or at least identify such reflections by the use of IR polarizers.

3.4.1.1 Transition from Directed to Diffuse Reflections from Surfaces

In conventional optics, in the visible spectral range, it is common knowledge that flat polished surfaces reflect part of the incident light, whereas the other part is refracted into the material (Figure 3.39). In physics and technology, reflection comes in two different forms: first, and primarily, reflection means specular (i.e., directed) reflection, which is described by the law of reflection (see also Figure 1.9 and Eq. (1.1)) that is, the angle of incidence is equal to the angle of reflection (Eq. (3.24)):

$$\alpha_1 = \alpha_1' \tag{3.24}$$

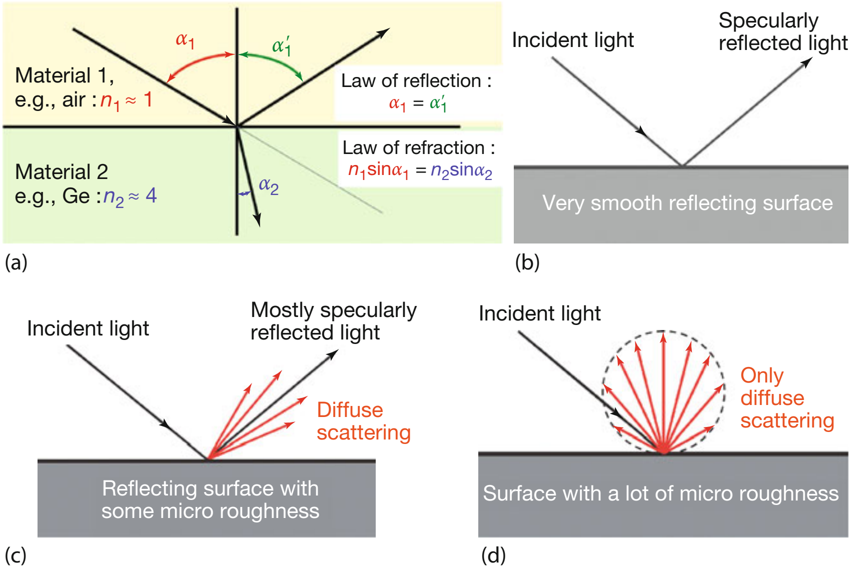
Material 1,
e.g., air : $n_1 \approx 1$
α_1
α_1'
Law of reflection :
$\alpha_1 = \alpha_1'$
Law of refraction :
$n_1 \sin\alpha_1 = n_2 \sin\alpha_2$
Material 2
e.g., Ge : $n_2 \approx 4$
α_2
(a)
Incident light
Specularly reflected light
Very smooth reflecting surface
(b)
Incident light
Mostly specularly reflected light
Diffuse scattering
Reflecting surface with some micro roughness
(c)
Incident light
Only diffuse scattering
Surface with a lot of micro roughness
(d)

Figure 3.39 Law of specular reflection and refraction (a) and transition from "normal" specular reflection (b) to diffuse scattering (c,d).

where the angles are defined as in Figure 3.39. The more common case of slightly rough surfaces – which predominate in everyday life – leads to diffuse scattering of incident light, as shown in Figure 3.39c,d. For perfect diffusely scattering surfaces, the angular distribution is that of a Lambertian source (Section 1.3.1.4).

In what follows, we refer to specular reflection when we mean conventional mirror reflection. Whenever diffuse scattering is meant, we explicitly say so. Mirrors should have reflectivities R (the portion of reflected light) close to 100% (1.00). Smaller reflectivities ($R < 1$) occur for every boundary between two media. The reflectivity is found in detail using the law of reflection to find the angle and then Fresnel's equations [34] to compute the reflectivity. In this chapter, all calculations that use the Fresnel equations assume perfectly flat surfaces without any influence of scattering (Figure 3.39a,b). Whenever scattering contributions due to rough surfaces become important, the ideal Fresnel equation results for reflectivity must be modified.

The material input parameter is the index of refraction, which is real for transparent materials and complex for absorbing materials. As an example for transparent materials, Figure 3.40 depicts the reflectivity for light impinging from air onto glass, characterized by an index of refraction $n = 1.5$. Obviously, the reflectivity strongly depends on the polarization of the incident light. The latter is given as the orientation of the electric field of the electromagnetic wave with respect to the plane of incidence, which is defined by the $\boldsymbol{k}$-vector, that is, the propagation direction of the light and the vector normal to the boundary of the surface. Usually, as shown in Figure 3.40, the plane of incidence is the drawing plane.

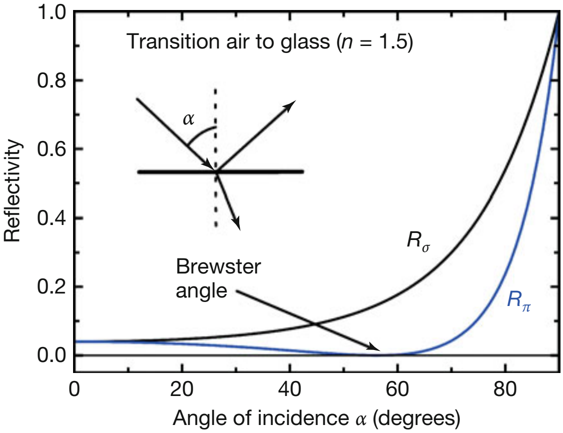

Figure 3.40 Reflectivity computed from Fresnel equations for a transparent material, defined by $n = 1.5$. This can be, for example, the transition from air to glass for visible light.

In this case, normal incidence ($\alpha = 0°$) leads to 4% reflection. Obviously, light polarized parallel (p or π) to the plane of incidence is not reflected at all if the angle of incidence is Brewster's angle, defined by $\tan\alpha = n_2/n_1$. Therefore, the reflected light is polarized perpendicular (s or σ) to the plane of incidence. This fact is used in photography: strong reflections from glass surfaces may easily be suppressed by the use of polarizing filters.

The reflection may not only be calculated for transparent bodies but also for absorbing materials like metals. Theory gives similar results, the main difference being that the materials are characterized by a complex index of refraction. The resulting reflectivity diagrams look similar to those for transparent materials (Figure 3.41); however, the minimum reflectivity usually does not reach zero, that is, the reflected light is only partially polarized. Still, the use of polarizing filters may be useful in partially suppressing reflections.

The situation is very similar when moving from visible light to the thermal IR spectral region. Depending on the materials under consideration and on the wave-

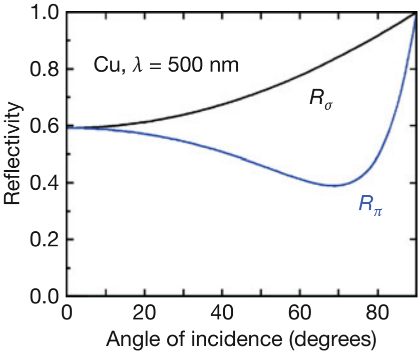

Figure 3.41 Reflectivity from a copper surface at $\lambda = 500$ nm according to Fresnel equations ($n \approx 1.12 + i2.6$).

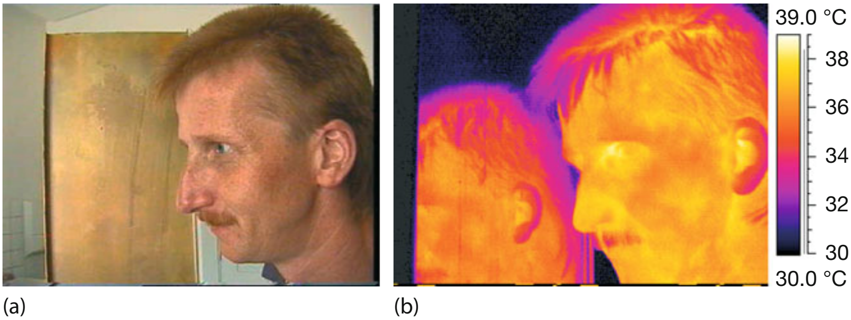

Figure 3.42 An oxidized old brass plate with a lot of surface roughness in the 1 μm scale or lower scatters light diffusely for visible light (a) but specularly, at least in part, for thermal IR radiation of $\lambda \approx 10\,\mu\text{m}$ (b).

length range, one may have nonabsorbing transparent materials such as NaCl ($\lambda < 20\,\mu\text{m}$) or absorbing materials such as metals.

Compared to the visible spectral range, the situation regarding reflections may become even worse, as illustrated in Figure 3.42, which depicts an old brass plate covered by oxide.

This plate is an atomically rough surface, as can be seen in the visible spectral range: no direct reflection can be seen. Investigating with a LW IR camera in the 8–14 μm wavelength range, one immediately sees reflections from the plate: obviously, the plate is a poor mirror in the visible range but a rather good one in the IR range. This behavior is due to the ratio of surface roughness and wavelength of the radiation. If λ is smaller or on the order of the dimension of the surface roughness, light is scattered diffusely, that is, a good mirror image is not seen. For wavelengths much larger than the roughness dimensions, the radiation is specularly reflected as from a mirror. A classical analogy is that of a soccer ball, which will most likely be reflected according to the law of reflection from a mesh wire if the mesh dimension is much smaller than the ball diameter. Now imagine using smaller balls!

In Figure 3.42, the IR wavelengths are more than a factor of 10 larger than the visible wavelengths, and one easily observes the transition from diffuse scattering to specular reflections [35].

Figure 3.43a depicts the specular reflectivity of the brass plate, as measured for an angle of incidence of 20° with respect to an optically polished Au surface for wavelengths from about 1.5 to 25 μm. Measurements were performed with FTIR spectroscopy [28, 29]. Obviously, the directed reflectivity strongly decreases toward the visible spectral range, that is, mostly diffuse scattering takes place in the visible range, explaining why no mirror image is seen. In contrast, at wavelengths of 10 μm, the reflectivity, which already amounts to about 70%, leads to the mirror image seen in Figure 3.42b.

To correlate the low specular reflectivity, that is, the large portion of diffuse scattering, to surface roughness, a small piece of the brass plate was analyzed

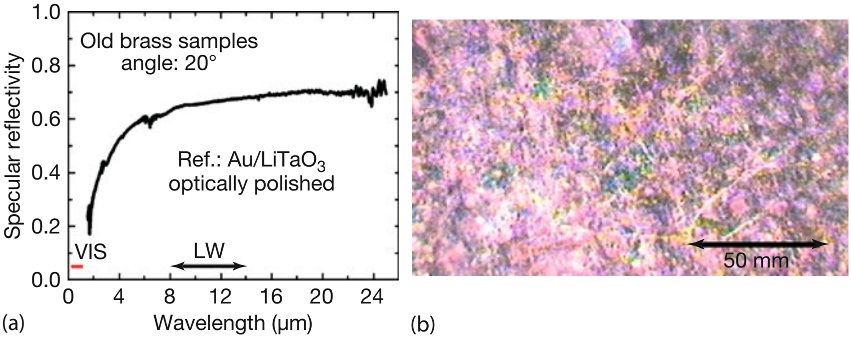

Figure 3.43 Analysis of brass plate. (a) Specular reflectivity as measured with a FTIR spectrometer and (b) light microscope image of surface of brass plate.

with conventional microscopy, dark field microscopy, and scanning electron microscopy. Figure 3.43b shows a typical example of an area of about $100 \times 165\ \mu m^2$ magnified with a light microscope. There are some scratches across the surface with widths in the 1–5 μm range and lengths of millimeters or more. In addition, there are many "pointlike" structures in the range of 1–3 μm as well as some larger ones, as is revealed by studying more pictures and also electron micrographs. These structures resemble surface roughness and are responsible for the transition from specular to diffuse scattering.

The consequence of this discussion is as follows. Flat and polished surfaces, in particular all kinds of metal surfaces, may easily result in reflections of IR radiation, even if they are do not reflect in the visible range. Therefore, all analysis of IR thermal images must consider the possibilities of thermal reflections.

If unnoticed, thermal reflections may be misinterpreted as sources of heat on the surfaces of the investigated reflecting bodies. Many possible thermal sources could serve as the origins of the reflections, for example, the sun for outdoor thermography or moving sources like humans for indoor thermography in the vicinity of objects under consideration.

It is, however, possible to identify thermal reflections and to suppress them. To achieve this, polarizers for thermal IR radiation in the MW (3.0–5.0 μm) and the LW range (8–14 μm) were used. The principle behind this is the same as in the suppression of reflections in visible photography: according to the Fresnel equations, radiation that is either polarized perpendicular or parallel to the plane of incidence will be reflected differently.

3.4.1.2 Reflectivities for Selected Materials in the Thermal Infrared Range

Reflectivities as a function of the angle of incidence have been computed for a number of selected materials in wavelength ranges of IR camera systems. The following examples are based on one set of optical parameters, although sometimes several sets were available [4]. Since all surface properties of materials may appreciably change by oxidation or corrosion, all theoretical examples should only give indications for the reflectivities. If very precise values are needed, each given sample needs to be characterized experimentally.

A quantitative description of how good the suppression by polarizers may be is possible by introducing the parameter z, which is defined for the angle $\varphi_{\min}$ of the minimum of the R_π curve:

$$z = \frac{R_\sigma(\varphi_{\min}) - R_\pi(\varphi_{\min})}{R_\sigma(\varphi_{\min})} \tag{3.25}$$

$z = 1$ would offer the possibility of complete suppression, whereas z close to 0 refers to the case of very small minima, that is, nearly no chance of suppression. In addition, practical requirements favor small Brewster angles that are, however, often not present. In such cases, it can still be helpful to get at least partial suppression or identification of thermal reflections. Hence, the following discussion focuses on minimum angles as well as on the parameter z. In the aforementioned example of Figure 3.40, $z = 1$ at 56.3° for glass and $z \approx 0.54$ at around 70° for copper in the visible range (Figure 3.41).

Metals

The most widely used metals are iron, iron alloys, or aluminum. Figure 3.44 depicts the reflectivity of iron for selected wavelengths in the MW and LW camera ranges. Similarly, Figure 3.45 gives examples for aluminum. The plots of Figures 3.44 and 3.45 are representative of the MW and the LW regions of thermography since the optical constants are functions that slowly but monotonously increase with wavelength. Obviously, the minima for R_π are at very large angles, that is, nearly grazing incidence for these (and many other) metals. This is not suitable for practical field work. Hence, a first conclusion is that suppression of thermal reflections will not be applicable to pure metal surfaces. However, even at angles in the range of 40–60°, many metals have z values in the range of several percent. This may be sufficient to at least identify thermal reflections.

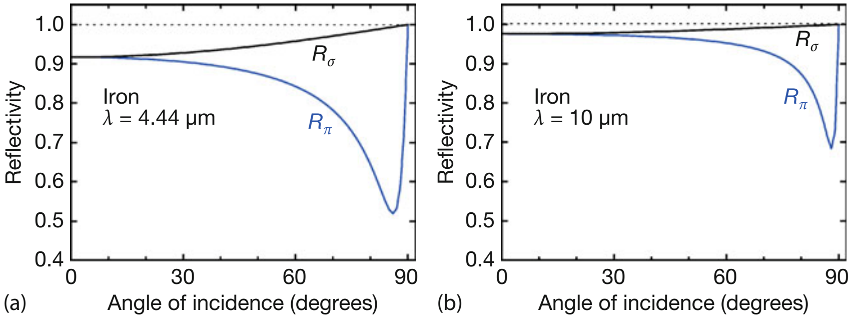

Figure 3.44 Reflectivity vs. angle of incidence for iron. (a) $\lambda = 4.44$ μm, $n = 4.59 + i13.8$; $\varphi_{\min} = 86°$, $z(86°) \approx 47\%$, $z(60°) = 12.5\%$; (b) $\lambda = 10.0$ μm, $n = 5.81 + i30.4$; $\varphi_{\min} = 88°$, $z(86°) \approx 32\%$, $z(60°) = 3.6\%$.

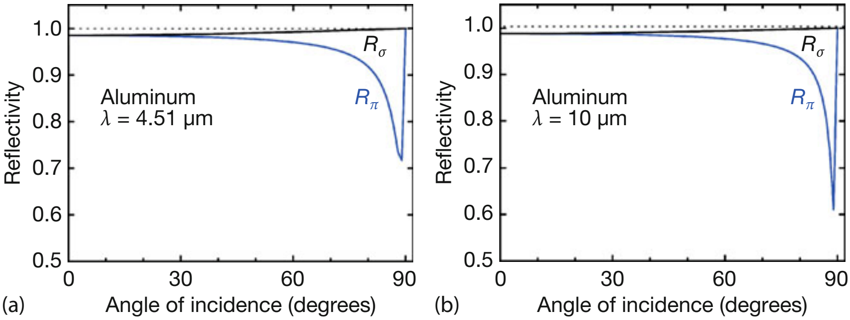

Figure 3.45 Reflectivity vs. angle of incidence for aluminum. (a) $\lambda = 4.51\ \mu\text{m}$, $n = 7.61 + \text{i}44.3$; $\varphi_{\text{min}} = 89°$, $z(86°) \approx 28\%$, $z(60°) = 2.2\%$; (b) $\lambda = 10.0\ \mu\text{m}$, $n = 25.3 + \text{i}89.8$; $\varphi_{\text{min}} = 89°$, $z(86°) \approx 40\%$, $z(60°) = 1.7\%$.

Nonmetals

In contrast to metals, other materials of practical use that absorb in the IR range offer much better options. Figure 3.46 illustrates the reflectivities for glass (SiO_2). In the MW region, $z = 1$, that is, 100% suppression should be possible at Brewster's angle. Also, an appreciable partial suppression should be possible for angles $> 30°$. Because of the absorption maximum of glass in the 8–10 μm range with a peak around $\lambda = 9\ \mu\text{m}$, a LW camera would not allow perfect suppression, but again, very satisfying results are already expected for angles $> 30°$.

As a final example, Figure 3.47 depicts reflectivity spectra for silicon. This example is motivated by investigations to study the temperatures of silicon wafers in situ with IR imaging. However, because of the large real part of the index of refraction of silicon of about 3.4, silicon wafers are very good mirrors for thermal radiation; hence, suppression of reflections is essential for correct measurements.

An obvious preliminary conclusion from these theoretical reflectivities is that the use of polarizing filters should be useful in suppressing thermal reflections for many materials, with the exception of metals, where the minimum angles are close to grazing incidence. A number of practical materials behave in a manner similar to the examples shown, for example, wood used for furniture or other indoor applications is often treated with lacquer, giving a very smooth reflecting surface.

3.4.1.3 Measuring Reflectivity Spectra: Laboratory Experiments

To verify the theoretical predictions and study their applicability for the suppression of thermal reflections, a series of laboratory experiments was carried out. The objects under study emit unpolarized IR radiation. In addition, disturbing thermal reflections from warm or hot objects in the surroundings were present. These reflections correspond to partially polarized radiation, which may be eliminated by appropriate polarizers.

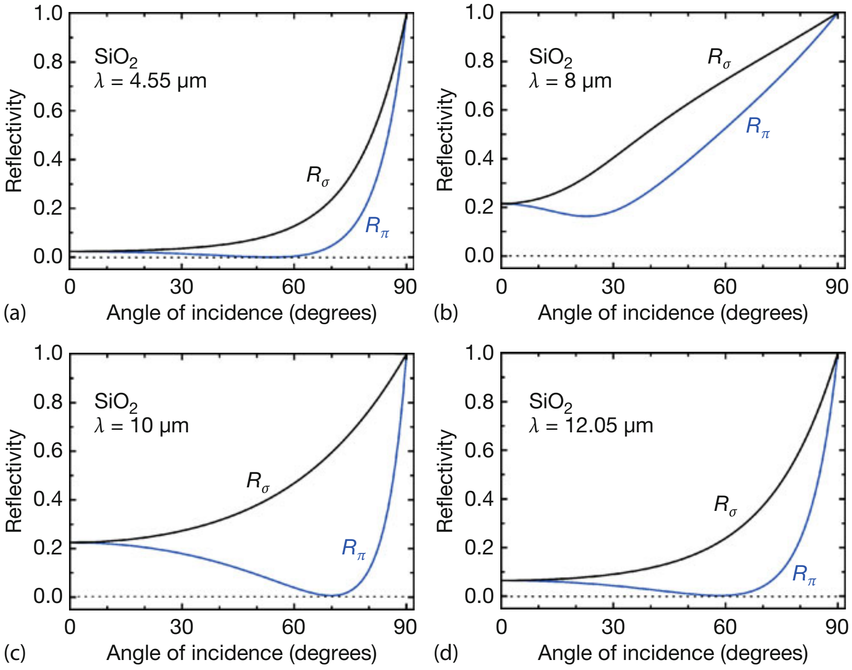

Figure 3.46 Reflectivity vs. angle of incidence for glass (SiO$_2$). (a) $\lambda = 4.55\,\mu m$, $n = 1.365 + i0.000\,256$; $\varphi_{min} = 54°$, $z(54°) \approx 1$; (b) $\lambda = 8\,\mu m$, $n = 0.4113 + i0.323$; $\varphi_{min} = 23°$, $z(23°) \approx 50\%$; (c) $\lambda = 10\,\mu m$, $n = 2.694 + i0.509$; $\varphi_{min} = 70°$, $z(70°) \approx 1$; and (d) $\lambda = 12.05\,\mu m$, $n = 1.615 + i0.267$; $\varphi_{min} = 58°$, $z(58°) \approx 1$.

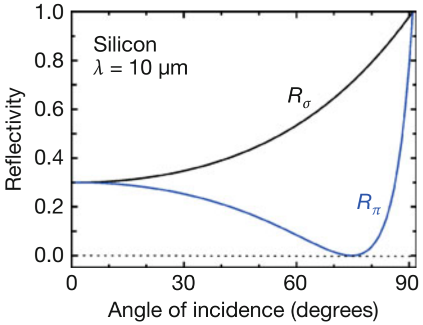

Figure 3.47 Reflectivities for silicon. $\lambda = 10\,\mu m$, $n = 3.4215 + i6.76 \cdot 10^{-5}$; $\varphi_{min} \approx 75°$, $z(75°) \approx 1$. The optical constants are nearly constant across the region of MW and LW thermal IR radiation; hence, results for $\lambda = 4\,\mu m$ look exactly the same as for the shown example of 10 µm.

Polarizers

Polarizers must be of a material that is transparent to IR radiation. In the studies described in what follows, polarizers with an aperture of 50 mm, made of Ge for the LW range and CaF$_2$ for the MW range, were used (in principle, the Ge polarizer can also be used for the MW range). The polarizing function is due to small metal strips on top of the corresponding substrates. For the Ge polarizer, they are 0.12 µm wide and made of aluminum with a grating constant of about

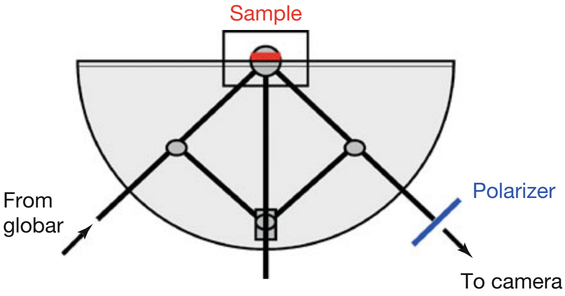

Figure 3.48 Arrangement for letting IR source and IR camera at fixed positions. Thermal radiation from a globar is reflected from the sample and passes a polarizer on its way to the camera. Under operation, the direction of the beam to the camera stays exactly collinear while the sample on the assembly is rotated. The incident radiation from the fixed globar is directed onto the entrance beam of the assembly by mirrors (not shown).

0.25 μm. Like metal grids for microwave radiation or Polaroid foils [34], only radiation with electric field vector pointing perpendicular to the strips will be transmitted. The Ge polarizer is equipped with an antireflection coating to minimize reflection losses.

Experimental Setup for Quantitative Experiments

The principal setup for quantitative angularly resolved measurements of reflectivity is shown in Figure 3.48. It was developed to simplify the experiments in keeping the IR source for the thermal reflections, a globar with T from 1000 to 1500 °C, and the detector, that is, an IR camera, at fixed positions while at the same time easily fulfilling the condition of the law of reflection. The whole assembly is mounted on a transparent plate with angular scale. With this assembly, angular measurements in a range between 27 and 85° are possible. For very large samples, the angular range can be extended to 89°, that is, grazing incidence that is necessary for metals.

Using this setup, a number of precise measurements were carried out with, for example, aluminum, iron, SiO_2 (glass), or silicon. The results confirm the theoretical expectations according to the Fresnel equations.

Example for Measured Reflectivity Curve

For selected materials, wavelength-dependent measurements of the reflectivities for parallel and perpendicular polarization were done. For polished and smooth surfaces, no deviations from the predictions of Fresnel's formulas are expected. If surface roughness comes into play, the influence of diffuse scattering could give rise to discrepancies. Experiments were done with the reflection accessory of a FTIR spectrometer. For selected angles, reflection spectra were recorded. Therefore, in principle, the spectra for all wavelengths are available. Figure 3.49 depicts some results for a silicon wafer, together with an enlarged view of the theoretical prediction, which is shown in Figure 3.47. The experimental values nicely coincide with the predictions for π-polarization.

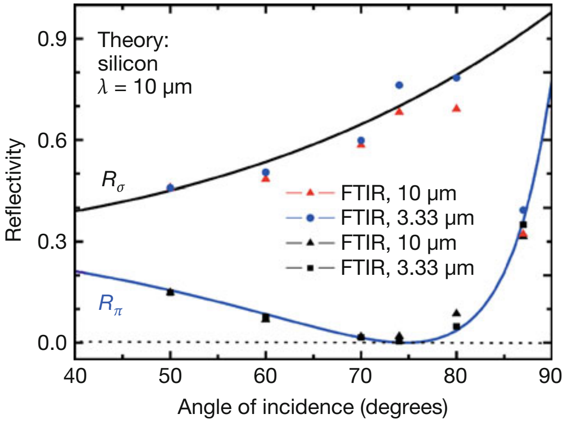

Figure 3.49 Angular dependence of reflectivities R_π and R_σ for silicon at wavelengths 10 and 3.33 μm compared to theoretical expectations.

3.4.1.4 Identification and Suppression of Thermal Reflections: Practical Examples

In what follows, three applications are described. First, reflections from a polished silicon wafer, then reflections from normal glass (which may be encountered quite often in different thermography applications, for example, buildings), and, finally, reflections from polished and varnished wood are discussed.

Silicon Wafer

From Figures 3.47 and 3.49 it is expected that thermal radiation polarized parallel to the plane of incidence may be completely suppressed at a wavelength of about 10 μm. The absorption coefficient does vary a bit over the wavelength range of LW cameras [4], however, this is not enough to significantly change the plot of Figure 3.47. For MW wavelengths between 3 and 5 μm, it is even lower. Therefore, to the first order, silicon should behave as shown in Figure 3.47 for IR radiation all across the MW and LW ranges.

The setup for this experiment and the one with glass is shown in Figure 3.50. An 8-in polished silicon wafer was attached to a clean glass plate. It sticks to it immediately via adhesion forces. A human face served as a source of IR radiation, which is reflected from the wafer. An LW IR camera is positioned in a direction corresponding to an angle of 75° with respect to the surface normal of the wafer, that is, close to its Brewster angle. Figure 3.51 depicts the resulting IR images.

Clearly, a perfect mirror image is seen in the visible as well as in the IR if the polarizer transmits the perpendicular component (Figure 3.51a). In particular, the reflections from the wafer and the glass can be studied simultaneously. Rotating the polarizer (Figure 3.51b) by 90°, the thermal mirror image on the wafer is more or less suppressed completely, whereas one may still see a part of the thermal reflection on the glass.

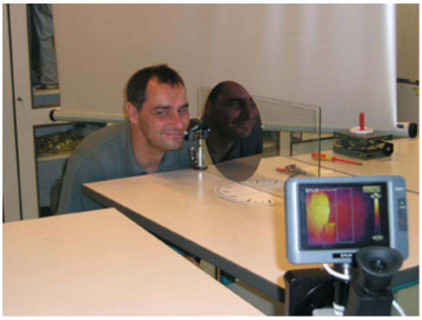

Figure 3.50 Experimental setup with glass plate and silicon wafer (attached to it by adhesion) oriented vertically. The face of a colleague served as an IR source. The angle of incidence (and reflection) was chosen close to 75°.

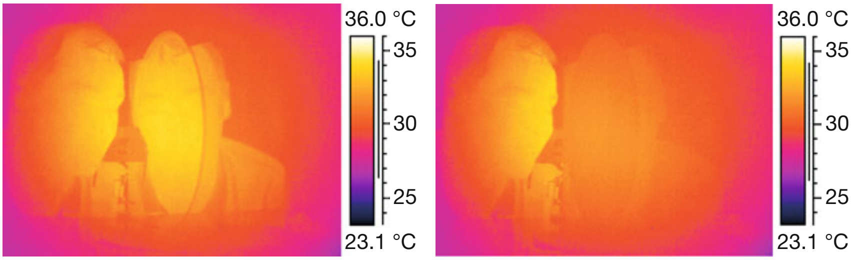

(a)

(b)

Figure 3.51 Suppression of thermal reflections from wafer as observed through IR polarizer oriented (a) perpendicular or (b) parallel to plane of incidence at angle of incidence of ≈ 75°.

Glass Plates

According to Figure 3.46, the angle of 75°, which is the Brewster angle for silicon, is not expected to work just as well for glass. This is why Figure 3.51 still showed the contours of a reflected image on the glass plate. This is an example of how the method works if the angle is not perfect: there is only partial suppression, but this is sufficient to at least identify thermal reflection sources. Still, thermal reflections from glass can also be suppressed more or less completely. Figure 3.52 depicts again the IR image of a person bending over a horizontal table with a vertically oriented glass plate.

The wafer was removed, that is, only reflections from the glass could occur. Obviously, pronounced thermal reflections from the glass plate can be observed.

Figure 3.53 shows the same scene with the IR polarizer being oriented either parallel or perpendicular to the plane of incidence. The change in absolute temperature is not relevant here; it is due to the fact that the warm polarizing filter was just placed in front of the camera. First, thermal reflections of the warm detector from the polarizer surface may contribute (the Narcissus effect); second, the IR camera was not calibrated with this filter. Hence, the results are more or less only qualitative.

Figure 3.53 nicely demonstrates the more or less complete suppression of the thermal reflections. According to Figure 3.46, it is not possible to easily attribute a specific Brewster angle for the λ range from 8 to 14 μm to glass since the reflectiv-

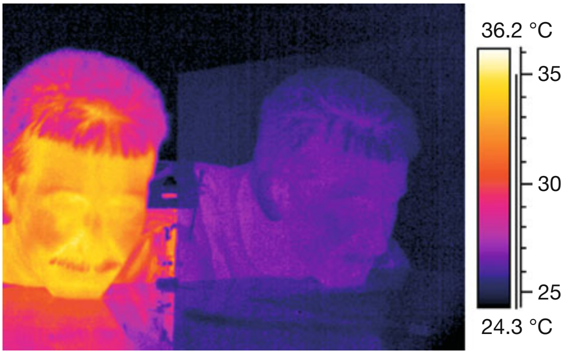

Figure 3.52 Thermal reflections from a glass plate, observed with a LW IR camera without any polarizing filter.

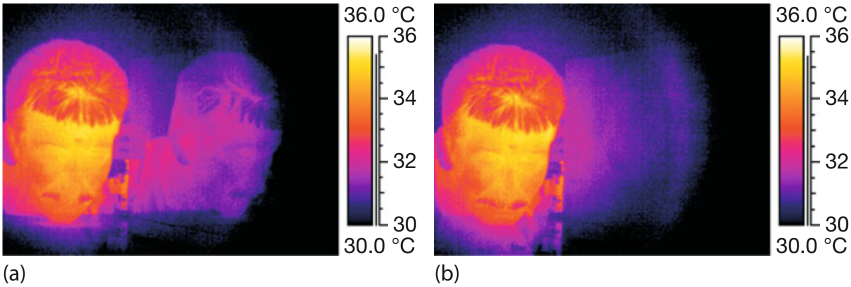

Figure 3.53 Thermal reflections from glass plate of Figure 3.52, observed with LW IR camera through IR polarizer oriented perpendicular (a) and parallel (b) to plane of incidence.

ity curves vary appreciably; therefore, the angle was optimized for these images, and it was probably around 60°. For different angles, the suppression would only be partial but still sufficient to identify disturbing thermal sources (see earlier example of silicon wafer).

Glass is used in many applications of thermography, in particular building thermography, and so care should be taken to assure that the signals from the camera are real and not due to reflections.

Varnished Wood

Varnished wood has very smooth surfaces, similar to thin films. Hence, specular reflections are to be expected, in particular at large angles of incidence. Figure 3.38 already demonstrated pronounced thermal reflections from such surfaces. In Figure 3.54, IR images of the same scene were recorded while looking through the Ge polarizer. As in the case of the silicon wafer and the glass plate, the reflections can be strongly suppressed if the polarizer is oriented parallel to the plane of incidence (Figure 3.54b).

In conclusion, thermal reflections are a nuisance in IR imaging. They are a common source of disturbing signal contributions to object signals and complicate any

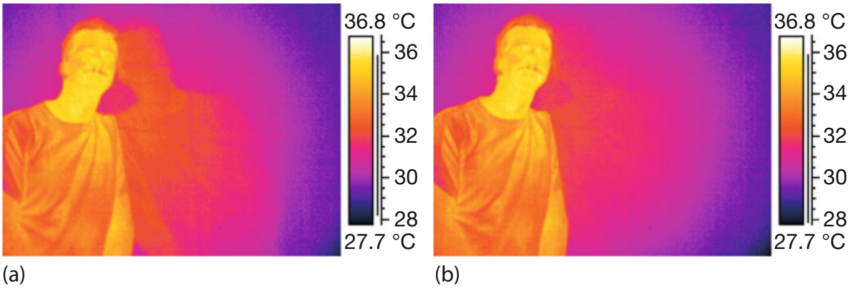

Figure 3.54 Suppression of thermal reflections from varnished wood as observed through IR polarizer oriented (a) perpendicular and (b) parallel to plane of incidence.

kind of quantitative analysis. Therefore, it is very important to identify sources of thermal reflections and, if possible, suppress them. So far, no commercial solutions are available. Laboratory experiments have, however, proven the suitability of polarizing filters to at least identify such reflections at nonnormal incidence. The results, demonstrated for several materials, are very encouraging and suggest that the method is applicable to a much wider range of materials.

3.4.2
Polarization-Sensitive Thermal Imaging

Polarization is a fundamental property of electromagnetic radiation (Section 1.2) and can provide important additional information not only in visual imaging [36] but also in IR thermal imaging investigations. Polarimetric sensing techniques and especially imaging polarimetry are widely used in such different fields as photography, microscopy, spectroscopy, atmospheric remote sensing, astronomy, and biomedical diagnostics [37].

In conventional IR imaging with commercial cameras, the object radiance within a defined waveband incident on the detector is measured. This signal depends on the object temperature and is not sensitive to the polarization state of incident IR radiation.

However, any radiation emitted from a source can be partially polarized and, utilizing the polarization, may help to enhance fine details of an object within an image. Since polarization (usually) does not depend on temperature, the display of polarization information in thermal images can obscure the temperature information. Therefore, polarization in IR imaging is mostly used as an additional qualitative tool to enhance contrast and detail in IR images. It can be due to two different, though related, mechanisms.

First, polarization in emitted IR radiation can occur if the object emissivity depends on the angle of observation. For example, the IR emissivity for water surfaces shows a distinct polarization dependence on the wavelength and the observation angle [38]. Second, scattering (including reflection) of unpolarized IR radiation from matter (Section 3.4.1) can lead to partial polarization of the radiation [36–39].

In recent years, IR imaging polarimetry has become more common in remote sensing owing to its demonstrated enhancement of sensitivity and image contrast [40, 41]. The resulting images reflect a mapping of the degree of polarization in an object scene, however, without including temperature information.

The typical setup for polarimetric imaging with a common IR camera just needs a suitable linear polarizer. The polarizer can be rotated in front of the camera in order to detect different polarization states depending on the polarizer orientation.

The following procedure is commonly used to construct a linear polarimetric image. The state of polarization is completely defined by the Stokes parameters S_0, S_1, S_2, and S_3 [36]. For a linear polarization imager (the most common class of imaging polarimeter) it is sufficient to determine the Stokes parameters S_0, S_1, and S_2 (S_3 refers to circular polarization; see [36, 42] for details). These Stokes parameters can be related to radiance measurements according to Eq. (3.26):

$$S_0 = L(0°) + L(90°) \tag{3.26a}$$

$$S_1 = L(0°) - L(90°) \tag{3.26b}$$

$$S_2 = L(+45°) - L(-45°) \tag{3.26c}$$

where $L(0°)$, $L(90°)$, $L(45°)$, $L(-45°)$ represent the measured radiance images for different linear polarizer orientations at angles 0°, 90°, +45°, −45°, respectively.

The degree-of-linear-polarization (DoLP) image is defined as [36, 42]

$$\text{DoLP} = \frac{\sqrt{S_1^2 + S_2^2}}{S_0} \tag{3.27}$$

and it may be easily calculated from the measured radiance images. It ranges between 0 (unpolarized) and 1.0 (linearly polarized).

The image quality improvement in terms of details within the resulting DoLP images of an object scene with a human (b) and an enlarged human face (d) with respect to conventional thermal images (a,c) are shown in Figure 3.55 (after [42, 43]). In DoLP images, facial contours are much more visible and the enhanced image contrast is clearly seen.

3.5
Processing of IR Images

IR images represent a spatial radiance distribution incident on the detector array. The first image processing is done inside the camera firmware by calculating the temperature of the object scene from the detector signals using the camera calibration parameters and various user-defined parameters, for example, emissivity, ambient temperature, humidity, and measurement distance. The result is a false color image of the temperatures, which must be interpreted by the observer.

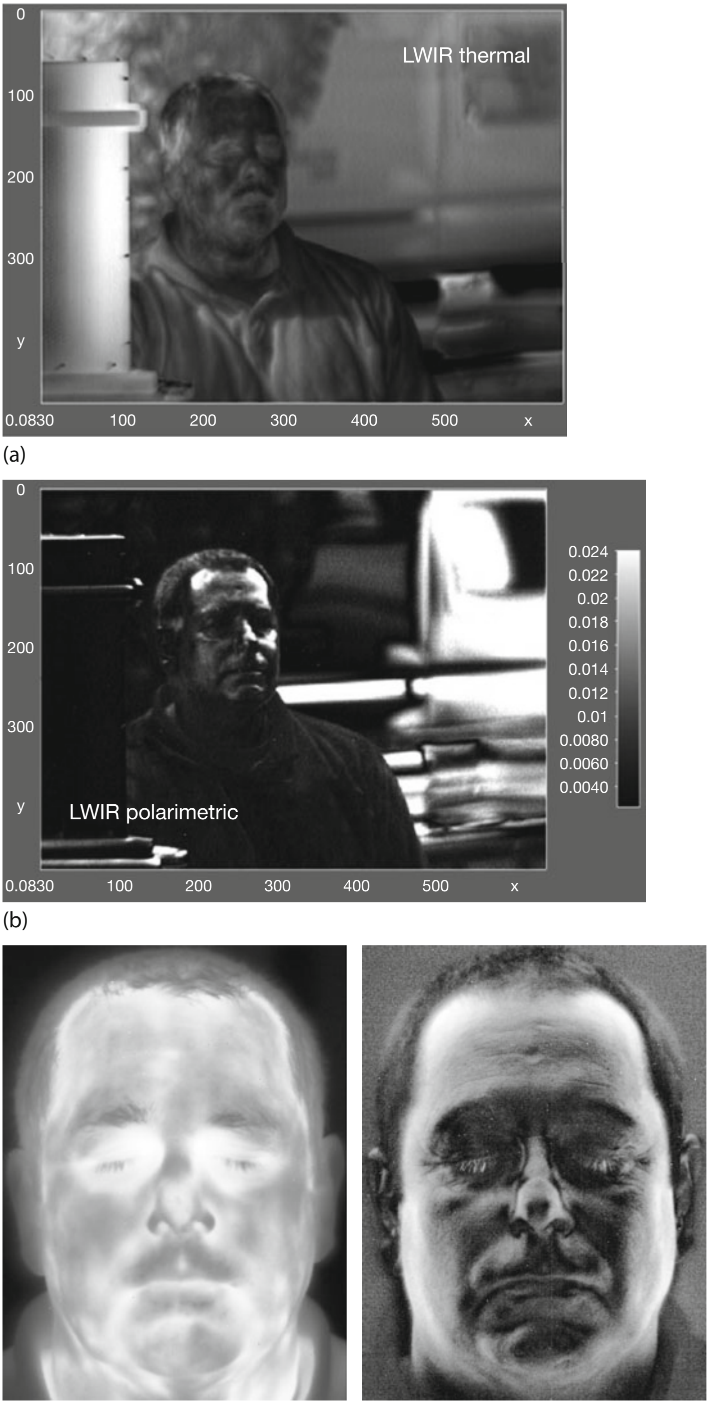

(a)

(b)

(c)

(d)

Figure 3.55 (a,c) Conventional long-wave-IR (LWIR) thermal image (grayscale) in which the facial features lack details. (b,d) The same scenes but displaying the polarimetric information as a DoLP image. Images courtesy K. Gurton and A. Juffa.

Further postrecording image processing can, on the one hand, help improve the pictorial information for human interpretation of IR images. On the other hand, it can prepare images for the measurements of predefined features. More advanced procedures of image processing will use the image data for autonomous machine perception.

3.5.1
Basic Methods of Image Processing

Some basic methods of image processing, for example, image fusion, image building, and image subtraction, can be applied using the typical R&D software in IR cameras. Moreover, numerous programs (e.g., Adobe Photoshop) can also be used for postprocessing of images, such as digital detail enhancement.

3.5.1.1 Image Fusion

In general, image fusion is a process of combining relevant information from different images into a single image [44]. In thermography, image fusion refers to the combination of IR images with VIS images from megapixel cameras. The IR image can be either superimposed on the VIS image (picture-in-picture overlay) (Figure 3.56) or merged with the VIS image (see following discussion). This significantly enhances the information content within a single image. For instance, the temperature distribution depicted by the IR image will sometimes not reflect the structural properties of the investigated object. Superimposing the IR image on the VIS image can also solve the problem of identifying observed temperature anomalies with features of the object. Overall, superposition of IR images on visible images simplifies the interpretation considerably.

Some IR cameras offer image fusion not only by superimposing IR images on visible ones but also by merging visual and IR images. This merging function operates in real time [45] and offers the possibility to highlight object areas in VIS

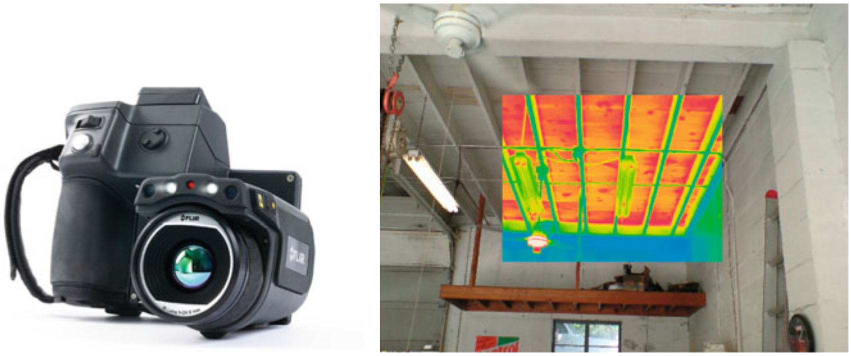
(a) (b)

Figure 3.56 (a) FLIR TG640 camera with 640 × 480 pixels IR resolution and 3.2 megapixel digital camera (above IR lens) allowing IR image overlay on VIS images. (b) Example overlay image of indoor inspection of roof area. (Image courtesy FLIR Infrared Training Center.)

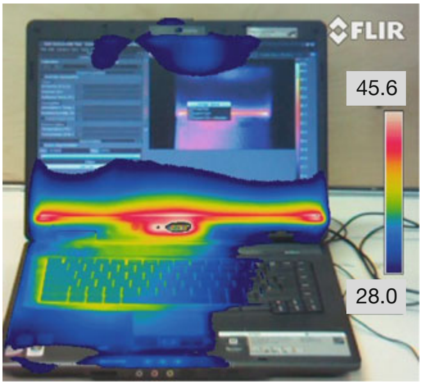

Figure 3.57 Example of merging IR and VIS image with FLIR camera T650sc (640 × 480 pixel in IR camera and 5 megapixel VIS camera).

images that are above or below a predefined temperature threshold or areas within a predefined temperature interval (Figure 3.57).

Such a thermal image fusion can also be done in a postrecording mode using image-processing software. Figure 3.58 depicts some examples of the merging of VIS and IR images. Note that close-up images may pose problems for the super-

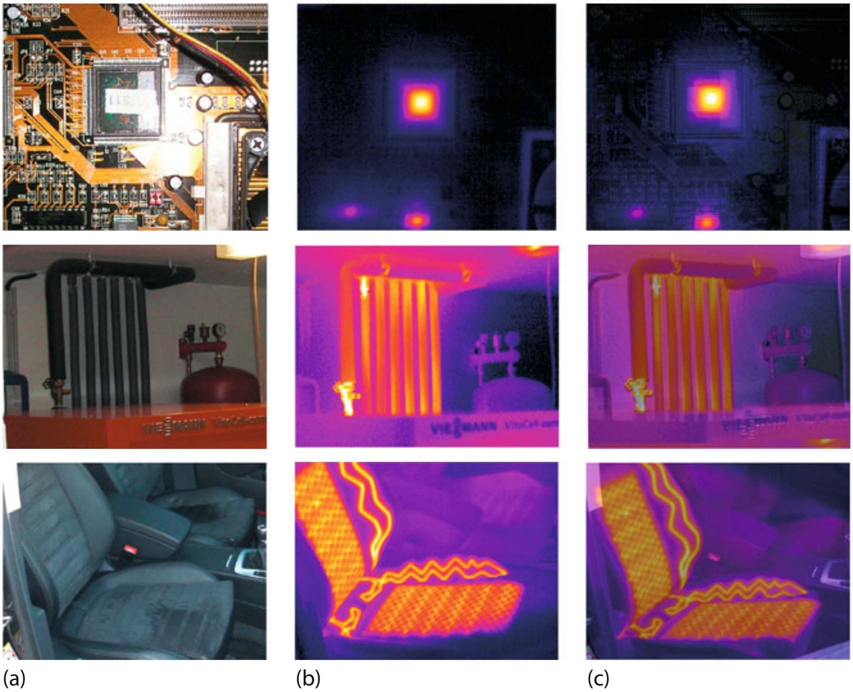
(a) (b) (c)

Figure 3.58 Examples of thermal image fusion. (a) VIS image; (b) IR image; (c) fusion image. Top: electronic board under load; middle: inspection of pipes of a heating system; bottom: car seat heating.

position since the lenses for the IR and the VIS camera are separated, that is, the images are slightly shifted with respect to each other.

Merging IR and VIS images is particularly important when dealing with inexpensive IR cameras having a small number of pixels, for example, the FLIR C2 camera with 80 × 60 IR pixels. Without additional VIS image information, overview IR images covering a large image field show little detail and are hard to interpret. Using an overlap with the VIS image (for the C2, for example, a 640 × 480 pixel VIS image), the user already gets a much better feeling for the location of thermal features that must be analyzed later on close up. The same applies to IR cameras acting either as smartphone accessories or already built into phones. Currently, there are IR cameras of reduced pixel numbers, for example, FLIR second-generation cameras for the Apple iPhone and Android systems have 160 × 120 IR pixels that are superimposed on a VGA ox 1440 × 1080 visible camera image. So far, one smartphone with an IR camera already integrated is available, the CAT S60 with 80 × 60 pixels IR camera, which is also superimposed on a VGA visible image.

Compared to the usual spatial resolution of commercial digital cameras, VIS images with VGA, that is, 640 × 480 pixels, do have lower quality. Therefore, additional image processing is applied, called, for example, MSX for FLIR cameras, which enhance the contrast of edges (see following discussion). These processed VGA images are then used for the superposition of even lower-resolution IR images.

The resulting superimposed and processed VIS-IR images look much nicer than IR images alone (which is of course why this is done anyway). Therefore, we point to the danger that these superimposed and processed images suggest a much better spatial resolution of the IR image than is available in reality.

3.5.1.2 **Image Building**

A typical practical problem of IR inspection is that the object scene is sometimes so large that the field of view (FOV) of the available camera optics can only capture part of it. This can, for example, be due to constraints regarding possible object distances. Alternatively, one may be able to get complete images of extended objects, with the disadvantage, however, of low spatial resolution owing to the required large object distance. Both these problems can be solved with image-building software tools. Such postrecording image-processing software has been developed, in particular, at the request of the building inspection industry and is image-assembling software that allows one to combine and align different images to create high-resolution overview images. Obviously, the method only works for stationary conditions since repositioning of the camera multiple times can require quite a large time span for the recording of a single large image.

We now discuss this application in more detail. The camera FOV is determined by the f-number of the camera optics (many standard lenses having a 20–24° FOV). The spatial resolution can be simply calculated by dividing the FOV by the linear number of FPA pixels and is represented by the instantaneous field of view (IFOV) (Section 2.5.3). If the object scene to be analyzed is too large, for example, an elongated building as shown in Figure 3.59, compared to the camera

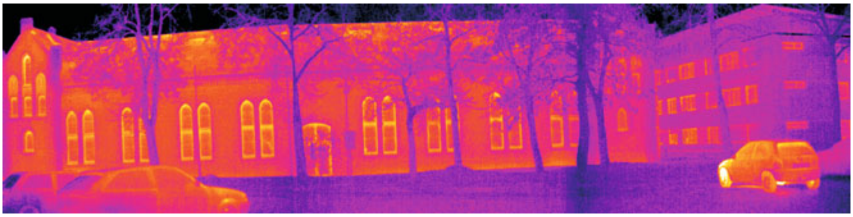

Figure 3.59 High-resolution overview image of a building with 932 × 230 pixels combined from three separate thermal images with 320 × 240 pixels per image.

FOV, the use of an additional wide-angle lens is possible. It increases the IFOV by some factor while at the same time reducing the spatial resolution by the same factor. The resolution reduction can cause measurement errors and misinterpretations for small object sizes (Section 2.4.4). This problem is avoided by capturing a number of thermal images that cover different parts of the object scene. All these frames offer spatial resolution according to the detector IFOV. The thermal images depicted in Figure 3.59 were recorded using a camera with a 1.3 mrad IFOV. Considering an object distance of about 40 m, the images will exhibit a spatial resolution of about 5 cm. The combined image is characterized by the same spatial resolution. If instead a wide-angle camera lens had been used to capture the same horizontal object size, the FOV would have increased by a factor of 3. In that case, the IFOV would have been about 4 mrad, and the image would have offered a spatial resolution of only 15 cm. This difference in spatial resolution is shown in Figure 3.60, which presents an example of the same object scene that was first recorded with a wide-angle lens with 45° FOV (Figure 3.60a). The same scene is shown in Figure 3.60b as a combined image of six single IR images recorded with a telephoto lens with 12° FOV. The difference in spatial resolution is obvious. If a quantitative analysis is requested, a high-resolution combined image would be much better, whereas the wide-angle image could cause wrong interpretations owing to the low spatial resolution.

IR image-building software usually offers fully radiometric composite images that can also be analyzed with the typical analysis software used for single images [45]. Image building is suitable for large static object scenes and can be used for a large variety of applications, for example, the inspection of buildings, electrical sytems at transformer stations, panels, and electronic boards.

As an additional example Figure 3.61 depicts a composite image of an electronic board. For the analysis, a 34/80 close-up lens of a 320 × 240 pixel LW camera was used to obtain a high spatial resolution of about 100 μm per pixel. The image field of a single image equals 34 × 25 mm^2 at an object distance of 80 mm.

3.5.1.3 Image Subtraction

Image subtraction is a method of image processing that can, first, help to identify small temperature changes, second, suppress the influence of thermal reflections, and, third, if applied consecutively, visualize time derivatives, for example, those due to transient phenomena.

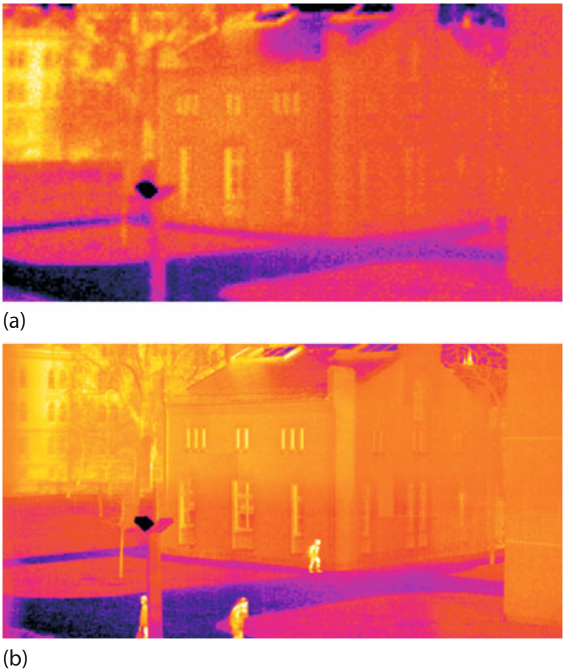
(a)

(b)

Figure 3.60 Thermal image captured with a 45° lens (a) compared to a combination of six individual images using a 12° lens and image-building software (b).

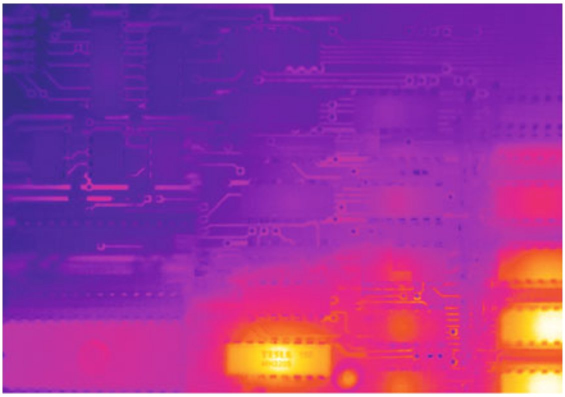

Figure 3.61 Composite IR image (864 × 602 pixels) of an electronic board with load. The image was assembled from 3 × 3 single images.

Image subtraction can be done in two ways: by subtracting a reference image from each image of a recorded sequence or by a consecutive process, that is, subtracting each image from its precursor. The first procedure results in a new sequence showing the temperature difference between each image of the sequence

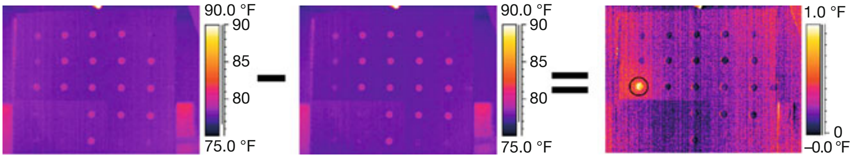

(a) Result (b) Baseline (c) Subtracted

Figure 3.62 Thermal images of a plate with holes. After grabbing the baseline image (b), one of the holes is heated by a microheater. The resulting image (a) shows the ensuing temperature distribution. The baseline image is subtracted from the resulting image. The ensuing subtracted image (c) clearly exhibits the temperature difference. (Image courtesy FLIR Infrared Training Center.)

and the reference image. Figure 3.62 presents an example of this procedure using a plate with holes. The temperature of one of the holes is slightly increased by about 0.6 °C using a microheater. It is very difficult to find this hot spot in Figure 3.62a (result) owing to the small temperature change compared to the temperature span in the IR image. Figure 3.62b (baseline) shows the temperature distribution before the hole is heated. The comparison of the baseline image and the result image does not really help find the position of the hot spot, but the subtracted image (Figure 3.62c) clearly depicts its position. The temperature is changed by about 1 °F (5/9 °C). This example demonstrates that image subtraction is suitable for detecting very small temperature changes in object scenes.

Image subtraction can also be used in applications where reflections of ambient temperature should be suppressed. Figure 3.63 shows an electronic board. From the visual as well as from the IR image, highly reflecting electronic devices are clearly seen. If the board is operated, these reflections will add to the emission of the current-induced self-heated electronic devices. Therefore, the simple IR image does not allow one to correctly estimate the temperature change under load.

The suppression of background radiation reflections can be understood from Eq. (2.37a). Neglecting atmospheric influences, the detected radiance will consist of the emitted object radiation and the reflected radiation of the background:

$$L_{\text{det}}(x, y) = \varepsilon(x, y) L_{\text{object}}^{\text{BB}}(T_{\text{object}}) + [1 - \varepsilon(x, y)] L_{\text{amb}}(T_{\text{amb}}) \tag{3.28}$$

The $\varepsilon(x, y)$ equals the object emissivity at the position (x, y). If we calculate the difference in signals detected for two different object temperatures but the same ambient temperature, the signal is no longer affected by the reflection:

$$\Delta L_{\text{det}}(x, y) = \varepsilon(x, y) \left\{ \left[L_{\text{object}}^{\text{BB}}(T_{2,\text{object}}) - L_{\text{object}}^{\text{BB}}(T_{1,\text{object}}) \right] \right\} \tag{3.29}$$

The subtracted image will depend only on the temperature difference. However, the correct emissivity must be applied to measure the correct temperature difference.

From Eqs. (3.28) and (3.29) it is clear that image alignment is critical for image subtraction. A small misalignment between the source and the reference image

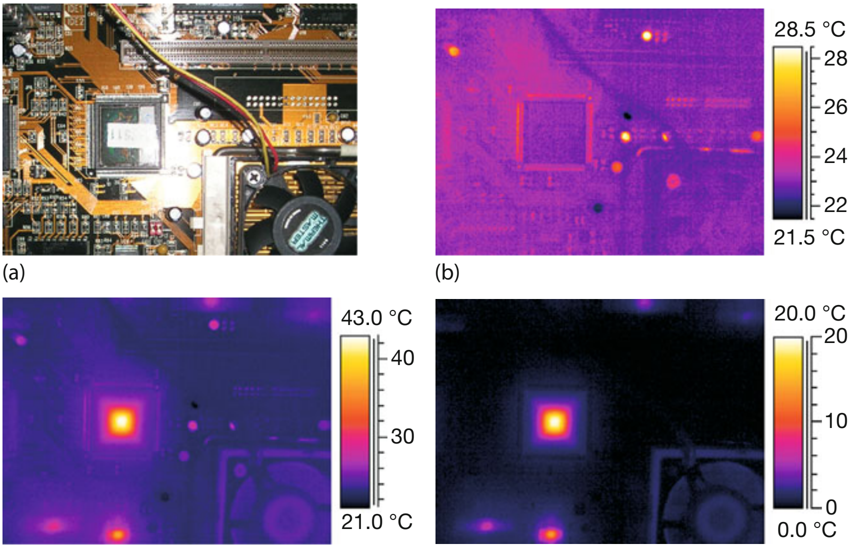

(a) (b) (c) (d)

Figure 3.63 Image subtraction applied to a thermographic analysis of an electronic board. (a) VIS image, (b) IR image at ambient temperature without applied voltage (reference image), (c) IR image of electronic board with applied voltage (source image), and (d) subtracted image (source image–reference image).

will cause different positions (x, y) with different emissivity values and the subtraction algorithm will fail. This is illustrated in Figure 3.64 for two similar IR images for the electronic board with no load. With proper alignment, the subtracted image resembles the image noise, whereas slight misalignments result in the presence of additional features, although no temperature change occurred during recording.

3.5.1.4 Consecutive Image Subtraction: Time Derivatives

In the second method of image subtraction, consecutive image subtraction is performed. In this case, the difference signal for a pixel (x, y) of the nth image in the sequence $\Delta S(x, y, n)$ is computed via

$$\Delta S(x, y, n) = S(x, y, n) - S(x, y, n-1) \tag{3.30}$$

Since subsequent images n and $n-1$ are separated by a time interval Δt, defined by the frame rate of the recording, consecutive image subtraction represents a calculation of the first derivative of the image in time domains. If this algorithm is applied to the self-heating process of the electronic board components shown in Figure 3.63, the differences in the time-dependent temperature increase become obvious. Figure 3.65 show a series of images that represent consecutive subtraction results during the self-heating process if a voltage is applied. From the consecutive image subtraction, the different time constants during the self-heating process are obvious. The component at the bottom of the board exhibits a faster

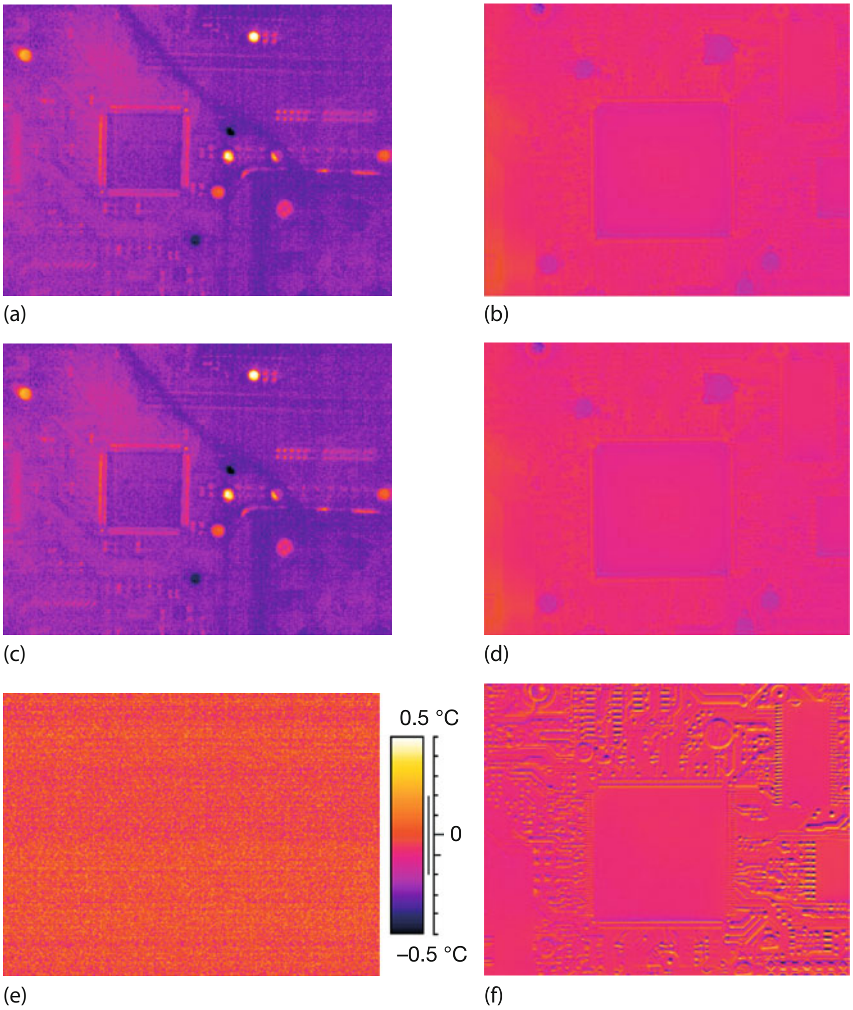

Figure 3.64 Influence of image misalignment on result of image subtraction. Source (top) and reference (middle) images for electronic boards with no load. Left: correct alignment of source (a) and reference image (c) will result in a correct subtracted image (e). Right: misalignment between source (b) and reference images (d) of a different board will result in an incorrect subtracted image (f).

temperature increase than the device in the middle. It reaches stationary conditions much faster during board operation. Therefore, it has already disappeared in the final subtracted images at times t_6 and t_7. The temperature of the device in the middle increases on a much longer timescale. At the end of the self-heating process, when stationary conditions are reached, all components will disappear in the consecutive subtracted images of the board.

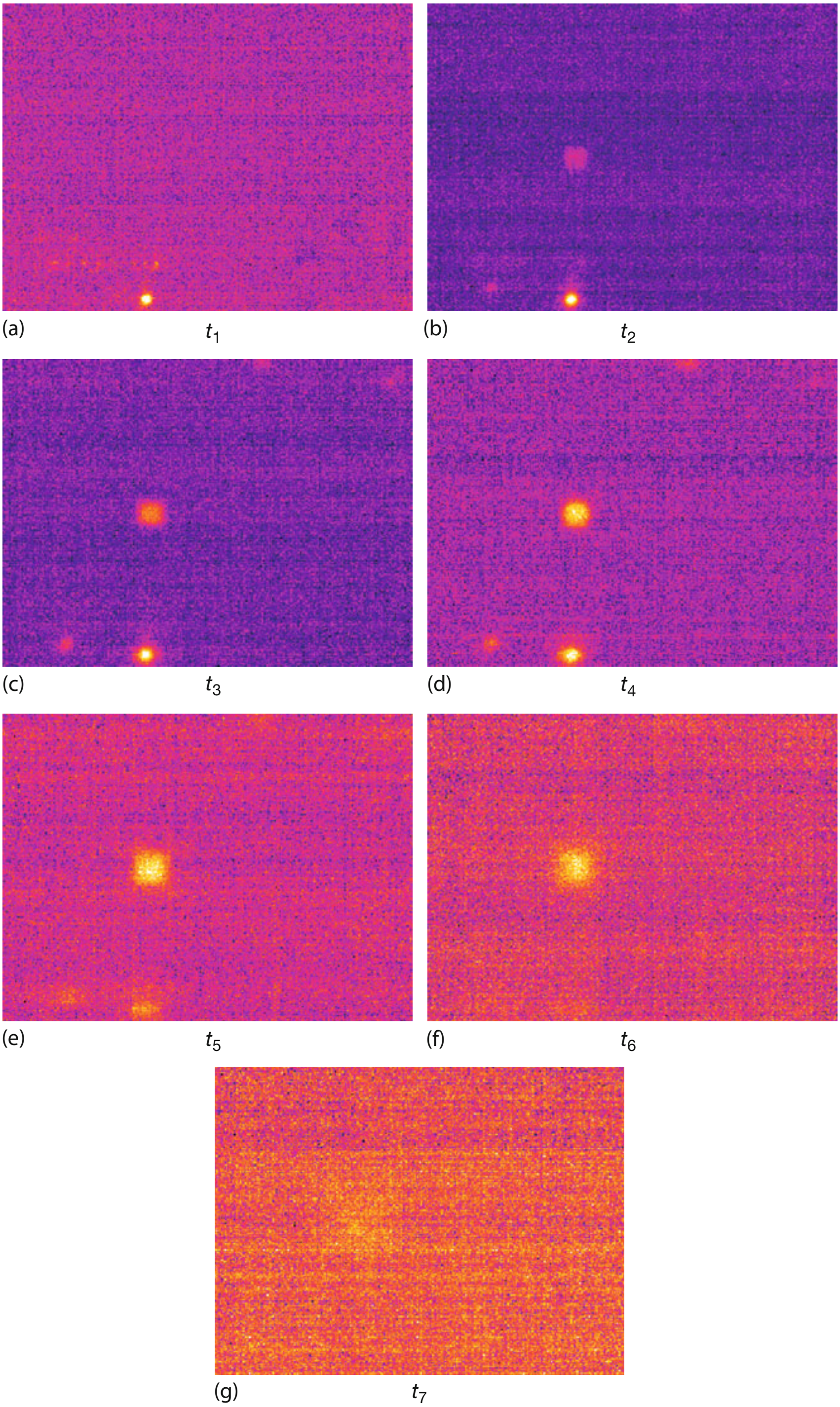
(a) t_1 (b) t_2

(c) t_3 (d) t_4

(e) t_5 (f) t_6

(g) t_7

Figure 3.65 Consecutive subtracted thermal images of an electronic board during self-heating due to applied voltage ($t_1 < t_2 < \dots < t_7$). Transient phenomena with different timescales are observed.

If the consecutive subtraction algorithm is applied a second time to an already consecutive subtracted image sequence, the second derivative of the temperature in time domains will be calculated. It can provide additional information about the time-dependent temperature behavior of the investigated object and is used, for example, in pulse thermography ([46] and Section 3.6.2).

Consecutive image subtraction can also be used to extract features of moving objects in real time if the object scene and the background are either more or less static [47] or featureless. Figure 3.66 presents an example of such a system: a water beaker was heated from below resulting in convection patterns at the upper surface (Section 5.3.4). Convection currents have only small temperature differences compared to the rest of the water, and features change rapidly. Whereas comparison of two consecutive images with regard to changes is difficult, the subtracted images clearly show only the locations where changes occur because of convection currents.

3.5.1.5 Consecutive Image Subtraction: High-Sensitivity Mode

Similar to Figure 3.66, some R&D software, for example FLIR ResearchIR, offer a type of consecutive image subtraction as an additional filter. The idea is that one observes not the live image sequence in real time, as in Figure 3.66a, but rather a consecutive subtraction image sequence in real time, such as in Figure 3.66b. This works as the image subtraction procedures operate in real time. They increase the sensitivity in IR thermal imaging by enhancing the differences between the consecutive images in a dynamic scene. FLIR has introduced this high-sensitivity mode (HSM) for gas leak detection using its GasFind cameras [45]. Figure 3.67 illustrates this HSM mode for the example of a 1000 mL/min CO_2 gas leak.

3.5.1.6 Image Derivative in Spatial Domain

For still, that is, static, images it is sometimes desirable to increase image contrast, for example, by enhancing the thermal contours of objects. The corresponding image-processing algorithm calculates spatial derivatives. This can be done by exporting the radiance or temperature data from the IR image into a spreadsheet program. The calculation of the derivative is done in the x- or y-coordinate direction by consecutive subtraction of columns or lines, respectively. This procedure will increase the image contrast for image regions with nonzero temperature gradients $\mathrm{d}T/\mathrm{d}x \neq 0$ or $\mathrm{d}T/\mathrm{d}y \neq 0$. In Figure 3.68, the original IR image is depicted in comparison to the calculated image derivative in the x-coordinate, that is, the horizontal, direction. Obviously, the image derivative exhibits enhanced contours of vertical and inclined features caused by the temperature gradients.

However, horizontal features, for example, the roof edge of the house, cannot be seen, as expected. For them to show up, the derivative in the y-coordinate direction must be computed.

Figure 3.69 depicts an example where the derivation algorithm was applied both to the x- and y-coordinate directions for an electronic board (again the one from Figure 3.63) under load. The derivative images for x and y can be combined to obtain improved information about the temperature gradients in both directions.

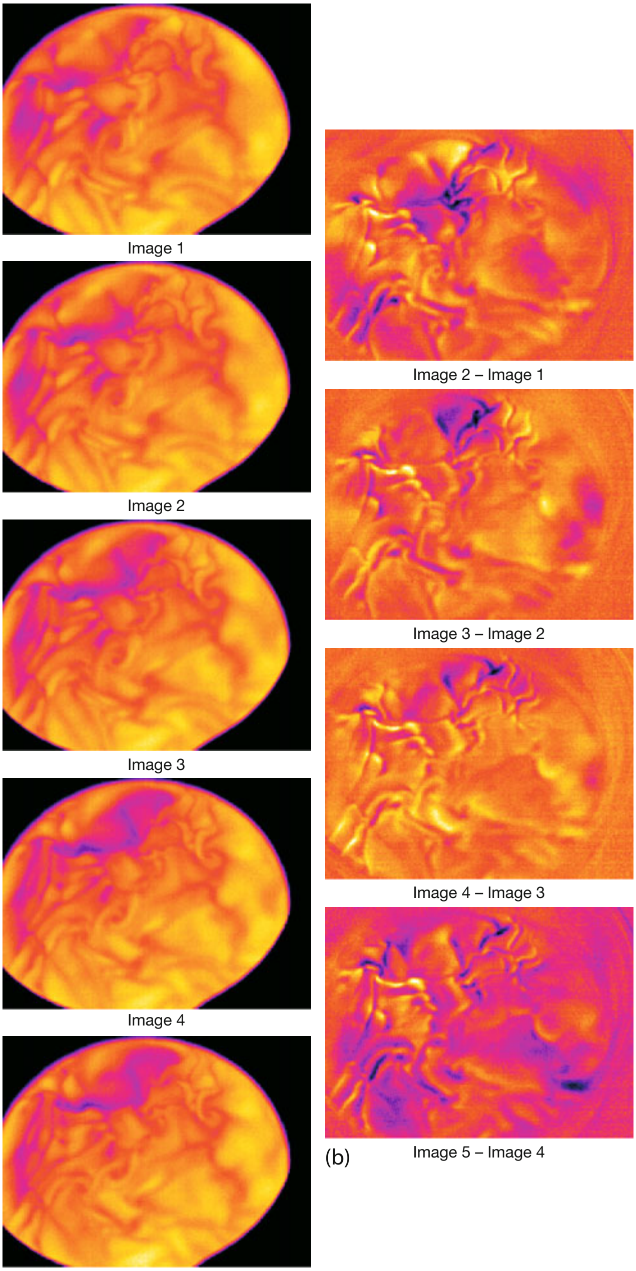

Image 1

Image 2

Image 3

Image 4

(a) Image 5

Image 2 – Image 1

Image 3 – Image 2

Image 4 – Image 3

(b) Image 5 – Image 4

Figure 3.66 Convection of heated water. (a) Original IR images grabbed every 0.2 s. (b) Images from consecutive subtraction.

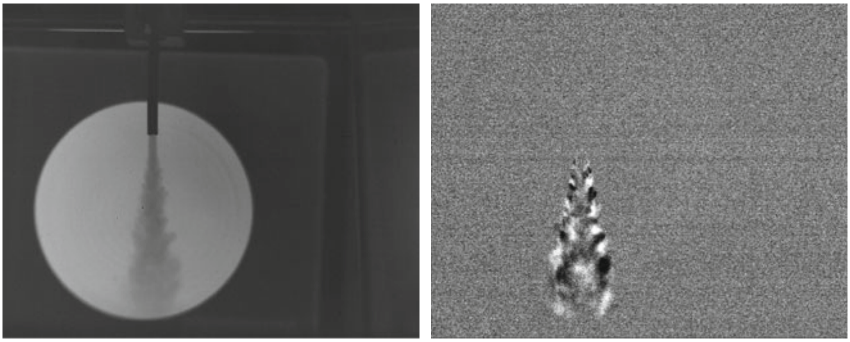
(a) (b)

Figure 3.67 IR image (a) of a CO_2 gas leak and sensitivity improvement using HSM with consecutive image subtraction (b).

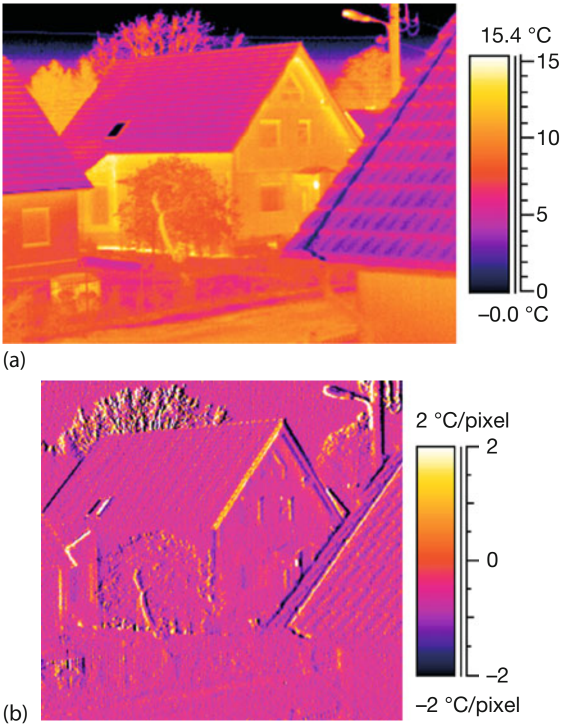

(a)
(b)

Figure 3.68 Comparison of original IR image (a) and its image derivative (b) in spatial domain along horizontal coordinate.

The combined image, however, still gives incorrect results at the corners of the self-heated processor because temperature gradients incorrectly aligned toward the coordinate axes are shown incorrectly.

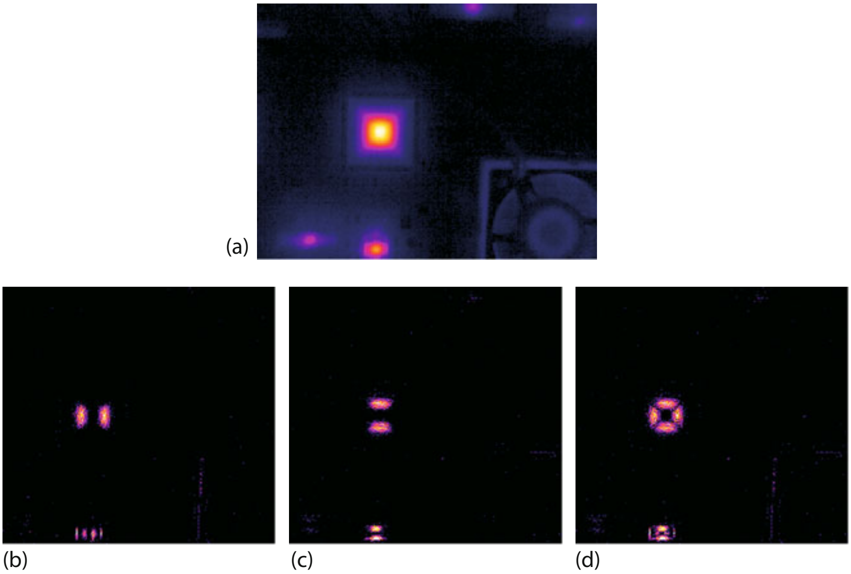

Figure 3.69 IR image of electronic board (a) processed to yield spatial derivatives along *x* (horizontal) coordinate (b) and *y* (vertical) coordinate (c) and combination of the two derivative images (d).

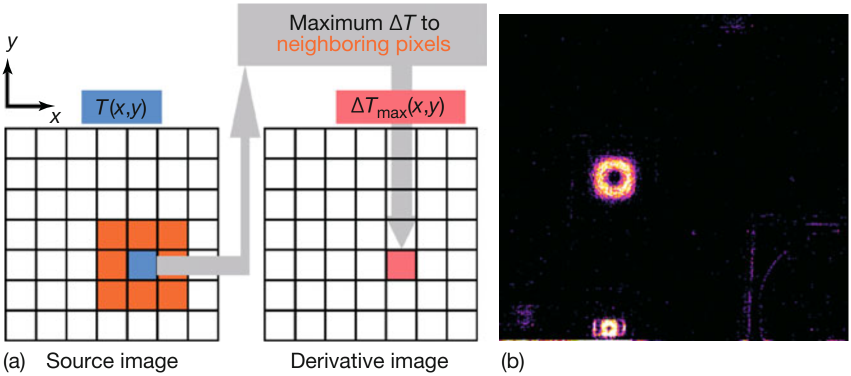

Figure 3.70 Calculation of image derivative in spatial domain using maximum temperature difference between neighboring image pixels.

Therefore, an improved procedure for calculating the temperature gradients within a thermal image should be applied. Figure 3.70a depicts the mathematical procedure. For each pixel, the signal difference for all eight neighboring pixels is calculated. The maximum difference is used as the new pixel signal. This algorithm is applied to all pixels of the image and results in the derivative image shown in Figure 3.70b. Obviously, the result of this algorithm reflects the contours of temperature changes of objects more accurately.

3.5.1.7 Infrared Image Contrast and Digital Detail Enhancement

Basic Idea of Digital Contrast and Detail Enhancement

Usually an IR camera signal contains 12–14 bit of information, which, in false color, resembles 4096–16 384 different hues. Still, perception problems may occur due to the limitation of human visual recognition. We discuss the grayscale images first.

A human observer can distinguish only approximately 128 levels of gray, which corresponds to 7 bit images. If automatic gain control (AGC) with linear gradation is applied in the IR image analysis software, the human observer cannot detect low-contrast objects within a high-dynamic-range object scene; see, for example, the image in Figure 3.71a. However, perception may be enhanced if the linear image gradation curve is changed to a nonlinear one that is characterized

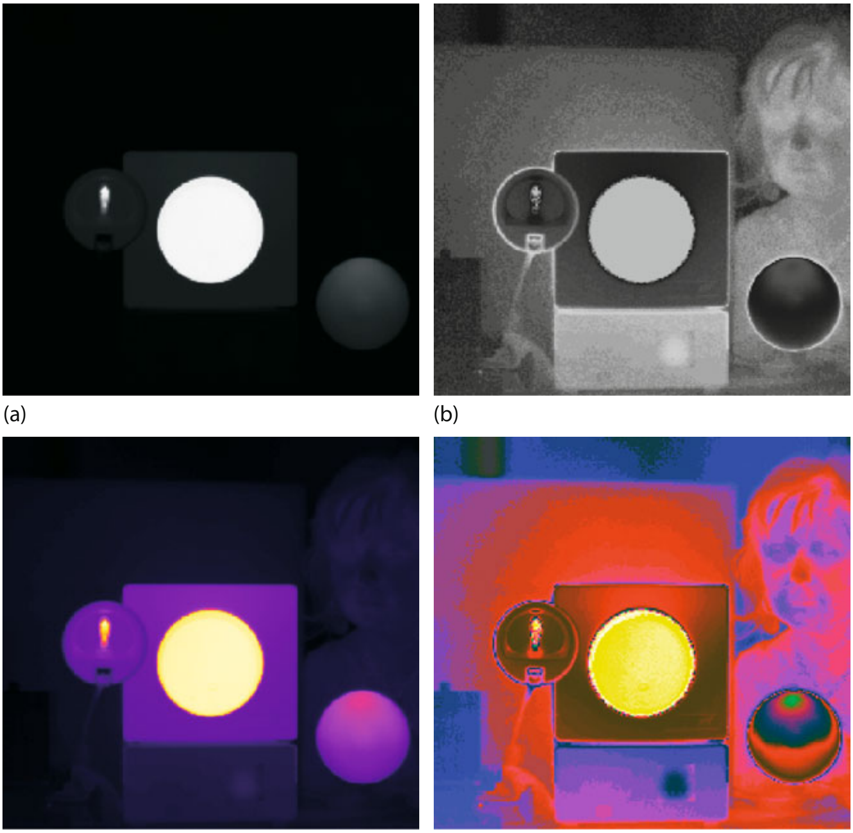

Figure 3.71 Detail enhancement by application of nonlinear gradation to a high-dynamic-range IR image. (a,b) 8 bit gray-level representation of high-dynamic-range IR image from Figure 3.37a: (a) with linear gradation curve; (b) with nonlinear gradation curve. (c, d) Same image, represented with 8 bit color scale (iron) representation: (c) with linear gradation curve; (d) with nonlinear gradation curve.

by small grayscale changes for large signal changes and large grayscale changes in regions with small signal changes. This so-called Digital Detail Enhancement (DDE) procedure has been applied to the image in Figure 3.71a, resulting in the changed image of Figure 3.71b. Apparently, this nonlinearity algorithm enables the observer to also detect low-contrast object details.

Figure 3.71 also compares grayscale and color representations of the same image, that is, the same content of information. Obviously, color scales are better suited for image enhancement procedures. Nevertheless, grayscale images are still often used in security and surveillance applications (Section 10.9), probably because they allow a direct comparison with low-light-level visual images that are grayscale images anyway. For all other purposes, color palettes are superior for image enhancement with regard to the visual detection of features by human observers.

Digital Contrast and Detail Enhancement in IR Imaging

Nowadays, detail and contrast enhancement algorithms are widely used in image processing not only in the visual range but also for IR images [48, 49]. Therefore, some methods are usually included in camera image-processing software, for example, in FLIR ResearchIR [45].

One of the most popular automatic procedures used for contrast enhancement is histogram equalization [50–52]. An image histogram represents the probability distribution of object signal or temperature values in an image. In what follows, we describe the procedure.

First we construct a histogram based on the temperature values in the object scene. This is done by dividing the entire temperature range in the IR image into a series of temperature intervals (bins) and then counting how many pixel temperature values in the image fall into each bin. Usually the bins are defined as consecutive, adjacent, and nonoverlapping equal intervals. Figure 3.72 shows an example of an IR image and the associated histogram.

The IR image in Figure 3.72b is displayed with automatic gain control (AGC) and a linear false color mapping within the image dynamic range. Four regions of well-separated temperatures, or regions of interest (ROIs), can be seen, but within each of these regions there is very low contrast. The histogram clearly shows that for this image the linear dynamic range mapping causes sharp peaks in the probability distribution. Although the image shows all relevant temperatures, a large temperature interval from about 34 to 68 °C, including all green and yellowish hues of the color representation, is not seen in the image. This results in low-contrast behavior, that is, a loss of detail information for the temperature spread within the ROIs, as seen in Figure 3.72. The idea in histogram equalization is to obtain a more uniform probability distribution in the histogram applying a mathematical operation. The corresponding nonlinear mapping of the image dynamic range will enhance the contrast within the ROIs of the image in a high-dynamic-range object scene.

An example of this procedure is shown in Figure 3.73 for an image histogram. The mathematical operation is called Plateau Equalization (PE scale). Existing

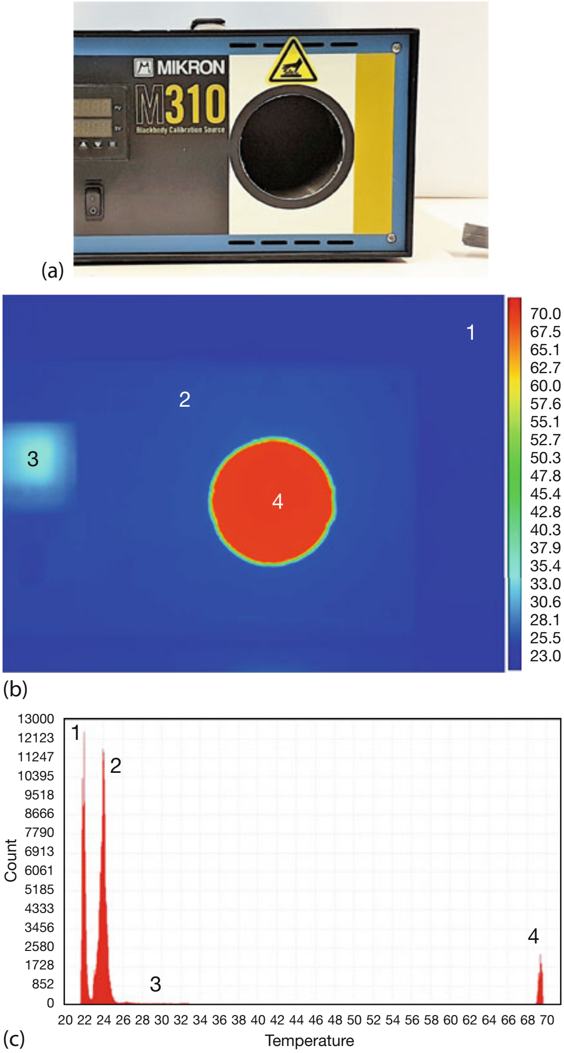

Figure 3.72 (a) VIS and (b) IR image of electrically heated blackbody ($T_{\mathrm{BB}} = 70\,°\mathrm{C}$). (c) Associated histogram of IR image with 20–72 °C temperature range. Numbers refer to chosen regions of interest. 1: background, 2: blackbody housing, 3: power switch region of blackbody, 4: blackbody emitter region.

object temperature ranges in the image are stretched on the color scale, whereas temperature ranges not present in the image are compressed by a plateaulike behavior of the mapping curve.

FLIR Systems has included such an advanced nonlinear image-processing algorithm in several analysis software packages in order to find low-temperature-contrast objects in a high-dynamic-range object scene [45, 53]. The relevant details of an image are enhanced within the total dynamic range of the original

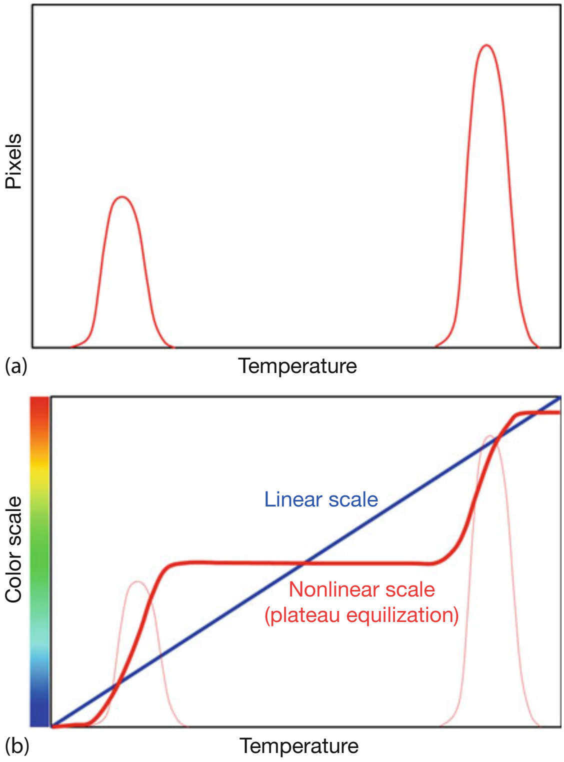

Figure 3.73 Image histogram (a) and exemplary nonlinear mapping function for a given color scale of temperature (b).

image. As a result of the algorithm, low- as well as high-contrast objects can be seen simultaneously by a human observer. This algorithm is especially important for a number of security and surveillance thermal imaging applications.

We use the IR image depicted in Figure 3.72b to demonstrate these IR image-contrast-enhancement techniques. Figure 3.74 depicts the results of a histogram PE for different degrees (moderate vs. very pronounced) of the equalization procedure. The improvement in contrast and perception of details in the processed image are obvious.

To describe and explain more details of the image processing techniques, we discuss the simpler grayscale representations. Figure 3.75 depicts the IR image of Figure 3.72b as a grayscale image and also gives its corresponding gray-value image histogram.

Obviously, it is difficult to detect any fine details within the grayscale image. Initially, we apply the PE algorithm (Figure 3.76). The contrast enhancement compared to the linear gradation curve image is clear. The histograms show that the PE algorithm has already spread the gray value scale for the ROIs by applying a

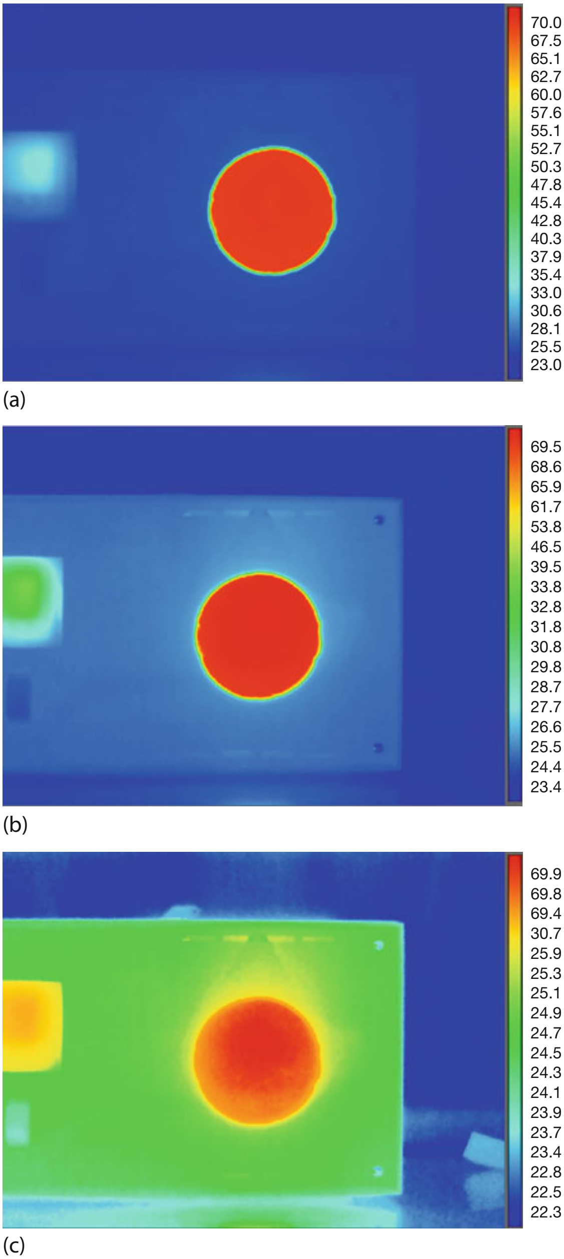

Figure 3.74 Image contrast enhancement and color-scale changes using PE of image histogram. (a) Original image with linear mapping function, (b) moderate PE algorithm, (c) very pronounced PE algorithm. Color scale in °C.

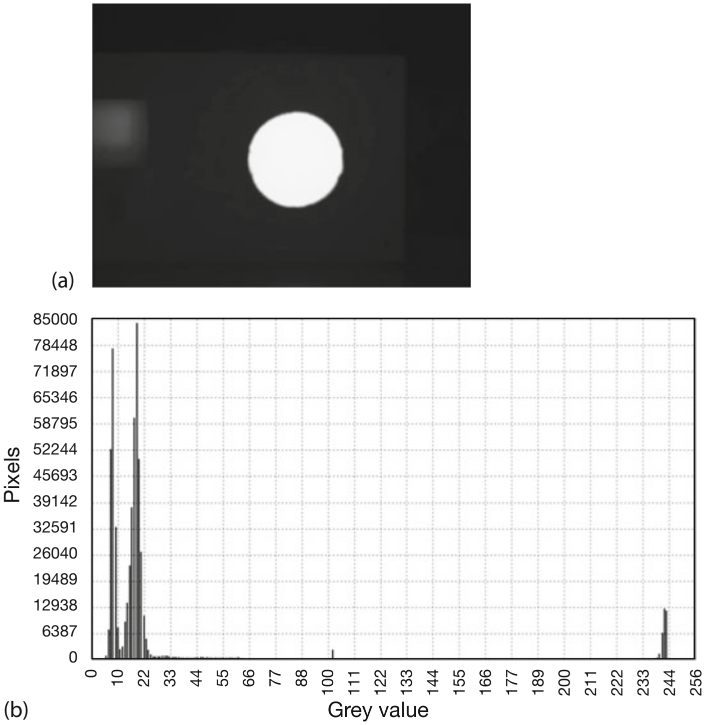

Figure 3.75 IR image of Figure 3.72b with linear gradation curve (a) and gray-value histogram of image (b). ROIs are the same as in Figure 3.72b,c.

nonlinear conversion of the pixel temperature data to the grayscale (gradation curve). This improves the visibility of details in these regions.

Further improvement is possible with the Advanced Plateau Equalization (APE) algorithm, which not only spreads the gray (or color) scale in the regions of interest but also leads to a much broader probability distribution curve in the image histogram of unused gray values (or colors). This results in a much improved contrast enhancement of the IR image (Figure 3.77).

Figure 3.78 shows a corresponding APE image in color scale that may be compared to the original IR image of Figure 3.72b.

Rather than having users adjust the parameters of a PE procedure in the software to optimize image quality, FLIR Systems also offers another advanced nonlinear image-processing algorithm (e.g., in the ResearchIR software package) that preserves details in high-dynamic-range imagery. This algorithm is called Digital Detail Enhancement (DDE). DDE images of the same scene as before are depicted in Figure 3.79. The degree, also called the *aggressiveness*, of the algorithm or the nonlinearity level of the gradation function is user selectable. At the highest degree level of the DDE PE algorithm the image histogram becomes nearly flat over the entire grayscale, causing a considerable contrast enhancement in the image, but also causing the loss of temperature information in the IR image.

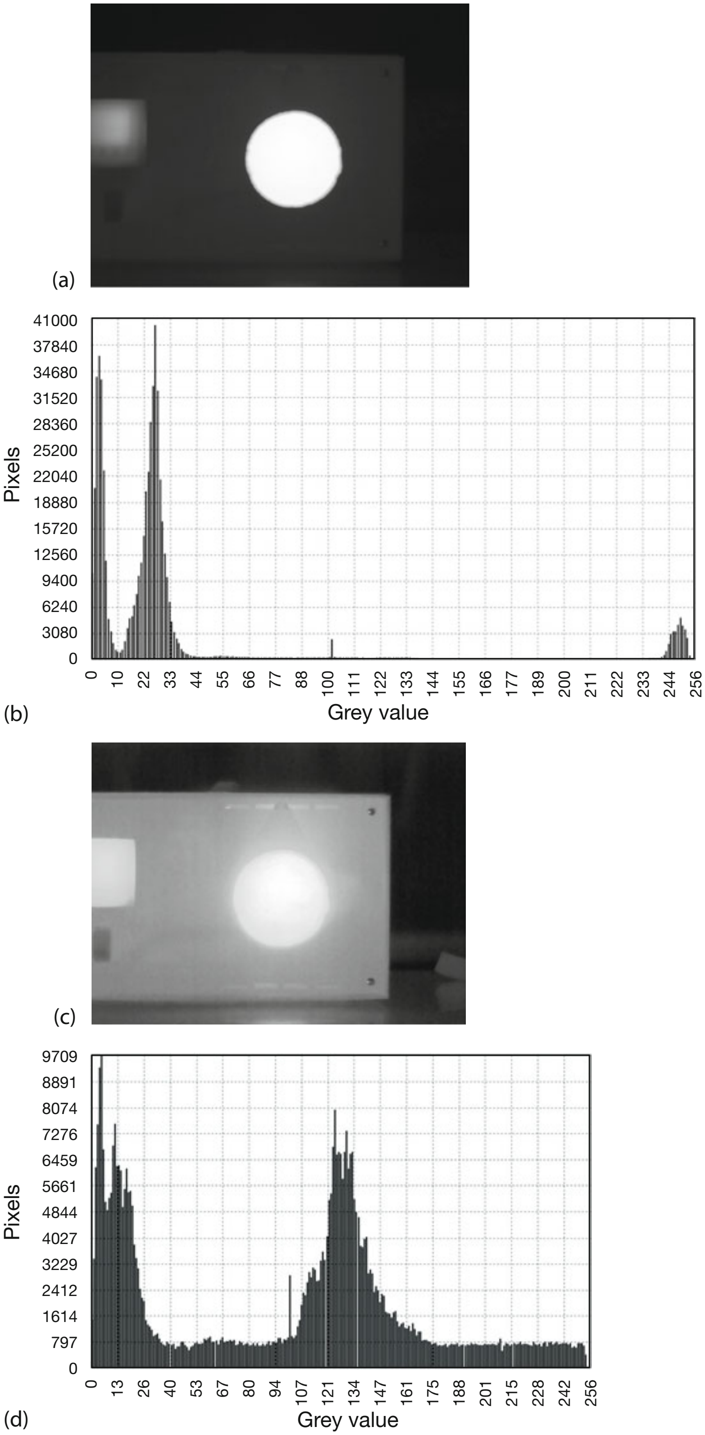

Figure 3.76 Comparison of PE scale images and histograms for moderate (a,b) and pronounced (c,d) PE.

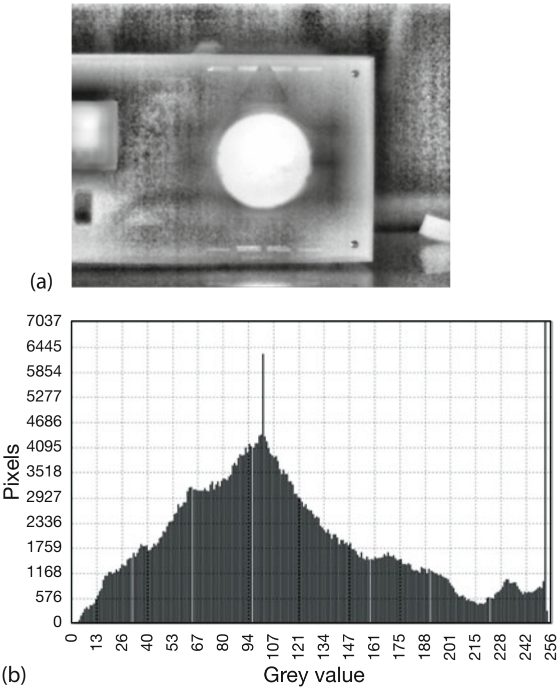

Figure 3.77 APE scale image (a) and image histogram (b).

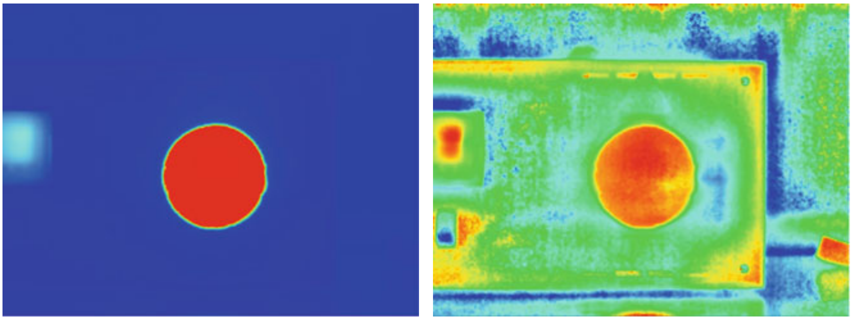

Figure 3.78 Processed IR image of Figure 3.72b using APE leads to much better contrast.

The DDE algorithm is applied to the original 14 bit data before any gradation curve is introduced to the data. This improves the performance with respect to clearly defined edges in the IR image. In the FLIR ResearchIR software, the DDE level and, thus, the sharpness of edges are also user selectable. Figure 3.80 presents an example of increasing sharpness of edges in an IR image at a higher DDE level.

The aforementioned methods of contrast and detail enhancement work well to improve the perception of fine details in IR images. However, because of the strongly nonlinear response curves, the color information in a processed image

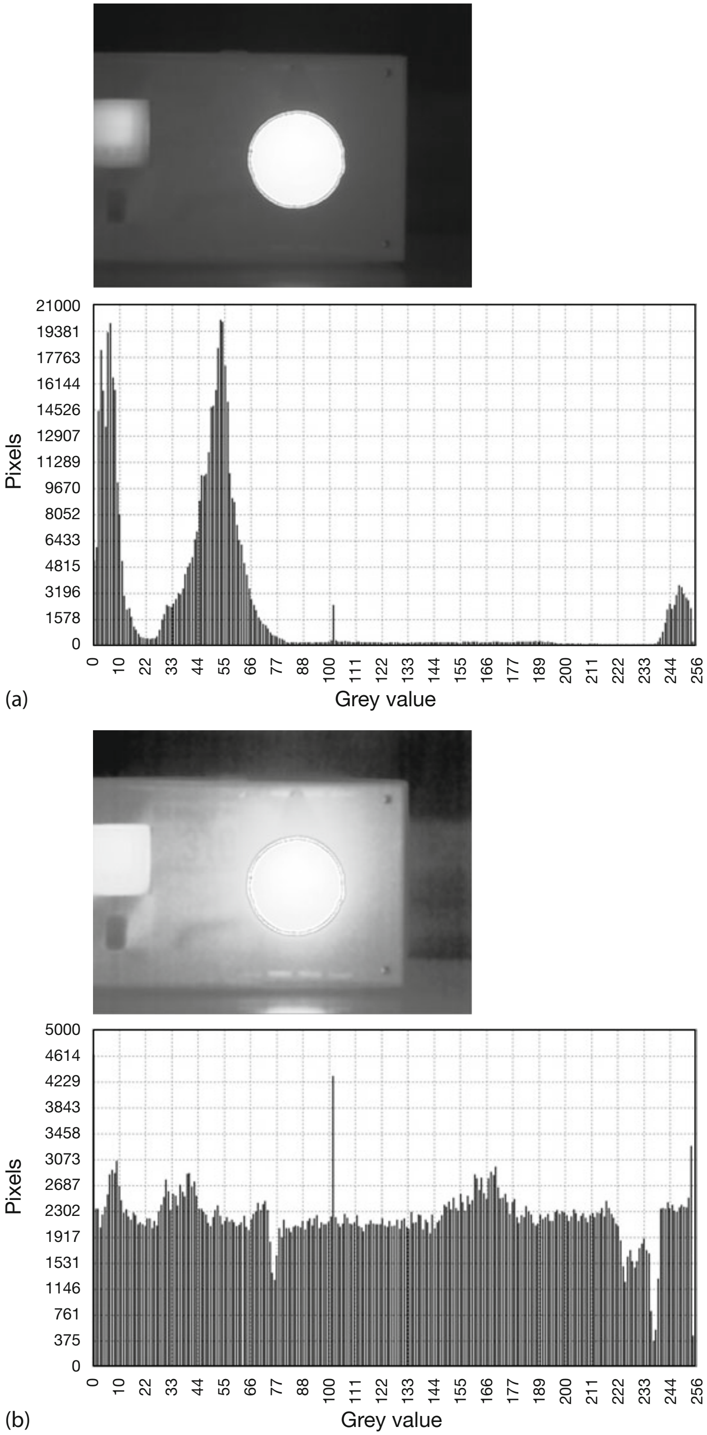

Figure 3.79 DDE images with different degree of histogram equalization: (a) weak equalization, (b) strongest equalization.

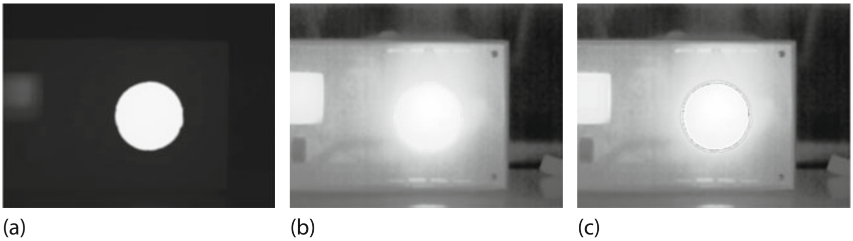

Figure 3.80 IR Image with linear gradation curve (a). Contrast enhancement with DDE (strong PE) for moderate level (b) and high level (c).

is no longer directly related to a given temperature. Often, the same color now means two or even more different temperatures (e.g., red hues in Figure 3.78). Therefore, associated processed color or grayscale images should only be used for better qualitative perception and not for quantitative temperature information. The latter is, of course, still contained in the raw data and becomes accessible if the images are loaded into the software.

3.5.2
Advanced Methods of Image Processing

Thermal-imaging systems with the goal of process visualization and computer-based process observation have become increasingly important in many industrial fields. However, experts guess that so far only 20% of all possible applications of industrial image processing are used. As a consequence, developments in the field of industrial image processing offer enormous potential for fast and sustained growth.

The enhanced use of image processing became possible owing to the fast development of, first, thermal imaging systems and, second, high-speed multicore processors. Twenty years ago, image-processing algorithms on a large number of pixels would have lasted several hours or days, whereas today, a full image inspection consisting of the whole visualization and classification process is finished within a few seconds. This means nearly real-time visualization, which offers the possibility of fast controlling or adjusting online production, for example, using robotics. The advantages are obvious, in particular if the visualization is applied in real-time quality control of industrial products.

The most important applications of industrial image processing are the inspection of single workpieces, band processes, recognition of characters, patterns, and codes, and the 2D or 3D survey of objects [54–59]. The variety of applications emphasizes the universal character of such image-processing software solutions. In industrial production processes, reliable and fast tools to minimize errors and prevent production breaks are essential to ensure high productivity and quality levels. This is why more and more industrial branches are investing in automatic process visualization systems. Another advantage of such automated image-processing systems is the possibility to collect important process parameters in databases for subsequent offline process analysis studies.

The following section gives only a brief general overview of some procedures applied in the processing of IR images for automation processes in industry. Compared with IR imaging, in this section, they are considered advanced since they are usually not included in typical IR image-processing software packages from the manufacturers of IR cameras.

In IR imaging, the basis of every processing model is a thermal image or a series of thermal images. Compared to the object scene, any thermal image already suffers from a loss of information because of the unavoidable transformation of real-world contours into pixels (problem of discretization). A limited number of pixels build a matrix of signal values, which is the basis of the subsequent mathematical processing steps. The goal is to extract relevant information like defect or pattern identification, such that reliable analysis and classification tools can be applied.

As an example, Figure 3.81 shows typical defects in a glass sheet that are not detectable in the visible spectrum but clearly seen in the thermal image. The defects are visible in the IR image since any defect in a glass sheet will exhibit a slightly different cooling behavior than the rest of the bulk material, that is, give rise to temperature differences. In addition, cracks in glass will cause slightly higher emissivities owing to the cavity effect (Sects. 1.4.4 and 1.4.6). Identifying these defects is crucial since they could easily result in product failure, for example, breaking of the glass before its guaranteed lifetime is reached. Therefore, in the case of Figure 3.81, the IR images are recorded immediately after the last thermal process during manufacturing. Obviously, if a large number of glass sheets is produced, image-processing algorithms can help analyze images and identify and classify such defects in real time. In the case of defect detection, the process operator will be notified. Such an automated procedure, hence, constitutes a quality control step.

Advanced image processing for automation or other purposes can be divided into three major parts: first, image preprocessing (noise reduction); second, seg-

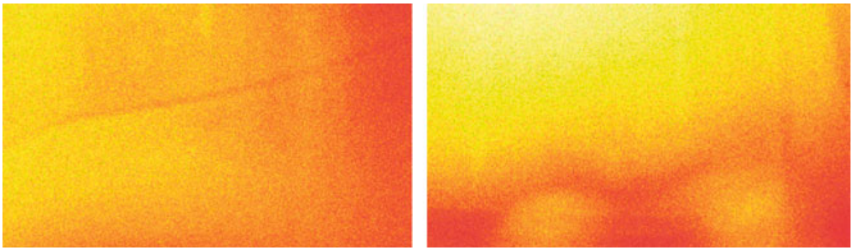

(a) (b)

Figure 3.81 Two possible defects visualized by thermal images: (a) a long break in a glass sheet and (b) a couple of hot spots in a glass sheet. (Image courtesy: Fluke Process Instruments GmbH, Berlin, Germany; www.flukeprocessinstruments.de.)

mentation (locate relevant information); and third, feature extraction and reduction. In some cases, feature extraction uses specific pattern recognition tools that produce as output false color images with especially marked defect locations. These can form the basis for quality control criteria.

3.5.2.1 **Preprocessing**

Perhaps the most important part of any image processing for pattern recognition or image classification is preprocessing of the raw data. On the one hand, it is necessary to reduce noise and eliminate pixel artifacts in images by applying low-pass filters; on the other hand, phenomena like distortion, twisting, scaling, and translation can occur in connection with the object geometry. This requires that input images be transformed geometrically.

Noise Reduction

Noise in IR images is given by random changes in pixel signals caused by single pixel noise as well as fixed pattern noise (Chapter 2). The filters used to reduce noise are characterized as low-pass filters. The frequency information (low pass means low frequency) refers to the spatial frequency of the system. Definitions are similar to those used in the treatment of diffraction in optics. Fixed pattern noise is characterized by a spatial periodicity referring to the pixel size, which can be regarded as analogous to wavelength λ. The quantity $2\pi/\lambda$ is referred to as the *wave vector* or *spatial frequency*. A small λ value implies a high spatial frequency and vice versa. Obviously, the pixel size is the smallest possible spatial periodicity in IR images, that is, it resembles the highest possible frequency $f_{\max}$. Therefore, fixed pattern noise (as well as single pixel errors) refers to high spatial frequencies. Consequently, it may be reduced by applying low-pass filters, which suppress high frequencies while at the same time preserving edges and contours. The easiest low-pass filters are just averaging pixels with their neighboring pixels, for example, each pixel may be computed as the average of its value with that of its 8 nearest neighbors (using neighbors at a distance of 1 pixel) or its 24 nearest neighbors (using neighbors at distances of up to 2 pixels) etc. Since the corresponding total filter widths are then either 3 pixels (8 nearest neighbors) or 5 pixels (24 neighbors), the corresponding frequencies are only one-third or one-fifth of the highest frequency $f_{\max}$.

The application of such averaging filters is mathematically described by matrices. Taking into account only nearest neighbors will lead to 3×3 matrices, including second-nearest neighbors to 5×5 matrices (Figure 3.82). Owing to limitations of computational power (easy but CPU-intensive calculations), the maximum filter size is usually described by 7×7 matrices. For simplicity, we present the principal idea for these and all subsequent filters using 3×3 matrices only.

The averaged pixel signal $\hat{S}(x, y)$ is mathematically evaluated by computing the trace of the matrix product of the averaging operator 3×3 matrix $\boldsymbol{A}$ and the 3×3

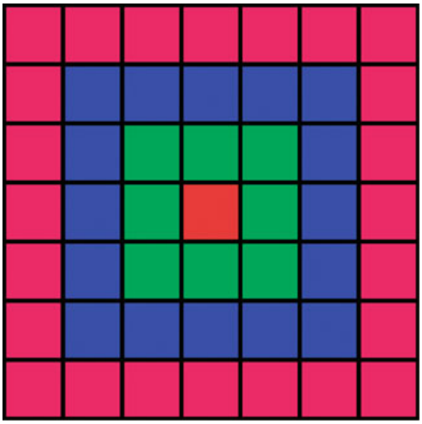

Figure 3.82 Section of pixel array of IR image. The new value of the signal of the center pixel (red) can be calculated by either averaging its signal values with its 8 nearest neighbors (green, operator: 3 × 3 matrix), with 24 neighbors (blue, operator: 5 × 5 matrix), or 48 neighbors (pink, operator: 7 × 7 matrix).

signal matrix centered around the pixel at row x and column y (Eq. (3.31)):

$$\hat{S}\,(x,y) = Tr\left\{\begin{pmatrix} a_{11} & a_{12} & a_{13} \\ a_{21} & a_{22} & a_{23} \\ a_{31} & a_{32} & a_{33} \end{pmatrix} \cdot \begin{pmatrix} S_{x-1,y-1} & S_{x-1,y} & S_{x-1,y+1} \\ S_{x,y-1} & S_{x,y} & S_{x,y+1} \\ S_{x+1,y-1} & S_{x+1,y} & S_{x+1,y+1} \end{pmatrix}\right\}$$

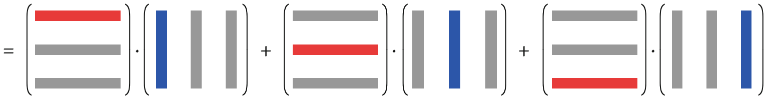

$$= \mathrm{a}_{11}\mathrm{S}_{x-1,y-1} + \mathrm{a}_{12}\mathrm{S}_{x,y-1} + \mathrm{a}_{13}\mathrm{S}_{x+1,y-1} + \mathrm{a}_{21}\mathrm{S}_{x-1,y} + \mathrm{a}_{22}\mathrm{S}_{x,y} + \mathrm{a}_{23}\mathrm{S}_{x+1,y} + \mathrm{a}_{31}\mathrm{S}_{x-1,y+1} + \mathrm{a}_{32}\mathrm{S}_{x,y+1} + \mathrm{a}_{33}\mathrm{S}_{x+1,y+1} \tag{3.31}$$

The colored bars denote the scalar product of the corresponding row of $\boldsymbol{A}$ with the column of the signal matrix. Since the trace is computed, only the indicated three diagonal components of the result matrix are needed. From Eq. (3.31) it is obvious that the resulting average value depends critically on the choice of the a_{ij} values of matrix $\boldsymbol{A}$.

Let us return to noise in IR images. The problem in averaging is the need to preserve edges and contours such that no relevant information in the image gets lost. Several filters are available, the most commonly used ones being simple box filters, Gauss filters, or median filters [55]. Some R&D thermal imaging software, for example, FLIR ResearchIR, offer these three different types of filters for noise reduction with variable kernel size, for example, 3 × 3 or 5 × 5 pixel.

As far as preserving edges and image details is concerned, the Gauss filter works best, the median filter is second, while less satisfying results are obtained for the simple averaging box filter.

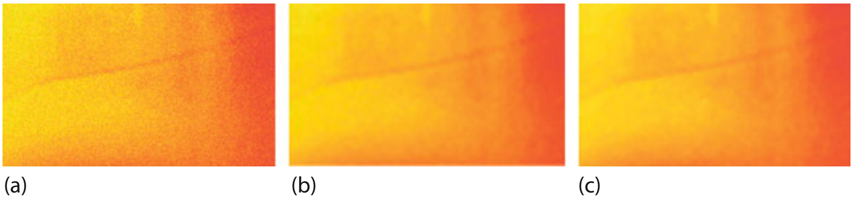

Figure 3.83 Comparison of different low-pass filters. (a) Original image (raw-data image). (b) Image after Gaussian filtering. (c) Image after median filtering. Both the Gaussian and median filtering preserve the edge. (Image courtesy: Fluke Process Instruments GmbH, Berlin, Germany; www.flukeprocessinstruments.de.)

The simple box averaging filter A_{box} and the Gauss filter A_{Gauss} are described by the matrices (here kernel size of 3×3 pixel)

$$A_{\text{box}} = \frac{1}{9}\begin{pmatrix} 1 & 1 & 1 \\ 1 & 1 & 1 \\ 1 & 1 & 1 \end{pmatrix} \quad A_{\text{Gauss}} = \frac{1}{16}\begin{pmatrix} 1 & 2 & 1 \\ 2 & 4 & 2 \\ 1 & 2 & 1 \end{pmatrix} \tag{3.32}$$

According to Eq. (3.31), it is quite easy to interpret the averaging procedure from the form of the matrices. The box filter applied to the signal matrix just computes an average where each of the nine pixels contributes with the same weight. In contrast, the center pixel has the largest weight for the Gauss filter, with the horizontal and vertical nearest neighbor pixels contributing twice as much as the more distant diagonal neighbors.

The median filter for a 3×3 signal matrix centered around pixel (x, y) resembles a procedure where the nine signal values of the pixels are ordered, and the middle value, for a 3×3 matrix the fifth value, is defined as a result. Because of this procedure, the median value is less sensitive to single value deviations, that is, single pixel errors, than the other filters.

Figure 3.83a depicts the thermal image of a glass sheet with a long break. The images after a Gaussian (b) and a median (c) filtering (both of size 7×7) are shown for comparison.

3.5.2.2 Geometrical Transformations

To compare a processed object with a reference object (e.g., manufactured products), both must have identical geometrical properties (position and orientation). But before that, it is appropriate to start with the challenging and exciting part of defect detection and image classification. Mathematically, the possible geometric variations are described by projective and affine transformations. Affine transformations consist of a multiplication of the original Cartesian coordinates with a 2×2 matrix and a vector addition to represent a translation. They can be described by

$$\begin{pmatrix} x' \\ y' \end{pmatrix} = \begin{pmatrix} a_{11} & a_{12} \\ a_{21} & a_{22} \end{pmatrix}\begin{pmatrix} x \\ y \end{pmatrix} + \begin{pmatrix} t_x \\ t_y \end{pmatrix} \tag{3.33}$$

and all affine transformations are special cases of that general equation. The three basic affine transformations are

1. Rotation by α:

$$\begin{pmatrix} a_{11} & a_{12} \\ a_{21} & a_{22} \end{pmatrix} = \begin{pmatrix} \cos\alpha & -\sin\alpha \\ \sin\alpha & \cos\alpha \end{pmatrix} \quad \text{and} \quad \begin{pmatrix} t_x \\ t_y \end{pmatrix} = \begin{pmatrix} 0 \\ 0 \end{pmatrix} \tag{3.34}$$

2. Translation by $\bar{t}$:

$$\begin{pmatrix} a_{11} & a_{12} \\ a_{21} & a_{22} \end{pmatrix} = \begin{pmatrix} 1 & 0 \\ 0 & 1 \end{pmatrix} \quad \text{and} \quad \begin{pmatrix} t_x \\ t_y \end{pmatrix} \neq \begin{pmatrix} 0 \\ 0 \end{pmatrix} \tag{3.35}$$

3. Scaling by s_x, s_y:

$$\begin{pmatrix} a_{11} & a_{12} \\ a_{21} & a_{22} \end{pmatrix} = \begin{pmatrix} s_x & 0 \\ 0 & s_y \end{pmatrix} \quad \text{and} \quad \begin{pmatrix} t_x \\ t_y \end{pmatrix} = \begin{pmatrix} 0 \\ 0 \end{pmatrix} \tag{3.36}$$

It is possible to simplify this representation by including the translation within a single 3 × 3 matrix operator:

$$\begin{pmatrix} x' \\ y' \\ 1 \end{pmatrix} = \begin{pmatrix} a_{11} & a_{12} & t_x \\ a_{21} & a_{22} & t_y \\ 0 & 0 & 1 \end{pmatrix} \begin{pmatrix} x \\ y \\ 1 \end{pmatrix} \tag{3.37}$$

Any change in position or scaling can be constructed by combining these basic affine transformations and applying them to every single pixel in the image.

Problems that can emerge are obvious. An input image with integer pixel coordinates is transformed by an affine transformation into a result image. After transformation back to the input image, noninteger coordinates result. Therefore, a loss of information may be caused by the constrained resolution of pixels and the affine transformations. For example, Figure 3.84 depicts the discretization and an affine transformation of an ellipse. In the transformed output image, the original ellipse is scaled, rotated, and translated.

The transformation can therefore result in a new pixel center position between four adjacent pixel centers (Figure 3.85).

The resulting signal strengths for each pixel are calculated by working in the subpixel area. A simple nearest-neighbor algorithm can be applied to calculate the closest pixel. The signal of the nearest-neighbor pixel will dominate the signal strength of the transformed pixel. A better interpolation results if the new signal is calculated from signals of all neighboring pixels weighted according to their center distances to the new pixel center (Figure 3.85).

3.5.2.3 Segmentation

Typically, the first step after preprocessing is segmentation of the input data, that is, searching for ROIs. The main goal is to determine the zones in the image in

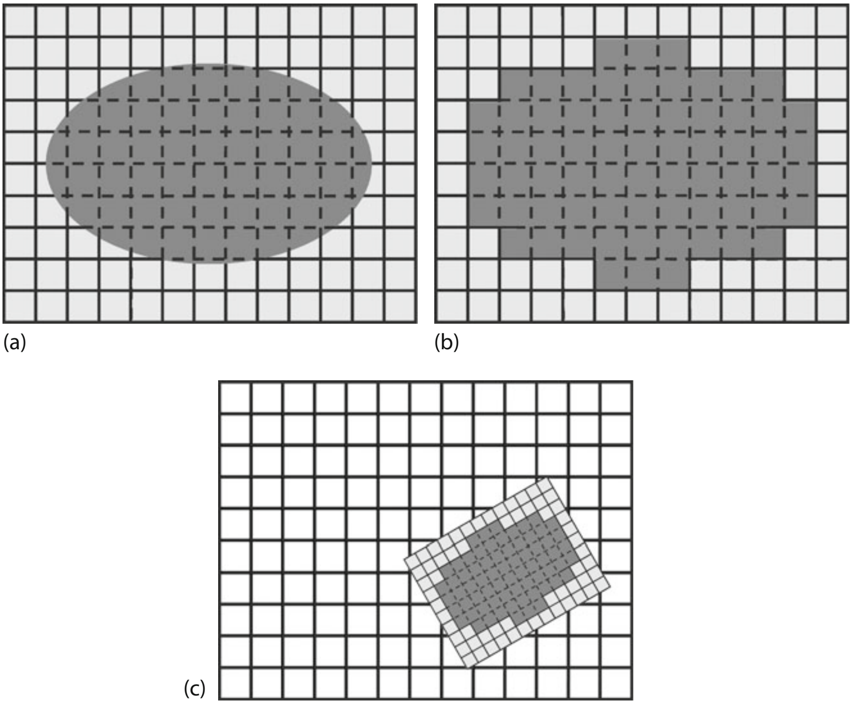

Figure 3.84 Problems caused by an affine transformation. (a) Ellipse with smooth contours. (b) Discretized and scaled ellipse. (c) Transformed ellipse (rotation, translation, scaling).

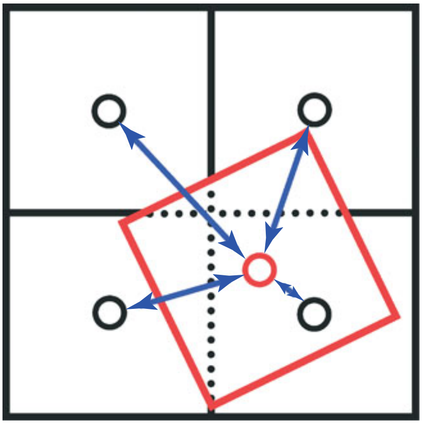

Figure 3.85 Geometry for calculating signal strength of transformed pixels. The lower right pixel is the nearest neighbor whose signal will dominate.

which the relevant information is located. There are several possibilities of image segmentation like region-growing segmentation, histogram-based segmentation, and edge detection. The decision on which type of segmentation procedure must be applied depends on the concrete goals of the image-processing procedure. In some cases, only a segmentation between foreground and background using a

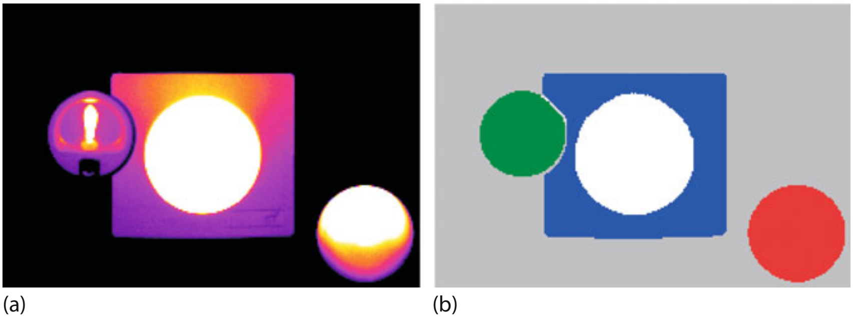

Figure 3.86 Segmentation of thermal image: determining ROIs. (a) Original thermal image and (b) colored ROI and gray background.

histogram method is necessary; in others, one may need to locate certain objects by edge detection algorithms.

All pixels classified as belonging to a particular ROI have one or more similar properties. In the thermal image depicted in Figure 3.86, for example, there are four ROIs (one rectangle, three circles). These objects can be segmented very easily from the background using the corresponding histogram and defining a temperature threshold. Alternatively, ROIs may be defined using edge detection and a fill algorithm.

3.5.2.4 Feature Extraction and Reduction

Following segmentation, that is, defining the ROIs in the image, the feature extraction procedure can start. Pixels in the signal matrix that represent noncontinuous jumps represent existing structures or edges in the image. To emphasize these discontinuities with sizes on the order of one pixel, high-pass filtering is needed, which is carried out by applying several local pixel operators.

Most of the different methods used may be grouped into two categories: gradient and Laplacian. Gradient methods detect edges by looking for extreme values (maxima and minima) of the first derivative of the image. In principle, the Laplacian method, which searches for positions where the second derivative of the image becomes zero, is equivalent.

The most commonly used local operators of the gradient method are the simple difference operator (Figure 3.70), Sobel masks (Eq. (3.38)), and Roberts cross operators (Eq. (3.39)):

$$So^y = \begin{pmatrix} -1 & -2 & -1 \\ 0 & 0 & 0 \\ +1 & +2 & +1 \end{pmatrix}, \quad So^x = \begin{pmatrix} -1 & 0 & +1 \\ -2 & 0 & +2 \\ -1 & 0 & +1 \end{pmatrix} \tag{3.38}$$

$$R_1 = \begin{pmatrix} -2 & -1 & 0 \\ -1 & 0 & +1 \\ 0 & +1 & +2 \end{pmatrix}, \quad R_2 = \begin{pmatrix} 0 & -1 & -2 \\ +1 & 0 & -1 \\ +2 & +1 & 0 \end{pmatrix} \tag{3.39}$$

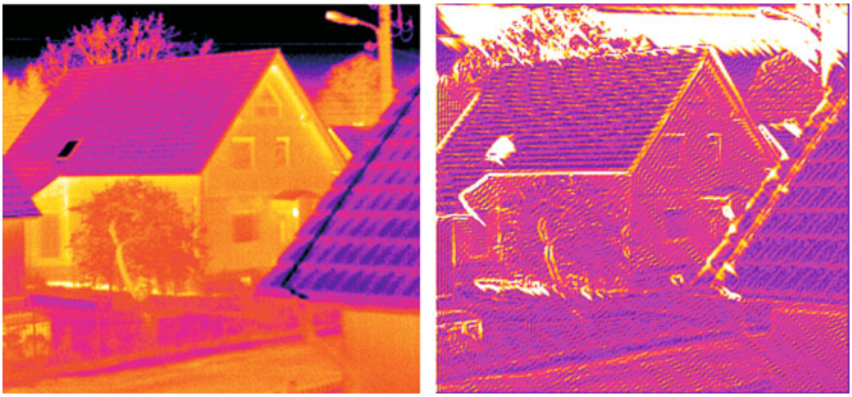
(a) (b)

Figure 3.87 Application of Sobel masks for edge detection. (a) Original image and (b) gradient image of $S_{i,j}$.

These matrices are applied to pixel areas exactly as discussed earlier. In contrast to the averaging matrices, which only contained positive numbers, the gradient operators must contain negative numbers, since they resemble derivatives, that is, the difference signals of neighboring pixels are calculated. From the structure of the matrices it is obvious that the Sobel mask computes the horizontal/vertical spatial derivatives, with more emphasis on the direct nearest neighbors in these directions. In contrast, the Roberts crosses resemble spatial derivatives in the directions of the two diagonals, with greater emphasis on the diagonal nearest neighbors.

As an example, the magnitude of the gradient for a pixel at row i and column j is calculated for the Sobel mask according to

$$So_{i,j} = \sqrt{\left(So_{i,j}^{x}\right)^{2} + \left(So_{i,j}^{y}\right)^{2}} \tag{3.40}$$

where $So_{i,j}^{x}$ and $So_{i,j}^{y}$ represent the results when applying the Sobel mask to the pixel area centered around image point (i, j). Figure 3.87 depicts the edge detection in an IR image using the Sobel masks according to Eq. (3.38) for all pixels of the original image.

Depending on the directional preference of the local operator, certain edges are preferentially extracted, while others may not be found. This is, of course, undesirable in some cases. This is why the use of isotropic operators can be advantageous. Examples of such isotropic (symmetric in all directions) operators are Laplace filters, which are approximations of the second-order derivatives (Eq. (3.41)):

$$\underbrace{L_1 = \begin{pmatrix} -1 & -1 & -1 \\ -1 & 8 & -1 \\ -1 & -1 & -1 \end{pmatrix} \quad L_2 = \begin{pmatrix} 1 & 0 & 1 \\ 0 & -4 & 0 \\ 1 & 0 & 1 \end{pmatrix} \quad L_3 = \begin{pmatrix} -1 & -2 & -1 \\ -2 & 12 & -2 \\ -1 & -2 & -1 \end{pmatrix}}_{\text{Laplace filters}} \tag{3.41}$$

The structure of the three chosen Laplacian operators leads to second derivatives. This can be seen from the calculation, which leads to the eight differences from the center pixel to all of its neighbors. If grouped in four pairs along the four major directions (vertical, horizontal, and two diagonals), the two differences for each direction have different signs, which means that, again, their difference is computed, namely, the second difference or derivative. The three chosen Laplacian operators $\boldsymbol{L}_1$, $\boldsymbol{L}_2$, and $\boldsymbol{L}_3$ differ in the following properties. $\boldsymbol{L}_1$ resembles just the average of the second derivatives in all four directions. $\boldsymbol{L}_2$ only calculates the second derivatives in the diagonal direction, and, again, $\boldsymbol{L}_3$ calculates the second spatial derivatives in all four directions, however, with twice as much weight of the horizontal and vertical nearest neighbors. Both the first- and second-order derivative operators are vulnerable to one-pixel disturbances such that a previous low-pass filtering is mandatory.

The most important goal of image processing is to find optimal edge detection algorithms. The most popular edge detection procedure is the so-called Canny algorithm, which claims to combine good detection, good localization, and minimal response. This means that as many existing edges as possible should be marked exactly at the correct position and independently of noise. In addition, no false edges should be detected owing to noise or pixel errors.

So-called optimal operators, such as the Canny or the Marr–Hildreth operators, have a multistep architecture [56]. In the Canny procedure, the image is first convoluted with a Gaussian matrix; then Sobel masks are used to extract the existing edges. To eliminate nonedge points, a non-maxima-suppression algorithm gets started as the third step. In this step, the gradient values and the gradient directions are evaluated such that pixels that are not local maxima in a 3×3 neighborhood and whose gradient direction is not the same as that of the maximum get classified as nonedge points. The advantage of this elimination procedure is good localization and ideal edges with a width of only one pixel. In the fourth step, a so-called hysteresis threshold algorithm can extract these edges directly via a contour-following algorithm. Therefore, an upper threshold for the gradient matrix of real edge points is set. These pixels build the starting points of the contour-following algorithm. All points along the contour above a defined lower threshold (mostly between two and three times smaller than the upper threshold) are the connecting pixels, which are used to define a complete contour.

Recently, FLIR Systems patented an image-processing feature using edge extraction to improve the thermal image quality [60]. Multi Spectral Dynamic Imaging (MSX®) uses both the IR image with typically submegapixel resolution, as well as the visible image with megapixel resolution from a digital camera. From the visible image characteristic, contours in the object scene are determined by an edge extraction procedure. The IR image is combined with the visible contour image using the image fusion procedure in real time. This feature produces extremely detail-rich images (Figure 3.88). If the visibility of objects in the IR image alone is limited owing to a lack of thermal contrast, the MSX fusion image will produce an enhanced representation of this object. This technique is used, for example, in smartphone cameras (see earlier discussion).

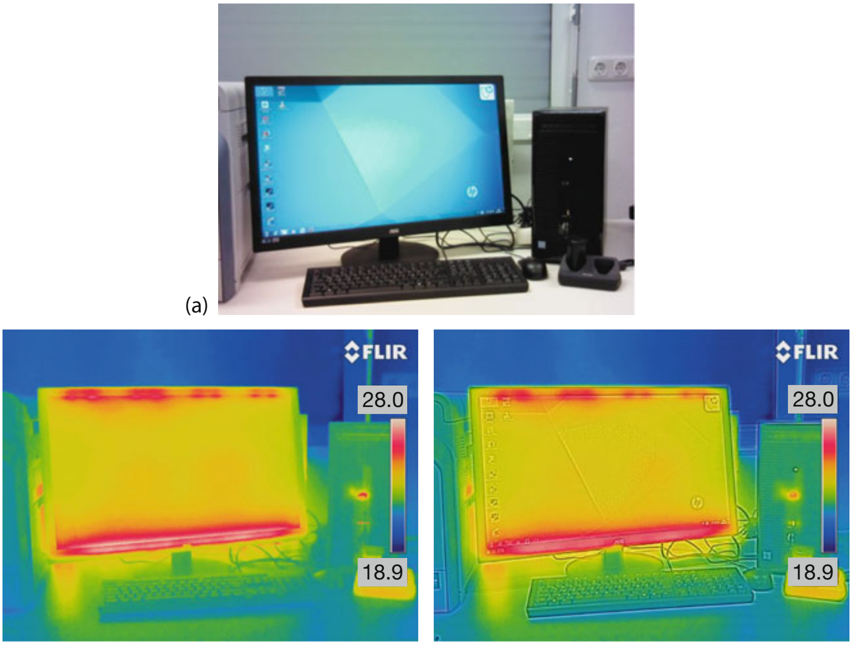

(a)

(b)

(c)

Figure 3.88 VIS (a) and IR image (b). Same thermal image using MSX.

3.5.2.5 Pattern Recognition

In some applications, the acquired images contain specific patterns or geometrically parameterizable objects like, for example, straight lines, parabola, circles, and so on. In these cases, a coordinate transformation from the original $x-y$ space to a so-called Hough space can be applied to extract these patterns. All pixels in the gradient matrix (result of feature extraction) with signal values above a certain threshold are used for the transformation. The simplest case is to search for collinear points or nearly straight lines.

Every straight line in Cartesian coordinates can be identified as one point in the corresponding Hough space. Figure 3.89 depicts the transformation procedure for the Hough space associated with linear features. A straight line $y = mx + b$ is plotted in Cartesian coordinates, that is, a rectangular (x, y) coordinate system. Within a Hough transformation, such a line is characterized by two other parameters (d, α), where $d = x_0 \cos(\alpha) + y_0 \sin(\alpha)$. The parameter d represents the shortest distance between the line and the origin, whose orientation is necessarily perpendicular to the chosen line. The angle $\alpha(-90° < \alpha < 90°)$ is the angle between the x-axis and this shortest-distance line. Angles lying outside the range $-90° < \alpha < 90°$ are replaced by $\alpha \pm 180°$.

To understand how the Hough transformation is applied to image analysis, a rule must be defined that states how extracted image features are treated. This rule and the corresponding procedure are described to give a simple example.

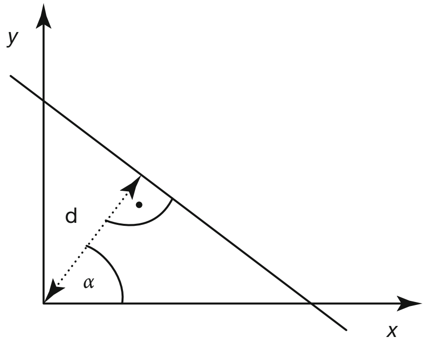

Figure 3.89 Principle of Hough transformation from (x, y) coordinates to (d, α) coordinates. The shortest connection from the origin to the line hits the line at point (x_0, y_0).

Each already extracted object image consists of a large number of pixels, that is, image points that were found via feature extraction. First, we consider one of these, a single point P, in the Cartesian object space. This point is transformed into a whole series of points in Hough space by first drawing an arbitrary line through P. This line refers to a well-defined point in Hough space. Second, we let the chosen line start to rotate with the rotation axis through P. This obviously defines a large number of lines in Cartesian space and, hence, also a large number of transformed points in Hough space. This means that each image pixel refers to a very large number of points in Hough space. Third, a second pixel point Q in the image is chosen, and again, all possible different lines through Q are transformed into Hough space. This procedure is repeated for each pixel, which was previously defined as a ROI in feature extraction. If the number of image points is large, an even much larger number of points result in Hough space.

The usefulness of Hough space becomes obvious if we consider, for example, a line defect found by a feature extraction algorithm. Arbitrarily distributed image points in the IR image would result in a distribution of points in Hough space that is quite homogeneous. If, however, pixels along a line in the image are transformed, each of the line pixels will also contribute to the same spot in Hough space since each pixel will contribute a line that is parallel to the image line. As a result, this line will lead to an accumulation point in Hough space.

Consequently, if all image pixels of extracted features are used for the transformation, one only needs to look for accumulation points. These define the line feature unequivocally according to the definition of Hough space (Figure 3.89). Therefore, a simple algorithm is applied to the problem: after all points of extracted features are transformed, the maxima, that is, accumulation points in Hough space, are rated via a threshold. Positively rated points are transformed back to visualize the problem areas of the extracted features.

Figure 3.90 shows an example to visualize the procedure with three straight lines that were defined as extracted ROIs. All image points along these lines were used to plot points in Hough space. Obviously, three accumulation points were found, which, as expected, resemble the three chosen lines.

Another advantage of such a representation is the independence of the algorithm with respect to noncontinuous structures that are mostly found in the ac-

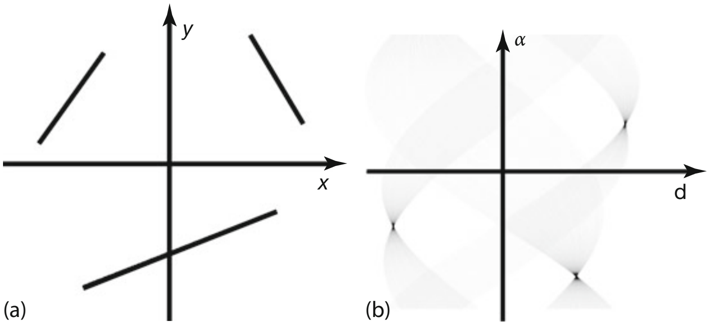

Figure 3.90 Hough transformation for three straight lines. (a) Straight lines in Cartesian coordinates and (b) corresponding accumulation points in Hough space.

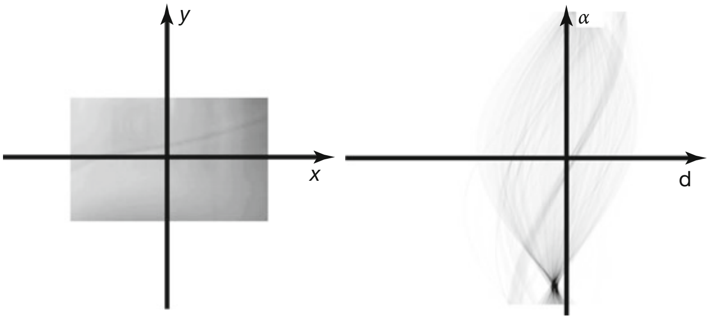

Figure 3.91 Hough transformation of a break in a glass sheet.

quired images. If, for example, only fragments of a line are detected in the IR image, they still lead to an accumulation point in Hough space.

Figure 3.91 depicts an application of the Hough transformation to the break in a glass sheet shown in Figure 3.81a.

The speed of calculation decreases with the dimension of the Hough space. The easiest 2D Hough space refers to linear features. If a search for objects that can be represented by circles is performed, one needs a 3D Hough space (the two center coordinates + the radius), and for an ellipse search one needs a 5D Hough space. In practice, these higher-dimensional Hough calculations are not used because of a lack of speed as a consequence of the higher number of dimensions. Several other, more advanced, methods, such as the generalized Hough transformation [61] or template matrices [62], can treat other structures and problems as well.

3.5.2.6 **Deblurring of Infrared Images**

A large number of advanced mathematical methods of signal processing have been developed to improve information extraction from images [54, 56, 58, 63]. One specific method, so-called image restoration, was developed to reconstruct images that, for several reasons, may have been changed from their original appearance. One of the most important image restoration methods is motion deblurring of images [64]. Motion blur is a well-known phenomenon in photography if objects within a scene move during the exposure time of the camera. This phenomenon is often seen in night shot images that use long exposure times, but it is also present in all situations where the exposure times are longer than the time it takes object images to move across several pixels in the detector array.

Motion blur therefore can also occur in thermal imaging of transient processes caused by moving objects. In commercial applications, mostly bolometer cameras are used. Owing to large detector time constants of about 10 ms in bolometer cameras, motion blur already occurs for quite low object or scene speeds (Section 2.5.5). Blur within IR images (Figure 2.104) is accompanied by an incorrect temperature measurement (Figure 2.105). This limits the applicability of quantitative thermal imaging with uncooled and inexpensive bolometer cameras for industrial process control.

Motion deblurring image processing can still help to extract the correct quantitative information from IR images by eliminating the influence of the bolometer detector properties upon recording and restoring original image information.

Quantitative recovery of an original, deblurred, that is, sharp, image requires a precise model of the blurring process. Mathematically the motion-blurred image represents a convolution of the deblurred image, f, and a distortion operator, h, producing the motion blur.

The distortion operator h is represented by the point spread function (PSF), which describes the response of the imaging system to a point source or point object. This means that the camera image of a moving point object corresponds to the PSF. The convolution result is often represented by

$$g = h \otimes f \tag{3.42}$$

which represents the convolution integral

$$g(t) = \int_{0}^{t} h(\tau) f(t - \tau) \,\mathrm{d}\tau \tag{3.43}$$

Figure 3.92 visualizes the convolution procedure. The relative movement of the PSF versus f as a function of time results in integral values (shaded areas) that define the convolution integral. For example, if f and h both represent rectangles, the convolution integral resembles a triangular, or as here trapezoid shape. In practice both shapes are more complicated, typically resulting in more complexly shaped convolution functions.

Because motion-blurred images represent convolutions, one needs to apply a deconvolution algorithm to remove the blur. In general, deconvolution is the process used to reverse the effects of convolution on recorded image data. This can usually be performed by, firstly, computing the Fourier transforms G and H of the recorded signal g and the transfer function h. Secondly, the deconvolution requires to calculate the Fourier transform of the unblurred image F by

$$F = \frac{H}{G} \tag{3.44}$$

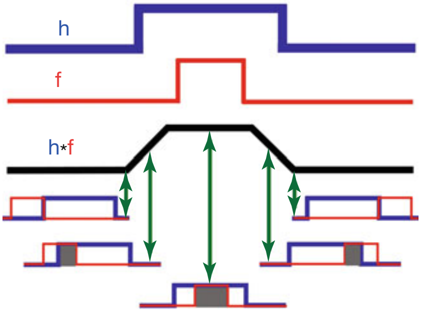

Figure 3.92 Visual representation of a convolution integral (see text for details).

Third, the inverse Fourier transform of F is calculated to find the desired deconvoluted original signal f. Let us apply this procedure to the motion-image blur of a falling ball in IR images recorded with bolometer cameras.

Bolometers are characterized by their thermal time constant τ, as discussed in Section 2.2.3. The time constant causes an exponential behavior of the normalized timescale PSF(t):

$$\mathrm{PSF}(t) = h(t) = \frac{1}{\tau}\mathrm{e}^{-\frac{t}{\tau}} \tag{3.45}$$

This PSF as a function of time can be converted into the spatial PSF as a function of pixels in the IR image considering the object speed v and image resolution Res given by pixels per length in the object scene:

$$\mathrm{PSF}(\mathrm{pixel}) = h(\mathrm{pixel}) = \frac{1}{\tau \cdot v \cdot \mathrm{Res}}\mathrm{e}^{-\mathrm{pixel}/(\tau \cdot v \cdot \mathrm{Res})} \tag{3.46}$$

The PSF is determined by the time constant of the detector signal generation in the bolometer. Therefore, strictly speaking, the PSF can only be applied to deblur detector (or object) signal images and not the corresponding temperature images (the relation between object temperature and detector signal is nonlinear – Section 2.4.5 – so the PSF to be used for temperature images would differ from the one in Eq. (3.46)). As a consequence, the IR image deblurring is usually done for the detector (object) signal images. Later on, the deblurred signal image can be transformed into the temperature image using a calibration curve. Only for small temperature differences in the object scene is it possible to linearize the calibration curve between detector signal and object temperature. In these cases the temperature images can be directly restored using the PSF given in Eq. (3.46). For all the following examples this assumption of sufficiently small temperature differences is valid and the deconvolution procedure based on Eq. (3.46) is applied.

The free-falling ball from Section 2.5.5 will now be used to illustrate, first, the motion blur in IR images and, second, the respective deblurring procedure. For simplicity, we consider only 1D motion along the line as shown in Figure 2.106a.

Figure 3.93 depicts the result of the convolution calculation for the falling ball in Figure 2.106a. The calculated blur of the ball image along the vertical line leads to a temperature profile that is in perfect agreement with the recorded image.

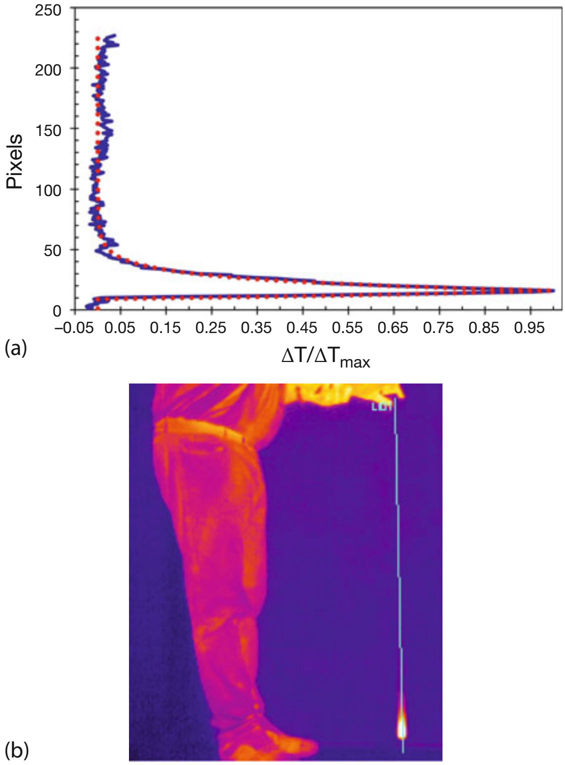

Figure 3.93 Motion blurring for falling ball shown in Figure 2.106a along line. (a) Red dotted line: convolution calculation result with PSF (pixel) from Eq. (3.46) (τ = 10 ms, resolution 227 pixels/m, v_{ball} = 4.27 m/s); blue line: measurement result. (b) IR image (Figure 2.106).

The deblurring algorithm for different kinds of object motions has been applied to various thermal images [65, 66]. One of the test objects was the small falling ball. Figure 3.94a depicts an IR image of a falling heated ball at a speed of about 1 m/s with the expected motion blur. Figure 3.94b depicts the corresponding measured temperature profile due to the image blur, similar to Figure 3.93a. The final deconvolution result using the exponential PSF with a 10 ms time constant of the bolometer detectors is shown in Figure 3.94c.

It nicely demonstrates that the circular ball shape can indeed be restored in the IR image. However, the deconvolution result in Figure 3.94c also indicates a typical problem in image restoration: restored images become noisy. Unfortunately, it is in practice not possible to recover the true image exactly owing to fluctuations or noise in the image recording process. This means that in any real case Eq. (3.42) needs to be modified by some noise contribution n generated during image acquisition:

$$g = h \otimes f + n \tag{3.47}$$

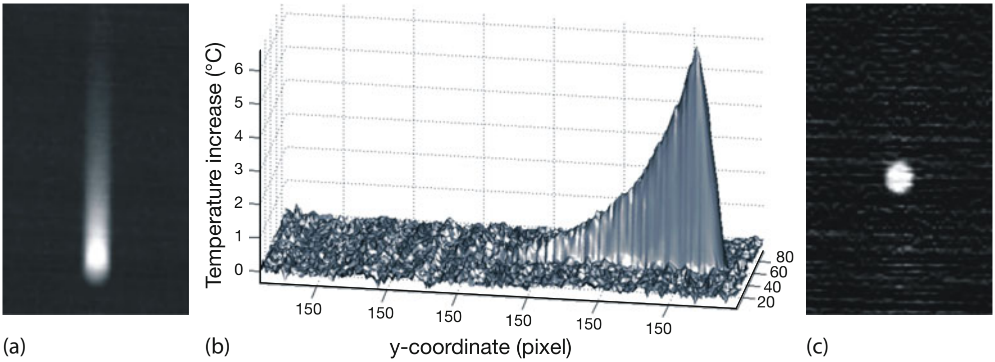

(a) (b) (c)

Figure 3.94 (a) Bolometer camera image of a falling ball at a speed of about 1 m/s and a camera spatial resolution of 288 pixels/130 mm. (b) Measured temperature caused by falling ball with respect to background temperature. (c) Restored image after deconvolution using exponential PSF with $\tau = 10$ ms; see Eq. (3.46). (Image courtesy: B. Oswald-Tranta, University of Leoben, Austria.).

For images recorded with microbolometer cameras it was shown that neglecting the noise in the deconvolution procedure will increase the noise after deblurring dramatically [65, 66] (Figure 3.95a). The original rectangular shaped signal whose blurred version is represented by a saw toothlike shape can be restored to its rectangular shape, however, with a very high noise level, as indicated by the amount of fluctuations.

Obviously, it is necessary to improve the restored images with respect to noise. Noise reduction in the deconvolution procedure can be done by applying special filters, like a Wiener filter [67]. The Wiener filter is a low-pass filter and suppresses the high-frequency noise amplified in the deconvolution [64, 65]. As discussed in Section 3.5.2.1, the problem of filtering is the need to preserve object edges and contours. With stronger filtering the noise can be efficiently suppressed, but the loss of high-frequency components will soften object edges and change object contours, as depicted in Figure 3.96.

The spatial smearing-out is associated with a decrease in object signal, which as a consequence also leads to a temperature measurement error. This problem increases with decreasing object size.

Motion deblurring of IR images is not limited to vertical or horizontal object motion along the image axes. Effective restoration can also be successfully applied to any arbitrary motion direction or rotational movements. Figure 3.97 [65, 66] presents an example of two balls rotating around the same center. The different image blurs of the two balls are corrected for in the reconstructed images, which nicely show the restored shape as well as quantitative original temperatures.

Figure 3.98 shows another successful example of blurred image reconstruction in automatic crack detection and failure classification of metal castings by thermographic inspection during induction heating [66]. The workpieces are falling through an induction coil and are heated by induced eddy currents.

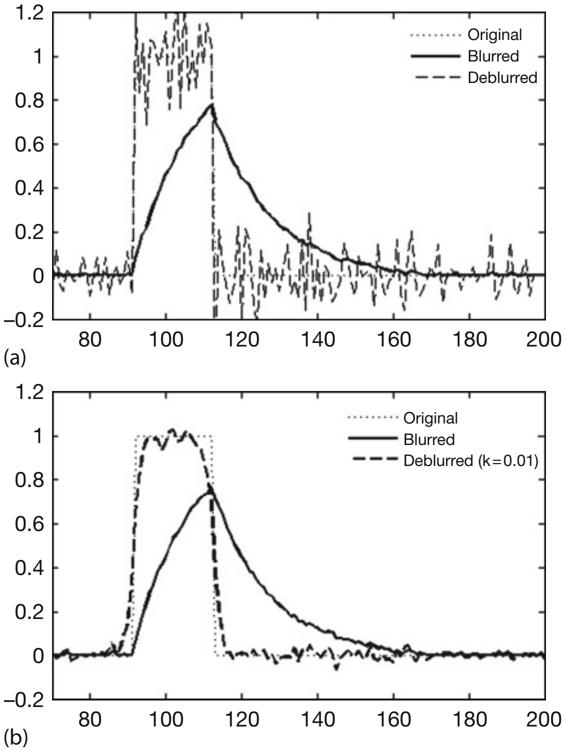

Figure 3.95 Deblurring of normalized signal of falling ball along pixel line with PSF according to Eq. (3.46) [65]. (a) Strong noise amplification caused by deblurring procedure using Eq. (3.44). (b) Suppression of noise using a Wiener filter in deblurring procedure. (Image courtesy: B. Oswald-Tranta, University of Leoben, Austria.).

The presented discussion of motion blur of IR images and their successful deblurring worked well as idealized conditions could be assumed. All objects investigated were perfectly separated from the background due to a significant higher object temperature, their speed was assumed to be known and it was comparatively small. If these assumptions are no longer valid, the deblurring problem becomes more complex. Whenever the object background or other objects at rest must also be considered, the PSF is no longer spatially invariant. Only the moving object is blurred but neither the background nor other objects at rest. Therefore, in this case, one must separate the moving object from the background first before starting the deconvolution. To conclude: motion deblurring can in principle be used to successfully restore IR images recorded with microbolometer cameras, but there are applicability limits for this method.

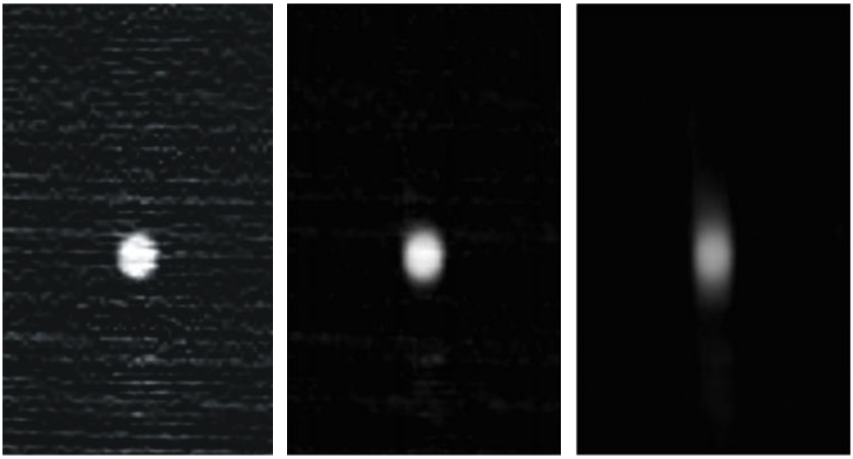
(a) (b) (c)

Figure 3.96 Restoration of falling-ball image from Figure 3.94a. (a) Direct deconvolution result without additional filter (original object contour and correct temperature measurement but strong noise). (b) Deconvolution result with weak Wiener filter (noise reduction, weak smearing of object contours). (c) Deconvolution with strong Wiener filter (perfect noise reduction, larger smearing, that is, loss of object contours and temperature measurement accuracy). (Image courtesy: B. Oswald-Tranta, University of Leoben, Austria.)

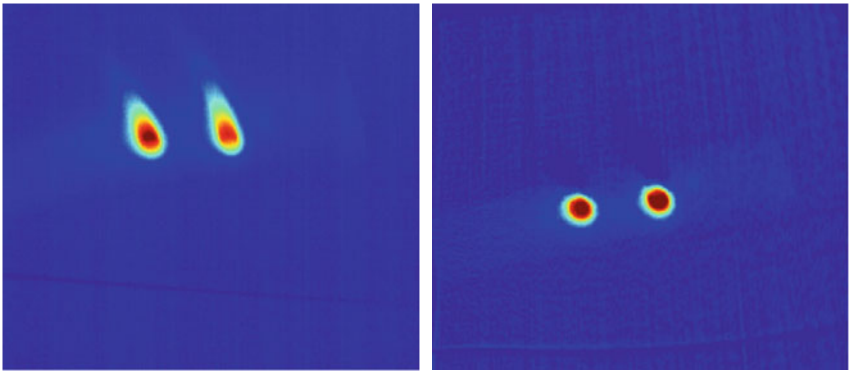
(a) (b)

Figure 3.97 Motion deblurring of two rotating balls at the same ball temperature. (a) Original image (right ball with larger distance from center of rotation, that is, higher speed, higher blurring, and higher temperature measurement error) may indicate rotation direction. (b) Restored image (both balls with circular contour, shown at same temperature). (Image courtesy: B. Oswald-Tranta, University of Leoben, Austria.).

3.6
Active Thermal Imaging

In most IR imaging applications, the investigation is done passively, that is, the camera observes a scene and detects the thermal radiation emitted from objects.

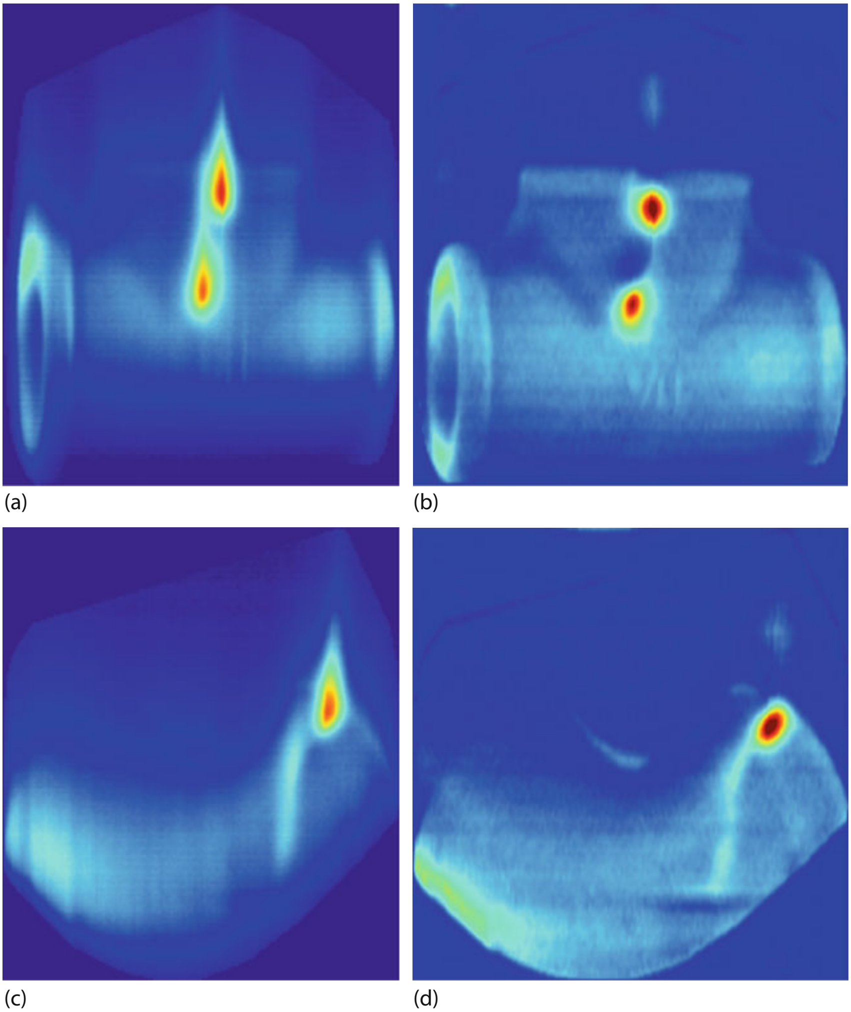

Figure 3.98 IR images of falling castings with cracks (hot spots). (a,c) Blurred original images. (b,d) Corresponding restored images. (Image courtesy: B. Oswald-Tranta, University of Leoben, Austria.)

Because of the thermal radiation from the surroundings, a thermal contrast in an image is observed only if temperatures differ from the ambient temperature. The method is called *passive* since the existing temperature distribution of the object scene is analyzed without imposing an additional heat flow to the object. This means that the observed temperature patterns are due solely to existing temperature differences. These often lead to nearly dynamic equilibrium conditions, that is, object surface temperatures do not change as a function of time (at least not very much). A typical example is a building inspection, where temperature differences are due to heating from inside while the outer walls are cooled by the surrounding air. Such passively recorded images may visualize the inner structural details of a building. A typical example is a half-timbered house (Section 7.2.1). The surface temperature differences measured by thermal imaging are caused by a spatial variation of the heat flow due to different thermal properties of the materials or constructions (Chapter 4).

Unfortunately, there are often situations where no natural temperature differences are present or, if they are present, may not be sufficiently large, or envelopes of objects may be too thick for an identification of structural elements below the surface. If one still wants to have a look beneath the surface, that is, detect structural details below the surface, active methods are needed.

They are based on the heating (in principle, cooling is also possible) of the surfaces to be investigated. These processes provide a nonstationary temperature gradient inside the structure being tested, which affects the observable surface temperature distributions.

Therefore, active thermography can also be treated as non-steady-state, nonequilibrium, or dynamic thermography. The surface temperatures of the sample are monitored as a function of time and the transient heat flow generated through the sample subsurface will cause transient anomalies in the surface temperature distribution. Figure 3.99 gives a brief overview of active thermal imaging techniques. A sample is heated by the absorption of radiation (as shown), electrical heating (current flowing through specimen), eddy currents, or, for example, ultrasound. The energy transfer to the sample can be either continuous, in a modulated continuous form (e.g., harmonic), or via pulses (rectangular or other shaped pulses). Detection of the heat transfer within the sample – which is affected by internal defects/structures – is done by measuring surface temperatures either in reflection or in transmission as a function of time. Neglecting the trivial cases of continuous heating or step heating, the most important methods of active thermal imaging are pulse thermography and lock-in thermography. They are applied widely in many different fields such as inspection of aircraft, solar panels, or objects made from composite materials with carbon or glass fiber structures and many more.

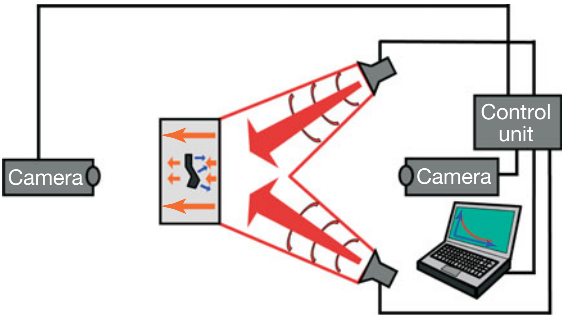

Figure 3.99 Schematic setup for active thermography techniques. A sample with an internal structure is heated, for example, by absorbing visible light. Surface temperatures are measured using IR cameras as a function of time. They are affected by structures/intrusions/anomalies within the sample.

The idea of nondestructive testing using transient temperature behavior has a long history and predates the development of the first thermal imagers. In the 1960s, a lot of laboratory work was done on the detection of transient surface temperature of objects. Temperature-sensitive colors, point-measuring sensors, and other instrumentation were used. All these methods were, however, severely limited by low temperature sensitivity and slow response times. For more detailed historical perspectives see [68]. The late 1970s mark the beginning of successful developments of both lock-in and pulse thermography methods [69, 70]. With the increasing use of thermal imaging systems and new heating methods, as well as electronic and computer technology in recent decades, these two methods became well established in the general field of nondestructive testing (NDT) [71].

This field is so broad that only a very brief overview of the fundamentals of transient heat transfer and active thermographic methods can be given here. For more detailed information about these methods, one should refer to the references [72, 73]. A large number of papers on the application of active thermography in NDT are available at the NDT database [74].

Active thermography methods are based on transient heat transfer in solids. The aim of all methods is to detect, locate, and characterize buried material discontinuities in solids [71, 75–80]. The correct quantitative description of 3D transient heat transfer in such systems is a very complex problem. The simulation of transient heat transfer in active thermography requires the prediction of the 3D temperature distribution using the 3D heat conduction differential equation for anisotropic thermal material behavior (e.g., for composites). A simplification of heat transfer using 1D or 2D models will only give rough estimates or qualitative information on the temperature distribution [71, 72] and will make the interpretation of the measurement result difficult. Nowadays, finite-element methods (FEMs) are the most promising tools for 3D heat transfer modeling if the experimental conditions are considered correctly [81]. A description of these methods is beyond the scope of this section. Here, we discuss first the relevant material parameters, which will help to understand whether a material discontinuity may be detectable with active techniques. Second, the simplest method, pulse thermography, is discussed briefly, along with some examples that demonstrate the sensitivity of the method. Third, the basics of lock-in thermography are presented with some applications to aircraft inspection. Finally, pulse phase thermography, which is simple to perform but complex in connection with data analysis, is briefly discussed.

3.6.1
Transient Heat Transfer – Thermal Wave Description

Transient heat transport in a solid body is characterized by two dynamic quantities. These are the thermal diffusivity a_{diff} and the thermal effusivity e_{eff}. Whereas the first describes how fast thermal energy diffuses through a material, the second represents some kind of thermal inertia. (In many publications, effusivity is simply denoted by e; here we rather use e_{eff} to distinguish it from Euler's number $\mathrm{e} = 2.718\ldots$).

As also discussed in Section 4.4, the thermal diffusivity a_{diff} is the ratio of the thermal conductivity λ to the volumetric heat capacity (i.e., the product of specific heat capacity and density):

$$a_{\mathrm{diff}} = \frac{\lambda}{\rho c_p} \tag{3.48}$$

Please note that λ uses the same Greek symbol that is usually reserved for wavelength. Rather than introducing additional subindices, which would unnecessarily complicate the notation, in particular when a distinction between thermal conductivities for different materials (indicated by subindices) will be made later, we stay with the same symbol since the context of the respective equations will usually make it absolutely clear which quantity – wavelength or thermal conductivity – is meant.

The thermal diffusivity is a measure of the rate of thermal energy diffusion through a material. The diffusion rate will increase with the ability to conduct heat and decrease with the amount of thermal energy needed to increase the temperature. Large diffusivity values mean that objects respond fast to changes in thermal conditions. Therefore, this quantity governs the timescale of heat transfer into materials. If a material has voids or pores in its structure, then the thermal conductivity and density decrease, which means the thermal diffusivity changes. As a result, the heat transfer within the material is affected, leading to observable changes in surface temperatures in the vicinity of the defects.

The *thermal effusivity*, e_{eff}, is defined as the square root of the product of the thermal conductivity and the volumetric heat capacity:

$$e_{\mathrm{eff}} = \sqrt{\lambda \rho c_p} \tag{3.49}$$

This quantity is often referred to as *thermal inertia*. If the response of a heat input is analyzed, the effusivity will represent the ability of the material to increase its temperature according to $T \sim 1/e_{\mathrm{eff}}$. Therefore, this quantity will govern how much the temperature of an object changes owing to the input of thermal energy. Again, if a defect below a surface has a different temperature than its surroundings, this will affect the observed surface temperatures.

The effusivity also has another effect on heat transfer within a material. Considering a thermal contact between two materials with different effusivities $e_{\mathrm{eff},1}$ and $e_{\mathrm{eff},2}$, one often characterizes the thermal behavior by the thermal mismatch factor Γ:

$$\Gamma = \frac{e_{\mathrm{eff},1} - e_{\mathrm{eff},2}}{e_{\mathrm{eff},1} + e_{\mathrm{eff},2}} \tag{3.50}$$

$\Gamma = 0$, that is, equal effusivities, implies that there is no thermal mismatch (the interface of the two materials cannot be detected by a temperature measurement at the surface). For a perfect thermally conducting first material, $\Gamma = 1$, and, for a perfect thermally insulating material, $\Gamma = -1$.

If the transient thermal behavior of a composite material is analyzed, the thermal mismatch factor will describe the change in thermal transit time compared to a homogeneous material. In this regard, the effusivity behaves similar to, for example, the index of refraction in optics when describing the reflection of optical waves being incident on the interface between two media. An optical interface cannot be detected if the two indices of refraction are identical. In this case, the wave just passes the interface undisturbed without changing its speed. In an even more general scheme, any wave is characterized by wave resistance or impedance, which depends on the material properties. If the wave hits an interface with another material, reflections can be observed only if there is a change in impedance.

As a matter of fact, one also often uses the concept of thermal waves in active thermography, in particular if periodical heating processes are described, for example, in lock-in thermography [71].

It can be shown that the Fourier equation, assuming harmonic object heating at the surface provides a harmonic temperature field within the object with the same frequency but different amplitude and phase. Therefore, the concept of thermal waves, which can be described by the theory of wave physics, can be introduced. The main characteristic of thermal waves is the strong decay as a function of depth in the object. This decay can be characterized by the thermal diffusion length, which resembles a thermal penetration depth:

$$\mu = \sqrt{\frac{a_{\text{diff}}}{\pi f}} \tag{3.51}$$

The thermal diffusion length depends on the thermal diffusivity a_{diff} and the frequency f of the thermal wave (or heat stimulation). This expresses the fact that low-frequency thermal waves will penetrate deeper into a material than high-frequency waves. The penetration depth will increase with increasing diffusivity. A first idea of possible depth ranges can be obtained from μ. Consider, for example, the outer skin of aircraft constructions, which is made of a few millimeters of aluminum and below some carbon fiber composite materials. Aluminum has a diffusivity of around $10^{-4}\,\text{m}^2\,\text{s}^{-1}$, which, for a frequency of 10 Hz, would result in a μ value of about 1.8 mm. Since μ corresponds to a depth where the signal has decreased exponentially to a value of $e^{-1} = 0.368$, it seems reasonable to assume that thermal signatures may be detectable at depths of several millimeters.

As discussed previously, compared to light waves, thermal waves are reflected at boundaries of materials only if the materials have different effusivities. If we look at the boundary between a solid and a gas, the effusivity of the solid is much higher than the effusivity of the gas. Applying Eq. (3.50) we will get $\Gamma = 1$ and the solid behaves as a thermal wave mirror for the gas–solid interface [71]. As a result, any reflection from internal boundaries will lead to changes in thermal wave propagation in the object, which will in turn cause changes of observable surface temperature distributions.

In summary, thermal waves exhibit all wave phenomena such as reflection, refraction, and interference. The propagation of thermal waves in inhomogeneous solids will be affected by these phenomena and will result in a well-defined time-dependent surface temperature distribution that can be analyzed by transient temperature measurements.

3.6.2
Pulse Thermography

Pulse thermography is one of the most popular methods in active thermography because it is extremely easy to carry out. The setup just requires the possibility of pulsed heating, for example, a system of flash lamps and time-dependent recording with an IR camera. The data analysis consists of analyzing IR images of the object as a function of time and thereby detecting surface temperature changes induced by subsurface structures. The only severe drawback is the limited spatial resolution with regard to depth on the one hand and lateral resolution on the other.

The experimental setup of pulse thermography was already shown in Figure 3.99. Short pulses are applied that last from a few milliseconds for high-conductivity material inspection such as metals to a few seconds for low-conductivity specimens such as plastics and graphite epoxy laminates [71]. Although appreciable heating powers are applied, the brief duration of the heating usually only leads to temperature rises of a few degrees above the initial component temperature, which prevents any thermally induced damage to the component.

Figures 3.100 and 3.101 depict two different situations for possible pulse thermography inspections. Figure 3.100 shows an object material that has three holes of different diameters and depths drilled from the bottom of the sample. The sample is heated with a pulse from the bottom. Thermal diffusion in the material can proceed faster in the region of the deepest holes, since heat must then only diffuse through a thin layer of object material before reaching the top surface. Therefore, the observable top surface temperatures are increased with respect to neighboring parts of the surface. This temperature difference will evolve as a function of time, the absolute values depending on the thermal diffusivity and effusivity of the material. Figure 3.100 depicts the situation schematically. Owing to the thermal diffusion, a lateral spreading takes place, and the hole with a smaller diameter will have a less pronounced thermal signature than the hole with a larger diameter but the same depth. Similarly, comparing the two holes with equal diameters but different depths, the temperature difference is smaller for the hole of lower depth. The various holes of different depths and diameters will also show up with the best thermal contrast at different times during such an experiment.

Figure 3.101 shows a second example. A solid material 1 (gray object) characterized by thermal diffusivity $a_{\text{diff},1}$, conductivity λ_1, and effusivity $e_{\text{eff},1}$, and so on has a subsurface structure of material 2 (black object), characterized by different values of thermal diffusivity $a_{\text{diff},2}$, conductivity λ_2, and effusivity $e_{\text{eff},2}$. Heat flow is induced by a thermal rectangular pulse from the bottom. If the effusivity $e_{\text{eff},2}$

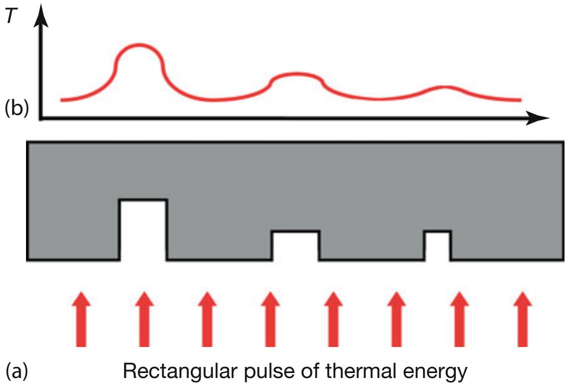

Figure 3.100 (a) Scheme of pulse thermography experiment with test structure composed of material containing holes of given diameter and depth. The structure is illuminated from the bottom, and temperatures are analyzed from the opposite side (b). Owing to better heat transfer through the thinner regions of the object, temperature anomalies appear, which depend on the ratio of thickness below the surface to the diameter of the structure.

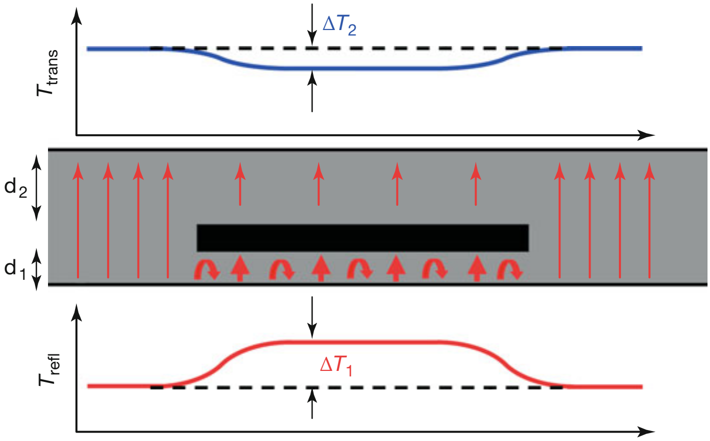

Figure 3.101 Scheme of pulse thermography experiment with test structure composed of material with embedded second material of different thermal properties. Observable surface temperature differences depend on thermal material properties of object and intrusion.

of the substructure is much lower than that of material 1, the heat flow will try to at least partially bypass the obstacle, that is, it will be lower behind the substructure. At the same time, blocking of heat flow by the obstacle (visualized by the curved arrows) leads to lower heat flow from the surface to the inside of the material. As a consequence, the surface temperatures at the bottom of the thermal energy input will decrease more slowly in the region of the intrusion, that is, the temperature profile across the structure will lead to a temperature rise above the region of intrusion. In contrast, the corresponding heat flow is lower on the opposite side, giving rise to a lower temperature with regard to adjacent parts of the object. Depending on the distance of the obstacle from the two surfaces, the temperature profiles will differ: the one at a greater distance will be shallower owing to lateral spreading by thermal diffusion within the material. In case the intrusion is of a material with much higher effusivity than the surrounding material, the corresponding temperature profiles from front and back would be inverted. If the distances d_1 and d_2 from the intrusion to object surfaces are different, then, on the one hand, the temperature profile for the larger distance will be more smeared out laterally due to the diffusion and, on the other hand, its thermal contrast will be lower.

A more quantitative analysis reveals [71] that the time to observe the maximum thermal contrast of an intrusion in depth z is proportional to z^2, that is, $t_{\text{obs}} \sim z^2/a_{\text{diff}}$, while at the same time, the thermal contrast C_{th} decreases because of lateral spreading of the thermal energy ($C_{\text{th}} \sim 1/z^3$). Deeper discontinuities will be observed later and with a reduced contrast. As a result, deep embedded structures usually appear very shallow with very poor thermal contrast. Overall, the size and depth of observable discontinuities are restricted. In isotropic media, the smallest detectable discontinuity should have a diameter of at least two times its depth below the surface. For anisotropic media, this restriction can even amount to a factor of 10. The criterion for still observing a structure is that the corresponding laterally induced observable surface temperature change ΔT is larger than the NETD of the camera.

Figure 3.102a illustrates a typical experimental arrangement for observation in reflection or in transmission. Which approach is chosen depends on whether both

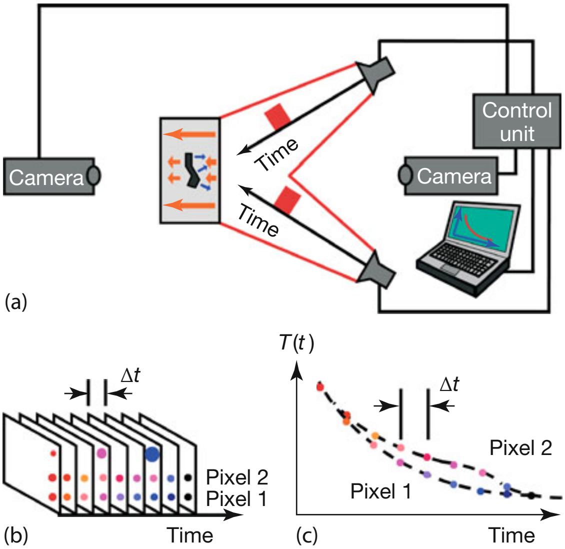

Figure 3.102 Principal and experimental arrangement of pulse thermography (a) and data acquisition/analysis (b,c). Images are recorded at time intervals Δt (b) and temperature plots of single pixels as functions of time (c) show a thermal contrast due to anomalies.

sides are accessible for recording and, if so, where the substructure is located. It can be better detected from the side where the depth below the surface is smaller.

A square pulse of thermal energy, in this case visible light from flash lamps, is incident on the sample. For example, total thermal energies of 10–15 kJ are typical for pulse widths of 0.2 s. Figure 3.102b schematically depicts a time series of IR images recorded from the side of the illumination. The frames are separated by time intervals Δt. In each frame, the temperature decrease of two selected pixels are

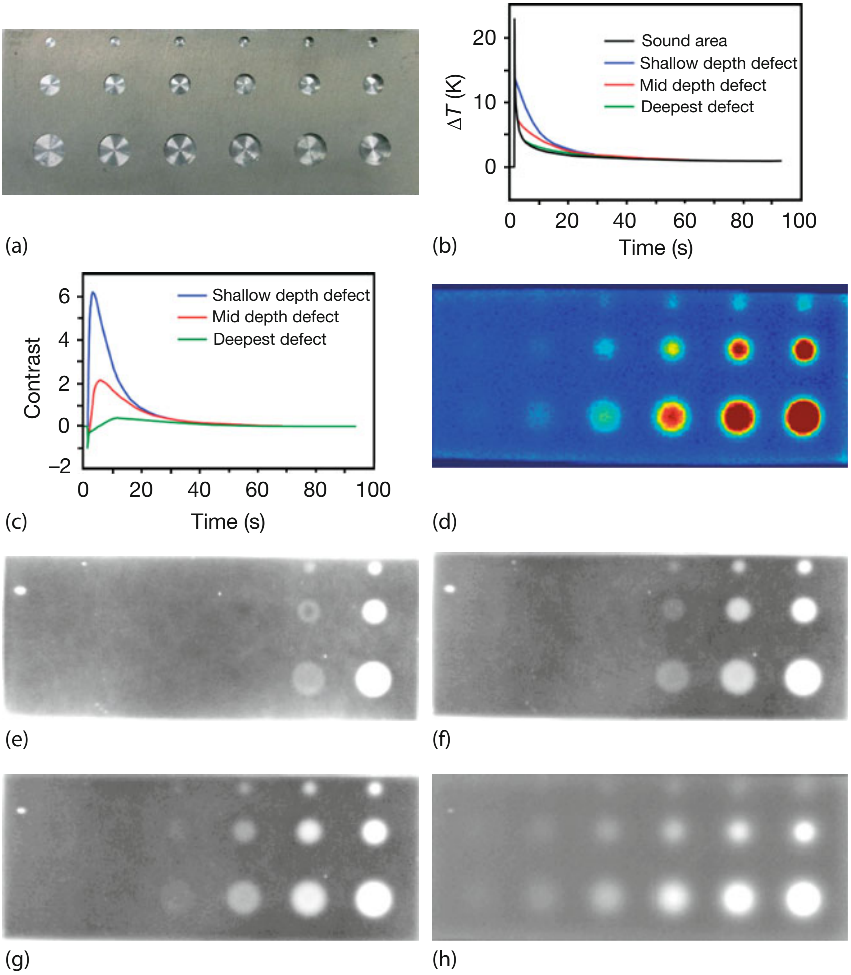

Figure 3.103 Flat-bottom holes of different depths in solid laminate composite. (a) VIS image from backside. (b) Temperature evolution (thermal pulse at $t = 0$). (c) Temperature contrasts between hole area and homogeneous part of sample. (d) False color representation of IR image at $t = 0.4$ s. (e) IR image at $t = 0.033$ s. (f) IR image at $t = 0.050$ s. (g) IR image at $t = 0.067$ s. (h) IR image at $t = 0.400$ s. (Image courtesy: National Research Council Canada, NRC Aerospace.).

indicated (different colors refer to different temperatures). The time dependence of the temperatures of these two pixels is schematically plotted in Figure 3.102c. The temperature at the surface drops after the initial pulse since the thermal energy diffuses into the material. In the example, the two chosen pixels differ in their transient behavior, one resembling the undisturbed material, the other a position with a subsurface structure that blocks heat flow, thereby leading to a higher surface temperature than in the other pixel. The lateral spreading of the thermal energy pulse is visualized by the top spot in the IR frame sequence (Figure 3.102b). It can be thought of as resembling a point source heating at the chosen given pixel. The corresponding spatially localized initial high temperature spreads out owing to thermal diffusion.

Figure 3.103 depicts a measurement result, recorded with a test structure similar to that in Figure 3.100. A solid laminate composite test object with three rows of flat-bottom holes of different diameters was investigated. The diameter of the holes increased from top to bottom and the depth of the holes increased from left to right. After pulsed excitation, IR images were recorded from the back side as a function of time. As expected, the deep holes were already clearly visible within short times after excitation. With increasing time, from panels e to h, holes with smaller depths also appear, but the structures are more blurred because of the lateral heat diffusion. Comparing the holes with different diameters but the same depths, it is also obvious – as expected – that the smaller the hole, the more it gets spread out laterally. This can be seen best, for example, for the third structure from the right in the top row. At short times, it is not visible. Then it starts to show up with good contrast and a rather sharp edge before beginning to get blurred edges and lower thermal contrast for long times.

Figure 3.104 shows an example of a practical application. Here, pulse thermography was used to detect impact damage in a solid laminate.

3.6.3
Lock-in Thermography

Lock-in thermography [71, 72] is very similar to pulse thermography in terms of the setup; however, the pulsed thermal excitation is replaced by a sinusoidal input of thermal energy (Figure 3.105). This is most easily brought about by illuminat-

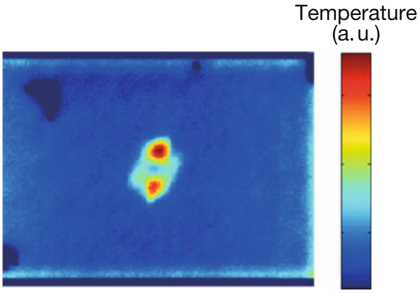

Figure 3.104 Impact damage of solid laminate. (Image courtesy: National Research Council Canada, NRC Aerospace.)

ing an extended sample using a modulated lamp. This periodic, to be specific harmonic, heating input leads to a similar transient harmonic variation of the surface temperature of the object. As mentioned in Section 2.4.1, harmonic heating at the surface also leads to harmonic temperature variations at given depths within the object, although with a strongly attenuated amplitude as a function of depth, described by the thermal diffusion length μ (Eq. (3.51)).

Let us assume thermal excitation using light absorption from a modulated light source. The harmonically varying input energy is partially absorbed, leading to a strong temperature increase of the surface during the maximum of the input energy. While the excitation energy drops and passes through a minimum, the surface temperature drops too, because the initially absorbed energy diffuses into the interior of the object. After another half period of excitation, the surface is again heated by maximum input of thermal energy, and so forth. As a result, the harmonic input will lead to a harmonically varying surface temperature distribution. Since the diffusion of thermal energy into the solid is taking place at the same time, one can also observe harmonic variation of temperature at certain depths of the object as a function of observation time. The observed surface temperature variation may be shifted by a phase angle with respect to the exciting light source owing to thermal inertia of the object. If the object is homogeneous, the phase shift will be similar for all observed surface pixels that were recorded with the IR camera. If, however, there is an intrusion or a thermal anomaly below the surface of the object, the thermal behavior changes. Either lower or higher heat flow due to the intrusion will manifest itself in a change of the phase of the observable surface temperature above the intrusion. Thus, any defect or structure within an object may lead to observable changes, here, predominantly an additional phase shift of the surface temperature with respect to the excitation. The analysis of the recorded images is therefore straightforward. One must record surface temperatures as a function of time for each pixel (x, y) and evaluate changes in the phase shift compared to a reference signal. Usually, it is sufficient to study a harmonic

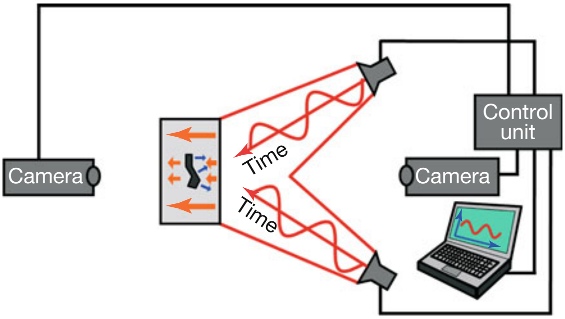

Figure 3.105 Setup for lock-in thermography: a sample is heated harmonically (sinusoidal excitation) as a function of time, for example, by modulated illumination, eddy currents, ultrasound, microwaves, and so on. The camera analyzes the spatial temperature distribution as a function of time by recording thermal images.

function by recording at least four data points per complete cycle (Figure 3.106), that is, the frame rate must be chosen according to the predefined frequency of excitation.

Consider four well-defined points, $P_1(t_1)$, $P_2(t_2)$, $P_3(t_3)$, and $P_4(t_4)$, of the modulated excitation, where t_1 corresponds to a zero crossing of the excitation signal. These points define the times at which the temperature signal is analyzed, that is, the surface temperatures $T_1(t_1)$, $T_2(t_2)$, $T_3(t_3)$, and $T_4(t_4)$ within one cycle. Usually, the signal is shifted by a phase angle difference $\Delta\phi$ with respect to excitation.

If the temperature signal is given by an average value and a modulation, that is, $T(t) = T_{av} + S(t)$, then one may construct two different resulting signals, an amplitude signal $A(x, y)$ and a phase signal $\phi(x, y)$, for each pixel (x, y) according to

$$A(x, y) = \sqrt{[S_1(x, y) - S_3(x, y)]^2 + [S_2(x, y) - S_4(x, y)]^2} \tag{3.52}$$

$$\phi(x, y) = \arctan\left[\frac{S_1(x, y) - S_3(x, y)}{S_2(x, y) - S_4(x, y)}\right] \tag{3.53}$$

The average temperatures cancel each other out because of the differences, that is, these signal functions depend only on the harmonically induced temperature differences. If the signals remained constant, the amplitude signal would be zero. A maximum amplitude signal results from a harmonic variation of temperature, that is, $S(t) = \Delta T_{max} \sin(\omega t + \phi)$, where the excitation varies as $\sin(\omega t)$. In this case, the amplitude signal would give $2\Delta T_{max}$, that is, the maximum temperature variation of the harmonic signal. The phase from Eq. (3.53), on the other hand, directly reflects the phase change between excitation and harmonic signal, as can be seen by calculating the signal differences and assuming that each of the various signals is separated from the next signal by 90°.

The amplitude signal depends on the sum of the squared temperature differences, whereas the phase signal only relates to the ratio of the respective temperature differences. Any local variations in illumination, absorption, or emissivity

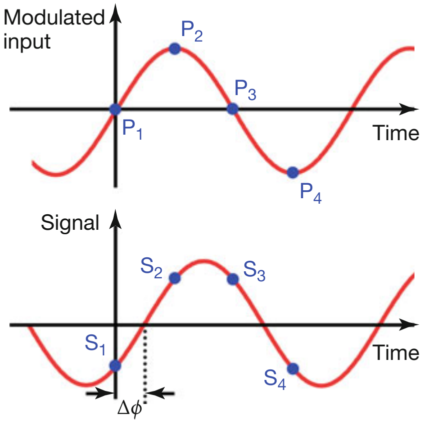

Figure 3.106 Measurement principle: the signal (surface temperature) varies harmonically but is shifted with respect to the excitation owing to the modulated input.

(i.e., higher or lower temperature differences between different pixels) will cancel out in the phase but show up in the amplitude signal. Therefore, one usually uses the phase signal, which is more sensitive to buried defects than the amplitude signal. It can be used to investigate a depth range of about twice the thermal diffusion length μ (Eq. (3.51)). Evaluating the phase signal for all pixels makes it possible to produce phase IR images, that is, the phase is correlated with a color or a grayscale (see below for examples). Images therefore reflect phase changes induced by subsurface structures or defects. The probed depth range depends on the frequency according to Eq. (3.51). Therefore, the input energy source must be used at an optimal frequency, which depends on both the thermophysical characteristics of the object and its thickness.

The definition of phase and amplitude also stress the fact that the recording frequency must be large enough for at least four data points to be recorded during one cycle of excitation. If the four chosen points were distributed over several cycles, the results would no longer be unequivocal. Therefore, the method resembles a phase-sensitive detection if the signal is locked to the excitation frequency. This is similar to the lock-in technique used in other measurement science applications and, hence, explains the name.

Before presenting practical examples, some advantages and disadvantages of lock-in thermography must be mentioned. Lock-in thermography detects defects in depth ranges, which are related to the excitation frequency according to Eq. (3.51). Therefore, an inspection covering a large range of depths requires longer times than other approaches, such as pulse thermography, since many different frequencies must be applied to a sample, and each time the dynamic equilibrium must be established before starting the measurement. Compared to pulse thermography, the method is, however, more sensitive and may be used for greater depths. Furthermore, the energy required to perform lock-in thermography is generally smaller than in other active techniques, which may be important if the inspected part suffers damage from high energy input. Lock-in thermography has been used in a large number of application fields. It can even be applied in building surveys [82] using the day-to-night cycle as periodic heating and cooling of buildings (Chapter 7).

3.6.3.1 Nondestructive Testing of Metals and Composite Structures

The main body of a passenger aircraft, also known as the *fuselage*, is built as a skeleton frame structure with a skin affixed to the frame elements. For reasons of weight, the skin only consists of a thin metal layer, usually aluminum, with a thickness (e.g., for the Boeing 737) on the order of 1 mm. Stability is achieved by attaching a composite material, usually a carbon-fiber-reinforced material, to a substantial portion of the interior surface of the skin layer. The fuselage must remain intact for many flights, that is, for many pressurizing and depressurizing cycles. Aging aircraft may suffer from material fatigue, for example, cracks in the skin or loose connections between skin and supporting frame, and so on, which can lead to failure. Therefore, the aircraft fuselage is regularly scanned for defects.

Figure 3.107 shows an example of aircraft testing [83]. Phase image lock-in thermography was performed on the outer skin of a Boeing 737 aircraft. Obviously the lock-in technique can easily look through the 1 mm aluminum skin and detect the supporting subsurface structure. One of the advantages of lock-in compared to conventional NDT techniques like ultrasound is that during a single measurement, large areas of typically 1 m^2 can be imaged. This considerably reduces the inspection times by a factor of 10 or so compared to conventional methods. It

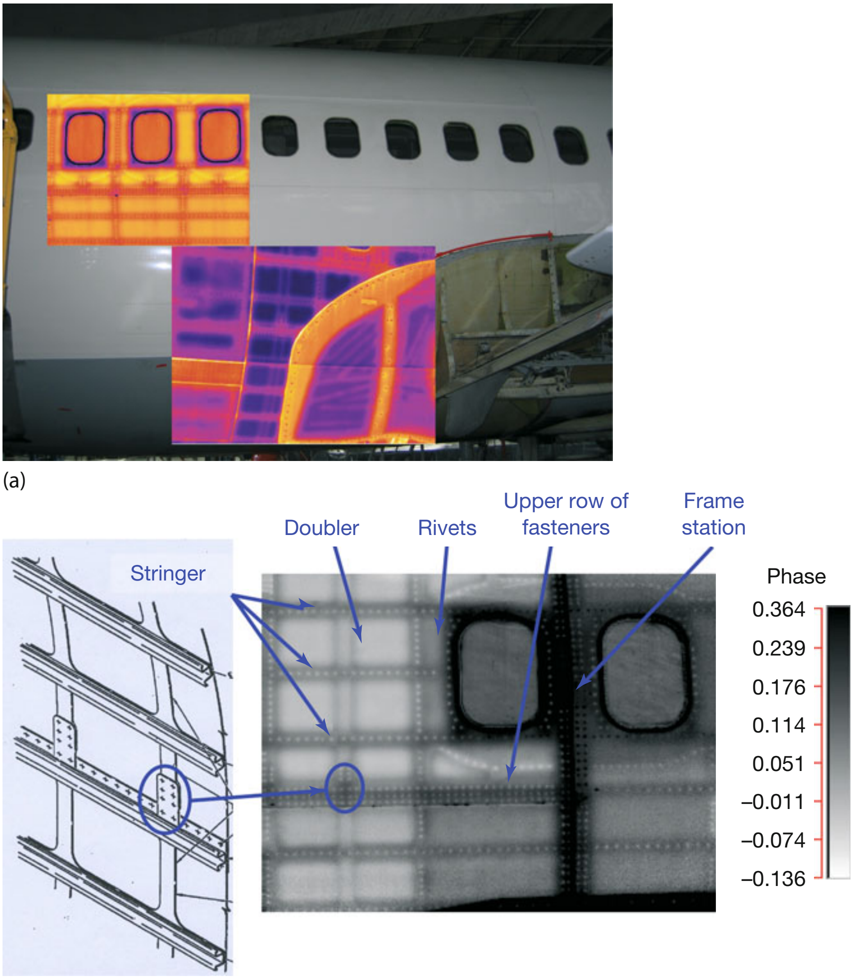

(b)

Figure 3.107 Lock-in thermography testing of a Boeing 737. The images show selected sections as overlays of thermal phase images and visible images (a). The subsurface structures are easily detected and investigated with regard to anomalies, which would indicate defects. Often results are shown as grayscale images (b). (Image courtesy: MoviTHERM, www.movitherm.com.)

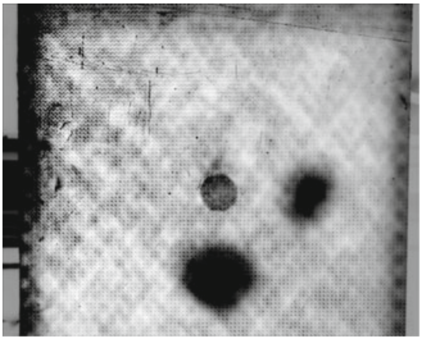

Figure 3.108 Lock-in phase image of honeycomb structure from an aircraft showing delaminations. (Image courtesy: MoviTHERM, www.movitherm.com.)

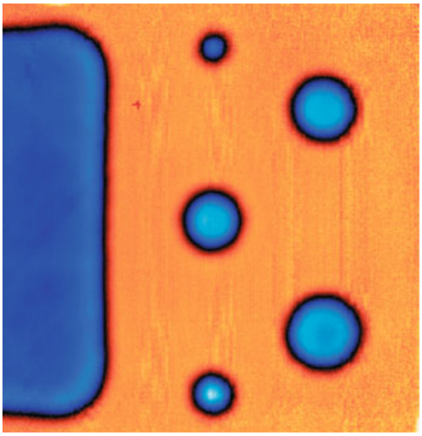

Figure 3.109 Lock-in thermography phase image of test structure of carbon fiber sample with flat-bottom holes and large milled-out area. (Image courtesy: MoviTHERM, www.movitherm.com.)

was estimated that a lock-in inspection of the complete fuselage of a Boeing 737 could be done within about 100 h. The method is, for example, approved by the US Federal Aviation Administration (FAA) and used by Boeing, Airbus, and, the airline Lufthansa, for example.

The thermal input, needed to perform the measurement, only leads to maximum temperatures of about 40 °C, that is, thermally induced damage is nonexistent. The technique can be used to detect all key defects such as delaminations, cracks, loose rivets, or water intrusions for metals (such as aluminum), carbon, or glass fiber-reinforced plastics, as well as honeycomb structures.

As an example of a defect, Figure 3.108 shows an example of delamination in a composite panel honeycomb structure from an Airbus aircraft.

Test structures similar to those used for pulse thermography (Figure 3.103) are shown in Figure 3.109. A carbon fiber sample was prepared with flat-bottom holes and a larger milled-out area (to the left). No structure can be seen visually from the other side, whereas the lock-in phase image easily detects all subsurface structures.

3.6.3.2 **Solar Cell Inspection**

Photovoltaic power generation is one of the most rapidly developing fields of renewable energy. The industry faces major challenges in terms of the quality control of solar cells. In particular, defects in the semiconducting materials can reduce cell efficiencies. Therefore, reliable test procedures of the modules are needed that can be adjusted to the typical areas of modules in the square-meter range.

Current solar cell tests, that is, photovoltaic cell tests, are based on three types of measurement: spectroscopy, electrical (contact) measurements, and IR imaging. Measured electrical parameters include the short-circuit current, open-circuit voltage, fill factor, ideality factor, series resistance, shunt resistance at 0.0 V, and reverse voltage breakdown. On the one hand, electrical contact measurements are straightforward and involve the collection of a complete set of parameters. Therefore, electrical cell tests can be quite time consuming. On the other hand, conventional IR imaging allows a faster detection of the major shunts by either applying a reverse bias voltage or by observing the cell temperature for normal operating conditions. The sensitivity and thermal resolution of standard thermography are, however, limited by the detector NETD (Section 2.5.2), which amounts to about 20 mK for cooled InSb detectors and up to 80 mK for uncooled microbolometers. Therefore, refined methods such as lock-in thermography are needed to detect a wider variety of defects below this limit with temperature resolutions in the microkelvin range, for example, shunt conditions below a solar cell's metallization layer. Figure 3.110 depicts a standard (panel a) and lock-in (panel b) thermal image of the same solar cell. The triangular shapes on the left- and right-hand sides (best seen in Figure 3.110a) are alligator clips that apply a bias voltage. The circular blue area of the standard IR image is a reflection of the cold detector of the InSb camera.

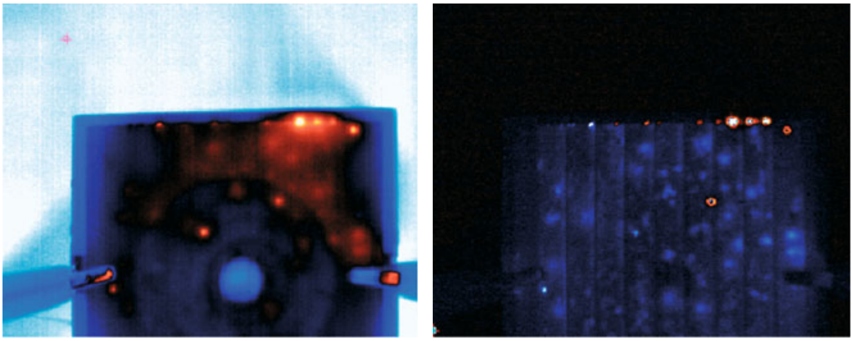
(a) (b)

Figure 3.110 Standard thermal image (a) recorded with an InSb camera of a $60 \times 60\,\text{mm}^2$ silicon solar cell. The lock-in image of the same cell (b) is the result of 800 individual images, recorded using a 10 Hz electrical AC input and an acquisition time of 20 s. Both images show shunt defects (orange areas) under steady-state reverse bias conditions. (Image courtesy: MoviTHERM, www.movitherm.com.)

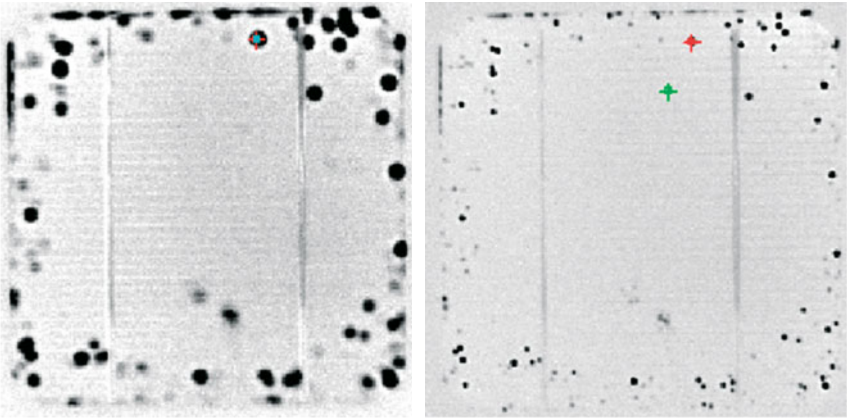
(a) (b)

Figure 3.111 Phase images of shunt defects from lock-in measurement system at 10 Hz (a) and 200 Hz (b) sine wave stimulation. (Image courtesy: MoviTHERM, www.movitherm.com.)

A direct comparison of the two images reveals that, whereas the standard image, recorded with a cooled InSb camera, shows thermal reflections from the detector as well as from the surroundings on the clips, no reflections are visible in the lock-in image. The InSb camera detects some hot spots (shunts) as blurred, that is, strongly diffused orange regions in the upper right half, whereas the lock-in image shows a very sharp image with well-localized shunts. The shunt detection in both images is limited by the sensitivity of the detector, which is 20 mK for the InSb camera, but only 0.02 mK for the lock-in image.

Therefore, only severely shunted areas become visible as bright orange and localized spots in the InSb image. The darker orange regions are a result of weaker shunt defects. Locating the origins of these weaker shunts is extremely difficult, if not impossible, owing to the thermal diffusion (spreading of thermal energy over time) as well as the weak thermal radiation of the defect itself.

Overall, image quality and methods of extracting quantitative information are strongly improved in the lock-in image. These sharp lock-in thermography images provide additional information, such as nonuniform heating of the cell, as revealed by lighter and darker blue areas. Therefore, the lock-in technique also requires much less thermal energy input to the solar cells during the test procedure.

Another example, which illustrates the effect of modulation frequency on the image, is presented in Figure 3.111, which shows the results of lock-in thermography testing for shunt defects on cells that were electrically excited with sine waves of different frequencies. Obviously – as expected – the image with a lower frequency, which relates to a larger depth within the cell, is more blurred.

As a final example, Figure 3.112 shows three images, which show the differences between a standard thermal image (panel a) and either amplitude (panel b) or phase (panel c) lock-in thermal images. Obviously, the phase image has the best quality, clearly detecting a shunt with high spatial resolution.

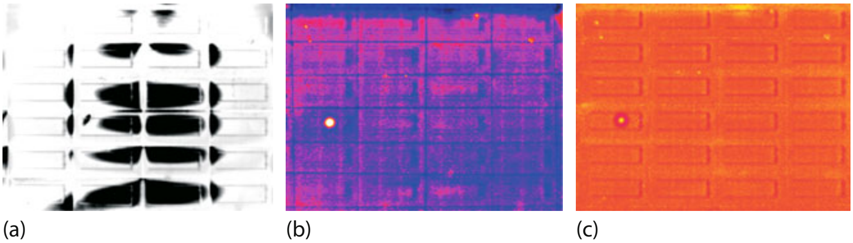

Figure 3.112 Comparison of different thermal images of an array of 5 × 10 mm^2 solar cells. (a) Standard image recorded with cooled InSb camera, again showing reflection of cold detector, that is, the Narcissus effect (Section 2.4.4.5). (b,c) Amplitude and phase lock-in images recorded using sinusoidal illumination with diode array operating at $\lambda = 850$ nm and frequency of 25 Hz. Shunts are clearly detected in both lock-in images. (Image courtesy PVflex Solar GmbH, Fürstenwalde, Germany.)

It should be noted, however, that which lock-in image is to be used may depend on the specific requirements and experimental conditions [72]. For IR imaging of solar power plants see Section 10.11.2.

3.6.4
Pulsed Phase Thermography

Pulse thermography is easy to perform; however, it suffers from limited thermal contrast and limited depth range. Lock-in thermography is better suited for locating depth ranges of defects by varying the frequency of excitation; however, this advantage is associated with longer measurement times.

To overcome the latter drawback while at the same time having a simple setup, pulsed phase thermography was introduced as a link between pulse thermography and lock-in thermography [71].

Pulsed phase thermography uses the concept of Fourier that any pulse of arbitrary shape can be described as a superposition of harmonic waves of different frequencies. Therefore, a square pulse, such as is used in pulse thermography, can also be considered as being composed of a multitude of different harmonic waves of different frequencies and associated amplitudes. The frequency distribution is unequivocally related to the shape of the pulse in the time regime, for example, a square pulse gives rise to a frequency spectrum defined by a $\text{sinc}(x) = \sin(x)/x$ function. The fundamental idea behind pulsed phase thermography is as follows. A square pulse is applied to a sample. This leads to heat flows into the sample, which may be changed owing to the presence of defects/substructures, exactly as explained for pulse thermography. Again, IR images of changing surface temperatures are recorded as a function of time. The difference between pulsed phase and pulse thermography is due simply to the data analysis procedure, that is, signal processing. In pulsed phase thermography, a fast Fourier transform is computed from the signals: since the input includes contributions of many frequencies simultaneously, the signal is thereby deconvoluted into the responses due to the individual frequencies. This means that results are obtained for a large spectrum of frequencies, thereby simultaneously probing different depth ranges of a sample.

Based on theory, the typical maximum frequencies associated with a pulse of width Δt can be computed. One finds, for example, that for a 10 ms pulse, the highest frequency that still has more than 90% of the maximum amplitude is 25 Hz; for a 0.1 s pulse, this maximum frequency is 2.5 Hz. Images must be recorded with at least twice the maximum frequency in order to avoid any aliasing effects.

References

1 De Witt, D.P. and Nutter, G.D. (1989) *Theory and Practice of Radiation Thermometry*, 2007 Proceedings, John Wiley & Sons Inc., pp. 129–139.

2 www.spectrogon.com (accessed May 2017).

3 www.schott.com (accessed May 2017).

4 Palik, E.P. (ed.) (1985) *Handbook of Optical Constants of Solids*, vol. 1, Academic Press;
(1991) vol. 2.

5 www.optris.com/thermal-imager-optris-pi-450-g7 (accessed May 2017)

6 Hunter, G.B., Allemand, C.D., and Eagar, T.W. (1984) An improved method for multi-wavelength pyrometry. Thermosense VII. Proc. SPIE, vol. 520, 40–46.

7 Hunter, G.B., Allemand, C.D., and Eagar, T.W. (1986) Prototype device for multiwavelength pyrometry. *Opt. Eng.*, **25** (11), 1223–1231.

8 Inagaki, T. and Okamoto, Y. (1994) Temperature measurement and radiometer pseudo gray-body approximation. Thermosense XVI. Proc. SPIE, vol. 2245 (34), 231–240.

9 Thevenet, J., Siroux, M., and Desmet, B. (2010) Measurements of brake disc surface temperature and emissivity by two-color pyrometry. *Appl. Therm. Eng.*, **30** (6-7), 753–759.

10 www.lumaseinc.com (accessed May 2017).

11 Coates, P.B. (1988) The least-squares approach to multi-wavelength pyrometry. *High Temp.-High Press.*, **20**, 433–441.

12 Saunders, P. (2000) Reflection errors and uncertainties for dual and multiwavelength pyrometers. *High Temp.-High Press.*, **32**, 239–249.

13 Neuer, G., Fiessler, L., Groll, M., and Schreiber, E. (1992) in *Temperature: Its Measurement and Control in Science and Industry*, vol. 4, (ed. J.F. Schooley), American Institute of Physics, New York, pp. 787–789.

14 Svet, D.Y. (2003) in *Temperature: Its Measurement and Control in Science and Industry*, vol. 7, (ed. D.C. Ripple), American Institute of Physics, New York, pp. 681–686.

15 Peacock, G.R. (2003) in *Temperature: Its Measurement and Control in Science and Industry*, vol. 7 (ed. D.C. Ripple), American Institute of Physics, New York, pp. 789–793.

16 Peacock, G.R. (2003) in *Temperature: Its Measurement and Control in Science and Industry*, vol. 7, (ed. D.C. Ripple), American Institute of Physics, New York, pp. 813–817.

17 Gibson, G.C., DeWitt, D.P., and Sorrell, F.Y. (1992) In-process temperature measurement of silicon wafers. *Temp. Meas. Control Sci. Ind.*, **6** (Part 2), 1123–1127.

18 Kourous, H., Shabestari, B.N., Luster, S., and Sacha, J. (1998) Online industrial thermography of die casting tooling using dual-wavelength IR imaging. Thermosense XX. Proc. SPIE, vol. 3361, 218–227.

19 Holst, G.C. (2000) *Common Sense Approach to Thermal Imaging*, SPIE Press, Bellingham.

20 Williams, G.M. and Barter, A. (2006) Dual-band MWIR/LWIR radiometer

for absolute temperature measurements. Thermosense XXVIII. Proc. SPIE, vol. 6205, 62050M.

21 Khan, M.S., Washer, G.A., and Chase, S.B. (1998) Evaluation of dual-band infrared thermography system for bridge deck delamination surveys. Proc. SPIE, vol. 3400, 224–235.

22 Moropoulou, A., Avdelidis, N.P., Koui, M., and Kanellopoulos, N.K. (2000) Dual band infrared thermography as a NDT tool for the characterization of the building materials and conservation performance in historic structures. MRS Fall Meeting: Nondestructive Methods for Materials Characterization, November 29–30 1999, Boston, vol. 591, Publication Materials Research Society, Pittsburgh, pp. 169–174.

23 Beecken, B.P., LeVan, P.D., and Todt, B.J. (2007) Demonstration of a dualband IR imaging spectrometer, Infrared Systems and Photoelectronic Technology II. Proc. SPIE, vol. 6660, 666004.1–666004.11.

24 Beecken, B.P., LeVan, P.D., Lindh, C.W., and Johnson, R.S. (2008) Progress on characterization of a dualband IR imaging spectrometer, Infrared Technology and Applications XXXIV. Proc. SPIE, vol. 6940, 69401R–69401R-9.

25 Farley, V., Belzile, C., Chamberland, M., Legault, J.-F., and Schwantes, K.R. (2004) Development and testing of a hyper-spectral imaging instrument for field spectroscopy. Proc. SPIE, vol. 5546, 29–36.

26 FIRST Hyper-Cam Datasheet, Telops Inc., Quebec, www.telops.com (accessed May 2017).

27 Möllmann, K.-P. and Vollmer, M. (2013) Teaching Fourier transform infrared spectroscopy in physics lab courses. *Eur. J. Phys.*, **34** (6), S123-S137.

28 Kauppinen, J. and Partanen, J. (2001) *Fourier Transformations in Spectroscopy*, John Wiley & Sons, Berlin.

29 Bell, R.J. (1972) *Introductory Fourier Transform Spectroscopy*, Academic Press, New York, London.

30 Moore, E.A., Gross, K.C., Bowen, S.J., Perram, G.P., Chamberland, M., Farley, V., Gagnon, J.-P., Lagueux, P., and Villemaire, A. (2009) Characterizing and overcoming spectral artifacts in imaging Fourier transform spectroscopy of turbulent exhaust plumes. Proc. SPIE, vol. 7304, 730416–730416-12.

31 Farley, V., Vallières, A., Villemaire, A., Chamberland, M., Lagueux, P., and Giroux, J. (2007) Chemical agent detection and identification with a hyperspectral imaging infrared sensor. Proc. SPIE, vol. 6739, 673918.

32 Harig, R., Gerhard, J., Braun, R., Dyer, C., Truscott, B., and Mosley, R. (2006) Remote detection of gases and liquids by imaging Fourier transform spectrometry using a focal plane array detector: first results, Chemical and Biological Sensors for Industrial and Environmental Monitoring II. Proc. SPIE, vol. 6378-16, doi: 10.1117/12.692922.

33 Richards, A. and Cromwell, B. (2004) Superframing: Scene dynamic range extension of infrared cameras. Proc. SPIE, vol. 5612, 199–205.

34 Hecht, E. (1998) *Optics*, 3rd edn, Addison-Wesley.

35 Vollmer, M., Henke, S., Karstädt, D., Möllmann, K.P., and Pinno, F. (2004) Identification and suppression of thermal reflections in infrared thermal imaging. Inframation 2004, Proceedings, vol. 5, pp. 287–298.

36 Goldstein, D.H. (2011) *Polarized Light*, 3rd edn, CRC Press, Taylor & Francis Group, Boca Raton.

37 Snik, F., Craven-Jones, J., Escuti, M., Fineschi, S., Harrington, D., de Martino, A., Mawet, D., Riedi, J., and Tyo, J.S. (2014) An Overview of Polarimetric Sensing Techniques and Technology with Applications to Different Research Fields, Proc. SPIE, vol. 9099, Polarization: Measurement, Analysis, and Remote Sensing XI, 90990B (21 May 2014); doi: 10.1117/12.2053245.

38 Shaw, J.A. (2007) A survey of infrared polarization in the outdoors. Proc. SPIE, vol. 6660, 666006-1.

39 Sandus, O. (1965) A review of emission polarization. *Appl. Opt.*, **4**, 1634–1642.

40 Tyo, J.S., Goldstein, D.L., Chenault, D.B., and Shaw, J.A. (2006) Review of passive imaging polarimetry for remote sensing applications. *Appl. Opt.*, **45** (22) 5453–5469.

41 Gurton, K.P. and Felton, M. (2012) Remote detection of buried land-mines and IEDs using LWIR polarimetric imaging. *Opt. Express*, **20** (20), 22344–22359.

42 Gurton, K.P., Yuffa, A.J., and Videen, G.W. (2014) Enhanced facial recognition for thermal imagery using polarimetric imaging. *Opt. Lett.*, **39** (13), 3857–3859.

43 Yuffa, A.J., Gurton, K.P., and Videen, G. (2014) Three-dimensional facial recognition using passive long-wavelength infrared polarimetric imaging. *Appl. Opt.*, **53** (36), 8514–8521.

44 Smith, M.I. and Heather, J.P. (2005) Review of image fusion technology in 2005. Thermosense XXVII. Proc. SPIE, vol. 5782, 29–45.

45 www.flir.com (accessed May 2017).

46 Avdelidis, N.P., Almond, D.P., Ibarra-Castanedo, C., Bendada, A., Kenny, S., and Maldague, X. (2006) Structural integrity assessment of materials by thermography. Conference Damage in Composite Materials CDCM, Stuttgart, www.ndt.net/article/cdcm2006/papers/maldague.pdf (accessed May 2017).

47 Mat Desa, S. and Salih, Q.A. (2004) Image subtraction for real time moving object extraction. International Conference on Computer Graphics, Imaging and Extraction CGIV'04, pp. 41–45.

48 Weth-Glushko, S. and Salvaggio, C. (2007) Quantitative analysis of infrared contrast enhancement algorithms. Proc. SPIE, vol. 6543, 1–11.

49 Zuo, C., Chen, Q., Liu, N., Ren, J., and Sui, X. (2011) Display and detail enhancement for high-dynamic-range infrared images. *Opt. Eng.*, **50** (12), 127401.

50 Singh, R.P. and Dixit, M. (2015) Histogram equalization: A strong technique for image enhancement. *Int. J. Signal Process. Image Process. Pattern Recogn.*, **8** (8), 345–352.

51 Kaur, M., Kaur, J., and Kaur, J. (2011) Survey of contrast enhancement techniques based on histogram equalization. *Int. J. Adv. Comput. Sci. Appl.*, **2** (7), 137–141.

52 www.flir.com/uploadedFiles/OEM/Products/LWIR-Cameras/Quark/FLIR-Camera-Adjustments-LWIR-AppNote.pdf (accessed May 2017).

53 Högasten, N. (2013) Systems and methods for processing infrared images, United States Patent, US 8,515,196 B1, 20 August 2013.

54 Jaehne, B. (2004) *Practical Handbook on Image Processing for Scientific and Technical Applications*, CRC Press LLC, Boca Raton.

55 Steger, C., Ullrich, M., and Wiedemann, C. (2008) *Machine Vision Applications and Algorithms*, John Wiley & Sons, Berlin.

56 Gonzalez, R.C. and Woods, R.E. (2008) *Digital Image Processing*, 3rd edn, Pearson Prentice Hall, Pearson Education, Inc., Upper Saddle River, New Jersey.

57 Möllmann, S. and Gärtner, R. (2009) New Trends in process visualization with fast line scanning and thermal imaging systems. p. 43–48 in Proceedings of the Conference Temperatur, PTB Berlin (Germany), ISBN 3-9810021-9-9 (in German).

58 Parker, J.R. (1997) *Algorithms for Image Processing and Computer Vision*, John Wiley & Sons, Inc., New York.

59 Russ, J.C. (2007) *The Image Processing Handbook*, 5th edn, CRC Press Taylor and Francis Group, LLC, Boca Raton.

60 Strandemar, K. (2015) Infrared resolution and contrast enhancement with fusion, US Patent, US 9171361 B2 (also published as US20120262584, US20140015982), 27 October 2015.

61 Ballard, D.H. (1981) Generalizing the Hough transform to detect arbitrary shapes. *Pattern Recognit.*, **13** (2), 111–122.

62 Brunelli, R. (2009) *Template Matching Techniques in Computer Vision: Theory and Practice*, John Wiley & Sons, Inc. Hoboken.

63 Young, S.S., Driggers, R.G., and Jacobs, E.L. (2008) *Signal Processing and Performance Analysis for Imaging Systems*, Artech House, Inc., Boston, London.

64 Rajagopalan, A.N. and Chellappa, R. (2014) *Motion Deblurring: Algorithms and Systems*, Cambridge University Press, Cambridge.

65 Oswald-Tranta, B., Sorger, M., and O'Leary, P. (2010) Motion deblurring of infrared images from a microbolometer camera. *Infrared Phys. Technol.*, **53** (4), 274–279.

66 Oswald-Tranta, B. (2012) Automated Thermographic Non-destructive Testing, Habilitation, Montanuniversität Leoben, Austria.

67 Wiener, N. (1949) *Extrapolation, Interpolation, and Smoothing of Stationary Time Series*, John Wiley & Sons, New York.

68 Shepard, S.M. (2007) Thermography of composites. *Mater. Eval.*, **65** (7), 690–696.

69 Milne, J.M. and Reynolds, W.N. (1985) The non-destructive evaluation of composites and other materials by thermal pulse video thermography. Proc. SPIE, vol. 520, 119.

70 Kuo, P.K., Ahmed, T., Huijia, J., and Thomas, R.L. (1988) Phase-locked image acquisition in thermography. Proc. SPIE, vol. 1004, 41–45.

71 Moore, P.O. (ed.) (2001) *Nondestructive Testing Handbook*, 3rd edn, American Society for Nondestructive Testing, Columbus.

72 Breitenstein, O. and Langenkamp, M. (2003) *Lock-in Thermography*, Springer, Berlin, Heidelberg.

73 Maldague, X.P.V. (2001) *Theory and Practice of Infrared Technology for Nondestructive Testing*, John Wiley & Sons, New York.

74 www.ndt.net (accessed May 2017).

75 Wu, D., Salerno, A., Schönbach, B., Hallin, H., and Busse, G. (1997) Phase sensitive modulation thermography and its application for NDE. Proc. SPIE, vol. 3056, 176–183.

76 Sagakami, T. and Kubo, S. (2002) Application of pulse heating thermography and Lock-In thermography to quantitative non-destructive evaluations. *Infrared Phys. Technol.*, **43**, 211–218.

77 Grinzato, E., Bison, P.G., Marinetti, S., and Vavilov, V. (2007) Hidden corrosion detection in thick metallic components by transient IR thermography. *Infrared Phys. Technol.*, **49**, 234–238.

78 Maldague, X., Benitez, H.D., Ibarra Castenado, C., Benada, A., Laiza, H., and Caicedo, E. (2008) Definition of a new thermal contrast and pulse correction for defect quantification in pulsed thermography. *Infrared Phys. Technol.*, **51**, 160–167.

79 Genest, M. and Fahr, A. (2009) Pulsed thermography for nondestructive evaluation (NDE) of aerospace materials. Inframation 2009, Proceedings, vol. 10, pp. 59–65.

80 Tarin, M. (2009) Solar panel inspection using Lock-in-Thermography. Inframation 2009, Proceedings vol. 10, pp. 225–237.

81 Weiser, M., Arndt, R., Röllig, M., and Erdmann, B. (2008) Development and test of numerical model for pulse thermography in civil engineering. ZIB-Report 08-45, Konrad-Zuse Zentrum für Informationstechnik, Berlin, December 2008.

82 Bortolin, A., Cadelano, G., Ferrarini, G., Bison, P., Peron, F., and Maldague, X. (2013) High resolution survey of buildings by lock-in IR thermography, Thermosense: Thermal Infrared Applications XXXV, (eds G.R. Stockton, F.P. Colbert), Proc. SPIE, vol. 8705, 870503.

83 Tarin, M. and Kasper, A. (2008) Fuselage inspection of boeing-737 using lock-in thermography. Proc. SPIE, vol. 6939, 1–10.

Chapter 4
Some Basic Concepts in Heat Transfer

4.1
Introduction

In this chapter, we discuss the relevance of measured surface temperatures of opaque objects (e.g., buildings, electrical components under load) due to their emitted infrared (IR) radiation using IR cameras. Taking nice IR images, that is, snapshots of object surface temperature distributions, is just the start of analyzing data and drawing conclusions concerning thermal properties of objects under study. The main objectives are, for example, to gain insight into heat loss problems owing to the thermal insulation properties of buildings or leakages in industrial installations, to understand heat sources that may lead to the failure of electrical components, and many more. In each case, one must generally start with the measured surface temperature and from that extract useful information. In general, the physics problem behind the issue can be formulated as follows. If the surface temperature of an opaque object at a certain time is given, what can we learn about the temperature distribution within the object, about the associated heat flows through the surfaces of the object, and about the transient changes in surface temperatures?

Disregarding emissivity for the moment, all objects that can be investigated have in common that they must have a different temperature than their surroundings. This means that either the objects have energy sources or sinks within them or they were heated or cooled before the observation started. In addition, during the observation, the temperature of objects may change, that is, thermal equilibrium conditions are usually never fulfilled. To interpret the results of surface temperature measurements, one must therefore know about all processes that might lead to temperature changes in objects. In this chapter, we briefly discuss the three basic heat transfer modes. More information can be found in textbooks (e.g., [1, 2]). Then the meaning of measured surface temperatures with regard to measurement conditions is discussed for a number of examples, that is, the problem of how the surface temperature can be used to extract meaningful information concerning objects under study.

Infrared Thermal Imaging, Second Edition. M. Vollmer and K.-P. Möllmann.
© 2018 WILEY-VCH Verlag GmbH & Co. KGaA. Published 2018 by WILEY-VCH Verlag GmbH & Co. KGaA.

4.2
The Basic Heat Transfer Modes: Conduction, Convection, and Radiation

Temperature differences in any situation result from energy flows into a system (heating by electrical power, contact to thermal bath, absorption of radiation, for example, microwaves or solar radiation) and energy flows from a system to the surroundings (Figure 4.1). The former leads to heating, whereas the latter results in the cooling of an object. In thermodynamics, any kind of energy flow (also called *heat transfer*) that is due to a temperature difference between a system and its surroundings is usually called *heat flow*. In physics, one usually distinguishes three kinds of heat flow: conduction, convection, and radiation. As a matter of fact, the underlying physical processes for conduction and convection are very similar, so the distinction is rather artificial.

4.2.1
Conduction

Conduction refers to the heat flow in a solid or fluid (liquid or gas) that is at rest (Figure 4.2). Conduction of heat within an object, for example, a wall of infinitesimally small thickness $\mathrm{d}s$, is usually assumed to be proportional to the temperature difference $\mathrm{d}T$ on the two sides of the object as well as the surface area A of the object, and inversely proportional to the thickness $\mathrm{d}s$ of the sample, that is,

$$\dot{Q}_{\mathrm{cond}} = \lambda \cdot A \cdot \frac{\mathrm{d}T}{\mathrm{d}s} \tag{4.1a}$$

For the specific example of a macroscopic one-dimensional (1D) wall of thickness $s = s_1 - s_2$, steady-state conduction leads to a temperature that varies linearly with distance. In this case,

$$\dot{Q}_{\mathrm{cond}} = \lambda \cdot A \cdot \frac{\mathrm{d}T}{\mathrm{d}s} \approx \frac{\lambda}{s} \cdot A \cdot (T_1 - T_2) = \alpha_{\mathrm{cond}} \cdot A \cdot (T_1 - T_2) \tag{4.1b}$$

In what follows, we mostly refer to the simplified heat conduction equation $\dot{Q}_{\mathrm{cond}} = \alpha_{\mathrm{cond}} \cdot A \cdot (T_1 - T_2)$. The heat transfer coefficient is defined as $\alpha_{\mathrm{cond}} = \lambda/s$,

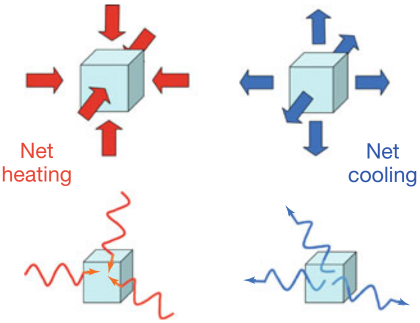

Figure 4.1 Energy flows (red) into a system, here a cube, lead to temperature rise. Energy flows (blue) from a system (cube) decrease the temperature. These energy flows are due to conduction, convection, and radiation acting via the surface of the system. For small absorption constants of the system material, radiation may also act within the volume.

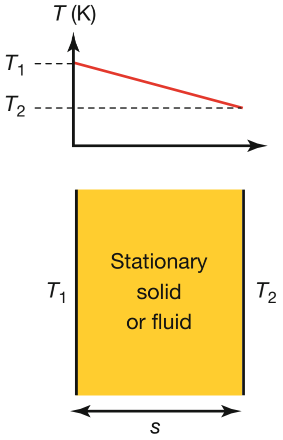

Figure 4.2 Conduction of heat takes place within a solid or stationary fluid.

where λ is the thermal conductivity of the wall material given in $\mathrm{W\,(m\,K)^{-1}}$ and s is the wall thickness given in meters. (Note that λ uses the same Greek symbol that is usually reserved for wavelength. Rather than introducing additional subindices that would unnecessarily complicate the notation, in particular when later a distinction between thermal conductivities for different materials – indicated by subindices – will be made, we will stick with the same symbol since the context of the corresponding equations will usually make it clear which quantity – wavelength or thermal conductivity – is meant.) The heat transfer coefficient α_{cond} describes heat transfer in watts per unit area and Kelvin, that is, $\mathrm{W\,(m^2\,K)^{-1}}$. Hence, the heat flux through the wall $\dot{Q}_{\mathrm{cond}}$ in watts gives the energy flow per second through the wall of surface area A if the temperature difference between the inner and outer surfaces is given. Table 4.1 gives typical values of thermal conductivities of materials as well as their corresponding heat transfer coefficients for $s = 10\,\mathrm{cm}$ "wall thickness."

Table 4.1 Some approximate values for thermal conductivity of materials at $T = 20\,°\mathrm{C}$ and the corresponding heat transfer coefficients for $s = 10\,\mathrm{cm}$. Values may vary depending on purity/composition.

Material	λ **(W (m K)$^{-1}$)**	$\alpha_{\mathrm{cond}} = \frac{\lambda}{s}$ **(W (m^2 K)$^{-1}$)**	**Material**	λ **(W (m K)$^{-1}$)**	$\alpha_{\mathrm{cond}} = \frac{\lambda}{s}$ **(W (m^2 K)$^{-1}$)**	**Material**	λ **(W (m K)$^{-1}$)**	$\alpha_{\mathrm{cond}} = \frac{\lambda}{s}$ **(W (m^2 K)$^{-1}$)**
Aluminum (99%)	220	2200	Concrete stones	0.5–2 0.5–1.2	5–20 5–12	Water	0.6	6
Copper	390	3900	Dry wood	0.1–0.2	1–2	Oils	0.14–0.18	1.4–1.8
Silver	410	4100	Foams, Styrofoam	0.02–0.05	0.2–0.5	Air	0.026	0.26
Steel	15–44	150–440	Glass	0.8–1.4	8–14	CO_2	0.016	0.16

Values of the heat transfer coefficient of conduction depend on the geometry and dimensions of an object. The description of geometrical effects can become quite complex mathematically, and they may, for example, be accounted for by shape factors [1]. Here we stick with one-dimensional (1D) problems and give a numerical example for change with dimensions. We consider walls with thickness $s = 10$, 20, or 30 cm made of stones with $\lambda = 1\,\mathrm{W\,(m\,K)^{-1}}$ and find $\alpha_{\mathrm{cond,10\,cm}} = 10\,\mathrm{W\,(m^2\,K)^{-1}}$, $\alpha_{\mathrm{cond,20\,cm}} = 5\,\mathrm{W\,(m^2\,K)^{-1}}$, and $\alpha_{\mathrm{cond,30\,cm}} = 3.3\,\mathrm{W\,(m^2\,K)^{-1}}$.

The microscopic processes responsible for conduction of heat are most easily explained for objects that are in contact with gases. In a gas, a large number of atoms/molecules move with different velocities and in different directions. The temperature of a gas determines the average kinetic energy and – in relation to it – the average velocity of the gas molecules; these averages are mean values of the corresponding energy and velocity distributions. Owing to the high average velocities of a few hundred meters per second at room temperature, each second a large number of collisions take place between gas molecules, which permanently exchange energy and momentum. Individual molecules may change their energy and velocity; overall, the average values, however, stay the same if the gas is characterized by a well-defined temperature.

Now consider a gas that is in thermal contact with a hot object of given high temperature and, for example, room temperature walls. Owing to collisions with the hot object, the gas will have high average kinetic energies and high average velocities in its vicinity. At a certain distance, the same gas may also be in contact with a room temperature wall. There the neighboring gas molecules have lower average kinetic energies and lower average velocities. In the space between the wall and the hot object, the gas molecules will undergo many collisions. These collisions will lead to energy transfer from high kinetic energies near the hot object to low kinetic energies near the wall. Obviously, conduction of heat just describes this energy transfer via molecular or atomic collisions within the gas. For liquids the situation is quite similar, the main difference being that molecular distances are much shorter. In solids, there are no free-moving atoms or molecules; however, the atoms in a crystal lattice can vibrate. In the language of solid-state physics, the corresponding vibrational quanta are called *phonons*. For solids that are in thermal equilibrium, there is a well-defined phonon distribution that gives rise to the corresponding average energy. If the solid is placed between two objects of different temperatures, the phonon distributions and, hence, the corresponding average energies will differ. Like collisions of gas molecules, phonon distributions change as a function of position between the two different temperatures. In conductors, in addition, free electrons contribute to heat conduction, which may even dominate over the contribution by phonons. In principle, the corresponding energy transfer is similar to that of gas molecules described earlier.

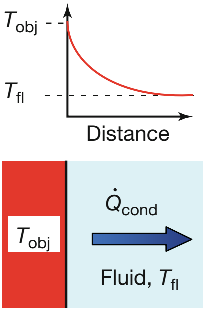

Figure 4.3 Convection of heat occurs between a surface and a moving fluid.

4.2.2
Convection

Convection refers to the heat flow between a solid and a fluid in motion (Figure 4.3).

The energy flow $\dot{Q}_{conv}$ per second from the surface of an object with temperature T_1 into a fluid of temperature T_2 owing to convection is usually assumed to follow a law similar to that of conduction, that is, it is proportional to the area and the temperature difference:

$$\dot{Q}_{conv} = \alpha_{conv} \cdot A \cdot (T_1 - T_2) \tag{4.2}$$

The heat transfer coefficient for convection depends on the nature of the motion of the fluid. In free convection, the current of the fluid is due to temperature-induced density differences in the fluid; in forced convection, the current of the fluid is due to external forces/pressure. Typical values for free convective heat transfer coefficients of gases above solids are cited as ranging between 2 and 25 W $(m^2\ K)^{-1}$, the exact value depending on flow conditions, wind speed, and moisture on the surface; for liquids they can be in a range of 50 to 1000 W $(m^2\ K)^{-1}$.

Compared to free convection, values for forced convection can be higher by an order of magnitude. A typical thermography application where forced convection plays a role is an outdoor building inspection when the wind speed is finite, but α_{conv} depends on wind speed [3]. Figure 4.4 shows as an example the range of values for convective heat transfer coefficients for outside walls of buildings reported in the literature.

A word of caution: in many heat transfer estimates, the convective heat transfer coefficients already include the radiative heat losses of the corresponding surfaces. The reason for this and the corresponding limitations are discussed in Section 4.5.

To understand the physical processes responsible for heat convection, one needs a microscopic model of the system. Owing to the movement of fluid across the surface, a boundary layer of a certain thickness is established. As a consequence, there is a velocity distribution of the fluid due to the molecular forces between fluid molecules and, first, surface molecules with zero velocity at the surface and, second, the bulk fluid velocity at distances greater than the thickness of the boundary layer. Convective heat transfer then comprises two different mech-

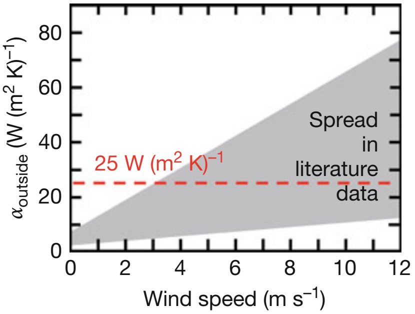

Figure 4.4 A large range of convective heat transfer coefficients for outside walls of buildings are reported as a function of wind speed. For many estimates of total heat transfer through walls (Section 4.3.3), a value of 25 W (m^2 K)$^{-1}$ is used.

anisms. First, it is due to the conduction of heat between the object surface and the fluid layer very close to the surface, that is, it is due to molecular motion and collision processes. The second convective contribution is due to the bulk motion of the fluid. The bulk motion of the fluid close to the boundary layer sweeps away the heat that was transferred via conduction from the surface. As a consequence, a detailed microscopic modeling is rather tedious and involves many phenomena of fluid dynamics.

4.2.3
Radiation

The emission of thermal radiation was already treated in Chapter 1. In any realistic situation in IR imaging, an object of temperature T_{obj} is surrounded by other objects of background temperatures T_{surr}. For simplicity, we assume a warm object that is completely surrounded by an enclosure of constant lower temperature (Figure 4.5). Whenever objects with different temperatures are present, one needs to compute the corresponding view factors (Sections 1.3.1.5 and 7.4.4) to find the net radiation transfer.

The object surface of T_{obj} emits radiation according to the laws of radiation (Section 1.3.2). The total emitted power is given by the Stefan–Boltzmann law (Eq. (1.19)) corrected for the emissivity of the object. In what follows, we assume gray objects. In addition, radiation from the surroundings is incident on the object. This finally leads to a net energy transfer from the warmer object with surface

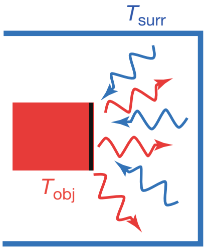

Figure 4.5 Whenever an object is placed in an environment of different temperature, there will be a net energy transfer via thermal radiation owing to the emission and absorption of radiation by the object.

area A to the colder surroundings,

$$\dot{Q}_{\mathrm{rad}} = \varepsilon \cdot \sigma \cdot A \cdot \left(T_{\mathrm{obj}}^4 - T_{\mathrm{surr}}^4 \right) \tag{4.3}$$

where $\sigma = 5.67 \cdot 10^{-8}\,\mathrm{W\,(m^2\,K^4)^{-1}}$.

This energy transfer equation differs from those for conduction and convection, which were of the form $\dot{Q} = \alpha \cdot A \cdot (T_1 - T_2)$, owing to the nonlinear dependence on temperature. Since any quantitative analysis concerning heat transfer is much easier for linear temperature differences, it is customary to approximate the radiative contribution also with a linear equation. This makes sense if temperature differences are small, that is, $(T_{\mathrm{obj}} - T_{\mathrm{surr}}) \ll (T_{\mathrm{obj}}, T_{\mathrm{surr}},)$ since in this case

$$\begin{aligned} \left(T_{\mathrm{obj}}^4 - T_{\mathrm{surr}}^4 \right) &= \left[(T_{\mathrm{obj}} + T_{\mathrm{surr}}) \cdot \left(T_{\mathrm{obj}}^2 + T_{\mathrm{surr}}^2 \right) \right] \cdot (T_{\mathrm{obj}} - T_{\mathrm{surr}}) \\ &= k_{\mathrm{appr}}(T) \cdot (T_{\mathrm{obj}} - T_{\mathrm{surr}}) \end{aligned} \tag{4.4}$$

where $k_{\mathrm{appr}}(T) \approx 4T_{\mathrm{surr}}^3$. Using $\alpha_{\mathrm{R}} = \varepsilon \cdot \sigma \cdot k_{\mathrm{appr}}$, we can then rewrite Eq. (4.3) as

$$\dot{Q}_{\mathrm{rad}} = \alpha_{\mathrm{rad}} \cdot A \cdot (T_{\mathrm{obj}} - T_{\mathrm{surr}}) \tag{4.5}$$

which is of the same type as the heat transfer equations for conduction and convection. To give a numerical example, we estimate the radiative heat loss of 1 m^2 of a gray object ($\varepsilon = 0.9$) of 310 K in 300 K surroundings. According to Eq. (4.3), we find 57.93 W, and from the approximation given by Eq. (4.5) we find 55.11 W, that is, a 4.9% lower value. The deviation decreases for a smaller temperature difference and only amounts to 0.5% for 301 K vs. 300 K.

A more thorough discussion of the applicability of the approximation of Eqs. (4.4) and (4.5) is given later in Section 4.5.

4.2.4
Convection Including Latent Heats

Usually microscopic models for convective heat transfer treat the energy transfer as being due to the combined effects of the conduction of heat within the boundary layer between solid and fluid and effects as being due to fluid motion. In this case, internal thermal energy of the fluid is transferred to a solid or from the solid to the fluid.

However, in addition, there are many convection processes where additional *latent heats* are exchanged. Such latent heats are associated with phase changes between the liquid and vapor states of the fluid. The most important and often used fluid in technology and nature is water. The corresponding heats for phase changes are called the *heat of condensation* or the *heat of vaporization* (when vaporization occurs at the liquid–gas interface, it is termed *boiling*). They add up to the transferred heat and give rise to strongly increased coefficients for the convective heat transfer, which can reach values between 2500 and 100 000 W (m^2 K)$^{-1}$.

Microscopically, heat transfer due to evaporation and condensation can be understood as follows:

1. If a solid is covered with liquid droplets or a liquid film and it is surrounded by a gaseous fluid with low vapor pressure, the liquid droplets or the film can evaporate. To do so, the heat of vaporization is needed, which is extracted from the solid, thereby transferring energy from the solid to the gaseous fluid (evaporative cooling of the solid).
2. If heat is transferred from a solid to a liquid around it, and the surface temperature exceeds the saturation temperature, vapor bubbles start to grow on the surface. Finally, upon growing they can detach from the surface, thereby transporting the energy that was used for their generation from the solid to the liquid (cooling of the solid).
3. Condensation occurs when the temperature of a vapor is reduced below its saturation temperature. In industrial applications (and in nature around us), this usually results from the contact of the vapor with a cold surface. Upon condensation, the latent heat of condensation is released, that is, the condensing vapor transfers energy from the vapor to the solid (heating of solid). Depending on whether droplets or a thin film is produced upon condensation, different microscopic theories are used for estimating the associated heat transfer coefficients.

For water, the latent heats are temperature dependent (Table 4.2).

Owing to the large value of latent heats for water, the associated heat transfer coefficients can have dramatic effects on temperature distributions of objects. For example, in outdoor building thermography, the surface temperature distributions of walls or enclosures of objects strongly depend on rain and wind. The phenomenon is also well known from personal experiences in summer. When getting out of a swimming pool, lake, or the ocean, one is usually still covered with many droplets of water. Sometimes one may start to shiver during a mild breeze while experiencing evaporative cooling.

A numerical example will illustrate the cooling potential of water. One gram, that is, 1 cm^3, of vaporizing water will transfer an amount of about 2450 J at a temperature of 20 °C. If this 1 cm^3 of water were spread as a thin film on an aluminum metal cube with side length 60 mm (as in the example in Section 4.4.4), the film would have a thickness of about 46 μm. This would strongly increase the heat transfer coefficient, in particular if a fan were used for artificial wind speed.

Table 4.2 Heat of vaporization for saturated water at various temperatures.

Temperature in K (°C/°F)	Heat of vaporization/condensation in kJ kg^{-1}
273.15 (0/32)	2501
283.15 (10/50)	2477
293.15 (20/68)	2453
303.15 (30/86)	2430
373.15 (100/212)	2257

Total vaporization of this water film would lead to a temperature drop of the cube from 20 °C by about 4.7 K to 15.3 °C, provided the system was thermally isolated from its surroundings. Experimental investigations of such effects are discussed in Chapter 7. We finally note that additional heat sources can be present, for example, reaction enthalpies while studying chemical reactions (Section 9.3). Whenever such special problems are investigated, the corresponding energies must be taken into account.

4.3
Selected Examples of Heat Transfer Problems

4.3.1
Overview

Obviously, any object that is studied by thermography can be characterized by heat transfer due to both conduction within a wall/an enclosure as well as convection at the inner (if applicable) and outer surfaces of the object. Typical examples are hot liquids transported within tubes, electrical wires heated from within due to current, or buildings heated from inside. In thermography, one measures the surface temperatures of objects with the goal of learning something about the object. The two potential extreme situations are pure qualitative studies and accurate quantitative analysis. In the first case, the relevant information is contained, for example, in the inhomogeneities of the thermal radiation, indicating thermal leaks in a qualitative manner. In the second case, one is interested in the absolute temperature values for quantitative analysis, for example, of the thermal insulation properties of a wall or a window. We treat the general problem of heat transfer for the example of building walls and will discuss examples of both cases.

Figure 4.6 depicts five standard situations that resemble typical measurement situations. The conditions for these situations are summarized in Table 4.3.

The least interesting situation for IR imaging is thermal equilibrium (a), that is, any initial temperature differences have vanished since no heat sources (e.g., heater) or sinks (e.g., cooling system) are available. If every parameter of the camera is properly adjusted, the IR image will just be a homogeneous area with no thermal signatures, even independent of emissivity contrast.

In cases (b) and (c), time-independent heat sources are present. In the case of building thermography, the heat source can be the heating system inside leading to a constant inside temperature and the heat sink is the outside of the house at a much lower constant temperature. For industrial applications, one may think of pipes transporting hot liquids. In this case, the hot liquid is filled in at constant flux, thereby providing the time-independent heat source. Again, the heat sink is the outside of the pipe at much lower but constant temperature. Since we assume time-independent behavior, that is, that the inside and outside temperatures do not change with time, a stationary temperature distribution within the wall is reached. After initializing the corresponding measurement setup or process, it

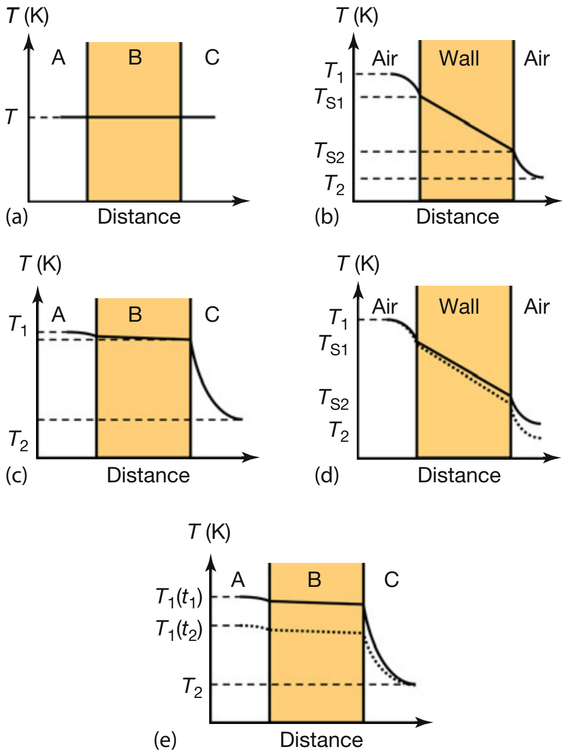

Figure 4.6 (a–e) Schemes for standard situations encountered in thermography. They can be distinguished according to differences in temperatures T_1 and T_2 of two fluids A and C (e.g., air on both sides of a wall), material properties of a solid material (the wall B), and time dependence of heat sources or sinks (for more details see text and Table 4.3).

may take quite a while to reach this dynamic thermal equilibrium. Depending on the material properties of the wall/tube, the temperature may vary with distance, as shown for the wall (b), or stay more or less constant within the tube (c). The relevant parameter is the Biot number, which is introduced in Section 4.3.2. Obviously, the case of large Biot numbers is usually encountered for buildings, where the temperature within walls may vary widely. In contrast, the measured surface temperature is close to the inner temperature for small Biot numbers. The stationary situations (b) and (c) are the easiest for quantitative analysis.

Unfortunately, the standard application in IR imaging deals with time-dependent heat sources or sinks. For building inspections, this is due to a number of factors like the night setback of the heating cycle, potential solar load effects of the outside wall during the daytime, potential night sky radiant cooling, and changes in the ambient outside temperature during the day and at night (e.g., cloudy vs. cloudless sky). In industrial applications with pipe systems, there can be transient changes both of the source (e.g., variations of initial temperature of the fluid) or of the sink (change in outside temperature). As a consequence, the spatial tem-

Table 4.3 Parameters/conditions, referring to the standard situations in thermography shown in Figure 4.6.

(a)	Thermal equilibrium	No heat sources or sinks, after a long time	IR images homogeneous, no thermal contrast
(b)	Temperature difference due to time-independent heat sources/sinks	Large Biot number (Section 4.3.2): variations of T within wall/solid, T profiles independent of time	For example, typical outside building inspections, measure $T_{S_2} < T_1$ (inside), useful information in spatial variations of T_{S_2}
(c)		Small Biot number: nearly no variations of T within wall/solid, T profiles independent of time	For example, pipe system with hot fluid measure $T_{S_2} \approx T_1$ (inside) useful information also in spatial variations of T_{S_2}
(d)	Temperature difference due to time-dependent heat sources/sinks	Large Biot number: variations of T within wall/solid	For example, typical outside building inspections, T_2 drops, measure $T_{S_2} = T_{S_2}(t)$
(e)		Small Biot number: nearly no variations of T within wall/solid	For example, pipe system with hot fluid, T_1 drops, measure $T_{S_2} = T_{S_2}(t)$

perature profiles additionally depend on time. This is illustrated for the case of large Biot numbers and lowering of the outside temperature in (d) and for small Biot numbers and lowering of the inside temperature in (e).

A number of questions arise in relation to this transient behavior. How much useful information can still be guessed? Is quantitative analysis still possible or only a qualitative one? And – if transient effects are to be avoided – how long are the corresponding time constants for these changes? As shown by many examples, the answers to the first two questions are easy: one can still extract a lot of useful information, in particular from the spatial variations across the investigated object surface. In most cases, comparison to earlier studies on the same object or similar objects also allows some semiquantitative analysis (e.g., criterion for potential failure of component). In the few cases where a quantitative analysis of absolute temperature is needed, one must, however, study the thermal time constants of the objects (see below).

In what follows we present a few selected examples in detail.

4.3.2
Conduction within Solids: The Biot Number

Consider a solid between two fluids of different but constant temperatures, T_1 and T_2, as shown in Figure 4.6b,c. Assuming steady-state conditions, the heat flow due to conduction, convection, and radiation will lead to a spatial temperature distribution within the object. It is possible to get some idea of the temperature within the solid using the so-called Biot number *Bi*:

$$Bi = \frac{\alpha_{\text{conv}}}{\alpha_{\text{cond}}} = \alpha_{\text{conv}} \cdot \frac{s}{\lambda} \tag{4.6}$$

where α is the corresponding heat transfer coefficient with α_{cond} being expressed by the dimension s of the object and the thermal conductivity λ of the object material.

In this book we only discuss the Biot number and, subsequently, the Fourier number, although many other dimensionless quantities are defined and used to describe the properties of heat and mass transfer depending on flow conditions [1, 2]. Such quantities as the Nusselt number, the Reynolds number, and the Prandtl number are particularly important for forced convection, where the heat transfer coefficient depends not only on geometry but also on whether the flow is laminar or turbulent.

The Biot number is a dimensionless quantity, usually describing the ratio of two adjacent heat transfer rates. In the present case, it describes the ratio of the outer heat flow from the surface to the surroundings, characterized by the convective heat transfer coefficient α_{conv} at the surface and the inner heat flow within the object characterized by the conductive heat transfer coefficient $\alpha_{\text{cond}} = \lambda/s$. For $Bi \gg 1$, the outer heat flow is much larger than the inner heat flow. Obviously, this results in a strong spatial variation of internal temperature within the object. This is typical for walls of buildings (Figure 4.6b). If, however, $Bi \ll 1$, the internal heat flow is much larger than the heat loss from the surface. Therefore, temperature will be near equilibrium within the object, that is, the temperature distribution will be homogeneous within the solid, and a large temperature drop will occur at the boundary of the object with the surrounding fluid [1]. This is, for example, typical for metal tubes transporting hot liquids (Figure 4.6c).

As an example of time-dependent effects, we now discuss the situation of the cooling of objects. Consider, for example, an initially hot object of temperature T_{obj} that is in contact with surroundings of lower temperature. There will be no further energy input into the object. For simplicity we consider a 1D object, such as a plate of thickness $2s$, that extends to infinity in the other dimensions (results are also approximately valid for finite plates if their thickness is small compared to the other dimensions).

Figure 4.7 gives a schematic representation of the temperature distributions within such initially hot plates as a function of time for different Biot numbers. For clarity, the temperature drops outside of the boundaries (similar to those in Figure 4.6) are omitted here. For Biot numbers less than 0.1, the temperature differences between the exact solution and that assuming equilibrium within the object only lead to a maximum of 2% deviation [2]; hence, whenever $Bi < 0.1$, one may assume a constant temperature throughout the solid [1].

For larger Biot numbers, the conductive heat transfer within the solid proceeds more slowly than the convective heat transfer from the surface boundary. Therefore, any heat transferred to the surface from within is immediately removed, that

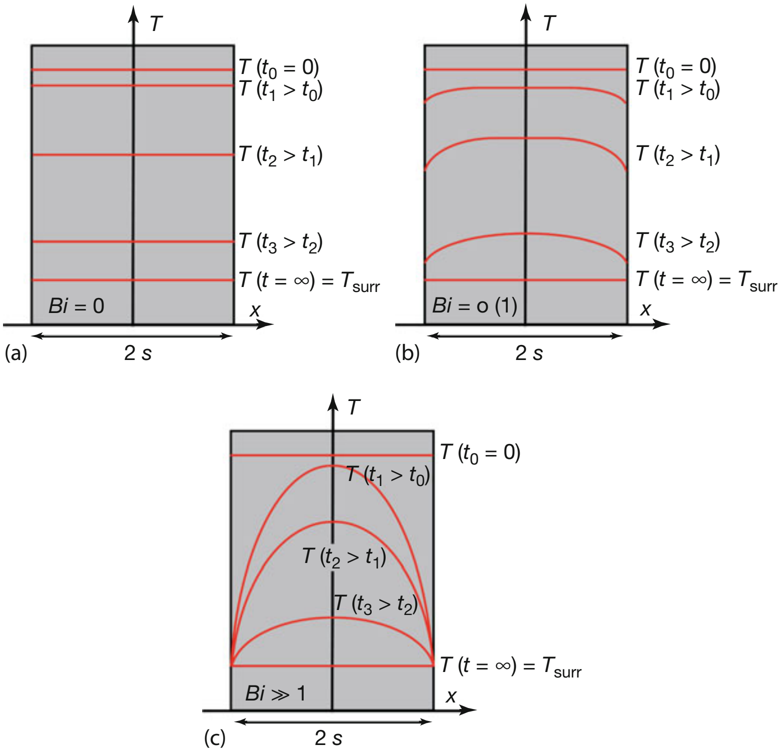

Figure 4.7 Schematic temperature distributions within solid objects upon cooling as a function of increasing Biot number. (a): *Bi* = 0; (b): *Bi* = *o*(1), that is, on the order of unity; (c): *Bi* ≫ 1. There is an additional temperature drop at the boundary to the surrounding fluid (omitted here).

is, the outside parts of the solid cool faster than the inside, and a spatial temperature profile results. In this case, the surface temperature does not seem to be a useful measure for the inside temperature or even an average temperature of the solid. For very large Biot numbers, the convective heat transfer dominates. The surface temperature drops very rapidly and then stays low, whereas the internal temperature drops only very slowly.

Figure 4.7 also gives an indication as to how cooling curves of initially hot objects change with time. For large Biot numbers the internal heat flow within the object is smaller than the heat flow due to convection from the boundary. Therefore, cooling takes longer for large Biot numbers.

Whenever we deal with situations like those in Figure 4.6, we should evaluate the Biot numbers. A typical wall may be 24 cm thick with stones of $\lambda = 0.5\,\mathrm{W\,(m\,K)^{-1}}$. In this case, the conductive heat transfer $\lambda/s \approx 2\,\mathrm{W\,(m^2\,K)^{-1}}$ is on the order of or less than the typical value for convective heat transfer of outside walls of 2 to 25 $\mathrm{W\,(m^2\,K)^{-1}}$. Hence, the corresponding Biot number, $Bi = 1 - 12.5$, is equal to or greater than unity, and we expect a large temperature drop within

Table 4.4 Some material properties of objects and the corresponding Biot numbers. In massive building materials like brick, the assumption $Bi \ll 1$ does not hold.

Object	**Material(s)**	α_{conv} $(\text{W}\,(\text{m}^2\,\text{K})^{-1})$	s (m)	λ $(\text{W}\,(\text{m}\,\text{K})^{-1})$	$\alpha_{\text{cond}} = \lambda/s$ $(\text{W}\,(\text{m}^2\,\text{K})^{-1})$	**Biot number**
Metal cubes	Aluminum, paint	2–25	$20\text{–}60 \cdot 10^{-3}$	220	11 000–3 670	< 0.01
Soft drink can (0.5 L)	Aluminum inside water	2	$\leq 1 \cdot 10^{-3}$ $3.3 \cdot 10^{-2}$ radius	220 0.6	$> 220\,000$ 18.2	$\ll 1$ ≈ 0.1
Bottle (0.5 L) in fridge	Glass inside water	2	$\approx 3 \cdot 10^{-3}$ $3.3 \cdot 10^{-2}$ radius	≈ 1 0.6	333 18.2	≈ 0.006 ≈ 0.1
Brick (for comparison)	Stone	2–25	$12 \cdot 10^{-2}$	≈ 0.6	5	0.4–1
Pipe	Stainless steel	2–25	$2 \cdot 10^{-2}$	15	750	0.033
Concrete (for comparison)	Composite with stones	2–25	$20 \cdot 10^{-2}$	≈ 1	5	0.4–1

the building wall. In contrast, a stainless steel metal tube 2 cm thick and with $\lambda = 15\,\text{W}\,(\text{m}\,\text{K})^{-1}$ gives $(\lambda/s) \approx 750\,\text{W}\,(\text{m}^2\,\text{K})^{-1}$. In this case, the Biot number is given by $Bi \ll 1$, that is, there is no temperature gradient within the tube wall.

Table 4.4 gives a summary of Biot numbers for some objects used in experiments plus several others for comparison. For small metallic objects or thin hollow objects filled with water, the condition $Bi < 0.1$ is usually fulfilled. However, in realistic building materials like brick or concrete of larger dimensions, this condition is not valid. The consequences for thermal time constants of objects are also discussed in what follows.

4.3.3
Steady-State Heat Transfer through One-Dimensional Walls and U-Value

Figure 4.8 depicts a 1D wall of an object. The fluid at the left side of the wall (e.g., the inside air) is at a high temperature T_1; the one at the right (e.g., the outside air) is at a lower temperature T_2. The heat transfer from left to right is described by heat transfer equations. As discussed previously, typical Biot numbers are larger than unity, and one expects appreciable temperature drops within walls. A typical qualitative result is shown in the figure.

Imagine this is a building. There is a temperature drop from the inside air temperature T_1 to the inner wall surface temperature T_{S_1}. Within the wall, the temperature drops to that of the outer wall surface, T_{S_2}, which is still above the outside air temperature T_2. Within a 1D wall, extended to infinity, there is a linear temperature drop. If the wall is composed of two or more different materials, there will be intermediate boundary temperatures T_{B}. In thermography one usually mea-

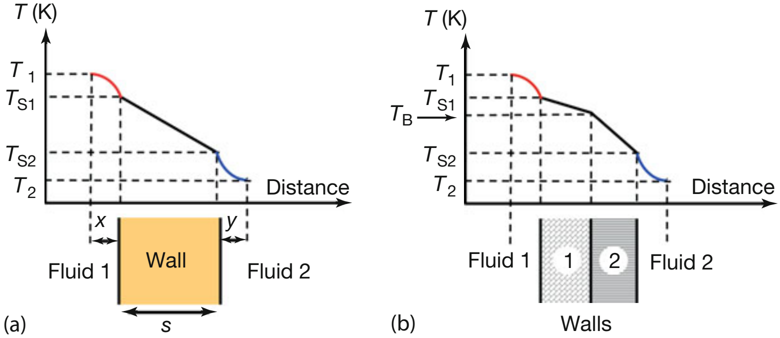

Figure 4.8 Schematic dependence of temperature changes owing to heat transfer through a 1D wall embedded in fluids of different temperatures (a) or a double-layer wall (b).

sures the surface temperatures, T_{S_1} or T_{S_2}, and not the fluid (air) temperatures, T_1 or T_2!

The x- and y-dimensions of the temperature boundary layers, that is, the distances δ_{th} from the walls where the corresponding fluid temperatures are reached, vary with the flow conditions [1, 2]. An order-of-magnitude estimate for the thermal boundary layer thickness δ_{th} is

$$\delta_{\text{th}} \approx \frac{\lambda}{\alpha} \tag{4.7}$$

where λ is the thermal conductivity of the fluid and α is the heat transfer coefficient for convection at the boundary [2]. Using $\alpha_{\text{inside}} = 8\,\text{W}\,(\text{m}^2\,\text{K})^{-1}$ and $\alpha_{\text{outside}} = 2\text{–}25\,\text{W}\,(\text{m}^2\,\text{K})^{-1}$ for air as well as $\lambda_{\text{air}} \approx 0.026\,\text{W}\,(\text{m}\,\text{K})^{-1}$, we find $\delta_{\text{inside}} \approx 3\,\text{mm}$ and $\delta_{\text{outside}} \approx 13\,\text{mm}$ to 1 mm, that is, the thicknesses of the thermal boundary layers for building walls are usually much smaller than other characteristic dimensions.

A note on the use of α_{outside} values: in many cases, α_{outside} ranges between 2 and $25\,\text{W}\,(\text{m}^2\,\text{K})^{-1}$. For building inspections one may think of the lower limit $2\,\text{W}\,(\text{m}^2\,\text{K})^{-1}$ as a no-wind situation. In most calculations concerning heat losses of building envelopes, the upper limit of $\alpha_{\text{outside}} = 25\,\text{W}\,(\text{m}^2\,\text{K})^{-1}$ is chosen (usually assumed for wind speeds below $5\,\text{m}\,\text{s}^{-1}$) to obtain the so-called worst-case scenario with the largest possible heat transfer rates. α_{outside} can, however, still be larger for even larger wind speeds (Figure 4.4). The upper limit value may also depend on moisture on the surface, leading to latent heat effects (Section 4.2.4).

The analysis of total heat transfer through the wall can be simplified using an analogy. The mathematical nature of Eqs. (4.1a), (4.1b), and (4.2) is very similar to that of Ohm's law for electrical circuits, suggesting an analogy between heat transfer and charge transfer (note that both charge and heat are usually described by the same symbol, Q; we stick to this notation and introduce no subindices since it is always clear from the context which quantity is meant). In an electrical circuit, the driving force for charge transfer $\text{d}Q/\text{d}t$ (i.e., current I) is the potential difference, that is, the voltage U, whereas in a thermal circuit the driving force for

Table 4.5 Equivalent quantities in electrical and thermal circuits. Note that Q has different meanings for the two cases.

Quantity	**Electrical circuit**	**Thermal circuit**
Driving force	Potential difference U (voltage) in V	Temperature difference ΔT in K
Resistance	Electric resistance R in Ω	Thermal resistance R_{th} in K/W
Transfer quantity	Charge transfer $I = \mathrm{d}Q/\mathrm{d}t$ in $\mathrm{C\,s^{-1}} = \mathrm{A}$	Heat transfer $\dot{Q}$ in $\mathrm{J\,s^{-1}} = \mathrm{W}$

heat transfer is the temperature difference ΔT:

$$I = \dot{Q} = \frac{U}{R} \quad \text{for charge} \quad \text{and} \quad \dot{Q} = \alpha \cdot A \cdot (T_1 - T_2) \quad \text{for heat} \tag{4.8}$$

This analogy suggests defining thermal resistances, $R_{\mathrm{th}} = 1/(\alpha \cdot A)$. Table 4.5 presents a comparison of the corresponding quantities. For conduction, the thermal resistance is $R_{\mathrm{th,cond}} = s/(\lambda \cdot A)$, and for convection it is defined as $R_{\mathrm{th,conv}} = 1/(\alpha_{\mathrm{conv}} \cdot A)$.

Using this analogy and the concept of thermal resistance, it is now easy to understand the limiting factors of heat transfer. A building wall constitutes a series connection of the thermal resistances of convection and conduction similar to an electrical series connection (Figure 4.9).

For the building wall of Figure 4.8, the thermal resistance R_{inside} of the inner convection leads to the temperature drop from the inside air temperature T_1 to the inner wall surface temperature T_{S_1}. Within the 1D wall, there is a linear temperature drop from T_{S_1} to T_{S_2} because of the thermal resistance R_{wall}, and the thermal resistance of the outer convection R_{outside} leads to a drop from the outer wall surface temperature T_{S_2} to the outside air temperature T_2.

Obviously, the total heat transfer for the wall problem can be written

$$\dot{Q} = \frac{\Delta T_i}{R_i} = \frac{T_1 - T_2}{R_{\mathrm{total}}} \tag{4.9}$$

where ΔT_i denotes the temperature drops at resistances R_i. The total thermal resistance is the sum of the individual resistances

$$R_{\mathrm{total}} = \frac{1}{\alpha_{\mathrm{conv,ins}} \cdot A} + \frac{1}{\alpha_{\mathrm{cond}} \cdot A} + \frac{1}{\alpha_{\mathrm{conv,out}} \cdot A} \tag{4.10}$$

As a consequence, the largest individual resistance dominates the total heat transfer.

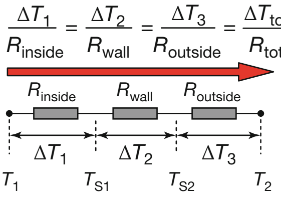
$\dot{Q} = \frac{\Delta T_1}{R_{\mathrm{inside}}} = \frac{\Delta T_2}{R_{\mathrm{wall}}} = \frac{\Delta T_3}{R_{\mathrm{outside}}} = \frac{\Delta T_{\mathrm{total}}}{R_{\mathrm{total}}}$
R_{inside}
R_{wall}
R_{outside}
ΔT_1
ΔT_2
ΔT_3
T_1
T_{S1}
T_{S2}
T_2

Figure 4.9 Equivalent electrical circuit for heat transfer through wall with convection on both sides.

For composite walls, it is often convenient to introduce an overall heat transfer coefficient U of a wall [1] (in Europe, it was previously also denoted by a k-value; in the United States, the reciprocal $1/U$ is also called the *R-value* [4]) by Eq. (4.11):

$$\dot{Q} = U \cdot A \cdot \Delta T \tag{4.11}$$

U is given in W (m^2 K)$^{-1}$ and describes the amount of energy per second, which is transmitted through a surface of 1 m^2 through a wall if the temperatures on both sides of the wall differ by 1 K. Adapting the actual surface areas and temperature differences then gives the total heat transfer according to Eq. (4.11) (for unit change to BTU/(h ft^2 F), see [4]). Comparing Eq. (4.11) with (4.9) gives

$$U = \frac{1}{R_{\text{total}} \cdot A} = \frac{1}{\dfrac{1}{\alpha_{\text{conv,ins}}} + \sum \frac{s_i}{\lambda_i} + \dfrac{1}{\alpha_{\text{conv,out}}}} \tag{4.12}$$

where the conduction term involves the sum over all parts of a multilayer wall. Equations 4.9, 4.11, and 4.12 allow us to compute the total heat transfer rates if thermal resistances, that is, heat transfer coefficients, are known or, conversely, if the temperatures are measured. This shall be illustrated with a specific example of a composite wall (Figure 4.10).

A brick wall that is 25 cm thick ($\lambda_{\text{br}} = 0.5$ W (m K)$^{-1}$) has on the inside a 12 mm thick layer of plaster ($\lambda_{\text{pl}} = 0.7$ W (m K)$^{-1}$) and on the outside a 60 mm thick layer of Styrofoam ($\lambda_{\text{st}} = 0.04$ W (m K)$^{-1}$). The Styrofoam is additionally covered with a thin layer of special plaster on the outside, whose thermal resistance is neglected for simplicity. The heat transfer coefficients for convection are assumed to be $\alpha_{\text{inside}} = 8$ W (m^2 K)$^{-1}$ and $\alpha_{\text{outside}} = 25$ W (m^2 K)$^{-1}$. From that the U-value is found to be $U = 0.46$ W (m^2 K)$^{-1}$. It would decrease to about 0.31 W (m^2 K)$^{-1}$ if the Styrofoam layer increased in thickness from 60 to 100 mm.

Assuming an inside temperature of $T_1 = 20\,°\text{C}$ and an outside temperature of $T_2 = -12\,°\text{C}$, the total heat flow per area $\dot{Q}/A = U \cdot \Delta T$ (Eq. (4.11)) is then about 14.7 W m^{-2} for 60 mm Styrofoam and 10.1 W m^{-2} for 100 mm Styrofoam. We only calculate internal temperatures for the 60 mm Styrofoam example. The inte-

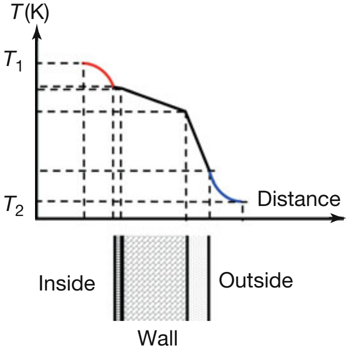

Figure 4.10 Example of composite stone wall of a building for winter conditions (for details see text).

rior temperatures follow from inverting Eq. (4.9) to give

$$\Delta T_i = \frac{\dot{Q}}{A} \cdot \frac{1}{\alpha_i} \tag{4.13}$$

with coefficients α_i from Eqs. (4.1a), (4.1b), and (4.2). Starting from the inside, we obtain the following temperatures:

Air in room inside	$T_1 = 20\,°\mathrm{C}$
Inside wall	$T_{\mathrm{S}_1} = 18.2\,°\mathrm{C}$
Boundary plaster–brick	$T_{\mathrm{B}_1} = 17.9\,°\mathrm{C}$
Boundary brick–Styrofoam	$T_{\mathrm{B}_2} = 10.6\,°\mathrm{C}$
Outside wall	$T_{\mathrm{S}_2} = -11.4\,°\mathrm{C}$
Air outside	$T_2 = -12\,°\mathrm{C}$

that is, the freezing point temperature lies in the Styrofoam layer, as desired. The necessity of building insulation becomes evident if we consider a wall system where the Styrofoam layer is missing and the brick stone thickness is larger by 60 mm such that the total thickness of 31 cm is the same. In this case, $U = 1.25\,\mathrm{W\,(m^2\,K)^{-1}}$ and the total heat flow per area would increase to $39.9\,\mathrm{W\,m^{-2}}$, that is, about a factor of 2.7 larger than that with insulation. Besides much larger energy costs for heating, the freezing point lies within the bricks, which may cause structural problems if moisture enters the wall.

Regarding the emerging energy crisis and consequent legislative measures like tighter energy conservation regulations for buildings, a typical future application of thermography may be the verification of building insulation by measuring U-values of building envelopes (Chapter 7). Table 4.6 gives some typical values for U for various materials or constructions.

Table 4.6 Typical *U*-values for certain building materials.

Material	**Thickness (cm)**	***U* (W (m² K)⁻¹)**
Walls		
Concrete wall, no thermal insulation	25	≈ 3.3
Brick wall	25	≈ 1.5
Brick wall plus thermal insulation	25 + 6	≈ 0.46
Brick wall	31	≈ 1.25
Massive wooden walls	25	≈ 0.5
Wooden or plastic entrance doors of houses		3–4
Windows (Section 4.3.4):		
Single pane		≈ 6
Double pane		≈ 2–3
For passive houses		≤ 1

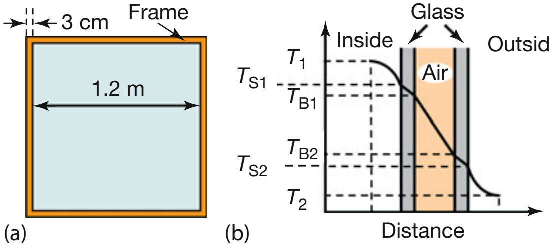

Figure 4.11 Front view (a) and cross-sectional view of glass part alone (b) of double-pane window.

4.3.4
Heat Transfer Through Windows

Windows are present in many thermography applications, in particular in building inspections, and they are usually eye catchers in IR images. Owing to their importance, we present typical heat transfer characteristics. Problems in correctly interpreting surface temperatures are discussed in Chapter 7.

Consider a window with a glass size of $1.2 \times 1.2\,\mathrm{m}^2$ and glass width of 4 mm and thermal conductivity $\lambda = 1\,\mathrm{W\,(m\,K)^{-1}}$. The glass is surrounded by either a metal frame or a wooden frame 3 cm wide and 5 cm thick ($\lambda = 220\,\mathrm{W\,(m\,K)^{-1}}$ and $\lambda = 0.15\,\mathrm{W\,(m\,K)^{-1}}$, respectively). The inside air temperature T_1 is 20 °C and the outside air temperature T_2 is −10 °C. The problem consists in calculating the U-value, the heat flux through the pane and frame, and the surface temperatures for a single-pane window and a double-pane window. In the latter case, the two panes will be separated by 10 mm of pure air with $\lambda = 0.026\,\mathrm{W\,(m\,K)^{-1}}$. The inner and outer heat transfer coefficients for convection will be assumed to be $\alpha_{\mathrm{inside}} = 8\,\mathrm{W\,(m^2\,K)^{-1}}$ and $\alpha_{\mathrm{outside}} = 25\,\mathrm{W\,(m^2\,K)^{-1}}$. Figure 4.11 depicts a front view of a window including the frame and a cross-sectional view of the glass part of the double-pane window.

We start the analysis with the glass alone and add the frame later. First, Eq. (4.12) is used to estimate U of the single-pane glass: $U_{\mathrm{single}} = 5.92\,\mathrm{W\,(m^2\,K)^{-1}}$. For the double-pane window (glass only), $U_{\mathrm{double}} = 1.79\,\mathrm{W\,(m^2\,K)^{-1}}$. From that the total heat transfer through the glass is found to be $\dot{Q}_{\mathrm{single}} = 255.6$ W and $\dot{Q}_{\mathrm{double}} = 77.5$ W. Using Eq. (4.13), the various glass surface temperatures are evaluated. For the single pane, one finds for the inside and outside glass surfaces $T_{\mathrm{S}_1} = -2.2\,°\mathrm{C}$ and $T_{\mathrm{S}_2} = -2.9\,°\mathrm{C}$. Obviously, a single-pane window is more or less isothermal. The very low inside glass surface temperature even allows for the generation of frost flowers. The double-pane window has the huge advantage of having an air-filled gap with low thermal conductivity. The surface temperatures for windows 1 (facing inside) and 2 (facing outside) are found to be as follows:

Air in room inside	$T_1 = 20\,°\mathrm{C}$
Inside surface glass	$T_{\mathrm{S}_1} = 13.3\,°\mathrm{C}$
First boundary: outside inner glass	$T_{\mathrm{B}_1} = 13.1\,°\mathrm{C}$
Second boundary: inside outer glass	$T_{\mathrm{B}_2} = -7.6\,°\mathrm{C}$
Outside surface glass	$T_{\mathrm{S}_2} = -7.8\,°\mathrm{C}$
Air outside	$T_2 = -10\,°\mathrm{C}$

Obviously, the window pane facing the inside now has much higher temperatures, which should be above typical dew point temperatures (Section 4.3.6). However, the inside of the outer window is very cold; therefore, care must be taken to ensure that the gas filling contains no water vapor in order to avoid condensation. Very often gas fillings with noble gases are used.

Second, the heat transfer through the frame will be estimated (for simplicity we assume a solid metal or wooden frame and neglect the fact that the glass needs to be partly embedded within the frame). The total frame area is about $0.148\,\mathrm{m}^2$, and Eq. (4.12) gives for the frame alone $U_{\text{Al-frame}} = 6.0\,\mathrm{W\,(m^2\,K)^{-1}}$ and $U_{\text{wood-frame}} = 2.0\,\mathrm{W\,(m^2K)^{-1}}$. Obviously, the heat transfer coefficients at the boundaries dominate the behavior. The heat flux through the frame alone is found to be $\dot{Q}_{\mathrm{Al}} = 26.8\,\mathrm{W}$ and $\dot{Q}_{\mathrm{wood}} = 8.9\,\mathrm{W}$. Adding up the total heat flux through window and frame, we can define U-values for the whole window. For the single-pane window, $U_{\text{single,Al}} = 5.93\,\mathrm{W\,(m^2\,K)^{-1}}$ and $U_{\text{single,wood}} = 5.55\,\mathrm{W\,(m^2\,K)^{-1}}$, and for the double-pane window, $U_{\text{double,Al}} = 2.19\,\mathrm{W\,(m^2\,K)^{-1}}$ and $U_{\text{double,wood}} = 1.81\,\mathrm{W\,(m^2\,K)^{-1}}$.

4.3.5
Steady-State Heat Transfer in Two- and Three-Dimensional Problems: Thermal Bridges

In realistic applications, any object investigated by thermography is usually 3D. The heat transfer in the corresponding geometries is more complex than the 1D case. In particular, rectangular structures lead to a new phenomenon called a *thermal bridge*. Consider, for example, the walls of a house. Figure 4.12 depicts a cross section of a corner segment of an outside wall. For the sake of simplicity, a wall made of a single material is shown. Figure 4.12a shows schematically several isotherms (i.e., lines of constant temperature) within the wall for an inside temperature of 20 °C and outside temperature (in winter) of –15 °C. Following the electrical analogy, isotherms in thermal physics correspond to equipotential lines in electrical situations. The current flows along electric fields, that is, the gradient of the electric potential. In the thermal situation, the heat flows along the gradients of the temperature distributions. This is indicated by the broken arrows.

In the planar sections of the wall (bottom and right-hand side), the isotherms are parallel to the wall surfaces and 1D calculations may be used. In this case, the heat that is transported to the outside wall area A comes from a similarly large surface area at the inside of the wall. In the corner section, however, the heat flow

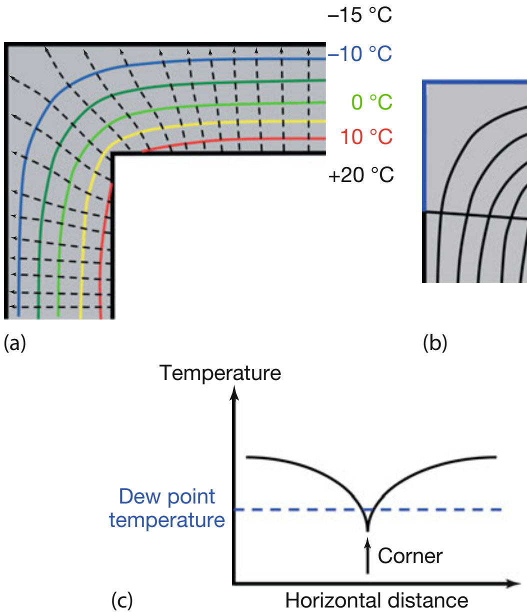

Figure 4.12 (a) Schematic illustration of a geometrical thermal bridge in a corner of a house during wintertime. The contours of constant temperature (colored isotherms) are curved and the heat flux is perpendicular to them (broken lines with arrows). (b) In the corner, the blue area of the outside wall, through which heat is transferred to the outside air, is much larger than the corresponding red area of the inside wall. (c) If the corner temperature drops below the dew point temperature, mold may grow.

follows curved trajectories. As a result, there is a much larger outside wall area A_{out} (blue line in Figure 4.12b) than the corresponding inner wall area (red line Figure 4.12b), from which the heat is transported. As a consequence, the inner wall temperature must decrease in a corner (Figure 4.12c). For buildings this is very important: one must make sure that the corner temperature does not drop below the dew point temperature, that is, the temperature where condensation starts at the wall. If unnoticed, mold starts to build up. This can happen already in situations with relative humidity around 80%.

Figure 4.12 is a schematic representation of the very general phenomenon called *thermal bridge*, which is observed in any building thermography. Thermal bridges can be due to geometry or to neighboring materials with different thermal properties. Since thermal bridges lead to temperature differences, they are naturally present in IR images, and the corresponding temperature change need not be due to a bad insulation. Thermal bridges are particularly important since temperatures may drop below the so-called dew point.

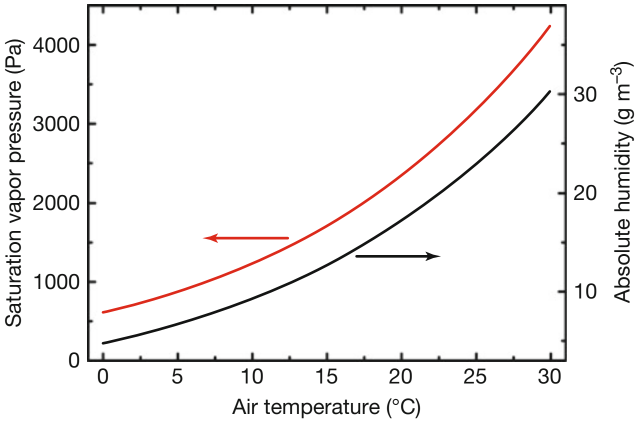

Figure 4.13 Vapor pressure (red curve) and maximum absolute humidity as a function of air temperature. Maximum absolute humidity corresponds to 100% relative humidity.

4.3.6
Dew Point Temperatures

In many applications of IR imaging, in particular from building thermography and outdoor inspections of industrial facilities, it is important to know whether the corresponding surfaces (of course, for otherwise dry weather conditions) are dry or wet since wet surfaces under wind load suffer evaporative cooling, which changes surface temperatures. Surfaces can become wet upon condensation of water vapor from the surrounding air, which happens whenever the air temperature drops below the corresponding dew point temperature.

Air at a given temperature is only able to accommodate a certain amount of water vapor. It is characterized either by the relative humidity or by the absolute humidity. The absolute humidity is a measure of the density of water vapor in air. Figure 4.13 depicts the maximum absolute humidity (corresponding to the saturation vapor pressure) as a function of air temperature. This is the maximum amount of water vapor that can be accommodated by air at this temperature. The relative humidity is a measure of the actual percentage of water vapor in the air in relation to the maximum possible water vapor content. Typical indoor situations refer to 50% relative humidity. Whenever air contains more water vapor than the maximum possible amount, the water vapor will condense on surrounding surfaces as droplets of a thin film. This usually happens during cold nights in spring or fall. Air of a given water vapor content, say 50% relative humidity, starts in the evening with a high temperature of, say, 20 °C. This means that it contains $0.50 \cdot 17.3\,\mathrm{g\,m^{-3}} = 8.65\,\mathrm{g\,m^{-3}}$ water vapor. During clear night conditions, the atmospheric temperature may drop to less than 5 °C.

However, the relative humidity of the air increases during cooling since colder air cannot accommodate as much water as warm air. In the present case, the air reaches 100% relative humidity at a temperature of 9.3 °C, which is the corre-

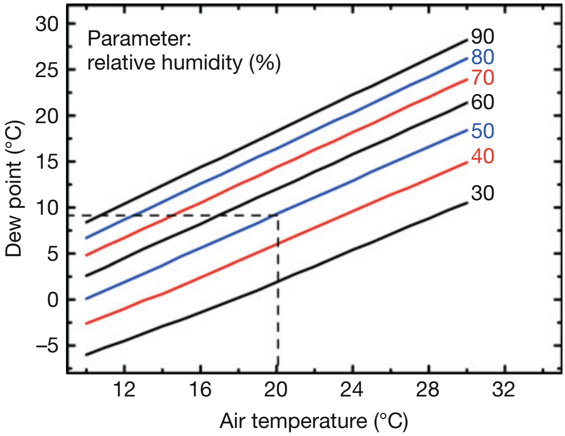

Figure 4.14 Dew point temperatures as a function of air temperature and relative humidity. For typical indoor temperatures of 20 °C and air with 50% relative humidity, the dew point is at 9.3 °C, that is, water will condense at any surface colder than 9.3 °C.

sponding dew point temperature. Since the air cools further, the excessive water vapor in the air starts to condense on colder surfaces of leaves of trees, grass, and so on. If this happens indoors, water vapor condenses at inside walls, which may lead to mold. Therefore, building inspections must look quantitatively at low temperatures, for example, from thermal bridges in corners, and so on, and investigate whether dew point temperatures are reached.

Figure 4.14 shows plots of dew point temperatures as a function of air temperature, the parameter being relative humidity.

4.4
Transient Effects: Heating and Cooling of Objects

So far, steady-state conditions have been assumed, that is, situations such as those shown in Figure 4.6b,c. In many cases, however, IR imaging is done while an object is either heated or is cooling down. Imagine, for example, a building wall exposed to the sun. It will absorb visible radiation and heat up, disguising any thermal signature of insulation problems of the wall itself. Similarly, electrical equipment under load may change temperature upon load changes during an investigation. In what follows, the simplest theoretical description of temperature changes of solid or liquid objects due to heat sources is discussed. Only opaque objects will be assumed, and the analysis must be modified for semitransparent objects [5]. Later on, we also only compute Biot numbers for quasi-steady-state conditions and neglect the transient case, which would require a more complex analysis with the need to introduce the Fourier number (e.g., [6]).

4.4.1
Heat Capacity and Thermal Diffusivity

Whenever an amount ΔQ of heat is transferred to or from an object, the object temperature changes according to

$$mc\Delta T_{\text{obj}} = \Delta Q \tag{4.14}$$

Here, m denotes the mass of the object and c the material-dependent specific heat (which, to first order, is assumed to be independent of T). Of course, a certain time is needed to reach the new thermal equilibrium within the object. The specific heat determines how much energy is needed for a given temperature change. Combined with the mass, $m \cdot c$ describes the energy storage ability of an object in Joules per Kelvin. To compare materials, one also uses the volumetric heat capacity $\rho \cdot c$ given in J $(\text{m}^3\,\text{K})^{-1}$, where ρ denotes the density of the material. This quantity describes the energy storage capacity of an object per volume. Table 4.7 summarizes these quantities for a number of materials.

Knowing the energy storage capacity of an object and its thermal conductivity, it is possible to define the thermal diffusivity a_{diff} given in square meters per second (Section 3.6):

$$a_{\text{diff}} = \frac{\lambda}{\rho \cdot c} \tag{4.15}$$

Diffusivity is defined as the ratio of thermal conductivity to energy storage capability. Note that sometimes in the literature, diffusivity is denoted by α. We

Table 4.7 Specific heat, density, and volumetric heat capacity of some materials at 20 °C. For gases, the specific heat refers to constant pressure.

Material	Specific heat c (J $(\text{kg K})^{-1}$)	Density ρ (g cm^{-3})	$\rho \cdot c$ (J $(\text{m}^3\,\text{K})^{-1}$)
Aluminum	896	2.7	$2.42 \cdot 10^6$
Copper	383	8.94	$3.42 \cdot 10^6$
Silver	237	10.5	$2.49 \cdot 10^6$
Steel	420–500	6.3–8.1	$(2.6–4) \cdot 10^6$
Concrete	840	0.5–5	$4.2 \cdot 10^5–4.2 \cdot 10^6$
Stones	700–800	2.4–3	$(1.7–2.4) \cdot 10^6$
Dry wood	1500	0.4–0.8	$6 \cdot 10^5–1.2 \cdot 10^6$
Foams Styrofoam	1300–1500	0.02–0.05	$(2.6–7.5) \cdot 10^4$
Glass	500–800	2.5–4.0	$(1.25–3.2) \cdot 10^6$
Water	4182	1.0	$4.18 \cdot 10^6$
Oils	1450–2000	0.8–1.0	$(1.2–2) \cdot 10^6$
Air	1005	$1.29 \cdot 10^{-3}$	$1.3 \cdot 10^3$
CO_2	837	$1.98 \cdot 10^{-3}$	$1.7 \cdot 10^3$

Table 4.8 Thermal diffusivity for certain materials. For those with varying composition (steel, concrete, stones, wood, glass, oil) either specific materials or reasonable average values are given.

Material (metals)	a_{diff} ($m^2\,s^{-1}$)	Material (other solids)	a_{diff} ($m^2\,s^{-1}$)	Material (liquids, gases)	a_{diff} ($m^2\,s^{-1}$)
Aluminum (99%)	$90 \cdot 10^{-6}$	Concrete, Stones	$0.66 \cdot 10^{-6}$	Water	$0.14 \cdot 10^{-6}$
Copper	$110 \cdot 10^{-6}$	Dry wood	$0.17 \cdot 10^{-6}$	Synthetic oil	$0.11 \cdot 10^{-6}$
Silver	$170 \cdot 10^{-6}$	Foams, Styrofoam	$0.7 \cdot 10^{-6}$	Air	$20 \cdot 10^{-6}$
Stainless steel	$4 \cdot 10^{-6}$	Quartz glass	$0.85 \cdot 10^{-6}$	CO_2	$9.4 \cdot 10^{-6}$

stick to a_{diff} since α is already used for the various heat transfer coefficients. The meaning of diffusivity becomes clear from a specific example. Consider a cube or sphere of a certain material at a given temperature immersed in a liquid of much higher temperature. The larger the thermal conductivity and the smaller the energy storage capacity within the object, the faster thermal equilibrium can be established. Therefore, large values of a_{diff} mean that objects/materials will respond very quickly to thermal changes, establishing a new thermal equilibrium, whereas small values reflect materials where the corresponding processes take longer. Table 4.8 compares the thermal diffusivity of a number of materials.

As shown in Table 4.8, metals have large diffusivities, that is, they redistribute heat much more quickly than other solids or liquids.

4.4.2
Short Survey of Quantitative Treatments of Time-Dependent Problems

The spatial and time-dependent distribution of energy in an object due to temperature differences is described by the heat diffusion equation [1] . The general form includes energy source or sink terms and the possibility of anisotropic thermal properties. Here we consider the simplest case of 1D heat transfer with no source or sink terms. In this case, the change of temperature with time at a given location within the object is connected to the spatial changes of temperature (Eq. (4.16)):

$$\frac{\partial T(x,t)}{\partial t} = a \cdot \frac{\partial^2 T(x,t)}{\partial x^2} \tag{4.16}$$

Here, a is the thermal diffusivity, introduced earlier (Eq. (4.15)). Equation 4.16 determines the temperature distribution completely, provided boundary conditions (e.g., initial temperature distribution, initial heat flux) are given. Unfortunately, Eq. (4.16) and, in particular, its 3D analog can only be solved analytically for a few special cases; mostly it is solved numerically. Here we sketch the solution for temperature distributions of the simple geometries of plane, cylinder, and

Table 4.9 Dimensionless quantities commonly used to represent solutions for $T(x, t)$.

Quantity	Dimensionless temperature Θ	Dimensionless time (Fourier number)	Biot number
Definition	$\Theta = \frac{T - T_\infty}{T_{\text{start}} - T_\infty}$	$Fo = \frac{a \cdot t}{s^2} = \frac{\lambda \cdot t}{\rho \cdot c \cdot s^2}$	$Bi = \frac{\alpha_{\text{conv}}}{\frac{\lambda}{s}}$
Meaning	Fraction of realized temperature change	Ratio of heat transfer to change in stored thermal energy of object	Ratio of heat transfer at boundary to that within object

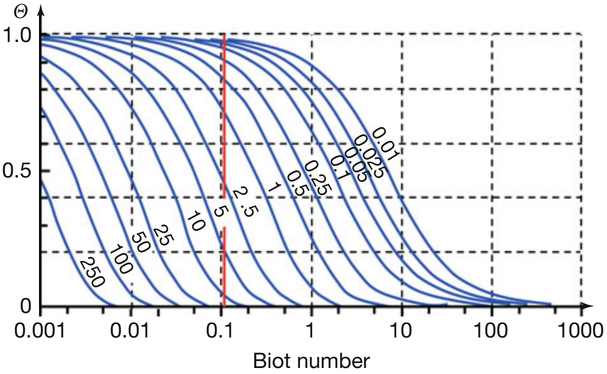

Figure 4.15 Schematic plots for dimensionless surface temperature Θ of a sphere as a function of Biot number, with the Fourier number as parameter (for details concerning the example (red line) see text, after [7]).

sphere upon a sudden change in temperature of the surrounding (think of putting an object in a fluid of different temperature).

The geometries are approximated by 1D objects, that is, we treat a plate of thickness $2s$ in the x-direction, but of infinite dimension in the y- and z-directions. An infinitely long cylinder with radial coordinate x and a sphere defined by its radius x are treated in a similar fashion. The solution $T(x, t)$ is usually expressed in terms of dimensionless temperature, dimensionless time (Fourier number), and Biot number (Table 4.9). $T(x, t)$ is then written as a so-called Fourier series expansion. Its numerical results are often depicted in terms of temperature at object surface (T_{surface}), temperature at object center (T_{center}), and temperature averaged over the object (T_{average}) as a function of Biot number, with the Fourier number being a parameter.

As an example, Figure 4.15 depicts results for the dimensionless surface temperature Θ of a sphere (similar results can be found for the other geometries [7]).

Such figures can be used to graphically solve problems of transient phenomena. As an example, let us assume a sphere of diameter $2R$ that is initially at temperature T_0. At time $t = 0$ it is put into a fluid (the fluid, for example water, is assumed not to change its temperature upon heating up the sphere) at temperature T_∞. The problem is to use Figure 4.15 to find the surface temperature as a function of time (and from similar plots the temperature at the center and the average temperature of the sphere). The solution is simple. One needs to calculate the thermal diffusivity, Biot number, and Fourier number as a function of time. For boiling water, one must assume a meaningful value for the convective heat transfer coefficient. The solution is then found as follows. Draw a vertical line at the position of the Biot number, which is relevant for the problem (e.g., red line in Figure 4.15). The intersections with the curves belonging to different Fourier numbers give the dimensionless temperatures for that Fourier number, which actually is a measure of time. Schematic results for the surface, center, and average temperatures of the sphere problem with small Biot numbers are given in Figure 4.16 for heating from 20 to 100 °C or cooling from 100 to 20 °C. They can be directly related to the temperature distribution within the sphere, as shown in Figure 4.16c (similar to plots in Figure 4.7).

Figures 4.15 and 4.16 illustrate the problems associated with the interpretation of surface temperature changes of spatial temperature distributions within objects. Figure 4.16, however, also shows that for small Biot numbers (as in this case), T_{surface} still resembles a more or less reasonable approximation for the average temperature T_{average}.

4.4.3
Demonstration of Transient Heat Diffusion

The transient diffusion of heat can be nicely visualized in a simple experiment that is often shown in introductory thermography training courses. A flat-iron or other compact heater is placed on top of a thick book with many pages, for example, a phone book, for a certain amount of time. Heat will be conducted from the iron to the book. How fast this happens depends on the energy storage of the paper pages and the thermal conductivity. As a qualitative result, it is obvious that deeper parts of the book will have reached lower temperatures only and that with increasing depth there will also be an increasing lateral heat diffusion. This can be observed easily with an IR camera by just flipping the pages after removing the iron. We will discuss this in more detail in Section 5.3.3.

4.4.4
Typical Time Constants for Transient Thermal Phenomena

In thermography, it is convenient to describe and interpret a thermal steady-state solution. Unfortunately, one often encounters situations where one observes a heating or cooling of objects owing to thermal contact with another object, owing to heat sources or sinks within the object, and so on. Whenever this happens, the interpretation of IR images can become complex. In this case, it is desirable to at least have a best guess for the respective time constants associated with temperature changes. This will be illustrated for cooling processes that are analyzed using IR imaging.

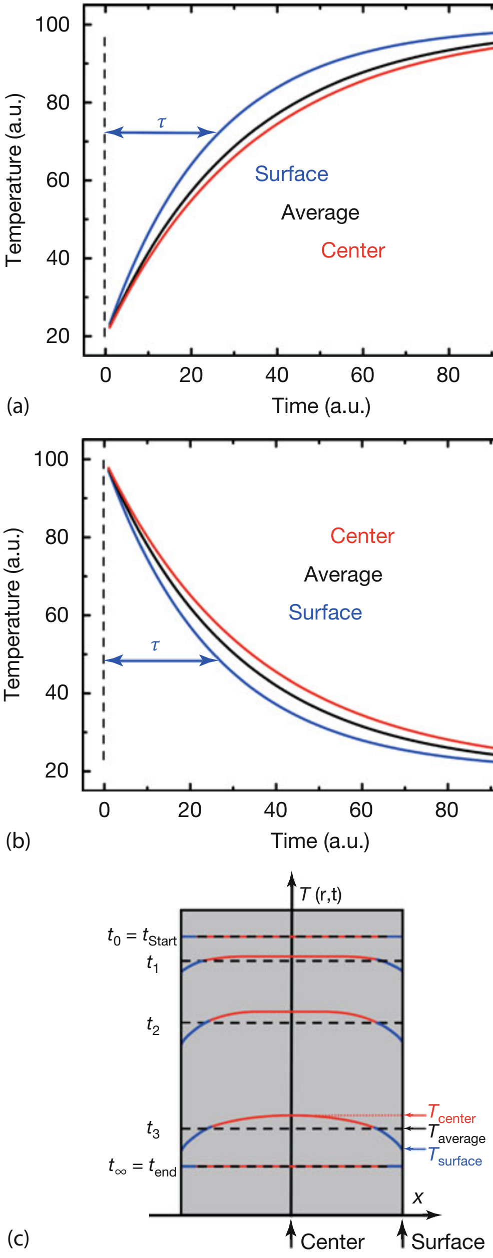

Figure 4.16 Schematic representation of surface, center, and average temperature of a sphere at a small Biot number, heated (a) or cooled (b) due to an abrupt temperature, after dropping it into a fluid. The corresponding temperature distributions within the sphere are depicted in (c). From such curves one may determine the corresponding time constants as indicated for the surface temperature plots.

4.4.4.1 Cooling Cube Experiment

Aluminum metal cubes with side lengths of 20, 30, 40, and 60 mm were heated up in a conventional oven on a metal grid. The cubes were covered with a high-temperature stable paint to provide high emissivity (in detail, three sides were covered with paint of $\varepsilon \approx 0.85$, whereas the other three sides were left as polished metal of $\varepsilon \approx 0.05$). Ample time for the heating was given such that all cubes were in thermal equilibrium within the oven at a temperature of 180 °C. The IR imaging experiment started when the oven was opened and the metal grid with the cubes was placed on thermal insulation on a table. Figure 4.17 shows two snapshots of the cooling process.

Obviously, the smallest cubes cool best, as can also be seen in the temperature profiles as a function of time (Figure 4.18). The temperature as a function of cooling time can be fitted with a simple exponential decrease, as seen in the expanded plot in Figure 4.18. Since we are dealing with small Biot numbers, this can be explained by simple theoretical assumptions.

4.4.4.2 Theoretical Modeling of Cooling of Solid Cubes

For the metal cubes, the Biot numbers follow from the values of heat conductivity $\lambda \approx 220\,\mathrm{W\,(m\,K)^{-1}}$, size s between 20 and 60 mm, and typical values for heat transfer coefficients for free convection (solids to gases) in the range 2 to $25\,\mathrm{W\,(m^2\,K)^{-1}}$. We find λ/s between 11 000 and $3667\,\mathrm{W\,(m^2\,K)^{-1}}$, giving $Bi \ll 1$, that is, we can expect a temperature equilibrium within any of the metal cubes. Supposing an initial temperature $T_{\mathrm{obj}}(t=0) = T_0$ of the cubes, energy conservation requires that any heat loss will lead to a decrease in the thermal energy of the cube, that is,

$$mc\frac{\mathrm{d}T_{\mathrm{obj}}}{\mathrm{d}t} = -\dot{Q}_{\mathrm{cond}} - \dot{Q}_{\mathrm{conv}} - \dot{Q}_{\mathrm{rad}} \tag{4.17}$$

where m is the mass of the cube, c the specific heat (here assumed to be independent of T), and $\mathrm{d}T_{\mathrm{obj}}/\mathrm{d}t$ the decrease in (uniform) the temperature of the objects (here cubes) due to the losses. Note that the signs of the (positive values of the) heat flows $\dot{Q}_i$ must be chosen properly to account for either cooling or heating processes. Here we assume initially a hot object that cools down, so there must be a minus sign in the differential Eq. (4.17) to ensure that $\mathrm{d}T < 0$ for a positive time interval $\mathrm{d}t$. For a heating process, there would be a positive sign of the heat flows leading to $\mathrm{d}T > 0$.

Using Eqs. (4.1)–(4.3) for the heat losses would lead to a nonlinear differential equation, which would be difficult to solve analytically. However, if the radiative cooling contribution can be used in the linearized form (Eq. (4.5)), then Eq. (4.17) turns into a conventional linear differential equation:

$$\begin{gathered} mc\frac{\mathrm{d}T_{\mathrm{obj}}}{\mathrm{d}t} = -\alpha_{\mathrm{total}} \cdot A \cdot (T_{\mathrm{obj}} - T_{\mathrm{surr}}) \quad \text{where} \\ \alpha_{\mathrm{total}} = \alpha_{\mathrm{cond}} + \alpha_{\mathrm{conv}} + \alpha_{\mathrm{rad}} = \alpha_{\mathrm{C}} + \varepsilon \cdot \sigma \cdot k_{\mathrm{appr}} \end{gathered} \tag{4.18}$$

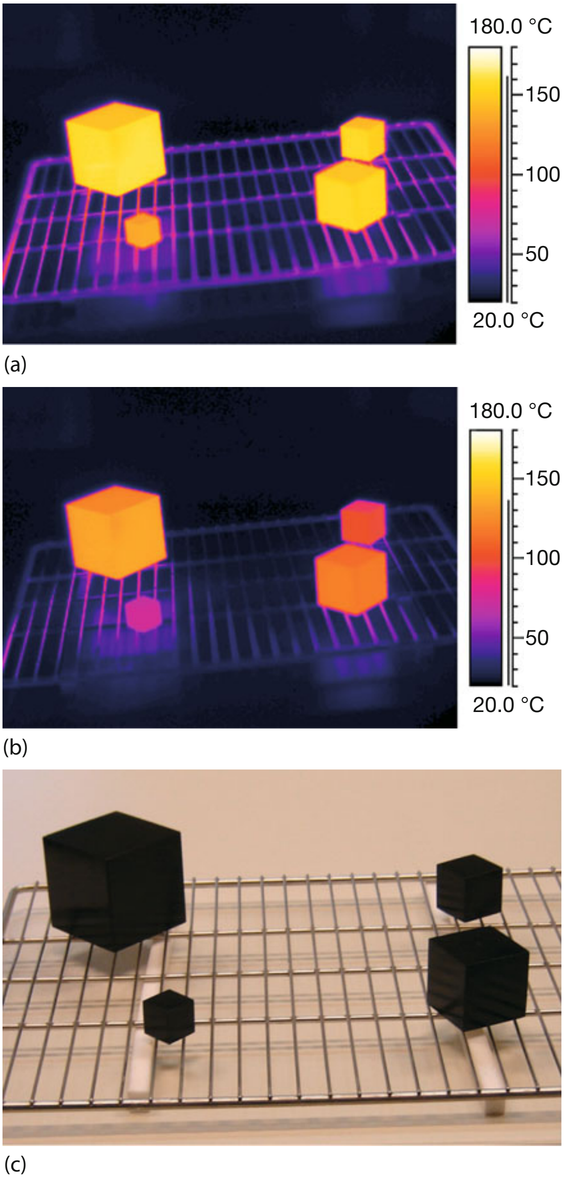

Figure 4.17 Two thermal imaging snapshots (a,b) during cooling of paint-covered aluminum cubes of different sizes and visible image (c) showing cubes on a grid and thermal insulation on lab table.

Here α_C accounts for the sum of conduction and convection. Using the boundary conditions $T_{obj}(t = \infty) = T_{surr}$ and $T_{obj}(t = 0) = T_0$ we find

$$T_{obj}(t) = T_{surr} + (T_0 - T_{surr}) \cdot e^{-\frac{t}{\tau}} \quad \text{with time constant} \tag{4.19a}$$

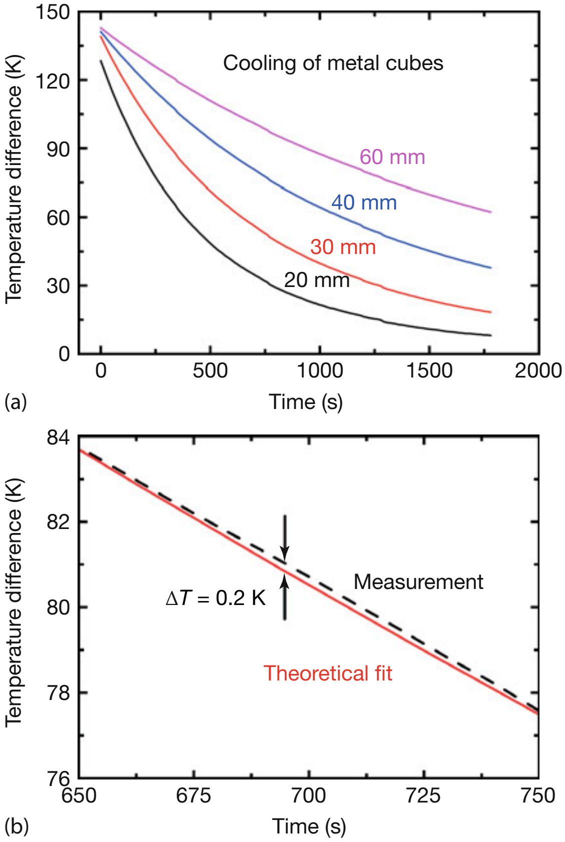

Figure 4.18 Temperature as a function of cooling time for aluminum cubes of various sizes (a) and example of a simple exponential fit for 40 mm cubes. (b) The fit is so close to the experimental data that only an expanded portion can illustrate the differences between theory and experiment.

$$\tau = \frac{\rho c(V/A)}{\alpha_{\text{total}}} \tag{4.19b}$$

Here, ρ is the density of the object material, c is the specific heat, and the volume-to-surface ratio V/A is proportional to x, the length of the cube. Equation 4.19 predicts that the difference between initial temperature T_0 and surrounding air temperature T_{surr} drops exponentially. The characteristic time constant τ describes the time after which the temperature difference has dropped to $1/\mathrm{e} \approx 0.368$ of its original value. In this type of problem, it depends on the ratio of size/α_{total}. As expected, the larger the size and the smaller the effective total heat transfer coefficient, the longer it takes to cool the cube.

4.4.4.3 Time Constants for Different Objects

For the practitioner it is important to get a feeling for the time constants τ involved in the heating and cooling of objects. In what follows, several examples are given for typical values/ranges of τ. Rather than analyzing every situation in detail, order-of-magnitude estimates are given using Eq. (4.19), assuming a constant $\alpha_{\text{total}} = 15\,\text{W}\,(\text{m}^2\,\text{K})^{-1}$ for the sum of convective and radiative heat transfer. Table 4.10 gives a summary. Numbers are rounded to give an indication of the order of magnitude. Equation 4.19 is based on the validity of $Bi < 0.1$. In all cases where Bi is larger, the time constants represent lower limits, that is, real times will be even longer. It must be kept in mind that within one time constant, a temperature difference ΔT only decreases to $(1/\text{e}) \cdot \Delta T$, that is, thermal equilibrium requires at least about five time constants.

Obviously, time constants for large buildings or walls can be in the range of many hours. This is crucial in outdoor building thermography, in particular if solar load or night sky radiant cooling are effective as time-dependent additional heat sources or sinks (Chapter 7).

Estimating time constants is easy if the temperature varies exponentially with time, as given in Eq. (4.19). The validity of the underlying assumption that the total heat transfer rates depend linearly on the temperature difference (sometimes this dependence is denoted as Newton's law) is, however, not straightforward. As a matter of fact, it is quite surprising that the linearization of Eqs. (4.4) and (4.5) seems to work over the extended temperature range of around $\Delta T = 100\,\text{K}$, as indicated in Figure 4.18. As shown in what follows, this unexpected behavior can be explained by the result that whenever temperature differences are below 100 K,

Table 4.10 Typical time constants for heating and cooling of objects.

Object	Dimensions	Material constants	Comment	Time constant τ (s)
Aluminum metal cube	20 to 60 mm	$\rho = 2700\,\text{kg}\,\text{m}^{-3}$ $c = 900\,\text{J}\,(\text{kg}\,\text{K})^{-1}$		≈ 500 to 1500
Halogen light bulb	Thickness 1 mm	$\rho = 2500\,\text{kg}\,\text{m}^{-3}$ $c = 667\,\text{J}\,(\text{kg}\,\text{K})^{-1}$		≈ 100
Liquid container for 0.5 L water	Cylinder, for example, $R = 3.35\,\text{cm}$, $h = 14.2\,\text{cm}$	$\rho = 1000\,\text{kg}\,\text{m}^{-3}$ $c = 4185\,\text{J}\,(\text{kg}\,\text{K})^{-1}$ for water	Container material can add to heat capacity and τ	Order of 4000
Single brick stone	$24 \times 12 \times 8\,\text{cm}^3$	$\rho = 1500\,\text{kg}\,\text{m}^{-3}$ $c = 850\,\text{J}\,(\text{kg}\,\text{K})^{-1}$	Typical for buildings	≈ 1700
Concrete	$0.3 \times 0.3 \times 1\,\text{m}^3$	$\rho = 2000\,\text{kg}\,\text{m}^{-3}$ $c = 850\,\text{J}\,(\text{kg}\,\text{K})^{-1}$	Typical for building foundation	≈ 10 000
Stone wall	$0.24 \times 3 \times 10\,\text{m}^3$	$\rho = 2000\,\text{kg}\,\text{m}^{-3}$ $c = 850\,\text{J}(\text{kg}\,\text{K})^{-1}$	Typical for stone buildings	≈ 14 000

a simple exponential function is sufficient to explain the heating and cooling of objects. In this case, time constants as derived previously may be used as estimates for the transient thermal behavior of the objects.

4.5
Some Thoughts on the Validity of Newton's Law

The cooling of objects with small Biot numbers according to Eq. (4.18) leads to an exponentially decreasing temperature difference with time (Eq. (4.19)). We briefly summarize the assumptions that led to Eq. (4.19), sometimes referred to as *Newton's law of cooling* [8]:

1. The object is characterized by a single temperature ($Bi \ll 1$).
2. For small temperature differences ΔT (i.e., $\Delta T \ll T_{\text{obj}}, T_{\text{surr}}$ with absolute temperatures in K), radiative heat transfer may be approximated by its linearized form, where the heat transfer coefficient is constant (does not depend on temperature). In what follows, we discuss in detail how small ΔT must be.
3. The convective heat transfer coefficient is assumed to remain constant during the cooling process.
4. The temperature of the surroundings stays constant during the cooling process; this means that the surroundings must be a very large thermal reservoir.
5. The only internal energy source of the object is the stored thermal energy.

It is quite easy to experimentally fulfill requirements 1, 4, and 5. The convective heat transfer (3) assumption is more critical. In experiments, it can be kept constant using steady airflow around objects, that is, for forced convections. If experiments use free convections, $\alpha_{\text{c}} = \alpha_{\text{conv}} + \alpha_{\text{cond}}$ may depend on the temperature difference. Usually convection dominates in α_{c} which explains why one often refers to α_{c} as the convection term. In the following theoretical analysis, however, we focus on the influence of the linearization of radiative heat transfer. In particular, we discuss the question of whether the linearization of Eq. (4.18) also works over extended temperature ranges.

In a more accurate description of the cooling process, the radiation contribution is treated in its original nonlinear form:

$$mc\frac{\mathrm{d}T_{\text{obj}}}{\mathrm{d}t} = -\alpha_{\text{c}} \cdot A \cdot (T_{\text{obj}} - T_{\text{surr}}) - \varepsilon \cdot \sigma \cdot A \cdot \left(T_{\text{obj}}^4 - T_{\text{surr}}^4\right) \tag{4.20}$$

4.5.1
Theoretical Cooling Curves

Equation 4.20 was numerically solved for a specific example of initially hot painted 40 mm aluminum cubes since such cubes were used in one of the experiments. They may serve as a theoretical model system with simple geometry. The cooling depends on three parameters: cube size (in general, this relates to the energy stor-

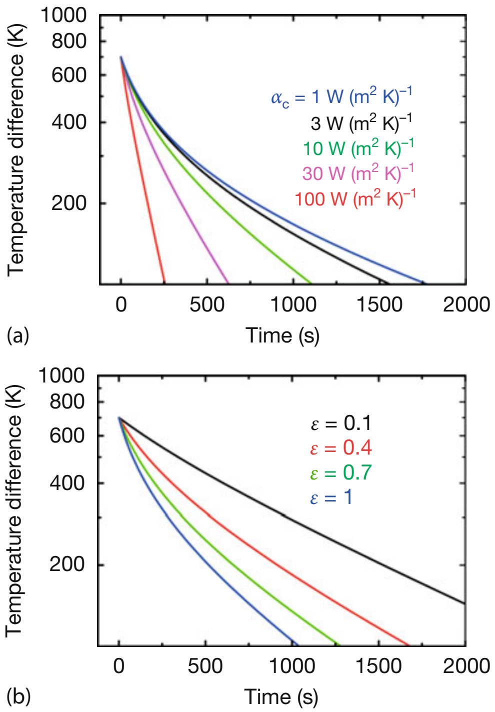

Figure 4.19 Numerical results of Eq. (4.20) for aluminum metal cubes. (a) Variation of heat transfer coefficient α_C from 1 to 100 W (m^2 K)$^{-1}$ for fixed size (s = 40 mm) and $\varepsilon = 0.9$. (b) Variation of emissivity for fixed α_C = 10 W (m^2 K)$^{-1}$ and cube size s = 40 mm.

age capability of the object), convective heat transfer coefficient (in this example, a cube in air, α_c is determined by convection), and object emissivity, that is, the contribution of radiative heat transfer. The variation of cube size directly relates to the fact that the time constant for cooling is linearly proportional to size.

Figure 4.19 depicts the results while varying convection and emissivity independently in semilogarithmic plots. Newton's law, being exponential as in Eq. (4.19), would be represented by straight lines in these plots.

Obviously, one observes curved cooling plots, that is, deviations from the simple exponential behavior (straight line) for all investigated sizes. Variation of the heat transfer coefficient α_c (Figure 4.19a) has a strong impact on the linearity of the plot. The larger α_c, the more the plot follows a straight line. Similarly, the variation of emissivity (Figure 4.19b) shows that very small emissivities (e.g., $\varepsilon < 0.2$), that is, small contributions of radiative heat transfer, clearly favor Newton's law, that is, exponential cooling. In practice, ε cannot be varied in such wide ranges. Polished metal cubes will have ε values on the order of 0.1, whereas those painted with high-emissivity paint will have emissivities around 0.9. For experiments, intermediate values for the total radiative heat transfer may be realized by painting only a few sides of the cubes and leaving the others polished.

The numerical results of Figure 4.19 were, of course, expected because they are a direct consequence of Eq. (4.20), which explains the conditions for having either linear or nonlinear behavior. If the convection term is large and the radiation contribution small, linear plots are expected, and vice versa, whereas changing the size (ratio of mass and area) only has an effect on the timescale of the cooling process.

The degree of deviation from a straight line is depicted for three different heat transfer coefficients α_{conv} of 3, 10, and 30 W $(\text{m}^2\,\text{K})^{-1}$ for 40 mm cubes and $\varepsilon = 0.9$ in Figure 4.20. The initial temperature differences were assumed to be 700 K in relation to ambient temperature.

It is quite obvious that all plots show deviations from straight lines (red broken lines), which nicely fits the low temperature data. The larger the heat transfer α_C, the smaller the deviations. For low convective losses of only 3 W $(\text{m}^2\,\text{K})^{-1}$, deviations can be expected for temperature differences as small as 40 K. In contrast, for very high convective losses of 30 W $(\text{m}^2\,\text{K})^{-1}$, simple exponential cooling seems to work quite well for $\Delta T < 100$ K.

The results demonstrate that there is no general number for ΔT describing the range of validity of Newton's law. Rather, the corresponding temperature range depends on the experimental conditions and how closely one looks for deviations. Plotting data only for small temperature differences can lead to the impression that the straight-line fits work quite well since deviations are not as pronounced as for the high temperature range.

We finally consider two extreme cases for cooling of objects, one where radiation dominates and another where convection dominates the cooling process (i.e., $\alpha_C \approx \alpha_{\text{conv}}$). Results are depicted in Figure 4.21. The smallest imaginable realistic value for convective heat transfer is in the 1 W $(\text{m}^2\,\text{K})^{-1}$ range, and the largest corresponding radiative heat transfer occurs for black bodies, that is, setting $\varepsilon = 1.0$, as may be realized by metal cubes covered with high-emissivity paint. In this case, the cooling curve starts to deviate from Newton's law for $\Delta T \approx 30$ K. In contrast, polished metal cubes with low emissivity reduce radiation losses. The convective losses may simultaneously be enhanced by directing fans with high air speed onto the objects. In this case, very high values of up to 100 W $(\text{m}^2\,\text{K})^{-1}$ seem possible. In this case, no deviation from the straight line plot is observable, that is, Newton's law would hold for the whole temperature range of $\Delta T = 500$ K.

4.5.2
Relative Contributions of Radiation and Convection

To further understand the relevance of the nonlinearities during the cooling of objects, we now consider the relative contributions of radiation and convective heat transfer (again, we assume that α_C is dominated by convection). Quick estimates for special cases are possible using Eqs. (4.2) and (4.3). Even close to room temperature, radiative losses are surprisingly large. This must be noted since many argue that radiation losses can be neglected close to room temperature, which is incorrect. Let us assume a background temperature of ≈ 20 °C, that is, $T_{\text{surr}} = 293$ K. At

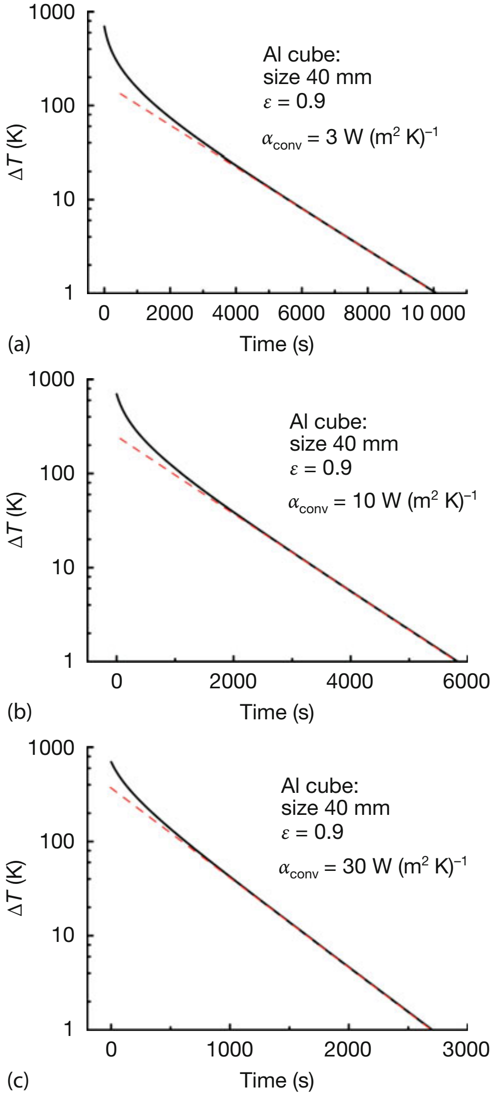

Figure 4.20 Theoretical cooling of aluminum metal cubes with size 40 mm and $\varepsilon = 0.9$ for different heat transfer coefficients α_{conv} (a–c). Newton's law would be a straight line such as the red broken lines, which closely describe the low temperature data, but show deviations for larger temperatures.

300 K, a blackbody ($\varepsilon = 1$) will then have an emission (Eq. (4.3)) of (459.3 W m^{-2}–417.9 W m^{-2}), that is, about 41 W m^{-2}, which is of the same order of magnitude as typical convection losses of 63 W m^{-2} (for $\alpha_C = 9\,\text{W}\,(\text{m}^2\,\text{K})^{-1}$) or 14 W m^{-2} (for $\alpha_C = 2\,\text{W}\,(\text{m}^2\,\text{K})^{-1}$).

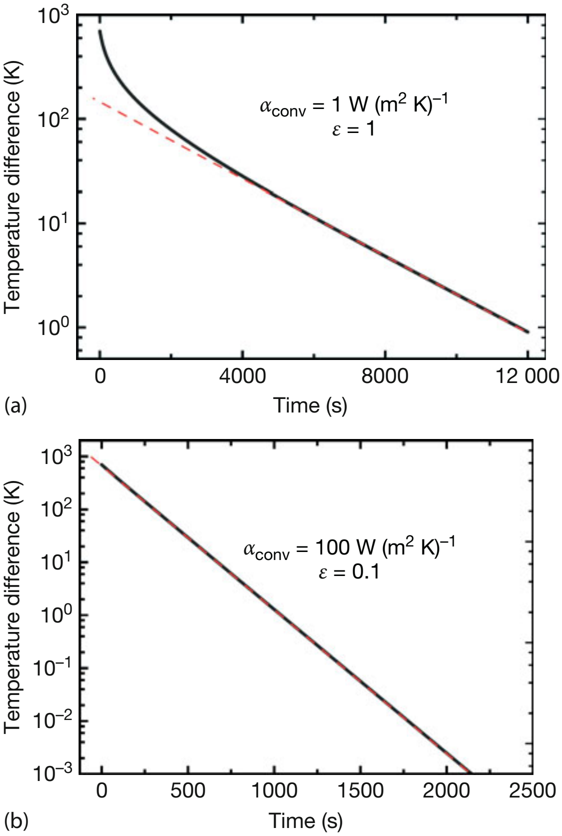

Figure 4.21 Extreme cases of cooling of aluminum metal cubes ($s = 40\ mm$): small convection with large radiation heat transfer (a) and large convection with small radiative heat transfer (b).

Figure 4.22 depicts the relative contributions of convective and radiative heat transfer for the 40 mm aluminum cubes by assuming $\varepsilon = 0.9$ and three different values, 3, 10, and 30 W (m^2 K)$^{-1}$, for convective heat transfer.

For a very small convective heat transfer of 3 W (m^2 K)$^{-1}$, radiation dominates the total energy loss of the object from beginning to end. This easily explains why in this case one would necessarily expect strong deviations from Newton's law for small temperature differences. For larger convection coefficients like 10 or 30 W (m^2 K)$^{-1}$, there is a transition temperature difference where the dominant cooling changes from radiation to convection. For 10 W (m^2 K)$^{-1}$, this happens at $\Delta T = 137$ K (after ≈ 840 s in a $T(t)$ plot), and for 30 W (m^2 K)$^{-1}$ it happens at $\Delta T = 415$ K (after 112 s). Qualitatively, it makes sense that the higher this transition temperature difference, the larger the range of validity of Newton's law of cooling. For a convective heat transfer of 100 W (m^2 K)$^{-1}$ and $\varepsilon = 0.1$ (Figure 4.21), convection would dominate radiation right from the beginning, which easily explains the linear plot.

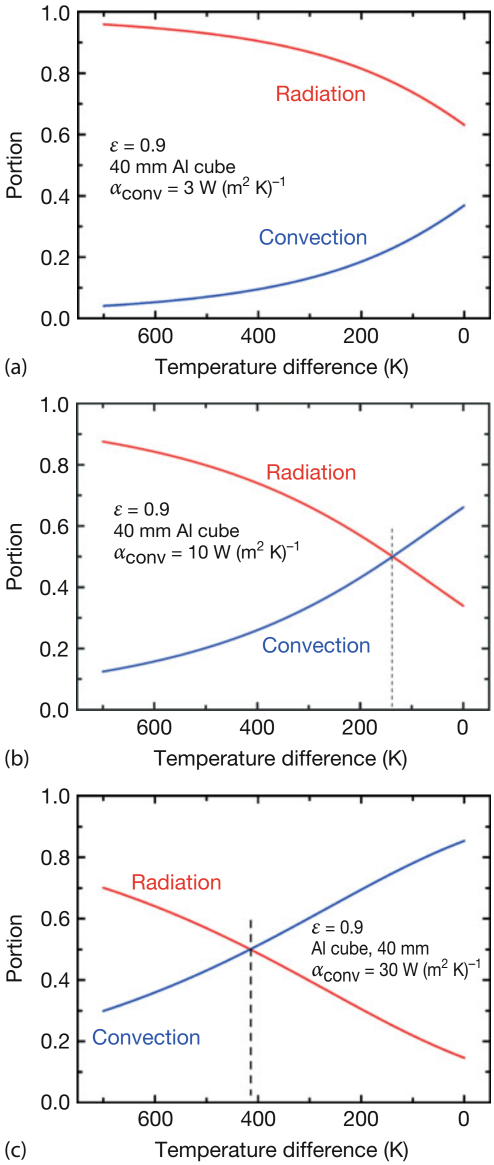

Figure 4.22 Relative contributions of convection and radiative cooling of aluminum cubes of 40 mm size with $\varepsilon = 0.9$ as a function of temperature. The initial temperature was 993 K, that is, $\Delta T = 700\,K$. For small convective heat transfer coefficients, radiative cooling is dominant throughout the cooling process, whereas for larger convection there will be a change in the dominant cooling contribution at a certain temperature.

The theoretical analysis make it clear that radiative cooling should lead to deviations from Newton's law of cooling above critical temperature differences, which, in some of the discussed cases, were below 100 K. This raises the question as to why many experiments report the applicability of Newton's law for a temperature difference of up to 100 K. The answer is simple [8]: if one waits long enough, any cooling process can be approximately described by a simple exponential function.

4.5.3
Experiments: Heating and Cooling of Light Bulbs

Owing to the oven used, the aluminum metal cubes could only be heated to about 180 °C. At these temperatures, the curvature of the cooling curves is not yet very pronounced, though definitely observable [8]. Therefore, to study higher temperatures experimentally, we used light bulbs. Several light bulbs with differing levels of power consumption and size were tested. Experiments were performed using small halogen light bulbs (nearly a cylinder, 11 mm in diameter and 17 mm in height) (Figure 4.23). Figure 4.24 shows an IR image of the halogen bulb when hot and measured surface temperatures.

For the following analysis, the maximum temperatures in a small area around the top of the light bulb were used. A test using average rather than maximum temperatures within the indicated area showed that the general form of normalized $T(t)$ curves as in Figure 4.24 changed very little, that is, conclusions drawn from time constants derived from these data do in fact hold.

For the measurement in Figure 4.24 the halogen light bulb was powered up until an equilibrium temperature was reached; then the power was turned off and the cooling curve recorded. Compared to the cooling of the metal cubes with times on the order of 1000 s, the cooling of the light bulb occurred much faster. This is mostly due to the small amount of stored thermal energy in the mass of the light bulb. This again illustrates the characteristic fact that small systems with small stored energy $c \cdot m \cdot \Delta T$ reach equilibrium much faster. The smaller the system, the smaller the corresponding time constants (Table 4.10, also Chapter 9).

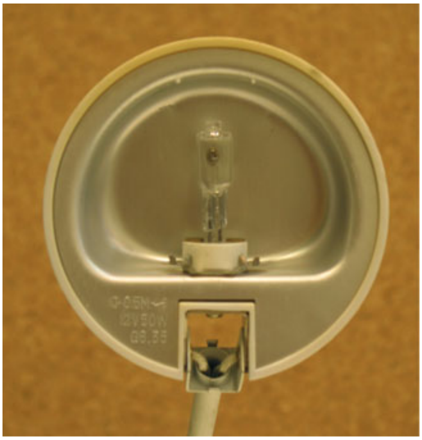

Figure 4.23 Example of investigated light bulbs. Samples were placed in front of a room temperature cork board.

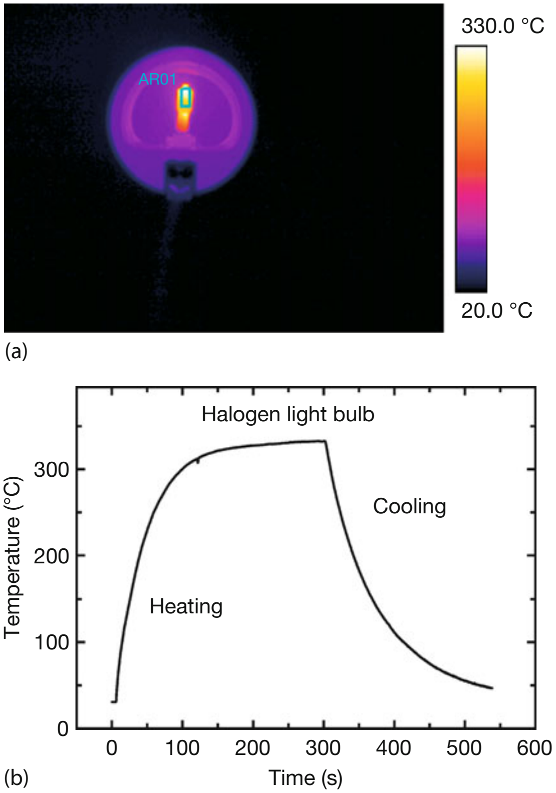

Figure 4.24 Halogen light bulbs reach maximum temperatures > 330 °C with small relative temperature variations (a). The heating and cooling of the halogen light bulb covers a temperature difference of more than 300 K (b).

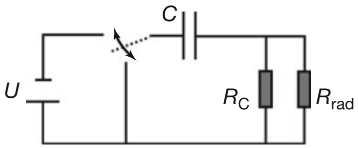

Figure 4.25 Equivalent electrical circuit representing heating and cooling of an object. Its heat capacity resembles the capacity. The thermal losses via convection/conduction and radiation are represented by two resistances in parallel.

Similar to Section 4.3.3, the heating and cooling of objects can be described by equivalent electrical circuits. Figure 4.25 depicts a RC circuit that can be connected to a voltage supply. The capacitor resembles the light bulb, and the resistances correspond to the losses due to convection and radiation. The charging of the capacitor corresponds to heating of the light bulb, the discharging to its cooling. Obviously, the voltage across the capacitor shows the same behavior as the temperature of the light bulb.

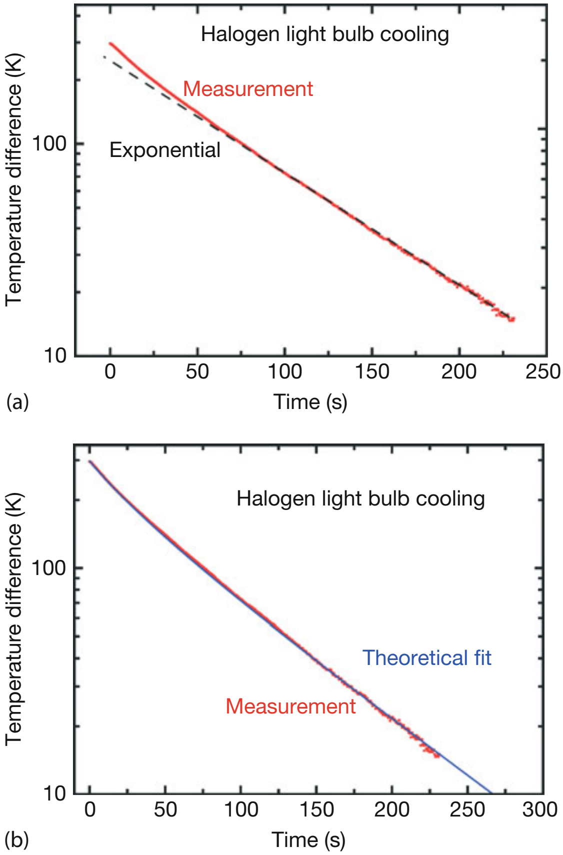

Figure 4.26 Cooling of halogen light bulb. Again, deviations occur for $\Delta T > 100$ K, as indicated by the straight line (a). The data can be fitted by a double exponential fit (b), where the time constant of the initial part is 16.7 s (amplitude 37.7 K) and that of the part with the slower decrease is 77.3 s (amplitude 259.3 K). For the smallest temperatures, the signal is very noisy. This is due to the fact that the temperature range of the camera was fixed at 80–500 K during the measurement; hence, data below 80 K must be considered with care.

Experimental results for the cooling of the halogen light bulb (Figure 4.26) are nicely represented by an exponential for small ΔT values, but they deviate for larger ΔT. This is exactly as expected theoretically.

References

1 Incropera, F.P. and DeWitt, D.P. (1996) *Fundamentals of Heat and Mass Transfer*, 4th edn, John Wiley & Sons, Inc., New York.

2 Baehr, H.D. and Karl, S. (2006) *Heat and Mass Transfer*, 2nd revised edn, Springer, Berlin, New York.

3 Möllmann, K.-P., Pinno, F., and Vollmer, M. (2007) Influence of wind effects on thermal imaging – Is the wind chill effect relevant? Inframation 2007, Proceedings, vol. 8, pp. 21–31.

4 Madding, R. (2008) Finding R-values of stud frame constructed houses with IR thermography. Inframation 2008, Proceedings, vol. 9, pp. 261–277.

5 Sazhin, S.S. (2006) Advanced models of fuel droplet heating and evaporation. *Prog. Energy Combust. Sci.*, **32**, 162–214.

6 Sazhin, S.S., Krutitskii, P.A., Martynov, S.B., Mason, D., Heikal, M.R., and Sazhina, E.M. (2007) Transient heating of a semitransparent spherical body. *Int. J. Therm. Sci.*, **46**, 444–457.

7 VDI Wärmeatlas (2006) *Verein Deutscher Ingenieure, VDI-Gesellschaft Verfahrenstechnik und Chemieingenieurwesen (GVC)*, 10th edn, Springer, Berlin (in German).

8 Vollmer, M. (2009) Newton's law of cooling revisited. *Eur. J. Phys.*, **30**, 1063–1084.

Chapter 5
Basic Applications for Teaching: Direct Visualization of Physics Phenomena

5.1
Introduction

Infrared (IR) thermal imaging allows quantitative and qualitative imaging of a multitude of phenomena and processes in physics, technology, and industry. Already over 15 years ago, thermography was proposed as a supporting qualitative visualization and quantitative measurement tool for physics education [1–3]. Meanwhile it has become increasingly popular for science and in particular physics teaching in schools as well as at universities since it allows visualization of phenomena dealing with (sometimes minute) energy transfer, which cannot be easily demonstrated with other methods [1–10]. In this chapter, the focus is on selected applications of qualitative IR imaging of phenomena for physics education. The examples should not only help to motivate students and increase their interest in natural sciences, but they should also inspire teachers to perform more experiments, thereby further demonstrating how IR imaging can be used in teaching physics and in visualizing fundamental principles and processes. Unfortunately, seemingly simple phenomena very often involve complex explanations. Therefore, despite the simplicity of the phenomena, a complete quantitative analysis is far beyond the scope of this chapter. The topics are arbitrarily divided into the classical categories of physics„ mechanics, thermal physics, electromagnetism, and optics, followed by radiation physics as an example for using thermography in "modern physics." Of course, many other applications, which are treated in other chapters can and should be used for physics teaching such as, for example, thermal reflections (Section 3.4.1), detection of gases (Chapter 8), building insulation (Chapter 7), heating and cooling of objects (Sections 4.4 and 4.5), heat sources in electrical components (Sections 10.3 and 10.4), and so on. More details regarding the physics of the various phenomena can be found in nearly every textbook on introductory physics (e.g., [11–13]).

Infrared Thermal Imaging, Second Edition. M. Vollmer and K.-P. Möllmann.
© 2018 WILEY-VCH Verlag GmbH & Co. KGaA. Published 2018 by WILEY-VCH Verlag GmbH & Co. KGaA.

5.2
Mechanics: Transformation of Mechanical Energy into Heat

A very important field for IR imaging in physics education is the visualization of mechanical phenomena involving friction. These most important everyday phenomena concern our ability to move around. Walking, riding bicycles and motorcycles, and driving cars are only possible due to frictional forces between the shoes/tires on the one hand and the floor/street on the other hand. Whenever some force acts along a given direction for a given distance, work is done that is eventually converted into thermal energy (often but not very precisely denoted as heat). For sliding friction, the work due to the frictional force will ultimately lead to a temperature rise of the two areas that are in contact. The situation is slightly different for static friction, which is the physical basis for walking or driving on vehicles with wheels. For example, a microscopic model of rolling friction includes inelastic deformations of one or both of the touching objects. These will also produce heat, which can be made visible with IR imaging.

5.2.1
Sliding Friction and Weight

Whenever two dry unlubricated solid surfaces slide over each other, there are frictional forces, which can be expressed by the empirical law $F_{\text{friction}} = \mu \cdot F_{\text{normal}}$, where $\mu < 1$ is the coefficient of friction and F_{normal} is the normal force with which each surface presses onto the other (e.g., [11–13]). One distinguishes coefficients for static friction μ_{static} (no movement yet) and for kinetic friction μ_{kinetic}, that is, after a sliding of the two surfaces has been realized. Some typical μ-values for sliding friction, for example, for wood on wood or a car tire on the pavement of a street, are in the 0.5 range. If some object is, for example, sliding across the floor, work must be done against frictional forces. Imagine that after a while the objects have a constant sliding velocity. In this case, the work is only used to overcome the kinetic frictional forces. It is ultimately converted into thermal energy, that is, the temperature of the two sliding surfaces will rise.

To analyze these effects of frictional energy transfer in more detail, two different weights, 1 and 5 kg, were placed on small wooden plates and drawn simultaneously at constant speed across the floor (Figure 5.1). The heavier weight led to a much larger warming of the floor, as expected since the normal force was increased by a factor of 5. The plate surfaces were also heated up (not shown here). This experiment qualitatively demonstrates the effects of frictional forces in mechanics. A quantitative analysis would be quite complex. First, it requires exact measurements of frictional forces. Second, the corresponding mechanical work is split up into heating of both surfaces, depending on their thermal material properties. Third, the diffusion of thermal energy from the directly heated contact surfaces into the interior of the material leads to transient effects, which means that a realistic modeling would require recording time sequences of this problem.

Figure 5.2 schematically illustrates (for the floor surface only) the transient effects of thermal energy diffusion into the bulk of the solid. It depicts a small object

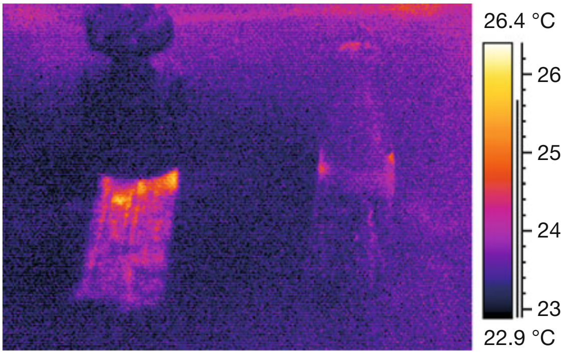

Figure 5.1 Two weights of 1 kg (right) and 5 kg (left) were placed on wooden plates and simultaneously drawn across the floor. The differing temperature rises of the floor are easily observed.

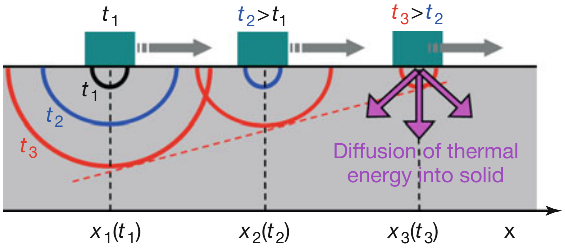

Figure 5.2 Transient thermal phenomena in sliding friction experiments arise from the fact that thermal energy diffuses into the bulk material, giving rise to time-dependent spatially varying surface temperatures. The distance of energy diffusion into the bulk material as a function of time is indicated by the semicircles.

(blue–green) that is moving at constant speed across a solid surface. Three snapshots are shown at times t_1, t_2, and t_3 at which the object was at location x_1, x_2, and x_3, respectively. Owing to the work done by the object, the temperature at the contact spots rises to a maximum and then drops as a function of time due to, first, a lateral diffusion, second, a diffusion of the energy into the bulk material, and third, heat transfer to the air. This transient behavior is characteristic of sliding friction phenomena.

Obviously, very simple looking basic physics phenomena become very complex in a realistic and quantitative analysis. This, however, is beyond the scope of this chapter, which only presents qualitative visualizations of physics phenomena.

5.2.2

Sliding Friction during Braking of Bicycles and Motorcycles

Very similar to the rising temperature of sliding planar surfaces as in the preceding example, the surfaces of bicycle, motorcycle, or automobile tires heat up during braking with blocked tires. The temperature of the contact spot of the tire with

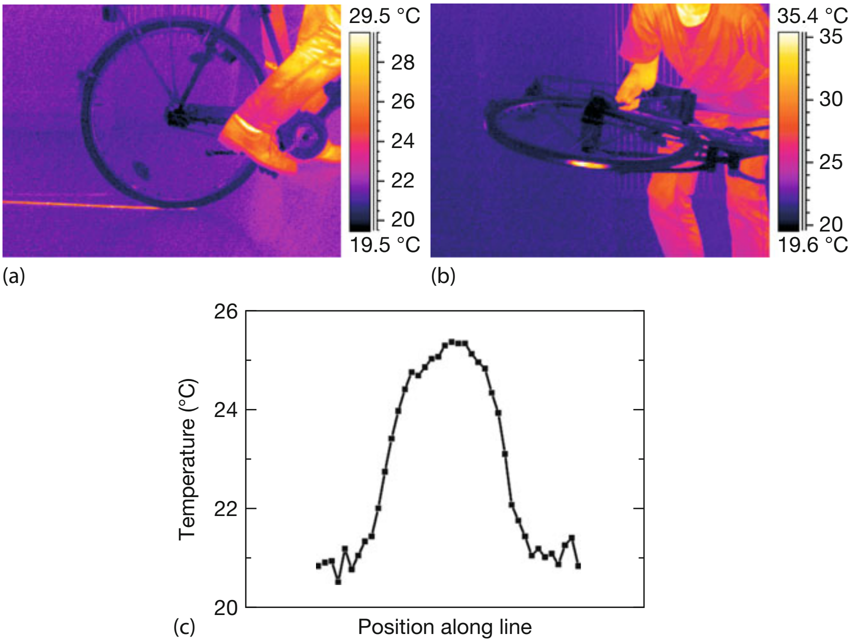

Figure 5.3 Sliding friction causes temperature to rise during braking of a bicycle tire with a blocked wheel, using the back pedal brake (a,b). The heat transfer into adjacent locations on the floor is illustrated as temperature profile along a line perpendicular to the trace on the floor (c), recorded several seconds after braking.

the pavement rises very quickly whenever the kinetic energy of the vehicle will be transferred into thermal energy. Figures 5.3 and 5.4 depict the temperature rise of the floor as well as of the tire on a bicycle after applying the back pedal brake and on a motorcycle on the road. For a motorbike braking from an initial velocity of 30 km h^{-1}, temperature rises can easily add up to more than 100 K for the tire. The temperature rise of the floor again depends on the floor material, its thermal conductivity, heat capacity, and so on. It is usually smaller than that on the tire since the thermal energy is spread over a much larger area during the braking procedure. Figure 5.3c shows the temperature across the braking trace on the floor. It may be easily observed as a function of time, illustrating the transient thermal effects.

The repeated heating during acceleration and braking of racing cars is nicely shown in a YouTube video [14]. In addition, Figure 5.5 illustrates the circular sliding of Red Bull Racing car tires on a road demonstrating the enormous thermal energies involved (see also the YouTube video in [15]).

A very similar sliding friction phenomenon involves the use of the rim brakes. The contact between the friction pads (usually made of some kind of rubber) and the metal rim of the rotating wheel again uses sliding friction forces to transform kinetic energy into thermal energy. Therefore, the rim itself as well as the friction

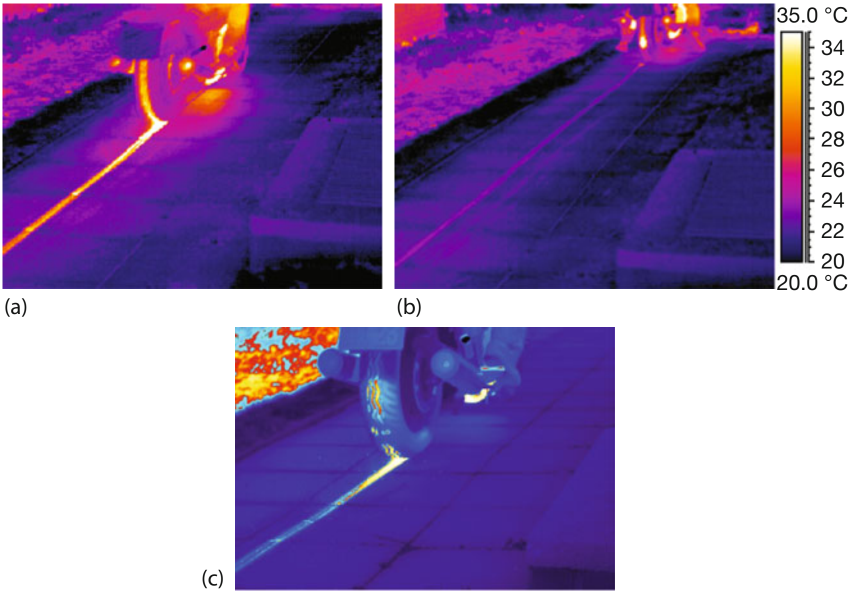

Figure 5.4 (a,b) Low-resolution LW camera image of braking of a motorcycle with blocked tires. The tire temperatures reach up to 100 °C immediately after stopping. (c) High-resolution image recorded with high-speed camera and smaller integration time.

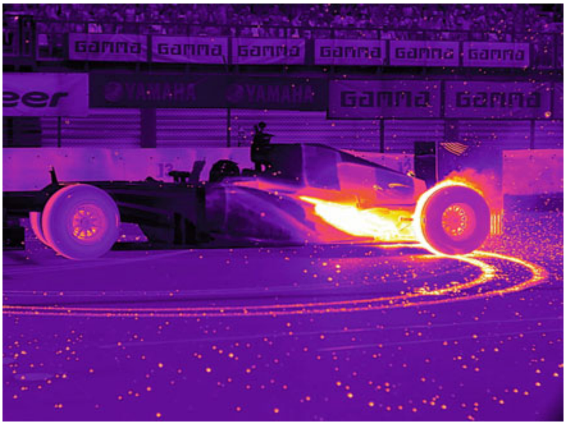

Figure 5.5 Red Bull Racing car with tire and road heating upon skidding on pavement. Courtesy Infiniti Red Bull Racing.

pads can become very warm. Figure 5.6 depicts the wheel before (panel a) and after (panel b) a braking maneuver.

Braking maneuvers with blocked tires are not good for the tires. The hot spots on the tires are accompanied by greater material ablation at those locations. This means that the lifetime of a tire will decrease with repeated braking maneuvers of

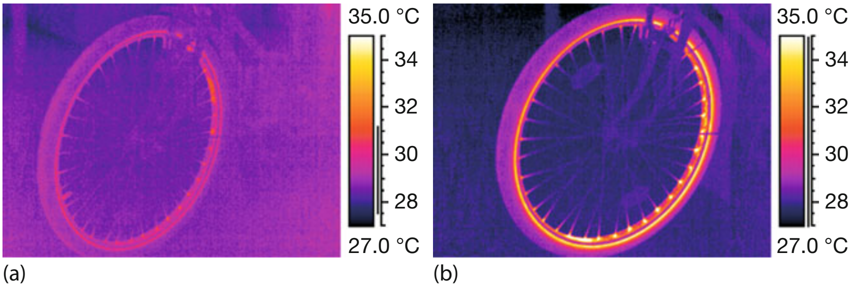

Figure 5.6 Sliding friction causes temperature rises during braking of a bicycle tire with a blocked wheel using the rim brake.

this type (the same happens for so-called jackrabbit starts where the accelerator pedal is pushed hard such that the wheels skid, leaving a black rubber trail like that left after braking with a blocked tire). In addition, the braking itself is not as efficient since the coefficient of sliding friction is lower than that for static friction. If sliding between tire and pavement is avoided, the slightly larger coefficient of static friction applies. In addition, it is not possible to maneuver a car while sliding. For these reasons, modern cars are equipped with systems to prevent sliding friction during braking.

5.2.3
Sliding Friction: the Finger or Hammer Pencil

A very simple but impressive demonstration of sliding friction and the corresponding temperature rises of surfaces can be made by the use of a hammer or just a finger to write texts or equations on any convenient surface, even the floor. The surfaces need not be too rough and their thermal conductivity should not be too large (in metals the thermal energy diffuses away very quickly; linoleum floors are excellent). Depending on the finger speed and contact pressure, it is easy to achieve temperature differences of several Kelvin. Figure 5.7 shows an example.

5.2.4
Inelastic Collisions: Tennis

Collisions are different mechanical phenomena that also involve energy transfer. One may think, for example, of two billiard balls colliding with each other. Usually, one distinguishes between elastic and inelastic collisions. Elastic collisions are those where the total kinetic energy of the objects before the collision is exactly equal to the total kinetic energy after the collision. Elastic collisions are idealized phenomena that are usually demonstrated in physics using apparatus to reduce any residual friction effects, for example, by using an air rail system. In practice, most collisions in everyday life are inelastic, that is, part of the kinetic energy of a moving object is transformed into thermal energy during the collision process.

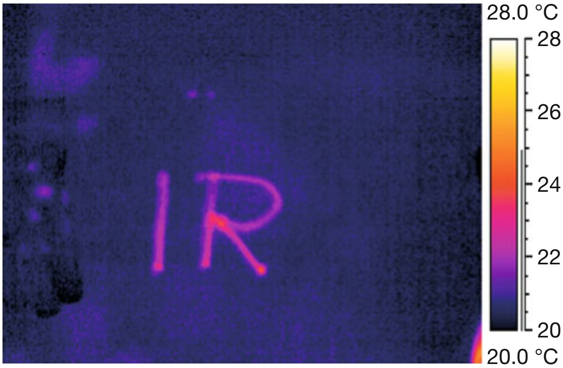

Figure 5.7 Finger writing: work against sliding frictional forces leads to temperature increase of the surface.

Think, for example, of a ball (e.g., tennis, soccer, volleyball, basketball, rubber ball) that falls from a certain height to the floor. It will collide with the floor, leading to a rebound. From energy conservation, an elastic collision of the ball with the floor would give the ball enough energy to reach the original height from which it was dropped. However, no real ball will reach the original height from which it was dropped; part of the initial kinetic energy is lost. New tennis balls (mass $\approx$ 57 g, diameter $\approx$ 6.5 cm), if dropped from a height of 2.54 m, must at least reach a rebound height of 1.35 m. This corresponds to a loss of kinetic energy of about 0.67 J, that is, about 47% of the initial kinetic energy is lost. Even super balls lose about 20% of their kinetic energy upon bouncing from a floor [16].

Microscopically, the ball and the surface deform upon impact of the ball. Consider, for example, the ball. If the deformation changes the ball's shape from the initially ideal spherical shape to a distorted shape while touching the floor, it stores potential energy. Such deformations are, however, never totally elastic, or reversible, because during deformations part of the energy is transformed into thermal energy. This means that when we observe falling objects colliding with surfaces, we expect temperature increases at the contact spot on the falling object as well as of the spot on the floor surface where it hits. Figure 5.8 shows an example of an inelastic collision of a tennis ball with a floor.

In this experiment, where the ball, hit with a racket by an amateur, reached velocities of around 100 km/h, a temperature rise of the floor of about 5 K was observed with a decay time of several seconds. Similar to the friction experiment, a quantitative analysis is more difficult. The tennis ball experiment is explained in more detail in Section 11.3 in a discussion of high-speed thermography.

Similar effects can be observed at much lower speeds when, for example, dropping a metal sphere (see also [9]), for example, a metallic Boule ball, from a height of 1.2 m to the floor or some other surface. The ball had an impact velocity of only around 5 m/s. Figure 5.9 depicts the result for dropping the ball on a linoleum floor. The 527 g metal ball bounced very little two to three times, and the first contact led to a small indentation of a few tenths of a millimeter. Before the bounce,

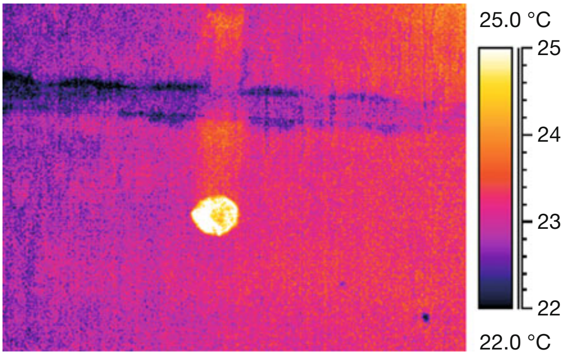

Figure 5.8 A tennis ball hits a carpet, resembling the court. The image was taken just after it touched the ground. The ball was also heated up during the collision but, because of its fast movement, only left a vertical trace.

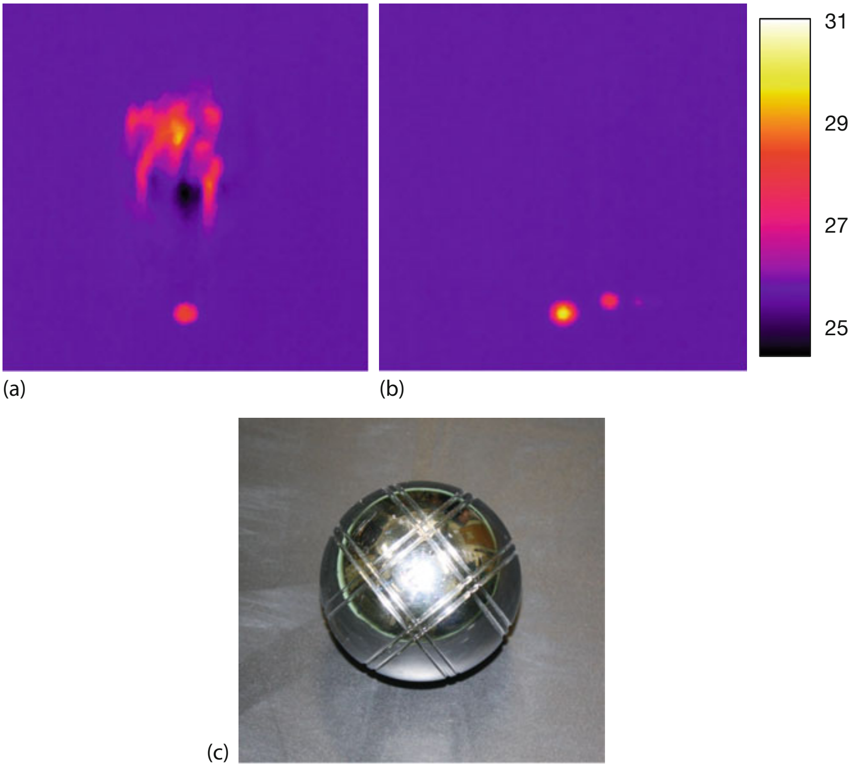

Figure 5.9 Metal sphere 7 cm in diameter (c) heating top of floor upon falling from 1.2 m height. (a) Right after impact (one can still see the upward-moving motion blurred sphere); (b) after another 3.5 s after reaching the largest *T* increase of 5.2 K. The *T* scale is from 24 to 31 °C.

the floor ($\varepsilon = 0.9$) had a temperature of 25 °C. Right after first contact, the temperature of the indented floor reached 27.8 °C, but (based on multiple experiments) it took about 3–5 s before the maximum temperature, which was more than 5 °C warmer than the adjacent floor, was reached. Usually, the ball bounced two to three times before coming to rest (and was then removed manually), which is why Figure 5.9b shows three contact points with decreasing temperatures.

In brief, the nearly incompressible metal ball deformed the more elastic floor surface, thereby dissipating about 10 to 20 % of its kinetic energy into heat. The latter process is time dependent owing to the subsequent slow lateral and vertical heat diffusion.

Many other inelastic collisions involving heat transfer may be studied with IR imaging. For example, so-called hopper popper toys consist of spherical rubber segments that bounce to enormous heights if properly loaded [17].

5.2.5
Inelastic Collisions: The Human Balance

If two objects stick together after a collision, the process is considered *completely inelastic*. Imagine, for example, a piece of putty falling to the floor. It will not rebound at all, that is, it loses all of its kinetic energy upon impact. The amount of energy transformed into thermal energy is larger than in inelastic collisions, and therefore the corresponding temperature changes may be more easily observed. For the observation it is, however, necessary to remove the object and turn it around after it has come to rest in order to measure the surface temperatures of the two contact areas.

Figure 5.10 shows an example of two people of different masses, $m_1 \approx 80\,\text{kg}$ and $m_2 \approx 120\,\text{kg}$, jumping down from a table onto the floor. Both are wearing the same type of shoes. After landing, they quickly step aside and the contact spots

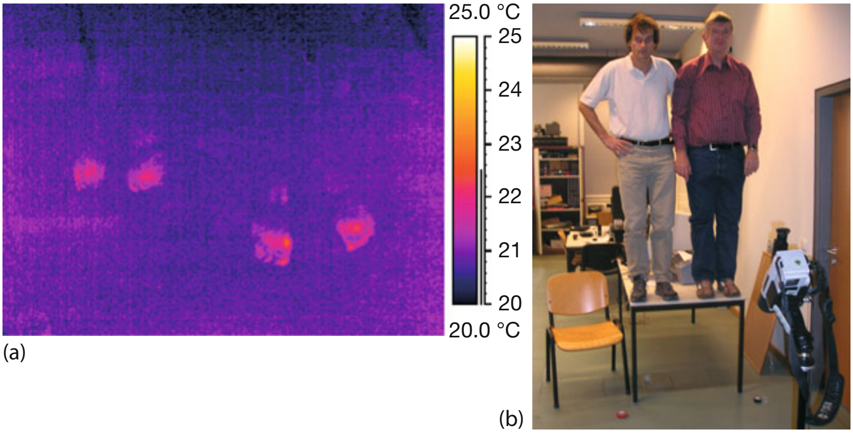

(a)

(b)

Figure 5.10 Human balance: the temperature rise due to an inelastic collision of people jumping from a table to the floor (a) can be used to compare the masses (weight forces) of the jumpers (b).

on the floor are examined by IR imaging. Quite obviously, the heavier jumper gives rise to a higher surface temperature on the floor. One could easily argue that this was expected since the heavier jumper started with a higher initial potential energy. This is correct, but again, a more thorough discussion would show that any kind of quantitative explanation requires much more information, for example, the contact area while hitting the floor may be made of different materials and, hence, involve different heat transfer properties of the shoe soles, and so on.

To elaborate, the two jumpers have different initial potential energies, $m_\mathrm{i}gh_\mathrm{i}$, in the earth's gravitational field, where h_i is the height difference between the floor and center of gravity of the individuals. In what follows, we assume people of about the same height, $h_1 = h_2 = h$. Just before reaching the floor the potential energy has been completely transformed into kinetic energy, $1/2m_\mathrm{i}v_\mathrm{i}^2$, where v denotes the velocity. During the completely inelastic collision, a first part of the kinetic energy is transferred to deformations of the floor and the shoes and a second part (i.e., the rest) into deformations within the body (e.g., muscles, knee joints). Ultimately, both parts will end up in thermal energy. Of course, it is only possible to measure the first part, that is, the temperature rise of the floor and the shoes, by IR imaging. Unfortunately, again, the amount of energy dissipation within the body will depend on the jumper, that is, on whether and how muscles are stretched, and it is not easy to guess the ratio of both contributions. Therefore, we assumed that both jumpers would try to jump in as similar a manner as possible, with muscles stretched. In this case, one expects that a similar ratio of energy would be dissipated into the shoe–floor contact area. It would then divide up into heating of the shoe and of the floor.

5.2.6
Temperature Rise of Floor and Feet while Walking

Walking on ice is very difficult, whereas walking on a dry street is easy. The difference between these two situations is that the frictional forces are much lower for the contact between shoes and ice as compared to that between shoes and street pavement. Obviously, friction is necessary for walking. However, although the phenomenon is one of the most natural for us, the details can be very complex. First, static friction is usually involved (the undesired sliding friction does apply to ice, though). Usually there is no sliding between shoe and floor during walking. The shoe just touches the floor and then lifts up again. Since there is no distance traveled along the direction of an acting force, no mechanical work is done that could be converted into thermal energy.

The energetics of human walking and running has been studied in detail [18–20]. It involves work for accelerating and decelerating the legs plus the gravitational work associated with lifting the trunk at each step. The total power exerted during walking finally leads to a heating up of the body, sweating, and, to a small extent, to a heating up of the two contact areas (this contribution has not been studied in detail so far; its portion of the total expenditure is probably at most in a small percentage range, most likely in the single percentage range). Micro-

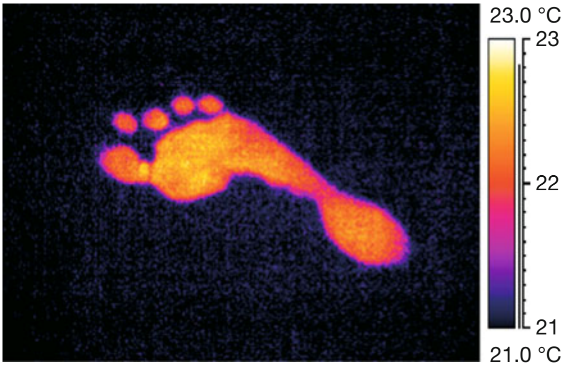

Figure 5.11 Energy dissipation due to walking can be visualized with IR imaging.

scopically, one may understand the mechanism for the heating from the inelastic collision experiment (Section 5.2.5). During each step, the shoe experiences something like an inelastic collision with the floor. Therefore, part of the original kinetic energy of the leg is transformed into deformation energy of the soles of the shoe as well as of the floor (and perhaps a small amount is transferred into the body of the walker). These deformation energies end up as thermal energy, that is, a temperature rise of the shoe and floor. How the total energy is split up depends again on the thermal properties of the two materials in contact.

Figure 5.11 shows an example of a heated linoleum floor after a person was walking on it at constant speed in bare feet (also minute heat transfer from warm feet).

Since the foot hits the floor only with part of its surface, one can clearly see the walking profile and the toes. The corresponding temperature rise, although still detectable, is smaller for shoes, in particular when running, that is, hitting the floor at a greater velocity (cf. Figure 5.10).

5.2.7

Temperature Rise of Tires during Normal Driving of a Vehicle

Like walking, driving a vehicle on wheels is based on static frictional forces [16]. When a vehicle moves forward, its wheels rotate such that the bottom surface does not slide on the ground. Instead, a portion of the surface of each wheel touches the ground, where it briefly experiences static friction. Then it moves up, with a new portion of the wheel surface taking its place. This touch-and-release process involves only static friction; therefore, like the walking discussed earlier, this mechanism alone is not able to convert mechanical energy via work into thermal energy.

However, the rolling of wheels on a surface involves more. The corresponding technical term for the resistance to motion is *rolling resistance* or *rolling friction*. When a wheel or tire rolls on a flat surface, it deforms the object as well as the surface. Static frictional forces are present at the contact point/area. Sliding fric-

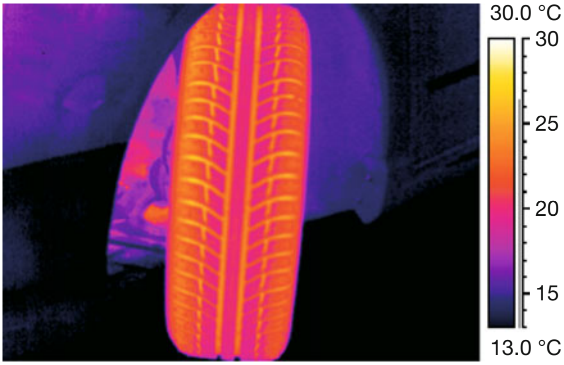

Figure 5.12 Homogeneous heating of tires during normal driving conditions. This is also a test of the quality of the tire profile; without the profile, the heating would be more homogeneous across the tire surface.

tion does not contribute since each contact spot on the tire is lifted up from the rolling. The deformation of the surface leads to reaction forces that have a component opposed to the direction of motion. As a matter of fact, the deformations of the surface lead to the seemingly paradoxical situation that any horizontally driving vehicle must drive upward (out of the hole due to the deformation).

As in the case of static and sliding friction, frictional force is described as $F_{\text{friction}} = \mu_{\text{roll}} \cdot F_{\text{normal}}$, with μ_{roll} being the rolling friction coefficient. This coefficient is much smaller than typical static or dynamic friction coefficients – for steel railroad wheels on steel rails it is less than 0.001, and for car tires on asphalt about 0.03. Ideally, deformations should be elastic, in which case no thermal energy is generated. In reality, part of the deformation is inelastic and the contact areas should warm up.

As a consequence, the tire of any transport vehicle will have elevated temperatures from driving, even in the absence of acceleration or deceleration. High-quality tires should have surfaces that heat homogeneously, provided no braking with blocked tires or wheel spinning during accelerating takes place. Figure 5.12 shows an example of a car tire after continuous driving for several minutes and very soft braking. As expected, the tire has heated up homogeneously, and no hot spots are evident; however, the spatial profile of the rather new tire is of course clearly visible.

This technique – investigation of tire surfaces after driving – is commonly used to analyze the quality of new tires, in particular of tires used on Formula One racing cars.

5.2.8
Generating Heat by Periodic Stretching of Rubber

Rubber is a thermoelastic material, that is, there is a close interaction between mechanical and thermal effects. In particular, a rubber band heats up when stretched

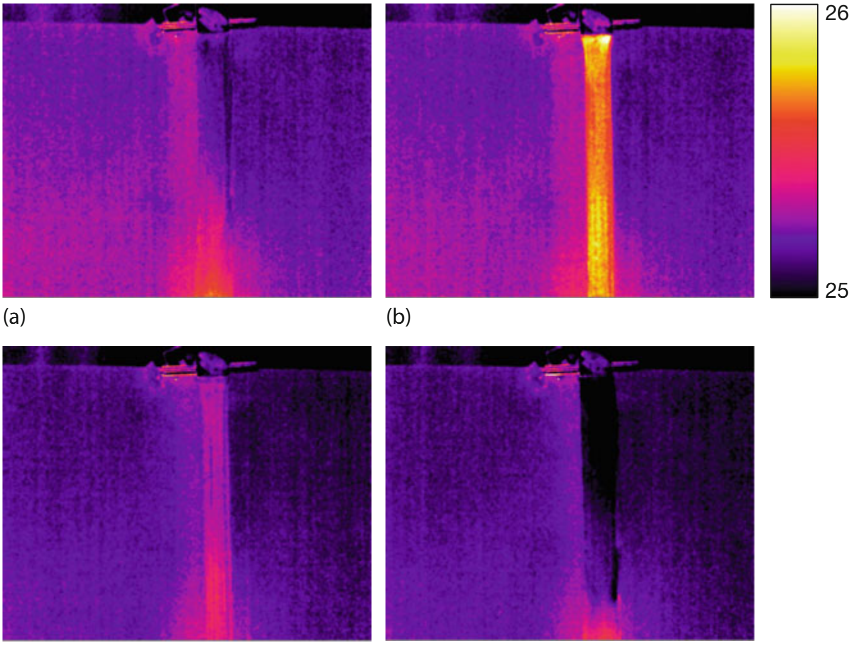

(a) (b) (c) (d)

Figure 5.13 Single stretching (a,b) and letting go (c,d) a rubber band leads to a temperature increase (here 0.9 K) and decrease (here 0.4 K) of the rubber, respectively. Width 4.1 cm, length without force 45 cm, thickness 1 mm.

and cools down when released (e.g., [21]). The temperature difference can easily amount to several Kelvin if the material is stretched by a factor of 3 to 5. Similarly, rubber expands upon a temperature increase and shrinks under a temperature decrease. The thermodynamic theory behind this behavior (which is somewhat similar to the behavior of gases that also heat up when under pressure and cool down when allowed to expand) is quite complex and involves the entropy, that is, the degree of order, associated with the polymer molecules in the rubber band [22]. The heating and cooling can easily be visualized with IR imaging. Figure 5.13a,b shows a rubber band in the LW IR range before and after stretching by a factor of 2. The band heats up by 0.9 K. After waiting a minute for an equilibrium to establish, the band is relaxed and cools down again by about 0.4 K upon the release of the stress (Figure 5.13c,d).

Fast periodic stretching and releasing lead to a larger temperature increase since the rubber cooling takes more time. Figure 5.14 shows the transient behavior of the band under heating and partial cooling in the upper third of the image, allowing for a count of about 20 stretching cycles. Ultimately, the band developed a fissure and broke apart. A maximum temperature of around 39 °C was observed for one of the experiments.

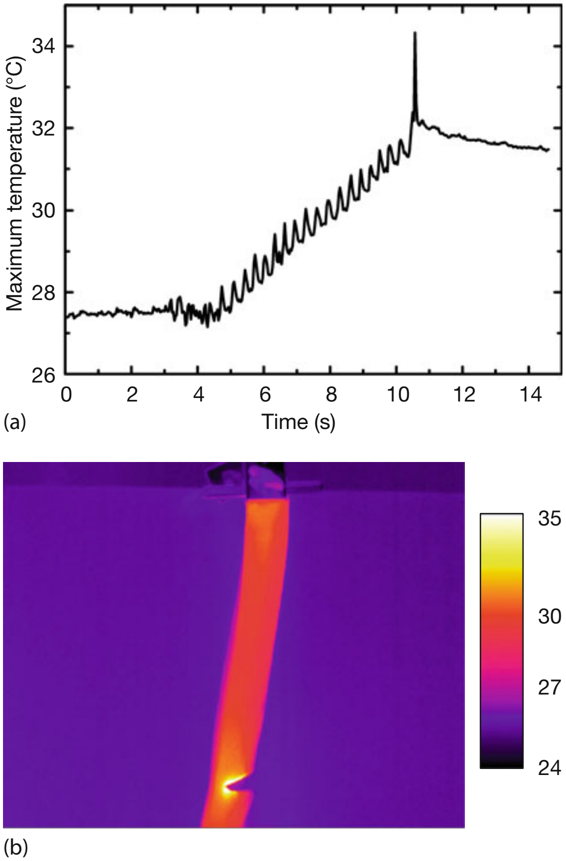

Figure 5.14 Heating and cooling of rubber band upon periodic stretching. The band finally broke apart due to a fissure (scale IR image 24–35 °C).

5.3
Thermal Physics Phenomena

Although nearly all applications of IR imaging involve thermal phenomena, for example, by transforming mechanical or electrical energy into thermal energy and a corresponding heating up of the surface of objects, some purely thermal physics phenomena can be visualized using thermography. These include characteristic properties of heating systems, material properties like thermal conductivity, and convection in liquids. IR imaging can be used to study the effect of phase transitions like in evaporative cooling or the consequences of adiabatic processes like temperature differences due to adiabatic cooling. Finally, IR imaging offers possibilities for quantitative analysis of the heating and cooling of many objects.

5.3.1
Conventional Hot-Water-Filled Heaters

Many indoor heating systems (e.g., wood, coal, or oil stoves or furnaces that use warm-air heating or water-filled radiators) can be analyzed by thermography. For physics teaching, it is very convenient to use hot water heaters whose hot water supply comes from a furnace. The hot water is usually driven by a pump and flows in pipes from room to room, and in each room it also flows through the radiators, which transfer the heat to the room via convection and radiation.

Since the water transfers energy to the heaters, it should be possible to detect a temperature difference between the inlet and outlet pipes of a radiator.

Figure 5.15 depicts a set of two radiator heaters in a lecture room close to a window as well as a vertical pipe system of inflow and outflow water. One of the heaters is turned on, the other is off. The image immediately visualizes the hot inlet water pipe and the slightly colder outlet water pipe. The water enters the radiator from the top, and slightly colder water flows out at the bottom, as expected.

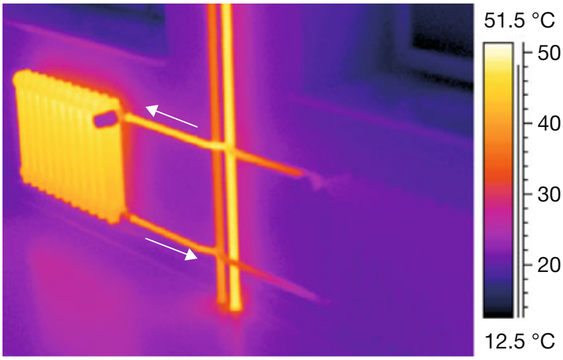

Figure 5.15 Water pipes and radiator heater with hot water inflow and slightly colder water outflow (arrows).

If IR image examples like these are shown when first introducing thermography, the confidence in the method increases. Probably many other well-known everyday-life objects whose surface temperatures can also be measured separately with thermocouples can similarly build up confidence in this measurement technique.

5.3.2
Thermal Conductivities

In Section 4.2.1, conduction of heat was introduced as representing heat flow within a solid or fluid at rest owing to a temperature difference between its ends. The simplest theoretical system, like a one-dimensional (1D) wall that extends laterally indefinitely, can obviously not be measured by thermography. One needs to measure the surface temperature of realistic objects.

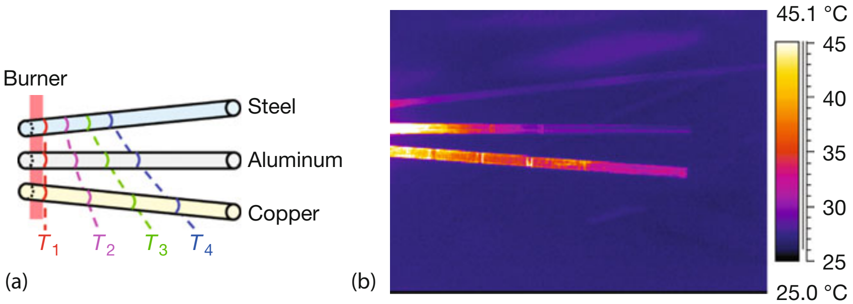

Figure 5.16 Typical setup of experiment to demonstrate thermal conductivity differences of materials (a). After heating has started, the diffusion of heat into the rods proceeds at different velocities, as indicated by the locations of the same temperature along the rods. (b) IR image of such a setup of steel, aluminum, and copper rods, heated from one end (not seen in image) with a Bunsen burner.

A typical setup to demonstrate differences in the thermal conductivity of solid materials is the following (Figure 5.16a). Thin rods of different materials are horizontally fixed in such a way that one of their ends is free and the other end heated (e.g., by flames of a Bunsen burner). Along the length of the rods, small pieces of wax can be attached at regular intervals (not shown in figure). The wax starts to melt at a certain temperature. The melting indicates that the critical temperature has been reached. The experiment is conducted by recording the times at which wax at given locations starts to melt. This allows visualization of the heat diffusion within the rods as a function of time. In particular, at a given distance from the heating location, the wax will start to melt earlier for rods with higher thermal conductivity. This experiment nicely, but only qualitatively, demonstrates thermal conductivity. Unfortunately, it is not thermal conductivity alone that determines the outcome of such an experiment. First, for any quantitative analysis of thermal conductivity, a well-defined temperature difference is needed. Since, however, the rod ends are usually not fixed in a heat bath, but just end in air at room temperature, the entire rods will start to warm up and the end temperature will also increase with time. Second, convective heat losses due to the surface area of the rods and, third, radiation losses will also contribute. As a consequence, it may well be that if these additional losses dominate, the temperature profile would not allow for any precise conclusion concerning the thermal conductivity.

Figure 5.16b presents an IR image of such an experiment. Three rods of the same diameter, made of steel (top), aluminum (middle), and copper (bottom), were heated at one end using a flat-flame Bunsen burner. The thermal conductivities (Table 4.1) increase from top to bottom. As expected, the copper rod with the largest thermal conductivity is heated up much more quickly than the steel and aluminum rods. To avoid saturation of the IR detectors close to the heating zone, it is best to first heat and then record images directly after turning off the heater. All rods were covered with a thin soot layer to ensure equally high emissivities.

A more well-defined setup for thermal conductivity measurements uses a fixed temperature difference between the two ends of a material, in this case water. A particularly simple experiment is depicted in Figure 5.17. An ice cube is crushed, and some pieces are put in a test tube. The tube is filled more or less completely with precooled water around 0 °C. Ice normally floats; therefore, we put a metal weight on top of the ice to keep the pieces at the bottom of the test tube. The ice within the water reaches the lower temperature of 0 °C at the bottom of the test tube. The upper end of the test tube is then heated using a Bunsen burner until the water in the upper few centimeters of the tube starts to boil, defining the upper temperature of 100 °C. The temperatures of 0 and 100 °C will be maintained as long as there is ice in the test tube (latent heat of melting) and as long as the upper parts are still covered by boiling water (latent heat of evaporation). Along the test tube, a temperature profile develops that is mainly governed by the thermal conductivity of the water (the glass has a somewhat larger thermal conductivity). Furthermore, the glass is very thin such that – to the first order – the Biot number can still be assumed to be small compared to unity. This means that the glass surface temperature should more or less resemble the water temperature inside the tube. Figure 5.17 depicts the experimental result from IR imaging. The line plot along the test tube shows that both glass and water are poor thermal con-

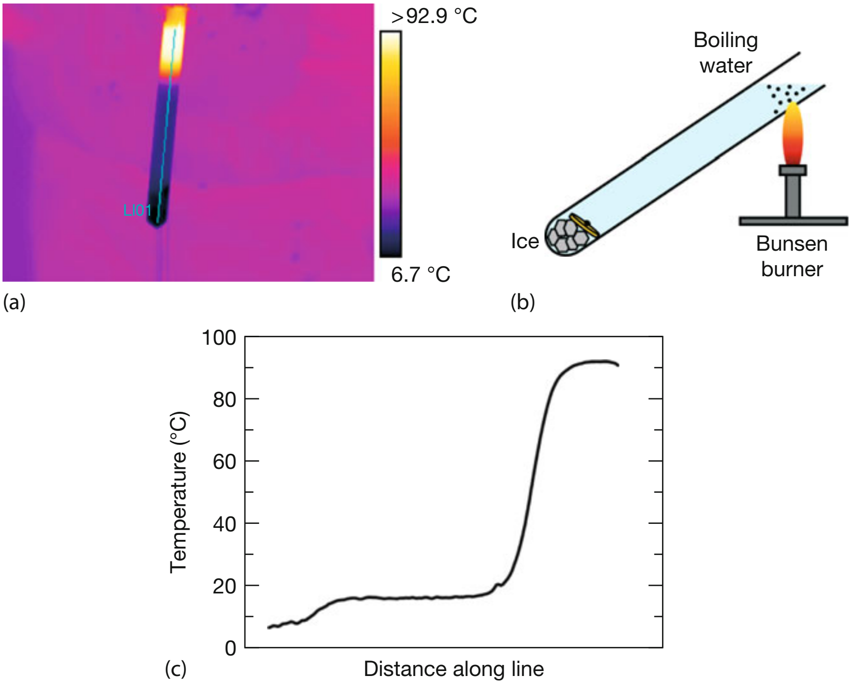

Figure 5.17 (a) IR image and setup for demonstration of thermal conduction in water. (b) The line plot of the temperature reveals ice water at bottom while water at top, recorded directly after turning off the burner, remains around 90 °C.

ductors. The water at the bottom is still around 0 °C, whereas the water at the top has just boiled. Of course, a long wait will also lead to heat conduction, which will eventually equalize the temperatures.

5.3.3
Conduction of Heat in Stack of Paper

A very instructive experiment (we are not sure who first described it) visualizes the conduction of heat from an electric iron to paper. The iron is turned on and placed for a certain amount of time, perhaps 30–60 s, on top of a telephone directory (Figure 5.18c) containing several hundred very thin pages. Then the surface temperatures at the top of the book and of certain pages down from the top are measured. Figure 5.18a,b presents some snapshots from a corresponding video sequence of 100 and 200 pages below the surface. Figure 5.18d shows a semi-quantitative analysis of inner page temperatures while turning the pages, starting from page 500, in 50 page steps to the top. It typically takes about 2 s between measurements of successive data points. Each time a page is exposed to the air, it cools down much faster owing to convection. For example, the top of the book – after removing the iron – had an initial temperature above 160 °C. In air, the page cooled down to less than 95 °C within 6 s. Figure 5.18 nicely visualizes the slow lateral and vertical diffusion of the heat into the paper. In our case, no effect of heat diffusion due to the iron could be detected for more than 300 pages, that is, depths below 7.2 mm.

5.3.4
Convection in Liquids

In Section 4.2.2, convection was introduced as representing heat flow between a fluid and a solid. It is composed of both heat transfer due to conduction in the boundary layer around the solid and heat transfer due to the bulk motion of the fluid that is outside the boundary layer. Both processes are difficult to visualize with IR imaging if the fluids are gases, unless the gases have strong absorption features in the thermal IR region (Chapter 8). Convections due to liquids are easier to observe. Figure 5.19 shows an ice cube floating in a glass beaker filled with water at room temperature. If initially the ice cube and water are just at rest, natural convection starts to build up, that is, water close to the ice cube gets cooler, thereby transferring part of its thermal energy to the cube, which starts to melt at the surface. The colder water has a higher density and will start to sink down in the beaker, thereby transporting warmer water to the surface. These slow convection currents would not be observable with IR imaging since water is not transparent in the thermal IR region (Section 1.5, Figure 1.54). However, the convective bulk motion of the surface water can be made visible by observation from above. The ice cube floats so we can study the water surface convection currents. Since no natural lateral force is driving such currents, the ice cube is given a little bit of an initial spin. Owing to this initial rotary movement, some volume elements of

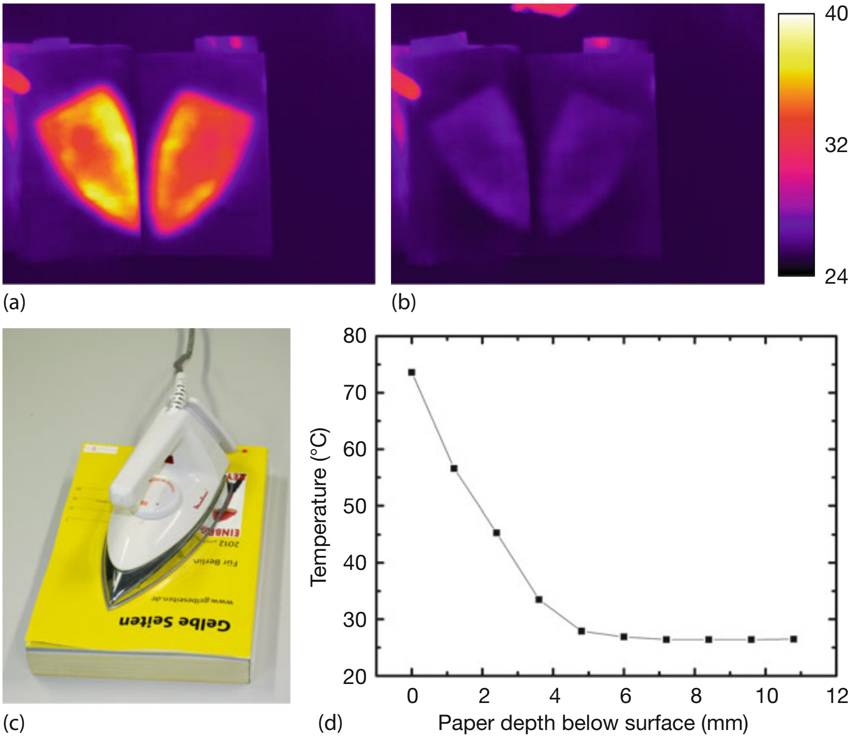

Figure 5.18 After a hot iron was placed on top of a thick phone book (c), the diffusion of the heat into the paper is studied by looking at the temperatures at various pages, that is, depth (a,b). A plot of temperature versus depth illustrates the heat diffusion (d).

the water that have touched the cube and had already cooled down move, that is, they flow away from the boundary layer. Therefore, new water volume elements can get close to the cube, transporting thermal energy from the water at room temperature to the ice cube at around freezing temperature. This leads to melting at the ice cube surface. In Figure 5.19, water with green shades is about 6–7 K cooler than the average water temperature. Figure 5.19 also demonstrates the heat conduction in the boundary layer. The line plot data in a "quiet" region show the expected gradual temperature increase from the ice cube ($T \approx 0\,°\mathrm{C}$) to the average water temperature of about 20 °C. In this case, the steep increase takes place over a distance of about 2 mm. For a nonmoving cube, the distance can easily be greater by a factor of 2. If an ice cube rests at the edge of the beaker in contact with the glass, it is also possible to directly observe the consequences of cold convection currents from the outside of the beaker. This is due to the cold water that would start to sink away from the ice cube inside the beaker, thereby cooling the adjacent glass surface.

Convections involving the transport of larger volume elements of fluids are usually driven by larger temperature differences. A well-known example in nature is

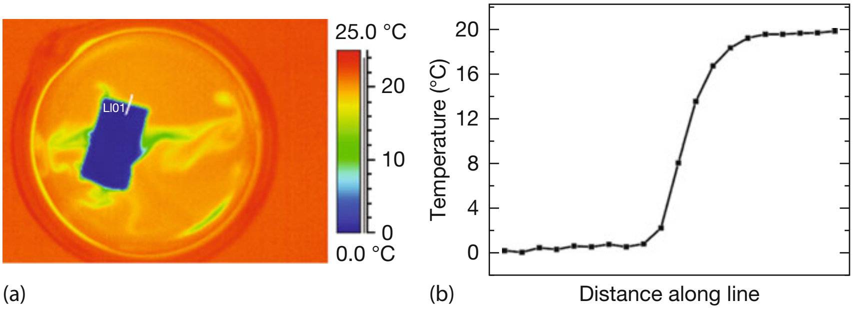

Figure 5.19 (a) Top view of water convection around a slowly rotating ice cube and (b) temperature profile along white line. See text for details.

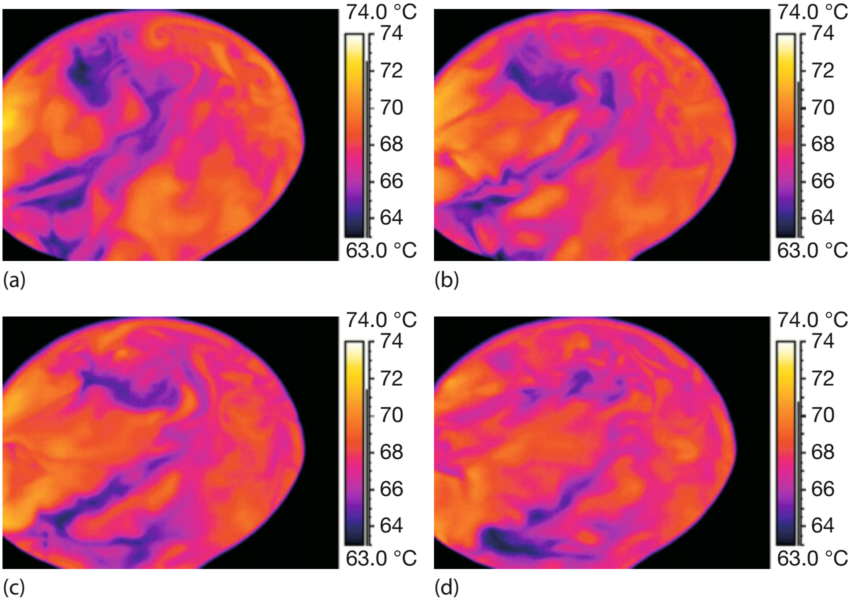

Figure 5.20 Convection features observed from a hot water surface, with the water being heated from below.

the convection cell structure, which can be observed at the surface of the sun. Figure 5.20 depicts a series of IR images, showing convection features of water within a large glass beaker being heated from below. Convection is a transient phenomenon and can be better observed in real time; however, the still images already show how structures are formed and transported across the surface of the water.

Similar convection cells are observable in everyday life when heating oil in a pan to very high temperatures. For appropriate temperature differences and oil thickness, this leads to so-called Bénard–Marangoni convections. Figure 5.21 il-

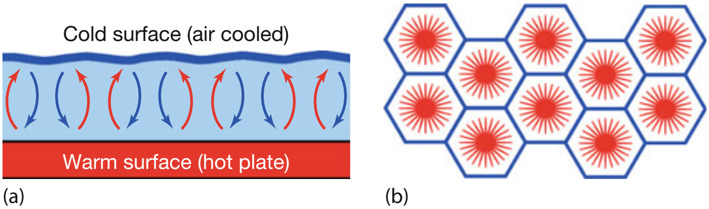

Figure 5.21 Formation of Bénard–Marangoni convections of a liquid heated from below and cooled from above. Warm oil (red) starts to rise, whereas colder oil (blue) sinks (a). This can result in (ideally) hexagonal 2D structures on the surface (b), where the rising oil is in the middle of the cells and the sinking one defines the cell boundaries.

lustrates how these convection structures form. Oil in the vicinity of the lower hot surface is heated and therefore starts to rise because of its lower density. Similarly, the colder and denser oil from the surface starts to sink. Of course, this process cannot take place simultaneously everywhere in the pan. For a given temperature difference, oil thickness, and diameter of the pan, regular cell structures start to form, which allow large quantities of hot oil to rise, while simultaneously the same amount of colder oil sinks to the bottom of the pan. In the 2D sketch of Figure 5.21, closed loops of flowing oil organize in such a way that neighboring loops rotate in opposite directions such that they do not disturb the flow of their neighbors. This process is self-organizing. The form and number of formed cells depend on the conditions, in particular the temperature difference. The complete theoretical modeling needs to take into account the buoyancy forces, temperature-dependent surface tension, and dynamic viscosity of the oil [23]. Since there are regions where colder oil sinks and others where warmer oil rises, a line plot of temperature across the surface will show a regular structure.

Figure 5.22 shows an example of an experimental result, investigated using IR imaging (care must be taken to avoid oil vapor on the camera optics; observe either via a mirror or a thin transparent plastic foil acting as a protective window). The oil was 3 mm thick and had a total diameter of about 9.5 cm. The structures start to form well above 100 °C. For constant temperature the cell structure is stable;

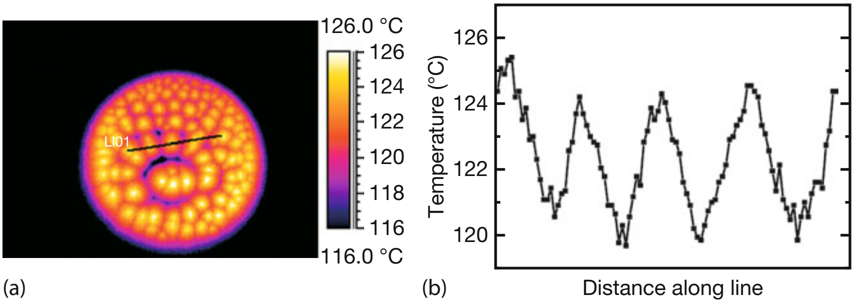

Figure 5.22 IR image of Bénard–Marangoni convection cells of oil in a pan, heated to about 120 °C (a). Convection leads to well-defined temperature variations across the surface (b).

however, its geometry and number density change with temperature. The temperature differences between the rising and sinking oil amount to about 4.5 K in Figure 5.22. In a pan heated to 150 °C, we observed T variations of up to 9 K.

Some expert cooks who want to prepare steaks in a pan use these convection cells as an indicator of the oil temperature. It is rather easy to observe the convection cells with the naked eye when looking at grazing incidence at the oil surface. The oil is not hot enough unless cells start to form.

5.3.5
Convection Effects Due to Gases

A simple demonstration of convective thermal effects of gases is breathing. Figure 5.23 shows two snapshots of inhaling and exhaling through the nose, recorded with an LW camera approximately vertically below the nose. The temperature of the observed portion of the inside of the nose is typically around 35 °C. While inhaling, the colder room temperature air decreases temperatures by nearly 10 °C to around 25 °C, whereas exhaling brings about elevated temperatures owing to the warmed air from the lungs. Portraitlike images indicate the temperature differences, but close-up images are more impressive. Similar though somewhat smaller temperature differences can be observed while inhaling and exhaling through the mouth.

5.3.6
Evaporative Cooling

The idea behind evaporative cooling can be gleaned from the following description of an ancient cooling system: "In the Arizona desert in the 1920s, people would often sleep outside on screened-in sleeping porches during the summer. On hot nights, bedsheets or blankets soaked in water would be hung inside the screens. Whirling electric fans would pull the night air through the moist cloth to cool the room" [24]. The same article [24] by the California energy commission also emphasizes that many new technologies have been inspired by this principle of evaporative cooling.

The physics behind evaporative cooling is quite simple. It requires air with relative humidity below 100% (Section 4.3.6) that is directed over water, wet surfaces, or through wet blankets. While passing over the given water surfaces, water molecules change their phase state from liquid to gas. Thus, the water molecules become part of the airflow, which will then have a higher humidity.

This phase change from liquid to gas does, however, require energy, to be specific, the heat of vaporization, which amounts to about $2400\,\text{kJ}\,\text{kg}^{-1}$ at around 30 °C (sometimes this number is also given as $43\,\text{kJ}\,\text{mol}^{-1}$, that is, as energy needed to vaporize 1 mol, here 18 g, of water or as 0.45 eV/molecule, where the fact that $1\,\text{eV} = 1.6 \cdot 10^{-19}\,\text{J}$ and 1 mol of water contains $6.022 \cdot 10^{23}$ molecules is used). This is an enormous amount of energy that must come from the water, the air, or both. Therefore, there should be two observable effects: both the water and the air

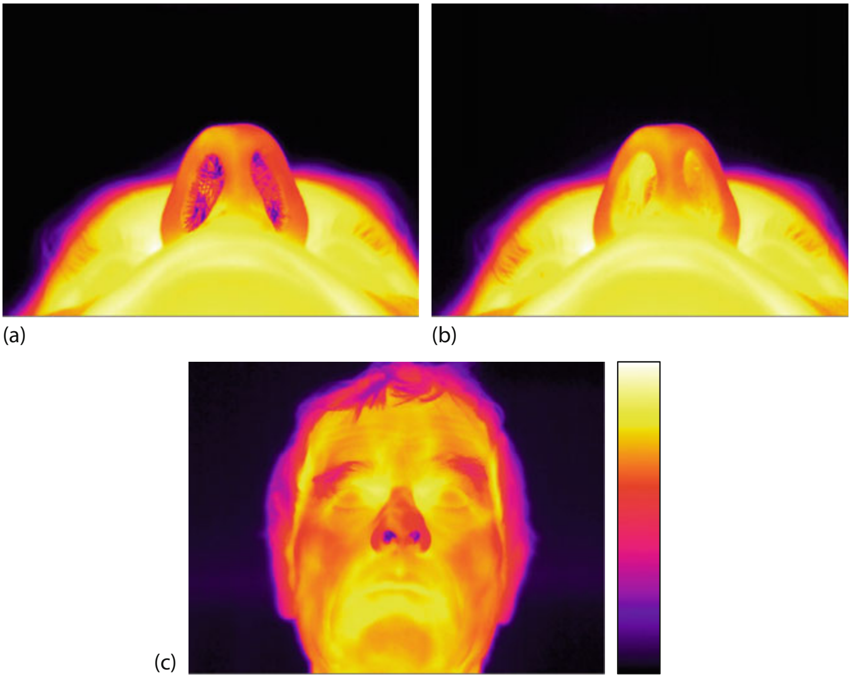

Figure 5.23 Temperature differences due to inhaling (a,c) and exhaling (b) air through the nose. *T* scale for close-ups (a,b): 24–36 °C, for portrait (c): 24–38 °C.

should cool down. The latter effect was described earlier: the hot air being pulled through the wet blankets loses part of its thermal energy, which is transferred to the blankets, providing the energy for evaporation. In dynamic equilibrium, the blanket temperature would not change anymore, and the energy needed for the evaporation of water per time unit would be transferred to the blanket from the air.

Obviously, IR imaging is not able to detect air temperature; rather, the temperature of wet surfaces that are exposed to airflow will be studied. For experiments, various liquids such as water and aftershave lotion (which contains alcohol) are used. It is well known that a lotion containing alcohol will lead to a much more dramatic cooling effect compared to the same amount of pure water. Although water and ethanol have about the same heats of vaporization (40–45 kJ mol^{-1}), they behave quite differently. This means that there is at least a second ingredient in evaporative cooling: the vapor pressure of the liquid at given ambient conditions. As shown in Figure 5.24, the saturation vapor pressure over a liquid increases sharply with temperature. The *saturation pressure* is defined as the equilibrium vapor pressure above a liquid. This means that some molecules will evaporate per time interval from a liquid (from liquid to gas phase) and some gas molecules will condense at the liquid again (from gas to liquid phase). For any given temperature, there is an equilibrium at which equal amounts of molecules evaporate

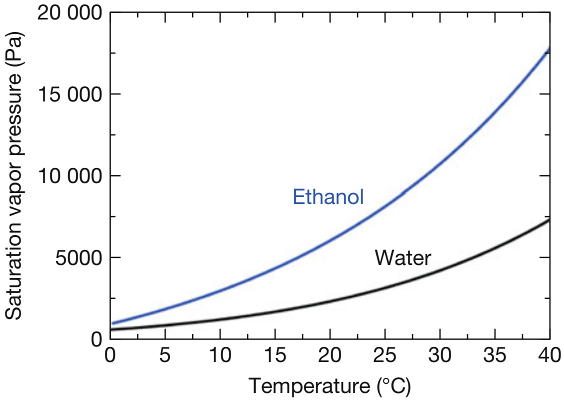

Figure 5.24 Saturation vapor pressure of ethanol and water. The differences are due to the lower boiling temperature of 78 °C, that is, the ethanol vapor pressure reaches the atmospheric pressure of about 1000 hPa already at 78 °C.

and condense. In this case, the gas pressure (being related to the number density of molecules in the gas phase) is the saturation vapor pressure. As shown in Figure 5.24, at any given ambient temperature between 10 and 30 °C, the ethanol vapor pressure is at least twice as large as that of water. As a consequence, compared to the evaporation of water molecules, twice as many molecules of ethanol vapor can evaporate, that is, the evaporative cooling effect can be much greater.

Two more factors that influence evaporative cooling are the relative humidity of the air and the speed of the airflow. If the air is already saturated with water vapor, it cannot accommodate more water. In this case, evaporative cooling cannot take place. The speed of the airflow can enhance evaporation quite significantly. This is plausible since air in close contact with water will acquire higher values of relative humidity, and so it can accommodate less water vapor. Blowing fresh air of lower relative humidity toward the water surface will therefore enhance evaporation. In addition, as was pointed out in Chapter 4 (Figure 4.4), the convective heat transfer coefficient increases with increasing airflow velocity. Therefore, larger amounts of energy for the vaporization of water vapor are available.

Figure 5.25a,b shows a water film on the wall surface of a house model. A warm air fan was directed onto the wall and the IR images were recorded. Owing to evaporative cooling, the wet wall segment was strongly cooled initially, although warm air was used. Later on, after equilibrium was established, the wall temperature remained constant. The consequences for building thermography are discussed in Chapter 7.

Similarly, Figure 5.25c,d depicts evaporative cooling following the use of aftershave. The ethanol rapidly evaporates, especially if air from a warm air fan is used, giving rise to enhanced cooling.

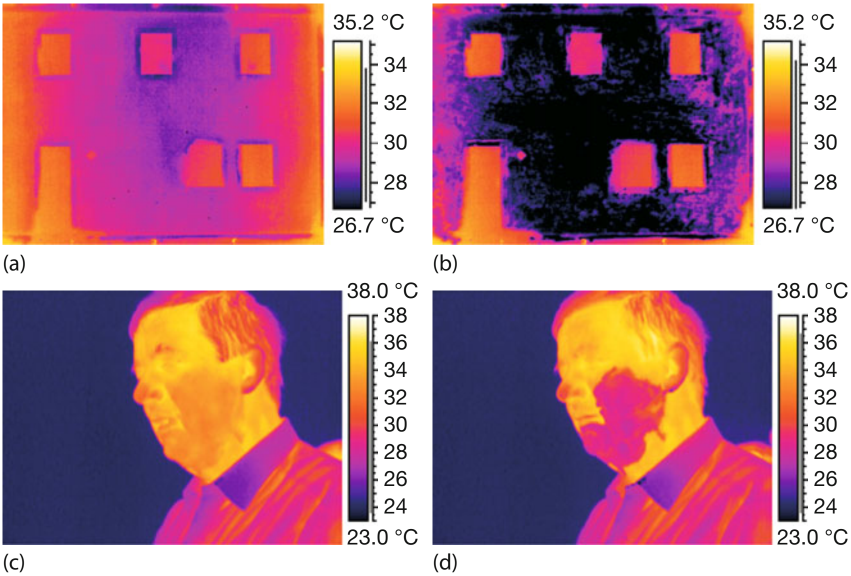

Figure 5.25 (a,b) Evaporative cooling due to water. A wet surface of a house model cools rapidly due to evaporative cooling, enhanced by a warm air fan (see Section 7.4 for details). (c,d) Evaporative cooling due to ethanol in aftershave, enhanced by a warm air fan.

5.3.7
Adiabatic Heating and Cooling

The state of a gas is usually characterized by three quantities. The most commonly used quantities are pressure, temperature, and volume; another is entropy. There are many ways of changing the state of a gas; for example, one may keep one of these quantities constant and change the other two. Two processes that are very important for technical applications are the so-called adiabatic expansions or compressions, the characteristic features of which are due to energy conservation.

Whenever a gas is compressed, work is done on the gas, which will lead to a change in its internal energy (which microscopically can be regarded as energies of the gas molecules). The first law of thermodynamics is a statement of energy conservation. It states that the internal energy of a gas can only change as a result of either heat transfer to/from the gas or work done on/by the gas. In most state changes of a gas, heat and work are exchanged. However, adiabatic processes are different. They take place too quickly for thermal equilibrium to be established, and therefore adiabatic processes take place without an exchange of heat. As an example, we consider the very fast compression of a gas. Assume that a gas is in a container with a movable piston. A typical example from everyday life would be a pump for bicycle tires with a closed outlet valve. If the piston is moved inward very rapidly (to compress the gas), there is no time for an exchange of heat, that is, the compression takes place as an adiabatic process. In such cases, the work done

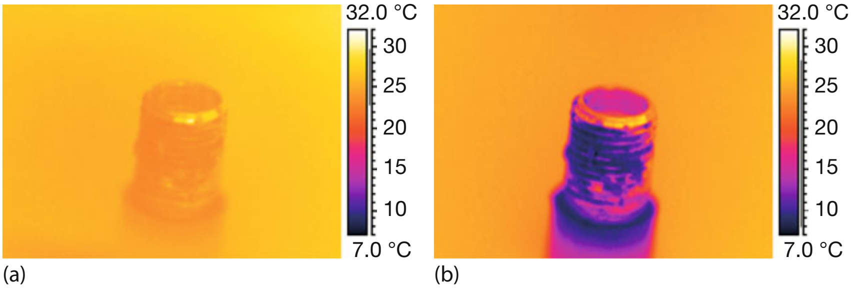

Figure 5.26 Valve of an automobile tire before (a) and after (b) opening the valve. Adiabatic cooling of expanding air from a bicycle tire also leads to a cooling of the valve with a large temperature drop.

during compression is entirely transformed into internal energy of the gas. As a consequence, it will heat up rapidly. Anyone who uses a bike hand pump knows that holding the pump close to the valve will cause the pump to get warm quickly since the hot gas inside will ultimately also lead to a warming of the containing metal or plastic tube.

We illustrate the reverse process, the adiabatic expansion of a gas, with IR imaging. Expansion of a gas requires that work be done (imagine that the gas moves a piston outward upon expansion). Since heat exchange is not possible, the energy needed for this work must come from the gas itself, that is, the gas must reduce its internal energy, which is accompanied by a temperature decrease. This means that any adiabatic expansion will result in a decrease in the gas's temperature. Such adiabatic processes may be brought about simply through the use of a bicycle tire that is pressurized to 3 bar. Opening the valve leads to a rapid expansion through the valve. Therefore, the gas needs to cool down. The cold airstream touches the valve and leads to a cooling of the valve. This is illustrated in Figure 5.26. We can easily observe valve temperatures as low as 3 °C.

Holding a piece of paper originally at 23 °C (ambient temperature) in front of an expanding airstream leads to a rapid cooling of the paper to around 5–7 °C, which is below its dew point at 50% relative humidity, that is, the paper gets wet during the cooling process.

A nice everyday experiment along the same lines is the opening of a bottle of champagne [25, 26]. The cooling of the gas streaming out causes condensation of water vapor from the surrounding air.

5.3.8
Heating of Cheese Cubes

Several examples of heating and cooling of objects like metal cubes and light bulbs were presented in Sections 4.4 and 4.5. In this section and Section 5.3.9, we present additional examples related to the heating and cooling of certain objects. Some of these examples very effectively illustrate the general physical principles

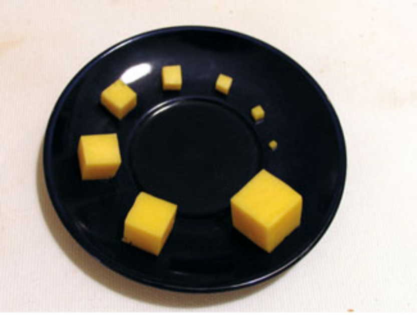

Figure 5.27 Differently sized cheese cubes on a plate set in a conventional or microwave oven.

of convection and radiation. In all cases, we assume small Biot numbers, that is, that the surface temperatures are somewhat close to the average temperatures of the objects (Section 4.3.2).

The first example [27] deals with cheese cubes. Imagine a piece of solid cheese, such as Gouda or cheddar, that contains no air holes. Cut the cheese into several, say 6–8, small cubes from 2 to 15 mm in size. Arrange the cubes in a circle on a small plate (Figure 5.27) and set the plate in a conventional electric oven preheated to 200 °C.

Question: What will happen to the cheese cubes? Will the small ones melt before the large ones, or will all cubes melt at the same time, or will some not melt at all? (The answer to this and the following question is given below so readers can think about it before finding out the solution.)

After tackling this introductory problem, repeat the experiment, that is, prepare an identical set of cheese cubes on an identical plate, but one that is microwavable. Then place the plate in a microwave oven set at full power (e.g., 800 W). The heating should take place for an integer number of revolutions of the turntable; this ensures that all cubes will experience the same microwave fields inside the oven. The question will be the same as before: What will happen to the cheese cubes? Will the small ones melt first or the large ones, or will all cubes melt at the same time, or will some cubes not melt at all?

Figure 5.28 shows the results of the cheese cube experiments heated in a conventional (Figure 5.28a) and a microwave oven (Figure 5.28b). In the conventional oven the small cubes will start to melt first, as demonstrated by the rounding off of the corners. In contrast, the cubes behave totally differently in a microwave oven. The largest cubes melt first, and cubes that are smaller than a critical size will not melt at all. Obviously, the different behaviors must be due to the different heating and cooling processes involved.

The temperature of the air within the conventional oven is much higher than the cheese temperature. Therefore, energy flows from the oven through the surface of the cubes into the cheese. The smaller cubes get heated throughout their interior much faster than the large ones and, hence, melt first. In contrast, heating in the microwave oven happens via the absorption of microwave radiation in the interior of the cheese cubes [28]. However, since the air temperature in the oven is about ambient temperature, the heated cheese cubes also start to cool via

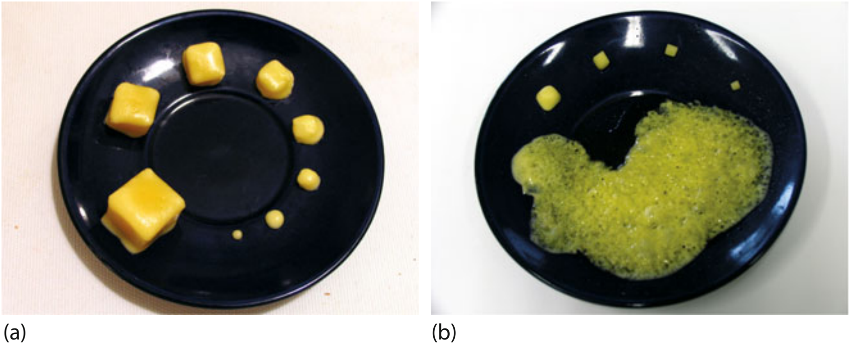

Figure 5.28 In the conventional preheated electric oven (a), the cubes were heated at 200 °C for about 70 s. The microwave oven (b) was operated at 800 W for about 30 s.

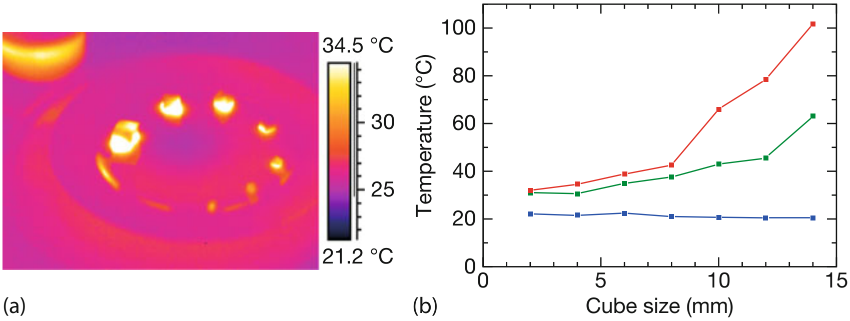

Figure 5.29 Cheese cubes after 10 s of heating (800 W) in a microwave oven (a) and measured maximum temperatures of cubes before (blue, bottom), after 10 s (green, middle) and after 30 s (red, top) of heating (b).

convection and radiation. The cooling power will be proportional to the surface area of the cubes, whereas the heating will be proportional to their volume. As a consequence, the surface-to-volume ratio determines the equilibrium maximum temperature of a cube. The smallest cubes will undergo the most dramatic cooling. Eventually, this can even prohibit melting. The equilibrium temperature will increase with cube size. This is shown in Figure 5.29, which shows the situation after 10 and 30 s of heating. Quantitative analysis revealed a strong dependence of temperature on cube size, and the temperatures of the largest cubes exceeded the melting temperatures of the cheese.

The heating and cooling of cheese cubes in the microwave oven can also be easily treated theoretically [27]. The power absorbed by each cheese cube of size a is proportional to its volume:

$$\frac{\mathrm{d}W_{\mathrm{abs}}}{\mathrm{d}t} = P_{\mathrm{absorb}} \propto V = k_1 a^3 \tag{5.1}$$

where k_1 is a constant that depends on the absorption coefficient of microwaves in cheese. The cooling, which is due to convection and radiation (Section 4.2), can

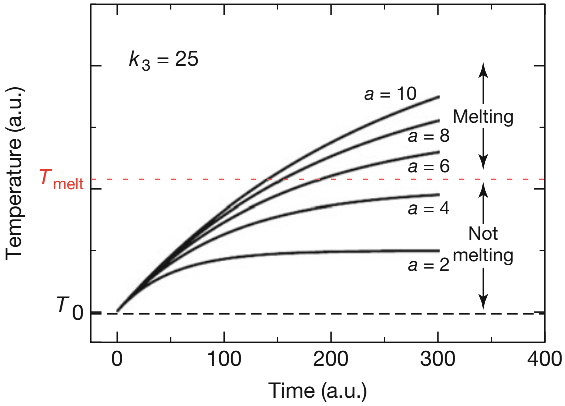

Figure 5.30 Temperatures of cheese cubes of different sizes a as a function of heating time in a microwave oven for a given value of $k_3 = 25$.

be approximated by

$$P_{\text{cool}} = k_2 \cdot a^2 \cdot (T_{\text{cheese}} - T_{\text{oven}}) \tag{5.2}$$

It depends linearly on the temperature difference between the cheese and its surrounding. The effective absorbed power leading to a temperature rise of the cheese is due to

$$P_{\text{eff. heating}} = P_{\text{absorb}} - P_{\text{cool}} \tag{5.3}$$

This leads to the differential equation

$$P_{\text{eff. heating}} = c \cdot m \cdot \frac{\mathrm{d}T}{\mathrm{d}t} = k_1 \cdot a^3 - k_2 \cdot a^2 \cdot (T(t) - T_0) \tag{5.4}$$

with the solution

$$T(t) = T_0 + \frac{k_1}{k_2} a \left[1 - \mathrm{e}^{-\frac{t-t_0}{\tau}}\right] \tag{5.5}$$

with the time constant $\tau = k_3 a$ ($k_3 = c\rho/k_2$, c: specific heat, ρ: density). Despite not knowing exact values for the constants, it is possible to plot the general form of $T(t)$ (Figure 5.30) for different values of cube size a. It follows from Eq. (5.5) that the temperature of each cube eventually reaches the asymptotic equilibrium value $T_0 + k_1/k_2 a$. If this temperature is below the melting temperature, the cheese will never melt. An interesting feature of Eq. (5.5) is that since the time constant τ is proportional to the cube size, the time until the maximum temperature is reached at equilibrium is shortest for small cubes. As shown in Figure 5.30, only the smallest cubes have reached the maximum possible temperature, whereas the largest cubes are still far from equilibrium. For $k_3 = 25$, we find, for example, $\tau = 50$ for $a = 2$, $\tau = 100$ for $a = 4$, $\tau = 200$ for $a = 8$, and so forth.

More details on this experiment can be found in [27].

5.3.9
Cooling of Bottles and Cans

The next example is an everyday experiment dealing with Newton's law of cooling (Section 4.5). Whenever an object of temperature T_{obj} is in a surrounding of lower temperature T_{surr}, it will cool down due to conductive, convective, and radiative heat transfer. Because of energy conservation, the heat transfer must lead to a decrease in thermal energy and, hence, in the temperature of the object. The cooling process can be described by

$$mc\frac{\mathrm{d}T_{\text{obj}}}{\mathrm{d}t} = -(\alpha_{\text{C}} + \alpha_{\text{R}}) \cdot A \cdot (T_{\text{obj}} - T_{\text{surr}}) \quad \text{where} \quad \alpha_{\text{R}} = \varepsilon \cdot \sigma \cdot k_{\text{appr}} \tag{5.6}$$

where m is the mass of the object, c its specific heat capacity, A its surface area in contact with the colder surroundings, and α_{i} corresponding heat transfer rates (Chapter 4). This differential equation has the solution

$$T_{\text{obj}}(t) = T_{\text{surr}} + (T_{\text{Init}} - T_{\text{surr}}) \cdot \mathrm{e}^{-t/\tau} \quad \text{with} \quad \tau = \frac{\rho c V}{(\alpha_{\text{C}} + \varepsilon \cdot \sigma \cdot k_{\text{appr}})A} \tag{5.7}$$

Here T_{Init} is the initial object temperature at the start of the cooling process, ρ its density, and V its volume. Equation 5.7 means that if Newton's law of cooling is satisfied, we expect an exponential decrease in the temperature difference with time, that is, a straight line in a semilogarithmic plot (Section 4.5). This expectation was checked by studying the cooling of soft drink cans and bottles. Particularly in summer time, the cooling of liquids in refrigerators is important. As two examples we present the cooling of cans and bottles filled with water (or other

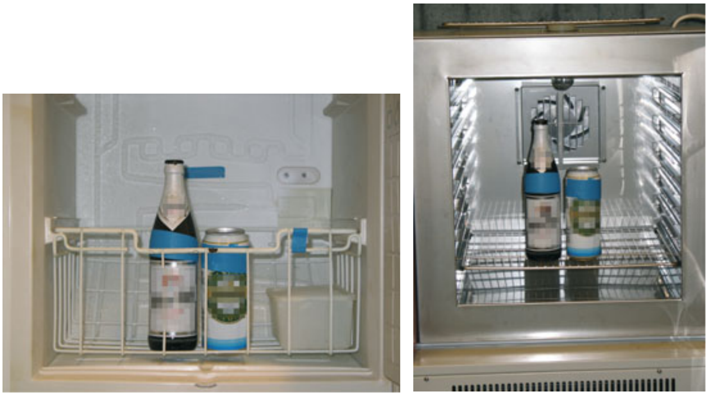
(a) (b)

Figure 5.31 Cooling cans and bottles of liquids in a conventional refrigerator ($T_{\text{final}} = 6\,°\text{C}$, not shown), a freezer ($T_{\text{final}} = -22\,°\text{C}$) (a), and an air convection cooler ($T_{\text{final}} = -5.5\,°\text{C}$) (b). A tape of known emissivity ($\varepsilon = 0.95$) was attached to the bottles and cans.

liquids) as a function of time for different cooling methods. Figure 5.31 shows the experimental setup.

The cooling power of the systems is expected to differ significantly. The conventional refrigerator and freezer both hold objects surrounded by still air, since the temperatures are usually too low to generate natural convections. Hence, the heat transfer coefficients and the cooling time constants of both should be the same. However, the refrigerator shows a smaller temperature difference than the freezer; therefore, the cooling power of the freezer is greater and the effective cooling times (times to reach a certain low temperature upon cooling) are smaller than in the refrigerator. The air convection cooler should have the fastest cooling time since the convective heat transfer coefficient increases strongly with airflow velocity. Therefore, the time constant should also decrease.

As samples, we used glass bottles and aluminum cans. A (blue) tape was attached to ensure equal emissivity values for all samples. The containers were filled with water slightly above room temperature and placed inside the refrigerator, freezer, and air convection cooler. During temperature recordings with the IR camera, taken every few minutes, the cooling unit doors were opened for at most 25 s each. Figure 5.32 shows the resulting plots of temperature difference between measured temperature and ambient temperature within the cooling system on a logarithmic scale. From Newton's law a straight line is expected. Obviously, this holds quite well for any cooling mechanism down to around 0 °C (indicated by the broken horizontal lines), where the phase transition of water to ice imposes a natural limit. At the end of the experiments in the freezer and air convection cooler, we indeed observed small pieces of ice floating on the surface of the water in the bottle and can.

The time constants τ from quantitative fits to the data agree well with theoretical expectations from Eq. (5.7). For the freezer and the refrigerator, $\tau \approx$ 8300–8400 s, whereas for the air convection cooler, the value of τ is halved. This is due to the increased convective heat transfer coefficient. Theory also accounts for the differences (a factor in τ of about 1.2) between cans and bottles. On the one hand, it is due to the different amounts of water; on the other hand, it is due to the differences in the stored thermal energy in the glass of the bottle as compared to that in the aluminum can.

Users of cold drinks are usually not interested in time constants; rather they would like to know when a drink will reach a certain temperature. Figure 5.33 depicts the experimental cooling curves for the 0.5 L bottles (linear scale). The initial temperature was about 28 °C. The refrigerator has the longest cooling time, whereas the air convection system cools fastest, in about 30 min from 28 °C to below 13 °C.

Obviously, from daily experience, an even faster way of cooling would use forced convective cooling with liquids rather than gases (placing bottles, for example, in a small cold-water river) due to the large density difference between gas and liquid.

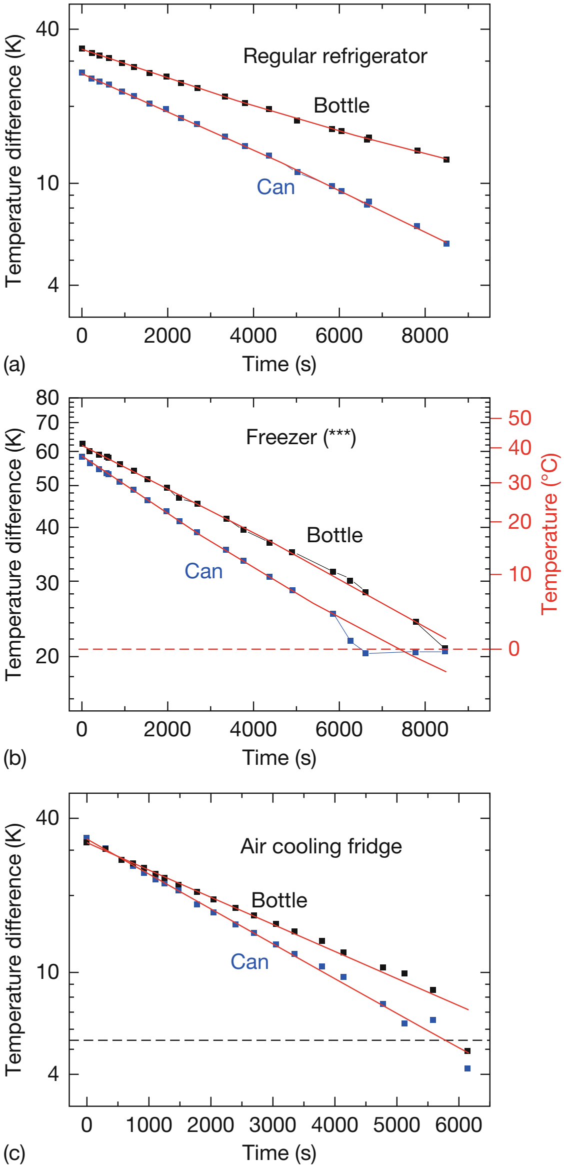

Figure 5.32 Cooling curves of can and bottles for a regular fridge, a freezer, and an air convection cooler. All plots can be fitted with a simple exponential, that is, they follow Newton's law of cooling.

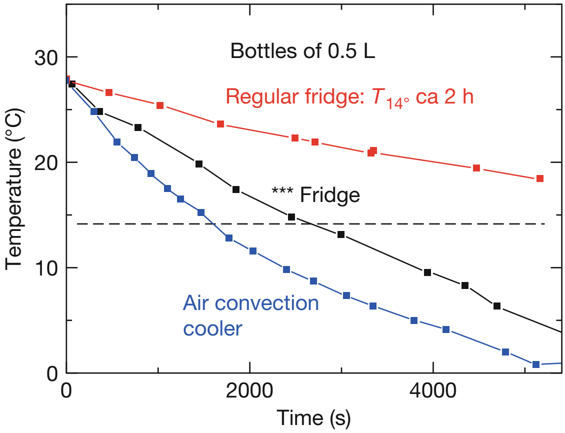

Figure 5.33 Cooling curves of 0.5 L bottles for a regular fridge, a freezer, and air convection cooler. The typical timescale for cooling from 28 to below 14 °C (which may be a suitable drinking temperature) is more than 2 h for the fridge, about 45 min for the freezer, and less than half an hour for the air convection cooler.

5.4
Electromagnetism

5.4.1
Energy and Power in Simple Electric Circuits

In any simple electric circuit that follows Ohm's law [11–13], electrical energy is transformed into internal thermal energy inside the resistor, manifesting itself

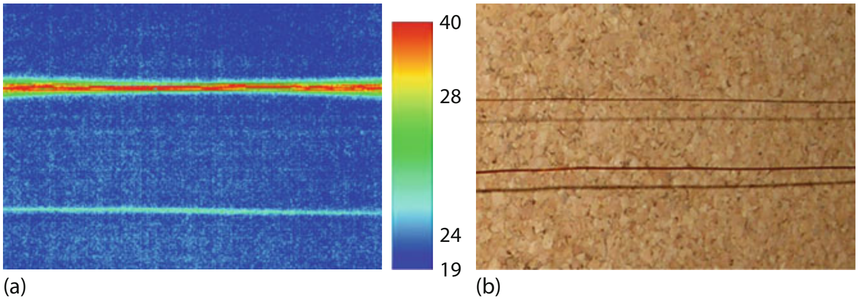

Figure 5.34 The electrical energy associated with a current flowing through a wire is dissipated, leading to a temperature rise of the resistor, that is, the wire (a). The (nonlinear) color bar spans a range from 19 °C (blue) to 40 °C (red). The VIS image (b) in front of a cork board also shows the wire shadows.

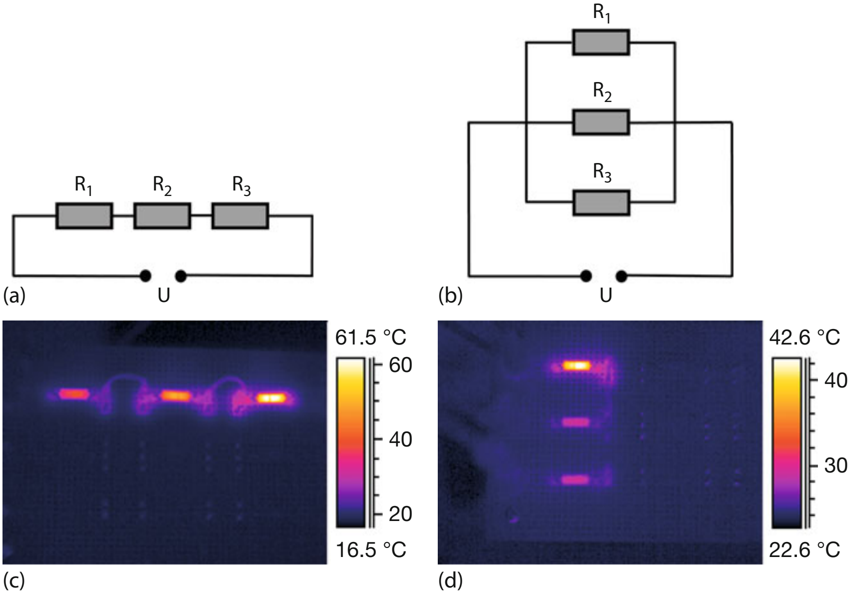

Figure 5.35 Scheme of three different resistances (a) in series and (b) in parallel as well as the corresponding IR images (c,d).

as a temperature rise of the resistor. Obviously, IR imaging can easily visualize this direct thermal consequence of electric currents through resistors. Figure 5.34 illustrates the simplest electrical circuit: a wire connected to a power supply. The wire itself is the resistor, which warms up while current is flowing through it. The wire need not be straight; it could be a coil or a wire spiral as in light bulbs. In the image, two copper wires of different diameters, 0.25 (top) and 0.55 mm (bottom), were used with the same current of 0.5 A. As expected, the thin wire became very hot, whereas the thick wire warmed up only slightly.

Figures like 5.34 can also visualize how the heating of a constant diameter wire is the same everywhere, for example, before and after a coil. This may help to eliminate misconceptions of students that a current may lose some of its "power" while traveling through a circuit, leading to less energy dissipation behind a coil.

Usually, in electrical circuits, metal wires are just the connecting elements. It is straightforward to design the next simple circuits with wires and resistors of varying sizes. Figure 5.35 shows series and parallel circuits of several resistors. Obviously, the resistors heat up according to the power $P = R \cdot I^2$ dissipated within them. Measurement of the surface temperatures of these resistors then allows for sorting them by size. Quantitative analysis, that is, finding the exact value of R from the surface temperature, is a more complex problem. In this case, all heat transfer modes, conduction, convection, and radiation must be treated. In any case, studying various combinations of resistors with IR imaging may be a nice visualization of Kirchhoff's rules in simple electric circuits.

5.4.2
Eddy Currents

Faraday's law of induction [11–13] leads to a phenomenon called an *eddy current*. When a conducting material in the form of a loop is exposed to a changing magnetic field, Faraday's law states that an electromotive force is induced. In a closed loop, this leads to a ring current. Any current in a conductor will dissipate energy according to $P = I^2 \cdot R$, that is, the current should heat up the object. The same thing happens if conductors of arbitrary geometrical form are exposed to changing magnetic fields. In any case, electromotive forces are induced that lead to closed-loop currents within the conductor, raising the temperature of the conductor. These are called *eddy currents*. These circulating currents by themselves create induced magnetic fields that oppose the change in the original magnetic field due to Lenz's law.

The effect of eddy currents can be made visible using IR imaging. Figure 5.36 shows the setup for a popular physics demonstration, the jumping ring experiment [29–31]. A nonmagnetic metal ring is placed on top of a solenoid over the core of a U-shaped demountable transformer unit. When AC power is applied to the solenoid, the ring is thrown off since the induced eddy currents induce secondary magnetic fields that are opposed to the primary magnetic field.

The heat generated by the eddy currents can be made visible by preventing the ring from being thrown off. Holding it in one's hand is not very wise; we arranged for a metal bar several centimeters above the solenoid to serve as a mechanical stop. Applying AC power to the solenoid leads to an upward acceleration of the ring. It comes to a stop at the metal bar, where it levitates for the rest of the experiment. Owing to the AC magnetic fields, eddy currents are permanently induced, that is, heat is continuously generated according to $P = I^2 \cdot R$, which leads to a rapid heating up of the ring. Figure 5.37 presents an example as observed after several seconds. One may study the heating as a function of time and changes due to different ring materials (e.g., copper vs. aluminum) or initial temperatures (e.g., −196 °C vs. 20 °C).

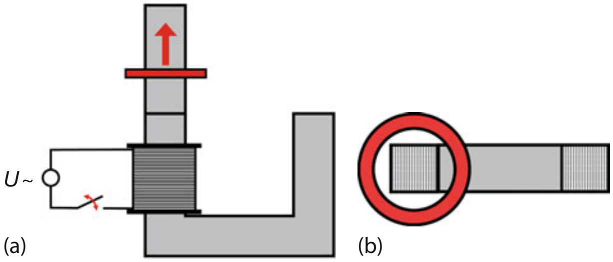

Figure 5.36 Setup for jumping ring experiment (a) from side and (b) from top. A conducting nonmagnetic metal ring (red) is placed over the extended vertical core of a demountable transformer.

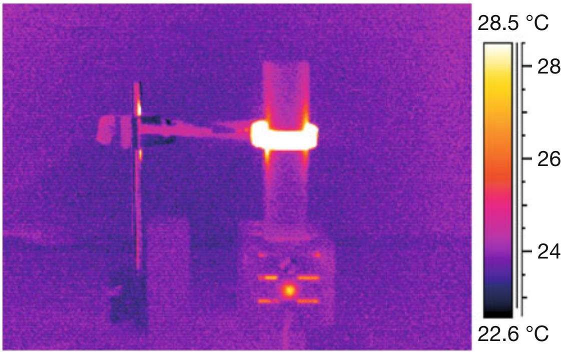

Figure 5.37 Eddy currents induced in a metal ring by an AC magnetic field in the solenoid of an open transformer unit led to a rise in temperature of the ring, which was stopped by a mechanical bar.

5.4.3
Thermoelectric Effects

A number of thermoelectric effects [32] are exploited in physics and technology (see also Section 1.7.2.1). Temperature measurements with thermocouples use the Seebeck effect (Figure 5.38a).

Two different metals, A and B, are joined at two points. If a temperature difference occurs between these two contact points, a small electric voltage U_{th} (typically, in the microvolts per Kelvin range) is produced that drives a thermoelectric current. The physics behind the effect is as follows: for each metal there exists a well-defined work function, which describes the minimum energy needed to remove an electron from the metal surface. If two different metals with differing values of their work functions touch each other, electrons will be transferred from the metal with the lower work function to the one with the higher work function. This leads to a contact potential. If two metals are bent such that they touch each other at two ends, the same contact potentials will result, that is, they will cancel each other. However, the number of electrons transferred from one metal to the other depends on the temperature of the contact point. Therefore, a temperature difference between the two contact spots of two metals in Figure 5.38 will lead to

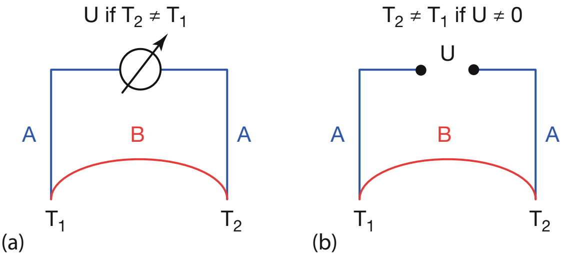

Figure 5.38 Thermoelectric Seebeck (a) and Peltier effects (b) for two metals A and B.

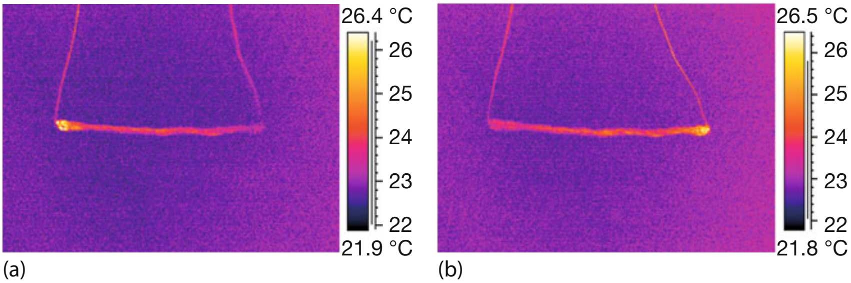

Figure 5.39 Demonstration of Peltier effect with wires of two different materials (vertical wires, copper; horizontal wire, constantan), which produce a thermoelectric force of 42.5 μV K^{-1} in a temperature range from −200 to 500 °C.

a net potential difference U_{th} that depends on temperature. After calibration, this voltage is used for a quantitative measurement of temperature. In conclusion, the Seebeck effect creates a potential difference (i.e., a voltage) from a temperature difference.

The opposite effect, called the *Peltier effect* (Figure 5.38b), uses an electric current to generate a temperature difference. In this case, an electric current is driven through a bimetallic circuit that is maintained at uniform temperature. Heat is generated at one junction, leading to an increase in temperature, and heat is extracted at the other junction, leading to a cooling of the junction. The direction of the current and the contact potentials determine which contact point is heated and which is cooled. Figure 5.39 provides an example using two copper wires (vertical) and one constantan wire. A direct current of 3 A leads to heating of one connection and cooling of the other (a). The effect is reversed if the direction of the current is reversed (b).

In this (macroscopic) experiment, the constantan wire was made much thicker (several parallel wires) since it has a higher resistance than the copper wire. If a single wire is used, the dissipation of energy by its resistance alone (the I^2R joule heat) would lead to a homogeneous heating along the wire, which would cover up the small effect due to the Peltier effect. Nowadays, the Peltier effect is widely used in microscopic setups of cooling systems for microelectronics and detectors (Section 9.5.2).

5.4.4
Experiments with Microwave Ovens

Microwave ovens, which are also part of everyday life, combine electromagnetism, the general behavior of electromagnetic waves, and thermal physics in a unique way. The most common application is the simple heating of food, but industrial ovens are also used to dry a variety of goods [33, 34]. Here, we discuss some experiments involving household microwave ovens (for more information see [28, 35–37]).

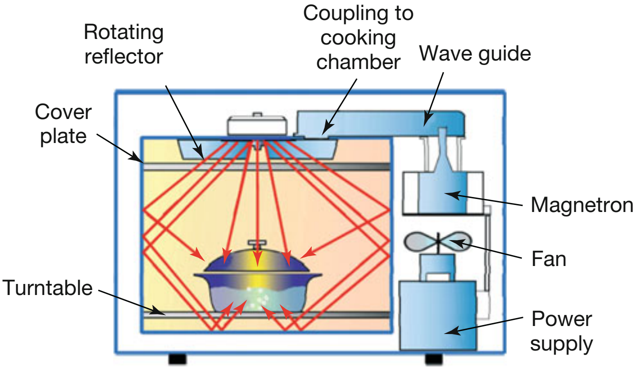

Figure 5.40 Schematic diagram of a microwave oven.

5.4.4.1 Setup

Figure 5.40 illustrates the main features of a microwave oven. The microwaves are generated within a magnetron and guided to the cooking chamber, which has metal walls. There, the microwave energy is absorbed [28, 33] by the food or the object placed in the chamber.

To the first order, a microwave oven with metallic walls resembles a 3D resonator for electromagnetic waves. The microwaves of typical ovens have frequencies of about 2.45 GHz, giving wavelengths of about 12.2 cm. The wave equation for electromagnetic waves is solved for an oven chamber with lengths L_x, L_y, and L_z (typical lengths range between 20 and 30 cm). Like the 1D case of standing waves on the string of a guitar, one finds 3D standing waves, that is, locations in the oven with a high energy density of the microwave field, and there will be nodes of standing waves with no energy density. With regard to geometry, one speaks of horizontal and vertical modes of the microwave field.

An obvious consequence of inhomogeneities of the microwave energy in the oven is that the absorption of microwave energy by food or other products will strongly depend on its position. To reduce uneven heating of food, the effect of the horizontal modes is usually smeared out through the use of a rotating turntable and sometimes a top rotating reflector.

5.4.4.2 Visualization of Horizontal Modes

To visualize the undisturbed mode structure in a microwave oven (i.e., without a turntable or rotating reflector) using thermography, we place a thin glass plate of appropriate dimensions inside the oven. Its height can be adjusted by placing Styrofoam underneath it. Glass does not absorb microwaves strongly. To measure the mode structure, we either put a wet paper on top of the plate or wet the glass plate by covering it with a thin film of water. The plate is then heated in the oven for a certain period (depending on the applied power). Right after heating, the door is opened and the plate is analyzed with the IR camera. Figure 5.41 shows three examples of the observed mode structure of the otherwise empty microwave

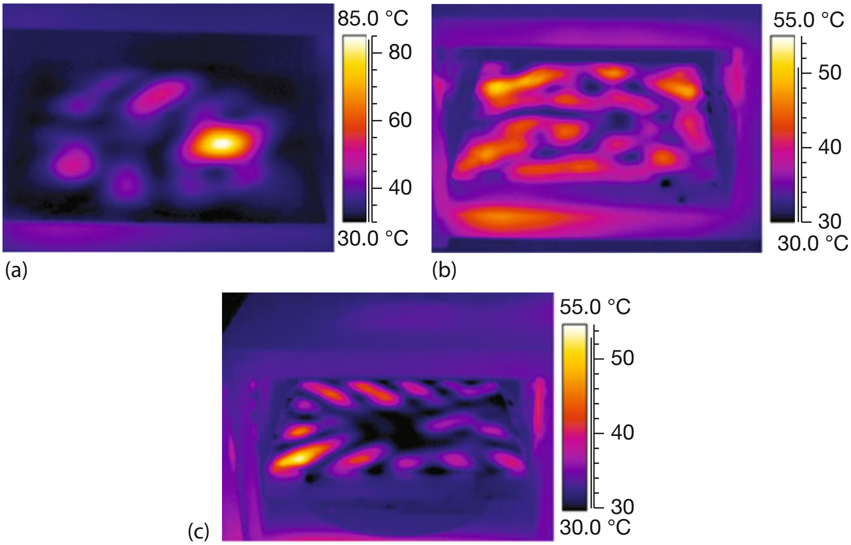

Figure 5.41 Visualization of horizontal mode structure in a microwave oven. A horizontal glass plate with a thin water film was heated for 15 s at a microwave power of 800 W without using the turntable. The plate was on the bottom (a), at a height of 3.5 cm (b), and at a height of 8 cm (c).

oven for a plate on the bottom of the oven and at heights of 3.5 and 8 cm. In all cases, the oven ran for 15 s at 800 W. One can see clearly striking differences; the horizontal mode structure also strongly depends on height.

Unfortunately, the situation is more complex for practical applications. Most importantly, the mode structure changes as the oven is filled. For example, when an object of a given geometry that can absorb microwave energy is placed in the oven, the electrodynamic calculation of the loaded oven gives different mode structures compared to the empty oven since the boundary conditions have changed.

5.4.4.3 **Visualization of Vertical Modes**

Although a turntable in a microwave oven may be useful in smearing out inhomogeneities of the horizontal mode structure, it does not have the same effect in vertical modes. Figure 5.42 shows IR images of a tall glass cylinder about 2 cm in diameter filled with water before and after heating in a microwave oven. The cylinder was placed in the center of the turntable, which is where most people put things in a microwave oven. Obviously, the heating is quite uneven. There are large temperature differences of more than 20 K between the bottom, middle, and top of the glass. In this case, we found the temperatures to be 76 °C at the top, 43 °C in the middle, and 62 °C at the bottom of the glass. If baby food is heated in this way, and the cold part is on top, one might mistakenly assume that the whole portion of food is cold enough to eat. For this reason, we recommend stirring food in tall containers before serving. Of course, the turntable may help somewhat, but only

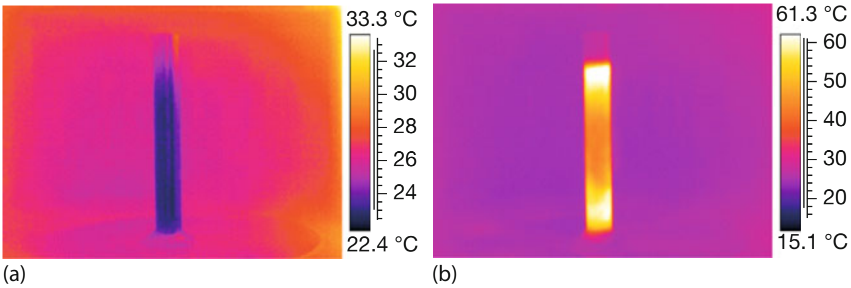

Figure 5.42 Visualization of vertical mode structure in a microwave oven. A glass cylinder (diameter 2 cm), filled with about 38 mL of water, was placed on the turntable and observed before (a) and after (b) heating for 15 s at a power of 800 W.

if the container is not placed in the center, since at a fixed height the object may eventually also move through maxima as well as minima of the mode structure, which may lead to some averaging.

5.4.4.4 Aluminum Foil in Microwave Ovens

One often hears that metals or objects with metallic parts should never be put in a microwave oven. Physicists know about the origin of this supposed “wisdom”; however, they are also aware of the limited extent of its validity. When microwaves interact with metals, they are not only effectively absorbed but also reradiate most of the energy. Since metals have a good thermal conductivity, the fraction of energy that is absorbed is rapidly distributed over the whole metallic body. If this body is very massive – for example, the walls of a microwave oven – the new equilibrium state, which depends on absorbed power, heat capacity, and heat losses, will correspond to a very small warming. The behavior of smaller metallic parts strongly depends, however, on their geometry and mass. Very thin metal sheets or similar bodies have only a very small heat capacity and can warm up quickly. This can even lead to glowing and evaporation, for example, from gold-trimmed plates. One should never put such plates in a microwave, unless the gold trim is to be removed.

This leads to the typical question of what happens to thin metal foils like aluminum foil in a microwave oven. Thin strips of foil can heat up quickly, but what happens if they have good thermal contact with another body that might absorb energy? Figure 5.43 shows two identical beakers filled with water before (Figure 5.43a) and after (Figure 5.43b) heating in the microwave oven. The right beaker in each image is surrounded by aluminum foil about 30 μm thick. This foil is thick enough that no microwave radiation will penetrate through it, that is, in this beaker, only radiation from the top may reach the water. The foil absorbs a small amount of energy, which is transferred to the water inside the beaker because of the good thermal contact. However, this transferred energy is much less than the energy absorbed in the other beaker by the water itself. Therefore, the beaker filled with water heats up much more quickly. Consequently, food should never be put in a microwave oven wrapped in thick aluminum foil.

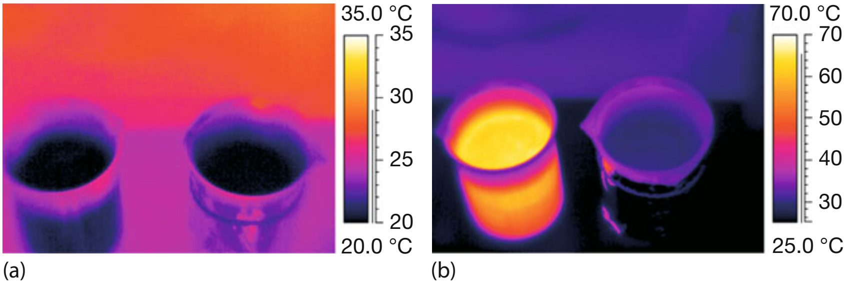

Figure 5.43 Two beakers are filled with water. The one wrapped in aluminum foil heats more slowly than the one without foil.

Many more experiments involving IR imaging and microwave ovens can be conducted [28, 35–37].

5.5
Optics and Radiation Physics

IR imaging can provide some fascinating insights into the optical properties of various materials and objects. Some objects are transparent in the VIS range, but opaque in the thermal IR and vice versa, and others are transparent in both spectral ranges. The general theoretical background was discussed in Section 1.5; some simple experimental results with VIS and LW IR images are presented here. More examples comparing VIS and SW IR optical material properties will be discussed in Chapter 6.

IR thermal imaging is based on the laws of radiation by Kirchhoff and on Planck's law, describing the spectrum of thermal radiation. It also depends on emissivity and whether gray or selective emitters are studied. Besides using these laws, one may, however, also use IR imaging to visualize these concepts.

5.5.1
Transmission of Window Glass, NaCl, and Silicon Wafers

Regular window glass and laboratory glass like BK7 show no transmission above $\lambda \approx 3\ \mu m$ (Figure 1.53). Therefore, any IR camera operating at longer wavelengths (LW cameras) will not be able to look through thick layers of glass, though MW cameras might still see a tiny bit of radiation (see also Figure 3.2). This fact must be known to thermographers doing outdoor building inspections.

Figure 5.44 depicts someone holding a plate of glass (thickness of several millimeters) partially obscuring his face. Obviously, it is not possible to look through glass, which is opaque in the IR spectral range. One may, of course, measure the surface temperature of the glass plate, something that is regularly done in building inspections. In addition, Figure 5.44 visualizes one of the major problems encoun-

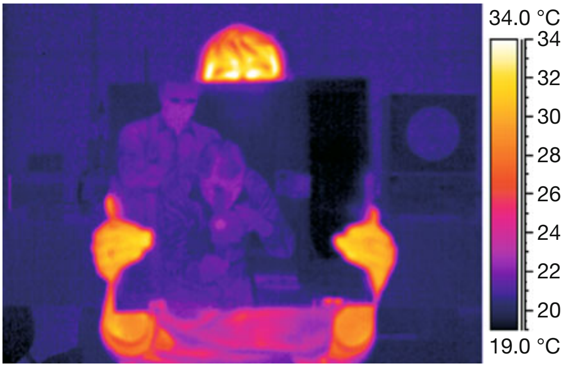

Figure 5.44 A room temperature glass plate is opaque to IR radiation. In addition, because of the flat surface, it serves as a source of thermal reflections. Here two people are behind an LW camera.

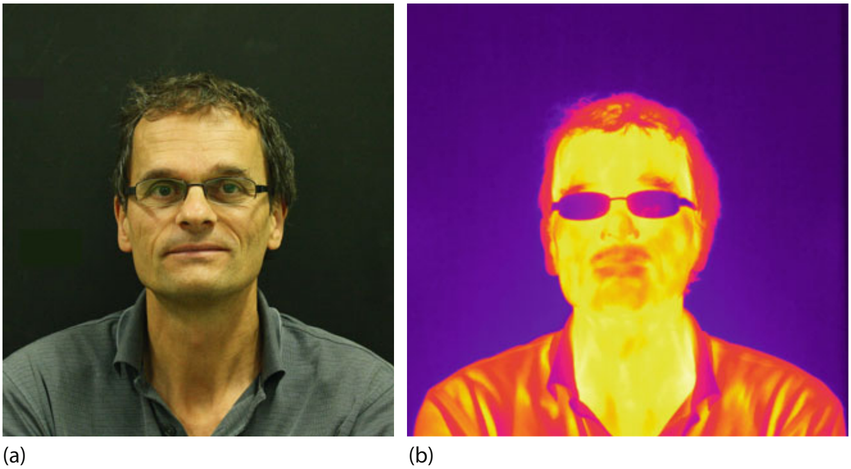

Figure 5.45 VIS (a) and LW IR image (b) of person wearing regular glasses. IR images can often erroneously suggest that dark sunglasses were worn.

tered in the thermography of flat surfaces: they may cause thermal reflections, which can give rise to problems in quantitative analysis (Section 3.4.1).

Objects made of glass are very often encountered in IR imaging, not only in building inspections but also when recording images of people. Everyone wearing regular glasses will appear in IR images as wearing very dark sunglasses (Figure 5.45) since the glass is opaque. But why is the glass temperature so much lower than the skin temperature? Glasses usually only have poor thermal contact with the face, and little thermal energy is conducted from the skin to the glasses at the three contact points at the nose and near the ears. Therefore, the heat transfer that occurs via convection from the ambient temperature air at the glass surfaces dominates and determines the surface temperature.

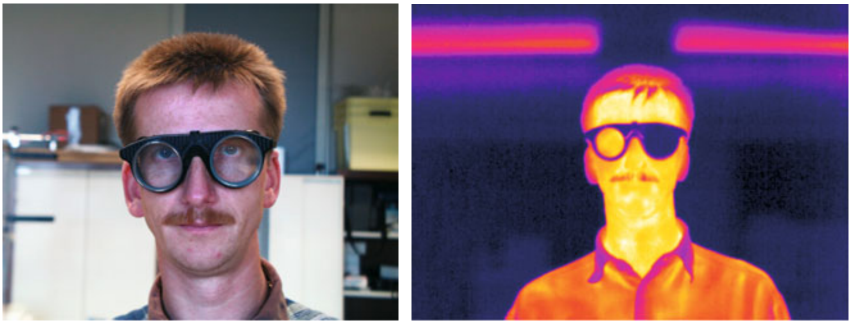
(a) (b)

Figure 5.46 A special pair of glasses made of two different materials; VIS radiation is transmitted by both materials, whereas thermal IR radiation is only transmitted by one of them.

Figure 5.46 depicts VIS and LW IR images of a person using a different pair of glasses. One lens is made of regular glass, the other of NaCl. Figure 1.47 shows clearly that NaCl will transmit VIS and thermal IR radiation; therefore, one can readily look through the lens and observe the higher temperature of the skin near the eyes. It is very easy to use the known theoretical transmission of NaCl (about 91%) and from that calculate correction factors to quantitatively measure temperatures behind the lens [38].

In contrast to glass and NaCl, both of which transmit VIS radiation, silicon wafers are opaque in the VIS spectral range (spectrum Figure 1.50). Therefore, it is not surprising that one cannot see through them using the unaided eye. However, IR imaging makes it possible to see through wafers (Figure 5.47). This feature is due to the energy gap of silicon of about 1.1 eV, corresponding to a wavelength of 1100 nm. Any higher energy radiation, that is, radiation with shorter wavelengths, can excite electrons across the gap and is thus absorbed: the wafer will turn opaque. Radiation with smaller energy levels, that is, energy with longer wavelengths such as LW IR radiation, will not be able to excite electrons, that is, it cannot be absorbed, meaning the material is transparent.

In an experiment, a 0.362 mm thick wafer was placed directly in front of an IR camera lens. The real part of its index of refraction ($n = 3.42$) leads to a transmission of about 53% in the LW range.

5.5.2
From Specular to Diffuse Reflection

Usually, only the law of mirror reflection (here called specular reflection) is treated (Eq. (1.2), Figure 1.9) when introducing reflection in optics. In contrast, diffuse reflection (Figure 1.11) is encountered much more often in everyday life and technology, or at least a combination of diffuse and regular reflection, as illustrated in Figure 5.48.

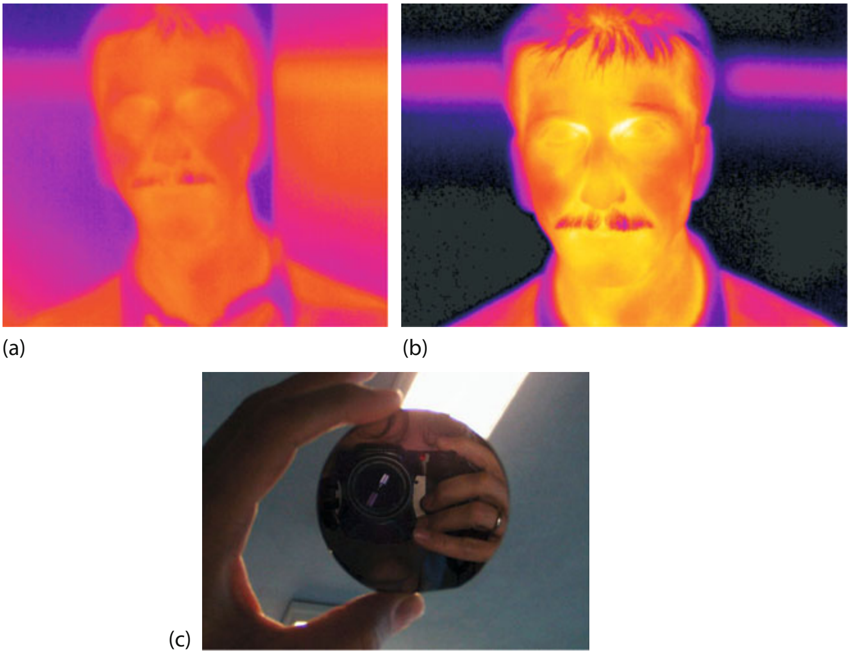

Figure 5.47 A silicon wafer, polished on both sides, is opaque under VIS light (c) but transmits thermal IR radiation (a). The IR signal with a wafer is attenuated compared to the image without a wafer (b) because of reflection losses at the interfaces.

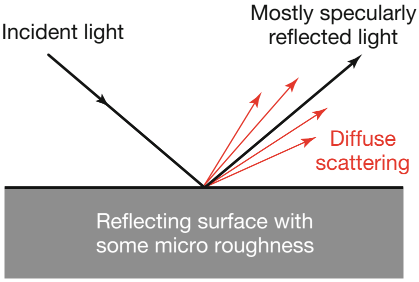
Incident light
Mostly specularly reflected light
Diffuse scattering
Reflecting surface with some micro roughness

Figure 5.48 Real surfaces have surface roughness. Therefore, reflection consists of a superposition of specularly reflected and diffusely scattered light.

The transition from pure diffuse scattering (e.g., from a wall or blackboard) to pure specular reflection (e.g., from a mirror) can be readily examined using IR imaging with LW cameras. Diffuse scattering takes place if the wavelength of the electromagnetic radiation is comparable to the dimensions of the surface roughness. However, if the latter dimensions are small compared to the wavelength, regular reflection takes place. Analogously, a table tennis ball thrown at a wire mesh with dimensions similar to those of the mesh will behave like a diffuse scatterer, whereas a much larger soccer ball will bounce off the wire mesh according to the law of reflection.

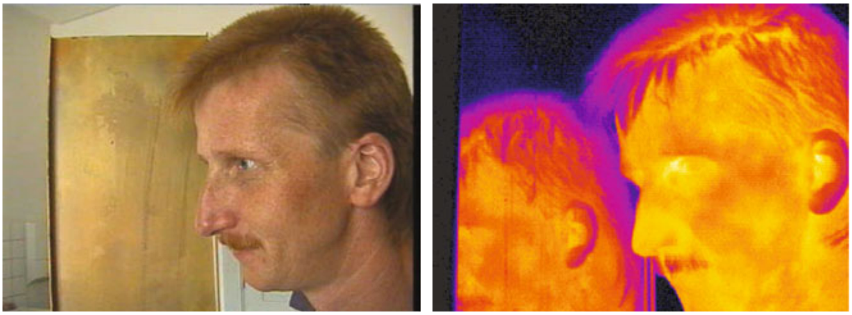
(a) (b)

Figure 5.49 Transition from specular to diffuse reflection. An oxidized brass plate scatters visible light diffusely (a), whereas LW IR radiation leads to a clearly observable specular reflection image (b). This behavior is due to microscopic roughness.

Using VIS and IR electromagnetic radiation the transition from diffuse to specular reflection can be demonstrated directly. Consider, for example, a person in front of a brass plate that is oxidized and a diffuse scatterer in the VIS range ($\lambda = 0.4$–$0.8\,\mu\text{m}$): no mirror image can be seen (Figure 5.49). However, the wavelength of the IR radiation, detected in $\lambda = 8$–$14\,\mu\text{m}$ IR cameras, is larger by a factor of about 10. Therefore, the IR image has a much larger portion of regular reflection (see Section 3.4.1 and [39] for more details).

5.5.3
Some Light Sources

Light sources, for example incandescent lamps and discharge lamps, present a lot of interesting physics lessons [40]. One particularly obvious feature is the periodic brightness variation. In incandescent lamps they can be related to periodic temperature variations of the filament, which are due to the 50 or 60 Hz AC voltage power supplies. These may be measured with suitable IR cameras [40].

A related phenomenon is known as the light emitting pickle experiment [41]. When a regular pickle is attached to either 110 or 230 V line voltage, it will soon start emitting yellow–orange light. The mechanism, though mostly known, was recently reinvestigated using spectroscopy and high-speed imaging, in addition to IR thermal imaging [41]. IR analysis showed that one or both electrodes become very hot, reaching up to a few hundred degrees Celsius. The whole process also acts electrolytically, that is, hydrogen by itself and hydrogen mixed with oxygen (oxyhydrogen) exist close to the electrodes, which may be ignited by sufficiently high electrode temperatures. In addition, the hot electrodes slice through the pickle, thereby stopping the whole process after a while. Figure 5.50a depicts the light emitted by the pickle, and Figure 5.50b shows an IR image with a very hot electrode.

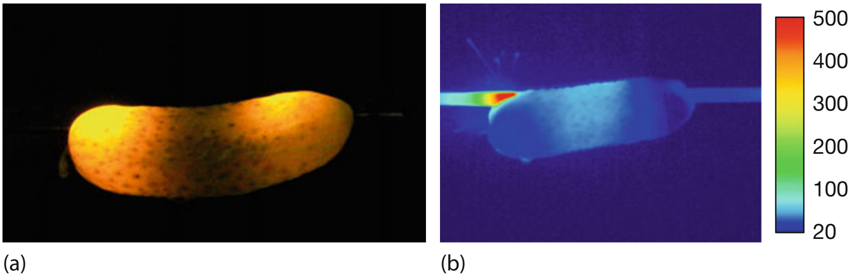

Figure 5.50 Light-emitting pickle recorded in VIS light (a) and in IR to measure electrode temperatures. (b) The T scale is from 20 to 500 °C.

5.5.4
Blackbody Cavities

It is believed that blackbody cavities (Section 1.4.6) give the best possible approximations to blackbody radiation on earth. Therefore, many analyses have been conducted on theoretical emissivities depending on the properties of the used cavities. According to an old theory by Gouffé, the total emissivity of a cavity resembling a blackbody is given by [42]

$$\varepsilon = \varepsilon_0'(1 + y) \tag{5.8}$$

where

$$\varepsilon_0' = \frac{\varepsilon^*}{\varepsilon^*(1 - s/S) + s/S} \tag{5.9a}$$

and

$$y = (1 - \varepsilon^*)\left[\left(\frac{s}{S} - \frac{s}{S_0}\right)\right] \tag{5.9b}$$

In these equations, ε^* denotes the emissivity of the wall material of the cavity, s and S are respectively the areas of the aperture and the interior surface, and S_0 denotes the surface area of an equivalent sphere, which would have the same depth as the cavity in the direction normal to the aperture. Usually, y is a small number; however, depending on the cavity shape, it can be positive or negative.

From Eqs. (5.8), (5.9a), and (5.9b) it becomes clear that even rather small values of material emissivity can yield quite large values for the total emissivity.

Figure 5.51 shows the results of an experiment. A set of three cylindrical holes in a metal block could be covered by the shiny cover plate on top with apertures to form cavities of different emissivities. IR images of the heated cavities revealed that the apparent temperature between the largest and smallest aperture cavities evaluated for constant emissivity would differ by more than 2 K. Assuming, however, that the differences in the detected IR radiation were due to changes in emissivity, the experiment nicely demonstrates the validity of Eqs. (5.8), (5.9a), and (5.9b).

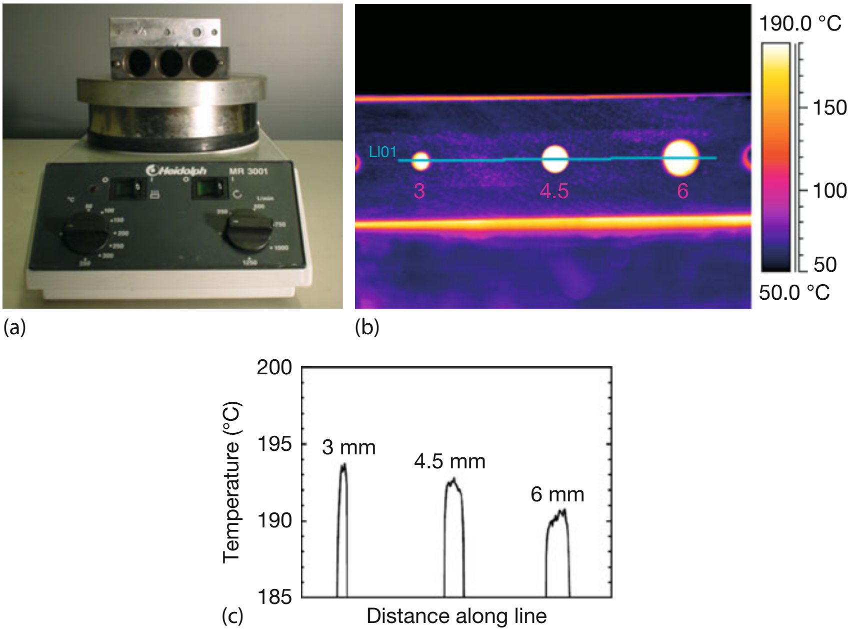

Figure 5.51 (a) A set of three cylindrical holes in a metal block, which may be covered by apertures of different sizes to form cavities of different emissivities. (b) IR radiation was detected when heating the cavities to a temperature of around 200 °C. (c) The temperature along a line through the centers of the holes was evaluated for constant emissivity (see text for more details).

The cylindrical holes had an inner diameter of 18 mm and a depth of 36 mm each. The apertures used had diameters of 3, 4.5, and 6 mm, leading to values of s/S of 0.28, 0.62, and 1.1%, respectively. The values of s/S_0 are even smaller; hence the correction term y is always less than 0.01. The metal walls of the cavity were already slightly corroded and had an ε^* value of approximately 0.21. This gives total emissivities of the three cavities of about 0.96 for the 6 mm aperture, 0.98 for the 4.5 mm aperture, and 0.99 for the smallest 3 mm aperture. These slight differences in emissivity directly and quantitatively explain the observed results from the IR analysis (Figure 5.51).

Note that the front plate looks much colder than the holes in the IR image. This is due to the lower emissivity of the cover plate (see VIS image in Figure 5.51a). Repeating this experiment for a long time leads to the oxidation of the front surfaces, which is accompanied by an increase in emissivity. Therefore, the actual IR image may change (i.e., the ratio of the signal from the holes to the cover plate changes) when the experiment is repeated, this means that the radiation from the cover plate may change. However, the cavity radiation does not change.

5.5.5
Emissivities and Leslie Cube

The angular dependence of emissivity can be seen in Figures 5.52 and 5.53. In Figure 5.52 (see also Figure 4.17), the aluminum cubes painted with high-emissivity black paint are shown shortly after being heated to about 160 °C. The top face of the cubes is observed from a much larger angle than the side faces. Therefore, according to Figures 1.30 and 1.31, its emissivity is lower than those of the side faces. As a result, the top face appears to be cooler, although it is the same temperature.

Figure 5.53 shows a cylindrical container (large glass beaker) with an attached tape of high emissivity. One can clearly see that close to the edge, where the viewing angle is much larger, the apparent temperature drops with respect to the near-normal observed areas of the object. A detailed analysis of the shape of the temperature profile is in agreement with the predictions of the drop of emissivity with the observation angle (Figure 1.30).

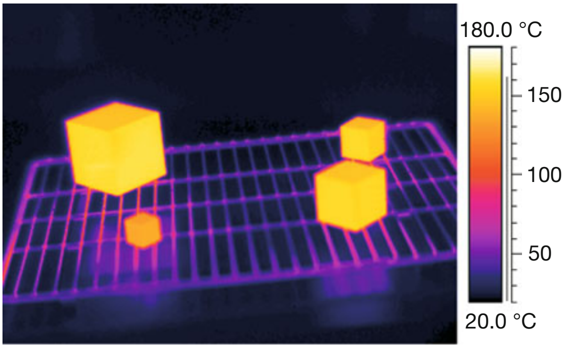

Figure 5.52 The normal emissivities of the faces of paint-covered metal cubes are the same. The two observable side faces are viewed from the same angle of about 45°, whereas the top face is seen from a larger angle. Owing to the angular dependence of emissivity, this leads to an apparently colder top face.

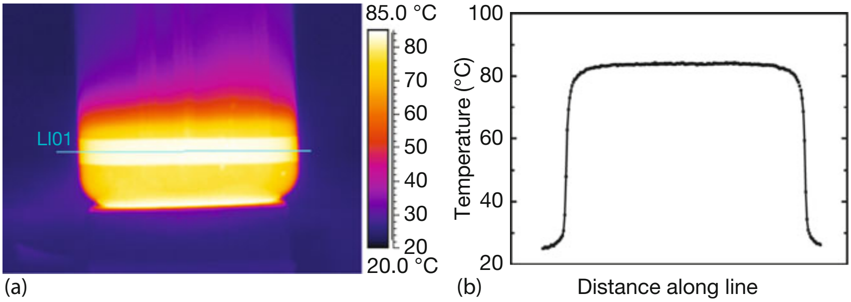

Figure 5.53 Glass cylinders filled with hot water make it possible to simultaneously observe emissivity effects due to a large variety of viewing angles. (a) IR image with line across a high-emissivity tape. (b) Temperature profile along the line.

Figure 5.54 shows an empty Leslie cube at room temperature, observed in such a way that two side faces and the bottom face are all viewed from about the same viewing angle. If warm objects (say, a person's finger) are nearby, thermal reflections are clearly observable. They are most easily seen for the polished copper metal surface but still detectable on the surfaces covered by white and black paint. This can be easily explained by Eq. (1.29) as the reflectivity $R = 1 - \varepsilon$ and the emissivity $\varepsilon_{\mathrm{Cu}} \ll \varepsilon_{\mathrm{paints}}$.

The same Leslie cube is shown in Figure 5.55 while and after being filled with hot water. Now the surfaces are much hotter than the surroundings and no additional warm objects are in the vicinity. Therefore, no thermal reflections are seen and the differences directly reflect the different surface emissivities at this fixed angle. The white and black painted surfaces show nearly the same emissivity for the LW camera, whereas the polished copper still has a lower emissivity compared to the diffusely scattering rough copper surface.

5.5.6
From Absorption to Emission of Cavity Radiation

In most experimental conditions in thermal physics, one must deal with nonequilibrium conditions. An instructive experiment uses a small cavity, which resembles some kind of blackbody radiator. Examples of such cavities include small graphite cylinders with an additional hole in the center of the side. Let us assume

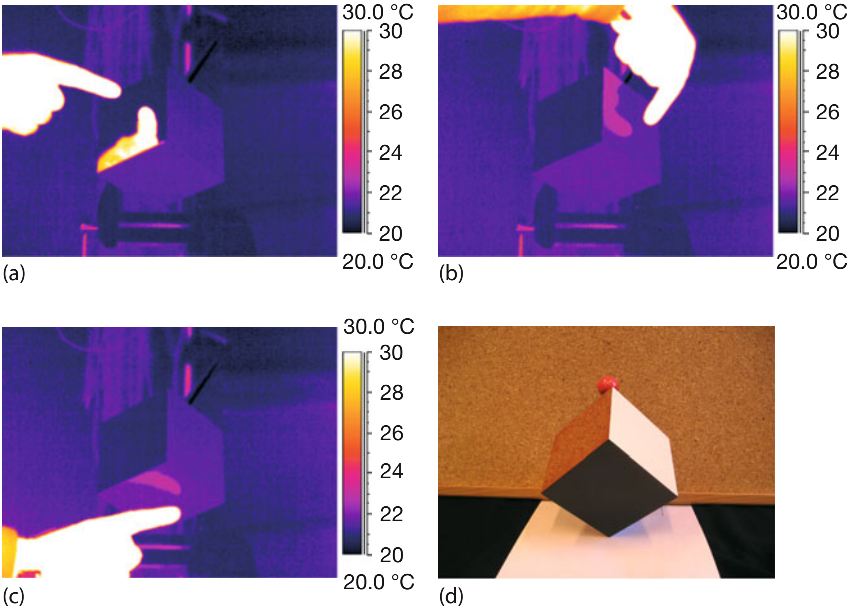

Figure 5.54 Empty (tilted) Leslie cube with thermal reflections from a finger observed from an angle such that the sides are viewed at the same angle: (a) polished Cu, (b) white paint, (c) black paint, (d) VIS image.

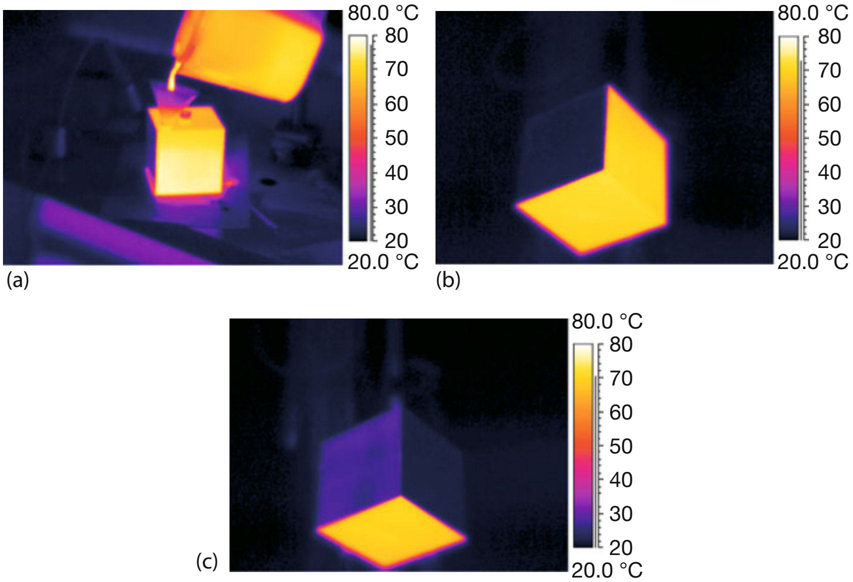

Figure 5.55 (a) Leslie cube while being filled with hot water. The cube is observed from a direction such that the sides are viewed at the same angle. (b) As in Figure 5.54d: polished copper, white paint, and black paint (lowest segment). (c) Cube after 90° rotation: rough copper, polished copper, and black paint surface.

that the graphite surface has an emissivity of, say, $\varepsilon = 0.9$, whereas the hole has a slightly larger emissivity, around 0.98 (the exact values do not really matter, just the difference between surface and cavity values). Such graphite tubes are standard sample holders in atomic absorption spectroscopy (AAS). The cavity can easily be heated while holding the end between one's fingers ($T > 30\,°\mathrm{C}$). After a dynamic thermal equilibrium between the fingers and the cavity is established, it is warmer than the surroundings, that is, the cavity is now not in thermal equilibrium with the colder surroundings. According to the laws of radiation, the temperature difference between cavity and surroundings will lead to a net emission of thermal radiation from the cavity, the amount being characterized by the emissivity. Since the cavity has a higher value of emissivity, it emits more radiation, as clearly shown in Figure 5.56a.

The situation may, however, also be reversed by cooling the cavity. This was done by placing it between two ice cubes. After a (dynamic) thermal equilibrium between ice cube and cavity is established, the cavity is now much colder than the surroundings at room temperature. The cavity itself has a high emissivity, that is, it also has a high absorptivity (according to Kirchhoff's law). Therefore, it will absorb more radiation from the surroundings than the surface of the graphite tube. This energy quickly flows away to the ice cubes owing to conduction, that is, we assume that the cavity temperature will remain low (this is why we speak of a dynamic equilibrium). The cavity will therefore emit radiation according to the

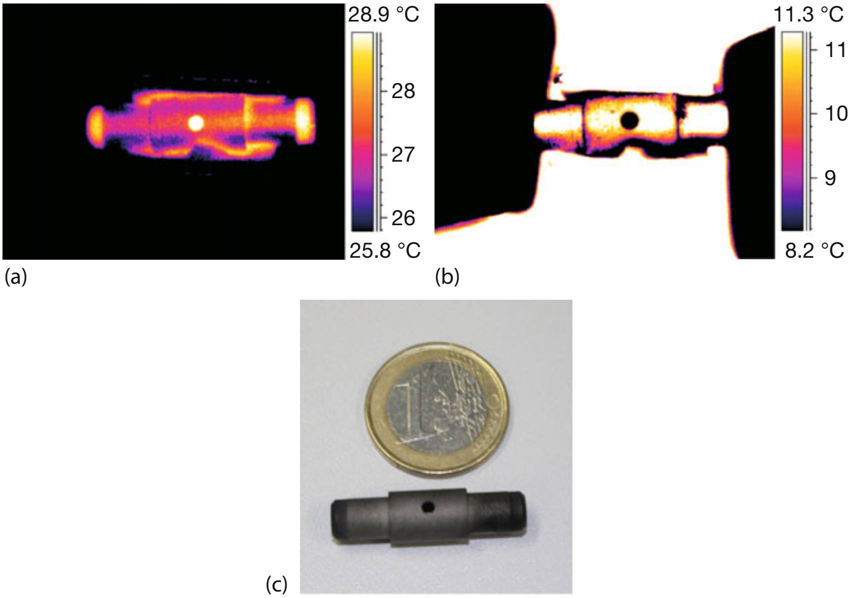

Figure 5.56 A graphite tube (length = 3 cm, inner diameter = 4 mm) with a small hole (diameter = 2 mm), which is commonly used as a sample holder in AAS, may serve as a cavity (c). A €1 coin was added for scale. The tube can be used to record IR images while studying the transition from emission (a) to absorption (b). The tube can be heated by holding its ends between one's fingers (a) or cooled (b) by attaching the ends to ice cubes.

cavity temperature, which is lower than that of the surroundings. This must be compared with the radiation from the graphite tube surface. Assuming the same temperature (thermal equilibrium within the tube), the radiation should be lower than that of the cavity due to the lower emissivity. However, since its emissivity is lower, its reflection coefficient is automatically much higher (Eq. (1.29)). Therefore, the amount of thermal radiation from the much warmer surroundings, which will be reflected from the tube surfaces, adds up to the pure thermal emission. This leads to a much larger total emission from the surface compared to the cavity. As a consequence, the cavity emits much less radiation than the tube surface, as shown in Figure 5.56b.

5.5.7
Selective Absorption and Emission of Gases

The transition from absorption to emission of radiation by a selective emitter can also be demonstrated very nicely using selectively absorbing and emitting objects like molecular gases (see Chapter 8 for details). Figure 5.57 illustrates experimental results recorded with an LW camera using SF_6 [43]. SF_6 was used to fill a plastic bag and cooled to about −20 °C in an air convection cooler. The cold gas bag was removed from the cooler, the valve of the bag was opened, and cold gas was

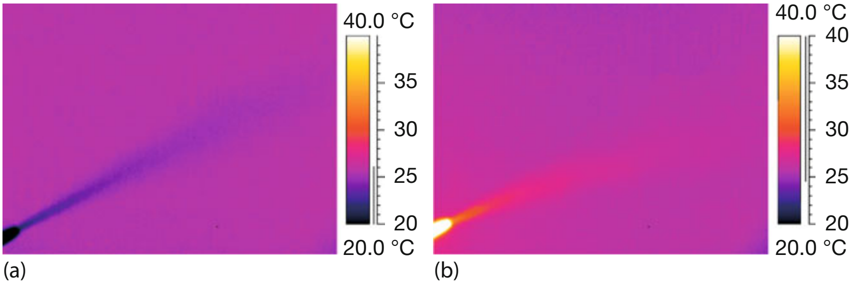

Figure 5.57 Absorption of cold SF_6 ($T \approx -20\,°C$) (a) and emission from warm SF_6 ($T \approx 80\,°C$) (b) in front of a wall at room temperature (detected with an LW camera).

pressed out of the valve. The process was observed with the IR camera using a wall at room temperature as background. As shown in Figure 5.57a, the IR radiation from the wall toward the camera is significantly attenuated owing to absorption within the gas. This is due to the strong absorption bands of SF_6 in a wavelength range of around 10–11 μm.

To observe emission at these wavelengths, we placed the gas-filled bag in our air convection heating system. The gas was heated to about 80 °C. It was removed from the heater, the valve was opened, the gas was pressed out of the valve, and the process was again observed with the same wall at room temperature as background. The result presented in Figure 5.57b clearly demonstrates the emission of the hot gas, which leads to an increase of IR radiation from the streaming gas. Details of gas absorption and emission, along with the corresponding technological applications, are discussed in Chapter 8.

References

1 Karstädt, D., Pinno, F., Möllmann, K.P., and Vollmer, M. (1999) Anschauliche Wärmelehre im Unterricht: ein Beitrag zur Visualisierung thermischer Vorgänge. *Prax. Naturwiss. Phys.*, **48** (5), 24–31.

2 Karstädt, D., Möllmann, K.P., Pinno, F., and Vollmer, M. (2001) There is more to see than eyes can detect: visualization of energy transfer processes and the laws of radiation for physics education. *Phys. Teach.*, **39**, 371–376.

3 Möllmann, K.-P. and Vollmer, M. (2000) Eine etwas andere, physikalische Sehweise–Visualisierung von Energieumwandlungen und Strahlungsphysik für die (Hochschul-) lehre. *Phys. Bl.*, **56**, 65–69.

4 Möllmann, K.-P. and Vollmer, M. (2007) Infrared thermal imaging as a tool in university physics education. *Eur. J. Phys.*, **28**, S37–S50.

5 Xie, C. and Hazzard, E. (2011) Infrared imaging for inquiry based learning. *TPT*, **49**, 368–372.

6 Xie, C. (2011) Visualizing chemistry with infrared imaging. *J. Chem. Educ.*, **88**, 881–885.

7 Haglund, J., Jeppsson, F., Hedberg, D., and Schönborn, K.J. (2015) Thermal cameras in school laboratory activities. *Phys. Educ.*, **50** (4), 424–430.

8 Haglund, J., Jeppsson, F., and Schönborn, K.J. (2015) Taking on the heat – A narrative account of how infrared cameras invite instant inquiry. *Res.*

Sci. Educ., **46**, 685–713. online first, doi:10.1007/s11165-015-9476-8.

9 Haglund, J., Jeppsson, F., Melander, E., Pendrill, A.-M., Xie, C., and Schönborn, K. J. (2016). Infrared cameras in science education. *Infrared Phys. Technol.*, **75** (March), 150–152, doi:dx.doi.org/10.1016/j.infrared.2015.12.009.

10 Vollmer, M. and Möllmann, K.-P. (2013) Characterization of IR cameras in student labs. *Eur. J. Phys.*, **34** (6), 73–90.

11 Halliday, D., Resnick, R., and Walker, J. (2001) *Fundamentals of Physics, Extended*, 6th edn, John & Wiley Sons, Inc.

12 Tipler, P.A. and Mosca, G. (2003) *Physics for Scientists and Engineers*, 5th edn, Freeman

13 Chabay, R. and Sherwood, B. (2002) *Matter and Interactions*, vol. 1 and 2, John Wiley & Sons, 4th edn 2015.

14 Tire heat of F1 Cars detected with onboard IR camera, see www.youtube.com/watch?v=VNYUkRKslEw (accessed May 2017).

15 https://www.youtube.com/watch?v=jvuBe6b2iVk, (accessed May 2017).

16 Bloomfield, L. (2007) *How Everything Works*, John Wiley & Sons, Inc.

17 Vollmer, M. and Möllmann, K.-P. (2015) Bouncing poppers. *Phys. Teach.*, **50**, 489–493.

18 Bellemans, A. (1981) Power demand in walking and pace optimization. *Am. J. Phys.*, **49**, 25–27.

19 Keller, J.B. (1973) A theory of competitive running. *Phys. Today*, **26**, 42–47.

20 Alexandrov, I. and Lucht, P. (1981) Physics of sprinting. *Am. J. Phys.*, **49**, 254–257.

21 Dart, S.L., Anthony, R.L., and Gut, E. (1942) Rise of temperature on fast stretching of synthetic and natural rubbers. *Ind. Eng. Chem.*, **34** (11), 1340–1342.

22 Ogden, R.W. (1992) On the thermoelastic modeling of rubberlike solids. *J. Therm. Stress.*, **15** (4), 533–557.

23 Maroto, J.A., Pérez-Muñuzuri, V., and Romero-Cano, M.S. (2007) Introductory analysis of the Bénard Marangoni convection. *Eur. J. Phys.*, **28**, 311–320.

24 www.energy.ca.gov (accessed May 2017).

25 Vollmer, M. and Möllmann, K.-P. (2012) Vapour pressure and adiabatic cooling from champagne: slow motion visualization of gas thermodynamics. *Phys. Ed.*, **47** (5), 608–615.

26 Liger-Belair, G., Bourget, M., Cilindre, C., Pron, H., and Polidori, G. (2013) Champagne cork popping revisited through high-speed infrared imaging: The role of temperature. *J. Food Eng.*, **116**, 78–85.

27 Planinsic, G. and Vollmer, M. (2008) The surface-to-volume-ratio in thermal physics: From cheese cubes to animal metabolism. *Eur. J. Phys.*, **29**, 369–384 and erratum on page 661.

28 Vollmer, M. (2004) Physics of the microwave oven. *Phys. Educ.*, **39**, 74–81.

29 Baylie, M., Ford, P.J., Mathlin, G.P., and Palmer, C. (2009) The jumping ring experiment. *Phys. Educ.*, **44** (1), 27–32.

30 Bostock-Smith, J.M. (2008) The jumping ring and Lenz's law – An analysis. *Phys. Educ.*, **43** (3), 265–269.

31 Tjossem, P.J.H. and Brost, E.C. (2011) Optimizing Thomson's jumping ring. *Am. J. Phys.*, **79**, 353–358.

32 Michalski, L., Eckersdorf, K., Kucharski, J., and McGhee, J. (2001) *Temperature Measurement*, 2nd edn, John Wiley & Sons, Ltd., Chichester.

33 Thuery, J. (1992) *Microwaves, Industrial, Scientific and Medical Applications*, Artech House, Boston.

34 Smith, B.L. and Carpentier, M.-H. (1993) *The Microwave Engineering Handbook*, vol. 1–3, Chapman & Hall, London.

35 Parker, K. and Vollmer, M. (2004) Bad food and good physics: the development of domestic microwave cookery. *Phys. Educ.*, **39**, 82–90.

36 Vollmer, M., Möllmann, K.-P., and Karstädt, D. (2004) More experiments with microwave ovens. *Phys. Educ.*, **39**, 346–351.

37 Vollmer, M., Möllmann, K.-P., and Karstädt, D. (2004) Microwave oven experiments with metals and light sources. *Phys. Educ.*, **39**, 500–508.

38 Vollmer, M., Möllmann, K.-P., and Pinno, F. (2007) Looking through matter: Quantitative IR imaging when ob-

serving through IR windows. Inframation 2007, Proceedings, vol. 8, pp. 109–127.

39 Henke, S., Karstädt, D., Möllmann, K.-P., Pinno, F., and Vollmer, M. (2004) Identification and suppression of thermal reflections in infrared thermal imaging, Inframation 2004, Proceedings, vol. 5, pp. 287–298.

40 Vollmer, M. and Möllmann, K.-P. (2015) Flickering lamps. *Eur. J. Phys.*, **36**, 035027 (20pp).

41 Vollmer, M. and Möllmann, K.-P. (2015) Light emitting pickles. *Phys. Educ.*, **50** (1), 94–104.

42 Wolfe, W.L. and Zissis, G.J. (eds) (1993) *The Infrared Handbook*, revised edition, 4th printing, The Infrared Information Analysis Center, Environmental Research Institute of Michigan, Michigan.

43 Vollmer, M., Karstädt, D., Möllmann, K.-P., and Pinno, F. (2006) Influence of gaseous species on thermal infrared imaging. Inframation 2006, Proceedings, vol. 7, pp. 65–78.

Chapter 6
Shortwave Infrared Thermal Imaging

6.1
Introduction

Applications for the three typical wavebands used in infrared (IR) thermal imaging can differ quite significantly. Though sometimes used qualitatively, for example, as optical gas imaging devices (Chapter 8), mid-wave (MW) and long-wave (LW) cameras are predominantly advertised as temperature-calibrated instruments for quantitative investigations. In contrast, short-wave (SW), also called near infrared (NIR), cameras are mostly used for qualitative visualization and their use as temperature-calibrated instruments is just one among many other potential applications. The reason for this difference compared to MW and LW cameras lies within the physics differences of NIR radiation and the corresponding optical properties of studied materials and objects. In this chapter NIR and SW are used synonymously.

6.2
The Why and How of SW Infrared Imaging

SW cameras operate in a spectral range of 0.8 μm to about 1.7 μm (Figure 1.8). They are not often advertised as being temperature-calibrated measurement devices because they cannot be used at the low temperatures where MW and LW cameras are common. Room temperature objects emit more or less negligible amounts of SW IR radiation (Figures 1.21 and 1.22). This means that, although they theoretically have advantages when it comes to temperature contrast, thermal reflections, and emissivity uncertainties (Section 2.3.3), the reduced detected radiances do not allow measurements for temperatures below around 200 or 300 °C. Therefore, temperature-calibrated systems usually start above 300 °C, depending on the wavelength range, and extend to a maximum of around 3000 °C. At these elevated temperatures, SW cameras can indeed resemble precise quantitative measurement devices like MW and LW cameras in the lower temperature ranges.

Infrared Thermal Imaging, Second Edition. M. Vollmer and K.-P. Möllmann.
© 2018 WILEY-VCH Verlag GmbH & Co. KGaA. Published 2018 by WILEY-VCH Verlag GmbH & Co. KGaA.

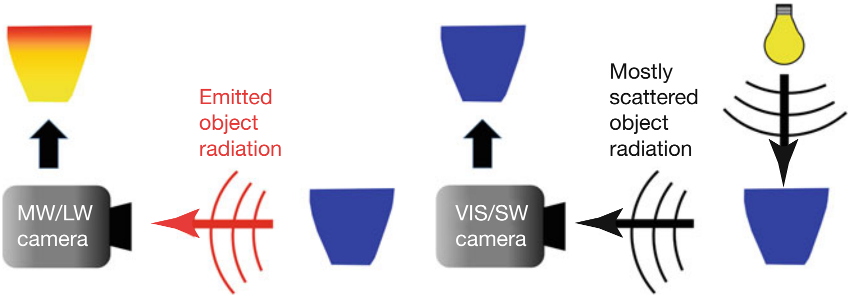

Figure 6.1 Main differences between IR imaging in MW/LW bands compared to SW band. Resulting images are visualized above the cameras.

Of course, there are industrial high-temperature applications, for example, the study of furnaces or molten glass and metals in various processes, and SW cameras are beginning to replace other spot measurement devices such as pyrometers. However, high-temperature applications alone would not have led to the enormous developments seen in the field. Many applications of SW cameras nowadays also involve the study of objects at much lower temperatures.

Figure 6.1 illustrates the major differences between IR imaging in the various spectral ranges. With MW and LW cameras, one usually detects the emitted thermal radiation even of room temperature objects. An MW or LW camera detects the radiation and gives a thermal image, which, if the camera is calibrated, allows one to measure surface temperatures, here of a cup filled with a hot liquid. In contrast, SW imaging works more or less as imaging in the visible (VIS) spectral range. One mostly detects scattered radiation from an object. The source may be the sun, an incandescent lamp, or light-emitting diodes, for example. Therefore, a SW camera usually cannot deduce object temperature but rather detects objects as any regular VIS camera does. For higher temperatures, a SW camera will of course in addition also detect emitted object thermal radiation. In this case it can in principle be used for temperature measurement if the amount of residual scattered radiation is small or well known.

In this sense Figure 6.1 also visualizes the well-known general difference between active and passive imaging systems. Passive systems just detect object radiation, whereas active systems use an additional radiation source such that an object scatters this radiation toward the sensor for image generation.

In outdoor use VIS cameras utilize solar radiation. Figure 6.2 illustrates a spectrum of solar radiation outside the atmosphere and at sea level at midlatitudes as a function of wavelength from the ultraviolet (UV) up to 2.5 μm, including the SW band. Obviously, although the radiation decreases strongly towards the IR (for a surface temperature of roughly 6000 K, the wavelength of maximum spectral irradiance is in the VIS range according to Wien's displacement law) (Eq. (1.16)), there is still enough radiation in the SW band, which may be used for imaging. Therefore, SW cameras should easily work outdoors when using scattered radiation for imaging.

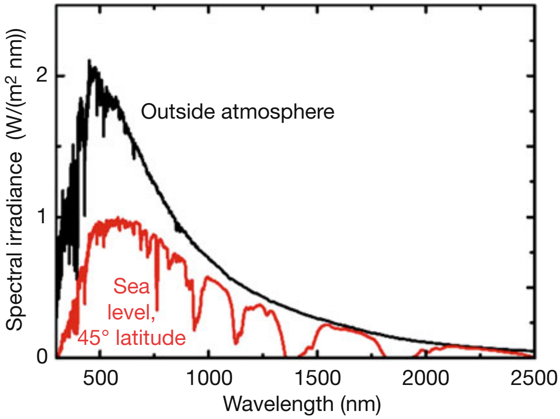

Figure 6.2 Solar radiation spectrum outside of atmosphere and for cloudless skies at 45° latitude at sea level from VIS to IR range. Considerable radiation is still available in the SW band (after [1]).

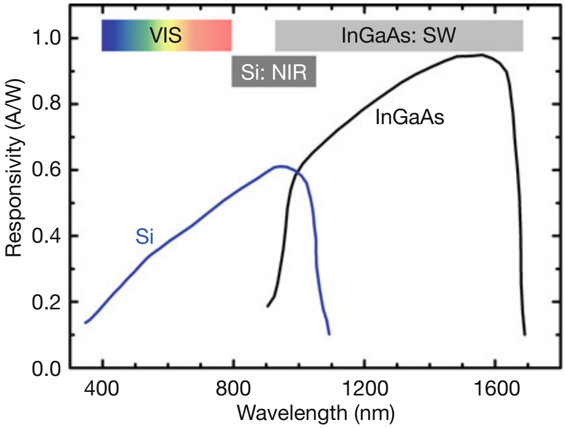

Figure 6.3 Typical reponsivity spectra of silicon and InGaAs detectors (after [2]). The colored bar refers to the VIS spectral range. The gray bars indicate the very NIR if detected with silicon-based camera sensors and the SW range detectable with InGaAs cameras.

Many different kinds of sensors are available for the SW range. Owing to recent progress in semiconductor technology, it is now possible to easily produce, for example, InGaAs sensors with quantum efficiencies above 80%, that is, every 100 incoming IR photons yield at least 80 electrons in the detector (this is already rather close to the ideal situation of 100%, where each photon creates a photoelectron; see Section 2.2.4.1). Since IR radiation has lower photon energies than VIS radiation, the detector sensitivity (usually defined for photodiodes in photocurrent per incident radiant power in A/W is higher for NIR diodes than for visible ones). This is illustrated in Figure 6.3, which depicts the responsivity of a Si and an InGaAs photodiode.

Current InGaAs technology can produce sensors with extended wavelength ranges starting at around 0.5 μm (although most manufacturers mention 0.4 μm; see subsequent discussion). At VIS wavelengths, the responsivity of these sensors is, however, always smaller than those made of silicon and decreases already below 0.2 A/W for $\lambda < 0.6$ μm. Commercial array sensors with 640 × 512 pixels are advertised as having below 0.37% bad pixels [2], that is, less than about 1200 out of 328 000 pixels may not work. The highest-grade IR cameras should have much smaller numbers, at least by a factor of 10.

Although InGaAs is the sensor of choice for most manufacturers, several other sensor types are used in SW cameras (see also Section 6.4). These include mercury cadmium telluride (MCT) detectors in a wavelength range from 0.8 to 2.5 μm, Ge detectors (0.4–1.6 μm) [3], InSb (0.4 μm up to 5 μm, for SW typically 0.9–2.5 μm), as well as silicon-based sensors (0.8–1.1 μm). For elevated temperature measurements, additional narrowband filters are used. A major advantage of SW compared to MW and LW cameras is that SW cameras operate in a region where glass optics is still transparent (Figure 1.53), that is, the optics is much less expensive than IR optics in the other ranges.

Focal-plane arrays (FPAs) typically have around 640 × 512 pixels; some, however, are already available in high-definition (HD) format with 1280 × 1024 pixels. Individual pixel sizes vary between 12.5 μm and around 30 μm. If variable, integration times start at around a minimum of 5 μs.

Knowing that many applications of SW cameras utilize scattered radiation and that the combination of sensors and available solar radiation in the SW and VIS ranges are similar, one might ask why nonradiometric SW cameras are produced and sold at all. The answer is simple: although the technologies and radiation sources are similar, we can already qualitatively gain a vast amount of new information in the SW band that is not available with VIS light imaging. The reason is hidden in the physics, which varies with wavelength. On the one hand, the optical properties of matter change with wavelength; on the other hand, the interaction processes between matter and radiation can change, too. We will illustrate some of these effects in the next section.

6.3
Some Applications of SW Infrared Imaging

Table 6.1 lists a number of typical applications of SW IR cameras. There is a great variety of different uses of NIR imaging, and they cover quantitative as well as qualitative imaging. In what follows, a few examples will be presented in more detail; however, no claim is being made as to the completeness of coverage of this rapidly evolving field. To understand the underlying physics, we first discuss the influence of the optical properties of water and water vapor since they are needed to explain the contrast observable in some SW images.

Table 6.1 Typical uses and application areas of SW cameras and summary of underlying physics. Examples with figures are given in Section 6.3.3. References are arbitrarily chosen for the various fields.

Specific use of NIR	Examples for application field	Physics for image contrast	References, figures
High-temperature measurement	Metal industry, furnaces	Thermal radiation	[4–8] Figures 6.8, 6.9
Vegetation changes, mineral mapping	Nature or airborne/satellite imaging	Different absorption/reflection/scattering depending on material	[9–17] Figures 6.10 and 6.11
Looking through haze/smoke	Wildfires, contrast enhancement sky/clouds	Different scattering of sky vs. clouds, air/smoke/dust, water	[1, 18–20] Figures 6.12–6.14
Sorting plastics	Recycling industry	Different absorption in plastic/water	[21–24] Figure 6.15
Looking through paints/inks	Art inspections, reflectography, detection of forged banknotes	Little absorption in paints, varnishes	[1, 18, 25–29] Figures 6.16–6.20
Fruits and vegetables: detect bruises before observable in VIS	Agricultural industries	Strong absorption in water below surfaces	[30–32] Figures 6.21 and 6.22
Optical material properties	Teaching	Different absorption of liquids in VIS and NIR range	[1, 28] Figures 6.23–6.25
Moisture detection	Remote sensing, building thermography	Strong absorption of water	[33–35] Figures 6.26 and 6.27
Surveillance and security, crime scene imaging	Vision enhancement, forensic sciences	Residual light in atmosphere: nightglow; spectra	[36–39]
Astronomy	NIR sensors for telescopes	Radiation emitting stars, dust, and so forth	[40, 41]
Hot glass inspections	Looking for defects		[31]
Wafer inspections	Microelectronics and solar cell industry		[42–44]
Telecommunication equipment testing	Laser beam mapping	Scattered laser light	[45, 46]
Medical use	Searching for blood vessels below skin, life images at surgery, air bubbles in syringes	Different scattering in skin, air, blood vessels	[1, 26, 47–51]

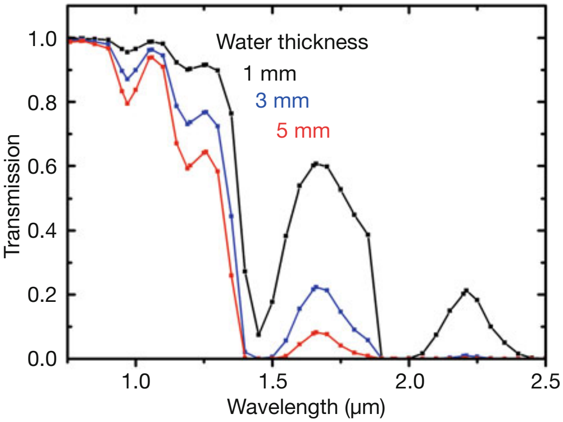

Figure 6.4 Liquid water absorption in NIR range (after optical constants from [52]).

6.3.1
Water Optical Material Properties

Water strongly influences contrast in SW IR imaging, as will be demonstrated later on in Section 6.3.3. The transmission of liquid water depends on its optical properties, as indicated by its index of refraction (Section 1.5.4.2). Figure 6.4 presents an enlarged view of Figure 1.54 focusing on the SW region. The transmission is based on literature data for the optical constants of water [52]. Water films with a thickness of just 1 mm already lead to observable absorption bands at 1 and 1.2 µm and much stronger absorption bands around 1.4 µm, 1.9 µm and well above 2.5 µm. Therefore, any macroscopic water film will show strong absorption features in the SW IR starting at wavelengths of 1 µm.

In addition to liquid water, SW cameras looks through the atmosphere, which contains water vapor, and images will strongly depend on the amount of water vapor. Figure 6.5 depicts the transmission of a 10 m path of air – similar to Figure 1.45a – however, expanding the SW IR region. The absorption bands in the gas phase are shifted with regard to those in the liquid phase (Figure 6.4). This is due to the additional hydrogen-bridge bonds between neighboring water molecules in the liquid phase. From Figure 6.5 it is obvious that water vapor absorption will have more impact on SW images (0.9–1.7 µm), in particular for long path lengths, but less so for NIR images (0.8–1.1 µm).

6.3.2
Cameras Used in the Experiments

For most of the examples shown in what follows, two types of SW IR camera were used (Figure 6.6), first, a commercial SW camera with an InGaAs detector operating from 0.9 to 1.7 µm and, second, a modified commercial digital single-lens reflex (DSLR) camera.

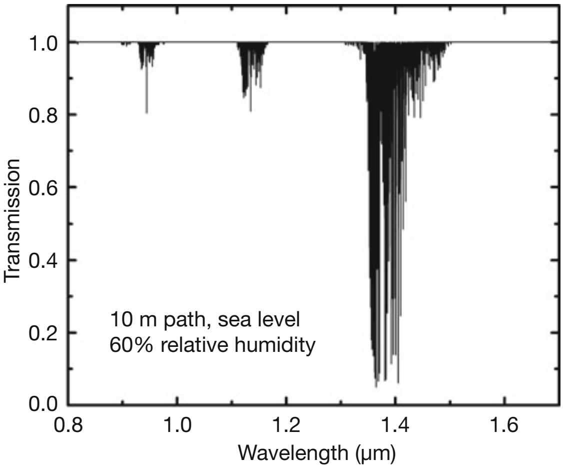

Figure 6.5 Transmission of a horizontal 10 m path in an atmosphere of 60% relative humidity. The absorption bands are due to rotational-vibrational excitations of the water molecules.

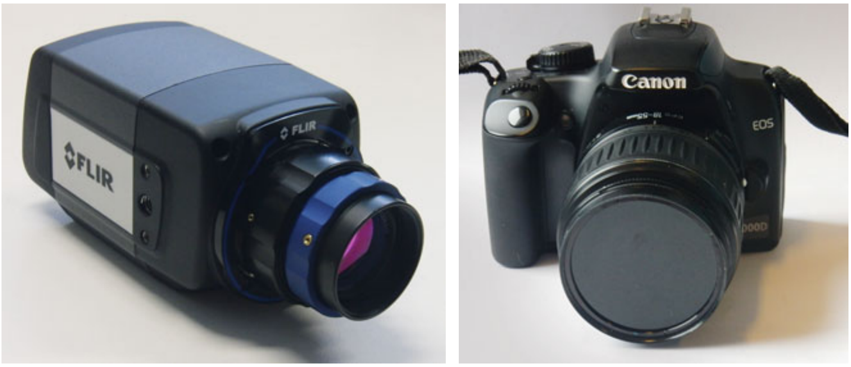

(a) (b)

Figure 6.6 SW IR cameras used for most experiments in this section. (a) SW camera FLIR SC2600 with InGaAs sensor (0.9–1.7 μm) and (b) modified Canon EOS1000D camera with silicon sensor (0.8–1.1 μm: NIR cutoff filter removed and VIS blocking filter added).

In regular compact digital cameras or DSLR cameras with silicon-based detector chips, the detector sensitivity is somewhat similar to that shown as left blue graph in Figure 6.3. While recording regular photos, the NIR part of the incident radiation is blocked by an IR cutoff filter (Figure 6.7a). For SW operation, this filter is removed and an additional filter is introduced to block the VIS light (Figure 6.7b [1, 28]). Depending on the cut-on wavelength of the latter filter, the modified camera then only detects NIR radiation between, for example, 800 and 1100 nm. Although CCD sensor efficiencies may slightly differ from those of silicon photodiodes (Figure 6.3), it is obvious that they are able to detect NIR radiation, as indicated by the gray “NIR” box between 800 and 1100 nm. (A word

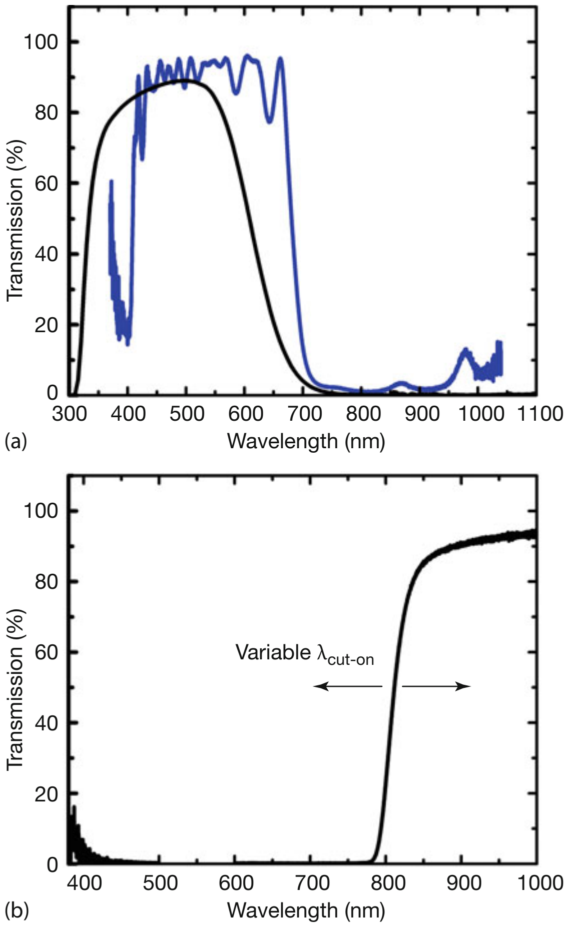

Figure 6.7 (a) Typical NIR blocking filters in DSLR camera and (b) VIS blocking filters used for NIR photography. The cut-on wavelength is variable (see [1] for more details).

of caution: removing the IR-blocking filter means opening the camera case, that is, any warranty will be voided, so only a specialist should perform the necessary camera modifications).

6.3.3
Selected Examples of SW Imaging

6.3.3.1 High-Temperature Measurements

Although it is not the primary use of SW cameras in industry, quantitative measurement of high temperatures is possible and has been demonstrated, for example, for the metal/steel industry, metal welding, manufacturing, and the study of furnace walls and wafers [4–6, 8]. The most often studied objects of high tem-

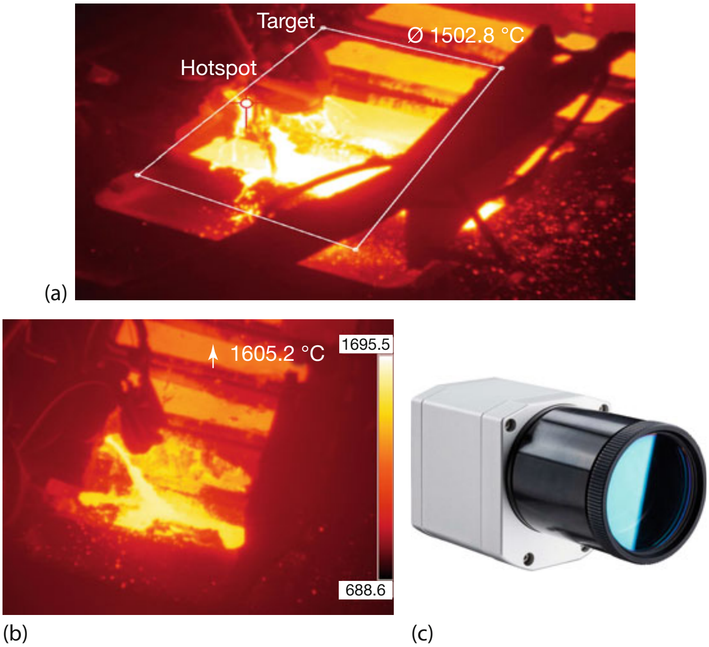

Figure 6.8 Quantitative images of liquid metals (a, b) recorded with an Optris PI1M NIR camera (c). Image courtesy: Optris GmbH, Berlin, Germany (www.optris.com).

peratures are metals. Figure 6.8c depicts an Optris NIR camera, operating with a CMOS sensor (764 × 480 pixels at 32 Hz or 72 × 56 pixels at 1 kHz) in a wavelength range between 0.85 and 1.1 μm. The camera comes radiometrically calibrated for temperatures up to 1800 °C with a noise-equivalent temperature difference of under 2 K at 1000 °C. Figure 6.8a,b shows two typical applications in the liquid metal industry, operating above 1500 °C. Figure 6.8a shows an example using the software tool hot spot tracker: it gives the temperature of the hottest spot within the indicated region of interest (ROI). Figure 6.8b shows another example outside the ROI. Here the maximum temperature within the image is given.

Since metals usually encounter the problem of unknown emissivity, which complicates any analysis, one often uses two-color ratio thermography for NIR or even VIS wavelengths. The technique and associated problems that might limit the achievable temperature accuracy were discussed in detail in Section 3.2.2.

We include a corresponding VIS ratio imaging example, recorded with a commercial camera. Figure 6.9 depicts an example of a MAG welding process [8], observed with a PyroCam (Table 6.2) operating at two nearby wavelengths of 663.1 and 679.5 nm at the red end of the VIS spectrum.

MAG welding refers to a metal active gas welding process, in which an electric arc is formed between a feed wire and the workpiece. A shield gas is injected, usually CO_2 or argon, which protects wire and workpiece from the oxygen and nitrogen in the air. MAG welding is used, for example, in the automotive industry

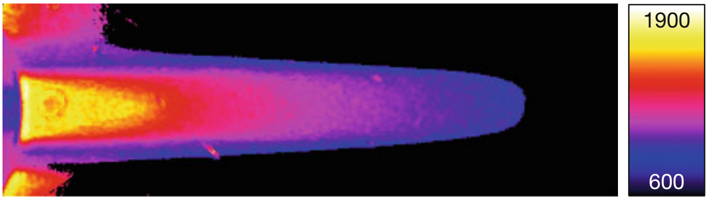

Figure 6.9 Surface temperatures of welding joint (width of image about 45 mm) between two metal sheets, recorded with a ratio thermal imaging PyroCam VIS camera operating at wavelengths of 663.1 and 679.5 nm. The temperature scale ranges from 600 °C up to 1900 °C. (see text for details; courtesy S. Goecke, TH Brandenburg/Germany).

for connecting metal sheets. The two metal sheets on top of each other are initially separated by a small gap. Upon welding the wire within, the arc melts and forms a weld joint between the two sheets. Figure 6.9 depicts the PyroCam image observed from above. The shown horizontal dimension amounts to about 40 mm, covered by 640 pixels. The arc moved from right to left. Temperatures are indicated by the false color bar within the arc area. The analysis revealed maximum values of around 1800 °C.

Another interesting example of quantitative high-temperature analysis with SW and VIS cameras dealt with wafer temperatures in molecular beam epitaxy processes. Substrate temperatures belong to the most important process variables and their accurate knowledge is therefore desirable. Image-based methods have advantages, in particular when studying temperature variations across a wafer. It was demonstrated that a simple and rather inexpensive method may use the silicon sensor of a modified DSLR camera, utilizing IR radiation with wavelengths longer than 720 nm. The camera was calibrated and then applied to wafers, detecting temperatures in a range of 400–600 °C [5].

These were just two examples, and there are of course many more potential applications for quantitative high-temperature measurements with such cameras.

6.3.3.2 Vegetation Studies

Vegetation has very characteristic features in the SW range that are exploited, for example, in satellite-based remote hyperspectral imaging (for an explanation of the technique see Section 3.2.3). An example is the Hyperion imager on board the EO-1 platform, which has 220 spectral bands in the 400–2500 nm wavelength range, a 30 m spatial resolution (corresponding to pixel size), and a 7.5 km swath [11]. The spectral signatures of green vegetation and minerals such as talc, dolomite, chlorite, white mica, and possibly tremolite are clearly resolvable. Several studies focused on green vegetation, and particularly coniferous forest canopy covers [10] and differences with deciduous forests [12]. Usually the difference in reflectance in NIR and VIS is compared [16, 17], which depends on chlorophyll content and plant health. From that one may distinguish between healthy and unhealthy vegetation before differences become apparent to the naked eye.

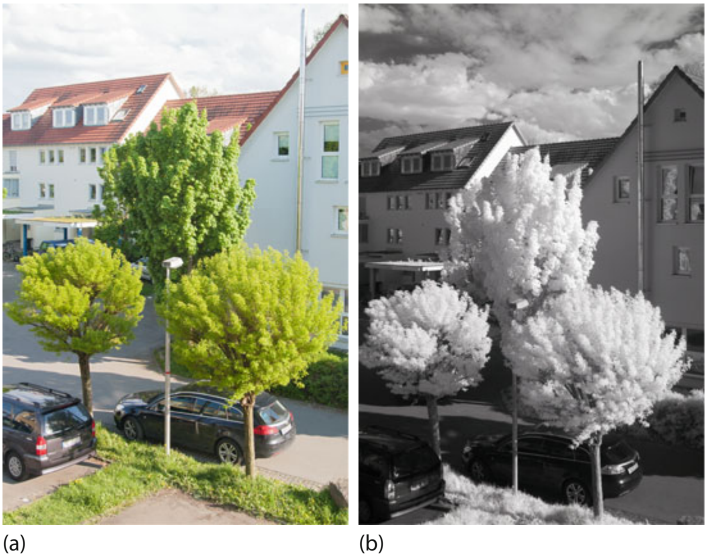

(a) (b)

Figure 6.10 Urban scene (a) in VIS (0.4–0.7 μm) and (b) in NIR (0.8–1.1 μm). Green vegetation appears spectacularly bright in the NIR, and the contrast between sky and clouds is much greater compared to the VIS photo (after [1]).

The main features of vegetation in the SW range become apparent already in recordings of everyday outdoor scenes. Figure 6.10 shows an example of conventional visible photos (Figure 6.10a) and a pure NIR photo (Figure 6.10b) of an urban scene containing houses, sky, clouds, and trees with green leaves. The most obvious differences are indeed much brighter vegetation, darker regions of clear sky, and higher contrast between clear sky and clouds. Already in 1910, the first NIR photographer, Wood, wrote: "… We obtain in this way photographs of objects taken by means of the infra-red radiations. They are quite different in appearance from ordinary photographs, their chief peculiarity lying in the intense blackness of the sky and the extreme brilliancy of the trees and grass. They resemble snow-covered landscapes in bright moonlight more than anything else …" [15]. In honor of his pioneering work on IR photography, the effect by which green vegetation looks extremely bright is called the *Wood effect* [13, 14].

The now commonly accepted explanation of this phenomenon (Figure 6.11a) assumes that light enters the epidermis of leaves and is scattered in deeper sections where there are many cellular walls of interior cells separated by air inclusions. This model is strongly supported by ray-tracing models [9]. Multiple scattering events finally give rise to very strong backscattering.

The strong NIR backscattering in leaves can also be verified experimentally by recording reflection spectra of sunlight from green vegetation. Figure 6.11b shows some examples of reflection spectra for green leaves. There is always a strong increase in reflectance starting around $\lambda = 700$ nm, which correlates well with the scattering observed in the photos. A biological consequence of high-NIR reflec-

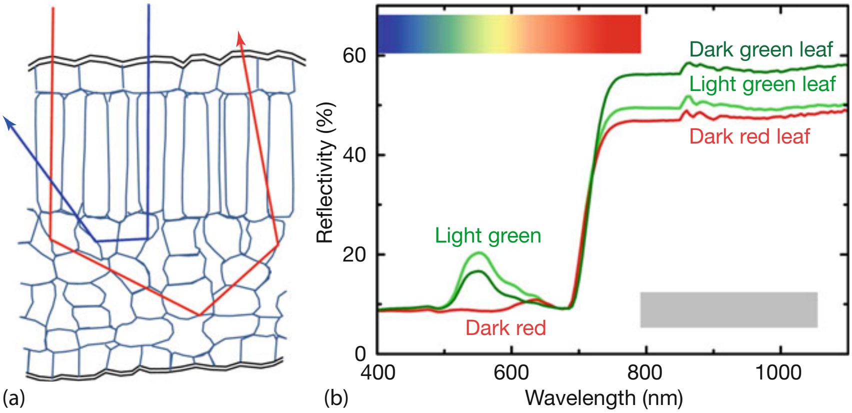

Figure 6.11 (a) Scheme of light paths through leaves: after entering the leaf epidermis, light may be multiply scattered at the cellular walls in deeper regions, as shown for two exemplary rays, the left one being scattered three times, the other one two times. (b) Reflectivity spectra of two green and one red leaf. The minimum thickness of the leaves was around 100 μm for the green and 200 μm for the red leaf (after [1]).

tivity is that plants will not heat up too much owing to incident solar radiation, which is important for survival in hot climates. Interestingly, the NIR behavior appears to be independent of the visual color of the leaf. One may note that the absorption features of chlorophyll, which are responsible for photosynthesis, are only important in the VIS spectral range.

6.3.3.3 Sky-to-Cloud Contrast Enhancement

Figure 6.10 also shows partly cloudy and hazy skies. Similarly, Figure 6.12 depicts a late winter scene with part of our university building, some grass but trees still without leaves and a more or less blue sky.

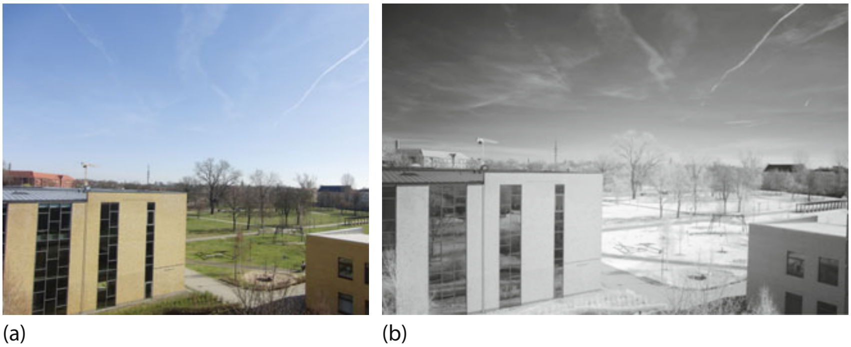

Figure 6.12 VIS (a) and NIR (0.8–1 μm) photo of a scene with blue sky and a few faint cloud shadows.

These images again clearly show that there is a much higher NIR contrast between the clear sky and the clouds. The reason lies in the scattering characteristics of molecules, haze particles, and the much larger cloud droplets.

Qualitatively, the molecular scattering efficiency by atmospheric gases undergoes a rapid ($1/\lambda^4$) falloff. In contrast, the scattering by much larger cloud droplets leads to a more gradual reduction of scattering efficiency with wavelength. The consequence is higher NIR contrast.

A quantitative explanation can be based on Figure 6.13, which depicts theoretical spectra of scattered light from the clear zenith sky (lower curve at long wavelengths) and an altostratus cloud (top curve at long wavelengths). Obviously, the clouds give rise to a much higher radiance in the NIR compared to the VIS spectral range. This means that clouds will have a much higher contrast in a NIR image compared to a VIS image and that they will be imaged as bright and sometimes quite spectacular objects compared to a clear sky.

A similar explanation applies to tiny haze particles. Their size lies in between those of molecules and cloud droplets but – like molecules – they still predominantly scatter light according to the ($1/\lambda^4$) law, that is, they will scatter much less in the NIR than in the VIS spectral range. Therefore, NIR images have also been considered to help in the reduction of haze effects in photography [20]. As a consequence, NIR imaging is also used as a means of contrast enhancement [19]. This is nicely illustrated in Figure 6.14, which shows NIR and VIS images of the San Francisco–Oakland Bay Bridge in haze (panels a,b) and of a forest fire, observed from a plane from a distance of several kilometers (panels c,d). NIR images were recorded with 640 × 512 pixels. The bridge was recorded in July 2008 with a lot of haze in the air. It was at a distance of about 10 km, the hills behind at about 40 km.

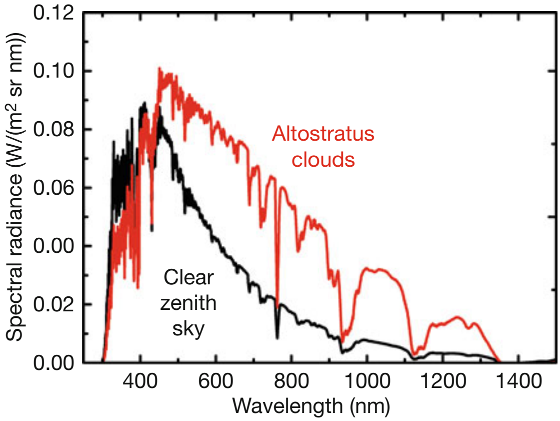

Figure 6.13 Spectra of scattered sunlight for clear zenith sky and altostratus cloud calculated with Modtran for solar zenith angle of 45° and the 1976 US Standard Atmosphere model, which represents quite typical midlatitude conditions that are relevant to much of the USA and Europe. The simulated cloud was characterized by a base at 2.4 km, top at 3.0 km, and total extinction of 128.1 km^{-1}, that is, the cloud optical depth is 0.6 km · 128.1 km^{-1} = 76.9 (after [1]).

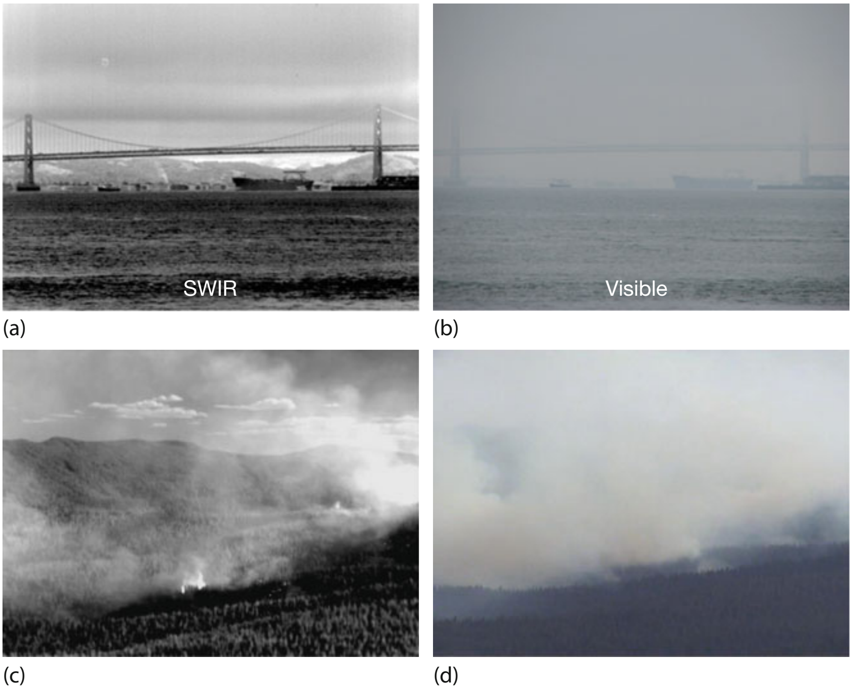

Figure 6.14 SW IR (a,c) and VIS (b,d) images side by side. (a,b) San Francisco–Oakland Bay Bridge and distant hills observed through haze. (c, d) Forest fire around Mt. Hood from plane. Images courtesy: UTC Aerospace Systems..

The difference in contrast and visibility with clear advantages for SW imaging is obvious. Similarly, SW radiation with its longer wavelengths than VIS light can penetrate forest fire smoke, which is also composed of tiny particles that scatter less at longer wavelengths. The images in Figure 6.14c,d were recorded in the Mt. Hood region from distances of around 2 to 7 km. Again, the SW radiation can more easily penetrate through the smoke such that the SW image reveals where the active hot spots are. We mention that for the purposes of looking through haze and forest fire surveillance, one may also use longer-wavelength IR cameras (Sections 10.9 and 11.5.2).

6.3.3.4 Sorting Plastics and Detecting Liquid Levels in Plastic Containers

Plastics are selective absorbers and emitters (Figure 1.55 and Section 10.8). This means that they are partially transparent to IR radiation. The rather sharp and characteristic absorption features in the spectra correspond to well-defined excitations in the polymer molecular structures in plastics. Therefore, different plastics have different IR spectra, in particular different SW spectra as well. This property has led to an industrial application involving the sorting of plastics in recycling facilities [21–23]. Similarly, different SW spectra have been used for the material classification of cellulose-based materials such as paper, pulp, and cardboard [24].

The task of plastic sorting is to identify and sort bales of crushed and commingled bottles and containers. Polyethylene terephthalate (PET) and polyvinyl chloride (PVC) bottles are difficult to distinguish by sight alone, but doing so correctly is crucial for the sorting of these particular polymers. Just a few parts per million of PVC in the PET remolding process will ruin the PET resin from recycled material and any products made from it. The distinction between PET and PVC is made by their dominant absorbance peaks in the SW IR range, which is at 1660 nm for PET and 1716 nm for PVC. Therefore, IR sensors analyze the plastic parts according to their spectra. The method has been used successfully to identify polymer types in samples of crushed, dirty bottles collected from a recycling plant.

The fact that plastics are selective emitters and absorbers, that is, are partly transmitting in the NIR range, has another interesting application. Consider, for example, colored plastic containers that are opaque in the VIS spectral range. When they contain strongly absorbing liquids such as water, a SW IR camera can detect the filling level [31]. The reason is simple: incident SW radiation is incident on the bottle and its content. It will be scattered toward the observer. However, water absorbs more than the air above it, so there will be a strong contrast indicating the filling level.

Figure 6.15a shows an example of a green and, in the VIS range, opaque plastic bottle. It is partly filled with water, the regular visible photo (Figure 6.15c) shows no change whatsoever. In contrast, if detected in the SW, there is a change from the empty (Figure 6.15b) to the partly filled bottle (Figure 6.15d).

6.3.3.5 **Looking Beneath the Surface**

The first time IR radiation was excessively utilized in a technique to investigate paintings below the paint layers was around 1956 [53]. Owing to the development of much better IR camera technology in subsequent decades, a method called *IR reflectography* for the investigation of artwork was established [54]. In brief, NIR radiation is able to penetrate below paint layers, thereby enabling a look beneath the surface. This makes it possible to reveal, for example, underdrawings and, thus, can help to establish whether a painting is genuine or a fake. IR reflectography now belongs to the established methods in art inspection, similar to X-ray radiography (see, e.g., also [25–27, 29]).

The principle idea behind IR reflectography or similar techniques to look beneath a surface covered with paint or varnish is illustrated in Figure 6.16. The layer names here refer to those used for paintings; however, the scheme may also be applied to other surfaces, covered with visibly opaque layers. A painting consists of a canvas covered by a ground layer. Quite often artists used a pencil or coal underdrawing on the ground layer before adding the paint layers and finally the varnish. For analysis, in particular IR reflectography, the painting is illuminated by VIS and NIR radiation. In visible light, the paint layer hides the ground and drawings due to absorption in the paint pigments and reflection, that is, the visible light cannot

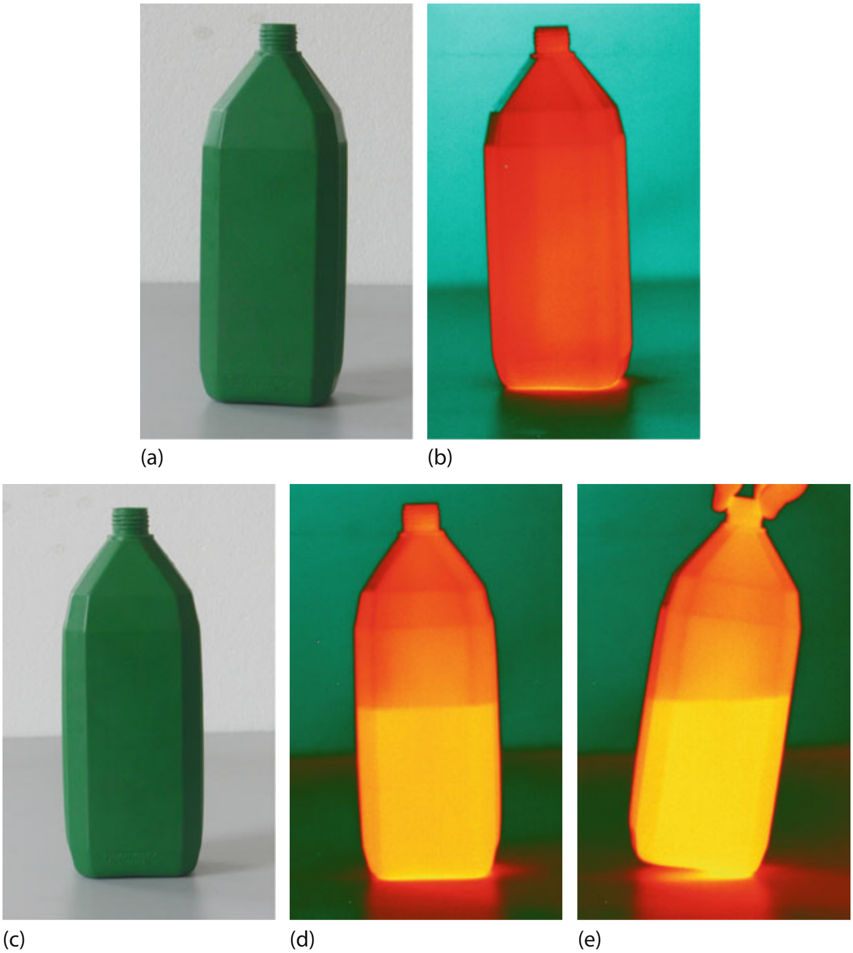

Figure 6.15 Visibly opaque dark green plastic bottle, either empty (a,b) or partly filled with water (c–e). The VIS camera image (c) shows no difference from (a), whereas the water level can be easily detected by the InGaAs SW camera (d,e).

penetrate the whole paint layer. In contrast, many pigments no longer absorb radiation of longer wavelengths in the SW range. Therefore, SW radiation can go as far as the drawings on top of the ground layer. How much radiation reaches the ground depends on the thickness of the paint layer and types of pigments used. Some paints will be transparent to SW, others will partially absorb, appearing gray or even black. As a rule, the longer the wavelength, the less absorption will take place. IR radiation that is backscattered either from pigments or the ground layer is imaged with a SW camera.

In art inspection sciences, the resulting image is called an *IR reflectogram*. Ideally, the ground layer is white and highly reflective and underdrawings are made from carbon-containing materials like carbon black. The latter have high absorp-

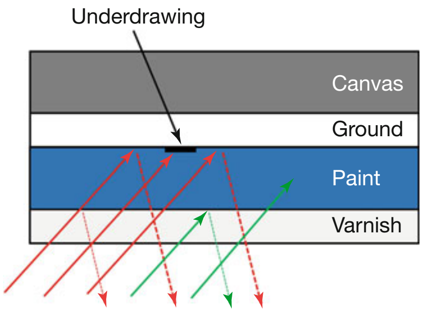

Figure 6.16 Scheme of working principle of IR reflectography or similar techniques to look beneath the surface layers of objects. NIR radiation (red) usually penetrates the paint layer but may be absorbed from underdrawings, whereas visible light (green) is absorbed in the paint layer (after [29]).

tion in the NIR range, that is, there is much less backscattered radiation from the underdrawing than from the ground, which results in high contrast.

Usually, InGaAs cameras are used in IR spectrography. Since art inspections almost always require high spatial resolution, specialized manufacturers now offer scanning systems with up to 16 megapixels [55]. A corresponding analysis may

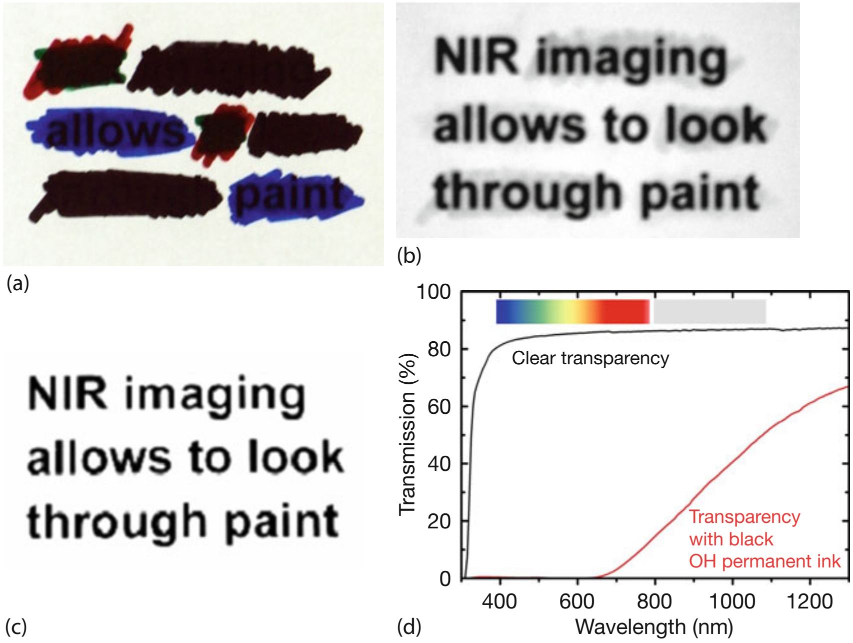

Figure 6.17 VIS (a), NIR (b), and InGaAs (c) photo of black text from a laser printer on regular paper as seen through various colored text markers. In the VIS (a) it is very difficult to read the text and one might just be able to see through the blue color. The NIR (b) and InGaAs photos (c) do, however, allow one to make out the text.

use a 250 lux illumination source and scan an image within 2 to 10 min at high resolution. To be sensitive to various paint layers (pigments), one can also use different spectral filters.

We demonstrate the principle of IR reflectography in a simple experiment [1, 28]. As paint we first use colored ink from permanent overhead transparency markers on top of black text from a laser printer on regular paper illuminated by an incandescent lamp. It is nearly impossible to read the text below the ink in the visible photo (Figure 6.17a). If anything at all is legible, it will likely be the text below the blue ink in light transmitted through the paper. In contrast, the NIR photo recorded using a modified DSLR camera (Figure 6.17b) demonstrates that the ink is more or less transparent to NIR radiation. The original photo (which still had some residual false color; see [1]) was transformed into a grayscale image and slightly contrast enhanced. Last but not least, the photo recorded with the InGaAs camera (Figure 6.17c) shows the text with good contrast and clearly demonstrates that it is very easy to see beneath surfaces. Figure 6.17d shows an exemplary transmission spectrum of the black ink, which was covering part of a clear overhead projector transparency. Clearly, the ink transmits nearly no visible light but is becoming transparent in the NIR range.

Similarly, Figure 6.18 shows an example of a text covered by thick layers of various acrylic color paints such that the text is no longer legible in the visible photo

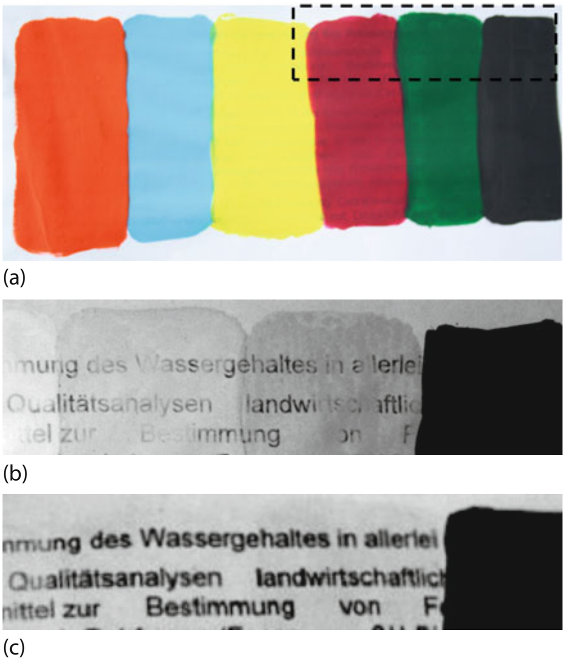
(a)
(b)
(c)
nmung des Wassergehaltes in allerlei
Qualitätsanalysen landwirtschaftlic
nittel zur Bestimmung von F

Figure 6.18 VIS (a), NIR (b), and SW IR (c) photo of black text seen through acrylic paints. The NIR and InGaAs images are enlarged sections from the upper right corner and cover black, green, red, and the beginning of the yellow color.

(Figure 6.18a). In contrast, the NIR photo by the DSLR camera (Figure 6.18b) and the InGaAs camera image (Figure 6.18c) allow us to read most of the text. The acrylic black does indeed absorb a lot of NIR as well as SW IR and is not transparent. The nearby green paint still absorbs part of the NIR radiation between 0.8 and 1.1 μm but becomes more transparent toward longer wavelengths, which explains the difference between panels b and c of Figure 6.18.

The paint layers in the preceding example were opaque, mostly because of absorption within the pigments. A second reason why objects can be opaque is scattering. Radiation transport through materials such as paper involves a lot of scattering but little absorption. Consider, for example, an optical structure such as, once again, black text on white paper (Figure 6.19a). If illuminated by light, an observer will see less light from the absorbing paint than from the surrounding white paper. This leads to contrast, and the text will be readable. If a sheet of paper is placed on top, one might be able to see through the paper and detect text with the naked eye if the paper is thin. For thick paper or two sheets of paper, for example, the eye will be unable to detect the underlying text (Figure 6.19b).

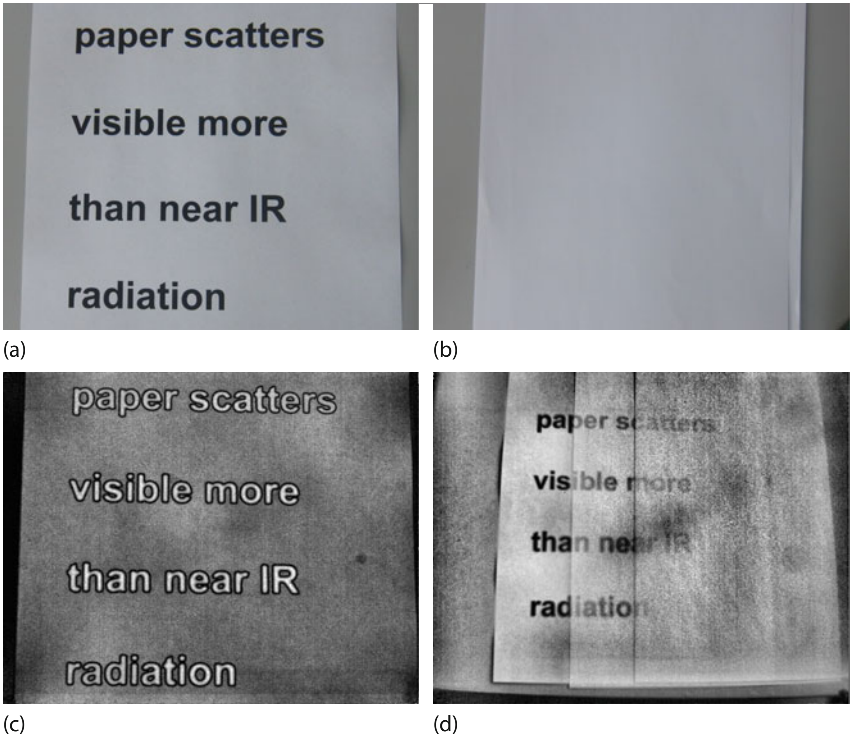

Figure 6.19 Visible (a,b) and SW images (c,d) of black text on paper. If the text (a) is covered with two sheets of paper (thickness around 200 μm, 80 g/m^2), it is no longer legible in the visible image, that is, the paper is opaque (b). For the SW image (d), the two sheets were displaced to better visualize the effect. The text is still clearly recognizable.

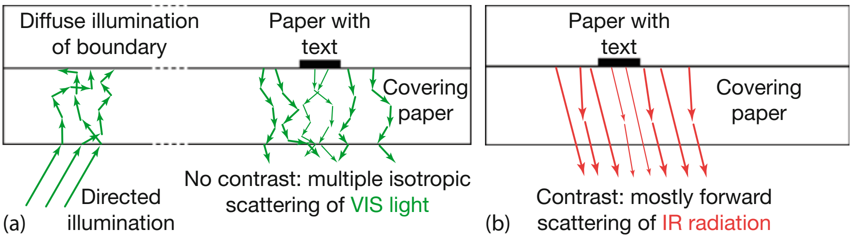
Diffuse illumination of boundary
Paper with text
Covering paper
Directed illumination
No contrast: multiple isotropic scattering of VIS light
(a)
Paper with text
Covering paper
Contrast: mostly forward scattering of IR radiation
(b)

Figure 6.20 (a) Visible light undergoes multiple scattering in paper such that any directional information is lost after a few scattering events. (b) NIR radiation scatters mostly in the forward direction.

The explanation is multiple scattering: after a large number of scattering events, any initial directional information of the visible light propagation (which may give rise to an image contrast) is lost (Figure 6.20a). This applies to potential directed illumination as well as diffusely scattered radiation from the inner boundary. Therefore, any contrast at the interface is washed out in a covering paper. The scattering efficiency of radiation in paper is, however, wavelength dependent. The longer NIR wavelengths are scattered less. Forward scattering dominates such that some of the text can still be read/guessed (Figure 6.19d), in particular if some image-processing contrast-enhancement technique is applied (either included in the software or supplementary program used after recording).

In transmission, that is, having the text and the paper between a light source and the camera, we could even see through up to 10 pages (1 mm thick).

Finally, NIR radiation can also be used in the inspection of banknotes. Most banknotes have a number of characteristic features that are used to test for forgery, and some of these features can be clearly seen in NIR radiation.

6.3.3.6 Undamaged Fresh Fruit/Vegetable Test

The fruit industry faces the general problem that before or during transport, some fruit may become damaged, for example, by bruises, which on the one hand decreases fruit quality and on the other can lead to much shorter ripening times.

Several inspection techniques are available, one of them being nondestructive inspection by NIR imaging.

The criterion for a bruise in this case is a change in reflectance with respect to undamaged fruit. Figure 6.21 illustrates how NIR reflection spectra in pears can change.

Fruit with bruises has lower reflection since damaged cells beneath the skin become filled with water. NIR radiation penetrates the skin and reaches this water accumulation where it will be more strongly absorbed compared to undamaged fruit flesh. This leads to a contrast in SW images where (if the false color or grayscale is not inverted) the bruises appear darker than undamaged parts from the same fruit. Since this technique is very sensitive, it is possible to detect bruises before they become visible to the naked eye. The sensitivity can be enhanced by comparing two images, one recorded using a filter within an absorption band,

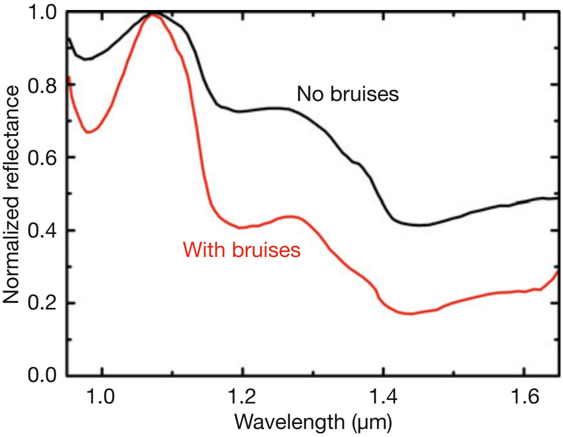

Figure 6.21 Normalized SW IR reflectance spectra in pears with and without bruises (after [32]).

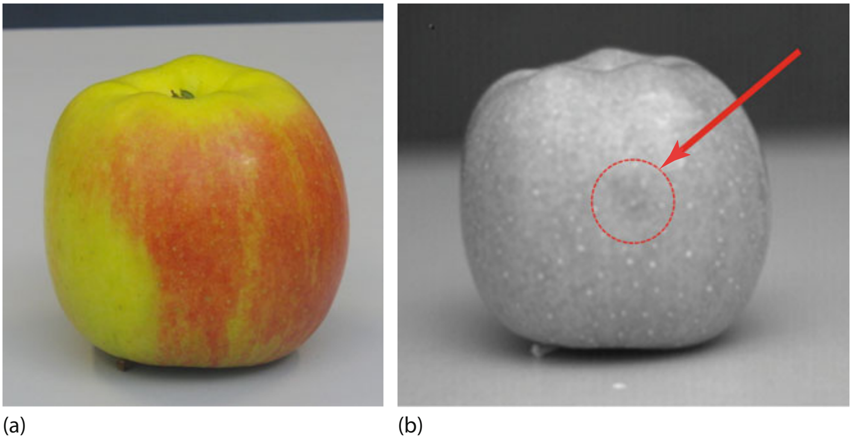
(a) (b)

Figure 6.22 An apple with a bruise that is not evident to the naked eye (a) but is detected by SW IR (b).

the other one outside. Overall this technique may be described as detecting the moisture uniformity and density of a product compared to a reference image taken from a similar object with known moisture content (see also [30–32]).

Figure 6.22 shows a VIS and a SW IR image of an apple with a bruise. It was not yet visible to the naked eye, but it was detectable to the SW camera.

6.3.3.7 **Material Properties of Liquids**

Some liquids that have very intense colors in the visible spectral range can appear colorless and highly transparent in the NIR. Figure 6.23 shows examples – recorded with a DSLR camera – of a red wine bottle made of green glass and a col-

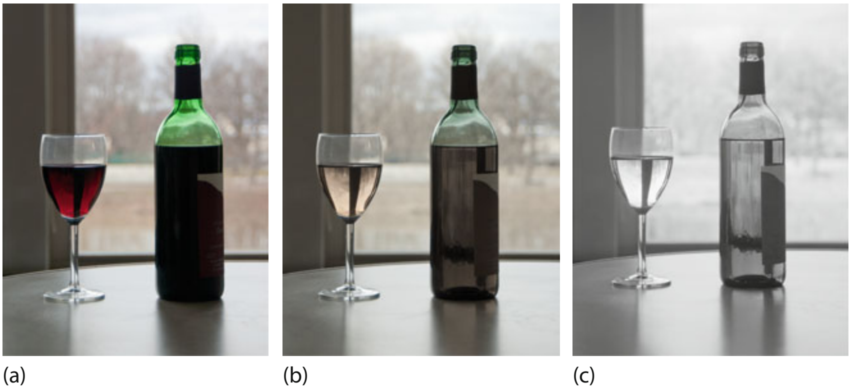

Figure 6.23 Images of a green wine bottle and a clear glass filled with red wine recorded with a modified DSLR camera. (a) For VIS light only, (b) for the whole range of VIS and NIR, and (c) for NIR only. Photos courtesy K. Mangold (after [1]).

orless wine glass filled with red wine. The first image (Figure 6.23a) was recorded with a normal IR cutoff filter ($\lambda = 400{-}700$ nm), the last (Figure 6.23c) with an IR-transmitting filter ($\lambda = 830{-}1100$ nm), and the middle one (Figure 6.23b) without any filter ($\lambda = 400{-}1100$ nm). The familiar looking VIS image (Figure 6.23a) shows a deep red color for the wine. In contrast, the NIR image (Figure 6.23c), recorded in grayscale mode, gives the impression that there is water in the glass and that the bottle is clear. This means that both the red wine and the green glass have turned transparent in the NIR range. When detecting VIS plus NIR radiation simultaneously (Figure 6.23b), the green bottle still looks greenish and the wine in the glass still has a red tint.

Figure 6.23b also explains why IR cutoff filters are used in digital photography: any photographer would be extremely puzzled since the photo shows some liquid that resembles a wine mixed with water more than pure red wine, that is, colors perceived by such a camera would not be the same as those observed with the naked eye. Similar images could also be recorded for other liquids, for example, Coke or coffee.

The explanation of the apparent liquid change from nearly opaque in the VIS (Figure 6.23a) to transparent in the NIR (Figure 6.23c) is simple when studying the corresponding transmission spectra. Figure 6.24 depicts the spectra of water compared to red wine. They were recorded for a 1 cm path length in glass cuvettes, so reflection losses from the glass interfaces with air and water account for the decrease in maximum transmission from 100% to about 91%. The red wine shows several absorption features in the VIS range with a steep increase in transmission for longer wavelengths. This explains the red color. However, compared to water, red wine is similarly transparent in the NIR up to about 1400 nm. However, thicker liquid samples, such as 5 cm for a glass or bottle, can exhibit a lower level of transmission than water owing to the residual differences in the 800–900 nm range.

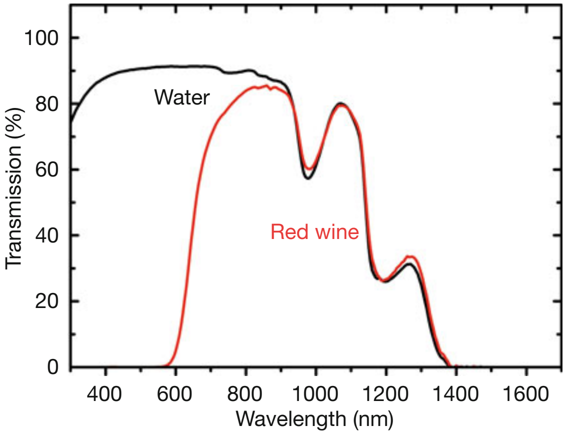

Figure 6.24 Transmission spectra of red wine and water for a liquid path length of 1 cm (see text for details) (after [28]).

Figure 6.25 shows a scene similar to that in Figure 6.23 but resembling a kind of puzzle. Now, besides a green wine bottle and two transparent glasses, there is also a transparent plastic bottle filled with water. The glass on the left is filled with red wine, that on the right with water. The first two images were recorded (Figure 6.25a) in the VIS spectral range, $\lambda = 400–700$ nm, and (Figure 6.25b) in the NIR ($\lambda = 830–1100$ nm) with the DSLR camera Canon EOS 1000D. The third image (Figure 6.25c) was recorded with an InGaAs camera ($\lambda = 900–1700$ nm).

The appearance of the water versus the wine differs considerably from one photo to the next. In the VIS, we have the expected behavior of transparent water but nearly opaque (i.e., very dark and red) wine. In the NIR, similar to Figure 6.23 and explained by the spectra of Figure 6.24, both the water and the wine look similar and are transparent.

However, probably unexpectedly, the InGaAs image (Figure 6.25c), compared to the NIR image of Figure 6.25b, shows both liquids as being nearly opaque. According to the spectra of Figure 6.24 and the detector sensitivities (Figure 6.3), one might have expected a transmission similar to that of the NIR camera, that is, at least partially transparent water and wine.

The explanation is simple but is based on a quantitative analysis. The observed signal is due to the wavelength dependence of detector sensitivity. For InGaAs it is quite small for the short wavelengths where the water and wine samples still have some transmission. For longer wavelengths, where sensitivity is high, the transmission is very small. As a consequence, the detector-waveband-integrated transmission signal of wine and water (now about 5 cm thick) only amounts to a small percentage of the transmission of a nonabsorbing specimen, that is, it must appear very dark.

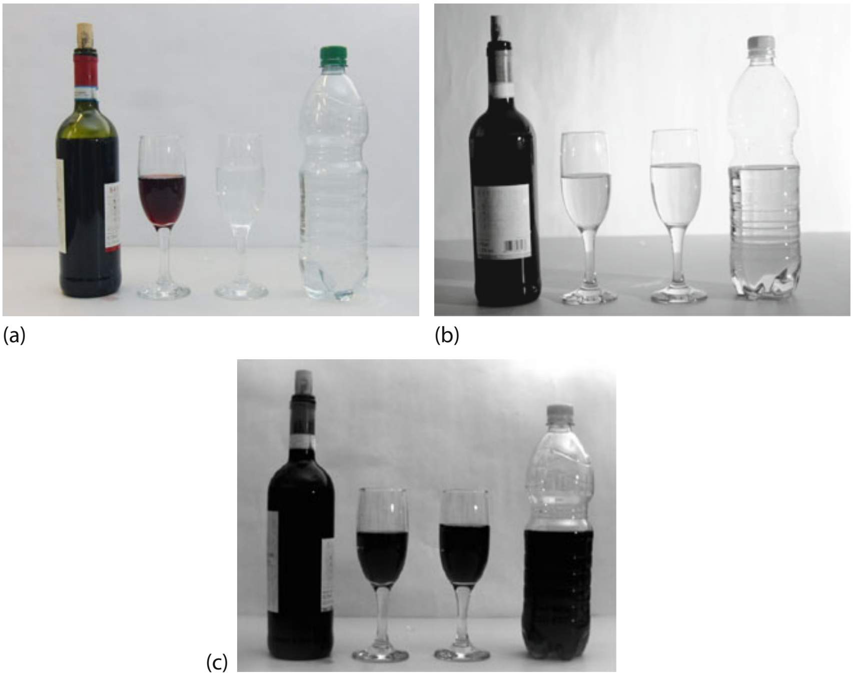

(a) (b) (c)

Figure 6.25 Scene with wine and water bottles and two glasses filled with red wine (left) and water (right). (a) VIS photo, (b) NIR photo recorded with Canon EOS1000 D, and (c) SW IR photo recorded with FLIR SC2600 InGaAs camera (after [28]).

6.3.3.8 **Moisture on Walls**

As mentioned earlier, satellite remote sensing techniques have been used extensively in recent decades to study, for example, the composition of soils and minerals and changes in vegetation. Owing to the strong water absorption bands in the SW IR, airborne and satellite imaging has also been used to study explicitly the water content in soils [33–35]. Of course, SW IR imaging does not require long distances and need not be done remotely. Rather, NIR cameras may be used to visualize hidden moisture in nearby objects, for example, wood [26]. Similarly, SW cameras are also useful for detecting moisture within walls of buildings, so they nicely complement information from LW building thermography cameras.

Figure 6.26 shows an example of a plain concrete wall with some light and electrical protection switches. The wall is covered with white paint. Using a thin wet paper towel rolled around a pen, some words were written as a very thin water film on the wall. They are, of course, not visible to either the naked eye or a VIS camera (Figure 6.26a) but are easily recognized in the NIR range (Figure 6.26b,c).

6.3.3.9 **Other Applications of SW Imaging**

As summarized in Table 6.1, there are many more uses of SW imaging. Here just another few shall be briefly mentioned. SW imaging has been used for wafer and

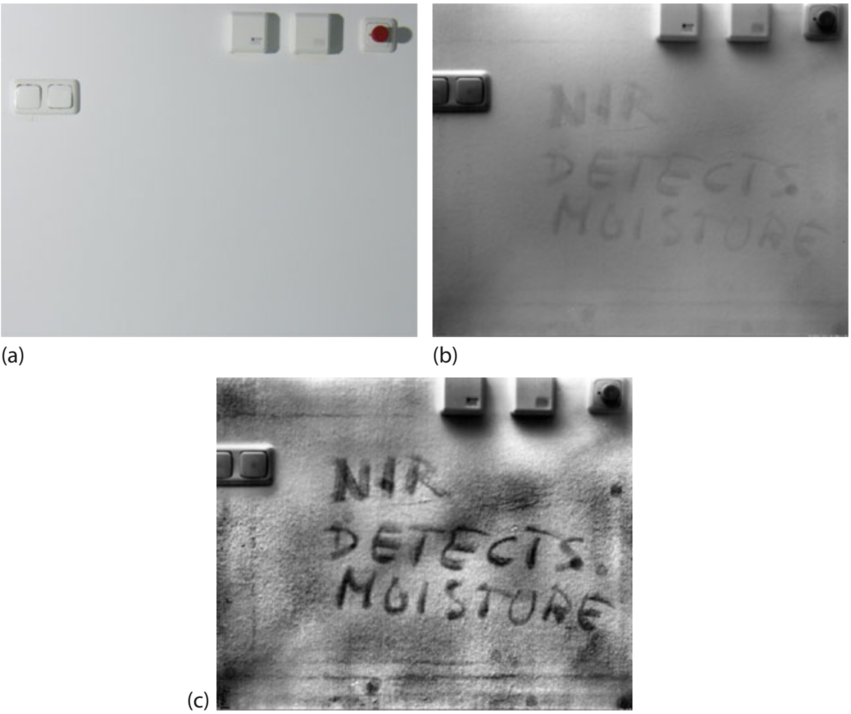

(a) (b) (c)

Figure 6.26 Writing with a wet paper towel on a wall produces a thin water film that is not visible in regular VIS images (a) but easily read by a NIR camera (b). Further contrast and image enhancement (c) help to filter the relevant information, here the moist wall from the dry wall. The scene was about 1 m wide. The text could be read for several minutes until the water had completely evaporated.

solar cell wafer inspections, using mostly photoluminescence at $\lambda = 1150$ nm [42–44]. It is also a standard technique for telecommunication equipment testing [45, 46]. For InGaAs cameras some typical applications include beam profiling, location of free space communications laser beams at 1.55 μm, dynamic imaging of routers and switches, and detection of laser operation.

From the multitude of medical applications [1, 26, 47–51], we may first mention that NIR images of humans look strange. The appearance of skin in NIR images is strongly influenced by its moisture content, which is much higher than that of hair. Moisture absorbs a lot of NIR radiation and thus reduces the signal from moisture-containing object parts. In contrast, hair is usually dry and shows up with larger radiation scattering signals, which becomes white in a grayscale image compared to the darker skin (Figure 6.27). The liquid in the surface layer of the eyes absorbs, which also makes the eyes look very dark. Note again that the dry eyebrows look white. As a consequence, people look much older since they appear to have white hair and strangely looking deep eyes. It may well be that such images have been used or will be used in horror movies (incidentally, the number below the image is not a prisoner identification number but details of the recording).

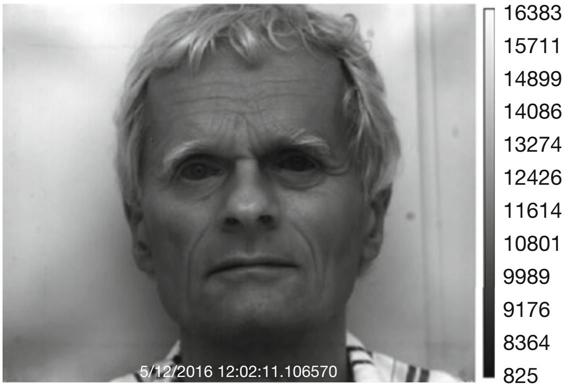

Figure 6.27 Strange looking human face in SW IR (recorded with InGaAs camera).

A very important practical medical application is the detection of blood vessels below the skin surface which may help to reduce pain in treating very small children. Astronomy has numerous applications in the SW IR spectral range, as discussed in Section 1.7.2.3 [40, 41]. Major results were collected by the Hubble Space telescope and many more are expected from follow missions of NASA and ESA concerning modern astronomical instruments. Finally, SW cameras have many applications in the field of surveillance, security, and crime scene analysis (see, for example, the advertisements of all the main manufacturers or [38, 39]). The high sensitivity of modern cameras even allows for vision enhancement in natural low light conditions using just the residual light from the so-called atmospheric nightglow [36, 37]. This natural light source is due to sunlight-induced photochemical dissociation processes of air molecules (e.g., O_2, H_2O, O_3, CH_4) during daytime. At night, molecular radicals may recombine. Many of the involved processes leading to molecules or atoms in excited vibrational or electronic states have characteristic times on the order of hours or days. In the NIR, mostly recombination radiation from OH hydroxyls in the upper atmosphere (heights of 70–300 km) contributes. The brightness of this atmospheric residual light is typically more than five times greater than that of starlight, spanning virtually the entire SW IR range from 1.0 to 1.7 μm.

6.4
Survey of Commercial Systems

Table 6.2 gives an overview of commercially available nonmilitary SW IR cameras. This selection may not be exhaustive and should be considered a snapshot of what is possible and available. Details on the camera systems, such as frame rates or integration times, can be obtained directly from the manufacturers.

Table 6.2 Commercial manufacturers/suppliers of SW cameras (alphabetical order, no claim of completeness, accessed May 2017); a no for T calibration means that it may be possible but is not offered. opt. means optional.

Name	Detector max. array size T calibration	Camera series or names/web site (all accessed May 2017)
Allied Vision	InGaAs 0.9–1.7 μm 640 × 512 no T cal.	Goldeye https://www.alliedvision.com/en/products/cameras.html
DIAS Infrared	Si 0.8–1.1 μm 768 × 576 up to 3000 °C InGaAs 1.4–1.6 μm 320 × 256 300–1200 °C	Pyroview www.dias-infrared.com
Edmund Scientific	InGaAs 1.46–1.6 μm 752 × 582 no T cal.	1460–1600 nm NIR Camera http://www.edmundoptics.de
FLIR	InGaAs 0.9–1.7 μm, opt. 0.4 – 1.7 μm 640 × 512 T cal. opt. ≤ 3000 °C	Examples: Tau SWIR, SC2600, A 6250sc SWIR www.flir.com
IMS Chips	Si 640 × 480 600–3000 °C	HDRC-Q-PyroCam Ratio thermography http://www.ims-chips.de
IR Cameras	InSb opt. 0.4–5 μm, SW: 0.9–2.5 μm, 1280 × 1024 no T cal.	IRC912-SWIR http://www.ircameras.com
Lumasense	Si: 0.78–1.08 μm 640 × 480 600–3000 °C	MCS640 http://www.lumasenseinc.com
Optris	Si: 0.92–1.1 μm 764 × 480 T cal. Yes	PI 1M http://www.optris.com
Photonic Science	InGaAs 0.9–1.7 μm opt. 0.4–1.7 μm 640 × 512 no T cal.	PSL SWIR cameras http://www.photonic-science.co.uk
Princeton	InGaAs 0.9–1.7 μm 640 × 512 no T cal.	NIRvana http://www.princetoninstruments.com
Sensors Unlimited	InGaAs 0.9–1.7 μm opt. 0.4(0.7)–1.7 μm up to 1280 × 1024 no T cal.	640HS SWIR www.sensorsinc.com
Xenics	InGaAs 0.9–1.7 μm opt. 0.4–1.7 μm 640 × 512 no T cal.	Bobcat http://www.xenics.com/en/

References

1 Mangold, K., Shaw, J.A., and Vollmer, M. (2013) The physics of near-infrared photography. *Eur. J. Phys.*, **34** (6), 51–71.

2 Hamamatsu InGaAs selection guide, https://www.hamamatsu.com/resources/pdf/ssd/ingaas_kird0005e.pdf (accessed May 2017).

3 Rafferty, C., King, C., Ackland, B., O'Neill, J., Aberg, I., Sriram, T.S., Mackay, A., and Johnson, R. (2008) Monolithic germanium SWIR imaging array, Proc. IEEE Conf. Technol. Homeland Security, 577–582.

4 Chen, J., Osborn, P., Paton, A., and Wall, P. (1993) CCD near infrared temperature imaging in the steel industry, Proc. Instrumentation and Measurement Technology Conf., IEEE 1993.

5 Jackson, A.W. and Gossard, A.C. (2007) Thermal imaging of wafer temperature in MBE using a digital camera. *J. Cryst. Growth*, **301/302**, 105–108.

6 Price, S., Cooper, K., and Chou, K. (2012) Evaluations of temperature measurements by near infrared thermography in powder-based electron-beam additive manufacturing, 2012 Solid Freeform Fabrication Symposium, http://sffsymposium.engr.utexas.edu/Manuscripts/2012/2012-57-Price.pdf (accessed May 2017).

7 Köhler, H., Jayaraman, V., Brosch, D., Hutter, F.X., and Seefeld, T. (2013) A novel thermal sensor applied for laser materials processing. *Phys. Proc.*, **41**, 502–508.

8 Goecke, S.-F. and Ebert-Spiegel, M. (2015) Towards a more robust automated MAG welding, Proc. 2015 IEEE Int. Conf. on Automation Science and Engineering (CASE), Gothenburg, Sweden.

9 Allen, W.A., Gausman, H.W., and Richardson, A.J. (1973) Willstatter–Stoll theory of leaf reflectance evaluated by ray tracing. *Appl. Opt.* **12** (10), 2448–2453.

10 Lobell, D.B., Asner, G.P., Law, B.E., and Treuhaft, R.N. (2001) Subpixel canopy cover estimation of coniferous forests in Oregon using SWIR imaging spectrometry. *J. Geophys. Res.*, **106** (D6), 5151–5160.

11 Cudahy, T.J., Hewson, R., Huntington, J.F., Quigley, M.A., and Barry, P.S. (2001) The Performance of the Satellite-borne Hyperion Hyperspectral VNIR-SWIR Imaging System for Mineral Mapping at Mount Fitton, South Australia, p. 314–316 in vol. 1 of Geoscience and Remote Sensing Symposium, 2001. IGARSS '01. IEEE 2001 International.

12 Cipar, J., Cooley, T., Lockwood, R., and Grigsby, P. (2004) Distinguishing between coniferous and deciduous forests using hyperspectral imagery, IGARSS 2004. 2004 IEEE International Geoscience and Remote Sensing Symposium Proceedings, vol. 4, pp. 2348–2351.

13 Finney, A. (2007) Infrared photography, in *Focal Encyclopedia of Photography*, (ed. M.R. Peres), 4th edition, Elsevier, Amsterdam, pp. 556–562.

14 Finney, A. (2007) The Wood effect. *RPS J.-R. Photogr. Soc.*, **147.8**, 366.

15 Wood, R.W. (1910) A new departure in photography. *Cent. Mag.*, 565–572.

16 Hogan, J.A. *et al.* (2012) Detection of leaking CO_2 gas with vegetation reflectances measured by a low-cost multispectral imager. *IEEE J. Sel. Top. Appl. Earth Obs. Rem. Sens.*, **5** (3), 699–706.

17 Shaw, J.A. *et al.* (2012) Multispectral imaging systems on tethered balloons for optical remote sensing education. *J. Appl. Rem. Sens.*, **6** (1), 063613.

18 Richards, A. (2001) *Alien Vision*, SPIE Press, Bellingham/Washington, see also: Emerging applications for high-performance near-infrared imagers, Proc. SPIE, vol. 4710, Thermosense XXIV, 450 (2002).

19 Malchow, D. NIR Trends: Penetrating The Haze of Scattered Light, Photonics Online newsletter (10/24/08) see www.photonicsonline.com/doc/nir-trends-penetrating-the-haze-of-scattered-0001 (accessed May 2017).

20 Schaul, L., Fredembach, C., and Süsstrunk, S. (2009) Color image dehazing using the near-infrared, Proc. IEEE Int. Conf. Image Pro-

cessing (ICIP), pp. 1629–1632, doi:10.1109/ICIP.2009.5413700.

21 Scott, D.M. (1995) A two-colour near-infrared sensor for sorting recycled plastic waste. *Meas. Sci. Technol.*, **6**, 156–159.

22 van den Broek, W.H.A.M., Wienke, D., Melssen, W.J., and Buydens, L.M.C. (1998) Plastic material identification with spectroscopic near infrared imaging and artificial neural networks. *Anal. Chim. Acta*, **361**, 161–176.

23 Kulcke, A., Gurschler, C., Spöck, G., Leitner, R., and Kraft, M. (2003) On-line classification of synthetic polymers using near infrared spectral imaging. *J. Near Infrared Spectrosc.*, **11** (1), 71–81.

24 Tatzer, P., Wolf, M., and Panner, T. (2005) Industrial application for inline material sorting using hyperspectral imaging in the NIR range. *Real-Time Imaging*, **11** (2), 99–107.

25 Dinwiddie, R.B. and Dean, S.W. (2006) Case study of IR reflectivity to detect and document the underdrawing of a 19th century oil painting, Proc. SPIE, vol. 6205, Thermosense XXVIII, 620510.

26 Ebeid, A., Rott, S., Talmy, E., Ibarra-Castanedo, C., Bendada, A., and Maldague, X. (2010) Near infrared imaging for multi-polar civilian applications, Proc. QIRT 2010-038, 10th Int. Conf. Quant. InfraRed Thermogr., 27–30 July 2010, Quebec.

27 Ambrosini, D., Daffara, C., Di Biase, R., Paoletti, D., Pezzati, L., Bellucci, R., and Bettini, F. (2010) Integrated reflectography and thermography for wooden paintings diagnostics. *J. Cult. Herit.*, **11**, 196–204.

28 Vollmer, M., Möllmann, K.-P., and Shaw, J.A. (2015) The optics and physics of near infrared imaging, in Education and Training in Optics and Photonics (ETOP), (ed. E. Cormier), Laurent Sarger, Proc. SPIE, vol. 9793, 97930Z.

29 Cosentino, A. (2016) Infrared technical photography for art examination, e-PreservationScience (e-PS), **13**, 1–6, www.morana-rtd.com/e-preservationscience/TOC.html (accessed May 2017)

30 Lu, R. (2003) Detection of bruises on apples using near infrared hyperspectral imaging. *Trans. Am. Soc. Agri. Eng.*, **46**, 523–530.

31 Ettenberg, M. and Malchow, D. (2006) Short-wave IR offers unique remote sensing solutions. *Laser Focus World*, 74–76.

32 Lee, W.-H., Kim, M.S., Lee, H., Delwiche, S.R., Bae, H., Kim, D.-Y., and Cho, B.-K. (2014) Hyperspectral near-infrared imaging for the detection of physical damages of pear. *J. Food Eng.*, **130**, 1–7.

33 Ben-Dor, E. (2002) Quantitative remote sensing of soil properties. *Adv. Agr.*, **75**, 173–243.

34 Lobell, D.B. and Asner, G.P. (2002) Moisture effects on soil reflectance. *Soil Sci. Soc. Am. J.*, **66**, 722–727.

35 Whiting, M.L. (2009) Measuring surface water in soil with light reflectance, Remote Sensing and Modeling of Ecosystems for Sustainability VI, Proc. SPIE, vol. 7454, 74540D.

36 Roach, F.E. (1964) The light of the night sky: Astronomical, interplanetary and geophysical. *Space Sci. Rev.*, **3**, 512–540.

37 Vallence Jones, A. (1973) The infrared spectrum of the airglow. *Space Sci. Rev.*, **15,** 355–400.

38 Vandersmissen, R. (2008) Night-vision camera combines thermal and low-light-level images. *Photon. Int.* **2008** (2), 2–4.

39 Kuul, J., Pölönen, I., Puupponen, H.-H., Selander, T., Reinikainen, T., Kalenius, T., and Saar, H. (2012) Using VIS/NIR and IR spectral cameras for detecting and separating crime scene details, Proc. SPIE Conf. Technol. for Homeland Security and Homeland Defense XI, Proc. SPIE, vol. 8359, 83590P.

40 Rieke, G.H. (2009) History of infrared telescopes and astronomy. *Exp. Astron.*, **25**, 125–141.

41 Clements, D.L. (2015) *Infrared Astronomy – Seeing the Heat*, CRC Press.

42 Trupke, T., Bardos, R.A., Schubert, M.C., and Warta, W. (2006) Photoluminescence imaging of silicon wafers. *Appl. Phys. Lett.*, **89**, 044107.

43 Malchow, D. (2009) NIR trends: Photoluminescence inspection of photovoltaics with SWIR imaging. *Photon. Online Newslett.*, (09/11/09), see www.photonicsonline.com/doc/photoluminescence-inspection-of-photovoltaics-0001 (accessed May 2017)

44 Olsen, E. and Flø, A.S. (2011) Spectral and spatially resolved imaging of photoluminescence in multicrystalline silicon wafers. *Appl. Phys. Lett.*, **99**, 011903.

45 Graff, J.H., Meyer, W.H., and Heidner, K.E. (2001) High-performance SWIR cameras for the telecom industry, Proc. SPIE, vol. 4369, Infrared Technology and Applications XXVII, 713.

46 Barton, J., Cannata, R., and Petroni, S. (2002) InGaAs NIR focal plane arrays for imaging and DWDM applications, Proc. SPIE, vol. 4721, Infrared Detectors and Focal Plane Arrays VII, 37.

47 Anderson, R.R. and Parrish, J.A. (1981) The optics of human skin. *J. Invest. Dermatol.*, **77**, 13–19.

48 Kienle, A. *et al.* (1996) Why do veins appear blue? A new look at an old question. *Appl. Opt.*, **35** (7), 1151–1160.

49 Smith, A.M., Mancini, M.C., and Nie, S. (2009) Second window for in vivo imaging. *Nat. Nanotechnol.*, **4**, 710–711.

50 Murkin, J.M. and Arango, M. (2009) Near-infrared spectroscopy as an index of brain and tissue oxygenation. *Br. J. Anaesth.*, **103** (Suppl 1), i3–i13.

51 Cupera, N.J. *et al.* (2013) The use of near-infrared light for safe and effective visualization of subsurface blood vessels to facilitate blood withdrawal in children. *Med. Eng. Phys.*, **35** (4), 433–440.

52 Irvine, W.M. and Pollack, J.B. (1968) Infrared optical properties of water and ice spheres. *Icarus*, **8**, 324–360.

53 Taubert, J. (1956) Dissertation Marburg, Zur kunstwissenschaftlichen Auswertung von naturwissenschaftlichen Gemäldeuntersuchungen, Abdruck in Studien aus dem Institut für Baugeschichte, Kunstgeschichte, Restaurierung mit Architekturmuseum, TU München (2001).

54 van Asperen de Boer, J.R.J. (1969) Reflectography of paintings using an infrared vidicon television system. *Stud. Cons.*, **14** (3), 96–118.

55 Manufacturer of IR cameras for art inspections: http://www.opusinstruments.com/ (accessed May 2017).

Chapter 7
IR Imaging of Buildings and Infrastructure

7.1
Introduction

Infrared (IR) thermal imaging is considered to be an excellent noninvasive inspection tool for monitoring and diagnosing the condition of buildings [1–10] by measuring the surface temperatures of the building envelope from either inside or outside (or both). The surface temperatures of buildings result from three basic mechanisms: the flow of heat, air, and moisture through the building envelope. These three factors not only determine a building's durability and its energy efficiency but also, most importantly, the feeling of comfort, health, and safety for its inhabitants.

Heat flow is the primary mechanism for heating up the surfaces of a building. Heat flows from the warm interior to the cold exterior, giving rise to an increase in outer wall surface temperatures. The corresponding physical quantities, like U-value, were discussed earlier in Section 4.3.3. In general, heat flow can lead to either warming up or cooling of building parts due to conductive differences, thermal bridges, or air infiltration or exfiltration.

Water intrusion into walls/insulation and surface moisture often reduce the measured surface temperatures due to evaporative cooling (Section 5.3.6). However, the huge heat capacity of water, that is, the capacity to store thermal energy, may (besides cooling) also lead to the warming of building parts, depending on conditions. Also, water intrusions into thermal insulation material may lead to an increased thermal conductivity from the inside to the outside with characteristic thermal signatures. Moisture is often present on flat roofs and may penetrate into buildings if the moisture barrier is not correctly installed.

Finally, uncontrolled airflows through air leaks may transport heat via additional convection losses. In addition, airflows affect temperatures in the vicinity of air leaks, for example, in window frames. The reduction of frame temperatures (mostly in corners) in wintertime to below the dew point can give rise to mold problems. Air leaks may also often occur close to wall openings for electrical wiring or plumbing and ducts.

Thermography can be used to identify problems associated with heat, water, and air flows through a building envelope. In this manner, it may be used to auto-

Infrared Thermal Imaging, Second Edition. M. Vollmer and K.-P. Möllmann.
© 2018 WILEY-VCH Verlag GmbH & Co. KGaA. Published 2018 by WILEY-VCH Verlag GmbH & Co. KGaA.

matically test, for example, the energy efficiency of new homes or plan the restoration of old ones. In particular, it may help to

- locate heating and cooling losses;
- locate building envelope water leakages, that is, moisture sources;
- locate structural problems (e.g., missing insulation, degradation of old insulation);
- locate problems in floor heating systems;
- compare pre- and postrestoration conditions.

Since – besides irradiation with ultraviolet (UV) light – the flows of heat and water are also the most important damage functions for buildings, IR inspections may help to save a lot of money for restoration. With regard to energy efficiency, it can help in saving energy needed for the heating of a building and thus reduce the emission of greenhouse gases. In some countries like the United States or Australia, thermography is also a useful tool in pest control, for example, by localizing termites (see Section 11.2.4 for references).

7.1.1
Publicity of IR Images of Buildings

Among the public, IR imaging of buildings is probably the best known application of thermography. This is due to several reasons. First, buildings offer a standard textbook example of thermography. In particular in wintertime, there is usually a large temperature difference between the inside and outside of a house such that defects in the thermal insulation can be easily detected as thermal losses from the building envelope. Hence, thermography is a valuable tool in diagnosing thermal insulation problems of buildings. Second, thermography usually provides false color images of objects. In the modern communication age, false color representations of nearly anything are often welcomed by journalists as eye catchers. In particular, thermographic false color images are often used in newspapers and on many web sites, and IR movie sequences are often shown in TV programs and increasingly on YouTube.

We believe that one reason for this may be that journalists and YouTube video producers, as well as those viewing the images, tend to think that they can immediately grasp the content and draw correct conclusions. And if those conclusions identify a problem previously unknown, the story will become widely known or the video will be downloaded many times, which is good for the author. As a matter of fact, a red color in an IR image is usually considered to be a very bad sign (Figure 7.1).

Unfortunately, it is very easy to produce false color images with IR cameras, and this will become even easier with the new class of low-price thermal imagers or those attachable to smartphones. The lower the price of the cameras, the less experienced and educated users will be and the less they will think about training courses whose cost may be a large part of the price of the camera itself. This will lead to problems.

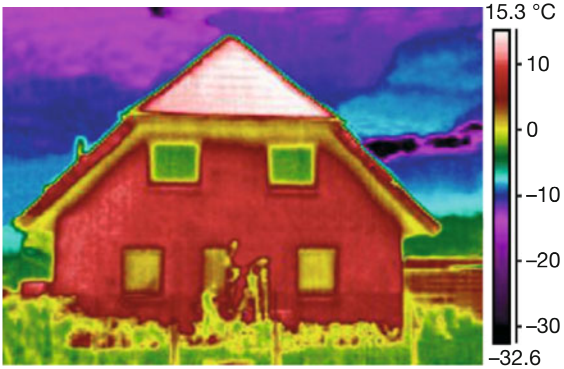

Ein sogenanntes Thermogramm lässt durch Rotfärbung erkennen, dass die Hauswände Wärme abgeben *Foto: dpa*

Figure 7.1 This IR thermal image of a house was published a while ago in a daily newspaper (23 May 2009 in *Berliner Morgenpost*, www.morgenpost.de/berlin/article1097945). The image was published in many newspapers, sometimes even without a temperature scale, the caption usually mentioning that the red color in the figure would indicate where the walls would lose heat. But that statement suggests the whole house needs renovating. Can that really be true?

In this section, we demonstrate that thermal imaging is indeed a very valuable tool in building inspections, and for that reason, it makes sense that buildings are the most common objects in thermal images published in newspapers. However, a large number of external influences may cause problems in the interpretation of thermal images. For this, we return to Figure 7.1 and point out potential problems in a much too easy interpretation of this attractively colored IR image.

7.1.2
Just Colorful Images?

In building thermography, the IR radiation signals contain information about emissivity and surface temperatures (this is often the very first mistake made by amateur thermographers: they interpret any image as showing only temperatures and they neglect any emissivity issues). The second problem is that amateurs often use a color scale and temperature span that exaggerate any slight differences seen. As a matter of fact, the choice of color palette, scale, and span can strongly affect the interpretation.

Therefore, we start by discussing color palettes, level, and span and their role in the initial – often intuitive – interpretation of thermal images. Then, assuming that camera and material parameters are known, we will focus on external influences. We will illustrate some of the major potential interpretation errors in the examination of buildings using thermography. It will be shown that a correct, detailed interpretation of thermal images is a complex problem since many different factors can affect the result of the measurement (e.g., [8]).

7.1.2.1 Level and Span

The lower the span, the more dramatic the appearance of the IR images, indicated by the images in Figure 7.2a–c for a 6 K temperature span (panel a) compared to a 10 K (panel b) or 30 K (panel c) span at the same level. By watching only the largest span image – image (c) $\Delta T = 30\,\mathrm{K}$ – one might not think there was a problem at all because of the small color variations across the image. Keeping the span constant, the change in level (panels d and e) also leads to significant color changes, and if the span is used under the simple notion that red or yellow is bad, one may interpret the house in panel d as a problem case and the one in panel e as fine.

7.1.2.2 Choice of Color Palette

The color palette for the images in Figure 7.2a–e was the same. Very often, color scales are used where red and yellow indicate higher temperatures. As a consequence, most people interpret all IR images accordingly, in particular, if images are shown without a side color bar (this may happen quite often, for example, in newspapers). Figure 7.2g shows the same image for a different color palette. In Figure 7.2h, the sequence of colors is inverted. Obviously these two images (with the same level and span as Figure 7.2b) look very different. For example, Figure 7.2g might suggest that the two skylights and the rectangular area close to the rooftop (a solar thermal power heating system) may present problems, although they are cold. Comparing the colored images of Figure 7.2 with an inverted grayscale image (Figure 7.2f) explains why color palettes are usually preferred. There are many more possibilities in the amplification of small signal differences.

7.1.2.3 More on Palette, Level, and Span

Owing to the variety of manufacturers and the different software packages for a single camera type, there is usually a large number of possible color palettes to select from. The palettes from Figures 7.1 and 7.2a–e are different – but in both cases, red and yellow indicate high temperatures. In contrast, however, the yellow areas in Figure 7.1 have lower temperatures than the red ones, whereas in Figure 7.2a–e, yellow refers to higher temperatures.

Why do we sometimes relate red and yellow to high temperatures and blue to cold? Maybe these colors are sometimes unconsciously associated with known objects such as flames or red glowing heating plates on the one hand and water or ice on the other. This is what we have learned as children and this is how most of us associate colors with temperature, and this may be the first reason for intuitive misinterpretations of false color IR images. By the way, this common human association of color with temperature is in contrast to blackbody radiation in physics, where higher temperatures shift spectra toward the blue, so so-called blue stars are hotter than red ones!

In thermography, the use of false color images is based on the principle that the color perception of the human eye makes it possible to distinguish about a million shades of color, differing in either hue or saturation. However, concerning brightness, the eye is limited to a few hundred levels for a given saturation and hue. Grayscale images differ only in brightness, whereas color images have the

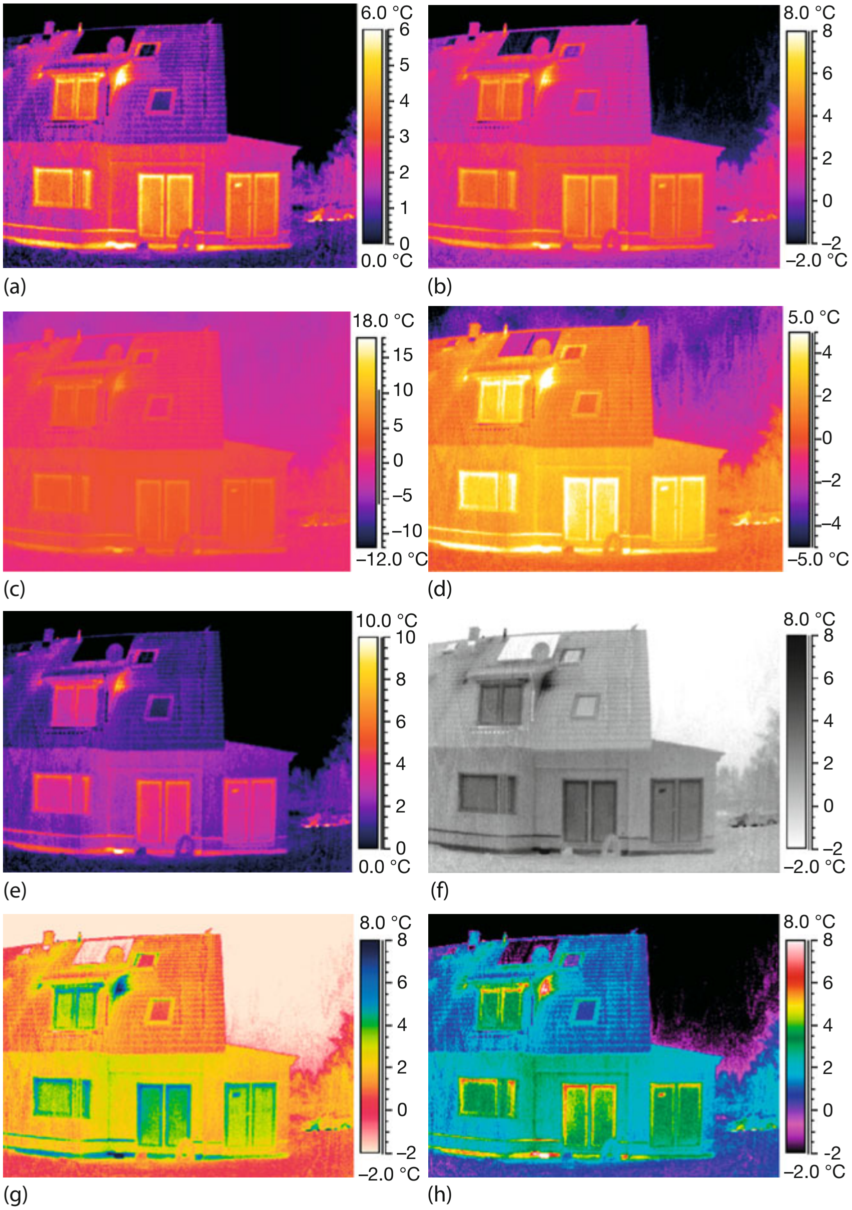

Figure 7.2 (a–f) IR thermal images of the same house displayed for a variety of temperature spans and color palettes. Emissivity was set at 0.96, distance 10 m, the outdoor ambient air temperature was 0 °C. The interior of the whole house was heated to about 20 °C.

additional parameters hue and saturation. Therefore, false color representation offers the ability to more clearly illustrate details and slight differences compared to grayscale image.

To our knowledge grayscales are nowadays only used in the life image mode of GasFind cameras (Chapter 8) as the standard palette. For their purposes, single images alone are not what's important but rather the change from one image to the next in live sequences. Such changes are already seen in grayscale, and considerably less memory space is needed for saving these files.

Figure 7.3 gives another example of various palettes used in thermography. The grayscale and inverted grayscale images (Figure 7.3a,b) look similar to black-and-white photos or the corresponding developed films. Obviously, fine details can be better detected in false color representations.

The use of the iron color palette (Figure 7.3c,d) in building thermography often leads to very low-contrast representations of the temperature distribution since only half of the possible color hues are used: green and blue are missing. Therefore, it is often difficult to recognize details in the temperature distribution, for example, on the roof of a building.

The use of structured palettes as the rainbow 1 (also called rain in Researcher Software) palette (Figure 7.3e,f) with more and stronger colors as the iron palette leads to higher contrast images with more details. But this palette can also be confusing sometimes.

For example, it is not intuitively obvious that bright purple is colder than dark blue. Color palettes with ambiguities are often not helpful for image viewing. In particular, the nonlinear color transitions in rainbow palette 1 can lead to an overemphasis on temperature differences within predefined temperature ranges. Though such representations may be useful for experts, for the majority of users the use of this rainbow palette may lead to misinterpretations.

For many users, palette rainbow 2 (also called rain900 in Researcher software) (Figure 7.3g,h) with its neglect of pink and suppression of cyan meets the demand for a more harmonic ordering of neighboring colors in an IR thermal image and a good color representation of temperature differences in a predefined temperature range much better. The rainbow 2 color palette solves temperature differences well and comes closest to the intuitive connection of color with temperature (see preceding discussion). Therefore, the inverted color scheme in this rainbow representation is particularly irritating: the roof seems to be much colder than the grass in front of the building. For any official report to nonexperts, the use of inverted or other irritating color scales should be avoided. The variation of level and span can strongly change the perception of the temperature distribution, as shown in Figure 7.4.

The choice of span determines the contrast of a thermal image. Both too high and too low a contrast should be avoided in thermal images. Figure 7.1 was an example of an extremely wide span that is totally unsuitable for detecting fine structures. If an unsuitably large span is chosen, then the visual impression of the temperature distribution within the image may not be very sensitive to temperature changes; cf. Figure 7.4c (16 °C span) and Figure 7.4a (4 °C span).

Figure 7.5 depicts a thermal image with an automatic setting of level and span, as is usually done within modern IR cameras. Both parameters, level $= 9.0\,°\mathrm{C}$ and

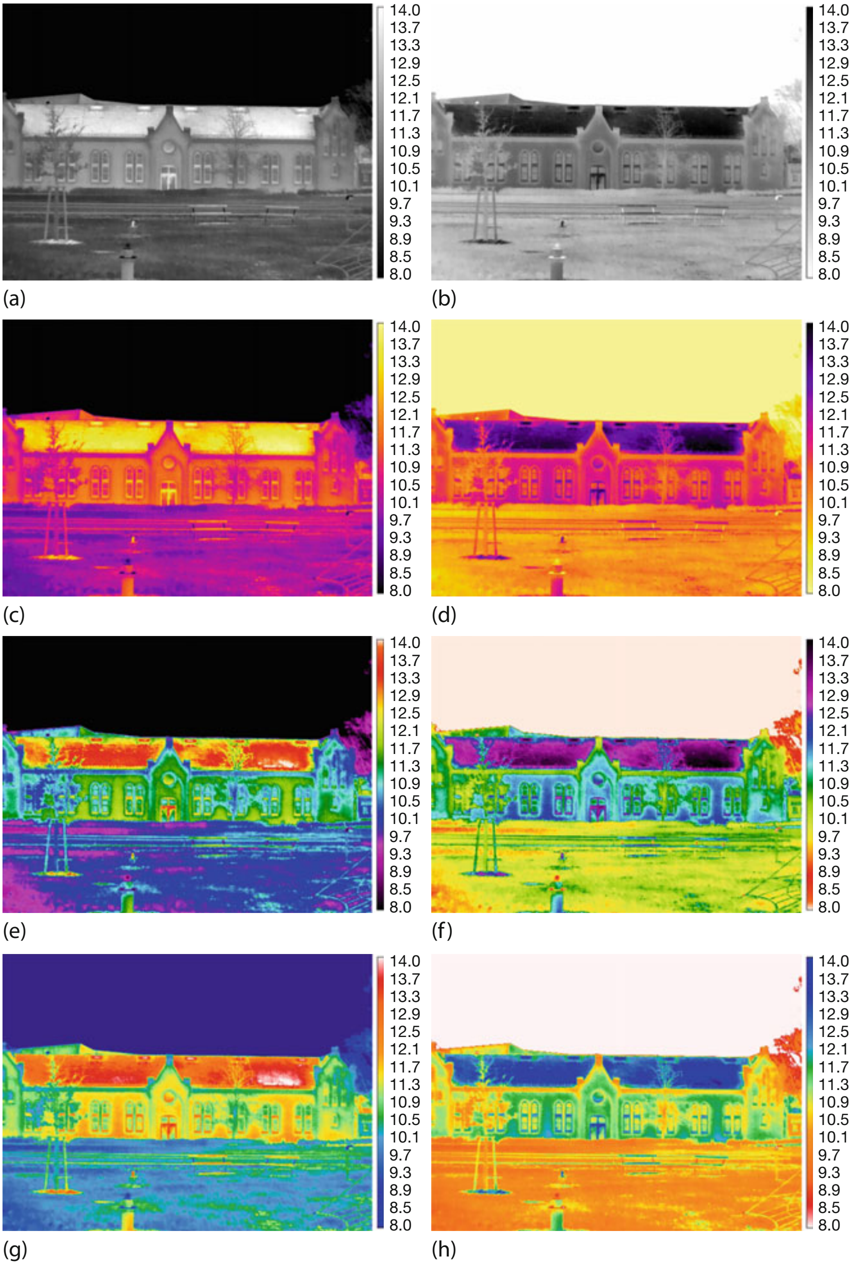

Figure 7.3 Representations of the same IR image of a building using different color palettes but the same level (11 °C) and span (6 °C) of linear scales. (a) grayscale; (b) grayscale inverted: (c) iron; (d) iron inverted; (e,g) two rainbow scales 1; (f,h) inverted rainbow scales.

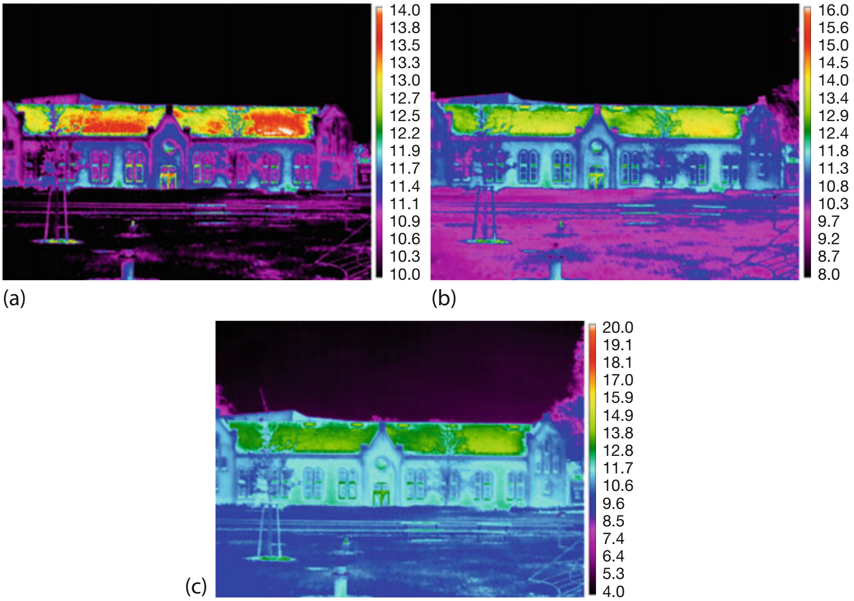

Figure 7.4 Comparison of image with a linear rainbow color palette for the same level (12 °C) but a variation of span: (a) 4 °C; (b) 8 °C; (c) 16 °C.

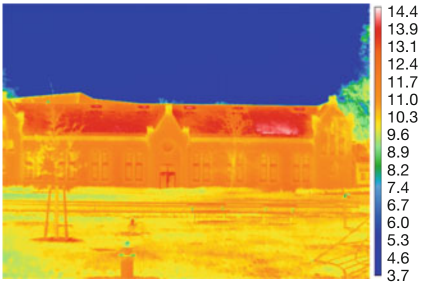

Figure 7.5 Thermal image with automatic level and span, and temperature range of 3.7–14.4 °C.

span = 10.7 °C, are calculated from the maximum/minimum temperature within the image.

This representation is unfavorable since the temperature range, which is of interest for the analysis of the temperature distribution of the building, is significantly smaller. The cold sky increases the span in this picture. This is clearly seen in the temperature histogram of the image (Figure 7.6). The histogram shows two accumulation regions on the temperature scale. The first region, 3–5 °C, results from the cold sky temperatures and only the second region, 7.5–13.5 °C, includes the relevant building temperatures. Therefore, the parameters' level and span should always be adapted to the temperature range under study. Figure 7.3e showed the corresponding level- and span-optimized thermal image of the building.

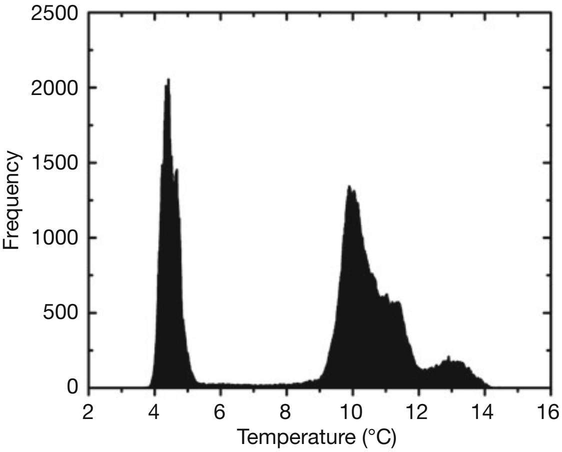

Figure 7.6 Temperature histogram of image in Figure 7.5.

These examples show how sensitively visual impressions depend on the selection of the correct color palette as well as the values of level and span when viewing a thermal image. A suitable representation is usually the first step after IR images are recorded; the more important second step is correctly interpreting the observations.

7.1.3
General Problems Associated with Interpretation of IR Images

Using the preceding discussion of color representation of data in IR images, we can take another first look at the bad (but published) example of Figure 7.1. The temperature span is unusually large – more than 47 °C – which means that any fine structure of the wall is completely lost. For a careful analysis, such a large color span is simply impractical. As can be seen from the image, all relevant parts of the house have temperatures in a range above −5 °C; therefore, the level and span should have been changed accordingly. In addition, heat transfer through windows is usually much greater than through walls (Table 4.6), so one would expect higher window temperatures compared to those of walls. In Figure 7.2, this is indeed observed, whereas, surprisingly, the windows in Figure 7.1 (and Figures 7.3–7.6) seem to have lower temperatures than the walls. Since it is very unlikely that the walls would have very bad thermal insulation (high U-value) while at the same time the windows in this house would have been top of the line (low U-value), we must think of another reason for this observed anomaly (see end of Chapter 7).

Concerning the interpretation of Figure 7.2, note all of the Figure 7.2 images show the area on the right-hand side of the dormer window and the spot in the lower left corner. A thorough investigation is needed to determine whether these indicate a real problem or whether they are due to structural or geometrical effects and, hence, expected (see discussion of Figure 7.26).

Table 7.1 External influences on outdoor thermography.

Influence	Problem caused
Wind	$\alpha_{\text{outside}} = \alpha_{\text{outside}}(v_{\text{wind}}) \Rightarrow$ transient wall temperatures (see also Section 4.3.3)
Solar radiation	Transient effects of wall heating, reflections of IR radiation (MW cameras)
Shadows	Transient effects of wall heating and cooling
Cloudy versus clear sky	Transient effects of radiant cooling of walls
View factor	Orientation-dependent radiative contributions from surroundings
Rain/moisture	Evaporation cooling, change of thermal time constant, usually reducing thermal contrast

As a matter of fact, surface temperatures of objects may be deduced from a thermal analysis, provided the corresponding surfaces, walls, windows, roofs, and so on are gray emitters and the emissivities are known. However, even measured surface temperatures alone mean nothing. Too many environmental factors can have an additional influence. The most crucial question is whether measurements are made from inside or outside a building. Outdoor thermography may provide an overview of a building envelope, giving an indication or orientation about where to look for more details. For home inspections, this can always be the first step toward a thorough investigation. Indoor thermography is much less affected by external factors and should be performed whenever possible. Sometimes, outdoor thermography is even useless, for example, for rear ventilated wall constructions.

The complications associated with outdoor thermography are manifold because a large number of external factors greatly complicate any analysis (Figure 7.7, Table 7.1) and often lead to wrong conclusions. The most important environmental factors are direct or indirect radiation from the sun, wind of varying speed, and moisture, for example, rain. In addition, sky conditions (cloudy or clear skies) and the view factor are particularly important when considering radiant cooling. Night sky radiant cooling and daytime exposure to solar radiation can cause strong variations of building envelope temperatures with long time constants. Therefore, absolute temperatures as measured in outdoor thermography are often unimportant since a detailed quantitative analysis would be too difficult.

In the following sections, the problems introduced by these external factors are illustrated by thermal images. In contrast, indoor thermography has the advantage of nearly quasi-stationary conditions (Figure 7.7), provided a few general rules are followed while preparing an IR thermal imaging study of a building:

- Required: $\Delta T = T_{\text{inside}} - T_{\text{outside}} > 15\,\text{K}$ for more than a few days (this implies that most investigations take place in wintertime);
- Try to enable quasi-stationary conditions inside by opening all doors and closing all windows;

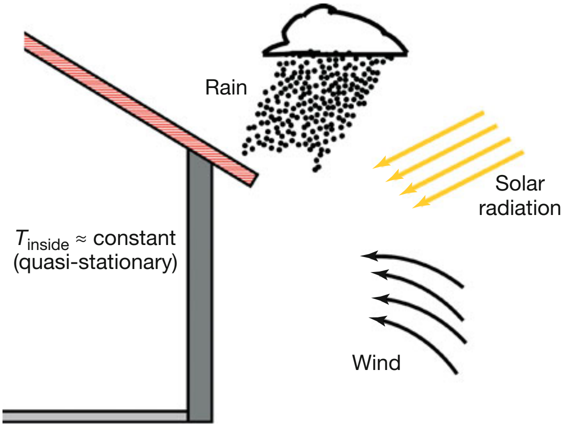

Figure 7.7 The inside building envelope can often be considered to be in a quasi-stationary state. In contrast, the outside walls of the building are subject to solar radiation (and shadows), wind of varying speed, and moisture due to rain.

- Move furniture away from walls;
- Let camera housing establish thermal equilibrium (at least 30 min).

In addition, the following conditions should be met when recording outdoor thermography images:

- Record before sunrise after a cloudy night (small night-to-day temperature changes);
- Avoid fog, rain, or snow;
- Avoid strong winds ($v_{\text{wind}} < 1\,\text{m/s}$);
- Let camera housing establish thermal equilibrium (at least 30 min).

The following conditions should definitely be recorded:

- Indoor and outdoor air temperatures;
- Indoor and outdoor reflected temperatures;
- Indoor and outdoor humidity;
- Outdoor wind speed;
- Distances from camera to walls: check geometrical resolution, perhaps change lenses;
- Emissivities of wall materials (e.g., tape);
- Orientation of surroundings with corresponding temperatures (view factor contributions);
- Visible photos of areas being investigated by IR imaging.

Despite its problems, outdoor thermography may sometimes be the only useful method of investigating a building, for example, when studying half-timbered structures behind plaster, when trying to locate water intrusions in building fronts, or when it is not possible, for various reasons, to get inside a building.

In interpreting indoor and outdoor IR images, one first tries to exclude all possible error sources as mentioned earlier (e.g., sun, shadows, thermal reflections). The resulting temperature profiles may then point to problems. Sometimes, however, there are no problems, but observed fluctuations are simply due to structurally expected thermal bridges or other factors, and within allowed limits.

To summarize, IR thermal images from buildings may yield apparently significant signal differences between various locations. After corrections for emissivity, some temperature differences might still remain. Even if all other disturbing effects are eliminated, they may still be within the expected range, for example, owing to geometrical details. As a consequence, not all differences in thermal images of buildings imply structural problems or leaks in thermal insulation; rather a very careful analysis is needed.

7.1.4
Energy Standard Regulations for Buildings

In times of environmental awareness and sustainable development, the need for a reduction of greenhouse gases by a reduction in the consumption of fossil fuels and the introduction of new renewable energies and technologies is obvious. In addition, over the years, the energy savings requirements for new homes regarding thermal insulation and heat losses through the building envelope have changed, and the specific heating power per area of a home has been continually decreasing (Figure 7.8). Starting after the first severe oil crisis, regulations were imposed restricting the allowed annual energy consumption for the heating of new buildings (the example here is for Germany) from around 200 to 300 kW h $(\mathrm{m}^2\,\mathrm{a})^{-1}$ in the 1960s and 1970s to less than 70 kW h $(\mathrm{m}^2\,\mathrm{a})^{-1}$ according to the 2002 regulation. The new regulations, starting in 2016, further reduce these numbers by around 30%, and there is no end in sight to this trend.

Already in 1995, new standards for special buildings were defined, the so-called low-energy or passive houses (e.g., [12]). The former range between ≈ 70 and 25 kW h $(\mathrm{m}^2\,\mathrm{a})^{-1}$. The latter were only allowed to consume 15 kW h $(\mathrm{m}^2\,\mathrm{a})^{-1}$, corresponding to a minimum of about 1.5 L oil/m^2 annually. Currently, even zero-energy houses or energy-producing houses are available.

Such laws, if enforced, can lead to a drastic reduction in primary energy consumption and of greenhouse gas emissions. However, since the lifetime of old buildings is in the range of many decades and since less strict regulations apply to the renovation of old buildings, the average value of energy needed for heating all buildings in a country will decrease slowly. Right now, in Germany this amounts to about 160 kWh/$(\mathrm{m}^2\,\mathrm{a})$. To accelerate the decrease, new energy standards for buildings have been defined in many countries; in addition, so-called energy passports (Figure 7.9) for buildings have been introduced and certificates issued for buildings (e.g., in Germany). New houses need such passports, which must include numbers for annual end energy and primary energy consumption as well as CO_2 emissions. The graphs usually also contain comparisons to various buildings such as single-family homes, larger apartment complexes, modernized

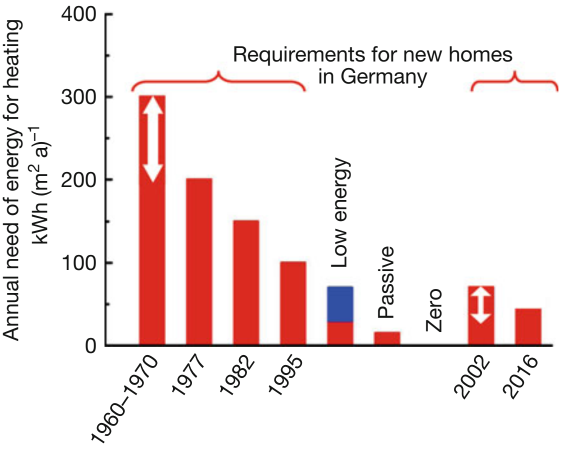

Figure 7.8 In many countries, the energy needed for the heating of a building per year is restricted by law. In the given example of Germany, regulations were imposed after the first oil crisis. They apply to new buildings. On the latest regulations, see [11].

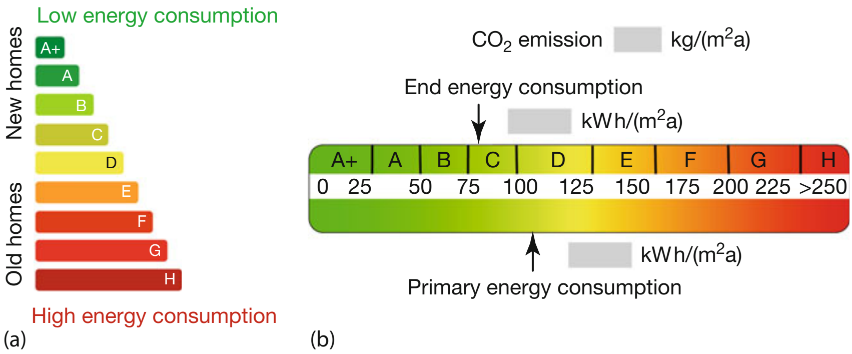

Figure 7.9 Possible energy performance certificates for buildings. They may be qualitative only (a) with a highlighted symbol of the present home or include a quantitative scale, for example, for energy consumption per area and year (b).

old buildings, nonmodernized old buildings, and the nationwide average of all buildings. A distinction is made between buildings for residence and others.

In the United States, the concept of energy ratings is different insofar as usually only a relative scale is used. For example, in the home energy rating system (HERS), a rating of 100 corresponds to a typical home built in 2006 [13]. Buildings requiring less energy have a lower index. A number of other indices exist, and reference [14] offers one example of a comparative discussion. Things change fast in this field, and many new developments may happen within the next few years around the world.

Thermal imaging can play a major role in this field of energy savings, leading to energy cost savings for private homes. In particular, thermography can test whether actions to save energy via better thermal insulation really work. The motivation of homeowners is mostly of a financial nature: very often the cost of installing improved thermal insulation is much less than what can be saved on energy costs within a few years, in particular if the costs of fossil-based energy sources are rising. Let us do a very naïve order-of-magnitude estimate of the energy cost savings from restoring an old house. Before restoration, the annual energy consumption in a 100 m^2 house should be 270 $kWh\,(m^2\,a)^{-1}$, and after restoration this figure should be reduced to only 70 $kWh\,(m^2\,a)^{-1}$. Obviously, this leads to energy savings of $100\,m^2 \cdot 200\,kWh\,(m^2\,a)^{-1} = 20\,000\,kWh\,a^{-1}$. If gas heating is used at a cost of 0.06 €/kWh, then the annual cost savings after restoration would amount to €1200.

7.2
Some Standard Examples for Building Thermography

In general, building thermography is a tool to locate hidden structures as a result of thermal anomalies, which may be due to a variety of causes. In any case, the heat transfer through a wall or part of a building causes differences in measured surface temperatures due to differences in heat conductivity or heat capacity of the building materials. Each thermal anomaly found via thermography must be discussed in detail considering the background knowledge of the construction, the materials used, and so on to determine whether the temperature anomaly would be expected and within so-called normal limits or whether it represents an actual insulation problem involving energy losses, structural damage, or both. We start this subsection by presenting a few qualitative examples of building thermography where the structures that give rise to specific thermal signatures are hidden beneath the surface but are well known from the construction of the building.

7.2.1
Half-Timbered Houses behind Plaster

In Europe, there are still many old houses that were built as half-timbered structures. In Germany, timber framing was the most popular building technique from the twelfth to the nineteenth centuries. The idea is to create framed structures of heavy timber held together by special joints. Some diagonal frames are used to stabilize the structure. The spaces between the timbers are filled with brick or, more often, with a woven lattice of wooden strips daubed with a sticky material usually made of some combination of wet soil, clay, sand, animal dung, and straw. In the twentieth century many of these old half-timbered structures were covered with an additional layer of plaster, and sometimes with thermal insulation, often because the restoration of the original structure would have been too expensive. Nowadays, houses with half-timbered structures are often considered to represent valuable old monuments that need to be preserved. In this context, IR thermal imaging can be a valuable tool to identify such houses, even if they are covered with a layer of plaster. Figure 7.10 shows an example of a house in Brandenburg/Havel in Germany, recorded in wintertime with temperature differences from inside to outside of about 15 K. The visible image (Figure 7.10b) gives no indication of what is beneath the outer layer of plaster. The IR image (Figure 7.10a), however, clearly shows the structure of the wooden frames. Several features need to be discussed.

1. The clear view of the half-timbered structure in the thermal image results from the differing thermal conductivity of the wood and the filled compartments of the rest of the wall (Table 7.2). As shown in the scheme of the heat flow (Figure 7.10c), the wood (brighter shaded areas) has lower thermal conductivity, resulting in less heat flow through the frames compared to the planar section of the filled compartments. The lateral heat flow is not large enough to establish thermal equilibrium at the outer surface, as the temperature plot and the corresponding color scale (arbitrarily chosen to resemble the color scale of the IR image) indicate. The most prominent feature in the thermal image is due to the open window in the center. The warm air from the inside heated

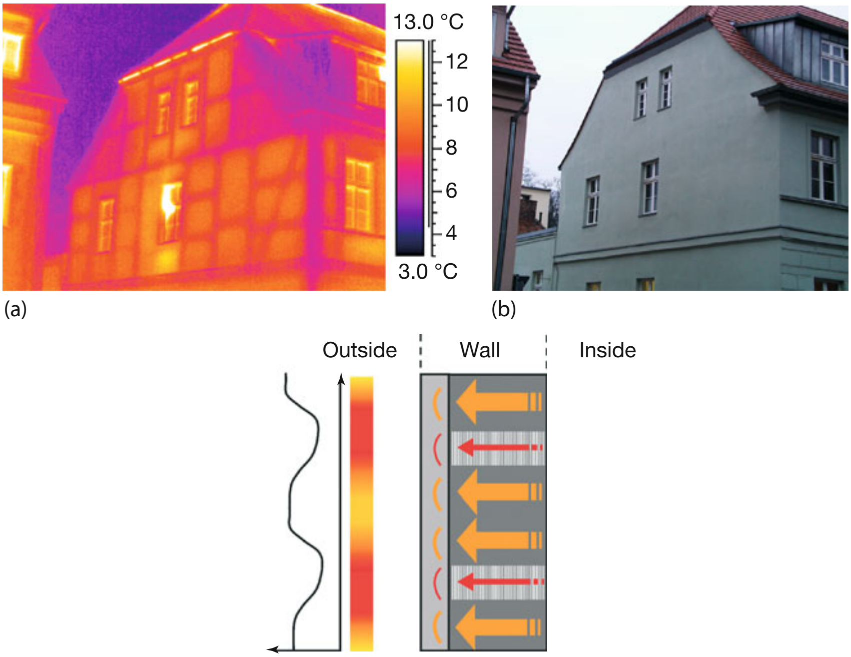

(a) (b)

(c) Temperature

Figure 7.10 (a,b) Half-timbered structures of a house, hidden behind plaster, recorded during wintertime (no sunshine). The visible image (b) shows no structures at all. The white spot in the center of the IR image (a) corresponds to a small top window, which was opened after recording the visible image. (c) Scheme of heat flow through a structured wall. Shaded areas (with red arrows) resemble wood, gray areas (with yellow arrows) the filled compartments.

Table 7.2 Material properties of wood and typical sandstone relevant for interpreting IR images.

	Thermal conductivity ($\mathrm{W\,(m\,K)^{-1}}$)	**Specific heat capacity ($\mathrm{kJ\,(kg\,K)^{-1}}$)**	**Density ($\cdot 10^3\,\mathrm{kg/m^3}$)**
Dry wood	≈ 0.15	≈ 1.5	≈ 0.6
Typical sand stones	≈ 1.8	≈ 0.7	≈ 2

up the parts adjacent to the window. Overall, the image shows the structures of the frames; however, the observed temperature differences across the wall surface do not indicate any energetic or thermal insulation problems.

2. The right-hand edge of the building seems to be colder than the plane wall. This is expected because of the geometrical thermal bridge (see Section 7.3) and does not pose a problem.
3. Only the middle section of the upper floor below the roof is heated, and the thermal insulation of the wall section is tolerable. However, the rooftop suffers from missing insulation. This needs more attention. We also note that the frame of the right-hand-side window is made of corroded metal with unknown emissivity; however, it is probably still slightly lower than that of the wall.
4. Furthermore, one can clearly observe a warmer wall section below the open window in the center due either to a heater or missing insulation. To a lesser extent, this can also be observed for the right window and the top floor windows. To determine whether this is energetically critical, more studies would be desirable. The present study focused only on detecting the half-timbered structures themselves.

To simulate half-timbered structures or, more generally, building structures with differing thermal conductivities and heat capacities, students were given the task of building a model of such a hidden structure. The differing thermal properties were established using Styrofoam, air, metal, and wood. Figure 7.11a shows the front and Figure 7.11b the back of the final model with dimensions of $62 \cdot 42\,\mathrm{cm}^2$ and a thickness of 2 cm. The IR imaging test was done by placing it in front of a planar, electrically heated $0.6 \cdot 0.9\,\mathrm{m}^2$ plate (which, within minutes, reached more or less homogeneous surface temperatures of about 130 °C). Figure 7.11c shows the result. The hidden structures became visible within a minute after starting to heat the plate. Other experiments with this model are discussed subsequently in the context of wind and moisture effects.

Half-timbered houses are examples of buildings that may not be investigated in wintertime alone (as shown in Figure 7.10). Since the heat capacity c and the density ρ of the used wall materials are quite different, thermal contrast can also be obtained after the wall is exposed to intense solar radiation even if indoor and outdoor air temperatures do not differ (appreciably). Dry wood has a larger specific heat capacity but much smaller density than stones or filling material.

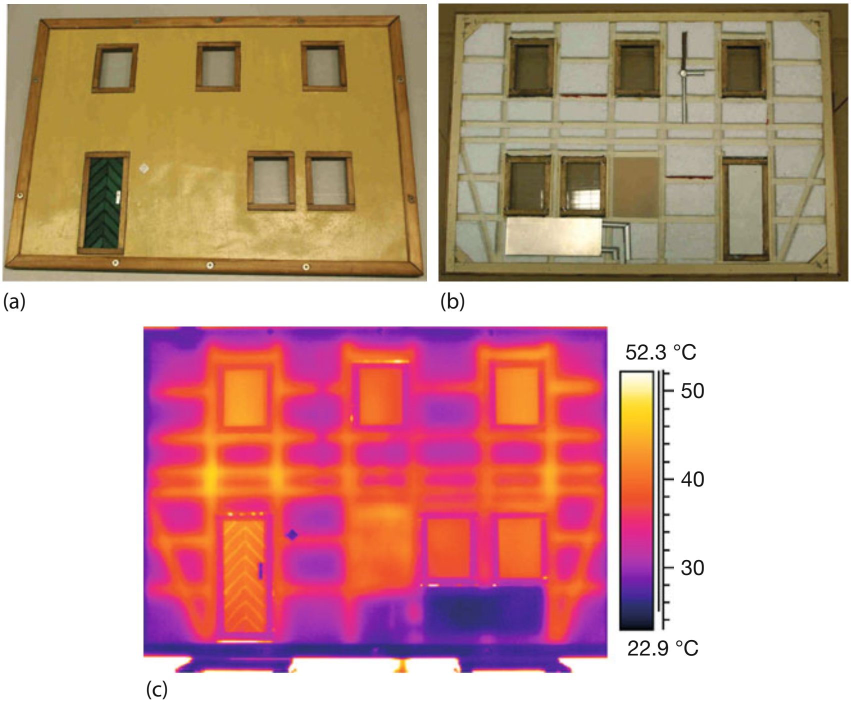

Figure 7.11 Model for hidden structure with front and back (a, b) as well as IR image (c) when heated from the back.

A simple analysis relates the temperature rise ΔT to the incident energy ΔQ via $\Delta Q = c \cdot m \cdot \Delta T$, where the mass m is given by density times volume. Therefore, upon receiving the same amount of incident energy ΔQ, the temperature rise of a material with a given volume depends inversely on the product of its specific heat and density. Dry wood has a smaller value of $c \cdot \rho$, so it will show up at a higher temperature. Of course, the structures are still behind the plaster, but the effect is clearly visible.

Depending on the recording conditions, the location of the wooden frames of half-timbered structures may thus show up in IR images either as colder or as warmer surface temperatures!

7.2.2
Other Examples with Outside Walls

Sometimes, buildings are modified, for example, building envelope openings like windows may be added or removed. Figure 7.12 depicts an example of the wall of a hotel building. As can be seen from the IR image, originally, there had been another window at the center of the wall, which was subsequently closed with masonry, before the wall was covered with plaster. If no more details about the work

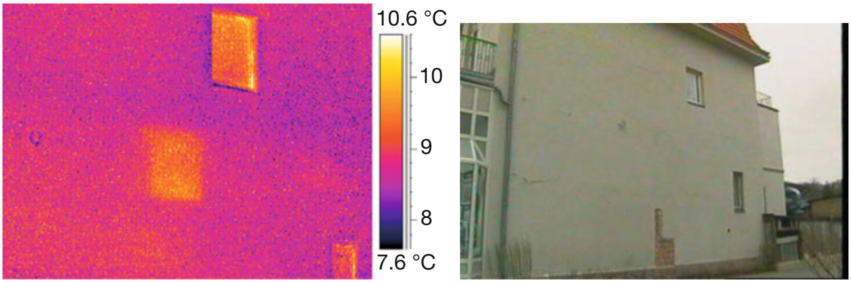

(a) (b)

Figure 7.12 Old window covered up with masonry and plastered over.

are available, one can only speculate about the reason. Perhaps the thermal insulation was forgotten during the process, the thermal conductivity of the chosen brick could be different from the original brick used for the rest of the wall, or heat was transferred to the wall (e.g., via radiation from the sun) prior to recording the image and the value of $c \cdot \rho$ of the chosen brick is smaller than for the rest of the wall, leading to a higher temperature. In this case, the owner immediately realized that the window was just filled with brick and covered with plaster without any thermal insulation attached.

Many European houses are equipped with stoves (oil, coal, or wood) and therefore need chimneys. Sometimes, these are at the outside walls of a building. Figure 7.13 shows an example of a three-story building with the chimney at the center of the wall. Obviously, the thermal insulation of the chimney is very bad or, at least, partially missing.

The observed temperature differences amounts to $\approx 2\,\mathrm{K}$ and the defect is energetically relevant. In addition, one can see that the connection of the ceiling of the second floor was also not properly insulated.

7.2.3
Determining whether a Defect Is Energetically Relevant

Interpreting outdoor IR images qualitatively is relatively easy (if all possible error sources are known and eliminated). However, the critical question of any homeowner is whether observed defects that do not point to structural damage and that need to be dealt with anyway are energetically relevant. Solving this problem is not always an easy task.

First, any thermal bridge that points to increased heat transfer through the building envelope means that energy needed for heating is lost to the environment. If this energy comes from fossil fuels, any such energy loss automatically implies that there is avoidable CO_2 emission: better thermal insulation means less primary energy needed for heating, that is, lower levels of CO_2 emissions. Hence any energy loss is CO_2 relevant.

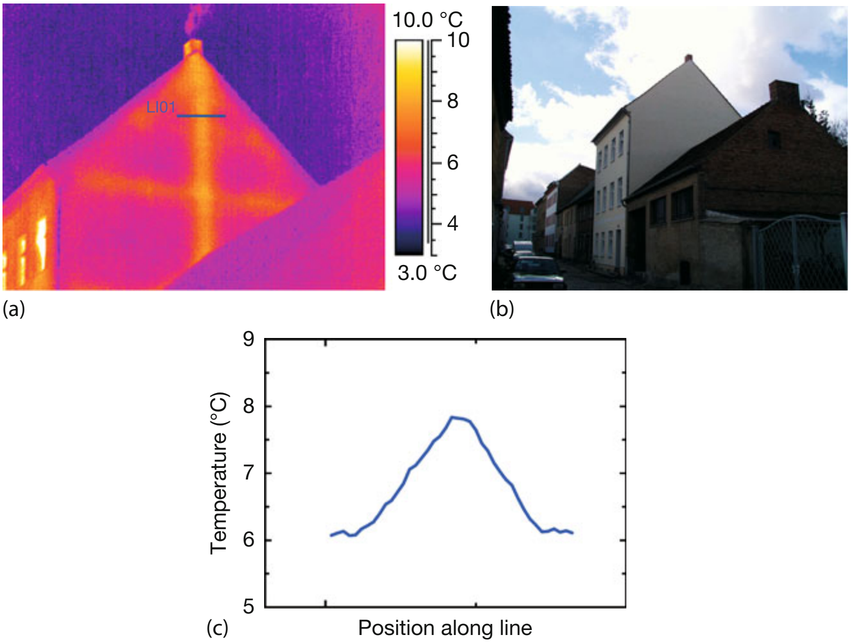

Figure 7.13 IR (a) and visible (b) image of a house. The location of the chimney can be easily seen through the outside wall. Temperature differences along the line in the IR image amount to about 2 K (c).

Second – and usually more important for homeowners – is the question of how much money could be saved per year if the observed energy loss were prevented. This savings in terms of money is then compared to the cost of restoration, and if the amortization time is, say, less than 5 years, the work may be done.

Restoration costs may depend on workers' wages, on the costs of materials, on the type of house, and so on, which are not discussed here. Rather, a very crude estimate is given of how much energy may be lost during a year owing to an observed defect. Of course, much more sophisticated finite-element models (computational fluid dynamics) are available [15], but for a first-order estimate, the simpler approach is sufficient.

The idea behind the estimate is the concept of the U-value or R-value introduced in Section 4.3.3, Eq. (4.10):

$$\dot{Q} = U \cdot A \cdot \Delta T \tag{7.1a}$$

where

$$U = \frac{1}{R_{\text{total}} \cdot A} = \frac{1}{1/\alpha_{\text{conv,ins}} + \sum s_i/\lambda_i + 1/\alpha_{\text{conv,out}}} \tag{7.1b}$$

Here $\alpha_{\text{conv,ins}}$ and $\alpha_{\text{conv,out}}$ represent the inside and outside wall heat transfer coefficients for convection, and the sum represents the heat transfer through wall segments of thickness s_i having a thermal conductivity λ_i. In Chapter 4, model calculations are discussed that make it possible to calculate all relevant temperatures, the corresponding U-values, and the total heat flux through a number of different walls.

If owing to a defect one of these contributions changes, the heat flow through the corresponding part of the building envelope changes. Once the relevant areas are known, one may estimate the total heat loss and from that calculate the corresponding energy costs. The best way to do this would be to measure U-values directly by thermal imaging. In principle, this is possible (Section 7.7). Alternatively, one could start with the known insulated wall structure U-value and relate it to the corresponding outside wall temperature. Since adjacent thermal bridges have a higher wall temperature, one could vary the thermal resistance of the wall materials in Eq. (7.1b) such that the observed wall temperature is reproduced. The corresponding thermal resistance will lead to a new, now larger, U-value that may be used to estimate the heat loss according to Eq. (7.1a).

Here we would like to give a simpler rough estimate example based on typical U-values for walls and windows. From Table 4.6, concrete walls with no thermal insulation have U-values of around $3\,\mathrm{W\,(m^2\,K)^{-1}}$, brick walls of $1.5\,\mathrm{W\,(m^2\,K)^{-1}}$, and brick walls with insulation of about $0.5\,\mathrm{W\,(m^2\,K)^{-1}}$. Let us assume a single-family home with about $50\,\mathrm{m}^2$ of floor space on two floors (i.e., $100\,\mathrm{m}^2$ of living space), and an overall (including roof) envelope area of $A = 300\,\mathrm{m}^2$. For simplicity, we assume that all homes (not insulated and insulated) would have similar U-values all around the envelope (including windows and roof). Table 7.3 gives results for the heat flux $\dot{Q}$ in W, the total heat transfer Q per year in kWh/a, the heat transfer per area and year in kWh/(m^2 a), and the corresponding energy costs per year in €/a. We assumed $t_{1\,\mathrm{year}} = 3.15 \cdot 10^7$ s, 1 kWh $= 3.6 \cdot 10^6$ J, and a cost of 0.06 €/kWh. Either the value for the temperature difference (inside to outside), here $\Delta T = 10$ K, or a time period of one year $t_{1\,\mathrm{year}}$ can be chosen to account for the actual duration of the heating period (e.g., at most half a year). The numbers in Table 7.3 can be used to estimate the improvement due to insulation, for example, from type 3 to type 2. If defects only occur at smaller areas, the corresponding numbers will be accordingly lower.

Table 7.3 Rough estimates of annual heating energy and corresponding energy costs for three different homes assuming $A = 300\,\mathrm{m}^2$, $\Delta T = 10$ K, and 0.06 €/KWh.

Type of house	**U value (W (m^2 K)$^{-1}$)**	**$\dot{Q} = U \cdot A \cdot \Delta T$ (W)**	**Q (kWh/a)**	**Q/A (kWh (m^2 a)$^{-1}$)**	**Cost (€/a)**
1. Not insulated concrete	3	9000	$7.9 \cdot 10^4$	263	4730
2. Not insulated brick	1.5	4500	$3.9 \cdot 10^4$	131	2360
3. Insulated brick or wood	0.5	1500	$1.3 \cdot 10^4$	44	790

7.2.4
The Role of Inside Thermal Insulation

The importance of thermal insulation of walls was discussed in detail in Section 4.3.3. In short, the thermal conductivities of thermal insulation of composite walls determine the temperature distribution within the wall (Figure 4.10). The largest temperature drop occurs in the thermal insulation layer made of Styrofoam. It is desirable that the freezing point should lie within this layer; therefore, thermal insulation should be attached to the outside of a building. However, one needs to consider what happens if additional thermal insulation is attached to an inside wall. Figure 7.14 shows an exterior wall of a classroom in a public school. The inner wall consists of studwork plates attached to metal poles. Just before recording the thermal image, a heavy and large whiteboard (dimensions about $1.6 \times 0.8\,\text{m}^2$) was removed from the wall. The vertical line structures are due to the thermal conductance of the metal poles to which the plates are attached. On both sides of the poles, air serves as thermally insulating material. The most prominent feature is that the whole wall area, which was covered by the whiteboard, has reduced surface temperatures by 2–2.5 K.

The explanation for this – at first glance – unusual behavior is simple. Figure 7.15 shows a schematic representation of a typical stone wall with inside plaster, masonry, and outside thermal insulation, together with the corresponding temperature along a perpendicular line through the wall (for details of the calculations, see Chapter 4). The inside and outside air temperatures are fixed. As expected, the outside thermal insulation gives rise to the most dramatic temperature drop. The black solid line shows the situation for the uncovered wall in stationary equilibrium, and the blue dotted line shows the same for an additional inside thermal insulation abbreviated as whiteboard in what follows.

In both cases, the inner surface temperature, that is, the plaster surface or the whiteboard surface (pink horizontal line), is the same. However, owing to the thermal insulation properties of the whiteboard, the temperature drops by several Kelvin at the interface of whiteboard and plaster. When removing the white-

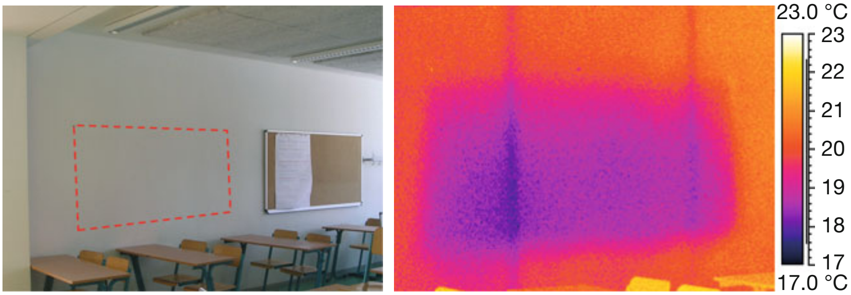

(a) (b)

Figure 7.14 VIS (a) and IR image (b) of an exterior wall segment in a classroom. Prior to recording the IR image, a large whiteboard, which was attached to the wall (position indicated in VIS image), was removed.

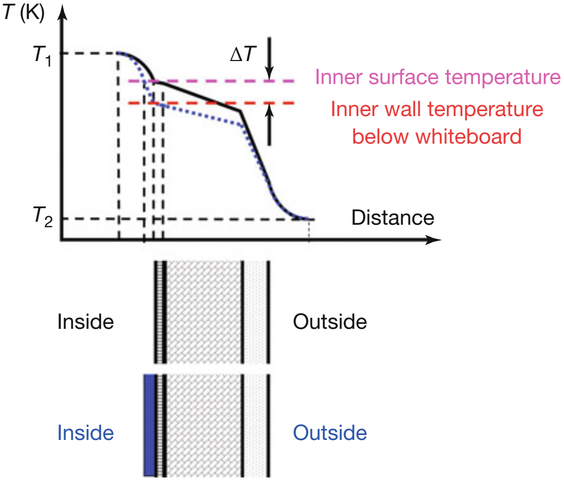
T (K)
T1
T2
ΔT
Inner surface temperature
Inner wall temperature below whiteboard
Distance
Inside
Outside
Inside
Outside

Figure 7.15 Scheme for a wall with additional thermal insulation (blue area) from the inside. The inner temperatures of the insulation surface and the neighboring wall without insulation are the same; however, the wall temperature below the insulation is reduced.

board, this interface becomes the new wall surface showing lower temperatures. In conclusion, one should try to avoid covering the inside of exterior walls with thermally insulating objects; the better the insulation, the lower the real wall surface temperature. This may, in the worst-case scenario, even lead to mold below the object.

7.2.5
Floor Heating Systems

A typical indoor thermography application in homes concerns floor heating systems. Hot water radiant floor heating systems, which are quite common in many European countries, have also become more popular in North America lately [16–18]. While applications in North America also include exterior systems, for example, for the melting rather than removal of snow in cold climates, the most popular use in northern and central Europe, particularly in Germany, are floor heating systems in private homes. Despite the higher initial costs during the construction of a house, this technique is very competitive compared to conventional heating systems since it uses lower temperatures during operation, which means lower fixed running costs. In addition, many homeowners prefer warm floors because they associate this with “just feeling good.” Also, the interior of a home, particularly near walls and windows, can be better used since heaters are absent.

Two tubing patterns, spiral and meander, are common in floor heating systems (Figure 7.16). They differ in the homogeneity of the surface temperatures: the meandering type structure usually shows a gradient from left to right as the flowing hot water cools down.

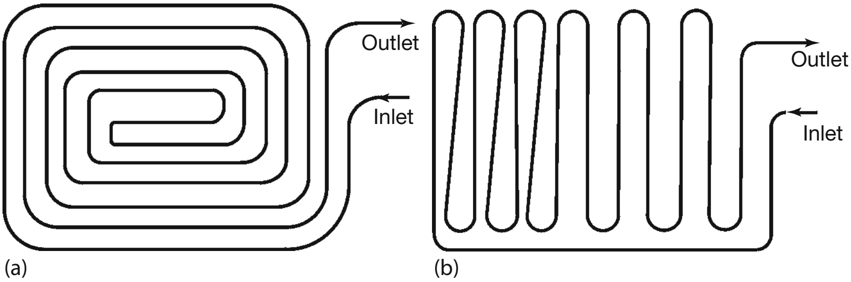

(a) (b)

Figure 7.16 Spiral (a) and meandering (b) tubing of a floor heating system. Here, the meandering tubes are mostly parallel, but that is not a requirement.

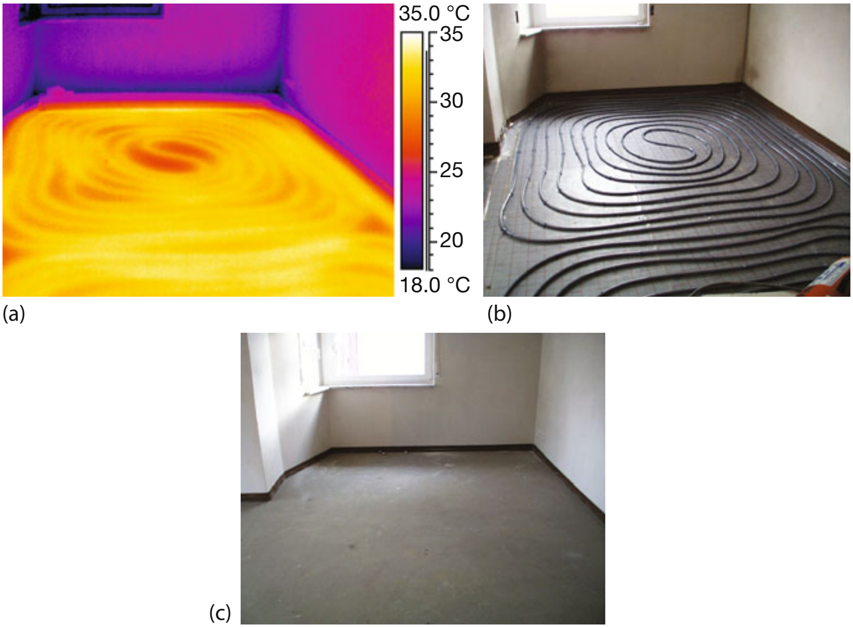

(a) (b) (c)

Figure 7.17 One zone of a spiral laying of a floor heating system (b). The tubing is on top of the concrete foundation slab. The IR picture (a) was taken after the tubing was covered by the floating floor screed (c).

Figure 7.17 depicts an example of the spiral zone of a system in a living room (dimensions $3 \times 3.2\,\mathrm{m}^2$).

Figure 7.17b shows the layout of the tubes before a floating floor screed about 6 cm thick was put on top (Figure 7.17c). The IR image in Figure 7.17a was taken several weeks after the tubing was buried below the floating screed.

Usually, such images are obtained when the heating is turned on after the floor was initially cold [16]. The image presented, here with just the screed on top of the tubing, was, however, obtained after many hours of heating at high power [17]. Obviously, under normal conditions with less heating, the temperature variations would not be pronounced, as shown here. Also, if additional floor coverage is used, like a wooden parquet floor, the temperature distribution at the surface of the floor is smeared out further laterally. In this case, the tubes can indeed only be seen with good contrast in the heating-up period. Figure 7.17 shows that the heating system is working very well; the only problem may arise in the center of the spiral, where the temperature variation on top of the screed reaches 5 K over a distance of about 0.3 m.

Thermography can, of course, also be used to analyze the usual accessories of floor heating systems, like the boiler and its exhaust pipes, as well as the insulation of the connecting tubes between pump and floor heating system [17].

7.3
Geometrical Thermal Bridges versus Structural Problems

Often, the structural differences beneath the building walls, which may give rise to a thermal signature in the IR image, are not known in advance. In this case, a detailed knowledge of typical and unavoidable thermal bridges is the prerequisite for avoiding wrong interpretations. In this subsection, we present first some qualitative examples of building thermography with geometrical thermal bridges and explain how they give rise to commonly observed thermal features of the building envelope. Then we proceed to examples of where the observed thermal bridges are due to structural defects like missing insulation.

7.3.1
Geometrical Thermal Bridges

As mentioned in Chapter 4, geometrical thermal bridges are present in corner sections of buildings owing to the details of the heat flow from a small warm inside area to a much larger, colder outside wall area (Section 4.3.5 and Figure 7.18). As a consequence, inside corner sections always show a minimum temperature compared to the adjacent flat area of outside walls.

The observation conditions for building corners from outside are often fluctuating because of weather conditions, sunshine, shadows, and so on (see following discussion), which may have already led to different wall temperatures at either side of a corner. However, under ideal outside conditions, late at night, with no wind and moisture in wintertime, it may also be possible to observe such geometrical thermal bridges due to corners with outdoor thermography. Figure 7.18c,d shows schematically the situation for the bottom plate of a building (gray shaded area) with heat transfer via convection to the outside air. Increased heat flux from outside corners will result in a lower temperature at the corner point, whereas reduced heat flux from the inside corner of a concrete bottom plate of a building will lead to a higher temperature at corner point B.

The situation of Figure 7.18c,d was observed for a building under construction (Figure 7.19). The concrete bottom plate ended at the boundary of the house. The

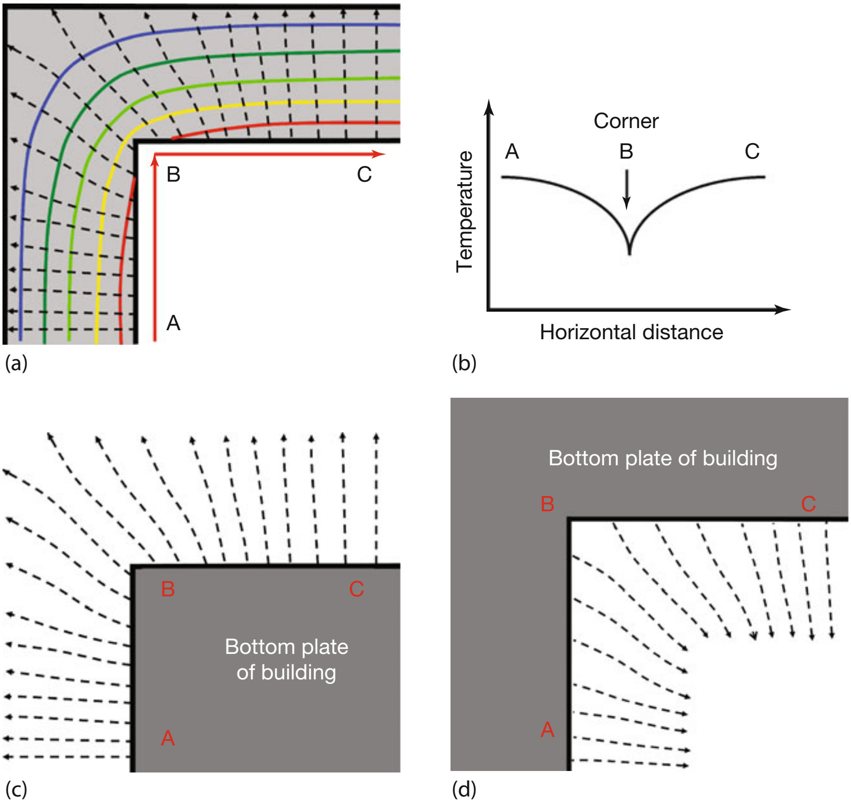

Figure 7.18 (a) Illustration of a geometrical thermal bridge in a corner of a house. The (colored) contours of constant temperature are curved and the heat flux is perpendicular to them (broken lines with arrows). (b) Plot of inside surface temperature of wall along line ABC. The temperature shows a pronounced minimum at corner point B. (c) Geometrical thermal bridges observable with outdoor thermography. Increased heat flux from the outside corner (90° angle) of a concrete bottom plate of a building should lead to a lower temperature at corner point B. (d) Reduced heat flux from the inside corner (270° angle) of a concrete bottom plate of a building should lead to a higher temperature at corner point B.

plate was heated due to the test of the floor heating system of the adjacent room. Since the patio was not yet built, the thermal insulation at the end faces of the plate had not yet been installed, and one could detect the plate in the overview thermal image. The geometry of the relevant portions (white circles) includes an outside corner with a plate angle of 120° and an inside corner with a plate angle of 240°. Although these angles differ from the schematic ones of 90° and 270° discussed earlier, the general argument still holds. Figure 7.20 shows IR images with expanded views of the corresponding corner sections.

The geometrical thermal bridge effect can be seen clearly. The plots of the measured temperature along the lines in the IR images reveal that temperature differences of as much as 3 K can result.

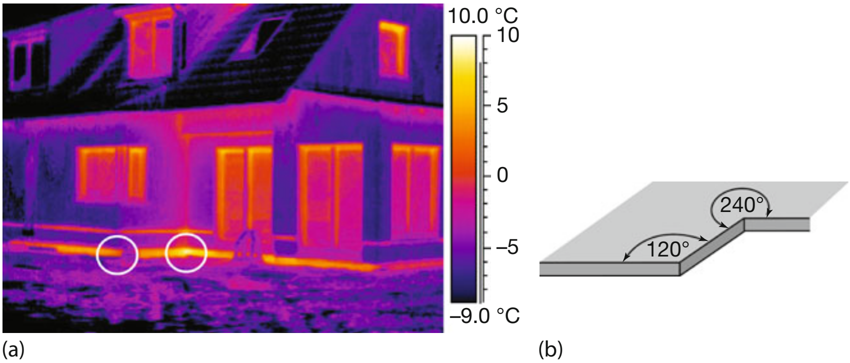

Figure 7.19 The geometrical thermal bridges of a concrete bottom plate of a building in the IR image (a) are due to inside and outside corners, as shown in the sketch of the geometry (b).

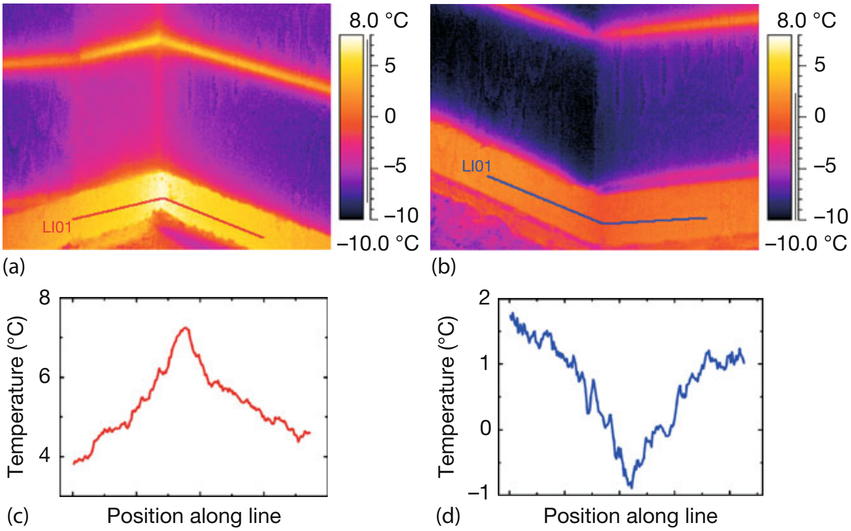

Figure 7.20 Thermal images (a,b) and temperature plots along shown lines (c,d) for the geometrical thermal bridges of Figure 7.18c,d. Left: 240° inside angle; right: 120° outside angle.

Although such geometrical thermal bridges are sometimes observable from outside, the effect is better known from indoor thermography. Figure 7.21a depicts an example of the inside corner of a room. The thermal bridges lead to a temperature drop along the edges and an even larger one in the lower and upper corners. An expanded view of the lower corner was investigated quantitatively. The temperature plots along the lines, shown in the IR image, indicate temperature drops of about 2–2.5 K just around the edge and more than 5 K in the lower corner, reaching minimum temperatures below 11 °C. These low temperatures were critical with regard to mold formation. First, the investigation was done for an outside temperature of 1 °C. In midwinter, temperatures often drop to below

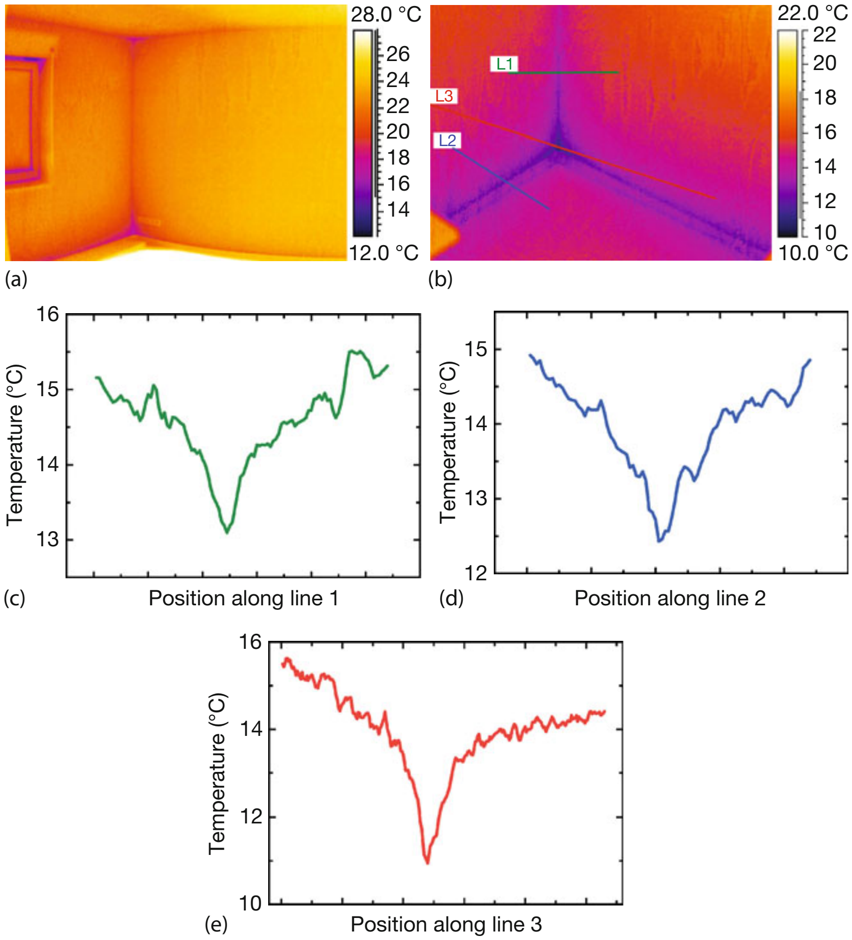

Figure 7.21 Geometrical thermal bridge observed for an inside corner of a basement room (no cellar) with two outside walls. The dark blue areas (a) indicate the lowest temperatures. An expanded view of the lower corner section was analyzed in more detail, as indicated by the three lines (b). (c–e) Corresponding temperature plots along lines. Outside air temperature: 1 °C.

zero and sometimes remain for several days to weeks below −5 or −10 °C. This will obviously lower the corresponding inside wall temperatures and those of the corner sections. Second, the dew point temperature (Section 4.3.6) for 50% humidity and an air temperature of 20 °C corresponds to 9.3 °C, that is, water will start to condense at wall areas with $T \leq T_{\text{dewpoint}}$. However, it was shown that in order for mold to grow, wall temperatures need not reach dew point temperatures; typically regions with 80–90% relative humidity are sufficient [19]. Owing to the low corner temperatures, the adjacent air will reach 80 or 90% relative humidity, which is already well above dew point temperature, in this case, between

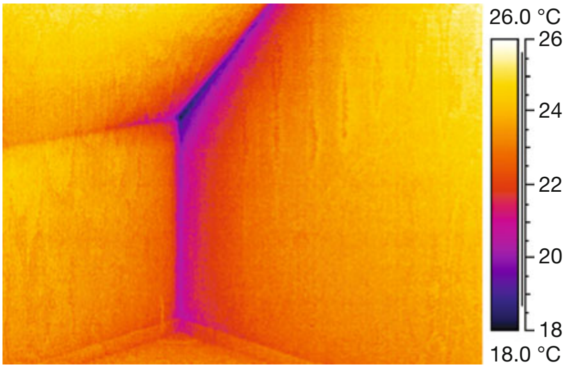

Figure 7.22 Another typical geometrical thermal bridge observed for inside corners of a bedroom below an inclined roof. The room was heated to around 26 °C for this study.

12.6 and 10.8 °C. This means that the edge, in particular the corner regions, may give rise to problems if air movement is restricted. As a consequence, such inside corners should be kept free of shelves or other furniture to allow for sufficient air ventilation.

Figure 7.22 shows another noncritical example of such geometrical thermal bridges. The temperature scale shows a very pronounced dark spot in the corner; however, minimum temperatures were well above 18 °C.

7.3.2
Structural Defects

In addition to geometrical thermal bridges observed at corners or edges, there is another class of common thermal bridges due to structural defects. Figure 7.23 shows two examples that may show up in IR images. First (Figure 7.23a), air gaps between adjacent parts of thermal insulation can give rise to linelike features or plastic anchor bolts with steel core for attaching the insulation to the masonry can show up as a series of spotlike features in IR images. Such problems can be avoided by using two laterally displaced layers of insulation and shorter anchor bolts (Figure 7.23b). Other potential problems concern badly insulated concrete plates, serving as ceiling or floor (Figure 7.23c) in large apartment buildings giving rise to air-filled cavities. They also lead to linelike features seen through the outside wall along the whole length of the plate. Such defects are energetically relevant. However, in addition to heat flow, moisture can leak into these air cavities, which also drastically reduces the lifetime of the whole structure, that is, they can easily lead to very expensive structural damage.

Figures 7.24 and 7.25 present examples of a nine-floor apartment building made of precast concrete slabs. This building technique was quite common in the 1960s, in particular in the German Democratic Republic. Figure 7.24 shows the visible (panel b) and the IR image (panel a) of part of the window front of the building. The IR images were recorded in the early morning hours before sunrise. The cen-

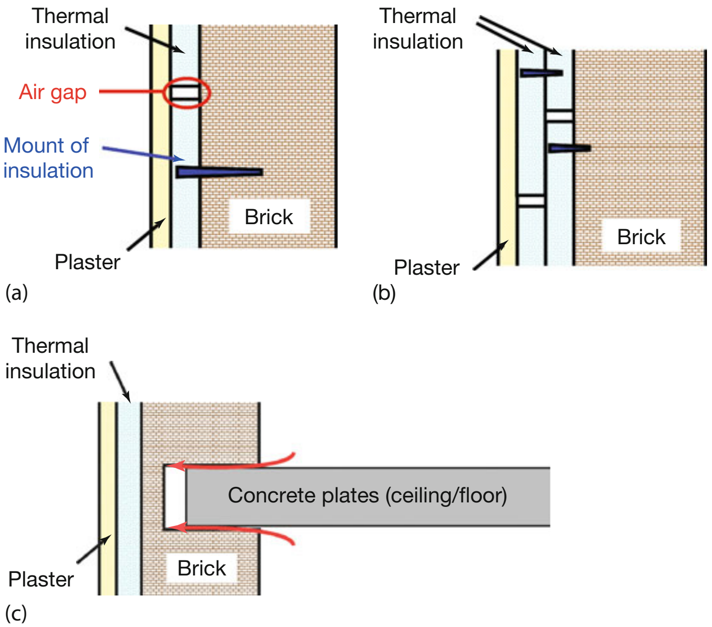

Figure 7.23 Structural defects can be, for example, air gaps between adjacent parts of thermal insulation or plastic anchor bolts with steel core for attaching the insulation to the masonry (a). Problems may be avoided by using two displaced layers of insulation and shorter anchor bolts (b). Other potential problems concern badly insulated concrete plates, serving as ceiling or floor in large apartment buildings (c).

tral window had remained closed for a long time and also during the recording (only the window partially visible in the lower right corner was open). One can clearly identify the structural problem of missing insulation of the concrete plates (floor/ceiling) as described in Figure 7.23. In addition, the window frames are particularly badly insulated since not only the window seals but also parts of the adjacent concrete plates are heated significantly. The worst problem is the missing thermal insulation of the concrete wall plate below the window. It simply does not exist; one can even see the position of the heater through the wall. In these old buildings, the heater could not be turned off or on at all, temperature was generally regulated by opening a window. This building suffered enormous heat losses, and heating costs were extraordinary. The building was, however, renovated in the late 1990s, and thermal insulation was added on the exterior wall.

Figure 7.25 shows two IR images of the windowless east wall of the same building recorded before and after restoration of the building envelope. The thermal imaging analysis demonstrated that the restoration work was indeed successful. The overall outside temperatures were much higher; however, the temperature span of the images after repairs was reduced to only 3 K, and still no structural thermal bridge could be detected.

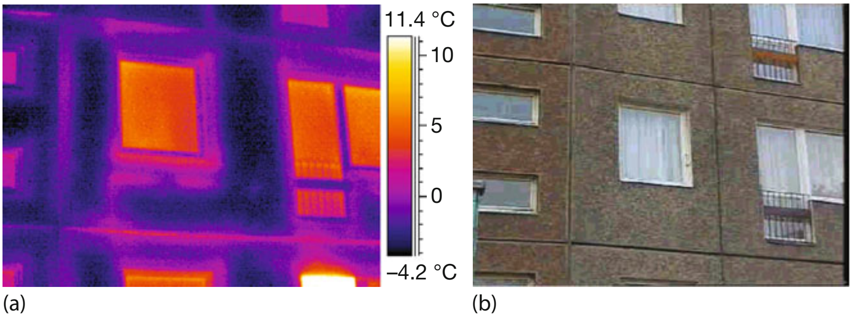

Figure 7.24 (a) A section of the window front of an apartment building made of precast concrete slabs before restoration work. (b) One can see the position of the concrete plates (ceiling/floor), the bad insulation of the window, and the heater below the window through the wall.

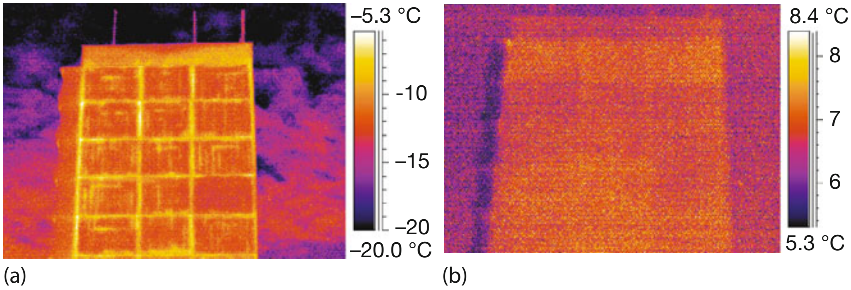

Figure 7.25 East side wall of building from Figure 7.24 before (a) and after (b) adding thermal insulation to the wall. The thermal bridges due to structural defects could not be detected after the repairs.

Finally, we want to mention another common thermal bridge effect. In the example in Figures 7.24 and 7.25, no thermal insulation was present anywhere, it was just not planned in the original design. In contrast, a large number of structural thermal bridges occur in buildings where thermal insulation is planned, of course, but not installed properly.

Figure 7.26a shows again an overview image of a family home (Figure 7.2). Besides the geometrical thermal bridges in the lower part, the feature near the dormer window needs attention. The window section is shown in more detail in Figure 7.26b, clearly indicating a problem that is energetically relevant. The problem consists in partially missing insulation at the connection of the wooden ceiling to the attic. The possible reasons are manifold: first, sometimes construction workers dispose of their trash (e.g., soft drink cans) by simply stuffing it into the insulation material. Second, the density of the insulation material, which is stuffed into openings, is still low when the morning break starts, but this is forgotten after the break. Third, some additional installation (e.g., electrical, plumbing) may be needed, so that insulation is removed but not added back after the work is finished, and so forth.

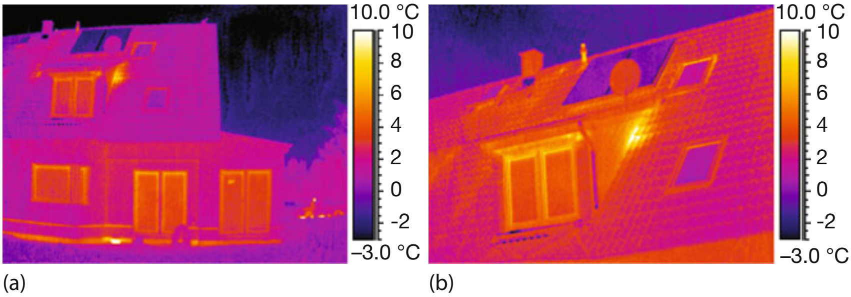

Figure 7.26 (a,b) Thermal bridge to right of dormer window owing to missing thermal insulation material.

7.4
External Influences

7.4.1
Wind

The surface temperature of objects is strongly influenced by the airflow around them. This is due to the fact that the heat transfer coefficient describing convection between the object surface and the surrounding air depends on the flow conditions, in particular, the flow velocity [20–22]. Large flow velocities can result in a strong cooling effect. This has an effect, for example, on the results of outdoor IR imaging of buildings or electrical equipment. Moreover, the wind not only reduces the surface temperature but also changes the thermal signature of the object surface. For most practitioners, this behavior is known and they use wind speed limits for their qualitative or quantitative analysis. Unfortunately, these limits are not standardized and the theoretical connection between the wind speed and the heat transfer due to forced convection at the surface is very complicated.

In any case, the heat transfer coefficient α_{conv} increases with flow velocity (Figure 7.27a), that is, wind speed. This leads to changes in observed surface wall temperatures, as shown in Figure 7.27b, which shows the calculated temperatures at the surface of an outside wall (calculation similar to the one in Section 4.3.3) for given conditions $T_{\text{inside}} = 20\,°\text{C}$, $T_{\text{outside}} = 0\,°\text{C}$, 24 cm brick wall with $\lambda = 1.4\,\text{W}\,(\text{m}\,\text{K})^{-1}$, and $\alpha_{\text{conv. inside}} = 7.69\,\text{W}\,(\text{m}^2\,\text{K})^{-1}$.

Obviously, both wall surface temperatures change with wind speed. For the outside wall, this change also leads to a strong decrease in thermal signature (i.e., the detected temperature difference between two adjacent spots, which are due to differences in thermal conductivity of the wall, will decrease for increasing wind speed) [22]. This behavior was demonstrated for our model half-timbered wall structure of Figure 7.11. The experimental arrangement is shown in Figure 7.28. The wall model was placed in front of a heating plate and a room temperature airflow was generated by a large fan. The wind speed was measured using a calibrated sensor, and the heat flux (in $\text{W}\,\text{m}^{-2}$) was determined using a calibrated

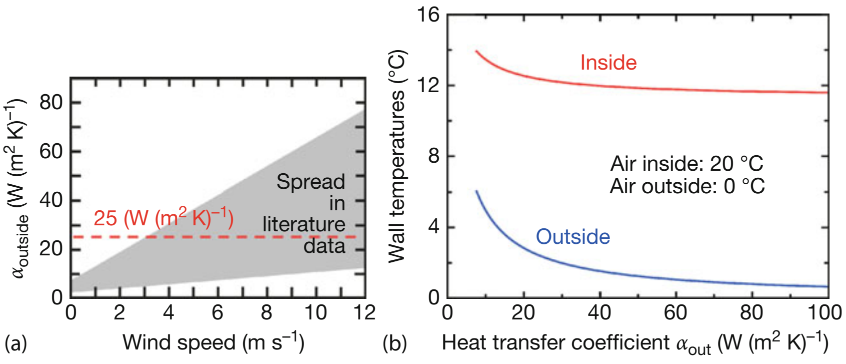

Figure 7.27 (a) Outside wall convective heat transfer coefficient as a function of wind speed and (b) corresponding theoretical wall surface temperatures for a single-layer wall with $\lambda = 1.4\,\text{W}\,(\text{m K})^{-1}$.

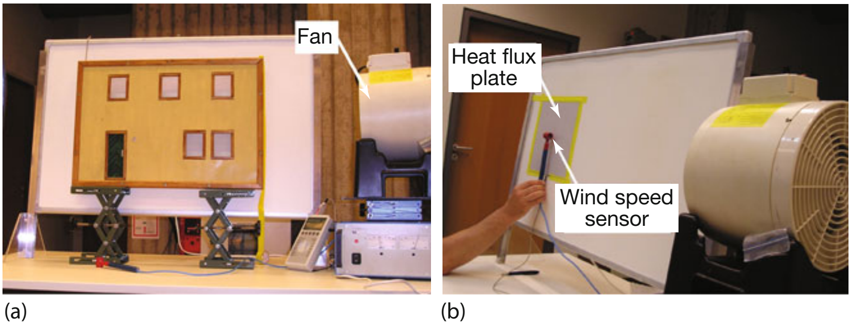

(a) (b)

Figure 7.28 Experimental setup for analyzing the effect of wind speed on surface temperatures and heat transfer rates.

heat flux plate. Determination of its surface temperature revealed the expected temperature drop with increasing wind speed as in Figure 7.27.

A demonstration of the wind speed effect for the house wall model is shown in Figure 7.29. Figure 7.29a shows the wall, heated from the rear, at zero wind speed, and Figure 7.29b refers to a maximum wind speed of $7.3\,\text{m}\,\text{s}^{-1}$. A quantitative analysis of two spots (good insulation of the wall, SP01; bad insulation of the wall, SP02) clearly demonstrates the decrease in thermal contrast (Figure 7.30). With increasing wind speed, both spot temperatures decrease as expected owing to forced convection. However, the temperature difference between the two spots – describing thermal contrast – also decreases (Figure 7.30b).

This means that outdoor thermography is less able to detect thermal bridges/temperature differences at high wind speeds.

The increase in the convective heat transfer coefficient with wind speed is also one of the physical principles underlying the so-called wind chill factor, well known from weather reports. The *wind chill temperature* is defined as the apparent temperature felt on exposed skin owing to the combination of air temperature

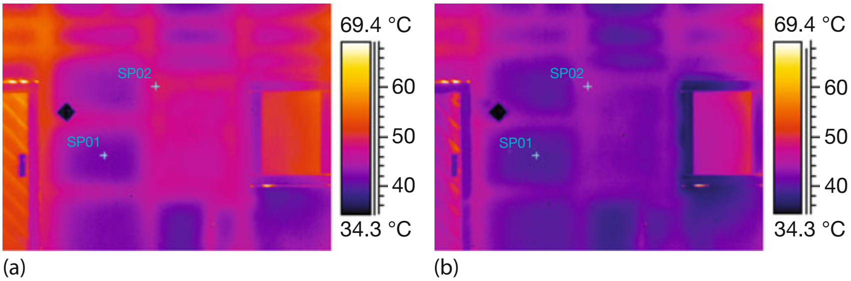

Figure 7.29 Change of thermal images with increasing wind speed. (a) $v_{\text{wind}} = 0\,\text{m/s}$ and (b) $v_{\text{wind}} = 7.3\,\text{m/s}$.

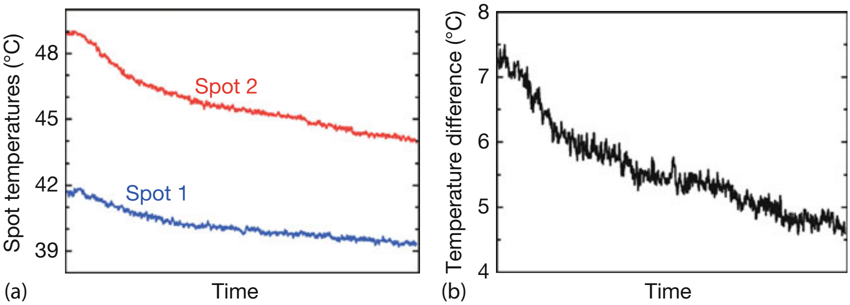

Figure 7.30 (a) Wall surface temperatures at spots 1 and 2 of Figure 7.29 as a function of time while increasing the wind speed from 0 to 7.3 m/s. (b) Corresponding difference in spot temperatures, which is a measure of the thermal signature.

and wind speed. Humans do not sense the temperature of the air, but heat flow due to the temperature difference between the skin temperature and the temperature of the surrounding air. When there is wind, the increasing α_{conv} between the skin and the air results in greater heat loss, that is, the temperature of the skin starts to get closer to the air temperature. This is interpreted as “it feels colder.” The exact definition of the wind chill index [23] also includes the human temperature perception and is therefore more complex.

7.4.2
Effect of Moisture in Thermal Images

Water damage can result in very high repair costs. Therefore, it is very important to know how to detect water in buildings and how water changes thermal signatures. As noted earlier, surface moisture on walls often reduces the measured surface temperatures owing to evaporative cooling. This effect must be considered separately from the water condensation on wall areas in corners or at edges, where the wall temperature is, in any case, already low owing to geometrical thermal bridges. In addition, the huge heat capacity of water may also lead to the warming up of building parts, depending on prevailing conditions.

Evaporative cooling occurs whenever a gas flows over a liquid surface [24]. This effect is well known and has been used in cooling for a long time. "In the Arizona desert in the 1920s, people would often sleep outside on screened-in sleeping porches during the summer. On hot nights, bedsheets or blankets soaked in water would be hung inside of the screens. Whirling electric fans would pull the night air through the moist cloth to cool the room" [25]. Evaporative cooling is a very common form of cooling buildings for thermal comfort since it is relatively cheap and requires less energy than many other forms of cooling.

In brief, all solids and liquids have a tendency to evaporate to a gaseous form, and all gases have a tendency to condense back. At any given temperature, for a particular substance such as water, there is a partial pressure at which the water vapor is in dynamic equilibrium with liquid water. With increasing wind speed the number of water molecules of the liquid water that experience collisions with the gas molecules increases. These collisions increase their energy, and they are able to overcome their surface-binding energy of the liquid. This results in an increasing evaporation effect. The energy necessary for the evaporation of the liquid comes from the internal energy of the liquid. Therefore, the liquid must cool down. This effect must be taken into account for all temperature measurements at objects with moist surfaces where the measured temperature depends on wind speed.

To demonstrate the consequences of evaporative cooling for buildings, laboratory experiments with the house wall model were carried out (Figure 7.31).

First, the dry surface of the house wall was analyzed (Figure 7.31a). Temperature differences due to different heat insulation quality are clearly seen as a thermal signature. Subsequent to moistening the surface, the thermal signature of the wall is changed. The thermogram shows a more homogeneous temperature distribution (Figure 7.31b), and the horizontal and vertical structural thermal bridges can no longer be detected. This effect is due to the evaporation cooling. Water evaporation increases at wall locations with higher temperatures, causing a higher cooling effect at these areas. As a consequence, a more homogeneous temperature distribution across the model wall can be observed. Additional air flows over the wall increase the evaporation effect (Figure 7.31c). This results in a further cooling of the wall surface by 5–6 K at a wind speed of 7.3 m s^{-1}.

It can be concluded that, first, an overall reduction of the absolute wall temperature happens and, second, evaporative cooling decreases the thermal contrast considerably, much more than wind over dry surfaces alone. On the one hand, this means that outdoor thermography during rain or with moist wall surfaces is very insensitive in terms of the detection of thermal bridges. On the other hand, one may just utilize the reduction of the wall temperature for increased airflow as a means to detect moisture.

We successfully tested an idea to use evaporative cooling consciously to check whether a cold spot on a wall is dry or moist. Figure 7.32 depicts the result of this experiment. At the wall in the lab, some areas were moistened with cold water (Figure 7.32b in black circle in IR image) and other areas were just cooled down using pieces of ice in a plastic bag (in white circle in Figure 7.32b) to avoid the

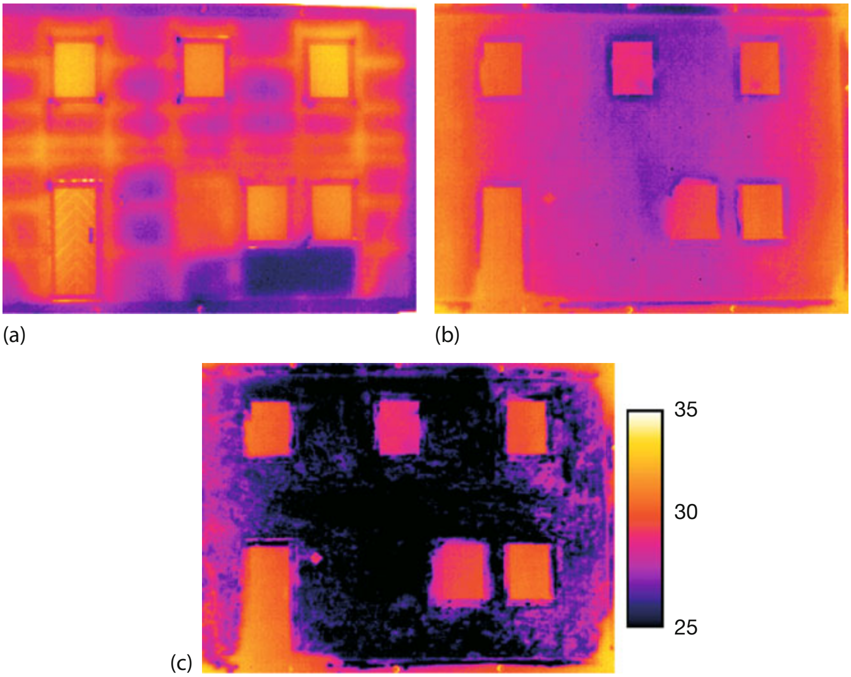

Figure 7.31 Thermal images of house wall model showing effect of evaporative cooling. (a) Dry surface; (b) moistened surface, no wind; and (c) moistened surface, wind speed 7.3 m/s. The temperature scale of 25–35 °C is the same for all images.

moistening of these areas. The water temperature was chosen such that approximately the same initial wall temperatures (without airflow) were measured. They were slightly below room temperature. It was not possible from the initial thermal image alone (Figure 7.32b) to determine which area was moist and which was dry.

If an additional airflow is directed onto the surface using a fan, the rate of evaporation of the water at the moist areas increases, resulting in a cooling down of these areas by 3–4 K within 10 s (Figure 7.32c,d). In contrast, the dry areas are heated by the room temperature airflow. In such experiments, a qualitative analysis to find moist areas on walls becomes possible with thermography by directing a fan toward the wall.

Quite a few investigations have been reported for moisture detection in building envelopes and on roofs using thermography (e.g., [26–32]). The idea behind this is usually to utilize evaporative cooling to detect moisture within a wall or ceiling [31]. Thermography was used to observe the walls and the ceiling before, during, and after water testing. In particular, the differences in moisture for roof assemblies, above-grade assemblies, and foundation wall assemblies were discussed in detail together with a methodology for exterior and interior inspections [28]. Other studies tried to quantitatively estimate moisture in masonry and wood structures [32] or to use solar loading to detect suspect areas [29]. In the

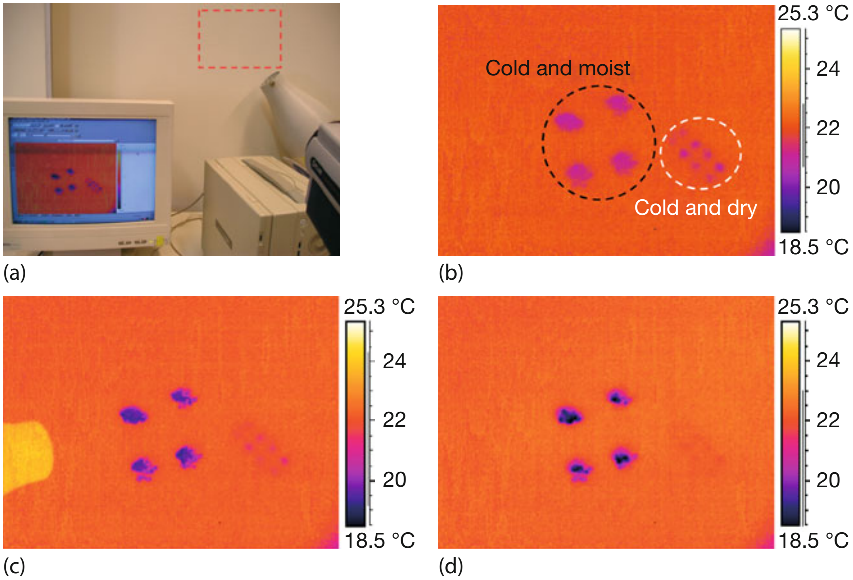

Figure 7.32 Analysis of dry and moist cold spots on a wall while applying airflow. (a) Experimental setup; red rectangle: observed area; (b) IR image of prepared wall without airflow; and (c,d) thermal images using airflow of 7.3 m/s after 2 s (left) and 11 s (right).

latter case, heating and cooling of the walls were observed. If water, which has a much higher heat capacity than building materials, is trapped in the walls, the corresponding regions will warm up more slowly.

Another study focused on the sometimes observable strange warm edges of moisture regions observable in building thermography [33], for example, when water is sprayed onto buildings to locate areas of intrusion. From evaporative cooling, one would expect cold regions if moisture is involved. However, transient warming up of the edges of moist regions may happen before this cooling starts to dominate.

Figure 7.33 shows an example of a laboratory experiment that demonstrated both evaporative cooling and a warm edge at the moisture front [33] for room temperature water poured at the upper right corner of a soft paper tissue. The warming is due to additional mechanisms as a result of exothermic chemical reactions, that is, reactions that release energy to the surroundings. Therefore, it is only observable in certain building materials, for example, some woods, paint filler materials, and cellulose-containing materials (e.g., wallpaper), but never in metallic parts, plastic, or glass. The paper tissue temperature at the spot in Figure 7.33 increased by about 5 K at the warm edge before cooling down to about 2 °C below room temperature after the moisture edge passed the spot.

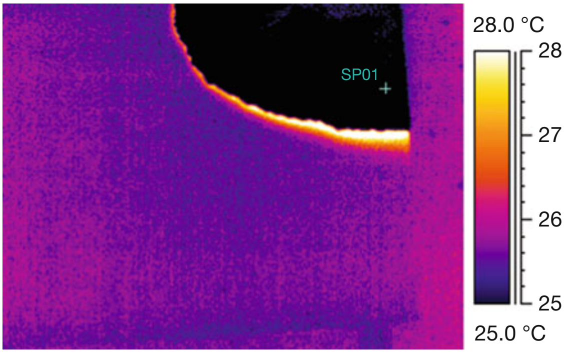

Figure 7.33 Snapshot from a time sequence after water was poured onto a soft paper tissue (after [33]). Besides the evaporative cooling, a warm edge can be observed.

7.4.3
Solar Load and Shadows

The outer walls of buildings are often subject to solar radiation. This solar load can lead to appreciable temperature rises within a wall [29]. However, even for clear sky conditions, the radiation flux incident on a wall changes during the day owing to the changing elevation and direction of the sun. Additional short-term changes may happen owing to cloud shadows or shadows from trees or neighboring buildings, which can move across the wall of a house. As a consequence, these external effects of solar load and shadows inevitably lead to transient effects: the surface temperatures of sun-facing walls and roofs will change continuously. In addition, all walls and roofs can experience night sky radiant cooling (Section 7.4.5), which also leads to transient effects. Following the description of simple model results of these effects, corresponding experiments and observations are presented.

7.4.3.1 Modeling Transient Effects Due to Solar Load

Measurements were done on two buildings with different but typical wall systems in Germany. Simple model calculations for the corresponding specific walls were studied but implementation for other wall systems is easily possible. The walls (Figure 7.34) consist of a layer system of gas concrete and exterior plaster (wall 1, Figure 7.34a) and the same system with an additional layer of 6 cm Styrofoam, also called *expanded polystyrene* (wall 2, Figure 7.34b). Styrofoam is a very good insulating material with low thermal conductivity. The table in Figure 7.34c gives a summary of the relevant properties of the used materials. The time dependence of wall heating and wall cooling depends on the construction and the properties of the wall materials. Owing to its insulation properties, it is expected that the Styrofoam coating will significantly affect the temperature distribution in the walls (Figure 4.10). Therefore, a difference in the time dependence of heating and cooling processes between the two wall models is expected.

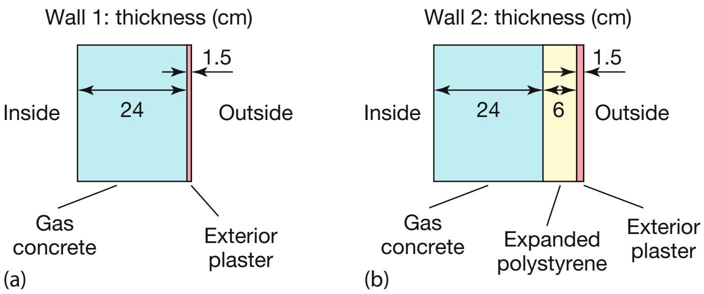

(c)

Material	Specific heat capacity *c* (J/(kg K))	Thermal conductivity λ (W/(m K))	Density ρ (kg/m^3)
Gas concrete	1000	0.1	400
Styrofoam (expanded polystyrene)	1200	0.04	12.5
Exterior plaster	1000	0.31	600

Figure 7.34 Wall models. (a) Wall 1, (b) wall 2 = wall 1 with additional thermal insulation, and (c) table of relevant material properties used in the model.

The surface temperatures of the wall and the temperature distribution within the wall were simulated using a freeware Excel program DynaTherm2000 [34]. The program uses the finite-element method to calculate the temperature distribution depending on the boundary conditions. It allows the calculation of transient heat conduction in any composite wall while taking into account the main meteorological influences – geographical position, solar conditions (sun elevation as a function of time during the day, day of year, geographical latitude, and longitude), and wind speed. In particular, it automatically includes the solar-load-induced wall heating.

Figure 7.35 shows the temperature distributions in the cross section of the wall models for several time periods after sunset and after the wall had been exposed to solar radiation for 5 h (this resembles a house that gets only afternoon sun). The steady-state conditions for the air temperatures were $T_{\text{inside}} = 20\,°\text{C}$ and $T_{\text{outside}} = 6\,°\text{C}$. Owing to the solar load, inner wall regions of gas concrete are heated up in Figure 7.34a. The Styrofoam insulation in wall 2, however, acts as a barrier for the solar-load-induced thermal flux. Therefore, the maximum gas concrete temperatures are below 21 °C in Figure 7.34b, which is much lower than in Figure 7.34a.

The larger amount of stored thermal energy within wall 1 will obviously lead to longer cooling times compared to wall 2. This cooling process will be governed by heat diffusion from the inside of the wall to the surface. To compare the results of simulations with the experimental results, it is necessary to calculate the outside wall surface temperatures due to the solar load. With the appropriate conditions of

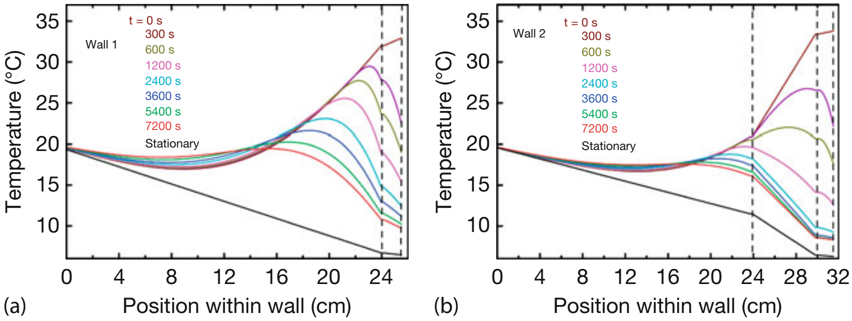

Figure 7.35 Simulation of temperature distributions in the model walls for different time periods after sunset. Stationary conditions (lowest curves) are $T_{\text{inside}} = 20\,°\text{C}$ and $T_{\text{outside}} = 6\,°\text{C}$ without any solar irradiance. The curve ($t = 0$ s) reflects the temperature distribution after 5 h of sunshine immediately after sunset.

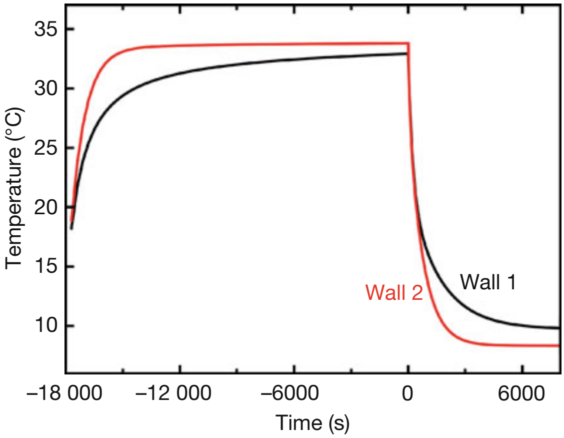

Figure 7.36 Simulation of surface temperatures of model walls 1 and 2 for $T_{\text{inside}} = 20\,°\text{C}$ and $T_{\text{outside}} = 6\,°\text{C}$. Solar irradiance started at $t \approx -18\,000$ s, yielding 5 h solar load. Time $t = 0$ corresponds to the end of solar irradiance, that is, the start of the subsequent cooling process. The timescale corresponds to times given in Figure 7.35.

solar irradiance, the modeled surface temperatures during the heating and cooling process are shown in Figure 7.36.

At first glance, the temperature rise and the cooling of the wall surface seem to exhibit a simple exponential behavior. This is motivated by the fact that it is possible to characterize a one-dimensional (1D) time-dependent cooling process for an infinite 1D wall with one material by

$$T = A_1 \cdot \exp\left(-\frac{t}{\tau}\right) + T_0 \tag{7.2}$$

where T is the surface temperature of the wall, T_0 is the wall temperature in stationary thermal equilibrium, and τ is the corresponding time constant.

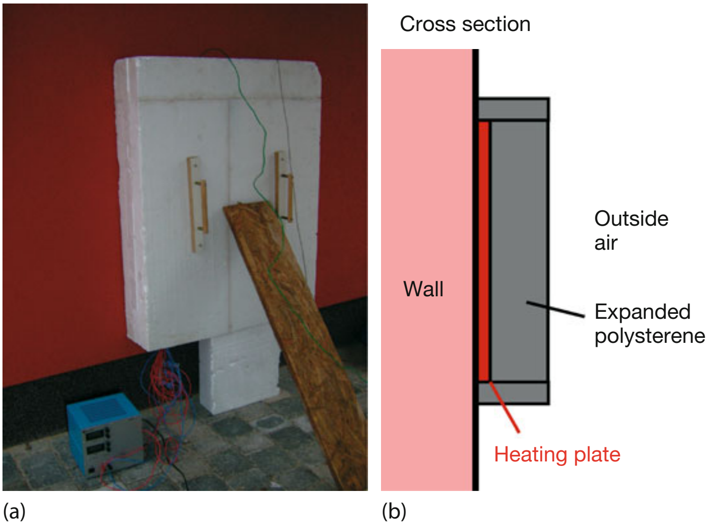

Figure 7.37 Experimental setup for electrical-heater-induced wall heating.

The cooling process of multilayer systems with nonhomogeneous initial temperatures within walls, like for walls 1 and 2, is more complicated. However, the simulations demonstrate that the model results may be fitted with the following equation:

$$T = A_1 \cdot \exp\left(-\frac{t}{\tau_1}\right) + A_2 \cdot \exp\left(-\frac{t}{\tau_2}\right) + T_0 \tag{7.3}$$

From these modeling results we conclude that, owing to the complex interplay between cooling due to convection and radiation from the outside and heat flow from stored energy in the wall to the outside surface, no simple Newtonian exponential cooling is expected [35]. Rather, we will try to fit the experimental results by the more complex double-exponential function of Eq. (7.3).

7.4.3.2 Experimental Time Constants

To analyze the cooling process of a wall experimentally [36], it was necessary to provide either solar load or an alternative wall-heating mechanism. In a first test, the wall was heated using an electrical heating plate ($A = 1.2\,\text{m}^2$) that could be attached to the outside surface of the walls. It was thermally insulated from the outside (Figure 7.37) and had more or less homogeneous surface temperatures across the whole area.

The cooling of the two walls after electrical heating was measured with IR cameras in the MW and LW regions by studying average temperatures within a centered area of about 200 cm^2. The resulting standard deviation within the area was typically less than 0.3 °C. As suggested in Section 4.5, we do not expect simple exponential cooling but rather fit the data with Eq. (7.3). The results for the LW measurements and both walls are shown in Figure 7.38. When comparing these

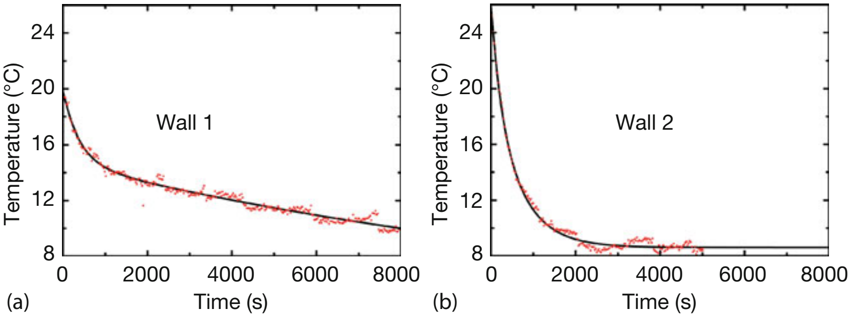

Figure 7.38 Measured surface temperatures of walls 1 and 2 immediately after removing the heater. The reason for the occasional drops in the data points are automatically performed camera calibrations.

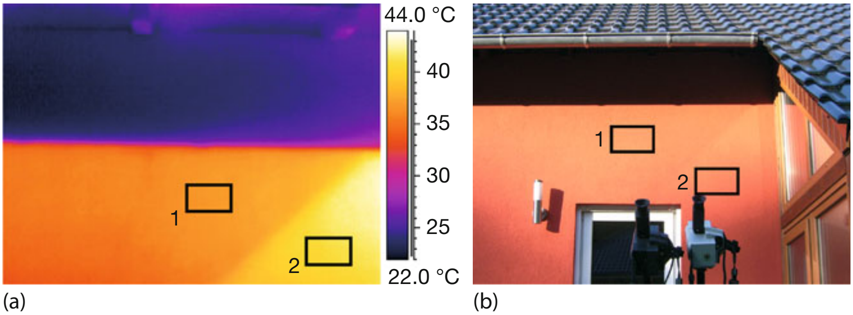

Figure 7.39 IR image of solar-radiation-heated wall 2 (a) and visible image (b) after 4 h afternoon solar load. LW camera, T(AR01) = 36 °C, T(AR02) = 42 °C, $T_{\text{amb. air}} = 20$ °C.

results with the rather crude infinite 1D wall model of the simulation, one finds the same trends between walls 1 and 2, that is, the cooling times of wall 1 are much larger than for wall 2.

In a second test, measurements using solar heating were done after 4 h of sunshine on wall 2 in the late afternoon. Figure 7.39 shows the measurement with analysis regions AR01 and AR02. The average temperature of AR02 is higher owing to the reflected radiation by the lateral window.

Figure 7.40 depicts the measured temperature differences $\Delta T = T_{\text{area}} - T_{\text{amb}}$ as a function of time, after the sun has stopped irradiating the wall (hidden behind forest trees). At $t = 1600$ s, part of the wall around AR01 was briefly irradiated again (suitable geometry of sun, clearing in forest, and house). Obviously, the solar load can easily lead to temperature differences of more than 20 K on walls and the corresponding time constants can easily amount to 1000 s. Since a signal has decayed to less than 1% of its original value only after about five time constants, this means that whenever a solar load is present on a wall, one should wait at least 1–2 h before the solar load effect no longer shows up in the IR image. For walls with larger time constants, these waiting times may be even longer.

7.4.3.3 **Shadows**

Figure 7.41 presents a typical example of outdoor building thermography. A house wall is illuminated by the sun, but part of it is already in the roof shadow. In addition, one clearly sees thermal reflections from the top of the right window frame. The shadows lead to transient effects of solar load heating and cooling of the wall.

A similar example, recorded in wintertime, is shown in Figure 7.42. The shadow of the rooftop of the neighboring house is clearly visible on the house wall. Owing to the change in position of the sun as a function of time (1° in 4 min), the shadow moves across the wall. From the geometry one may estimate a typical change of, say, 20 cm in 5 min. In the center of the shadow (to the left of the vertical metal chimney), the house wall is about 17 K colder compared to locations fully exposed to solar radiation for hours. Figure 7.42b shows the temperature along the line visualizing the temperature gradient. The broken red line indicates the expected

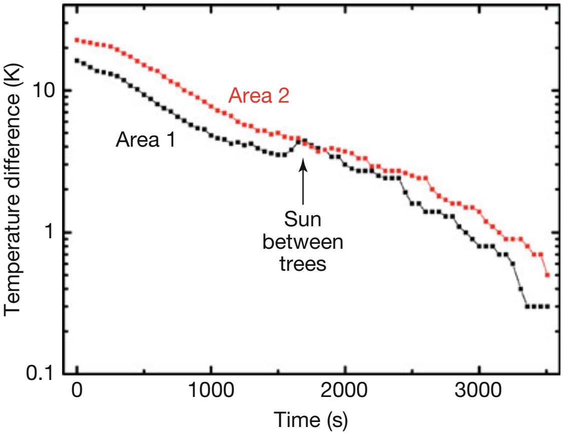

Figure 7.40 Temperature difference ΔT between average temperatures of areas AR01 and AR02 of Figure 7.39 and $T_{\text{amb. air}}$ as a function of time.

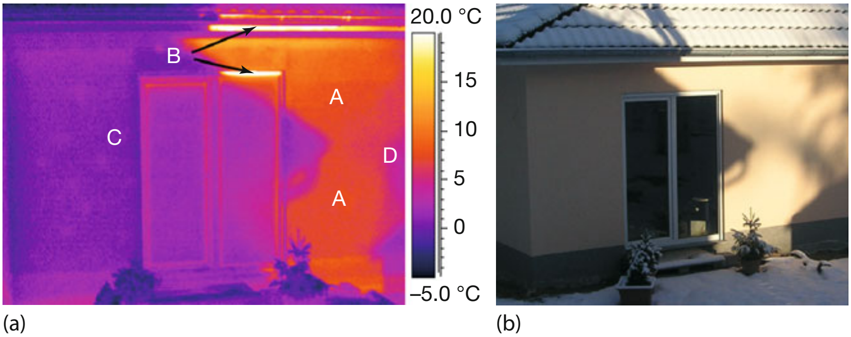

(a)

(b)

Figure 7.41 MW IR image (a) and VIS image (b) of a wall with solar-induced wall heating (A), solar reflections (B), shadowing effects of neighboring building (C), and tree branches (D).

behavior of the house wall. The lower signals are due to the lower emissivity of the metal chimney.

Such transient effects may lead to misinterpretation. Imagine, for example, that the shadow of a tall structure had been on a wall and then the sun disappeared behind clouds. Still, the wall would present a thermal image of this shadow for more than an hour. If one were unaware that the thermal feature was due to solar load and shadows, one might think of structural defects, which would be a totally wrong interpretation.

7.4.3.4 Solar Load of Structures within Walls

Solar load effects not only affect plane walls but may also change the thermal features of structures within walls as a function of time. This was studied for the house shown in Figure 7.43. As an example, Figure 7.44 illustrates the difference

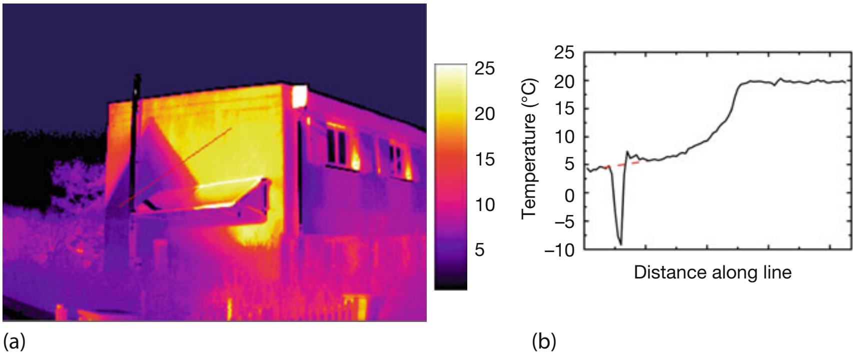

Figure 7.42 IR image (a) and line plot (b) visualizing temperature gradient of transient cooling due to shadow and heating by sun on a house wall. Scale: 1–25 °C.

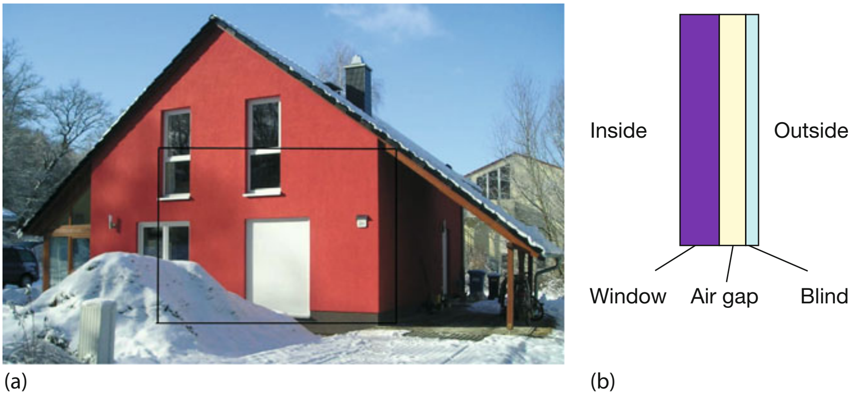

Figure 7.43 House wall with windows and a closed blind (a) covering a window with an air gap. This resembles a composite wall structure (b) similar to Figure 7.34, however, with different material properties.

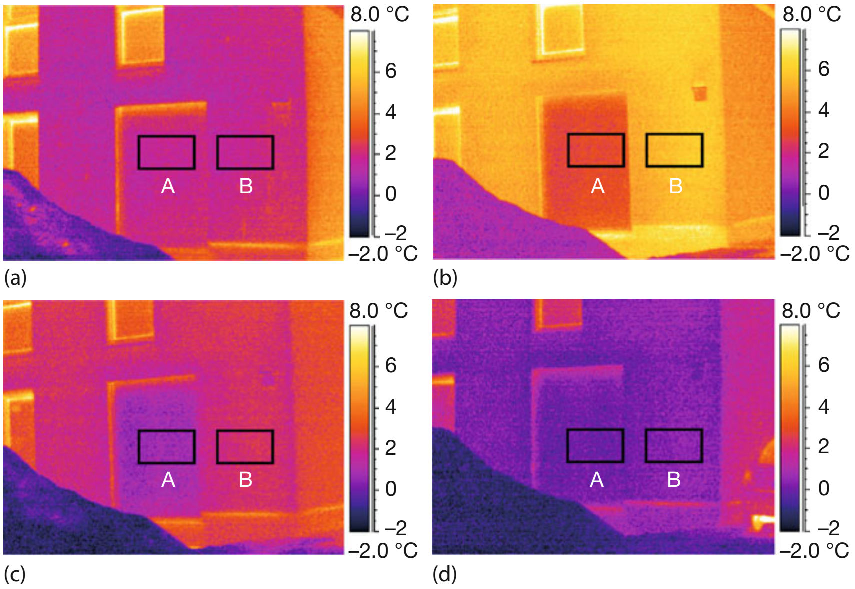

Figure 7.44 MW camera thermal images of closed blind (A) and thermally insulated wall (B). (a) At 7:30 a.m. before sunrise, $\Delta T = 0$ K; (b) at 3:50 p.m., 30 min after 4 h of irradiance by the sun ended, $\Delta T = 2.6$ K; (c) at 4:50 p.m., $\Delta T = 1.3$ K; and (d) at 5:50 p.m., $\Delta T \approx 0$ K again.

in time-dependent cooling processes between a thermally insulated plane wall section (B) and an adjacent closed blind (A).

Figure 7.44 shows measurement results before sunrise (Figure 7.44a), 30 min (Figure 7.44b), 90 min (Figure 7.44c), and 150 min (Figure 7.44d) after solar-load-induced heating (4 h with interruptions) had ended. Average surface temperatures were analyzed. Initially, that is, in the morning before sunrise, the temperature of the two areas was the same. Solar load led to an increased wall temperature compared to the blind. This temperature difference ΔT slowly decreased with cooling time. Owing to the very low thermal heat capacity and the good insulation from the window by the air gap, the closed blind cooled down after sunset more rapidly than the solid wall. Absolute temperatures depend on material properties. From this we can conclude that solar load can also affect the thermal contrast between a wall and its composite structures.

We note that solar-load-induced temperature variations of different building materials was also used in nondestructive testing [37]. The daily cycle of solar irradiation was used as input for lock-in thermography (Section 3.6.3), that is, the corresponding thermal wave had a period of 24 h. This made it possible to probe the walls of buildings with a penetration depth on the order of several centimeters.

7.4.3.5 Direct Solar Reflections

Solar irradiation is not completely absorbed by a wall, so it does not just lead to a heating up but also results in a diffuse reflection from rough surfaces and spec-

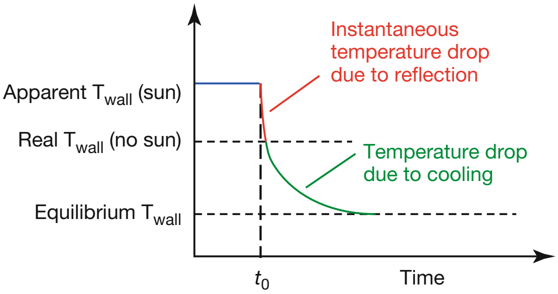

Figure 7.45 Detecting wall reflections. The temperature of a wall exposed to solar irradiation for a long time is described by a steady-state temperature (blue). A shadow on the wall leads to an instantaneous drop (red) of this apparent wall temperature due to solar reflections before cooling processes start (green curve).

ular reflections from polished surfaces. Owing to the spectrum of the radiation from the sun, this effect should be more pronounced for MW cameras than for LW systems. Initially, we neglect specular reflections from polished surfaces (B in Figure 7.41) but focus on rough wall reflections.

There is a simple way to test the effect of wall reflections. A wall is exposed to solar irradiation until nearly steady-state conditions are reached after several hours. If at time t_0 some object is placed between the sun and wall such that part of the wall surface is in shade, the apparent surface temperature measured with IR cameras will exhibit the kind of behavior shown in Figure 7.45. At first, there is a very rapid, instantaneous drop, owing to the now missing direct reflection of the solar radiation. Later, the wall area in the shadow starts to cool down with time constants as discussed earlier. The initial instantaneous drop indicates the temperature measurement error.

The physics behind the signal change was already discussed in Chapters 1 and 2 (Eqs. (1.29) and (2.37)). The radiometric chain for gray bodies with $\varepsilon < 1$ usually neglects reflected solar radiation and only treats the reflected background radiation. This is fine as long as there is either no direct sun present or that detection is in a long-wavelength IR region such that solar reflections can be neglected with respect to the other signal contributions. Here, however, we treat the case where solar reflections cannot be neglected. For simplicity let us assume that reflections from the surroundings at ambient temperature as well as atmospheric contributions can be neglected ($\tau_{\text{atm}} = 1$). In this case, Eq. (2.37a) would have one signal contribution only. Including the solar reflections, a modified equation for the radiant power from a (sun-irradiated) opaque wall at equilibrium wall temperature T_{wall} will have two contributions:

$$\Phi(\lambda) = \varepsilon \cdot \Phi_{\text{wall,BB}}(\lambda, T_{\text{wall}}) + (1 - \varepsilon) \cdot \Phi_{\text{sun}}(\lambda, T_{\text{sun}}) \tag{7.4}$$

In practice, we need to evaluate these signals for the limited wavelength ranges of the cameras used (see below).

If the complete signal is interpreted as being solely due to the thermal wall radiation (first term), one will then detect an apparently larger signal, that is, a wall

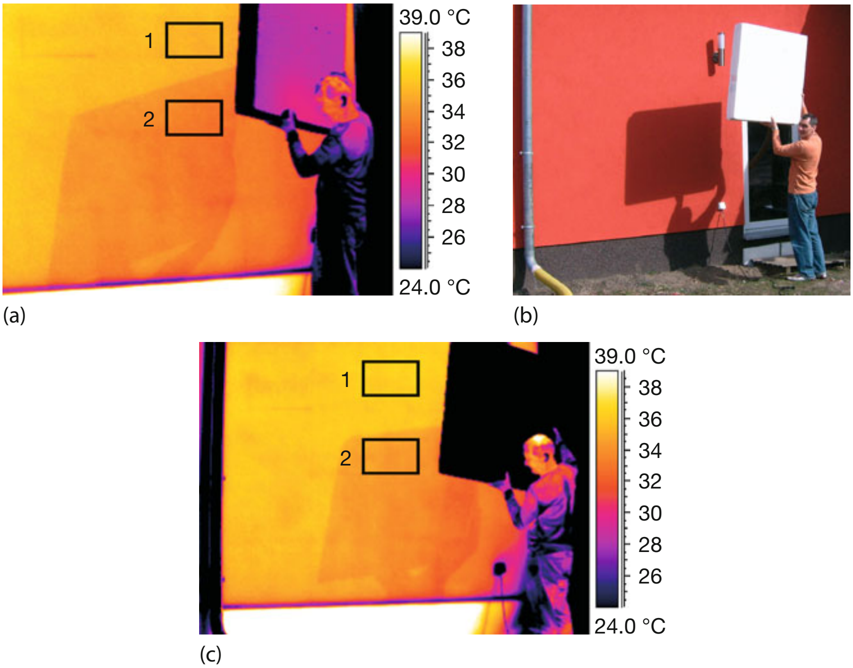

Figure 7.46 VIS image (b) and MW camera IR image of wall 2 immediately after shadowing recorded (a), indicating detection of direct solar reflections. Detection with a LW camera (c) was less sensitive to reflections; however, the shadow could be detected via the wall cooling (here after 35 s).

temperature reading, if there is also a solar reflection contribution (second term). However, when the wall is no longer being irradiated by the sun (second term really absent), the signal will instantaneously drop to the real signal contribution of the wall, that is, the real wall temperature can be detected.

The experimental setup and measurements of this effect are shown in Figure 7.46. A wall was exposed to solar radiation for about 3 h. The shadow was produced on the wall using a large Styrofoam block. Detecting surface temperatures (around 35 °C for $\varepsilon = 0.94$) with the MW camera, we found a temperature drop $\Delta T = 1.8\,\text{K}$ immediately after shadowing. With a LW camera the instantaneous drop is nearly nonexistent ($\Delta T \leq 0.4\,\text{K}$). However, the subsequent cooling due to the persistent shadow became visible later (1.5 K after 35 s).

From Figure 7.46 we conclude that solar reflections can become very important for MW camera systems with apparent temperature effects of up to 2 K. The size of this effect is surprising since walls have very rough surfaces, that is, high emissivity and very low diffuse reflectivity. Obviously, roof tiles typically with more flat surfaces may exhibit much stronger directional reflectivity, thereby amplifying the solar reflection contributions.

Figure 7.47 shows an example of a roof observed with MW and LW cameras. The geometry is shown in Figure 7.48. The measured apparent roof temperature

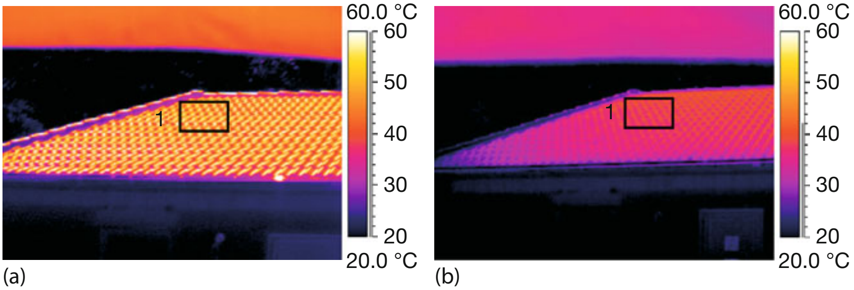

Figure 7.47 IR images of a roof recorded with a MW camera (a) and a LW camera (b) at $T_{amb} = 20$ °C. The MW camera detects a higher IR signal and therefore apparent temperature due to solar reflections. T_{ave} (AR01) = 48.6 °C for MW (a) and T_{ave} (AR01) = 38.1 °C for LW (b) using $\varepsilon = 0.8$.

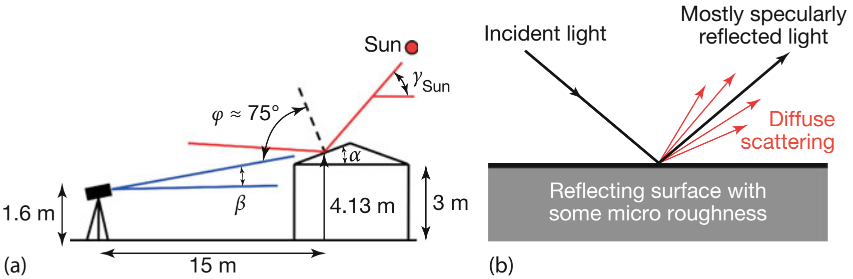

Figure 7.48 (a) Geometry of measurement $\gamma_{sun} = 53°$ at noon, $\alpha_{roof} = 24°$, $\beta_{camera} = 9°$. (b) Scattering of radiation from surface with microroughness (after [38]).

differences between MW and LW amount to more than 10 °C! In what follows we will try to quantitatively interpret these images.

From the known angles (solar elevation, roof angle, camera observation angle) it was found that the observation was in a direction rather close ($\approx 14°$) to the specular reflection of solar radiation. Therefore, one may expect a strong contribution of diffuse reflections (Figure 7.48b). Analyzing the geometry in detail, we found the observation direction to be at $\approx 75°$ with respect to the surface normal of the roof tile. For such large angles, the emissivity decreases to a value of about $\varepsilon(75°) \approx 0.8$, as has been tested in the laboratory, giving a reflectivity of $\rho = 0.2$ for the subsequent roof analysis.

To quantitatively estimate the influence of reflected solar radiation on wall and roof signals in MW and LW regions, we need to introduce the blackbody radiation functions from band emission (Section 1.3.2.5). $F_{(0\to\lambda)}$ gives the fraction of total blackbody radiation in the wavelength interval from 0 to λ (Eq. (1.20)) compared to the Stefan–Boltzmann law, that is, the total emission from 0 to ∞ (M_λ denotes the spectral emissive power). Under assumptions of constant detector sensitivity in a wavelength interval (λ_1, λ_2) and a constant emissivity ε, $F_{(0\to\lambda)}$ can be used to calculate the fraction $\Delta F(\lambda_1, \lambda_2)$ of radiation in the MW and LW ranges

Table 7.4 Results of fraction of reflected solar radiation in MW and LW range.

IR region in μm	**ΔF (6000 K)**	**S_{refl}: fraction of reflected solar radiation (W/m^2)** **Winter, $I = 200$ W/m^2**	 **Summer, $I = 800$ W/m^2**
MW 3–5	$1.45 \cdot 10^{-2}$	0.174	0.696
LW 8–14	$9.88 \cdot 10^{-4}$	$1.18 \cdot 10^{-2}$	$4.74 \cdot 10^{-2}$

(Eq. (1.21)). The detailed argument will be given for the wall example (Figure 7.46); extrapolation with different ε for the roof example is straightforward.

For a sun temperature $T_{\text{sun}} = 6000\,K$, reflectivity of the wall $R = 0.06$, solar irradiance in winter $I = 200\,\text{W m}^{-2}$ and in summer $I = 800\,\text{W m}^{-2}$, we define the fraction of reflected solar radiation

$$S_{\text{refl}} = R \cdot \Delta F \cdot I \quad \text{in W/m}^2 \tag{7.5}$$

With that one finds the results shown in Table 7.4.

These numbers depend strongly on the actual value of R. Larger reflectivities (i.e., smaller emissivities) can dramatically increase the reflected solar radiation, particularly in the MW band, since $\Delta F_{\text{MW}} \approx 15 \cdot \Delta F_{\text{LW}}$.

To judge the effect of these reflected solar radiations S_{refl} on the IR camera readings, we estimate the necessary thermally induced radiant signal changes $\Delta S_{\text{thermal}}$, which result in an apparent $\Delta T = 1$ K increase in temperature of a wall from, say, $T_1 = 307$ K to $T_2 = 308$ K. It is calculated from

$$\Delta S_{\text{thermal,MW}} = \varepsilon \cdot \left(\Delta F_{\text{MW}}(T_1)\sigma T_1^4 - \Delta F_{\text{MW}}(T_2)\sigma T_2^4\right) \tag{7.6}$$

$$\Delta S_{\text{thermal,LW}} = \varepsilon \cdot \left(\Delta F_{\text{LW}}(T_1)\sigma T_1^4 - \Delta F_{\text{LW}}(T_2)\sigma T_2^4\right) \tag{7.7}$$

With an emissivity of the wall of $\varepsilon = 0.94$, we find $\Delta S_{\text{thermal}}(\text{MW}) = 0.25\,\text{W m}^{-2}$. The spectrally resolved irradiances from a wall surface ($\varepsilon = 0.94$, $R = 0.06$) for reflected solar radiation S_{refl} and the thermally induced radiant signal change $\Delta S_{\text{thermal}}$ from 307 to 308 K is plotted in Figure 7.49. The blue and red regions denote respectively the MW and LW camera ranges. The hatched areas below the plots of $S_{\text{refl}}(\lambda)$ and $\Delta S_{\text{thermal}}(\lambda)$ correspond to the computed values. For example, for $200\,\text{W m}^{-2}$

$$S_{\text{refl}} = \int_{3\,\mu\text{m}}^{5\,\mu\text{m}} S_{\text{refl}}(\lambda)\,\text{d}\lambda \approx 0.174\,\text{W/m}^2 \quad \text{and}$$

$$\Delta S_{\text{thermal}} = \int_{3\,\mu\text{m}}^{5\,\mu\text{m}} S_{\text{thermal}}(\lambda)\,\text{d}\lambda \approx 0.25\,\text{W/m}^2 \tag{7.8}$$

Of course, the graphs for $\Delta S_{\text{thermal}}$ in Figure 7.49 will change if the object temperature T is changed. The interpretation will, however, be the same. As is obvious

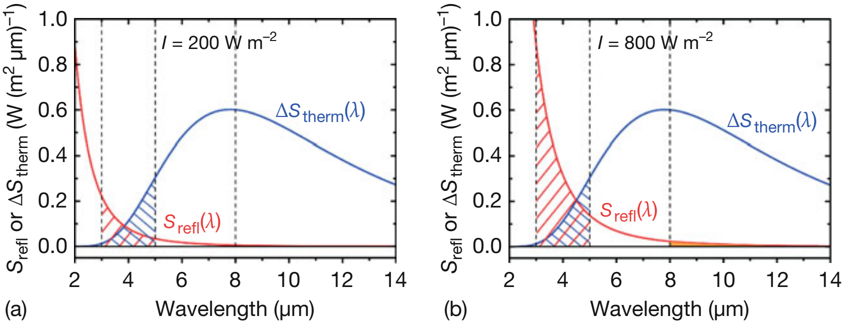

Figure 7.49 Reflected spectral radiance of sun S_{refl} for $\varepsilon = 0.94$, that is, $R = 0.06$ for a given irradiance of 200 W m^{-2} (a) and 800 W m^{-2} (b), compared to a signal change of the thermal radiation of the object at 307 K. ΔS_{th} induced by $\Delta T = 1$ K change.

from Figure 7.49, solar reflections are negligible, that is, they are much smaller for LW camera systems compared to MW cameras.

The preceding analysis can help understand the differences in solar reflection from wall and roofs. In the wall measurement (Figure 7.46), the reflected portion of the sun's radiation amounted to an apparent temperature drop $\Delta T = 1.8$ K, which (at $T_1 = 307$ K) corresponds to $1.8 \cdot 0.25$ W m^{-2} = 0.45 W m^{-2}. If this additional irradiance were due to reflected solar radiation, one would need a solar irradiation of (0.45 W m^{-2}/0.174 W m^{-2}) · 200 W m^{-2} ≈ 520 W m^{-2}, which is reasonable for a clear day in May at noon.

For the roof, however, the angle of emission of around 75° with respect to the surface normal led to a reduced emissivity ($\varepsilon(75°) = 0.8$), that is, increased reflectivity ($R = 0.2$). Repeating the preceding calculation for the higher basis temperature of the roof (38 °C), we find for the same solar irradiation of 520 W m^{-2} that the reflected portion of MW radiation will cause a temperature difference of about 7 K. Experimentally, the temperature difference between the LW and MW cameras amounted to about 10 K, which – considering the simplicity of our theoretical approach – is reasonably close.

7.4.4
General View Factor Effects in Building Thermography

Besides transient effects due to solar loads, shadows, and changes in wind and rain with time, there is another very important fundamental parameter that has a strong impact on outside building temperatures: the geometry of the surroundings. In Chapter 1, the laws of blackbody radiation and radiative transfer between objects of different temperatures were introduced. Consider the simplest arrangement, which deals with a gray object of given temperature T_{obj} within isotropic surroundings of constant temperature T_{surr}. For simplicity, the space between object and surroundings should be a vacuum such that conduction and convection can be neglected. In this case, the radiation exchange between object and sur-

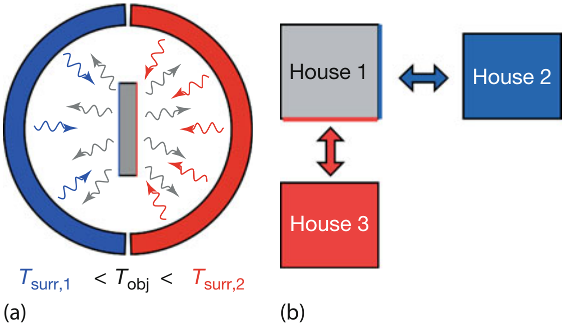

Figure 7.50 An object surrounded by other objects with differing temperatures will have a different radiative transfer in the various directions (a). The situation is similar to a house facing two neighboring buildings of different temperatures (b). This will lead to differences in the temperatures of the corresponding object sides.

roundings is due to the radiant power $\varepsilon \cdot \sigma \cdot T_{obj}^4 \cdot A_{obj}$ emitted by the object and the corresponding radiant power $\varepsilon \cdot \sigma \cdot T_{surr}^4 \cdot A_{obj}$ received by the object from the surroundings. Hence the net radiant power emitted ($T_{obj} > T_{surr}$) or received ($T_{obj} < T_{surr}$) by an object is given by

$$\Phi = \varepsilon \cdot A_{obj} \cdot \sigma \left(T_{obj}^4 - T_{surr}^4 \right) \tag{7.9}$$

However, when an object is not surrounded by an isothermal surface, the situation becomes more difficult. Consider, for example, the situation depicted in Figure 7.50a. An object is surrounded by two hemispheres of different temperatures. In this case, the left side of the object (in the center) emits more radiation than it receives, whereas the right side of the object receives more than is emitted. As a consequence, the left and right object surfaces may have different temperatures, unless the thermal conductivity of the object is extremely high. The same thing may happen to buildings. Consider the situation depicted in Figure 7.50b. House 1 has two neighboring buildings of different temperatures. House 2 has colder and house 3 warmer outside surfaces than house 1. Assuming again only a finite thermal conductivity of the wall material (which is reasonable), the wall facing house 3 should become warmer than the wall facing house 2. Figure 7.50 is, of course, only a simplified description. Usually any object (e.g., a building) is surrounded by many different objects (e.g., houses, trees and plants, ground, sky, clouds), and one must consider the radiation balance including all parts. Quantitatively the radiative contribution from each part of the surroundings is described by the corresponding view factor, introduced in Section 1.3.1.5.

Rather than presenting the complex calculations, the effect of the view factor on building thermography is illustrated schematically in Figure 7.51 for three different typical situations in the field of outdoor building thermography.

For buildings, there are usually three objects of different temperatures around. First is the ground, including vegetation, at T_{ground}; second are neighboring objects (buildings) that, owing to internal heating, may have different surface tem-

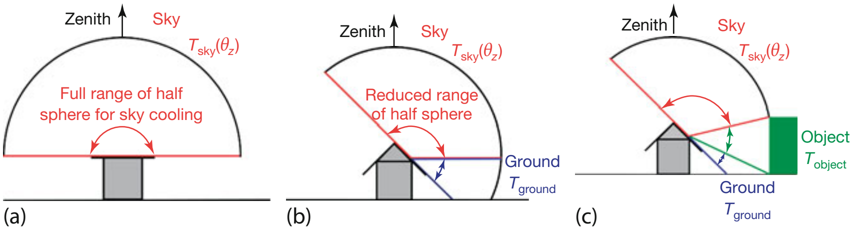

Figure 7.51 (a–c) View factor for different situations with respect to radiation exchange.

peratures, T_{object}; and finally is the sky, which may be clear or blocked by clouds and which has a temperature T_{sky}. The question of how much each part of the surroundings contributes is given by the view factor. Qualitatively, it is larger for two objects facing each other compared to the case where there is an angle involved. Figure 7.51a depicts a flat-roof building facing the sky. The radiative exchange of the roof with the surroundings is described by the view factor. It is calculated by integrating over the half sphere above the roof. Therefore, only the sky contributes. For a building with a tilted roof (Figure 7.51b) the sky can only contribute in a reduced angular range to the radiative exchange of the roof. In addition, part of the roof also faces the ground, which will have a different temperature. In this case, two view factors must be calculated, and the separate contributions need to be summed up accordingly. Qualitatively, one could immediately argue that the overall effect will be a larger or smaller radiative exchange depending on whether the additional ground temperature is larger or smaller than the sky temperature. Finally, Figure 7.51c again shows a building with a tilted roof that in addition faces another neighboring building. Now there are three contributions to the radiative exchange of the roof surface, a further reduced sky contribution, a reduced ground contribution, and an additional object contribution. Obviously, the situation becomes more complex as more objects of different temperatures are added. Different parts of the building, such as the walls, will have different contributions depending on their orientation.

A test involving a heat flux plate showed [39] that for a clear night sky (see below) the measured heat flux from the plate toward the surroundings could amount to as much as 60 W m^{-2} if oriented horizontally (i.e., the plate normal facing the zenith angle 0°). Changing the angle between plate normal and zenith from 0° to 90° (the latter corresponds to a vertically oriented plate, the surface normal being horizontal) led to a decrease in observed heat flux to only 10 W m^{-2}.

Owing to the fact that building walls or roofs usually have only low values of thermal conductivity, the different surrounding temperatures may easily lead to temperature differences on the building envelope, even if wall thicknesses are the same and no thermal insulation problems exist. Examples are given in what follows after a more detailed discussion on night sky radiant cooling.

7.4.5
Night Sky Radiant Cooling and the View Factor

The three typical temperatures of the surroundings of buildings, T_{ground}, T_{obj}, and T_{sky}, vary within different limits. Typical building temperatures (T_{obj}) can vary due to solar load and shadows during the daytime and due to cooling effects during the night; however, since there is internal heating in wintertime, the building envelope temperatures will usually not drop below the outside air temperature. Similarly, ground temperatures will not drop significantly below the air temperatures (see also following discussion). In contrast, the sky can show the most dramatic temperature variations. The greatest temperature difference occurs between clear and cloud-covered skies. This is due to the fact that clouds are opaque objects in the IR and have temperatures based on their minimum altitude. In contrast, the measured temperatures of clear skies are due to contributions from all atmospheric altitudes since the emissivity of thin layers of air within the atmosphere is quite small.

Nearly everyone with access to an IR camera has probably once pointed it toward a clear sky, maybe just out of curiosity. Figure 7.52 shows one such thermal image, which includes the horizon. The emissivity was chosen near unity to get a reasonable measure for the objects close to the horizon within a distance of about 100 m (air temperature 10 °C). The sky shows a colored band (in the chosen color palette) with apparent temperatures (along the line of IR image) decreasing to about −40 °C at the top of the image.

Of course, these apparent temperatures are absolutely useless; they refer to some kind of effective sky temperature averaged over the whole line of sight. A more thorough quantitative analysis of IR emissivities of sky radiation leads to emissivity values on the order of 0.8 [40]. Using these emissivities, effective sky temperatures were defined using the net radiant heat flux from an object of temperature T toward the hemispherical sky with effective temperature T_{sky}. In a sim-

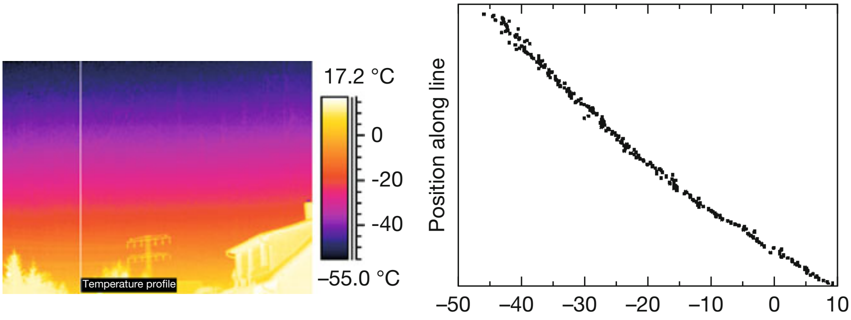

(a) (b)

Figure 7.52 Typical thermal image of a clear night sky, angular range 24° (a) and apparent temperature profile for constant emissivity along chosen line (b).

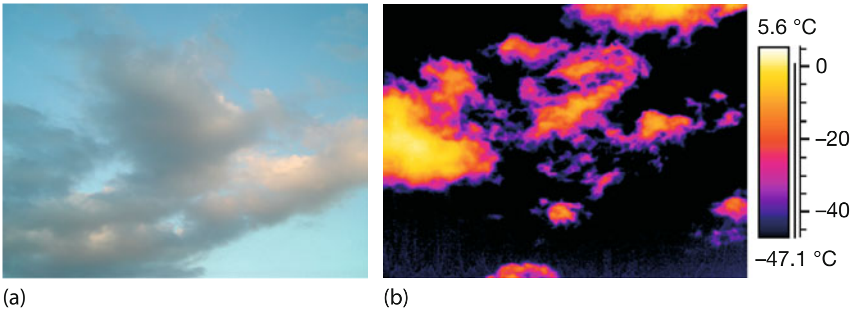

Figure 7.53 Influence of clouds on detected IR camera temperature (VIS image taken during the day, IR image taken at night). Clouds can have much larger apparent temperatures than the clear sky.

plified model, the effective sky temperatures depend on dew point temperature, ambient temperature, and cloud cover [40].

Figure 7.53 depicts VIS and IR images of clouds and a clear sky in the background. Owing to their low altitude, the clouds have much higher temperatures than the clear sky in the background. High cirrus clouds with a base at 10 km can, however, easily have temperatures as low as −55 °C [41] (for more details on sky and clouds, see Section 11.5.1).

The possible very low effective clear sky temperatures can have a dramatic influence on outdoor IR thermal imaging of buildings, in particular if the rule for outdoor thermography – that recordings should be made in the early morning hours before sunrise – is obeyed. Clear skies strongly increase radiative losses compared to completely cloud-covered skies. They can therefore lead to large time-dependent temperature drops of walls, roofs, and windows of buildings. In this case, weather conditions of the previous night define the thermal behavior of the outside building envelope. For hot climates, this effect has been proposed as a cooling mechanism [42].

From everyday experience (in climates that occasionally experience freezing temperatures) it is well known that air temperatures can get unusually low after nights with clear skies, in contrast to the case of completely cloud-covered skies. Therefore, very low morning air temperatures are an indication of night sky radiant cooling [39] (of course, the process also takes place during clear days; however, it may then be obscured by solar load effects since clear daytime skies automatically correlate with daytime solar loads). In the following sections, a number of examples are discussed that illustrate the importance of the view factor in building thermography, in particular when night sky radiant cooling is involved.

7.4.5.1 Cars Parked Outside or Below a Carport

It is known that parking a car in a carport can prevent the cooling down of the car windshield to a temperature below the dew point or the freezing point of water. This behavior is shown in Figure 7.54. In Figure 7.54a,c two cars are parked: one inside and the other outside of a carport. The carport roof consists of 3.5 mm

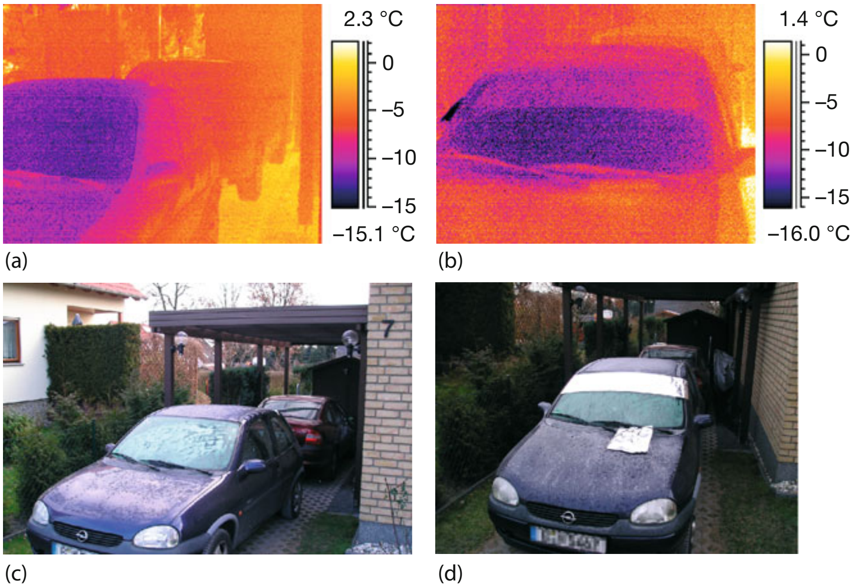

Figure 7.54 (a,c) Two parked cars (one in and one outside a carport with a plastic roof) after a clear sky night during winter. (b,d) On another night the windshield and engine hood of the car parked outside (d) was partially covered with aluminum foil, which was removed right before the IR image was taken.

thick sheet of plastic and is opaque in the IR range. The effective clear night sky temperature is much lower than the ambient air temperature and cools down the carport roof and the car outside the carport. The windshield of the car below the carport roof, however, is much warmer than the one outside. It sees only a small angular part of the clear night sky and a much larger part of the inner roof with a temperature well above the sky temperature. Therefore, it suffers less radiative losses to the surroundings than the car outside the carport.

During a clear night sky the windshield of the car parked outside (Figure 7.54a,c) directed to the sky was strongly cooled down to −12 °C. In contrast, the windshield temperature of the car within the carport was approximately equal to the ambient temperature of −4 °C.

A well-known and often used way to avoid a frozen windscreen on a car parked outside is to attach a foil blanket on top. Figure 7.54d shows a partially covered windshield of a car parked outside with an ordinary aluminum foil about 30 μm thick. The high reflectivity ($R \geq 95\%$) of the aluminum foil causes a low emissivity $\varepsilon \leq 0.05$ of the covered area. The radiant energy loss during the night is reduced below the foil, and the corresponding IR image (Figure 7.54b) recorded directly after removing the foil clearly shows the higher temperature of the previously foil-covered area. The thermal conductivity of glass, at $\lambda_{\text{glass}} \approx 0.7\,\text{W}\,(\text{m K})^{-1}$, is very low. Therefore, the temperature difference of about 5 K between the two areas of the windshield can be observed. For comparison, aluminum foil was also placed

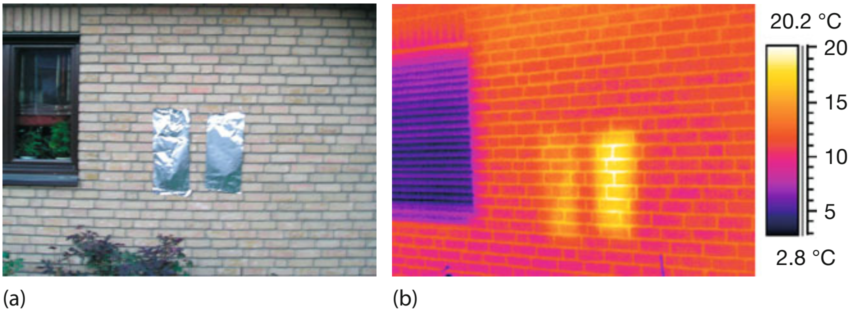

Figure 7.55 Areas of an outside building wall (facing no other warm objects/buildings) covered with aluminum foil (a). Thermal image of wall immediately following removal of aluminum foil 4 h after sunset (b).

on an area of the engine hood. The IR image does not show a temperature difference on the engine hood because the thermal conductivity of the metal, at $\lambda_{\text{steel}} \approx 50\,\text{W}\,(\text{m K})^{-1}$, is much greater, which leads to a fast temperature equalization.

Figure 7.54 also illustrates the fact that objects can indeed cool down far below the ambient temperature when the nighttime sky is clear since the large loss in radiant heat cannot be accounted for fast enough by heat transfer due to convection.

7.4.5.2 **Walls of Houses Facing a Clear Sky**

For vertical walls of buildings the view factor for night sky cooling is much smaller than for car windshields because there is a 90° angle to the zenith. To analyze the influence of clear sky radiant cooling on the temperature of a wall without any neighboring objects (imagine the situation as depicted in Figure 7.51b for vertical surfaces), two areas of a wall were covered with aluminum foil at sunset (Figure 7.55). The foil was removed and a thermal image taken 4 h after sunset. Like the car windshield, the previously covered areas exhibited a higher temperature with a ΔT reading up to 6 K caused by the reduced night sky cooling. This means that house walls facing clear skies do also cool down, though not as much as roofs.

7.4.5.3 **View Factor Effects: Partial Shielding of Walls by Carport**

Carport roofs also present opportunities to study the differences in the radiant night sky cooling of building walls. Figure 7.56 shows again the carport from Figure 7.54. As mentioned earlier, the temperature of its upper roof surface has decreased during the night sky radiant cooling but, because of air convection, remains at a higher temperature level than the effective night sky temperature. It is interesting to compare the three house wall segments indicated by areas AR01, AR03, and AR04. They all belong to the same wall with the same construction and no geometrical thermal bridges. The radiant energy loss of the wall below the carport roof (AR01) is much smaller than the energy loss of the wall above the roof (see temperatures of AR04) owing to the differences in view factor with respect

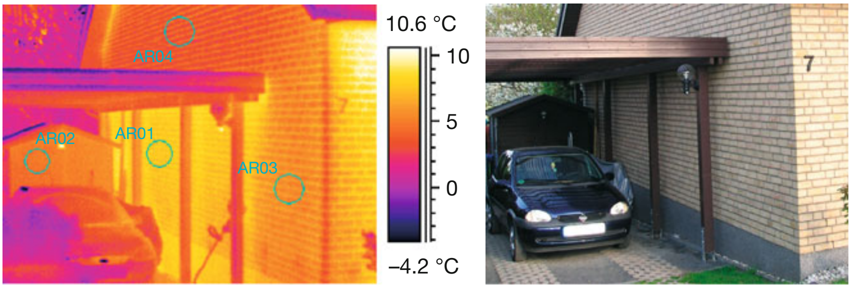

(a) (b)

Figure 7.56 Influence of different view factors on radiant cooling rates of building walls. The thermal image was taken 4 h after sunset.

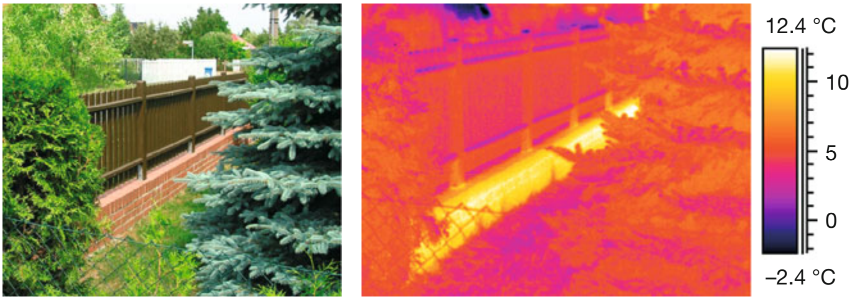

(a) (b)

Figure 7.57 Transient temperature distribution of a fence and its base caused by different thermal time constants. The IR image was recorded shortly before sunrise.

to the clear sky and the long thermal time constants of the wall. The temperature differences 4 h after sunset amount to about 3 °C. The wall temperatures of AR03 are in between, since this wall segment is still partially shielded from the night sky (resembling a viewing angle smaller than that in Figure 7.51) by the carport roof.

The small wooden house at the rear of the carport is also completely covered by the carport roof. The temperature of this wooden house (AR02) is, however, smaller than the temperature of the adjacent building wall (AR01). This effect is caused by the much smaller thermal capacitance (smaller thermal time constant). Obviously, without consideration of the view factor, the thermal image in Figure 7.56 could be erroneously interpreted as a typical example of very bad thermal insulation of the wall segment below the carport roof.

The difference in thermal time constants of brick versus wood is also illustrated in Figure 7.57. It shows a wooden garden fence on a base of concrete and bricks, recorded shortly before sunrise. A typical wrong interpretation of such an image could be the assumption that heating pipes are below the fence. In reality, the garden fence cools down very quickly due to its low thermal mass. The base, however, can store much more thermal energy and cools down more slowly. The cooling

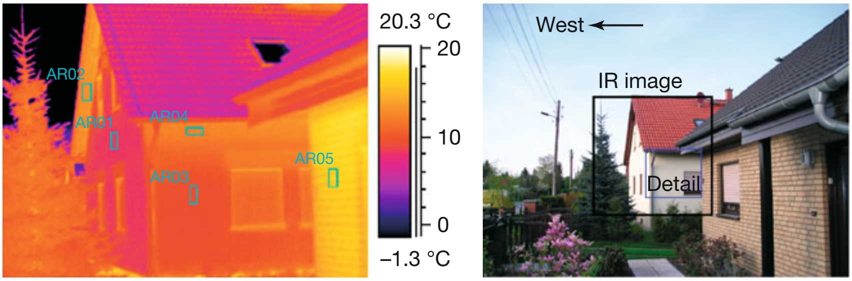

(a) (b)

Figure 7.58 Influence of radiant night sky cooling and view factor on apparent wall temperatures (see text for details).

time constants of objects can be estimated from their thermal properties [35, 43]. In the present case, for the base of the fence, one finds a cooling time constant of about 3 h.

7.4.5.4 View Factor Effects: The Influence of Neighboring Buildings and Roof Overhang

Figure 7.58 presents another example of a possible erroneous interpretation of IR images if the view factor is not properly taken into account. The figure shows two neighboring houses. To the west of both houses there is no surrounding property, that is, there are only view factor contributions of the clear sky and of the flat ground, but none of warmer buildings. In contrast, the southern side wall of the more distant white house faces the house in the foreground of the VIS image. Therefore, its view factor contribution to the cold clear night sky and ground is strongly reduced and instead replaced by a contribution due to the warmer neighboring house. Therefore, this wall (AR03) is warmer than the west-facing wall (AR01) (it was checked experimentally that there is no influence of an angle-dependent emissivity on the thermal imaging results).

The marked areas A02 and A04 in Figure 7.58 depict the effect of the roof overhang on the radiant cooling rate. Just below the overhang (AR02) the temperature is much higher owing to the strongly reduced radiant cooling. The decrease of the view factor for the cold sky in the upper region of the side wall by the overhang (AR04) also causes an area with a higher temperature level compared to the lower wall (AR03). Just looking at such experimental results without thinking about the physics behind them can easily lead to misinterpretations of thermal images. The higher-temperature areas caused by reduced radiant cooling are often misinterpreted as thermal leakages.

Another example of a possible misinterpretation of thermal images concerns the temperatures of the western walls of the two buildings. The measured wall temperature of the foreground house (AR05) is significantly higher than that of the background house (AR01). This is caused by the different wall constructions and not by a different thermal insulation. The house wall exhibiting the higher temperature (foreground house) consists of a brick wall on the outside, an air gap, and an insulated inner wall. Owing to the high thermal capacitance, the heat storage capacity is large. The wall of the background house consists of a thin (2 cm) layer of plaster followed by thermal insulation and an inner wall. The thermal storage capacitance of the plaster is much smaller than that of the brick wall. Therefore, the wall of this house exhibits a lower temperature at the surface if there is significant heat loss at the surface due to the radiant cooling. The measured temperatures do not represent the energy loss of the houses but rather the transient effect of cooling during the night after heating during the day (sun and air).

7.5
Windows

7.5.1
General Features

Windows are among the most prominent features in any IR image of buildings, for two reasons. First, glass surfaces are usually very flat, providing excellent conditions for mirror images, that is, thermal reflections. Second, the connection of window frames to the building wall is critical with respect to thermal insulation. Figure 7.59 shows a schematic, very simplified view of a window frame attached to a building wall. Nowadays, double- and triple-pane windows are available with U-values that are quite low (Table 4.6); however, the critical energy loss comes from the frame. There may be associated problems, for example, bad insulation (hollow space between frame and masonry incompletely filled with insulating foam) leading to airflow (red arrow) to the outside. In addition, the corner geometry of windows in their frames also represent geometrical thermal bridges. Therefore, window frames usually show up in thermal images. The important question is whether the associated temperatures are above or below the typical dew point temperatures. Therefore, a careful IR analysis from the inside of a building will always check window frames with regard to dew point temperatures.

Figure 7.60a shows an indoor inspection of a living room window. It is a split window with a 120° wall corner angle. The most prominent feature is clearly the thermal reflection of the thermographer himself (for more details on thermal reflections see Section 3.4.1.4). The most prominent feature regarding the quality of the window insulation is the cold spot in the upper corner between the two

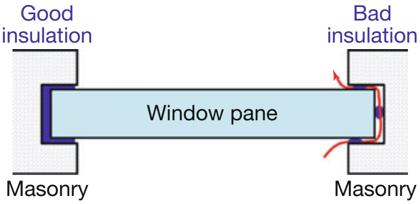

Figure 7.59 Schematic view of a window and its connection to the building wall.

window parts. Figure 7.60b is an expanded view of this critical section. Owing to missing thermal insulation in the frame at the edge, the minimum temperature came to only 8 °C, which is below the corresponding dew point temperature for 50% relative humidity. This leak is relevant in terms of mold formation.

Another example of bad thermal insulation in a window frame is shown for a skylight window within a tilted roof (Figure 7.61). For the same inside–outside conditions as in Figure 7.60, the lower right corner had an even lower temperature of only 7.3 K, clearly below the dew point temperature. The window often showed a wet frame after cold winter nights and was replaced.

In contrast, Figure 7.62 shows an example of a large window front on the top floor of a house from outside as well as inside. Although the window frames clearly show up in the images, the inspection showed no problems. The features are due to the expected geometrical thermal bridges of the frame as well as the slightly lower U-values of the frames compared to the panes. The double-pane windows themselves are slightly warmer than the brick wall owing to their slightly larger

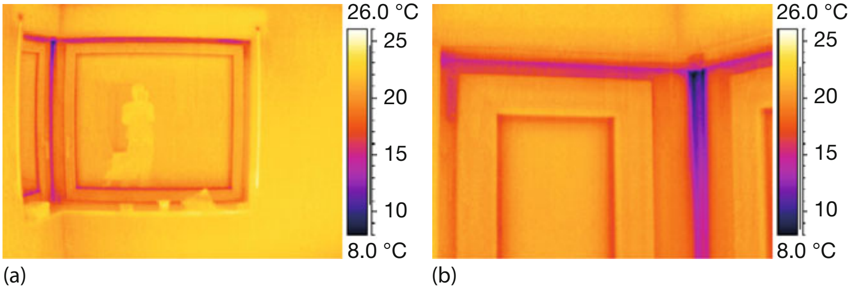

Figure 7.60 (a) Overview of living room window showing thermal reflections. (b) Expanded view of critical section. Conditions: outside air: 0 °C; inside air: 21 °C; and minimum at leak: 8 °C.

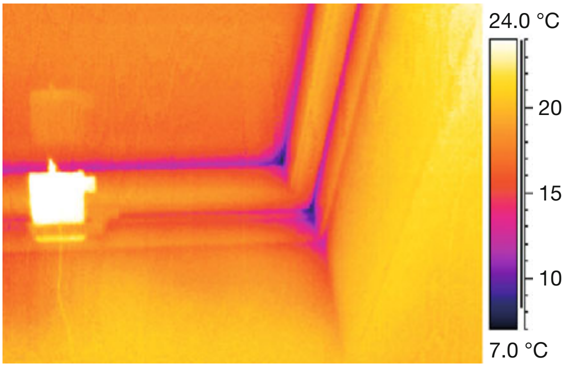

Figure 7.61 Skylight window with bad thermal insulation of frame. The lower corner edge had a minimum temperature of only 7.3 °C, well below the corresponding dew point temperature. The bright feature to the left is a 28 °C warm display of a digital thermometer used to initially convince the construction workers that the IR images were showing correct temperatures.

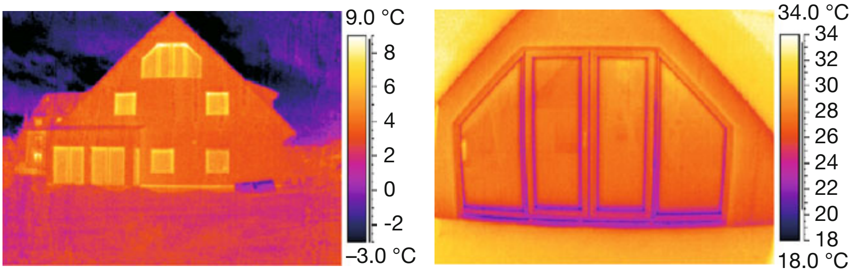

(a) (b)

Figure 7.62 Outside (a) and inside (b) view of a four-part window section on the top floor of a house for $T_{\text{inside}} - T_{\text{outside}} \approx 20\,\text{K}$.

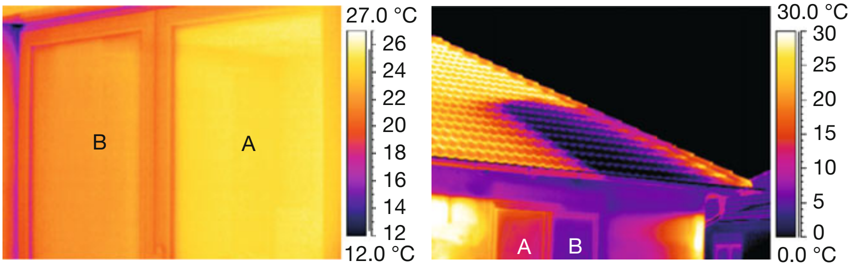

(a) (b)

Figure 7.63 (a) Interior IR image of two window panes, showing quite different temperatures. (b) Exterior analysis of the same window. Part A was within sunshine, whereas part B was in the shadow of a neighboring building.

U-value (Table 4.6). Even close-up imaging of the window frames from inside revealed no problems, and frame temperatures were well above dew point temperatures for lower inside temperatures.

Shadows of neighboring buildings can also have a dramatic influence on the appearance of windows in thermal images [44]. Figure 7.63a shows an indoor thermal image of two adjacent double-pane windows, A and B. Without considering the outside conditions (Figure 7.63b reveals that window B is in shadow), one might think that window B was defective, perhaps having a gas leak. However, the residual absorption of glass in the LW band caused a slight heating of window A upon solar irradiation.

In contrast, Figure 7.64 shows a real gas leak of a double-pane window. Such insulating glass is usually filled with dry air (to avoid condensation) or special gases (mostly argon). The window part A in Figure 7.64 had a gas leak. As a consequence, the low U-value of the double-pane window must be replaced by larger U-values of two single-pane windows, which means that the corresponding glass surfaces will be colder from inside and warmer from outside. Besides the gas leak in the window, Figure 7.64 also shows an additional defect in the rubber gasket of the window frame itself (B). This could only be detected from the inside. In the

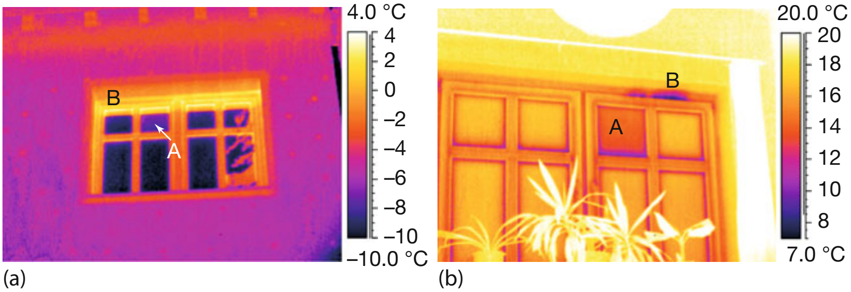

Figure 7.64 A gas leak (A) in a window detected using a combination of indoor (b) and outdoor (a) thermography. Feature B is an additional defect in the rubber gasket.

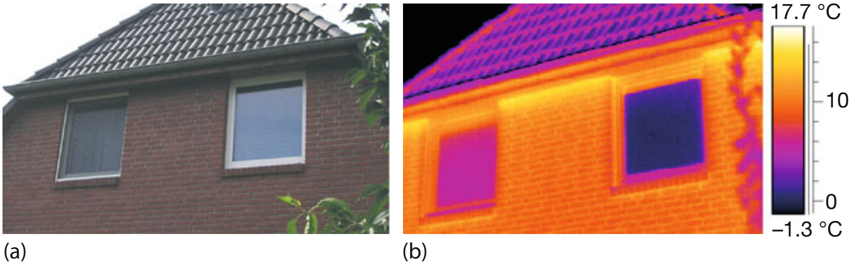

Figure 7.65 Influence of differing view factor contributions of cold sky and warm nearby objects (measurement taken 4 h after sunset).

outside image, thermal reflections from the window frame overhang were dominating and hiding this thermal feature.

A similar example with an apparently warmer strip below the roof is shown in Figure 7.65b. It results from reduced radiative losses (view factor effects) owing to the roof overhang. In addition, one clearly sees the effect of less insulation directly above the windows owing to reduced thermal insulation within and around the roller shutter housing. Figure 7.65 shows an additional effect: the right-hand-side window reflects the night sky (IR recorded during night, VIS during daytime), whereas the left-hand-side windows reflects radiation from a neighboring building. Therefore, the various view factor contributions of night sky and warmer nearby objects differ, leading to a colder right window. Again, this has nothing to do with a badly insulated window.

The left-hand part of Figure 7.66 shows vertical windows (areas A and B) and a skylight window (C). Owing to the different tilt angle of the windows with respect to the zenith, window C will undergo more night sky radiant cooling and is much colder. In addition, part B of the window on the left appears warmer owing to a reflection from the roof overhang.

A final example of night sky radiant cooling on the appearance of windows is shown in Figure 7.67.

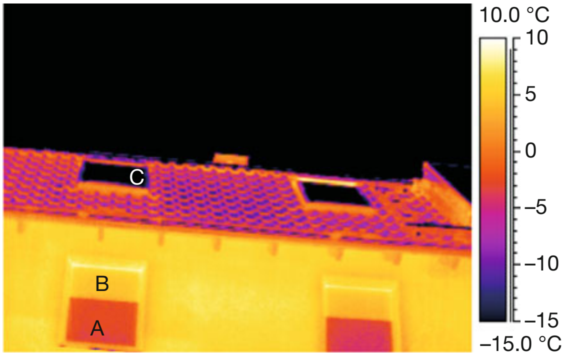

Figure 7.66 Two sections, A and B, of normal windows and skylight windows, C. Differences in temperatures are due to view factor effects of the night sky and the roof overhang.

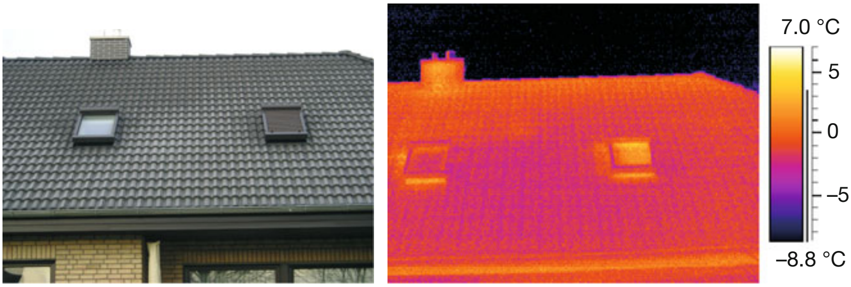

(a) (b)

Figure 7.67 Influence of a rolling shutter on the outside temperature of skylight window panes. The shutter on the skylight window on the right was opened right before the IR image measurement was taken at sunrise.

It illustrates the use of rolling shutters for skylight windows to reduce the heat transfer due to night sky radiant cooling. A roof with two dual-pane skylight windows was analyzed. During a night with a clear sky, the rolling shutter on the left-hand side in Figure 7.67 was open and the right one was closed. The closed shutter of the right-hand-side window was then opened right before the IR image was taken (for the thermal imaging, a MW camera was used; for detailed information about temperature measurements at window panes with MW cameras see [44]).

The temperature of the skylight window previously shielded by the closed roller shutter exhibits a higher temperature with a ΔT reading up to 5 K owing to the reduced night sky cooling. Consequently, the temperature difference between the inside and outside window pane temperatures is lower than for the other window. This causes less heat loss through the skylight window. One may conclude that shutters can indeed help to conserve energy, in particular in cold clear night sky conditions.

As discussed earlier, analyzing windows using IR cameras can be very interesting, and the thermographer may get quite excited if anomalies are detected. Here some caution is appropriate: the inhabitants of a house can feel like someone is watching them and even taking pictures through the window. They might even get angry if you look too closely at their bedroom windows.

7.5.2
Optically Induced Thermal Effects

Besides thermal insulation problems due to frame defects or gas leaks in multiple-pane systems, windows can have additional thermal features that are due to optically induced effects. Such features already arise for regular building windows [45, 46], but they can become much more pronounced for skyscrapers [47, 48], where they can cause severe problems.

Double-pane windows (Figure 4.11) consist of two glass panes separated by a volume filled with some inert gas. This inner volume is airtight. Therefore, the two panes are only parallel to each other if the outside/inside pressures and temperatures are the same as during manufacturing.

However, whenever pressure or temperatures changes, the panes may deform, leading to either convex or concave surfaces (Figure 7.68). Owing to the glass reflectivity, these shapes resemble curved mirrors, which may focus or defocus incident light. Incident parallel solar radiation will become focused by one pane while being defocused by the other. If it is projected onto a given surface, complex images will result. Since windows are usually rectangular rather than spherical, these images will usually not be spherically symmetric [45].

Figure 7.69a shows a close-up visible view of such a reflection on a neighboring building. A crosslike feature surrounded by an ellipse is observed on the bricks, the cross being due to focused radiation and the ellipse to the defocused part [45]. Focusing of radiation onto a wall leads to absorption and therefore heating up of

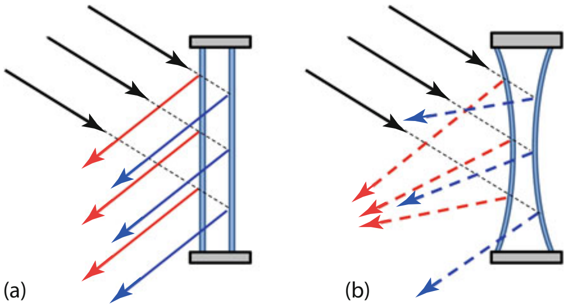

Figure 7.68 Double-pane window for equilibrium conditions with planar surfaces (a) and if deformed owing to external pressure and temperature changes (b). Incident parallel solar radiation (black arrows) is reflected, giving rise to either parallel reflected rays (a) or focused and defocused rays (b).

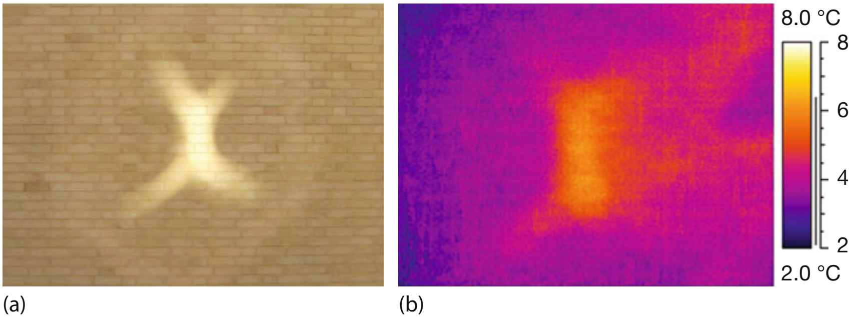

Figure 7.69 (a) Enlarged section of light focus owing to reflected sunlight from a single double-pane window on wall of a neighboring building. (b) Temperature distribution of focal area owing to irradiation of the wall.

the wall. In this case, a 2 K temperature difference was detected with a LW camera (Figure 7.69b).

Although thermal effects due to an individual double-pane window are small, the effect of many windows could add up, in particular, if the wall with the windows is curved. Modern skyscrapers with glass fronts are nice to look at; however, they are also excellent examples of potential troublemakers with regard to optically induced thermal problems. These can happen in particular if the curved shape is pointed southward (in the northern hemisphere) and if architectural glass with reflectivities higher than that of plain glass is used and covers most of the building envelope [47, 48]. In such a case, the now much larger curved reflecting area can indeed cause severe problems ranging from sunburn of people in the focus to even melting of plastics on bags, in cars, and so forth. Some sensational stories in the media even reported on skyscraper death rays!

The physics behind this phenomenon is similar to that of double-pane windows; however, skyscrapers usually have a more cylindrical symmetry. Figure 7.70a,b shows a problematic building in Las Vegas that made the phenomenon popular and a miniaturized model made of mirror foils. Figure 7.70c is an IR image of the optically induced heating of the wooden bottom plate of the model from normal irradiation with sunlight. For the most unfavorable conditions, that is, the best achievable focus, the model showed huge temperature increases above 30 K within seconds and above 100 K within minutes depending on the materials and geometry used. It could have melted plastic and fried eggs! A computer modeling analysis was able to explain peak irradiation values, which were up to a factor of 100 greater than regular solar irradiation. The problem exists only for certain geometries, times of day, and times of year for any given building [47]. It can also easily be avoided by choosing a proper orientation of the glass façade of the building.

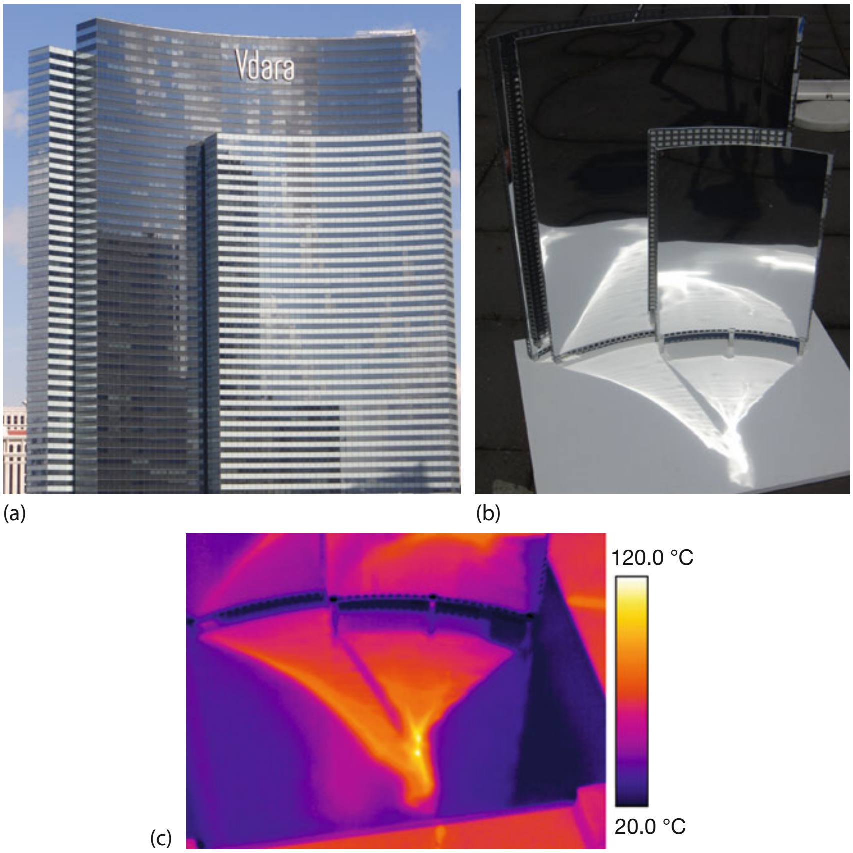

Figure 7.70 Curved glass front of a skyscraper (a), miniaturized model (b), and LW IR image of focus-induced heating of wooden bottom plate of model upon being irradiated by the sun (c).

7.6

Thermography and Blower-Door Tests

No building is 100% airtight. The air exchange rate is a quantitative number that describes how much air is exchanged in a building per unit of time with regard to the volume of the building. For example, an air exchange rate of 3 means that air with three times the inside volume of a building is exchanged per hour. If all natural openings in a building (windows and doors) are closed, air exchange will take place only through air leaks in the building envelope that could be, for example, small channels of missing insulation or fissures and crevices in seals of windows or doors, and so on. Figure 7.71 shows an example of an air leak within a wall socket in an exterior wall. The problem was due to missing thermal insulation in the wire channel and socket hole that could be easily resolved. Incoming cold air was flowing down and cooling adjacent parts of the wall and floor.

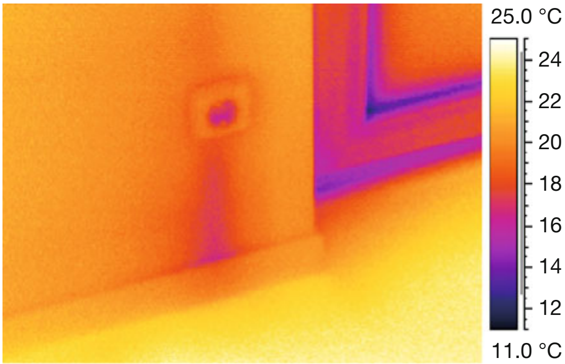

Figure 7.71 Leaks within a wall socket in an exterior wall leads to a steady flow of cold air, which flows downward and thereby cools the adjacent wall.

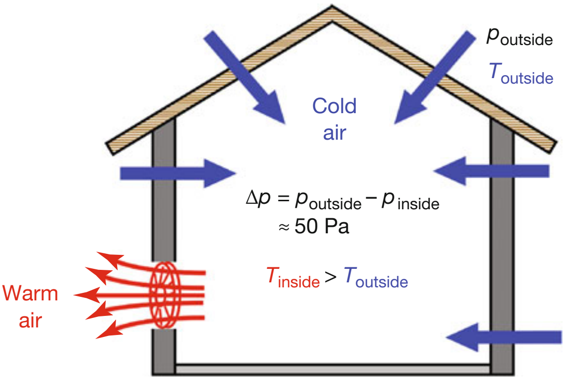
p_{outside}
T_{outside}
Cold air
$\Delta p = p_{\text{outside}} - p_{\text{inside}}$
≈ 50 Pa
$T_{\text{inside}} > T_{\text{outside}}$
Warm air

Figure 7.72 Blower-door technique for measuring air exchange rates: a powerful fan creates a pressure difference of typically 50 Pa. As a consequence, cold air from outside is flowing in through holes in the building envelope. Besides measuring the volume flow at the fan, the technique can be combined with thermography to locate leaks. The cold airflow will lead to a temperature decrease at the corresponding parts of the window frame, wall, and so on.

In such cases, that is, when air is streaming through channels, it is well known from aerodynamics and fluid dynamics that the volume flow through pipes or tubes depends linearly on the pressure difference on both sides (Hagen–Poiseuille law). This linear dependence of the air exchange rate is easily measured as a function of pressure difference. Typically, a standard pressure difference of 50 Pa between the inside and outside of a building is chosen for localizing leaks and giving standardized air exchange rates. The corresponding method is called the *blower-door technique* (Figure 7.72) [49].

A powerful fan is attached to a metal frame that can be adjusted airtight to any door opening. The fan can be operated at variable pressure differences to the outside atmospheric pressure, which is usually measured at a distance of at least 10 m from the building. Both higher and lower pressure is possible within the building, though mostly a lower pressure of 50 Pa is used. Once all windows and doors are closed, the resulting low pressure leads to the inflow of air through holes in the building envelope. Large airflows can often be detected by the skin. Alternatively, smoke sources were used from the inside or outside to visualize the airflow directly. However, the best visualization is possible with IR thermal imaging, provided that measurements are taken while large enough temperature differences exist between outside and inside air. This means that measurements are typically performed in winter (see Section 7.1.3 for precautions and requirements of thermal imaging of buildings). In this case, cold air is flowing into the building, thereby cooling parts adjacent to the leaks. The problem is that leaks often occur, for example, close to window frames or parts of a wall, or roof constructions that no matter what show up in IR images as thermal bridges. Therefore, the proper way of analyzing thermal images while applying the blower-door technique is to record images with and without a pressure difference and to subtract the IR images [19]. Image subtraction is a simple image-processing technique (Chapter 3) that is commonly available in commercial camera software packages. The resulting image only shows the additional changes induced by the airflow. A few examples of blower-door thermal imaging are reported in the literature (e.g., [15, 50–53]). In what follows we will first give examples as close-up views and second as overview images to identify problem areas.

7.6.1
Close-Up Studies

Paned front doors are fancy, but often their window frames are sources of thermal bridges. Figure 7.73 shows two IR images at ambient and reduced pressure. Each image alone shows geometry-based structures but make it impossible to determine whether there are real leaks. Direct comparison of the two images seems to indicate an air leak at the door sealing, but it is not clear whether there are also leaks at the window segments of the door. The problem is solved by studying the subtracted image (Figure 7.73c), which clearly shows that there is only a sealing leak (B); the window panes are fine (A).

The cause of air infiltration at the sealing was a gap with a dimension of around 2 mm between door gasket and door frame: the gasket had to be realigned.

The next example, Figure 7.74 shows a window frame in the kitchen recorded at normal pressure (Figure 7.74a) and reduced pressure (Figure 7.74b). Both images reveal features around the frame that are more pronounced for reduced pressure, though. The visible image (Figure 7.74d) gives no hint as to these observed temperature anomalies. Figure 7.74c depicts the result of image subtraction of Figure 7.74a,b. The temperature difference scale ranges from −1 to +1 °C.

The geometrical thermal bridges of the window frame are more or less absent in the subtraction image, and the residual features reflect real air leaks. Three different features are obvious, a leaky blind box (A), an improperly sealed opening into the blind box (B), and a tiny leak (C) due to a defective gasket.

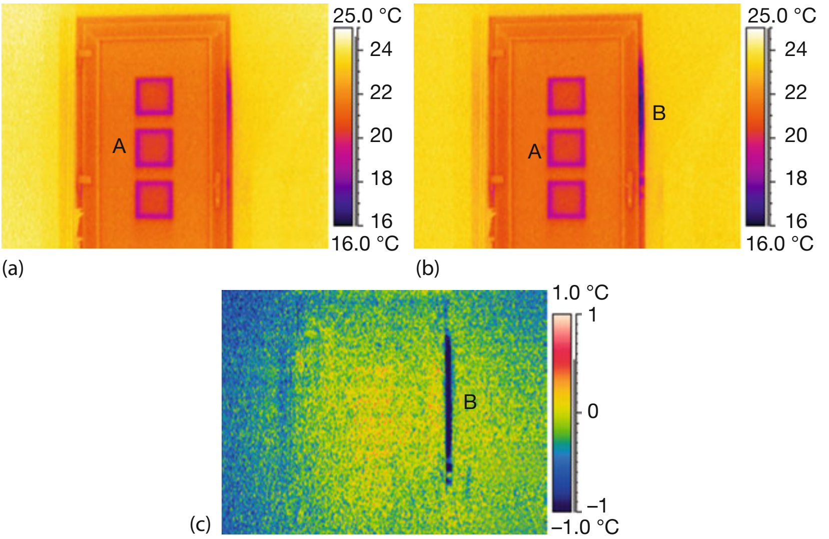

Figure 7.73 IR images of a front door of a house, recorded at normal pressure (a) and at standard inside pressure lowered by 50 Pa (b). The subtraction of the two images (c) shows that window feature A causes no problems, whereas the sealing air leak B is relevant. Stationary conditions are $T_{\text{inside}} = 23\,°\text{C}$ and $T_{\text{outside}} = 13\,°\text{C}$, MW camera 320 × 240 pixels.

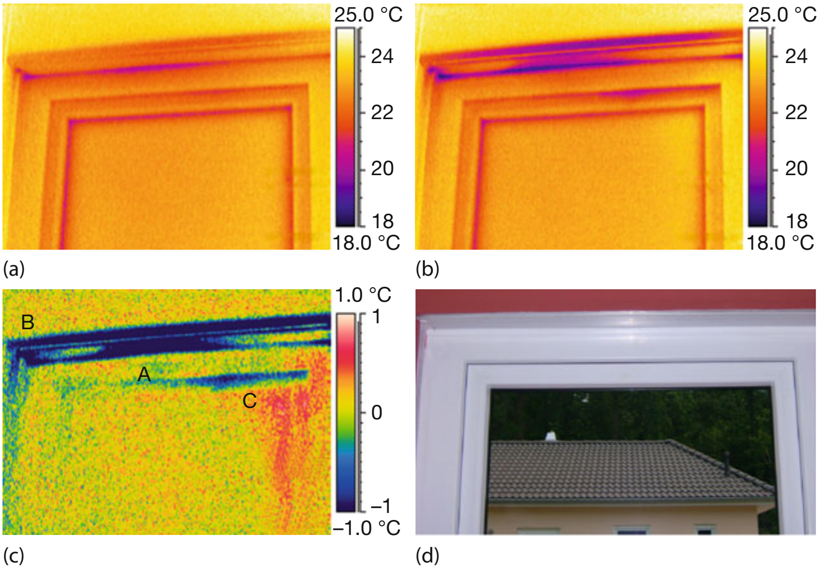

Figure 7.74 IR images of upper part of a kitchen window with blind box above recorded from inside at normal pressure (a) and at reduced pressure of –50 Pa (b). The subtraction (c) visualizes three problems: a leaky blind box (A), a badly sealed opening into the blind box (B), and defective gasket (C). These were not obvious in the visible image (d). Conditions: $T_{\text{inside}} = 23\,°\text{C}$, $T_{\text{outside}} = 13\,°\text{C}$, MW camera.

Figure 7.75 shows a typical feature/problem of blower-door image analysis for another window. It depicts again IR images at normal (Figure 7.75a) and reduced pressure (Figure 7.75b). At reduced pressure (Figure 7.75b) an air leak (A) due to a defective seal tape between brick wall and wooden material is obvious. Of course, it also shows up in the image subtraction (Figure 7.75c) but not in the visible image (Figure 7.75d). The subtraction image offers higher sensitivity and also detects the smaller air leak B due to a defective gasket. However, Figure 7.75c also reveals a problem that is commonly encountered when using image subtraction with the blower-door technique: surprisingly the subtracted image shows not only air leaks but also, and perhaps unexpectedly, the plant leaves. The solution to this puzzle is quite easy and of practical origin: during a blower-door analysis, one first records IR images at normal pressure and then turns on the fan. After waiting for equilibrium to establish, one starts the IR analysis for reduced pressure. This means that there is always a time difference between the recordings of the two images. In the present case it was about 30 min. During this period, ambient conditions change and the plant leaf temperature increases. As a result, the leaves show up as unexpected additional structures.

Artifacts of this kind can of course be minimized by reducing the time between the two images, but there will always be a residual time limit imposed by practicability.

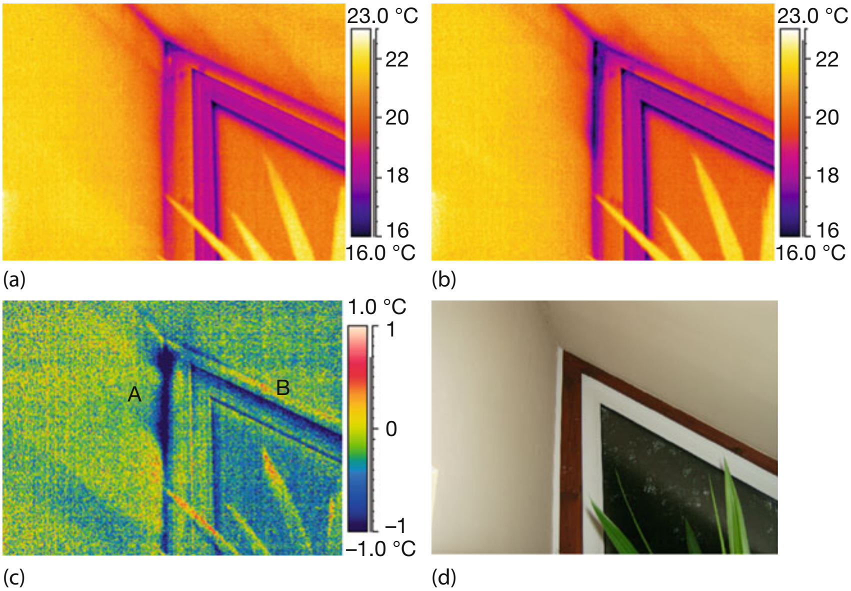

(a) (b)

(c) (d)

Figure 7.75 IR images of a window in the sun porch recorded from inside at normal pressure (a) and at reduced pressure of minus 50 Pa (b) with a recording time difference of 30 min. The subtraction (c) visualizes a defect seal tape (A), a defective gasket (B), and in particular the influence of recording time difference on the subtraction image. The visible image is shown in (d). Conditions: $T_{\text{inside}} = 22\,°\text{C}$, $T_{\text{outside}} = 1\,°\text{C}$, LW camera.

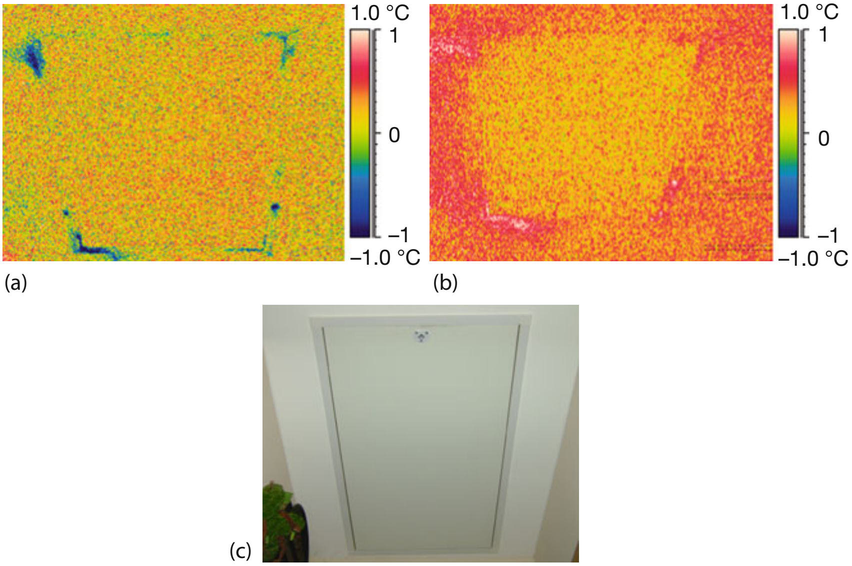

Figure 7.76 Subtraction images of trapdoor to cold roof attic (normal pressure and reduced by 50 Pa) in winter with $T_{\text{in}} = 22\,°\text{C}$ and $T_{\text{attic}} = 2\,°\text{C}$ (a) and summer with $T_{\text{in}} = 24\,°\text{C}$ and $T_{\text{attic}} = 34\,°\text{C}$ (b) as well as visible image (c). Both subtraction images (more or less from the same position) show defective gaskets (left line shapes) and leakage due to a screw connection (pointlike feature in lower right corner), however, either as cold or warm features.

A final close-up view example is shown in Figure 7.76. It depicts a trapdoor (used for inspection purposes) from the residential area of a house to the thermally insulated attic. The roof of this house was built without thermal insulation as a so-called cold roof, that is, the attic should be sealed airtight. The blower-door technique was used to check the thermal insulation and air tightness of the trapdoor. Owing to this construction, large temperature differences between the residential area and the attic are expected in summer as well as winter. Therefore, leakages may be visible due to either colder (winter) or warmer (summer) regions in the subtracted images.

Figure 7.76a shows the subtraction of two IR images at normal and reduced pressure in winter ($\Delta T = 20\,\text{K}$), and Figure 7.76b shows the same in summer ($\Delta T = 10\,\text{K}$). Both images reveal tiny air leaks due to defective gaskets (A) and a bad screw connection in the door frame.

The detected temperature differences are small, and these tiny leaks are not critical for energy loss, but in summer, the warm wet air infiltration from the residential area to the attic under normal pressure conditions may lead to mold problems.

7.6.2
Overview Studies

Figure 7.77d shows a visible image of a room in a penthouse with the pitch of the roof. The most prominent features are two skylights and the rafter at the roof edge. The IR image (Figure 7.77a) was recorded at normal pressure. The fan was then operated to reduce the inside pressure, and the image in Figure 7.77b was recorded at a pressure difference of 50 Pa to atmospheric pressure. Obvious differences are present. However, as mentioned earlier, all window frames already have typical edge structures due to thermal bridges. To find the effects solely due to the airflow, one needs to subtract the two images, as shown in Figure 7.77c.

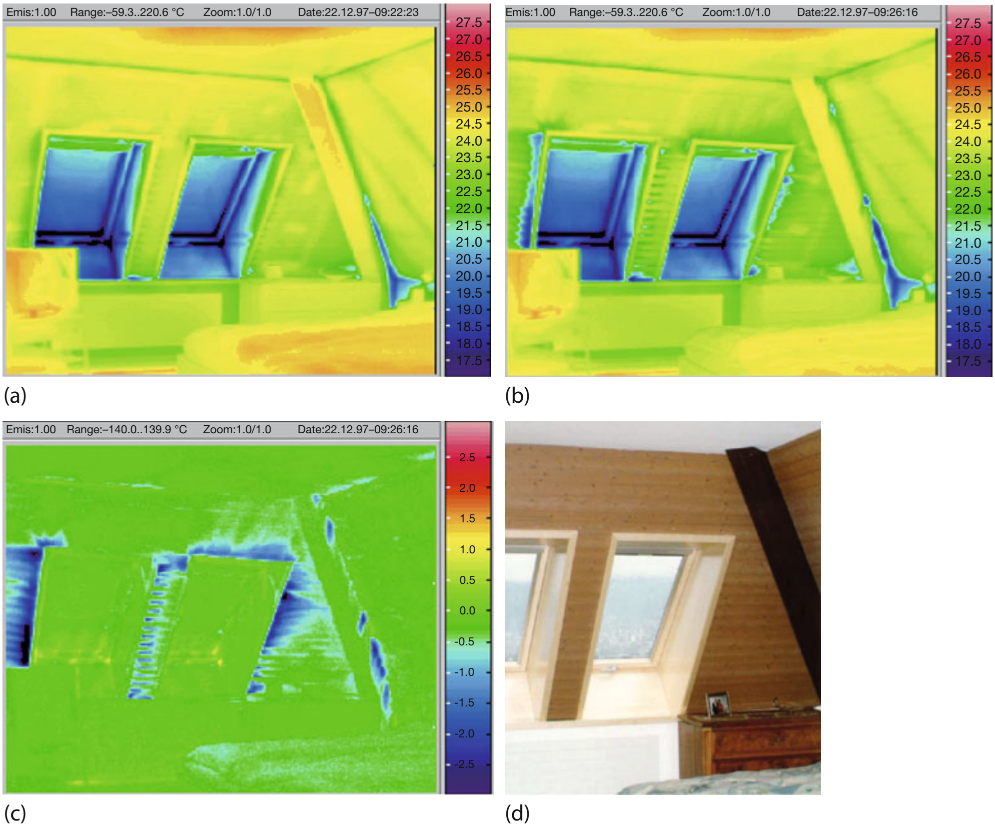
Emis:1.00 Range:–59.3..220.6 °C Zoom:1.0/1.0 Date:22.12.97–09:22:23
27.5
27.0
26.5
26.0
25.5
25.0
24.5
24.0
23.5
23.0
22.5
22.0
21.5
21.0
20.5
20.0
19.5
19.0
18.5
18.0
17.5
(a)
Emis:1.00 Range:–59.3..220.6 °C Zoom:1.0/1.0 Date:22.12.97–09:26:16
(b)
Emis:1.00 Range:–140.0..139.9 °C Zoom:1.0/1.0 Date:22.12.97–09:26:16
2.5
2.0
1.5
1.0
0.5
0.0
-0.5
-1.0
-1.5
-2.0
-2.5
(c)
(d)

Figure 7.77 Visible (d) and thermal images (a,b) of a room in a penthouse with roof pitch. Images were recorded at normal pressure (a) and at an inside pressure lowered by 50 Pa (b). The lower IR image (c) results from subtraction of the two upper images. Thermal images were recorded with a LW NEC TH 3101 camera (256 × 207 pixels, HgCdTe detector). Images courtesy Christoph Tanner, QC-Expert AG.

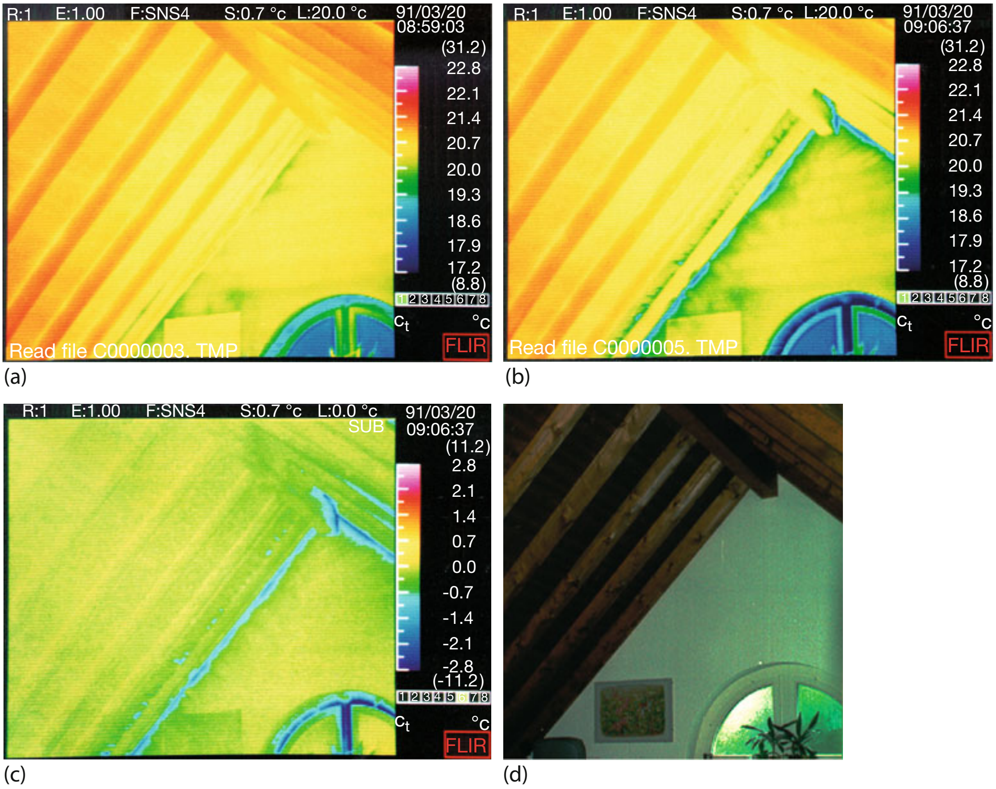

Figure 7.78 Visible (d) and thermal images (a, b) of roof section of upper floor of house. Images were recorded at normal pressure (a) and at an inside pressure lowered by 50 Pa (b). The lower IR image (c) results from subtraction of two upper images. Thermal images were recorded with FLIR 6200 camera. Images courtesy Christoph Tanner, QC-Expert AG.

The air leaks become visible instantaneously: they are most pronounced at the left edge of the left window and the right edge of the right window and partially also at the lower part of the rafter.

Another set of IR images of the roof area of the upper floor of a house is shown in Figure 7.78. The most prominent features in these images are the rafters, the ridge at the rooftop, and the upper part of a round arc window. Similar to Figure 7.77, Figure 7.78a was recorded at normal pressure and Figure 7.78b at a reduced pressure of 50 Pa below atmospheric pressure. The subtracted image (Figure 7.78c) proves that the roof itself is fine, whereas the connection between the roof and wall has leaks all along the edge. Similarly, the ridge connection to the wall has problems related to airflow. In addition, the window frame and window middle seal show air leaks.

All of these examples clearly demonstrate the usefulness of the blower-door technique when combined with thermal imaging: only the areas with air leaks are visualized.

7.7
Quantitative IR Imaging: Total Heat Transfer through Building Envelope

So far, thermography has mostly been used in building diagnostics to qualitatively locate thermal bridges and interpret them in terms of air leakages, geometrical effects, missing insulation, design flaws, moisture problems, and so on. It is then more or less a matter of experience to directly judge the importance of any detected thermal signatures with respect to their being energy relevant or even relevant concerning building damage. In many cases, quantitative analysis means at most that the measured surface temperatures are usually compared to corresponding dew point temperatures in order to judge whether problems might arise with mold or condensation. Of course, this difficulty in direct quantitative analysis is due to the possibly large variety of building types, wall constructions, and so on. Obviously, it would be highly desirable to use thermography to directly and quantitatively judge the heat transfer rates through building envelopes.

As shown in Section 4.3.3, heat transfer through any composite wall may be described by a single number, the so-called U-value in Europe or its reciprocal value, the R-value ($R = 1/U$) in the United States. The U-value is given in W (m^2 K)$^{-1}$ and describes the amount of energy per second that is transmitted through a surface of 1 m^2 through a wall under steady-state conditions if the temperatures on both sides of the wall differ by 1 K. Hence, the overall heat transfer rate (in W) through a wall of area A and a temperature difference ΔT is given by

$$\frac{\mathrm{d}Q}{\mathrm{d}t} = U \cdot A \cdot \Delta T = \left(\frac{1}{R}\right) \cdot A \cdot \Delta T \tag{7.10}$$

Note that the R-value is often not given in SI units, m^2 K W^{-1}, but in the old (and internationally totally uncommon) units, ft^2 F/(BTU/h). In the following sections we will use $1/U$ when referring to the R-value because the thermal resistances are also usually abbreviated by the symbol R.

These values (U or $1/U$) are easily calculated from the respective heat conductivities of the building materials assuming a standard convection coefficient for the outside wall (Section 4.3.3). Therefore, architects must promise that new buildings will at least satisfy the requirements for U-values given by the corresponding national regulations. However, until recently, it was very difficult to directly measure these values. The situation changed when Madding proposed a simple method based on IR thermal imaging to directly evaluate the R-values for exterior wall segments [54]. Meanwhile, other similar studies have been reported (e.g., [55, 56]). The good news is that this method has been tested for a few standard wall constructions and so far seems to be successful and reliable. The drawback is that a user cannot just hit a button on the camera and get the results; rather, some background knowledge is needed for a correct measurement and analysis. In what follows, the idea behind the method is briefly described.

According to the definition given by Eq. (7.10) (see also Figure 4.9), the R-value can be written

$$\frac{1}{U} = \frac{A \cdot \Delta T_{\text{inside–outside}}}{\dot{Q}} \tag{7.11}$$

Therefore, we need to know the area A of a wall, the temperature difference $\Delta T_{\text{in–out}}$ between inside and outside air (easy to measure), and the total heat transfer rate $\mathrm{d}Q/\,\mathrm{d}t$ through the wall. The latter is the same, however, anywhere within the wall since the energy that flows from inside to outside must pass through all components of the wall, which is in steady state. Therefore (Eq. (4.9)),

$$\dot{Q} = \frac{\Delta T_i}{R_i} = \frac{T_{\text{inside,air}} - T_{\text{outside,air}}}{R_{\text{total}}} \tag{7.12}$$

where ΔT_i and R_i denote any selected temperature drop owing to the corresponding thermal resistance (Section 4.3.3) and R_{total} the total thermal resistance across the wall. Obviously, one just needs to know the thermal resistances to calculate the heat transfer from temperature measurements alone. Madding proposed the use of the thermal resistance between the inside room temperature and the inside wall surface temperature to calculate the heat flow. The argument can be summarized as follows.

The heat transfer between the inside wall surface and the surroundings inside the room is due to radiation and convection. Both contributions are theoretically well known. The heat transfer rate due to radiation is given by

$$\dot{Q}_{\text{rad}} = \varepsilon \cdot \sigma \cdot A \cdot \left(T^4_{\text{inside,wall}} - T^4_{\text{inside,surr}} \right) \tag{7.13}$$

where $T_{\text{inside,surr}}$ is the temperature of the inner surfaces of the room. It is assumed that these inner surfaces act as a large thermal reservoir (no change in temperature) and thus serve as the reference temperature. In thermography, this temperature is also known as the *apparent reflected temperature.* As shown in Chapter 4, Eq. (7.13) can be linearized for small temperature differences to give

$$\dot{Q}_{\text{rad}} = 4\varepsilon \cdot \sigma \cdot A \cdot T^3_{\text{mean}} \cdot (T_{\text{inside,wall}} - T_{\text{inside,surr}}) \tag{7.14}$$

where T_{mean} is the average temperature $(1/2) \cdot (T_{\text{inside,wall}} + T_{\text{inside,surr}})$.

The heat transfer rate between the inside wall surface and the air inside the room due to convection is given by

$$\dot{Q}_{\text{conv}} = \alpha_{\text{conv}} \cdot A \cdot (T_{\text{inside,air}} - T_{\text{inside,wall}}) \tag{7.15}$$

where α_{conv} is the convective heat transfer coefficient.

Combining Eqs. (7.11), (7.14), and (7.15), one finally arrives at

$$\frac{1}{U} = \frac{T_{\text{inside,air}} - T_{\text{outside,air}}}{4\varepsilon \cdot \sigma \cdot T^3_{\text{mean}} \cdot (T_{\text{inside,wall}} - T_{\text{inside,surr}}) + \alpha_{\text{conv}} \cdot (T_{\text{inside,air}} - T_{\text{inside,wall}})} \tag{7.16}$$

Equation 7.16 is the basis for determining the R-value $R = 1/U$ of a wall; it would be even more straightforward to use the nonlinear relation Eq. (7.13) rather than Eq. (7.14). One needs to know combinations of the following quantities:

ε	emissivity of wall
σ	Stefan–Boltzmann constant $5.67 \cdot 10^{-8}\,\mathrm{W\,(m^2\,K^4)^{-1}}$
α_{conv}	convective heat transfer coefficient
$T_{\mathrm{inside,air}}$	inside bulk air temperature (distance from wall large enough such that $T = const$)
$T_{\mathrm{outside,air}}$	outside bulk air temperature
$T_{\mathrm{inside,wall}}$	inside wall surface temperature
$T_{\mathrm{inside,surr}}$	reflected apparent temperature, that is, temperature of inner surfaces of room
T_{mean}	average temperature $(1/2) \cdot (T_{\mathrm{inside,wall}} + T_{\mathrm{inside,surr}})$

Three temperature differences and one mean temperature value need to be measured with thermography. Bulk air temperatures can be measured by placing a piece of cardboard at a safe distance (e.g., 0.5 m) from the walls, wait until thermal equilibrium is established, and then measure the surface temperature of the cardboard. The inside wall temperature is directly measured with the camera. One may use a trick to measure the reflected apparent temperature by crumbling a piece of aluminum foil in an area large enough to be spatially resolved by the IR camera. This piece can be attached to the cardboard (at a safe distance from the wall) used for measuring the inside air temperature. The foil has very low emissivity and is strongly reflecting (however, it is diffuse due to the crumbling). Therefore, the measured temperature from the foil directly yields the temperatures of the inner walls. By measuring ΔT values for interior wall surface to interior bulk air and to the reflected apparent temperature in a single IR image, one reduces measurement uncertainty significantly. Using the same IR camera to measure the bulk outdoor air temperature has a similar advantage.

Besides the temperatures and the emissivity, one needs to know α_{conv}. This is probably the most critical input parameter since such coefficients depend on the airflow conditions (laminar vs. turbulent) and the actual temperature difference between wall surface and the air. Fortunately, one may safely assume laminar flow; nevertheless, different formulas are known. Typical values of α_{conv} for inside walls are on the order of 2–$8\,\mathrm{W\,(m^2\,K)^{-1}}$.

Further, steady-state or near-steady-state conditions are crucial, that is, the inside to outside temperature difference should be stable, and the outside walls should not suffer solar or wind loading. In addition, the inside walls must be free of pictures and other objects, avoiding any additional thermal insulation. The temperature differences between inside air and inside wall, as well as inside wall to inside surroundings, can be very small (e.g., 0.3 K for good insulation and up to 6 K for bad insulation). To test for good insulation, the IR camera should therefore have a low NETD of less than 50 mK. Cameras with much larger NETDs are not suitable.

Madding successfully measured the R-values of stud frame constructed houses including laboratory models [54] and structural insulated panel as well as insulated concrete form wall constructions [55]. He showed good agreement with measurement deviations amounting to less than 5% and less than 12% compared to values calculated by summing the R-values of materials used in construction. The latter differences are also influenced by uncertainties in stated material R-values compared to actual as-built conditions. The biggest problem in experimentally estimating U-values is studying the measurement under only near-steady-state conditions because external ambient conditions can vary significantly over time.

7.8
New Developments and Conclusions

As one of the most popular applications of thermal imaging, building diagnostics is a well-developed field. Nevertheless, some recent developments have potential new applications in the field.

These include active thermography applications, for example, lock-in or pulse thermography with artificial [57] or natural [37] light sources to study cultural heritage buildings. Another new approach is called *time lapse thermography* and uses time lapse sequences of IR images of up to several days (similar periods were observed in studies of lock-in thermography with solar load [37]) with, for example, 30 min intervals between images to detect defects in building construction [58]. In a differently motivated study, thermography was used to study the more subjective comfort conditions in office-type environments [59].

Finally, we want to discuss a bit more extensively an interesting development regarding the energy efficiency of buildings and the prevention of surface damage. The walls of private homes and office buildings are often covered with colorful paints. In the past, these paints were chosen mostly for aesthetic reasons. Unfortunately, many dark colors often absorb a lot of solar radiation and heat up effectively, meaning there is a strong thermal input into building walls in summertime. On the one hand, this may lead to increased cooling needs for the building interior; on the other hand, high surface temperatures can damage plaster, by forming cracks, or insulation materials below. Part of the problem can be solved by creating selectively absorbing and reflecting paints in the VIS and NIR region of the solar spectrum. Selective absorbers are well known in the field of solar collectors, and it was just a matter of time until paint producers also offered corresponding selective paints for the building industry with high-NIR reflection to reduce the thermal load. Several groups working on this topic have independently carried out relevant studies [60–63].

The industry calls the corresponding selectively absorbing/scattering paints total solar reflectance (TSR) paints. As stated by one manufacturer (e.g., [64]), they should primarily reduce the solar load and thus prevent the plaster from heating up above 70 °C, which could cause damage in the form of cracks or the deformation of lower insulation materials.

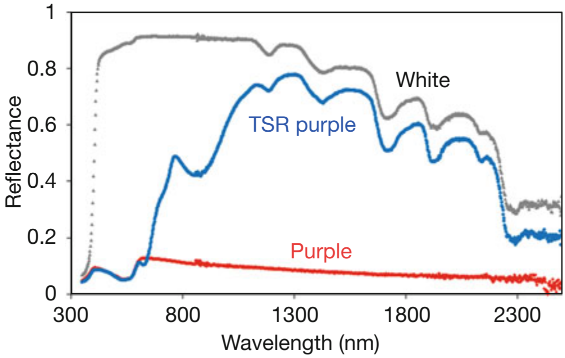

Figure 7.79 Reflection spectra of various paints on plaster. Although the two pink paints look similar in the VIS range, they behave quite different in the NIR.

Figure 7.79 depicts reflection spectra for three wall paint samples in the spectral range of maximum solar load from the UV to the NIR. The first sample is simple white plaster, the second a regular dark pink wall color on white plaster, and the third a visually very similar looking special pink TSR color, again on white plaster.

The white and regular pink color samples are opaque (transmission $T = 0$), i.e. absorption $A = (1 - R)$, see Eqs. (1.28a) and (1.28b). The TSR color alone can, however, have high NIR transmission and $A = (1 - R - T)$. Up to a wavelength of 650 nm, the two pink colors show more or less the same absorption, that is, visually they are perceived as the same color. In the NIR however, the TSR paint has a much higher transmission, that is, much lower absorption. The radiation penetrates the pink TSR paint and is reflected from the opaque underlying white paint layer. This results in the overall high reflectance of the TSR paint seen in Fig. 7.79, which closely resembles the one of the white paint. A wall painted with such a color should therefore not heat up appreciably.

It is obvious from the spectra that a house covered with just white plaster or white painted plaster with a spectrum as shown in Figure 7.70 would always allow for the best heat management. It would always absorb less (reflect more) than any colored regular paint and hence heat up less. Therefore, houses in hot climates should preferably use white paint. If this is not desired for aesthetic reasons, one should at least use TSR paints.

Of course, the heating also depends on wall structures. If the paint is only on a thin layer of plaster on top of low-thermal-conductivity insulating material, the heating effect will be very pronounced, whereas if it is on a material with better thermal conductivity or on a thicker layer with larger thermal mass, the effect will be smaller.

For field studies, a $0.6 \times 1.2\,\text{m}^2$ large sample of an outer wall, that is, 0.7 cm plaster on a 7.3 cm insulating material was prepared whose top surface was covered by about 0.1 mm regular paint as well as TSR paint of the same visual color. Figure 7.80a shows a VIS photo of this sample leaning against the wall of a building covered with a regular rather dark black paint.

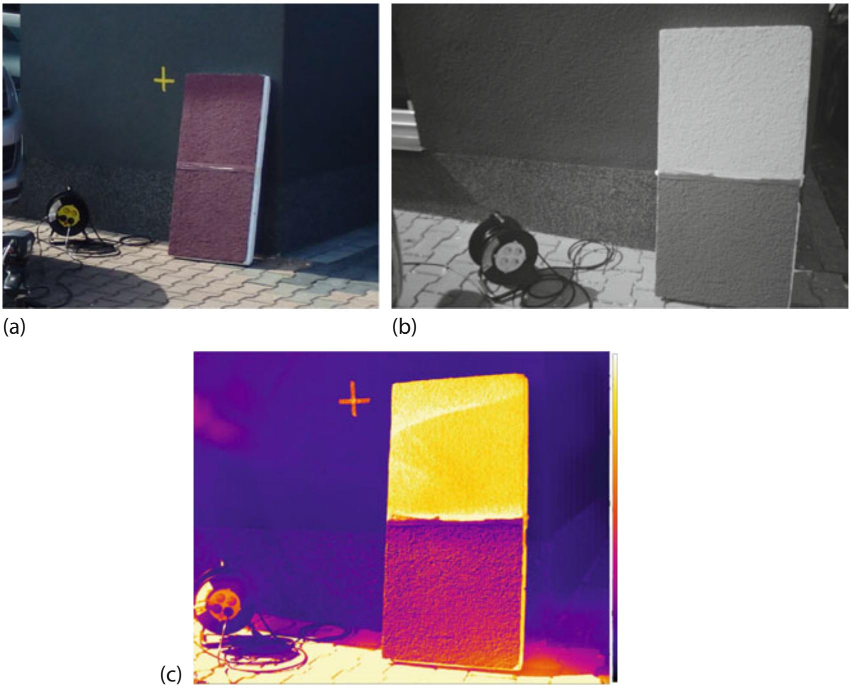

Figure 7.80 Examples of split paint probe in front of a building with regular paint. (a) VIS, (b) NIR image, and (c) SW IR image. The NIR and SW IR images show the differences in reflection.

Figure 7.80b depicts a NIR camera image of the same scene. It was recorded with a modified VIS camera acting as NIR camera detecting radiation in the range between 830 and 1100 nm (Chapter 6). Upon solar radiation it is obvious that the top part of the sample is covered by the TSR paint, which appears quite bright (strong reflection), whereas the lower regular paint is much darker. In comparison to these two samples, the painted black wall appears quite dark, which indicates that it is a regular paint that does not reflect a lot in the NIR. This also shows up in the SW IR image of a commercial camera operating from 0.9 up to 1.7 μm (Figure 7.80c).

Another example – this time of a house wall covered by a TSR paint – is shown in Figure 7.81. The VIS image Figure 7.81a shows the model leaning against the red painted house wall. Figure 7.81b depicts the SW IR image clearly again showing the strong scattering by the topmost TSR paint and much lower reflectance from the bottom regular one. In contrast, the house wall appears quite bright, that is, its paint is strongly scattering in the NIR, leading to an elevated NIR reflectance. Finally, Figure 7.81c shows a LW IR image of the same scene after the house wall has been in sunshine for several hours and the model for at least 30 min (which is sufficient to reach thermal equilibrium as was tested in the lab). As expected, the TSR paint of the model as well as of the house wall has led to lower solar

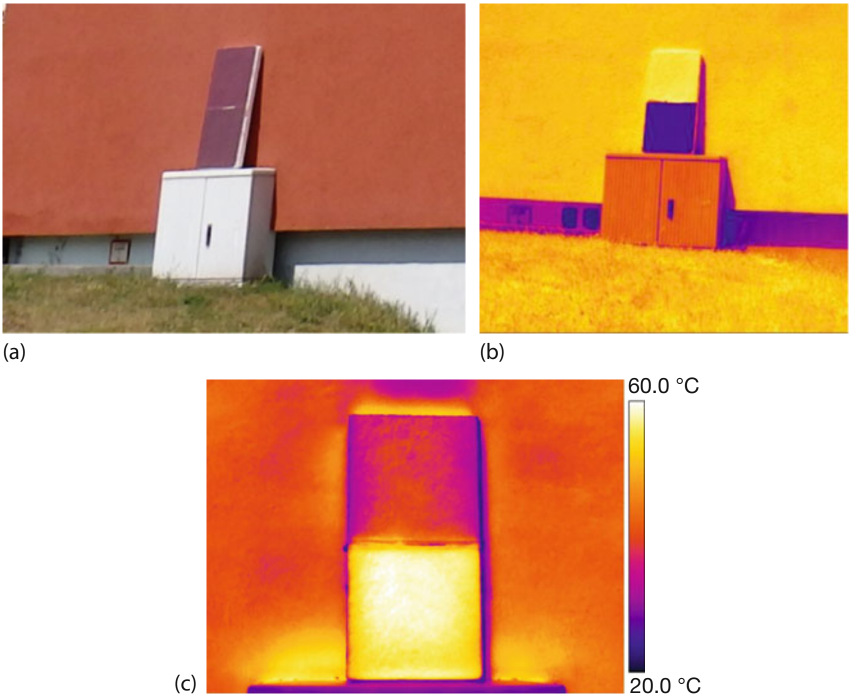

Figure 7.81 Examples of split paint probe in front of a building with a TSR paint. (a) VIS, (b) NIR image, and (c) LW IR image. The NIR shows the differences in reflection that manifest themselves in a lower temperature of the wall similar to the TSR-painted model wall segment.

absorption, so they are cooler than the regular paint model. It can be expected that more studies along these lines will be done in the near future.

In conclusion, building thermography is probably the most popular field in IR thermal imaging; however, it is not the easiest with regard to quantitative analysis, and it is often even difficult to extract useful qualitative information. As discussed earlier, several external factors are important such as wind, solar load, shadows, moisture, view factors, and night sky radiant cooling. If outdoor thermography is needed, the following are the best rules: avoid solar load, that is, measure at night; avoid transient effects due to night sky radiant cooling, that is, cloudy nights are better than clear nights; try to avoid transient effects due to large temperature fluctuations of buildings, that is, it is best to measure after a cloud-covered night that followed a cloud-covered day; and avoid rain and wind.

Knowing all the problems, we finally return to the example of Figure 7.1, discussed at the beginning of this chapter. The mentioned comment that the red color indicates where this building is losing energy is probably absurd. The large signal from the roof section can only be understood if it is a tilted roof, probably directly exposed to the sun. The solar load leads to the absorption of energy in the roof tiles, heating it up considerably. If an image is taken with a MW camera, there may also be an appreciable amount of direct solar reflections involved. Owing to differences in view factor, the solar-load-induced warming of the walls is lower compared to the roof (vertical wall, tilted roof). This solar load wall heating also explains why the windows seem colder than the wall. Usually, owing to U-values, it should be the other way around.

The fact that the basement and first-floor windows show different temperatures is most likely due to the fact that the basement was heated but the first floor was not heated. This outdoor IR thermal image is absolutely useless, unless one wants to indicate all possible errors in one's interpretation of IR images.

References

1 Holst, G.C. (2000) *Common Sense Approach to Thermal Imaging*, SPIE Optical Engineering Press, Washington.

2 Kaplan, H. (1999) Practical applications of infrared thermal sensing and imaging equipment, in *Tutorial Texts in Optical Engineering*, 2nd edn, vol. TT34, SPIE Press, Bellingham.

3 Grinzato, E., Vavilov, V., and Kauppinen, T. (1998) Quantitative infrared thermography in buildings. *Energ. Build.*, **29** (1), 1–9.

4 Hoyano, A., Asano, K., and Kanamaru, T. (1999) Analysis of the sensible heat flux from the exterior surface of buildings using time sequential thermography. *Atmos. Environ.*, **33**, 3941–3951.

5 Balaras, C.A. and Arigiriou, A.A.S. (2002) Infrared thermography for building diagnostics. *Energ. Build.*, **34**, 171–183.

6 Kylili, A., Fokaides, P.A., Christou, P., and Kalogirou, S.A. (2014) Infrared thermography (IRT) applications for building diagnostics: A review. *Appl. Energ.*, **134** 531–549.

7 Lehmann, B., Wakili, K.G., Frank, T., Collado, B.V., and Tanner, C. (2013) Effects of individual climatic parameters on the infrared thermography of buildings. *Appl. Energ.*, **110**, 29–43.

8 Möllmann, K.-P. and Vollmer, M. (2013) The Allure of Multicolored Images – Building Thermography Examined Closely, Inframation 2013 Proceedings, vol. 14 (on DVD only).

9 Vollmer, M. and Möllmann, K.-P. (2013) The allure of multicolored images – Building thermography examined closely, in *Renewable Energy – Sustainable Concepts for the Energy Change*, (eds R. Wengenmayr and T. Bührcke), 2nd edn, Wiley VCH-Verlag GmbH.

10 Asdrubali, F., Baldinelli, G., and Bianchi, F. (2012) A quantitative methodology to evaluate thermal bridges in buildings. *Appl. Energ.*, **97** 365–373.

11 Verordnung über energiesparenden Wärmeschutz und energiesparende Anlagentechnik bei Gebäuden (Energieeinsparverordnung – EnEV), Stand Oktober 2015, http://www.bmub.bund.de/themen/bauen/energieeffizientes-bauen-und-sanieren/energieeinsparverordnung/ (accessed May 2017).

12 Feist, W. and Schnieders, J. (2009) Energy efficiency – A key to sustainable housing. *Eur. Phys. J. Spec. Top.*, **176**, 141–153.

13 http://www.resnet.us/hers-index-score-card (accessed May 2017).

14 http://energy.gov/sites/prod/files/2013/11/f5/existing_labels.pdf (accessed May 2017).

15 Fronapfel, E. and Kleinfeld, J. (2005) Analysis of HVAC system and building performance utilizing IR, physical measurements and CFD modeling. Inframation 2005, Proceedings, vol. 6, pp. 219–229.

16 Amhaus, E.G. (2004) Infrared applications for post construction radiant

heating systems. Inframation 2004, Proceedings, vol. 5, pp. 1–8.

17 Karstädt, D., Möllmann, K.P., Pinno, F., and Vollmer, M. (2005) Using infrared thermography for optimization, quality control and minimization of damages of floor heating systems. Inframation 2005, Proceedings, vol. 6, pp. 313–321.

18 Consumer information of the US Department of Energy http://www.energy.gov/eere/office-energy-efficiency-renewable-energy (accessed May 2017).

19 Tanner, C. (2000) *Die Gebäudehülle – Konstruktive, Bauphysikalische und Umweltrelevante Aspekte*, EMPA Akademie, Fraunhofer IRB Verlag, Stuttgart, p. 2437.

20 Madding, R.P. and Lyon, B.R. (2000) Wind effects on electrical hot spots – some experimental data. Thermosense XXII. Proc. SPIE, vol. 4020, 80–84.

21 Madding, R.P., Leonard, K., and Orlove, G. (2002) Important measurements that support IR surveys in substations. Inframation 2002, Proceedings, vol. 3, pp. 19–25.

22 Möllmann, K.-P., Pinno, F., and Vollmer, M. (2007) Influence of wind effects on thermal imaging results – Is the wind chill effect relevant? Inframation 2007, Proceedings, vol. 8, pp. 21–31.

23 Oscevski, R. and Bluestein, M. (2005) The new wind chill equivalent temperature. *Bull. Am. Meteorol. Soc.*, **86** (10), 1453–1458.

24 Incropera, F.P. and DeWitt, D.P. (1996) *Fundamentals of Heat and Mass Transfer*, 4th edn, John Wiley & Sons, Inc., New York.

25 www.consumerenergycenter.org/residential/heating_cooling/evaporative.html (accessed May 2017).

26 Grinzato, E. and Rosina, E. (2001) Infrared and thermal testing for conservation of historic buildings, in *Nondestructive Testing Handbook, Infrared and Thermal Testing*, vol. 3, Chapt. 18.5 (ed. P.O. Moore), 3rd edn, American Society for Nondestructive Testing, Inc., Columbus.

27 Wood, S. (2004) Non-invasive roof leak detection using infrared thermography. Inframation 2004, Proceedings, vol. 5, pp. 73–82.

28 Colantonio, A. and Wood, S. (2008) Detection of moisture within building enclosures by interior and exterior thermographic inspections. Inframation 2008, Proceedings, vol. 9, pp. 69–86.

29 Kleinfeld, J.M. (2004) IR for detection of exterior wall moisture and delamination: a case study and comparison to FEA predictions. Inframation 2004, Proceedings, vol. 5, pp. 45–57.

30 Royo, R. (2007) Looking for moisture: inspection of a tourist village at the south of Spain. Inframation 2007, Proceedings, vol. 8, pp. 39–49.

31 Pinno, F., Möllmann, K.-P., and Vollmer, M. (2013) Moisture detection at building walls using evaporative cooling, Inframation 2013 Proceedings, vol. 14 (on DVD only).

32 Ludwig, N., Redaelli, V., Rosina, E., and Augelli, F. (2004) Moisture detection in wood and plaster by IR thermography. *Infrared Phys. Technol.*, **46** 161–166.

33 Vollmer, M., Möllmann, K.-P., and Wood, S. (2012) Surprising warm edges associated with moisture on surfaces, Inframation 2012, Proceedings, vol. 13.

34 Internet source for download: www.holznagels.de/DYNATHERM/download/index.html DynaTherm2000.zip, (accessed May 2017).

35 Vollmer, M. (2009) Newton's law of cooling revisited. *Eur. J. Phys.*, **30**, 1063–1084.

36 Pinno, F., Möllmann, K.-P., and Vollmer, M. (2009) Solar load and reflection effects and respective time constants in outdoor building inspections. Inframation 2009, Proceedings, vol. 10, pp. 319–330.

37 Bortolin, A., Cadelano, G., Ferrarini, G., Bison, P., Peron, F., and Maldague, X. (2013) High-resolution survey of buildings by lock-in IR thermography, Proc. SPIE, vol. 8705, Thermosense: Thermal Infrared Applications XXXV, 870503.

38 Henke, S., Karstädt, D., Möllmann, K.P., Pixnno, F., and Vollmer, M. (2004) Identification and suppression of thermal reflections in infrared thermal imaging. Inframation Proceedings, vol. 5, pp. 287–298.

39 Möllmann, K.-P., Pinno, F., and Vollmer, M. (2008) Night sky radiant cooling – influence on outdoor thermal imaging analysis. Inframation 2008, Proceedings, vol. 9, pp. 279–295.

40 Martin, M. and Berdahl, P. (1984) Characteristics of infrared sky radiation in the United States. *Solar Energ.*, **33**, 321–336.

41 Shaw, J.A. and Nugent, P.W. (2013) Physics principles in radiometric infrared imaging of clouds in the atmosphere. *Eur. J. Phys.*, **34**, 111–121.

42 Moyer, N. (2008) Using thermography in the evaluation of the NightCool nocturnal radiation cooling concept. Inframation 2008, Proceedings, vol. 9, pp. 309–319.

43 Vollmer, M., Möllmann, K.-P., and Pinno, F. (2008) Cheese cubes, light bulbs, soft drinks: An unusual approach to study convection, radiation and size dependent heating and cooling. Inframation 2008, Proceedings, vol. 9, pp. 477–492.

44 Pinno, F., Möllmann, K.-P., and Vollmer, M. (2008) Thermography of window panes – problems, possibilities and troubleshooting. Inframation 2008, Proceedings, vol. 9, pp. 355–362.

45 Vollmer, M., Möllmann, K.-P., and Schlichting, H.J. (2014) Double pane windows – elastic deformations, gas thermodynamics, thermal and optical phenomena. *Eur. J. Phys.*, **35**, 045023.

46 Möllmann, K.-P., Vollmer, M., and Winburn, M. (2011) Optics of glass fronts of buildings: the science of skyscraper “death rays”, Inframation 2011, Proceedings, vol. 12, pp. 79–92.

47 Vollmer, M. and Möllmann, K.-P. (2012) Caustic effects due to sun light reflections from skyscrapers: simulations and experiments. *Eur. J. Phys.*, **33,** 1429–1455.

48 Möllmann, K.-P. and Vollmer, M. (2012) Thermal effects due to focused light from glass fronts, Inframation 2012, Proceedings, vol. 13.

49 http://energyconservatory.com/applications/ (accessed May 2017)

50 Streinbronn, L. (2006) Building air barrier testing and verification using infrared thermography and blower doors as part of the building commissioning process. Inframation 2006, Proceedings, vol. 7, pp. 129–144.

51 Amhaus, E.G. and Fronapfel, E.L. (2005) Infrared imaging and log construction thermal performance. Inframation 2005, Proceedings, vol. 6, pp. 285–292.

52 Coloantonio, A. and Desroches, G. (2005) Thermal patterns due to moisture accumulation within exterior walls. Inframation 2005, Proceedings, vol. 6, pp. 249–260.

53 Pinno, F., Vollmer, M., and Möllmann, K.-P. (2010) Improved sensitivity for blower door thermography using image subtraction, Inframation 2010, Proceedings, vol. 11, pp. 29–40.

54 Madding, R. (2008) Finding *R*-values of stud frame constructed houses with IR thermography. Inframation 2008, Proceedings, vol. 9, pp. 261–277.

55 Madding, R. (2009) Finding *R*-values of SIP and ICF wall construction with IR thermography. Inframation 2009, Proceedings, vol. 10, pp. 37–47.

56 Fokaides, P.A. and Kalogirou, S.A. (2011) Application of infrared thermography for the determination of the overall heat transfer coefficient (U-value) in building envelopes. *Appl. Energ.*, **88** 4358–4365.

57 Maierhofer, C., Röllig, M., and Krankenhagen, R. (2010) Integration of active thermography into the assessment of cultural heritage buildings. *J. Mod. Opt.*, **57** (18), 1790–1802.

58 Fox, M., Coley, D., Goodhew, S., and De Wilde, P. (2015) Time-lapse thermography for building defect detection. *Energ. Build.*, **92**, 95–106.

59 Revel, G.M., Sabbatini, E., and Arnesano, M. (2012) Development and experimental evaluation of a thermography measurement system for real-time monitoring of comfort and heat rate exchange in the built environment. *Meas. Sci. Technol.*, **23**, 035005 (12pp).

60 Pinno, F., Möllmann, K.-P., and Vollmer, M. (2012) Dark colors of building walls – thermal problems due to

solar load, Inframation 2012, Proceedings, vol. 13.

61 Coser, E., Moritz, V.F., Krenzinger, A., and Ferreira, C.A. (2015) Development of paints with infrared radiation reflective properties. *Polímeros*, **25** (3), 305–310.

62 Cozza, E.S., Alloisio, M., Comite, A., Di Tanna, G., and Vicini, S. (2015) NIR-reflecting properties of new paints for energy-efficient buildings. *Solar Energ.*, **116**, 108–116.

63 Pinno, F., Karstädt, D., Möllmann, K.-P., and Vollmer, M. (2016) Beating the summer heat: thermal building insulation with TSR – colors, Presentation at Inframation.

64 http://www.brillux.com/applications-and-solutions/thermal-insulation/daemmsysteme/facade-insulation/dunkle-fassaden/?L=1. (accessed May 2017)

Chapter 8
Industrial Application: Detection of Gases

8.1
Introduction

In most applications of infrared (IR) thermal imaging, the IR radiation from objects to be studied passes through gases before reaching the camera detector. The most common gas is air, and therefore IR absorption features of atmospheric air are important for any quantitative analysis using thermography (Section 1.5.2). The most prominent spectral absorption features in the range of commercial IR cameras are due to water vapor and carbon dioxide (Figure 1.45), and therefore relative humidity and object distance are needed as input parameters to correct for transmission losses between the object and the camera.

In this chapter, we want to focus in more detail on the influence of gaseous species on IR imaging. After a short introduction to spectral features of gases in general, we focus on absorption, emission, and scattering of radiation by molecular gases due to rotational–vibrational excitations in the thermal IR spectral range. These lead to changes in detected IR radiation from objects passing through gases. Although a quantitative description is difficult, qualitative and semiquantitative applications are possible, which has led to the development of commercial qualitative gas-detecting cameras. Nowadays, thermography is an established commercial technique for detecting leaks of volatile organic compounds (VOCs), refrigerants, sulfur hexafluoride, ammonia, carbon monoxide, and, recently, carbon dioxide. The corresponding industrial topics are known as optical gas imaging (OGI) and leak detection and repair (LDAR). The influence of atmospheric absorption and scattering on the range of IR cameras is a related topic that is discussed in the context of surveillance systems (Section 10.9).

8.2
Spectra of Molecular Gases

One of the most prominent manifestations of atomic physics in optics is the observation of absorption or emission of radiation. In the visible spectral range, an illustrative example is shown in Figure 8.1a depicting the Fraunhofer lines in the solar

Infrared Thermal Imaging, Second Edition. M. Vollmer and K.-P. Möllmann.
© 2018 WILEY-VCH Verlag GmbH & Co. KGaA. Published 2018 by WILEY-VCH Verlag GmbH & Co. KGaA.

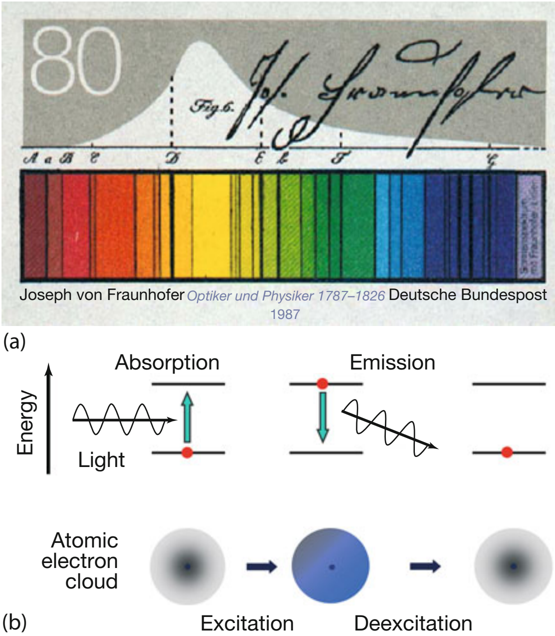

Figure 8.1 German stamp illustrating famous Fraunhofer absorption lines in spectrum of sun due to electronic excitations in atoms (a) and scheme of electronic excitation and deexcitation in atoms (b).

spectrum. They are a result of absorption of solar radiation in the outer atmosphere of the sun owing to the presence of colder elemental gases. In atomic theory, a ladder of possible energy levels of atoms can be computed. Absorption (excitation) or emission (deexcitation) of light corresponds to electronic transitions between two of these levels. While changing the energy level, the electron charge distribution around the atomic nucleus changes, too, as shown in Figure 8.1b.

Most electronic excitations of atoms and of molecules are in the ultraviolet or visible spectral range. Therefore, electronic excitations are only of minor importance when considering the influence of gaseous species in the thermal IR with wavelengths ranging from 1 to 14 μm. This spectral range is, however, the region of spectroscopic fingerprints of thousands of molecules owing to vibrational and rotational excitations.

The easiest molecules are diatomic. Molecules composed of two atoms of a kind (e.g., N_2, O_2) are called *homonuclear molecules*, whereas those composed of different atoms are heteronuclear molecules (e.g., NO, CO, HCl). In addition to electronic excitations, molecules can exhibit vibrations and rotational excitations. Figure 8.2 shows a schematic view of the vibration and rotations of a diatomic molecule. In a semiclassical description, the two atoms of the molecule can be considered to be connected by a spring (Figure 8.2a) whose spring constant determines the oscillation frequency (in introductory mechanics, the oscillation of a mass m attached by a spring (spring constant K) to some fixed mount is given

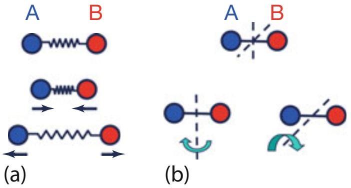

Figure 8.2 Vibration (a) and rotations (b) of a diatomic molecule.

by $\omega = (K/m)^{1/2}$). In addition, the molecule may rotate around the two axes, perpendicular to the chemical bond. From quantum mechanics, it is known that with each of these possible movements – vibration as well as rotation – energy levels are associated similar to those of the electronic excitations from Figure 8.1b, but with much lower energy separation. In particular, the vibrational frequencies of many molecules lie in the thermal IR spectral range and are important for IR imaging.

Whether vibrations of molecules can lead to absorption of IR radiation depends on so-called selection rules. The most important rule is that the electric dipole moment of a molecule must change during a vibrational excitation if IR radiation is to be absorbed. An electric dipole consists of two opposite charges separated by a distance d. Each heteronuclear diatomic molecule resembles such an electric dipole, since different atoms have different abilities to attract the electron cloud around the nucleus. For example, in a HCl molecule, the electron charge from the hydrogen atom is more strongly attracted by the chlorine atom, which means that, overall, the chlorine end of the molecule has more negative charge and the hydrogen end more positive charge. In this case, the molecule has an electric dipole moment defined by the charge times the bond length. If the bond length of this molecule increases and decreases periodically during a vibration, the dipole moment also changes periodically, that is, heteronuclear diatomic molecules may absorb IR radiation.

In contrast, homonuclear diatomic molecules like N_2 and O_2 do not have a dipole moment initially, and hence there can be no change in dipole moment during a vibration of the molecule. Therefore, such gases are not able to directly absorb thermal IR radiation. This is, of course, very good for life on earth: if the main constituents, oxygen and nitrogen, absorbed IR radiation, the earth's atmosphere would resemble a gigantic greenhouse, which, like the greenhouse planet Venus (atmosphere with 96.5% of the greenhouse gas CO_2), would have temperatures well above the boiling point of water, making human life impossible.

The next simple kind of molecule is triatomic molecules. They present a new possibility: the molecules can be either linear or nonlinear. As an example, consider H_2O and CO_2 molecules, which act as greenhouse gases in the atmosphere. Figure 8.3 schematically depicts the fundamental vibrational modes possible for these triatomic linear (CO_2) and nonlinear (H_2O) molecules (after [1]). Besides vibrations, each molecule can also have two (CO_2) or three (H_2O) modes of rotational motion, as indicated by the axes (broken lines) in Figure 8.3.

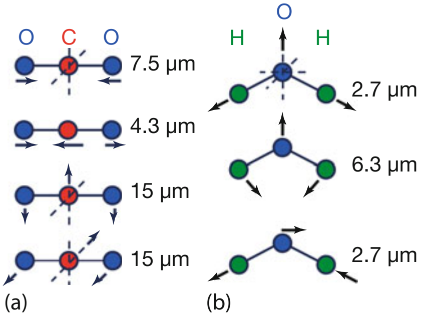

Figure 8.3 Examples of vibrational modes of linear (CO_2) and nonlinear (H_2O) triatomic molecules. Oscillation frequencies are often given as a so-called wavenumber in cm^{-1}. To find the wavelength in micrometers, divide 10 000 by the wavenumber in cm^{-1}. Example: $10\,000/2349\,\text{cm}^{-1} = 4.26\,\mu\text{m}$.

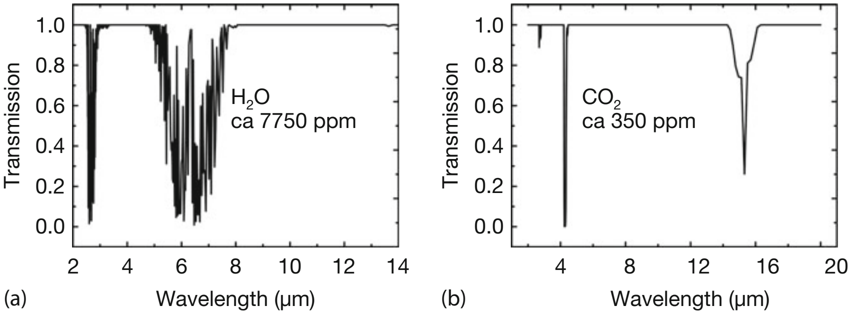

Figure 8.4 Survey spectra of H_2O vapor (a) and (b) CO_2 vapor over a path length of 10 cm as a function of wavelength. The features reflect the IR active vibrational modes of Figure 8.3. If CO_2 spectra are recorded at a higher resolution, each absorption feature is further split into a multitude of individual absorption lines (Figure 8.10).

Applying the dipole moment rule to the four vibrational modes of CO_2, it is obvious that the mode for $\lambda = 7.5\,\mu\text{m}$ cannot be excited by the absorption of IR radiation since CO_2 is a symmetric molecule that does not have a dipole moment at rest (small negative charges at the ends, small positive charge at center ⇒ two dipoles cancel each other). Therefore, a breathing-type oscillation (top vibration in Figure 8.3a) cannot change the dipole moment. In contrast, modes where the oxygen and carbon atoms move out of the linear geometry lead to a finite dipole moment, and so these modes can absorb IR radiation. Water molecules, on the other hand, can absorb IR radiation with all three possible fundamental oscillation modes. Figure 8.4 depicts the corresponding IR absorption spectra of water and carbon dioxide molecules. The spectra reveal quite complex shapes, since, in reality, vibrations are coupled to rotational excitations, and therefore one usually speaks of rotational–vibrational bands.

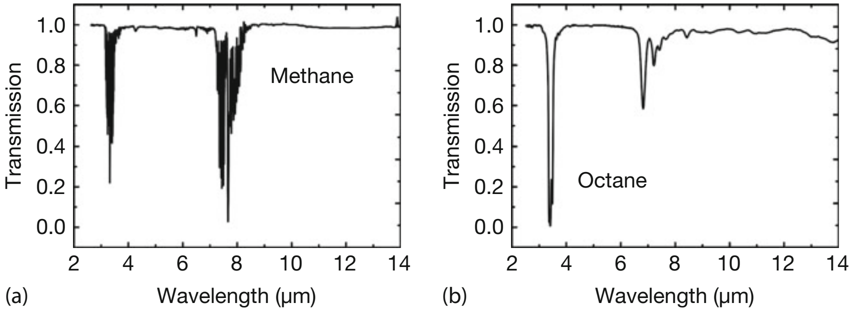

Figure 8.5 Survey spectra of methane (CH_4, high resolution) (a), (author's own FTIR measurements) and octane (C_8H_{18}, low resolution) (b), after NIST (National Institute of Standards) data, as a function of wavelength between 2 and 10 μm (these and other spectra only indicate the resonance positions; for quantitative information about concentrations, see, for example, [2]).

Obviously, the situation for triatomic molecules is more complex than the one for diatomic molecules. Molecules with four atoms exhibit another possibility: geometrically they can be linear (C_2H_2), planar (SO_3), or even three-dimensional in shape (NH_3). If more atoms are added, the molecule usually has a three-dimensional shape. For example, methane (CH_4) has a tetrahedral shape with the C atom being in the center and the hydrogen atoms at the four corners.

In general, a molecule composed of N atoms has $3N$ different ways to store energy (also called *degrees of freedom*). Three ways are the kinetic energies in the three directions of space. Then molecules can rotate around two axes for linear molecules (Figure 8.3) or around three axes for nonlinear molecules, giving two or three additional ways to store energy (the rotation around the bond axis of linear molecules is forbidden according to the quantum mechanical treatment; in the semiclassical description, the necessary excitation energies would be way too large). This finally gives either $3N$-5 (linear) or $3N$-6 (nonlinear) different ways to store energy in vibrations, respectively. For example, triatomic molecules ($N = 3$) can have four vibrational modes like CO_2 or three vibrational modes like H_2O. A molecule like methane with $N = 5$ atoms will therefore, in principle, have nine different vibrational modes and larger molecules will have even more.

Fortunately, the respective IR spectra are, however, still very simple (e.g., methane and octane spectra in Figure 8.5). Although methane should have 9 different vibrational modes and octane even 72 different modes, the spectra look astonishingly simple and – since both belong to the same group of simple hydrocarbons with single bonds – even similar.

The spectrum for methane may be understood in the following way: as a tetrahedron, methane is a very symmetric molecule, so some of the modes that resemble so-called breathing modes cannot be excited (no change in dipole moment). In addition, the symmetry forces some of the allowed modes for IR excitation to lie very close to each other and some of them may be suppressed by other quantum mechanical selection rules.

Obviously, the larger the number of atoms in a molecule, the larger the number of possible vibrational modes. But why does the octane spectrum from a molecule with 26 atoms look so simple and even similar to the one from methane, in particular concerning the spectral feature around $\lambda = 3.3\ \mu\text{m}$? As a matter of fact, many different kinds of organic hydrocarbon molecules (spectra in Appendix 8.A) show similar spectral features around the wavelength range of 3.1 to about 3.5 μm, which by the way also explains the success of commercial cameras for detecting these species.

Each absorption feature in a spectrum corresponds to a specific vibrational excitation of the molecule. The interactions of the various vibrations with each other and with rotations can lead to very complex spectra, however, with very characteristic spectral features. According to the foregoing discussion on diatomic molecules, the vibrational frequency depends on the "spring constant," that is, the strength of the chemical bond between the two atoms and their masses. Therefore, if a molecule has atom pairs with different chemical bonds (e.g., single, double, or triple covalent bonds or bonds of different strengths), vibrations between adjacent atoms will take place at quite different frequencies [1, 3]. This allows us to characterize a complex molecular spectrum in terms of the vibrations of some of its constituent atomic pairs. For example, the spectral regions due to C–H, C–C, C–O, C–N bonds, and so on are quite well separated in a spectrum, since the mass of the carbon atom partner changes appreciably (the larger the mass, the lower the oscillation frequency, that is, the larger the wavelength [1]).

All simple hydrocarbons, for example, octane, have two different functional groups within the carbon chain, CH_2 groups in the middle of the chain and CH_3 groups at the ends of the chain. Some other hydrocarbons have CH groups only. Owing to the similarity of the molecules, these functional groups dominate the spectral features by their various stretching and bending vibrational modes. In particular, the stretching modes of the CH, CH_2, and CH_3 groups contribute considerably around wavenumbers between 2800 and 3000 cm^{-1}. In addition, deformation modes (bending vibrations) give rise to spectral features around 1300–1500 cm^{-1}. This explains why quite different molecules (methane and octane) exhibit similar spectra. The same holds for numerous other hydrocarbon species (spectra in Appendix 8.A). These similarities are utilized in IR thermal imaging of gases, which uses a broad spectral region (see subsequent discussion) for mostly qualitative analysis. However, it should be emphasized that the spectra of these different molecules, though similar, differ enough from each other that high-resolution detection makes it possible to clearly identify each molecule separately via its spectroscopic fingerprint. In this respect, high-resolution IR spectroscopy is an important quantitative tool in gas detection as well.

In Appendix 8.A, we present a selection of IR spectra of inorganic as well as organic gases (Table 8.A.1). Some of them were recorded with conventional prism or grating spectrometers, others with Fourier transform IR spectroscopy (FTIR) [4, 5]. These spectra indicate which IR camera may be used for the detection of a specific gas. The commercial cameras only operate in a narrow predefined spectral band, whereas research cameras with exchangeable filters allow the detection of a larger variety of species. More information on spectra can be found, for example, in [2].

8.3
Influences of Gases on IR Imaging: Absorption, Scattering, and Emission of Radiation

8.3.1
Introduction

For many years, gases in IR imaging were restricted to being the medium through which the IR radiation of objects was transmitted before reaching the detector of the camera. Therefore, gases should neither absorb nor emit any IR radiation so as not to change the camera signals. These restrictions for the gas encountered in most applications, that is, atmospheric air, define the typical spectral ranges of IR cameras (cf. Figure 1.8 with Figure 1.45 or Figure 8.4). In the wavelength ranges of commercial IR camera systems, the residual extinction of atmospheric gases can be nicely compensated, and quantitative measurements are possible even for large distances [6].

In contrast, the qualitative detection of gases themselves by thermal imaging is a rather new application, first reported, to our knowledge, in 1985 [7]. This has meanwhile led to the development of new IR cameras. They all utilize the absorption or emission of IR radiation [8] in ro-vibrational bands of molecules contributing in the thermal IR region between 1 and 15 μm. Although strong absorption/emission features allow the detection of gases with broadband IR cameras operating in the MW and LW ranges [8], more sensitive commercial cameras [9] use narrowband cold filters in front of the detector. At present, commercial gas-detecting cameras are available for the detection of many VOCs, including refrigerants [10], SF_6 [11], CO, and, most recently, CO_2. Alternatively, warm filters may also be used for sensitive gas detection [12, 13]. A survey of new developments and manufacturers of commercial systems will be given in Section 8.6

One of the key issues associated with any kind of IR imaging of gases is whether it gives qualitative results in terms of visualizing the gas or quantitative numbers for the respective gas concentrations. Most commercially available gas-detecting cameras are only operated in the qualitative mode. The problems associated with quantitative imaging are discussed in Section 8.4.

8.3.2
Interaction of Gases with IR Radiation

As outlined in Section 8.2, IR radiation can be absorbed by molecules due to the excitation of rotational–vibrational bands. For simplicity we assume just two discrete energy levels representing ground and excited states of a molecule within such bands. We may then distinguish three different possibilities for gas molecules to interact with IR radiation (Figure 8.6):

- First, suitable IR radiation may be absorbed if the molecules are initially in the ground state (Figure 8.6a). In this case, directed IR radiation from an object behind the gas is attenuated by the gas, that is, less radiation is detected than without gas.
- Second, suitable IR radiation may be emitted isotropically if the molecules are initially in the excited state (Figure 8.6b). In this case, one would detect more IR radiation in the direction of an object than would be detected without the gas.
- Third, IR radiation may be scattered by molecules. This process happens if molecules are initially in the ground state (Figure 8.6c). They may then be excited by suitable IR radiation, for example, due to hot objects that are close by, but not in the line of sight of the camera. Immediately after excitation they reemit this IR radiation more or less isotropically. In this case, one would also detect more IR radiation in the direction of an object than would be detected without the gas.

Both the emission and the scattering processes lead to additional IR radiation due to the gas. If the population of the excited state of the gas is due to its temperature (thermal excitation) and the gas is optically thick (see below), the spectrum of the emission process can be described by Planck's law of blackbody radiation. If it is optically thin, the spectrum is obtained by multiplying Planck's law with a suitable emissivity that may be wavelength dependent (Section 1.4).

Scattering, on the other hand, does not need an initial population of an excited state. Scattering of electromagnetic radiation from molecules is well known. One usually distinguishes resonant from nonresonant scattering. In resonant scattering, the energy of the incident photons matches the required energy for excitation of the molecule to an excited state. The corresponding process is called *resonance fluorescence*. The best-known example of nonresonant scattering, that is, when the photon energy does not match the energy for an excitation, is Rayleigh scattering, which is responsible for blue skies (due to visible light scattering with energy lower than that for electronic excitations and higher than that for vibrational excitations of air molecules). If nonresonant radiation is incident on molecules, one may also observe an additional phenomenon where the scattered light has

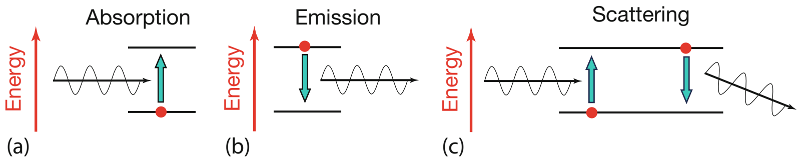

Figure 8.6 Interaction of IR radiation with two specific energy levels corresponding to rotational–vibrational excitations of a molecule. (a) Radiation may be absorbed from an initially low-lying state; the molecule ends up in a different rotational–vibrational state; (b) radiation may be emitted from an initially excited state; or (c) radiation may be scattered (absorption–emission cycle).

a slightly different energy compared to the incident light. This process is called *Raman scattering* and is an established technique of IR spectroscopy.

In the thermal IR range, the probability of nonresonant scattering from molecules is very small compared to resonant scattering, and therefore only scattering processes at the corresponding transition wavelengths must be considered. Such scattering processes from molecular gases may be thought of as resembling something like thermal reflections known from the study of solid objects.

This explains an additional difficulty when trying to quantitatively measure the influence of gases: one needs to know the contribution of scattering. This may be solved using an approach similar to reducing thermal reflections in conventional thermography: one must reduce the amount of scattered IR radiation by shielding the observed gases from any hot objects that could provide the IR radiation needed for the excitation of the scattering process.

8.3.3
Influence of Gases on IR Signals from Objects

The impact of gas absorption, emission, or scattering on IR thermal imaging is schematically illustrated in Figures 8.7–8.9. The top row of Figure 8.7 depicts the situation of an object observed by an IR camera through a cold gas of temperature T_{gas}. The object should have a temperature $T > T_{\text{gas}}$. The left line graph of the middle row of Figure 8.7 shows the object radiation (e.g., radiance) whose spectrum for a blackbody would follow Planck's law. An IR camera only uses a predefined spectral range, which is indicated by the pink area below the curve. This area corresponds to the object signal seen by a detector if no additional attenuation of the radiation takes place on its path from object to detector. If, however, the cold gas has absorption features within the IR camera spectral range (indicated by transmission spectrum below the cold gas in the middle row of Figure 8.7), the detected object signal (spectrum below the camera) is lower (smaller pink area).

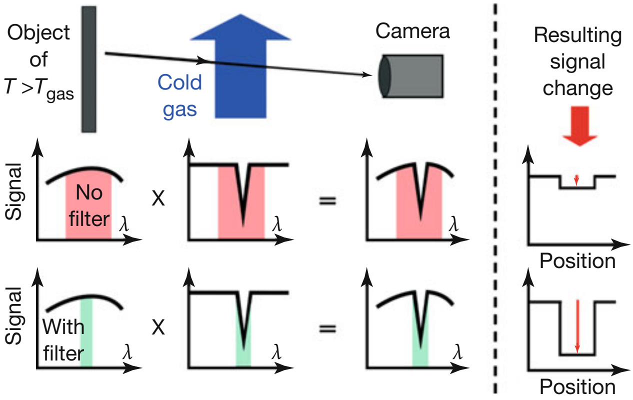

Figure 8.7 Detecting cold gases in front of a warm background with or without a filter. The shaded regions reflect the detected spectral range of the camera system.

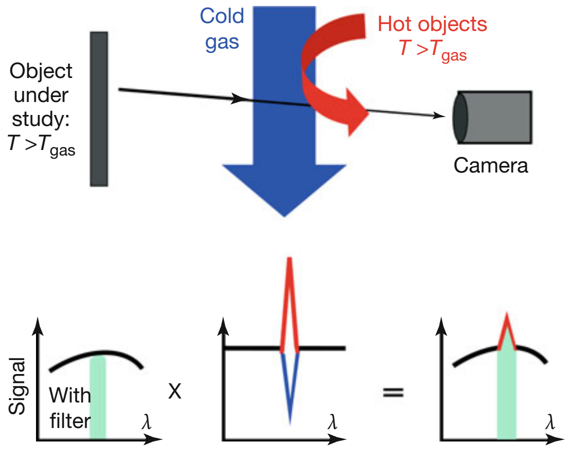

Figure 8.8 Detecting warm objects through cold gases if additional hot objects are close by. These may lead to a kind of thermal reflection, thereby altering the signal strength.

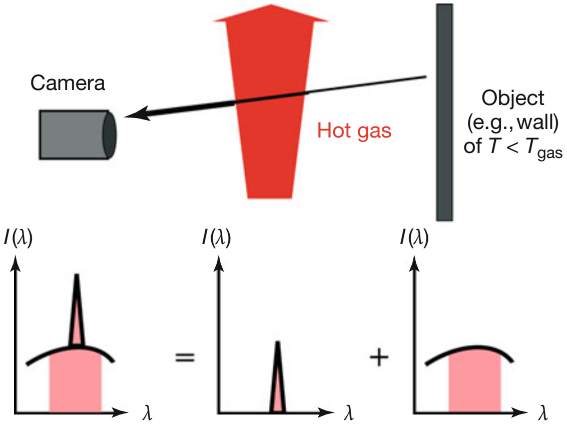

Figure 8.9 Detecting hot, thermally emitting gases in front of a colder background with a broadband IR camera. The shaded regions reflect the detected spectral range of the camera system.

This means that observation through a gas stream leads to a decrease in the object signal.

If a narrowband spectral filter is used in front of the camera detector (bottom row in Figure 8.7), the object signal (green area) is on the one hand smaller than that obtained by broadband detection. On the other hand, if it is tuned to the absorption feature of the gas, the relative signal change due to absorption by the gas is much larger, that is, one may improve the signal contrast and achieve more sensitive detection (right side of Figure 8.7). A detailed analysis must also consider the corresponding change in the signal-to-noise ratio (Section 3.2.1).

Figure 8.8 illustrates the measurement situation where, in addition to the object under study, other warm or hot objects that emit thermal IR radiation are close by. The hot surrounding objects emit thermal radiation, which may lead to resonant scattering processes from the molecular gas. This closely resembles the effect of thermal reflections known from solid objects (Section 3.4.1).

The detected camera signal may change according to the relative importance of gas absorption (blue, signal decrease) and resonant scattering (red, signal increase). Scattering effects can often be observed using gas-detecting cameras if the geometry/orientation of the camera is changed and, as a consequence, the amount of thermal reflections from the gas varies.

Now let us consider the influence of hot gases. The top row of Figure 8.9 depicts the ideal situation of an object observed by a broadband IR camera through a warm or hot gas of temperature T_{gas}. The object should have a temperature $T < T_{\text{gas}}$. If the gas is optically thick, the thermal emission from the gas would be described by Planck's law using the gas temperature. However, for realistic situations, gases under study are optically thin, that is, they are spectral emitters with emissivities below unity. In any case, the hot gas radiation may add up to the object signal. This means that observation through a hot gas stream leads to an increase in the object signal.

We note that Figure 8.9 can be extended to also illustrate the use of narrowband filters (as in Figure 8.7), and it is furthermore also possible in this setup for additional hot objects to lead to resonant scattering (like in Figure 8.8), thereby changing object signals.

As demonstrated in Figures 8.7–8.9, absorption, emission, or scattering of IR radiation by gases can have an influence on IR thermal imaging signals. The improvement in signal contrast and sensitivity from the use of narrowband filters is common to many cameras optimized for gas detection. As an example, Figure 8.10 shows an expanded high-resolution view of the 4.3 μm absorption band of CO_2 (Figure 8.4), together with the transmission spectrum of a typical commercially available filter in this wavelength region. Such a filter easily serves the purpose of IR imaging. A multitude of narrowband and broadband filters are available in the thermal IR range [14].

Further improvement in sensitivity results from using cold rather than warm filters since the detected background signal will be reduced, in particular if the filter material is also absorbing IR radiation (Section 3.2.1). This gas detection method with cold filters is commonly used with many commercial cameras for detecting VOCs. In addition, some cameras do not need filters at all: cameras with quantum well narrowband detectors (QWIP systems), their wavelength being tuned to molecular absorption bands, for example, to that of SF_6, need no additional filter. Other systems without filters are discussed in Section 8.6.

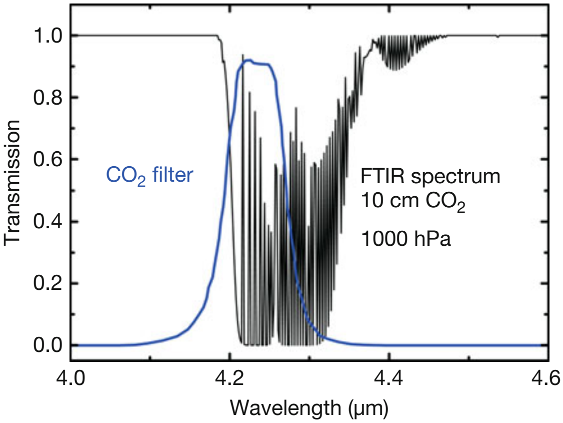

Figure 8.10 The 4.3 μm band spectrum of CO_2 with superimposed filter transmission curve.

8.4
Absorption by Cold Gases: Quantitative Aspects

In principle, a quantitative analysis of absorption of IR radiation by gases is possible. However, we only give a schematic description since any adaptation to a specific gas measurement requires taking into account the quantitative details of the corresponding gas absorption, the specifics of the geometry of the surroundings, measurement conditions, and so on [15]. Other preliminary studies to quantitatively measure gas sensitivities of thermal imagers for methane have been reported [16], and a systematic PhD-level study was published that demonstrates that, in principle, IR cameras may be used for quantitative gas leak measurements (Section 8.6) A recent commercial solution will be discussed in Section 8.6.

The reasoning for a quantitative analysis is as follows:

- First, quantitative gas spectra must be known;
- Second, one may calculate from that any decrease in IR radiation (e.g., its radiance) induced by a certain gas as a function of gas parameters, the used spectral range of the IR detector, and the geometry;
- Third, this leads to quantitative signal estimates, that is, a kind of calibration curve for an IR camera.

8.4.1
Attenuation of Radiation by a Cold Gas

The attenuation losses of IR radiation passing through a gas are described by Bouguer's law (sometimes also called *Lambert–Beer's law*), which states that the change in radiance passing through matter as a function of traveled distance L is given by

$$I(\tau) = I_0(\lambda) \cdot e^{-\tau(\lambda,c,L)} \tag{8.1}$$

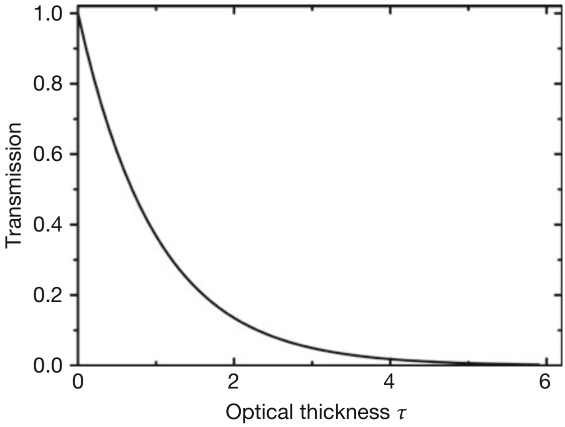

Figure 8.11 IR radiation passing through a gas is attenuated. The relevant quantity is the optical thickness τ of the gas.

Here I_0 defines the radiance entering the matter. Figure 8.11 shows a graphical representation of Eq. (8.1) in terms of transmission $T(\tau) = I(\tau)/I_0$. The quantity $\tau(\lambda, c, L)$ is the optical thickness of the gas. It depends on wavelength λ, gas concentration c, and length L of optical path through the gas. The gas concentration may be written in a number of ways. It may be given as mass density $\rho = m/V$, that is, mass per volume (kg m^{-3}), as number density $n = N/V$, that is, number of molecules per unit volume (in m^{-3}), or as pressure p (in hPa or atm), since, according to the ideal gas law, p is proportional to number density n.

For a gas of constant density n (molecules per unit volume) over the whole optical path, τ can be written in two different ways:

$$\tau(\lambda, c, L) = \sigma_{\text{ext}}(\lambda) \cdot n \cdot L = k(\lambda) \cdot p \cdot L \tag{8.2}$$

where the extinction cross section $\sigma_{\text{ext}}(\lambda)$ accounts for scattering as well as absorption losses. In what follows, we only deal with absorption features. $k(\lambda)$ is the spectral gas absorption coefficient, usually given in units of 1/(atm m). Once $k(\lambda)$ is known, one may quantitatively calculate the transmission $T(\lambda, p, L) = I(\lambda, p, L)/I_0(\lambda)$ of radiation through any gas of given pressure p and dimension L from Eq. (8.1). Obviously, Eqs. (8.1) and (8.2) are the key for any quantitative analysis of gas absorption: one needs to know the absorption coefficient $k(\lambda)$ very precisely. Then it is straightforward to compute the portion of transmitted radiation through a gas of given length at given pressure.

We note that the situation may be more complex if, for example, the gas is not distributed homogeneously. In this case the optical thickness is calculated from

$$\tau(\lambda) = \int_0^L \sigma(\lambda) \cdot n(x)\,\mathrm{d}x = \int_0^L k(\lambda) \cdot p(x)\,\mathrm{d}x \tag{8.3}$$

that is, contributions must be summed up over the total length of the optical path considered. In all of what follows, we use the description with the absorption constant k.

Transmission decreases exponentially, as shown in Figure 8.11. After five optical thicknesses, transmission $T = e^{-5}$ is below 1%. If, as in this case, it is very difficult to still detect IR radiation through the gas, one speaks of an optically thick gas.

8.4.2
From Transmission Spectra to Absorption Constants

The main problem in quantitatively evaluating camera signal changes due to gas absorption is the precise knowledge of the absorption coefficient k. Starting points are theoretical or experimental literature data for transmission spectra. To extract k values from such spectra according to Eqs. (8.1) and (8.2), the precise values of pressure p and path length L through the gas must be known. It is sometimes not very easy to get hold of reliable data since literature data may deviate from each other appreciably [15].

As an example, Figure 8.12 depicts CO_2 spectra (the analysis scheme in this chapter is presented for CO_2). The various literature data [2, 17, 18] may differ from each other, the main differences usually being due to the chosen spectral resolution. Low-resolution spectra only show averaged absorption and do not allow us to resolve individual ro-vibrational lines within the spectrum. The spectrum presented in Figure 8.12 was originally recorded at high resolution to resolve fine structures. Then a low-resolution spectrum was generated by averaging with neighboring data points (smoothed spectrum). If recording conditions (gas pressure p, length of optical path through gas L) are chosen unfavorably, the spectrum may show saturation behavior (zero transmission) at the center of the resonance between $\lambda = 4.2$ and 4.35 μm, which complicates the analysis.

Using Eqs. (8.1) and (8.2), the transmission spectra of Figure 8.12 are used to extract the absorption constants if the pressure p and length L of the recorded spectrum are known. Obviously, the extraction of data from regions in the spectrum where transmission is close to zero is difficult since errors in k get very large. Similar arguments hold for transmission close to unity. Regarding additional uncertainties of 0% and 100% lines (in particular for old literature spectra), we propose that reasonable transmission values for k-value extraction should lie in the interval $\{0.1, 0.9\}$ for the transmission data. Figure 8.13 schematically depicts the absorption coefficient k evaluated from the spectra of Figure 8.12 using Eqs. (8.1) and (8.2).

8.4.3
Transmission Spectra for Arbitrary Gas Conditions and IR Camera Signal Changes

Once the absorption constant k of a gas is known, the transmission of the gas for any pressure and optical path length may easily be computed according to

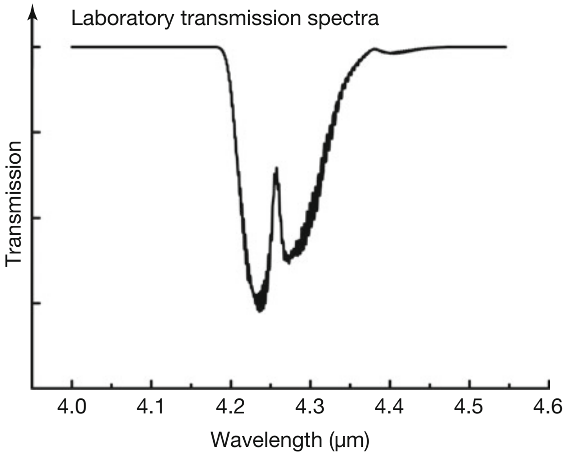

Figure 8.12 Starting point for quantitative analysis: a typical transmission spectrum of a gas, here CO_2, recorded, for example, with FTIR spectroscopy.

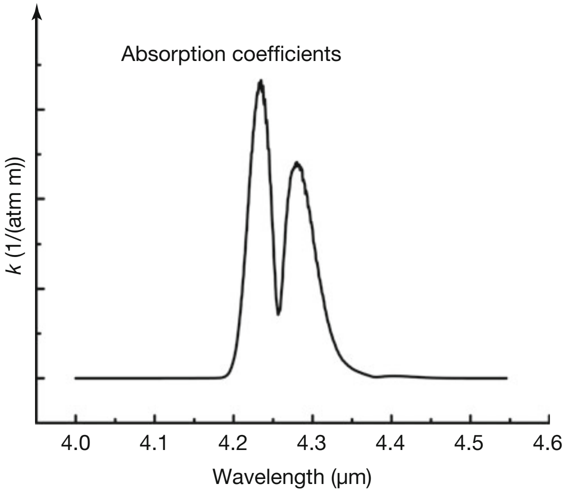

Figure 8.13 Absorption coefficients *k* extracted from transmission spectra of Figure 8.12.

Eqs. (8.1) and (8.2). As an example, Figure 8.14 depicts a number of transmission spectra for selected $p \cdot L$ values.

Modeled transmission spectra like these, due to given concentrations and path lengths, can be used to estimate the changes, induced on the object radiance of hot objects, observed through cold gases. In addition, one needs to know (Figure 8.15) the following information:

1. Object radiation (here the M_λ dλ spectrum) referring to object temperature;
2. Object emissivity;

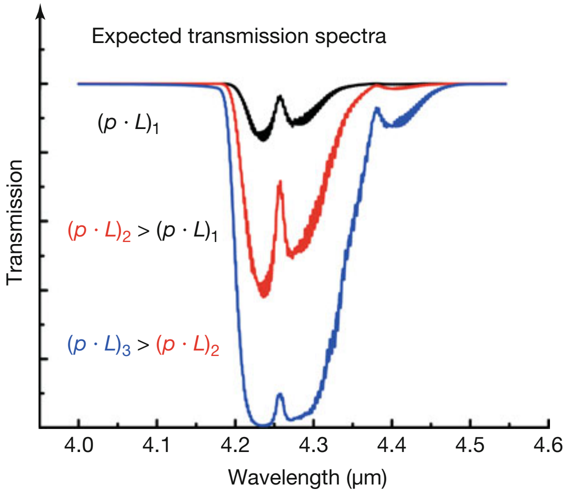

Figure 8.14 Transmission spectra for various conditions of $p \cdot L$, computed from k spectra of Figure 8.13.

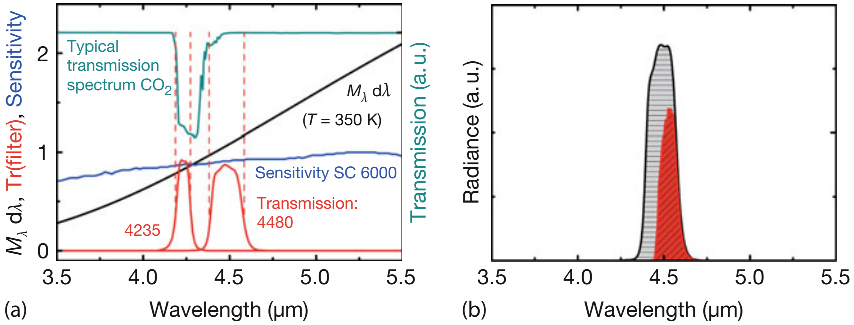

Figure 8.15 (a) Planck blackbody radiance M_λ dλ, detector sensitivity for SC6000, transmission of two commercially available filters [14], as well as a typical transmission spectrum for CO_2, all given in arbitrary units. (b) Schematic camera signals with and without gas absorption when using the 4480 narrowband filter.

3. Detector sensitivity (here of the midwave SC6000 camera used in some experiments), determining the detected wavelength band of the used camera; and
4. Transmission of optics, in particular of narrowband filters (here denoted 4235 and 4480).

Figure 8.15a illustrates the idea behind the quantitative analysis of an object (350 K) observed through a gas (gas + background at 300 K). The region of interest is defined by the absorption bands of CO_2. The detected radiance as a function of wavelength is proportional to the product of the object's Planck function, object emissivity, detector sensitivity, filter transmission, and transmission through the

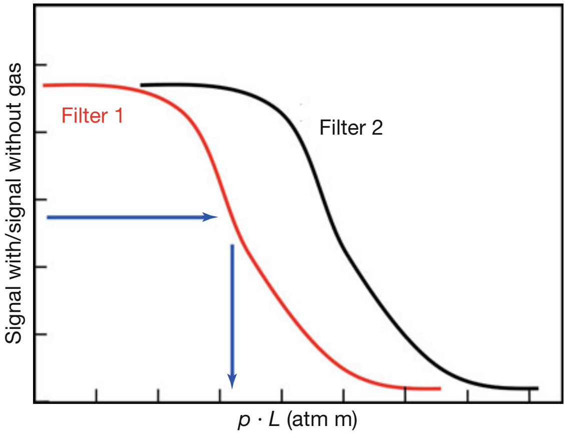

Figure 8.16 Schematic normalized plots of signal changes expected upon CO_2 gas absorption for given T_{object} as a function of gas pressure and optical path length through gas. The range of sensitive gas detection can be shifted by the use of appropriate filters.

gas under study. The filter transmission changes most rapidly, and hence it dominates the shape of the resulting detected spectral radiance function. The total detected IR radiation (Figure 8.15b) is proportional to the area under the spectral radiance function.

If there is no absorbing gas (CO_2 transmission 100%), the gray-shaded area determines the maximum possible signal. If, however, there is attenuation due to absorption by CO_2, the spectral radiance is reduced and the new signal is determined by the red-shaded area. This reduction in area corresponds to the signal reduction of Figure 8.7.

8.4.4
Calibration Curves for Gas Detection

The change in IR signal due to the gas is determined by the value of $p \cdot L$ (pressure times path length in gas). Figure 8.16 illustrates the fact that for very small absorption (small value of $p \cdot L$), both signals will be about equal (plateau region to the left), whereas for very large values of $p \cdot L$, nearly all of the IR radiation from the object is absorbed (signals drop close to zero). For any intermediate value of $p \cdot L$, an intermediate signal ratio will result. Hence, if such a calibration curve is known, one may easily find the $p \cdot L$ value from the measured signal attenuation (blue arrows).

How sensitive the method can be depends on the gas under study (value of k constants) and the use of filters. A camera is considered to be sensitive to a certain amount of gas if slight changes in $p \cdot L$ induce large changes in the signal. The two filters in Figure 8.16 lead to two separated sensitive regions that lie between 10% and 90% of the respective saturation values. Filter 1 may detect smaller $p \cdot L$ values, that is, it allows the detection of smaller amounts of gas.

Obviously, the lowest $p \cdot L$ value for a gas is defined by the given k value of the gas and the used narrowband filter. If the filter is on resonance, that is, completely overlapping the ro-vibrational absorption bands, the signal decrease for fixed $p \cdot L$ has its maximum value and the lowest detectable $p \cdot L$ values are reached (e.g., graph of filter 1 in Figure 8.16). This is nearly the case for the 4235 filter in Figure 8.15. If, however, the filter is slightly off resonance (e.g., filter 4480 in Figure 8.15), less radiation passing through the filter may be absorbed. Therefore, the $p \cdot L$ value belonging to the same signal attenuation must increase. As a consequence, the calibration curve is shifted to larger $p \cdot L$ values (e.g., graph of filter 2 in Figure 8.16), resembling a less-sensitive detection. This may be necessary if a gas has very strong absorption bands and is present at high pressure and over a long path. In practice, it may be desirable to switch from a high-sensitivity mode to a lower-sensitivity mode in a camera when studying, for example, very large gas leaks (in this case, the camera would probably not receive any background signal since strong gas absorption would block the detection of any object radiation).

The only remaining question is how a calibration curve, such as that shown in Figure 8.16, can be obtained for given gas conditions. The easiest way is to use calibration procedures. In principle, it seems possible to include a database in the camera with signal attenuations as a function of $p \cdot L$ at certain background object temperatures and distances. This could be done by calibration upon production of the camera. One would need several gas containers with IR windows such as heatable cells of various lengths, say, between 20 cm (for subsequent close-up studies) up to, say, 10 m. Then the procedure for evaluating the gas absorption effects would be similar to those in the study by Richards [6], who studied the influence of long atmospheric paths (up to 1 km). The camera needs to be directed onto a blackbody source of given temperature, and the signal changes are recorded as a function of increasing pressure or length. There would be a multitude of such graphs as a function of temperature.

8.4.5
Problem: the Enormous Variety of Measurement Conditions

Before 2015, no commercial quantitative gas-detecting camera was available. However, a patent was issued very recently, and the first quantitative analysis systems that can be combined with other commercial cameras are now being advertised (Section 8.6). Difficulties are connected with the fact that in practice, there is such an enormous variation in measurement parameters (e.g., geometrical distribution of gas densities, background object temperatures, ambient temperatures) that for each measurement situation, an individual calibration curve would be necessary. Even if calibration curves were available and measurements gave as a result a certain $p \cdot L$ value, there would still be the problem of interpreting it.

To estimate concentrations from the product $p \cdot L$ (p is proportional to the volume concentration according to the ideal gas law), one needs to have a good estimate of the length. Three measurement conditions seem possible: a homogeneous gas distribution, a localized gas leak with rather well-defined gas flow, and a

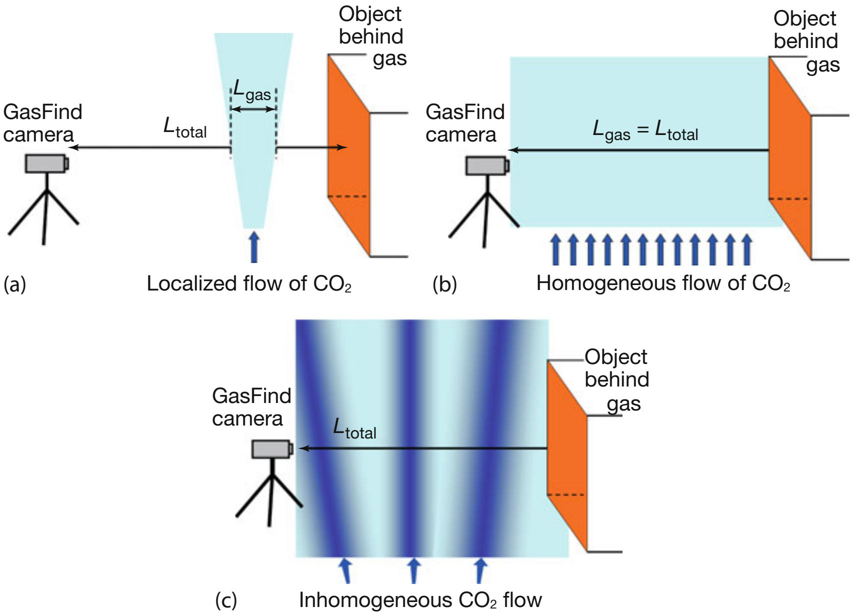

Figure 8.17 (a–c) Three typical measurement situations when studying gas absorption with IR cameras.

complex inhomogeneous distribution of gas, which may be due to localized leaks, in combination with diffusion processes that can lead to turbulent mixing with the surrounding air. These three conditions are depicted schematically in Figure 8.17.

For a homogeneous distribution of the gas between the camera and the observer (Figure 8.17b), the analysis is straightforward since L_{total} can be guessed easily using, for example, a laser range finder. From the measurement of the signal change, $p \cdot L$ is extracted, which means that p follows directly, and from that the volume concentration.

The most general and most difficult case is depicted schematically in Figure 8.17c. Such a situation may be the result of localized leaks; however, diffusion processes and turbulent mixing with the surrounding air can easily obscure the localized signature of laminar flow from a leak, especially if observed from a distance (this may be advisable for security reasons). In this case, the change in signal will just give the optical thickness, which is due to an averaged value $p_{average} \cdot L_{total}$ and which results from integration over the optical path. In this case, only an average concentration may be deduced, and high-concentration gas leak spots may be hidden.

For localized gas leaks with gas streaming out from a nozzle or a hole in some pipe and so on, one usually expects an inhomogeneous distribution, which, close to the leak, would still resemble a laminar flow like the one shown in Figure 8.17a (see also examples in [12, 13] and Section 8.7). If it is possible to estimate the actual gas flow diameter L_{gas} while measuring over a distance of L_{total}, the related localized pressure value p_{gas} follows from the measured average pressure p over L_{total} according to $p_{\text{gas}} \cdot L_{\text{gas}} = p \cdot L_{\text{total}}$. In any case, the net result would be at best a volume concentration of a gas.

Obviously, many practical applications require a knowledge of gas flows. From the preceding discussion it follows that these cannot be estimated *per se* by IR imaging. However, as has been demonstrated for the example of artificial CO_2 gas leaks [12, 13], sensitive detection with small gas flows is possible, and for given leak sizes, calibration measurements are possible.

8.5
Thermal Emission from Hot Gases

Although in practice one will likely encounter mostly cold gases (see preceding subsections), we also want to briefly focus on the case of colder objects observed through hot gases, in particular for cases where the gases are thermally emitting IR radiation. In this case (Figure 8.9), gas thermal emission adds up to the object radiation, that is, the original signal (without gas) is enlarged. Some experimental examples are described in Section 8.7; here we focus on the problem of quantitative analysis, for which one needs to know the emissivity of the hot gas. This problem is raised quite often by practitioners searching for a method to estimate gas temperatures from hot flames with IR imaging.

The absorption constant $k(\lambda)$ is related to the directed emissivity of a gas. The total average volume emissivity ε_{gas} is then given by (e.g., [19])

$$\varepsilon_{\text{gas}}(T, p_{\text{tot}}, p_{\text{gas}}, L) = \frac{1}{\sigma T^4} \int (1 - \mathrm{e}^{-k(\lambda,T)\cdot p\cdot L}) M_\lambda(T)\,\mathrm{d}\lambda \tag{8.4}$$

Results for gases depend on the optical thickness; usually they are depicted as a function of $p \cdot L$. They are well known for H_2O vapor and CO_2 at elevated temperatures since these gases are byproducts in combustion processes, and it is important to know the radiative heat load on the interior walls of furnaces. This was the original motivation for calculating the emissivities of CO_2, so data are mostly available for elevated temperatures. Still, they can give some insight into general behavior. Figure 8.18a (after [20] using data of Hottel) shows ε_{gas} (CO_2) for a variety of $p \cdot L$ values [17, 19, 21–23]. The parameter is given in feet times atmosphere, with 1 ft = 0.3 m. Slightly above room temperature and at standard pressure, CO_2 with $p \cdot L = 1$ atm m (≈ 3 atm ft) gives $\varepsilon_{\text{gas}} \approx 0.18$. The peculiar form of the $\varepsilon(T)$ curves can be understood from the basic physics of blackbody radiation and the corresponding band absorption.

Figure 8.18b illustrates which absorption bands of CO_2 contribute as a function of temperature for $p \cdot L = 1$ ft atm. For low temperature, the $M_\lambda(T)$ spectra peak in the LW region, and hence the 15 μm absorption band, will dominate absorption for low temperatures. For larger temperatures, the contribution of the 15 μm band will decrease and the 4.2 μm band contribution will increase as $M_\lambda(T)$ shifts to the MW range. For still larger temperatures, the 4.2 μm band contribution decreases,

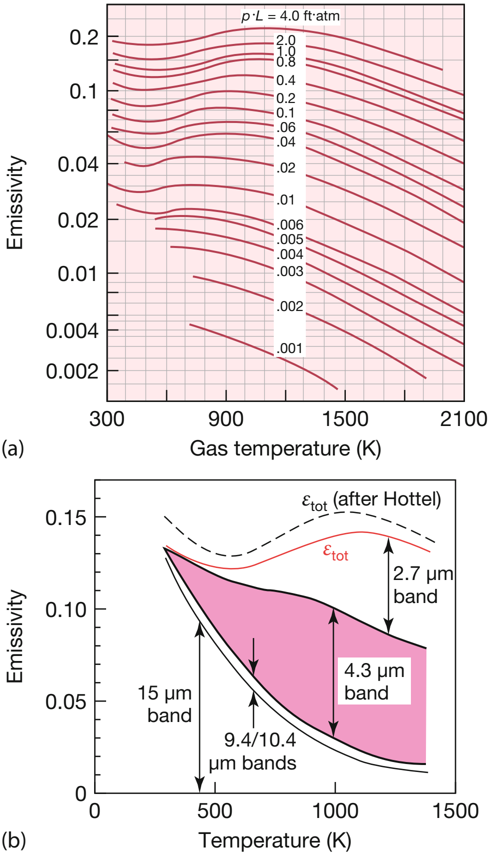

Figure 8.18 (a) Volume emissivities of CO_2 for various values of $p \cdot L$ as a function of temperature (a) (from [20] after Hottel). (b) The total emissivity (red solid line theory) has contributions from absorption of the various ro-vibrational bands, shown here for $p \cdot L = 1$ ft atm (after [17]).

whereas now the 2.7 μm contribution can still increase. The changes in the various contributions from different absorption bands to the total emissivity as a function of temperature can be calculated from transition matrix elements, which give the respective oscillator strengths. Changes result more or less from the fact that the total oscillator strength is finite and transitions from the various bands compete with each other.

When discussing measurements with MW cameras, we would not deal with the total gas emissivity from Figure 8.18a but rather with the smaller pink shaded contribution of the 4.3 μm band, as indicated in Figure 8.18b. This means that any MW camera would be dealing with much smaller emissivities, for example, $\varepsilon_{4.3\text{-}\mu\text{m band}} \approx 1/4\ \varepsilon_{\text{gas}}$ at $T \approx 500\,\text{K}$, and so on.

Obviously, Figure 8.18 indicates that the emissivities of hot gases and dimensions on the order of 1 m are still quite low, that is, the corresponding thermal gas radiation is far from resembling a Planck black or gray body source (for a discussion of typical gas dimensions needed to reach thermal equilibrium and emissivity $\varepsilon = 1$ for atomic hydrogen gas, see [24]).

8.6
New Developments

Many optical methods are known for gas sensing [25]; here we will restrict ourselves to imaging systems. We will try to provide a survey but cannot claim completeness in this rapidly evolving market. The first commercial IR OGI cameras worked qualitatively with a single fixed cold filter in front of MW cooled photoelectric focal plane array (FPA) detectors. Meanwhile, several different methods were developed for OGI in the thermal IR spectral range that led to a number of commercial products. Table 8.1 summarizes the techniques and physics principles of the various detection methods.

Table 8.1 Different techniques used in OGI.

Technique	Single cold filter	Filter wheel	Circular filter wheel	Diffractive element	FTIR + scanning/FPA
Principle	Narrowband cooled filter directly in front of cooled detector	Measure gas (1) without filter and (2) with cut-on filter (no gas influence) (Figure 8.19)	Broad- or narrowband, quasi-hyperspectral detection using conventional filters + wheel with narrowband interference filters (Figure 8.20)	Varying distance between diffractive element and FPA (Figure 8.21)	True hyperspectral: combine FTIR spectrometer with either scanning option or FPA (Section 3.2.3, Figure 8.22)
Manufacturer (example)	FLIR, EyeC-Gas [26, 27]	Second Sight [28, 29]	CI systems [30]	GIT Sherlock [31]	Bruker, Telops, Telops2 [32–35]
Details	About 6 to 7 different filters (cameras) available		Up to 80 spectral bands, $d\lambda/\lambda = 0.5\%$, 7.8–12 μm, 320×256 pixels 2 s for image	VOCs (MW) and SF_6 (LW)	IFOV < 1 mrad, typical spectral resolution $4\,cm^{-1}$, 256×256/ 320×256 pixels, MW and LW systems, cooled detectors, airplane use possible

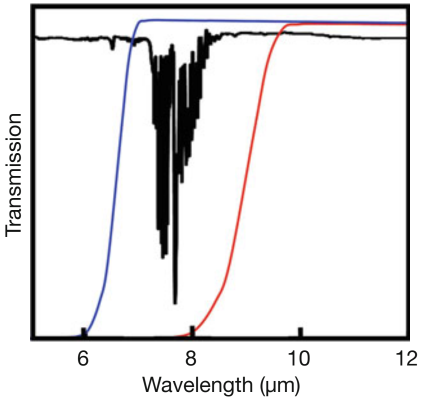

Figure 8.19 Scheme for gas detection with cut-on filters. The shown gas spectrum corresponds to pure methane (see text for details).

The basics of gas detection with single narrowband filters were explained in Sections 8.3 and 8.4. Here we briefly summarize new commercial developments without going into details of the related detection limits, cooled versus uncooled filters, signal-to-noise ratios, and so forth.

A potential improvement in cameras with fixed single filters are filter wheels. These have been available for quite a long time, however, only in research cameras. Meanwhile they are also used commercially for gas imaging. Besides wheels with various narrowband filters, gas detection and discrimination is also possible using (a number of) cut-on filters [29]. The scheme is depicted in Figure 8.19. For example, a gas with an absorption band in the LW IR may first be detected using the whole broad LW band or a (blue) filter with cut-on wavelength below the absorption feature. In a second step, a filter is inserted with cut-on wavelength above the absorption feature. Without gas, the signal decrease would just correspond to the reduced width of the detected band. If an absorbing gas is present, the signal decrease will be larger.

Another filter wheel system [30] is advertised as being able to detect radiation, either broadband, narrowband, or (quasi-) hyperspectral. Figure 8.20 depicts the scheme of such a setup.

One half of the filter wheel can accommodate a number of filters that allow for broadband or narrow band detection at various center wavelengths. In addition, the other half (in Figure 8.20a, the lower one) of the wheel is a specially manufactured narrowband precision interference filter with variable center wavelengths, which depends on the wheel rotation angle α (Figure 8.20b). Such an assembly is available for the LW band between 7.8 and 12 μm with up to 80 spectral channels (which is why it is advertised as hyperspectral) and spectral resolution $d\lambda/\lambda = 0.5\%$.

The physics underlying a quite different patented technique [31] is illustrated in Figure 8.21. The object radiation – and we assume objects that emit black or gray body broadband radiation – passes through a diffractive element before reach-

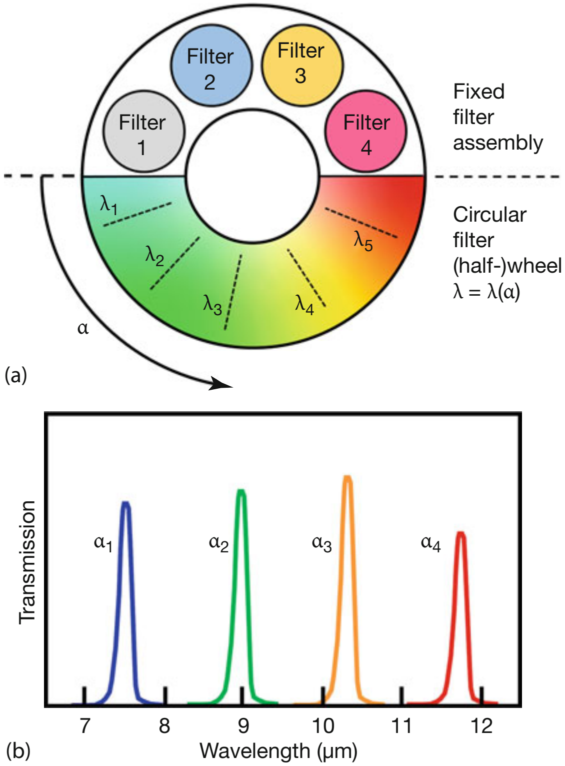

Figure 8.20 (a) Filter setup to either detect broadband or narrowband IR radiation with normal filters or perform quasi-hyperspectral imaging using a circular filter wheel with narrow interference filter transmission as a function of rotation angle α. (b) Schematic example of transmission of interference filters on wheel as function of angle.

ing the detector FPA. For simplicity we assume the diffractive element to be a common, that is, chromatic, lens. Each lens made of a given material suffers from dispersion, that is, the index of refraction is wavelength dependent, with longer wavelengths usually having smaller index values than shorter wavelengths. The focal length of a lens depends on the index, so longer wavelengths usually have longer focal lengths, and consequently, for any optical imaging they also have longer image distances than those of shorter wavelengths. To keep it simple, this is illustrated (in a geometrical optics diagram) only for those limiting rays in Figure 8.21a that form an image on the optical axis. The short rays (blue) have a shorter image distance than green and red rays. As shown, for a given distance between the lens and the FPA, the green rays form a sharp image on the central pixel on the optical axis, whereas blue and red rays have their images closer to the lens or further from it. As a consequence, the detector will receive different amounts of radiation from the three shown wavelengths (Figure 8.21b). The more widely spread the radiation is at the FPA, the smaller the amount an individual pixel will receive. Therefore, as depicted, radiation of wavelength λ_2 will be dom-

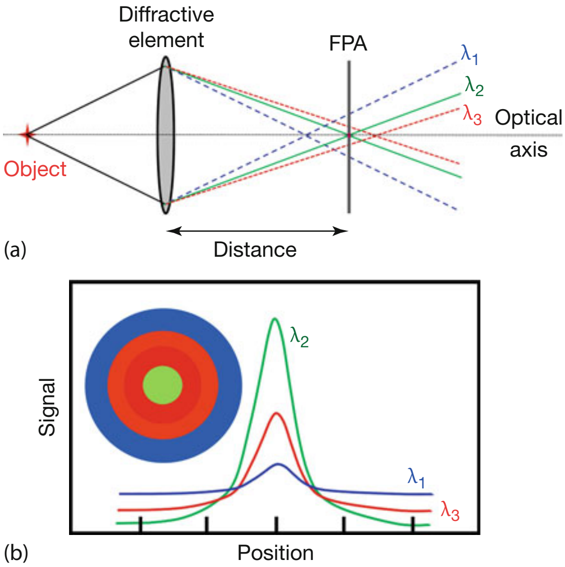

Figure 8.21 (a) Scheme to detect IR spectra using a diffractive element (e.g., longitudinal chromatic aberrations of dispersive lens).The distance between the element and the detector FPA is varied. (b) At fixed distance, a given pixel receives more radiation for the wavelength, which focuses the object onto the FPA.

inant, that is, in the example given, the pixel receives more or less narrowband radiation centered around λ_2.

An interesting effect occurs if the image distance between lens and FPA detector can be varied. In this case, changing the distance causes a change in the detected radiation wavelength. This allows a conceptually simple way of recording spectra by varying the distance between diffractive element and detector array.

Finally, (true) hyperspectral imaging (Section 3.2.3) has also made progress in the field of OGI [32–35]. To repeat briefly: in true hyperspectral imaging, IR spectra are recorded for each pixel using FTIR. This ensures the highest possible spectral resolution, better than that of the filter wheel.

In addition to the information given in Section 3.2.3, we briefly discuss two types of commercial hyperspectral systems for OGI. The first uses a single detector and an optical scanning system. It has the advantage of having best detector performance but the disadvantage of longer recording times for extended object scenes. Even if 16 spectra are recorded per second (and it is not possible to do this much faster), and one spectrum is used for each pixel only, images of 256 × 256 pixels would require about 4000 s, or more than an hour. Obviously, this technique is only useful for studying regions of interest with low spatial resolution if the situation does not change with time. If, however, FPAs are used, the recording time is drastically reduced and quasi-life images can be seen (depending more on the speed of the fast Fourier transform and subsequent image processing than on data recording).

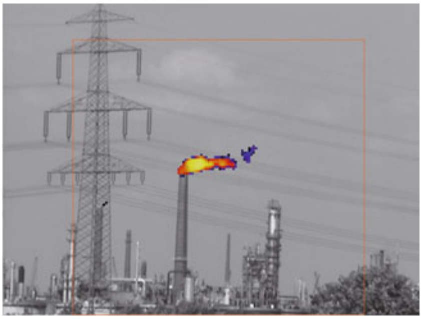

Figure 8.22 Example of detection of industrial SO_2 emission from a distance of 1.5 km using a hyperspectral imaging system, HI90 (image courtesy Bruker Optics).

Figure 8.22 shows an industrial example of SO_2 detection from a distance of about 1.5 km [32]. The spectra of the recorded pixels are compared to internally stored sets of spectral data of many gases. Whenever a measured spectrum coincides with a certain gas, this is marked in the image. Another example of a detailed study refers to a coal-burning power plant smokestack [35]. The plume was strongly emissive across 1800 to 3000 cm^{-1}, and the spectra revealed simultaneous emissions of at least six gases: CO_2, CO, H_2O, NO, SO_2, and HCl.

The latest developments in OGI include the use of drones or, more generally, unmanned aerial vehicles (UAVs). Obviously, UAVs equipped with IR cameras can help to increase safety in inspections, in particular if hazardous gases are being investigated. In addition, it makes it possible to be much closer to objects, such as chimneys, that may otherwise be difficult to inspect (see also Section 10.11).

Another important field of research is to develop real quantitative gas-detecting cameras. As mentioned earlier in Section 8.4, quantitative analysis is in principle possible but requires a lot of additional knowledge. Recently, an extensive piece of related research was published in a PhD thesis [36], which resulted in the first commercial solutions for quantitative imaging with common cameras [37]. It will be worthwhile to follow these developments.

Finally, coming back to the most commonly used OGI cameras for practitioners who use narrowband filters, we summarize in Table 8.2 those gases that are advertised as being detectable. Obviously, using just a single filter does not allow one to determine which or how many of the gases with absorption features within the filter bandwidth are detected. This is possible only if the exact species is known from the specifics of an object under study (e.g., searching for SF_6 or CO leaks). In general, however, if the camera detects a gas-induced signal, it can be asserted only that one of many gases must be present. More detailed knowledge would be possible with a hyperspectral imaging system. Alternatively, once a leak is found, ground-based chemical or spectroscopic inspections can be conducted to definitely identify the relevant gas species.

Table 8.2 also contains a column (filter 3.8–4.05 μm) that is somewhat out of place, let us say, complementary to the other cameras. In this system, the filter is

Table 8.2 Characterization of commercially available OGI cameras using narrowband filters (e.g., FLIR, EyecGas); advertised list of detectable gases for leak detection and repair (LDAR).

Spectral range	MW	MW	MW	MW	LW	LW
Filter wavelengths in µm	3.2–3.4	3.8–4.05	4.2–4.4	4.52–4.67	8–8.6	10.3–10.7
Type of gas	Hydrocarbons		CO_2	CO	refrigerants	
Gases	Examples: • Benzene • Butane • Ethane • Ethylbenzene • Ethylene • Heptane • Hexane • Isoprene • Methyl ethyl ketone (MEK) • Methane • Methanol • MIBK • Octane • Pentane • 1-Pentane • Propane • Propylene • Toluene • Xylene • …	*Used in spectral region where there is no absorption by CO_2 or H_2O*	CO_2	CO Also: • Acetonitrile • Acetyl cyanide • Arsine • Bromine isocyanate • Butyl isocyanide • Chlorine isocyanate • Chlorodimethylsilane • Cyanogen bromide • Dichloromethylsilane • Ethenone • Ethyl thiocyanate • Germane • Hexyl isocyanide • Ketene • Methyl thiocyanate • Nitrous oxide • Silane	Freon MEK ClO_2 … • R125 • R134A • R143A • R245fa • R404A • R407C • R410A • R417A • R422A • R507A	SF_6 NH_3 Also • ClO_2 • Ethylene • a large number of hydrocarbon chlorides, bromides, fluorides
Application areas	Natural gas Petrochemical Oil refining Offshore platforms	Industrial furnace surface inspection Looking through flames	CO_2 industries Enhanced oil recovery CCS	Petrochemical Chemical manufacturing steel industry	Food production Pharmaceutical Automotive Air conditioning	Electrical utilities Ammonia plants Fertilizer production

tuned to specifically avoid gas absorption, in particular by H_2O and CO_2, which dominate absorption within furnaces. These cameras may therefore be used to inspect furnaces during operation.

8.7
Practical Examples: Gas Detection with Commercial IR Cameras

In this section, we present a selection of IR images of different gases, detected via absorption or emission processes of the gas between camera and a background object under study. Some studies were performed using broadband cameras, others using cameras equipped with narrowband filters. The spectra of all investigated gases are given in Appendix 8.A. Most examples shown here are qualitative only, with the exception of a few studies on CO_2 detection.

8.7.1
Organic Compounds

The first commercial IR camera developed for the sole purpose of detecting gases was an OGI camera called GasFind [9, 10] that was sensitive for VOCs. Although some countries have definitions of VOCs, there is no generally accepted one. Qualitatively, VOCs are volatile organic compounds with rather high vapor pressure under normal conditions such that there is significant vaporization. In the European Union, for example, a VOC is any organic compound having an initial boiling point less than or equal to 250 °C measured at a standard atmospheric pressure of 1013 hPa. Obviously, this vague definition explains why there are millions of different compounds – natural as well as synthetic – that can be classified as VOCs. Typical examples are fuels, solvents, drugs, pesticides, or refrigerants. Since many VOCs are toxic (e.g., benzene compounds) or dangerous for the earth's climate (e.g., greenhouse gases, chlorofluorocarbons for the ozone layer), they are often regulated, and efficient means of detecting them are needed. The most important single application field of IR gas imaging of VOCs is probably the petrochemical industry.

The simplest and best-known VOC molecule is methane. According to the spectrum shown in Figure 8.5, there are two major absorption bands, one centered around 3.3 μm in the MW band and the other between 7 and 8 μm. This means that either MW or LW cameras are suitable for its detection. The first commercial GasFind cameras were MW cameras with cold narrowband filters adjusted in a wavelength range between 3 and 3.5 μm. Just a year later, it was shown that LW cameras could also be used for detecting VOCs and many other species [8]. This idea was followed up by several manufacturers, as summarized in Section 8.6. In comparison to methane, propane shows similar spectral features; however, the relative strengths of the bands are changed. Compared to methane, propane's absorption in the LW band is reduced with respect to the MW band.

Figure 8.23 compares two camera types (GasFind MW with narrowband cold filter and a typical broadband LW) for the detection of methane and propane, flowing out at atmospheric pressure from a nozzle in front of a blackbody source at around 55 °C. The two images of each gas were recorded nearly simultaneously – the tube with the gas flow was sometimes moved for better detection in real time image sequences. Three things are obvious:

1. It does not really matter which wavelength region is used for the detection of gases, the only prerequisite being that there must be an absorption band.
2. These images indicate the improvement that is due to the narrowband filter in the GasFind camera. Its images (a, c) have a much better signal contrast. In real-time observations, this is even more obvious. We note, however, that here the two cameras have different spectral ranges. Below, we present another example with CO_2 where the comparison between broad- and narrowband filter detection is shown for the same spectral range.

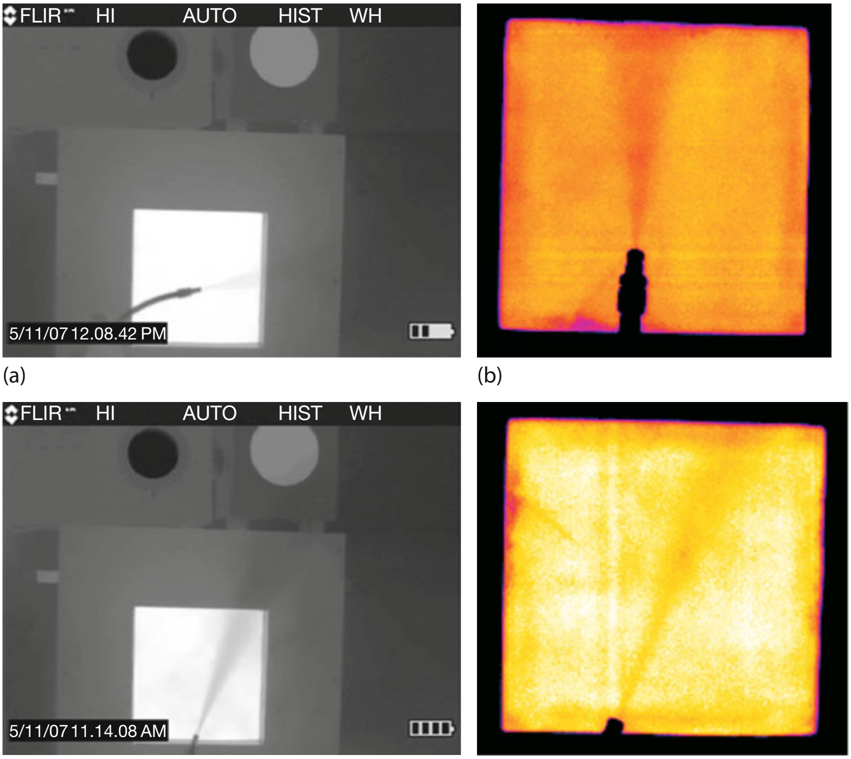

(a) (b) (c) (d)

Figure 8.23 IR images of pure methane (a,b) and propane (c,d) flowing out of a nozzle in front of a blackbody source. (a,c) MW FLIR GasFind camera images and (b, d) broadband LW FLIR P640 camera images. Images recorded at laboratory in Brandenburg, Germany.

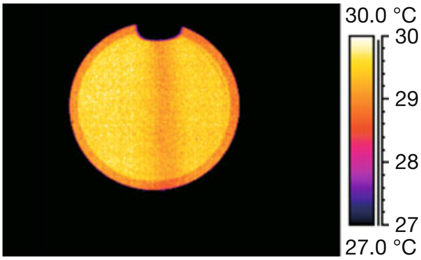

Figure 8.24 IR image of gas of camping burner recorded with LW FLIR SC2000 camera.

3. The differences between the spectra show up in the images. For propane, MW detection improved considerably because of the much higher absorption constants (the two spectra in Appendix 8.A refer to the same gas pressure and sample length).

The commercial VOC GasFind cameras will detect a variety of gaseous species. Since the corresponding spectra sometimes shift around the fixed filter region, some gases may be detected slightly more easily than others. This may give rise to additional changes when detecting different gases.

Together with propane, butane is another very important gas encountered in everyday life. In Europe, mixtures of these two gases are commonly used in lighters or camping burners. Butane shows absorption features very similar to those of propane. Figure 8.24 shows an image of the gas (no flame) flowing out of a camping burner. The burner was turned upside down since propane and butane are both heavier than air.

A variety of other organic compounds have been investigated experimentally using broadband LW cameras [8], mostly to demonstrate the possibility of detecting these species with broadband systems. Of course, narrowband detection is more sensitive. Here, ethanol and gasoline are discussed as two more examples.

Ethanol is probably the most important alcohol species. To detect just the effects of pure ethanol, we used laboratory-grade ethanol (Figure 8.25). Upon opening the flask at room temperature (about 18 °C) in front of a blackbody source at about 35 °C, one immediately observes the absorption effects of the vapor. This becomes even more obvious when the alcohol is poured into a shallow dish while the dish is moved gently.

IR cameras are sensitive enough to detect ethanol alcohol vapor in the breath right after the consumption of a high percentage of alcohol (of course, more sensitive spectroscopic methods are available). The IR images in Figure 8.26 show the results of the following experiment: a volunteer drinks either pure water or alcohol and then exhales (it is sufficient to flush the mouth without swallowing, and care must be taken to exhale gas and not liquid droplets). Exhaling after drinking water shows no noticeable effect (Figure 8.26a), whereas the alcohol in the breath is easily observable (Figure 8.26b).

Figures 8.27 and 8.28 depict two typical examples of onsite analysis of VOCs recorded with GasFind cameras. A very common use of VOCs is as gasoline for

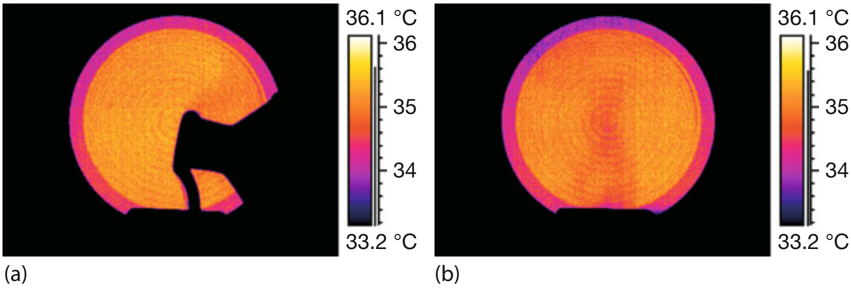

Figure 8.25 Room temperature pure ethanol poured into a dish in front of temperature-stabilized blackbody source (a) and ethanol vapor, above dish (b).

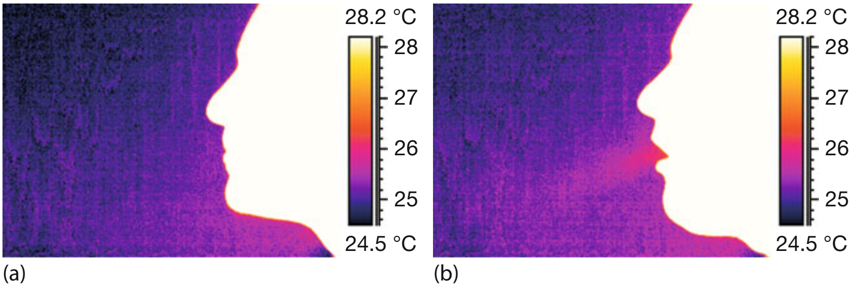

Figure 8.26 Normal breathing and exhaling after drinking water has no observable effect on LW IR thermal imaging (a). In contrast, drinking alcohol does lead to alcohol vapor in the breath that is detectable (b).

cars. While pumping gas at gas stations, the VOC fumes, due to the vapor pressure of the liquids, may be emitted into the environment. This can be clearly seen in Figure 8.27, which depicts the situation before (Figure 8.27a) and after starting the fill-up. To reduce these emissions, the hose may be equipped with a surrounding tube, which pumps the fumes away. Figure 8.28 shows an example of a refinery where one could detect VOC fumes leaking out from below the cover of a waste-water tank.

8.7.2
Some Inorganic Compounds

Ammonia is a very common substance used in the chemical industry. Opening a bottle with pure ammonia leads to the escape of the vapor pressure above the liquid. Figure 8.29 depicts this vapor in front of a temperature-stabilized blackbody source at around 41 °C used as background object. The strong absorption of the vapor in the LW range (spectrum in Appendix 8.A) immediately leads to clearly observable features in the IR images.

Whereas ammonia can be sensed by humans due to its bad smell, sulfur hexafluoride (SF_6) cannot be detected by human senses, and whereas ammonia shows

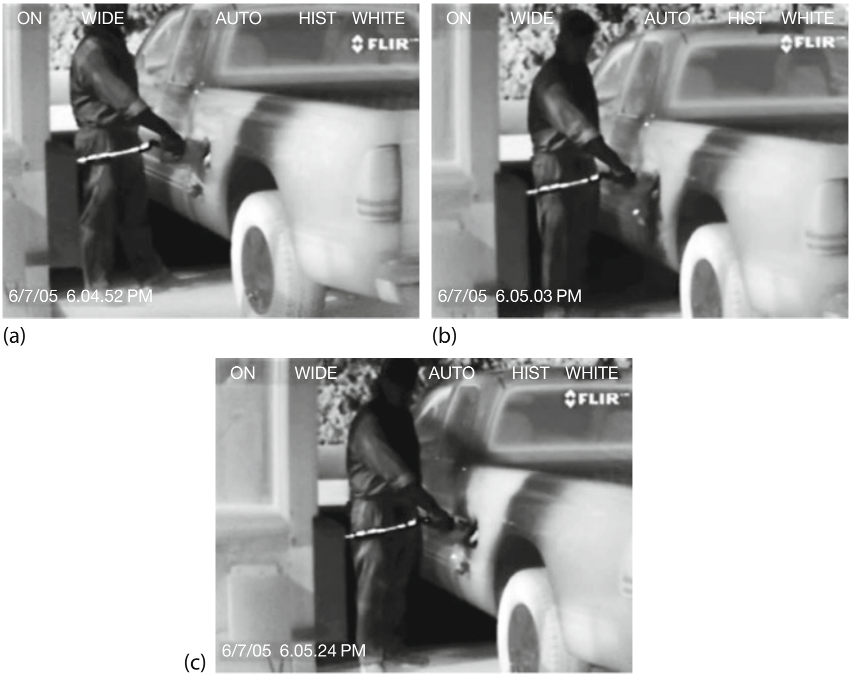

Figure 8.27 Three snapshots of fill-up of a car tank with gasoline at a regular gas station. Before starting the fill-up (a), no fumes can be seen. (b) Immediately after the gas starts being pumped, fumes are detected. (c) Though heavier than air, they are driven by air currents and may also be blown toward the customer. (Courtesy Infrared Training Center, FLIR Systems Inc.)

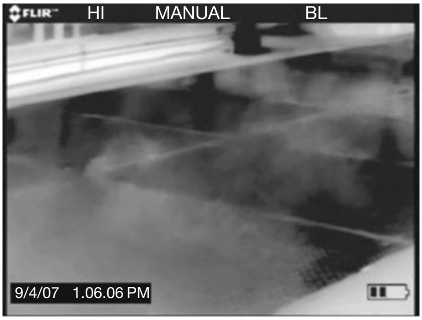

Figure 8.28 Fumes of VOCs leaking through covers of wastewater holding tanks in a refinery. Such tanks separate the oil from the water. (Courtesy Infrared Training Center, FLIR Systems Inc.)

strong broadband absorption in the LW and some small absorption features in the MW band, SF_6, due to its high symmetry, only shows one pronounced and very strong absorption feature in the thermal IR range around 10 μm. In the following experiments (after [8]), SF_6 was injected into a balloon, and its effects on IR signals were studied by positioning it in front of a blackbody source. Then a valve was opened and the gas was pressed out of the balloon. Figure 8.30 shows some examples with room temperature gas (about 24 °C) and varying object temperature for

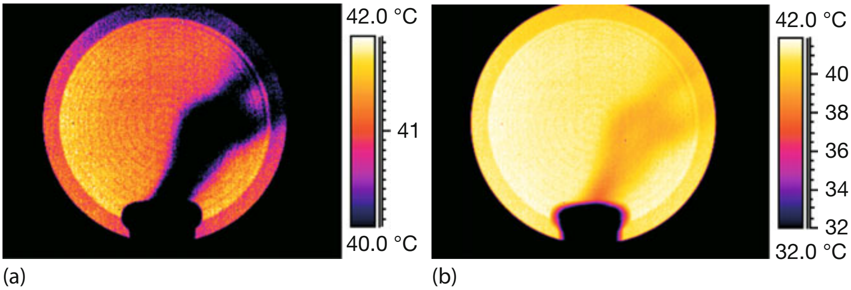

Figure 8.29 Room temperature ammonia vapor in front of warmer object is easily visible with a LW camera, not only for a 2 K span (a) but also for a larger 10 K span (b).

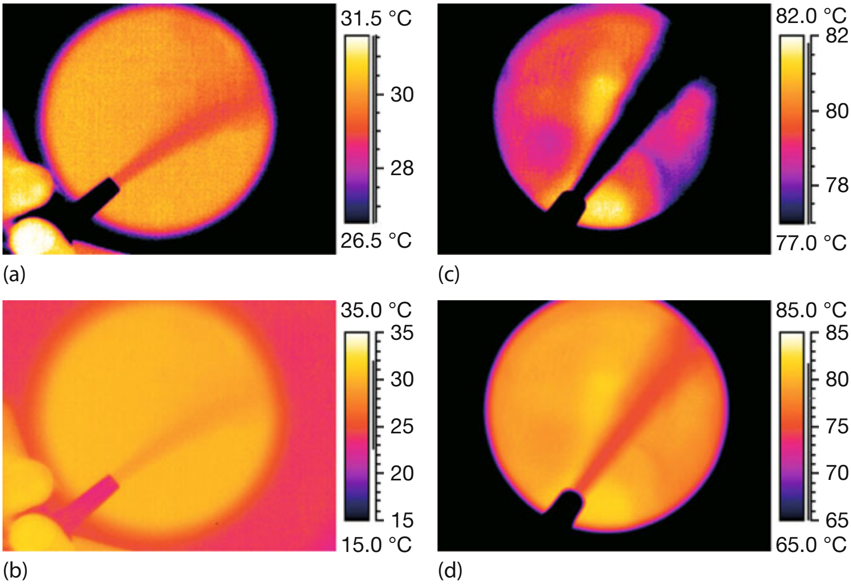

Figure 8.30 Room temperature SF_6 in front of a blackbody of 32 °C (a,b) and 82 °C (c,d). Both images were recorded with a broadband LW camera and a 5 K span (a,c) and 20 K span (b,d).

spans of 5 and 20 K. These images show the increase in contrast with increasing temperature difference between the gas and the object. Furthermore, the good signal contrast also for a large span clearly demonstrates that SF_6 can easily be detected without carefully adjusting the level and span. As a consequence, a narrowband LW GasFind camera for SF_6 and species with absorption around 10 μm wavelength was introduced [11].

The gas-filled bags with SF_6 were quite easy to handle and allowed us to study the changes in IR images when varying the gas temperature in relation to the surroundings. This was done by placing the gas balloons in a temperature-stabilized oven for times long enough to establish thermal equilibrium. One balloon with

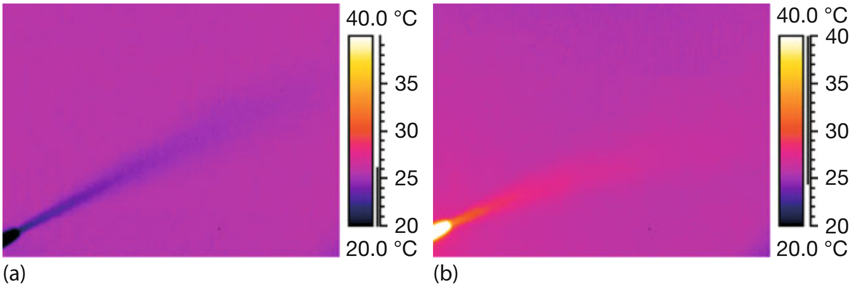

Figure 8.31 Cold (a) and hot (b) SF_6 in front of a room temperature wall.

SF_6 was cooled down to −20 °C and a second was heated to +80 °C, that is, one gas bag was much colder than the ambient temperature while the other was much warmer. Figure 8.31 depicts the respective gas flows observed in front of a room temperature wall. These images nicely demonstrate the change from absorption of IR radiation by the cold gas to the thermal emission of IR radiation by the hot gas.

8.7.3
CO_2: Gas of the Century

The final section on gas detection with IR cameras discusses applications for probably the most important gas of the twenty-first century. Carbon dioxide (CO_2) is a natural gas that has found numerous applications in various industries. In addition, it is a byproduct of the combustion of carbon-based energy sources. As a result, at present, it makes the most important contribution to the anthropogenic greenhouse effect [38, 39]. To mitigate climate change due to anthropogenic emissions of greenhouse gases, many large corporations in the field of energy plan to introduce so-called carbon capture and storage (CCS) technologies. The concept of CCS is briefly summarized in Figure 8.32 (from [40]).

CO_2 from primary sources, for example large power plants, is captured and transported to several storage sites (mostly in pipelines). Storage can occur, for example, in deep geological formations, oil wells, the deep ocean, or in the form of mineral carbonates.

The introduction of CCS technologies will raise the following issues:

- Verification that power plants do indeed no longer emit CO_2;
- Verification that pipelines do not leak;
- Verification that underground storage is safe, that is, that there are no leaks.

For all of these verification issues, analytical tools are needed that easily allow monitoring of pipelines or sites by sensitive detection systems for gaseous CO_2.

As demonstrated by the examples below, IR thermal imaging provides an excellent tool for this purpose [12, 13, 41]. As an imaging device it offers in particular the possibility of fast leak detection in large areas. Once leaks are localized, the

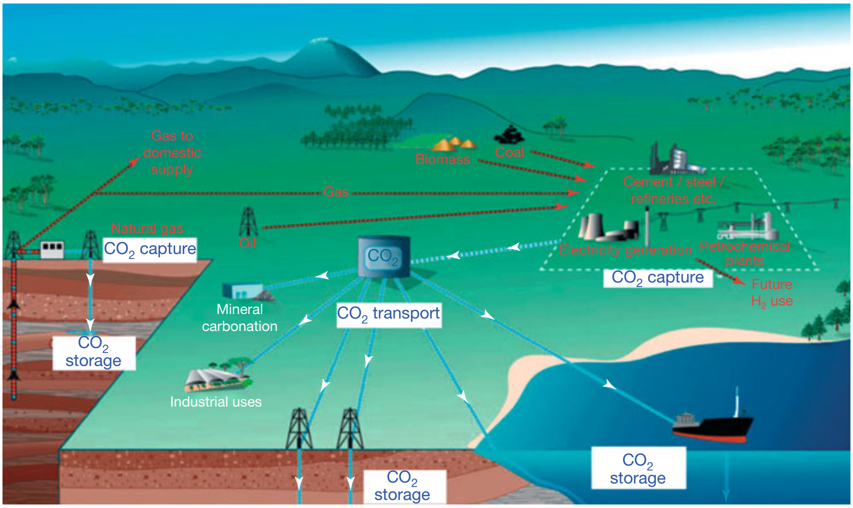

Figure 8.32 CCS systems showing carbon sources for which CCS might be relevant and options for the transport and storage of CO_2. (Reproduced from [40], Chapter 4, Energy supply, Figure 4.22.)

method may be combined with other conventional and very sensitive spot measurement techniques for CO_2. We also note that recently, a passive technique was developed to detect large amounts of CO_2 degassing from the earth's surface by secondary thermal effects [42].

In what follows, a number of different thermal imaging experiments with CO_2 are presented [12, 13]. These include a comparison of broadband detection versus narrowband detection in the MW range, detection of low concentrations on the order of 500 ppm over short distances, detection of CO_2 in exhaled air and in combustion processes, and the visualization of absorption versus scattering and emission of radiation by gases. Most importantly, detection of well-defined gas flows, simulating gas leaks, is presented, and it is demonstrated that CO_2 gas flows as small as $1\,\text{mL min}^{-1}$ corresponding to CO_2 masses of about 1 kg/year may be detected.

The principles of two of the used setups are shown in Figure 8.33. MW cameras were used to observe a blackbody emitter that served as background of well-defined temperature and emissivity. In some cases, the blackbody emitter was replaced by a large-area hot plate, which was not as homogeneous, but still nicely served as background object. We used both a broadband THV 550 Agema camera (3–5 μm range/PtSi detector/320 × 240 pixels) as well as a broadband FLIR SC6000 camera (1.5–5 μm range/InSb detector/640 × 512 pixels). The latter allowed us to insert commercially available room temperature narrowband spectral filters adjusted to the absorption feature of CO_2 gas (here Spectrogon 4235 filter [14]).

CO_2 was introduced between the camera and the blackbody source either in cells of well-defined length at well-defined pressures (Figure 8.33a) or while flow-

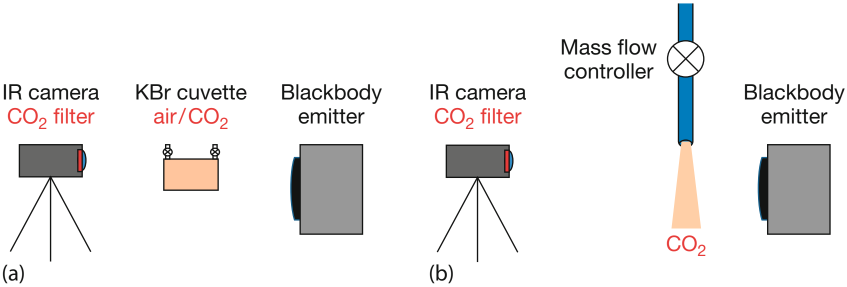

Figure 8.33 Experimental setup. An IR camera with or without a filter detects radiation changes from a background object of known temperature and emissivity.

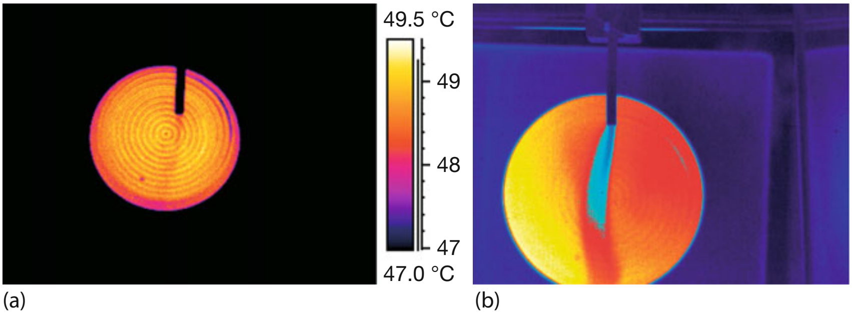

Figure 8.34 Detection of same flow of CO_2 gas (100 mL min^{-1}, tube inner diameter 6 mm) with a broadband MW camera (THV 550) (a) and a narrowband camera (SC6000 plus filter) (b).

ing out of a tube of well-defined diameter with a known flux, defined by mass flow controllers (Figure 8.33b), or it could be emitted in unknown concentrations and gas flows due to a variety of processes.

8.7.3.1 Comparison of Broadband and Narrowband Detection

Although broadband MW cameras may already easily detect CO_2 by its absorption [8, 13], it is customary to use narrowband filters. Figure 8.34 illustrates a comparison between IR images of a broadband MW camera (3–5 μm) and a narrowband camera (SC6000 with warm filter 4235). Both cameras observe the same CO_2 flow in front of a blackbody source, operated at around 50 °C.

Whereas the broadband camera hardly detects this small CO_2 flow of only 100 mL min^{-1}, the narrowband detection substantially improves the sensitivity of the camera. In addition, the InSb detector of the SC6000 camera is more sensitive than the PtSi detector of the THV 550 camera. Reducing the gas flow allows us to estimate the differences in sensitivity. In the present case for the given conditions (T_{BB} = 50 °C, tube inner diameter 6 mm), the difference in the lowest detectable gas flows was around a factor of 20–30, that is, the narrowband camera system allowed us to detect gas flows that were smaller by a factor of 20–30 than those observed with a broadband camera (see following discussion on detection lim-

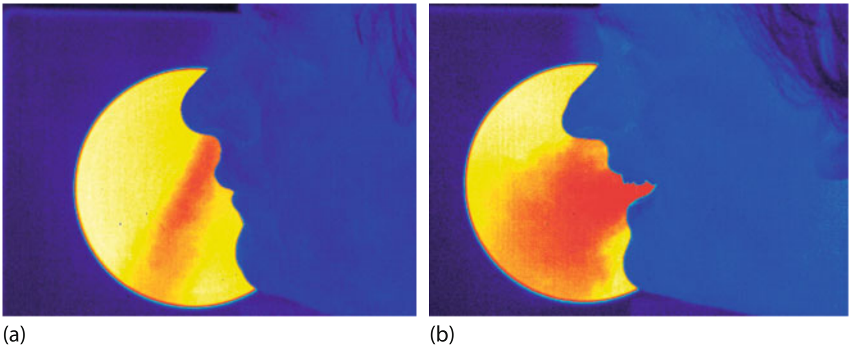

(a) (b)

Figure 8.35 The authors (K.-P.M. (a), M.V. (b)) while exhaling through the nose and (while laughing) through the mouth in front of a 50 °C blackbody source.

its). *For the practitioner, the smallest detectable gas flows will always be seen much easier as signal changes in life image sequences.* This is due to the fact that the image processing within the brain is in general very sensitive to movements in our field of view, that is, image changes as a function of time. In still images, it is much harder to detect such small variations of gas concentrations. All of the following CO_2 experiments were recorded with the narrowband camera system.

8.7.3.2 Detecting Volume Concentration of CO_2 in Exhaled Air

Being the "exhaust gas" of human breathing, CO_2 is directly related to human energy production upon oxygen intake. The average CO_2 concentration in the air, that is, the concentration while inhaling air, is about 400 ppm (in the open air) and up to around 800 ppm in closed rooms (depending on the size of the room, number of people in the room as function of time, ventilation of the room, etc.). The increase of CO_2 concentration in closed rooms is due to breathing. Typical carbon dioxide concentration in exhaled air is around 4–5 vol% (40 000–50 000 ppm), that is, around a factor of 100 larger than typical concentrations in fresh air.

Figure 8.35 depicts qualitative examples for detection of CO_2 concentrations upon exhaling air. Exhaling may occur through the nose (opening diameter around 1 cm) (Figure 8.35a) or through the mouth (opening diameter 4–5 cm) (Figure 8.35b). In both cases, the absorption of background IR radiation due to the colder gas is easily visible.

8.7.3.3 Absorption, Scattering, and Thermal Emission of IR Radiation

Figure 8.36 depicts the influence on scattering of hot objects nearby on IR gas imaging. The background blackbody source was set to 80 °C, the CO_2 gas was at room temperature (about 20 °C), and as additional radiation source we used a soldering iron tip at 400 °C, which could be freely moved in the region close to the gas flow. The orientation of camera, gas tube, and blackbody source was not changed.

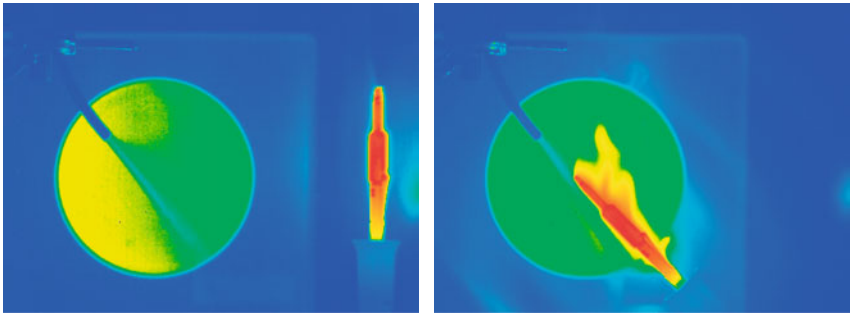
(a) (b)

Figure 8.36 Room temperature CO_2 gas flow at 700 ml min^{-1} in front of black body source set to 80 °C. (a) The cold gas leads to attenuation of IR radiation. (b) Scattering of IR radiation from a hot soldering iron at 400 °C, allows simultaneous observation of gas absorption and scattering. The soldering iron was placed several centimeters in front of the gas flow.

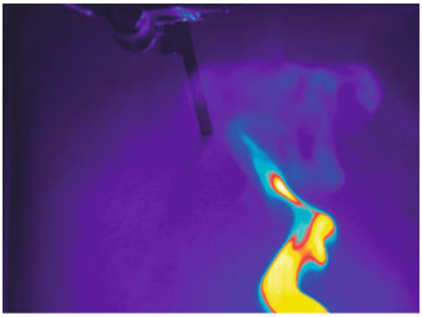

Figure 8.37 CO_2 flow from tube in front of slightly warmer background as well as hot CO_2 combustion product of a lighter flame (the visual flame top was about 10 cm below the lower edge of the IR image).

In Figure 8.36a, the cold gas (blue) clearly attenuated the IR radiation from the blackbody source (yellow–green). If the additional hot object, the soldering iron (red), is far away (Figure 8.36a), scattering contributions from CO_2 are too small to be detected. However, moving the iron tip to a distance of several centimeters from the outflow of cold gas (Figure 8.36b), one immediately observes gas features of apparently higher temperature due to the scattering of IR radiation.

In principle, it is also possible to have a small amount of thermal emission from the heated gas close to the soldering iron tip and in practice it may become difficult to separate the scattering from the thermal emission contribution of the gas. In order to estimate the amount of thermal emission, one needs to calculate its emissivity and its optical thickness (Section 8.5). Qualitatively, thermal emission may be observed isolated by studying combustion processes which produce hot CO_2. In the laboratory setup, a cigarette lighter was placed below the blackbody source. It was observed with the IR camera such that the visually observable flame top was about 10 cm below the lower edge of the IR image. Figure 8.37 shows an example: hot CO_2 gas was rising and – while still being hot – emitting IR radiation. Besides, in the upper part of the image, one can still observe the colder gas flowing out of the tube.

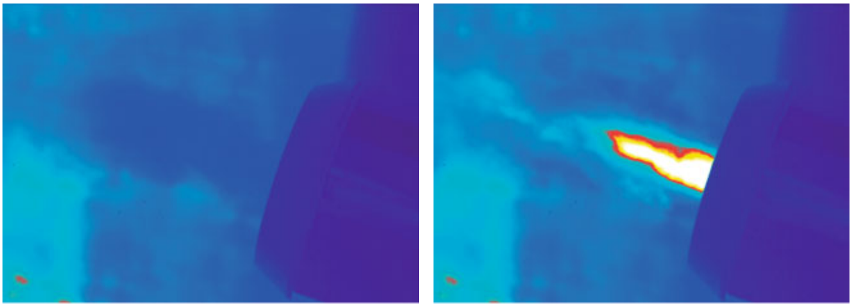
(a) (b)

Figure 8.38 Warm (a) and hot (b) CO_2 exhaust gas from combustion in a motorcycle engine. The background was at a temperature of about 80 °C. (Use of motorcycle, thanks to F. Pinno.)

An even more impressing visualization of CO_2 combustion products is obtained by studying the exhaust of combustion engines. Figure 8.38 depicts the exhaust pipe of a motorcycle (Suzuki 1100 GSXF, 98 hp) in front of a heating plate which had an inhomogeneous temperature distribution with an average temperature of about 80 °C.

Figure 8.38a shows CO_2 absorption in the exhaust after starting the engine and running it at low power. Obviously, the exhaust gases had enough time to cool down within the exhaust pipe. Therefore, only some absorption of IR radiation in front of the warm background was observed. However, while the engine was operated (for a short time) at full power, rather hot exhaust gases were emitted, which showed up in the IR image Fig. 8.38b.

8.7.3.4 Quantitative Result: Detecting Minute Amounts of CO_2 in Air

For quantitative measurements of CO_2, we used a cell of 10 cm in length with KBr windows of about 95% transmission. It can be filled with any desired partial pressure. At first, the cell was evacuated and observed while ambient air was streaming in with typical CO_2 volume concentrations in closed rooms of around 400–800 ppm. Figure 8.39 shows the following result: the change in CO_2 content is due to the 10 cm cell while the total measurement distance was about 1 m. The observed change means that we are able to detect minute changes in CO_2 concentrations of 40–80 ppm over measurement distances of 1 m.

The high sensitivity of the measurements even allowed us to detect the additional attenuation due to pressure broadening. Figure 8.40 compares signals of the same partial pressure of CO_2 (51 hPa) for two different total pressures of 51 hPa (pure CO_2) and 1029 hPa. Higher atmospheric pressure results in pressure broadening, which itself leads to larger attenuation of the IR radiation.

8.7.3.5 Quantitative Result: Detection of Well-Defined CO_2 Gas Flows from a Tube

The most important application of any GasFind camera should be its leak detection capability. Figure 8.41 depicts results for varying CO_2 flow in front of a blackbody source operating at around 50 °C. The CO_2 flow (100 vol%) was adjusted

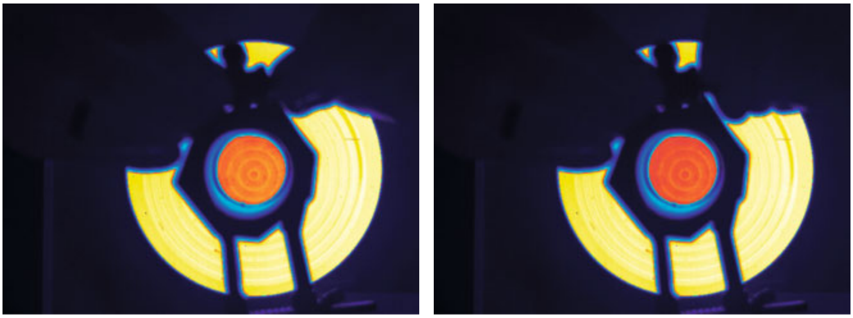
(a) (b)

Figure 8.39 Cell with vacuum (a) and filled (b) with room temperature air (CO_2 concentration 400–800 ppm).

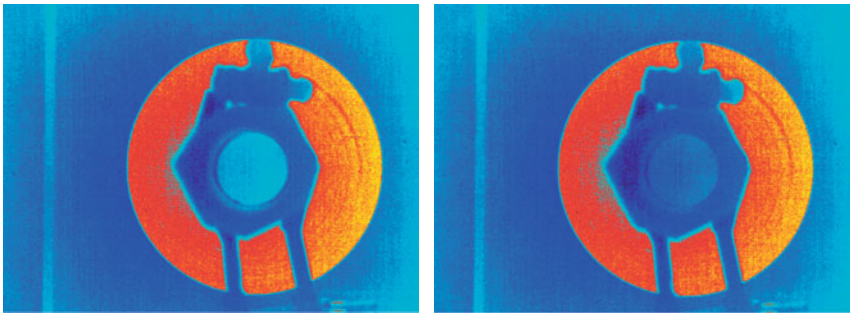
(a) (b)

Figure 8.40 Pressure broadening in CO_2 spectra: cell of 10-cm length with KBr windows in front of blackbody source ($T = 35\,°C$). The CO_2 partial pressure was 51 hPa in both cases with total pressures of 51 hPa (a) and 1029 hPa (b).

using a mass flow controller, the gas was exiting a tube of 6 mm inner diameter several centimeters from the source.

The sequence in Figure 8.41 shows results for mass flows between 5 and 1000 mL min^{-1}. Despite the large density of CO_2 compared to air, small flow rates lead to fumes which are easily driven by currents of the surrounding air. Flow rates between 100 and 500 mL min^{-1} result in nearly laminar flow. For flow rates around 1000 mL min^{-1}, turbulences develop.

The main question concerns the lower limit of detectable gas flow. It depends on a combination of background signal and chosen integration time for the detector (most commercial IR cameras do not allow the user to select integration time). In order to more closely resemble typical outdoor situations, experiments were carried out for blackbody background temperatures only slightly above room temperature ($T_{BB} = 35\,°C$). Owing to the corresponding lower radiation signal (with respect to a 50 °C blackbody) longer integration times could be used, yielding a better signal-to-noise ratio. So far, gas flows as low as 1 mL min^{-1} could be

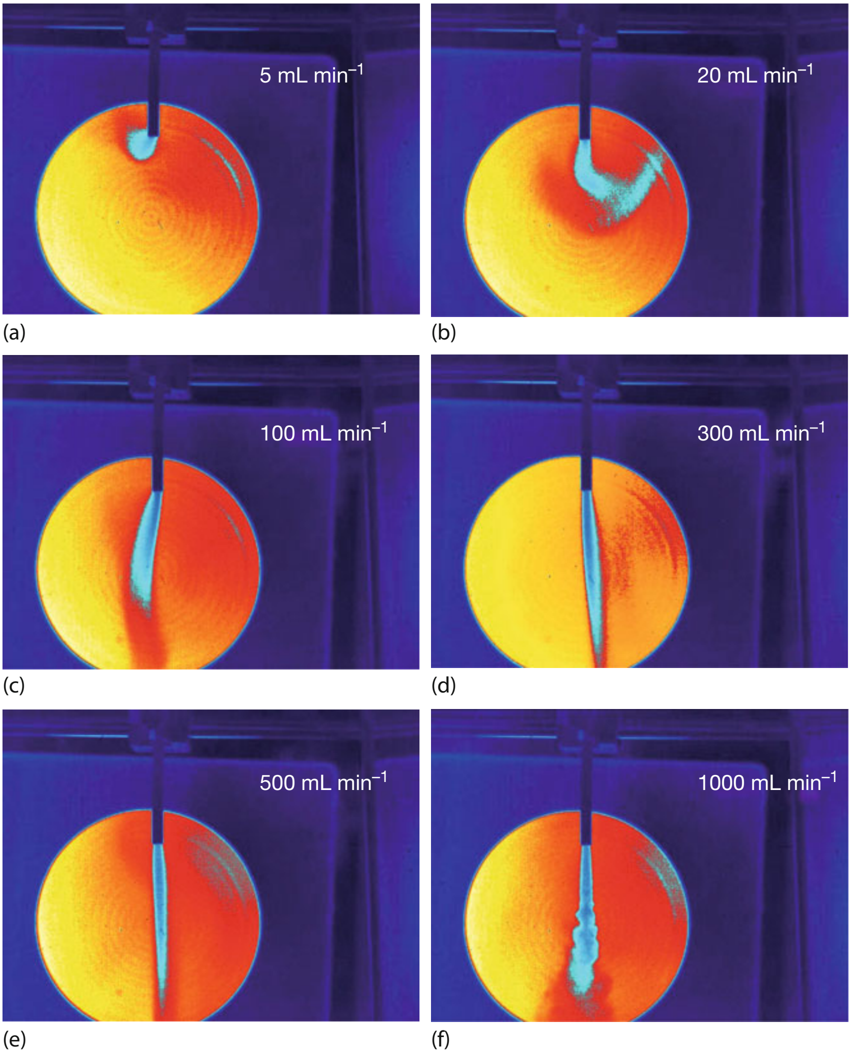

Figure 8.41 Raw data of detected CO_2 flows (in milliliters per minute): 5 (a), 20 (b), 100 (c), 300 (d), 500 (e), and 1000 (f). The SC6000 camera was operated with an uncooled narrow band filter in front of a black body emitter operated at $T = 50\,°C$.

detected. In still images, such a small gas flow is sometimes hard to detect; it is easier to observe changes in life images. GasFind cameras use a high-sensitivity mode (HSM) that is based on a consecutive image subtraction procedure (Section 3.5.1.4, also Figure 3.67).

The laboratory results suggest that CO_2 with IR cameras is suitable for analyzing gas leaks. The lowest detected gas flows so far of 1 mL min^{-1} would correspond to 0.06 L h^{-1}, 1.44 L/day, or $\approx$ 0.5 m^3/year. Using a density of CO_2 (about

$2\,\mathrm{kg\,m^{-3}}$), it is therefore possible to detect emissions as low as about 1 kg/year from individual leaks. Even for much less favorable conditions in industry, the lowest detectable gas flows of, say, $100\,\mathrm{mL\,min^{-1}}$, that is, $\approx$ 100 kg/year, should be readily observable. Once leaks are localized, the method may be combined with other more sensitive CO_2 spot measurement techniques.

It is indeed a pleasant surprise to learn that now, about 8 years after commercial CO_2 cameras were first proposed by one of the authors while on sabbatical at FLIR/ITC in Boston [12, 13], they are finally available.

Looking to the future, we mention another possibility for increasing the sensitivity of such gas-sensitive cameras. As is well known from other spectroscopic techniques, it would make sense to use two warm filters (of nonabsorbing materials) to detect the object signal through the gas, one being off resonance (no absorption) and the other one on resonance (absorption). The ratio of these two signals directly reflects the gas absorption very sensitively. Inserting warm filters in IR cameras should pose no problems. It is already common practice when changing the temperature ranges of IR cameras.

8.A
Appendix: Survey of Transmission Spectra of Various Gases

Here a qualitative survey of the spectra of important VOCs and inorganic molecules is given. Spectra are from own calculations, own measurements, and after data from [2]. They were recorded using a variety of methods (prism and grating spectrometers as well as FTIR spectrometers) by many different groups. Although for many of these spectra recording conditions would allow for a quantitative description, we only show qualitative spectra since conditions like gas pressure and optical path length differ from sample to sample such that the transmission at the center of the absorption bands will be similar. More details can be found, for example, on the web [2]. We note that spectra are usually recorded as a function of wavenumber, which is proportional to the frequency or energy of the radiation. Here we present the data as a function of wavelength since the various camera systems are usually characterized in terms of wavelength ranges. Table 8.A.1, reproduced here for completeness, summarizes all substances whose spectra can be found in this appendix.

Table 8.A.1 Some natural and industrial gases, including hydrocarbons and other organic compounds, that absorb in the thermal IR region.

Inorganic compounds	**Simple hydrocarbons**	**Simple multiple bond compounds**	**Benzene compounds**
H_2O water vapor	CH_4 methane	C_2H_2 ethylene	C_6H_6 benzene
CO_2 carbon dioxide	C_2H_6 ethane	C_3H_6 propylene	C_7H_8 toluene
CO carbon monoxide	C_3H_8 propane	C_4H_6 butadiene	C_8H_{10} *p*-xylene
NO nitric oxide	C_4H_{10} butane	**Some alcohols**	C_8H_{10} ethylbenzene
N_2O nitrous oxide	C_4H_{10} isobutane	CH_3OH methanol	$C_{10}H_8$ naphthalene
NH_3 ammonia	C_5H_{12} pentane	C_2H_5OH ethanol	**Hydrocarbons with halogens**
O_3 ozone	C_6H_{14} hexane	C_3H_7OH propanol	CCl_2F_2 Freon 12 (CFC12)
H_2S hydrogen sulfide	C_8H_{18} octane	**Ketones/ethers**	$CHClF_2$ Freon 22 (CFC22)
SO_2 sulfur dioxide	C_8H_{18} isooctane	C_3H_6O acetone	CHF_3 Freon 23 (CFC23)
CS_2 carbon disulfide	$C_{12}H_{26}$ dodecane	C_4H_8O MEK	$CHCl_3$ chloroform
SF_6 sulfur hexafluoride	$C_{16}H_{34}$ hexadecane	$C_6H_{12}O$ MIBK	CCl_4 carbon tetrachloride
–	–	$C_5H_{12}O$ MTBE	$COCl_2$ carbonyl chloride

8.A.1
Inorganic Compounds 1

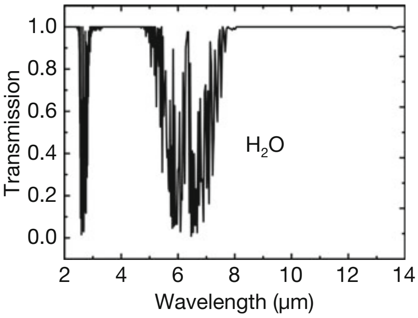

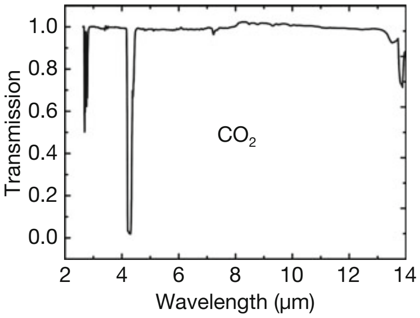

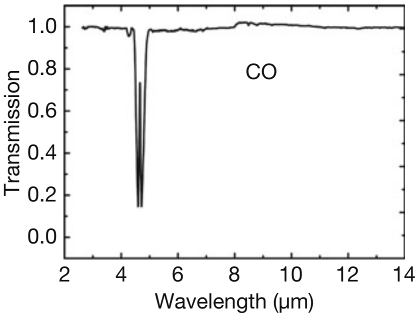

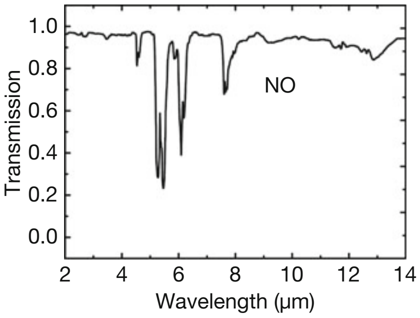

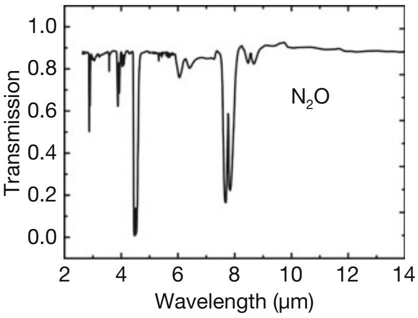

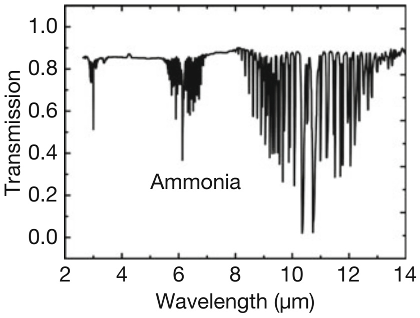

8.A.2
Inorganic Compounds 2

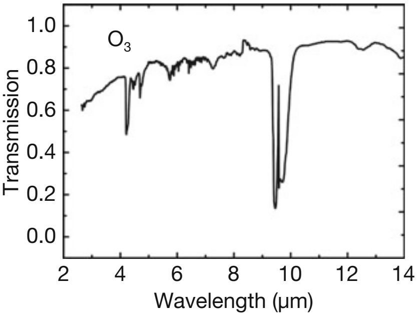

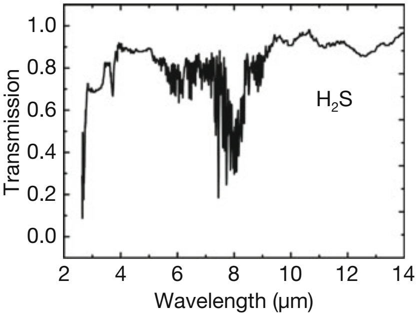

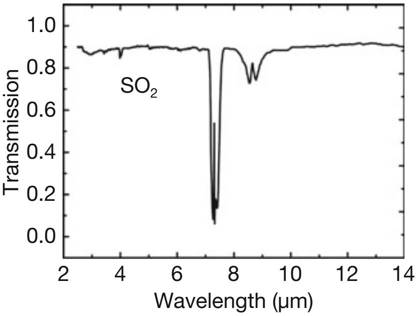

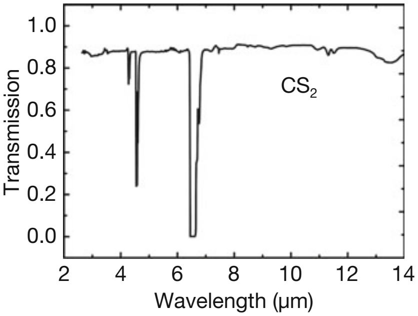

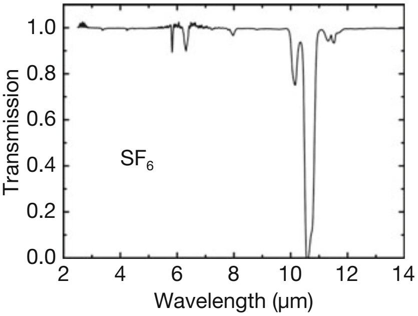

8.A.3

Simple Hydrocarbons 1

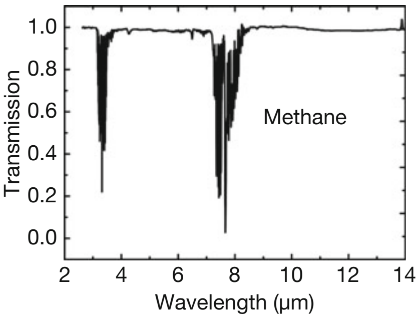

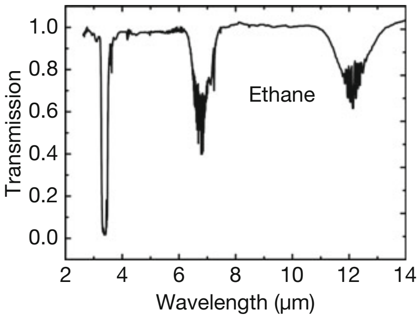

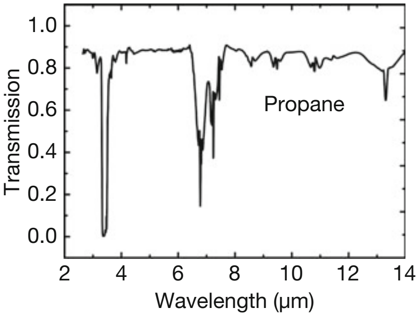

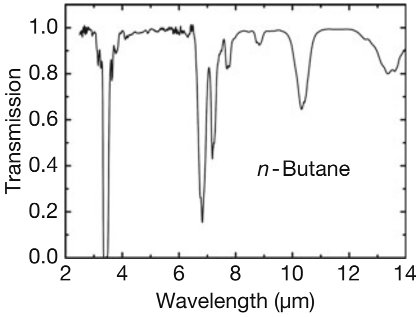

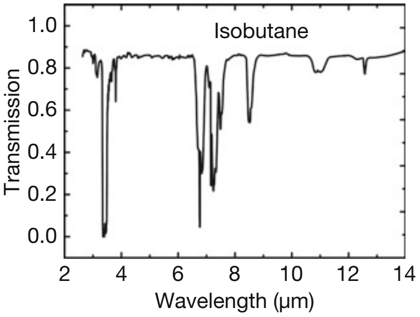

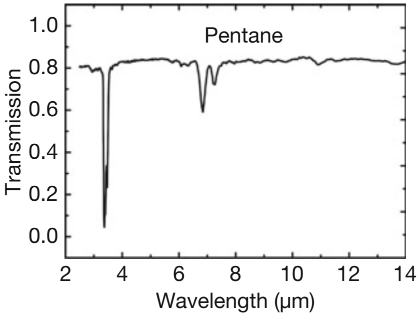

8.A.4
Simple Hydrocarbons 2

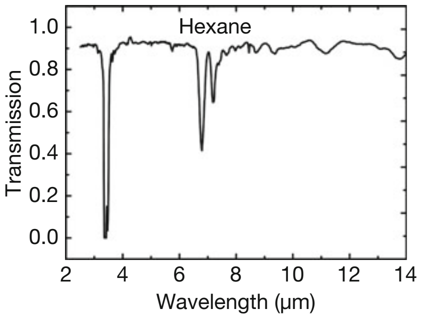

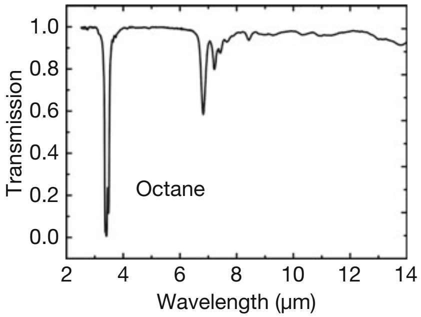

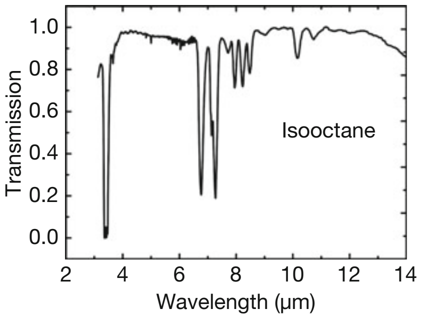

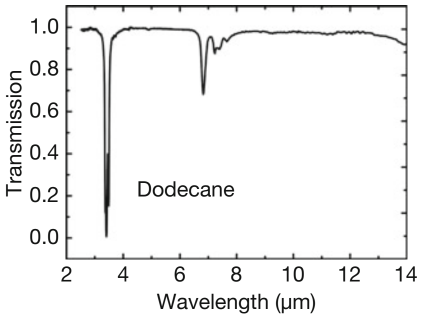

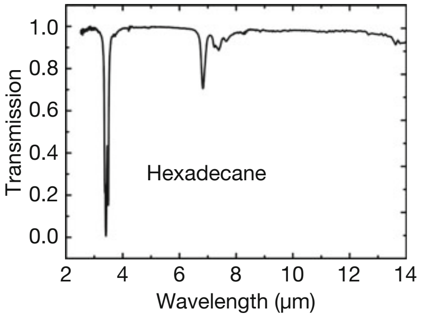

8.A.5

Simple Multiple Bond Compounds and Some Alcohols

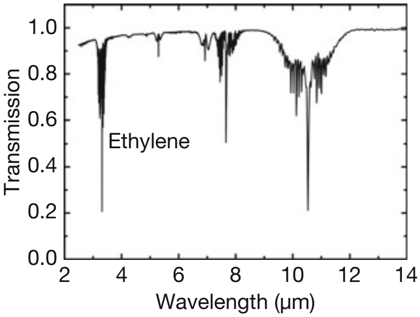

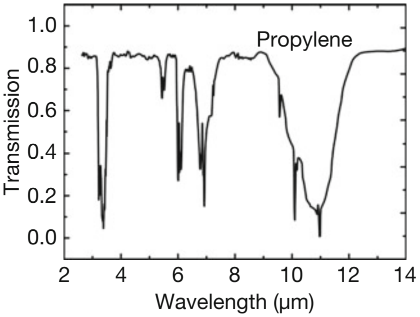

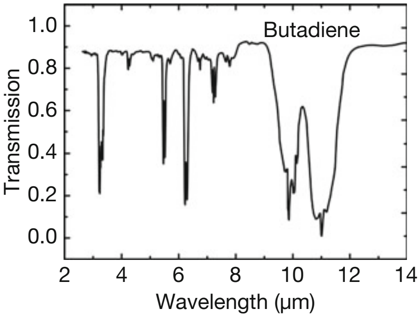

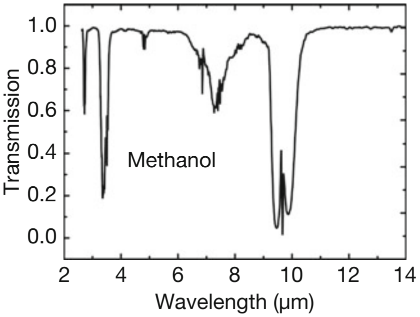

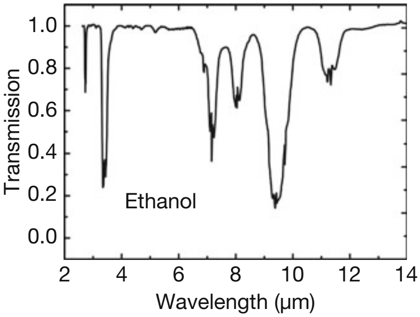

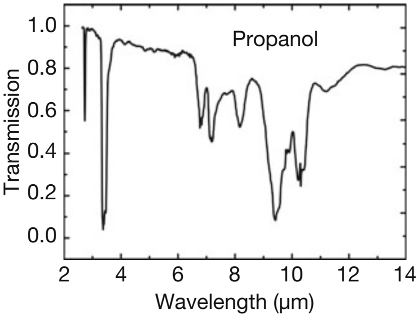

8.A.6
Some Ketones/Ethers

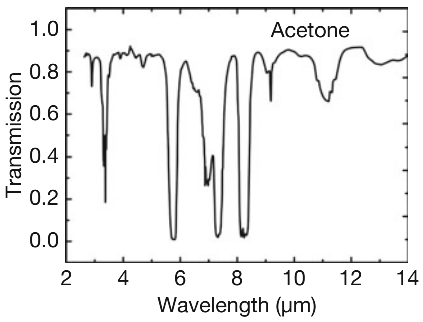

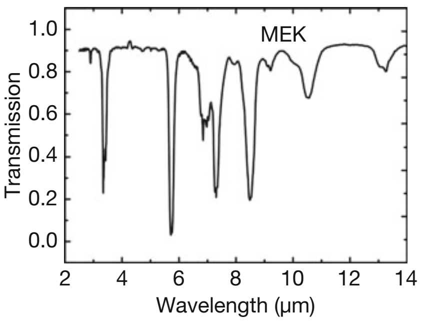

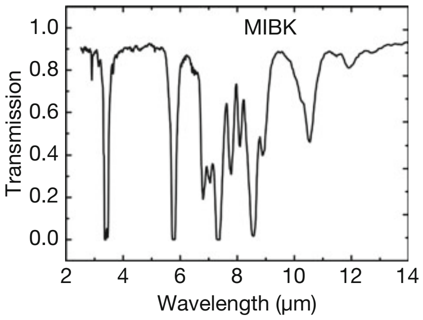

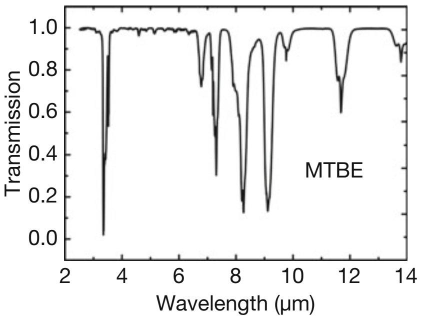

8.A.7

Some Benzene Compounds

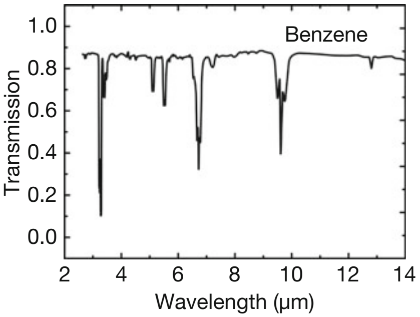

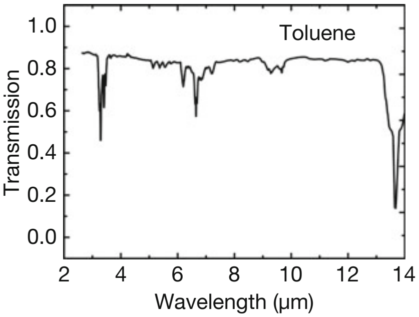

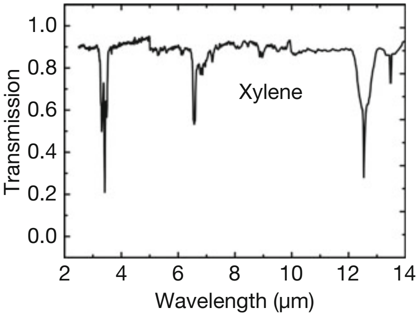

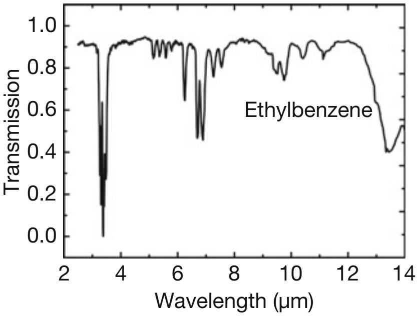

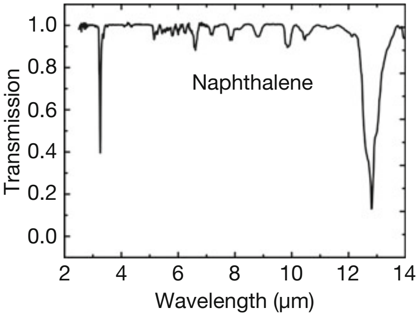

8.A.8

Some Hydrocarbons With Halogens

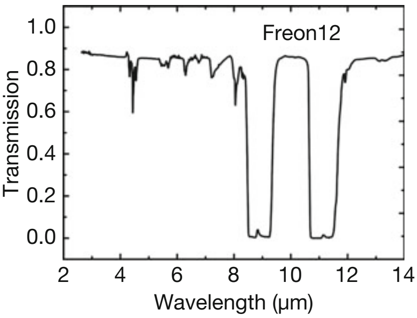

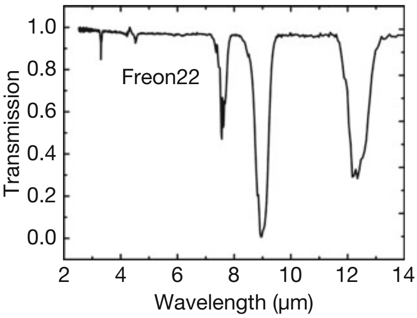

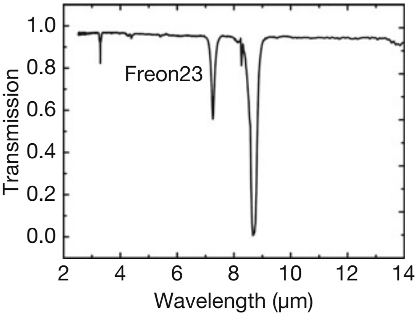

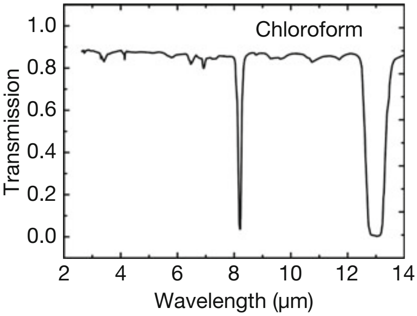

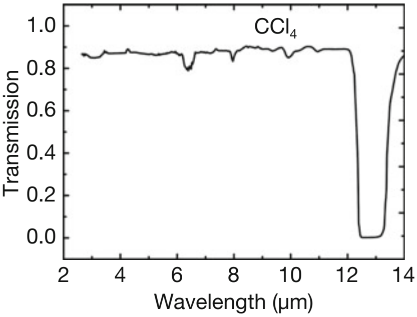

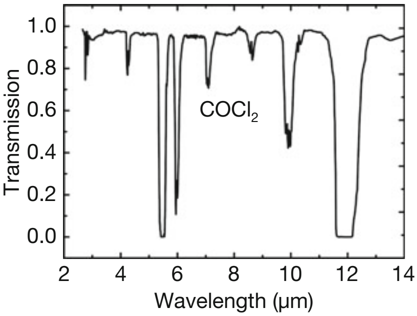

References

1 Günzler, H. and Gremlich, H.-U. (2002) *IR Spectroscopy – An Introduction*, Wiley-VCH Verlag GmbH.

2 Database of IR Spectra and Properties of Chemical Compounds. http://webbook.nist.gov/chemistry/form-ser.html (accessed May 2017).

3 Socrates, G. (2001) *Infrared and Raman Characteristic Group Frequencies, Tables and Charts*, 3rd edn, John Wiley & Sons, Inc.

4 Bell, R.J. (1972) *Introductory Fourier Transform Spectroscopy*, Academic Press, New York.

5 Kauppinen, J. and Partanen, J. (2001) *Fourier Transform in Spectroscopy*, Wiley-VCH Verlag GmbH, Berlin.

6 Richards, A. and Johnson, G. (2005) Radiometric calibration of infrared cameras accounting for atmospheric path effects. Thermosense XXVII. Proc. SPIE, vol. 5782, 19–28.

7 Strachan, D.C. *et al.* (1985) Imaging of hydrocarbon vapours and gases by infrared thermography. *J. Phys. E: Sci. Instrum.*, **18**, 492–498.

8 Karstädt, D., Möllmann, K.P., Pinno, F., and Vollmer, M. (2006) Influence of gaseous species on thermal infrared imaging. Inframation 2006. Proceedings, vol. 7, pp. 65–78.

9 www.flir.com (accessed May 2017).

10 Furry, D., Richards, A., Lucier, R., and Madding, R.P. (2005) Detection of Volatile Organic Compounds (VOC's) with a spectrally filtered cooled midwave infrared camera. Inframation 2005, Proceedings, vol. 6, pp. 213–218.

11 Madding, R. and Benson, R. (2007) Sulphur Hexafluoride (SF6) insulating gas leak detection with an IR imaging camera. Inframation 2007, Proceedings, vol. 8, pp. 89–94.

12 Vollmer, M. and Möllmann, K.-P. (2009) Perspectives of IR imaging for industrial detection and monitoring of CO_2. Proc. Conf. Temperature PTB, Berlin. ISBN:3-9810021-9-9.

13 Vollmer, M. and Möllmann, K.-P. (2009) IR imaging of gases: potential applications for CO_2 cameras. Inframation 2009, Proceedings, vol. 10, pp. 99–112.

14 www.spectrogon.com (accessed May 2017).

15 Vollmer, M. and Möllmann, K.-P. (2009) IR imaging of gases: Quantitative analysis. Inframation 2009, Proceedings, vol. 10, pp. 113–123.

16 Benson, R.G., Panek, J.A., and Drayton, P. (2008) Direct measurements of minimum detectable vapor concentration using passive infrared optical imaging systems. Paper 1025 of Proc. 101st ACE meeting (held June 2008 in Portland/Oregon) of the Air & Waste and Management Association.

17 Edwards, D.K. (1960) Absorption by infrared bands of carbon dioxide gas at elevated pressures and temperatures. *J. Opt. Soc. Am.*, **50**, 617–626.

18 Burch, D.E. *et al.* (1962) Total absorptance of CO_2 in the infrared. *Appl. Opt.*, **1**, 759–765.

19 Lapp, M. (1960) Emissivity calculations for CO_2. part 1 of PhD thesis, Cal Technology.

20 Incropera, F.O. and DeWitt, D.P. (1996) *Fundamentals of Heat and Mass Transfer*, 4th edn, John Wiley & Sons, Inc.

21 Schack, K. (1970) Berechnung der Strahlung von Wasserdampf und Kohlendioxid. *Chem. Ing. Tech.*, **42** (2), 53–58.

22 DeWitt, D.P. and Nutter, G.D. (1988) *Theory and Practice of Radiation Thermometry*, John Wiley & Sons, Inc., New York.

23 (a) Baehr, H.D. and Stephan, K. (2006) *Wärme – und Stoffübertragung*, 5th German edn, Springer-Verlag;
(b) Baehr, H.D. and Stephan, K. (2006) *Heat and Mass Transfer*, 2nd English edn, Springer, Berlin.

24 (a) Vollmer, M. (2005) Hot gases: transition from line spectra to thermal radiation. *Am. J. Phys.*, **73**, 215–223; see also comment by
(b) Nauenberg, M. (2007) *Am. J. Phys.*, **75**, 947; reply to comment (2007) *Am. J. Phys.*, **75**, 949.

25 Hodgkinson, J. and Tatam, R.P. (2013) Optical gas sensing: A review. *Meas. Sci. Technol.*, **24**, 012004 (59pp).

26 http://flir.com/GF-Series/ (accessed May 2017).

27 http://eyecgas.com/ (accessed May 2017).

28 System Second Sight® MS, www.bertin-instruments.com/products-range/gas-detection/ (accessed May 2017); and white paper from website: http://www.generalmonitorssystems.com/downloads/white_papers/Improving-plant-safety-with-IR-gas-cloud-imaging.pdf (accessed May 2017).

29 Naranjo, E., Baliga, S., and Bernascolle, P. (2010) IR Gas Imaging in an Industrial Setting, Thermosense XXXII, (eds R.B. Dinwiddie and M. Safai), Proc. SPIE, vol. 7661, 76610K.

30 www.ci-systems.com/SR-7000-Hyperspectral-Camera (accessed May 2017).

31 http://www.gitint.com/ MW VOC and LW SF6 systems available (accessed May 2017)

32 Application Note AN #91, *HI 90 - Hyperspectral Imaging System*, see www.bruker.com/products/infrared-near-infrared-and-raman-spectroscopy.html (accessed May 2017).

33 Harig, R., Matz, G., Rusch, P., Gerhard, H.-H., Gerhard, J.-H., and Schlabs, V. (2005) New Scanning Infrared Gas Imaging System (SIGIS 2) for emergency response forces. Proc. SPIE, vol. 5995, 174–181, doi:10.1117/12.630818.

34 Telops application note, Airborne Midwave Infrared Mapping for Environmental Monitoring Applications, www.telops.com, accessed April 2016, see also Kastek, M., Piątkowski, T., and Trzaskawka, P. (2011) Infrared imaging Fourier transform spectrometer as the stand-off gas detection system. *Metrol. Meas. Syst.*, **XVIII** (4), 607–620.

35 Gross, K.C., Tremblay, P., Bradley, K.C., Chamberland, M., Farley, V., and Perram, G.P. (2010) Instrument calibration and lineshape modeling for ultraspectral imagery measurements of industrial smokestack emissions. Proc. SPIE, vol. 7695, 769516-1.

36 Safitri, A. (2011) Infrared optical imaging techniques for gas visualization and measurement, PhD thesis, Texas A&M Univ.

37 http://www.providenceeng.com/services/technology/Optical-Gas-Imaging (accessed May 2017), see also US patent 9225915 B2, published 29 Dec. 2015; Y. Zeng, J. Morris, *Calibration and quantification method for gas imaging camera*

38 Houghton, J.T. *et al.* (eds) (2001) Climate Change 2001, The Scientific Basis, Contribution of Working Group I to 3rd Assessment Report of the Intergovernmental Panel on Climate Change, IPCC.

39 Solomon, S. *et al.* (eds) (2007) Climate Change 2007, The Physical Science Basis, Contribution of Working Group I to 4th Assessment Report of the Intergovernmental Panel on Climate Change, IPCC.

40 Metz, B. *et al.* (eds) (2007) Climate Change 2007, Mitigation of Climate Change, Contribution of Working Group III to 4th Assessment Report of the Intergovernmental Panel on Climate Change, IPCC.

41 Yoon, H.W. *et al.* (2006) Flow visualization of heated CO_2 gas using thermal imaging. Thermosense XXVIII. Proc. SPIE, vol. 6205, 62050U-1.

42 Tank, V., Pfanz, H., and Kick, H. (2008) New remote sensing techniques for the detection and quantification of earth surface CO_2 degassing. *J. Volcanol. Geotherm. Res.*, **177**, 515–524.

Chapter 9
Microsystems

9.1
Introduction

Microsystems engineering is likely to be a key technology in the twenty-first century. Microsystems promise to revolutionize nearly every product category. Microelectromechanical systems (MEMS) are the integration of mechanical, optical, and fluidic elements, sensors, actuators, and electronics through microfabrication technologies. MEMS are made up of components with a characteristic size in the micrometer region. They are also referred to (in Japan) as *micromachines* or (in Europe) microsystems technology or MST. Microsystems engineering is an enabling technology that allows the development of smart products. It augments the computational ability of microelectronics with the perception and control capabilities of microsensors and microactuators and expands the range of possible applications. Upon production, every technical product will be characterized such that its properties upon variation of relevant parameters are known.

The concepts of measuring and testing technology known from, for example, microelectronics or precision mechanics can, however, only be partially applied to microsystems because of the small size and the variety of physical principles used in the microsystem operation. Therefore, new testing methods must be developed to characterize the operation and important performance parameters of microsystems.

Many microsystems are characterized either by a uniform temperature or by a spatial temperature distribution. In addition, thermal response times belong to the most important system parameters. Owing to the small heat capacitance, any contact probe for temperature measurement will induce appreciable thermal conductive heat transfer, which will either complicate the analysis or even make it impossible. Therefore, a contactless measurement is needed to analyze spatial and transient temperature distributions for microsystem components (reactors, sensors, actuators). Obviously, thermography can play an important role in the thermal characterization of different microsystems. It can support the research and development work and control the system operation without modifying system performance [1, 2].

Infrared Thermal Imaging, Second Edition. M. Vollmer and K.-P. Möllmann.
© 2018 WILEY-VCH Verlag GmbH & Co. KGaA. Published 2018 by WILEY-VCH Verlag GmbH & Co. KGaA.

In what follows, exemplary results are presented for microfluidic systems, sensors, and microsystems that utilize an electric-to-thermal energy conversion during operation.

9.2
Special Requirements for Thermal Imaging

The thermography of microsystems is affected by a number of problems that are usually not encountered in the study of macroscopic objects. The specific requirements concern suppression of mechanical instabilities and vibrations, the need for close-up lenses or microscope objectives, and the possibility of high-speed recording.

9.2.1
Mechanical Stability of Setup

Owing to the small size of microstructures, a very stable mechanical construction of a test bench is necessary to avoid the effects of mechanical instabilities or mechanical vibrations on the thermal imaging results. A breadboard or, even better, a vibration-insulated optical table with adjustable sample and camera holders is well suited for microscopic thermal imaging analysis (Figure 9.1).

9.2.2
Microscope Objectives, Close-up Lenses, Extender Rings

The study of microsystems usually requires a spatial resolution of thermal imaging much better than 1 mm. In practice, the requirement depends on the microstructure size. Infrared (IR) cameras with standard objectives only allow spatial resolutions of around 1 mm, so they must be equipped with an additional close-up lens to increase the spatial resolution (Section 2.4.4.3). For cameras with exchangeable lenses, one may also use extender rings (Section 2.4.4.4). The maximum spatial resolution is achieved using microscope optics (Figure 2.77).

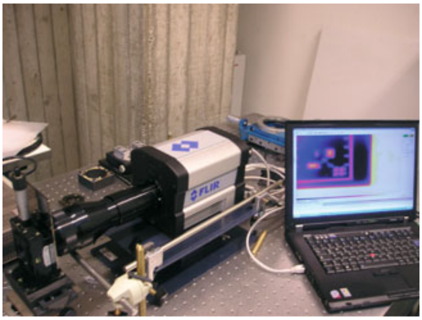

Figure 9.1 Experimental setup for microscopic thermal imaging using an optical table.

Figure 9.2 demonstrates an improvement of the optical resolution for a miniaturized thermal emitter in a transistor housing using different components. The use of additional optical components to increase the spatial resolution of the imaging is accompanied by a decreasing working distance (camera objective to object). Thus, the Narcissus effect for nonblack objects may become important (Section 2.4.4.5) [3].

Before analyzing the temperatures of microscopic structures, the spatial resolution of the used equipment needs to be determined to avoid temperature measurement errors. An easy method to determine spatial resolution uses chromium structures with a well-defined size on a photolithography mask with a glass substrate. The mask should be heated, and the emissivity contrast of the mask can be used for the measurement. Figure 9.3 depicts a measurement across a 34 μm thick line on the mask. Compared to the visible microscope image (Figure 9.3a, top), the IR image appears blurred (Figure 9.3a, bottom). Raw signal data across the line were analyzed and a signal plateau was formed by about six pixels (Figure 9.3b). If this number of pixels is compared with the linewidth of 34 μm, one may conclude that for this camera equipment resolution per pixel is around 5–6 μm.

For a more detailed analysis, the modulation transfer function should be analyzed as described in Section 2.5.4.

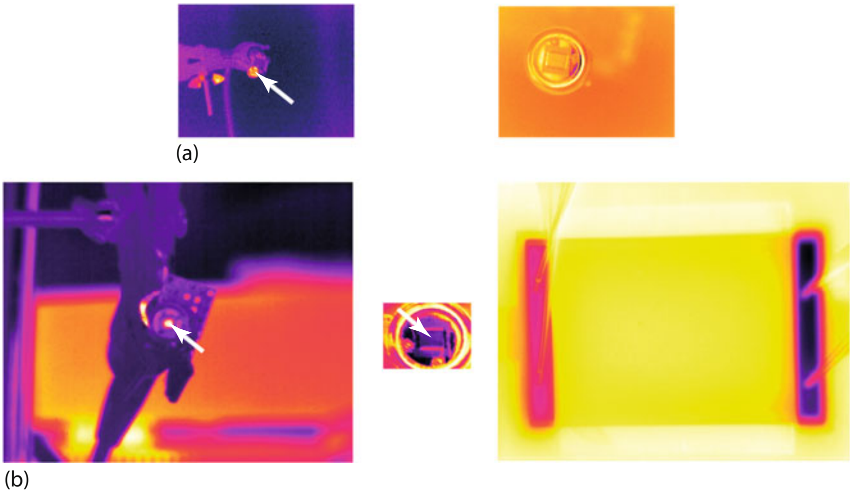

Figure 9.2 IR images of miniaturized IR emitter (size 2.1 × 1.8 mm^2) in TO-39 housing. Region of interest as indicated by arrows in images on left and in middle is shown expanded in images on right. (a) MW camera FLIR THV 550 (320 × 240 pixels) with a 24 optics (left) and an additional close-up lens (right). (b) MW camera FLIR SC6000 (640 × 512 pixels) with a 25 mm lens (left), additional extender ring (middle with 160 × 120 pixels), and microscope optics (right).

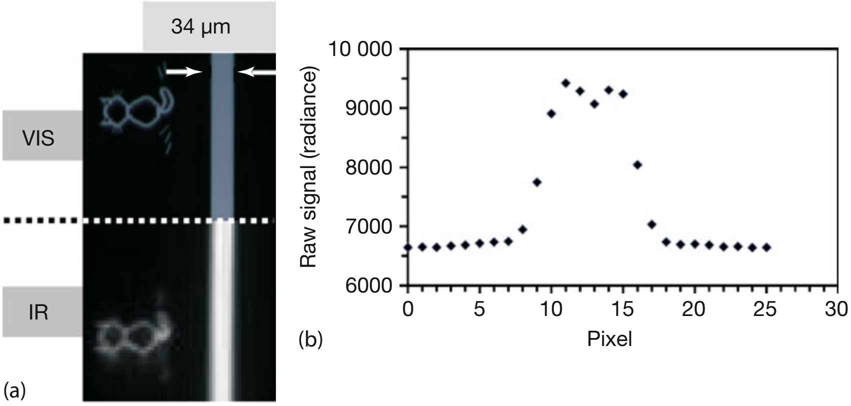

Figure 9.3 VIS microscope image (a) (top) and IR image (bottom) of a line with a width of 34 µm on a chromium mask. Raw signal profile of line measured in IR image (b) using SC6000 camera.

9.2.3
High-Speed Recording

Thermal processes such as heat transfer and temperature changes in microsystems are mostly characterized by small time constants in the millisecond to microsecond range owing to the low heat capacitance or thermal mass. For time-resolved thermal imaging, high-speed data acquisition is necessary. The limitation of the time resolution is given by the response time of the IR camera. For cameras with photon detectors the sometimes selectable integration time (microseconds to milliseconds) and for cameras with thermal detectors the detector time constant itself (some milliseconds) determine the camera response time (Section 2.5.5). Accurate temperature values and time-dependent temperature changes for transient thermal processes can only be measured if the response time of the camera is much smaller than the time constant of the microsystem. Therefore, the suitability of cameras equipped with bolometer focal-plane arrays and rather large time constants of 10 ms is limited. Instead, mostly photodetector cameras are used for transient thermal microsystem investigations.

9.2.4
Temperature Measurement

Accurate temperature measurements by radiation thermometry require an accurate knowledge of the object emissivity. Emissivity determination of objects within microsystems is, however, a complex problem.

Microsystems are made from a large variety of materials that are commonly not well suited for thermal imaging owing to their emissivity properties. Problems exist, for example, for highly reflecting materials (metals), semitransparent materials (glass or silicon), or selectively emitting materials (plastics). Surface modification by additional colors or emissivity strips as used in standard thermal imaging applications fails because this would modify the physical properties of the microsystems dramatically. If the determination of absolute temperature values is necessary, the emissivity can be determined by tempering the microsystem to a known temperature using a climatic exposure test cabinet. The emissivity adjustment at the camera is changed to measure the known object temperature. The object emissivity is given by the correct emissivity adjustment at the camera. The emissivity can also be estimated by IR spectroscopic measurements using an IR microscope [2].

9.3
Microfluidic Systems

9.3.1
Microreactors

Microreactors are devices in which chemical reactions take place in microchannels with typical lateral dimensions below 1 mm. Microreactors are normally operated continuously and offer many benefits compared to conventional-scale chemical reactors [4], such as large heat exchange coefficients owing to large surface-to-volume ratios. This allows fast and precise cooling, heating, or temperature stabilization, which are important for strong exothermic and dangerous chemical reactions.

Microreactors are fabricated using metals, glass, silicon, or ceramics. During the design process of a microreactor, first a theoretical model is established considering many parameters, for example, the chemistry of the reaction process and the fluidic properties of the reactants. However, studying reaction products alone without a detailed analysis of reactor temperatures and temperature distributions is usually insufficient if optimum operation parameters are to be found. Here thermal imaging comes into play.

Chemical reactions are connected with heat consumption or heat production, so the experimental analysis of the spatial reactor temperature distribution and the time-dependent temperature behavior along the reaction channels is important for reactor control. Measured temperatures can be used to verify and to improve design models. For this purpose, exemplary well known exothermal chemical reactions are used to characterize a microreactor during operation. Thermal imaging then allows one to find optimum operation parameters, that is, it can help to optimize reactor construction. The following examples will demonstrate the potential of thermal imaging in microreactor technologies.

9.3.1.1 Stainless Steel Falling Film Microreactor

The design and operational principle of the falling film reactor are shown in Figure 9.4. It can be used, for example, for gas–liquid reactions [5–8]. Figure 9.4b illustrates how thin films in the micrometer range are generated on a reaction

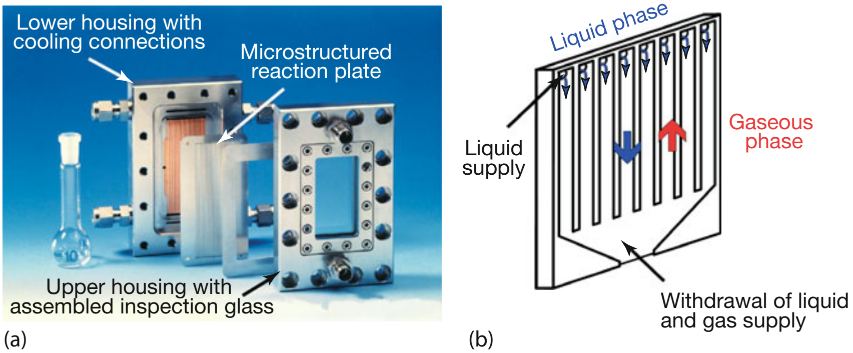
Lower housing with cooling connections
Microstructured reaction plate
Upper housing with assembled inspection glass
(a)
Liquid phase
Gaseous phase
Liquid supply
Withdrawal of liquid and gas supply
(b)

Figure 9.4 (a) Components of falling film microreactor (total height 10 cm) and (b) a microstructured reaction plate of falling film reactor (channel width and depth 300 × 100 or 1200 × 400 μm^2) after [1]. (VIS image courtesy: Fraunhofer IMM, Mainz, Germany [6].)

plate with microchannels. The fluid enters the reaction channels on the top of the reaction plate and flows downward to the withdrawal zone at the bottom. While the flow direction of the liquid reactant corresponds to the direction of gravity, the gas phase reactant can be guided either parallel or antiparallel to the liquid phase.

To detect the zone where the chemical reaction actually takes place and to measure fluid equipartition and temperature profiles of the fluid films on the reaction plate, a FLIR SC2000 IR camera with a 24° lens was used. To enable thermal process control, the microreactor was equipped with an IR-transparent inspection window (626 μm thick silicon wafer). In addition, the use of a close-up lens allowed measurements at a high spatial resolution of about 200 μm. This is sufficient to reveal details smaller than the characteristic dimensions of the microreactor.

One of the most important preconditions for an optimum operation of the reactor is the fluid equipartition in the reaction channels. Mostly, the reaction fluids are transparent in the visible but opaque in the IR spectral region. Therefore, the homogeneity of the microchannels can be tested by studying the wetting behavior of the reaction plate using isopropanol under *no-reaction* conditions by thermal imaging in the LW IR region utilizing the emissivity contrast between the fluid and the reaction plate material. The isopropanol film was heated above room temperature to 30 °C by an integrated micro heat exchanger. The emissivity of the microstructured reaction plate manufactured in high-alloy stainless steel ($\varepsilon \approx 0.5$) differs strongly from that of isopropanol ($\varepsilon \approx 0.9$) in the LW IR region. Therefore, areas wetted with preheated isopropanol show up with a larger signal (indicated as bright white color in the used false color scale), whereas dry areas emit less radiation and are indicated in black. This effect was used to image the fluid equipartition in parallel channels. In Figure 9.5, a sequence of the initial wetting behavior at a volume flow of 250 mL h^{-1} isopropanol is shown for a reaction plate with 15 channels over a period of 2.5 s. It is obvious that a very uniform spa-

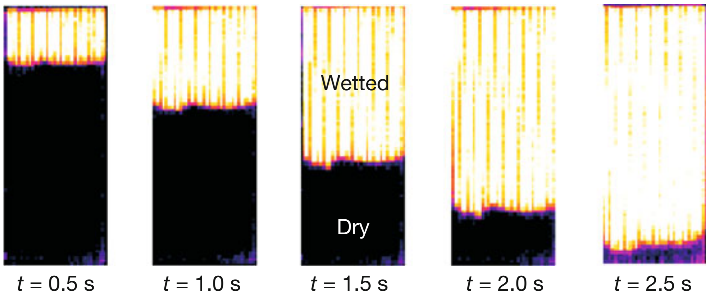

Figure 9.5 Wetting behavior of a reaction plate with channels 1200 × 400 μm^2 loaded with a volume flow of 250 mL h^{-1} isopropanol and heated to 31 °C as a function of time.

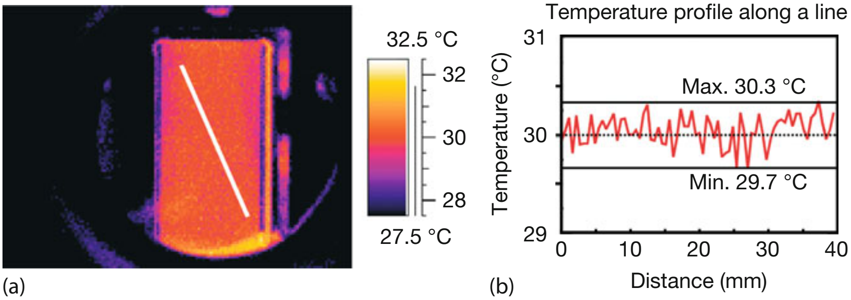

Figure 9.6 (a,b) IR image with temperature profile of heated reaction plate wetted with isopropanol.

tial distribution was achieved for each time, since the fluid front moved the same distance in all microchannels.

Heat management plays an important role in many reactions since most reaction rates strongly depend on temperature. Thermal imaging allows one to record temperature profiles across the whole reaction plate with a single measurement at a high spatial resolution sufficient to reveal details smaller than the characteristic dimensions. Figure 9.6a shows an IR image of the temperature distribution of a reaction plate wetted with isopropanol under *no-reaction* conditions after thermal equilibrium has been established. Figure 9.6b depicts a temperature plot along the inclined line indicated in the IR image that crosses several microchannels. Apart from the reflection of environmental radiation at the bottom of the reaction plate, the temperature profile is very homogeneous. The maximum deviation from the set value of 30 °C amounts to ±0.3 °C along the line, and for the whole reaction plate of the $27 \cdot 65\,\text{mm}^2$ area it amounts to about ±0.5 °C.

The temperature changes and the spatial temperature distribution of the liquid phase during reactor operation can be monitored by thermal imaging analysis of an exothermic test reaction with a gaseous reactant [7, 8]. The investigations were performed in a batchwise manner: the reaction plate was loaded with a well-defined liquid flow of NaOH under stationary conditions, and an overstoichio-

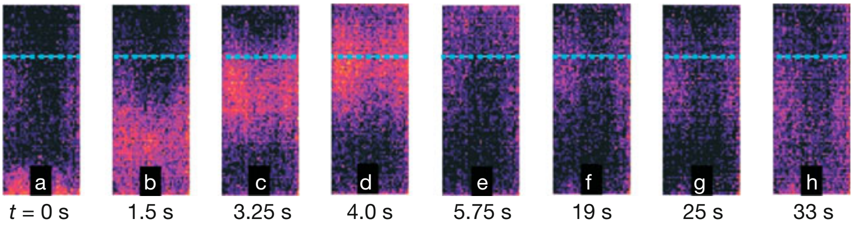

Figure 9.7 Heat release of CO_2 absorption into 2.0 M solution of NaOH. CO_2 was fed into the chamber from 0 to 6 s. The reaction plate with channels of $1200 \times 400\ \mu m^2$ was loaded with $250\ mL\ h^{-1}$, and the temperature was set to 25 °C. The IR scale corresponds to a span of $\Delta T = 2$ K from blue to red. The blue line indicates a position used subsequently for a temporal plot analysis.

metric amount of pure CO_2 was fed into the gas chamber in counterflow to the falling film.

The molar concentration of the NaOH solution was 2.0 M, the liquid load of NaOH was $250\ mL\ h^{-1}$, and the reaction plate was heated to 25 °C by the integrated heat exchanger. In Figure 9.7, a sequence of IR images illustrates the transient upward moving reaction front via the heat release of the NaOH solution after opening a valve for CO_2 supply.

The varying position of the reaction zone within the series of images can be explained as follows. As CO_2, which is heavier than air, is fed into the gas chamber from the bottom, the reaction front rises as the CO_2 level increases in the gas chamber (Figure 9.7a–d). The gas chamber is completely filled with CO_2 when the top of the reaction front leaves the observable area of the reaction plate and the reaction starts to be quenched at the bottom (Figure 9.7e). At $t = 5.75$ s the gas chamber is filled with an excess of CO_2. The reaction now only takes place at the entrance port of NaOH. Then at $t = 6$ s the CO_2 supply is stopped. As the CO_2 level in the chamber decreases, the reaction front starts moving again downward (Figure 9.7f,g), thereby consuming the remaining CO_2 in the chamber. Whereas the streaming in of the CO_2 at the beginning of the experiment is a fast process, the consumption of the remaining CO_2 is a slow diffusion process showing a broad reaction zone with a small temperature peak.

The CO_2 absorption into a 2.0 M solution of NaOH results in a significant temperature increase of about 0.5 °C (Figure 9.8). This temperature increase corresponds to the theoretically calculated data [9].

Such an analysis allows for optimization of the flow rates for the chemical reactants in the microreactor. In particular, it helps to ensure that the chemical reaction does indeed take place in the center of the microstructured reaction plate as planned. Furthermore, the requirements for the reaction plate cooling (for stronger exothermic reactions) can be specified from the temperature increase and the spatial temperature distribution across the reaction plate for stationary operating conditions.

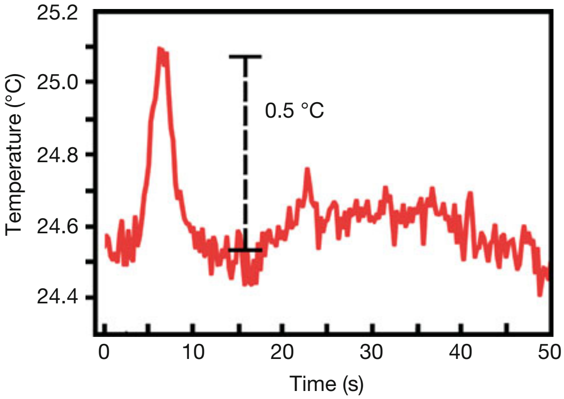

Figure 9.8 Transient temperature profile of CO_2 absorption into 2.0 M solution of NaOH from start until complete consumption of all CO_2. The temperature values are averages along the blue line indicated in Figure 9.7.

9.3.1.2 **Glass Microreactor**

Glass is widely used in the manufacture of chemical reaction vessels. The use of glass is due to its unique physical and chemical properties, for example, its excellent resistance to many chemicals, optical transparency, mechanical hardness, and high temperature stability. Traditional micromachining technologies known from silicon-based processes have been adapted to glass processing.

Fraunhofer ICT developed a glass microreactor for controlled liquid–liquid chemical reactions with strongly exothermic behavior [10, 11]. This reactor, shown in Figure 9.9, is made from photoetchable, chemically resistant, and temperature-stable Foturan® glass.

The reacting liquids are injected through input reactants 1 and 2 (Figure 9.9). The chemical reaction occurs within the mixing and reaction channels (width approximately 120 μm). A separate cooling system is integrated in the microsystem behind the reaction channels.

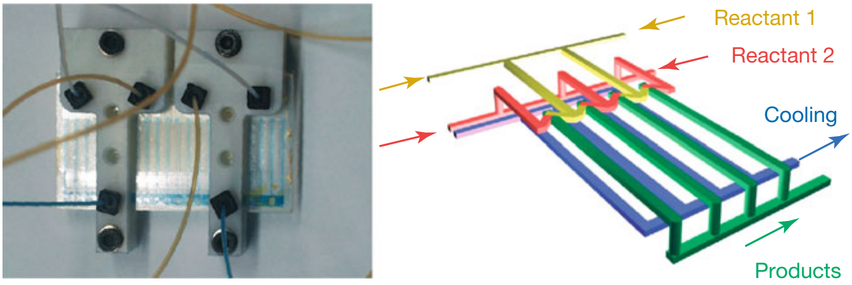

Figure 9.9 Micro glass reactor (total dimension of depicted area: 6 × 8 cm^2; drain outputs blue, reactant 1 inputs gray, reactant 2 inputs yellow, colors refer to left image, cooling system not connected) for strongly exothermic liquid–liquid reactions after [1]. (VIS image courtesy Fraunhofer ICT, Pfinztal, Germany [11].)

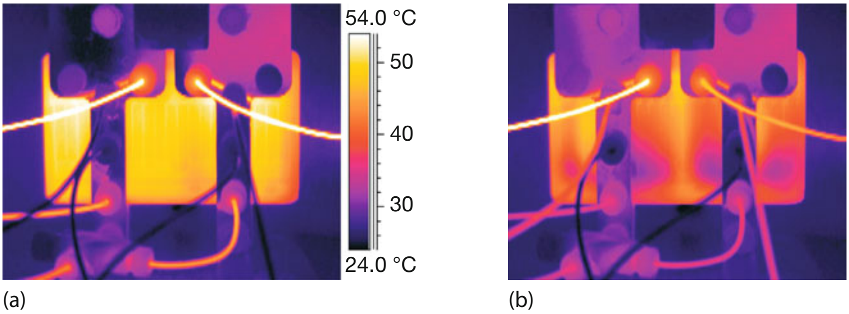

Figure 9.10 Test of microreactor with H_2O (80 °C) without (a) and with (b) cooling (IR image for $\varepsilon \approx 0.9$) recorded with an AGEMA THV 550 camera.

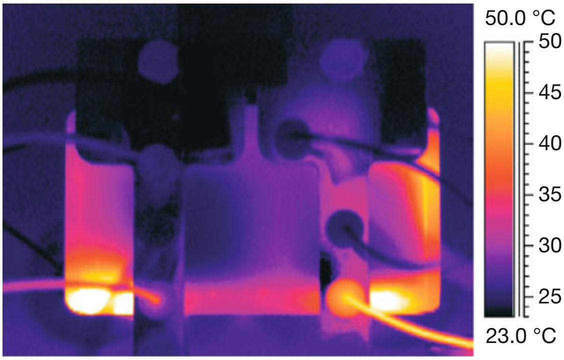

Figure 9.11 A dilution reaction of 96% sulfuric acid with water in the glass microreactor occurred in the drain owing to unfavorable fluid flows at equilibrium.

Thermal imaging of glass microreactors became possible because Foturan® glass is fortunately semitransparent within the wavelength region of 3–5 μm. The raw data signal of a MW camera measured for a blackbody with a temperature of 50 °C will drop to 50% if a 1 mm thick Foturan® glass plate is placed in front of the camera. Therefore, thermal processes inside the reactor can be easily observed using a MW camera.

During the first tests with hot water ($T \approx 80$ °C), strong temperature inhomogeneities were found (Figure 9.10). These inhomogeneities were amplified when additional cooling was applied with room temperature water. Such results can be used to optimize the assembly of the reacting and cooling channels.

For the characterization of the reactor operation within an exothermal chemical test reaction, sulfuric acid (96%) was diluted with water. As shown in Figure 9.11, the flow rates or flow rate ratio of the reactants was unfavorably selected. Therefore, the chemical reaction did not occur in the microchannels as desired but was uncontrolled and without necessary cooling within the drain.

Figure 9.11 demonstrates that temporally and spatially resolved thermography is a powerful method for adjusting and controlling process parameters in chem-

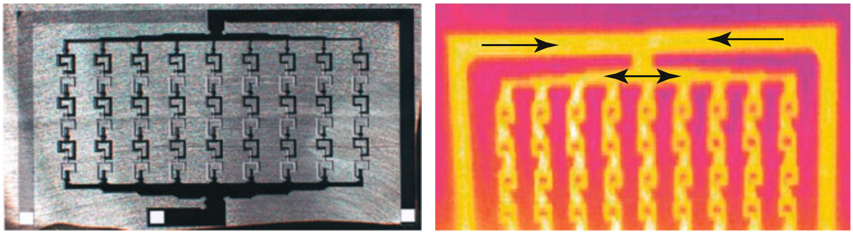

Figure 9.12 Cutaway view of silicon microreactor and IR image of reaction channels filled with hot water (arrows: flow directions).

ical microreactors. The results of experiments with varying flow parameters are used to improve the design of the microreactor to ensure a homogeneous and controlled chemical reaction inside the reaction channels.

9.3.1.3 **Silicon Microreactor**

Silicon is the best-known and best-mastered material in microtechnology. Its large mechanical strength, very good thermal properties, and a good chemical stability of silicon combined with the well-established silicon micromachining technologies offer excellent possibilities for fabricating microreactors. Such reactors are suitable for chemical reactions at elevated temperatures and pressures.

Silicon is nonabsorbing in the MW region and is characterized by a flat wavelength dependence of the transmission at about 50% (Figure 1.48). In the LW region absorption features affect transmission (Section 1.5.4). However, for the typical thickness of a silicon wafer below 1 mm transmission decreases by only 10% compared to the MW range (Figure 1.50). Therefore, temperatures of the chemical reactants inside silicon microreactors can be analyzed by either MW or LW cameras.

The silicon microreactor shown in Figure 9.12 was developed for process-controlled strong exothermic liquid–liquid chemical reactions within nine parallel microchannels (channel width approximately 300 μm). The special geometry and the configuration were designed using computer simulations to allow optimum mixing of the reactants.

The silicon microreactor was tested, for example, for the nitration of diethyl urea with N_2O_5. The thermal imaging of this reaction results in an unexpected result. Contrary to expectations, inhomogeneous reactions occur with hot spots along the reaction channels (Figure 9.13). Depending on the pressure, the flow rates, and the temperature of the reactants within the reaction zone, the IR images show time-dependent localized hot spots like “thunderbolts” in different reaction channels.

So far, the reasons for these unexpected results are unknown. Obviously, Figure 9.13, however, nicely demonstrates how temporally and spatially resolved temperature distributions are extremely valuable tools for reactor optimization. The thermal imaging results led to a complete redesign of the structures and the geometries in order to get a homogeneous and continuous distribution of the chemical reaction across the whole reactor.

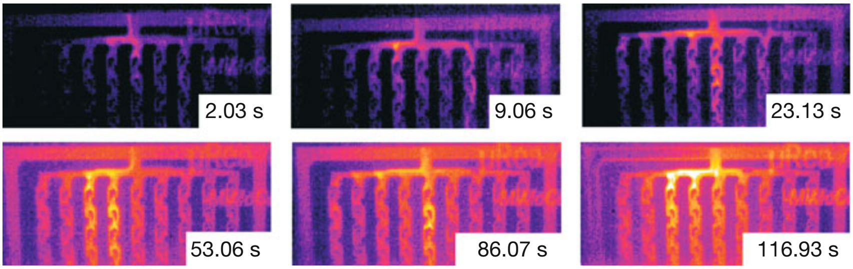

Figure 9.13 Thermal imaging of a nitration reaction of urea in silicon microreactor, recorded with THV 550 MW camera. The numbers indicate the elapsed time after start of reaction.

9.3.2
Micro Heat Exchangers

Micro heat exchangers are heat exchangers with microchannels for flowing fluids; typically their dimensions below 1 mm. Such microscale thermal devices with very large surface-to-volume ratios are motivated by the fact that the heat transfer coefficient increases if the channel diameter and the channel distance decrease [12, 13]. Micro heat exchangers are fabricated using metals, glass, silicon, or ceramics. Like microreactors, micro heat exchangers made of silicon and glass can be analyzed by thermal imaging during operation. An example of such a thermal analysis will be demonstrated for a glass micro heat exchanger.

The US company Invenios has special know-how in the development of microstructured glass components [14]. One of the developments of Invenios is a micro heat exchanger made from photoetchable Foturan® glass. This type of glass was also used in a cover for a glass microreactor.

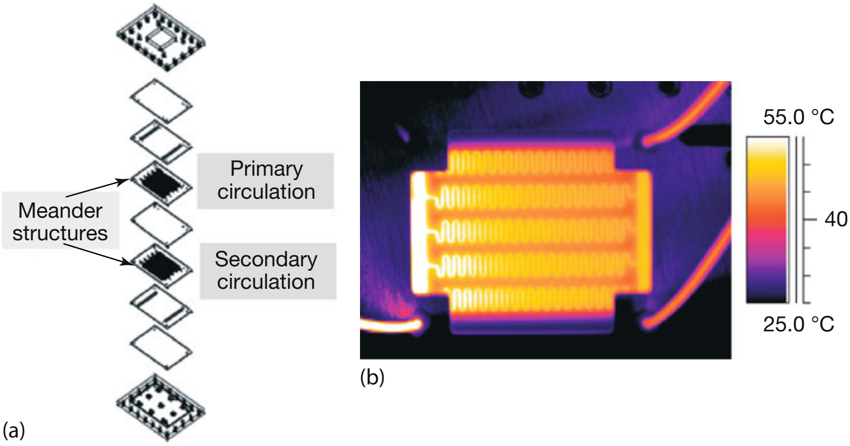

Figure 9.14 (a) Assembly of micro heat exchange system and (b) an IR image (MW AGEMA THV 550 camera) of the primary circuit with hot water flow inside.

The assembly of a micro heat exchange system is shown in Figure 9.14. The primary and secondary circuits consist of identical meander structures. The channels of the primary and secondary circuits are directly on top of each other and separated by a Foturan® glass plate with a thickness of 200 μm. Both circuits branch out to five meanders with a channel width of approximately 700 μm.

Applying temporally and spatially resolved thermography, the thermal processes and the heat transfer in the micro heat exchanger can be studied precisely. The different operation methods (parallel and antiparallel mode, that is, cocurrent and countercurrent flow) can be characterized very accurately (Figure 9.15).

The IR images show very smoothly varying temperatures across the heat exchanger. Owing to the small temperature gradient, the system operation is remarkably homogeneous. This is shown in Figure 9.16. Obviously all five meanders show about the same temperature gradient, especially for antiparallel flow operation.

Time-resolved thermal imaging offers the possibility for a detailed analysis of thermal processes as shown for antiparallel flow in Figure 9.17. The time-dependent temperatures at selected measuring spots can be used to determine the time response and the heat transfer efficiency. The statistically occurring spikes of the temperatures are caused by small air bubbles within the channels.

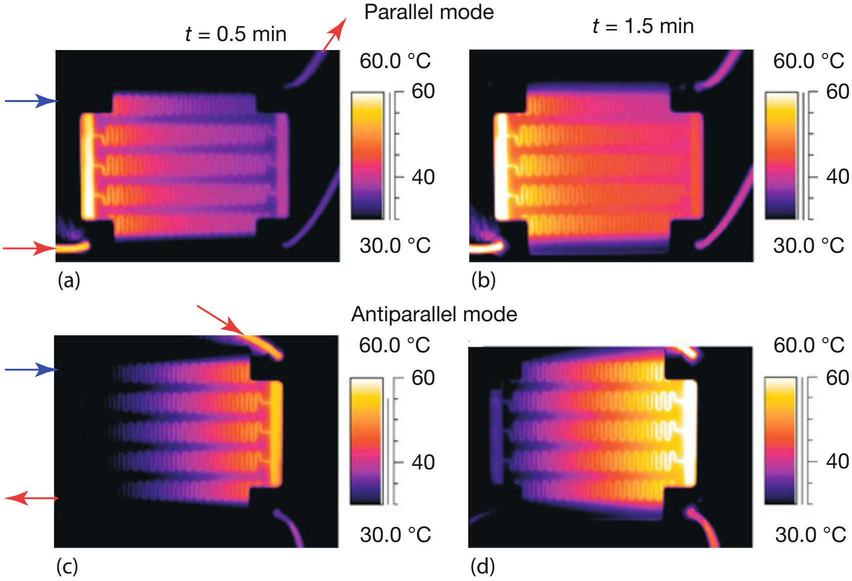

Figure 9.15 IR image of primary circuit (AGEMA THV 550). Temperature rise of heat exchanger at parallel flow (a,b) and antiparallel flow (c,d) after 30 s (a,c) and 90 s (b,d). Input (water at $T = 60\,°C$) and output of primary circuit are marked by red arrows and the cooling water input ($T = 25\,°C$) is marked by a blue arrow. At $t = 0$ the hot water flow was started while the cold water was running continuously.

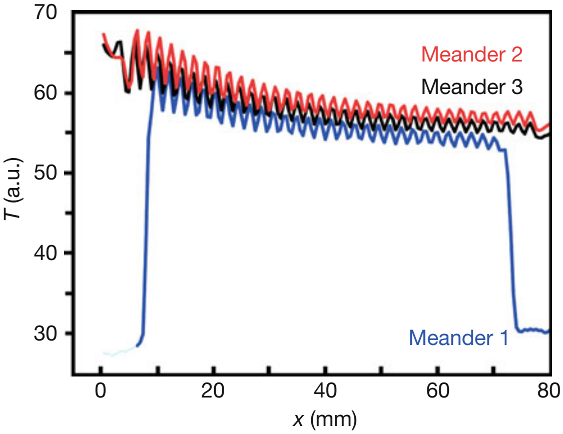

Figure 9.16 Temperature profiles from Fig. 9.15c (line from right to left) along selected meanders after about 30 s (antiparallel primary and secondary circuit, noncalibrated temperatures). Meander 1 is partially covered by the housing.

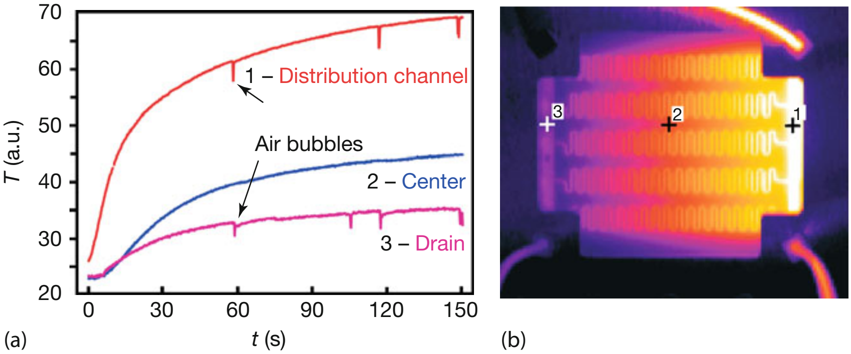

Figure 9.17 (a,b) Time-dependent temperatures at selected test points (antiparallel flow).

The corresponding apparent temperature change is caused by the change of emissivity between water and air.

9.4
Microsensors

9.4.1
Thermal IR Sensors

The performance of thermal radiation sensors is determined by the efficiencies and the properties of the two transduction steps first from incident radiation power to temperature change (Section 2.2.3) and second from the temperature change to the electrical output signal (Section 2.4.5). Usually responsivity and time constant measurements for thermal radiation detectors utilize both transduction steps simultaneously. For a more detailed analysis, however, the characterization of each individual transduction step would be desirable. The first step from energy deposition in the sensor element to temperature increase is of particular interest because two of the most important thermal parameters, heat capacitance and thermal conductance, can be determined directly from this transduction process. The following examples will demonstrate the potential of thermal imaging for characterization of thermal IR sensors.

9.4.1.1 IR Thermopile Sensors

Radiation thermocouples are probably the oldest IR detectors [15]. They utilize the Seebeck effect [16] (Section 1.7.2.1, Figure 1.68) for signal generation and consist of alternate junctions of two different materials. Alternate junctions are defined as hot and cold junctions. For any temperature difference between the alternate junctions, a voltage is generated that is proportional to the temperature difference. To increase their voltage responsivity, a large number of individual thermocouples are often combined to form thermopiles. Thermopiles exhibit lower responsivities compared to other thermal detectors such as bolometers or pyroelectric detectors. However, thermopiles do not require a bias for operation and exhibit low noise at low frequencies. Thermopiles are frequently used as IR sensors in pyrometers because of their excellent properties in DC operation not requiring temperature stabilization, in contrast to bolometers (Section 2.2.3).

A typical thermopile used as an IR sensor is shown in Figure 9.18. It consists of 72 thermocouples with one type of junction ("hot junction") in the center of a thin micromachined Si_3N_4 membrane and the other type ("cold junction") connected to the outside silicon substrate [16, 17]. The IR radiation must be absorbed on the thermopile in order to be detected, so the center is coated with an absorption

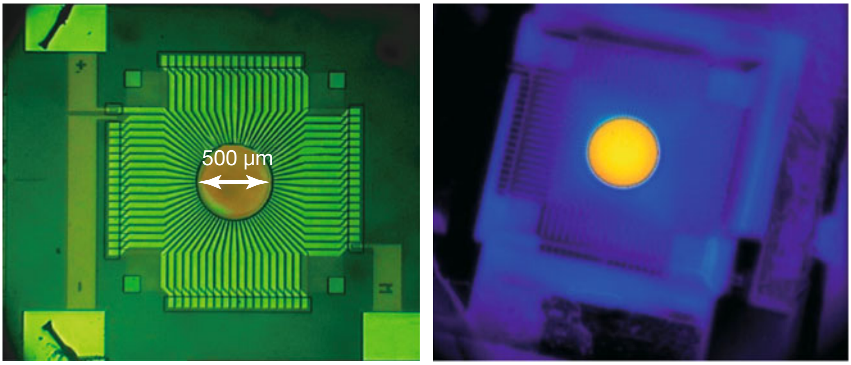

(a) (b)

Figure 9.18 Visible microscope image (a) and IR image (b) (homogeneous temperature distribution, emissivity contrast only) of a thermopile (with 72 thermocouples) in stationary thermal equilibrium.

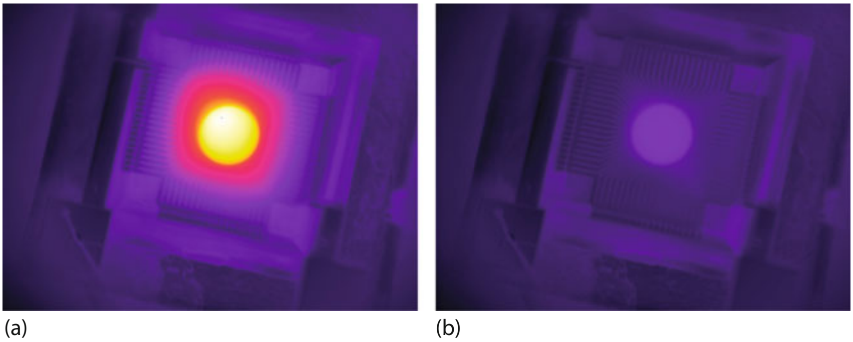

(a) (b)

Figure 9.19 Thermopile operated as a Peltier element: an electrical voltage is applied to the thermopile detector such that the thermocouples in the center are heated (a). For comparison, an image without applied voltage is shown (b). The false color scale differs from that in Figure 9.18.

layer (500 μm diameter and about 1 μm thickness). The IR image (Figure 9.18) of a homogeneously tempered thermopile (sensor temperature slightly higher than ambient temperature) is only owing to emissivity contrast, that is, the emissivity difference between the absorption layer and the surrounding sensor area.

The absorption layer should define the radiation-sensitive area. However, incident radiation is also partially absorbed on the uncovered membrane area, which causes an additional contribution to the temperature increase of the membrane. Therefore, the sensor exhibits a larger radiation-sensitive area as defined by the size of the absorption layer. This undefined radiation-sensitive sensor area can cause problems in quantitative application of the sensors.

The Peltier effect is a reverse Seebeck effect (Figure 1.68), and a thermopile consequently represents a Peltier element if it is operated accordingly [18]. If a voltage is applied to the thermopile, one type of junction is heated up and the other type is cooled down. The direction of the applied voltage determines which type is heated or cooled. Figure 9.19 depicts a thermopile detector operated as a Peltier element.

The used polarity of the voltage causes a heating of the junctions in the center of the membrane. The corresponding temperature distribution on the radiation-sensitive sensor area is determined by the value of the applied voltage. If a voltage pulse is applied, the sensor time constant can be determined as well.

The spatial sensitivity distribution is usually determined by a laser microprobe using a spatial scan of a focused laser beam. The detector signal is measured for the different laser beam positions at the sensor area. Figure 9.20c,e depicts a 2D sensitivity profile and a sensitivity false color representation of the spatial sensitivity distribution resulting from such a laser spot measurement. These results can be compared with the thermal imaging results for the Peltier element operation of the thermopile (Figure 9.20a,b,d). Obviously, the thermal imaging gives the same results as the laser spot measurement with respect to the spatial sensitivity distribution of the sensor. However, the IR measurement by thermal imaging is

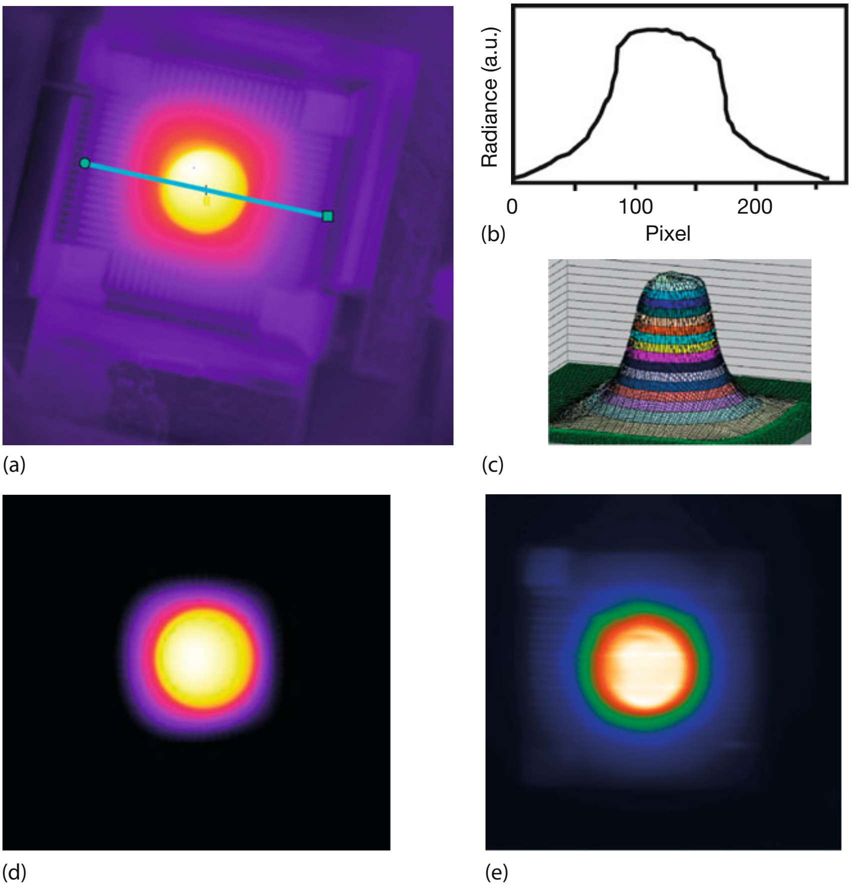

Figure 9.20 IR image of a thermopile operated as a Peltier element with heated thermocouples in the center (a). Comparison of temperature line profile of center heated thermopile (b) with 2D sensitivity profile from laser spot measurement (c). False color representation of temperature distribution (d) owing to Peltier effect with IR imaging and of spatial sensitivity distribution with laser scanning (e).

advantageous compared to the laser spot measurement because the sensor is characterized in the same IR spectral region where it is used, whereas for laser spot measurements characterization is due to visible laser radiation. Also, IR imaging needs no scanning, that is, it allows a much faster testing of the sensors.

If the thermopile is operated with a square wave pulsed voltage, the sensor time constant can be determined from the temperature rise and decay during the Peltier element operation (Figure 9.21). For the determination of the time constant, the raw signal data (representing the radiance) were used. Owing to the fact that there is only a small change in the sensor temperature of several degrees Celsius, one can assume a linear relation between radiance and temperature. The determined 40 ms time constant accords well with the results of frequency-

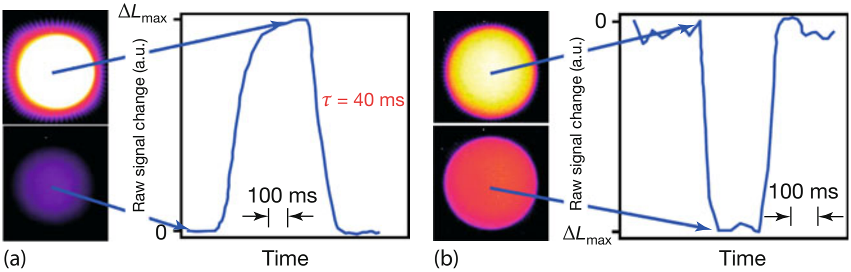

Figure 9.21 Time-resolved measurement of emitted radiation (raw data signal) for center heating (a) and center cooling of thermopile (b) owing to Peltier effect during a 250 ms square wave voltage pulse (integration time 0.75 ms, 1 kHz frame rate).

dependent sensitivity measurements using modulation and signal rise/decay measurements with pulses of incident radiation. Temperature rise and decay are characterized by slightly different time constants. This behavior is caused by the complex thermal conditions within the heated thermopile area [12]. Thermal energy is generated by the electrical heating at the center of the membrane structure. The transient heat transfer in the structure is, however, initiated by convection to the surrounding gas and by the 2D heat conduction into the substrate (outside the membrane structure).

9.4.1.2 IR Bolometer Sensors

Microbolometers play a very important role in the IR industry (Chapter 2). The excellent achievable detector performance of microbolometers can be used not only for IR thermal imaging but for other applications as well, for example, for nondispersive gas detection, pyrometry, or IR spectroscopy applications. Therefore, a technology to produce single microbolometers and measurement techniques for characterizing bolometer performance, including microthermography, have been developed [19].

A single bolometer consists of a thin layer of a material with a high temperature coefficient of resistivity (TCR) with electric contacts (Section 2.2.3). The layer is thermally insulated from the surroundings. Figure 9.22a,b depicts the layout of a single microbolometer.

A bulk micromachining technology based on anisotropic silicon etching was used [19]. First a silicon substrate was covered with a thin Si_3N_4 layer forming the membrane for the bolometer structure. A new bolometer material with a high TCR of -2.5 to $-3\%\,K^{-1}$ was developed. For perfect conversion of the incident radiation to heat, an absorbing layer structure (maximum absorbance 0.95, adjustable wavelength for maximum absorbance within 2–14 μm) was evaporated on top of the sensor area. Finally, an inverse pyramid shape cavity of $500 \times 500\ \mu m^2$ was etched into the silicon substrate. KOH is a wet etch that attacks silicon preferentially in the (100) plane, producing a characteristic V etch, with (111) planes as sidewalls that form a 54.7° angle with the surface [17, 20]. The bolometers are thermally insulated from the silicon substrate by supporting legs, which simulta-

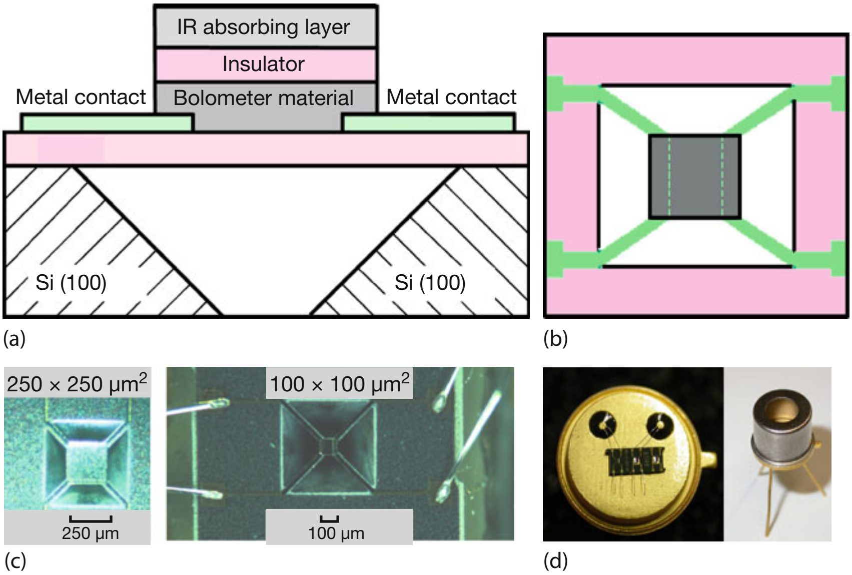

Figure 9.22 Layout (not correctly scaled) of microbolometer structure (a) and top view of bolometer (b). Visible microscope images of micromachined 250 × 250 and 100 × 100 µm^2 bolometers with support legs (c). Mounted microbolometer and complete microbolometer with housing (d). (Image courtesy of iris GmbH, Berlin, Germany.)

neously act as electric contacts. Bolometers with pixel pitches of 100 and 250 µm were tested. Figure 9.22c,d depicts a microscopic image of the bolometers after complete technological process (c) and of a bolometer in a TO housing (well-known semiconductor package system mainly used for transistors; d). The packaging can be completed by mounting of a transistor cap with an IR transparent window.

The heat capacitance C_{th} and the heat conductance G_{th} of the bolometer structure are important parameters for the performance of the bolometer [21] (Section 2.2.3). Therefore, the thermal design of the microbolometer structure has a strong influence on the performance of the detector. The voltage responsivity depends reciprocally on G_{th} and the time constant of the sensor equals the ratio of C_{th} to G_{th} (Figure 2.2).

Within the layout process, a detailed thermal analysis of the structures was done. To compare the results of the numerical simulation with the parameters characterizing the processed bolometer structures and for further improvement of the detector performance, the two values C_{th} and G_{th} must be determined separately. Usually these two parameters are determined experimentally from time constant and sensitivity measurements. To increase the accuracy of the determination of these two parameters, an electrical measurement combined with microthermography has been developed utilizing the self-heating process of the bolometer if a voltage is applied [19]. Figure 9.23 depicts the self-heating of the 100 µm bolometer owing to the applied voltage. The thermal conductance can

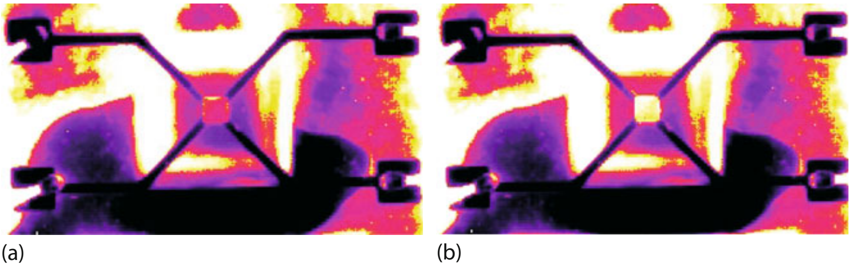
(a) (b)

Figure 9.23 IR image of a 100 × 100 μm^2 microbolometer electrically heated by an applied voltage pulse without voltage (a) and with applied voltage (b).

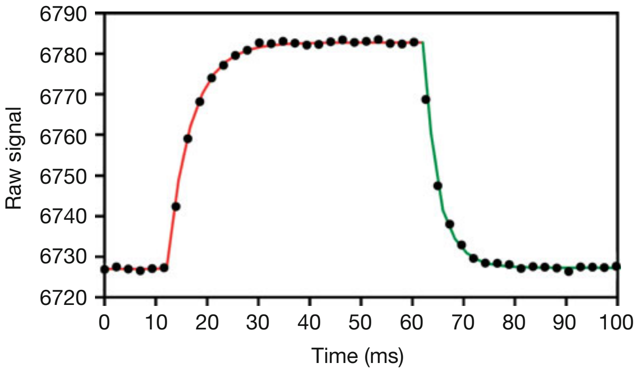

Figure 9.24 Bolometer temperature rise and decay (measured as the raw data camera signal) during an applied 50 ms voltage pulse (FLIR SC6000 camera parameters: integration time 0.8 ms, frame rate 430 Hz). Fit curves of the signal rise and decay by exponential functions led to a time constant of 4.7 ms (rise, red curve) and 3.4 ms (decay, green curve).

be determined from the ratio of the electric power dissipated in the bolometer structure and the observed temperature change.

The temperature of the bolometer during this self-heating process can be analyzed using microscopic thermal imaging for direct temperature determination or from the changed bolometer resistance with the known temperature-dependent bolometer resistance. For the 100 × 100 μm^2 bolometer depicted in Figure 9.23, a heat conductance of $G_{th} = 4\,\mu W\,K^{-1}$ was determined.

In addition, a time constant of about 4 ms of the microbolometer was determined from transient thermal imaging during pulsed heating and the subsequent cooling process (Figure 9.24). As in the analysis of the miniaturized emitters, different time constants for temperature rise and decay were found. The heat capacity was determined from the heat conductance $G_{th} = 4\,\mu W\,K^{-1}$ and the time constant $\tau \approx 4$ ms to be $C_{th} \approx 1.6 \cdot 10^{-8}\,J\,K^{-1}$.

Furthermore, the thermal images of the electrically self-heated bolometer can be used to analyze the homogeneity of the temperature distribution on the bolometer area and the temperature drop owing to thermal conductivity of the

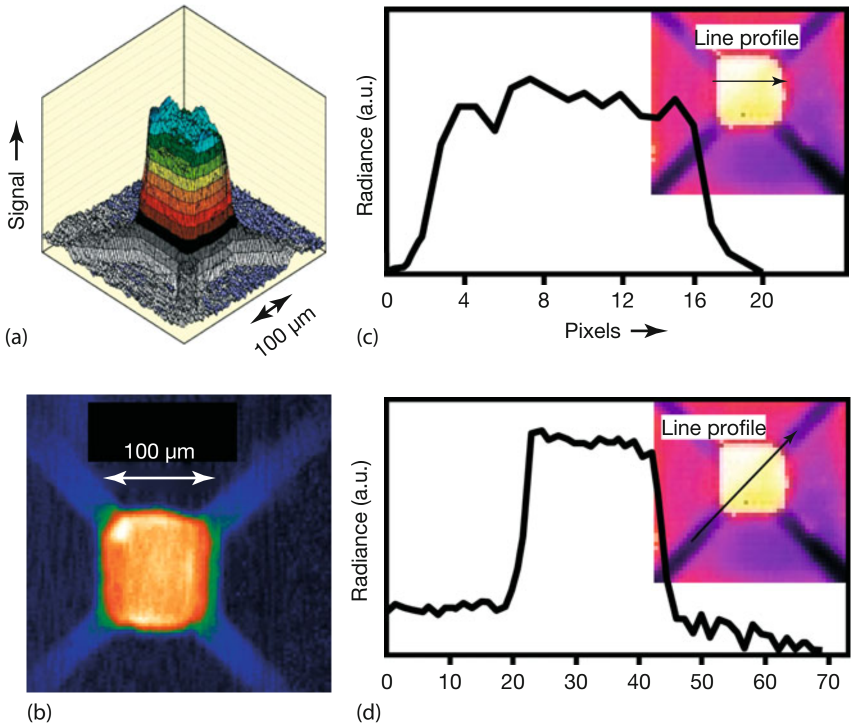

Figure 9.25 Spatial sensitivity distribution determined by a laser spot measurement and thermal imaging of a 100 × 100 μm^2 bolometer. (a) 2D sensitivity distribution from a laser spot measurement. (b) False color representation of spatial sensitivity distribution from the laser spot measurement. (c,d) IR image of heated bolometer with raw signal line profile.

supporting legs of the bolometer. The IR image of the self-heated bolometer in Figure 9.25 allows one to estimate the spatial sensitivity distribution. Owing to the fabrication process, any effects increasing the effective detector area can be excluded. These results are confirmed by the results of laser spot and IR imaging measurements (Figure 9.25).

9.4.2
Semiconductor Gas Sensors

Gas sensors are of prime industrial interest because of their applications in important fields such as security, environment, control, automotive, and domestic applications. A particularly interesting class of gas sensors is based on the resistivity change of metal oxide semiconductor thin films (e.g., made of SnO_2) induced by adsorbed gases. The reversible reactions of adsorption and desorption of different gases are controlled by the operational temperature (an integrated heater on the sensor chip makes it possible to vary the temperature between 150 and 900 °C) and the type of metal oxides used. Such sensors allow for the analysis of

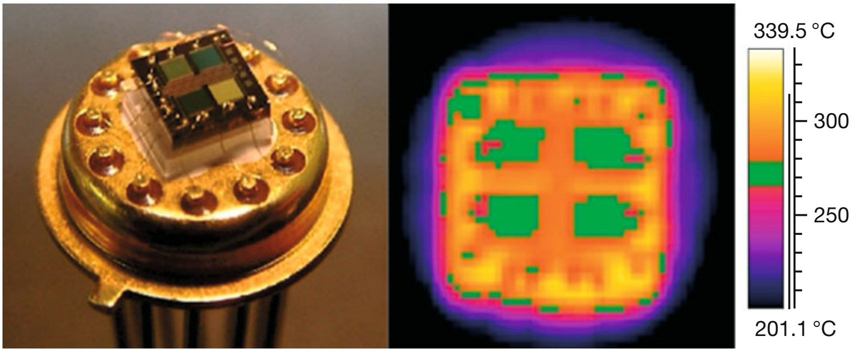

Figure 9.26 Photo of a sensor chip (size approximately 5 × 5 mm^2) and IR image (with a green isotherm $\Delta T = 12$ K) of metal oxide gas sensors after [1]. (VIS image courtesy: Fraunhofer IPM, Freiburg, Germany [22].)

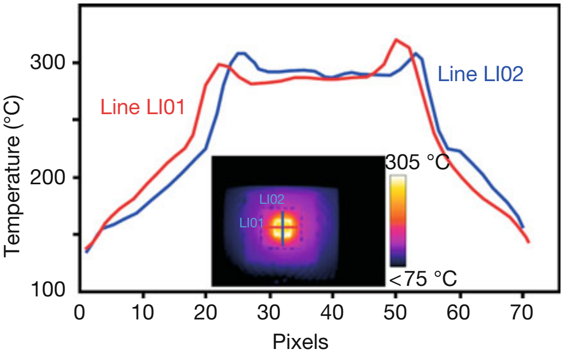

Figure 9.27 Temperature distribution on chip. The center of the temperature plateau corresponds to the center of the chip.

various trace gases such as CO_x, NO_x, NH_3, and hydrocarbons down to minimum concentrations in the lower parts-per-million range.

Over the last few decades, mostly thick-film devices have been used, although their inherent high power consumption is undesirable, especially for portable systems. Meanwhile, the technological problems associated with the production of thin-film devices have been solved, and Fraunhofer IPM [22] develops gas sensor arrays for implementation in commercial systems based on the combination of thin-film deposition techniques, CMOS-compatible microfabrication, and bulk silicon micromachining. As an example, Figure 9.26 shows such a sensor composed of four quadratic gas-sensitive areas with the heater in the center of the chip.

As in the thermopile and bolometer studies, thermal imaging was used to analyze the surface temperature of the sensors, the thermal response time to heat up the sensor to the operational temperature, and the spatial temperature distribution on the chip (Figures 9.26 and 9.27). The temperature distribution across the sensitive sensor area is very homogeneous, with $\Delta T \approx 10$ K.

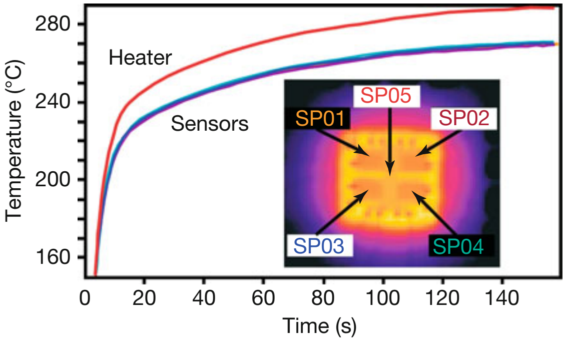

Figure 9.28 Time-dependent temperatures at sensor areas (SP01-SP04) during heating of chip. The heater temperature (SP05) is slightly higher.

The time response during heating is shown in Figure 9.28. All four sensors show nearly the same behavior during the time-dependent temperature rise with deviations below 2 K. The heating process shows two time constants (very fast heating up at the beginning and then a slow temperature increase). Because the sensitivity strongly depends on the sensor temperature, these results are now used to optimize the chip structures to obtain short time constants of the gas sensor.

9.5
Microsystems with Electric to Thermal Energy Conversion

Thermal imaging allows for the thermal characterization of miniaturized systems that transform electrical energy into thermal energy, for example, electrically heated radiation emitters, Peltier elements, or cryogenic actuators. For optimum operation of these systems, the efficiency of energy transfer, the absolute temperature values, and the temperature distribution during operation, as well as characteristic thermal time constants, are important.

9.5.1
Miniaturized IR Emitters

New micromachined thermal IR emitters in TO-39 housing with a protective cap, reflector, or IR-transparent window are available for compact IR spectroscopy applications and nondispersive IR (NDIR) gas analysis [23]. Typical emitter areas are in the range of several square millimeters. Figure 9.29 depicts two types of miniaturized IR emitters. The miniaturized emitters consist of a resistive heating element on top of a thin insulating membrane suspended by a micromachined silicon substrate. Owing to the low thermal mass of the MEMS structure (heated membrane with a thickness in the micrometer range), these emitters exhibit a time constant in the millisecond range. The maximum emitter temperature is up to 750 °C. The emitters are characterized by wavelength-independent large emissivity values (typically 0.95 in the 2–14 μm range), low electrical power consump-

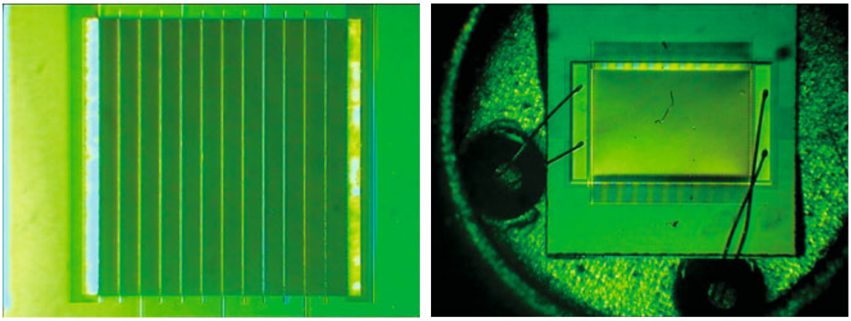
(a) (b)

Figure 9.29 VIS microscope images of two types of commercial miniaturized emitters. (a) Type 1, maximum temperature 450 °C, emitter area 2.1 × 1.8 mm^2. (b) Type 2, maximum temperature 750 °C, emitter area 2.8 · 1.8 mm^2.

tion, high electrical to IR radiation output efficiency, excellent long-term stability, and reproducibility. One of the most important benefits of these emitters is the possibility of fast electrical modulation with high modulation depth (typical 80% at 10 Hz), that is, a chopper wheel for radiation modulation is no longer needed.

Using microscopic and high-speed thermal imaging during emitter operation, the time constant and the temperature distribution can be analyzed as shown in Figures 9.30 and 9.31, respectively. The spatial temperature distribution influences the angular dependence of the emitted radiation.

The radiance measurements indicate a spatially varying temperature distribution across the emitting area. This behavior is caused by the construction of the miniaturized emitter. The heated area is placed on a membrane area that is connected to the silicon substrate at its edges. A large part of the heat generated in the element is transported by thermal conduction to these edges via the membrane material. Owing to the large thermal conductance of bulk silicon, the temperature at the edges will not increase during heating of the membrane. Therefore, the maximum temperature is achieved at the center of the membrane. The IR image of the type 1 emitter exhibits additional lines with reduced radiance (Figure 9.30c, left). These lines, which are also visible in the microscopic image (Figure 9.29), are the contact lines for current supply to the emitter. They are made of metal with reduced emissivity. Therefore, the emitted radiance is also reduced.

A time constant of $\tau \approx 32$ ms is determined from the measurement of the temperature signal of the emitter surface temperature during voltage pulsed operation of the IR emitter (Figure 9.31). In terms of frequency response, the emitter represents a low-frequency pass and can be characterized by a limiting frequency $f = 5$ Hz for $\omega\tau = 1$ operation.

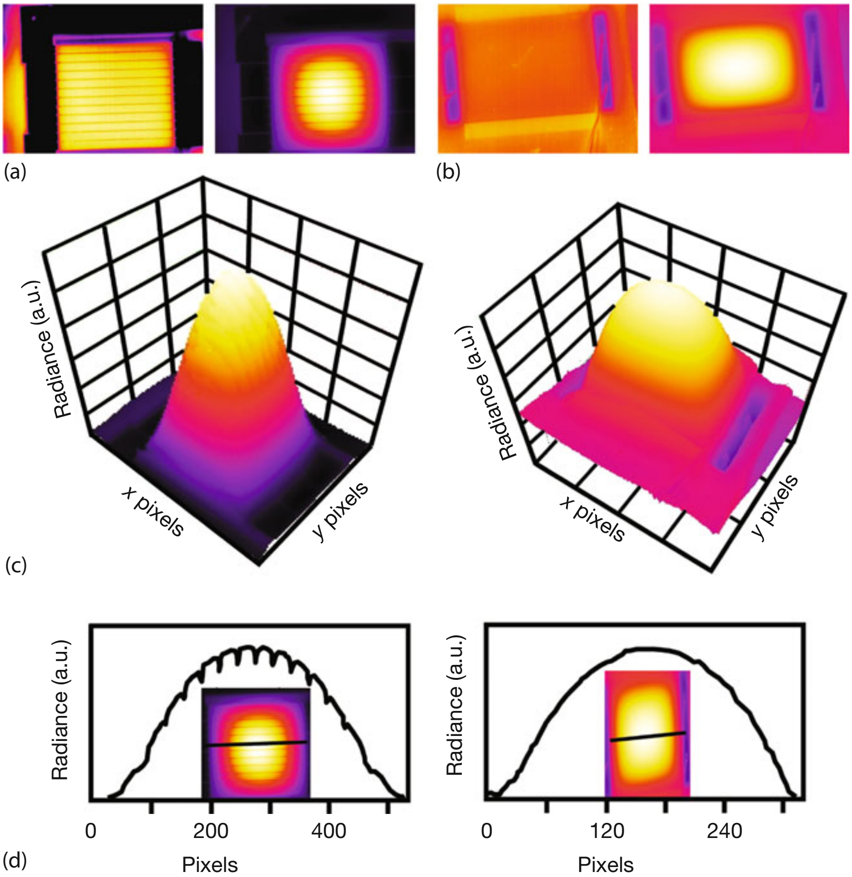

Figure 9.30 Thermal images of stationary spatial radiance distributions at emitter surfaces – (a) type 1, (b) type 2 – without (left) and with (right) applied voltage. (c) 2D plots of measured raw data signal distributions on emitter surfaces of type 1 (left) and type 2 (right) with applied voltage. (d) Line profiles of respective measured raw data for applied voltages.

9.5.2
Micro Peltier Elements

Micro Peltier coolers for spot cooling or temperature stabilization and micro thermogenerators are in high demand for many micro- and optoelectronic applications owing to the increase of miniaturization in these technological fields. Examples are chip cooling in microelectronics or temperature control for telecommunication lasers.

Peltier coolers and thermogenerators offer the typical advantages of microsystems, such as short response time and small area combined with a high thermoelectric energy conversion. Infineon Technologies AG and Fraunhofer IPM

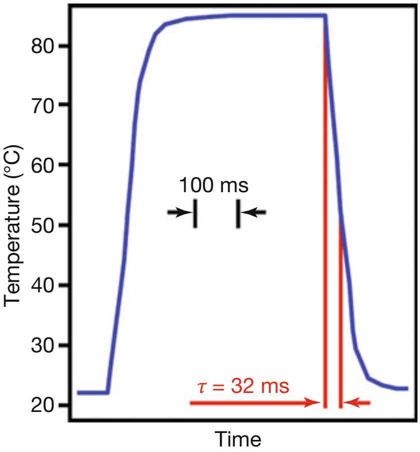

Figure 9.31 Determination of time constant from transient temperature signal of emitter surface temperature for emitter type 1 following 500 ms square wave electrical pulse (measurement at 600 Hz frame rate and 0.8 ms integration time; spot temperature measurement at center of emitter surface).

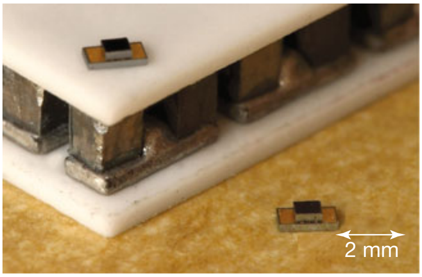

Figure 9.32 Miniaturized thermoelectric elements compared to a “classical” Peltier element after [1]. (VIS image courtesy: Fraunhofer IPM, Freiburg, Germany [22].)

developed the first Peltier devices based on the V–VI compounds Bi_2Te_3 and $(Bi,Sb)_2Te_3$, which can be manufactured by means of regular thin-film technology, in combination with microsystem technology [24] (Figure 9.32). Nowadays dimensions of as small as $1 \times 0.5\,mm^2$ can be achieved.

MicroPelt®, the new generation of thermoelectric components, was analyzed by thermography. Some examples are shown in Figures 9.33 and 9.34. Such optimized elements offer many outstanding properties, such as cooling densities $> 100\,W\,cm^{-2}$, achievable temperature differences $\Delta T > 40\,K$, and a time response on the order of 10 ms [25, 26]. Obviously, contactless IR imaging techniques are extremely useful for temporally and spatially resolved characterization of the surface temperatures of these systems.

9.5.3
Cryogenic Actuators

Cryo grippers from NAISS GmbH in Berlin, Germany [27], are a new patented kind of grippers that form a connection between the grippers’ contact surface and the object under study with freezing vapor (Figure 9.35). This method can be used for any hydrophilic material. The resulting connection creates a high holding force without straining the material. Cryo grippers can be used for automatic handling

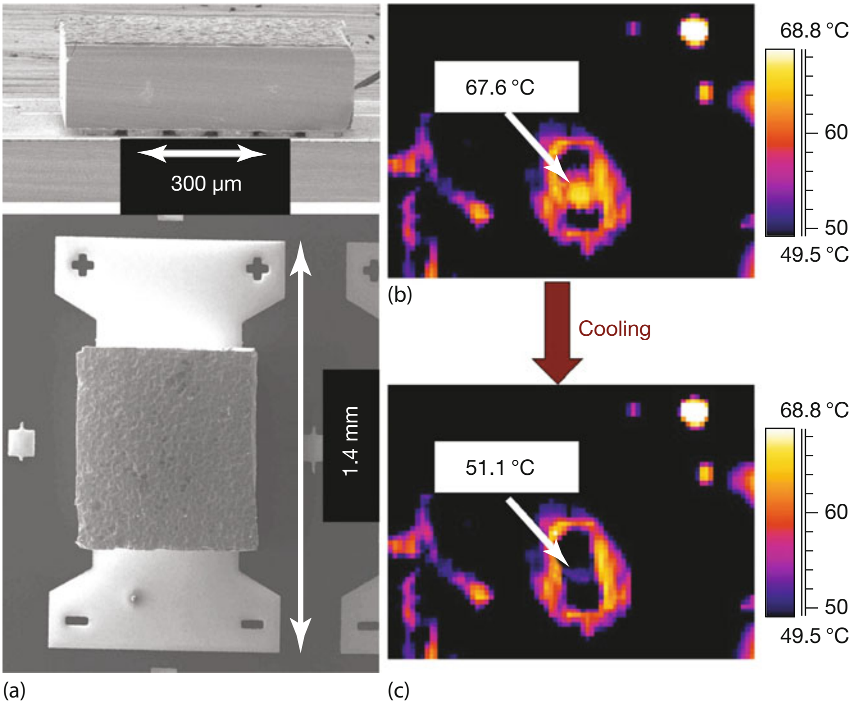

Figure 9.33 Side and top view of a MicroPelt® Peltier cooler as VIS photos (a) and IR images before (b) and while (c) applying a voltage pulse after [1]. (VIS image courtesy: Fraunhofer IPM, Freiburg, Germany [22].)

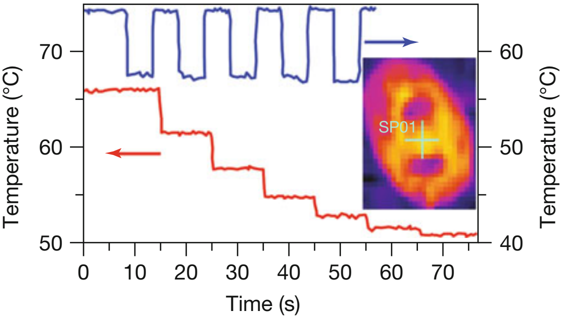

Figure 9.34 Two different time responses of miniaturized Peltier cooler from a thermography measurement (square pulsed voltage – blue curve; step pulsed voltage – red curve). A typical IR image is shown in the inset.

of microprobes without applying any tension force. The probes may be permeable to air, made of nonrigid materials, or of miniaturized components.

Time-resolved thermography is a powerful tool for optimizing the handling process (cooling and heating). Gripping is based on water vapor near the material.

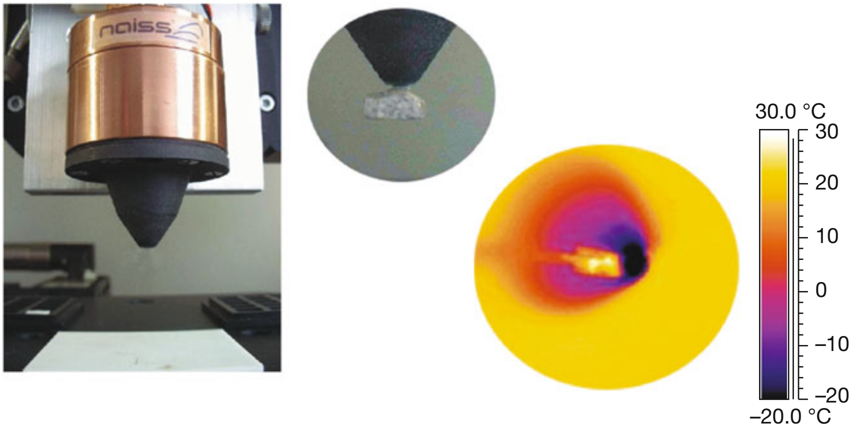

Figure 9.35 Photo of cryogenic actuator and IR image (recorded at an angle from below the gripper) during cooling (after [1]). (VIS image courtesy: NAISS GmbH, Berlin, Germany [27].)

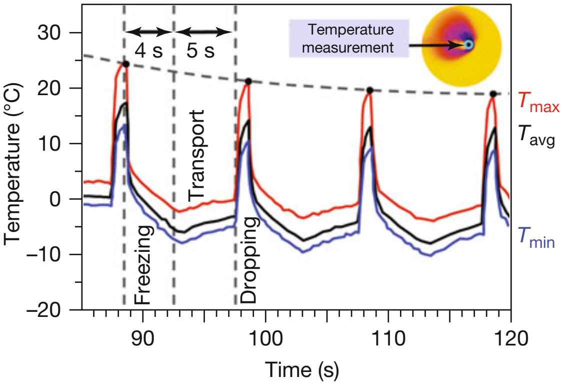

Figure 9.36 Time-dependent temperatures at cryogenic actuator during cooling and heating.

An integrated nozzle in the holder is used to spray the water vapor on the gripping spots only. The freezing of the vapor is due to a Peltier cooling element. This ensures freezing of small amounts of water within a second. Actuators work by picking up probes and dropping them at their destination. For dropping probes, the frozen vapor (i.e., ice) will be liquefied again by heating. Besides melting, the heating also dries by vaporizing the material at the same time. The whole task takes only a few seconds.

To optimize the gripper, a detailed knowledge of the thermal properties at the top of the gripper is necessary. Therefore, time-resolved measurements of the temperature distribution were carried out. Figure 9.36 shows the temperatures at the top of the gripper during periodic freezing, transporting, and heating of the system. From these results the operating parameters, that is, the current for the Peltier cooler/heater at the top of the gripper with regard to the cycle times, are optimized.

References

1 Möllmann, K.-P., Lutz, N., Vollmer, M., and Wille, C. (2004) Thermography of microsystems. Inframation 2004, Proceedings, vol. 5, pp. 183–196.

2 Möllmann, K.-P., Pinno, F., and Vollmer, M. (2009) Microscopic and high-speed thermal imaging: A powerful tool in physics R&D. Inframation 2009, Proceedings, vol. 10, pp. 303–317.

3 Holst, G.C. (2000) *Common Sense Approach to Thermal Imaging*, SPIE Press, Bellingham.

4 Roberge, D.M., Ducry, L., Bieler, N., Cretton, P., and Zimmermann, B. (2005) *Microreactor Technology: A Revolution for the Fine Chemical and Pharmaceutical Industries?* Chemical Engineering and Technology, vol. 28, No. 3, Wiley-VCH Verlag GmbH & Co. KgaA, Weinheim.

5 Hessel, V., Ehrfeld, W., Golbig, K., Haverkamp, V., Löwe, H., Storz, M., Wille, C., Guber, A., Jähnisch, K., and Baerns, M. (2000) Conf. Proc. 3rd Int. Conf. Micro-reaction Technol., Springer-Verlag, Frankfurt a.M., April 18th–21st 1999, pp. 526–540.

6 www.imm.fraunhofer.de/en.html (accessed May 2017).

7 Hessel, V., Ehrfeld, W., Herweck, T., Haverkamp, V., Löwe, H., Schiewe, J., Willle, Ch., Kern, Th., and Lutz, N. (2000) Conference Proceedings of the 4th International Conference on Microreaction Technology, AIChE, Atlanta, 5–9 March 2000.

8 Wille, C., Ehrfeld, W., Haverkamp, V., Herweck, T., Hessel, V., Löwe, H., Lutz, N., Möllmann, K.-P., and Pinno, F. (2000) Dynamic monitoring of fluid equipartion and heat release in a falling film microreactor using real-time thermography. Proc. MICRO.tec 2000 VDE World Microtechnologies Congress, 25–27 September 2000, Expo 2000, Hannover, Germany, VDE Verlag, Berlin und Offenbach, pp. 349–354.

9 Danckwerts, P.V. (1970) *Gas/Liquid Reactions*, McGraw-Hill Book Company, New York, pp. 35, 37, 45, 47, 55.

10 Marioth, E., Loebbecke, S., Scholz, M., Schnürer, F., Türke, T., Antes, J., Krause, H.H., Lutz, N., Möllmann, K.-P., and Pinno, F. (2001) Investigation of microfluidics and heat transferability inside a microreactor array made of glas. Proc. 5th Int. Conf. Microreaction Technol., 27–30 May 2001, Strasbourg.

11 http://www.ict.fraunhofer.de/en.html (accessed May 2017).

12 Incropera, F.P. and DeWitt, D.P. (1996) *Fundamentals of Heat and Mass Transfer*, 4th edn, John Wiley & Sons, Inc., ISBN: 0-471-30460-3.

13 Brandner, J.J., Benzinger, W., Schygulla, U., Zimmermann, S., and Schubert, K. (2007) Metallic micro heat exchangers: properties, applications and long term stability. ECI Symposium Series, vol. RP5: Proc. 7th Int. Conf. Heat Exchanger Fouling Cleaning – Challenges and Opportunities, Engineering Conferences International, Tomar, Portugal, 1–6 July 2007 (eds H. Müller-Steinhagen, M.R. Malayeri, and A.P. Watkinson).

14 www.invenios.com (accessed May 2017).

15 Seeger, K. (1991) *Semiconductor Physics*, Springer Series in Solid State Science, 5th edn, Springer, New York, Berlin, Heidelberg.

16 www.leibniz-ipht.de/en/ (accessed May 2017).

17 Madou, M. (1997) *Fundamentals of Microfabrication*, CRC Press, Boca Raton, London, New York, Washington.

18 Rowe, D.M. (ed.) (2005) *Thermoelectrics Handbook: Macro to Nano*, CRC Press, Boca Raton, London, New York, Washington.

19 Möllmann, K.-P., Trull, T., and Mientus, R. (2009) Single Microbolometer as IR Radiation Sensors Results of a Technology Development Project, Proc. Conf. Temperature, PTB, Berlin, ISBN: 3-9810021-9-9.

20 Gerlach, G. and Doetzel, W. (2008) *Introduction to Microsystem Technology*, Wiley-VCH Verlag GmbH.

21 Hudson, R.D. and Hudson, J.W. (eds) (1975) *Infrared Detectors*, John Wiley & Sons, Inc., Dowden, Hutchinson, Ross.

22 http://www.ipm.fraunhofer.de/en.html (accessed May 2017).

23 www.leister-group.com/de-de/products-and-markets/axetris?nr=true (accessed May 2017).

24 www.micropelt.com (accessed May 2017).

25 Böttner, H. (2002) Thermoelectric micro devices: current state, recent developments and future aspects for technological progress and applications. Proc. 21st Int. Conf. Thermoelectrics, 25–29 August 2002, Long Beach, pp. 511–518.

26 Böttner, H., Nurnus, J., Gavrikov, A., Kuhner, G., Jagle, M., Kunzel, C., Eberhard, D., Plescher, G., Schubert, A., and Schlereth, K.-H. (2004) New thermoelectric components using microsystem technologies. *J. Microelectromech. Syst.*, **13**, 414–420.

27 www.naiss.de/index_en.html (accessed May 2017).

Chapter 10
Selected Topics in Industry

10.1
Introduction

Applications in industry of IR imaging are manifold. In this chapter, a number of different topics are discussed, starting with the general issue of predictive maintenance (PdM) and condition monitoring (CM). These are relevant for all kinds of industry, but here we give examples from power plants, the petrochemical industry, polymer molding, fire testing, and a variety of electrical utilities. We proceed with examples from the metal industry at high temperatures, including a discussion of the problem of emissivity.

In the following sections, specific quality control, safety enhancement, and research applications are presented from different fields, for example, automobiles, airplanes, spacecraft, and surveillance and security. After further treatment of plastic foils, we end the chapter by an extensive discussion of the new emerging field of IR remote sensing, in particular IR imaging with drones.

10.2
Miscellaneous Industrial Applications

10.2.1
Predictive Maintenance and Quality Control

In the preceding chapters of this book exemplary applications of thermography in various fields were presented. Nowadays, thermography is so widely used in industry that it is no longer possible to give examples from all application areas. It is, however, possible to identify the fundamental application fields of IR thermal imaging in industry. Thermography is, on the one hand, mostly used as a tool in CM within PdM programs. On the other hand, it offers some unique possibilities in the field of quality control.

PdM programs are major tools in industry that are used to reduce costs in the long term. In general, PdM using CM techniques should help determine the condition of in-service equipment in order to predict when maintenance should be

Infrared Thermal Imaging, Second Edition. M. Vollmer and K.-P. Möllmann.
© 2018 WILEY-VCH Verlag GmbH & Co. KGaA. Published 2018 by WILEY-VCH Verlag GmbH & Co. KGaA.

performed in order to avoid system failure. The goal is for repair or maintenance tasks to be performed only when needed. Ideally, maintenance may also be scheduled in advance when it is also most cost-effective, for example, during regular shutdown periods of the machinery. This method is much cheaper than time-based maintenance programs, where parts are maintained or replaced not because they may need it, but because a predefined time interval has passed.

To monitor when equipment or parts of it loses optimum performance, PdM programs use CM. In CM, inspections of equipment are performed while it is in service, that is, CM should not affect regular system operation, but at the same time it should give reliable information on significant changes in equipment parameters that are indicative of a developing failure.

Besides qualitative visual inspections that are cheap and quite reliable if performed by experts, the most common CM techniques – depending on the equipment to be tested – are the following nondestructive testing methods:

- Vibrational analysis (in particular, of equipment with rotating parts, using seismic, piezoelectric, or eddy current transducers, combined with fast Fourier transform analysis);
- Oil inspections (spectrographic analysis of chemical composition of oil);
- Ultrasound (mechanical applications, high-pressure fluid flows); and
- Thermography.

In recent years, IR analysis with thermography has become an important tool since high surface temperatures of parts are often indicative of a developing failure of components, for example, of degrading electrical contacts and terminations. It may also detect a multitude of other thermal anomalies like missing or rotting thermal insulation around tubes or leakages from tubes and valves. In all tests, a deviation from a reference value (e.g., a specific vibration behavior, oil quality, temperature value) must occur to identify impending damage.

Quality control is another important factor in any industry. It should ensure that given industrial products have properties as designed. Quality control, therefore, deals with failure testing in the design and production of products. Obviously, all kinds of destructive as well as nondestructive test methods may be applied. Again, thermography is a nondestructive test tool that has the advantage of being contactless while measuring the thermal properties of products either during or after manufacture.

Obviously, there are many applications of thermography in the fields of PdM, CM, and quality control [1–3]. Examples have been reported for fossil [4], gas [5], and nuclear power plants [6, 7], an electrical power converter system with a capacity of 3 GW [8], the chemical and petroleum industry [9], coal mines [10], the sand mining industry [11], the sugar industry [12], the paper industry [13–15], a crankshaft production line [16], the inspection of marine vessels [17, 18] or pipelines [19, 20], refineries [21, 22], large mail distribution centers [23, 24], solar panel inspections using lock-in techniques [25], wind energy rotor blade inspections [26], and cooled food in supermarkets/grocery stores [27].

Each application would deserve a section of its own. Here we present only a few examples: first, PdM of tubes and valves in a power plant; second, detection of the levels of liquids in large storage tanks in the petrochemical industry; third, an example of quality control in the production line of bicycle helmets using polymer welding techniques; and fourth rack-storage fire tests. The wide field of electrical applications is discussed in a later section.

10.2.2
Pipes and Valves in a Power Plant

Power plants are very complex systems that have a large variety of equipment ranging from electrical to fluid dynamic components. For most parts of the equipment, thermal signatures provide important information for CM systems. Therefore, thermography is already in common use as an established technique for power plant PdM programs. Many examples for early detection of problems have been reported [6, 7]. They include the detection of hot spots in a cable connection for a large chiller, a hot bus bar connection in a critical panel, a complicated compressor issue, hot spots on a terminal board, remote monitoring for pump seal leakage, leak detection of critical valves, evaluation of loading on compressors, and the study of hot spots in generator equipment, switchyard equipment, and motor control centers. Because of the complexity of power plants, it has proven important to prepare careful documentation of detected irregularities in the form of case histories, which enter, for example, a component health database. This can also help to judge the severity of an identified anomaly and give hints as to the most important question of how long a component that is showing irregularities will last.

Figure 10.1 shows an example of remote monitoring of a pump seal leakage from a high-energy feed pump. Recording IR images of leakage from remote drain piping eliminates the need to enter the room, providing a safer means of monitoring the equipment condition. If the temperature remains constant in the piping profile, the leakage should also remain relatively constant. The repair can be deferred until the end of a 2-year cycle.

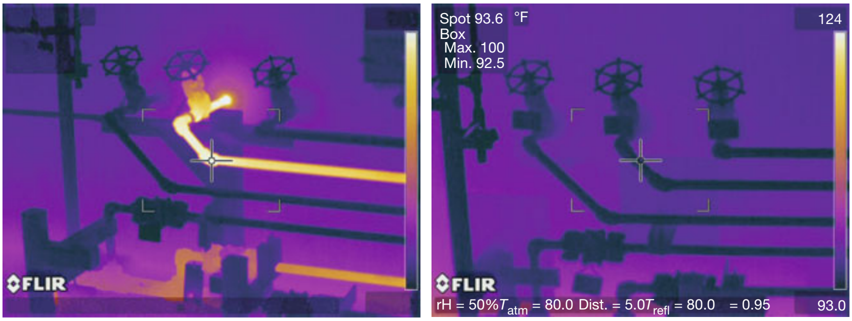
FLIR
Spot 93.6 °F
Box
Max. 100
Min. 92.5
124
FLIR
rH = 50% T_{atm} = 80.0 Dist. = 5.0 T_{refl} = 80.0 = 0.95
93.0

(a) (b)

Figure 10.1 IR images of a seal leak (a) and of a companion pump without leak (b). (Images courtesy Michael J. Ralph, Exelon Nuclear.)

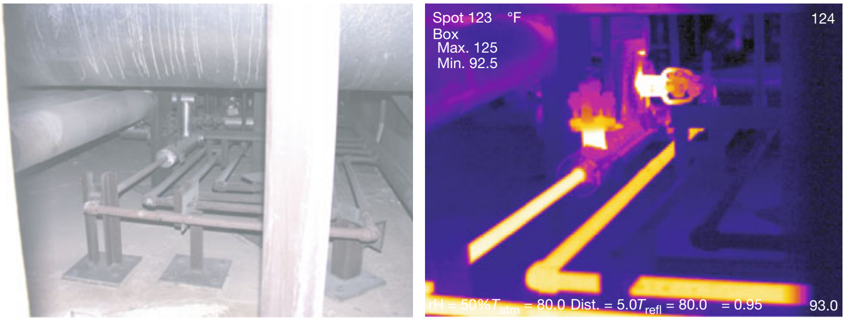
Spot 123 °F
Box
Max. 125
Min. 92.5
124
rH = 50% T_{atm} = 80.0 Dist. = 5.0 T_{refl} = 80.0 = 0.95
93.0

(a) (b)

Figure 10.2 Photo of drain valve arrangement (a) and IR image of hot pipes from leaking drain valves (b). (Images courtesy Michael J. Ralph, Exelon Nuclear.)

Figure 10.2 shows an IR image and the corresponding photo of drain lines with leaking valves from the main steam lines. This leakage had minimal effect on plant efficiency, but it was causing concern over the waste-processing equipment, which handled the inputs of high-temperature water. It was imperative to accurately identify which of potentially dozens of valves were leaking in order to make the repair during a scheduled refuel outage.

10.2.3
Levels of Liquids in Tanks in Petrochemical Industry

The petrochemical industry makes intensive use of IR thermal imaging not only for the detection of volatile organic compounds with GasFind cameras (Chapter 8) but also for other equipment [21, 22]. As an example, the process conditions within oil field production vessels can be studied with IR thermal imaging [28, 29].

In particular, thermography was used to monitor the crude oil conditions in various storage, treatment, and transfer tanks used in oil production fields, and it was shown that the levels of liquids and solids in tanks and vessels were easily detected with thermography. Thermography is useful for locating levels in tanks and silos since other methods are often unreliable. The need for precise information is often critical, for example, to verify whether there is still enough space in a tank to be filled.

The primary focus in the example presented in what follows was to ensure that foaming, solids, and other crude oil process conditions are known and properly handled to optimize the cost of handling, processing, and transferring. The technique has been demonstrated for the production of gunbarrel tanks, water storage tanks, oil storage tanks, oil heaters, and production vessels.

A *gunbarrel* is a large tank that is used to separate oil from water as it flows from the production wells. Such tanks typically range from 500 barrels up to 10 000 barrels (1 barrel corresponds to a volume of ≈ 159 L). They are made of either steel or fiberglass and are usually painted black. Gunbarrels are located within a tank battery, which also includes a number of oil and water storage tanks and a unit to monitor the oil being sold to the pipeline companies. If the contaminants in the oil (water, sediment, and other matter) exceed a preset limit, usually 1%, the oil is diverted back to a storage tank for treatment. This oil will go through another treating process to be within acceptable limits before it can be introduced back into the sales tank. The gunbarrel is a vital part of the crude oil sales and water-treating process. The crude from the producing wells goes directly into the gunbarrel, where the gas, oil, water, and small amounts of solids go through a separation process. The oil separates and floats upward, and the gas also goes to the top of the gunbarrel. The heavier water and solids settle to the bottom.

IR thermal imaging can then be used to identify all these layers from outside a gunbarrel tank [29]. The layer between the oil and water is called the *interface pad*. It is a normal part of the separation process, but sometimes the paraffin, asphaltenes, and iron compounds can become suspended within the interface pad. When this happens, the pad becomes thicker and can become hard, inhibiting the separation process and causing a number of operational problems. Using IR to locate these pads and their thickness, one can take measures to break it up before it gets too thick and hard. For example, chemicals can be added to break up the suspensions within the gunbarrel. Another method is to shut down operations to the gunbarrel and physically remove the contents, which usually requires personnel to go in and scrape out the solids, load them into trucks, and dispose of the waste materials.

Oil and water storage tanks are another area where IR has become an important CM tool. Water storage tanks are usually associated with water injection plants and receive the water from the crude oil batteries and gunbarrels. The water is then reinjected into the producing formations to enhance oil production. Some problems associated with water tanks are oil that has not been separated from the water and, as with the gunbarrels, solids and other unwanted compounds. IR thermography can be used to locate these levels of "bottoms" – settlements and oil layers floating on water that can be recovered and sold. Storage tanks with a large accumulation of bottoms are also more prone to tank bottom corrosion problems.

Figure 10.3 presents a thermal image of a water storage tank with a substantial amount of oil floating on water. It provides the data needed to understand what is going on inside these tanks and vessels, instead of just making an educated guess. This knowledge allows prioritization of maintenance efforts on these tanks and to go right to the most critical problems first, minimizing the potential environmental risks of tank overflows and leaks. It also helps not only in identifying those tanks and vessels that are high-priority risks, but it also allows deferral of maintenance on tanks that do not need attention.

Obviously, one needs a thermal contrast to record such an image [30]. This is due to the fact that materials in a tank or silo, whether solids, liquids, or gases, behave in different ways when subjected to a thermal transition. Gases typically

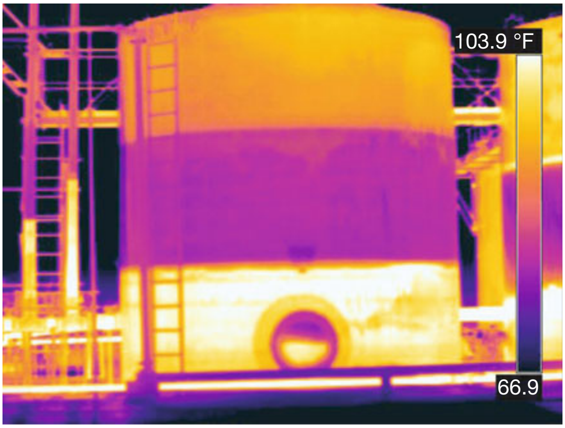

Figure 10.3 Locating levels of liquids in tanks. The shown tank has an outer diameter of about 4.7 m and a height of 4.9 m, which corresponds to a capacity of 500 barrels (79.5 m^3). At a height of about 1.5 m, a cool oil layer pad is floating on top of warmer water. The oil layer itself corresponds to about 23.9 m^3 of oil. (Image courtesy Danny Sims, Chevron USA.)

change temperature much more easily than liquids because of their much lower heat capacity. Consider, for example, air and water. If the same amount ΔQ of thermal energy is added to equal volumes of air and water, the resulting temperature changes differ appreciably. From the general relation $\Delta Q = cm\Delta T$, where c is the specific heat capacity and $m = \rho V$ the mass (ρ: density, V: volume) of the gas, liquid, or solid, it follows that

$$\frac{\Delta T_{\text{air}}}{\Delta T_{\text{water}}} = \frac{c_{\text{water}} \cdot \rho_{\text{water}}}{c_{\text{air}} \cdot \rho_{\text{air}}} \tag{10.1}$$

From known specific heats and densities (air: $c_p \approx 1\,\text{kJ}\,(\text{kg}\,\text{K})^{-1}$, $\rho = 1.293$ kg m^{-3}; water: $c = 4.182\,\text{kJ}\,(\text{kg}\,\text{K})^{-1}$, $\rho = 1000\,\text{kg}\,\text{m}^{-3}$) it follows that air temperature differs by a factor of more than 3000 from that of water. Now imagine a tank with a liquid and a gas on top. If the tank is heated from the outside, for example, owing to solar load, the gas can easily increase its temperature, that is, it will adapt its temperature to that of the tank wall. In contrast, the liquid below will show a much smaller temperature rise due to its large thermal heat capacity. This obviously results in a thermal signature on the outside wall at the interface between liquid and gas. If different liquids with different thermal heat capacity are present, the same mechanism leads to thermal signatures at the liquid interface.

In tanks, one may also have solids like sludge. Since liquids and solids have similar densities, the temperature rises due to the same thermal input energy are not as pronounced as compared to the gases. In this case, the thermal contrast is also affected by the different methods of heat transfer (Section 4.2). In solids, heat is transported by conduction, whereas in liquids, convections also play a major role. If heated from the wall of the tank, the various heat transfer mechanisms inside the solid and liquid give rise to the observed thermal signature.

How was the thermal contrast achieved in the example discussed here? The weather conditions in Texas include a lot of sunshine, which means solar load on the tank walls. In Figure 10.3, the gases on top of the oil layer (upper third of image) have a low heat capacity, which means that the wall temperature is mainly due to solar load. Below, that is, in the middle part, the oil layer cools the outside wall. At the bottom, however, there is warmer water which heats the wall. Because of the large heat capacity of the fluids, quasi-stationary conditions are achieved.

10.2.4
Polymer Molding

Shape and block molding of expanded polymers such as polystyrene, polypropylene, and various blends therefrom are nowadays widely used in the manufacture of many everyday-life products, ranging from simple packaging materials or picnic supplies to technical industrial products, for example, automotive bumpers, bicycle helmets, or aircraft structural parts. Besides being used in the direct creation of products, such foams are also used, for example, in metal–foam casting processes (Section 10.5.6).

The manufacture of foam-molded parts requires precise molding control, such as precise amounts of steam energy delivered to the mold and later extracted in the subsequent cooling cycles. Accomplishing this so-called energy balance is critical in molding good-quality parts. Besides quality control, one also wants to reduce excessive energy use.

Characterization of freshly molded parts is possible with IR thermal imaging. The parts will have varying moisture contents and thermal gradients from the manufacturing process. Quantitative analysis of the gradients can lead to process improvement and the identification of defect areas in the manufactured parts. In particular, thermal gradients are often directly related to mechanical property variations in the related locations.

Figure 10.4 shows examples of the manufacture of protective bicycle helmets [31]. These are molded in presses. The press halves separate after completion of the process and the frame slides out to allow retrieval of the freshly molded helmets. Figure 10.4 shows two images of the frames with helmets at the time of helmet ejection, showing significant temperature gradients for the molds and the helmets (line plots on right).

The IR image of the helmet shown in Figure 10.5 was recorded 60 s after its ejection from the mold. To determine whether the observed temperature gradient has an impact on helmet properties, an X-ray mass profile was made of the part. The helmet was inspected in slices by scanning the cross section of the helmet in several sections. These are also plotted in Figure 10.5.

The higher mass profile on one side of the helmet coincides with the thermal behavior in the press. This may imply a bead-filling issue on one side that when coupled with a differing steam distribution across the helmet results in differing fusion and density profiles [31]. Such features can lead to a nonuniformity of the mechanical properties of the helmet. In this case, the asymmetry of the

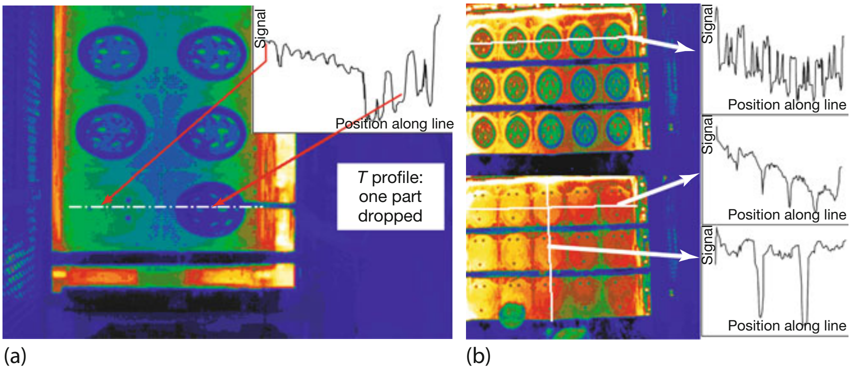

Figure 10.4 Thermal images of two thermal presses at point of bicycle helmet ejection. (Images courtesy G.V. Walford.)

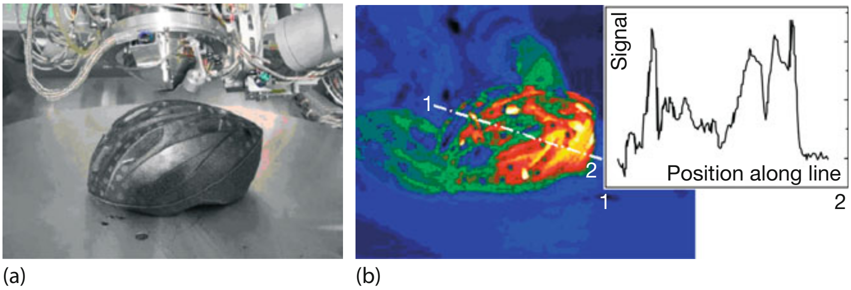

Figure 10.5 Visible (a) and thermal image (b) of a helmet removed from press. The helmet was subsequently analyzed using X-ray profiling; see inset at thermal image. (Images courtesy G.V. Walford.)

helmet was readily observable with thermal imaging. Such nonuniformities can have a significant impact on the end application, be it helmets or other mold parts, since mechanical properties are correspondingly modified from the original design specification.

10.2.5
Rack-Storage Fire Testing

Today's warehouses are larger and taller than ever before. Using automatic storage systems, commodities may be placed on racks at heights of about 30 m or higher. As a consequence, a fire in such a warehouse carries great risk. Therefore, quantitative modeling and real test measurements of large warehouse fires yield important information not only for the warehouse owner but for insurance companies as well. IR cameras have been useful in such experimental studies for two reasons. First, they make it possible to look through the smoke and steam and, thus, to see the details of how the fire spreads (smoke and steam develop rather quickly once the water sprinkling system is activated). Second, if properly

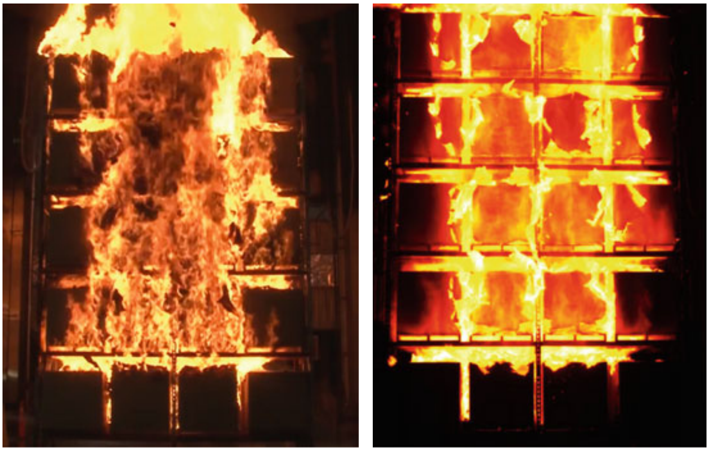

(a) (b)

Figure 10.6 Visible (a) and thermal image (b) of a rack fire. (Images courtesy J. de Vries, FM Global. See text for details.)

calibrated, the data yield quantitative surface temperatures that may be used to validate numerical model results. Successful firefighting and mitigation relies on the understanding of fire development and location [32, 33].

Figure 10.6 shows some results from a front view of a large test fire with a maximum heat release rate of up to 30 MW for a 2 × 4 × 5 tier high rack storage system. The horizontal and vertical dimensions of the system are about 5.1 and 7.3 m, respectively. Figure 10.6a shows a visible and Figure 10.6b a LW IR image recorded 200 s after ignition. The measurement range of the IR camera had been extended up to 1200 °C using an aperture of 12.7 mm in front of the lens and subsequent recalibration. When looking through the flames at the rack, the used LW IR range ensured that H_2O or CO_2 emissions played a minor role. However, heated soot particles could pose a problem. The corresponding tests showed that the flames only contributed about 50 K to the measured rack temperatures. The observed and modeled maximum temperatures inside some of the horizontal flue spaces reached up to 1400 K.

10.3
Low-Voltage Electrical Applications

There are many examples of IR thermal imaging in the field of low-voltage electrical applications [34]. They range from low-voltage indoor surveys and the study of components on electrical assemblies or electrical circuit boards and electronic components [35–38] to electric motors (e.g., [39]).

In what follows, just a few select examples of microelectronic boards are discussed. Some other low-voltage examples of electrical heating within wires, microwave oven, thermoelectric effects, or eddy currents were already treated in Chapter 5.

10.3.1
Early Microelectronic Boards

Because of the ongoing miniaturization of all electronic components, in particular in the microelectronic boards of computers, the problem of the malfunctioning of whole boards has become important. Although the voltages and the currents are very low, they still produce heat, and many components malfunction above a critical temperature. The old 486 processors from the early 1990s still operated uncooled and sometimes at working temperatures above 80 °C. Starting with the Pentium series in 1993, processors were air cooled by fans. Still, it is necessary to separate all heat-producing elements on a board from each other to avoid the overheating of individual parts. To test or design new boards, it is essential to operate the boards under working conditions and analyze, for example, IR images. Figure 10.7 shows an example of a board containing a fan-cooled Pentium processor. Upon turning the computer on, two integrated circuit chips and another processor on the board were also heated, however, typically only to 15 °C above room temperature.

As can be seen in the visible image, the board is made of different materials; therefore, the IR images usually reflect temperature as well as emissivity contrast. If emissivities are quite high ($\varepsilon > 0.9$), slight variations in their values are not critical. However, whenever small emissivities are present, in particular those of hot objects, the quantitative analysis must be performed very carefully. To overcome such problems, it was recently suggested that electronic boards be covered with a thin coating of known emissivity, which does not change the electric properties of the components [35]. In this case, the boards will show homogeneous emissivity and, hence, allow sensitive relative temperature measurements across them.

Besides the design of microelectronic boards for computers, IR imaging may also be used to study the behavior of simpler electronic boards. As an example,

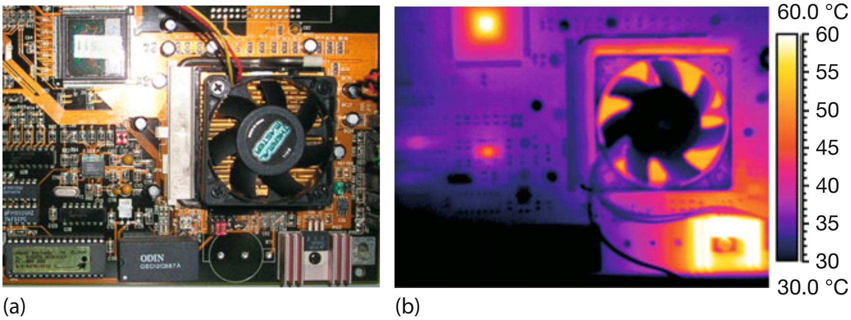

Figure 10.7 Microelectronic board with Pentium 100 processor below a fan. The heat sources are well separated on this board. For demonstration purposes, the fan was not run.

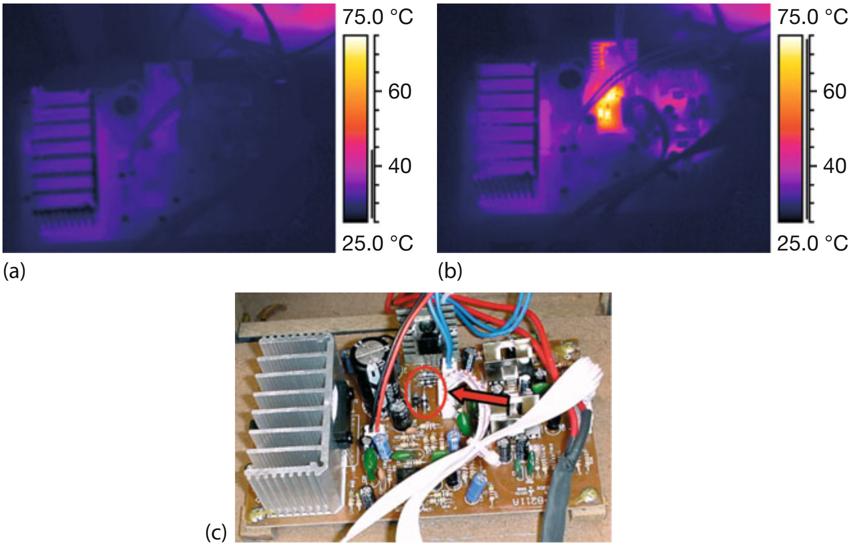

Figure 10.8 Visible (c) and IR images of electronic board of a speaker connected to a computer. First, the speaker was turned on but operated without emitting any sound (a), and then the speaker was used to play music that was clearly audible (b). Obviously, the four diodes on the board (red circle in VIS image) heated up to about 75 °C during operation of the speaker.

Figure 10.8 shows the electronic board of a small loudspeaker of a type that is usually connected to computers. The visible image shows the board that is mounted on the back cover of the speaker, which was opened for the experiment. Playing music obviously led to a heating up of four diodes on the board, whereas the power transistors were sufficiently cooled by the metallic cooling fins.

10.3.2
Macroscopic Electric Boards

Electric switchboards are related to typical industrial applications in engineering since the regular testing and surveying of electrical switches is essential for reducing service shutdown times and, hence, for guaranteeing a high productivity of machines in factories. Therefore, a student project [40] dealt with an electrical switch assembly to simulate malfunctioning and subsequently identify the relevant parts. To visualize typical defects occurring in low-voltage applications ($U < 1\,\text{kV}$), we prepared an old electric fuse board previously used in industry. Several typical failures were included artificially for student teaching. Figure 10.9 shows the visual image as well as an expanded view of the upper section. Several different defects can be clearly seen, such as a broken connection, a deformed (squeezed) wire connection, a loose connection (loose screw) with transition resistance, and a very old oxidized 16-A fuse. Whenever such anomalies are ob-

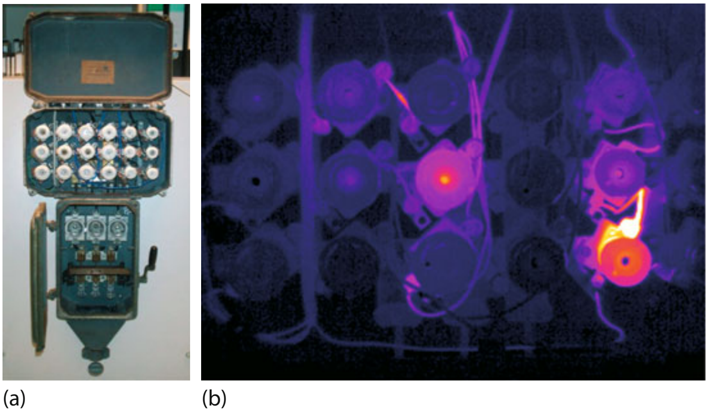

Figure 10.9 Visible (a) and IR image (b) of (very) old electrical equipment. The board was modified to include three typical thermal features of malfunctioning. Top row of fuses: broken wire within insulation gives resistance, heating up the wire. Middle row: an old oxidized fuse heats up. Bottom row, right: loose connection giving a transition resistance.

served in IR thermal imaging, one must take a closer look, which will usually lead to identifying and resolving the problem immediately.

10.3.3
Modern Microelectronic Boards

Modern microelectronic components are getting smaller with each development cycle. Therefore, IR cameras used to study the thermal behavior of the corresponding boards should have four features. First, they need an appropriate close-up lens; second, the resolution should be at least 640 × 480 pixels (better if possible); third, they should also record VIS images; and fourth, the image software should use digital detail enhancement (DDE) techniques (Section 3.5.1.7). Figure 10.10 shows an example clearly demonstrating the capabilities of IR imaging for electronic board inspections.

10.4
High-Voltage Electrical Applications

In addition to low-voltage applications, there are numerous medium- or high-voltage applications for IR thermal imaging, ranging from oil-filled circuit breakers [41], transformers, and substations [42, 43] to the study of high-voltage lines, sometimes only observed from helicopters [44]. For any quantitative outdoor inspections, potential wind speed effects on temperature readings of the components under study must be taken into account [45].

Since thermography inspections of electrical equipment make sense only if components are under full load, covers of electrical panels and other components

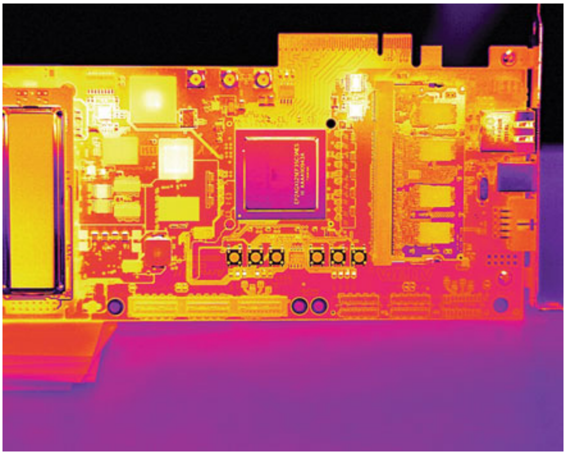

Figure 10.10 High-resolution DDE IR image (1280 × 1024 pixel) of a modern electronic board of a computer (image courtesy FLIR Systems Inc.).

must usually be removed [46] unless special IR windows are used [47, 48], which make it possible to study the objects from a safe distance. In any case, whenever high-voltage or high-power equipment under load is investigated, special personal protection precautions must be taken to avoid arc flash hazards [49–52].

10.4.1
Substation Transformers

A very important electrical application for thermography are high-voltage power lines and their connection to transformer units. Figure 10.11 shows an example of a 115–23 kV substation transformer unit [53]. The distance between the camera and the transformer, which was run at about 40% of the maximum allowed load, was determined by a laser range finder to be around 11 m. At least two of the phases show problems. Figure 10.11 also illustrates a typical problem of outdoor electrical applications encountered when studying high-voltage equipment. Since the distances between observer (camera) and the targets are often above 10 m – with no chance for the thermographer to get closer – and targets (like the 19 mm cables in Figure 10.11) are sometimes just a few centimeters in size, the spatial resolution of the camera can impose problems for a quantitative analysis. In the example presented, three different measurements of the same targets were made at about the same time and from the same distance under the same environmental and load conditions. Three different cameras (high, medium, and low number of pixels) were used, which differed only by their detector arrays (high: 640 × 480 pixels, medium: 320 × 240 pixels, and low: 160 × 120 pixels). Since the field of view (FOV) determined by the standard optics was similar, the instantaneous field of view (IFOV) of the cameras differed (0.65, 1.3, and 2.6 mrad, re-

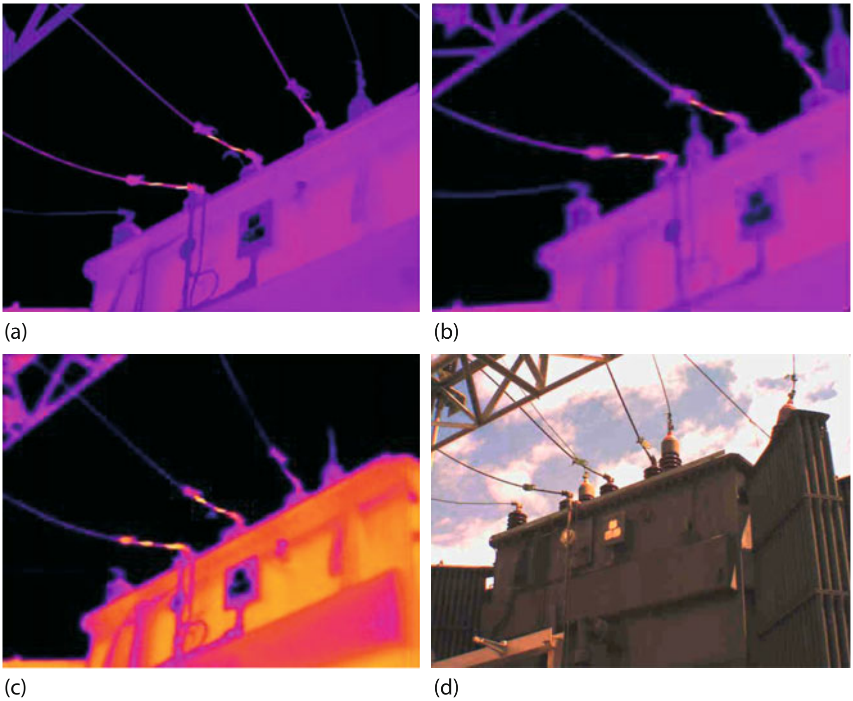

Figure 10.11 Thermal images of 115–23 kV substation transformer, low side. (a) High-resolution (640 × 480 pixels), (b) medium-resolution (320 × 240 pixels), (c) low-resolution (160 × 120 pixels), and (d) visible image. Significant thermal anomalies can be clearly observed with all cameras; quantitative analysis, however, results in large differences (see text for details). (Images courtesy: Infrared Training Center, FLIR Systems.)

spectively). As a consequence, the number of pixels is directly related to the spatial resolution (Section 2.5.3).

A cable of 2 cm at a distance of 11 m corresponds to an angular size of about 1.8 mrad or 0.1°. As mentioned in Chapter 2, the minimum object size should be about two to three times the IFOV in order to get reliable temperature measurements. This condition is only fulfilled for the high-resolution camera with IFOV = 0.65 mrad. Therefore, it is to be expected that the medium- and low-resolution cameras will show appreciably lower temperatures, since the background temperature of the clear sky behind the cables was well below 0 °C and the detectors received signals not only from the hot cable but also from the much colder background.

The two problem areas with thermal anomalies of the jumpers from the bushings were detected with all cameras. The jumpers from the bushings to the feed were stranded cables where some of the strands had broken over time or were not well connected electrically. This caused overloading of the remaining good conductors, resulting in significant heating. Preliminary conclusions indicated that one may detect thermal anomalies with all cameras.

However, the question arises as to whether these anomalies create a problem that needs to be dealt with. Obviously, one must quantitatively estimate the temperature increases of the problem areas. The maximum temperature of the leftmost phase in Figure 10.11 was analyzed for all three images. Not surprisingly, the temperature rise with respect to ambient temperature differed appreciably for the three cameras showing 50 °C (low), 95 °C (medium), and 117 °C (high) for 40% load of the transformer.

This 40% load situation was observed in early June when the weather was cool and electrical demand in the area was low. Obviously, later in the summer, the use of air conditioners would lead to much higher demand. Therefore, the temperature rises were also estimated for 100% load (for load correction [45]). It was found that temperature differences would significantly increase to 211 °C (low), 402 °C (medium), and even 494 °C (high). Whether a temperature rise is critical or not depends on the criteria [54], for example, those of the American Electric Power Research Institute (EPRI). In this case, the problem severity according the EPRI criteria was already critical at 40% load for the medium- and high-resolution measurements! For the estimate of 100% load, results indicated a very high probability of major failure.

The example of Figure 10.11 nicely demonstrates the importance of knowing the exact spatial resolution of the camera used, in particular if the distance to small targets is quite large. For the conditions presented here, a cheap and simple low-resolution camera of 160 × 120 pixels is useless.

It should also be mentioned that whenever surface temperatures are measured from high-voltage electrical components, small measured values at the outside surface may correspond to large internal temperature rises. This can, for example, be the case for oil circuit breakers [55]. In this case, power loss calculations, including convective and radiative heat transfer, can be based on measured surface temperatures to estimate the total power loss, and from that the internal electrical resistance can be calculated.

10.4.2
Overheated High-Voltage Line

Figure 10.12 shows a number of 130 kV lines under load. Three cables are clearly overheated, as can be seen in direct comparison with the other (blue color) cables, which were much colder. It turned out that the load on these three cables was occasionally enlarged without taking into account whether they were being run with the load above the specified limit. The diameter of the cables needs to be increased, too, to reduce their resistance, that is, the electrical power consumption by the cables themselves.

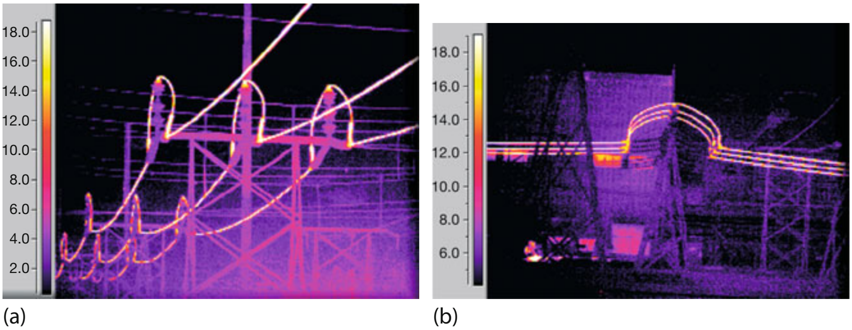

Figure 10.12 About 130 kV high-voltage lines that are clearly overheated. Temperature scale in °C. (Images courtesy J. Giesecke.)

10.4.3
Electric Fan Defects

Transformer units at substations are critical components. Their housings are usually cooled from their sides by a series of powerful fans. Figure 10.13 shows an array of nine fans capable of cooling an area of about 4 m^2 of a transformer housing. The center fan in the image suffered a severe malfunction. The fan motor was overheated and only allowed for a strongly reduced cooling operation, as can be seen by the elevated transformer wall temperatures. When this unit was exposed to extremely high solar load, the reduced cooling sometimes resulted in problems, that is, the fan motor had to be exchanged or repaired immediately.

10.4.4
Oil Levels in High-Voltage Bushings

A very crucial application of IR imaging is monitoring oil levels in bushings of high-voltage power equipment [56, 57]. This is an important application because it deals indirectly with the most costly piece of equipment in a power grid, the power transformer. Bushings are devices that allow electrical current to pass through a barrier and provide an electrical connection on each side while pro-

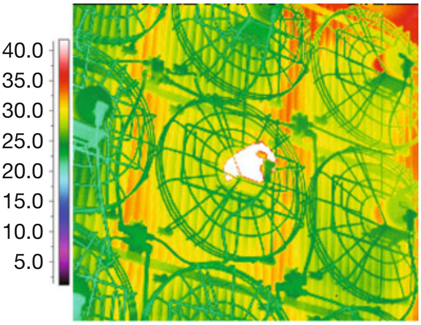

Figure 10.13 Housing of a transformer unit cooled by a series of electric fans. The center fan is malfunctioning leading to reduced cooling power. Temperature scale in °C. (Image courtesy J. Giesecke.).

viding electrical insulation between the center conductor and the ground. The inside conductor is surrounded by electrical insulation. In higher-voltage bushings, it consists of concentric layers of insulation and layers of conductor foils. These layers of insulation and conductors form a concentric capacitor between the high-voltage center core and the bushing flange at ground potential. In most modern bushings above 26 kV, paper provides the skeleton for the insulation system. The paper is impregnated with mineral oil to provide more insulation.

One of the most important failure modes of high-voltage bushings are oil leakages. Whatever the reason for the leakage, moist air may enter the bushing and replace the oil. Since the paper will become devoid of oil, the insulation ability of the bushing decreases. Eventually, electrical discharges (corona discharges) can develop, which may eat like worms through the paper, causing the foil layers to short out. In the worst case, the dry insulation may flash and lead to million-dollar losses (the cost of high-voltage transformer units). Therefore, it is of the utmost importance to regularly check the oil levels in such high-voltage transformer bushings.

IR thermal imaging is a very useful method for determining the oil levels in such bushings in PdM programs. The method for detecting oil levels is simple. In any transformer, there are energy losses that lead to a temperature increase in the transformer coils. These heat up the oil in the tank of the transformer and, via thermal conduction, the oil filling in the attached bushing. Because of the thermal conductivity through the wall of the bushing and heat capacitance of the oil with respect to that of the air above it, the bushing oil level can be seen. So the bushings will appear warmer where the oil is and cooler where there is no oil. The IR image (Figure 10.14) shows two bushings, the one on the right being full of

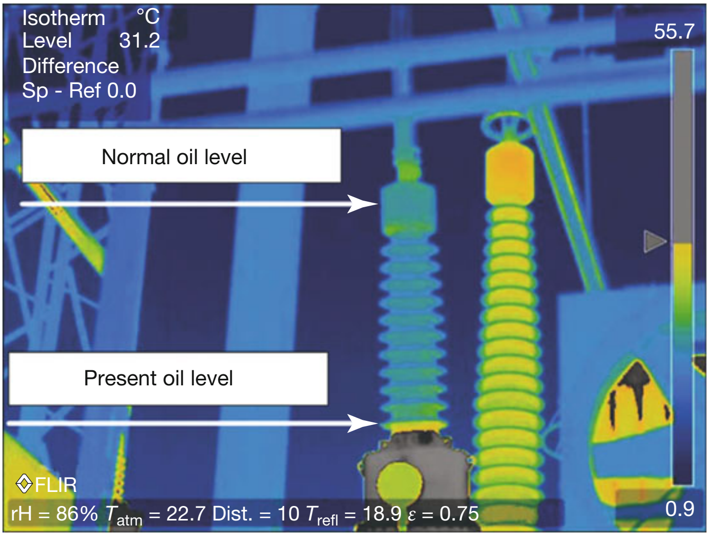

Figure 10.14 Checking oil levels in bushings of high-voltage power equipment. See text for details. (Image courtesy M.B. Goff.)

oil and the other one being only partially filled. The oil-filled bushing is warmer (around 31 °C) owing to the heat conduction from the warm transformer tank full of oil up the bushing all the way to the top. In contrast, the bushing with a low oil level is much colder, here only around 15 °C, since there is no oil in the bushing to conduct the heat from the transformer to the bushing. Only the very lowest part of the bushing on the left shows signs of heat being conducted, thus marking the location of the oil level. After verifying the low oil level, the transformer was immediately removed from service for repair to avoid possible catastrophic failure.

10.5
Metal Industry and High Temperatures

The metal industry deals with all aspects of working with metals to create individual parts, assemblies, or large-scale structures. Metal working generally is divided into three categories: forming, cutting, and, joining. Each of these categories contains various processes. Forming processes modify the work pieces by deforming the object without removing any material. This is done with heat and pressure, with mechanical force, or both. In casting, a specific form of metallic objects is achieved by pouring molten metal into a form and allowing it to cool. Cutting and joining consists of a collection of processes, wherein the material is brought to a specified geometry by either removing excess material using various kinds of tooling or by joining two metal parts by processes like welding. With regard to materials, one often distinguishes the steel industry from the light metal industry (e.g., aluminum, magnesium, titanium) and industries dealing with other nonferrous metals (e.g., copper, platinum, noble metals).

Obviously, the metal industry offers a large variety of different processes, some of them associated with very high temperatures. Therefore, it is natural that attempts have been made to measure the associated temperatures with IR thermal imaging. In particular, it seems promising at first glance to measure temperatures of metal molds, for example, in steel or aluminum casting.

10.5.1
Direct Imaging of Hot Metal Molds

Figure 10.15 shows an example of an aluminum cast. Although contact measurements resulted in large temperatures of around 800 °C, IR imaging is not very accurate in determining temperatures. There are several reasons for this. First, metals have very low emissivities in the thermal IR range (Section 1.4), and small ε variations can lead to large changes in measured temperature. The variations in emissivity of metal molds are due to the dependence of ε on temperature itself, the thickness of the molten slag (which has lower density and lies atop the pure metal), the angle of observation, and so on. In addition, metal molds behave like liquids [58]. In particular, they may exhibit convection cells (like the Bénard con-

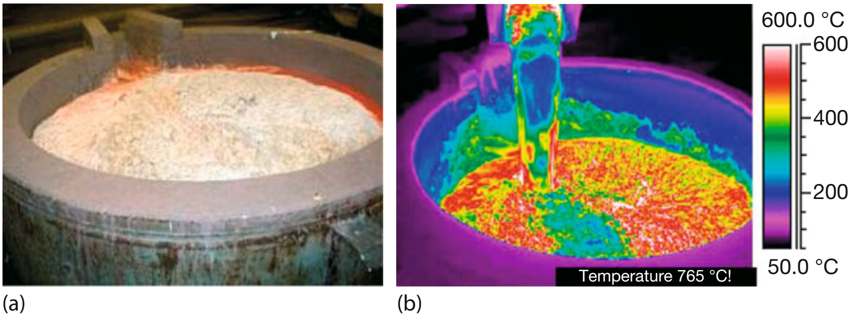

Figure 10.15 Aluminum casting. (a) Visible image. (b) Thermal imaging shows huge variations of temperatures of the mold owing to various parameters that affect emissivity. (Images courtesy H. Schweiger [59].)

vections, Section 5.3.4), which induce temperature fluctuations at the mold surface. All these effects can lead to measurement errors of several hundred Kelvin!

This example indicates that to measure the temperatures of molten metals, conventional thermography is usually unsuitable. Rather, a method that is independent of emissivity, such as ratio thermometry, is needed (Section 3.2.2). In pyrometry, the related instruments are called *two-color pyrometers* [60]. In addition, for high-temperature metal applications, it may be useful to use SW imaging rather than LW or MW cameras (Chapter 6).

10.5.2
Manufacturing Hot Solid Metal Strips: Thermal Reflections

Once pure and solid metals are available, the machining of the metals still requires high temperatures. As an example, Figure 10.16 shows a scene from an aluminum factory during the production of aluminum metal strips. In the foreground is seen a hot pure aluminum metal strip (thickness around 3 cm, width about 2 m), mov-

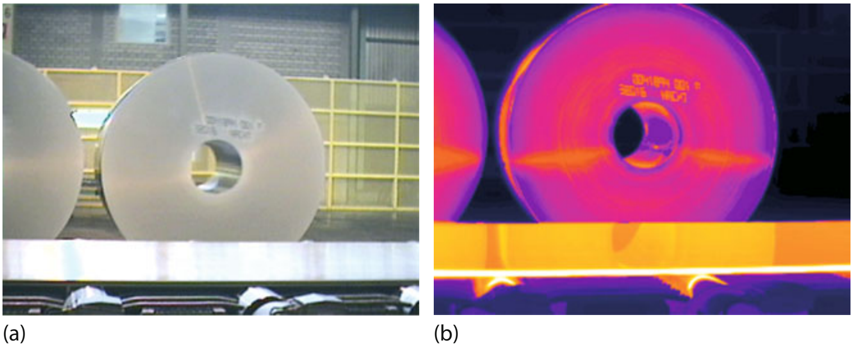

Figure 10.16 Cold aluminum rolls ($T < 200\,°C$) behind a hot ($T = 480\,°C$) aluminum strip with very low emissivity ($\varepsilon = 0.065$). Thermal reflections are evident.

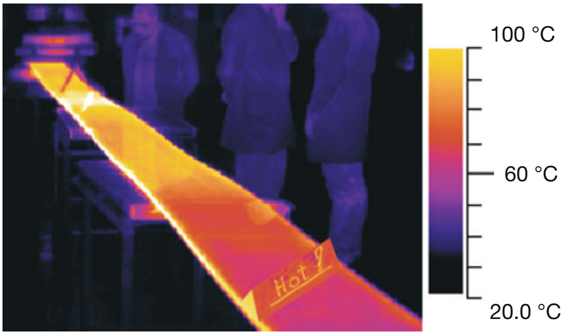

Figure 10.17 Thermal image of a hot and low-emissivity aluminum strip (near 200 °C) with strong reflections, demonstrating the influence of inhomogeneous background radiation.

ing at a velocity of about 2 m s^{-1}, that has surface temperatures of around 480 °C. Because of the manufacturing, the aluminum strip surfaces are very flat and have very low emissivities of around $\varepsilon = 0.065$. In the background can be seen colder aluminum rolls (thinner strips with thickness usually between 2 and 5 mm at a lower temperature of around 200 °C rolled to form a cylinder for transport). Similarly, Figure 10.17 shows an example of another aluminum strip (width about 0.6 m) produced for research purposes. The strip was supported by several tables to cool down slowly. At the time of the measurement, it still had a temperature of about 200 °C. Both IR images clearly show thermal reflections owing to the very flat surfaces.

In Figure 10.16, the reflections of the 200 °C background cylinders show up as apparently higher temperature on the 480 °C aluminum band in the foreground. This seems paradoxical at first glance: why should a colder metal give rise to a larger radiation signal when observed as thermal reflection from a much hotter metal strip? The answer is simple: the emissivity of the front side is increased largely due to the surface roughness, which is induced by rolling the thin metal strips to form the cylinder. The IR image shows another feature: the left-hand side of the cylinder allows a grazing incidence view of the strip surface. At such large angles, emissivities of conductors increase (Figure 1.31), which explains why the perimeter surface of the cylinder emits more radiation than its front. This feature is also apparent in the thermal reflection image from the hot aluminum strip.

A similarly surprising feature is shown in Figure 10.17, where thermal reflections of people with skin and clothing temperatures of around 30 °C show up as thermal reflections with greater IR emissions from the hot aluminum strip of 200 °C. Again, the people in the image have much higher emissivities compared to the hot metal.

This effect of thermal reflections of cold objects showing up as strong IR radiation sources in thermal reflections from very hot objects can also be understood quantitatively, provided the emissivity ε_{obj} of the object is known. Besides the emitted object radiation $\varepsilon_{\text{obj}} S_{\text{obj}}$, the detected radiation signal S_{det} from highly re-

Table 10.1 Signal contributions for an IR camera in 8–14 µm spectral range for pure aluminum with an emissivity of 0.02 and background at $T = 25\,°\text{C}$.

Al temperature (°C)	Signal portion of reflected background radiation (%)	Signal portion of emission (%) from Al surfaces
70	83.4	16.6
200	59.2	40.8
400	34.0	66.0

flecting surfaces also contains the reflected background radiation $(1 - \varepsilon_{\text{obj}})S_{\text{backgr}}$:

$$S_{\text{det}} = \varepsilon_{\text{obj}} S_{\text{obj}} + (1 - \varepsilon_{\text{obj}})S_{\text{backgr}} \tag{10.2}$$

S_{obj} is the radiation signal detected from a blackbody object of the same temperature. For aluminum, the emissivities ε_{obj} are very low, typically $\varepsilon_{\text{obj}} = 0.02\text{–}0.2$ depending on the alloy composition, surface roughness, and temperature. Table 10.1 compares the signal contributions of reflected background to object emission in the spectral region of a LW camera (8–14 µm). Surprisingly, the signal from aluminum of 200 °C with $\varepsilon_{\text{obj}} = 0.02$ is still smaller than the radiation of reflected objects of 25 °C. Obviously, background objects of higher temperatures shift the signal ratio to an even more unfavorable value (see also Section 2.3.3.3).

10.5.3
Determination of Metal Temperatures if Emissivity Is Known

Low emissivities and corresponding reflections from object surfaces are well known theoretically, and manufacturers of IR camera systems usually implement a reflectivity correction in order to be able to determine object temperatures. However, such corrections assume a constant ambient temperature of all background objects and precisely known object emissivities. They work reasonably well only if ε_{obj} is large. For very small ε values of metals, variations in object emissivity and fluctuation of background temperatures may lead to deviations. If the exact emissivity is known, the latter problem may be overcome using a homogeneous background illumination (hemispherical illumination) of known background temperature. Figure 10.18 illustrates this procedure for two different background temperatures in cold aluminum rolling where the emissivity is not changed by the temperature treatment. The aluminum strip (emissivity of the aluminum strip 0.05, pure aluminum alloy with a very smooth and homogeneous surface) was illuminated by two emitters (with emissivity of 0.98, temperatures 30 and 140 °C). To determine the strip temperatures, the emitter temperatures were used as the ambient temperatures. The results fit the aluminum strip temperature of 125 °C, with an uncertainty lower than 5°.

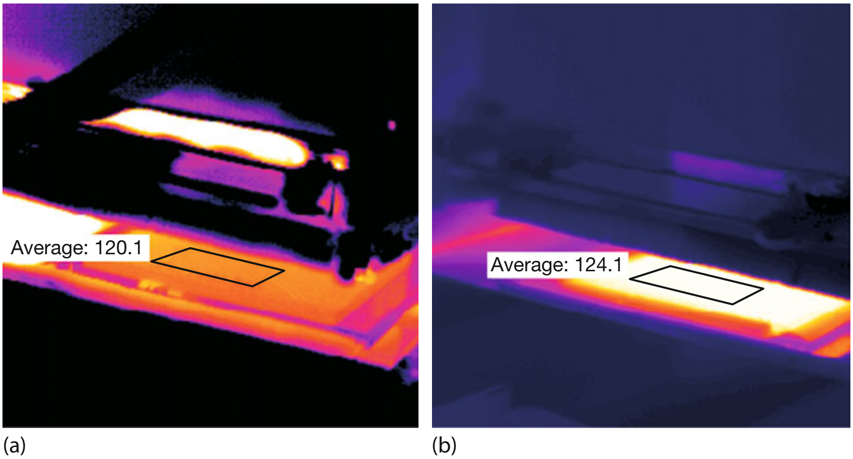

Figure 10.18 Temperature measurement at a 125 °C aluminum strip, background illuminated with black emitters at different temperatures: (a) 30 °C and (b) 140 °C.

10.5.4
Determining Metal Temperatures for Unknown Emissivity: Gold Cup Method

The typical situation for industrial applications is more complex (Figure 10.19). In most cases, the emissivity is not known accurately, and it changes over the course of the production process. The object signal is strongly influenced by thermal reflections of background objects (a structured, that is, inhomogeneous, background) at different temperatures and changing angles. Because of the strong influence of varying reflections (compare Table 10.1), the object signal may change by as much as 20%, resulting in large temperature measurement errors.

The so-called gold cup method [61] uses a highly reflecting hemisphere with a small hole for the camera (similar to an integrating sphere) placed near the surface of the object. All radiation sources for thermal reflections are blocked, and

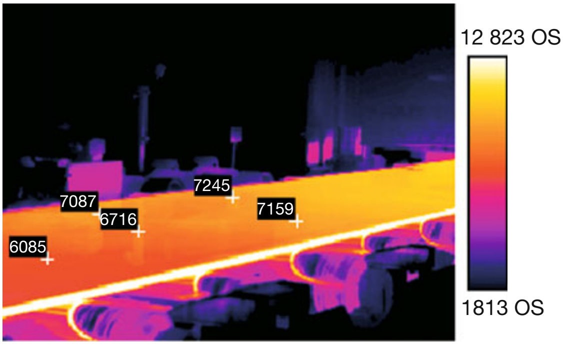

Figure 10.19 Measured object signals at different points of aluminum strip.

the multiple reflections inside the cavity increase the apparent emissivity to close to unity. The application of this method requires, however, a very clean environment to avoid a decrease in the reflectivity inside the hemisphere and very small working distances to suppress any thermal reflection from outside background. Within most industrial processes, such clean conditions and small distances are unobtainable.

10.5.5
Determining Metal Temperatures for Unknown Emissivity: Wedge and Black Emitter Method

There are two possible solutions to solve this problem under industrial conditions with varying emissivities. First, the wedge method [61] can be used for aluminum rolling. In this application, highly polished rollers form an aluminum strip. These rollers and the strip form a wedge (Figure 10.20) that acts as a cavity (multiple reflections) and therefore has an increased emissivity [62]. Figure 10.20 demonstrates that, in principle, wedges enhance emissivity and, thus, IR emission; however, a quantitative analysis still requires precise knowledge of the emissivity.

To estimate changes in ε induced by a wedge, a test measurement was performed with an aluminum strip of known temperature (provided with a contact

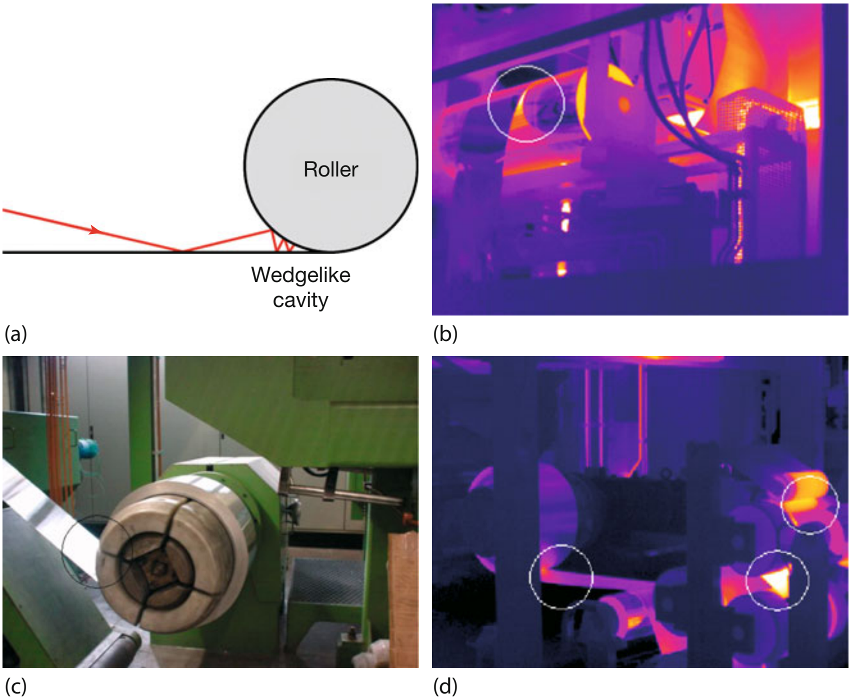

Figure 10.20 Wedges formed by roller and aluminum strip. (a,c) Scheme and VIS photo and (b,d) example of IR images.

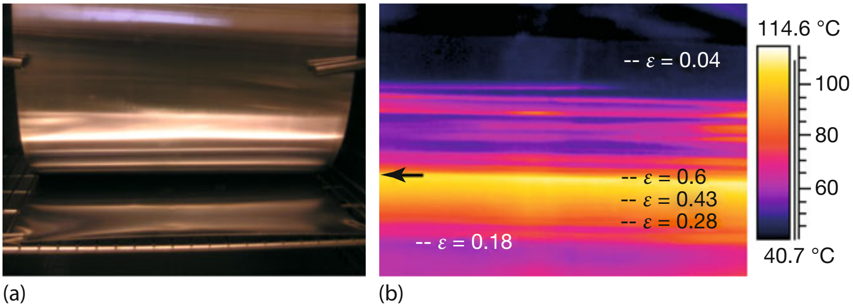

Figure 10.21 Thermal imaging of aluminum using wedge measurement technique (temperature 110 °C, temperature scale for emissivity setting 0.6); ε = calculated emissivity.

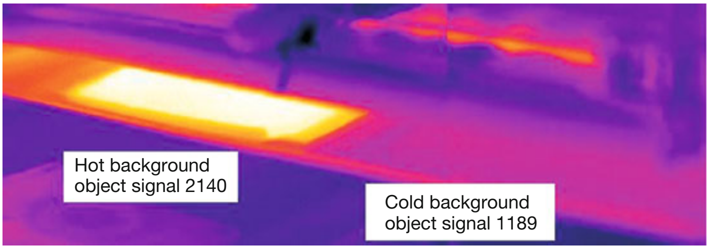

Figure 10.22 Projection of blackbody emitters with different temperatures on aluminum strip. Analysis of the two signals yields emissivity as well as metal temperature.

measurement). Because of the purity and the smooth and shiny surface of the aluminum strip, the emissivity in the 8–14 μm region was as low as 0.04 (Figure 10.21). The visible image shows the cavity effect with strongly increased absorptance within the formed wedge. The emissivity in the LW region increased from 0.04 to 0.6. The maximum emissivity value is limited by the geometric resolution of the thermal imaging system. Obviously, it is difficult to correctly guess exact emissivity values; therefore, the wedge method is not suitable as a standard method to quantitatively measure metal temperatures.

A second and much better way to estimate correct temperatures from low-emissivity metals uses two blackbody emitters. The object whose temperature is to be measured is illuminated (approaching hemispherical illumination) with two blackbody emitters that have different temperatures (Figure 10.22). Using Eq. (10.2) with the two different background temperatures, both the emissivity as well as the emitted radiation (object signal) of the measuring object can be determined. Using the calibration curve (temperature versus radiance) of the imager, the object temperature can be determined accurately. For a detailed analysis of a corresponding radiation thermometry of aluminum, see [63, 64].

Two-color pyrometry (Section 3.2.2) can also accurately measure metal temperatures, provided the emissivities are the same in both chosen wavelength bands.

10.5.6
Other Applications of IR Imaging in Metal Industry or at High Temperatures

There are many more applications of IR thermal imaging in the metal industry; for an early review of radiation thermometry in the steel and aluminum industries, see [60]. In this chapter, a few more examples with IR cameras are mentioned.

First, thermography applications have recently been reported for equipment in steel works [65], mostly within a PdM program. Examples include machinery, electrical systems including motors and substation conditions, and pipeline inspections.

A second example concerns casting, in particular, lost-foam casting processes. Lost-foam casting is an evaporative-pattern casting process. First, a pattern in the shape of the desired part is made from polystyrene foam such that the final pattern contains mostly air and a few percent polystyrene. Next, it is coated with a ceramic that forms a barrier so that molten metal does not penetrate. It is then placed inside a flask and backed by sand (or other molding media), which is compacted. Then, the mold is ready to be poured. The molten metal causes the foam to evaporate, that is, it replaces the foam until the form is completely filled with the desired metal form. The pyrolysis products escape through the porous ceramic coating into the surrounding porous medium (sand). After cooling and solidifying, the cast is removed from the flask.

During lost-foam casting, it is important to avoid defect formation such as flaws that could subsequently lead to failure of the part in service. The cause of such fold formation in aluminum lost-foam casting is the presence of retained foam residues during metal fill and solidification. Therefore, a detailed study using real-time MW IR imaging at 10 frames/s was conducted to examine the effects of various process parameters on the metal fill and the casting quality [66]. For this purpose, the flask contained a ceramic window for MW IR inspections at mold temperatures of up to 700 °C. It was found that lowering the heat loss rate during the liquid metal cooling should reduce fold formation.

In many industrial chemical processes, furnaces are used for high-temperature processes. Our third and final example deals with the investigation of furnace tubes (which transport liquids through fire chambers). Characterizations of temperatures within a furnace during operation are quite difficult to obtain. First, one needs to know the emissivities; second, one must address the reflected apparent temperature; third, the atmosphere within a furnace absorbs and emits radiation, so one needs to know the flame spectrum. Here, a MW camera was used with a spectral filter at 3.9 μm, where the flame has around 100% transmission. Still, quantitative measurements are very difficult [67], whereas qualitative inspections can yield valuable information.

Figure 10.23a shows an IR image of furnace tubes in operation that clearly demonstrates patterns resembling temperature variations on the tubes. These may be due first to outer surface deposits as a result of oxidation processes which change the local emissivity. In our study these changes were negligible. A second and more severe cause of temperature fluctuations is coking of the tubes

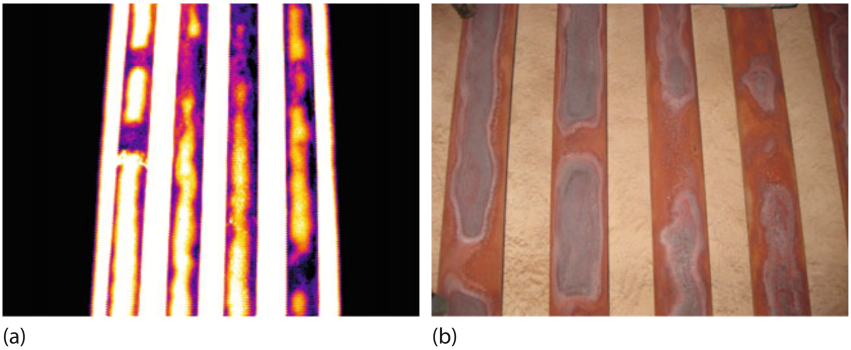

Figure 10.23 Thermal patterns observable owing to furnace tube coking (a); they also show up in visible images (b). Image courtesy Andy Whitcher, Tecpinions Ltd.

from the inside. This may happen if the outside of the tubes has been locally overheated. As a consequence, the (usually carbon-rich) process fluid inside the tube breaks down and creates an inside layer of carbon, called coke deposition. Coke depositions resemble heat resistances, which lead to further local overheating (which may also lead to outer surface changes that directly reflect the inside coking). This may finally result in tube rupture, with catastrophic results. In one case study, it was also possible to record visible images of the furnace tube (Figure 10.23b) while the furnace was shut down for inspection. The significant changes in surface conditions matched the thermal pattern owing to the coking patterns.

10.6
Automobile Industry

The car industry is a key industry for many countries not only with regard to the large number of employees but also because it is a field where new high-tech innovations are continually being introduced. In this respect, it was only a question of time for IR thermal imaging to bridge the gap between analysis tool for the manufacture and implementation in the product itself. Applications of thermography in the car industry are, therefore, at least threefold. First, it may be used for CM and PdM of all kinds of equipment in factories (Section 10.2); second, it can be used to check product quality; and third, IR imaging is used as a new technology to enhance safety while driving at night. Examples of CM and PdM in the automobile industry that do not differ from their uses in other industries, for example, checking electrical panels, robotic welders, motors, and so on [68, 69], are not discussed here.

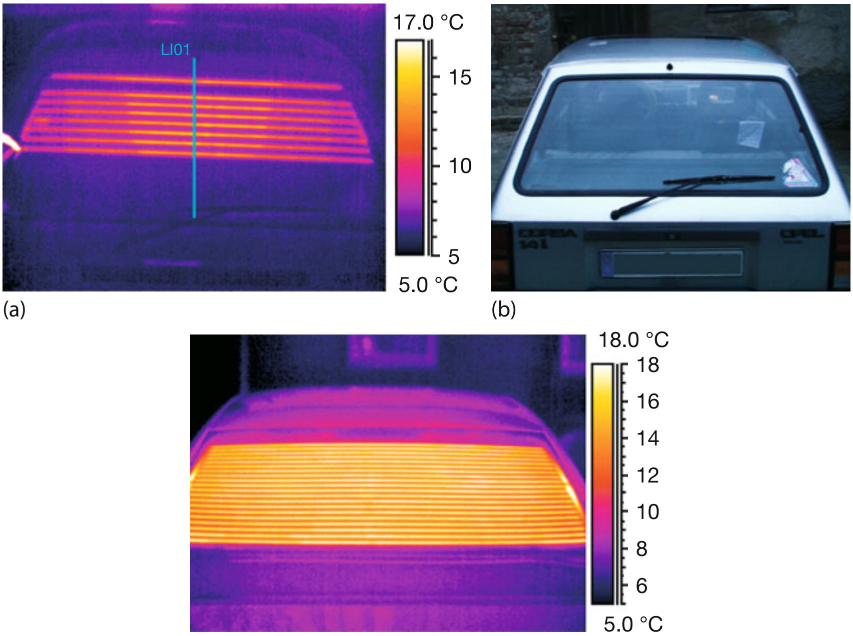

(a) (b)

(c)

Figure 10.24 IR (a) and visible (b) image of defective rear-window heater and (c) example of a properly working heater of a more expensive car (more wires separated by smaller distances).

10.6.1
Quality Control of Heating Systems

The car industry offers many examples of directly using thermography to check the quality of certain components of cars. Figures 10.24–10.26 give some examples. Figure 10.24 displays a defective rear-window electrical heater (also called a *defogger*), which originally consisted of a row of 12 parallel wires attached to the window. As a result of scraping ice off the window, some wires were damaged: the second one from the top and the lowest three wires are clearly not working. Besides detecting new damage to rear-window defoggers, the technique is also used in quality control. Recently, a modern car manufacturer had announced a previous failure rate of 1 out of 50 rear-window defoggers. To overcome this, IR thermal inspections were used as a means of quality control and were found to be successful [70].

Similarly, modern cars also have front windshield heaters (Figure 10.25), and it is popular to have seat heaters in cars (Figure 10.26).

Other examples for the use of IR thermal inspections in the car industry include testing of brakes [71] and, in particular, quality control of tires. Besides regular tires, IR imaging is also regularly used to test the special tires of racing cars (see Section 10.6.3).

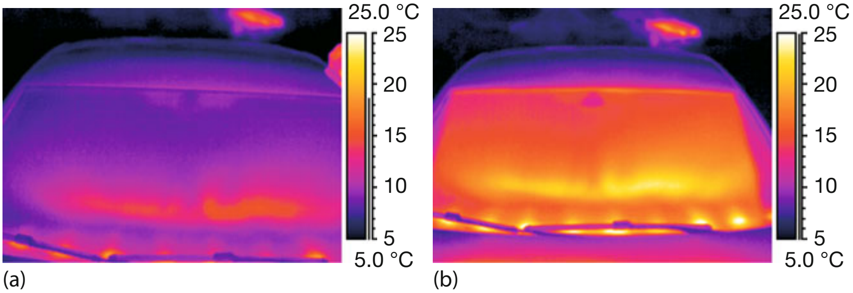

Figure 10.25 Front windshield heaters work using hot air from a fan (eight equidistant openings at bottom) as well as many very small heating wires embedded in glass, ensuring very fast defogging.

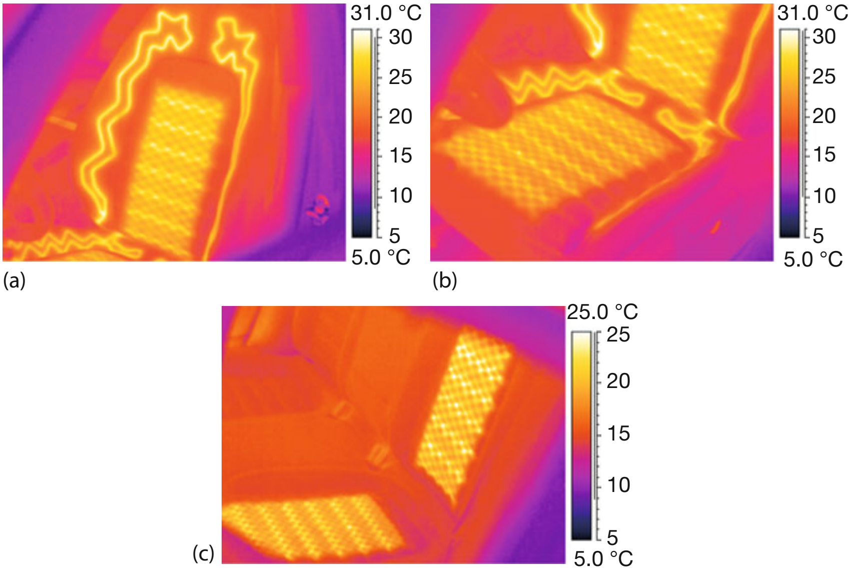

Figure 10.26 (a,b) Front-seat heater and (c) rear-seat heater in a car.

A number of different patents are associated with car tires and thermography. For example, one European patent application proposed to measure temperatures across a tire profile using high-speed IR imaging [72] and another US patent involved forecasting tire wear using high-speed thermography [73].

10.6.2
Active and Passive IR Night Vision Systems

A very recent, perhaps the most important, innovation of IR imaging in the car industry in recent decades, took place in the field of driving safety. Driving during the day presents no problems to observing the road and potential obstacles ahead for several hundred meters, while at night only the portion of the road that is illuminated by the headlights is visible. Although there have been many innovations in lighting, for example, intelligent headlight beams that bend while driving on curves, the visual range in night driving is drastically reduced. Problems arise in particular if either cold objects like rocks or trees are blocking the road ahead or if warm objects like animals cross the road or people are moving along the road, say if their car breaks down. If the headlights catch such obstacles very late at night, meaning the driver sees them very late, reaction time limits for avoiding an accident can become very short. This limited visual detection ability by drivers can be overcome through the use of IR thermal imaging. Two different types of night vision systems are currently available for models of (so far mostly expensive) cars. One system (used, for example, in Mercedes Benz) uses an active technique, while the other (used, for example, in BMWs) utilizes passive IR imaging. These night vision systems currently run for around €2000. Both systems have specific properties: active systems have the advantage of also observing cold objects, and passive systems can detect warm obstacles at greater distances.

In the active system, near-IR (NIR) radiation is emitted by special IR headlights close to the regular visible headlights, and a NIR camera behind the windshield detects the scattered NIR radiation, similar to the scattered visible light from objects illuminated by headlights as detected by the human eye. The IR signals are then displayed as grayscale images on an 8-in thin-film-transistor (TFT) display in the center of the cockpit (Figure 10.27).

The technique works for distances of up to about 100 m, corresponding to the usual range of long-distance light, but without blinding the drivers of oncoming vehicles. As shown in Figure 10.27, it is easy to detect so-called hot objects such as pedestrians. In addition, cold objects, such as an abandoned car on the side of the road, can also be seen in advance.

Passive systems use regular but miniaturized IR cameras (focal-plane array (FPA) bolometer LW systems, 8–14 μm, usually with 320 × 240 pixels, camera size about $6 \times 6 \times 7\,\text{cm}^3$) with a wide-angle lens (36° horizontal and 27° vertical field of view), which can easily detect IR radiation for distances of up to 300 m. This system does not need active illumination but uses the emitted radiation of hot objects. Therefore, it may easily identify animals or humans, but it may not detect cold objects like rocks on the road. Like the active system, images are displayed on a monitor on the dashboard. This means that the driver must move his/her head slightly, but this would likely become a natural movement similar to checking the rearview mirror. The IR camera optics is equipped with electrical heating to prevent fog or ice on the lens.

Figure 10.28 shows two examples of IR images as displayed on the monitor from the passive system. Outside city limits, one could see wild animals such as deer crossing the street (Figure 10.28a) and in towns with poorly lit roads, one could encounter pedestrians with pets (Figure 10.28b).

Similarly, Figure 10.29 shows other examples while driving out of town.

Both active and passive systems, meanwhile, also use additional software for pattern recognition. Whenever animals or humans are detected, the systems

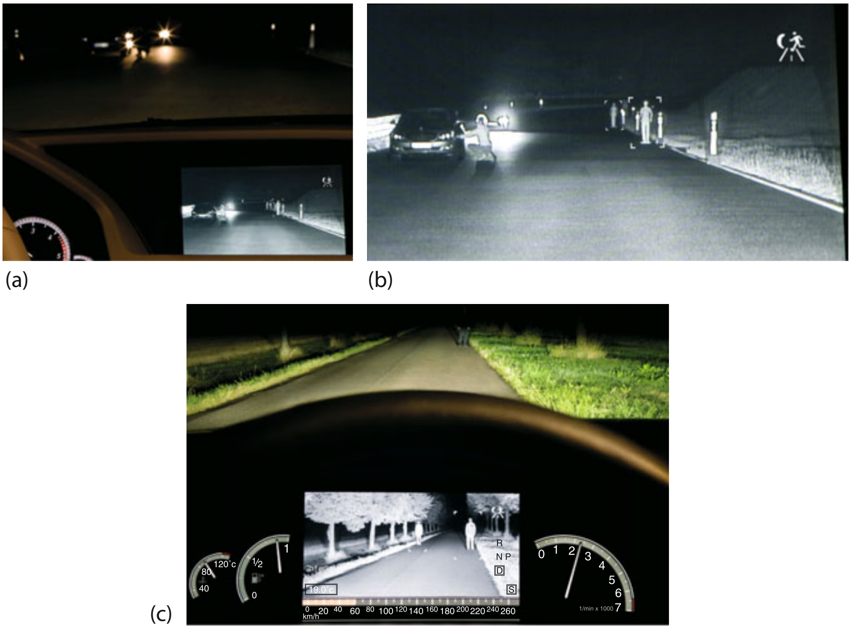

(a) (b) (c)

Figure 10.27 Examples of active IR imaging while driving at night with the Mercedes night vision system. (a) View from inside car and (b) expanded IR image of screen; (c) another night scene. Warm and cold objects can be clearly seen within the range of the IR headlights. The speed is indicated in the lower portion of the screen. (Images courtesy Daimler AG.)

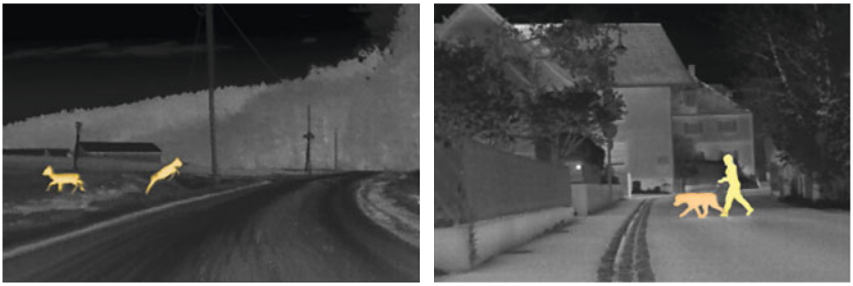

(a) (b)

Figure 10.28 Two IR images as displayed on monitor of a BMW car. Both the deer (a) and the pedestrian with dog (b) were outside the range of the visible light headlights, but they could be clearly detected with IR using the passive night vision system. (Images courtesy BMW AG, Munich, Germany.)

warn the driver. First, the respective objects are highlighted on the monitor (Figure 10.28). Second, warning signs are shown on the display. Third, acoustic warning signs are given. Fourth, when animals or pedestrians come into the range of the regular headlights, they are intermittently illuminated by sepa-

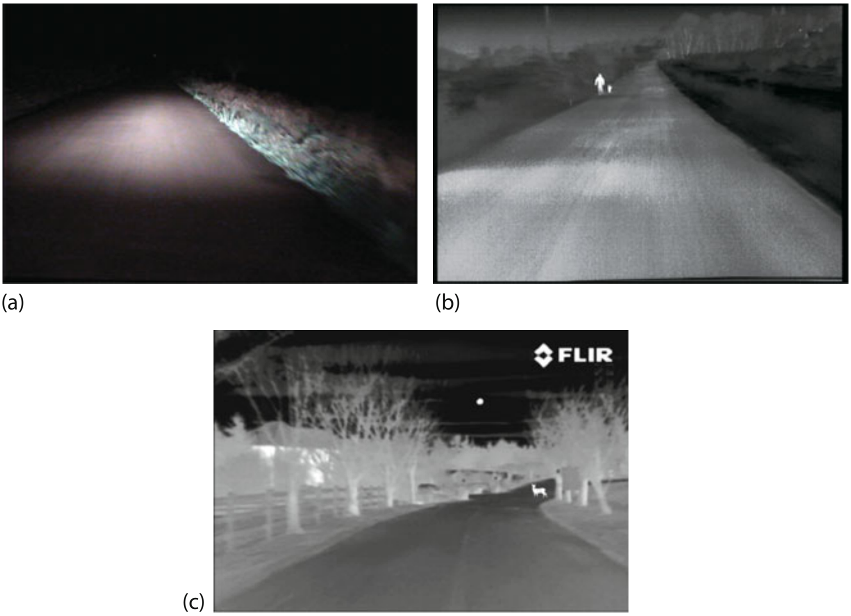

Figure 10.29 View of a night scene on a road. (a) VIS image as observed using the naked eye. (b) Man with dog as observed with night vision. (c) Deer crossing a road as observed with night vision. (Images courtesy FLIR Systems Inc.)

rate high-performance spotlights that will warn both the driver and the animals/pedestrians. Fifth, the braking system will kick into alert mode.

Last but not least, an indirect application associated with the car industry is that IR thermal imaging can also be used as a method for quality control in the pavement industry [74–78].

10.6.3
IR Imaging of Race Cars

Since IR imaging worked well for the conventional car industry, it was just a matter of time before its potential as analysis tool was put to use in Formula One racing cars. Figure 10.30 shows an example of a race car skidding in a circle. Besides making it possible to study the quality of the tires, such images are very suitable for advertisement, too. Meanwhile, IR cameras have sometimes been installed in the front of race cars, making it possible to study the thermal effects of the front tires of the driver's car and of those of the cars ahead [79]. In addition, IR imaging may be used to characterize the engines of race cars.

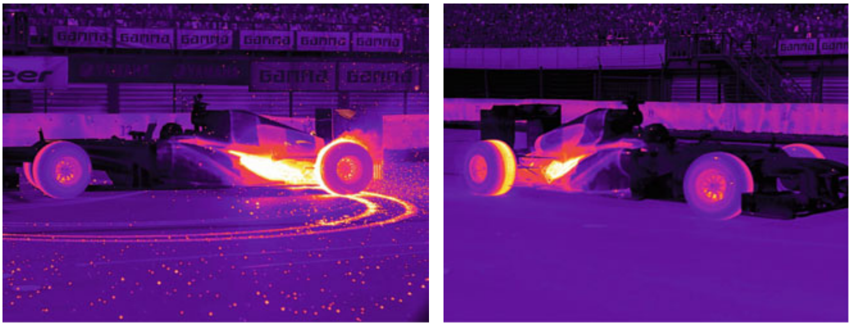

Figure 10.30 Two snapshots of a sliding Formula One race car. (Images courtesy Infiniti Red Bull Racing.)

10.6.4
Motorcycles

Thermal features of motorcycles are very similar to those of cars (see, for example, discussion on braking of motorcycles in Section 5.2). Here we present another application of IR imaging. Figure 10.31 shows a very nicely arranged image of a Harley Davidson, recorded with a one megapixel MW SC8300 IR camera. One can see thermal reflections on the floor, emissivity variations, and some real temperature variation: the engine is still warmer than the rest of the bike.

10.7
Airplane and Spacecraft Industry

10.7.1
Imaging of Aircraft

National and international air traffic has increased enormously in recent decades. Besides occasional use for airport inspections, the associated industry utilizes IR imaging extensively in various fields. For example, with regard to PdM (Sec-

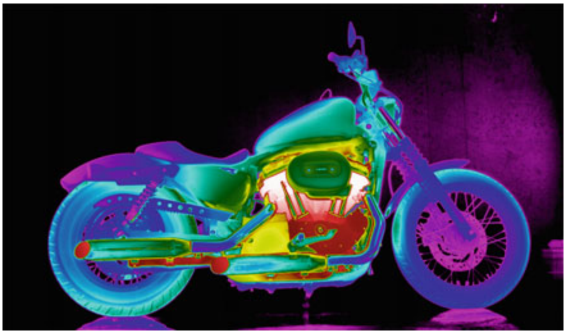

Figure 10.31 Harley Davidson motorcycle recorded with a cooled FLIR MW SC8300 camera, 1344 × 782 pixels. (Image courtesy Dave Bursell, FLIR Systems.)

tion 10.1), thermography has been used as a nondestructive testing method in general [80–82] for engine analysis, electrical and hydraulics inspections, detecting bleed air leaks, and studying the composite materials of, for example, propellers [83]. Other applications include inspections of aircraft fuselages using lock-in thermography [84] (Section 3.6.3).

In a research-oriented context, thermography has also been used to study new propulsion systems [85]. Here we want to mostly show qualitative images of aircraft from the outside. The features within thermal images of airplanes depend on the type of propulsion system. Propeller-driven planes and helicopters will have a characteristic thermal feature owing to the exhaust plume from the engines. Similarly, the different exhaust plumes of turbines are characteristic of jet planes. If they are recorded during takeoff or landing, then thermal reflections are clearly visible from the runway. Regardless of the kind of airplane being investigated, it will usually cover an extremely large range of temperatures or object radiances starting from relatively cold surroundings (e.g., sky) to the ambient temperature hull of the plane to the very hot engines or exhaust plumes. This large range of object temperatures usually leads to radiance differences exceeding more than an order of magnitude. Therefore, an image cannot be recorded by a camera with a given set of parameters (integration time, filters) without experiencing either low-signal nonlinearities or high-signal saturation effects of the detectors. Therefore, airplanes are ideal for superframing (Section 3.3) in order to have a very large dynamic range of several orders of magnitude in radiance within a single image. In addition, planes are usually fast-moving objects, which means that high-speed thermal imaging is needed with small integration times and high frame rates to obtain sharp still images. Figures 10.32–10.34 present examples for different types of aircraft. Figure 10.32 shows six snapshots from a start sequence of a jet plane. One can easily see the thermal reflections of the cold sky on the top hull and wings, but also the hot exhaust gases and engines on the colder runway. We will return to airplane start and landing and associated observable mirage effects in Section 11.5.4.

Figure 10.33 shows an example of a hot engine of a much smaller propeller-driven plane that was also used to describe superframing in Section 3.3.2.

Finally, Figure 10.34 shows a state-of-the-art IR image of the Lockheed Martin F-35, a vertical takeoff plane, recorded at the Farnborough International Air Show in July 2016 using the FLIR 380-HDc camera. The camera comes with a 1280 × 720 InSb FPA allowing short integration times and, hence, the study of fast-moving objects. It has an IR zoom lens with a 40° to 1° FOV. In the image, the vertical takeoff plane was hovering, that is, nearly immobile in the air. The exact focal lens used is not known; however, if the camera had operated with a 1° FOV, the 16 m long plane would have been at a distance of around 2000 m from the camera. If it had been closer, the lens focal length would have been reduced, that is, the FOV would have been increased. The image nicely demonstrates the enormous amount of hot exhaust gases of the engine that enable a vertical takeoff or landing.

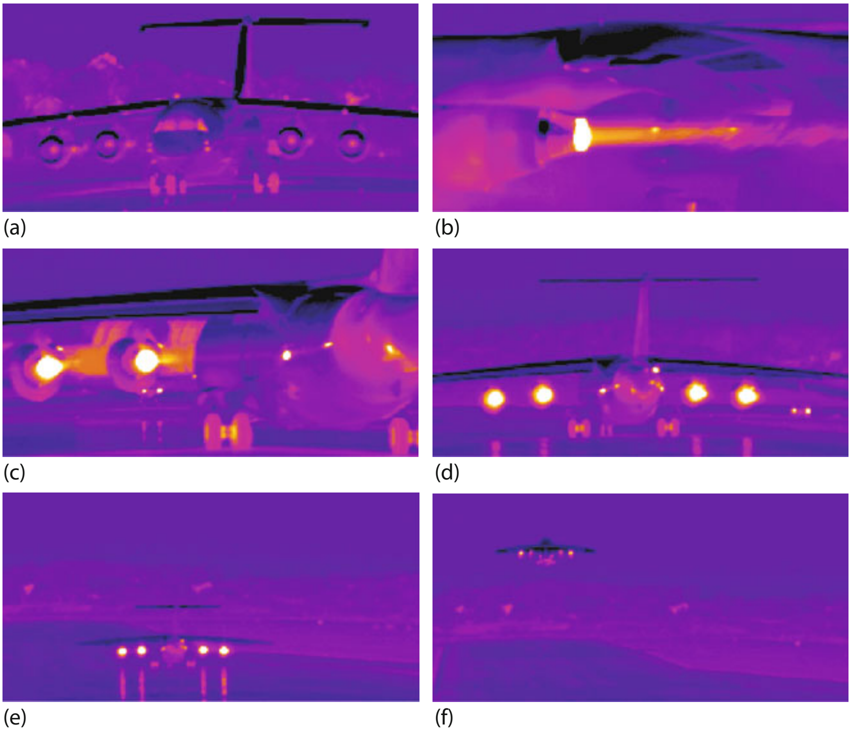

Figure 10.32 Qualitative IR image sequence of a plane during takeoff recorded with a high-speed Agema 900 camera. The exhaust gas is still optically thin when observed from the side. The hot engines give rise to thermal reflections from the runway. (Courtesy FLIR Systems AB.)

10.7.2
Imaging of Spacecraft

Nondestructive testing of aerospace structures is a challenging task owing to the exceptional demands on the materials and processes used [80]. All spacecraft that fly into space and return to earth need to be equipped with a heat shield. This is essential for a safe reentry of the vehicle into the atmosphere since the frictional forces between a fast-moving object and air of the atmosphere can easily lead to temperatures of several thousand degrees. A corresponding natural phenomenon is the occurrence of meteor showers and shooting stars – the sometimes spectacular night sky phenomenon when small meteorites enter the earth's atmosphere, heat up very fast, and finally evaporate upon the emission of light.

Spacecraft like Apollo or Soyuz incorporated techniques with heat shields for single use; in contrast, multiple-use vehicles, such as the space shuttles, required heat shields, which could be repaired as needed. After the accident of space shuttle Columbia in 2003, efforts were made to perform in-orbit inspections and potential damage assessments of the outer shell of the shuttle using IR cameras [86–88].

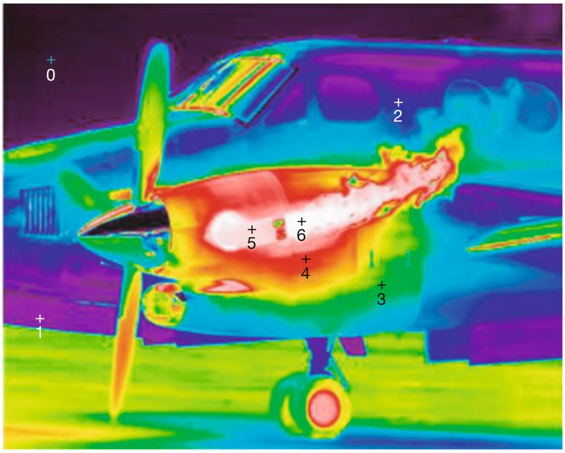

Figure 10.33 Small propeller-driven plane before takeoff. Because of the large temperature differences, the image was recorded using superframing. Temperatures increased from spot 1 to spot 6 in a range between 26 and 140 °C. Higher temperatures cannot be seen because the exhaust gas is not yet optically opaque. (Image courtesy FLIR Systems Inc.)

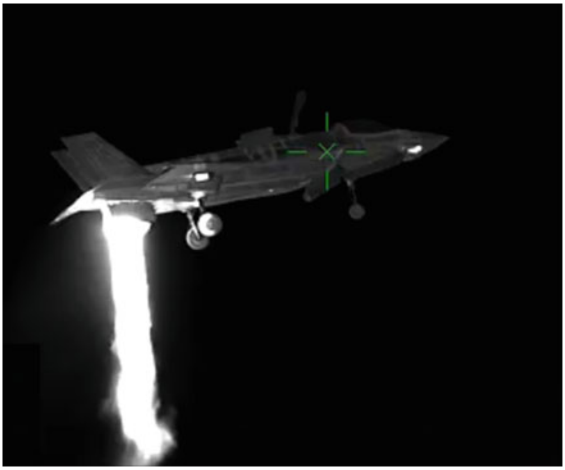

Figure 10.34 Snapshot MW IR image of a vertical takeoff plane. (Image courtesy FLIR Systems Inc.) See also YouTube video: https://www.youtube.com/watch?v=AzyH0M4C8TY.

For this purpose, a commercial IR camera had to be turned into a space-hardened camera ready for extra-vehicular activities in space. The first successful inspections in space – also of the International Space Station (ISS) (Figure 10.35) – took place during the mission STS 121 of space shuttle Discovery [89].

During this mission, the IR camera was also used to inspect an array of predamaged reinforced carbon–carbon samples – resembling parts of the heat shield – which were studied to test new adhesive repair techniques.

Some years ago researchers at NASA reported the use of IR thermal imaging to study the heat patterns on the surface of the space shuttle during reentry into the earth's atmosphere [90, 91]. So far, three missions of the shuttles Atlantis and

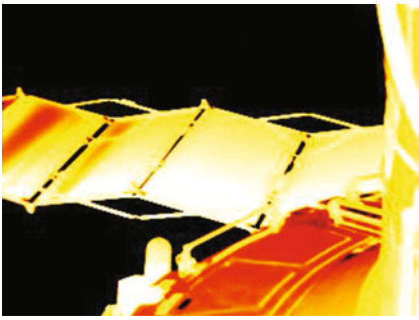

Figure 10.35 One of the first qualitative IR images recorded in space during space shuttle mission STS 121 with a commercial modified IR camera. Besides investigating shuttle heat shield samples, astronauts Sellers and Fossum also directed the camera toward an array of radiator fins of the ISS for later analysis on earth. (Image courtesy: NASA/Langley Research Center.)

Discovery (Figure 10.36) have been investigated for a project called Hypersonic Thermodynamic Infrared Measurements (HYTHIRM) [92–95]. The project was developed for the inspection and protection of shuttle missions in response to the Columbia disaster in 2003 when damage to the shuttle's wing compromised its heat-resistant shield, causing it to lose structural integrity and break apart during reentry.

Some goals of the project were to create 3D surface-temperature maps during reentry, compare them to measurements from thermal sensors on the shuttle's underbelly surface, and model these temperature maps using computational fluid dynamics. Once it is understood when and where peak temperatures occur, one may design the type of material for a protection system and the size of the system for the successor of the space shuttle whose missions ended in July 2011with STS 135.

Because of the very high temperatures, imaging of the shuttle upon reentry into the earth's atmosphere within the HYTHIRM project was done using a camera with filters for NIR radiation. The camera was on board an aircraft flying as close as 37 km to the space shuttle, thereby acquiring data for about 8 min. The calibration of sensors makes it possible, in principle, to calculate surface temperatures, once corrections for the varying atmospheric path from shuttle to camera are taken into account. The research focused on the underbelly of the shuttle, which is covered by about 10 000 thermal protective tiles. The highest temperature areas were found to be near the nose and along the leading edge of each wing. As the shuttle enters the atmosphere, it pushes air molecules out of the way. In that way, a boundary layer – acting as a protective layer – forms around the shuttle with temperatures between about 1100 and 1650 °C. Outside this protective boundary layer, temperatures can rise to around 5500 °C. The successful measurements [92–95] could indeed provide many useful insights, and measured temperatures were within the ranges of the model calculations.

Obviously, any damage to the tiles or bumps on the surface of the shuttle must be avoided since they can cause breaks in the boundary layer. In this case, the extreme heat from the outside may flow to the surface, leading to critical damage. To study such effects, artificial tiny bumps were added to the wing of Discovery. Similarly, heat shield materials for future spacecraft were tested. Figure 10.36 shows some qualitative results of the space shuttle thermal imaging for the shut-

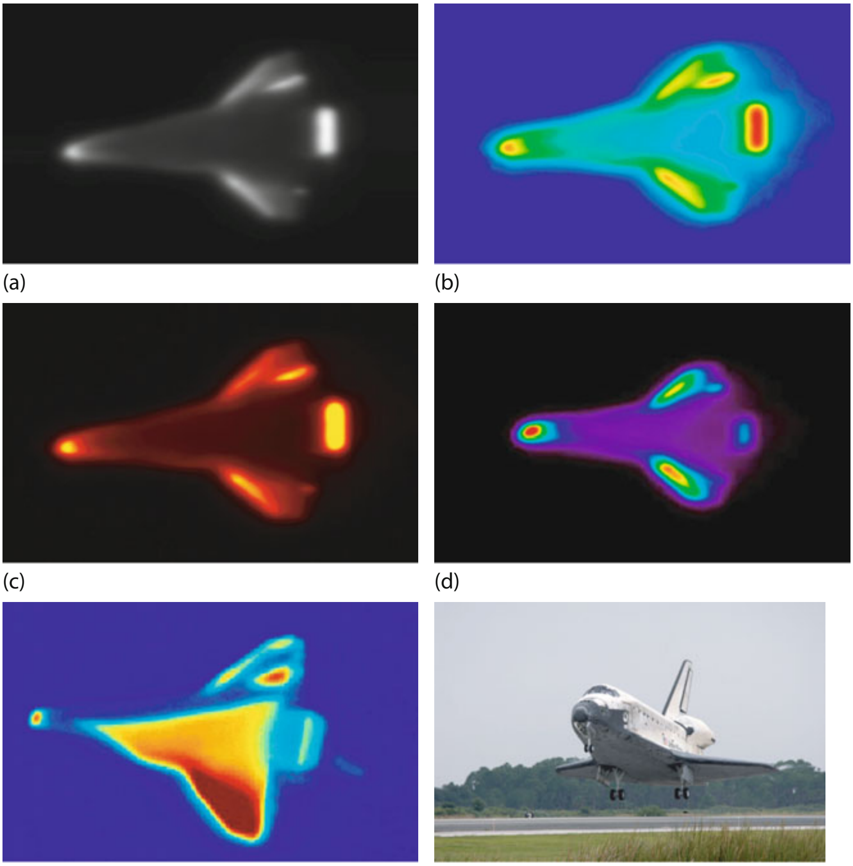

(a) (b) (c) (d) (e) (f)

Figure 10.36 Thermal and visible images of space shuttles Atlantis and Discovery. (All images courtesy NASA/Langley Research Center.) (a,b) Discovery on mission STS 128. Original data result in black-and-white images (a). In the false color image (b), blue refers to the lowest and red to the highest temperatures. (c,d) Discovery during boundary-layer experiment on mission STS 128 (c) and Atlantis on mission STS 125 with hot spots at nose and wings while traveling at 8 km s^{-1} (d). (e,f) Discovery on mission STS119 while traveling at about 4.8 km s^{-1} (e) and VIS image of space shuttle Discovery upon landing of missions STS121 (f).

tles Atlantis and Discovery recorded during the three missions STS119, STS125, and STS128. Figure 10.37 shows an example of the final start of a space shuttle, the mission STS 135. Superframing was used to create this fused image. The photographers recorded the start with five visible high-speed cameras operating with different exposure times. To also capture the thermal details in the exhaust gas plume, they added a MW IR camera. The overexposed areas in the visible image were replaced by those from smaller exposure time settings. The IR results only contributed to the hot exhaust gases in the plume of the solid rocket booster en-

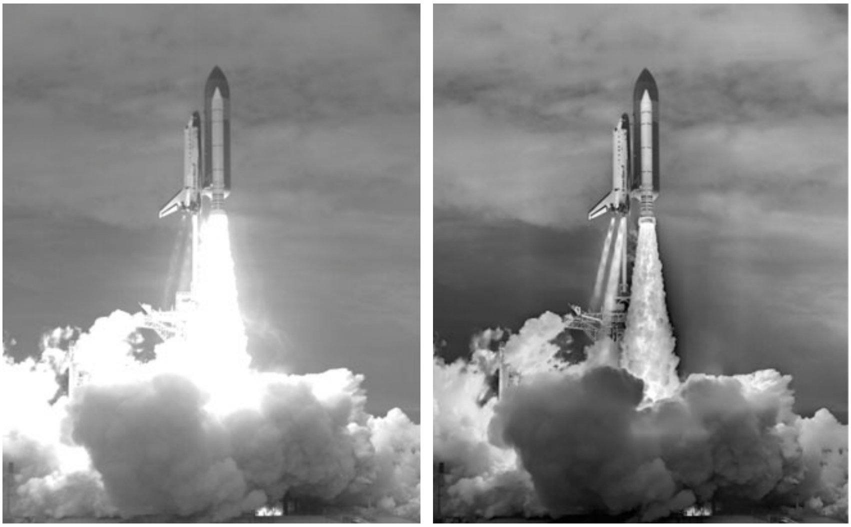

(a) (b)

Figure 10.37 (a) Snapshot of STS 135 launch recorded with a single visible camera whose exposure time was set such that the shuttle itself is readily seen. (b) Fusion image using five visible and IR imagery to create a composite that also shows details within the plume. (Image courtesy NASA, MSFC, KSC, and AMES, Darell Gaddy.)

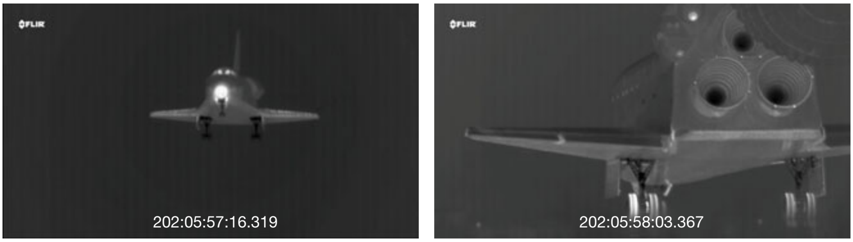

(a) (b)

Figure 10.38 IR snapshots of STS 135 landing recorded with FLIR SC8300 camera equipped with 1000 mm telelens. (Image courtesy NASA, MSFC, KSC, and AMES, Darell Gaddy).

gines as well as the exhaust of the space shuttle engines itself. More images of the start as well as further information related to the composite image can be found in the official NASA sources [96].

Finally, Figure 10.38 shows the final phase of a landing of a space shuttle in an IR image. Several landings at day and night were recorded [97, 98]. Note that the nose of the shuttle is still quite warm (Figure 10.38a). A bit earlier, at a more oblique angle, one could also see that the belly is still warmer than the top. In addition, one may observe that upon touch down, the wheels heat up rapidly owing to friction with the ground. Figure 10.38b shows the shuttle from behind after touchdown. Clearly, the wheels are the hottest parts.

10.8
Plastic Foils

10.8.1
Spectra: Selective Emitters

Accurate temperature measurements are crucial to any process in the plastics industry where temperature is a relevant factor. There is a large variety of applications for thermal imaging in extrusion, coating, thermoforming, laminating, and embossing. However, plastics present problems in connection with IR imaging because they are selective emitters (Section 1.4).

Thin plastic foils are typically selective emitters. Their spectral emissivity equals the spectrally dependent absorptance $\alpha(\lambda)$. Reflectances are very small (order of %) and neglected here. Figure 10.39 gives examples of absorptance spectra of several foils, computed from the transmission spectra according to $\alpha(\lambda) \approx 1 - T(\lambda)$.

As is obvious from Figure 10.39, the emissivity of thin plastic foils (e.g., polyvinyl chloride, polyester, polyethylene, polypropylene, nylon) changes strongly within the spectral ranges of the MW and LW thermal imaging systems. Such foils are selective emitters. In addition, they are not opaque, that is, an IR camera partially looks through such a foil. As a consequence, any broadband thermal imaging gives

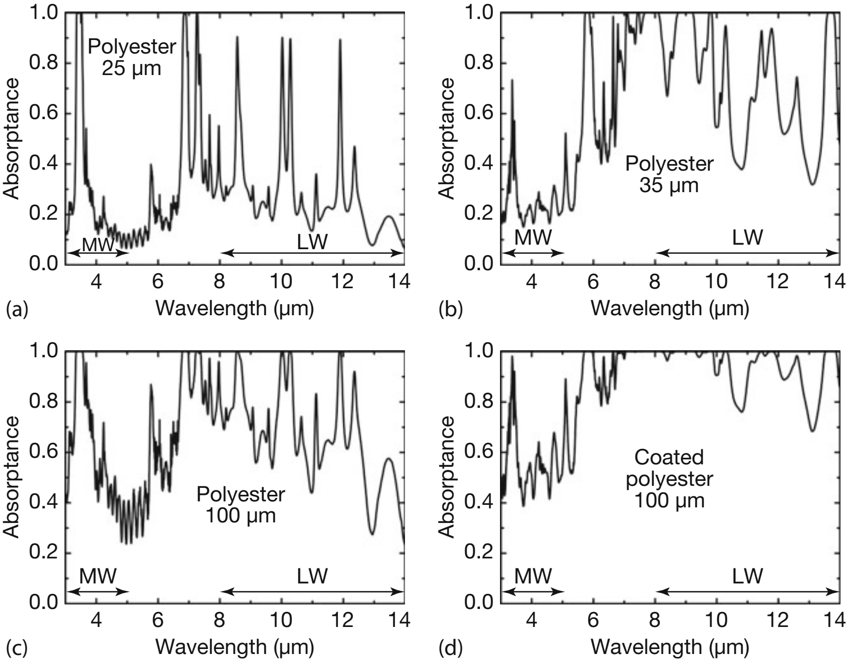

Figure 10.39 Spectral dependence of absorptance (emissivity) of polyester foils with different thickness (measured with a Bruker IFS 66 Fourier transform spectrometer).

inaccurate temperature values, particularly if other hot objects are behind the foil.

Even if background radiation is negligible, a quantitative analysis is tricky. One may, for example, think of correcting the changing emissivities by averaging the absorptance in the spectral range of the imaging system. It is, however, not possible to calculate simply an average emissivity because the spectral distribution of the emitted radiation follows Planck's law (Section 1.3.2). Therefore, an "effective emissivity" within the spectral bands used for thermal imaging depends on the object temperature [99], as has been shown for selectively transmitting IR windows.

An experiment was performed to illustrate this effect. One half of a heated blackbody source was covered with a 25 μm polyester foil (only during the measurement to prevent a temperature increase of the foil). The camera radiometric signals with and without foil were recorded and compared for MW (3–5 μm) and LW (8–14 μm) cameras (Figure 10.40). For the MW camera, a nearly constant ratio (decreasing from about 0.9 to 0.8 for the observed T range) between the two object signals with and without foil is observed, indicating that an "effective emissivity" value may be used to characterize the foil absorption. This is due to the fact that in the MW region, the Planck curves are still rising and the main effect of the foil is just to make the detected spectral region a little bit narrower owing to the absorption peak around 3.43 μm.

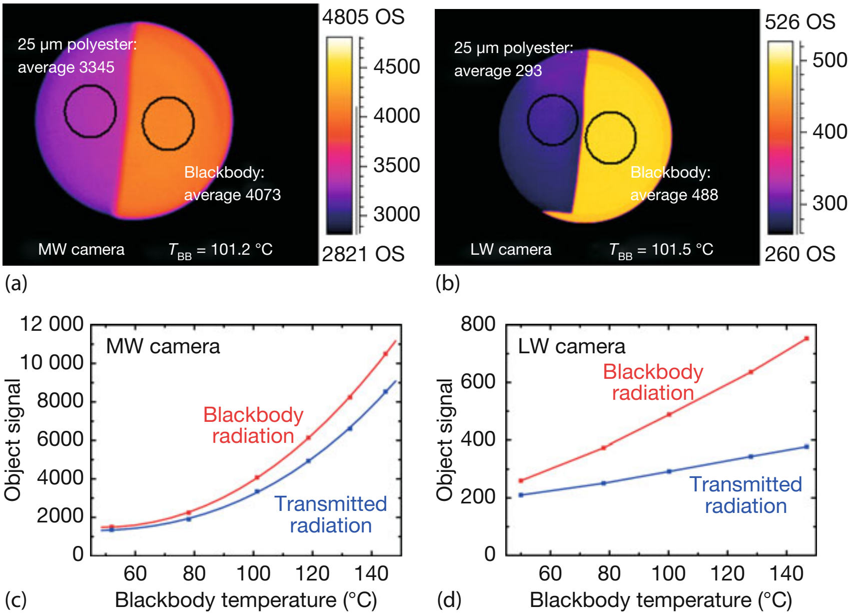

Figure 10.40 Temperature-dependent absorptance/emissivity of 25 μm polyester foil within MW and LW spectral range (object signals measured at different emitter temperatures).

This nearly constant ratio no longer holds for the LW region since the shift of the Planck curve with temperature is now affected by the absorption bands around 8.5, 10, and 12 μm. The ratio decreases from about 0.8 to 0.5 when changing T from 50 to 150 °C. We conclude that MW cameras are better suited to measure temperatures of such thin plastic foils.

From the spectrum of Figure 10.39d, it is, however, also clear that LW cameras are well suited to analyze temperatures of coated plastics (and also of foils with thickness > 250 μm) since emissivity is high with only a minor wavelength dependence.

The best choice to measure the temperature of thin plastic foils is to use a filter adapted to a narrow absorption band in the spectrum. The wavelengths of the absorption bands depend on the type of plastics and can be determined by an IR transmittance measurement.

10.8.2
Images: Looking through Plastics

From the spectra it is obvious that thin plastic foils are partially transparent to broadband IR radiation. This is demonstrated in Figure 10.41, which shows a

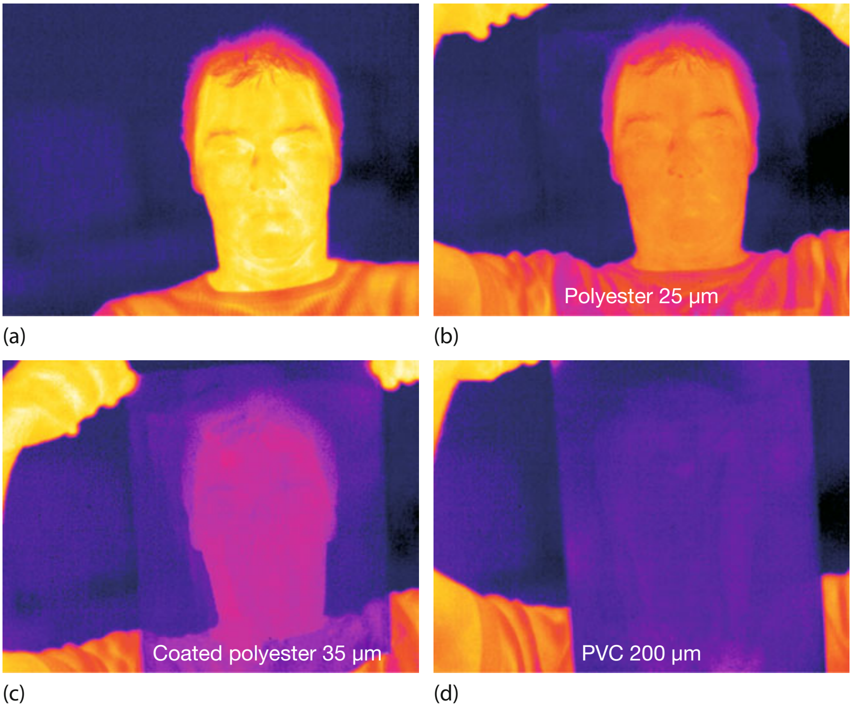

Figure 10.41 Demonstration of transmittance of various plastic foils in LW IR spectral region using thermal imaging.

person recorded without (Figure 10.41a) and with three different plastic foils (Figure 10.41b–d) between a LW camera and the person. The transmittance depends on the material and the thickness [58]. It is easy to see through the thin foil (Figure 10.41b), coated polyester still shows a small residual transmission (Figure 10.41c), whereas a thick foil is more or less opaque (Figure 10.41d).

The same phenomenon is observed looking through visibly opaque plastics. Figure 10.42a shows a person later covered by a black garbage bag (Figure 10.42c). The corresponding LW IR images (Figure 10.42b,d) show that one can easily see through the plastic and make out the face, although the bag is completely opaque in the visible spectral range. This behavior is of course very similar to looking through plastic in the SW range (e.g., Figure 6.15).

Finally, we note that looking through plastic or related materials can also be useful in surveillance and security (next section). In 2013, the Boston bomber was found, through the use of IR cameras, hiding under a plastic tarp in a boat. He was invisible to human eyes, but the police helicopters were equipped with IR cameras and could easily locate him thanks to the residual transmission of the plastic.

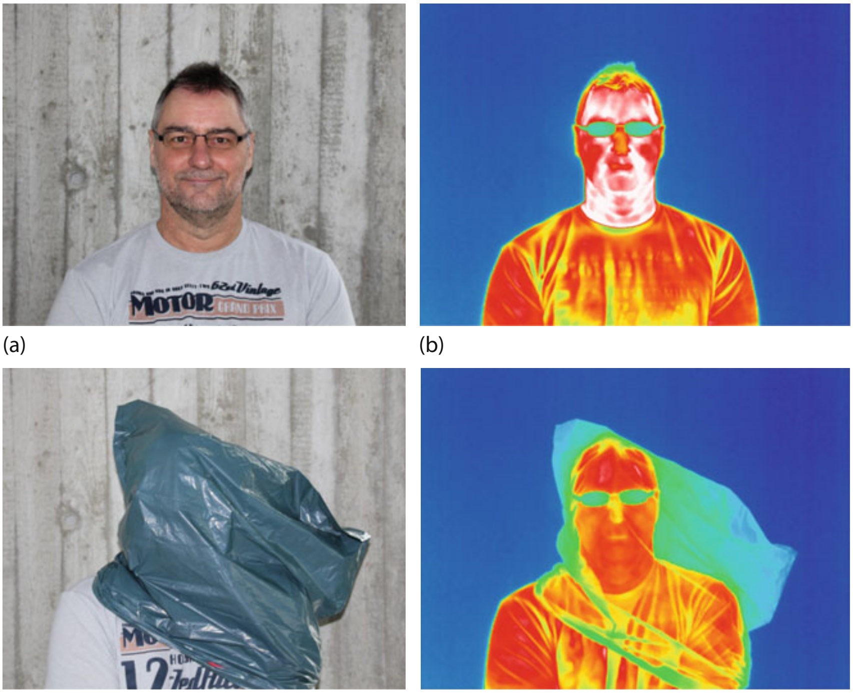
(a) (b) (c) (d)

Figure 10.42 Demonstration of transmittance of a visibly opaque plastic garbage bag in LW IR spectral region. Besides the transmission of plastic, one can also see the opaqueness of glass (see also Chapter 5).

10.9
Surveillance and Security: Range of IR Cameras

10.9.1
Applications in Surveillance

Not surprisingly, IR thermal imaging has found many applications in the field of security and surveillance. Here modern camera systems have many advantages compared to classical NIR image intensifier systems [100]. IR imaging is used extensively for the protection of critical infrastructure, that is, industrial assets such as airports, power plants, petrochemical installations, or warehouses. In particular, it is used for perimeter monitoring. Nowadays, it is even possible to construct sophisticated "thermal fences" around any facility using a series of IR cameras with overlapping fields of view and appropriate software tools. If an object of elevated temperature crosses such a line, an automated alarm is triggered. All kinds of IR cameras can be used as regular surveillance tools, the only difference with other imaging applications being the fact that these cameras must be operated under all weather circumstances, whether extremely warm or extremely cold, whether it is sunny, raining, or foggy. Therefore, surveillance cameras mostly have a special design.

Figures 10.43 and 10.44 show two typical examples. Surveillance cameras may be used to monitor large and dark parking lots (Figure 10.43) or the fenced perimeter of an industrial facility at night (Figure 10.44).

Besides security applications, IR imaging is also used when searching for missing persons, for example, disoriented people, fugitives, or even shipwrecked people at sea [101]. Surveillance cameras are available with either cooled MW detectors or uncooled microbolometer LW detectors, which now typically have a standard 640 × 480 pixels (320 × 240 pixels are available, too) and a variety of lenses and FOVs. To avoid ice buildup on lenses in wintertime, cameras are usually equipped with a lens heater (which is also standard for the cameras in cars) (Section 10.6.2). This also helps to avoid water films on lenses in situations of high humidity.

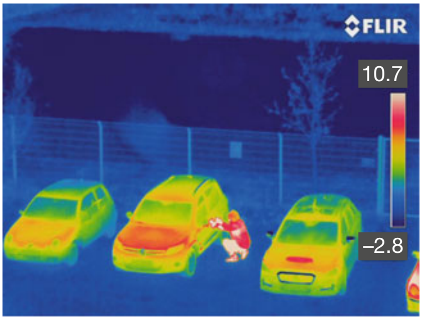

Figure 10.43 Monitoring a secured parking lot at night with a surveillance camera. Potential car thieves can be detected.

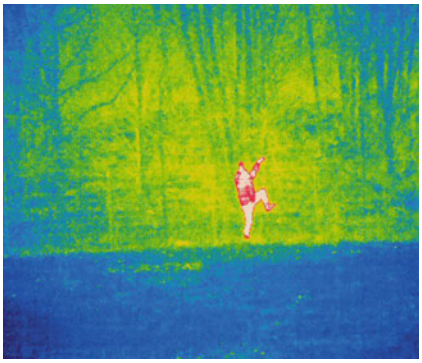

Figure 10.44 Monitoring a fenced-in property at night at a distance of about 100 m with an IR surveillance camera. In contrast to the IR image, no visual camera image would be able to detect anything.

10.9.2
Range of IR Cameras

There is one major question that is usually raised in surveillance issues that is not as important in regular thermal imaging applications (with the exception of passive IR in cars): is it possible to see through haze, fog, and rain, and what is the resulting range of an IR camera? This question is related to quite a few aerospace applications. For example, safety issues during landing at airports under unfavorable weather conditions like fog have raised the issue of whether IR cameras can improve visibility and thus help approaching aircraft during landing [102].

A similar question has been addressed from a different perspective: what is the influence of long atmospheric paths of tens to hundreds of meters through a hazy atmosphere with respect to radiometric calibrations of MW IR cameras? This problem was investigated by comparing experimental data to atmospheric MODTRAN modeling results [103]. For the MW range, the two major attenuating species are CO_2 and H_2O vapor. The aerosol contribution is usually modeled by the type of aerosol (see following discussion) and the visual range. It was found that deviations occur between experiment and theory, which means that quantitative radiometric measurements can usually not be performed over distances of hundreds of meters to 1 km.

The question of what is the actual range of an IR camera, however, requires no quantitative radiometric data; hence, much larger distances may be expected. However, a number of factors will have an influence on actual ranges of IR cameras:

1. Spectral range, type of detector (cooled or uncooled), and sensitivity;
2. Lens and size of object;
3. Temperature of target and background;
4. Atmospheric transmission for ideal clear sky conditions;
5. Humidity of the air;
6. Aerosol contribution in the atmosphere: haze;
7. Additional atmospheric properties: fog, rain.

The first three factors are common to all applications. The range is related to the reduction in apparent contrast [104, 105]. In the visible part of the spectrum, the visual range is defined by a reduction in the apparent contrast radiance between target and background to 2%. The range for IR cameras is related to the minimum resolvable temperature difference and the noise-equivalent temperature difference (NETD) (Section 2.5). In one model [102], the IR range was determined by analyzing the temperature difference of a bar pattern versus background. The *range* was then defined as the distance where this radiation temperature difference equals the NETD.

The attenuation of IR radiation along the path from object to observer is due to the molecular species in the atmosphere (Chapter 8), in particular, the strongly varying humidity. In addition, various kinds of aerosols may scatter or absorb IR radiation. For easier modeling, only six climate types were defined: tropical climate, midlatitude summer, midlatitude winter, subarctic summer, subarctic winter, and US standard. Each climate could in addition be combined with different types of aerosols. The following aerosol types were analyzed: rural, urban, maritime, advection fog, radiative fog, and desert.

Each aerosol type is characterized by size and material contributions with well-defined absorption and scattering properties of radiation. The concentration of these aerosols is usually characterized by the corresponding visual range or meteorological optical range [106].

Rather than speak of aerosols in the air, one often refers to a hazy atmosphere. Haze refers to the fact that dust, smoke, and other dry particles (e.g., from traffic, industry, wildfires) can obscure the clarity of the sky, thereby reducing visibility. Besides haze, the World Meteorological Organization also classifies horizontal obscuration in the atmosphere by the categories fog, mist, haze, smoke, volcanic ash, dust, sand, and snow.

Usually, dry haze refers to small particles made of dust or salt with typical sizes on the order of 0.1 μm. These particles interact with radiation mostly according to Rayleigh scattering, which favors short-wavelength scattering. If the relative humidity of the air increases above 75%–80%, these tiny aerosol particles of dry haze act as condensation nuclei, thereby producing wet haze. It is composed of small liquid droplets with sizes in the micrometer range. They are able to scatter light much more efficiently than dry haze, thereby reducing the range. If the nuclei grow much larger, fog may result, with droplet sizes in the range of 10 μm, which is similar to droplet sizes in clouds. Again the scattering efficiency of these droplets increases with size, which further reduces the range.

IR radiation can have a much larger range than visible light under certain circumstances. Such a situation is easiest for dry haze with scattering particles of diameters below, say, 500 nm. For this size range, visible light is greatly scattered. The dominant Rayleigh scattering mechanism decreases strongly with increasing wavelength (scattering is proportional to $1/\lambda^4$). Therefore, IR radiation in a SW range of 0.9–1.7 μm is much less affected. This means that NIR radiation can give much sharper images through such haze than visible light (see also Section 6.3.3.3). Examples where NIR radiation was used to detect objects at hori-

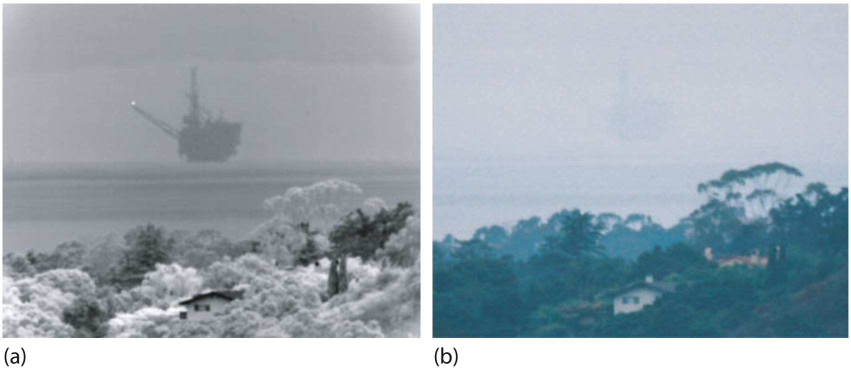
(a) (b)

Figure 10.45 Example of SW IR image (a) (recorded with InGaAs camera and telescope optics) versus VIS images (b) (regular color film) of oil platform at a distance of 47 km. (Images courtesy A. Richards, FLIR Systems Inc.).

zontal distances at sea level of around 50 km are shown in Figure 10.45. Obviously, the corresponding visible light produced only very fuzzy images – if they could be observed at all.

In principle, attenuation in the atmosphere due to Rayleigh scattering decreases for the even longer wavelengths of MW and LW cameras, which is why one might suspect that these systems would have even larger ranges. This is not the case, however. The major reason it is not is that NIR long ranges are usually observed during the day, when sunlit objects are observed at great distances. Therefore, the detected radiation consists of scattered radiation from the sun in this wavelength range, which is still very large compared to contributions in the MW or LW spectral region (cf. Figure 7.49). LW cameras, for example, will detect a comparably negligible amount of scattered sunlight. To see long-range objects, a thermal signature is required, for example, the objects must be much warmer than the surroundings. For the observed objects in Figure 10.45, this is not the case. And their small temperature differences with respect to the surroundings only give small object signals, which are attenuated due to aerosol scattering and absorption by water vapor and by carbon dioxide.

As a consequence, NIR cameras are the best option for long ranges in dry, hazy environments during daylight conditions. At night, when directly scattered radiation is absent, SW cameras also depend solely on thermal object radiation; hence, only very hot objects will be detectable at large ranges.

For dry and wet haze, that is, situations with fog, model calculations with MODTRAN, an atmospheric radiative transfer code, have been performed to characterize the range of IR cameras with respect to the visual range [102]. Parameters for the model are the climate and aerosol type, humidity, visibility, the geometry, and lengths of the atmospheric path, as well as the temperature and emissivity of the object and background. Transmission spectra are computed from the UV to the millimeter wavelength region at a spectral resolution of 1 cm^{-1} for the aforementioned climate models and differing locally prevailing aerosols. Typically 25

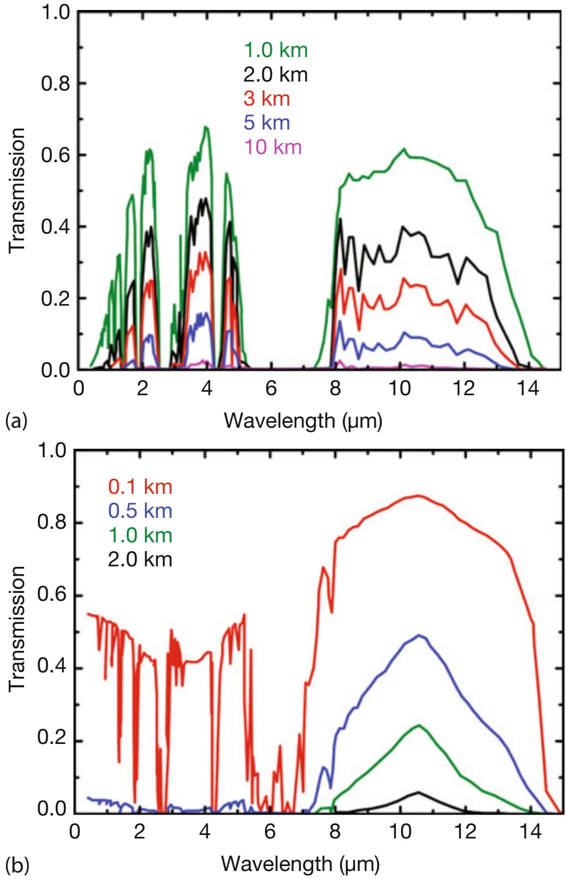

Figure 10.46 Spectral transmission for predefined climate and aerosol models. (a) Midlatitude summer climate and rural aerosol, visual range 1220 m. (b) Midlatitude winter, radiative fog, visual range 610 m. Parameter: atmospheric path length. Image after [102], courtesy Deutsches Zentrum für Luft- und Raumfahrt (DLR).

atmospheric species are included, in addition to pressure, temperature, and mixing ratios for 50 atmospheric layers from sea level to an altitude of 120 km.

In general, maritime aerosols have the lowest ranges since they are usually comprised of larger particles, for example, rural or urban aerosols. In situations where there is fog, the range also depends very sensitively on the type of fog, that is, its size distribution and the concentration of the droplets. Figure 10.46a shows an example of a reasonable visual range in the visible. It is due to rural aerosol particles, that is, pure dry aerosols that are typically smaller than 1 μm. The transmission in the visible band is significantly lower than in both IR bands due to the strong influence of Rayleigh scattering. Path ranges of more than 5 km still show reasonable transmission, that is, they are still detectable in both IR bands. As a consequence, the IR range is expected to be larger by at least a factor of four compared to the visual range.

Figure 10.46b shows the results for radiative fog in midlatitude winter [102]. The visual range was assumed to be around 0.61 km. Results for the IR show a similar low transmission for the MW range, whereas LW IR radiation shows a much larger transmission. In this case, the LW camera is expected to have a range of about a factor of four larger than in the VIS or the MW IR. Finally, very dense fogs with visibilities below 300 or 90 m will have similar transmission spectra for VIS, MW, or LW IR. Radiation does just not penetrate through this dense fog in all spectral bands (VIS, NIR, MW, and LW), that is, the atmosphere itself is the limiting factor for the range, which is the same in the VIS and the IR.

These transmission spectra have been used to actually determine the range according to the NETD criterion mentioned earlier. The temperature differences between object and background were varied between 1 and 100 K. Figure 10.47

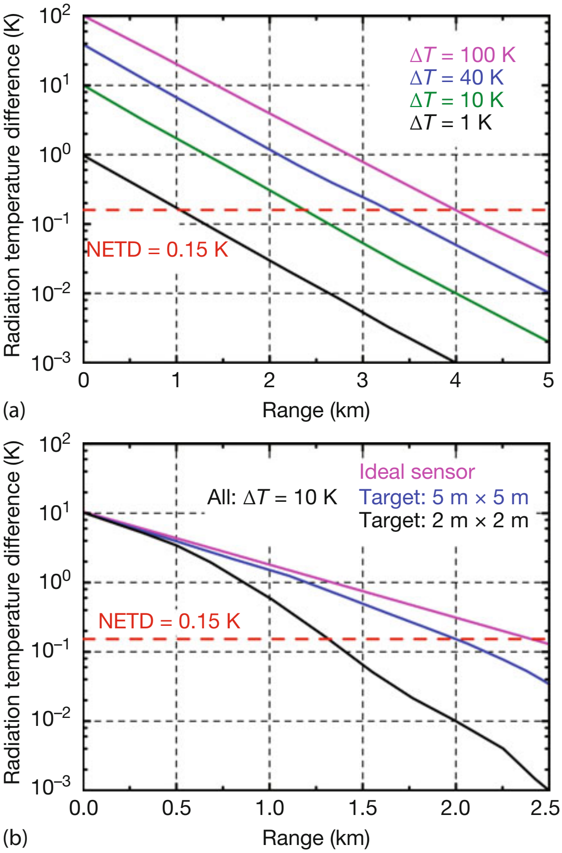

Figure 10.47 Ranges for LW IR cameras (see text for details) for the case of Figure 10.46b with midlatitude winter, radiative fog, visual range 610 m. (a) Ideal situation, only due to atmospheric conditions for $\Delta T = 1$, 10, 40, and 100 K. (b) Comparison of ideal (MTF = 1) with realistic conditions (MTF < 1) for $\Delta T = 10$ K. Images after [102], courtesy Deutsches Zentrum für Luft- und Raumfahrt (DLR).

shows the results assuming a NETD of 0.15 K of the camera (indicated by the red broken line; lower NETD values would just lead to a lowering of this horizontal line).

The detection range increases with a temperature difference between the object and the background and has a value of about 2.4 km for $\Delta T = 10$ K, which is a factor of four larger than for the visual range. Lowering the NETD would also lead to longer ranges. These ideal, sensor-independent results must still be corrected for the sensor properties, in particular, the limited spatial and radiometric resolution of the camera due to the optics, the detector, and the system noise. Finally, it is mostly the apparent angular size of the object (having an influence on the MTF; see Chapter 2) that will determine the achievable range. Figure 10.47b shows results for a $\Delta T = 10$ K difference of the object versus background as a function of distance. The limited spatial resolution is dominant, as can be seen from a comparison of the results for different target sizes. The smaller targets will become invisible at much shorter distances.

Overall, these model results suggest that fog penetration is higher in the LW IR compared to that in the MW IR band. LW systems have the additional advantages of being less affected by CO_2 absorption and being cheaper than MW cameras.

Rainfall consists of even larger droplets, with sizes in the millimeter range. Their increased scattering contribution and absorption properties significantly reduce the range for both LW IR and MW IR. Depending on the density of rain droplets, the signal decreases strongly and the range is seldom above 500 m. Another rain-related issue is whether raindrops (or dirt) on the lenses are important. First of all, if small particles are on a lens, they will be out of focus and, hence, will not affect image quality (similar to normal photography in the VIS range). Second, in most cameras, the lenses also have heaters to prevent condensation.

As a practical example, Figure 10.48 shows VIS and IR images while looking at distant objects through a slightly foggy atmosphere. The IR image is obviously quite clear and even allows one to identify the pedestrian and his mirror image in the lake, which is not easily done for the still image in the visible spectral range.

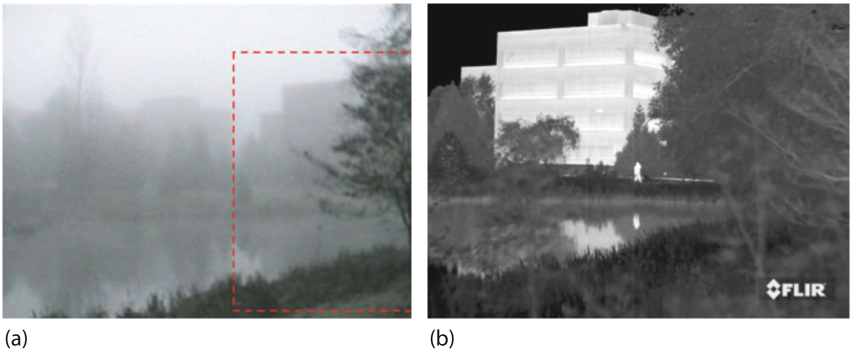

(a) (b)

Figure 10.48 Example of looking through slightly foggy atmosphere with (a) VIS and (b) IR cameras. (Images courtesy FLIR Systems Inc.)

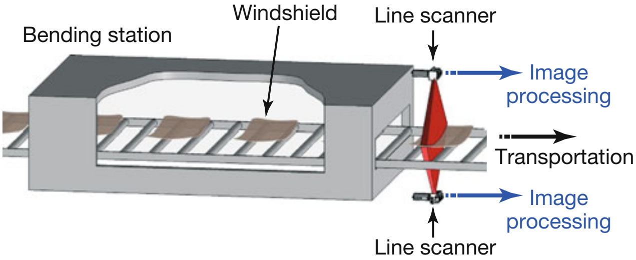

Figure 10.49 Measurement of temperature distribution of windshields at exit of bending station for automotive glass production. (Image courtesy Fluke Process Instruments GmbH Berlin)

10.10
Line Scanning Thermometry of Moving Objects

Quite often, technological, industrial, or everyday-life processes of moving objects need to be considered. Depending on the speed of the objects, different techniques are used. The best solution would be very high-speed IR cameras. If those are not available or, more importantly, if less expensive solutions are needed for mass production equipment, IR line scanners are the first choice.

Figure 10.49 shows a typical industrial example. Some products, here windshields, are transported with a certain velocity during production. The task is to analyze product quality during movement. In the example of Figure 10.49, windshields enter the bending station, and a test should be conducted to determine whether the bending process introduces any defects in them.

Using a high-speed IR camera was considered too expensive. Therefore, line scanners (Section 2.4.1, Figure 2.55) were used. As a matter of fact, line scanners are ideal candidates for monitoring industrial processes at a constant velocity: the lateral dimension is recorded along lines with short integration times. The longitudinal dimension (parallel to the velocity) is automatically recorded by the time sequence of the line scans.

Consider, for example, commercial line scanners that are available typically with up to 1024 pixels. It is clearly an advantage to have the largest possible number of pixels compared to the maximum number of 640 from the current standard 640 × 480 pixel cameras (owing to their higher cost, one megapixel IR cameras are still rather the exception than the rule). The operating wavelength for glass measurements is about 5 μm. This is achieved using broadband detectors with a narrow filter (Section 3.2.1). Glass is opaque with a high emissivity value at this wavelength, which enables studies of the surface-temperature distribution of windshields. Line scanners have the advantage of having a very large FOV, about 90°, which means that short distances between scanner and windshield are possible. In contrast, most standard lenses for IR cameras offer a maximum FOV of 45°.

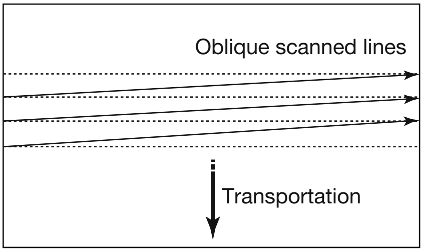

Figure 10.50 Line scans of a moving object lead to gridlines that are tilted with respect to the object.

Let us consider an example of a scanner with 256 pixels, which allows, for example, a 150 Hz frame rate, that is, a time of 6.6 ms between two scans (1024 pixels would allow, for example, 40 Hz). Assuming a velocity of $1\,\mathrm{m\,s^{-1}}$ of the windshields on the band, two subsequent line scans correspond to a distance of 6.6 mm (25 mm for 1024 pixels). Figure 10.50 shows how the windshield is scanned. The sequential readout given by the scan speed leads to scan lines that are slightly rotated with respect to the transverse object direction. The distance between two consecutive scans results in a line grid that is superimposed on the object area and forms a 2D slightly rotated IR image of the object. Its transverse spatial resolution is given by the number of pixels, and the longitudinal spatial resolution is defined by the distance between two scan lines (6.6 mm in the preceding example). The tilt angle depends on the ratio of scan speed to object speed.

Figure 10.51 shows an IR image of a windshield with a defect recorded with this method. The IR image was first treated with advanced image-processing techniques, which made it possible to get rid of the tilt angle and noise. Obviously, such IR images can detect any extended inhomogeneities of the temperature distribution, for example, owing to fissures, scratches, and so on, unless they are exactly parallel to the scan lines and are missed due to the line distance (in the example, 6.6 mm). Point defects of smaller sizes would be difficult to detect. The windshield is still warm owing to the manufacturing process. Any fissures or other defects can therefore show up in the IR image since such defects can lead first to inhomogeneities in emissivity and, second, they may change the heat transfer mechanisms like conduction in the vicinity of the defect. Images such as that in Figure 10.51 can then be analyzed online using image processing software tools (Section 3.5) adapted to the problem. Thereby, automated alarms could be installed if a certain defect level is detected.

10.11
Remote Sensing Using IR Imaging

10.11.1
Survey of Methods

In the context of this section, remote sensing refers to the use of sensors on satellites or other flying objects in order to gather information about objects on earth.

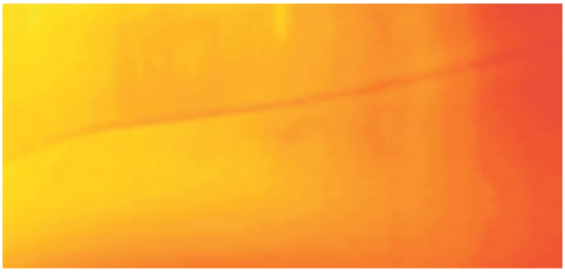

Figure 10.51 Thermal image of a windshield showing a line-type defect. (Image courtesy Fluke Process Instruments GmbH Berlin.)

The type of information defines the use, which early on was primarily of a military nature. Later on, scientific investigations followed, and recently civilian uses such as IR imaging applications have started to flourish.

The aerial platforms for the sensors can be divided into manned and unmanned vehicles (Table 10.2). They also differ in achievable heights, maximum payloads, range, operating times, and – importantly for users – price.

Regarding IR imaging, height is a crucial factor in connection with spatial resolution. Nowadays commercial telephoto lenses of 7° for 640 × 480 pixel IR cameras are available, which means about 0.2 mrad IFOV. Research systems can easily have much higher resolutions (much more expensive optics), but standard thermographers will use commercial equipment. Of course, a decrease by a factor of two

Table 10.2 Platforms for remote sensing systems.

Sensor host	Typical height	Manned	Unmanned	Typical payload	Range order of	Operating time	Price for investigation
Satellite	Above 500 km		×	o (10 kg)[a]	Global	Years	High
Jet airplane	10 km	×		o (100–1000 kg)[a]	1000 km	Hours	High
Helicopter	Below 3 km	×		o (10–100 kg)[a]	100 km	Hours	Medium
Small-propeller aircraft	Below 3 km	×		o (10–100kg)[a]	100 km	Hours	Variable
Fixed wing UAV	From 100 m up to 20 km		×	o (10 kg)[a]	Variable	Hours	Variable
Tethered balloon	Below 300m		×	< 5 kg	10 m	1 h	< $1000
Copter drones	Below 300 m		×	1–20 kg	0.1–1 km	15–30 min	< $500 to $10 000

a) o (… kg) means “order of … kg”.

for the IFOV could be attainable at reasonable prices in the near future (perhaps driven by drone applications); however, so far, an estimate for a lowest IFOV is about 0.2 mrad. In addition, initially it is often desirable to get overview images of an object, which requires a wider FOV. Therefore, standard lenses for IR cameras for drones have larger IFOV values on the order of 1 mrad. Table 10.3 gives typical lateral dimensions of observed objects from given heights corresponding to the best available and standard IFOV values. Since useful quantitative measurements would always require at least 3 pixels, that is, 3 IFOV (Section 2.5.3), we give the corresponding values as well.

Obviously, if IR applications require a spatial resolution below 10 cm, the allowed maximum height is on the order of 100 m, meaning low flying vehicles are required. This is the range in which most civilian IR applications are expected to fall. Therefore, satellites and jet airplanes are of no interest for applied IR imaging.

In the long term, the cost of hiring a small airplane or a helicopter is usually much greater than using a self-owned unmanned vehicle. Therefore, helicopters or small aircraft are currently mostly utilized if range is an important issue, for example, if a survey of hundreds of kilometers of high-voltage lines is the task. Since tethered balloons are a strictly local solution, drones based on small unmanned helicopters – also called copter drones – are generally the system of choice. Fixed-wing unmanned aerial vehicles (UAVs) are often used for special science or military applications. Drones in the form of multiple-rotor small helicopters have seen an enormous surge in demand over the last decade. Depending on the number of rotors, they are sometimes called quadro-copters (four engines), hexa-copters (six engines), or octo-copters (eight engines).

On the one hand, they are sold as toys for indoor use below $100 and commercial consumer products for outdoor use starting at a few hundred dollars. On the other hand, professional systems that can handle larger payloads, longer flight times, and higher maximum altitudes can cost up to $10 000. They are usually radio controlled by an operator who stays in sight of the vehicle. The drones are equipped with GPS and the sensors allow moving-image broadcasts of VIS and IR to the operators. An incomplete list of some of today's state-of-the-art systems is given in [107–114]. This field is rapidly evolving such that new systems may have been developed in the meantime with other properties/parameters, so one

Table 10.3 Spatial dimensions corresponding to 1 IFOV and 3 IFOV for a camera with 0.2 mrad IFOV (top two rows) and a commercial standard camera with wider field of view and IFOV = 1.2 mrad (bottom two rows) as function of height above ground.

Height	10 m	100 m	1 km	10 km	500 km
Dimension for IFOV = 0.2 mrad	2 mm	2 cm	20 cm	2 m	100 m
Dimension for 3 IFOV = 0.6 mrad	6 mm	6 cm	60 cm	6 m	300 m
Dimension for IFOV = 1.2 mrad	12 mm	12 cm	1.2 m	12 m	600 m
Dimension for 3 IFOV = 3.6 mrad	36 mm	36 cm	3.6 m	36 m	1.8 km

should always do an Internet search when looking for a new system. At present, typical drones used for IR cameras have weights in a range of 2–10 kg, operate with between four and eight rotors, offer maximum payloads of 1–9 kg, and can achieve maximum speeds in still air of up to 20 m/s (72 km/h, or 45 miles/h). They are typically specified for heights of up to around 500 m above ground, but maximum altitudes of 3000 m. The key parameter is the maximum flight time, which does of course depend on the payload. With no payload, maximum flight times can reach up to 30–45 min, whereas a typical payload reduces this time appreciably to typically 15 or 20 min or so. Of course, no operator of an IR camera will risk losing the camera, so typical operating times are at most 10 to 15 min for each flight.

Several companies have responded to the need for inexpensive, lightweight, state-of-the-art IR cameras for drone inspections. For example, a FLIR VuePro R 640 LW camera has dimensions of only about $45 \times 45 \times 63\,\text{mm}^3$ with a total weight (depending on the lens, without cables) of around 110 g (4 ounces). It has an average power consumption of only 2.1 W, stores radiometric images with 640 × 512 pixels on a SD card and allows analog (and with additional accessory also digital) video output. Three lens options are available ranging from wide angle (62° × 56°) down to a small-angle (32° × 24°) system. There are also a few other supplies of special low-weight cameras suitable for drones (e.g., [115, 116]). Meanwhile it is even possible to buy complete drone-plus-camera systems (e.g., [117–119]). Other companies specialize in customized software [120] to use with IR cameras and drones.

With the enormous increase in sold systems, many political and legal issues arose (e.g., [121–123]) ranging from privacy issues and intrusiveness to safety for other air traffic. Regulations on drones are handled at the national level. For example, the laws are rather strict in the United States concerning weight and allowed flight altitudes as well as training of drone operators.

Out of the vast literature in the field, we will mention just a few works [124–144]. IR remote sensing has many fields of application besides for the military. They range from science (e.g., polar research, volcanoes, wildlife census, biology, crop health, hurricanes, archeology) to law enforcement (e.g., monitoring of illegal activities like waste disposal, search and rescue operations for missing persons, disaster relief, locating terrorists like the Boston bomber) to a huge variety of governmental and civilian applications (e.g., fire mapping, bridge and building inspections, photovoltaic systems, pipelines, high-voltage lines, roof moisture on buildings, energy theft).

One attempt at a useful classification scheme of IR imaging [135] with unmanned vehicles differentiates between detection (is it there?), identification (what is it?), and analysis (what does it mean?). Detection may, for example, already be done at a greater altitude. Seeing a thermal anomaly may subsequently lead to decreasing the drone altitude to get a better spatial resolution and, thus, localize, or identify, the defect. For the analysis part of an investigation one may even need to have a close-up look and investigate in person.

10.11.2
Some IR Imaging Applications Using Drones

The last few years have seen a dramatic increase in the number of papers published on IR imaging with drones (e.g., [133–143]).

These relate to the detection of illegal waste disposal, analysis of buildings, in particular roofs, finding locations of remnants of archeological sites, studies of still active volcanoes, or investigating other geothermal activities. It was even recently proposed that active thermography be performed from UAVs [137]. Currently, the most popular topic in IR drone inspections deals with all kinds of photovoltaic systems [138–141], starting with small ones on individual houses to large power plants with hundreds of modules.

Figure 10.52 presents an example. The small solar field in San Diego, California (Figure 10.52) consists of 24 arrays, arranged in 6 columns of 3 to 5 rows. Each array consists of 4 × 7 individual solar panels, each having a size of approximately $2 \times 1\,\text{m}^2 = 2\,\text{m}^2$. This means that one array has dimensions of about $4 \times 14\,\text{m}^2$. Each panel is made up of individual cells, the typical size for these industrial panels being between 12 and 16 cm side length for each cell. The drone that recorded these images from a height of around 140 m used a FLIR Vue Pro R 640 camera with a 13 mm lens. The IR image is displayed as a composite image. The spatial resolution for a single pixel corresponds to about 16.5 cm, that is, around the size of an individual cell. Therefore, the resolution is insufficient (Section 2.5.3) to quantitatively measure individual cell temperatures; however, the image can easily serve to provide a qualitative overview to spot problem areas.

The IR image revealed the following problems (indicated by the yellow dotted lines), which were also checked from the ground. The small individual spots seen, for example, in row 1 (top row) and column 1 (left column) and elsewhere are individual cell failures. The individual bright panel in row 3, column 1 is likely an unplugged panel. The 2 × 7 panels in the top half of row 2, column 5 are brighter, resembling two dead strings. The same applies to the 2 × 7 panels in the bottom half of row 4, column 6. Finally, the center panel in row 2, column 6 is warmer, which indicates that it is unplugged.

Figure 10.53 shows another example of an IR drone inspection of a solar power plant in Germany (data courtesy M. Hambsch [145]). Here the drone was used at lower altitudes, giving a better spatial resolution.

The Optris IR camera images of 640 × 480 pixels [116] were recorded with a 33° HFOV lens, that is, about 0.9 mrad HIFOV. The solar panels had typical dimensions of 1.7 m length and 1 m width, which makes it possible to estimate the drone altitudes for each individual image. In the overview image Figure 10.53, the drone operated at altitudes of about 35–40 m, and for the subsequent close-up inspections, it was typically brought down to between 15 and 25 m above the ground. The most obvious feature of Figure 10.53 is the elevated temperature of the lower section. This section was not yet connected and therefore just heated up as a result of absorbed solar radiation.

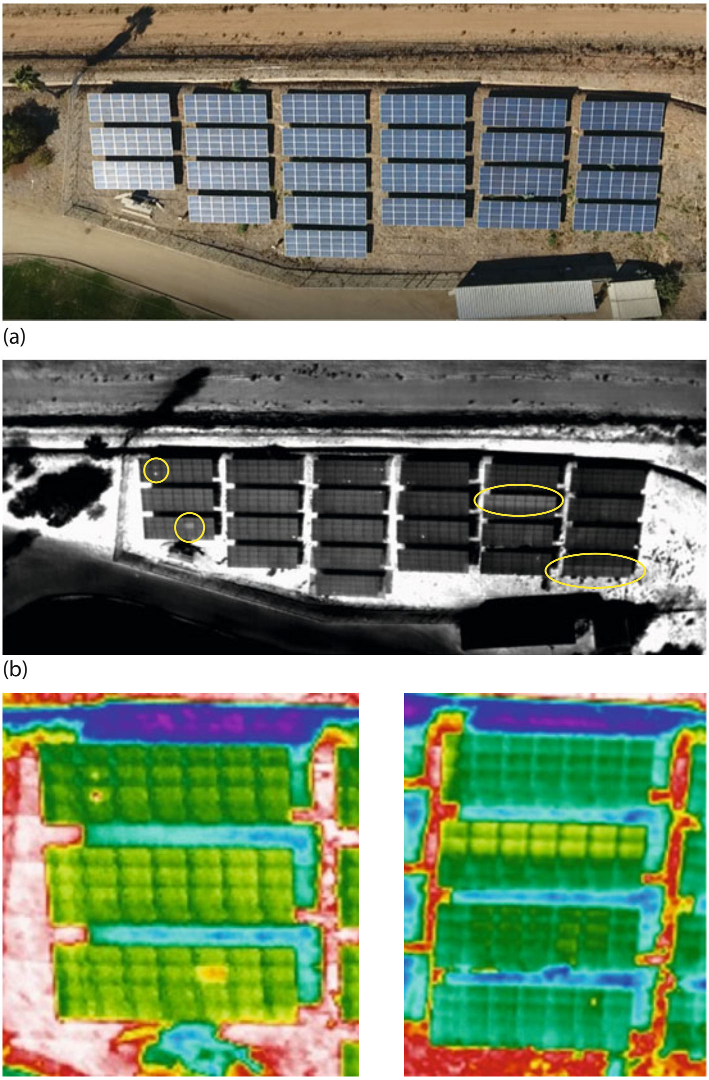
(a)
(b)
(c) (d)

Figure 10.52 VIS (a) and IR (b–d) images of a small solar field in San Diego, CA. The observed thermal anomalies (see discussion in text) clearly identify problems that need to be addressed on the ground. (c) and (d) are enlarged and processed images of columns 1 and 5. (Images courtesy Peter Hopkins, United Infrared, Inc.)

Figure 10.54 shows a sequence of three close-up views of different parts of the field. Like Figure 10.52, it shows typical problems that may be observed during drone IR inspections. In Figure 10.54a,b, vertical stripes of either one-third or two-thirds width within a panel show up at elevated temperatures. These typically amount to around 5 K (Figure 10.54c), meaning they are easily detected.

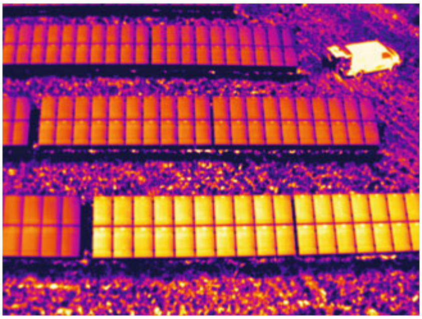

Figure 10.53 Overview image of part of an investigated solar power plant with a car parked to the side. The drone altitude was around 35–40 m. (Image courtesy M. Hambsch [145].)

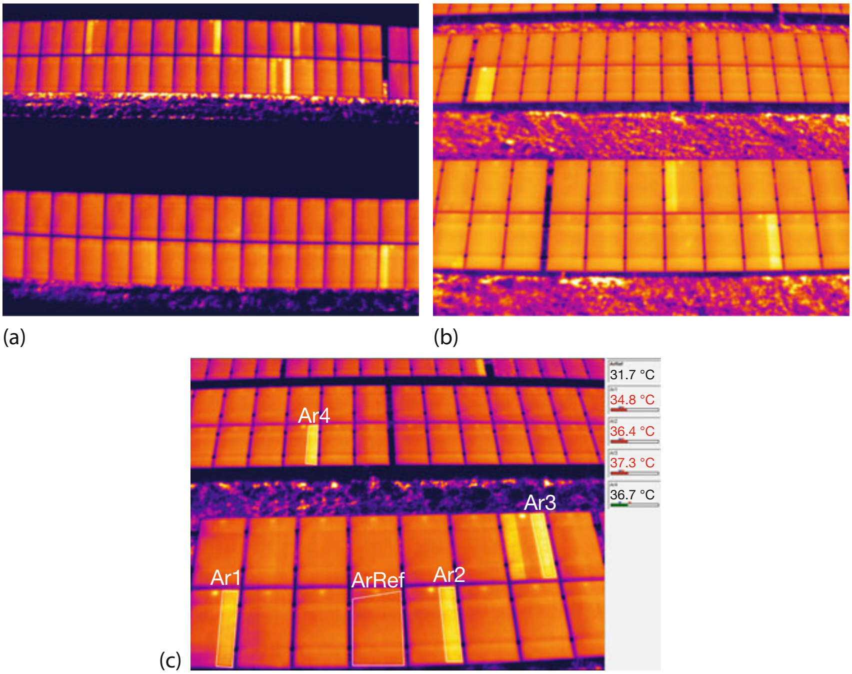

(a) (b)

(c)

Figure 10.54 (a,b) Typical thermal features of problem areas in solar panels and associated temperature differences (c). See text for details. (Images courtesy M. Hambsch [145].)

Since there are, for example, 6 × 10 individual cells within a panel, the stripes usually contain either 2 or 4 series of individual cells). The likely issues encountered here are either dead strings (no power output at all) or potential induced degradation (PID). The latter occurs due to leakage currents between the semiconductor material and other elements of the module (e.g., glass, frame). As a consequence, the output power of the respective cells connected in series of a module decreases, which leads to observable heating of these parts We emphasize that a drone inspection just shows the problem areas; the final conclusion about the cause of a problem is only possible after a close-up inspection on the ground.

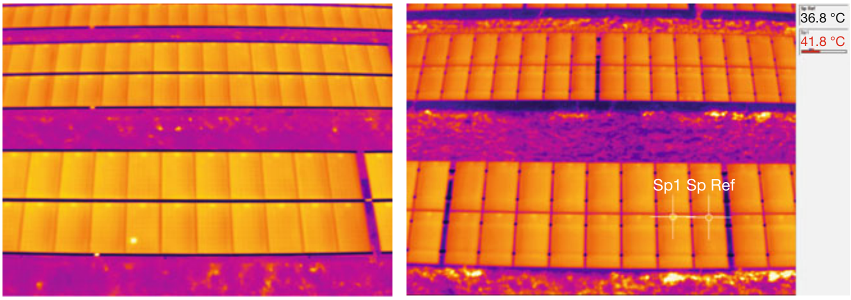

(a) (b)

Figure 10.55 Spotlike thermal features observed in IR drone inspections of solar fields (a) and analysis of the connection box influence (b). See text for details. (Images courtesy M. Hambsch [145].)

Finally, low drone altitudes, that is, high spatial resolution, allow one to observe features of individual cells. Figure 10.55a shows a feature due to a defective individual cell (bottom row, lower part). In addition, the resolution is sufficient to detect the thermal signature of the connection boxes attached close to the upper edge below each panel. The respective temperature differences are also on the order of 5 K (Figure 10.55b) and reflect normal operating behavior.

References

1. Schultz, C. (2004) Developing and implementing an infrared predictive maintenance program. *Maint. Technol.*, May 2004, 28–32.
2. Bagavathiappan, S., Lahiri, B.B., Saravanan, T., Philip, J., and Jayakumar, T. (2013) Infrared thermography for condition monitoring – A review. *Infrared Phys. Technol.*, **60**, 35–55.
3. Huda, A.S.N. and Taib, S. (2013) Application of infrared thermography for predictive/preventive maintenance of thermal defect in electrical equipment. *Appl. Therm. Eng.*, **61**, 220–227.
4. May, K.B. (2003) Predictive maintenance inspections – boilers in fossil power plants. Inframation 2003, Proceedings, vol. 4, pp. 161–166.
5. Updegraff, G. (2005) Infrared thermography program at a gas-fired turbine generation plant. Inframation 2005, Proceedings, vol. 6, pp. 293–300.
6. Ralph, M.J. (2004) Power Plant Thermography – Wide Range of Applications. Inframation 2004, Proceedings, vol. 5, pp. 241–248.
7. Ralph, M.J. (2009) The continuing story of power plant thermography. Inframation 2009, Proceedings, vol. 10, pp. 253–258.
8. Didychuk, E. (2006) Predictive maintenance of HVDC converter stations within Manitoba Hydro. Inframation 2006, Proceedings, vol. 7, pp. 409–422.
9. Bales, M.J., Berardi, P.G., Bishop, C.C., Cuccurullo, G., Grover, P.E., Mack, R.T., McRae, T.G., Pelton, M.W., Seffrin, R.J., and Weil, G.J. (2001) Chemical and petroleum applications of infrared and thermal testing, in *Nondestructive Testing Handbook*, Infrared and Thermal Testing, vol. 3, 3rd edn, Chapter 17 (ed. P.O. Moore), American Society for Nondestructive Testing, Inc., Columbus. pp. 571–600.
10. Massey, L.G. (2007) IR keeps West Virginia coal miners safe. Inframation 2007, Proceedings, vol. 8, pp. 327–334.

11 Blanch, M. (2008) Thermal imaging extracting faults in the sand mining industry. Inframation 2008, Proceedings, vol. 9, pp. 45–48.

12 Blanch, M. (2008) How sweet it is using infrared thermography. Inframation 2008, Proceedings, vol. 9, pp. 49–51.

13 Thon, R.J. (2002) Troubleshooting paper machine problems through thermal imaging. Inframation 2002, Proceedings, vol. 3, pp. 191–194.

14 Baird, L.W. and Bushee, R.L. (2003) Paper mill predictive maintenance utilizing infrared. Inframation 2003, Proceedings, vol. 4, pp. 17–24.

15 Thon, R.J. (2007) Using thermography to reduce energy costs in paper mills. Inframation 2007, Proceedings, vol. 7, pp. 553–555.

16 Bremond, P. (2004) IR imaging assesses damage in mechanical parts. *Photon. Spectra*, February 2004, 62–64.

17 Allison, J.N. (2005) Applying infrared imaging techniques to marine surveying. Inframation 2005, Proceedings, vol. 6, pp. 1–13.

18 Allison, J.N. (2008) Infrared thermography as part of quality control in vessel construction. Inframation 2008, Proceedings, vol. 9, pp. 11–16.

19 Ershov, O.V., Klimova, A.G., and Vavilov, V.P. (2006) Airborne detection of natural gas leaks from transmission pipelines by using a laser system operating in visual, near-IR and mid-IR wavelength bands. Thermosense XXVIII. Proc. SPIE, vol. 6205, 62051G.

20 Miles, J.J., Dahlquist, A.L., and Dash, L.C. (2006) Thermographic identification of wetted insulation on pipelines in the arctic oilfields. Thermosense XXVIII. Proc. SPIE, vol. 6205, 62051H.

21 Bonin, R.G. (2002) Infrared applications in the petrochemical refinery. Inframation 2002, Proceedings, vol. 3, pp. 13–17.

22 Whitcher, A. (2004) Thermographic monitoring of refractory lined petroleum refinery equipment. Inframation 2004, Proceedings, vol. 5, pp. 299–308.

23 Susralski, B.D. and Griswold, Th. (2000) Predicting mechanical systems failures using IR thermography. Inframation 2000, Proceedings, vol. 1, pp. 81–87.

24 Pearson, J. and Pandya, D.A. (2006) IR thermography assessment enhanced compressed air system operations & indirectly slashed $26 K utility bills at New Jersey international and bulk mail center. Inframation 2006, Proceedings, vol. 7, pp. 117–121.

25 Tarin, M. (2009) Solar panel inspection using lock-in thermography. Inframation 2009, Proceedings, vol. 10, pp. 225–237.

26 Aderhold, J., Meinlschmidt, P., Brocke, H., and Jüngert, A. (2008) Rotor blade defect detection using thermal and ultrasonic waves. Proc. 9th Int. German Wind Energy Conf. DEWEK, held 26–27 November 2008, Bremen, http://08.dewek.de/; see also www.wki.fraunhofer.de/en.html (accessed May 2017).

27 Moore, S. (2007) Thermography improves operations at grocery stores. Inframation 2007, Proceedings, vol. 8, pp. 181–186.

28 Sims, D. (2001) Using infrared imaging on production tanks and vessels. Inframation 2001, Proceedings, vol. 2, pp. 119–125.

29 Sims, D. (2004) Monitoring the process conditions in oil field production vessels with infrared technology. Inframation 2004, Proceedings, vol. 5, pp. 273–280.

30 Snell, J. and Schwoegler, M. (2004) Locating levels in tanks and silos using infrared thermography. Proceedings of the Thermosense XXVI. Proc. SPIE, vol. 5405, 245–248.

31 Walford, G.V. (2008) Use of infrared imaging techniques to understand and quantify expanded polymer molding operations and part quality. Inframation 2008, Proceedings, vol. 9, pp. 493–503.

32 de Vries, J. (2013) Application of Mid-Wave and Long-Wave Imaging in Large-Scale Rack-Storage Fires, 2013-020 in Inframation Proc. 2013, Infrared Training Center.

33 de Vries, J., Ren, N., and Chaos, M. (2015) Temperature measurements on

solid surfaces in rack-storage fires using IR thermography, Proc. SPIE, vol. 9485, Thermosense: Thermal Infrared Applications XXXVII, 94850H (12 May 2015); doi:10.1117/12.2177042.

34 Bosworth, B.R., Eto, M., Ishii, T., Mader, D.L., Okamoto, Y., Persson, L., Rayl, R.R., Seffrin, R.J., Shepard, S.M., Snell, J.R., Teich, A.C., Westberg, S.-B., and Zayicek, P.A. (2001) Electric power applications of infrared and thermal testing, in *Nondestructive Testing Handbook*, Infrared and Thermal Testing, vol. 3, 3rd edn, Chapter 16 (ed. P.O. Moore), American Society for Nondestructive Testing, Inc., Columbus, pp. 527–570

35 Bennett, R. (2009) Normalizing the E-values of components on a printed circuit board. Inframation 2009, Proceedings, vol. 10, pp. 157–162.

36 Fergueson, D.E. (2006) Applications of thermography in product safety. Inframation 2006, Proceedings, vol. 7, pp. 203–206.

37 Fishbune, R.J. (2000) IR thermography for electronic assembly design verification. Inframation 2000, Proceedings, vol. 1, pp. 211–217.

38 Wallin, B. and Wiecek, B. (2001) Infrared Thermography of electronic components, in *Nondestructive Testing Handbook*, Infrared and Thermal Testing, vol. 3, 3rd edn, Chapter 19 (ed. P.O. Moore), American Society for Nondestructive Testing, Inc., Columbus, pp. 659–678

39 Radford, P. (2008) Ship's stearing gear motor problem diagnosed using IR technology. Inframation 2008, Proceedings, vol. 9, pp. 373–376.

40 Möllmann, K.-P. and Vollmer, M. (2007) Infrared thermal imaging as a tool in university physics education. *Eur. J. Phys.*, **28**, S37–S50.

41 Madding, R.P. (2001) Finding internal electrical resistance from external IR thermography measurements on oil-filled circuit breakers during operation. Inframation 2001, Proceedings, vol. 2, pp. 37–44.

42 Leonard, K. (2006) What if? Inframation 2006, Proceedings, vol. 7, pp. 123–127.

43 Maple, C. (2003) Secure Plant infrastructure through remote substation monitoring. Inframation 2003, Proceedings, vol. 4, pp. 151–159.

44 Brydges, D. (2005) Aerial thermography surveys find insulator and other problems. Inframation 2005, Proceedings, vol. 6, pp. 193–202.

45 Madding, R.P. (2002) Important measurements that support IR surveys in substations. Inframation 2002, Proceedings, vol. 3, pp. 19–25.

46 Gierlach, J. and DeMonte, J. (2005) Infrared inspections on electric panels without removing covers: Can the inspection be completed correctly? Inframation 2005, Proceedings, vol. 6, pp. 203–212.

47 www.iriss.com (accessed May 2017), free download of "The Ten Things You Need To Know About Infrared Windows".

48 Robinson, M. (2007) Infrared Windows: Where do I start? Inframation 2007, Proceedings, vol. 8, pp. 291–307.

49 Newton, V. (2008) Arc flash and electrical safety for thermographers. Inframation 2008, Proceedings, vol. 9, pp. 321–332.

50 Theyerl, M.N. (2008) Arc Flash concerns & detecting early signs. Inframation 2008, Proceedings, vol. 9, pp. 447–457.

51 Androli, D. (2006) A thermographers common sense approach to arc flash safety. Inframation 2006, Proceedings, vol. 7, pp. 207–214.

52 Woods, B. (2005) Reducing arc flash hazards through electrical system modifications. Inframation 2005, Proceedings, vol. 6, pp. 15–21.

53 Madding, R.P., Orlove, G.L., and Lyon, B.R. (2006) The importance of spatial resolution in IR thermography temperature measurement – Three brief case studies. Inframation 2006, Proceedings, vol. 7, pp. 245–251.

54 Giesecke, J.L. (2006) Adjusting severity criteria. Inframation 2006, Proceedings, vol. 7, pp. 33–35.

55 Madding, R.P., Ayers, D., and Giesecke, J.L. (2002) Oil circuit breaker thermography. Inframation 2002, Proceedings, vol. 3, pp. 41–47.

56 Goff, M.B. (2001) Substation equipment (bushings). Inframation 2001, Proceedings, vol. 2, pp. 113–117.

57 Goff, M.B. (2008) The secrets of bushing oil level. Inframation 2008, Proceedings, vol. 9, pp. 167–174.

58 Möllmann, K.P., Karstädt, D., Pinno, F., and Vollmer, M. (2005) Selected critical applications of thermography: convections in fluids, selective emitters and highly reflecting materials. Inframation 2005, Proceedings, vol. 6, pp. 161–173.

59 http://www.thermokameras.com (accessed May 2017).

60 De Witt, D.P. and Nutter, G.D. (1988) *Theory and Practice of Radiation Thermometry*, John Wiley & Sons, Inc., New York.

61 Holst, G.C. (2000) *Common Sense Approach to Thermal Imaging*, SPIE Optical Engineering Press, Washington.

62 Vollmer, M., Henke, S., Karstädt, D., Möllmann, K.P., and Pinno, F. (2004) Challenges in infrared imaging: Low emissivities of hot gases, metals, and metallic cavities. Inframation 2004, Proceedings, vol. 5, pp. 355–363.

63 Schmidt, V., Möllmann, K.-P., Muilwijk, F., Kalz, S., and Stoppiglia, H. (2002) Radiation thermometry on aluminium. VIR[*]-Conference 2002, Ijmuiden, vol. 78, October 2002, pp. 897–901.

64 Gärtner, R., Klatt, P., Loose, H., Lutz, N., Möllmann, K.-P., Pinno, F., Muilwijk, F., Kalz, S., and Stoppiglia, H. (2004) New aluminium radiation thermometry. VIR[*]-Conference 2004, Brussels, vol. 80, June 2004, pp. 642–647.

65 Papp, L. (2004) Using IR surveys in DUNAFERR steelworks complex diagnostic systems. Inframation 2004, Proceedings, vol. 5, pp. 371–386.

66 Nolan, D., Zhao, Q., Abdelrahman, M., Vondra, F., and Dinwiddie, R.B. (2006) The effect of process characteristics on metal fill and defect formation in aluminum lost foam casting. Inframation 2006, Proceedings, vol. 7, pp. 51–64.

67 Whitcher, A. and Rees, K. (2013) Furnace tube choking – a case study, Inframation 2013, Proceedings, vol. 14, 2013-074

68 Calmes, F. (2000) Infrared inspections of robotic welders in automotive assembly. Inframation 2000, Proceedings, vol. 1, pp. 25–23.

69 Sinclair, D. (2004) Infrared cameras enhance productivity and safety at GM. Inframation 2004, Proceedings, vol. 5, pp. 281–286.

70 Predmesky, R. and Ruane, T. (2004) Using infrared cameras for process control. Inframation 2004, Proceedings, vol. 2, pp. 27–29.

71 Royo, R. (2004) Characterization of automation brake thermal conditions by the use of infrared thermography. Inframation 2004, Proceedings, vol. 5, pp. 259–266.

72 Infrared detection of standing waves. European patent application 1255102, see http://www.freepatentsonline.com/EP1255102.pdf (accessed May 2017).

73 Kurata, T. (2005) Tire wear forecasting method and apparatus. US patent 6883962.

74 Putman, B.J. and Amirkhanian, S.N. (2006) Thermal segregation in asphalt pavements. Inframation 2006, Proceedings, vol. 7, pp. 233–244.

75 Steyn, W.JvdM. (2005) Applications of thermography in pavement engineering. Inframation 2005, Proceedings, vol. 6, pp. 81–89.

76 Monem, T.A., Olaufa, A.A., and Mahgoub, H. (2005) Asphalt crack detection using thermography. Inframation 2005, Proceedings, vol. 6, pp. 139–150.

77 Amirkhanian, S.N. and Hartman, E. (2004) Applications of infrared cameras in the paving industry, Inframation 2004, Proceedings, vol. 5, pp. 91–99.

78 Philipps, L., Willoughby, K., and Mahoney, J. (2003) Infrared thermography revolutionizes hot-mix asphalt paving. Inframation 2003, Proceedings, vol. 4, pp. 213–221

79 Red Bull Racing's RB8 Tearing it Up in Infrared: www.youtube.com/watch?v=jvuBe6b2iVk (accessed May 2017).

80 Crane, R.L. *et al.* (2001) Aerospace applications of infrared and thermal testing, in *Nondestructive Testing Handbook*, Infrared and Thermal Testing, vol. 3, 3rd edn, Chapter 15 (ed. P.O.

Moore), American Society for Nondestructive Testing, Inc., Columbus, pp. 489–526.

81 Spring, R.W. (2001) An overview of infrared thermography applications for nondestructive testing in the aerospace industry. Inframation 2001, Proceedings, vol. 2, pp. 191–196.

82 Genest, M. and Fahr, A. (2009) Pulsed thermography for nondestructive evaluation (NDE) of aerospace materials. Inframation 2009, Proceedings, vol. 10, pp. 59–65.

83 Figg, J. and Daquila, T. (2001) Applying the benefits of infrared thermography in naval aviation. Inframation 2001, Proceedings, vol. 2, pp. 207–214.

84 Tarin, M. and Kasper, A. (2008) Fuselage inspection of Boeing-737 using lock-in thermography. Proc. Thermosense XXX. Proc. SPIE, vol. 6939, SPIE Press, Bellingham, electronic file: 693919-1 to 693919-10.

85 Holleman, E., Sharp, D., Sheller, R., and Styron, J. (2007) IR characterization of Bi-propellant reaction control engines during auxiliary propulsion systems tests at NASA's White Sands test facility in Las Cruces, New Mexico. Inframation 2007, Proceedings, vol. 8, pp. 95–107.

86 Gazarek, M., Johnson, D., Kist, E., Novak, F., Antill, Ch., Haakenson, D., Howell, P., Jenkins, R., Yates, R., Stephan, R., Hawk, D., and Amoroso, M. (2005) Infrared on-orbit RCC inspection with the EVA IR camera: development of flight hardware from a COTS system. Inframation 2005, Proceedings, vol. 6, pp. 273–284.

87 Gazarik, M., Johnson, D., Kist, E., Novak, F., Antill, C., Haakenson, D., Howell, P., Pandolf, J., Jenkins, R., Yates, R., Stephan, R., Hawk, D., and Amoroso, M. (2006) Development of an extra-vehicular (EVA) infrared (IR) camera inspection system. Proc. Thermosense XXVIII. Proc. SPIE, vol. 6205, 62051C.

88 Elliott Cramera, K., Winfreea, W.P., Hodgesb, K., Koshtib, A., Ryanc, D., and Reinhardt, W.W. (2006) Status of thermal NDT of space shuttle materials at NASA. Proceedings of the Thermosense XXVIII. Proc. SPIE, vol. 6205, 62051B.

89 (2006) *ITC Newsletter*, **7** (9), 2.

90 Sauser, B. (2009) http://www.technologyreview.com/computing/23533/, published by MIT, Monday, Image Credit: NASA/HYTHIRM team (28 September 2009; accessed May 2017)

91 http://www.youtube.com/watch?v=-H0GsU2Z6uc (accessed May 2017).

92 Horvath, T.J. *et al.* (2010) The HYTHIRM Project: Flight Thermography of the Space Shuttle during Hypersonic Reentry, Proc. 48th AIAA Aerospace Sci. Meeting Conf., AIAA 2010-241.

93 Schwartz, R.J. *et al.* (2011) Remote Infrared Imaging of the Space Shuttle during Hypersonic Flight: HYTHIRM Mission Operations and Coordination, Proc. 42nd AIAA Thermophysics Conf., AIAA 2011-3326.

94 Wood, W.A. and Oliver, A.B. (2011) Assessment of CFD Hypersonic Turbulent Heating Rates for Space Shuttle Orbiter, Proc. 42nd AIAA Thermophys. Conf., AIAA 2011-3327.

95 Zalameda, J.N. *et al.* (2012) Thermographic Imaging of the Space Shuttle during Re-Entry Using a Near Infrared Sensor, Proc. SPIE, vol. 8354 Thermosense XXXIV, 83540F.

96 http://www.youtube.com/watch?v=rVJDYI1BQA4; https://www.nasa.gov/topics/shuttle_station/features/sts-135_launch_fused_imagery.html (accessed May 2017).

97 http://www.youtube.com/watch?v=JoTBB9gmUkw (accessed May 2017).

98 http://www.youtube.com/watch?v=lJxnZ2opM38 (accessed May 2017).

99 Madding, R.P. (2004) IR window transmittance temperature dependence. InfraMation 2004, Proceedings, vol. 5, pp. 161–169.

100 Rogalski, A. and Chrzanowski, K. (2006) Infrared devices and techniques, in *Handbook of Optoelectronics*, vol. 1 (eds J.R. Dakin and R.G.W. Brown), Taylor and Francis, New York, pp. 653–691.

101 Zieli, M. and Milewski, S. (2006) Thermal images and spectral characteristics of objects that can be used to aid in rescue of shipwrecked people at sea. Inframation 2006, Proceedings, vol. 7, pp. 279–286.

102 Beier, K. and Gemperlein, H. (2004) Simulation of infrared detection range at fog conditions for enhanced vision systems. *Civ. Aviat. Aerosp. Sci. Technol.*, **8**, 63–71.

103 Richards, A. and Johnson, G. (2005) Proceedings of the Thermosense XXVII (2005), Proc. SPIE, vol. 5782, SPIE Press, Bellingham, pp. 19–28.

104 Duntley, S.Q. (1948) The reduction of apparent contrast by the atmosphere. *J. Opt. Soc. Am.*, **38**, 179–191.

105 Jha, A.R. (2000) *Infrared Technology*, John Wiley & Sons, Inc.

106 Mason, N. and Hughes, P. (2001) *Introduction to Environmental Physics*, Taylor and Francis.

107 www.acecoretechnologies.com/ (accessed May 2017).

108 www.aibotix.com/products/aibot-x6 (accessed May 2017).

109 www.airborne-robotics.com/en/drone/professionell/drone-air6 (accessed May 2017).

110 www.globe-flight.de/ScaraBot-X8 (accessed May 2017).

111 heighttech.com/en/products/ht-8/ (accessed May 2017).

112 www.jamcopters.cz/en/rtf/dji-matrice-600-hexakopt%C3%A9ra (accessed May 2017).

113 videodrone.fi/en/videodrone/videodrone-x4s/ (accessed May 2017).

114 http://www.dji.com/products/drones (accessed May 2017).

115 www.drone-thermal-camera.com/wiris/ (accessed May 2017).

116 www.optris.com/pi-lightweight-netbox (accessed May 2017).

117 www.flir.com/suas/content/?id=74946 (accessed May 2017).

118 www.dji.com/zenmuse-xt (accessed May 2017).

119 www.viper-drones.com (accessed May 2017).

120 www.dronedeploy.com (accessed May 2017).

121 Congress information 2012: Elias, B., Pilotless Drones: Background and Considerations for Congress Regarding Unmanned Aircraft Operations in the National Airspace System, Congressional Research Service 7-5700 www.crs.gov R42718, 10 September 2012.

122 Congress information 2016: Elias, B., Unmanned Aircraft Operations in Domestic Airspace: US Policy Perspectives and the Regulatory Landscape, Congressional Research Service 7-5700 www.crs.gov R44352, 27 January 2016.

123 Smith, K.W. (2015) Drone technology: Benefits, risks, and legal considerations. *Seattle J. Environ. Law*, **5** (1), Article 12 Available at: http://digitalcommons.law.seattleu.edu/sjel/vol5/iss1/12.

124 LaFay, M. (2015) *Drones for Dummies*, John Wiley & Sons.

125 Janssen, S.L. (2015) Assessing the perception of drones in the construction industry, Bachelor thesis, University of Twente.

126 Ariwoola, R.T. (2016) Use of drone and infrared camera for a campus building envelope study, Electronic Theses and Dissertations, Paper 3018 (May 2016) http://dc.etsu.edu/etd/3018 (accessed May 2017).

127 Marris, E. (2013) Fly and bring me data. *Nature*, **498**, 156–158.

128 Diaz, T.J. (2015) Lights, drone, action – An expert guide to drone videography. *Spectrum IEEE North American*, 36–41, see also http://spectrum.ieee.org/aerospace/aviation/the-insiders-guide-to-drone-videography (accessed May 2017).

129 Stockton, G.R. and Tache, A. (2006) Advances in applications for aerial infrared thermography, Proc. SPIE, vol. 6205, Thermosense XXVIII, 62050C (18 April 2006).

130 Stockton, G.R. and Lucas, R.G. (2012) Using aerial infrared thermography to detect utility theft of service, Proc. SPIE, vol. 8354, Thermosense: Thermal Infrared Applications XXXIV, 83540T (18 May 2012).

131 Lunden, B. (1985) Aerial thermography: A remote sensing technique applied to detection of buried archaeological remains at a site in Dalecarlia, Sweden. *Geografiska Annaler A*, **67**, 161–166.

132 Lega, M. and Napoli, R.M.A. (2008) A new approach to solid waste landfills aerial monitoring. Waste management and the environment IV. *WIT Trans. Ecol. Environ.*, **109**, 193–199.

133 Lega, M., Ferrara, C., Persechino, G., and Bishop, P. (2014) Remote sensing in environmental police investigations: Aerial platforms and an innovative application of thermography to detect several illegal activities. *Environ. Monit. Assess.*, **186** (12), 8291–8301.

134 Amici, S., Turci, M., Giulietti, F., Giammanco, S., Buongiorno, M.F., La Spina, A., and Spampinato, L. (2013) Volcanic environments monitoring by drones – Mud volcanic case study. *Int. Arch. Photogramm. Rem. Sens. Spat. Inf. Sci.*, **XL-1** (W2), 5–10.

135 Stark, B., Smith, B., and Chen, Y.Q. (2014) Survey of Thermal Infrared Remote Sensing for Unmanned Aerial Systems, Proc. Int. Conf. on Unmanned Aircraft Systems (ICUAS), 1294–1299, IEEE, doi:10.1109/ICUAS.2014.6842387.

136 Casana, J., Kantner, J., Wiewel, A., and Cothren, J. (2014) Archaeological aerial thermography: A case study at the Chaco-era Blue J community, New Mexico. J. *Archaeol. Sci.*, **45**, 207–219.

137 Mavromatidis, L.E., Dauvergne, J.-L., Saleri, R., and Batsale, J.-C. First experiments for the diagnosis and thermophysical sampling using impulse IR thermography from Unmanned Aerial Vehicle (UAV), paper 213, Proc. Conf. QIRT 2014 (Bordeaux), see http://dx.doi.org/10.21611/qirt.2014.213 (accessed May 2017).

138 Photovoltaic systems thermography from the air using drones, FLIR application story 2012, see www.flir.co.uk/instruments/building/display/?id=60636 (accessed May 2017).

139 Tyutyundzhiev, N., Lovchinov, K., Martínez-Moreno, F., Leloux, J., and Narvarte, L. (2015) Advanced PV modules inspection using multirotor UAV, Proc. 31st European Photovoltaic Solar Energy Conference and Exhibition, September 2015, Hamburg, see www.pvcrops.eu/sites/default/files/u10/Advanced_PV.pdf (accessed May 2017).

140 Dotenco, S., Dalsass, M., Winkler, L., Wurzner, T., Brabec, C., Maier, A., and Gallwitz, F. (2016) Automatic Detection and Analysis of Photovoltaic Modules in Aerial Infrared Imagery, Proc. 2016 IEEE Winter Conference on Applications of Computer Vision (WACV), see https://www.computer.org/csdl/proceedings/wacv/2016/0641/00/07477658-abs.html (accessed May 2017).

141 Muntwyler, U., Schüpbach, E., and Lanz, M. (2015) Infrared (IR) Drone For Quick and Cheap PV Inspection, Proc. 31st European Photovoltaic Solar Energy Conference (EU PVSEC) pp. 1804–1806, doi:10.4229/EUPVSEC20152015-5CO.15.6.

142 Harvey, M.C. and Luketina, K. (2015) Thermal Infrared Cameras and drones: A match made in heaven for cost-effective geothermal exploration, monitoring and development, Proc. 37th New Zealand Geotherm. Workshop 2015, New Zealand, see www.geothermalworkshop.co.nz/ (accessed May 2017).

143 Harvey, M.C., Rowland, J.V., and Luketina, K.M. (2016) Drone with Thermal Infrared Camera Provides high resolution georeferenced imagery of the Waikite Geothermal Area, New Zealand. *J. Volcanol. Geotherm. Res.*, **325**, 61–69.

144 Shaw, J.A., Nugent, P.W., Kaufman, N.A., Pust, N.J., Mikes, D., Knierim, C., Faulconer, N., Larimer, R.M., DesJardins, A.C., and Knighton, W.B. (2012) Multispectral imaging systems on tethered balloons for optical remote sensing education and research. *J. Appl. Rem. Sens.*, **6**, 063613-1-11.

145 www.kitawa.de/en (accessed May 2017).

Chapter 11
Selected Applications in Other Fields

In this final chapter, a number of miscellaneous topics are discussed that at first glance may seem too complex or beyond the interests of practicing thermographers in science and industry. At second glance, however, one may realize that such interdisciplinary examples are becoming increasingly popular and reveal a huge new field of potential applications. We start with thermal imaging in the (human) medical sciences as a diagnostic tool and then treat veterinary applications as well as the thermal imaging of zoo animals and wildlife studies. Changing topics, we proceed with IR imaging in various aspects of sports before discussing some exemplary applications in the arts. The final section deals with the beauty of nature around us. Nearly all thermographers – upon completion of their professional duties – probably point their camera to things around them in nature, for example, the sky, the Moon, or the Sun. Here explanations will be given about what may be observed and why. Finally, some of the most spectacular thermal features in nature around us will be presented: natural phenomena such as geysers, hot pools, and volcanoes.

11.1
Medical Applications

11.1.1
Introduction

Thermal imaging is becoming increasingly accepted by physicians as a supplementary diagnostic as well as monitoring tool for various diseases. This is based on the fact that diseases and injuries lead to changes in body surface temperature, which are recorded by sensitive IR cameras [1–4].

The surface temperature of an extremity reflects the result of a complex combination of central and local regulatory systems [5]. As a living organism, the human body tries to maintain homeostasis, that is, an equilibrium of all systems within the body, for all physiological processes, which (among other things) leads to dynamic changes in heat emission. They depend on internal (e.g., blood flow, hormones, food intake, in particular alcohol, smoking, exercise, emotion) and ex-

Infrared Thermal Imaging, Second Edition. M. Vollmer and K.-P. Möllmann.
© 2018 WILEY-VCH Verlag GmbH & Co. KGaA. Published 2018 by WILEY-VCH Verlag GmbH & Co. KGaA.

ternal (e.g., room temperature, humidity, clothing, cosmetics, jewelry) conditions. This makes inevitable the development of standard operating procedures that enable interpreting thermal imaging results that might influence a physician's decision regarding further steps in the diagnostic process and treatment.

The most important factor for the surface temperatures seems to be arterial blood flow because the temperatures increase with intensified blood flow, whereas augmented venous blood flow correlates with a temperature decrease (e.g., physical exercise leads to a dilation of veins in order to cool down the core body temperature) [6]. This physiological process is maintained by many factors: the activation of the sympathetic nervous system and hormones/catecholamines seem to play an important role. If activated, the sympathetic nervous system – partly controlled by hormones and catecholamines – leads to vasoconstriction. In a healthy person, skin temperature is symmetrical. Nevertheless, acral temperature varies more than the temperature in the area of the trunk, where it is usually higher than in more distal parts [7].

The major advantage of medical IR imaging, next to being an easy-to-handle tool in diagnostics and monitoring, is that the progress of a disease or the effects of therapeutic measures can be visualized for patients. Especially in the beginning of a treatment, patients may not notice sufficient relief. In this case, IR images can help to demonstrate the onset of changes and increase compliance for intensified or time-demanding efforts of the medical staff. This is best illustrated for pressure ulcers in patients with diabetes: because of the underlying disease, perception of healing is impaired by polyneuropathies. Here, IR images can visualize the positive effects of treatment before obvious macroscopic improvement. The advantages of thermography with modern camera systems are the high spatial resolution and fast data recording.

Standard conditions in thermographic imaging have been discussed copiously [8]. However, they are not put in place regularly, first because of a lack of time, second because of patients' noncompliance, and third because of a lack of knowledge. For example, room temperature as well as humidity and medication, which may have an impact on surface blood flow, should be included in reports. For standardization, the five following major conditions should be fulfilled in order to avoid common errors [9]:

1. Proper room conditions
   a) Minimum size of 9 m^2
   b) Constant room temperature (23.5 °C)
   c) Humidity of 45–60%
   d) No turbulent airflow, that is, no heat emitters, ventilators, or air conditioning close to the patient
   e) If necessary, shades should be installed to reduce the effect of sunlight
   f) Proper selection of material on walls and ceiling to avoid thermal reflections
2. Proper preparation of patient

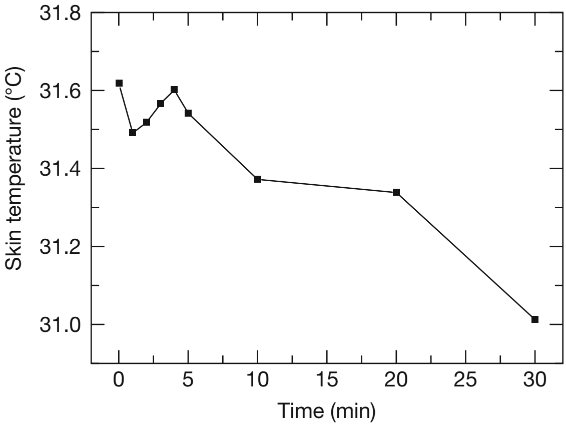

Figure 11.1 Decrease in skin temperature (hands) over a period of 30 min after an acclimatization period of 15 min. (Graph courtesy K. Agarwal.)

   a) Acclimatization for at least 15 min in a proper room (resting in a natural position, light clothing without feeling too hot or too cold), taking off clothes from areas to be examined
   b) No intake of food, alcohol, nicotine, coffee, or tea 2 h before examination
   c) No physical exercise 24 h before examination
   d) No deodorants, crèmes, perfumes, solutions, or shaving at the body surface areas to be monitored
   e) No acupuncture, transcutaneous electrical nerve stimulation, or invasive procedures before examination
   f) Jewelry removed 4 h before examination
   g) No excessive tanning or sunburns 7–10 days before examination
3. Standardized equipment
   a) Calibrated IR camera, low noise-equivalent temperature difference
   b) Camera switched on at least 1 h before examination in the same room (see switch on behavior and thermo shock, Section 2.4.6)
4. Proper recording and storage of acquired images
   a) Avoid grazing incidence of radiation on camera, select viewing angle close to 0° since $\varepsilon = \varepsilon$ (angle) (Section 1.4)
   b) Files should include gender, age, diagnosis, current medication, size, weight, room conditions, and date
5. Representation of images
   a) Standardized temperature scale (color palette, level, span), often a range of 23–36 °C or 24–38 °C is chosen.

In many books on dermatology or physiology, normal skin temperature is defined as falling in a range of 32–34 °C. In addition, despite proper acclimatization, skin temperature continues to drop at least 30 min into an examination (Figure 11.1). Even if all of the aforementioned items are followed strictly, the human

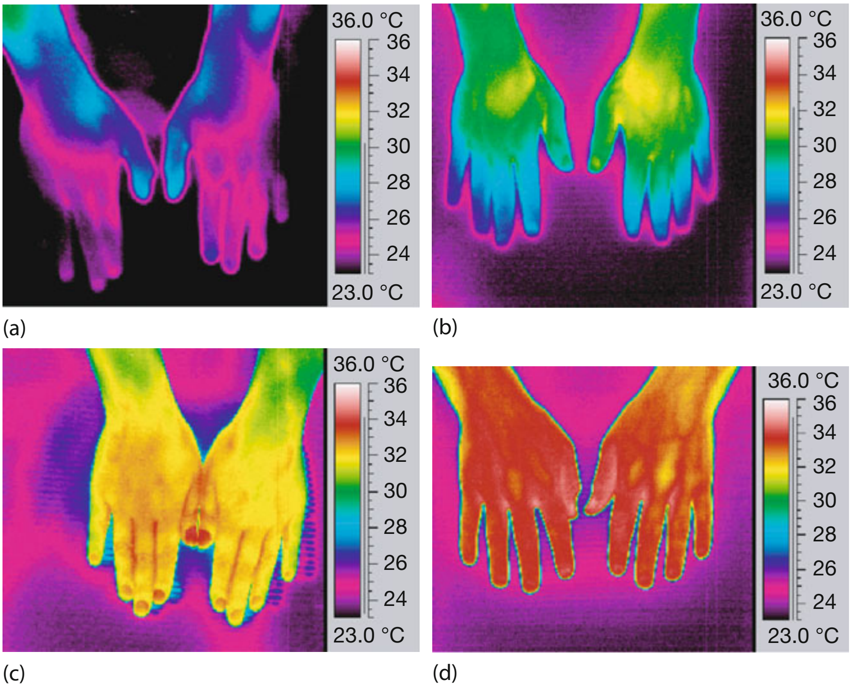

Figure 11.2 IR images of four healthy subjects – (a,c) female, (b,d) male, all age 25 recorded before a/b and after c/d) – after acclimatization for 15 min at standardized conditions. (Images courtesy K. Agarwal.)

body is a highly dynamic organism, so even under the same conditions, surface temperature may vary intra- (0.4–11 K) and interindividually (up to 12.3 K) without any obvious cause, the largest variations occurring at the extremities (Figure 11.2). This makes interpreting thermograms even more complicated [10].

For each application, different aspects are important; thus, here only a few case studies of medical applications – pain management, acupuncture, and breast cancer – are discussed in more detail; others are mentioned only briefly. Exemplary results will be presented based on the extensive work of K. Agarwal [10–15], though of course many more researchers work in this field.

11.1.2
Diagnosis and Monitoring of Pain

Objectively determining pain intensity is a key element of pain management. Unfortunately, so far no tool has been developed that sufficiently fulfills this task; hence, it is extremely difficult to conclude whether some treatment being offered to a patient is helpful or not. In particular forms of pain, that is, neuropathic and sympathetically maintained pain, blocks of the sympathetic nervous system are performed to diminish pain intensity. They often result in significant relief, though there is no way to prove that the relief did not result from blocking structures other than the sympathetic nervous system like spinal nerves or if it is just a psychological effect. Because sympathetic fibers affect blood flow by varying the size of vessels, a rise in skin temperature is expected from sympathetic blocks because variation of skin perfusion correlates with surface temperature. The configuration of changes in skin temperature provides us with precious information on the success of interventions besides the patient's subjective impression. Therefore, it has been proposed [11–13] that IR thermography can obviously be utilized as a diagnostic tool with extraordinary sensitivity and repeatability, although it has been rarely applied in that manner so far. Two examples of pain treatment are discussed in more detail [14].

First, the complex regional pain syndrome (CRPS) is a painful syndrome usually affecting distal extremities of the body and manifesting itself with a wide variety of symptoms. The most outstanding feature is unbearable pain, including spontaneous pain, allodynia, hyperpathia, and hyperalgesia. Usually, the affected extremity displays changes in color or temperature (vasomotor disturbances), edema, alterations in transpiration, hair and nail growth (sudomotor disturbances), and muscular atrophy or dysfunction (motortrophic disturbances). In some cases, a specific initiating event can be identified, for example, trauma or surgery, but occasionally it is observed after stroke, myocardial infarction, infection, or even without an obvious causing event. The course of the disease varies interindividually. If proper treatment is not available, or in some cases despite treatment, it may lead to persisting diminished function of the affected limb, which deeply impairs the patient's quality of life.

Temperature variations are commonly considered to be a major criterion in the diagnosis of CRPS; hence, IR thermography can be utilized as a diagnostic tool in CRPS with extraordinary sensitivity and repeatability, though it is not specific (Figure 11.3). As a matter of fact, good correlation is found between skin temperature and skin sympathetic nerve activity, so skin temperature can be regarded as a very good predictor of sympathetic activity.

The CRPS malady can be treated with blocks of the sympathetic nervous system, which in turn will have an impact on skin perfusion (Figure 11.4). Pain can usually be reduced within a few hours after injecting a local anesthetic, but complete treatment is very time consuming; patients often lose patience. To increase compliance to continue therapy, IR images are very useful.

Second, osteomyelitis is a painful infection of the bone and marrow. In adults it primarily affects digits of the feet and is most often associated with diabetes mellitus. Very often it is accompanied by neuropathic pain, which refers to an assortment of pain states with a common feature: symptoms are suggestive of dysfunction or lesion of nerves.

Treatment may be complicated and time consuming, often requiring prolonged antibiotic therapy for weeks or months, and sometimes surgical intervention may be required [14]. The lack of efficacy of antibiotic treatments may correlate with diminished blood flow in the affected area. This can be easily detected using thermography. In particular, it may reveal physiological changes that cannot be

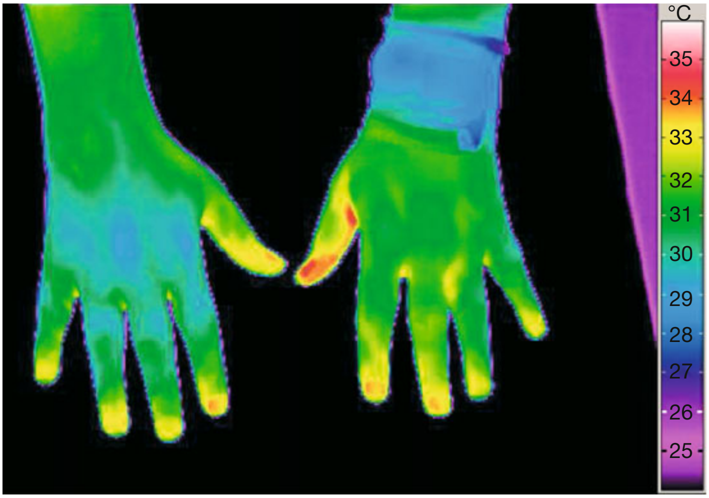

Figure 11.3 IR image prior to sympathetic block in a female patient with CRPS; note that the surface temperature on the right hand is about 2 K lower than in the unaffected left hand. (Images courtesy K. Agarwal.)

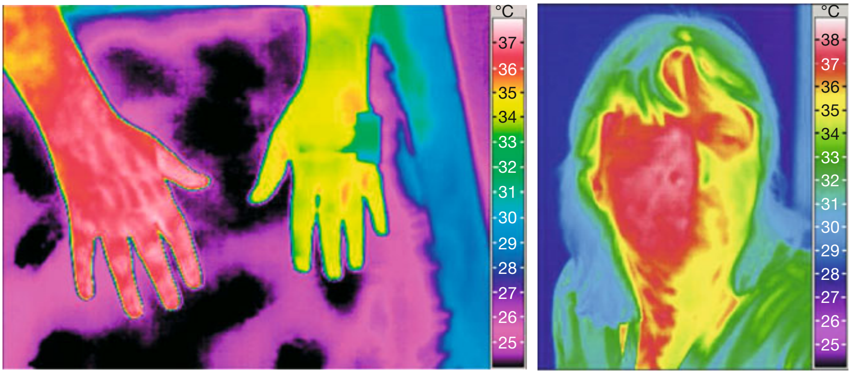

(a) (b)

Figure 11.4 IR images 2 h after sympathetic block of hands in the same patient; the block was performed on the right side, and hence perfusion of that hand and that side of the face led to an increase in skin temperature of up to $\Delta T \approx 10$ K, as opposed to $\Delta T \approx 3$ K contralaterally. All images were recorded using the aforementioned standardized procedure. (Images courtesy K. Agarwal.)

demonstrated by ultrasound, computed tomography (CT), or magnetic resonance imaging (MRI). A healthy human usually presents a symmetric surface temperature that correlates with tissue blood flow, which is influenced by sympathetic activity. In the treatment of sympathetically maintained pain, thermography is used to prove the efficacy of sympathetic chain blocks in order to determine whether neuroablation is indicated and might be effective. Figures 11.5–11.7 dis-

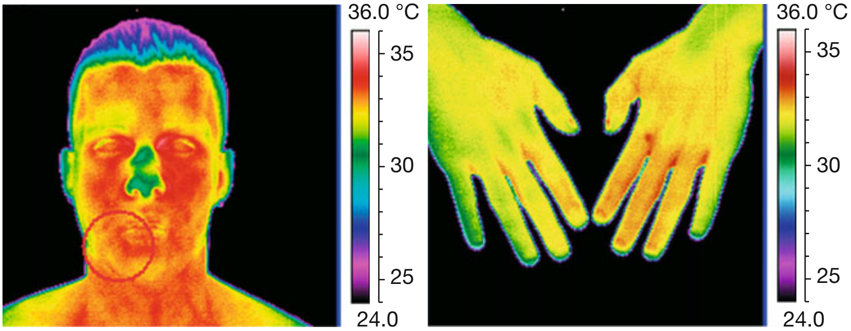

(a)

(b)

Figure 11.5 IR images of patient before treatment. (a) Facial image; circle: location of infection. (b) Dorsal IR image of hands. (Images courtesy K. Agarwal.)

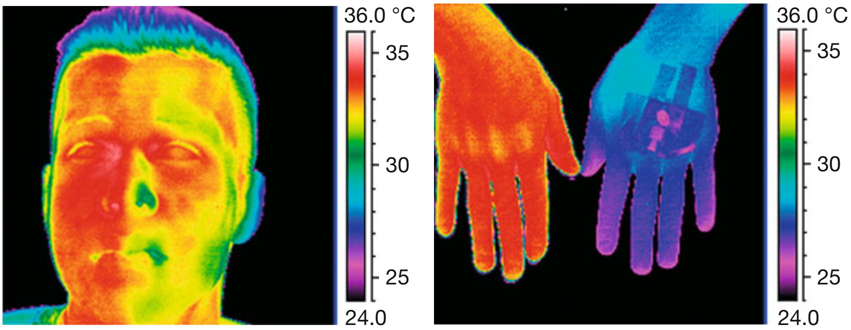

(a)

(b)

Figure 11.6 IR images of patient during treatment. (a) Facial image, indicating increased blood flow on right side of face. (b) Palmar IR image of hands. The pink dots and dark blue shades on the dorsal surface of the hand originate from an intravenous access that was taped to the skin. (Images courtesy K. Agarwal.)

play IR images of a young male who suffered from osteomyelitis in his jaw for more than 5 years following an accident. He had undergone initial surgery, including bony reconstruction of the jaw, and received multiple doses of antibiotics; still, healing would not progress as desired and he suffered from neuropathic pain in the affected area that started spreading over his whole face. As sufficient blood supply is inevitable for the delivery of satisfactory amounts of antibiotics to the affected site, the primary aim in treating this patient was to increase perfusion in the area involved.

Figure 11.5 shows the patient's face and hands prior to treatment. On the basis of the hypothesis that the whole disease might be sustained by the sympathetic nervous system, he received blocks of the stellate ganglion and the thoracic sympathetic chain. Figure 11.6 shows IR images during continuous infusion of a local anesthetic. The increased blood flow led to higher skin temperature on the right side of the face, as intended. The same applies to the hand, which proves that

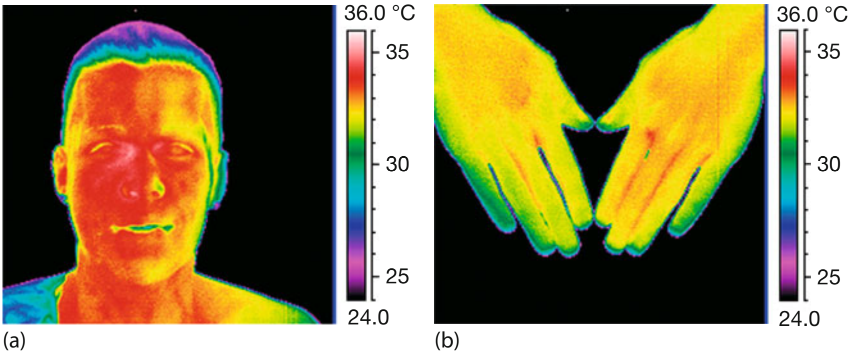

Figure 11.7 IR images of patient after treatment. (a) Facial image; blood flow is augmented all over. (b) Perfusion of hands returns to preinterventional level. (Images courtesy K. Agarwal.)

the effect is most likely sustained by the sympathetic nervous system. Figure 11.7 presents IR images following 10 days of infusion treatment with local anesthetics: facial blood flow is augmented all over, whereas the perfusion of the hands has returned to the preinterventional level. The patient was still feeling well 15 months after the treatment.

11.1.3
Acupuncture

Acupuncture is an ancient Chinese approach to treating various kinds of diseases. In Western societies, where it is considered to be a nontraditional approach, it has been particularly adapted to the treatment of pain. Recently it has been increasingly applied in therapeutic concepts for treating multiple illnesses, especially because of the growing demand by patients themselves, who believe this treatment to be less harmful and a "softer" method than Western medicine, avoiding the chemicals contained in regular medication and pills. The demand for acupuncture has also grown in cases where Western medicine may not offer a solution, for example, if no morphologic correlates can be found in laboratory specimens or other diagnostic procedures like imaging techniques.

The most important effective structural elements of acupuncture are acupoints. According to traditional Chinese medicine (TCM), their distribution defines the system of channels, also called *meridians*, through which *qi* flows. No generally accepted proof for meridians has so far been given. There is no exact translation for *qi* into a term recognized by Western medicine, though it is often referred to as "vital energy." In acupuncture, needles are inserted into acupoints. In this case, patients often indicate feeling a strange sensation that may include a feeling of warmth, cold, strong emotions, or relaxation referred to as the *deqi sensation*. So far, scientists have not been able to attribute this feeling to a specific bodily reaction, and so far no scientific proof for the efficacy of acupuncture has been found. Several theories of why and how acupuncture might work have been put forth.

Because of a lack of scientific evidence, conventional medicine often does not accept or believe in symptom alleviation by acupuncture. Recent research revealed that at least at the *Hegu* point, a specific effect occurs: needling of this acupoint results in a massive increase in skin temperature, whereas needling of the skin or muscle (so-called sham needling or false needling) or no needling leads to a decrease (Figure 11.8). The study was performed with 50 healthy volunteers as a randomized single-blinded placebo-controlled crossover clinical trial [15].

The visualization of acupoint distributions as well as the course of the meridians by measuring the skin surface temperatures has aroused controversy. Because meridian-like structures could be located by some researchers, others claimed that inferior techniques would produce these phenomena. Litscher [16] could not visualize structures based on meridians as described in TCM. With the aid of various IR cameras with diverging properties like resolution and with different methods of stimulation (e.g., Moxibustion, acupuncture, LASER), they were clearly able to objectively quantify technical reflection artifacts from the moxa-cigar on the skin of healthy probands that appeared to be meridian-like at first

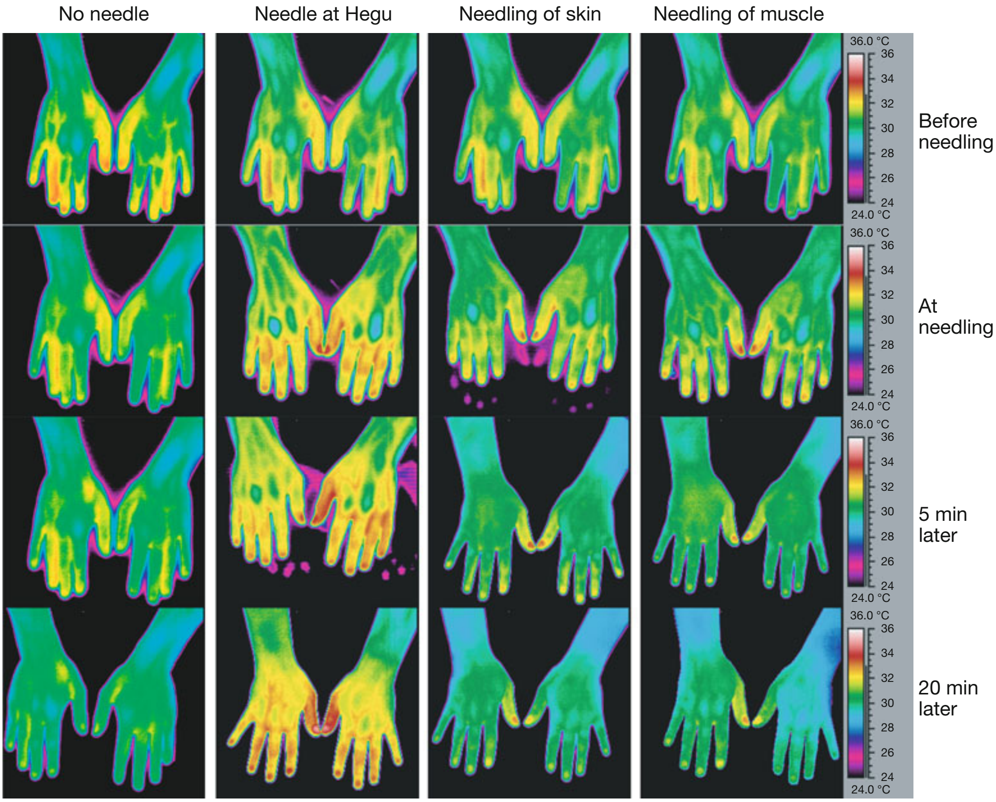

Figure 11.8 Thermograms of hands before, during, and after needling at the *Hegu* point, the skin, and muscle. (Images courtesy K. Agarwal.)

sight. No thermal reflection phenomena were present, and no meridians could be detected as soon as stimulation without heat was applied. Other authors describe channel-like pathways not known to TCM. Considering all the facts discovered so far, clearly an underlying anomalous dispersion must be insinuated.

11.1.4
Breast Thermography and Detection of Breast Cancer

Because of its noninvasive, nonradiating, and passive nature, IR thermal imaging is becoming more accepted in the early detection of anomalies of the breast. Usually, clinical breast exams, mammograms, and ultrasound are utilized in diagnosing pathologies of the breast. Although conventional breast-imaging techniques routinely include mammography and ultrasound, growing interest in other approaches has drawn increasing attention to exploiting the anatomical and physiological basis for understanding breast cancer. With the aid of thermography, tumors in the breast are to be identified due to elevated surface temperature caused by the increased blood flow as a response to augmented cellular activity.

In detail, breast thermography is based on the premise that before abnormal cells can grow, a constant blood supply must be circulated to the growth area. Thermography measures the breast surface temperatures and, hence, the heat generated by the microcirculation of blood in the breast during this process.

The chemical and blood vessel activity in both precancerous tissue and the area surrounding a developing breast cancer is almost always higher than in the normal breast [17–19]. Since cancerous masses are highly metabolic tissues, they need an abundant supply of nutrients to maintain their growth, which is achieved by increasing blood supply to their cells. The resulting increase in regional surface temperatures of the breast can be detected with IR breast imaging.

In 1956, thermography was introduced into screening but was abandoned 20 years later because it was not on par with previously mentioned methods, though no single tool provides excellent sensitivity and specificity. In the United States, breast thermography was later approved by the Food and Drug Administration in 1982 as an adjunctive diagnostic screening procedure for the detection of breast cancer. Protocols have also been standardized concerning patient preparation, image collection, and reporting [18].

Being a passive procedure, thermography application, especially in younger men and women, is favored because cumulating hazardous effects of radiation might be minimized. An assemblage that incorporates thermography might enhance accuracy. It is desirable to develop new approaches including regression analysis, highly precise diagnosis using thermography techniques, and high-resolution digital camera systems [20]. In the past few years, many studies on breast thermography have been reported not only in the medical but also in the IR community [17–19, 21–23].

Figure 11.9 shows two examples of IR images of two high-risk patients. Such images are evaluated following standard procedures that include analyzing the symmetry of thermal patterns between breasts, the consistency of thermal pat-

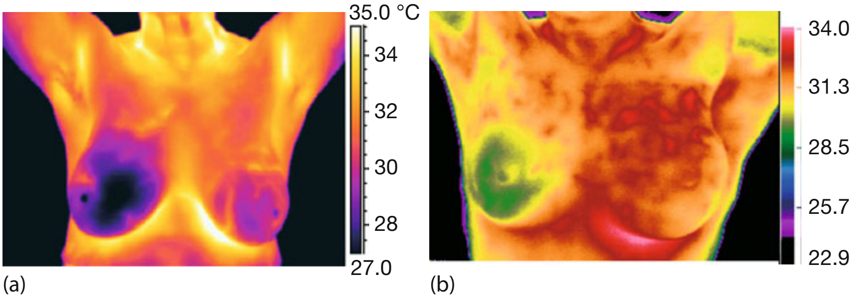

Figure 11.9 Two IR images of breast screens following standard procedures. (a) Temperature differences of around 2 K suggest additional diagnostic tools and closer observation. In this case, the mammogram was negative. (b) Example of thermogram of patient with regular negative annual mammography examination. Reexamination after this high-risk thermography finding confirmed breast cancer, which led to the mastectomy of the left breast. (Images courtesy A. Mostovoy.)

terns with normal anatomy, and the quantitative temperature differences between breasts [18]. In Figure 11.9, both patients show temperature anomalies in the range of 2 K or higher. All images are analyzed using specialized software, and the images of the breasts are grouped in five risk categories from TH-1 to TH-5, with TH-1 indicating the lowest possible risk of developing breast disease and TH-5 the highest risk. Any abnormal thermographic scan result of the breast clearly demonstrates abnormal areas of heat. This should be considered an alert that something might be wrong with the physiology of the breast. It could be an infection, inflammatory disease, trauma, or cancer.

As a consequence, thermal imaging is definitely not a standalone screening examination. It is simply a method to detect physiological changes associated with the presence or increased risk for the development of breast cancer. Breast thermography has been studied for over 60 years, and over 800 peer-reviewed breast thermography studies have been published. In the Index Medicus database, well over 250 000 women have been included as study participants. As a result, breast thermography has an average sensitivity and specificity of 90% [18].

11.1.5
Other Medical Applications

11.1.5.1 Raynaud's Phenomenon

In Raynaud's phenomenon, episodic, long-lasting recurrent vasospasms occur primarily in the extremities in response to cold or emotional stress, though other acral parts, such as the ears, chin, nose, nipples, and tongue, may be affected, too. Patients experience reversible discomfort and color changes (pallor, cyanosis, and erythema). The disease is common in cold climates. Young women are more often affected than other groups. Pathophysiology may result from an exaggerated α_2-adrenergic response, triggering vasospasms. Sometimes an association with rheumatic conditions can be recognized. IR thermography may reveal clinically

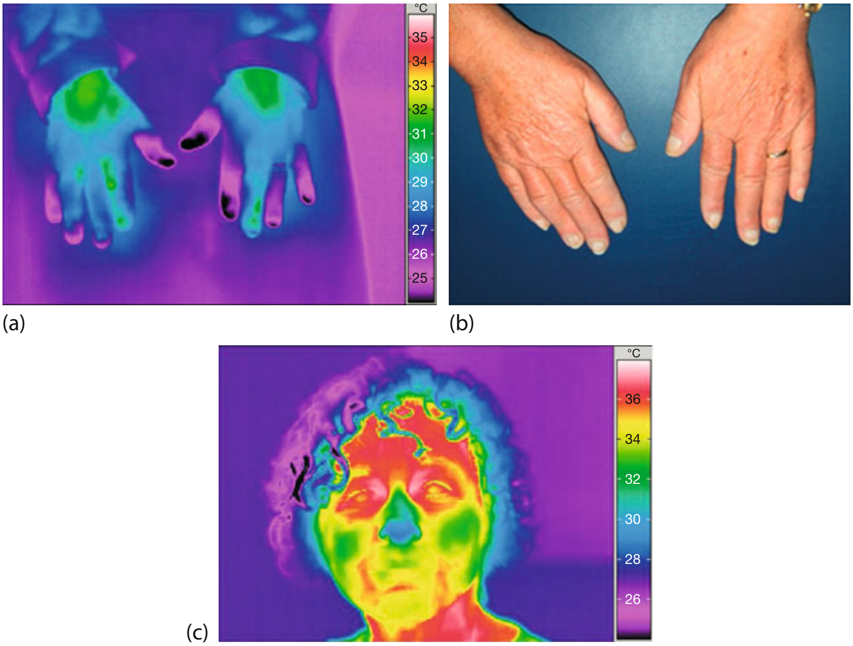

(a) (b) (c)

Figure 11.10 Thermogram of hands (a) and face (c) in Raynaud's phenomenon; note that clinically no pathology was found in the VIS picture (b) of the hands. In the IR image of the face, however, a markedly reduced temperature ($\Delta T = 7.6$ K) of the nose is evident. (Images courtesy K. Agarwal.)

undiagnosed Raynaud's syndromes, in particular if the skin sometimes looks normal upon inspection, though patients report pain or paresthesias (Figure 11.10).

11.1.5.2 **Pressure Ulcers**

Pressure ulcers (bedsores, decubiti) occur as tissue is compressed between bony prominences and a solid underground, leading to skin defects ranging from simple erythema to skin loss with extensive soft-tissue necrosis. Older patients or people suffering from impaired circulation, immobilization, malnutrition, and incontinence are prone to this complication, and bacterial superinfection is a serious risk. The clinical appearance of a lesion usually suffices to diagnose an ulcer, though depth and extent may be difficult to verify. Constant and repetitive assessment is compulsory for successful management of the disease. Serial photographs, that is, conventional pictures as well as IR images, aid in documenting the course of healing (Figure 11.11).

Several other successful medical thermography applications have been reported. As examples, we mention, first, evaluating the coronary flow during a myocardium revascularization operation [24], second, using IR imaging as a tool in medical emergencies to quickly gain triage information, that is, help to decide which victims, for example, of car accidents need help first [25], and third, the development of new expanded medical imaging by registering and merging 2D IR imagery with 3D MRI techniques [26].

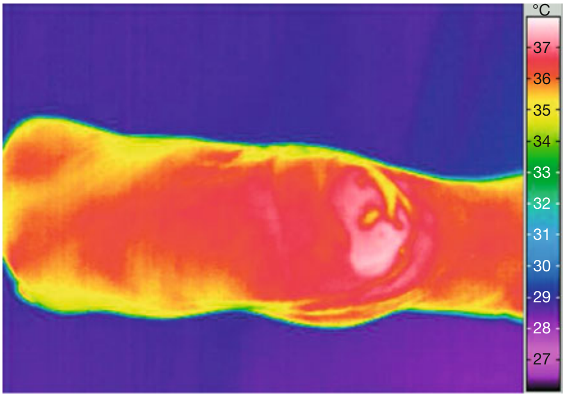

Figure 11.11 Pressure ulcer on right heel. (Image courtesy K. Agarwal.)

Finally, new medical applications of IR cameras are sometimes also due to topical issues. One example is the outbreak of severe acute respiratory syndrome (SARS) some years ago. In 2003, the SARS outbreak resulted in 813 deaths worldwide in half a year, with 8437 people officially reported as being infected [27]. SARS is transmitted by respiratory droplets or by contact with respiratory secretions of patients. It can spread very rapidly through public transport such as trains and airplanes. Therefore, soon after the outbreak, authorities arranged for screening procedures of travelers, looking for fever symptoms [28]. The goal was to prevent spreading of the disease by identifying the few infected people with fever out of thousands without fever by screening, for example, the large number of passengers arriving at airports from abroad. Because of the large numbers, traditional oral thermometers or spot IR thermometers were not practicable. Rather, IR imaging systems were used [27, 28] to find potentially febrile individuals. Because of the political pressure to stop a developing pandemic, large numbers of IR camera systems and IR spot pyrometers were needed, which provided a momentary stimulus to the industry. Finally, we mention that there are additional medical applications of near-IR (NIR) imaging (e.g., finding blood vessels below the skin in infants; see Section 6.3.3.9).

11.2
Animals and Veterinary Applications

Animals like humans vary in response to painful changes, be it illness or injury, in their bodies. Most often, increased or decreased blood flow to the related body regions leads to temperature changes from normal. Therefore, many diseases or structural changes due to injuries can be seen indirectly via thermal anomalies or asymmetries on the animal surface. The important issue is that the body of an animal – even if not showing acute signs of pain – usually develops a thermal signature or asymmetry, and often such temperature changes are the first indication of a problem. Thermal imaging is the proper tool to identify changes in heat patterns, and this information can be used in diagnosis [29, 30].

Consider, for example, horses experiencing pain in a leg: some become obviously lame, some may experience minor changes, but in any case significant methods of examination are required to detect the cause of the change. In contrast, other horses will mask their pain and show no visible obvious change in their gait [31]. In the latter case, IR cameras are valuable tools for evaluating and detecting such lameness issues, which otherwise could take up to 2 weeks before showing up with obvious signs. If used in conjunction with the evaluation of a veterinarian, thermal imaging makes it possible to make immediate changes, possibly preventing disastrous effects for the animal.

However, whenever thermography is used for veterinary purposes, it must be kept in mind that the method should usually be combined with other examination methods like X-ray scans, if needed. When thermal anomalies are detected, additional methods, such as X-ray, CT scan, or MRI, should be applied as well, and the information from methods should be combined for a diagnosis.

Consider, for example, X-rays: they are helpful in identifying bone changes and some changes in soft tissue, but they do not have the capability to evaluate soft tissue changes to the extent that thermal imaging does. Thermal imaging shows physiological changes such as increased or decreased blood circulation, lack of or diminished nerve function, and swelling. It can therefore give additional information that complements other examination techniques. Since it is a noninvasive technique, it has the additional advantage that it reduces stress in the owner and the animal.

Nowadays, animal IR imaging may be divided into thermography of either pets and zoo animals on the one hand and wildlife on the other. From an economic point of view the distinction would be more between equine thermography and studies of other animals. This is most probably due to the fact that horses are quite expensive animals, especially those used in sports. Therefore, owners are willing and able to invest much more money in the animals' welfare than is usually the case for other animals. Nevertheless, there has been an enormous increase in thermal imaging applications for all kinds of animals lately (e.g., [32–36]).

11.2.1
Pets

Most owners of IR cameras have probably recorded some images of animals – mostly their own pets when they are in good health (Figure 11.12). Such IR images have no relation to veterinary applications. They are usually fun to look at, but they may also point out differences between various animals, for example, in body temperatures or thermal insulation due to fur or bare skin, and so on. For example, cats' noses are usually the point of lowest temperature owing to evaporation, while eye and ear holes are the warmest regions. After being outside in the cold, the fur serves an insulating function quite well and quickly warms up the cat when it first enters the house again, though the paws can stay cold for quite a while.

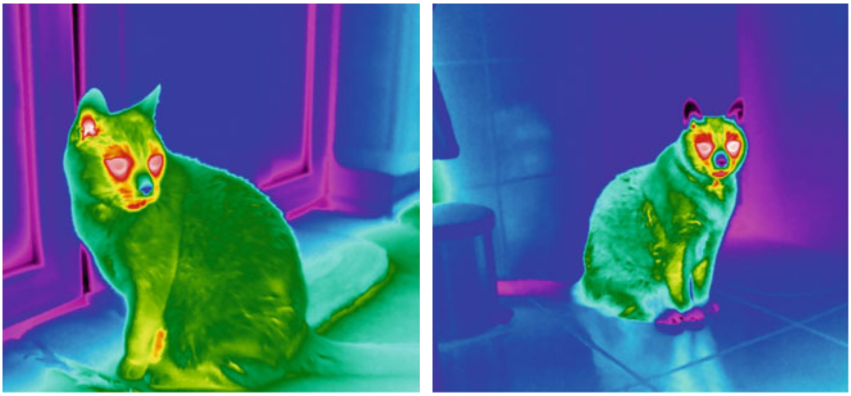
(a) (b)

Figure 11.12 (a) IR images of a cat inside a house (21 °C) or (b) after being outside for a while at air temperatures below 5 °C.

Figure 11.12a also shows the frame of a glass door to the patio with the usual characteristic geometrical thermal bridge features, and Figure 11.12b shows the cat's reflection from the ceramic tiles of a bathroom.

Of course, regular observations of one's pet can also help to detect illnesses or injuries since a comparison with "healthy" IR images will reveal thermal anomalies or asymmetries. In this respect, the pets of thermographers could very well receive the best possible benefit from thermal veterinary imaging. The following examples discuss some cases of zoo animals where thermography proved to be a versatile and successful diagnostic tool.

11.2.2
Zoo Animals

Many major cities around the world have zoos with a large variety of animals in captivity. Obviously, veterinary care for zoo animals is a primary concern, and thermography has proven to be a valuable tool in diagnosis, documentation, and monitoring in particular for very large animals such as elephants or camels [37, 38].

Figure 11.13 shows an example of IR images of two giraffes [31]. The front giraffe (Figure 11.13a) had a known injury to the left rear leg. The IR image clearly shows a thermal anomaly in the form of lower temperature compared to the other legs. This is due to a lack of blood circulation in the leg.

Figure 11.14a shows a northern white rhinoceros, an extremely rare and endangered species, in the San Diego zoo that was behaving strangely. IR imaging could clearly identify some abscesses (Figure 11.14c) and demonstrated the complex blood circulation in the animal's head and the temperature gradient on the horn (Figure 11.14b). Unfortunately, this rhino died later and at present, only a few white rhinos are known worldwide, living in a conservancy in Kenya.

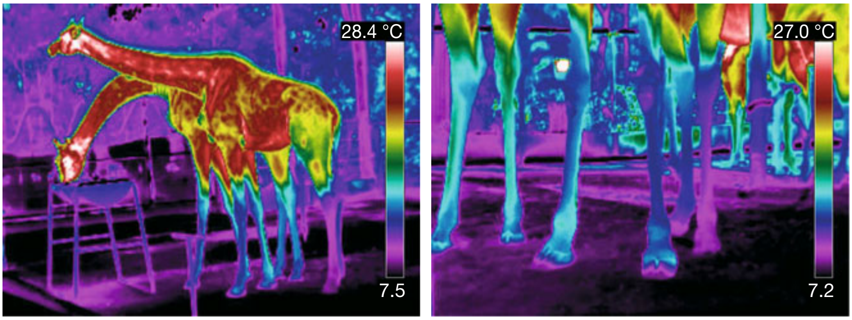

(a) (b)

Figure 11.13 (a) IR images of giraffes, one of them having a known injury in the left rear leg. (b) The dark blue-purple color in the leg and the purple-lavender in the foot indicate lower temperatures due to a lack of circulation or nerve conduction. (Images courtesy of Peter Hopkins, United Infrared, Inc. [39].)

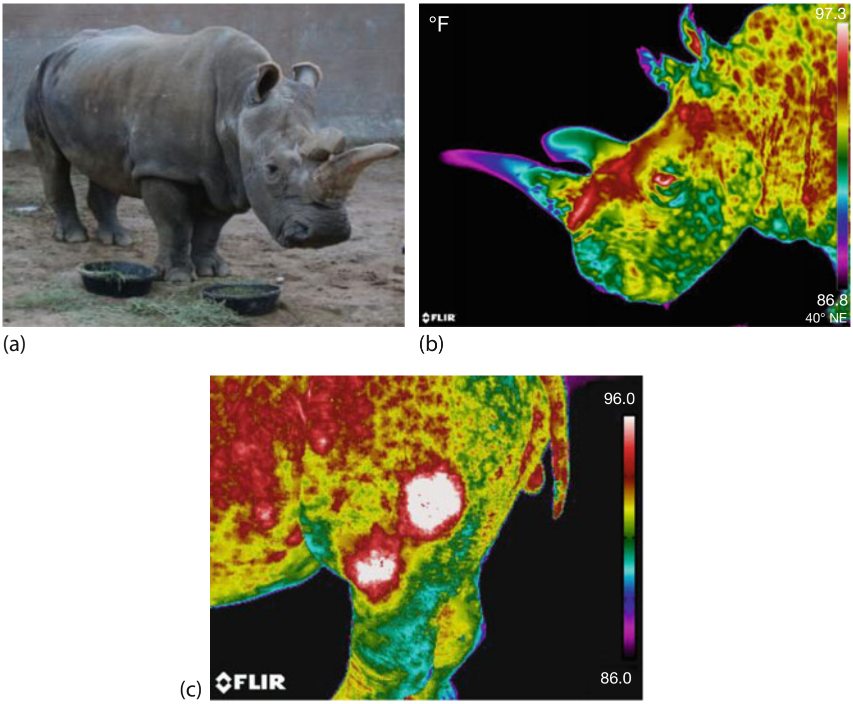

(a) (b)

(c)

Figure 11.14 VIS (a) and IR (b) images of a northern white rhino in a zoo. IR imaging was used to identify abscesses (c). Temperature scales are in Fahrenheit. (Images courtesy Peter Hopkins, United Infrared, Inc. [39].)

11.2.3
Equine Thermography

Equine thermography was one of the first applications of thermography to animals and is currently a fast growing field of veterinary applications of IR imaging [31]. It is extremely useful in the study of thermal asymmetries. As an example, Figure 11.15 shows a routine scan done on a racehorse scheduled to leave for the track 7 days after the recording. The IR scan identified an abnormal hot spot that was confirmed later as a fracture in the cannon bone. In addition, the rear leg hoof temperature was cooler. This was a consequence of the horse shifting its weight because of the previously unknown injury.

Another example is shown in Figure 11.16. The IR images of the horse were recorded after an emergency evacuation took place during a barn fire. The be-

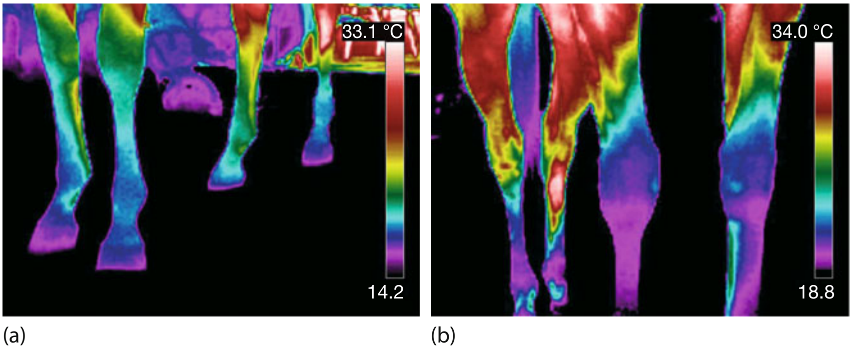

(a) (b)

Figure 11.15 Routine scans of racehorses. (a) Abnormal hot spot in leg (second leg from left) later confirmed as fracture of cannon bone. (b) The lower temperature of the left rear leg hoof (first leg from right) indicated shifting weights owing to the cannon bone injury. (Image courtesy Peter Hopkins, United Infrared, Inc. [39].)

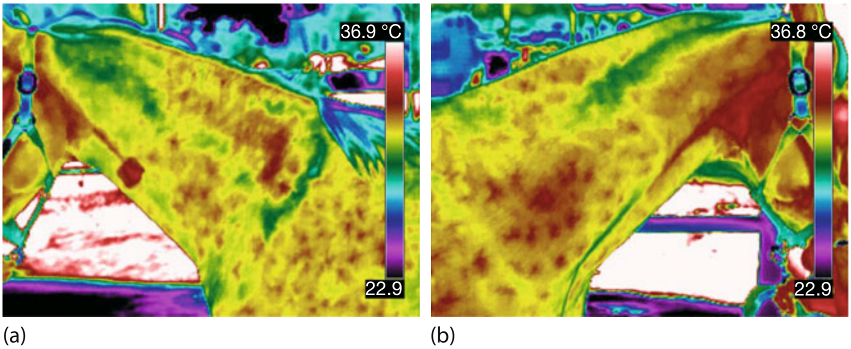

(a) (b)

Figure 11.16 Scans of left (a) and right (b) sides of neck of a horse indicated a thermal asymmetry, which was later confirmed as lower cervical neck injury (C6/7 fracture). (Image courtesy Peter Hopkins, United Infrared, Inc. [39].)

havior of the horse changed after the incident, and it was suspected that an injury may have occurred during the evacuation. The thermal scan shows an asymmetry in the neck, possibly indicating a lower cervical neck injury. Later it was confirmed via a radiograph that a C6/7 fracture had in fact occurred.

Thermography is also used to detect laminitis, one of the most serious horse diseases [40].

11.2.4
Wildlife

A variety of other animals have been studied using thermography. The examples range from nice shots of animals still living in their natural environment, for example, whales, elephants, leopards, or seals [41, 42], to purposeful studies like rescue, recovery, and rehabitation of birds following oil spills [43]. The detection of birds [44] or bats in flight [45] can raise some important question about the time response of detectors (Chapter 2). Slow cameras with microbolometer detectors usually show streaks behind flying birds. Of course, these must not be interpreted as air warmed as the bird was flying by. Rather, they represent the effect of detector integration time (Section 2.5.5). An example of a flying bird (a hummingbird) is shown in Figure 11.17. Hummingbirds can practically stay in midair while rapidly flapping their wings in order to get access to nectar in flowers. Because of the rapid wing movements, images must be recorded with high-speed cameras.

Another typical veterinary application is in the dairy and poultry industry [38]. For example, it has been demonstrated that IR imaging can be used as an early identifier of bovine respiratory disease in bison or in the detection of mastitis in dairy cows. In the poultry industry, thermography has also been used to study the feather cover, which in itself is an important factor determining animal welfare.

Another important application of animal thermography in certain parts of the world is the field of termite and pest detection [46, 47]. For example, termites do more damage in the United States each year than fires and storms combined [47]. The most destructive termite species in the world is the Formosan subterranean termite because they can secrete an acid that dissolves, for example, concrete, steel, lead, copper, glass, and wood. One colony can consume more than 1 kg of

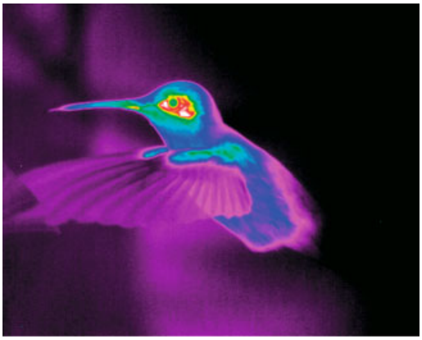

Figure 11.17 A hummingbird in flight, recorded with a MW camera at a rate of 430 frames/s. (Image courtesy A. Richards, FLIR systems Inc.)

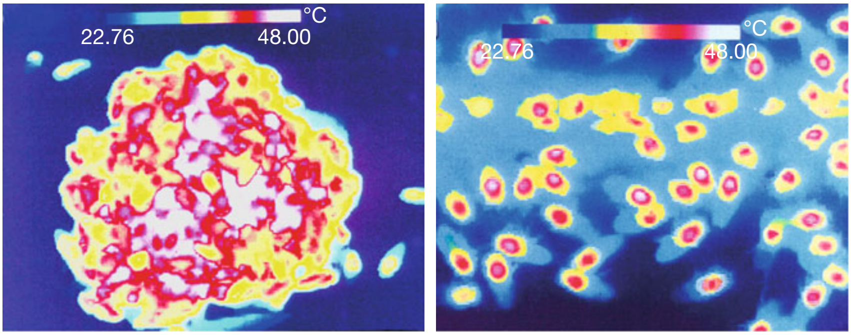

(a) (b)

Figure 11.18 Hot defensive ball consisting of many bees, raising the inside temperature to about 47 °C (a) and individual defender bees crawling around the nest entrance. Their thoracic temperature is already elevated (b). (Images courtesy M. Ono, Tokyo.)

wood per day, which means that wooden homes can be destroyed very fast when infected. If moisture sources are available within the structure, nests are built above ground somewhere in walls. This is where thermography comes in. Termites create irregular heat patterns due to two facts. On the one hand, the mud tubes they construct have high moisture content, and IR imaging techniques to detect moisture can be applied. On the other hand, heat is released from the digestive system of the termites in the form of CO_2. This leads to thermal changes on the surfaces of walls, ceilings, and floors, creating irregular temperature patterns that can be detected with IR imaging.

Another fascinating example of insect temperature study using thermography was reported recently [48]. The Japanese giant hornet is a predator of bees and wasps, and often several hornets join forces for a mass attack of a bee nest. Unlike European honey bees, Japanese honeybees have developed an ingenious strategy to respond to a hornet attack. Since individual counterattacks are useless, they use heat produced by a large group of bees to kill hornets that try to enter the nest. If warned of an attack, typically many worker bees wait inside the entrance, and once a hornet tries to enter, it is quickly engulfed within a ball of about 500 workers. Whereas the temperature of a typical worker without defending is about 35 °C, the temperature within the ball quickly rises to 47 °C (Figure 11.18). This temperature is lethal to the hornet (the upper lethal temperature of Japanese hornets is 44–46 °C) but not to the bees (the upper lethal temperature of Japanese honeybees is 48–50 °C).

Besides bees' reactions to attacks, bee populations themselves may also be studied with IR imaging as noninvasive method. The information thus obtained is important not only for understanding natural behavior in agricultural pollination and honey production, but also for other uses of bees, for example, in detecting land mines or explosives [49]. Figure 11.19 shows an IR image of six beehives. The color bar indicates radiance ($W\,m^{-2}\,sr^{-1}$) and corresponds to temperatures between −12 and 0 °C.

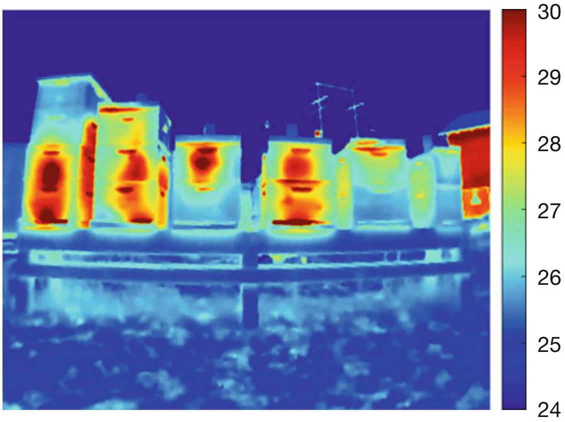

Figure 11.19 LW image of six beehives, with color bar calibrated in radiance (W m^{-2} sr^{-1}). The scale corresponds to temperatures of −12 to 0 °C; the air temperature was around −4 °C. Camera with 324 × 256 pixels, distance 3–4 m. Image courtesy Joe Shaw, Montana State University, Bozeman, Montana.

The idea is to use radiometrically calibrated camera signals from the exterior of the hive and relate it to the number of frames that are populated by bees inside each hive. The best results are obtained just before sunrise, when there is maximum thermal contrast between the hive and the background. After sunrise, the onset of solar heating rapidly obscures the thermal structure of the hive's interior. The hive population is estimated from a count of pixels that have a radiance greater than a predefined value. The connection to the actual population only requires a single initial manual inspection in order to enable a unique relation between hive, camera, and population. The subsequent noninvasive method allows rapid estimations of the population without further opening of the hive, which would disturb the bees and endanger the queen.

Finally, IR imaging is also becoming much more popular for wild carnivores, such as bears, mountain lions, and wolves. The well-known wildlife photographer Casey Anderson has provided fascinating footage [50–52] and (probably) the very first close-up IR images of a grizzly bear. As an example, Figure 11.20 depicts Brutus the Grizzly bear, who was born in captivity and was kind of adopted by Anderson while still a cub.

The image nicely demonstrates how IR imaging can be used in the wilderness. Bears, mountain lions, and other carnivores are warm-blooded animals with body temperatures typically well above 35 °C. When they are outside in the cold, their fur serves as thermal insulation. Still, they can usually be detected easily against the colder background. Often, wild animals being observed at night anticipate that people close by are not able to detect them and may therefore still behave quite naturally. This allows for spectacular observations when filming with infrared cameras [52].

Figure 11.20 Brutus the grizzly bear. (Image courtesy Casey Anderson, Vision Hawk Films.)

11.3
Sports

In sports, many processes involve heat transfer. Quite often, these processes are also fast and require high-speed data acquisition. Examples include all kinds of game activities that involve balls that are hit by a racket (e.g., tennis, squash), with the hands (e.g., Volleyball) or feet (soccer), or by something else (e.g., billiards). For these activities, IR thermal imaging may record the temperature changes following inelastic collision processes. The corresponding information may have varied uses, depending on the sport. For example, one can directly determine whether a tennis serve has landed in the service box or gone out. In what follows, first a number of applications involving inelastic collisions and frictional forces are presented. Then other potential benefits from IR imaging in sports are discussed.

11.3.1
High-Speed Recording of Tennis Serve

An introduction to the collision of a tennis ball with the court was already briefly discussed in Section 5.2.4. Here, we discuss the problem in more detail. Modern tennis balls are pressurized rubber balls covered with felt. They have masses of around 57–58 g and diameters of about 6.7 cm. They are quite elastic, and new balls are required to bounce back to a height of at least 1.35 m when dropped from a height of 2.5 m. Energy conservation requires that all of the initial potential energy of the ball be transformed into other kinds of energy. Just before hitting the floor, a dropped ball has a maximum of kinetic energy, which is about as large as the initial potential energy (friction due to the surrounding air is negligible at these slow speeds). The bouncing back, however, starts with less kinetic energy, which is why, later on, the ball comes to a stop at a lower height (at least 54% of the original height for a new ball). The difference in energy before and after the collision is due to the deformation of the ball upon hitting the floor. Thus, part of the kinetic energy is transformed into deformation energy. Because the deformation is not

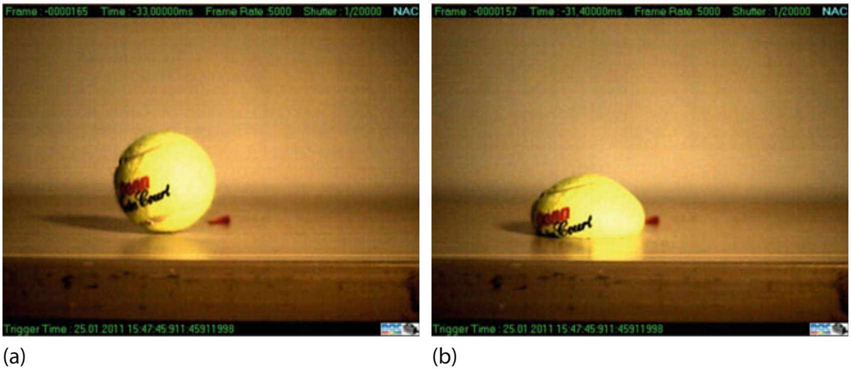
Frame : -0000165 Time : -33.00000ms Frame Rate 5000 Shutter : 1/20000 NAC
Trigger Time : 25.01.2011 15:47:45.911:45911998
Frame : -0000157 Time : -31.40000ms Frame Rate 5000 Shutter : 1/20000 NAC
Trigger Time : 25.01.2011 15:47:45.911:45911998
(a) (b)

Figure 11.21 Visual high-speed camera images of a tennis ball hitting the floor at a speed of about 77 km h^{-1}.

purely elastic, a part of this energy is converted into thermal energy, that is, ball and floor are heated up a little bit. Energy conservation, thus, means that potential energy is converted into the sum of kinetic energy and thermal energy.

The resulting temperature increase is quite small when a ball is dropped from a height of just 2.5 m. However, the serves of the top 10 tennis players can reach speeds of around 250 km h^{-1} (around 70 m/s). If a tennis ball traveling at this speed hits the court surface (whether grass or artificial), the inelastic collision will lead to an enormous deformation of the tennis ball. Figure 11.21 displays a visual image of a tennis ball first before and then while hitting the floor at a speed of only about 77 km h^{-1}. During the inelastic collision, upon hitting the floor the ball is compressed significantly to about half its original volume during the contact time of $\approx$ 4 ms with the floor [53]. After hitting the floor, the velocity of the bouncing ball drops by about a factor of 2.

This difference in the kinetic energies of the ball before and after the collision is converted into thermal energy, that is, one may expect both the ball and the floor to heat up. Figure 11.22 shows two thermal images recorded with a LW IR microbolometer camera operated at a 30 Hz frame rate [54]. The first image depicts the situation right after the ball has hit the court. Since the ball was going too fast, it just left a comet-like streak behind, similar to the examples of the falling balls discussed in Section 2.5.5. If the ball at an initial speed of 77 km h^{-1} had converted 40% of its kinetic energy into thermal energy, it would have left the image field of view (FOV) within 25 ms after making contact with the court, which roughly equals the 33 ms of the frame rate, that is, the ball would only be observable in at most 2 subsequent images recorded at this frame rate.

With these images it is not possible to quantitatively analyze the whole collision process, since first only the heating up of the floor is recorded while the ball itself has left the scene at an undefined temperature. Second, the heating is a transient phenomenon that depends on heat conduction within the ball and the court as well as on the respective heat capacities. However, it is possible to at least analyze the court surface heating as a function of time. Figure 11.22c shows the maximum

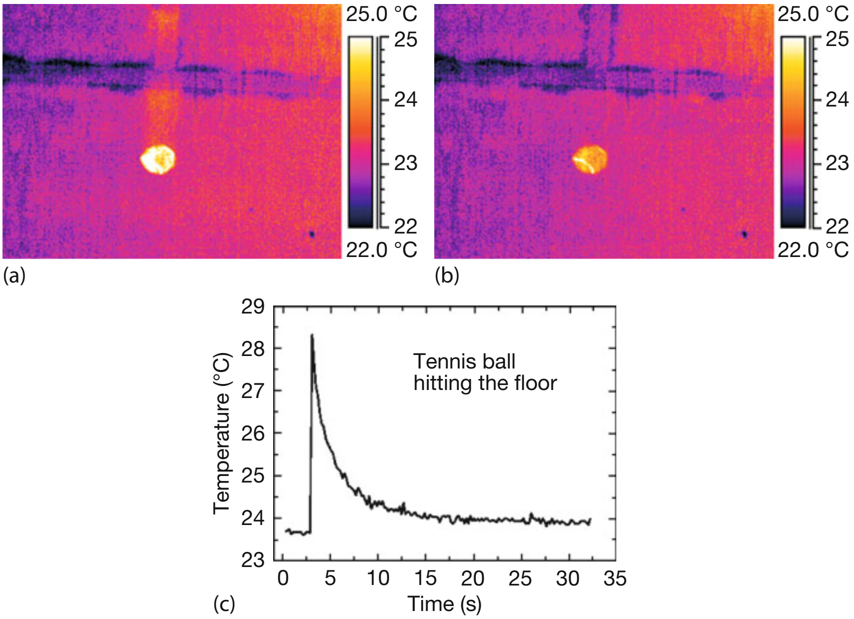

Figure 11.22 Tennis ball recorded with SC2000, 30 Hz. (a) First image after ball hits court, (b) 1.7 s after ball has hit court, and (c) measured surface temperature of contact spot on court as function of time.

temperature of the hot spot on the court as a function of time. The initial temperature rise in this case was about 5 K and the time constant was several seconds. Top players can easily reach ΔT values of 10–15 K, with an easy-to-observe signal for more than a minute. Therefore, the IR detection of the collision of a ball with the floor is easily detected, which means that it can in principle be used to determine the location of the serve in the opponent's court. This idea was tested more than 20 years ago at the ATP finals 1996 in Hannover, Germany. The side lines of the court in our experiment were just roughly marked with white chalk on a carpet, which yielded only a slight emissivity difference. On a real tennis court, the lines can be made visible using the large emissivity contrast of court and metals by having thin metal threads woven into the line material. Unfortunately, the method, though available as instant replay in near real time, was not chosen as an aid for referees in tennis – probably because of the costs of using several IR cameras.

Figure 11.22b shows the IR image about 1.7 s after making contact with the court. It nicely demonstrates the different thermal properties of the fuzz-covered area and the rubber lines on the tennis ball surface. On the one hand, the smooth surface of the rubber lines allowed for a much better thermal heat transfer; on the other hand, the thermal diffusion was also larger. As a result, the rubber lines achieved a higher temperature than the rest of the ball.

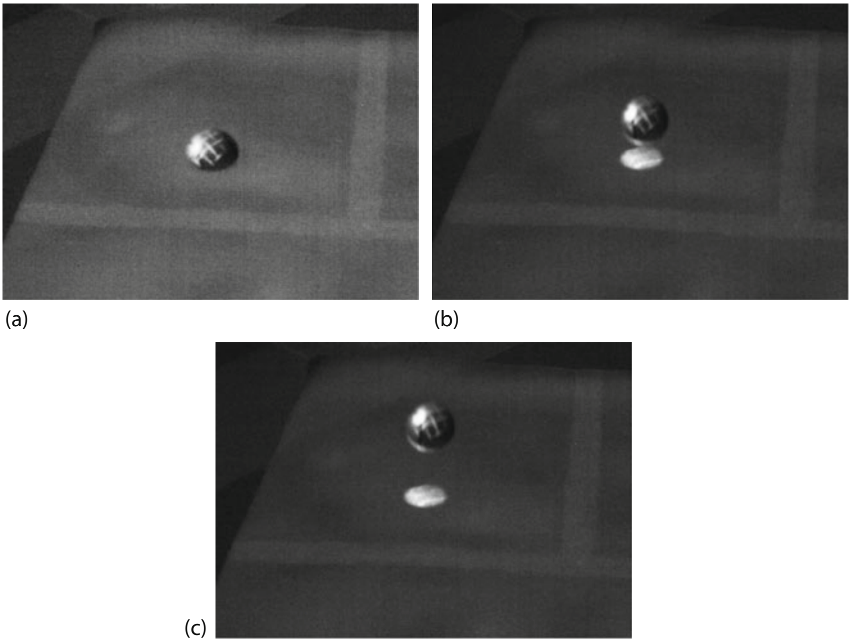

Figure 11.23 IR images of tennis ball while hitting court (a) and while bouncing up again (b,c) recorded at a frame rate of 400 Hz and integration time of 0.75 ms. The position on the ball that was hit by the racket, in particular the heated lines from contact with the string grid made of nylon or polyester synthetic materials, is clearly seen. During the rebound of the ball (b,c), the warming of the contact spot on the floor becomes visible.

To also observe the tennis ball itself, a high-speed IR camera (SC6000) was used to observe the collision. Figure 11.23 depicts three images of a slightly slower ball recorded at a frame rate of 400 Hz and an integration time of 0.75 ms. Because of the short integration time, more or less sharp and focused images result [55]. The first image represents the maximum deformation of the ball. On its upper surface, one can still see the structure of the string grid with which it was hit by the racket. The second and third images show the situation after collision with the floor. Now the floor has also heated up. One may even observe a slight rotation of the tennis ball in the thermal image. On the one hand, such experiments directly visualize the kinematics of inelastic collision processes; on the other hand, they make it possible to study the energetics involved.

11.3.2
Squash and Volleyball

Like tennis, squash consists of a repetition of inelastic collisions of a ball with walls and rackets. Squash balls consist of small rubberlike balls a few centimeters in diameter and filled with air. When dropped from a height of 1 m, they do not bounce very well, meaning they are quite inelastic. The near permanent collisions during

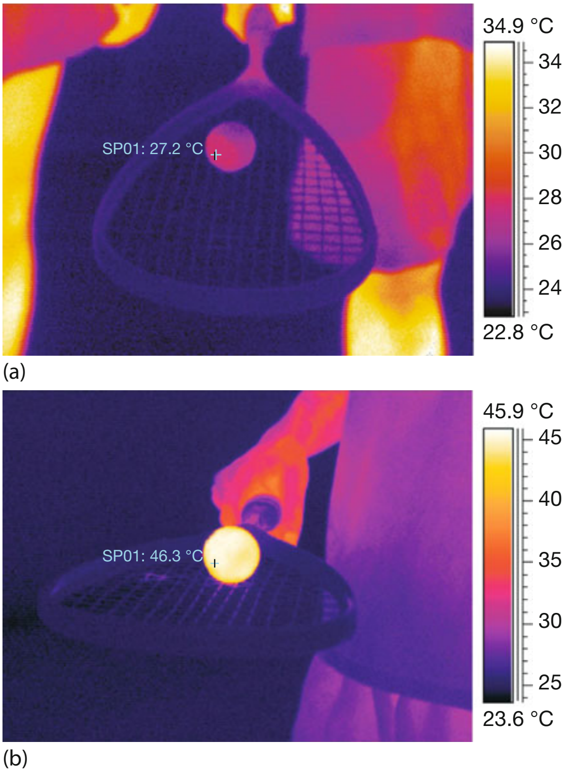

Figure 11.24 The temperature of a squash ball increases by about 20 °C after playing for several minutes.

a game will obviously lead to heating of the ball. Assuming steady-state conditions, that is, hitting the ball at a given frequency with similar strength each time, will lead to a dynamic equilibrium of heat transfer to the ball due to the inelastic collision processes and heat transfer from the ball due to convection and radiation and to a small extent also conduction to the walls during the short contact times. Figure 11.24 shows a squash ball before starting to play and after a few minutes of play. The ball temperature has risen by about 20 °C, and the ball is nearly homogeneously heated across its entire surface.

Volleyballs have a diameter of about 21 cm and a mass of typically 270 g. Several types of inelastic collisions are observable in volleyball games, for example, when serving the ball or spiking with one hand, when defending with both arms, or as the ball hits the floor. In a spike, the hand hits the ball and deforms it, which already leads to heating of the ball. Second, when a spiked ball (at velocities of up to $30\,\mathrm{m\,s^{-1}}$) hits the floor, that also leads to heating of the floor, much like with a tennis ball.

The available kinetic energy of a volleyball is similar to that of a tennis ball: the mass is about a factor of 4 higher, whereas the maximum velocity is about a

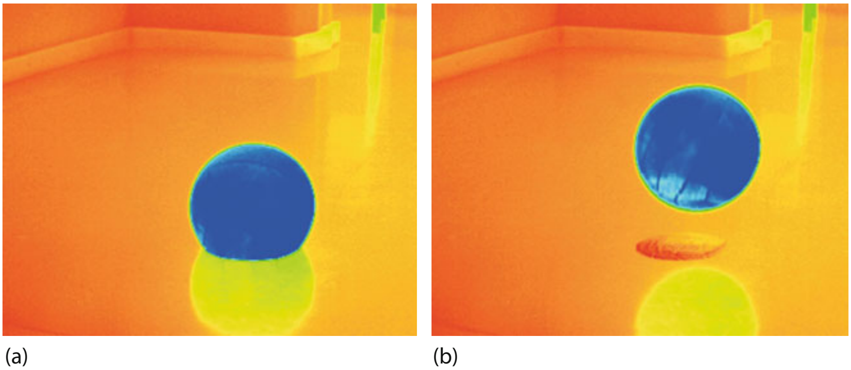

Figure 11.25 Two snapshots of a volleyball hitting the floor. Upon impact it is deformed appreciably, which leads to a temperature increase of floor and ball. In addition, thermal reflections of the previously frosted ball can be seen.

factor of 2 lower. Hence, we may assume a similar amount of energy can be transferred to heat the ball and the floor. However, because of its much larger diameter, the contact area of a volleyball with the floor is much larger, so the thermal energy is transferred to a larger area. Overall, a smaller temperature rise is to be expected. Figure 11.25 shows the results of a ball hitting the floor at high speed, again recorded with the high-speed IR camera SC6000. Like the tennis ball, the floor heats up appreciably and one may even see the geometrical structure of the ball surface on the floor owing to the different heat transfer rates.

11.3.3
Other Applications in Sports

There are many more IR imaging applications related to sports [56–61]. For example, sneakers have been tested using thermography, or sports injuries, which result in thermal asymmetries or anomalies, may be studied. Here, one more example dealing with the study of heat-loss patterns in athletes is discussed briefly [56]. During exercise and any kind of athletic activity, working muscles produce heat, that is, the body temperature increases. This heating up is counteracted by various thermoregulatory mechanisms, all of which dissipate the excess heat to the external environment. Two mechanisms are particularly important: first, sweating by cooling via the heat of vaporization and, second, direct radiative cooling from the body surface to the environment. These cooling mechanisms are essential for athletes to avoid heat illness, which may lead to decreased performance or, in the worst case, to severe injuries or even death. In the period between 1995 and 2008, 33 high school, college, and professional football player fatalities were attributed to heat stroke!

A particularly critical sport with regard to heat dissipation by the athlete is professional American football, because players must wear extensive padding on their chest, shoulders, and legs, as well as gloves and other equipment, all of which reduces the effectiveness of many of the body's methods for eliminating excess heat. Therefore, besides part of the arms and legs, the face itself can serve as a heat-dissipating surface when the helmet is removed, say, during breaks.

The results of a recently published investigation [56] involved the use of IR imaging to analyze the heat patterns of a venous plexus in the face for 53 National League Football players in 12 regular season games. These facial regions have shown to be effective at heat dissipation due to increased blood flow when body temperature rises during exercise. Players were filmed while resting on the sideline during brief recovery periods following strenuous exertion, yielding 1858 images. IR tracking of the skin temperatures proved to be a useful technique for understanding physiological heat exchange patterns in the cheek region after intense exertion. Characteristic trends were discernible during the postexertion period. For example, many players typically display a period of significant cutaneous temperature increase in the cheek region across the initial 0–3 min interval following exertion.

11.4
Arts: Music, Contemporary Dancing, and Paintings

Surprisingly many applications of IR thermal imaging have already been reported in the arts. Two examples, one in music and another in contemporary dancing, are discussed in more detail, and others concerning paintings and other artwork are briefly discussed.

11.4.1
Musical Instruments

Musical wind instruments produce sound when warm air from the musician's breath is blown into the instrument. Therefore, the instrument's temperature will change once the ambient temperature differs from body temperature, which is usually the case. In what follows, brass instruments are discussed. Playing brass instruments indoors, for example, in concert halls, leads to an effective temperature of the air in the inner cavity, which determines the intonation of the instrument. Intonation is a measure of the deviations of the fundamental frequencies of tones from those of a reference scale. Usually, one refers to the equally tempered scale, where one octave is divided into 12 half-tone steps of equal interval size (defined by the frequency ratios). For quantitative analysis, one octave is divided into 1200 intervals of 1 cent each, that is, each half-tone interval is divided into 100 cents.

The average temperature indoors is relatively stable and musicians can vary the intonation of their instrument to some extent by their blowing techniques; therefore, there are seldom any problems of intonation changes in an orchestra, which relate to the ambient temperature. In other words, there is more or less a temperature equilibrium within instruments after short times of several minutes. The situation, however, changes outdoors at low temperatures, say below 10–15 °C. Again, an instrument will be characterized by an effective temperature that determines its intonation. However, musical pauses, which occur quite frequently for brass instruments during a concert (e.g., around Christmastime), lead to a cooling of the inner cavity air. Therefore, the intonation changes during these breaks [62, 63]. If the temperature differences are too large, the necessary corrections done by the musicians using the strength of the lips may become tedious. These problems become more severe for large brass instruments, which, on the one hand, have a large heat conductivity because of the metallic surfaces and, on the other hand, are too big to be kept warm by pressing them against the body or by holding them under one's clothes.

Intonation changes were measured while, simultaneously, the temperature across the first upper slide of a trombone was measured using IR thermal imaging. As a result, it was found that the warming up of the instrument due to warm airflow through the mouth piece leads to a change in intonation of about 3 cents K^{-1}. The change occurs for all natural tones similarly, that is, the instrument does not change its characteristics during temperature changes. Even at low temperatures of 5 °C, the process of warming up takes less than 10 min, meaning the instrument can be characterized as stable with respect to intonation after this time. To correct the tuning, trombonists either correct the length of their instrument by its tuning slide or in the worst case by exerting different lip strengths.

Figure 11.26 depicts two IR images obtained while a trombone was being played. Obviously, a temperature gradient evolves and there is a pronounced effect at the crook of the main slide. After several minutes of continuous playing, steady-state conditions are achieved, characterized by approximately body temperature at the mouthpiece and a much smaller temperature gradient at a higher temperature level.

Surprisingly, quite a few more applications of IR thermal imaging in music have been reported. They are, however, mostly related to finding specific health prob-

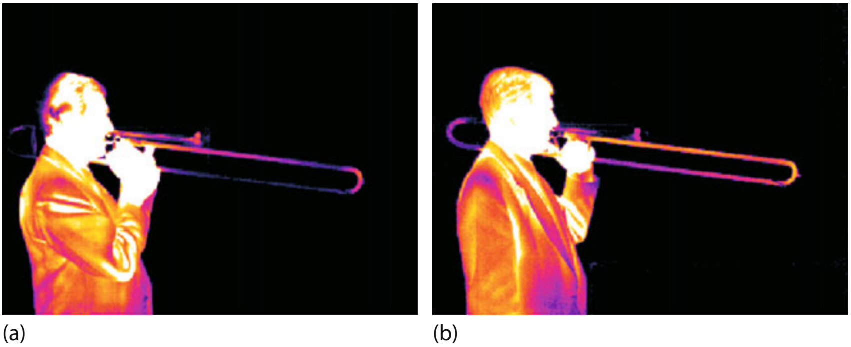

(a) (b)

Figure 11.26 Two IR images of a trombone being played. At the beginning (a), quite a large temperature gradient can be observed, whereas after several minutes of playing (b), steady-state conditions are reached.

lems (pain, fatigue, or musculoskeletal disorders) of musicians that are due to their partly unnatural body positions and movements when playing their instruments (e.g., [64, 65]).

11.4.2
Contemporary Dance

Pointed spotlights often suffer from the problem that, although people or objects are illuminated with a high light flux as desired, they usually also produce disturbing shadows. In addition, stage technicians must often manually direct the spots at the chosen points in real time. To overcome both drawbacks, a new illumination technique was invented by Milos Vujković [66, 67] based on IR thermal imaging. Using IR–visible feedback loops that are coupled to spotlights for target-based illumination, it could be demonstrated that shadows of any kind can be avoided upon illumination. Furthermore, this innovative technique of personalized spotlights requires no manual adjustments of the spots. The technique was demonstrated for contemporary dancing, enabling real-time movements of dancers on stage while only their bodies remain fully illuminated [67].

In general, feedback describes a situation where an output signal from a phenomenon is used to somehow affect the same phenomenon in the future. If the respective signals are used in a causal way, that is, if the output signal (or part of the output signal) of a phenomenon is used as an input signal to create a changed new output signal, one speaks of feedback loops. Such feedback loops are well known from many different areas in science, industry, and technology. Typical examples range from electronic circuits, where feedback loops are used in the design of amplifiers, oscillators, and logic circuit elements, to mechanical, audio, and video feedback phenomena.

In the arts, optical feedback is sometimes used to achieve special effects. The feedback occurs when an optical signal, for example, the image on a television screen, a computer monitor, or a video beamer, is observed by a camera whose output is fed into the monitor/beamer (Figure 11.27). The feedback loop creates an infinite series of images of the same object, all within the same image. The actual appearance of the resulting image depends on camera and monitor settings, for example, light amplification, contrast, distance, angle, and so on.

Using IR cameras rather than cameras in the visible spectral range, a very similar IR–visible feedback loop can be generated. The idea is to record a scene with an

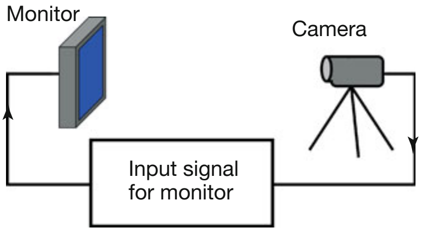

Figure 11.27 Setup for optical feedback loop.

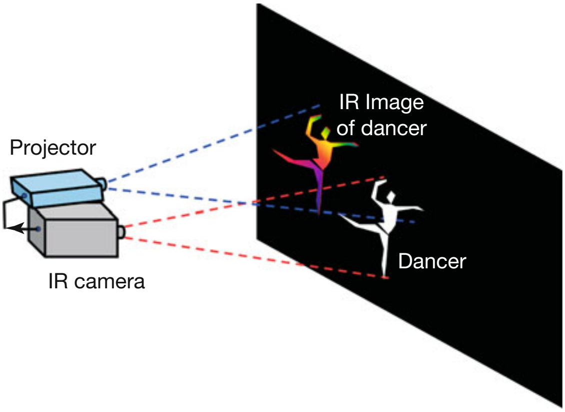

Figure 11.28 Scheme for an IR-optical feedback loop. An IR camera records an image of a dancer, which serves as an input signal of a projector.

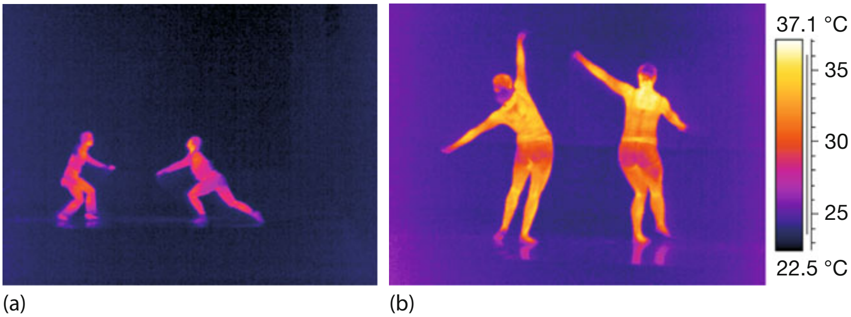

Figure 11.29 Two examples of IR images of contemporary dancing.

IR camera, for example, a performing dancer (Figure 11.28). The life signal of the camera can be fed into a video beamer, which projects the IR image onto a screen, which is behind the dancer. If the screen were be spatially separated from the dancer, one would just project typical IR images (Figure 11.29) onto the screen.

If the projector is aligned as close as possible to the IR camera (it is best to use a telephoto lens such that the distances from the camera plus projector are large compared to the size of the dancers), that is, if both are nearly in collinear alignment, the output signal of the video projector can be superimposed onto the dancers. By adjusting the telephoto lens of the video projector, it is possible to adjust the size of the projected image to that of the dancers (Figure 11.30). For demonstration purposes, the size of the projected image can be chosen slightly larger than that of the dancer (Figure 11.30a). In principle, the size can, however, be reduced such that only the dancer is illuminated (Figure 11.30b).

The idea behind this optical-IR feedback loop seems so simple that one might try to carry out this illumination using a visual camera. But that would raise the following problem. A visual light camera does need a certain light level for oper-

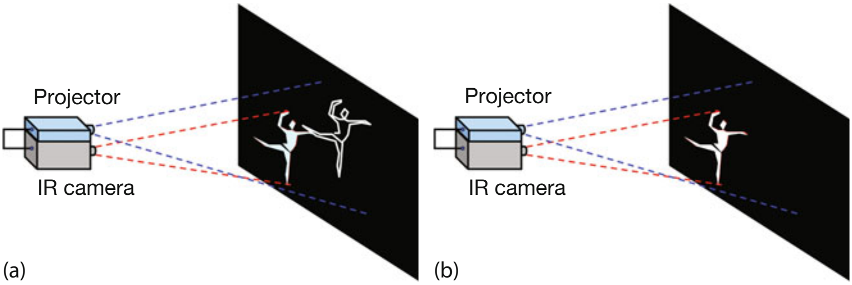

Figure 11.30 (a,b) Two useful alignments for the IR–visual feedback loop (see text for details).

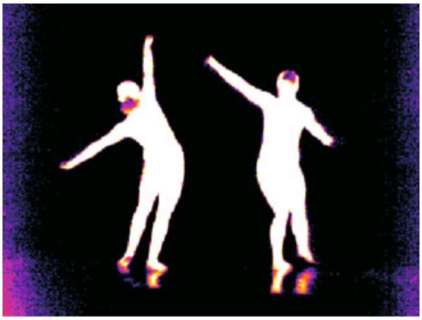

Figure 11.31 IR image of Figure 11.29b with different temperature span in order to reach saturation in image of dancers. This image can be used for the optical feedback signal to the projector.

ation, which automatically means that the background would also be visible and amplified by the feedback loop. This would lead to bad contrast between dancers and the background. The use of an IR camera, however, easily overcomes this problem, since it detects the surface temperature of the dancers, which is much higher than that of the background. The contrast can be made very large by simply changing the temperature span of the IR image (Figure 11.31). If this feedback signal is used, the background remains very dark and only the warm skin and clothes of the dancers remain visible. The result is a whitish projection, which fits nearly perfectly to the geometrical form of the dancing bodies.

Figure 11.32 shows several still images from a video sequence, which refer to the situation in Figure 11.32a. The projected image was chosen to be slightly larger than the dancer. This made it possible to simultaneously observe the edge of the projected image and the moving shadow of the dancer. Movie sequences analyzed in slow motion reveal that the projection can be made very fast so that the projection follows even very rapid movements of dancers in real time.

In the experiments [67], a SC6000 research IR camera (wavelength range 1.5–5 μm) with 640 × 512 pixel was used. It provides a 30 Hz analog output signal, which could be used directly as an input for the video projector. The IR-optical feedback loop can be easily used even for the fast body movements in contemporary dance and any kind of IR camera with 30 Hz output may be used for these experiments, although it is desirable to have at least 640 × 512 pixels. A number of improvements for the future were suggested, for example, using several cameras

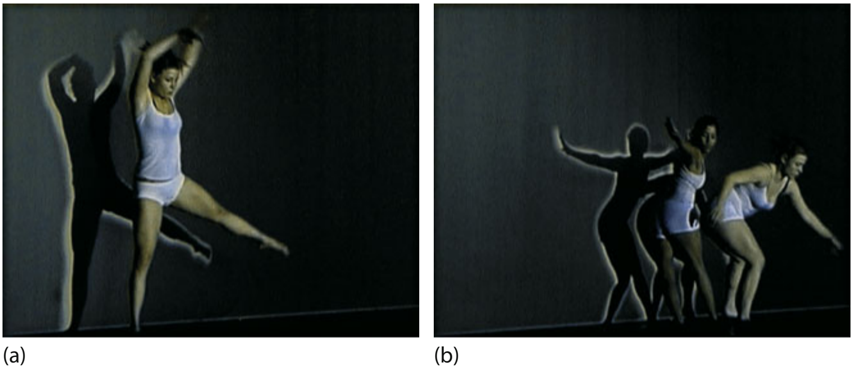
(a) (b)

Figure 11.32 (a,b) Some photos of dancers on stage which were illuminated with a slightly larger projected IR image of themselves. For more details on the art aspect, see [66].

simultaneously from the front and sides, using cameras with higher frequency analog output, or including a computer between the IR camera and the projector for manipulations of the camera signal.

11.4.3
Paintings

The restoration of paintings in museums requires a lot of sophisticated equipment. Some of the related techniques also allow one to look beneath the various layers of paint. One particularly interesting technique, IR reflectography, uses SW IR cameras like the SW cameras operating in a wavelength range from 1 to 2.5 μm [68]. IR reflectography (detailed discussion see Section 6.3.3.5) utilizes the fact that in certain lighting conditions, oil paints can appear transparent to the IR camera because they allow specific IR wavelengths to pass through them and be reflected below by the canvas. Graphite sketches on canvas do not reflect IR light and thus can be seen as dark areas on the canvas. The opaqueness of paint layers increases with paint thickness. If the paint is not too thick, the optimum wavelength to see through it while maintaining the ability to detect graphite lines against a white background has been shown to be around 2 μm. These images are referred to as *infrared reflectographs* since images are made using reflected light, rather than thermally self-emitted radiation (thermographs). In this way, art historians can study the thought processes of artists, that is, see where artists may have changed their minds between the stage of sketching a scene and painting it. In the 1960s, cameras with PbS detectors (peak responsivity at 2 μm) were used to study the underdrawings of a sixteenth-century painting using an active mode with the painting illuminated by a tungsten lamp.

In a recent investigation, a Phoenix SW camera with a 320 × 256 InGaAs (sensitive from 0.9 to 1.7 μm) focal-plane array was used. Lighting of the painting in the museum was by incandescent tungsten bulbs. An underdrawing test panel was made to optimize the camera settings and filter selection. This test panel consisted

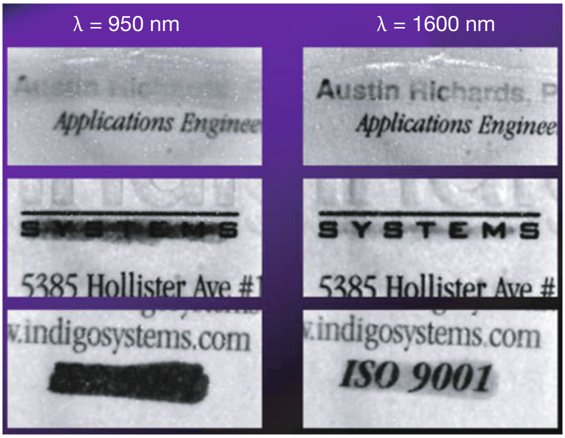

Figure 11.33 Detection of letters covered by correction fluid or ink using SW imaging. (Courtesy FLIR Systems Inc.)

of an ordinary primed artist canvas with vertical black stripes drawn by a charcoal pencil. These stripes were then covered with different colors of oil paint. The InGaAs IR camera was successful at imaging an underdrawing present below the specific chosen original painting attributed to Lloyd Branson. The underdrawing was oriented in the landscape direction, whereas the top painting was oriented in the portrait direction. Besides paintings, IR thermal imaging has also been used as a nondestructive test method to study historical wall paintings, frescoes, or other indoor and outdoor stone materials constituting cultural heritage (see [69–73] and references in Chapter 6).

Very similar techniques are used in forensic sciences [74]. Criminologists often use SW imaging techniques to examine documents for possible alterations. Similar to the examples presented in Chapter 6, Figure 11.33 shows examples of several documents that have been altered by covering some letters with either correcting fluid or ink, for example, from a ballpoint pen. The ink and correcting fluid neither absorb nor reflect SW IR radiation; therefore, they are more or less transparent to the radiation of 1.6 μm wavelength. The underlying paper does, however, reflect IR as well as VIS radiation. The printer toner ultimately absorbs the SW IR light, which leads to image contrast.

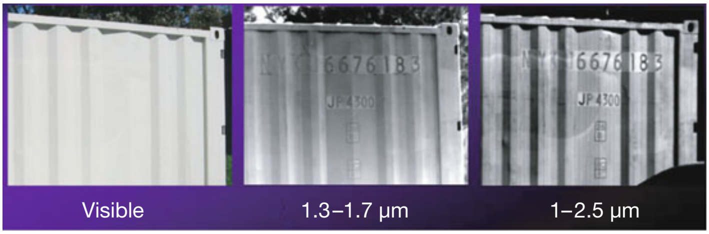

Figure 11.34 SW imaging looking through paint. (Courtesy FLIR Systems Inc.)

Similarly, it is possible to look through thin layers of paint with SW IR radiation, as demonstrated on metal containers whose serial numbers were covered by paint (Figure 11.34). In the VIS range, it is not possible to detect the numbers, whereas SW radiation between 1.3 and 2.5 μm readily detects hidden numbers below paint.

11.5
Nature

11.5.1
Sky and Clouds

Nearly everyone who owns an IR camera has probably directed it at least once at the sky. Optically thick (i.e., opaque) clouds allow one to measure cloud temperatures. Clear skies, however, pose a problem. The "measured" apparent temperature is useless since the atmosphere is not optically thick in the IR spectral range. Figure 11.35a displays a spectrum of the vertical atmosphere in the NIR range. Obviously, both in the LW and MW ranges, vertical transmission has values below 100% due to scattering and absorption losses. As a consequence of absorption, the vertical atmosphere also emits radiation, that is, an IR camera also detects residual radiation contributions from the atmosphere. Figure 11.35b depicts the corresponding expected emitted radiance for the vertical atmosphere, which is mostly due to H_2O vapor, meaning it is sensitive to relative humidity, and CO_2. It is the superposition of the emission contributions of all atmospheric height layers. Each layer contributes based on its absorption and the corresponding atmospheric temperature but – owing to the pressure (and gas concentration) reduction with height – the dominant contributions come from the lower atmosphere. As a thought experiment, suppose H_2O and CO_2 strongly absorb in the whole thermal IR range. In this case, one would expect that the atmospheric emission spectrum – if interpreted as a blackbody spectrum – would relate to a temperature of around 280 or 290 K, or the typical lower atmosphere temperature of these gases. According to Figure 1.21, such spectra would start around 4 μm and have a maximum around 10 μm before decreasing again.

In reality, H_2O and CO_2 absorption is strong only between 4 and 8 μm and above 14 μm. In the LW range between 8 and 14 μm, absorption and, hence, emission are reduced. This explains the general form of the emitted radiance spectrum in Figure 11.35b. In the range 4–8 μm and above 14 μm it resembles more or less a blackbody spectrum for a temperature of 280–290 K, but in between, where LW IR cameras operate, the residual radiance is strongly reduced.

The overall shape of the spectrum therefore nicely represents a blackbody spectrum of average atmospheric temperature multiplied by (1–atmospheric transmission). The exact amount of emitted radiation within the LW IR window depends sensitively on the precipitable water vapor (PWV). The chosen value of 1 cm in Figure 11.35 corresponds to typical dry winter months in Europe or the central United States.

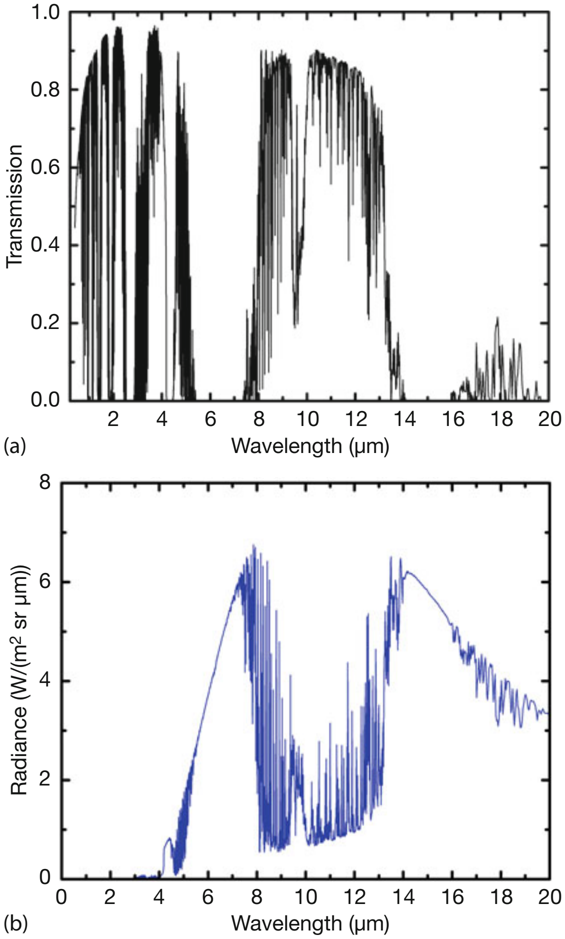

Figure 11.35 (a)Transmission spectrum of vertical atmosphere from sea level, 1 cm precipitable water vaport (PWV), and 400 ppm CO_2 in the thermal IR spectral range. (b) Corresponding emitted radiance spectrum. MODTRAN spectra, courtesy Joe Shaw, Paul Nugent, MSU Bozeman.

Owing to the high transmission of the vertical atmosphere within the atmospheric windows, a LW IR camera detects not only atmospheric radiation but also radiation from the (much colder) background, that is, space. The latter is, however, more or less negligible compared to the atmospheric radiance contributions.

To conclude, the measured radiance contribution from the clear zenith sky is the sum of the (more or less negligible) background radiance from outer space (3 K) (Figure 1.23), emissions of atmospheric gases (Figure 11.35b), and perhaps additional aerosols. The latter contribution is the least known. It depends on the temperature of the aerosols, that is, on their height, and may strongly fluctuate owing to transient sources such as volcanic eruptions, wildfires, or anthropogenic

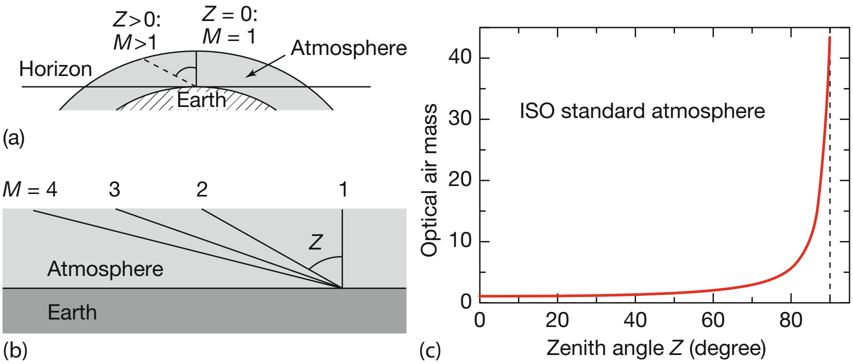

Figure 11.36 Spherical (a) and planar (b) geometry for explanation of air mass M and (c) resulting air mass as a function of zenith angle Z.

activities. As a consequence of all emission contributions, the measured zenith "sky temperatures" are always well above the expected 3 K background radiation of the universe, and they resemble some average atmospheric height temperature owing to the dominant contributions of atmospheric emissions.

To make the situation more complicated, the apparent sky temperature is also a function of the zenith angle. This is due to the so-called air mass: radiation that penetrates the atmosphere not from the zenith sky but under well-defined zenith angles will pass a longer distance, thereby interacting with more matter. The total amount of matter is accounted for by the dimensionless parameter air mass, which can reach a value of about 38 near the horizon (Figure 11.36b) [75].

This means that radiation that penetrates the atmosphere along a tangential path from the horizon to an observer must pass 38 times the amount of matter compared to the vertical, that is, the zenith direction. Consequently, it has a much higher chance of being scattered, absorbed, or emitted, and the overall radiance will accordingly increase at an increasing zenith angle. Emitted IR radiance from a direction close to the horizon will be greatest (longest path through low heights with large concentrations of H_2O) and it will be lowest for the zenith direction. In between, the apparent sky temperature derived therefrom will decrease from horizon toward the zenith (Figure 11.37, see also Figure 7.52).

Owing to the complex signal integration through the atmosphere, measured signals are only used by scientists to extract useful information about the clear sky atmosphere. In contrast, users of commercial IR cameras will just produce nice qualitative images. When trying to quantitatively describe their results in terms of "sky temperatures," they would be faced by quite a few additional problems.

First, the typical measured temperatures are at the lower end or even below the minimum temperature of the lowest measurement range. This means that the detectors are not really sensitive enough, that is, they are not suitable for this kind of low-temperature measurement. The second problem consists in the proper choice of the distance. Distances used in the camera software usually refer to horizontal paths ending at opaque objects. The atmosphere is, however, not opaque

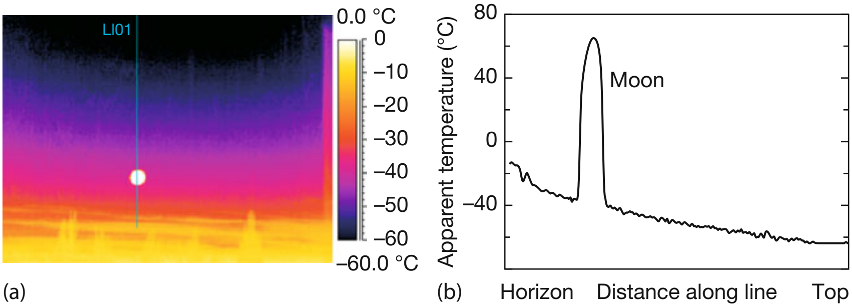

Figure 11.37 View of horizon and sky with setting moon on a cold winter morning ($T_{\text{air}} = -10\,°\text{C}$). The apparent temperature of the sky drops with increasing angle above the horizon. The exact values depend on the chosen distance and emissivity (here arbitrarily $\varepsilon = 0.95$ and 2000 m).

and the paths are not horizontal. In addition, the maximum distance input in the camera software (for internal corrections) is usually limited to, say, 10 km. The next issue relates to such questions as what value of averaged emissivity should be used for the atmosphere, what kind of relative humidity should be used, and which values for the reflected temperatures should be used. Humidity and temperatures in the atmosphere vary with height quite significantly, for example, T amounts to about –60 °C at a height of 10 km.

As a consequence, any thermographer should interpret apparent temperatures of sky images at best qualitatively. For the camera recording Figure 11.37, the lowest temperature range started at –60 °C. The apparent sky temperature dropped below this value already at elevations of around 7° above the horizon (zenith angles of 83°) at the top of the line plot!

Figure 11.37 also includes an image of the moon. The moon or any other hot object observed through the atmosphere also gives rise to an apparent temperature, which is due to different radiance contributions (Section 11.5.3).

Looking again at Figure 11.35, we also note that the spectrum of the vertical atmosphere may be compared to a corresponding spectrum for a horizontal path, for example, at a distance of 1 km, as shown in Figure 1.45. Both spectra are very similar, the main difference being the absorption feature between 9 and 10 μm, which is due to the ozone layer at heights above 20 km. Of course, it does not show up in the sea level horizontal spectrum.

Besides their usefulness in imaging the sky itself, low temperatures of clear skies at night have additional applications with relevance to IR imaging. On the one hand, they can be used for cooling purposes [76], and on the other hand, clear night sky radiative cooling will have an impact on outdoor building thermography (Chapter 7). For the corresponding radiative transfer rates, it is often useful to define effective sky temperatures, which resemble average values, defined by the overall energy transfer [77]. These effective sky temperatures depend primarily on dew point temperature and cloud cover.

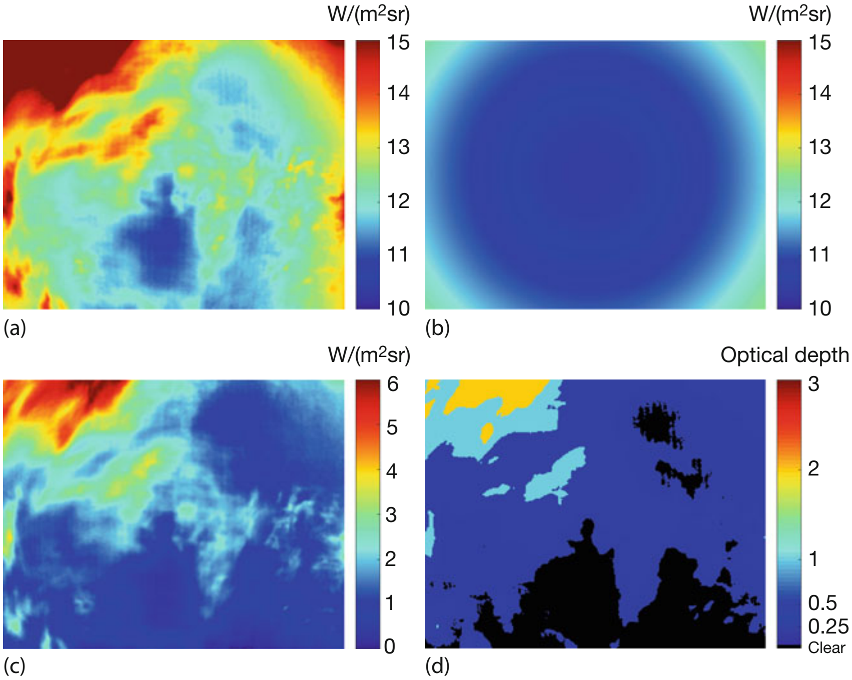

Figure 11.38 LW IR images of partially cloud-covered skies recorded in July 2012 in Alaska. (a) Measured total radiance from sky and clouds; (b) calculated clear sky radiance for camera and given atmospheric conditions; (c) residual radiance which is only due to the clouds. Images courtesy Joe Shaw, Paul Nugent, Montana State University, Bozeman, Montana.

Clouds in the sky often have their bases at certain heights and therefore emit IR radiation according to the temperature at the corresponding height. Since optically thick clouds are opaque, they usually emit more radiation than the corresponding clear sky in the same direction (Figure 7.53) [78, 79]. This fact was utilized to estimate cloud cover in remote regions like the Arctic in an automated way. Figure 11.38 illustrates the principle. A radiance-calibrated IR camera detects the sky. Then the clear sky radiance is subtracted, which gives a residual radiance distribution due to clouds. Finally, a clever image-processing tool computes the cloud cover and cloud optical thickness. Knowledge of these values at many locations on earth, and in particular in the Arctic and Antarctic regions during polar nights, is important since these data enter climate models.

11.5.2
Wildfires

Unplanned wildfires occur all over the world, mostly in hot and dry seasons. They can have devastating impacts on the environment by consuming thousands of hectares of productive timber, destroying wildlife habitats, and filling the air with smoke and tons of carbon dioxide.

Wildfires are due to either natural (as a result of lightning activity) or human causes and require immediate and effective suppressive actions. In some regions like southern Europe (e.g., Italy, Spain, and Greece), the United States (e.g., California), Canada (e.g., Alberta), or Australia, wildfires are well-known regular events. For example, the province of Alberta alone suffers from an average of about 1380 of these devastating events annually [80]. This resulted in the burning of more than 107 000 ha in the decade between 1998 and 2007, alone. Lightning accounted for 49% of these wildfires; the remaining 51% were preventable human-caused wildfires.

Therefore, detection and fast reporting of wildfires as well as protective actions for the land, the people, and wildlife are very important. In what follows, an exemplary program of the Alberta Sustainable Resource Development, Forestry Division, is presented, which uses a multiple IR approach to support wildfire suppression activities. This program is based on more than 30 years of thermal IR operations in the field. It uses, first, handheld IR cameras (primary use of IR scanning, for example, from helicopters), second, low- and high-altitude surveys (gyro-stabilized gimbal mounted on a helicopter or fixed at wing aircraft for high altitudes), and third, satellite-based systems (using the moderate-resolution imaging spectroradiometer, MODIS).

Overall, IR imaging helps to first detect holdover fires that are a result of winter burning, such as site clearings, power and pipeline construction, brush piles, and so forth, second to determine the most effective location for air tanker drops in heavy smoke conditions, and third to obtain hot spot locations and perimeters of ongoing wildfires. Overall, the allocation of limited firefighting resources is based on the following priorities: human life, communities, sensitive watersheds and soils, natural resources, and important infrastructure.

A typical use of handheld IR imaging is to use a camera on a helicopter by removing the helicopter door. The operator must wear a safety harness. He scans a wildfire and marks the identified spots with marking material and the use of GPS coordinates. Such handheld scanning works best for wildfires on areas of less than 1000 ha or when hot spots need to be located along portions of the fire line.

Low-altitude IR scanning involves the use of a light helicopter (Bell 206) with a gyro-stabilized gimbal-mounted IR camera under the aircraft. These (more expensive) systems allow a more flexible scanning of larger areas of typically 1000–10 000 ha. The spatial resolution of the hot spot ranges from 2.5 to 30 cm (1 in to 1 ft) for a maximum altitude of 250 m (1000 ft) above ground level. Approximately 100 km of perimeter can be scanned each day, depending on the number of hot spots and the speed of the aircraft.

In general, IR imaging of wildfires does not always work the same way, for several reasons:

- Rainfall causes the ground to cool through evaporation. This cooling reduces the heat signature and can drive hot spots into the ground, where they can smolder within organic material. Hot spots with sufficient energy can resurface, creating a potential risk. By scanning immediately following a rainfall, one may miss such hot spots. Therefore, depending on the amount of moisture, IR surveys following rainfall should wait for some dry days before trying to find resurfacing hot spots.

- The time of a scan may have an impact on the result due first to solar gain and second to solar reflectance. Both effects can lead to a false-positive identification of hot spots. Therefore, one should observe the same spot while changing the observation angle of the target.
- Imaging is not possible through solid objects (such as tree trunks, but also windows in helicopters), which are opaque in the IR.
- IR radiation can penetrate smoke to a much larger extent than visible light. Therefore, IR imaging is able to identify the perimeters or the head of wildfires through smoke from a safe distance. However, smoke may change the detected IR signal owing first to the absorption of the hot spot signal behind the smoke, second, to the emission of an IR signal from the smoke itself depending on the smoke's temperature and emissivity (which depend on its optical thickness), and third to the scattering of IR radiation. The importance of these effects depends on the ratio of the size of smoke particles (typically larger than VIS and smaller than IR wavelengths) and the wavelength of the relevant radiation. For wildfire smoke, LW camera signals are less susceptible to absorption and scattering than is the case for VIS detection.

The temperature range of hot spots found in wildfires ranges from above 800 °C for flaming combustion to below 100 °C for hot areas buried below a lot of white ash and observed through smoke. The latter spots are very difficult to detect by other means.

Figure 11.39 displays an example (VIS and IR image) of a low-altitude inspection for the detection of wildfire hot spots.

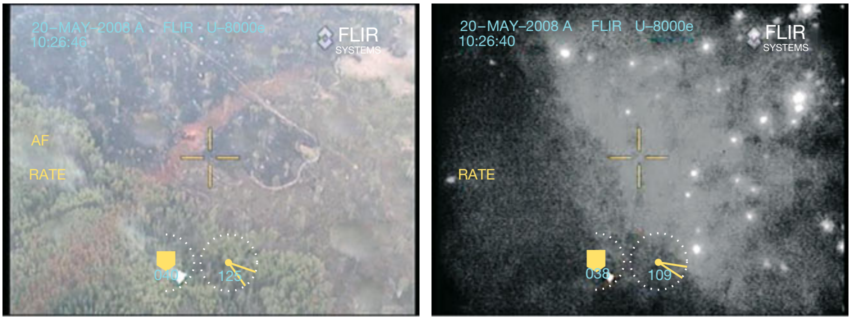

(a)

(b)

Figure 11.39 Hot spots of a wildfire observed with low-altitude IR imaging (a) and corresponding visible image (b). The colored line in the VIS image resembles the retardant used to slow down an advancing fire. Courtesy of Department of Agricultural and Forestry, Alberta/Canada.

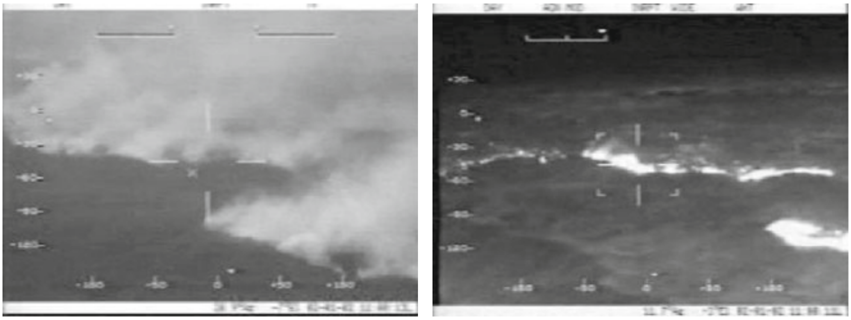

(a) (b)

Figure 11.40 Head of a wildfire in thermal IR (a) and VIS image (b). IR radiation penetrates through smoke and makes it possible to identify the head of the fire front. Courtesy of Department of Agricultural and Forestry, Alberta/Canada.

High-altitude IR scanning is done by mounting a gyro-stabilized gimbal and IR camera on the nose or wing of an aircraft. The spatial resolution of the method, which is useful for wildfires covering areas larger than 10 000 ha, ranges between 0.5 and 30 m on the ground. The images can precisely locate the head and flank of a wildfire, thereby effectively supporting the drops of retardant and water by air tankers, which are often hindered by poor visibility owing to heavy smoke (Figure 11.40). Because of the velocity of the moving aircraft, images sometimes appear slightly fuzzy, but that does not affect the information about hot spots or fire heads, for example.

The largest-scale scans of hot spots are performed using the MODIS and Aqua MODIS imaging spectroradiometer instruments aboard earth-orbiting satellites. They view the entire earth's surface every 1–2 days and cover the province of Alberta twice a day. Fire detection data are derived from the data, and a variety of products related to hot spot detection are available daily [81]. The data have a spatial resolution of approximately 1 km; hence, satellite data can give overviews of what is happening on a large scale.

Of course, IR imaging techniques, in particular those used on helicopters and planes, are expensive. For example, thermal IR operations cost the Alberta government approximately $1.6 million for each fire season [80]. However, this must be seen in relation to the huge benefits. Besides the use of LW cameras, SW imaging is very promising, too, when looking through smoke at forest fires (Section 6.3).

11.5.3
Sun and Moon

After finishing an early morning outdoor IR application like outdoor building thermography, one may just catch the sun rising or the moon setting. And for any observer, the most natural thing to do is to point a camera at these celestial bodies. In Section 11.5.1 we discussed the problems encountered when trying to measure temperatures of clear skies or clouds; here we discuss first whether it is recommended to direct an IR camera toward the sun. Second, we focus on problems in measuring the corresponding apparent surface temperature of the sun. Third, similar measurements of the moon are presented.

To the first order, the sun represents a blackbody source with a temperature between 5700 and 6000 K, which according to Wien's displacement law corresponds to a wavelength of maximum emission in the VIS spectral range (Figure 1.22, Eq. (1.16)). The high temperature combined with the rather high transmission of MW or LW IR radiation (Figure 11.35a) poses the first problem in connection with any measurement using a commercial IR camera. The typical measurement ranges are below 400 °C and even the high temperature option usually reaches up to only 2000 °C. Therefore, any commercial calibrated camera sensor would be saturated, meaning additional attenuation is required to avoid potential damage to the sensor. One way to achieve this is to insert either narrowband filters or broadband attenuators such as silicon wafers with high reflection losses. Alternatively (or in addition), one may use the natural attenuation in the atmosphere if the sun is very low, that is, close to the horizon, owing to the increased air mass (Figure 11.36). Whatever attenuation mechanism is chosen, the camera needs to be recalibrated. Therefore, the measurement – though possible – requires an accurate analysis.

The second potential problem, encountered in studies of the sun (as well as moon) is the spatial resolution. Older cameras with 320 × 240 pixels – even those equipped with 10° FOV lenses – would only give around 15 pixels across the 0.5° diameter of the sun or moon. This may be just enough to obtain a measure from the central pixel but does not produce an appealing image. Therefore, we used 500 mm regular VIS zoom optics for our extended MW camera (λ-range 1.5–5 μm) corresponding to about 180 pixels across the solar disk [82]. The glass also attenuates as a selective filter. Figure 11.41 depicts a raw image (Figure 11.41a), vertical and horizontal line plots across the solar disk (Figure 11.41), and expected signals along the line plots (Figure 11.41c). Owing to the high solar elevation, the line plots are symmetrical.

The line profiles show a decrease toward the edge that corresponds to the well-known limb-darkening effect ([82] and refs. therein). Scientifically a quantitative analysis poses no problem. It is even possible to estimate solar temperatures from commercial cameras if filter transmission is properly accounted for. Temperatures were in a range above 5000 K, the largest uncertainty being due to exact knowledge of the atmospheric transmission [82].

The situation for the moon is only similar with respect to the spatial resolution since the moon has an angular diameter of 0.5°, similar to that of the sun. Its average surface temperature, however, is due to the thermal equilibrium between the solar irradiance and the emitted thermal radiation. As a result, the expected maximum lunar temperatures range around 394 K (121 °C) in the center, which is easily accessible to commercial cameras. Owing to the reduced irradiance toward the edge, the temperature decreases sharply [82, 83]. At full moon, LW IR images (e.g., Figure 11.42a) show a very symmetrical radiance, that is, a symmetric temperature distribution across its disk that is nearly in accordance with the theoret-

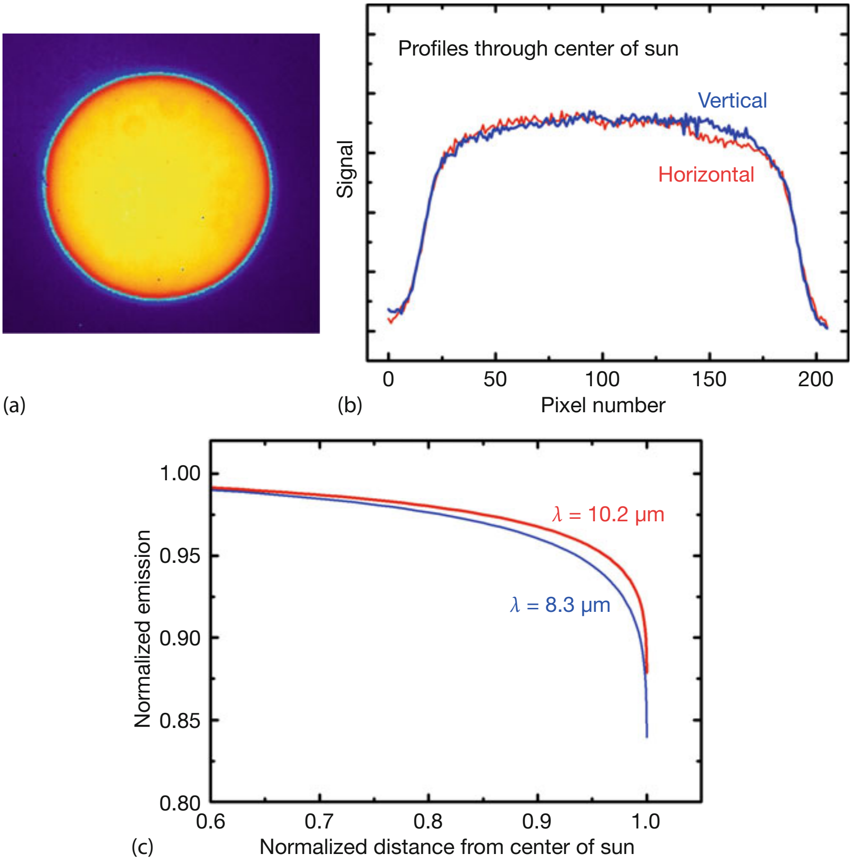

Figure 11.41 (a) IR image of sun recorded with FLIR SC6000 camera (1.5–5 μm, $f = 500$ mm lens, 17 May 2010, 11:30 a.m., clear sky); (b) horizontal and vertical line plots across sun disk; (c) expected line plot signals from limb darkening.

ically expected one (Figure 11.42c). These IR images of the moon were recorded using a radiometrically calibrated Photon 640 LW camera (640 × 512 pixel) combined with a 200 mm telescope optics. This resulted in about 100 pixels across the disk of the moon.

The quantitative analysis is not easy, mainly because there can always be additional aerosol layers in the atmosphere. They may be optically thin, that is, almost invisible to the naked eye or a VIS camera image. Still they can produce enough absorption that the atmospheric corrections due to atmospheric radiance as well as transmission no longer yield correct surface temperatures.

However, since lunar IR emission and surface temperatures are well known, one may turn the argument around and use the lunar IR images as calibration signals that allow one to estimate aerosol optical depths [83]. In Figure 11.42c and similar figures, the measured temperatures were close to, but always below,

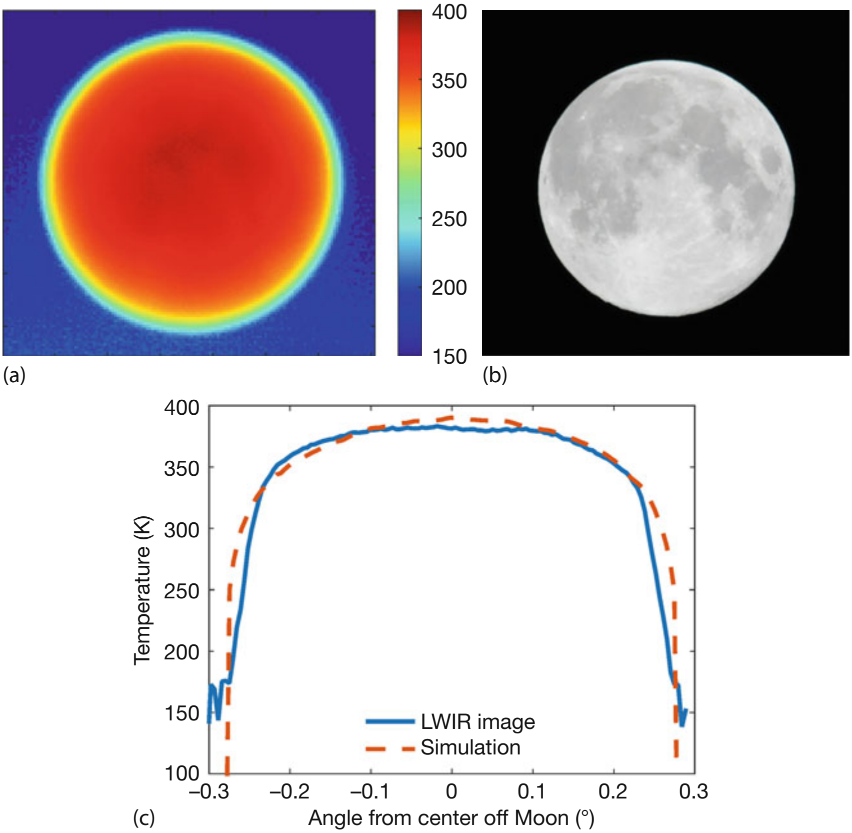

Figure 11.42 LW IR (a) and VIS (b) images of moon from 2 August 2012, 1.7 h after full moon, lunar elevation 30°. Temperatures in (a) are in Kelvin. (c) Horizontal line profile of measurement (blue line) and simulation (red dotted line). Images courtesy Joe Shaw, Paul Nugent, Montana State University, Bozeman, Montana.

the theoretically expected ones, sometimes up to 15 K. This reduction could be attributed to aerosols with optical depths between 0.04 and 0.1.

11.5.4
Infrared Mirages

Mirages are among the most documented atmospheric optical phenomena observable with the naked eye. They are rather frequent and easy to observe and record. Mirages are formed when light rays bend as they propagate through regions where the atmospheric refractive index varies. As a result, an observer sees additional images. One specific type, so-called inferior mirages, appear below the object; typical examples include scenes perceived by occupants of a car who are anticipating a lake or puddle of water in the road ahead of them – although it is just a mirror image of the sky. The typical FOV is just a few degrees.

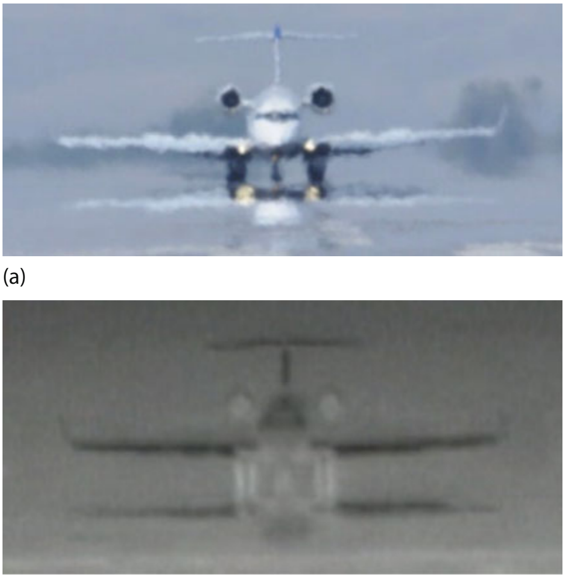
(a)

(b)

Figure 11.43 VIS (a) and LW IR images (b) of an airplane at takeoff at Bozeman, MT, airport. Inferior mirages are clearly seen in both wavelength ranges.

Of course, light is an electromagnetic wave, so mirages should also be a common phenomenon of other electromagnetic waves traveling through the atmosphere. In particular, mirages are also observable in the IR spectrum.

However, concerning mirage observations, commercial IR cameras have a severe disadvantage compared to VIS cameras. The telephoto lenses required for a small field of view are much more expensive. Therefore, we used a mirror telescope optics of 200 mm focal length combined with a LW FLIR Tau 640 camera (640 × 512 pixels) providing a 3.1° × 2.5° FOV. Inferior mirages were observed for airplanes at takeoff and landing on the runway of Bozeman airport over a distance of up to 3.4 km [84].

Figure 11.43 depicts a visible and an IR image of a jet plane during takeoff. The inferior mirages look very similar, though there are also pronounced differences (for more details, see [84]). The bright visible mirage parts come from the white painted body and wings of the aircraft, which scatter visible light best. In contrast, the IR object (the plane) as well as the mirage are brightest at the warmest spots. These are the engines due to the hot exhaust gases and the tires, which have heated up as a result of the plane's acceleration on the runway. The wings appear coldest since they reflect the cold sky.

11.5.5
Geothermal Phenomena

11.5.5.1 Geysers and Hot Springs

Geothermal phenomena are among not only the most spectacular but also the most dangerous phenomena in nature. A safe observation of geothermal physics is possible in US national parks such as Yellowstone or in Iceland, where spectacular geyser eruptions taking place at well-defined time intervals. Geyser eruptions are observed if hot water is in a cavern under high pressure due to the water column that extends from the cavern up to the surface, ending, for example, in a small pond. Because of geothermal heat, the water temperature in the cavern rises above the boiling point, which may well be above 100 °C due to the high pressure. Whenever the temperature exceeds a critical limit, boiling starts and gas bubbles form in the cavern. On their way up the channel to the surface their volume expands rapidly with decreasing pressure, thereby ejecting the water column on top of it at high velocities. Figure 11.44 depicts such a geyser eruption with hot water ejection as observed in Iceland. The fountain top is above 20 m, as can be seen by the spectators in the foreground, which were of course at a safe distance from the hot water.

Similarly, Figure 11.45 displays a snapshot from a summer eruption of the world's most famous geyser, Old Faithful in Yellowstone National Park. It erupts on average every 90 min for up to 5 min with maximum fountain heights of about 55 m. The image is calibrated and gives temperatures in °C. It also nicely shows clouds and partly clear skies.

Besides geysers, hot springs and pools are among the most fascinating natural thermal phenomena [85–87]. Being connected to underground thermal reservoirs, they maintain very high temperatures all year long. They are usually very colorful since thermopiles, the kind that depend on temperature, may grow on the hot pool walls. Combined with residual scattering in the crystal clear water, colors

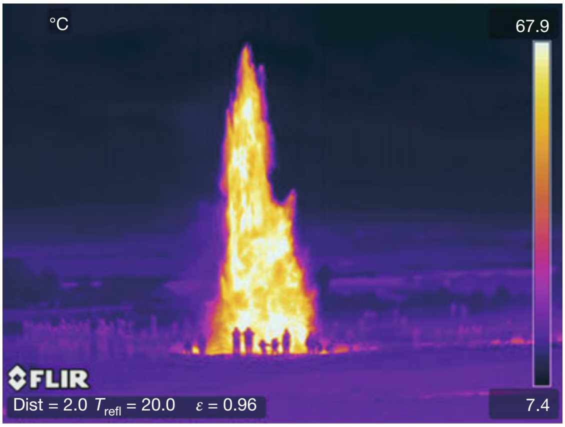

Figure 11.44 Eruption of a geyser in Iceland. Image courtesy Infrared Training Center.

spanning the complete visible spectral range result [85, 86]. Figure 11.46 shows a panoramic view of the world's third largest hot pool, Grand Prismatic Spring in Yellowstone National Park. Its extensions are about $75 \times 115\,\text{m}^2$ with a maximum depth of around 50 m. The average surface temperatures vary across the seasons, typically between 63 and 74 °C.

One can easily see the hot outflows and thermal reflections of the boardwalk with tourists. The hot steam feature in the background is due to the much smaller Excelsior Geyser. Its temperature is near boiling (at the geyser's location in the park), around 92 °C, which make it among the hottest pools. For a more detailed discussion of thermal features of Yellowstone National Park, see [87].

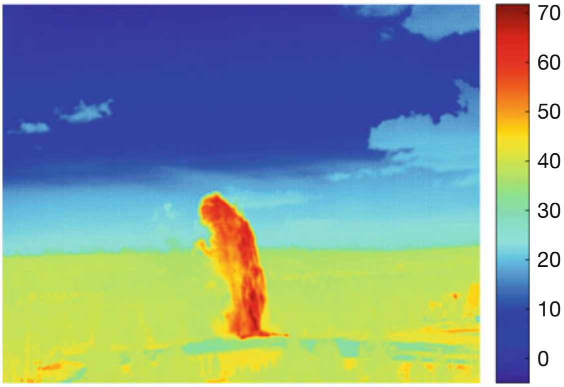

Figure 11.45 Old Faithful eruption from a distance (temperatures in °C). Image: Joe Shaw, Paul Nugent.

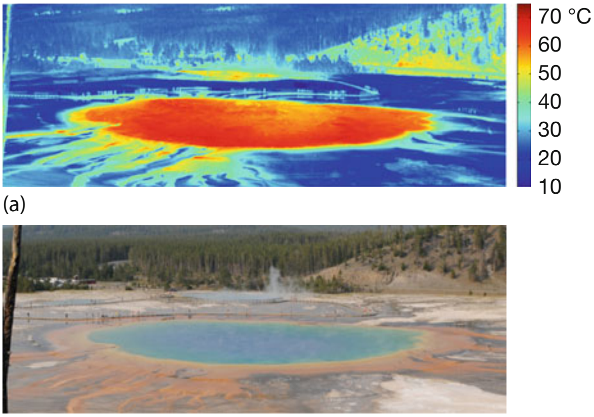

Figure 11.46 LWIR (a) and VIS (b) images of Grand Prismatic Spring in Yellowstone National Park, recorded in summer 2012 (see text for details). Images courtesy Joe Shaw, Paul Nugent, Montana State University, Bozeman, Montana.

11.5.5.2 **IR Thermal Imaging in Volcanology**

The value of ground-based thermal radiometry in volcanology has been recognized for decades [88]. Mostly thanks to the development of powerful radiometric imagers in the form of handheld IR cameras, however, it is only recently that this method has become routine and has included data capture from helicopters and from the sea [89–94].

In recent years, thermal IR measurements of active volcanic features have been used for the following applications:

1. Recognize magma movements in the uppermost volcanic conduits;
2. Detect the upward movement of shallow feeder dikes;
3. Track eruptive activity, for example, in craters even through the thick curtain of gases;
4. Distinguish and measure the thermal and rheological properties of active basaltic lava flows, lava tubes, and silicic lava flows, as well as sea-entry thermal anomalies;
5. Track the development of the structures on lava flow fields such as channels, tubes, tumuli, and hornitos;
6. Analyze the evolution of fumarole fields;
7. Study active eruption plumes, strombolian activity, and persistent degassing;
8. Obtain effusion rates for active lava flows;
9. Detect potential failure planes on recently formed cinder cones and fractures developing just before flank collapse at active volcanoes; and
10. Analyze active lava lakes.

Thus, thermal imaging has contributed to a detailed eruption chronology and understanding of lava flow and eruption processes operating during eruption. Thermal mapping has proven essential during effusive eruptions, since it distinguishes lava flows of different ages and concealed lava tubes' paths, improving hazard evaluation. In particular, the 2002/2003 Mount Etna and Stromboli eruptions were analyzed in detail with thermal imaging using more than 100 000 thermal images recorded before, during, and after eruptions. The analysis of these images was combined with information from visible images, as well as data on seismicity, ground deformation, and gas geochemistry collected routinely during the eruption. This allowed improved quantification of eruptive parameters, such as effusion rate and maximum temperature at the bottom of the summit craters, qualitative tracking of lava flow features, fissures, and vents in situations where traditional, ground-based measurements were difficult and dangerous, and in general a greater understanding of eruptive phenomena.

On Mount Etna, thermal images recorded monthly on the summit of the volcano revealed the opening of fissure systems several months in advance. After the onset of the 2002 flank eruption, daily thermal mapping made it possible to monitor a complex lava flow field spreading within a forest below a thick plume of ash and gas. At Stromboli, helicopter-borne thermal surveys made it possible to recognize the opening of fractures along Sciara del Fuoco 1 h before the large failure that caused severe destruction on the island on 30 December 2002. This was the

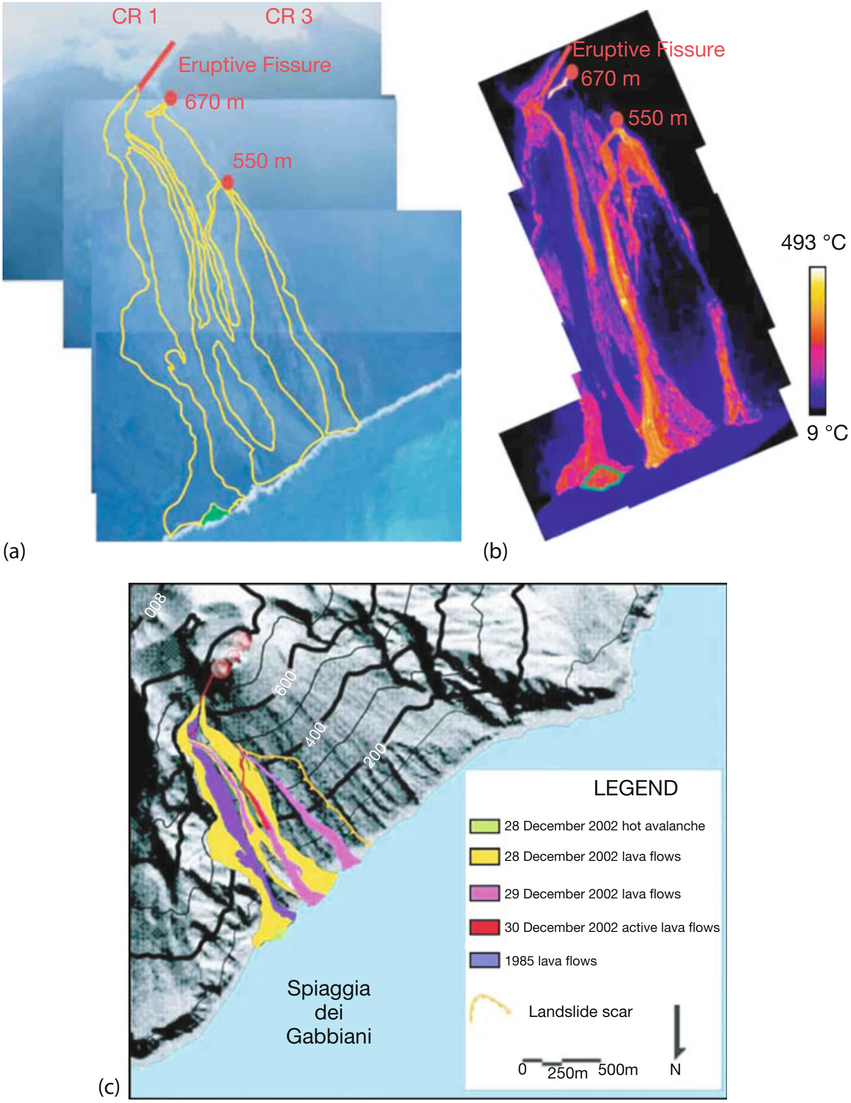

Figure 11.47 (a) Composite photo, (b) thermal image, and (c) map, view from the north, of the eastern half of Sciara del Fuoco, Stromboli volcano in southern Italy, showing the 28, 29, and 30 December 2002 lava flows, the 1985 lava flow, the hot avalanche on the Spiaggia dei Gabbiani beach, and part of the 30 December 2002 landslide scar. Images courtesy Sonia Calvari, Istituto Nazionale di Geofisica e Vulcanologia, Catania.

first time that a volcanic flank collapse had been monitored with a thermal camera. In addition, the exceptional explosive event of 5 April 2003 at Stromboli was observed from a helicopter with a thermal camera recording images immediately before, during, and after the huge explosion. As a consequence of these investiga-

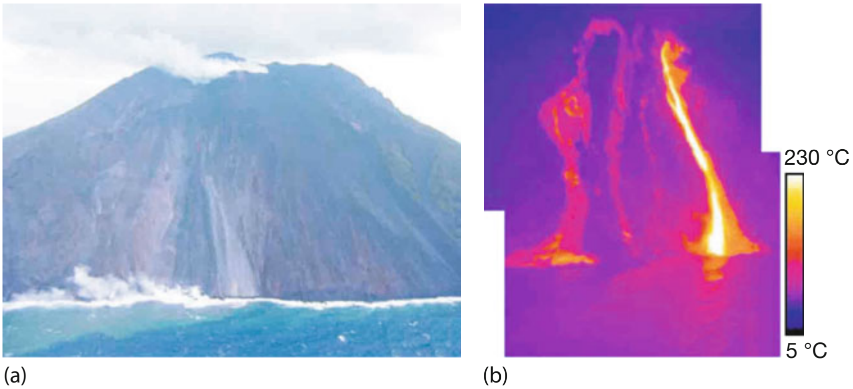

Figure 11.48 (a) View from north of Sciara del Fuoco (Stromboli volcano), showing the lava flow field erupted from the 500 m elevation vent. Thermal image (b) of active (yellow) and inactive (red-purple) single flow units entering the sea on 3 January 2003, one may easily detect thermal reflections from the water surface. Images courtesy Sonia Calvari, Istituto Nazionale di Geofisica e Vulcanologia, Catania.

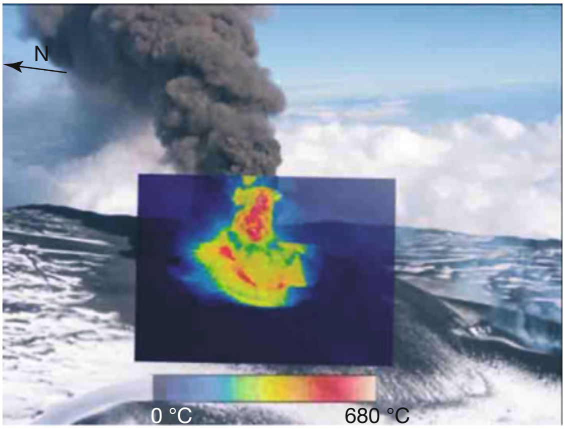

Figure 11.49 Explosive Strombolian activity and ash column detected by thermal and visible images. An example is shown of the 2750 m vent, with digital photos and overlaps of the corresponding thermal images of the 19 November 2002 transitional activity with the ash plume bent over close to the vent by the wind. Image courtesy Letizia Spampinato, Istituto Nazionale di Geofisica e Vulcanologia, Catania.

tions, it is argued that a more extended use of thermal cameras in volcano monitoring, on the ground, from fixed positions, from drones, and from helicopters, will significantly improve our understanding of volcanic phenomena and hazard evaluations during volcanic crises. It is expected that if thermal imaging is applied to the daily tracking of volcanic features, it will contribute significantly to volcano surveillance and hazard evaluation.

Figures 11.47 and 11.48 display some typical examples of thermal images from lava flows. Fresh lava flows at Mount Etna can have inside temperatures of up

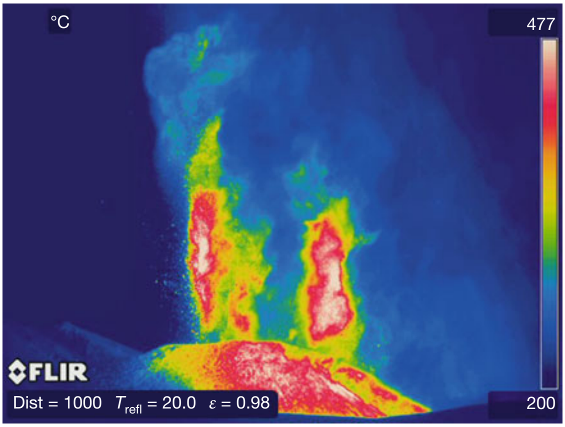

Figure 11.50 Lava fountain observed from a distance of about 1000 m through thick smoke during an eruption of the South East crater of Mount Etna on 12 August 2011. The lower-temperature blue shaded region resembles fine ash blown eastward by the wind. Camera: FLIR SC660 with 640 × 480 pixels. Image courtesy Sonia Calvari, Istituto Nazionale di Geofisica e Vulcanologia, Catania.

to 1085 °C [94] and outer surface temperatures of up to 900 °C (maximum temperatures at other volcanoes can be higher, as is, for example, the case in Hawaii). Figure 11.49 shows explosive Strombolian activity with an ash plume. Figure 11.50 shows similar activity with a lava fountain recorded during an August 2011 eruption of Mount Etna. The ash plumes are optically thick, but sometimes they allow one to estimate the maximum temperatures. For example, temperatures of about 900 °C were typically measured at distances of 250 m for Stromboli. However, for any quantitative analysis of volcanic features, one must take into account the special properties of the surroundings, for example, strong absorption due to SO_2 and aerosol absorption within the line of sight [92]; see also the spectrum of SO_2 in the appendix in Chapter 8.

Last but not least, the current development of powerful drones and other unmanned aerial vehicles has already led to the first applications in volcanology [95]. Owing to the reduced risk for observers, drone-based volcanic IR studies are expected to become more frequent in the future.

References

1 Diakides, M., Bronzino, J.D., and Peterson, D.R. (eds) (2013) *Medical Infrared Imaging, Principles and Practices*, CRC Press, Taylor and Francis, Bota Raton.

2 Ring, F., Jung, A., and Zuber, J. (eds) (2015) *Infrared Imaging, A casebook in clinical medicine*, IOP Publishing, Bristol.

3 Lahiri, B.B., Bagavathiappan, S., Jayakumar, T., and Philip, J. (2012) Medical applications of infrared thermography: A review. *Infrared Phys. Technol.*, **55**, 221–235.

4 Hildebrandt, C., Raschner, C., and Ammer, K. (2010) An overview of recent application of medical infrared thermography in sports medicine in Austria. *Sensors*, **10**, 4700–4715.

5 Jessen, C. (2003) in *Lehrbuch der Physiologie*, 4th edn (ed. S. Klinke), Thieme, Stuttgart.

6 Bennaroch, E. (2007) Thermoregulation: Recent concepts and remaining questions. *Neurology*, **69**, 1293–1297.

7 Uematsu, S. (1988) Quantification of thermal asymmetry. Part 1: normal values and reproducibility. *J. Neurosurg.*, **69** (4), 553–555.

8 Leroy, P. and Filasky, R. (1992) in *Evaluation and Treatment of Chronic Pain*, 2nd edn (ed. G. Aronoff), Williams and Wilkins, Baltimore, London, Hong Kong, Munich, pp. 202–212.

9 Cockburn, W. (2006) Common errors in medical thermal imaging. Inframation 2006, Proceedings, vol. 7, pp. 165–177

10 Agarwal, K., Lange, A.-Ch., and Beck, H. (2007) Thermal imaging in healthy humans, what is normal skin temperature? Inframation 2007, Proceedings, vol. 8, pp. 399–403.

11 Agarwal, K., Spyra, P.-S., and Beck, H. (2008) Monitoring treatment effects in Osteomyelitis with the aid of infrared thermography. Inframation 2008, Proceedings, vol. 9, pp. 1–6.

12 Agarwal, K., Spyra, P.-S., and Beck, H. (2007) Thermographic imaging for interventional pain management. Inframation 2007, Proceedings, vol. 8, pp. 391–394.

13 Agarwal, K., Spyra, P.-S., and Beck, H. (2007) Thermal imaging provides a closer look at stellate blocks in pain management. Inframation 2007, Proceedings, vol. 8, pp. 391–394.

14 Agarwal, K., Spyra, P.-S., and Beck, H. (2008) Monitoring effects of sympathicolysis with infrared-thermography in patients with complex regional pain syndromes (CRPS). Inframation 2008, Proceedings, vol. 9, pp. 7–10.

15 Agarwal-Kozlowski, K., Lange, A.C., and Beck, H. (2009) Contact free infrared thermography for assessing effects of acupuncture: A randomized single-blinded placebo-controlled cross-over clinical trial. *Anesthesiology*, **111** (3), 632–639.

16 Litscher, G. (2005) Infrared Thermography Fails to Visualize Stimulation-induced Meridian-like Structures, BioMedical Engineering, online http://www.biomedical-engineering-online.com/content/4/1/38 (accessed May 2017).

17 Ng, E.Y.-K. (2009) A review of thermography as promising non-invasive detection modality for breast tumor. *Int. J. Therm. Sci.*, **48**, 849–859.

18 Mostovoy, A. (2008) Breast thermography and clinical applications. Inframation 2008, Proceedings, vol. 9, pp. 303–307.

19 Mostovoy, A. (2009) Clinical applications of medical thermography. Inframation 2009, Proceedings, vol. 10, pp. 23–27.

20 Kennedy, D.A., Lee, T., and Seely, D. (2009) A comparative review of thermography as a breast cancer screening technique. *Integr. Cancer Ther.*, **8** (1), 9–16.

21 Cockburn, W. (2007) Functional thermography in diverse medical practice. Inframation 2007, Proceedings, vol. 8, pp. 215–224.

22 Bretz, P. and Lynch, R. (2007) Melding Three emerging technologies: pharmacogenomics, digital infrared and argon gas, to eliminate surgery, chemotherapy and radiation in diagnosing and treating

breast cancer. Inframation 2007, Proceedings, vol. 8, pp. 225–234.

23 Bretz, P., Lynch, R., and Dreisbach, P. (2009) Breast cancer in tough economic times – is there a new diagnostic and treatment paradigm? Inframation 2009, Proceedings, vol. 10, pp. 435–448.

24 Brioschi, M.L., Vargas, J.V., and Malafaia, O. (2004) Review of recent developments in thermographic applications in health care. Inframation 2004, Proceedings, vol. 5, pp. 9–17.

25 Brioschi, M.L., Silva, F.M.R.M., Matias, J.E.F., Dias, F.G., and Vargas, J.V.C. (2008) Infrared imaging for emergency medical services (EMS): Using an IR camera to identify life-threatening emergencies. Inframation 2008, Proceedings, vol. 9, pp. 549–560.

26 Brioschi, M.L., Sanches, I., and Traple, F. (2007) 3D MRI/IR imaging fusion: A new medically useful computer tool. Inframation 2007, Proceedings, vol. 8, pp. 235–243.

27 Wu, M., Stop outbreak of SARS with Infrared Cameras, (2004) Thermosense XXVI (2004), Proc. SPIE, vol. 5405, SPIE Press, Bellingham, pp. 98–105.

28 Tan, Y.H., Teo, C.W., Ong, E., Tan, L.B., Soo, M.J., Development and deployment of Infrared Fever Screening Systems, (2004) Thermosense XXVI (2004), Proc. SPIE, vol. 5405, SPIE Press, Bellingham, pp. 68–78.

29 Harper, D.L. (2000) The value of infrared thermography in the diagnosis and prognosis of injuries in animals. Inframation 2000, Proceedings, vol. 1, pp. 115–122.

30 Rekant, S.I., Lyons, M.A., Pacheco, J.M., Arzt, J., and Rodriguez, L.L. (2016) Veterinary applications of infrared thermography. *Am. J. Vet. Res.*, **77** (1), 98–107.

31 Hopkins, P. and Bader, D.R. (2009) Mammals communicate, infrared listens utilizing infrared imaging for injury identification. Inframation 2009, Proceedings, vol. 10, pp. 179–188

32 Lavers, C., Franks, K., Floyd, M., and Plowman, A. (2005) Application of remote thermal imaging and night vision technology to improve endangered wildlife resource management with minimal animal distress and hazard to humans. *J. Phys. Conf. Ser.*, **15**, 207–212.

33 Lavers, C., Franklin, P., Franklin, P., Plowman, A., Sayers, G., Bol, J., Shepard, D., and Fields, D. (2009) Nondestructive high-resolution thermal imaging techniques to evaluate wildlife and delicate biological samples. *J. Phys. Conf. Ser.*, **178**, 012040.

34 Cilulko, J., Janiszewski, P., Bogdaszewski, M., and Szczygielska, E. (2013) Infrared thermal imaging in studies of wild animals. *Eur. J. Wildl. Res.*, **59**, 17–23.

35 Chrétien, L.-P., Théau, J., and Ménard, P. (2015) Wildlife multispecies remote sensing using visible and thermal infrared imagery acquired from an unmanned aerial vehicle (UAV). *Int. Arch. Photogramm. Rem. Sens. Spatial Inf. Sci.*, **XL-1** (W4), 241–248.

36 Brawata, R.L., Raupach, T.H., and Neeman, T. (2013) Techniques for monitoring carnivore behavior using automatic thermal video. *Wildl. Soc. Bull.*, **37** (4), 862–871.

37 Reese, J. (2006) Applications of infrared imagery in the monitoring and diagnosis of zoo animals in anchorage, Alaska. Inframation 2006, Proceedings, vol. 7, pp. 145–150.

38 Church, J.S., Cook, N.J., and Schaefer, A.L. (2009) Recent applications of infrared thermography for animal welfare and veterinary research: Everything from chicks to elephants. Inframation 2009, Proceedings, vol. 10, pp. 215–224.

39 www.unitedinfrared.com, www.equineir.com (accessed May 2017).

40 West, M. (2007) The odd couple … the professor and the thermographer. Inframation 2007, Proceedings, vol. 8, pp. 281–289.

41 Allison, J.N. (2007) Infrared goes on safari. Inframation 2007, Proceedings, vol. 8, pp. 353–359.

42 Whitcher, A. (2006) Hunting seals with infrared. Inframation 2006, Proceedings, vol. 7, pp. 155–164.

43 Reese-Deyoe, J. (2008) Practical applications of infrared thermography in the rescue, recovery, rehabilitation and release of wildlife following external exposure to oil. Inframation 2008, Proceedings, vol. 9. pp. 389–402.

44 McCafferty, D.J. (2013) Applications of thermal imaging in avian science. *Ibis*, **155** (1), 4–15.

45 Schwahn, B. (2009) Infrared thermal imaging to prevent bat mortality at wind farms. Inframation 2009, Proceedings, vol. 10, pp. 385–392.

46 Rentoul, M. (2007) The practice of detecting termites with infrared thermal imaging compared to conventional techniques. Inframation 2007, Proceedings, vol. 8. pp. 15–19.

47 Bruni, B. (2004) Three ways the pest professional can use infrared thermography. Inframation 2004, Proceedings, vol. 5, pp. 109–119.

48 Ono, M., Igarashi, T., and Ohno, E. (1995) Unusual thermal defense by a honeybee against mass attack by hornets. *Nature*, **377**, 334–336.

49 Shaw, J.A., Nugent, P.W., Johnson, J., Bromenshenk, J.J., Henderson, C.B., and Debnam, S. (2001) Long-wave infrared imaging for non-invasive beehive population assessment. *Opt. Exp.* **19** (1), 399–408.

50 www.VisionHawkFilms.com (accessed May 2017).

51 www.CaseyAnderson.tv (accessed May 2017).

52 https://www.youtube.com/watch?v=zurTwzdtl0Y (accessed May 2017).

53 Vollmer, M. and Möllmann, K.-P. (2011) Exploding balloons, deformed balls, strange reflections, and breaking rods: Slow motion analysis of selected hands-on experiments. *Phys. Educ.*, **46** (4), 472–485.

54 Möllmann, K.-P. and Vollmer, M. (2007) Infrared thermal imaging as a tool in university physics education. *Eur. J. Phys.*, **28**, S37–S50.

55 Vollmer, M. (2013) Jenseits unserer Wahrnehmung. *Phys. J.*, **12** (8/9), 47–51.

56 Garza, D., Rolston, B., Johnston, T., Sungar, G., Ferguson, J., and Matheson, G. (2009) Heat-loss patterns in national football league players as measured by infrared thermography. Inframation 2009, Proceedings, vol. 9, pp. 541–547.

57 Hildebrandt, C., Raschner, C., and Ammer, K. (2010) An overview of recent application of medical infrared thermography in sports medicine in Austria. *Sensors*, **10**, 4700–4715.

58 Arfaoui, A., Polidori, G., Taiar, R., and Popa, C. (2012) Infrared thermography in sports activity, in *Infrared Themrograpohy*, (ed. R.V. Prakash), Published by InTech, pp. 141–168, www.intechopen.com (accessed May 2017).

59 Costello, J., Stewart, I.B., Selfe, J., Karki, A.I., and Donnelly, A. (2013) Use of thermal imaging in sports medicine research: A short report. *Int. Sport Med. J.*, **14** (2), 94–98.

60 Korman, P., Zielinski, J., Kusy, K., and Straburzynska-Lupa, A. (2016) Possible uses of infrared thermography in sport. *Trends Sport Sci.*, **2** (23), 57–62.

61 Quesada, P., and Ignacio, J. (eds) (2017) *Application of Infrared Thermography in Sports Science*, Springer Series Biol, Med. Phys., Biomed, Eng, Springer.

62 Vollmer, M. and Wogram, K. (2005) Zur Intonation von Blechblasinstrumenten bei sehr niedrigen Umgebungstemperaturen. *Instrumentenb. Z. Musik Int.*, **59** (3–4), 69–74.

63 Karstädt, D., Möllmann, K.P., Pinno, F., and Vollmer, M. (2001) There is more to see than eyes can detect: Visualization of energy transfer processes and the laws of radiation for physics education. *Phys. Teach.*, **39**, 371–376.

64 Podnar, M. and Bertsch, M.A. (2013) Infrared thermography as diagnostic tool for physiotherapeutic taping support of musicians, Proc. Int. Symp. Performance Sci., pp. 504–510.

65 Clemente, M., Coimbra, D., Silva, A., Gabriel, J., Aguiar Branco, C., and Pinho, J.C. (2015) Application of infrared thermal imaging in a violinist with temporomandibular disorder. *Med. Probl. Perf. Art.*, **30** (4), 251–254.

66 Coram Populo! – A Mystery, International Dance Theatre Production (2008), project proposal by Miloš Vujković, Arthouse Tacheles Berlin; contact: milosh@tacheles.de.

67 Vollmer, M., Vujković, M., Trellu, Y., and Möllmann, K.-P. (2009) IR feedback loops to spotlights: Thermography and contemporary dancing. Inframation 2009, Proceedings, vol. 10, pp. 89–97.

68 Dinwiddie, R.W. and Dean, S.W. (2006) Case study of IR reflectivity to detect and document the underdrawing of a 19th century oil painting. Proceedings of the Thermosense XXVIII, Proc. SPIE, vol. 6205, pp. 620510/1–12.

69 Grinzato, E. and Rosina, E. (2001) Infrared and thermal testing for conservation of historic buildings, in *Nondestructive Testing Handbook, Infrared and Thermal Testing*, vol. 3, 3rd edn, Chapter 18.5 (ed. P.O. Moore), American Society for Nondestructive Testing, Inc., Columbus, pp. 624–646.

70 Humphries, H.E. (2001) Infrared and thermal testing for conservation of fine art, in *Nondestructive Testing Handbook, Infrared and Thermal Testing*, vol. 3, 3rd edn, Chapter 18.6 (ed. P.O. Moore), American Society for Nondestructive Testing, Inc., Columbus, pp. 647–658.

71 Poksinska, M., Wiecek, B., and Wyrwa, A. (2008) Thermovision investigation of frescos in Cistercian monastery in Lad (Poland). Proc. 9th Int. Conf. Quantitative InfraRed Thermography in Krakow, QIRT 2008, pp. 653–658.

72 Poksinska, M., Cupa, A., and Socha-Bystron, S. (2008) Thermography in the investigation of gilding on historical wall paintings. Proc. 9th Int. Conf. Quantitative InfraRed Thermography in Krakow, Poland, QIRT 2008, pp. 647–652.

73 Magyar, M. (2006) Thermography applied to cultural heritage. Inframation 2006, Proceedings, vol. 7. pp. 325–332.

74 Richards, A. (2001) *Alien Vision*, SPIE Press, Bellingham.

75 Vollmer, M. and Gedzelman, S. (2006) Colors of the sun and moon: the role of the optical air mass. *Eur. J. Phys.*, **27**, 299–309.

76 Möllmann, K.-P., Pinno, F., and Vollmer, M. (2008) Night sky radiant cooling – influence on outdoor thermal imaging analysis. Inframation 2008, Proceedings, vol. 9, pp. 279–295.

77 Martin, M. and Berdahl, P. (1984) Characteristics of infrared sky radiation in the United States. *Solar Energy*, **33**, 321–336.

78 Shaw, J.A. and Nugent, P.W. (2013) Physics principles in radiometric infrared imaging of clouds in the atmosphere. *Eur. J. Phys.*, **34**, S111–S121.

79 Nugent, P.W. (2016) Deployment of the third-generation infrared cloud imager: A two-year study of arctic clouds at Barrow Alaska, PhD thesis, Montana State University Bozeman/MT, July 2016.

80 Simser, S. (2008) Utilization of thermal infrared technology on wildfires in Alberta. Inframation 2008, Proceedings, vol. 9, pp. 417–428.

81 http://fsapps.nwcg.gov/afm (accessed May 2017).

82 Vollmer, M., Möllmann, K.-P., and Pinno, F. (2010) Measurements of sun and moon with IR cameras: effect of air mass. Inframation 2010, Proceedings, vol. 11, 57–74

83 Shaw, J.A., Nugent, P.W., and Vollmer, M. (2015) Infrared moon imaging for remote sensing of atmospheric smoke layers. *Appl. Opt.*, **54** (4), B64–B75.

84 Vollmer, M., Shaw, J.A., and Nugent, P.W. (2015) Visible and invisible mirages: Comparing inferior mirages in the visible and thermal infrared. *Appl. Opt.*, **54** (4), B76–B84.

85 Nugent, P.W., Shaw, J.A., and Vollmer, M. (2015) Colors of thermal pools at Yellowstone National Park. *Appl. Opt.*, **54** (4), B128–B139.

86 Shaw, J.A., Nugent, P.W., and Vollmer, M. 2015 Colors of the Yellowstone Thermal Pools for Teaching Optics, Education and Training in Optics and Photonics (ETOP) 2015, (eds E. Cormier and L. Sarger), Proc. SPIE, vol. 9793, 97931S.

87 Shaw, J.A., Nugent, P.W., Harris, W., and Vollmer, M. (2017) Yellowstone in infrared. *Opt. Photon. News*, **28** (6), 36–43.

88 Birnie, R.W. (1973) Infrared radiation thermometry of Guatemalan volcanoes. *Bull. Volcanol.*, **37**, 1–36.

89 Calvari, S., Lodato, L., and Spampinato, L. (2004) Proceedings of the Thermosense XXVI (2004), Proc. SPIE, vol. 5405, SPIE Press, Bellingham, pp. 199–203.

90 Calvari, S., Spampinato, L., Lodato, L., Harris, A.J.L., Patrick, M.R., Dehn, J., Burton, M.R., and Andronico, D. (2005) Chronology and complex volcanic processes during the 2002–2003 flank eruption at Stromboli volcano (Italy) reconstructed from direct observations and surveys with a handheld thermal camera. *J. Geophys. Res.*, **110**, B02201, doi: 10.1029/2004JB003129.

91 Calvari, S., Spampinato, L., and Lodato, L. (2006) The 5 April 2003 vulcanian paroxysmal explosion at Stromboli volcano (Italy) from field observations and thermal data. *J. Volcanol. Geotherm. Res.*, **149**, 160–175.

92 Sawyer, G.M. and Burton, M.R. (2006) Effects of a volcanic plume on thermal imaging data. *Geophys. Res. Lett.*, **33**, L14311.

93 Spampinato, L., Calvari, S., Oppenheimer, C., and Lodato, L. (2008) Shallow magma transport for the 2002–2003 Mt. Etna eruption inferred from thermal infrared surveys. *J. Volcanol. Geotherm. Res.*, **177**, 301–312.

94 Calvari, S., Coltelli, M., Neri, M., Pompilio, M., and Scribano, V. (1994) The 1991–1993 Etna eruption: Chronology and lava flow-field evolution. *Acta Vulcanolo.*, **4**, 1–14.

95 Amici, S., Turci, M., Giulietti, F., Giammanco, S., Buongiorno, M.F., La Spina, A., and Spampinato, L. (2013) Volcanic environments monitoring by drones – mud volcanic case study. *Int. Arch. Photogramm. Rem. Sens. Spatial Inform. Sci.*, **XL-1** (W2), 5–10.

Index

a
active thermal imaging 327
– lock-in thermography 337
– nondestructive testing of composites 340
– pulse thermography 333
– pulsed phase thermography 345
– solar cell inspection 343
– thermal waves 330
adiabatic processes 417
air mass 744
airplanes 676
ambient temperature 143
animals 721
– bees 727
– grizzly bear 729
– humming bird 726
– pets 722
– zoo animals 723
antireflection coatings 65
arts 735
– contemporary dance 737
– musical instruments 735
– paintings 740
atmospheric emission 143, 742
atmospheric temperature 143
atmospheric transmission 53, 143, 691, 742
attenuation/transmission of IR radiation 50
– absorbing slabs 55
– nonabsorbing slabs 54
automobile industry 670
– heating systems 671
– Night Vision in 672
autoshutter 183

b
Background Noise Limited Detection 120
background reflections 155
bad pixels 186
Biot number 361
blackbody calibration standards 45
blackbody radiation 21
– band emission 26
– Planck's law 22
– Stefan–Boltzmann Law 26
– Wien's displacement law 24
blower-door test 541
bolometer 137, 632, *see also* detectors, thermal detector
Bouguer's law 572
Brewster angle 14
buildings 477
– blower-door test 541
– carport 529, 531
– energy standards 488
– external influences 486, 507
– floor heating system 498
– general rules 486
– half-timbered houses 490
– image representation 479
– inside thermal insulation 497
– moisture 509
– optically induced thermal effects 539
– quantitative analysis 549
– radiative cooling 528
– relevance of defects 494
– shadows 518
– solar load 519
– solar reflections 520
– structural defects 504
– thermal bridges 500
– TSR paints 552
– view factor effects 525, 533
– wind 507
– windows 534

Infrared Thermal Imaging, Second Edition. M. Vollmer and K.-P. Möllmann.
© 2018 WILEY-VCH Verlag GmbH & Co. KGaA. Published 2018 by WILEY-VCH Verlag GmbH & Co. KGaA.

c

calibration of IR camera 200
camera software 208
– color palette 204, 208, 480
– level 204, 208
– level and span 480
– span 204, 208
camera system performance 209
– NETD 210
– spatial resolution (IFOV, SRF) 213, 658
– temperature accuracy 209
– temperature resolution 210
– time resolution 221
camera systems 173
– comparison 186
carbon capture and storage (CCS) 594
cavity blackbodies 47, 437
chromatic aberrations 191
close-up lens 616
clouds 742
CO_2 imaging 594
condition monitoring 645
– polymer molding 651
– power plants 647
– tank levels 649
conduction *see* heat transfer
convection *see* heat transfer
convection experiments 410
– Bénard–Marangoni 412
– water 412
Cooling, Newton's law 383, *see also* detectors

d

D* *see* detectors, performance parameters
detector noise
– Johnson-Nyquist noise 113
– short noise 119
– temperature fluctuation noise 113
detectors 107
– (HOT) detectors 132
– bariode 136
– cooling 123, 188
– dual-band FPA 140
– performance parameters 108
– photon detectors 117, 125
– temperature stabilization 117, 188
– thermal detector 111
– type II strained layer superlattice (T2SLS) detectors 137
dew point 372
diffuse reflections 272
diffusivity *see* thermal diffusivity
digital detail enhancement (DDE) *see* image processing
dispersion 11
drone *see* remote sensing
dynamic range 204, 265, 266

e

eddy currents 426
electrical equipement *see* high voltage applications, low voltage applications
electromagnetic waves 6
– polarization 7
– specta 8
emissivity 31
– angular dependence 35, 440
– blackbody calibration standards 45, 437
– change with temperature 42
– change with wavelength 41
– classification 32
– definitions 31
– gray body 32
– Kirchhoff's law 32
– Leslie cube 36
– measurement 44
– parameters 34
– selective emitters 32, 61
– uncertainties 158
evaporative cooling 414, 510
experiments
– heating and cooling 379, 389
– optical material properties 433
– selective emitters 443
– thermal conductivity 407, 410
– thermal reflections 436
– visualization for teaching 393
extender rings 195, 616

f

field of view (FOV) 108, 192
filters 229
focal-plane arrays (FPA) 114, 176
frame rate 175, 221
Fresnel equations 12
friction 394, 395
– bicycle 396
– cars 397, 403
– motorcycle 397
– weights 394
FTIR spectroscopy 258
furnace tubes 669

g
gas sensors 635
gases 443, 561
– absorption 567, 597
– broadband vs. narrowband 569
– calibration curves 577
– CO_2 564, 571
– compilation of spectra 564, 603
– emission 567, 580, 597
– exhaust gases 599
– GasFind cameras 588
– H_2O 564
– hydrocarbons 565
– inorganic compounds 591
– measurement conditions 578
– measurements 588
– molecular spectra 561
– organic compounds (VOCs) 588
– quantitative analysis 572
– scattering 567, 597
– SF_6 593
– spectrally resolved imaging 582
– theory 561
gasoline 592
geometrical optics 10
– laws of reflection and refraction 11
geysers 754
gray body 32

h
heat capacity 374
heat diffusion equation 375
heat transfer
– 1-dim. wall 364
– analogy thermal/electrical circuits 365
– conduction 352
– convection 355, 507
– radiation 356
– relative contributions of radiation and convection 385
– windows 369
heating system 407, 498
hidden structures
– half-timbered houses 490
– paint 740
high speed imaging/recording 268, 618
high voltage applications 656
– fan defects 660
– HV bushings 660
– HV lines 659
– substation transformers 657
history of IR science 69
history of IR technology 76
hot springs 754
humidity air 372
hyperspectral imaging *see* multi- and hyperspectral imaging

i
IFOV *see* camera system performance
image formation 173
– bad pixel correction 186
– fill factor 180
– NUC 180
– pixel number 178
image processing 285
– advanced methods 309
– contrast and digital detail enhancement 300
– deblurring of infrared images 321
– feature extraction 316
– geometrical transformations 313
– high-sensitivity mode (HSM) 296
– image building 289
– image fusion 287
– image subtraction 290, 543
– noise reduction 311
– pattern recognition 319
– segmentation 314
– spatial derivatives 296
– time derivatives 293
image quality 216
inelastic collisions 398, 401
integration time 221
IR cameras 3
– parameters 4
– signal contributions 142
ir reflectography 461
IR spectral regions 10

k
Kirchhoff's law 32

l
latent heats 357
Leslie cube 36, 439
line scanning 174, 694
– principle 175
– windshields 695
lock-in thermography *see* active thermal imaging
low voltage applications 653
– electric boards 655
– microelectronic boards 654
– simple circuits 424

m
measurement process 142
measurements 443
medical applications 709
– acupuncture 716
– breast thermography 718
– pain management 712
– pressure ulcers 720
– Raynaud's phenomenon 719
– standard conditions 710
metal industry 662
– Al strips 663
– black emitter method 667
– gold cup method 666
– hot molds 662
microscope objectives 616
microsystems 615
– cryogenic actuators 640
– measurement requirements 616
– micro heat exchangers 626
– microelectromechanical systems (mems) 615
– microreactors 619
– miniaturized IR emitters 637
– Peltier elements 639
– thermal IR sensors 628
microwave ovens 429
mirages 752
moisture detection 470
moon 749
MTF, MRTD and MDTD *see* image quality
multi- and hyperspectral imaging 256
music *see* arts

n
narcissus effect 196
nature *see* clouds, geysers, mirages, moon, sky, sun, volcanology
NEP *see* detectors, performance parameters
NETD 210, *see also* detectors, performance parameters; camera system performance
Newton's law of cooling 383
NonUniformity Correction (NUC) *see* image formation

o
optical components IR camera 191
optical materials properties 49
– antireflection coatings 65
– atmospheric transmission 53
– thin film coatings 62
– transmission spectra of materials 56
– water 452

p
paintings *see* arts
Peltier element 188, 639
petrochemical industry 588, 648
photo diodes *see* detectors, photon detectors
photoelectrical effect 117
photon detectors *see* detectors
photonconductors *see* detectors, photon detectors
pixel number *see* image formation
Planck's law 22
polarization 271
– Brewster angle 277
– imaging polarimetry 284
– thermal reflections 272
predictive maintenance 645
PtSi 128
pulse thermography *see* active thermal imaging

q
QWIP *see* detectors, photon detectors

r
rack storage fire testing 652
radiation transfer 20, 356
radiative cooling *see* buildings
radiometric chain 142
radiometry 14
– excitance 15
– irradiance 15
– Lambertian emitters 17
– Lambertian radiators 35
– radiance 17
– radiant intensity 17
– radiant power 15
– radiation transfer 20
– spectral radiometric quantities 15
– view factor 20
range of IR cameras 688
ratio thermography 236, *see also* two color thermography
Rayleight-Jeans approximation 240
reflection, specular and diffuse 12, 435
reflectography 740
remote sensing 695
– drone applications 699
– platforms 696
R-value *see* U-value

s
selective emitters 32, 61
– plastic experiments 684
– plastic spectra 683

Signal-Noise-Limited Detection 119
sky 742
software tools 208
solar cell inspections 343
solar constant 30, 76
solar power plants 699
solar spectrum 449
solid angle 16
Space shuttle 678
– reentry 681
– STS 135 682
specific heat 374
– heat capacity 374
spectral filters 66, 199, 230
specular reflections 272
sports 729
– american football 734
– squash 732
– tennis 398, 729
– volleyball 732
Stefan–Boltzmann Law 26
Stirling cooler 190
sun 749
superframing 265
surveillance and security 687
SW imaging 447
– application areas 451
– cameras 452
– commercial systems 473
– contrast enhancement 458
– differences to VIS, MW and LWIR 447
– high-temperature measurement 454
– liquids 452, 467
– plastics 460
– vegetation 456
switch-on behavior 205

t
teaching physics 393
– electromagnetism 424
– mechanics 394
– optics/radiation physics 432
– thermal physics 406
temperature accuracy 209
temperature contrast 151
temperature resolution 210
temperature scales 6
thermal bridges 370, 500
thermal conductivity 353
thermal diffusivity 374
thermal mismatch 331, *see also* active thermal imaging, thermal waves
thermal penetration depth 332, *see also* active thermal imaging, thermal waves
thermal reflections 155, 272
– Fresnel equation 273
– identification and suppression 281
– measurements 280, 664
thermal shock behavior 206
thermal time constants 377, 382, 516
thermoelectricity 427
– Peltier effect 428, 630
– Seebeck effect 629
time resolution 221
transient effects
– modeling 379, 513
transient heating/cooling 373
– cheese cubes 418
two color thermography 236
– application 248
– comparison to single bond method 247

u
U-value 364, 495, 549

v
veterinary applications 721
– equine thermography 725
– zoo animals 723
view factor 20, 525
volcanology 756

w
Wavebands 146
Wien approximation 241
Wien's displacement law 24
wildfires 746
windows 534